Golio, Mike "Frontmatter"
The RF and Microwave Handbook
Editor in Chief Mike Golio
Boca Raton: CRC Press LLC,2001

Library of Congress Cataloging-in-Publication Data

The RF and microwave handbook / editor-in-chief, Mike Golio.
p. cm.—(The electrical engineering handbook series)
Includes bibliographical references and index.
ISBN 0-8493-8592-X (alk. paper)
1. Microwave circuits. 2.Radio circuits. 3. Wireless communication systems. I. Golio, John Michael, 1954- II. Series.

TK7876 .R493 2000
621.381′32—dc21 00-052885

This book contains information obtained from authentic and highly regarded sources. Reprinted material is quoted with permission, and sources are indicated. A wide variety of references are listed. Reasonable efforts have been made to publish reliable data and information, but the author and the publisher cannot assume responsibility for the validity of all materials or for the consequences of their use.

Direct all inquiries to CRC Press LLC, 2000 N.W. Corporate Blvd., Boca Raton, Florida 33431.

Trademark Notice: Product or corporate names may be trademarks or registered trademarks, and are used only for identification and explanation, without intent to infringe.

No claim to original U.S. Government works
International Standard Book Number 0-8493-8592-X
Library of Congress Card Number 00-052885
Printed in the United States of America 1 2 3 4 5 6 7 8 9 0
Printed on acid-free paper

Preface

The field of microwave engineering has undergone a radical transformation in recent years as the Defense and Government work effort that once dominated the industry is now exceeded by commercial wireless efforts. The explosive growth of commercial wireless markets has not only altered the Defense/non-Defense work balance, but also brought about significant shifts in the perspective and focus of working microwave and RF engineers. Engineering emphasis has changed from optimum performance design to design for manufacturing, from one-of-a-kind parts to high volume production, from performance at all cost to minimum cost with acceptable performance, from widest possible bandwidth to regulated narrow band, etc. Even engineers and researchers working in the traditional high performance, low volume microwave markets have seen a shift in emphasis of their work as every effort is made to reduce cost through the re-use of commercial-off-the-shelf (COTS) parts. Although the physics and mathematics of microwave and RF engineering is the same, the job of the typical microwave engineer has changed dramatically. The modern microwave and RF engineer is expected to be knowledgeable of customer expectations, market trends, manufacturing technologies, and factory models to a degree that is unprecedented in the history of RF/microwave engineering. Unfortunately, the 40+ years of close association of the microwave industry solely with Defense/Government agencies has left a legacy of microwave literature that is narrowly focused on high performance, low volume applications and is deficient in many areas of critical importance today. This handbook comes at a time when there is an emerging interest in a broader range of microwave material with more balance than that which has been previously available.

The purpose of *The RF and Microwave Handbook* is to provide a single-volume comprehensive reference for modern microwave and RF engineers. The articles that comprise the handbook provide important information for practicing engineers in industry, government, and academia. The intended audience also includes microwave and other electrical engineers requiring information outside of their area of expertise as well as managers, marketers, and technical support workers who need better understanding of the fields driving and affected by their decisions.

The book is organized into nine chapters, with all but the first chapter consisting of several articles on related topics. The first chapter consists of a single introductory article that provides important definitions and spectral information. Two appendices containing useful information for practicing microwave engineers are also included. By design, there is some overlap of information presented in some of the chapters. This allows the reader to investigate a topic without needing to make numerous references to other portions of the handbook. A complete table of contents is presented at the front of the book to provide the reader with a means of locating desired information as easily and rapidly as possible. Finally, all of the articles provide the reader with additional references to related expert literature.

Acknowledgments

Developing a handbook like this one is a big job — much bigger than I originally anticipated. This handbook would simply never have been completed if it were not for the efforts of the managing editor, Janet Golio. Her focus, persistence, software expertise, and organizational skills were essential to the project. Her efforts can be measured in the nearly 10,000 pieces of email correspondence she handled, the 100+ telephone conversations she initiated, or the tracking of approximately 80 articles from initial contact to commitment to receipt to review through final modification and submission. Yet all of these metrics combined do not completely capture the full magnitude of her contribution to this handbook. I cannot offer enough gratitude to compensate for the many long evenings she spent on this project.

I am also significantly indebted to the Handbook Editorial Board. This Board contributed to every phase of the handbook development. Their efforts are reflected in the organization and outline of the material, selection and recruitment of authors, article contributions, and review of the articles. Their labors were essential to the project and I am happy to acknowledge their help.

And, of course, I must thank the handbook professionals at CRC Press. Richard Dorf, Editor for the CRC Electrical Engineering Handbook series, and Ron Powers, President of Book Publishing, were instrumental in getting this project started. Special thanks is extended to Nora Konopka, Acquisitions Editor, who has worked most closely with the project during article development and has been more patient and encouraging than I deserve. Finally, Helena Redshaw, Production Manager, has taken the stacks of manuscripts, disks and CDs, identified and added the missing bits and pieces, and turned them into a book. Thanks also to all the CRC staff that I have not had the pleasure to work closely with, but who have contributed to this effort.

Editor-in-Chief

Mike Golio received his B.S.E.E. degree from the University of Illinois in 1976. He worked designing microwave oscillators and amplifiers for electronic counter-measure applications for two years before returning to school to complete his M.S.E.E. and Ph.D. degrees at North Carolina State University in 1980 and 1983, respectively. After graduate school, he worked as an Assistant Professor of Electrical Engineering before returning to industry. He spent five years developing MMIC circuits, tools, and techniques for microwave satellite applications prior to participating in the establishment of a GaAs fabrication facility. The GaAs facility was constructed to manufacture devices and circuits to serve commercial wireless markets — including cellular telephone, pager, and wireless LAN businesses. His role shifted from individual technical contributor to Group Manager during this time. He is currently the Director of the Rockwell Collins RF/Power Design Center tasked with identifying, acquiring, developing, and implementing emerging RF and power conversion technologies. The Center provides design expertise in the radio frequency (RF), microwave, and millimeter wave domain. This includes receivers, transmitters, antennas, frequency control circuitry, and power supplies for commercial and military avionics applications.

Dr. Golio's research has resulted in 15 patents and over 200 professional presentations and publications. His technical publications include four book chapters, one book, and one software package. He was selected to serve as the IEEE Microwave Theory and Techniques-Society (MTT-S) Distinguished Microwave Lecturer from 1998 to 2000. He is currently co-editor of the I*EEE Microwave Magazine,* to which he contributes a regular column. He serves as a member of the MTT-S Administrative Committee, has organized several professional workshops and panel sessions, and served as a member of the Technical Program Committee for several professional conferences. He was elected Fellow of the IEEE in 1996.

Managing Editor

Janet R. Golio received her B. S. in Electrical Engineering Summa Cum Laude from North Carolina State University in 1984. Prior to that she was employed by IBM. Between 1984 and 1996 she worked at Motorola in Arizona. Since 1996, she has been at Rockwell Collins in Cedar Rapids, IA. She holds one patent and has written four technical papers. When not working, she actively pursues her interests in archaeology, trick roping, and country western dancing. She is also the author of young adult books, *A Present From the Past* and *A Puzzle From the Past.*

Advisory Board

Peter A. Blakey obtained a B.A. in Physics from the University of Oxford in 1972, a Ph.D. in Electronic Engineering from University College London in 1976, and an MBA from the University of Michigan in 1989. Between 1972 and 1983 he worked on the theory and simulation of microwave semiconductor devices and circuits, with an emphasis on the impact of non-local transport phenomena. Between 1983 and 1995 he worked on the development, application, and commercialization of technology CAD software for silicon VLSI applications. Since 1995, he has been the manager of Predictive Engineering in the GaAs Technology Department at Motorola.

Lawrence P. Dunleavy received the B.S.E.E. degree from Michigan Technological University in 1982, and the M.S.E.E. and Ph.D. degrees in 1984 and 1988, respectively, from the University of Michigan. He has worked in industry for E-Systems and Hughes Aircraft Company and was a Howard Hughes Doctoral Fellow. In 1990 he joined the Electrical Engineering Department at the University of South Florida, where he now holds the title of Associate Professor. From August 1997 to to August 1998 he enjoyed a 1-year sabbatical research appointment with the Microwave Metrology Group of the National Institute of Standards and Technology (NIST) in Boulder, CO. His current research interests are in the area of accurate microwave and millimeter-wave measurements, measurement-based active and passive component modeling, MMIC design, and wireless systems characterization and CAD. Dr. Dunleavy is a Senior Member of IEEE, is very active in the IEEE MTT Society, and has been an ARFTG member since 1986.

Dr. Dunleavy has served as local host and technical program chair for ARFTG, as MTT/ARFTG liaison, and as conference chair for various conferences. He has also served ARFTG as the Short Course Coordinator from 1995 to 1998, as Director from 1998 to present, as Chair of the Education Committee from 1997 to present, and as a member of the Executive Committee from 1998 to present.

Jack East received his B.S.E., M.S., and Ph.D. degrees from the University of Michigan. He is presently with the Solid State Electronics Laboratory at the University of Michigan conducting research in the areas of high speed microwave device design, fabrication, and experimental characterization of solid state microwave devices, nonlinear device and circuit modeling for communications circuits and low energy electronics, and THz technology.

Patrick J. Fay is an Assistant Professor in the Department of Electrical Engineering at the University of Notre Dame. Dr. Fay received the B.S. degree in electrical engineering from the University of Notre Dame in 1991, and the M.S. and Ph.D. degrees in electrical engineering from the University of Illinois at Urbana-Champaign in 1993 and 1996, respectively. From 1992 to 1994, he was a National Science Foundation Graduate Research Fellow. After graduation, Dr. Fay served as a visiting assistant professor in the Department of Electrical and Computer Engineering at the University of Illinois at Urbana-Champaign in 1996 and 1997.

Dr. Fay joined the University of Notre Dame as an assistant professor in 1997. His educational activities have included the development of an advanced undergraduate laboratory course in microwave circuit design and characterization, and graduate courses in optoelectronic devices and electronic device characterization. His research interests include the design, fabrication, and characterization of microwave and high-speed optoelectronic devices and circuits for ultra-fast analog and digital signal processing, wireless communications, and fiber optic telecommunications. His research also includes the development and use of micromachining techniques for the fabrication of active and passive microwave components.

Dr. Fay is a member of the IEEE Microwave Theory and Techniques Society, the Solid-State Circuits Society, and the Electron Device Society. He was awarded the Department of Electrical Engineering's IEEE Outstanding Teacher Award in 1998–1999, and has served as a consultant for the Division of Electrical and Communications Systems at the National Science Foundation.

David Halchin received the Ph.D. degree in electrical engineering from North Carolina State University in 1987. From 1987 to 1989 he was an Assistant Professor in the ECE Department of Santa Clara University in Santa Clara, CA. His main interests in teaching and research were device modeling and microwave design. From 1989 until 1996 he was with Motorola Corporate Research and SPS in Phoenix, AZ. While at Motorola, he worked on a wide variety of projects. These included microwave and millimeter wave characterization of MESFETs and PHEMTs, modeling of PHEMTs and MESFETs, load pull measurements, device (MESFETs and PHEMTs) engineering and process development. From 1996 until 1997 he worked for Rockwell International in Newbury Park, CA as the head of a team tasked to develop and implement into production a linear MESFET and PHEMT for wireless PA applications. He rejoined Motorola SPS in 1997 for 1 year and again worked with the PHEMT/MESFET device development team in Phoenix. In 1998 he joined RF Micro Devices in Greensboro, NC working as a PA designer and a group leader in the area of WCDMA applications. He is a member of the Technical Program Committee for the GaAs IC Symposium, a reviewer for Transactions on Electron Devices and a member of the Editorial Board for Microwave Theory and Techniques and an IEEE member. He has 3 issued U.S. patents and several pending.

Roger B. Marks received his B.A. in Physics in 1980 from Princeton University and his Ph.D. in Applied Physics in 1988 from Yale University. Following a postdoctoral appointment at the Delft University of Technology (The Netherlands), he began a professional career with U.S. Commerce Department's National Institute of Standards and Technology (NIST) in Boulder, CO.

In 1998, Dr. Marks initiated an effort to standardize fixed broadband wireless access within the IEEE 802 LAN/MAN Standards Committee. This effort led to creation, in March 2000, of the IEEE 802.16 Working Group on Broadband Wireless Access. With Dr. Marks as Chair, 802.16 has grown to include three projects and hundreds of participants from over 100 companies.

A Fellow of the IEEE and the author of over 70 journal and conference publications, Dr. Marks has received many awards, including an IEEE Technical Field Award (the 1995 Morris E. Leeds Award). He has served in numerous professional capacities. In the IEEE Microwave Theory and Techniques Society, he served on the Adminstrative Committee and as Distinguished Microwave Lecturer. He developed the IEEE Radio and Wireless Conference (RAWCON) and chaired it from 1996 through 1999. He served as Vice Chair of the 1997 IEEE MTT-S International Microwave Symposium.

Dr. Marks lives in Denver, CO with his wife, Robbie Bravman Marks, and their children, Dan and Amy. His drumming can be heard on the RAWCON theme song and in a recording by the band Los Lantzmun.

Alfy Riddle operates Macallan Consulting, which specializes in solving RF and microwave circuit design problems as well as selling Mathematica-based design software. Dr. Riddle also teaches a course in electronic noise at Santa Clara University. He received his Ph.D. from North Carolina State University in 1986 for work on oscillator noise. After spending several years employed in the electronics industry, he began Macallan Consulting in 1989. When he is not working, he can be found on the tennis courts, hiking in the Sierras, taking pictures with an old Leica M3, or making and playing Irish whistles.

Robert J. Trew serves as Director of Research for Department of Defense (DoD). He has management oversight responsibility for the $1.2 billion yearly basic research programs of the Military Services and Defense Agencies. Dr. Trew has extensive experience in industry, academia, and government. He received the Ph.D. degree in electrical engineering from the University of Michigan in 1975. His industrial experience includes employment at General Motors Corp. in Michigan and Watkins-Johnson Company in California. In addition to his present DoD assignment, he worked for the U.S. Army Research Office as a program manager for five years. Dr. Trew was on the faculty of North Carolina State University where he served as Professor of Electrical and Computer Engineering from 1976 to 1993. From 1993 to 1997 he was George S. Dively Professor of Engineering and Chair of the Department of Electrical Engineering and Applied Physics at Case Western Reserve University. He was a Visiting Professor at the University of Duisburg in Germany in 1985. Dr. Trew is a Fellow of the IEEE and serves on the Microwave Theory and Techniques Society ADCOM. He is currently serving as Chair of the Publications Committee and was the Editor-in-Chief of the *IEEE Transactions on Microwave Theory and Techniques* from 1995 to 1997. He is currently co-editor of the new *IEEE Microwave Magazine*. Dr. Trew was the recipient of the 1998 IEEE MTT Society Distinguished Educator Award. He received the 1992 Alcoa Foundation Distinguished Engineering Research Award and a 1991 Distinguished Scholarly Achievement Award from NCSU. He was a recipient of an IEEE Third Millennium Medal award, and is currently an IEEE Microwave Distinguished Lecturer. Dr. Trew has 3 patents and has published more than 140 technical articles, 13 book chapters, and given over 250 scientific and technical presentations.

Contributors

David Anderson
Maury Microwave Corporation
Ontario, Canada

Carl Andren
Intersil
Palm Bay, Florida

Saf Asghar
Advanced Micro Devices, Inc.
Austin, Texas

Avram Bar-Cohen
University of Minnesota
Minneapolis, Minnesota

James L. Bartlett
Rockwell Collins
Cedar Rapids, Iowa

Melvin L. Belcher, Jr.
Georgia Tech
Smyrna, Georgia

Peter A. Blakey
Motorola
Tempe, Arizona

Mark Bloom
Motorola
Tempe, Arizona

Nicholas E. Buris
Motorola
Schaumburg, Illinois

Prashant Chavarkar
CREE Lighting Company
Goleta, California

John C. Cowles
Analog Devices–Northwest Laboratories
Beaverton, Oregon

Walter R. Curtice
W.R. Curtice Consulting
Princeton Junction, New Jersey

W.R. Deal
Malibu Networks, Inc.
Calabasas, California

Lawrence P. Dunleavy
University of South Florida
Tampa, Florida

Jack East
University of Michigan
Ann Arbor, Michigan

Stuart D. Edwards
Conway Stuart Medical Inc.
Sunnyvale, California

K.F. Etzold
IBM Thomas J. Watson Research Center
Yorktown Heights, New York

Leland M. Farrer
Cadence Design Systems, Inc.
Sunnyvale, California

John Fakatselis
Intersil
Palm Bay, Florida

Patrick Fay
University of Notre Dame
Notre Dame, Indiana

S. Jerry Fiedziuszko
Space Systems/LORAL
Palo Alto, California

Paul G. Flikkema
Northern Arizona University
Flagstaff, Arizona

Karl J. Geisler
University of Minnesota
Minneapolis, Minnesota

Ian C. Gifford
M/A-COM, Inc.
Lowell, Massachusetts

Mike Golio
Rockwell Collins
Cedar Rapids, Iowa

Madhu S. Gupta
San Diego State University
San Diego, California

Ramesh K. Gupta
COMSTAT Laboratories
Clarksburg, Maryland

R.E. Ham
Consulting Engineer
Austin, Texas

Mike Harris
Georgia Tech Research Institute
Atlanta, Georgia

Robert D. Hayes
RDH Incorporated
Marietta, Georgia

T. Itoh
University of California
Los Angeles, California

Daniel E. Jenkins
Dell Computer Corp.
Austin, Texas

Nils V. Jespersen
Lockheed Martin Space Electronics and Communications
Reston, Virginia

Christopher Jones
M/A-COM TycoElectronics
Lowell, Massachusetts

J. Stevenson Kenney
Georgia Institute of Technology
Atlanta, Georgia

Ron Kielmeyer
Motorola
Scottsdale, Arizona

Allan D. Kraus
Allan D. Kraus Associates
Beachwood, Ohio

Andy D. Kucar
4U Communications Research, Inc.
Ottawa, Ontario, Canada

Jakub Kucera
Infineon Technologies
Munich, Germany

Jean-Pierre Lanteri
M/A-COM TycoElectronics
Lowell, Massachusetts

Michael Lightner
University of Colorado
Boulder, Colorado

William Liu
Texas Instruments
Dallas, Texas

Urs Lott
Acter AG
Zurich, Switzerland

Leonard MacEachern
Carleton University
Ottawa, Ontario, Canada

John R. Mahon
M/A-COM TycoElectronics
Lowell, Massachusetts

Michael E. Majerus
Motorola
Tempe, Arizona

Donald C. Malocha
University of Central Florida
Orlando, Florida

Tajinder Manku
University of Waterloo
Waterloo, Ontario, Canada

Brent A. McDonald
Dell Computer Corp.
Austin, Texas

Umesh K. Mishra
University of California
Santa Barbara, California

Karen E. Moore
Motorola
Tempe, Arizona

Charles Nelson
California State University
Sacramento, California

Josh T. Nessmith
Georgia Tech
Smyrna, Georgia

Robert Newgard
Rockwell Collins
Cedar Rapids, Iowa

John M. Osepchuk
Full Spectrum Consulting
Concord, Massachusetts

Anthony E. Parker
Macquarie University
Sydney, Australia

Anthony M. Pavio
Motorola
Tempe, Arizona

Jeanne S. Pavio
Motorola
Phoenix, Arizona

Jim Paviol
Intersil
Palm Bay, Florida

Michael Pecht
University of Maryland
College Park, Maryland

Benjamin B. Peterson
U.S. Coast Guard Academy
New London, Connecticut

Ronald C. Petersen
Lucent Technologies Inc./Bell Labs
Murray Hill, New Jersey

Brian Petry
3Com Corporation
San Diego, California

Y. Qian
University of California
Los Angeles, California

Vesna Radisic
HRL Laboratories, LLC
Malibu, California

Arun Ramakrishnan
University of Maryland
College Park, Maryland

James G. Rathmell
University of Sydney
Sydney, Australia

Alfy Riddle
Macallan Consulting
Milpitas, California

Arye Rosen
Drexel University
Philadelphia, Pennsylvania

Harel D. Rosen
UMDNJ/Robert Wood Johnson
Medical School
New Brunswick, New Jersey

Matthew N.O. Sadiku
Avaya, Inc.
Holmdel, New Jersey

George K. Schoneman
Rockwell Collins
Cedar Rapids, Iowa

Jonathan B. Scott
Agilent Technologies
Santa Rosa, California

Warren L. Seely
Motorola
Scottsdale, Arizona

John F. Sevic
UltraRF, Inc.
Sunnyvale, California

Michael S. Shur
Renssalaer Polytechnic Institute
Troy, New York

Thomas M. Siep
Texas Instruments
Dallas, Texas

Richard V. Snyder
RS Microwave
Butler, New Jersey

Jan Stake
Chalmers University
Goteborg, Sweden

Wayne E. Stark
University of Michigan
Ann Arbor, Michigan

Joseph Staudinger
Motorola
Tempe, Arizona

Michael B. Steer
North Carolina State University
Raleigh, North Carolina

Daniel G. Swanson, Jr.
Bartley R.F. Systems
Amesbury, Massachusetts

Toby Syrus
University of Maryland
College Park, Maryland

Manos M. Tentzeris
Georgia Institute of Technology
Atlanta, Georgia

Robert J. Trew
U.S. Department of Defense
Arlington, Virginia

Karl R. Varian
Raytheon
Dallas, Texas

John P. Wendler
M/A–Com Components Business Unit
Lowell, Massachusetts

James B. West
Rockwell Collins
Cedar Rapids, Iowa

James C. Wiltse
Georgia Tech
Atlanta, Georgia

Jerry C. Whitaker
Technical Press
Morgan Hill, California

Contents

Fay, Patrick "Introduction"
The RF and Microwave Handbook
Editor in Chief Mike Golio
Boca Raton: CRC Press LLC,2001

1 Introduction

Patrick Fay
University of Notre Dame

1.1 Overview of Microwave and RF Engineering

Modern microwave and radio frequency (RF) engineering is an exciting and dynamic field, due in large part to the symbiosis between recent advances in modern electronic device technology and the current explosion in demand for voice, data, and video communication capacity. Prior to this revolution in communications, microwave technology was the nearly exclusive domain of the defense industry; the recent and dramatic increase in demand for communication systems for such applications as wireless paging, mobile telephony, broadcast video, and tethered as well as untethered computer networks is revolutionizing the industry. These systems are being employed across a broad range of environments including corporate offices, industrial and manufacturing facilities, and infrastructure for municipalities, as well as private homes. The diversity of applications and operational environments has led, through the accompanying high production volumes, to tremendous advances in cost-efficient manufacturing capabilities of microwave and RF products. This, in turn, has lowered the implementation cost of a host of new and cost-effective wireless as well as wired RF and microwave services. Inexpensive handheld GPS navigational aids, automotive collision-avoidance radar, and widely available broadband digital service access are among these. Microwave technology is naturally suited for these emerging applications in communications and sensing, since the high operational frequencies permit both large numbers of independent channels for the wide variety of uses envisioned as well as significant available bandwidth per channel for high speed communication.

Loosely speaking, the fields of microwave and RF engineering together encompass the design and implementation of electronic systems utilizing frequencies in the electromagnetic spectrum from approximately 300 kHz to over 100 GHz. The term “RF” engineering is typically used to refer to circuits and systems having frequencies in the range from approximately 300 kHz at the low end to between 300 MHz and 1 GHz at the high end. The term “microwave engineering”, meanwhile, is used rather loosely to refer to design and implementation of electronic systems with operating frequencies in the range of from 300 MHz to 1 GHz on the low end to upward of 100 GHz. Figure 1.1 illustrates schematically the electromagnetic spectrum from audio frequencies through cosmic rays. The RF frequency spectrum covers the medium frequency (MF), high frequency (HF), and very high frequency (VHF) bands, while the microwave portion of the electromagnetic spectrum extends from the upper edge of the VHF frequency range to just below the THz radiation and far-infrared optical frequencies (approximately 0.3 THz and above). The wavelength of free-space radiation for frequencies in the RF frequency range is from approximately 1 m (at 300 MHz) to 1 km (at 300 kHz), while those of the microwave range extend from 1 m to the vicinity of 1 mm (corresponding to 300 GHz) and below.

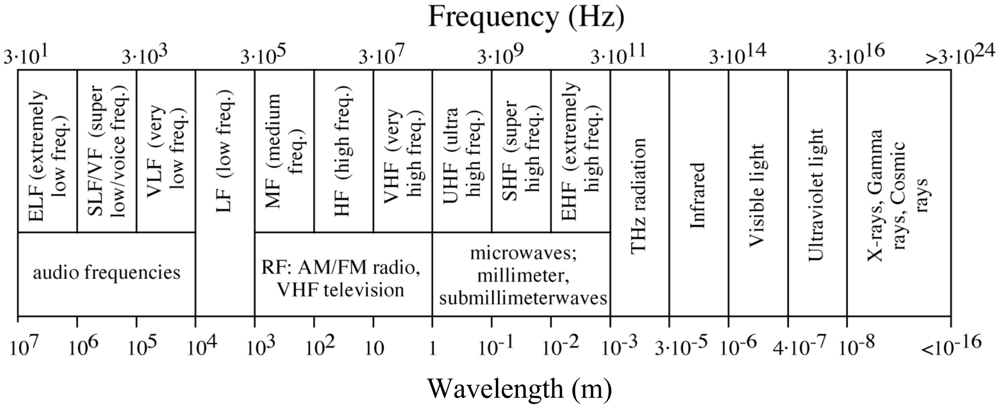

FIGURE 1.1 Electromagnetic frequency spectrum and associated wavelengths.

The boundary between "RF" and "microwave" design is both somewhat indistinct as well as one that is continually shifting as device technologies and design methodologies advance. This is due to implicit connotations that have come to be associated with the terms "RF" and "microwave" as the field has developed. In addition to the distinction based on the frequency ranges discussed previously, the fields of RF and microwave engineering are also often distinguished by other system features as well. For example, the particular active and passive devices used, the system applications pursued, and the design techniques and overall mindset employed all play a role in defining the fields of microwave and RF engineering. These connotations within the popular meaning of microwave and RF engineering arise fundamentally from the frequencies employed, but often not in a direct or absolute sense. For example, because advances in technology often considerably improve the high frequency performance of electronic devices, the correlation between particular types of electronic devices and particular frequency ranges is a fluid one. Similarly, new system concepts and designs are reshaping the applications landscape, with mass market designs utilizing ever higher frequencies rapidly breaking down conventional notions of microwave-frequency systems as serving "niche" markets.

The most fundamental characteristic that distinguishes RF engineering from microwave engineering is directly related to the frequency (and thus the wavelength) of the electronic signals being processed. For low-frequency and RF circuits (with a few special exceptions such as antennae), the signal wavelength is much larger than the size of the electronic system and circuit components. In contrast, for a microwave system the sizes of typical electronic components are often comparable (i.e., within approximately 1 order of magnitude) to the signal wavelength. This gives rise to a reasonable working definition of the two design areas based on the underlying approximations used in design. Since in conventional RF design, the circuit components and interconnections are generally small compared to a wavelength, they can be modeled as lumped elements for which Kirchoff's voltage and current laws apply at every instant in time. Parasitic inductances and capacitances are incorporated to accurately model the frequency dependencies, but these quantities can, to good approximation, be treated as lumped elements. For microwave frequencies, however, the finite propagation velocity of electromagnetic waves can no longer be neglected. For these frequencies, the time delay associated with signal propagation from one end of a component to the other is an appreciable fraction of the signal period, and thus lumped-element descriptions are no longer adequate to describe the electrical behavior. A distributed-element model is required to accurately capture the electrical behavior, in contrast to RF models. The time delay associated with finite wave propagation velocity that gives rise to the distributed circuit effects is a distinguishing feature of the mindset of microwave engineering. An alternative viewpoint is based on the observation that microwave engineering lies in a "middle ground" between traditional low-frequency electronics and optics, as shown in Fig. 1.1. As a consequence of RF, microwaves, and optics simply being different regimes of the same electromagnetic phenomena, there is a gradual transition between these regimes. The continuity of these regimes results in constant reevaluation of the appropriate design strategies and trade-offs as device and circuit technology advances. For example, miniaturization of active and passive components often increases the frequencies at which lumped-element circuit models are sufficiently accurate, since by reducing component dimensions, the time delay for propagation through a component is proportionally reduced. As a consequence, lumped-element components at “microwave” frequencies are becoming increasingly common in systems previously based on distributed elements due to significant advances in miniaturization, even though the operational frequencies remain unchanged. Component and circuit miniaturization also leads to tighter packing of interconnects and components, potentially introducing new parasitic coupling and distributed-element effects into circuits that could previously be treated using lumped-element RF models.

The comparable scales of components and signal wavelengths has other implications for the designer as well, since neither the ray-tracing approach from optics nor the lumped-element approach from RF circuit design are valid in this middle ground. In this regard, microwave engineering can also be considered to be “applied electromagnetic engineering,” as the design of guided-wave structures such as waveguides and transmission lines, transitions between different types of transmission lines, and antennae all require analysis and control of the underlying electromagnetic fields. The design of these guided-wave structures is treated in detail in Section 9.3.

The distinction between RF and microwave engineering is further blurred by the trend of increasing commercialization and consumerization of systems using what have been traditionally considered to be microwave frequencies. Traditional microwave engineering, with its historically military applications, has long been focused on delivering performance at any cost. As a consequence, special-purpose devices intended solely for use in high performance microwave systems and often with somewhat narrow ranges of applicability were developed to achieve the required performance. With continuing advances in silicon microelectronics, including SiGe heterojunction bipolar transistors (HBTs) and conventional scaled CMOS, microwave frequency systems can now be reasonably implemented using the same devices as conventional low-frequency baseband electronics. In addition, the commercialization of low-cost III-V compound semiconductor electronics, including ion-implanted metal-semiconductor field-effect transistors (MESFETs), pseudomorphic high electron mobility transistors (PHEMTs), and III-V HBTs, has dramatically decreased the cost of including these elements in high-volume consumer systems. This convergence, with silicon microelectronics moving ever higher in frequency into the microwave spectrum from the low-frequency side and compound semiconductors declining in price for the middle of the frequency range, blurs the distinction between “microwave” and “RF” engineering, since “microwave” functions can now be realized with “mainstream” low-cost electronics. This is accompanied by a shift from physically large, low-integration-level hybrid implementations to highly integrated solutions based on monolithic microwave integrated circuits (MMICs). This shift has a dramatic effect not only on the design of systems and components, but also on the manufacturing technology and economics of production and implementation as well. A more complete discussion of the active device and integration technologies that make this progression possible is included in Chapter 7.

Aside from these defining characteristics of RF and microwave systems, a number of physical effects that are negligible at lower frequencies become increasingly important at high frequencies. Two of these effects are the skin effect and radiation losses. The skin effect is caused by the finite penetration depth of an electromagnetic field into conducting material. This effect is a function of frequency; the depth of penetration is given by $\delta_s = \frac{1}{\sqrt{\omega f \mu \sigma}}$, where μ is the permeability, f is the frequency, and σ is the conductivity of the material. As the expression indicates, δ_s decreases with increasing frequency, and so the electromagnetic fields are confined to regions increasingly near the surface as the frequency increases. This results in the microwave currents flowing exclusively along the surface of the conductor, significantly increasing the effective resistance (and thus the loss) of metallic interconnects. Further discussion of this topic can be found in Sections 9.2 and 9.6.1. Radiation losses also become increasingly important as the signal wavelengths approach the component and interconnect dimensions. For conductors and other components of comparable size to the signal wavelengths, standing waves caused by reflection of the electromagnetic waves from the boundaries of the component can greatly enhance the radiation of electromagnetic energy. These standing waves can be easily established either intentionally (in the case of antennae and resonant structures) or unintentionally (in the case of abrupt transitions, poor circuit layout, or other imperfections). Careful attention to transmission line geometry, placement relative to other components, transmission lines, and ground planes, as well as circuit packaging is essential for avoiding excessive signal attenuation and unintended coupling due to radiative effects.

A further distinction in the practice of RF and microwave engineering from conventional electronics is the methodology of testing. Due to the high frequencies involved, the capacitance and standing-wave effects associated with test cables and the parasitic capacitance of conventional test probes make the use of conventional low-frequency circuit characterization techniques impractical. Although advanced measurement techniques such as electro-optic sampling can sometimes be employed to circumvent these difficulties, in general the loading effect of measurement equipment poses significant measurement challenges for debugging and analyzing circuit performance, especially for nodes at the interior of the circuit under test. In addition, for circuits employing dielectric or hollow guided-wave structures, voltage and current often cannot be uniquely defined. Even for structures in which voltage and current are well-defined, practical difficulties associated with accurately measuring such high-frequency signals make this difficult. Furthermore, since a DC-coupled time-domain measurement of a microwave signal would have an extremely wide noise bandwidth, the sensitivity of the measurement would be inadequate. For these reasons, components and low-level subsystems are characterized using specialized techniques. These approaches are treated in detail in Chapter 4.

1.2 Frequency Band Definitions

The field of microwave and RF engineering is driven by applications — originally for military purposes such as radar and, more recently, for commercial, scientific, and consumer applications. As a consequence of this diverse applications base, microwave terminology and frequency band designations are not entirely standardized, with various standards bodies, corporations, and other interested parties all contributing to the collective terminology of microwave engineering. Figure 1.2 shows graphically some of the most common frequency band designations, with their approximate upper and lower bounds. As can be seen, some care must be exercised in the use of the "standard" letter designations; substantial differences in the definitions of these bands exist in the literature and in practice. Diagonal hashing at the ends of the frequency bands in Fig. 1.2 indicates variations in the definitions by different groups and authors; dark regions in the bars indicate frequencies for which there appears to be widespread agreement in the literature. The double-ended arrows appearing above some of the bands indicate the IEEE definitions for these bands. Two distinct definitions of K-band are in use; the first of these defines the band as the range from 18 GHz to approximately 26.5 GHz, while the other definition extends from 10.9 to 36 GHz. Both of these definitions are illustrated in Fig. 1.2. Similarly, L-band has two overlapping frequency range definitions; this gives rise to the large "variation" regions shown in Fig. 1.2. In addition, some care must be taken with these letter designations, as the IEEE and U.S. military specifications both define an L-band, but with very different frequencies. The IEEE L-band resides at the low end of the microwave spectrum, while the military definition of L-band is from 40 to 60 GHz. The IEEE designations (L–W) are presently used widely in practice and the technical literature, with the newer U.S. military designations (A–N) having not yet gained widespread popularity outside of the military community.

1.3 Applications

The field of microwave engineering is currently experiencing a radical transformation. Historically, the field has been driven by applications requiring the utmost in performance with little concern for cost or manufacturability. These systems have been primarily for military applications, where performance at nearly any cost could be justified. The current transformation of the field involves a dramatic shift from defense applications to those driven by the commercial and consumer sector, with an attendant shift in

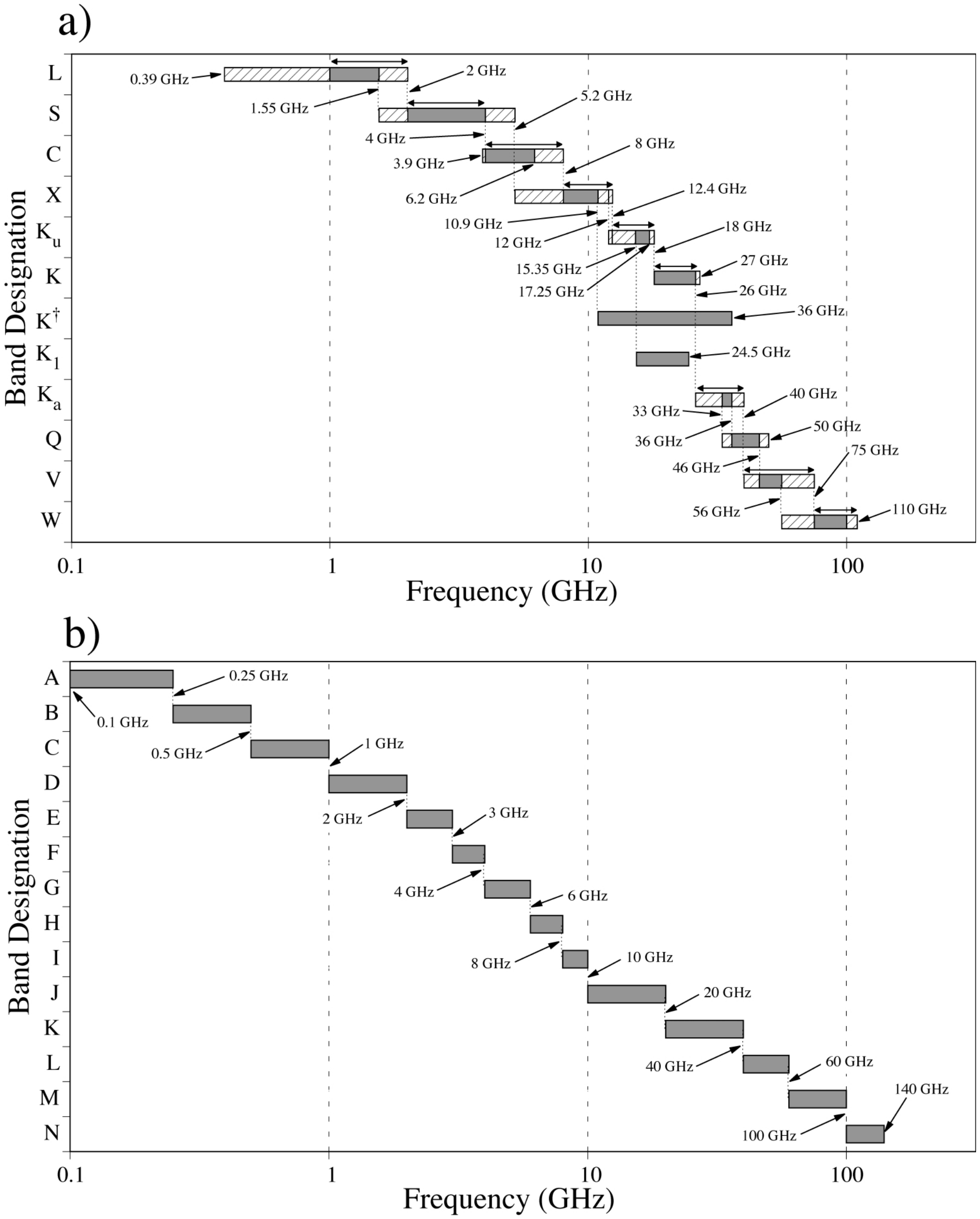

FIGURE 1.2 Microwave and RF frequency band designations.[1-5] (a) Industrial and IEEE designations. Diagonal hashing indicates variation in the definitions found in literature; dark regions in the bars indicate frequencies for which there is widespread agreement. Double-ended arrows appearing on bands indicate the current IEEE definitions for these bands where they exist, and K† denotes an alternative definition for K-band found in Reference 5. (b) U.S. military frequency band designations.[1-3]

focus from design for performance to design for manufacturability. This transformation also entails a shift from small production volumes to mass production for the commercial market, and from a focus on performance without regard to cost to a focus on minimum cost while maintaining acceptable performance. For wireless applications, an additional shift from broadband systems to systems having very tightly regulated spectral characteristics also accompanies this transformation.

For many years the driving application of microwave technology was military radar. The small wavelength of microwaves permits the realization of narrowly focused beams to be achieved with antennas small enough to be practically steered, resulting in adequate resolution of target location. Long-distance terrestrial communications for telephony as well as satellite uplink and downlink for voice and video were among the first commercially viable applications of microwave technology. These commercial communications applications were successful because microwave-frequency carriers (f_c) offer the possibility of very wide absolute signal bandwidths (Δf) while still maintaining relatively narrow fractional bandwidths (i.e., $\Delta f/f_c$). This allows many more voice and data channels to be accommodated than would be possible with lower-frequency carriers or baseband transmission.

Among the current host of emerging applications, many are based largely on this same principle, namely, the need to transmit more and more data at high speed, and thus the need for many communication channels with wide bandwidths. Wireless communication of voice and data, both to and from individual users as well as from users and central offices in aggregate, wired communication including coaxial cable systems for video distribution and broadband digital access, fiber-optic communication systems for long- and short-haul telecommunication, and hybrid systems such as hybrid fiber-coax systems are all poised to take advantage of the wide bandwidths and consequently high data carrying capacity of microwave-frequency electronic systems. In addition to the explosion in both diversity and capability of microwave-frequency communication systems, radar systems continue to be of importance with non-military and non-navigational applications including radar systems for automotive collision avoidance and weather and atmospheric sensing becoming increasingly widespread.

In addition to these “traditional” microwave applications, other fields of electronics are increasingly encroaching into the microwave frequency range. Examples include wired data networks based on coaxial cable or twisted-pair transmission lines with bit rates of over 1 Gb/s, fiber-optic communication systems with data rates well in excess of 10 Gb/s, and inexpensive personal computers and other digital systems with clock rates of over 1 GHz. The continuing advances in the speed and capability of conventional microelectronics is pushing traditional circuit design ever further into the microwave frequency regime. These trends promise to both invigorate and reshape the field of microwave engineering in new and exciting ways.

References

1. Collin, R. E., *Foundations for Microwave Engineering*, McGraw-Hill, New York, 1992, 2.
2. Harsany, S. C., *Principles of Microwave Technology*, Prentice-Hall, Upper Saddle River, NJ, 1997, 5.
3. Laverghetta, T. S., *Modern Microwave Measurements and Techniques*, Artech House, Norwood, MA, 1988, 479.
4. Rizzi, P. A., *Microwave Engineering*, Prentice-Hall, Englewood Cliffs, NJ, 1988, 1.
5. *Reference Data for Radio Engineers*, ITT Corp., New York, 1975.

Flikkema, Paul G. et al. "Microwave and RF Product Applications"
The RF and Microwave Handbook
Editor in Chief Mike Golio
Boca Raton: CRC Press LLC,2001

2

Microwave and RF Product Applications

Paul G. Flikkema
Northern Arizona University

Andy D. Kucar
4U Communications Research, Inc.

Brian Petry
3Com Corporation

Saf Asghar
Advanced Micro Devices, Inc.

Jim Paviol
Intersil

Carl Andren
Intersil

John Fakatselis
Intersil

Thomas M. Siep
Texas Instruments

Ian C. Gifford
M/A-Com, Inc.

Ramesh K. Gupta
COMSAT Laboratories

Nils V. Jespersen
Lockheed Martin Space Electronics and Communications

Benjamin B. Peterson
U.S. Coast Guard Academy

James L. Bartlett
Rockwell Collins

James C. Wiltse
Georgia Tech

Melvin L. Belcher, Jr.
Georgia Tech

Josh T. Nessmith
Georgia Tech

Robert D. Hayes
RDH Incorporated

Madhu S. Gupta
San Diego State University

Arye Rosen
Drexel University

Harel D. Rosen
UMDNJ/Robert Wood Johnson Medical School

Stuart D. Edwards
Conway Stuart Medical, Inc.

2.1 Cellular Mobile Telephony

Paul G. Flikkema

The goal of modern cellular mobile telephone systems is to provide services to telephone users as efficiently as possible. In the past, this definition would have been restricted to mobile users. However, the cost of wireless infrastructure is less than wired infrastructure in new telephone service markets. Thus, wireless mobile telephony technology is being adapted to provide in-home telephone service, the so-called wireless local loop (WLL). Indeed, it appears that wireless telephony will become dominant over traditional wired access worldwide.

The objective of this section is to familiarize the RF/microwave engineer with the concepts and terminology of cellular mobile telephony ("cellular"), or mobile wireless networks. A capsule history and a summary form the two bookends of the section. In between, we start with the cellular concept and the basics of mobile wireless networks. Then we take a look at some of the standardization issues for cellular systems. Following that, we cover the focus of the standards battles: channel access methods. We then take a look at some of the basic aspects of cellular important to RF/microwave engineers: first, modulation, diversity, and spread spectrum; then coding, interleaving, and time diversity; and finally nonlinear channels. Before wrapping up, we take a glimpse at a topic of growing importance: antenna array technology.

A Brief History

Mobile telephone service was inaugurated in the U.S. in 1947 with six radio channels available per city. This evolved into the manual Mobile Telephone System (MTS) used in the 1950s and 1960s. The year 1964 brought the Improved MTS (IMTS) systems with eight channels per city with — finally — no telephone operator required. Later, the capacity was more than doubled to 18. Most importantly, the IMTS introduced narrowband frequency modulation (NBFM) technology. The first cellular service was introduced in 1983, called AMPS (Advanced Mobile Phone Service). Cities were covered by cells averaging about 1 km in radius, each serviced by a base station. This system used the 900 MHz frequency band still in use for mobile telephony. The cellular architecture allowed frequency reuse, dramatically increasing capacity to a maximum of 832 channels per cell.

The age of digital, or second-generation, cellular did not arrive until 1995 with the introduction of the IS-54 TDMA service and the competing IS-95 CDMA service. In 1996–1997, the U.S. Federal Communications Commission auctioned licenses for mobile telephony in most U.S. markets in the so-called PCS (Personal Communication System) bands at 1.9 GHz. These systems use a variety of standards, including TDMA, CDMA, and the GSM TDMA standard that originated in Europe. Outside the U.S., a similar evolution has occurred, with GSM deployed in Europe and the PDC (Personal Digital Cellular) system in Japan. In other countries there has been a pitched competition between all systems. While not succeeding in the U.S., so-called low-tier systems have been popular in Europe and Japan. These systems are less robust to channel variations and are therefore targeted to pedestrian use. The European system is called DECT (Digital European Cordless Telephony) and the Japanese system is called PHS (Personal Handyphone System).

Third-generation (or 3G) mobile telephone service will be rolled out in the 2001–2002 time frame. These services will be offered in the context of a long-lived standardization effort recently renamed IMT-2000 (International Mobile Telecommunications–2000) under the auspices of the Radio Communications Standardization Sector of the International Telecommunications Union (ITU-R; see http://www.itu.int). Key goals of IMT-2000 are:[13]

1. Use of a common frequency band over the globe.
2. Worldwide roaming capability.
3. Transmission rates higher than second-generation systems to handle new data-over-cellular applications.

Another goal is to provide the capability to offer asymmetric rates, so that the subscriber can download data much faster than he can send it.

Finally, it is hoped that an architecture can be deployed that will allow hardware, software, and network commonality among services for a range of environments, such as those for vehicular, pedestrian, and fixed (nonmoving) subscribers. While also aiming for worldwide access and roaming, the main technical thrust of 3G systems will be to provide high-speed wireless data services, including 144 Kbps service to subscribers in moving vehicles, 384 Kbps to pedestrian users, 2 Mbps to indoor users, and service via satellites (where the other services do not reach) at up to 32 Kbps for mobile, hand-held terminals.

The Cellular Concept

At first glance, a logical method to provide radio-based communication service to a metropolitan area is a single, centrally located antenna. However, radio-frequency spectrum is a limited commodity, and regulatory agencies, in order to meet the needs of a vast number of applications, have further limited the amount of RF spectrum for mobile telephony. The limited amount of allocated spectrum forced designers to adopt the cellular approach: using multiple antennas (base stations) to cover a geographic area, each base station covers a roughly circular area called a cell. Figure 2.1 shows how a large region can be split into seven smaller cells (approximated by hexagons). This allows different base stations to use the same frequencies for communication links as long as they are separated by a sufficient distance. This is known as frequency reuse, and allows thousands of mobile telephone users in a metropolitan area to share far fewer channels.

There is a second important aspect to the cellular concept. With each base station covering a smaller area, the mobile phones need less transmit power to reach any base station (and thus be connected with the telephone network). This is a major advantage, since, with battery size and weight a major impediment to miniaturization, the importance of reducing power consumption of mobile phones is difficult to overestimate.

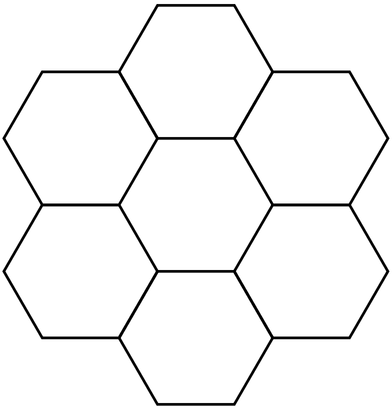

FIGURE 2.1 A region divided into cells. While normally the base stations are placed at the center of the cells, it is also possible to use edge-excited cells where base stations are placed at vertices.

If two mobile units are connected to their respective base stations at the same frequency (or more generally, channel), interference between them, called *co-channel interference,* can result. Thus, there is a trade-off between frequency reuse and signal quality, and a great deal of effort has resulted in frequency assignment techniques that balance this trade-off. They are based on the idea of clustering: taking the available set of channels, allocating them in chunks to each cell, and arranging the cells into geographically local clusters. Figure 2.2 shows how clusters of seven cells (each allocated one of seven mutually exclusive

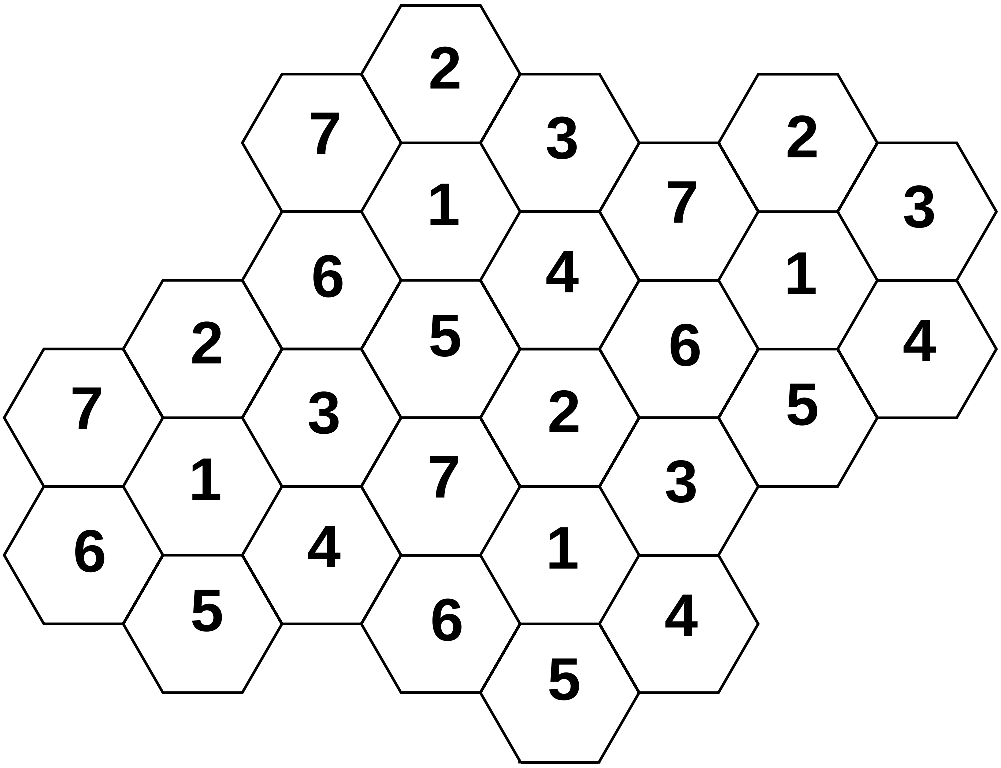

FIGURE 2.2 Cell planning with cluster size of 7. The number in each cell indexes the subset of channels allocated to the cell. Other cluster sizes, such as 4, 7, or 12 can be used.

channel subsets) are used to cover a large region; note that the arrangement of clusters maximizes the reuse distance — the distance between any two cells using the same frequency subset. Increasing the reuse distance has the effect of reducing co-channel interference.

Although it might seem attractive to make the cells smaller and smaller, there are diminishing returns. First, smaller cell sizes increase the need for management of mobile users as they move about. In other words, smaller cell sizes require more handoffs, where the network must transfer users between base stations. Another constraint is antenna location, which is often limited by available space and esthetics. Fortunately, both problems can be overcome by technology. Greater handoff rates can be handled by increases in processing speed, and creative antenna placement techniques (such as on lamp posts or sides of buildings) are allowing higher base station densities.

Another issue is evolution: how can a cellular system grow with demand? Two methods have been successful. The first is cell splitting: by dividing a cell into several cells (and adjusting the reuse pattern), a cellular service provider can increase its capacity in high-demand areas. The second is sectoring: instead of a single omnidirectional antenna covering a cell, a typical approach is to sectorize the cell into N_S regions, each served by an antenna that covers an angular span of $2\pi/N_S$ ($N_S = 3$ is typical). Note that both approaches increase handoff rates and thus require concurrent upgrading of network management. Later we will describe smart antennas, the logical extension to sectorization.

Networks for Mobile Telephony

A communication network that carries only voice — even a digital one — is relatively simple. Other than the usual digital communication system functions, such as channel coding, modulation, and synchronization, all that is required is call setup and takedown. However, current and future digital mobile telephony networks are expected to carry digital data traffic as well.

Data traffic is by nature computer-to-computer, and requires that the network have an infrastructure that supports everything from the application (such as Web browsing) to the actual transfer of bits. The data is normally organized into chunks called packets (instead of streams as in voice), and requires a much higher level of reliability than digitized voice signals. These two properties imply that the network must also label the packets, and manage the detection and retransmission of packets that are received in error. It is important to note that packet retransmission, while required for data to guarantee fidelity, is not possible for voice because it would introduce delays that would be intolerable in a human conversation.

Other functions that a modern digital network must perform include encryption and decryption (for data security) and source coding and decoding. The latter functions minimize the amount of the channel resource (in essence, bandwidth) needed for transferring the information. For voice networks this involves the design of voice codecs (coder/decoders) that not only digitize voice signals, but strip out the redundant information in them. In addition to all the functions that wired networks provide, wireless networks with mobile users must also provide mobility management functions that keep track of calls as subscribers move from cell to cell.

The various network functions are organized into *layers* to rationalize the network design and to ease internetworking, or the transfer of data between networks.[11] RF/microwave engineering is part of the *physical layer* that is responsible for carrying the data over the wireless medium.

Standards and Standardization Efforts

The cellular industry is, if anything, dense with lingo and acronyms. Here we try to make sense of at least some of the important and hopefully longer-lived terminology.

Worldwide, most of the cellular services are offered in two frequency bands: 900 and 1900 MHz. In each of the two bands, the exact spectrum allocated to terrestrial mobile services varies from country to country. In the U.S. cellular services are in the 800 to 900 MHz band, while similar services are in the 800 to 980 MHz band in Europe under the name GSM900. (GSM900 combines in one name a radio communication standard — GSM, or Global System for Mobile Communications — and the frequency band in which it is used. We will describe the radio communication, or *air interface*, standards later). In the mid-1990s, the U.S. allocated spectrum for PCS (Personal Communication Services) from 1850 to 2000 MHz; while many thought PCS would be different from cellular, they have converged and are interchangeable from the customer's perspective. Similarly, in Europe GSM1800 describes cellular services offered using the 1700 to 1880 MHz band.

The 1992 World Administrative Radio Conference (WARC '92) allocated spectrum for third-generation mobile radio in the 1885 to 1980 and 2110 to 2160 MHz bands. The ITU-Rs IMT-2000 standardization initiative adopted these bands for terrestrial mobile services. Note that the IMT-2000 effort is an umbrella that includes both terrestrial and satellite-based services — the latter for areas where terrestrial services are unavailable.

Please note that all figures here are approximate and subject to change in future WARCs; please consult References 2 and 13 for details.

The cellular *air interface* standards are designed to allow different manufacturers to develop both base station and subscriber (mobile user handset) equipment. The air interface standards are generally different for the downlink (base station to handset) and uplink (handset to base station). This reflects the asymmetry of resources available: the handsets are clearly constrained in terms of power consumption and antenna size, so that the downlink standards imply sophisticated transmitter design, while the uplink standards emphasize transmitter simplicity and advanced receive-side algorithms. The air interface standards address channel access protocols as well as traditional communication link design parameters such as modulation and coding. These issues are taken up in the following sections.

Channel Access

In a cellular system, a fixed amount of RF spectrum must somehow be shared among thousands of simultaneous phone conversations or data links. *Channel access* is about (1) dividing the allocated RF spectrum into pieces and (2) allocating the pieces to conversations/links in an efficient way.

The easiest channel access method to envision is FDMA (Frequency Division Multiple Access), where each link is allocated a sub-band (i.e., a specific carrier frequency; see Fig. 2.3). This is exactly the access method used by first generation (analog) cellular systems. The second generation of cellular brought two newer channel access methods that were enabled by progress in digital process technology. One is TDMA (Time Division Multiple Access), wherein time is divided into *frames*, and links are given short *time slots* in each frame (Fig. 2.4). FDMA and TDMA can be seen as time/frequency duals, in that FDMA subdivides the band into narrow sub-bands in the frequency domain, while TDMA subdivides time into slots, during which a link (within a cell) uses the entire allocated bandwidth.

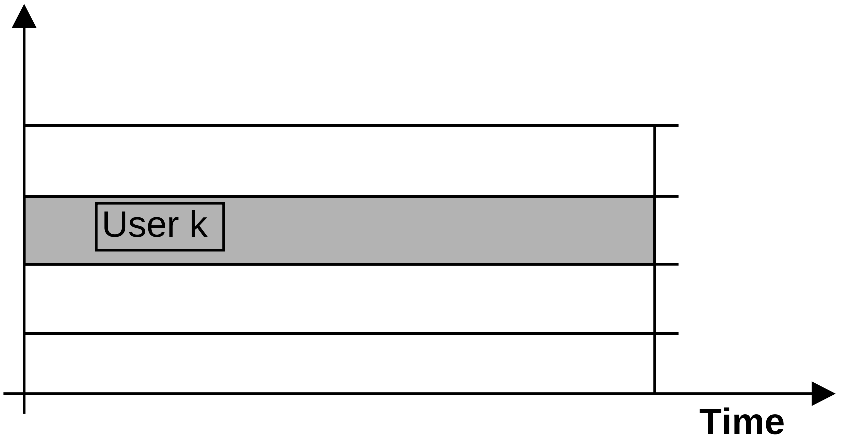

FIGURE 2.3 FDMA depicted on the time-frequency plane, with users assigned carrier frequencies, or channels. Not shown are guard bands between the channels to prevent interference between users' signals.

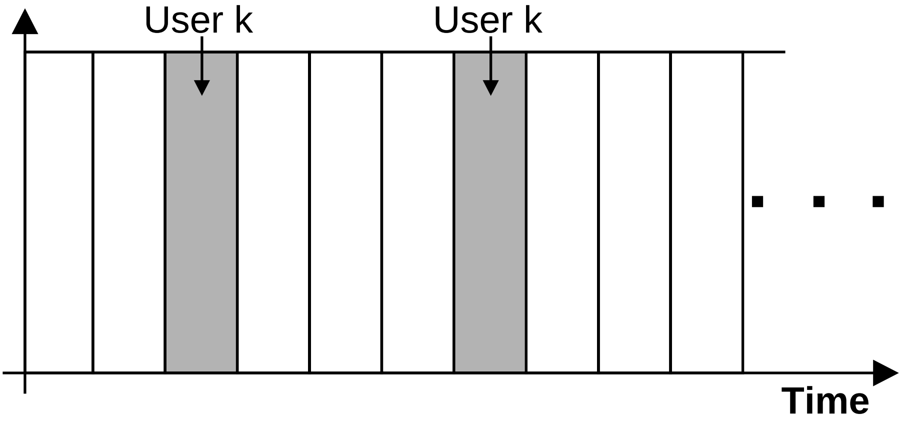

FIGURE 2.4 Depiction of TDMA on the time-frequency plane. Users are assigned time slots within a frame. Guard times (not shown) are needed between slots to compensate for timing inaccuracies.

The second generation of cellular also brought CDMA (Code Division Multiple Access). In CDMA, all active links simultaneously use the entire allocated spectrum, but sophisticated codes are used that allow the signals to be separated in the receiver.[1] We will describe CDMA in more depth later.

It should be noted that both TDMA- and CDMA-based cellular systems also implicitly employ FDMA, although this is rarely mentioned. The reason is that the cellular bands are divided into smaller bands (a form of FDMA), and both TDMA and CDMA are used within these sub-bands.

In the U.S., the TDMA and CDMA standards are referred to by different acronyms. The TDMA standard originally was called IS-54, but with enhancements became IS-136. The CDMA standard was called IS-95, and has been re-christened as cdmaOne by its originator, Qualcomm. These standards were created under the auspices of the Telecommunications Industry Association (TIA) and the Electronic Industries Alliance (EIA).

In Europe, the second generation brought digital technology in the form of the GSM standard, which used TDMA. (The GSM acronym originally referred to Group Special Mobile, but was updated to capture its move to worldwide markets.) Japan also chose TDMA in its first digital offering, called PDC (Personal Digital Cellular).

The three multiple access approaches use different signal properties (frequency, time, or code) to allow the distinguishing of multiple signals. How do they compare? In the main, as we move from FDMA to TDMA to CDMA (in order of their technological development), complexity is transferred from the RF section to the digital section of the transmitters and receivers. The evolution of multiple access techniques has tracked the rapid evolution of digital processing technology as the latter has become cheaper and faster. For example, while FDMA requires a tunable RF section, both TDMA and CDMA need only a fixed-frequency front end. CDMA relieves one requirement of TDMA — strict synchronization among the various transmitters — but introduces a stronger requirement for synchronization of the receiver to the received signal. In addition, the properties of the CDMA signal provide a natural means to exploit the multipath nature of the digital signal for improved performance. However, these advantages come at the cost of massive increases in the capability of digital hardware. Luckily, Moore's Law (i.e., that processing power roughly doubles every 18 months at similar cost) still remains in effect as of the turn of the century, and the amount of processing power that will be used in the digital phones in the 21st century will be unimaginable to the architects of the analog systems developed in the 1970s.

[1] It is fashionable to depict CDMA graphically using a "code dimension" that is orthogonal to the time-frequency plane, but this is an unfortunate misrepresentation. Like any signals, CDMA signals exist (in fact, overlap) in the time-frequency plane, but have correlation-based properties that allow them to be distinguished.

Modulation

The general purpose of modulation is to transform an information-bearing message signal into a related signal that is suitable for efficient transmission over a communication channel. In *analog modulation,* this is a relatively simple process: the information-bearing analog (or continuous-time) signal is used to alter a parameter (normally, the amplitude, frequency, or phase) of a sinusoidal signal (or carrier, the signal carrying the information). For example, in the NBFM modulation used in the AMPS system, the voice signal alters the frequency content of the modulated signal in a straightforward manner.

The purpose of *digital modulation* is to convert an information-bearing discrete-time symbol sequence into a continuous-time waveform. Digital modulation is easier to analyze than analog modulation, but more difficult to describe and implement.

Modulation in Digital Communication

Before digital modulation of the data in the transmitter, there are several processing steps that must be applied to the original message signal to obtain the discrete-time symbol sequence. A continuous-time message signal, such as the voice signal in telephony, is converted to digital form by sampling, quantization, and source coding. *Sampling* converts the original continuous-time waveform into discrete-time format, and *quantization* approximates each sample of the discrete-time signal using one of a finite number of levels. Then *source coding* jointly performs two functions: it strips redundancy out of the signal and converts it to a discrete-time sequence of symbols.

What if the original signal is already in discrete-time (sampled format), such as a computer file? In this case, no sampling or quantization is needed, but source coding is still used to remove redundancy.

Between source coding and modulation is a step critical to the efficiency of digital communications: channel coding. This is discussed later; it suffices for now to know that it converts the discrete-time sequence of symbols from the source coder into another (better) discrete-time symbol sequence for input to the modulator. Following modulation, the signal is upconverted, filtered (if required), and amplified in RF electronics before being sent to the antenna. All the steps described are shown in block-diagram form in Fig. 2.5. In the receiver, the signal from the antenna, following filtering (again, if required), is amplified and downconverted prior to demodulation, channel decoding, and source decoding (see Fig. 2.5).

What is the nature of the digital modulation process? The discrete-time symbol sequence from the channel coder is really a string of symbols (letters) from a *finite* alphabet. For example, in *binary* digital modulation, the input symbols are 0's and 1's. The modulator output converts those symbols into one of a *finite* set of waveforms that can be optimized for the channel.

While it is the finite set of waveforms that distinguishes digital modulation from analog modulation, that difference is only one manifestation of the entire paradigm of *digital communication.* In a good digital communication design, the source coder, channel coder, and modulator all work together to maximize the efficient use of the communication channel; even two of the three are not enough for good performance.

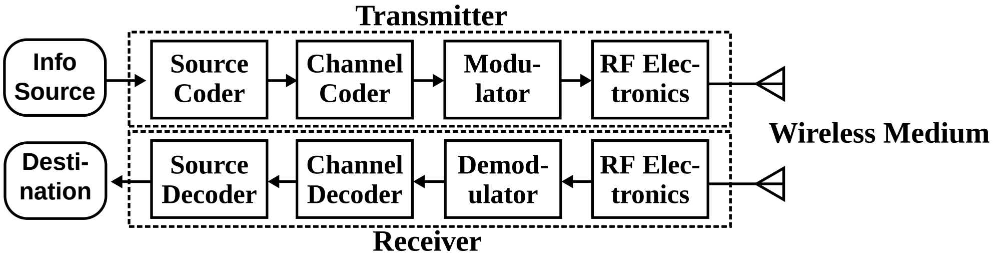

FIGURE 2.5 Communication system block diagram for wireless communication. In the wireless medium, multipath propagation and interference can be introduced. For system modeling purposes, the two blocks of RF electronics are combined with the wireless medium to form the wireless channel — a channel that distorts the signal, and adds noise and interference. The other blocks are designed to maximize the system performance for the channel.

Selection of Digital Modulation Formats

There are several (often conflicting) criteria for selection of a modulation scheme. They are:

- BER (bit error rate) performance
  - in wireless, particularly in cellular mobile channels, the scheme must operate under conditions of severe fading
  - cellular architectures imply co-channel interference
  - Typically, a BER of 10^{-2} or better is required for voice telephony, and 10^{-5} or better is required for data.
- Spectral (or bandwidth) efficiency (measured in bits/s/Hz)
- Power efficiency (especially for hand-held/mobile terminals)
- Implementation complexity and cost

In the U.S. cellular market, complexity is of special importance: with the number of standards growing, many handsets are now dual- and triple-mode; for example, a phone might have both GSM and 3G capability. While some hardware can be shared, multimode handsets clearly place additional constraints on the allowable complexity for each mode.

Classification of Digital Modulation Schemes

Broadly, modulation techniques can be classified into two categories.

Linear methods include schemes that use combinations of amplitude and phase modulation of a pulse stream. They have higher spectral efficiencies than constant-envelope methods (see the following), but must use more-expensive (or less efficient) linear amplifiers to maintain performance and to limit out-of-band emissions.

Examples of linear modulation schemes include PSK (phase-shift keying) and QAM (quadrature amplitude modulation). QAM can be viewed as a generalization of PSK in that both the amplitude and the phase of the modulated waveform are altered in response to the input symbols.

Constant-envelope methods are more complicated to describe, but usually are sophisticated methods based on frequency modulation. Their key characteristic is a constant envelope (resulting in a constant instantaneous signal power) regardless of the source symbol stream. They allow use of less expensive amplification and/or higher amplification efficiencies (e.g., running amplifiers in the nonlinear region), at the expense of out-of-band emissions. Historically, they are limited to spectral efficiencies of about 1 bit/s/Hz.

Examples of constant envelope methods include FSK (frequency-shift keying) and more sophisticated methods such as MSK and GMSK (these will be described shortly). These methods can be thought of as digital (finite alphabet) FM in that the spectrum of the output signal is varied according to the input symbol stream.

The spectral occupancy of a modulated signal (per channel) is roughly

$$S_O = B + 2\Delta f,$$

where B is the bandwidth occupied by signal power spectrum and Δf is the maximum one-way carrier frequency drift.[2] We can express the bandwidth

$$B = \frac{R_d}{\epsilon},$$

where R_d is the channel data rate (in bits/s) and ϵ is the spectral efficiency (in bits/s/Hz). Combining, we obtain

$$S_O = \frac{R_d}{\epsilon} + 2\Delta f.$$

[2] This drift can be caused by oscillator instability or Doppler due to channel time variations.

Thus, to minimize spectral occupancy (thus maximizing capacity in number of users) we can:

1. Reduce R_d by lowering the source coding rate (implying more complexity or lower fidelity), or
2. Improve the spectral efficiency of the modulation (implying higher complexity), or
3. Improve the transmitter/receiver oscillators (at greater cost).

Modulation, Up/Downconversion, and Demodulation

To transmit a string of binary information symbols (or bits — zeros and ones), $\{b_0, b_1, b_2, \ldots\}$, we can represent a 1 by a positive-valued pulse of amplitude one, and a 0 by a negative pulse of the sample amplitude. This mapping from the bit value at time n, b_n, to amplitude a_n can be accomplished using

$$a_n = 2b_n - 1.$$

To complete the definition, we define a pulse of unit amplitude with start time of zero and stop time of T as $p_T(t)$. Then the modulated signal can be efficiently written as

$$u(t) = \sum_n a_n p_T(t - nT).$$

This signal is at baseband — centered at zero frequency — and is therefore unsuitable for wireless communication media. However, this signal can be upconverted to a desired RF by mixing with a sinusoid to get the passband signal

$$x(t) = u(t)\cos(2\pi f_c t) = \cos(2\pi f_c t)\sum_n a_n p_T(t - nT),$$

where f_c is the carrier frequency.

Multiplying a sinusoid by ±1 is identical to changing its phase between 0 and π radians, so we have

$$x(t) = \cos\left(2\pi f_c t + \sum_n d_n p_T(t - nT)\right),$$

where we assign $d_n = 0$ when $a_n = -1$ and $d_n = \pi$ when $a_n = 1$. This equation shows that we are simply shifting the phase of the carrier between two different values: this is BPSK (binary phase-shift keying).

Why not use more than two phase values? In fact, four are ordinarily used for better efficiency: pairs of bits are mapped to four different phase values, 0, $\pm\pi/2$, and π. For example, the CDMA standards employ this scheme, known as quaternary PSK (QPSK).

In general, the baseband signal will be complex-valued, which leads to the general form of upconversion from baseband to passband:

$$x(t) = \sqrt{2}\Re\left\{u(t)e^{j2\pi f_c t}\right\},$$

where the $\sqrt{2}$ factor is simply to maintain a consistency in measurement of signal power between passband and baseband. The motivation of using the baseband representation of a signal is twofold: first, it retains the amplitude and phase of the passband signal, and is thus independent of any particular carrier frequency; second, it provides the basis for modern baseband receiver implementations that use high-speed digital signal processing. The baseband representation is also known as the *complex envelope* representation.

BPSK and QPSK are linear modulation methods; in contrast, FSK is a constant-envelope modulation scheme. For binary FSK (BFSK), there are two possible signal pulses, given at baseband by

$$u_0(t) = Ae^{-j\pi\Delta ft} p_T(t), \quad u_1(t) = Ae^{j\pi\Delta ft} p_T(t),$$

where A is the amplitude. Notice that we have two (complex) tones separated by Δf. MSK (minimum-shift keying) and GMSK (Gaussian prefiltered MSK) are special forms of FSK that provide greater spectral efficiency at the cost of higher implementation efficiency. The GSM standard and its next-generation version, currently known as EDGE (for Enhanced Data Rates for Global Evolution), use GMSK.

At the receiver, the RF signal is amplified and downconverted with appropriate filtering to remove interference and noise. The downconverted signal is then passed to the demodulator, whose function is to detect (guess in an optimum way) what symbol stream was transmitted. Following demodulation (also referred to as detection), the symbol stream is sent to subsequent processing steps (channel decoding and source decoding) before delivery to the destination.

At this point it is typical to consider the BERs and spectral efficiencies of various digital modulation formats, modulator and demodulator designs, and the performance of different detection strategies for mobile cellular channels. This is beyond the scope of this section, and we direct the reader to a good book on digital communications (e.g., References 1, 4, 6, 7, 8) for more information.

Diversity, Spread Spectrum, and CDMA

A mobile wireless channel causes the transmitted signal to arrive at the receiver via a number of paths due to reflections from objects in the environment. If the channel is linear (including transmit and receive amplifiers), a simple modeling approach for this multipath channel is to assume that it is specular, i.e., each path results in a specific amplitude, time delay, and phase change. If the channel is also at least approximately time-invariant, its impulse response under these conditions can be expressed as[3]

$$h(t) = \sum_{\lambda=0}^{\Lambda} \alpha_\lambda e^{j\theta_\lambda} \delta(t - \tau_\lambda),$$

where α_λ, τ_λ, and θ_λ are, respectively, the amplitude, time delay, and phase for the λ-th path.

Let the transmitted signal be

$$s(t) = \sum_n a_n f_n(t),$$

a sequence of pulses $f_n(t)$ each modulated by a transmitted symbol a_n at a symbol rate of $1/T$. When transmitted via a specular multipath channel with Λ paths, the received signal — found by the convolution of the transmitted signal and the channel impulse response — is

$$y(t) = \sum_{\lambda=0}^{\Lambda} \alpha_\lambda e^{j\theta_\lambda} s(t - \tau_\lambda).$$

For simplicity, consider sending only three symbols a_{-1}, a_0, a_1. Then the received signal becomes

$$y(t) = \sum_{n=-1}^{1} a_n \sum_{\lambda=0}^{\Lambda} \alpha_\lambda e^{j\theta_\lambda} f_n(t - \tau_\lambda).$$

[3] Here $\delta(t)$ denotes the Dirac delta function.

Two effects may result: fading and intersymbol interference. *Fading* occurs when superimposed replicas of the same symbol pulse nullify each other due to phase differences. *Intersymbol interference (ISI)* is caused by the convolutive mixing of the adjacent symbols in the channels. Fading and ISI may occur individually or together depending on the channel parameters and the symbol rate T^{-1} of the transmitted signal.

Let us consider in more detail the case where the channel *delay spread* is a significant fraction of T, i.e., τ_Λ is close to, but smaller than T. In this case, we can have both fading and ISI, which, if left untreated, can severely compromise the reliability of the communication link. Direct-sequence spread-spectrum (DS/SS) signaling is a technique that mitigates these problems by using clever designs for the pulses $f_n(t)$. These pulse designs are wide bandwidth (hence "spread spectrum"), and the extra bandwidth is used to endow them with properties that allow the receiver to separate the symbol replicas.

Suppose we have a two-path channel, and consider the received signal for symbol a_0. Then the DS/SS receiver separates the two replicas

$$\alpha_0 e^{j\theta_0} a_p f_0\left(t-\tau_0\right), \quad \alpha_1 e^{j\theta_1} a_0 f_0\left(t-\tau_1\right).$$

Then each replica is adjusted in phase by multiplying it by $e^{-j\theta\lambda}$, $\lambda = 0, 1$ yielding (since $zz^* = |z|^2$)

$$\alpha_0 a_0 f\left(t-\tau_0\right), \quad \alpha_1 a_0 f\left(t-\tau_1\right).$$

Now all that remains is to delay the first replica by $\tau_1 - \tau_0$ so they line up in time, and sum them, which gives

$$\left(\alpha_0 + \alpha_1\right) a_0 f\left(t-\tau_1\right).$$

Thus DS/SS can turn the multipath channel to advantage — instead of interfering with each other, the two replicas are now added constructively. This *multipath combining* exploits the received signal's inherent *multipath diversity,* and is the basic idea behind the technology of RAKE reception[4] used in the CDMA digital cellular telephony standards.

It is important to note that this is the key idea behind all strategies for multipath fading channels: we somehow exploit the redundancy, or *diversity* of the channel (recall the multiple paths). In this case, we used the properties of DS/SS signaling to effectively split the problematic two-path channel into two benign one-path channels. Multipath diversity can also be viewed in the frequency domain, and is in effect a form of *frequency diversity.* As we will see later, frequency diversity can be used in conjunction with other forms of diversity afforded by wireless channels, including time diversity and antenna diversity.

CDMA takes the spread spectrum idea and extends it to the separation of signals from multiple *transmitters.* To see this, suppose M transmitters are sending signals simultaneously, and assume for simplicity that we have a single-path channel. Let the complex (magnitude/phase) gain for channel m be denoted by $\beta^{(m)}$. Finally, the transmitters use different spread-spectrum pulses, denoted by $f^{(m)}(t)$. If we just consider the zeroth transmitted symbols from each transmitter, we have the received signal

$$y\left(t\right) = \sum_{m=1}^{M} \beta^{(m)} a_0^{(m)} f^{(m)}\left(t - t_m\right)$$

where the time offset t_m indicates that the pulses do not necessarily arrive at the same time.

[4] The RAKE nomenclature can be traced to the block diagram representation of such a receiver — it is reminiscent of a garden rake.

The above equation represents a complicated mixture of the signals from multiple transmitters. If narrowband pulses are used, they would be extremely difficult — probably impossible — to separate. However, if the pulses are spread-spectrum, then the receiver can use algorithms to separate them from each other, and successfully demodulate the transmitted symbols. Of course, these ideas can be extended to many transmitters sending long strings of symbols over multipath channels.

Why is it called CDMA? It turns out that the special properties of the signal pulses $f^{(m)}(t)$ for each user (transmitter) m derive from high-speed *codes* consisting of periodic sequences of chips $c_k^{(m)}$ that modulate chip waveforms $\varphi(t)$. One way to envision it is to think of $\varphi(t)$ as a rectangular pulse of duration $T_c = T/N$. The pulse waveform for user m can then be written

$$f^{(m)}(t) = \sum_{k=0}^{N-1} c_k^{(m)} \varphi(t - kT_c).$$

The fact that we can separate the signals means that we are performing code-division multiple access — dividing up the channel resource by using codes. Recall that in FDMA this is done by allocating frequency bands, and in TDMA, time slots. The pulse waveforms in CDMA are designed so that many users' signals occupy the entire bandwidth simultaneously, yet can still be separated in the receiver. The signal-separating capability of CDMA is extremely important, and can extend beyond separating desired signals within a cell. For example, the IS-95 CDMA standard uses spread-spectrum pulse designs that enable the receiver to reject a substantial amount of co-channel interference (interference due to signals in other cells). This gives the IS-95 system (as well as its proposed 3G descendants) its well-known property of universal frequency reuse.

The advantages of DS/SS signals derive from what are called their *deterministic correlation* properties. For an arbitrary periodic sequence $\{c_k^{(m)}\}$, the deterministic *autocorrelation* is defined as

$$\phi^{(m)}(i) = \frac{1}{N} \sum_{k=0}^{N-1} c_k^{(m)} c_{k+i}^{(m)},$$

where i denotes the relative shift between two replicas of the sequence. If $\{c_k^{(m)}\}$ is a direct-sequence spreading code, then

$$\phi^{(m)}(i) \approx \begin{cases} 1, & i = 0 \\ 0, & 1 < |i| < N. \end{cases}$$

This "thumbtack" autocorrelation implies that relative shifts of the sequence can be separated from each other. Noting that each chip is a fraction of a symbol duration, we see that multipath replicas of a symbol pulse can be separated even if their arrival times at the receiver differ by less than a symbol duration.

CDMA signal sets also exhibit special deterministic *cross-correlation* properties. Two spreading codes $\{c_k^{(l)}\}$, $\{c_k^{(m)}\}$ of a CDMA signal set have the cross-correlation property

$$\phi^{(l,m)}(i) = \frac{1}{N} \sum_{k=0}^{N-1} c_k^{(l)} c_{k+i}^{(m)} \approx \begin{cases} 1, & l = m, i = 0, \\ 0, & l = m, 0 < |i| < N, \\ 0, & l \neq m. \end{cases}$$

Thus, we have a set of sequences with zero cross-correlations and "thumbtack" autocorrelations. (Note that this includes the earlier autocorrelation as a special case.) The basic idea of demodulation for CDMA is as follows: if the signal from user m is desired, the incoming received signal — a mixture of multiple transmitted signals — is correlated against $\{c_k^{(m)}\}$. Thus multiple replicas of a symbol from user m can be separated, delayed, and then combined, while all other users' signals (i.e., where $l \neq m$) are suppressed by the correlation.

Details of these properties, their consequences in demodulation, and descriptions of specific code designs can be found in References 3, 4, 7, and 10.

Channel Coding, Interleaving, and Time Diversity

As we have mentioned, channel coding is a transmitter function that is performed after source coding, but before modulation. The basic idea of channel coding is to introduce highly structured redundancy into the signal that will allow the receiver to easily detect or correct errors introduced in the transmission of the signal.

Channel coding is fundamental to the success of modern wireless communication. It can be considered the cornerstone of digital communication, since, without coding, it would not be possible to approach the fundamental limits established by Shannon's information theory.[9,12]

The easiest type of channel codes to understand are *block codes:* a sequence of input symbols of length k is transformed into a code sequence (codeword) of length $n > k$. Codes are often identified by their rate R, where $R = k/n \leq 1$. Generally, codes with a lower rate are more powerful. Almost all block codes are *linear,* meaning that the sum of two codewords is another codeword. By enforcing this linear structure, coding theorists have found it easier to find codes that not only have good performance, but have reasonably simple decoding algorithms as well.

In wireless systems, *convolutional codes* are very popular. Instead of blocking the input stream into length-k sequences and encoding each one independently, convolutional coders are finite-state sequential machines. Therefore they have memory, so that a particular output symbol is determined by a contiguous sequence of input symbols. For example, a rate-1/2 convolutional coder outputs two code symbols for each information symbol that arrives at its input. Normally, these codes are also linear.

Error-correcting codes have enough power so that errors can actually be corrected in the receiver. Systems that use these codes are called *forward error-control (FEC)* systems. *Error-detecting codes* are simpler, but less effective: they can tell *whether* an error has occurred, but not where the error is located in the received sequence, so it cannot be corrected.

Error-detecting codes can be useful when it is possible for the receiver to request retransmission of a corrupted codeword. Systems that employ this type of feedback are called *ARQ,* or Automatic Repeat-reQuest systems.

As we have seen, the fading in cellular systems is due to multipath. Of course, as the mobile unit and other objects in the environment move, the physical structure of the channel changes with time, causing the fading of the channel to vary with time. However, this fading process tends to be slow relative to the symbol rate, so a long string of coded symbols can be subjected to a deep channel fade. In other words, the fading from one symbol to the next will be highly correlated. Thus, the fades can cause a large string of demodulation (detection) errors, or an *error burst.* Thus, fading channels are often described from the point of view of coding as *burst-error channels.*

Most well-known block and convolutional codes are best suited to random errors, that is, errors that occur in an uncorrelated fashion and thus tend to occur as isolated single errors. While there have been a number of codes designed to correct burst errors, the theory of random error-correcting codes is so well developed that designers have often chosen to use these codes in concert with a method to "randomize" error bursts.

This randomization method, called *interleaving,* rearranges, or scrambles, the coded symbols in order to minimize this correlation so that errors are isolated and distributed across a number of codewords. Thus, a modest random-error correcting code can be combined with interleaving that is inserted between the channel coder and the modulator to shuffle the symbols of the codewords. Then, in the receiver, the de-interleaver is placed between the demodulator and the decoder is reassemble the codewords for decoding.

We note that a well-designed coding/interleaving system does more than redistribute errors for easy correction: it also exploits *time diversity.* In our discussion of spread-spectrum and CDMA, we saw how the DS/SS signal exploits the frequency diversity of the wireless channel via its multipath redundancy. Here, the redundancy added by channel coding/interleaving is designed so that, in addition to the usual performance increase due to just the code — the *coding gain* — there is also a benefit to distributing the redundancy in such a way that exploits the time variation of the channel, yielding a *time diversity gain.*

In this era of digital data over wireless, high link reliability is required. This is in spite of the fact that most wireless links have a raw bit error rate (BER) on the order of 1 in 1000. Clearly, we would like to see an error rate of 1 in 10^{12} or better. How is this astounding improvement achieved? The following two-level approach has proved successful. The first level employs FEC to correct a large percentage of the errors. This code is used in tandem with a powerful error-detecting algorithm to find the rare errors that the FEC cannot find and correct. This combined FEC/ARQ approach limits the amount of feedback to an acceptable level while still achieving the necessary reliability.

Nonlinear Channels

Amplifiers are more power-efficient if they are driven closer to saturation than if they are kept within their linear regions. Unfortunately, nonlinearities that occur as saturation is approached lead to *spectral spreading* of the signal. This can be illustrated by observing that an instantaneous (or memoryless) nonlinearity can be approximated by a polynomial. For example, a quadratic term effectively squares the signal; for a sinusoidal input this leads to double-frequency terms.

A more sophisticated perspective comes from noting that the nonlinear amplification can distort the symbol pulse shape, expanding the spectrum of the pulse. Nonlinearities of this type are said to cause AM/AM distortion. Amplifiers can also exhibit AM/PM conversion, where the output phase of a sinusoid is shifted by different amounts depending on its input power — a serious problem for PSK-type modulations.

A great deal of effort has gone into finding transmitter designs that allow more efficient amplifier operation. For example, constant-envelope modulation schemes are insensitive to nonlinearities, and signaling schemes that reduce the peak-to-average power ratio (PAPR) of the signal allow higher levels. Finally, methods to linearize amplifiers at higher efficiencies are receiving considerable attention.

Modeling and simulating nonlinear effects on system performance is a nontrivial task. AM/AM and AM/PM distortions are functions of frequency, so if wideband amplifier characterization is required, a family of curves is necessary. Even then the actual wideband response is only approximated, since these systems are limited in bandwidth and thus have memory. More accurate results in this case can be obtained using Volterra series expansions, or numerical solutions to nonlinear differential equations. Sophisticated approaches are becoming increasingly important in cellular as supported data rates move higher and higher. More information can be found in References 1 and 5 and the references therein.

Antenna Arrays

We have seen earlier how sectorized antennas can be used to increase system performance. They are one of the most economical forms of multielement antenna systems, and can be used to reduce interference or to increase user capacity. A second use of multielement systems is to exploit the *spatial diversity* of the wireless channel. Spatial diversity approaches assume that the received antenna elements are immersed in a signal field whose strength varies strongly with position due to a superposition of multipath signals arriving via various directions. The resulting element signal strengths are assumed to be at least somewhat statistically uncorrelated. This spatial uncorrelatedness is analogous to the uncorrelatedness over time or frequency that is exploited in mobile channels.

One of the simplest approaches is to use multiple (normally omnidirectional in azimuth) antenna elements at the receiver, and choose the one with the highest signal-to-noise ratio. More sophisticated schemes combine — rather than select just one of — the element signals to further improve the signal-to-noise ratio at the cost of higher receiver complexity. These approaches date from the 1950s, and do not take into account other interfering mobile units. These latter schemes are often grouped under the category of *antenna diversity* approaches.

More recently, a number of proposals for systems that combine error-control coding mechanisms with multiple elements have been made under the name of *space-time coding*. One of the main contributions of these efforts has been the recognition that multiple-element transmit antennas can, under certain conditions, dramatically increase the link capacity.

Another approach, beamforming or phased-array antennas, is also positioned to play a role in future systems under the new moniker *smart antennas*. Space-time coding and smart antenna methods can be seen as two approaches to exploiting the capabilities of multiple-input/multiple-output (MIMO) systems. However, in contrast to space-time coding approaches, strong inter-element correlation based on the direction of arrival of plane waves is assumed in smart antennas. The basic idea of smart antennas is to employ an array of antenna elements connected to an amplitude- and phase-shifting network to adaptively tune (steer electronically) the antenna pattern based on the geographic placement of mobile units. Much of the groundwork for smart antenna systems was laid in the 1950s in military radar research. The ultimate goal of these approaches can be stated as follows: to track individual mobile units with optimized antenna patterns that maximize performance (by maximizing the ratio of the signal to the sum of interference and noise) minimize power consumption at the mobile unit, and optimize the capacity of the cellular system. One can conjecture that the ultimate solution to this problem will be a class of techniques that involve joint design of channel coding, modulation, and antenna array processing in an optimum fashion.

Summary

Almost all wireless networks are distinguished by the characteristic of a shared channel resource, and this is in fact the key difference between wireless and wired networks. Another important difference between wired and wireless channels is the presence of multipath in the latter, which makes diversity possible. What is it that distinguishes cellular from other wireless services and systems? First, it historically has been designed for mobile telephone users, and has been optimized for carrying human voice. This has led to the following key traits of cellular:

- efficient use of spectrum via the cellular concept;
- system designs, including channel access mechanisms, that efficiently handle large numbers of uniform — i.e., voice — links; and
- difficult channels: user mobility causes fast variations in channel signal characteristics compared with other wireless applications such as wireless local area networks.

We close by mentioning two apparent trends. First, as we mentioned at the outset of this article, wireless local loop services, where home telephone subscribers use wireless phones — and the “last mile” is wireless rather than copper — are a new application for mobile wireless technology. Secondly, at this time there is a great deal of effort to make next-generation cellular systems useful for data networking in addition to voice. Certainly, the amount of data traffic on these networks will grow. However, one of the largest questions for the next ten years is whether mobile wireless will win the growing data market, or if new data-oriented wireless networks will come to dominate.

References

1. Zeng, M., Annamalai, A., and Bhargava, V. K., Recent advances in cellular wireless communications, *IEEE Communications Magazine*, 37, 9, 128–138, September 1999.
2. Walrand, J., and Varaiya, P., *High-Performance Communication Networks*, Morgan Kaufman, San Francisco, CA, 1996.
3. Chaudhury, P., Mohr, W., and Onoe, S., The 3GPP proposal for IMT-2000, *IEEE Communications Magazine*, 37 (12), 72–81, December 1999.

4. Anderson, J. B., *Digital Transmission Engineering,* IEEE Press, Piscataway, NJ, 1999.
5. Lee, E. A., and Messerschmitt, D. G., *Digital Communication,* Kluwer Academic, second edition, 1994.
6. Proakis, J. G., *Digital Communications,* 3rd ed., McGraw-Hill, New York, 1995.
7. Haykin, S., *Communication Systems,* Wiley, New York, 1994.
8. Proakis, J. G., and Salehi, M., *Communication Systems Engineering,* Prentice-Hall, Englewood Cliffs, NJ, 1994.
9. Flikkema, P., Introduction to spread spectrum for wireless communication: a signal processing perspective, *IEEE Spectrum Processing Magazine,* 14, 3, 26–36, May 1997.
10. Viterbi, A. J., *CDMA: Principles of Spread Spectrum Communication,* Addison-Wesley, 1995.
11. Shannon, C. E., Communication in the presence of noise, *Proceedings of the IRE,* 37, 1,10–21, January 1949.
12. Wyner, A. D., and Shamai (Shitz), S., Introduction to "Communication in the presence of noise" by C. E. Shannon, *Proceedings of the IEEE,* 86, 2, 442–446, February 1998. Reprinted in the *Proceedings of the IEEE,* vol. 86, no. 2, February 1998, 447–457.
13. Jeruchim, M. C., Balaban, P., and Shanmugan, K. S., *Simulation of Communication Systems,* Plenum, New York, 1992.

2.2 Nomadic Communications

Andy D. Kucar

Nomadic peoples of desert oases, tropical jungles, steppes, tundras, and polar regions have shown a limited interest in mobile radio communications, at the displeasure of some urbanite investors in mobile radio communications. The focus of this contribution with a delegated title *Nomadic Communications* is on terrestrial and satellite mobile radio communications used by urbanites while roaming urban canyons or golf courses, and by suburbanites who, every morning, assemble their sport utility vehicles and drive to urban jungles hunting for jobs. The habits and traffic patterns of these users are important parameters in the analysis and optimization of any mobile radio communications system. The mobile radio communications systems addressed in this contribution and illustrated in Fig. 2.6 include:

1. the first generation *analog cellular mobile radio systems* such as North American AMPS, Japanese MCS, Scandinavian NMT, and British TACS. These systems use analog voice data and frequency modulation (FM) for the transmission of voice, and coded digital data and a frequency shift keying (FSK) modulation scheme for the transmission of control information. Conceived and designed in the 1970s, these systems were optimized for vehicle-based services such as police and ambulances operating at possibly high vehicle speeds. The first generation *analog cordless telephones* include CT0 and CT1 cordless telephone systems, which were intended for use in the household environment;
2. the second generation *digital cellular and personal mobile radio systems* such as *Global System for Mobile Communications* (GSM), *Digital* AMPS > IS–54/136, DCS 1800/1900, and *Personal Digital Cellular* (PDC), all Time Division Multiple Access (TDMA), and IS–95 *spread spectrum Code* Division Multiple Access (CDMA) systems. All mentioned systems employ digital data for both voice and control purposes. The second generation *digital cordless telephony systems* include CT2, CT2Plus, CT3, *Digital Enhanced Cordless Telephone* (DECT), and *Personal Handyphone System* (PHS); *wireless data mobile radio systems* such as ARDIS, RAM, TETRA, *Cellular Digital Packet Data* (CDPD), IEEE 802.11 *Wireless Local Area Network* (WLAN), and recently announced Bluetooth; there are also projects known as *Personal Communication Network* (PCN), *Personal Communications Systems* (PCS) and FPLMTS > UMTS > IMT–2000 > 3G, where 3G stands for the third generation systems. The second generation systems also include *satellite mobile radio systems* such as INMARSAT, OmniTRACS, MSAT, AUSSAT, Iridium, Globalstar, and ORBCOMM.

After a brief prologue and historical overview, technical issues such as the repertoire of systems and services, the airwaves management, the operating environment, service quality, network issues and cell

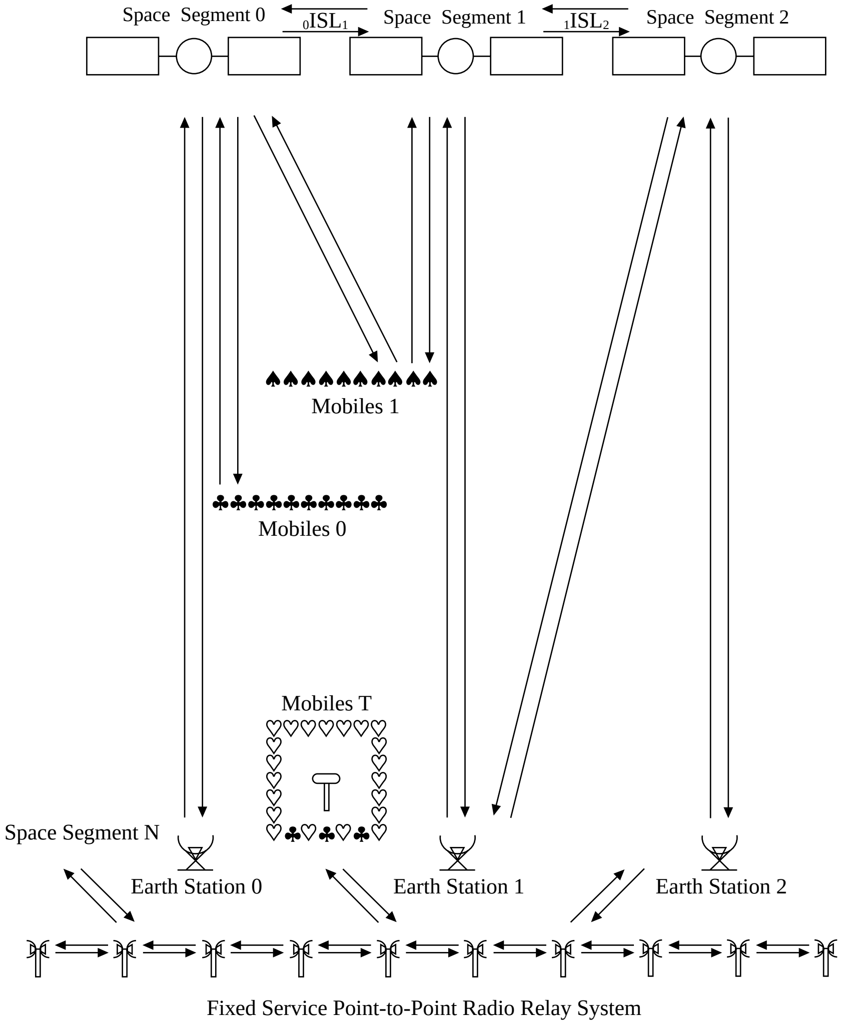

FIGURE 2.6 A Model of Fixed and Mobile, Satellite and Terrestrial Systems.

size, channel coding and modulation, speech coding, diversity, multiple broadcasting (FDMB, TDMB, CDMB), and multiple access (FDMA, TDMA, CDMA) are briefly discussed.

Many existing mobile radio communications systems collect some form of information on network behavior, users' positions, etc., with the purpose of enhancing the performance of communications, improving handover procedures and increasing the system capacity. Coarse positioning is usually achieved inherently, while more precise positioning and *navigation* can be achieved by employing LORAN-C and/or GPS, GLONASS, WAAS signals, or some other means, at an additional, usually modest, increase in cost and complexity.

Prologue

Mobile radio systems provide their users with opportunities to travel freely within the service area while being able to communicate with any telephone, fax, data modem, and electronic mail subscriber anywhere in the world; to determine their own positions; to track the precious cargo; to improve the management of fleets of vehicles and the distribution of goods; to improve traffic safety; to provide vital communication links during emergencies, search and rescue operations, to browse their favorites Websites, etc. These

TABLE 2.1 Glossary of Terms

AMPS	Advanced Mobile Phone Service
ASIC	Application Specific Integrated Circuits
BER	Bit Error Rate
CAD	Computer Aided Design
CB	Citizen Band (mobile radio)
CDMA	Spread spectrum Code Division Multiple Access
CEPT	Conference of European Postal and Telecommunications (Administrations)
CT	Cordless Telephony
DOC	Department of Communications (in Canada)
DSP	Digital Signal Processing
FCC	Federal Communications Commission (in USA)
FDMA	Frequency Division Multiple Access
FPLMTS	Future Public Land Mobile Telecommunications Systems
GDSS	Global Distress Safety System
GOES	Geostationary Operational Environmental Satellites
GPS	Global Positioning System
GSM	Groupe Spécial Mobile (now Global System for Mobile communications)
ISDN	Integrated Service Digital Network
ITU	International Telecommunications Union
MOS	Mean Opinion Score
MMIC	Microwave Monolithic Integrated Circuits
NMC	Network Management Center
NMT	Nordic Mobile Telephone (system)
PCN	Personal Communications Networks
PCS	Personal Communications Systems
PSTN	Public Switched Telephone Network
SARSAT	Search And Rescue Satellite Aided Tracking system
SERES	SEarch and REscue Satellite
TACS	Total Access Communication System
TDMA	Time Division Multiple Access
WAAS	Wide Area Augmentation System
WARC	World Administrative Radio Conference
WRC	World Radiocommunications Conference

Source: 4U Communications Research Inc., 2000.06.10~00:09, Updated: 2000.05.03

tieless (*wireless, cordless*) communications, the exchange of information, and the determination of position, course, and distance traveled are made possibly by the unique property of the radio to employ an *aerial* (*antenna*) for radiating and receiving electromagnetic waves. When the user's radio antenna is stationary over a prolonged period of time, the term *fixed radio* is used. A radio transceiver capable of being carried or moved around, but stationary when in operation, is called a *portable radio*. A radio transceiver capable of being carried and used, by a vehicle or by a person on the move, is called *mobile radio, personal and/or handheld device*. Individual radio users may communicate directly, or via one or more intermediaries, which may be *passive radio repeater(s), base station(s)*, or *switch(es)*. When all intermediaries are located on the Earth, the terms *terrestrial radio system* and *radio system* have been used. When at least one intermediary is a satellite borne, the terms *satellite radio system* and *satellite system* have been used. According to the location of a user, the terms *land, maritime, aeronautical, space,* and *deep-space radio systems* have been used. The second unique property of all terrestrial and satellite radio systems is that they share the same natural resource — the *airways* (*frequency bands* and *space*).

Recent developments in microwave monolithic integrated circuit (MMIC), application specific integrated circuit (ASIC), analog/digital signal processing (A/DSP), and battery technology, supported by computer-aided design (CAD) and robotics manufacturing allow the viable implementation of miniature radio transceivers at radio frequencies as high as 6 GHz, i.e., at wavelengths as short as about 5 cm. Up to these frequencies additional spectra have been assigned to mobile services; corresponding shorter wavelengths allow a viable implementation of adaptive antennas necessary for improvement of the quality of transmission and spatial frequency spectrum efficiency. The continuous flux of market forces (excited by the possibilities of a myriad of new services and great profits), international and domestic standard forces (who manage a common natural resource — the airwaves), and technology forces (capable of creating viable products) acted harmoniously and created a broad choice of communications (voice and data), information, and navigation systems, which propelled the explosive growth of mobile radio services for travelers.

A Glimpse of History

Late in the 19th century, Heinrich Rudolf Hertz, Nikola Tesla, Alexander Popov, Edouard Branly, Oliver Lodge, Jagadis Chandra Bose, Guglielmo Marconi, Adolphus Slaby, and other engineers and scientists experimented with the transmission and reception of electromagnetic waves. In 1898 Tesla made a demonstration in Madison Square Garden of a radio remote controlled boat; later the same year Marconi established the first wireless ship-to-shore telegraph link with the royal yacht Osborne. These events are now accepted as the birth of the mobile radio. Since that time, mobile radio communications have provided safe navigation for ships and airplanes, saved many lives, dispatched diverse fleets of vehicles, won many battles, generated many new businesses, etc.

Satellite mobile radio systems launched in the seventies and early eighties use ultrahigh frequency (UHF) bands around 400 MHz and around 1.5 GHz for communications and navigation services.

In the fifties and sixties, numerous private mobile radio networks, citizen band (CB) mobile radio, ham operator mobile radio, and portable home radio telephones used diverse types and brands of radio equipment and chunks of airwaves located anywhere in the frequency band from near 30 MHz to 3 GHz. Then, in the seventies, Ericsson introduced the *Nordic Mobile Telephone* (NMT) system, and AT&T Bell Laboratories introduced *Advanced Mobile Phone Service* (AMPS). The impact of these two *public land mobile telecommunication systems* on the standardization and prospects of mobile radio communications may be compared with the impact of Apple and IBM on the personal computer industry. In Europe systems like AMPS competed with NMT systems; in the rest of the world, AMPS, backed by Bell Laboratories' reputation for technical excellence and the clout of AT&T, became *de facto* and *de jure* the technical standard (British TACS and Japanese MCS–L1 are based on). In 1982, the Conference of European Postal and Telecommunications Administrations (CEPT) established Groupe Spécial Mobile (GSM) with the mandate to define future Pan-European cellular radio standards. On January 1, 1984, during the phase of explosive growth of *AMPS* and similar cellular mobile radio communications systems and services, came the divestiture (breakup) of AT&T.

Present and Future Trends

Based on the solid foundation established in 1970s the buildup of mobile radio systems and services at the end of the second millennium is continuing at an annual rate higher than 20%, worldwide. Terrestrial mobile radio systems offer analog and digital voice and low- to medium-rate data services compatible with existing public switching telephone networks in scope, but with poorer voice quality and lower data throughput. Wireless mobile radio data networks are expected to offer data rates as high as a few Mbit/s in the near future and even more in the portable environment.

Equipment miniaturization and price are important constraints on the systems providing these services. In the early fifties, mobile radio equipment used a considerable amount of a car's trunk space and challenged the capacity of car's alternator/battery source while in transmit mode. Today, the pocket-size, ≈100-gram handheld cellular radio telephone, manual and battery charger excluded, provides a few hours of talk capacity and dozens of hours in the standby mode. The average cost of the least expensive models of battery powered cellular mobile radio telephones has dropped proportionally and has broken the $100 U.S. barrier. However, one should take the price and growth numbers with a grain of salt, since some prices and growth itself might be subsidized. Many customers appear to have more than one telephone, at least during the promotion period, while they cannot use more than one telephone at the same time.

These facts need to be taken into consideration while estimating growth, capacity, and efficiency of recent wireless mobile radio systems.

Mobile satellite systems are expanding in many directions: large and powerful single unit geostationary systems; medium-sized, low orbit multi-satellite systems; and small-sized, and low orbit multi-satellite systems, launched from a plane, see [Kucar, 1992], [Del Re, 1995]. Recently, some financial uncertainties experienced by a few technically advanced LEO satellite systems, operational and planned, slowed down explosive growth in this area. Satellite mobile radio systems currently offer analog and digital voice, low to medium rate data, radio determination, and global distress safety services for travelers.

During the last five years numerous new digital radio systems for mobile users have been deployed. Presently, users in many countries have been offered between 5 and 10 different mobile radio communications systems to choose from. There already exists radio units capable of operating on two or more different systems using the same frequency band or even using a few different frequency bands. Overviews of mobile radio communications systems and related technical issues can be found in [Davis, 1984], [Cox, 1987], [Mahmoud, 1989], [Kucar, 1991], [Rhee, 1991], [Steele, 1992], [Chuang, 1993], [Cox, 1995], [Kucar, 1991], [Cimini, March 1999], [Mitola, 1999], [Cimini, July 1999], [Ariyavisitakul, 1999], [Cimini, November 1999], [Oppermann, 1999] and [Oppermann, 2000].

Repertoire of Systems and Services

The variety of services offered to travelers essentially consists of information in analog and/or digital form. Although most of today's traffic consists of analog or digital voice transmitted by analog frequency modulation FM (or phase modulation PM), or digital quadrature amplitude modulation (QAM) schemes, digital signaling, and a combination of analog and digital traffic, might provide superior frequency reuse capacity, processing, and network interconnectivity. By using a powerful and affordable microprocessor and digital signal processing chips, a myriad of different services particularly well suited to the needs of people on the move could be realized economically. A brief description of a few elementary systems/services currently available to travelers follows. Some of these elementary services can be combined within the mobile radio units for a marginal increase in the cost and complexity with respect to the cost of a single service system; for example, a mobile radio communications system can include a positioning receiver, digital map, Web browser, etc.

Terrestrial systems. In a terrestrial mobile radio network labeled Mobiles T in Fig. 2.6, a repeater was usually located at the nearest summit offering maximum service area coverage. As the number of users increased, the available frequency spectrum became unable to handle the increase traffic, and a need for frequency reuse arose. The service area was split into many subareas called cells, and the term *cellular radio* was born. The frequency reuse offers an increased overall system capacity, while the smaller cell size can offer an increased service quality, but at the expense of increased complexity of the user's terminal and network infrastructure. The trade-offs between real estate complexity, and implementation dynamics dictate the shape and the size of the cellular network. Increase in the overall capacity calls for new frequency spectra, smaller cells, which requires reconfiguration of existing base station locations; this is usually not possible in many circumstances, which leads to suboptimal solutions and even less efficient use of the frequency spectrum.

The *satellite systems* shown in Fig. 2.6 employ one or more satellites to serve as base station(s) and/or repeater(s) in a mobile radio network. The position of satellites relative to the service area is of crucial importance for the coverage, service quality, price, and complexity of the overall network. When a satellite encompass the Earth in 12-hour, 24-hour etc. periods, the term *geosynchronous orbit* has been used. An orbit inclined with respect to the equatorial plane is called an *inclined orbit*; an orbit with an inclination of about 90° is called a *polar orbit*. A circular geosynchronous 24-hour orbit in the equatorial plane (0° inclination) is known as the *geostationary orbit* (GSO), since from any point on the surface of the Earth, the satellite appears to be stationary; this orbit is particularly suitable for land mobile services at low latitudes, and for maritime and aeronautical services at latitudes of $< |80|°$. Systems that use geostationary satellites include INMARSAT, MSAT, and AUSSAT. An elliptical geosynchronous orbit with the inclination angle of 63.4° is known as *Tundra orbit.* An elliptical 12-hour orbit with the inclination angle of 63.4° is known as *Molniya orbit.* Both Tundra and Molniya orbits have been selected for coverage of the Northern latitudes and the area around the North Pole — for users at those latitudes the satellites appear to wander around the zenith for a prolonged period of time. The coverage of a particular region (*regional coverage*), and the whole globe (*global coverage*), can be provided by different constellations of satellites including ones in inclined and polar orbits. For example, inclined circular orbit constellations have been used by GPS (18 to 24 satellites, 55 to 63° inclination), Globalstar (48 satellites, 47° inclination), and Iridium (66 satellites, 90° inclination — polar orbits) system. All three systems provide global coverage. ORBCOM system employs Pegasus launchable low-orbit satellites to provide uninterrupted coverage of the Earth below ±60° latitudes, and an intermittent, but frequent coverage over the polar regions.

Satellite antenna systems can have one (*single beam global system*) or more beams (*multibeam spot system*). The multibeam satellite system, similar to the terrestrial cellular system, employs antenna directivity to achieve better frequency reuse, at the expense of system complexity.

Radio paging is a non-speech, one-way (from base station toward travelers), personal selective calling system with alert, without message, or with defined messages such as numeric or alphanumeric. A person wishing to send a message contacts a system operator by public switched telephone network (PSTN), and delivers his message. After an acceptable time (queuing delay), a system operator forwards the message to the traveler, by radio repeater (FM broadcasting transmitter, VHF or UHF dedicated transmitter, satellite, or cellular radio system). After receiving the message, a traveler's small (roughly the size of a cigarette pack) receiver (pager) stores the message in its memory, and on demand either emits alerting tones or displays the message.

Global Distress Safety System (*GDSS*) geostationary and inclined orbit satellites transfer emergency calls sent by vehicles to the central earth station. Examples are: *COSPAS,* Search And Rescue Satellite Aided Tracking system, *SARSAT,* Geostationary Operational Environmental Satellites *GOES,* and SEarch and REscue Satellite *SERES*). The recommended frequency for this transmission is 406.025 MHz.

Global Positioning System (*GPS*), [ION, 1980, 1984, 1986, 1993]. U.S. Department of Defense Navstar GPS 24–29 operating satellites in inclined orbits emit L band (L1 = 1575.42 MHz, L2 = 1227.6 MHz) spread spectrum signals from which an intelligent microprocessor–based receiver extracts extremely precise time and frequency information, and accurately determines its own three-dimensional position, velocity, and acceleration, worldwide. The coarse accuracy of < 100 m available to commercial users has been demonstrated by using a handheld receiver. An accuracy of meters or centimeters is possible by using the precise (military) codes and/or differential GPS (additional reference) principals and kinematic phase tracking.

Glonass is Russia's counterpart of the U.S.'s GPS. It operates in an FDM mode and uses frequencies between 1602.56 MHz and 1615.50 MHz to achieve goals similar to GPS.

Other systems have been studied by the European Space Agency (*Navsat*), and by West Germany (*Granas, Popsat,* and *Navcom*). In recent years many payloads carrying navigation transponders have been put on board of GSO satellites; corresponding navigational signals enable an increase in overall availability and improved determination of users positions. The comprehensive project, which may include existing and new radionavigation payloads, has also been known as the *Wide Area Augmentation System* (*WAAS*).

LORAN-C is the 100 kHz frequency navigation system that provides a positional accuracy between 10 and 150 m. A user's receiver measures the time difference between the master station transmitter and secondary station signals, and defines his hyperbolic line of position. North American LORAN-C coverage includes the Great Lakes, Atlantic, and Pacific Coast, with decreasing signal strength and accuracy as the user approaches the Rocky Mountains from the east. Recently, new LORAN stations have been augmented, worldwide. Similar radionavigation systems are the 100 kHz *Decca* and 10 kHz *Omega.*

Dispatch two-way radio land mobile or satellite systems, with or without connection to the PSTN, consist of an operating center controlling the operation of a fleet of vehicles such as aircraft, taxis, police cars, tracks, rail cars, etc.

TABLE 2.2 The Comparison of Dispatch WAN/LAN Systems

Parameter	US	Sweden	Japan	Australia	CDPD	IEEE 802.11
TX freq, MHz						
Base	935–941 851–866	76.0–77.5	850–860	865.00–870.00 415.55–418.05	869–894	2400–2483 2470–2499
Mobile	896–902 806–821	81.0–82.5	905–915	820.00–825.00 406.10–408.60	824–849	2400–2483 2470–2499
Duplexing method	sfFDD[a]	sFDD	sFDD	sfFDD	FDD	TDD
Channel spacing, kHz	12.5 25.00	25.0	12.5	25.0 12.5	30.0	1000
Channel rate, kb/s	≤9.6	1.2	1.2	≤	19.2	1000
# of Traffic channel	480 600	60	799	200	832	79
Modulation type:						
Voice	FM	FM	FM	FM		
Data	FSK	MSK-FM	MSK-FM	FSK	GMSK	DQPSK

[a] sfFDD stands for semi-duplex, full duplex, Frequency Division Duplex.

Similar systems are used in the Netherlands, U.K., USSR, and France.

ARDIS is a commercial system compatible with U.S. specs. 25 kHz spacing; 2FSK, 4FSK, ≤19.2 kb/s.

MOBITEX/RAM is a commercial system compatible with U.S. specs. 12.5 kHz spacing; GMSK, 8.0 kb/s.

Source: 4U Communications Research Inc., 2000.06.10~00:09, c:/tab/dispatch.sys

A summary of some of the existing and planned terrestrial mobile radio systems, including MOBITEX RAM and ARDIS, is given in Table 2.2.

OmniTRACS dispatch system employs a Ku-band geostationary satellite located at 103° W to provide two-way digital message and position reporting (derived from incorporated satellite-aided LORAN-C receiver), throughout the contiguous U.S. (CONUS).

Cellular radio or public land mobile telephone systems offer a full range of services to the traveler similar to those provided by PSTN. The technical characteristics of some of the existing and planned systems are summarized in Table 2.3.

Vehicle Information System and Intelligent Highway Vehicle System are synonyms for the variety of systems and services aimed toward traffic safety and location. This includes: traffic management, vehicle identification, digitized map information and navigation, radio navigation, speed sensing and adaptive cruise control, collision warning and prevention, etc. Some of the vehicle information systems can easily be incorporated in mobile radio communications transceivers to enhance the service quality and capacity of respective communications systems.

Airwaves Management

The airwaves (frequency spectrum and the space surrounding us) are a limited natural resource shared by several different radio users (military, government, commercial, public, amateur, etc.). Its sharing (among different users, services described in the previous section, TV and sound broadcasting, etc.), coordination, and administration is an ongoing process exercised on national, as well as on international levels. National administrations (Federal Communications Commission (FCC) in the U.S., Department of Communications (DOC), now Industry Canada, in Canada, etc.), in cooperation with users and industry, set the rules and procedures for planning and utilization of scarce frequency bands. These plans and utilizations have to be further coordinated internationally.

The International Telecommunications Union (ITU) is a specialized agency of the United Nations, stationed in Geneva, Switzerland, with more than 150 government and corporate members, responsible for all policies related to Radio, Telegraph, and Telephone. According to the ITU, the world is divided into three regions: Region 1 — Europe, including the Soviet Union, Outer Mongolia, Africa, and the Middle East west of Iran; Region 2 — the Americas, and Greenland; and Region 3 — Asia (excluding

TABLE 2.3 Comparison of Cellular Mobile Radio Systems in Bands Below 1 GHz

	System Name										
	AMPS	MCS L1	NMT	NMT	R.com		TACS		IS–54	IS–95	PDC
Parameter	NAMPS	MCS L2	900	450	2000	C450	UK	GSM	IS–136	USA	Japan
TX freq, MHz											
Base	869–894	870–885	935–960	463–468	424.8–428	461–466	935–960	890–915	869–894	869–894	810–826
Mobile	824–849	925–940	890–915	453–458	414.8–418	451–456	890–915	935–960	824–849	824–849	890–915
Max b/m eirp, dBW	22/5	19/7	22/7	19/12	20.10	22/12	22/8	27/9	27/9	/–7	/5
Multiple access	F	F	F	F	F	F	F	F/T	F/T	F/C	F/T
Duplex method	FDD	FDD	FDD	FDD	FDD	FDD	FDD	FDD	FDD	FDD	FDD
Channel bw, kHz	30.0	25.0	12.5	25.0	12.5	20.0	25.0	200.0	30.0	1250	25
	10.0	12.5				10.0	12.5				
Channels/RF	1	1	1	1	1	1	1	8	3	42	3
Channels/band	832	600	1999	200	160	222	1000	125 × 8	832 × 3	*n* × 42	640 × 3
	2496	1200									
Voice/Traffic:	analog	analog	analog	analog	analog	analog	analog	RELP	VSELP	CELP	VSELP
comp. or kb/s	2:1	2:1	2:1	2:1	2:1	2:1	2:1	13.0	8.0	≤9.6	6.7
modulation	PM	PM	PM	PM	PM	PM	PM	GMSK π/4	B/OQ	π/4	
kHz and/or kb/s	±12	±5	±5	±5	±2.5	±4	±9.5	270.833	48.6	1228.8	42.0
Control:	digital	digital	digital	digital	digital	digital	digital	digital	digital	digital	digital
modulation	FSK	FSK	FFSK	FFSK	FFSK	FSK	FSK	GMSK	π/4	B/OQ	π/4
bb waveform	Manch.	Manch.	NRZ	NRZ	Manch.	NRZ	NRZ	NRZ	NRZ		
	NRZ	NRZ									
kHz and/or kb/s	±8.0/10	±4.5/0.3	±3.5/1.2	±3.5/1.2	±1.7/1.2	±2.5/5.3	±6.4/8.0	270.833	48.6	1228.8	42.0
Channel coding:	BCH	BCH	B1 Hag.	B1 Hag.	Hag.	BCH	BCH	RS	Conv.	Conv.	Conv.
base→mobile	(40,28)	(43,31)	burst	burst	(19,6)	(15,7)	(40,28)	(12,8)	1/2	6/11	9/17
mobile→base	(48,36)	a.(43,31)	burst	burst	(19,6)	(15,7)	(48,36)	(12,8)	1/2	1/3	9/17
		p.(11,07)									

Note: Multiple Access: F = Frequency Division Multiple Access (FDMA), F/T = Hybrid Frequency/Time DMA, F/C = Hybrid Frequency/Code DMA.
π/4 corresponds to the π/4 shifted differentially encoded QPSK with α = 0.35 square root raised–cosine filter for IS–136 and α = 0.5 for PDC.
B/OQ corresponds to the BPSK outbound and OQPSK modulation scheme inbound.
comp. or kb/s stands for syllabic compandor or speech rate in kb/s; kHz and/or kb/s stands for peak deviation in kHz and/or channel rate kb/s.
IS–634 standard interface supports AMPS, NAMPS, TDMA and CDMA capabilities.
IS–651 standard interface supports **A** GSM capabilities and **A**+ CDMA capabilities.
Source: 4U Communications Research Inc., 2000.06.10~00:09

parts west of Iran and Outer Mongolia), Australia, and Oceania. Historically, these three regions have developed, more or less independently, their own frequency plans, which best suit local purposes. With the advent of satellite services and globalization trends, the coordination between different regions becomes more urgent. Frequency spectrum planning and coordination is performed through ITU's bodies such as: Comité Consultatif de International Radio (CCIR), now ITU-R, International Frequency Registration Board (IFRB), now ITU-R, World Administrative Radio Conference (WARC), and Regional Administrative Radio Conference (RARC).

ITU-R, through it study groups, deals with technical and operational aspects of radio communications. Results of these activities have been summarized in the form of reports and recommendations published every four years, or more often, [ITU, 1990]. IFRB serves as a *custodian* of a common and scarce natural resource — the *airwaves*; in its capacity, the IFRB records radio frequencies, advises the members on technical issues, and contributes on other technical matters. Based on the work of ITU-R and the national administrations, ITU members convene at appropriate RARC and WARC meetings, where documents on frequency planning and utilization, the *Radio Regulations,* are updated. The actions on a national level follow, see [RadioRegs, 1986], [WARC, 1992], [WRC, 1997]. The far-reaching impact of mobile radio communications on economies and the well-being of the three main trading blocks, other developing and third world countries, and potential manufacturers and users, makes the airways (frequency spectrum) even more important.

The International Telecommunications Union (ITU) recommends the composite *bandwidth-space-time* domain concept as a measure of spectrum utilization. The *spectrum utilization factor* $U = B \cdot S \cdot T$ is defined as a product of the frequency bandwidth B, spatial component S, and time component T. Since mobile radio communications systems employ single omnidirectional antennas, their S factor will be rather low; since they operate in a single channel arrangement, their B factor will be low; since new digital schemes tend to operate in a packet/block switching modes which are inherently loaded with a significant amount of overhead and idle traffic, their T factor will be low as well. Consequently, mobile radio communications systems will have a poor spectrum utilization factors.

The model of a mobile radio environment, which may include different sharing scenarios with fixed service and other radio systems, can be described as follows. Objects of our concern are *events* (for example, conversation using a mobile radio, measurements of amplitude, phase and polarization at the receiver) occurring in *time* $\{u^0\}$, *space* $\{u^1, u^2, u^3\}$, *spacetime* $\{u^0, u^1, u^2, u^3\}$, *frequency* $\{u^4\}$, *polarization* $\{u^5, u^6\}$, and *airwaves* $\{u^0, u^1, u^2, u^3, u^4, u^5, u^6\}$, see Table 2.4. The coordinate $\{u^4\}$ represents frequency resource, i.e., bandwidth in the spacetime $\{u^0, u^1, u^2, u^3\}$. Our goal is to use a scarce natural resource — the airwaves in an environmentally friendly manner.

TABLE 2.4 The Multidimensional Spaces Including the Airwaves

u^0	time		
u^1			
u^2	space	spacetime	
u^3			airwaves
u^4	frequency/bandwidth		
u^5	polarization		
u^6			
u^7			
u^8	Doppler		
u^9			
u^A	users: government/military, commercial/public, fixed/mobile, terrestrial/satellite …		
u^B			
⋮			
u^n			

Source: 4U Communications Research Inc. 2000.06.10~00:09, c:/tab/airwaves.1

When users/events are divided (sorted, discriminated) along the time coordinate u^0, the term *time division* is employed for function $f(u^0)$. A division $f(u^4)$ along the frequency coordinate u^4 corresponds to the *frequency division*. A division $f(u^0, u^4)$ along the coordinates (u^0, u^4) is usually called a *code division* or *frequency hopping*. A division $f(u^1, u^2, x^3)$ along the coordinates (u^1, u^2, u^3) is called the *space division*. Terrestrial cellular and multibeam satellite radio systems are vivid examples of the space division concepts. Coordinates $\{u^5, u^6\}$ may represent two orthogonal polarization components, horizontal and vertical or right-handed and left-handed circular; a division of users/events according to their polarization components may be called the *polarization division*. Any division $f(u^0, u^1, u^2, u^3, u^4, u^5, u^6)$ along the coordinates $(u^0, u^1, u^2, u^3, u^4, u^5, u^6)$ may be called the *airwaves division*. Coordinates $\{u^7, u^8, u^9\}$ may represent velocity (or Doppler frequency) components; a division of users/events according to their Doppler frequencies similar to the moving target indication (MTI) radars may be called the *Doppler frequency division*. We may also introduce coordinate $\{u^4\}$ to represent users, divide the airways along the coordinate $\{u^A\}$ (military, government, commercial, public, fixed, mobile, terrestrial, satellite, and others) and call it the *users division*. Generally, the segmentations of frequency spectra to different users lead to uneven use and uneven spectral efficiency factors among different segments.

In analogy with division, we may have time, space, frequency, code, airwaves, polarization, Doppler, users, $\{u^\alpha, \ldots, u^\omega\}$ *access* and *diversity*. Generally, the signal space may be described by m coordinates $\{u^0, \ldots, u^{m-1}\}$. Let each signal component has k degrees of freedom. At the transmitter site, each signal can be radiated via n_T antennas, and received at n_R receiver antennas. There is a total of $n = n_T + n_R$ antennas, two polarization components, and L multipath components, i.e., paths between transmitter and receiver antennas. Thus, the total number of degrees of freedom $m = k \times n \times 2 \times L$. For example, in a typical land mobile environment 16 multipath components can exist; if one wants to study a system with four antennas on the transmitter side and four antennas on the receiver side, and each antenna may employ both polarizations, then the number of degrees of freedom equals $512 \times k$. By selecting a proper coordinate system and using inherent system symmetries, one might be able to reduce the number of degrees of freedom to a manageable quantity.

Operating Environment

A general configuration of terrestrial FS radio systems, sharing the same space and frequency bands with FSS and/or MSS systems, is illustrated in Fig. 2.6. The emphasis of this contribution is on mobile systems; however, it should be appreciated that mobile systems may be required to share the same frequency band with fixed systems. A *satellite system* usually consists of many earth stations, denoted Earth Station 0 … Earth Station 2 in Fig. 2.6, one or many space segments, denoted Space Segment 0 … Space Segment N, and in the case of a *mobile satellite system* different types of mobile segments denoted by ♣ and ♠ in the same figure. Links between different Space Segments and mobile users of MSS systems are called *service links*; links connecting Space Segments and corresponding Earth Stations are called *feeder links*. FSS systems employ Space Segments and fixed Earth Station segments only; corresponding connections are called *service links*. Thus, technically similar connections between Space Segments and fixed Earth Station segments perform different functions in MSS and FSS systems and are referred to by different names. Administratively, the feeder links of MSS systems are often referred to as FSS.

Let us briefly assess spectrum requirements of an MSS system. There exist many possibilities of how and where to communicate in the networks shown in Fig. 2.6. Each of these possibilities can use different spatial and frequency resources, which one needs to assess for sharing purposes. For example, a mobile user ♣ transmits at frequency f_0 using a small hemispherical antenna toward Space Segment 0. This space segment receives a signal at frequency f_0, transposes it to frequency F_{n+0}, amplifies it and transmits it toward Earth Station 0. This station processes the signal, makes decisions on the final destination, sends the signal back toward the same Space Segment 0, which receives the signal at frequency f_{m+0}. This signal is transposed further to frequency F_{k+0} and is emitted via *inter-satellite link* ${}_0\text{ISL}_1$ toward Space Segment 1, which receives this signal, processes it, transposes it, and emits toward the earth and mobile ♠ at frequency F_1. In this process a quintet of frequencies $(f_0, F_{n+0}, f_{m+0}, F_{k+0}, F_1)$ is used in one direction.

Once the mobile ♠ receives the signal, its set rings and sends back the signal in reverse directions at a different frequency quintet (or a different time slot, or a different code, or any combination of time, code, and frequency), thus establishing the two-way connection. Obviously, this type of MSS system uses significant parts of the frequency spectrum.

Mobile satellite systems consist of two directions with very distinct properties. A direction from an Earth Station, also called a *hub* or *base station,* which may include a *Network Management Center* (NMC), toward the satellite space segment and further toward a particular mobile user is known as the *forward* direction. In addition, we will call this direction the *dispatch* direction, *broadcast* direction, or *division* direction, since the NMC dispatches/broadcasts data to different users and data might be divided in frequency (F), time (T), code (C), or a hybrid (H) mode. The opposite direction from a mobile user toward the satellite space segment and further toward the NMC is known as the *return* direction. In addition, we will call this direction the *access* direction, since mobile users usually need to make attempts to access the mobile network before a connection with NMC can be established; in some networks the NMC may poll the mobile users, instead. A connection between NMC and a mobile user, or between two mobile users, may consist of two or more hops, including inter-satellite links, as shown in Fig. 2.6.

While traveling, a customer — a *user of a cellular mobile radio system* — may experience sudden changes in signal quality caused by his movements relative to the corresponding base station and surroundings, multipath propagation, and unintentional jamming such as man-made noise, adjacent channel interference, and co-channel interference inherent in cellular systems. Such an environment belongs to the class of nonstationary random fields, on which experimental data is difficult to obtain; their behavior hard to predict and model satisfactorily. When reflected signal components become comparable in level to the attenuated direct component, and their delays comparable to the inverse of the channel bandwidth, *frequency selective fading* occurs. The reception is further degraded due to movements of a user relative to reflection points and the relay station, causing Doppler frequency shifts. The simplified model of this environment is known as the *Doppler Multipath Rayleigh Channel.*

The existing and planned cellular mobile radio systems employ sophisticated narrowband and wideband filtering, interleaving, coding, modulation, equalization, decoding, carrier and timing recovery, and multiple access schemes. The cellular mobile radio channel involves a *dynamic interaction* of signals arriving via different paths, adjacent and co-channel interference, and noise. Most channels exhibit some degree of memory, the description of which requires higher order statistics of — *spatial and temporal* — multidimensional random vectors (amplitude, phase, multipath delay, Doppler frequency, etc.) to be employed.

A model of a multi-hop satellite system that incorporates interference and nonlinearities is illustrated and described in Fig. 2.7. The signal flow in the forward/broadcast direction, from Base to Mobile User, is shown on the left side of the figure; the right side of the figure corresponds to the reverse/access direction. For example, in the forward/broadcast direction, the transmitted signal at the Base, shown in the upper left of the figure, is distorted due to nonlinearities in the RF power amplifier. This signal distortion is expressed via differential phase and differential gain coefficients DP and DG, respectively. The same signal is emitted toward the satellite space segment receiver denoted as point 2; here, noise N, interference I, delay τ, and Doppler frequency ${}_D f$ symbolize the environment. The signals are further processed, amplified and distorted at stage 3, and radiated toward the receiver, 4. Here again, noise N, interference I, delay τ, and Doppler frequency ${}_D f$ symbolize the environment. The signals are translated and amplified at stage 5 and radiated toward the Mobile User at stage 6; here, additional noise N, interference I, delay τ, and Doppler frequency ${}_D f$ characterize the corresponding environment. This model is particularly suited for a detailed analysis of the link budget and for equipment design purposes. A system provider and cell designer may use a statistical description of a mobile channel environment, instead.

An FSS radio channel is described as the Gaussian; the mean value of the corresponding radio signal is practically constant and its value can be predicted with a standard deviation of a fraction of a dB. A terrestrial mobile radio channel could exhibit dynamics of about 80 dB and its mean signal could be predicted with a standard deviation of 5 to 10 dB. This may require the evaluation of usefulness of existing radio channel models and eventual development of more accurate ones.

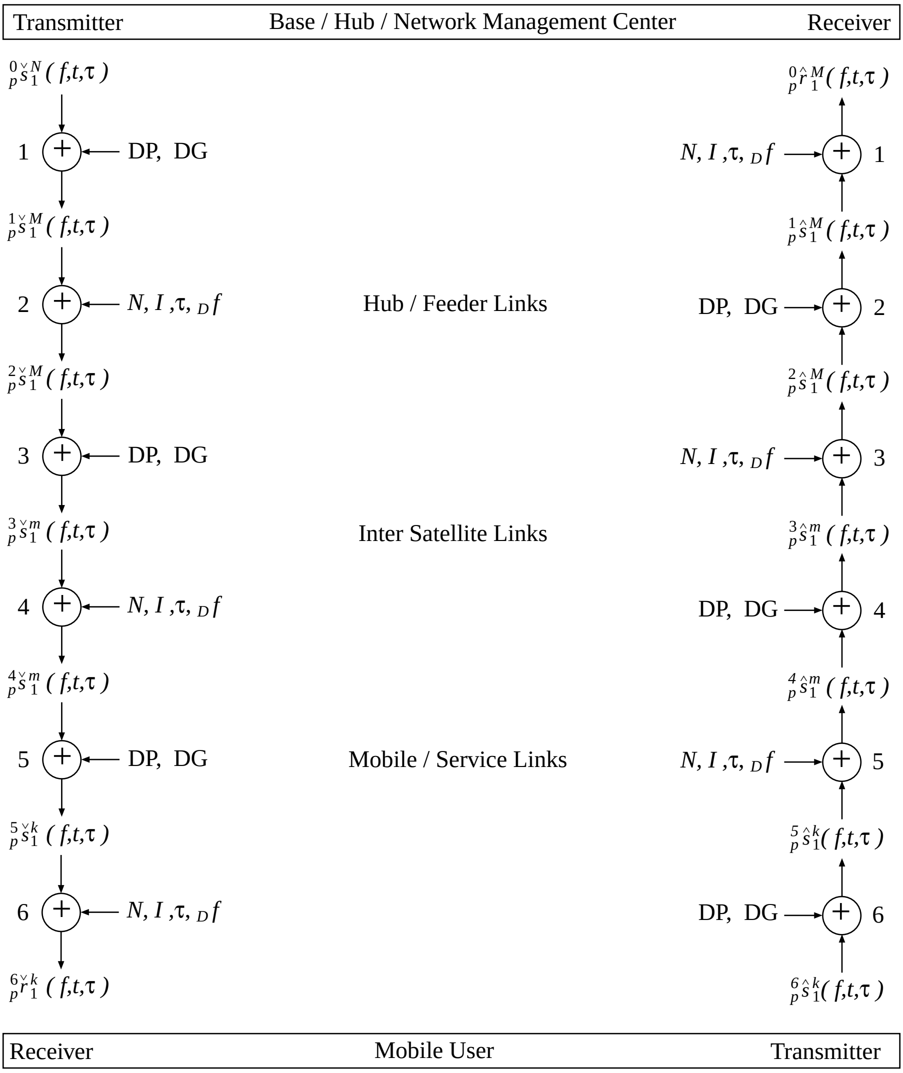
Transmitter
Base / Hub / Network Management Center
Receiver
$^0_p\check{s}^N_1(f,t,\tau)$
$^0_p\hat{r}^M_1(f,t,\tau)$
1
DP, DG
$N, I, \tau, {}_Df$
1
$^1_p\check{s}^M_1(f,t,\tau)$
$^1_p\hat{s}^M_1(f,t,\tau)$
2
$N, I, \tau, {}_Df$
Hub / Feeder Links
DP, DG
2
$^2_p\check{s}^M_1(f,t,\tau)$
$^2_p\hat{s}^M_1(f,t,\tau)$
3
DP, DG
$N, I, \tau, {}_Df$
3
$^3_p\check{s}^m_1(f,t,\tau)$
Inter Satellite Links
$^3_p\hat{s}^m_1(f,t,\tau)$
4
$N, I, \tau, {}_Df$
DP, DG
4
$^4_p\check{s}^m_1(f,t,\tau)$
$^4_p\hat{s}^m_1(f,t,\tau)$
5
DP, DG
Mobile / Service Links
$N, I, \tau, {}_Df$
5
$^5_p\check{s}^k_1(f,t,\tau)$
$^5_p\hat{s}^k_1(f,t,\tau)$
6
$N, I, \tau, {}_Df$
DP, DG
6
$^6_p\check{r}^k_1(f,t,\tau)$
$^6_p\hat{s}^k_1(f,t,\tau)$
Receiver
Mobile User
Transmitter

FIGURE 2.7 Signals and Interference in a Multihop Satellite System. $^q_px^M_1(f,\ t,\ \tau)$ represents signals $x = r, s$, where r is the received and s is the sent/transmitted signal, $\check{x}$ represents the dispatch/forward direction and $\hat{x}$ represents access/return direction; p is the polarization of the signal at location q and the number of signal components ranges from 1 to M; $f,\ t,\ \tau$ are frequency, time and delay of a signal at the location q, respectively. DP, DG are Differential Phase and Differential Gain (include AM/AM and AM/PM); $N,\ I,\ \tau,\ {}_Df$ are the noise, interference, absolute delay and Doppler frequency, respectively.

Cell engineering and prediction of service area and service quality in an ever-changing mobile radio channel environment, is a very difficult task. The average path loss depends on terrain microstructure within a cell, with considerable variation between different types of cells (i.e., urban, suburban, and rural environments). A variety of models based on experimental and theoretic work have been developed to predict path radio propagation losses in a mobile channel. Unfortunately, none of them are universally applicable. In almost all cases, excessive transmitting power is necessary to provide adequate system performance.

The *first generation* mobile satellite systems employ geostationary satellites (or payload piggy-backed on a host satellite) with small 18 dBi antennas covering the whole globe. When the satellite is positioned directly above the traveler (at zenith), a near constant signal environment, known as *Gaussian channel,* is experienced. The traveler's movement relative to the satellite is negligible (i.e., Doppler frequency is practically zero). As the traveler moves — north or south, east or west — the satellite appears lower on the horizon. In addition to the direct path, many significant strength-reflected components are present, resulting in a degraded performance. Frequencies of these components fluctuate due to movement of traveler relative to the reflection points and the satellite. This environment is known as the *Doppler Ricean Channel.* An inclined orbit satellite located for a prolonged period of time above 45° latitude north and 106° longitude west, could provide travelers all over the U.S. and Canada, including the far North, a service quality unsurpassed by either geostationary satellite or terrestrial cellular radio. Similarly, a satellite located at 45° latitude north and 15° longitude east, could provide travelers in Europe with improved service quality.

Inclined orbit satellite systems can offer a low start-up cost, a near Gaussian channel environment, and improved service quality. Low orbit satellites, positioned closer to the service area, can provide high signal levels and short (a few milliseconds long) delays, and offer compatibility with the cellular terrestrial systems. These advantages need to be weighted against network complexity, inter-satellite links, tracking facilities, etc.

Terrestrial mobile radio communications systems provide signal dynamics of about 80 dB and are able to penetrate walls and similar obstacles, thus providing inside building coverage. Satellite mobile radio communications systems are power limited and provide signal dynamics of less than 15 dB; the signal coverage is, in most cases, limited to the outdoors.

Let us compare the efficiency of a Mobile Satellite Service (MSS) with the Fixed Satellite Service (FSS); both services are assumed to be using the GSO space segments. A user at the equator can see the GSO arc reaching ±81°; if satellites are spaces 2° apart along the GSO, then the same user can reach 81 satellites simultaneously. An MSS user employs a hemispherical antenna having gain of about 3 dBi; consequently, he can effectively use only one satellite, but prevent all other satellite users from employing the same frequency. An FSS user employs a 43 dBi gain antenna that points toward a desired satellite. By using the same transmit power as an MSS user, but employing larger and more expensive antenna, this FSS user can effectively transmit about 40 dB (ten thousand times) wider bandwidth, i.e., 40 dB more information. The FSS user can, by adding 3 dB more power into an additional orthogonal polarization channel, reuse the same frequency band and double the capacity. Furthermore, the same FSS user can use additional antennas to reach each of 81 available satellites, thus increasing the GSO are capacity by 80 times. Consequently, the FSS is power-wise 10,000 times more efficient and spatially about 160 times more efficient than corresponding MSS. Similar comparisons can be made for terrestrial systems. The convenience and smallness of today's mobile systems user terminals is traded for low spatial and power efficiency, which may carry a substantial economic price penalty. The real cost of a mobile system seems to have been subsidized by some means beyond the cost of cellular telephone and traffic charges (both often $0).

Service Quality

The primary and the most important measure of service quality should be *customer satisfaction.* The customer's needs, both current and future, should provide guidance to a service offerer and an equipment manufacturer for both the system concept and product design stages. In the early stages of the product life, mobile radio was perceived as a necessary tool for performing important tasks; recently, mobile/personal/handheld radio devices are becoming more like status symbols and fashion. Acknowledging the importance of every single step of the complex service process and architecture, attention is limited here to a few technical merits of quality:

1. *Guaranteed quality level* is usually related to a percentage of the service area coverage for an adequate percentage of time.
2. *Data service quality* can be described by the average bit error rate (e.g., BER < 10^{-5}), packet BER (PBER < 10^{-2}), signal processing delay (1 to 10 ms), multiple access collision probability (< 20%), the probability of a false call (false alarm), the probability of a missed call (miss), the probability of a lost call (synchronization loss), etc.

3. *Voice quality* is usually expressed in terms of the mean opinion score (MOS) of subjective evaluations by service users. MOS marks are: bad = 0, poor = 1, fair = 2, good = 3, and excellent = 4. MOS for PSTN voice service, pooled by leading service providers, relates the poor MOS mark to a single-to-noise ratio (S/N) in a voice channel of S/N $\approx$ 35 dB, while an excellent score corresponds to S/N > 45 dB. Currently, users of mobile radio services are giving poor marks to the voice quality associated with a S/N $\approx$ 15 dB and an excellent mark for S/N > 25 dB. It is evident that there is significant difference (20 dB) between the PSTN and mobile services. If digital speech is employed, both the speech and the speaker recognition have to be assessed. For more objective evaluation of speech quality under *real conditions* (with no impairments, in the presence of burst errors during fading, in the presence of random bit errors at BER = 10^{-2}, in the presence of Doppler frequency offsets, in the presence of truck acoustic background noise, in the presence of ignition noise, etc.), additional tests such as the diagnostic acceptability measure DAM, diagnostic rhyme test DRT, Youden square rank ordering, Sino-Graeco-Latin square tests, etc., can be performed.

Network Issues and Cell Size

To understand ideas and technical solutions offered in existing schemes, and in future systems one needs also to analyze the reasons for their introduction and success. Cellular mobile services are flourishing at an annual rate higher than 20%, worldwide. The first generation systems, (such as AMPS, NMT, TACS, MCS, etc.), use *frequency division multiple access* FDMA and digital modulation schemes for access, command and control purposes, and analog phase/frequency modulation schemes for the transmission of an analog voice. Most of the network intelligence is concentrated at fixed elements of the network including base stations, which seem to be well suited to the networks with a modest number of medium to large-sized cells. To satisfy the growing number of potential customers, more cells and base stations were created by the cell splitting and frequency reuse process. Technically, the shape and size of a particular cell is dictated by the base station antenna pattern and the topography of the service area. Current terrestrial cellular radio systems employ cells with 0.5 to 50 km radius. The maximum cell size is usually dictated by the link budget, in particular the grain of a mobile antenna and available output power. This situation arises in a rural environment, where the demand on capacity is very low and cell splitting is not economical. The minimum cell size is usually dictated by the need for an increase in capacity, in particular in downtown cores. Practical constraints such as real estate availability and price, and construction dynamics limit the minimum cell size to 0.5 to 2 km. However, in such types of networks, the complexity of the network and the cost of service grow exponentially with the number of base stations, while the efficiency of present handover procedures becomes inadequate. Consequently, the second generation of all-digital schemes, which handle this increasing idle traffic more efficiently, were introduced. However, handling of the information, predominantly voice, has not been improved significantly, if at all.

In the 1980s extensive studies of then existing AMPS- and NMT-based systems were performed, see Davis et al. (1984) and Mahmoud et al. (1989), and the references therein. Based on particular service quality requirements, particular radio systems and particular cell topologies, few empirical rules had been established. Antennas with an omnidirectional pattern in a horizontal direction, but with about 10 dBi gain in vertical direction provide the frequency reuse efficiency of N_{FDMA} = 1/12. It was anticipated that base station antennas with similar directivity in a vertical direction and 60° directivity in a horizontal direction (a cell is divided into six sectors) can provide the reuse efficiency N_{FDMA} = 1/4, which results in a threefold increase in the system capacity; if CDMA is employed instead of FDMA, an increase in reuse efficiency $N_{FDMA} = 1/4 \rightarrow N_{CDMA} = 2/3$ may be expected. However, this does not necessarily mean that a CDMA system is more efficient than a FDMA system. The overall efficiency very much depends on spatiotemporal dynamics of a particular cell and the overall network.

Recognizing some of limitations of existing schemes and anticipating the market requirements, the research in *time division multiple access* (TDMA) schemes aimed at cellular mobile and DCT services, and in *code division multiple access* (CDMA) schemes aimed toward mobile satellite systems and cellular and personal mobile applications, followed with introduction of nearly ten different systems. Although employing different access schemes, TDMA (CDMA) network concepts rely on a smart mobile/portable unit that scans time slots (codes) to gain information on network behavior, free slots (codes), etc., improving frequency reuse and handover efficiency while hopefully keeping the complexity and cost of the overall network at reasonable levels. Some of the proposed system concepts depend on low gain (0 dBi) base station antennas deployed in a license-free, uncoordinated fashion; small size cells (10 to 1000 m in radius) and an emitted isotropic radiated power of about 10 mW (+10 dBm) per 100 kHz are anticipated. A frequency reuse efficiency of N = 1/9 to N to 1/36 has been projected for DCT systems. N = 1/9 corresponds to the highest user capacity with the lowest transmission quality, while N = 1/36 has the lowest user capacity with the highest transmission quality. This significantly reduced frequency reuse capability of proposed system concepts, will result in significantly reduced system capacity, which needs to be compensated for by other means including new spectra.

In practical networks, the need for a capacity (and frequency spectrum) is distributed unevenly in space and time. In such an environment, the capacity and frequency reuse efficiency of the network may be improved by *dynamic channel allocation,* where an increase in the capacity at a particular hot spot may be traded for a decrease in the capacity in cells surrounding the hot spot, the quality of the transmission, and network instability. The first generation mobile radio communications systems used omnidirectional antennas at base stations. Today, three-sector 120°-wide cells are typical in a heavy traffic urban environment, while entry-level rural systems employ omnidirectional antennas; the most demanding environments with changing traffic patterns employ adaptive antenna solutions, instead.

To cover the same area (space) with smaller and smaller cells, one needs to employ more and more base stations. A linear increase in the number of base stations in a network usually requires an $(n(n-1)/2)$ increase in the number of connections between base stations, and increase in complexity of switches and network centers. These connections can be realized by fixed radio systems (providing more frequency spectra available for this purpose), or, more likely, by a cord (wire, cable, fiber, etc.).

An increase in overall capacity is attributed to

- increase in available bandwidth, particularly above 1 GHz, but to the detriment of other services,
- increased use of adaptive antenna solutions which, through spatial filtering, increase capacity and quality of the service, but at a significant increase in cost,
- trade-offs between service quality, vehicular vs. pedestrian environments, analog vs. digital voice, etc.

The *first generation* geostationary satellite system antenna beam covers the entire Earth (i.e., the cell radius equals ≈6500 km). The *second generation* geostationary satellites use large multibeam antennas providing 10 to 20 beams (cells) with 800 to 1600 km radius. Low orbit satellites such as Iridium use up to 37 beams (cells) with 670 km radius. The *third generation* geostationary satellite systems will be able to use very large reflector antennas (roughly the size of a baseball stadium), and provide 80 to 100 beams (cells) with a cell radius of ≈200 km. If such a satellite is tethered to a position 400 km above the Earth, the cell size will decrease to ≈2 km in radius, which is comparable in size with today's small size cell in terrestrial systems. Yet, such a satellite system may have the potential to offer an improved service quality due to its near optimal location with respect to the service area. Similar to the terrestrial concepts, an increase in the number of satellites in a network will require an increase in the number of connections between satellites and/or Earth network management and satellite tracking centers, etc. Additional factors that need to be taken into consideration include price, availability, reliability, and timeliness of the launch procedures, a few large vs. many small satellites, tracking stations, etc.

Coding and Modulation

The conceptual transmitter and receiver of a mobile system may be described as follows. The transmitter signal processor accepts analog voice and/or data and transforms (by analog and/or digital means) these signals into a form suitable for a double-sided suppressed carrier amplitude modulator [also called quadrature amplitude modulator (QAM)]. Both analog and digital input signals may be supported, and either analog or digital modulation may result at the transmitter output. Coding and interleaving can also be included. Very often, the processes of coding and modulation are performed jointly; we will call this joint process *codulation.* A list of typical modulation schemes suitable for transmission of voice and/or data over Doppler-affected Ricean channel, which can be generated by this transmitter is given in Table 2.5. Details on modulation, coding, and system issues can be found in Kucar (2000), Proakis, (1983), Sklar, (1988), and Van Trees, (1968–1971).

Existing cellular radio systems such as AMPS, TACS, MCS, and NMT employ hybrid (analog and digital) schemes. For example, in access mode, AMPS uses a digital codulation scheme (BCH coding and FSK modulation), while in information exchange mode, the frequency-modulated analog voice is merged with discrete *SAT* and/or *ST* signals and occasionally blanked to send a digital message. These hybrid codulation schemes exhibit a constant envelope and as such allow the use of power efficient radio frequency (RF) nonlinear amplifiers. On the receiver side, these schemes can be demodulated by an inexpensive, but efficient limiter/discriminator device. They require modest to high $C/N = 10 - 20$ dB, are very robust in adjacent (a spectrum is concentrated near the carrier) and co-channel interference (up to $C/I = 0$ dB, due to capture effect) cellular radio environment, and react quickly to the signal fade outages (no carrier, code, or frame synchronization). Frequency-selective and Doppler-affected mobile radio channels will cause modest to significant degradations known as the *random phase/frequency modulation.* By using modestly complex extended threshold devices C/N as low as 5 dB can provide satisfactory performance.

Tightly filtered codulation schemes, such as $\pi/4$ QPSK additionally filtered by a square root, raised-cosine filter, exhibit a nonconstant envelope that demands (quasi) linear, less D.C. power efficient amplifiers to be employed. On the receiver side, these schemes require complex demodulation receivers, a linear path for signal detection, and a nonlinear one for reference detection — differential detection or carrier recovery. When such a transceiver operates in a selective fading multipath channel environment, additional countermeasures (inherently sluggish equalizers, etc.) are necessary to improve the performance — reduce the *bit error rate floor.* These codulation schemes require modest $C/N = 8 - 16$ dB and perform modestly in adjacent and/or co-channel (up to $C/I = 8$ db) interference environment.

Codulation schemes employed in spread spectrum systems use low-rate coding schemes and mildly filtered modulation schemes. When equipped with sophisticated amplitude gain control on the transmit and receive side, and robust rake receiver, these schemes can provide superior $C/N = 4 - 10$ dB and $C/I < 0$ dB performance. Unfortunately, a single transceiver has not been able to operate satisfactorily in a mobile channel environment. Consequently, a few additional signals have been employed to achieve the required quality of the transmission. These pilot signals significantly reduce the spectrum efficiency in the forward direction and many times in the reverse direction. Furthermore, two combined QPSK-like signals have up to (4×4) different baseband levels and may look like a 16QAM signal, while three combined QPSK-like signals may look like a 64QAM signal. These combined signals, one information and two pilot signals, at user's transmitter output, for example, exhibit high peak factors and total power that is by 3 to 5 dB higher than the C/N value necessary for a single information signal. Additionally, inherently power inefficient linear RF power amplifiers are needed; these three signal components of a CDMA scheme may have been optimized for minimal cross-correlation and ease of detection. As such, the same three signals may not necessarily have states in the QAM constellation that optimize the peak-to-average ratio, and vice versa.

Speech Coding

Human vocal tract and voice receptors, in conjunction with language redundancy (coding), are well suited for face-to-face conversation. As the channel changes (e.g., from telephone channel to mobile radio channel), different coding strategies are necessary to protect against the loss of information.

TABLE 2.5 Modulation Schemes, Glossary of Terms

Abbreviation	Description	Remarks/Use
ACSSB	Amplitude Companded Single SideBand	Satellite transmission
AM	Amplitude Modulation	Broadcasting
APK	Amplitude Phase Keying modulation	
BLQAM	Blackman Quadrature Amplitude Modulation	
BPSK	Binary Phase Shift Keying	Spread spectrum systems
CPFSK	Continuous Phase Frequency Shift Keying	
CPM	Continuous Phase Modulation	
DEPSK	Differentially Encoded PSK (with carrier recovery)	
DPM	Digital Phase Modulation	
DPSK	Differential Phase Shift Keying (no carrier recovery)	
DSB-AM	Double SideBand Amplitude Modulation	
DSB-SC-AM	Double SideBand Suppressed Carrier AM	Includes digital schemes
FFSK	Fast Frequency Shift Keying ≡ MSK	NMT data and control
FM	Frequency Modulation	Broadcasting, AMPS, voice
FSK	Frequency Shift Keying	AMPS data and control
FSOQ	Frequency Shift Offset Quadrature modulation	
GMSK	Gaussian Minimum Shift Keying	GSM voice, data, and control
GTFM	Generalized Tamed Frequency Modulation	
HMQAM	Hamming Quadrature Amplitude Modulation	
IJF	Intersymbol Jitter Free ≡ SQORC	
LPAM	L-ary Pulse Amplitude Modulation	
LRC	LT symbols long Raised Cosine pulse shape	
LREC	LT symbols long Rectangularly EnCoded pulse shape	
LSRC	LT symbols long Spectrally Raised Cosine scheme	
MMSK	Modified Minimum Shift Keying ≡ FFSK	
MPSK	M-ary Phase Shift Keying	
MQAM	M-ary Quadrature Amplitude Modulation	A subclass of DSB-SC-AM
MQPR	M-ary Quadrature Partial Response	Radio-relay transmission
MQPRS	M-ary Quadrature Partial Response System ≡ MQPR	
MSK	Minimum Shift Keying	
m-*h*	multi-*h* CPM	
OQPSK	Offset (staggered) Quadrature Phase Shift Keying	
PM	Phase Modulation	Low capacity radio
PSK	Phase Shift Keying	4PSK ≡ QPSK
QAM	Quadrature Amplitude Modulation	
QAPSK	Quadrature Amplitude Phase Shift Keying	
QPSK	Quadrature Phase Shift Keying ≡ 4 QAM	Low capacity radio
QORC	Quadrature Overlapped Raised Cosine	
SQAM	Staggered Quadrature Amplitude Modulation	
SQPSK	Staggered Quadrature Phase Shift Keying	
SQORC	Staggered Quadrature Overlapped Raised Cosine	
SSB	Single SideBand	Low and High capacity radio
S3MQAM	Staggered class 3 Quadrature Amplitude Modulation	
TFM	Tamed Frequency Modulation	
TSI QPSK	Two-Symbol-Interval QPSK	
VSB	Vestigial SideBand	TV
WQAM	Weighted Quadrature Amplitude Modulation	Includes most digital schemes
XPSK	Crosscorrelated PSK	
$\pi/4$ DQPSK	$\pi/4$ shift DQPSK with $\alpha = 0.35$ raised cosine filtering	IS-54 TDMA voice and data
3MQAM	Class 3 Quadrature Amplitude Modulation	
4MQAM	Class 4 Quadrature Amplitude Modulation	
12PM3	12 state PM with 3 bit correlation	

Source: 4U Communications Research Inc., 2000.06.10~00:09, c:/tab/modulat.tab

In (analog) companded PM/FM mobile radio systems, speech is limited to 4 kHz, compressed in amplitude (2:1), pre-emphasized, and phase/frequency modulated. At a receiver, inverse operations are performed. Degradation caused by these conversions and channel impairments results in lower voice quality. Finally, the human ear and brain have to perform the estimation and decision processes on the received signal.

In digital schemes for sampling and digitizing of an analog speech (source) are performed first. Then, by using knowledge of properties of the human vocal tract and the language itself, a spectrally efficient source coding is performed. A high rate 64 kb/s, 56 kb/s, and AD-PCM 32 kb/s digitized voice complies with ITU-T recommendations for toll quality, but may be less practical for the mobile environment. One is primarily interested in 8 to 16 kb/s rate speech coders, which might offer satisfactory quality, spectral efficiency, robustness, and acceptable processing delays in a mobile radio environment. A glossary of the major speech coding schemes is provided in Table 2.6.

TABLE 2.6 Digitized Voice. Glossary of Terms

Abbreviation	Description	Remarks/Use
ADM	Adaptive Delta Modulation	
ADPCM	Adaptive Differential Pulse Code Modulation	Digital telephony, DECT
ACIT	Adaptive Code sub-band excIted Transform	GTE
APC	Adaptive Predictive Coding	
APC–AB	APC with Adaptive Bit allocation	
APC–HQ	APC with Hybrid Quantization	
APC–MQL	APC with Maximum Likelihood Quantization	
AQ	Adaptive Quantization	
ATC	Adaptive Transform Coding	
BAR	Backward Adaptive Reencoding	
CELP	Code Excited Linear Prediction	IS-95
CVSDM	Continuous Variable Slope Delta Modulation	
DAM	Diagnostic Acceptability Measure	
DM	Delta Modulation	A/D conversion
DPCM	Differential Pulse Code Modulation	
DRT	Diagnostic Rhyme Test	
DSI	Digital Speech Interpolation	TDMA FSS systems
DSP	Digital Signal Processing	
HCDM	Hybrid Companding Delta Modulation	
LDM	Linear Delta Modulation	
LPC	Linear Predictive Coding	
MPLPC	Multi Pulse LPC	
MSQ	Multipath Search Coding	
NIC	Nearly Instantaneous Companding	
PCM	Pulse Code Modulation	Digital Voice
PVXC	Pulse Vector eXcitation Coding	
PWA	Predicted Wordlength Assignment	
QMF	Quadrature Mirror Filter	
RELP	Residual Excited Linear Prediction	GSM
RPE	Regular Pulse Excitation	
SBC	Sub Band Coding	
TASI	Time Assigned Speech Interpolation	TDMA FSS systems
TDHS	Time Domain Harmonic Scalling	
VAPC	Vector Adaptive Predictive Coding	
VCELP	Vector Code Excited Linear Prediction	
VEPC	Voice Excited Predictive Coding	
VQ	Vector Quantization	
VQL	Variable Quantum Level coding	
VSELP	Vector–Sum Excited Linear Prediction	IS–136, PDC
VXC	Vector eXcitation Coding	

Source: 4U Communications Research Inc., 2000.06.10~00:09, c:/tab/voice.tab

TABLE 2.7 Comparison of Cordless Telephone (CT) Systems

	System Name							
Parameter	CT0	CT1/+	JCT	CT2/+	CT3	DECT	CDMA	PHT
TX freq, MHz								
Base	22,26,30,31,46,48,45	914/885	254	864–8, 994–8	944–948	1880–1900		1895–1907
Mobile	48,41,39,40,69,74,48	960/932	380	864–8, 944–8	944–948	1880–1990		1895–1907
Multiple access band	FDMA	FDMA	FDMA	F/TDMA	TDMA	TDMA	CDMA	F/TDMA
Duplexing method	FDD	FDD	FDD	TDD	TDD	TDD	FDD	TDD
Ch. spacing, kHz	1.7,20,25,40	25	12.5	100	1000	1728	1250	300
Channel rate, kb/s				72	640	1152	1228.80	384
Channels/RF	1	1	1	1	8	12	32	4
Channels/band	10,12,15,20,25	40,80	89	20	2	5		20
Burst/frame length, ms				1/2	1/16	1/10	n/a	1/5
Modulation type	FM	FM	FM	GFSK	GMSK	GMSK	B/QPSK	π/4
Coding				Cyclic, RS	CRC 16	CRC 16	Conv 1/2, 1/3	
Transmit power, mW				≤10	≤80	≤100	≤10	≤80
Transmit power steps				2	1	1	many	many
TX power range, dB				16	0	0	≥80	
Vocoder type	analog	analog	analog	ADPCM	ADPCM	ADPCM	CELP	ADPCM
Vocoder rate, kb/s				fixed 32	fixed 32	fixed 32	≤9.6	fixed 32
Max data rate, kb/s				32	ISDN 144	ISDN 144	9.6	384
Processing delay, ms	0	0	0	2	16	16	80	
$\boxed{3}$ Minimum				1/25	1/15	1/15	1/4	
Average				1.15	1/07	1/07	2/3	
Maximum				$\boxed{1}$ 1/02	$\boxed{1}$ 1/02	$\boxed{1}$ 1/02	3/4	
$\boxed{4}$				100 × 1	10 × 8	6 × 12	4 × 32	
$\boxed{5}$ Minimum				4	5–6	5–6	$\boxed{2}$ 32 (08)	
Average				7	11–12	11–12	85 (21)	
Maximum				$\boxed{1}$ 50	$\boxed{1}$ 40	$\boxed{1}$ 40	96 (24)	

Note: $\boxed{1}$ The capacity (in the number of voice channels) for a single isolated cell. $\boxed{2}$ The capacity in parenthes may correspond to a 32 kbit/s vocoder. $\boxed{3}$ Reuse efficiency. $\boxed{4}$ Theoretical number of voice channels per cell and 10 MHz. $\boxed{5}$ Practical number of voice channels per 10 MHz. Reuse efficiency and associate capacities reflect our own estimates.

Source: 4U Communications Research Inc., 2000.06.10~00:09 c:/tab/cordless.sys

At this point, a partial comparison between analog and digital voice should be made. The quality of 64 kb/s digital voice, transmitted over a telephone line, is essentially the same as the original analog voice (they receive nearly equal MOS). What does this *near equal MOS* mean in a radio environment? A mobile radio conversation consists of one (mobile to home) or a maximum of two (mobile to mobile) mobile radio paths, which dictate the quality of the overall connection. The results of a comparison between analog and digital voice schemes in different artificial mobile radio environments have been widely published. Generally, systems that employ digital voice and digital codulation schemes seem to perform well under modest conditions, while analog voice and analog codulation systems outperform their digital counterparts in fair and difficult (near threshold, in the presence of strong co-channel interference) conditions. Fortunately, present technology can offer a viable implementation of both analog and digital systems within the same mobile/portable radio telephone unit. This would give every individual a choice of either an analog or digital scheme, better service quality, and higher customer satisfaction. Trade-offs between the quality of digital speech, the complexity of speech and channel coding, as well as D.C. power consumption have to be assessed carefully, and compared with analog voice systems.

Macro and Micro Diversity

Macro diversity. Let us observe the typical evolution of a cellular system. In the beginning, the base station may be located in the barocenter of the service area (center of the cell). The base station antenna is omnidirectional in azimuth, but with about 6 to 10 dBi gain in elevation, and serves most of the cell area (e.g., > 95%). Some parts within the cell may experience a lower quality of service because the direct path signal may be attenuated due to obstruction losses caused by buildings, hills, trees, etc. The closest neighboring (the first tier) base stations serve corresponding neighboring area cells by using different sets of frequencies, eventually causing adjacent channel interference. The second closest neighboring (the second tier) base stations might use the same frequencies (frequency reuse) causing co-channel interference. When the need for additional capacity arises and/or a higher quality of service is required, the same nearly circular area may be divided into three 120°-wide sectors, six 60°-wide sectors, etc., all served from the same base station location; now, the same base station is located at the edge of respective sectors. Since the new sectorial antennas provide 5 dB and 8 dB larger gains than the old omnidirectional antenna, respectively, these systems with new antennas with higher gains have longer spatial reach and may cover areas belonging to neighboring cells of the old configuration. For example, if the same real estate (base stations) is used in conjunction with 120° directional (in azimuth) antennas, the new designated 120°-wide wedge area may be served by the previous base station and by two additional neighboring base stations now equipped with sectorial antennas with longer reach. Therefore, the same number of existing base stations equipped with new directional antennas and additional combining circuitry may be required to serve the same or different number of cells, yet in a different fashion. The mode of operation in which two or more base stations serve the same area is called the *macro diversity.* Statistically, three base stations are able to provide better coverage of an area similar in size to the system with a centrally located base station. The directivity of a base station antenna (120° or even 60°) provides additional discrimination against signals from neighboring cells, therefore, reducing adjacent and co-channel interference (i.e., improving reuse efficiency and capacity). Effective improvement depends on the terrain configuration, and the combining strategy and efficiency. However, it requires more complex antenna systems and combining devices.

Micro diversity is when two or more signals are received at one site (base or mobile):

1. *Space diversity* systems employ two or more antennas spaced a certain distance apart from one another. A separation of only $\lambda/2$ = 15 cm at f = 1 GHz, which is suitable for implementation on the mobile side, can provide a notable improvement in some mobile radio channel environments. Micro space diversity is routinely used on cellular base sites. Macro diversity, where in our example the base stations were located kilometers apart, is also a form of space diversity.
2. *Field-component diversity* systems employ different types of antennas receiving either the electric or the magnetic component of an electromagnetic signal.
3. *Frequency diversity* systems employ two or more different carrier frequencies to transmit the same information. Statistically, the same information signal may or may not fade at the same time at different carrier frequencies. Frequency hopping and very wide band signaling can be viewed as frequency diversity techniques.
4. *Time diversity* systems are primarily used for the transmission of data. The same data is sent through the channel as many times as necessary, until the required quality of transmission is achieved automatic repeat request (ARQ). *Would you please repeat your last sentence* is a form of time diversity used in a speech transmission.

The improvement of any diversity scheme is strongly dependent on the combining techniques employed, i.e., the selective (switched) combining, the maximal ratio combining, the equal gain combining, the feedforward combining, the feedback (Granlund) combining, majority vote, etc., see [Jakes, 1974].

Continuous improvements in DSP and MMIC technologies and broader availability of ever-improving CAD electromagnetics tools is making adaptive antenna solutions more viable than ever before. This is particularly true for systems above 1 GHz, where the same necessary base station antenna gain can be achieved with smaller antenna dimensions. An adaptive antenna could follow spatially shifting traffic patterns, adjust its gain and pattern, and consequently improve the signal quality and capacity.

Multiple Broadcasting and Multiple Access

Communications networks for travelers have two distinct directions: the *forward link* — from the base station (via satellite) to all travelers within the footprint coverage area, and the *return link* — from a traveler (via satellite) to the base station. In the forward direction a base station distributes information to travelers according to the previously established protocol, i.e., no multiple access is involved; this way of operation is also called *broadcasting.* In the reverse direction many travelers make attempts to access one of the base stations; this way of operation is also called *access.* This occurs in so-called *control channels,* in a particular time slot, at a particular frequency, or by using a particular code. If collisions occur, customers have to wait in a queue and try again until success is achieved. If successful (i.e., no collision occurred), a particular customer will exchange (automatically) the necessary information for call setup. The network management center (NMC) will verify the customer's status, his credit rating, etc. Then, the NMC may assign a channel frequency, time slot, or code, on which the customer will be able to exchange information with his correspondent.

The optimization of the forward and reverse links may require different coding and modulation schemes and different bandwidths in each direction.

In *forward link,* there are three basic distribution (multiplex broadcasting) schemes: one that uses discrimination in frequency between different users and is called *frequency division multiplex broadcasting* (FDMB); another that discriminates in time and is called *time division multiplex broadcasting* (TDMB); and the last having different codes based on spread spectrum signaling, which is known as *code division multiplex broadcasting* (CDMB). It should be noted that hybrid schemes using a combination of basic schemes can also be developed. All existing mobile radio communications systems employ an FDM component; consequently, only FDMB schemes are pure, while the other two schemes are hybrid, i.e., TDMB/FDM and CDMB/FDM solutions are used; the two hybrid solutions inherit complexities of both parents, i.e., the need for an RF frequency synthesizer and a linear amplifier for *single channel per carrier* (SCPC) FDM solution, and the need for TDM and CDM overhead, respectively.

In *reverse link,* there are three basic access schemes: one that uses discrimination in frequency between different users and is called *frequency division multiple access* (FDMA); another that discriminates in time and is called *time division multiple access* (TDMA); and the last having different codes based on spread spectrum signaling, which is known as *code division multiple access* (CDMA). It should be noted that hybrid schemes using combinations of basic schemes can also be developed.

A performance comparison of multiple access schemes is a very difficult task. The strengths of FDMA schemes seem to be fully exploited in narrowband channel environments. To avoid the use of equalizers, channel bandwidths as narrow as possible should be employed, yet in such narrowband channels, the quality of service is limited by the maximal expected Doppler frequency and practical stability of frequency sources. Current practical limits are about 5 kHz.

The strengths of both TDMA and CDMA schemes seem to be fully exploited in wideband channel environments. TDMA schemes need many slots (and bandwidth) to collect information on network behavior. Once the equalization is necessary (at bandwidths > 20 kHz), the data rate should be made as high as possible to increase frame efficiency and freeze the frame to ease equalization; yet, high data rates require high RF peak powers and a lot of signal processing power, which may be difficult to achieve in handheld units. Current practical bandwidths are about 0.1 to 1.0 MHz. All existing schemes that employ TDMA components are hybrid, i.e., the TDMA/FDM schemes in which the full strength of the TDMA scheme is not fully realized.

CDMA schemes need large spreading (processing) factors (and bandwidth) to realize spread spectrum potentials; yet, high data rates require a lot of signal processing power, which may be difficult to achieve in handheld units. Current practical bandwidths are up to about 5 MHz. As mentioned before, a single transceiver has not been able to operate satisfactorily in a mobile channel environment. Consequently, a few CDMA elementary signals, information and pilot ones, may be necessary for successful transmission. This multisignal environment is equivalent to a MQAM signaling scheme with a not necessarily optimal state constellation. Significant increase in the equipment complexity is accompanied with a significant increase in the average and peak transmitter power. In addition, an RF synthesizer is needed to accommodate the CDMA/FDM mode of operation.

Narrow frequency bands seem to favor FDMA schemes, since both TDMA and CDMA schemes require more spectra to fully develop their potentials. However, once the adequate power spectrum is available, the later two schemes may be better suited for a complex (micro) cellular network environment. Multiple access schemes are also message sensitive. The length and type of message, and the kind of service will influence the choice of multiple access, ARQ, frame and coding, among others.

System Capacity

The recent surge in the popularity of cellular radio and mobile service in general, has resulted in an overall increase in traffic and a shortage of available system capacity in large metropolitan areas. Current cellular systems exhibit a wide range of traffic densities, from low in rural areas to overloaded in downtown areas with large daily variations between peak hours and quiet night hours. It is a great system engineering challenge to design a system that will make optimal use of the available frequency spectrum, while offering a maximal traffic throughput (e.g., Erlangs/MHz/service area) at an acceptable service quality, constrained by the price and size of the mobile equipment. In a cellular environment, the overall system capacity in a given service area is a product of many (complexly interrelated) factors including the available frequency spectra, service quality, traffic statistics, type of traffic, type of protocol, shape and size of service area, selected antennas, diversity, frequency reuse capability, spectral efficiency of coding and modulation schemes, efficiency of multiple access, etc.

In the seventies, so-called analog cellular systems employed omnidirectional antennas and simple or no diversity schemes offering modest capacity, which satisfied a relatively low number of customers. Analog cellular systems of the nineties employ up to 60° sectorial antennas and improved diversity schemes. This combination results in a three- to fivefold increase in capacity. A further (twofold) increase in capacity can be expected from narrowband analog systems (25 kHz $\rightarrow$ 12.5 kHz) and nearly threefold increase in capacity from the 5 kHz-wide narrowband AMPS, however, slight degradation in service quality might be expected. These improvements spurned the current growth in capacity, the overall success, and the prolonged life of analog cellular radio.

Conclusion

In this contribution, a broad repertoire of terrestrial and satellite systems and services for travelers is briefly described. The technical characteristics of the dispatch, cellular, and cordless telephony systems are tabulated for ease of comparison. Issues such as operating environment, service quality, network complexity, cell size, channel coding and modulation (codulation), speech coding, macro and micro diversity, multiplex and multiple access, and the mobile radio communications system capacity are discussed.

Presented data reveals significant differences between existing and planned terrestrial cellular mobile radio communications systems, and between terrestrial and satellite systems. These systems use different frequency bands, different bandwidths, different codulation schemes, different protocols, etc. (i.e., they are not compatible).

What are the technical reasons for this incompatibility? In this contribution, performance dependence on multipath delay (related to the cell size and terrain configuration), Doppler frequency (related to the carrier frequency, data rate, and the speed of vehicles), and message length (may dictate the choice of multiple access) are briefly discussed. A system optimized to serve the travelers in the Great Plains may not perform very well in mountainous Switzerland; a system optimized for downtown cores may not be well suited to a rural radio; a system employing geostationary (above equator) satellites may not be able to serve travelers at high latitudes very well; a system appropriate for slow moving vehicles may fail to function properly in a high Doppler shift environment; a system optimized for voice transmission may not be very good for data transmission, etc. A system designed to provide a broad range of services to everyone, everywhere, may not be as good as a system designed to provide a particular service in a particular local environment — as a decathlete world champion may not be as successful in competitions with specialists in particular disciplines.

However, there are plenty of opportunities where compatibility between systems, their integration, and frequency sharing may offer improvements in service quality, efficiency, cost and capacity (and therefore availability). Terrestrial systems offer a low start-up cost and a modest per user in densely populated areas. Satellite systems may offer a high quality of service and may be the most viable solution to serve travelers in scarcely populated areas, on oceans, and in the air. Terrestrial systems are confined to two dimensions and radio propagation occurs in the near horizontal sectors. Barostationary satellite systems use the narrow sectors in the user's zenith nearly perpendicular to the Earth's surface having the potential for frequency reuse and an increase in the capacity in downtown areas during peak hours. A call setup in a forward direction (from the PSTN via base station to the traveler) may be a very cumbersome process in a terrestrial system when a traveler to whom a call is intended is roaming within an unknown cell. However, this may be realized earlier in a global beam satellite system.

References

Ariyavisitakul, S.L., Falconer, D.D., Adachi, F., and Sari, H., (Guest Editors), Special Issue on Broadband Wireless Techniques, *IEEE J. on Selected Areas in Commun.,* 17, 10, October 1999.

Chuang, J.C.-I., Anderson, J.B., Hattori, T., and Nettleton, R.W., (Guest Editors), Special Issue on Wireless Personal Communications: Part I, *IEEE J. on Selected Areas in Commun.,* 11, 6, August 1993, Part II, *IEEE J. on Selected Areas in Commun.,* 11, 7, September 1993.

Cimini, L.J. and Tranter W.H., (Guest Editors), Special Issues on Wireless Communication Series, *IEEE J. on Selected Areas in Commun.,* 17, 3, March 1999.

Cimini, L.J. and Tranter, W.H., (Guest Editors), Special Issue on Wireless Communications Series, *IEEE J. on Selected Areas in Commun.,* 17, 7, July 1999.

Cimini, L.J. and Tranter, W.H., (Guest Editors), Special Issue on Wireless Communications Series, *IEEE J. on Selected Areas in Commun.,* 17, 11, November 1999.

Cimini, L.J. and Tranter, W.H., (Guest Editors), Special Issue on Wireless Communications Series, *IEEE J. on Selected Areas in Commun.,* 18, 3, March 2000.

Cox, D.C., Hirade, K., and Mahmoud, S.A., (Guest Editors), Special Issue on Portable and Mobile Communications, *IEEE J. on Selected Areas in Commun.,* 5, 4, June 1987.

Cox, D.C. and Greenstein, L.J., (Guest Editors), Special Issue on Wireless Personal Communications, *IEEE Commun. Mag.,* 33, 1, January 1995.

Davis, J.H. (Guest Editor), Mikulski, J.J., and Porter, P.T. (Associated Guest Editors), King, B.L. (Guest Editorial Assistant), Special Issue on Mobile Radio Communications, *IEEE J. on Selected Areas in Commun.,* 2, 4, July 1984.

Del Re, E., Devieux Jr., C.L., Kato, S., Raghavan, S., Taylor, D., and Ziemer, R., (Guest Editors), Special Issue on Mobile Satellite Communications for Seamless PCS, *IEEE J. on Selected Areas in Commun.,* 13, 2, February 1995.

Graglia, R.D., Luebbers, R.J., and Wilton, D.R., (Guest Editors), Special Issue on Advanced Numerical Techniques in Electromagnetics. *IEEE Trans. on Antennas and Propagation,* 45, 3, March 1997.

Institute of Navigation (ION), *Global Positioning System,* Reprinted by The Institute of Navigation. Volume I. Washington, D.C., USA, 1980; Volume II. Alexandria, VA, USA, 1984; Volume III. Alexandria, VA, USA, 1986; Volume IV. Alexandria, VA, USA, 1993.

International Telecommunication Union (ITU), *Radio Regulations,* Edition of 1982, Revised in 1985 and 1986.

International Telecommunication Union (ITU), Recommendations of the CCIR, 1990 (also Resolutions and Opinions). *Mobile Radiodetermination, Amateur and Related Satellite Services,* Volume VIII, XVIIth Plenary Assembly, Düsseldorf, 1990. Reports of the CCIR, (also Decisions), *Land Mobile Service, Amateur Service, Amateur Satellite Service,* Annex 1 to Volume VIII, XVIIth Plenary Assembly, Düsseldorf, 1990. Reports of the CCIR, (also Decisions), *Maritime Mobile Service,* Annex 2 to Volume VIII, XVIIth Plenary Assembly, Düsseldorf, 1990.

Kucar, A.D. (Guest Editor), Special Issue on Satellite and Terrestrial Systems and Services for Travelers, *IEEE Commun. Mag.,* 29, 11, November 1991.

Kucar, A.D., Kato, S., Hirata, Y., and Lundberg, O., (Guest Editors), Special Issue on Satellite Systems and Services for Travelers, *IEEE J. on Selected Areas in Commun.*, 10, 8, October 1992.

Kucar, A.D. and Uddenfeldt, J., (Guest Editors), Special Issue on Mobile Radio Centennial, *Proceedings of the IEEE,* 86, 7, July 1998.

Mahmoud, S.A., Rappaport, S.S., and Öhrvik, S.O., (Guest Editors), Special Issue on Portable and Mobile Communications, *IEEE J. on Selected Areas in Commun.*, 7, 1, January 1989.

Mailloux, R.J., (Guest Editor), Special Issue on Phased Arrays, *IEEE Trans. on Antennas and Propagation,* 47, 3, March 1999.

Mitola, J. III, Bose, V., Leiner, B.M., Turletti, T., and Tennenhouse, D., (Guest Editors), Special Issue on Software Radios, *IEEE J. on Selected Areas in Commun.,* 17, 4, April 1999.

Oppermann, I., van Rooyen, P., and Kohno, R., (Guest Editors), Special Issue on Spread Spectrum for Global Communications I, *IEEE J. on Selected Areas in Commun.,* 17, 12, December 1999.

Oppermann, I., van Rooyen, P., and Kohno, R., (Guest Editors), Special Issue on Spread Spectrum for Global Communications II, *IEEE J. on Selected Areas in Commun.,* 18, 1, January 2000.

Rhee, S.B., Editor), Lee, W.C.Y., (Guest Editor), Special issue on Digital Cellular Technologies, *IEEE Trans. on Vehicular Technol.,* 40, 2, May 1991.

Steele, R., (Guest Editor), Special Issue on PCS: The Second Generation, *IEEE Commun. Mag.,* 30, 12, December 1992.

World Administrative Radio Conference (WARC), *FINAL ACTS of the World Administrative Radio Conference for Dealing with Frequency Allocations in Certain Parts of the Spectrum* (WARC-92), Málaga-Torremolinos, 1992). ITU, Geneva, 1992.

World Radiocommunications Conference (WRC), *FINAL ACTS of the World Radiocommunications Conference* (WRC-97. ITU, Geneva, 1997.

Further Information

This trilogy, written by participants in AT&T Bell Labs projects on research and development in mobile radio, is the Holy Scripture of diverse cellular mobile radio topics:

Jakes, W.C. Jr. (Editor), *Microwave Mobile Communications,* John Wiley & Sons, Inc., New York, 1974.

AT&T Bell Labs Technical Personnel, Advanced Mobile Phone Service (AMPS), *Bell System Technical Journal,* 58, 1, January 1979.

Lee, W.C.Y., *Mobile Communications Engineering,* McGraw-Hill Book Company, New York, 1982.

An in-depth understanding of design, engineering, and use of cellular mobile radio networks, including PCS and PCN, requires knowledge of diverse subjects such as three-dimensional cartography, electromagnetic propagation and scattering, computerized analysis and design of microwave circuits, fixed and adaptive antennas, analog and digital communications, project engineering, etc. The following is a list of books relating to these topics:

Balanis, C.A., *Antenna Theory Analysis and Design,* Harper & Row, Publishers, New York 1982; Second Edition, John Wiley & Sons, Inc., New York, 1997.

Bowman, J.J., Senior, T.B.A., and Uslenghi, P.L.E., *Electromagnetic and Acoustic Scattering by Simple Shapes,* Revised Printing. Hemisphere Publishing Corporation, 1987.

Hansen, R.C., *Phased Array Antennas*, John Wiley & Sons, Inc., New York, 1998.

James, J.R. and Hall, P.S., (Editors), *Handbook of Microstrip Antennas*, Volumes I and II. Peter Peregrinus Ltd., Great Britain, 1989.

Kucar, A.D., *Satellite and Terrestrial Wireless Radio Systems: Fixed, Mobile, PCS and PCN, Radio vs. Cable. A Practical Approach*, Stridon Press Inc., 2000.

Lo, Y.T. and Lee, S.W., (Editors), *The Antenna Handbook*, Volumes I–IV, Van Nostrand Reinhold, USA, 1993.

Mailloux, R.J., *Phased Array Antenna Handbook*, Artech House, Inc., Norwood, MA, 1994.

Proakis, John G., *Digital Communications*, McGraw-Hill Book Company, New York, 1983.

Silvester, P.P. and Ferrari, R.L., *Finite Elements for Electrical Engineers*, 3rd Edition, Cambridge University Press, Cambridge, 1996.

Sklar, B., *Digital Communications. Fundamentals and Applications*, Prentice-Hall Inc., Englewood Cliffs, NJ, 1988.

Snyder, J.P., *Map Projection — A Working Manual*, U.S. Geological Survey Professional Paper 1395, United States Government Printing Office, Washington: 1987. (Second Printing 1989).

Spilker, J.J., Jr., *Digital Communications by Satellite*, Prentice-Hall Inc., Englewood Cliffs, NJ, 1977.

Stutzman, W.L., Thiele, G.A., *Antenna Theory and Design*, John Wiley & Sons, Inc., New York, 1981. 2nd Edition, John Wiley & Sons, Inc., New York, 1998.

Van Trees, H.L., *Detection, Estimation, and Modulation Theory*, Part I, 1968, Part II, 1971, Part III, John Wiley & Sons, Inc., New York, 1971.

Walker, J., *Advances in Mobile Information Systems*, Artech House, Inc., Norwood, MA, 1999.

2.3 Broadband Wireless Access: High Rate, Point to Multipoint, Fixed Antenna Systems

Brian Petry

Broadband Wireless Access (BWA) broadly applies to systems providing radio communications access to a core network. Access is the key word because a BWA system by itself does not form a complete network, but only the access part. As the "last mile" between core networks and customers, BWA provides access services for a wide range of customers (also called subscribers), from homes to large enterprises. For enterprises such as small to large businesses, BWA supports such core networks as the public Internet, Asynchronous Transfer Mode (ATM) networks, and the Public Switched Telephone Network (PSTN). Residential subscribers and small offices may not require access to such a broad set of core networks — Internet access is likely BWA's primary access function. BWA is meant to provide reliable, high throughput data services as an alternative to wired access technologies.

This article presents an overview of the requirements, functions, and protocols of BWA systems and describes some of today's efforts to standardize BWA interfaces.

Fundamental BWA Properties

Currently, the industry and standards committees are converging on a set of properties that BWA systems have, or should have, in common. A minimal BWA system consists of a single base station and a single subscriber station. The base station contains an interface, or interworking function (IWF), to a core network, and a radio "air" interface to the subscriber station. The subscriber station contains an interface to a customer premises network and of course, an air interface to the base station. Such a minimal system represents the point-to-point wireless transmission systems that have been in use for many years. Interesting BWA systems have more complex properties, the most central of which is point-to-multipoint (P-MP) capability. A single base station can service multiple subscriber stations using the same radio channel. The P-MP property of BWA systems feature omnidirectional or shaped sector radio antennas at the base station that cover a geographic and spectral area that efficiently serves a set of customers given the allocation of radio spectrum. Multiple subscriber stations can receive the base station's downstream transmissions on the same radio channel. Depending on the density and data throughput requirements of subscribers in a given sector, multiple radio channels may be employed, thus overlaying sectors. The frequency bands used for BWA allow for conventional directional antennas. So, in the upstream transmission direction, a subscriber's radio antenna is usually highly directional, aimed at the base station. Such configuration of shaped sectors and directional antennas allow for flexible deployment of BWA systems and helps conserve radio spectrum by allowing frequency bands to be reused in nearby sectors.

With such P-MP functions and a sectorized approach, more BWA properties unfold and we find that BWA is similar to other other well-known access systems. A BWA deployment is cellular in nature, and like a cellular telephone deployment, requires complicated rules and guidelines that impact power transmission limits, frequency reuse, channel assignment, cell placement, etc. Also, since subscriber stations can share spectrum in both the upstream and downstream directions, yet do not communicate with each other using the air interface, BWA systems have properties very similar to hybrid fiber coaxial (HFC) access networks that coexist with cable television service. HFC networks also employ a base station (called a head end) and subscriber stations (called cable modems). And subscriber stations share channels in both downstream and upstream directions. Such HFC networks are now popularized by both proprietary systems and the Data-over-Cable System Interface Specifications (DOCSIS) industry standards [1]. In the downstream direction, digital video broadcast systems have properties similar to BWA. They employ base stations on the ground or onboard satellites: multiple subscribers tune their receivers to the same channels. With properties similar to cellular, cable modems, and digital video broadcast, BWA systems borrow many technical features from them.

BWA Fills Technology Gaps

Since BWA is access technology, it naturally competes with other broadband, high data rate access technologies, such as high data rate digital cellular service, digital subscriber line (DSL) on copper telephone wires, cable modems on coaxial TV cables, satellite-based access systems, and even optical access technologies on fiber or free space. To some, the application of BWA overlaps with these access technologies and also appears to fill in the gaps left by them. Following are some examples of technology overlaps where BWA fills in gaps.

High data rate digital cellular data service will be available by the time this book is published. This service is built "on top of" digital cellular telephone service. The maximum achievable data rate for these new "third generation" digital cellular systems is intended to be around 2.5 Mbps. At these maximum speeds, high data rate cellular competes with low-end BWA, but since BWA systems are not intended to be mobile, and utilize wider frequency bands, a BWA deployment should be able to offer higher data rates. Furthermore, a BWA service deployment does not require near ubiquitous service area coverage. Before service can be offered by mobile cellular services, service must be available throughout entire metropolitan areas. But for BWA, service can be offered where target customers are located before covering large areas. Thus, in addition to higher achievable data rates with BWA, the cost to reach the first subscribers should be much less.

Current DSL technology can reach out about 6 km from the telephone central office, but the achievable data rate degrades significantly as the maximum distance is reached. Currently, the maximum DSL data rate is around 8 Mbps. Asymmetric DSL (ADSL) provides higher data rates downstream than upstream, which is ideal for residential Internet access, but can be limiting for some business applications. BWA can fill in by providing much higher data rates further from telephone central offices. BWA protocols and deployment strategies enable the flexibility necessary to offer both asymmetric and symmetric services.

HFC cable modem technology, which is also asymmetric in nature, is ideal for residential subscribers. But many subscribers — potentially thousands — often share the same downstream channels and contend heavily for access to a limited number of available upstream channels. A key advantage of HFC is consistent channel characteristics throughout the network. With few exceptions, the fiber and coaxial cables deliver a consistent signal to subscribers over very long distances. BWA fills in, giving a service provider the flexibility to locate base stations and configure sectors to best service customers who need consistent, high data rates dedicated to them.

Satellite access systems are usually unidirectional, whereas less available bidirectional satellite-based service is more expensive. Either type of satellite access is asymmetric in nature: unidirectional service requires some sort of terrestrial "upstream," and many subscribers contend for the "uplink" in bidirectional access systems. Satellites in geostationary Earth orbits (GEO) impose a minimum transit delay of 240 ms on transmissions between ground stations. Before a satellite access system can be profitable, it must overcome the notable initial expense of launching satellites or leasing bandwidth on a limited number of existing satellites by registering many subscribers. Yet, satellite access services offer extremely wide geographic coverage with no infrastructure planning, which is especially attractive for rural or remote service areas that DSL and cable modems do not reach. Perhaps high data rate, global service coverage by low Earth orbiting (LEO) satellites will someday overcome some of GEO's limitations. BWA fills in by allowing service providers to locate base stations and infrastructure near subscribers that should be more cost effective and impose less delay than satellite services.

Optical access technologies offer unbeatable performance in data rate, reliability, and range, where access to fiber-optic cable is available. But in most areas, only large businesses have access to fiber. New technology to overcome this limitation, and avoid digging trenches and pulling fiber into the customer premises is free space optical, which employs lasers to extend between a business and a point where fiber is more readily accessible. Since BWA base stations could also be employed at fiber access points to reach non-fiber-capable subscribers, both BWA and free space optical require less infrastructure planning such as digging, tunneling, and pulling cables under streets. Although optical can offer an order of magnitude increase in data rate over the comparatively lower frequency/higher wavelength BWA radio communications, BWA can have an advantage in some instances because BWA typically has a longer range and its sector-based coverage allows multiple subscribers to be serviced by a single base station.

Given these gaps left by other broadband access technologies, even with directly overlapping competition in many areas, the long-term success of BWA technology is virtually ensured.

BWA Frequency Bands and Market Factors

Globally, a wide range of frequency bands are available for use by BWA systems. To date, systems that implement BWA fall into roughly two categories: those that operate at high frequencies (roughly 10 to 60 GHz) and those that operate at low frequencies (2 to 11 GHz). Systems in the low frequency category may be further subdivided into those that operate in licensed vs. unlicensed bands. Unlicensed low frequency bands are sometimes considered separately because of the variations of emitted power restrictions imposed by regulatory agencies and larger potential for interference by other "unlicensed" technologies. The high frequencies have significantly different characteristics than the low frequencies that impact the expense of equipment, base station locations, range of coverage, and other factors. The key differing characteristics in turn impact the type of subscriber and types of services offered as will be seen later in this article.

Even though available spectrum varies, most nationalities and regulatory bodies recognize the vicinity of 30 GHz, with wide bands typically available, for use by BWA. In the United States, for instance, the FCC has allocated Local Multipoint Distribution Service (LMDS) bands for BWA. That, coupled with the availability of radio experience, borrowed from military purposes and satellite communications, influenced the BWA industry to focus their efforts in this area. BWA in the vicinity of 30 GHz is thus also a target area for standardization of interoperable BWA systems. Available spectrum for lower frequencies, 2 to 11 GHz, varies widely by geography and regulatory body. In the United States, for instance, the FCC has allocated several bands called Multipoint/Multichannel Distribution Services (MDS) and licensed them for BWA use. The industry is also targeting the lower spectrum, both licensed and unlicensed, for standardization.

Radio communications around 30 GHz have some important implications for BWA. For subscriber stations, directional radio antennas are practical. For base stations, so are shaped sector antennas. But two key impairments limit how such BWA systems are deployed: line-of-site and rain. BWA at 30 GHz almost strictly requires a line-of-sight path to operate effectively. Even foliage can prohibitively absorb the radio energy. Some near line-of-sight scenarios, such as a radio beam that passes in close proximity to reflective surfaces like metal sheets or wet roofs, can also cause significant communications impairments. Rain can be penetrated, depending on the distance between subscriber and base station, the droplet size, and rate of precipitation. BWA service providers pay close attention to climate zones and historical weather data to plan deployments. In rainy areas where subscribers require high data rate services, small cell sizes can satisfy a particular guaranteed service availability. Also, to accommodate changing rain conditions, BWA systems offer adaptive transmit power control. As the rate of precipitation increases, transmit power is boosted as necessary. The base station and subscriber station coordinate with each other to boost or decrease transmit power.

Impairments aside, equipment cost is an important issue with 30 GHz BWA systems. As of today, of all the components in a BWA station, the radio power amplifier contributes most to system cost. Furthermore, since the subscriber antenna must be located outdoors (to overcome the aforementioned impairments), installation cost contributes to the equation. A subscriber installation consists of an indoor unit (IDU) that typically houses the digital equipment, modem, control functions, and interface to the subscriber network, and an outdoor unit (ODU), which typically houses the amplifier and antenna. Today these factors, combined with the aforementioned impairments, typically limit the use of 30 GHz BWA systems to businesses that both need the higher-end of achievable data rates and can afford the equipment. BWA technology achieves data rates delivered to a subscriber in a wide range, 2 to 155 Mbps. The cost of 30 GHz BWA technology may render the lower end of the range impractical. However, many people project the cost of 30 GHz BWA equipment to drop as the years go by, to the point where residential service will be practical.

In the lower spectrum for BWA systems, in the range of approximately 2 to 11 GHz, line-of-sight and rain are not as critical impairments. Here, a key issue to contend with is interference due to reflections, also called multipath. A receiver, either base station or subscriber, may have to cope with multiple copies of the signal, received at different delays, due to reflections off buildings or other large objects in a sector. So, different modulation techniques may be employed in these lower frequency BWA systems, as opposed to high frequency systems, to compensate for multipath. Furthermore, if the additional expense can be justified, subscribers and/or base stations, could employ spatial processing to combine the main signal with its reflections and thus find a stronger signal that has more data capacity than the main signal by itself. Such spatial processing requires at least two antennas and radio receivers. In some cases, it may even be beneficial for a base station to employ induced multipath, using multiple transmit antennas, perhaps aimed at reflective objects, to reach subscribers, even those hidden by obstructions, with a better combined signal than just one.

Unlike BWA near 30 GHz, BWA in the lower spectrum today has the advantage of less expensive equipment. Also, it may be feasible in some deployments for the subscriber antenna to be located indoors. Further, the achievable data rates are typically lower than at 30 GHz, with smaller channel bandwidths, in the range of about 2 to 15 Mbps. Although some promise 30 GHz equipment costs will drop, these factors make lower frequency BWA more attractive to residences and small businesses today.

Due to the differing requirements of businesses and residences and the different capabilities of higher frequency BWA vs. lower, the types of service offered is naturally divided as well. Businesses will typically subscribe to BWA at the higher frequencies, around 30 GHz, and employ services that carry guaranteed quality of service for both data and voice communications. In the business category, multi-tenant office buildings and dwellings are also lumped in. At multi-tenant sites, multiple paying subscribers share one BWA radio and each subscriber may require different data or voice services. For data, Internet Protocol (IP) service is of prime importance, but large businesses also rely on wide area network technologies like asynchronous transfer mode (ATM) and frame relay that BWA must efficiently transport. To date, ATM's capabilities offer practical methods for dedicating, partitioning, and prioritizing data flows, generally called quality of service (QoS). But as time goes on (perhaps by this reading) IP-based QoS capabilities will overtake ATM. So, for both residential and business purposes, IP service will be the data service of choice in the future. Besides data, businesses rely on traditional telephony links to local telephone service providers. Business telephony services, for medium-to-large enterprises, utilize time division multiplexed (TDM) telephone circuits on copper wires to aggregate voice calls. Some BWA systems have the means to efficiently transport such aggregated voice circuits. Due to the economic and performance differences between low frequency BWA and high frequency BWA, low frequency BWA generally carries residential- and small business-oriented services, whereas high frequency BWA carries small- to large-enterprise services.

Since BWA equipment for the lower frequencies may be less expensive and less sensitive to radio directionality, and therefore more practical to cover large areas such as residential environments, subscriber equipment can potentially be nomadic. Nomadic means that the equipment may be moved quickly and easily from one location to another, but is not expected to be usable while in transit. Whereas at the higher frequencies, with more expensive subscriber equipment, the decoupling of indoor and outdoor units, the highly directional nature of radio communications in that range, and subscriber-oriented services provisioned at the base station, subscriber stations are fixed. Once they are installed, they do not move unless the subscriber terminates service and re-subscribes somewhere else.

Standards Activities

Several standards activities are under way to enable interoperability between vendors of BWA equipment. The standardization efforts are primarily focused on an interoperable "air interface" that defines how compliant base stations interoperate with compliant subscriber stations. By this reading, some of the standards may have been completed — the reader is encouraged to check the status of BWA standardization. Some standards groups archive contributions by industry participants and those archives, along with the actual published standards, provide important insights into BWA technology. Currently, most activity is centered around the Institute for Electronics and Electrical Engineers (IEEE) Local Area Network/Metropolitan Area Network (LAN/MAN) Standards Committee (LMSC), which authors the IEEE 802 series of data network standards. Within LMSC, the 802.16 working group authors BWA standards. The other notable BWA standards effort, under the direction of the European Telecommunications Standards Institute (ETSI), is a project called Broadband Radio Access Networks/HyperAccess (BRAN/HA). The IEEE LMSC is an organization that has international membership and has the means to promote their standards to "international standard" status through the International Organization for Standardization (ISO) as does ETSI. But ETSI standards draw from a European base, whereas LMSC draws from a more international base of participation. Even so, the LMSC and BRAN/HA groups, although they strive to develop standards each with a different approach, have many common members who desire to promote a single, international standard. Hopefully, the reader will have discovered that the two groups have converged on one standard that enables internationally harmonized BWA interoperability.

To date, the IEEE 802.16 working group has segmented their activities into three main areas: BWA interoperability at bands around 30 GHz (802.16.1), a recommended practice for the coexistence of BWA systems (802.16.2) and BWA interoperability for licensed bands between 2 and 11 GHz (802.16.3). By the time this book is published, more standards activities may have been added, such as interoperability for some unlicensed bands. The ETSI BRAN/HA group is focused on interoperability in bands around 30 GHz.

Past standards activities were efforts to agree on how to adapt existing technologies for BWA: cable modems and digital video broadcast. A BWA air interface, as similar to DOCSIS cable modems as possible, was standardized by the radio sector of the International Telecommunications Union (ITU) under the ITU-R Joint Rappateur's Group (JRG) 9B committee [2]. The Digital Audio-Video Council (DAVIC) has standardized audio and video transport using techniques similar to BWA [3]. Similarly, the Digital Video Broadcasting (DVB) industry consortium, noted for having published important standards for satellite digital video broadcast, has also published standards, through ETSI, for terrestrial-based digital television broadcast over both cable television networks and wireless. DVB has defined the means to broadcast digital video in both the "low" (<10 Gbps) and "high" (>10 Gbps) BWA spectra [4, 5]. These standards enabled interoperability of early BWA deployment by utilizing existing subsystems and components. Technology from them provided a basis for both the IEEE LMSC and ETSI BRAN/HA standardization processes. However, the current IEEE and ETSI efforts strive to define protocols with features and nuances more particular to efficient BWA communications.

Technical Issues: Interfaces and Protocols

A BWA access network is perhaps best described by its air interface: what goes on between the base station and subscriber stations. Other important interfaces exist in BWA systems, such as:

- interfaces to core networks like ATM, Frame Relay, IP, and PSTN
- interfaces to subscriber networks like ATM, Ethernet, Token Ring, and private branch exchange (PBX) telephone systems
- the interface between indoor unit (IDU) and outdoor unit (ODU)
- interfaces to back-haul links, both wired and wireless, for remote base stations not co-located with core networks
- air interface repeaters and reflectors

These other interfaces are outside the scope of this article. However, understanding their requirements is important to consider how a BWA air interface can best support external interfaces, particularly how the air interface supports their unique throughput, delay, and QoS requirements.

Protocols and Layering

Network subsystems following the IEEE LMSC reference model [6] focus on the lower two layers of the ISO Basic Reference Model for Open Systems Interconnection [7]. The air interface of a BWA system is also best described by these two layers. In LMSC standards, layers one and two, the physical and data link layers, are typically further subdivided. For BWA, the important subdivision of layer 2 is the medium access control (MAC) sublayer. This layer defines the protocols and procedures by which network nodes contend for access to a shared channel, or physical layer. In a BWA system, since frequency channels are shared among subscriber stations in both the downstream and upstream directions, MAC layer services are critical for efficient operation. The physical layer (PHY) of a BWA system is responsible for providing a raw communications channel, employing modulation and error correction technology appropriate for BWA.

Other critical functions, some of which may reside outside the MAC and PHY layers, must also be defined for an interoperable air interface: security and management. Security is divided two areas: a subscriber's authorized use of a base station and associated radio channels and privacy of transported data. Since the communications channel is wireless, it is subject to abuse by intruders, observers, and those seeking to deny service. BWA security protocols must be well defined to provide wire-like security and allow for interoperability. Since to a great extent, HFC cable TV access networks are very similar to BWA regarding security requirements, BWA borrows heavily from the security technology of such cable systems. Similarly, interoperable management mechanisms and protocols include the means to provision, control and monitor subscribers stations and base stations.

The Physical Layer

The physical layer (PHY) is designed with several fundamental goals in mind: spectral efficiency, reliability, and performance. However, these are not independent goals. We can not have the best of all three because each of those goals affects the others: too much of one means too little of the others. But reliability and performance levels are likely to be specified. And once they are specified, spectral efficiency can be somewhat optimized. One measure of reliability is the bit error ratio (BER), the ratio of the number of bit errors to the number of non-errored bits, delivered by a PHY receiver to the MAC layer. The physical layer must provide for better than 10^{-6} BER, and hopefully closer to 10^{-9}. The larger error ratio may only be suitable for some voice services, whereas a ratio closer to the lower end of the range is required for reliable data services that could offer equivalent error performance as local area networks (LANs). Reliability is related to availability. Business subscribers often require contracts that guarantee a certain level of availability. For instance, a service provider may promise that the air interface be available to offer guaranteed reliability and performance 99.99% (also called "four nines") of the time.

Performance goals specify minimum data rates. Since, in BWA systems, the spectrum is shared by subscribers, and allocation of capacity among them is up to the MAC layer, the PHY is more concerned with the aggregate capacity of a single radio channel in one sector of a base station than for capacity to a given subscriber. But if one subscriber would offer to purchase all the available capacity, the service provider would undoubtedly comply. For instance, a capacity goal currently set by the BRAN/HA committee is 25 Mbps on a 28 MHz channel. Without considering deployment scenarios, however, PHY goals are meaningless. Obviously, higher capacity and reliability could be better achieved by shorter, narrower sectors (smaller cells) rather than wider, longer sectors (larger cells). And the same sized sector in a rainy, or obstructed, terrain offers less guaranteed capacity than one in the flattest part of the desert. In any case, the industry seems to be converging on a goal to provide at least 1 bps/Hz capacity in an approximately 25 MHz wide channel with a BER of 10^{-8}. Many deployments should be able to offer much greater capacity.

In addition to such fundamental goals, other factors affect the choice of PHY protocols and procedures. One is duplex mode. The duplex mode can affect the cost of equipment, and some regulatory bodies may limit the choice of duplex mode in certain bands. Three duplex modes are considered for BWA: frequency division duplex (FDD), time division duplex (TDD), and half-duplex FDD (H-FDD). In FDD, a radio channel is designated for either upstream- or downstream-only use. Some bands are regulated such that a channel could only be upstream or downstream, thus requiring FDD if such bands are to be utilized. In TDD mode, one channel is used for both upstream and downstream communications. TDD-capable BWA equipment thus ping-pongs between transmit and receive mode within a single channel; all equipment in a sector is synchronized to divisions between transmit and receive. TDD is useful for bands in which the number of available, or licensed, channels is limited. TDD also allows for asymmetric service without reconfiguring the bandwidth of FDD channels. For instance, a service provider may determine that a residential deployment is more apt to utilize more downstream bandwidth than upstream. Then, rather than reallocating or sub-channeling FDD channels, the service provider can designate more time in a channel for downstream communications than upstream. Additionally, TDD equipment could potentially be less expensive than FDD equipment since components may be shared between the upstream and downstream paths and the cost of a duplexor may be eliminated. However, the third option, H-FDD, is a reasonable compromise between TDD and FDD. In H-FDD mode, a subscriber station decides when it can transmit and when it can receive, but cannot receive while transmitting. But the base station is usually full duplex, or FDD. For subscriber stations, H-FDD equipment can achieve the same cost savings as TDD, and offers the flexibility of asymmetric service. But H-FDD does not require all subscribers in a sector to synchronize on the same allocated time between transmit and receive.

Another important factor affecting spectral efficiency, upgradability, and flexible deployment scenarios, is adaptive modulation. In BWA, the channel characteristics vary much more widely than wired access systems. Rain, interference and other factors can affect subscriber stations individually in a sector, whereas in wired networks, such as HFC cable TV, the channel characteristics are consistent. Thus, to make good use of available bandwidth in favorable channel conditions, subscribers that can take advantage of higher data rates should be allowed to do so. And when it rains in one portion of a sector, or other impairments such as interference occur, subscriber stations can adapt to the channel conditions by reducing the data rate (although transmit power level adjustment is usually the first adaptive tool BWA stations use when it rains). Besides adapting to channel conditions, adaptive modulation facilitates future deployment of newer modulation techniques while retaining compatibility with currently installed subscriber stations. When the service provider upgrades a base station and offers better modulation to new customers, not all subscriber stations become obsolete. To achieve the most flexibility in adaptive modulation, BWA employs "per-subscriber" adaptive modulation to both downstream and upstream communications. Per-subscriber means that each subscriber station can communicate with the base station using a different modulation technique, within the same channel. Some BWA equipment offers per-subscriber adaptive modulation in both the downstream and upstream directions. But other equipment implements a compromise that allows for equipment or components, similar to cable modems or digital video broadcast systems, to require all subscribers to use the same modulation in the downstream direction at any one point in time. Most BWA equipment implements adaptive modulation in the upstream direction. The overriding factor for the PHY layer, with regard to adaptive modulation, is burst mode. Adaptive modulation generally requires burst mode communications at the PHY layer. Time is divided into small units in which stations transmit independent bursts of data. If the downstream employs per-subscriber adaptive modulation, the base station transmits independent bursts to the subscribers. Each burst contains enough information for the receiver to perform synchronization and equalization. However, if per-subscriber adaptive modulation is not employed in the downstream direction, the base station can transmit in continuous mode, in very large, continuous chunks, each chunk potentially containing data destined for multiple subscribers. In burst mode downstream communications, the base station informs subscriber stations, in advance, which burst is theirs. In this way, a subscriber station is not required to demodulate each burst to discover which bursts are for the station, but only to demodulate the "map." The base station encodes the map using the least common denominator modulation type so all subscriber stations can decode it. Conversely, continuous mode downstream, in which per-subscriber adaptive modulation is not used, requires all subscriber stations to demodulate prior to discovering which portions of data are destined for the station. So, per-subscriber adaptive modulation in the downstream affords more flexibility, but a continuous mode downstream may also be used. The standards efforts currently are attempting to work out how both downstream modes may be allowed and yet still have an interoperable standard.

Burst size and the choice of continuous downstream mode in turn affect the choice of error correction coding. Some coding schemes are more efficient with large block sizes, whereas others are more efficient with smaller block sizes.

The fundamental choice of modulation type for BWA varies between the upper BWA bands (~30 GHz) and lower bands (~2 to 11 GHz). In the upper bands, the industry seems to be converging on Quadrature Phase Shift Keying (QPSK) and various levels of Quadrature Amplitude Modulation (QAM). These techniques may also be used in the lower bands, but given the multipath effects that are much more prevalent in the lower bands, BWA equipment is likely to employ Orthogonal Frequency Division Multiplexing (OFDM) or Code Division Multiple Access (CDMA) technology that have inherent properties to mitigate the effects of multipath and spread transmit energy evenly throughout the channel spectrum.

The Medium Access Control Layer

The primary responsibility of the Medium Access Control Layer (MAC) is to allocate capacity among subscriber stations in a way that preserves quality-of-service (QoS) requirements of the services it transports. For instance, traditional telephony and video services could require a constant, dedicated capacity with fixed delay properties. But other data transport services could tolerate more bursty capacity allocations and a higher degree of delay variation. ATM service is notable for its QoS definitions [8]. Although not mature as of this writing, the Internet Protocol (IP) QoS definitions are also notable [9,10]. Though QoS-based capacity allocation is a complex process, the BWA MAC protocol defines the mechanisms to preserve QoS as it transports data. Yet the MAC protocol does not fully define *how* MAC mechanisms are to be used. At first glance, this does not seem to make sense, but it allows the MAC protocol to be defined in as simple terms as possible and leave it up to implementations of base stations and subscriber stations how to best utilize the mechanism that the protocol defines. This approach also allows BWA vendors to differentiate their equipment and still retain interoperability. To simplify capacity allocation, the smarts of QoS implementation reside in the base station, since it is a central point in a BWA sector and is in constant communication with all of the subscriber stations in a sector. The base station is also administered by the service provider, and therefore can serve as the best point of control to keep subscribers from exceeding their contractual capacity limitations and priorities.

Capacity Allocation Mechanisms — An overview of the mechanisms employed by the MAC layer to allocate capacity follows. In the downstream direction, the MAC protocol informs subscriber stations what data belongs to what subscriber by means of per-subscriber addressing and within a subscriber, by per-data-flow addressing. All subscribers in a sector "listen" to the downstream data flow and pick off transmissions belonging to them. If the downstream channel employs per-subscriber adaptive modulation, some subscriber stations may not be able to decode the modulation destined to other subscribers. In this case, the base station informs subscribers what bursts it should observe, with a downstream "map." The downstream map indicates what offsets in a subsequent transmission may contain data for the specified subscriber. The MAC must communicate this information to the PHY layer to control its demodulation.

For upstream capacity allocation and reservation, the MAC employs slightly more complicated schemes. The upstream channel is the central point of contention: all subscriber stations in a channel are contending for access to transmit in the upstream channel. Some subscribers require constant periodic access, others require bursty access with minimum and maximum reservation limits. Still other data flows may not require any long-standing reservations but can request a chunk of capacity when needed and survive the inherent access delay until the base station satisfies the request. On top of these varying data flow requirements, which are specified by subscriber stations and granted by the base station, priorities increase complications. The base station administers both priorities and QoS parameters of each data flow in each subscriber station. How a base station keeps track of all the flows of subscribers and how it actually meets the reservation requirements is usually beyond the scope of the BWA air interface in standards documents. But base stations likely employ well-known queuing algorithms and reservation lists to ensure that it assigns capacity fairly and meets subscribers' contractual obligations. Yet, as mentioned earlier, room is left for BWA base station vendors to employ proprietary "tricks" to differentiate their equipment from others. To communicate capacity allocation to subscribers, the base station divides time into multi-access frames (e.g., on the order of 1 to 5 milliseconds) in which multiple subscribers are assigned capacity. To accomplish this, a fixed allocation unit, or time slot, is defined. So, the upstream channel is divided into small, fixed-length time slots (e.g., on the order of 10 microseconds) and the base station periodically transmits a "map" of slot assignments to all subscribers in a channel. The slot assignments inform the subscriber stations which slots are theirs for the upcoming multi-access frame.

Periodically, a set of upstream slots is reserved for "open contention." That is, any subscriber is authorized to transmit during an open contention period. A subscriber can utilize open contention for initial sign-on to the network (called "registration"), to transmit a request for upstream capacity, or even to transmit a small amount of data. Since a transmission may collide with that of another subscriber station, a collision avoidance scheme is used. A subscriber station initiates transmission in a randomly chosen open contention slot, but cannot immediately detect that its transmission collided with another. The only way a subscriber station can determine if its transmission collided is if it receives no acknowledgment from the base station. In this case, the subscriber backs off a random number of open contention slots before attempting another transmission. The process continues, with the random number range getting exponentially larger on each attempt, until the transmission succeeds. The random back-off interval is typically truncated at the sixteenth attempt, when the subscriber station starts over with its next attempt in the original random number range. This back-off scheme is called "truncated binary exponential back-off," and is employed by popular MAC protocols such as Ethernet [11].

To mitigate the effects of potentially excessive collisions during open contention, the MAC protocol defines a means to request bandwidth during assigned slots in which no collision would happen. For instance, active subscriber stations may receive from the base station a periodic slot for requesting capacity or requesting a change in a prior reservation. This form of allocation-for-a-reservation-request is called a "poll." Also, the MAC protocol provides a means to "piggy-back" a request for capacity with a normal upstream data transmission. Subscriber stations that have been inactive may receive less frequent polls from the base station so as to conserve bandwidth. So, with a means for contentionless bandwidth reservation, the only time subscriber stations need to use the open contention window is for initial registration.

Slot-based reservations require that the base stations and subscribers be synchronized. Of course, the base station provides a timing base for all subscriber stations. To achieve accurate timing, subscriber stations need to determine how far they are from the base station so their transmissions can be scheduled to reach the base station at the exact point in time, relative to each other. The procedure to determine this distance, which is not really a measured linear distance, but a measurement of time, is called "ranging." Each subscriber station, coordinating with the base station, performs ranging during its registration process.

To maintain efficient use of bandwidth and accommodate PHY requirements of transmit power control, and flexible duplex modes, the MAC protocol performs even more gyrations. If interested, the reader is encouraged to read BWA MAC protocol standards, or drafts in progress, to learn more.

Automatic Repeat Request (ARQ) Layer

Some BWA systems trade off the bandwidth normally consumed by the PHY's error correction coding for the potential delays of ARQ protocol. An ARQ protocol employs sequence numbering and retransmissions to provide a reliable air link between base station and subscriber. ARQ requires more buffering in both the base station and subscriber station than systems without ARQ. But even with a highly-coded PHY, some subscriber stations may be located in high interference or burst-noise environments in which error correction falls apart. In such situations, ARQ can maintain performance, or ensure the service meets contractual availability and reliability requirements. Standards groups seem to be converging on allowing the use of ARQ, but not requiring it. The MAC protocol is then specified so that when ARQ is not used, no additional overhead is allocated just to allow the ARQ option.

Conclusion

This article has provided an overview of how BWA fits in with other broadband access technologies. It was also a short primer on BWA protocols and standards. To learn more about BWA, the reader is encouraged to read currently available standards documents, various radio communications technical journals, and consult with vendors of BWA equipment.

References

1. SCTE SP-RFI-105-981010: *Data-Over-Cable Service Interface Specifications: Radio Frequency Interface Specification,* The Society of Cable Telecommunications Engineers, Exton, Pennsylvania, 1999.
2. Draft Recommendation F.9B/BWA.- Radio transmission systems for fixed broadband wireless access (BWA) based on cable modem standard, International Telecommunications Union, Geneva, 1999.
3. DAVIC 1.4.1 *Specification Part 8: Lower Layer Protocols and Physical Interfaces,* Digital Audio-Visual Council, Geneva, 1999.
4. ETS 300 748, *Digital Video Broadcasting (DVB): Multipoint Video Distribution Systems (MVDS) at 10 GHz and above,* European Telecommunications Standards Institute, Geneva, 1997.
5. ETS 300 749, *Digital Video Broadcasting (DVB): Digital Video Broadcasting (DVB); Microwave Multipoint Distribution Systems (MMDS) below 10 GHz,* European Telecommunications Standards Institute, Geneva, 1997.
6. IEEE Std 802-1990, *IEEE Standards for Local and Metropolitan Area Networks: Overview and Architecture*, Institute for Electrical and Electronics Engineers, Piscataway, NJ, 1990.
7. ISO/IEC 7498-1:1994, *Information Technology — Open Systems Interconnection — Basic Reference Model: The Basic Model*, International Organization for Standardization, Geneva, 1994.
8. Bermejo, L. P. et al., Service characteristics and traffic models in broadband ISDN, *Electrical Commun.,* 64-2/3, 132–138, 1990.

9. Blake, S. et al., *RFC-2475 An Architecture for Differentiated Service*, Internet Engineering Task Force, 1998.
10. Braden, R. et al., *RFC-2205 Resource ReSerVation Protocol (RSVP) — Version 1 Functional Specification*, Internet Engineering Task Force, 1997.
11. IEEE Std 802.3, *Information Technology — Telecommunications and information exchange between systems — Local and metropolitan area networks — Specific requirements — Part 3: Carrier sense multiple access with collision detection (CSMA/CD) access method and physical layer specifications*, Institute for Electronics and Electrical Engineers, Piscataway, NJ, 1998.

2.4 Digital European Cordless Telephone

Saf Asghar

Cordless technology, in contrast to cellular radio, primarily offers access technology rather than fully specified networks. The digital European cordless telecommunications (DECT) standard, however, offers a proposed network architecture in addition to the air interface physical specification and protocols but without specifying all of the necessary procedures and facilities. During the early 1980s a few proprietary digital cordless standards were designed in Europe purely as coexistence standards. The U.K. government in 1989 issued a few operator licenses to allow public-access cordless known as telepoint. Interoperability was a mandatory requirement leading to a common air interface (CAI) specification to allow roaming between systems. This particular standard (CT2/CAI), is described elsewhere in this book. The European Telecommunications Standards Institute (ETSI) in 1988 took over the responsibility for DECT. After formal approval of the specifications by the ETSI technical assembly in March 1992, DECT became a European telecommunications standard, ETS300-175 in August 1992. DECT has a guaranteed pan-European frequency allocation, supported and enforced by European Commission Directive 91/297. The CT2 specification has been adopted by ETSI alongside DECT as an interim standard I-ETSI 300 131 under review.

Application Areas

Initially, DECT was intended mainly to be a private system, to be connected to a private automatic branch exchange (PABX) to give users mobility, within PABX coverage, or to be used as a single cell at a small company or in a home. As the idea with telepoint was adopted and generalized to public access, DECT became part of the public network. DECT should not be regarded as a replacement of an existing network but as created to interface seamlessly to existing and future fixed networks such as public switched telephone network (PSTN), integrated services digital network (ISDN), global system for mobile communications (GSM), and PABX. Although telepoint is mainly associated with CT2, implying public access, the main drawback in CT2 is the ability to only make a call from a telepoint access point. Recently there have been modifications made to the CT2 specification to provide a structure that enables users to make and receive calls. The DECT standard makes it possible for users to receive and make calls at various places, such as airport/railroad terminals, and shopping malls. Public access extends beyond telepoint to at least two other applications: replacement of the wired local loop, often called cordless local loop (CLL), (Fig. 2.8) and neighborhood access, Fig. 2.9. The CLL is a tool for the operator of the public network. Essentially, the operator will install a multiuser base station in a suitable campus location for access to the public network at a subscriber's telephone hooked up to a unit coupled to a directional antenna. The advantages of CLL are high flexibility, fast installation, and possibly lower investments. CLL does not provide mobility. Neighborhoods access is quite different from CLL. Firstly, it offers mobility to the users and, secondly, the antennas are not generally directional, thus requiring higher field strength (higher output power or more densely packed base stations). It is not difficult to visualize that CLL systems could be merged with neighborhood access systems in the context of establishments, such as supermarkets, gas stations, shops, etc., where it might be desirable to set up a DECT system for their own use and at the

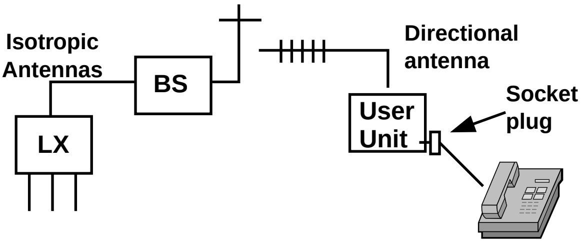

FIGURE 2.8

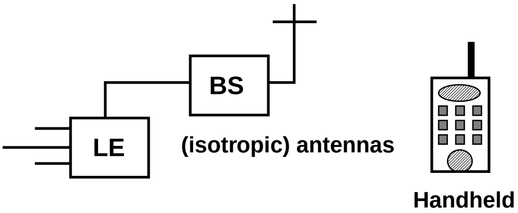

FIGURE 2.9

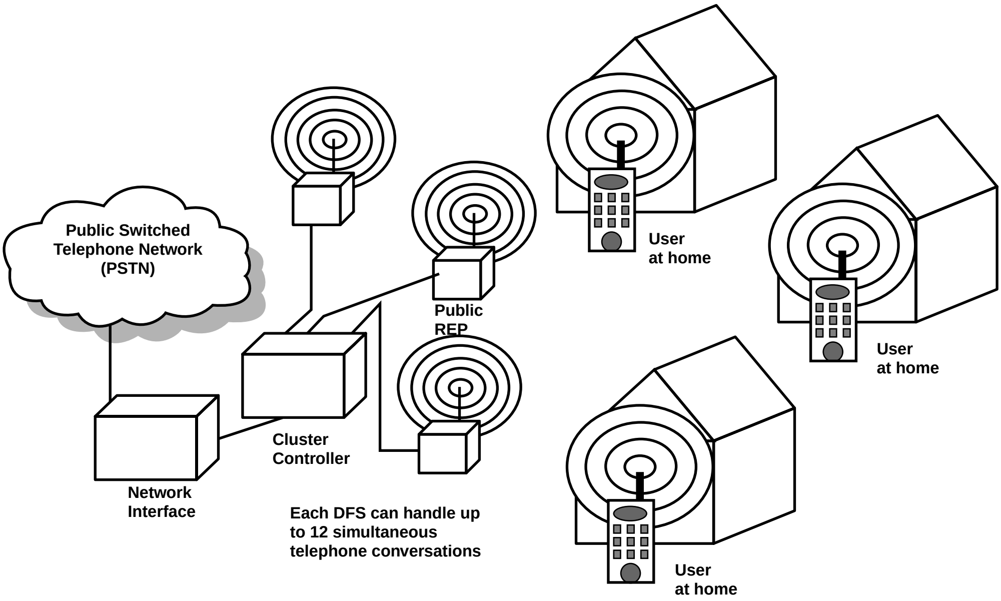

FIGURE 2.10

same time also provide access to customers. The DECT standard already includes signaling for authentication, billing, etc. DECT opens possibilities for a new operator structure, with many diversified architectures connected to a global network operator (Fig. 2.10). DECT is designed to have extremely high capacity. A small size is used, which may seem an expensive approach for covering large areas. Repeaters placed at strategic locations overcome this problem.

DECT/ISDN Interworking

From the outset, a major objective of the DECT specification was to ensure that ISDN services were provided through the DECT network. Within the interworking profile two configurations have been defined: DECT end system and DECT intermediate system. In the end system the ISDN is terminated in the DECT fixed system (DFS). The DFS and the DECT portable system (DPS) may be seen as ISDN terminal equipment (TE1). The DFS can be connected to an S, S/T, or a P interface. The intermediate system is fully transparent to the ISDN. The S interface is regenerated even in the DPS. Both configurations have the following services specified: 3.1-kHz telephony, i.e., standard telephony; 7-kHz telephony; i.e., high-quality audio; video telephony; group III fax, modems, X.25 over the ISDN; and telematic services, such as group IV fax, telex, and videotax.

DECT/GSM Interworking

Groupe Speciale Mobile (GSM) is a pan-European standard for digital cellular radio operation throughout the European community. ETSI has the charter to define an interworking profile for GSM and DECT. The profile describes how DECT can be connected to the fixed network of GSM and the necessary air interface functions. The users obviously benefit from the mobility functions of GSM giving DECT a wide area mobility. The operators will gain access to another class of customer. The two systems when linked together will form the bridge between cordless and cellular technologies. Through the generic access profile, ETSI will specify a well-defined level of interoperability between DECT and GSM. The voice coding aspect in both of these standards is different; therefore, this subject will be revisited to provide a sensible compromise.

DECT Data Access

The DECT standard is specified for both voice and data applications. It is not surprising that ETSI confirmed a role for DECT to support cordless local area network (LAN) applications. A new technical committee, ETSI RES10 has been established to specify the high performance European radio LAN similar to IEEE 802.11 standard in the U.S. (Table 2.8).

TABLE 2.8 DECT Characteristics

Parameters	DECT
Operating frequency, MHz	1880–1990 (Europe)
Radio carrier spacing, MHz	1.728
Transmitted data rate, Mb/s	1.152
Channel assignment method	DCA
Speech data rate, kb/s	32
Speech coding technique	ADPCM G.721
Control channels	In-call-embedded (various logical channels C, P, Q, N)
In-call control channel data rate, kb/s	4.8 (plus 1.6 CRC)
Total channel data rate, kb/s	41.6
Duplexing technique	TDD
Multiple access-TDMA	12 TDD timeslots
Carrier usage-FDMA/MC	10 carriers
Bits per TDMA timeslot, b	420 (424 including the 2 field)
Timeslot duration (including guard time), μs	417
TDMA frame period, ms	10
Modulation technique	Gaussian filtered FSK
Modulation index	0.45–0.55
Peak output power, mW	250
Mean output power, mW	10

How DECT Functions

DECT employs frequency division multiple access (FDMA), time division multiple access (TDMA), and time division duplex (TDD) technologies for transmission. Ten carrier frequencies in the 1.88- and 1.90-GHz band are employed in conjunction with 12 time slots per carrier TDMA and 10 carriers per 20 MHz of spectrum FDMA. Transmission is through TDD. Each channel has 24 times slots, 12 for transmission and 12 for receiving. A transmission channel is formed by the combination of a time slot and a frequency. DECT can, therefore, handle a maximum of 12 simultaneous conversations. TDMA allows the same frequency to use different time slots. Transmission takes place for ms, and during the rest of the time the telephone is free to perform other tasks, such as channel selection. By monitoring check bits in the signaling part of each burst, both ends of the link can tell if reception quality is satisfactory. The telephone is constantly searching for a channel for better signal quality, and this channel is accessed in parallel with the original channel to ensure a seamless changeover. Call handover is also seamless, each cell can handle up to 12 calls simultaneously, and users can roam around the infrastructure without the risk of losing a call. Dynamic channel assignment (DCA) allows the telephone and base station to automatically select a channel that will support a new traffic situation, particularly suited to a high-density office environment.

Architectural Overview

Baseband Architecture

A typical DECT portable or fixed unit consists of two sections: a baseband section and a radio frequency section. The baseband partitioning includes voice coding and protocol handling (Fig. 2.11).

Voice Coding and Telephony Requirements

This section addresses the audio aspects of the DECT specification. The CT2 system as described in the previous chapter requires adaptive differential pulse code modulation (ADPCM) for voice coding. The DECT standard also specifies 32-kb/s ADPCM as a requirement. In a mobile environment it is debatable whether the CCITT G.721 recommendation has to be mandatory. In the handset or the mobile it would be quite acceptable in most cases to implement a compatible or a less complex version of the recommendation. We are dealing with an air interface and communicating with a base station that in the residential situation terminates with the standard POTS line, hence compliance is not an issue. The situation changes in the PBX, however, where the termination is a digital line network. DECT is designed for this case, hence compliance with the voice coding recommendation becomes important. Adhering to this strategy for the base station and the handset has some marketing advantages.

G.721 32-kb/s ADPCM from its inception was adopted to coexist with G.711 64-kb/s pulse code modulation (PCM) or work in tandem, the primary reason being an increase in channel capacity. For

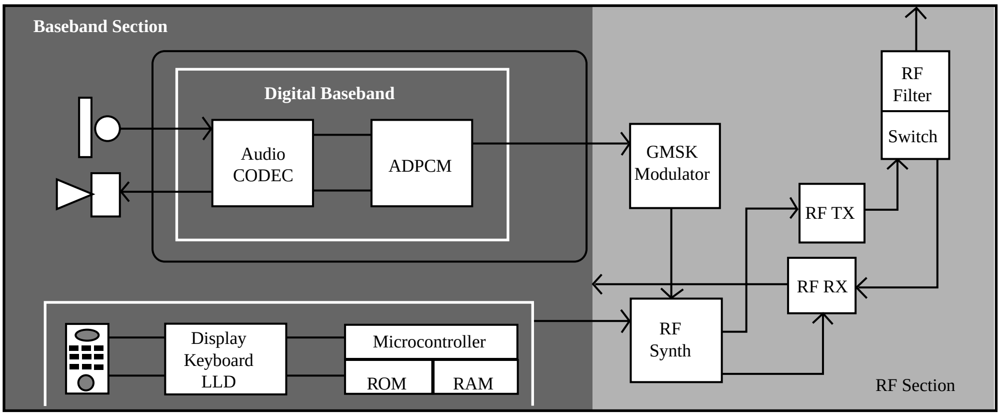

FIGURE 2.11

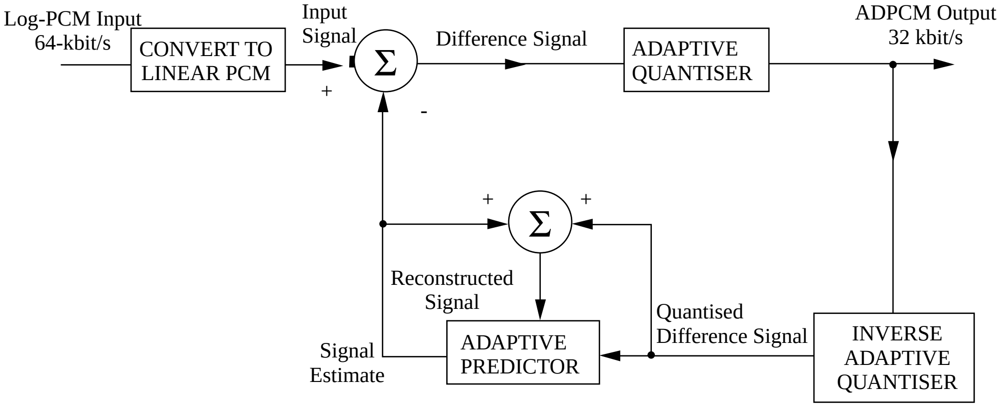

FIGURE 2.12 ADPCM encoder.

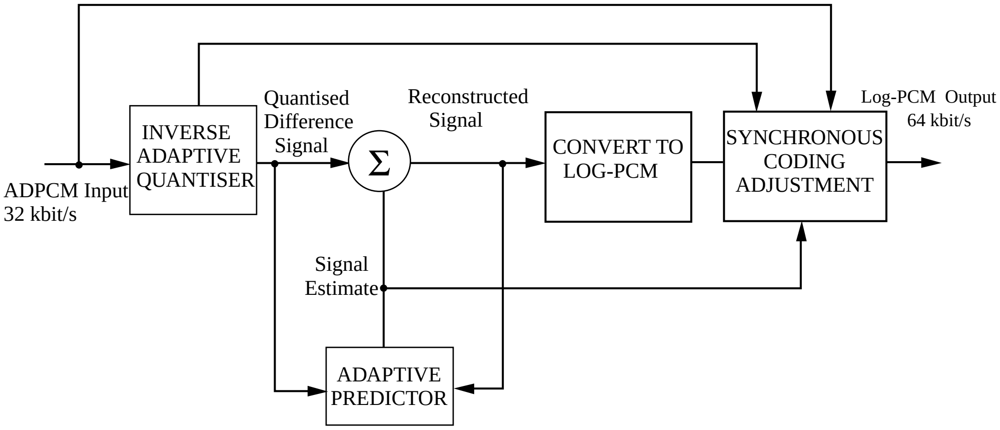

FIGURE 2.13 ADPCM decoder.

modem type signaling, the algorithm is suboptimal in handling medium-to-high data rates, which is probably one of the reasons why there really has not been a proliferation of this technology in the PSTN infrastructure. The theory of ADPCM transcoding is available in books on speech coding techniques, e.g., O'Shaughnessy, 1987.

The ADPCM transcoder consists of an encoder and a decoder. From Figs. 2.12 and 2.13 it is apparent that the decoder exists in the encoder structure. A benefit derived from this structure allows for efficient implementation of the transcoder.

The encoding process takes a linear speech input signal (the CCITT specification relates to a nonwireless medium such as a POTS infrastructure), and subtracts its estimate derived from earlier input signals to obtain a difference signal. This difference signal is 4-b code with a 16-level adaptive quantizer every 125 µs, resulting in a 32-kb/s bit stream. The signal estimate is constructed with the aid of the inverse adaptive quantizer that forms a quantized difference signal that added to the signal estimate is also used to update the adaptive predictor. The adaptive predictor is essentially a second-order recursive filter and a sixth-order nonrecursive filter,

$$S_0(k) = \sum_{i=1}^{2} a_i(k-1)\varepsilon_r(k-i) + \sum_{i=1}^{6} b_i(k-1)d_q(k-i) \tag{2.1}$$

where coefficients *a* and *b* are updated using gradient algorithms.

As suggested, the decoder is really a part of the encoder, that is, the inverse adaptive quantizer reconstructs the quantized difference signal, and the adaptive predictor forms a signal estimate based on the quantized difference signal and earlier samples of the reconstructed signal, which is also the sum of the current estimate and the quantized difference signal as shown in Fig. 2.13. Synchronous coding adjustment tries to correct for errors accumulating in ADPCM from tandem connections of ADPCM transcoders.

ADPCM is basically developed from PCM. It has good speech reproduction quality, comparable to PSTN quality, which therefore led to its adoption in CT2 and DECT.

Telephony Requirements

A general cordless telephone system would include an acoustic interface, i.e., microphone and speaker at the handset coupled to a digitizing compressor/decompressor analog to uniform PCM to ADPCM at 32 kb/s enabling a 2:1 increase in channel capacity as a bonus. This digital stream is processed to be transmitted over the air interface to the base station where the reverse happens, resulting in a linear or a digital stream to be transported over the land-based network. The transmission plans for specific systems are described in detail in Tuttlebee, 1995.

An important subject in telephony is the effect of network echoes [Weinstein, 1977]. Short delays are manageable even if an additional delay of, say, less than 15 µs is introduced by a cordless handset. Delays of a larger magnitude, in excess of 250 µs (such as satellite links [Madsen and Fague, 1993]), coupled to cordless systems can cause severe degradation in speech quality and transmission; a small delay introduced by the cordless link in the presence of strong network echoes is undesirable. The DECT standard actually specifies the requirement for network echo control. Additional material can be obtained from the relevant CCITT documents [CCITT, 1984–1985].

Modulation Method

The modulation method for DECT is Gaussian filtered frequency shift keying (GFSK) with a nominal deviation of 288 kHz [Madsen and Fague, 1993]. The *BT*, i.e., Gaussian filter bandwidth to bit ratio, is 0.5 and the bit rate is 1.152 Mb/s. Specification details can be obtained from the relevant ETSI documents listed in the reference section.

Digital transmission channels in the radio frequency bands, including the DECT systems, present serious problems of spectral schemes congestion and introduce severe adjacent/co-channel interference problems. There were several schemes employed to alleviate these problems: new allocations at high frequencies, use of frequency-reuse techniques, efficient source encoding, and spectrally efficient modulation techniques.

Any communication system is governed mainly by two criteria, transmitted power and channel bandwidth. These two variables have to be exploited in an optimum manner in order to achieve maximum bandwidth efficiency, defined as the ratio of data rate to channel bandwidth (units of bit/Hz/s) [Pasupathy, 1979]. GMSK/GFSK has the properties of constant envelope, relatively narrow bandwidth, and coherent detection capability. Minimum shift keying (MSK) can be generated directly from FM, i.e., the output power spectrum of MSK can be created by using a premodulation low-pass filter. To ensure that the output power spectrum is constant, the low-pass filter should have a narrow bandwidth and sharp cutoff, low overshoot, and the filter output should have a phase shift $\pi/2$, which is useful for coherent detection of MSK; see Fig. 2.14.

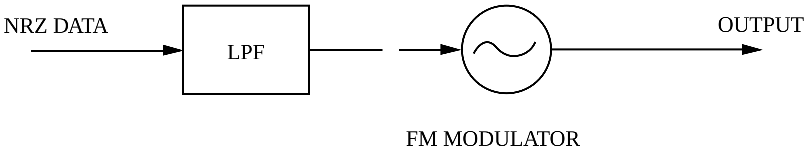

FIGURE 2.14 Premodulation baseband-filtered MSK.

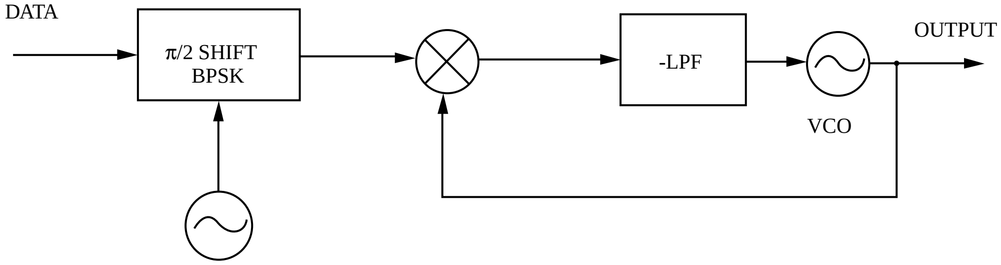

FIGURE 2.15 PLL-type GMSK modulator.

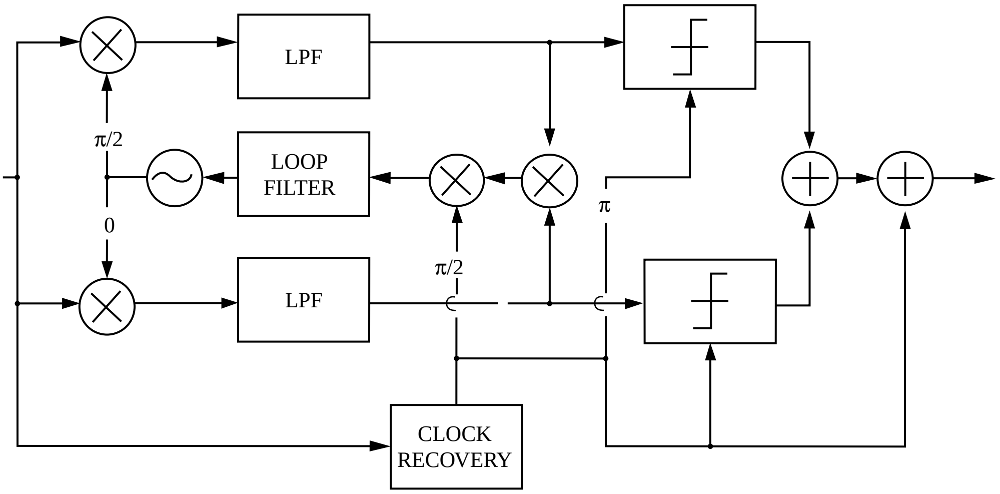

FIGURE 2.16 Costas Loop.

Properties of GMSK satisfy all of these characteristics. We replace the low-pass filter with a premodulation Gaussian low-pass filter [Murota and Hirade, 1981]. As shown in Fig. 2.15, it is relatively simple to modulate the frequency of the VCO directly by the baseband Gaussian pulse stream, however, the difficulty lies in keeping the center frequency within the allowable value. This becomes more apparent when analog techniques are employed for generating such signals. A possible solution to this problem in the analog domain would be to use a phase-lock loop (PLL) modulator with a precise transfer function. It is desirable these days to employ digital techniques, which are far more robust in meeting the requirements talked about earlier. This would suggest an orthogonal modulator with digital waveform generators [de Jager and Dekker, 1978].

The demodulator structure in a GMSK/GFSK system is centered around orthogonal coherent detection, the main issue being recovery of the reference carrier and timing. A typical method, is described in de Buda, 1972, where the reference carrier is recovered by dividing by four the sum of the two discrete frequencies contained in the frequency doubler output, and the timing is recovered directly from their difference. This method can also be considered to be equivalent to the Costas loop structure as shown in Fig. 2.16.

In the following are some theoretical and experimental representations of the modulation technique just described. Considerable literature is available on the subject of data and modulation schemes and the reader is advised to refer to Pasupathy (1979) and Murota and Hirade (1981) for further access to relevant study material.

Radio Frequency Architecture

We have discussed the need for low power consumption and low cost in designing cordless telephones. These days digital transmitter/single conversion receiver techniques are employed to provide highly

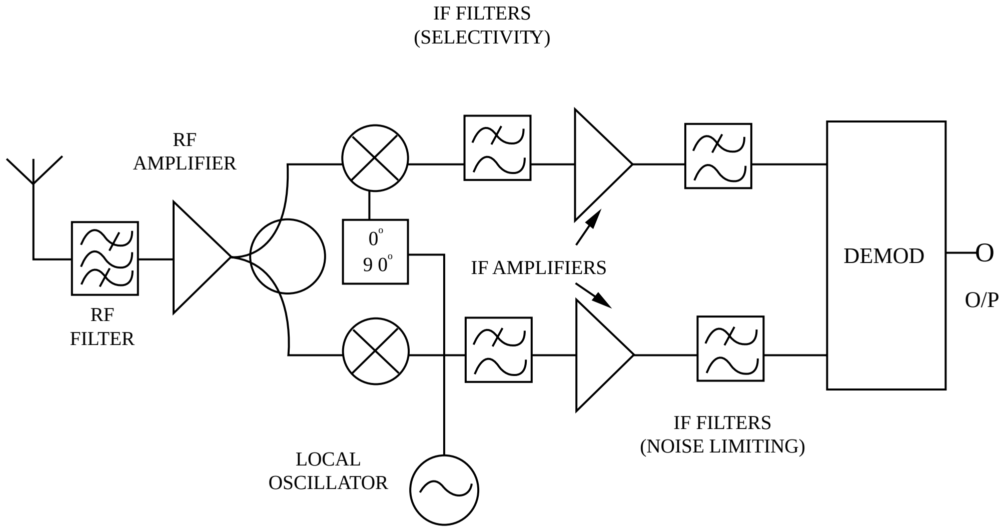

FIGURE 2.17 Direct conversion receiver architecture.

accurate quadrature modulation formats and quadrature downconversion schemes that allow a great deal of flexibility to the baseband section. Generally, one would have used digital signal processors to perform most of the demodulation functions at the cost of high current consumption. With the advent of application-specific signal processing, solutions with these techniques have become more attractive.

From a system perspective, range, multipath, and voice quality influence the design of a DECT phone. A high bit rate coupled with multipath reflections in an indoor environment makes DECT design a challenging task. The delay spread (multipath) can be anywhere in the 100 to 200 ns range, and a DECT bit time is 880 ns. Therefore, a potential delay spread due to multipath reflections is 1 to 20% of a bit time. Typically, antenna diversity is used to overcome such effects.

DECT employs a TDMA/TDD method for transmission, which simplifies the complexity of the radio frequency end. The transmitter is on for 380 ms or so. The receiver is also only on for a similar length of time.

A single conversion radio architecture requires fast synthesizer switching speed in order to transmit and receive on as many as 24 timeslots per frame. In this single conversion transmitter structure, the synthesizer has to make a large jump in frequency between transmitting and receiving, typically in the order of 110 MHz. For a DECT transceiver, the PLL synthesizer must have a wide tuning bandwidth at a high-frequency reference in addition to good noise performance and fast switching speed. The prescaler and PLL must consume as low a current as possible to preserve battery life.

In the receive mode the RF signal at the antenna is filtered with a low-loss antenna filter to reduce out-of-band interfering signals. This filter is also used on the transmit side to attenuate harmonics and reduce wideband noise. The signal is further filtered, shaped, and downconverted as shown in Fig. 2.17. The signal path really is no different from most receiver structures. The challenges lie in the implementation, and this area has become quite a competitive segment, especially in the semiconductor world.

The direct conversion receiver usually has an intermediate frequency nominally at zero frequency, hence the term zero IF. The effect of this is to fold the spectrum about zero frequency, which result in the signal occupying only one-half the bandwidth. The zero IF architecture possesses several advantages over the normal superheterodyne approach. First, selectivity requirements for the RF filter are greatly reduced due to the fact that the IF is at zero frequency and the image response is coincident with the wanted signal frequency. Second, the choice of zero frequency means that the bandwidth for the IF paths is only half the wanted signal bandwidth. Third, channel selectivity can be performed simply by a pair of low-bandwidth low-pass filter.

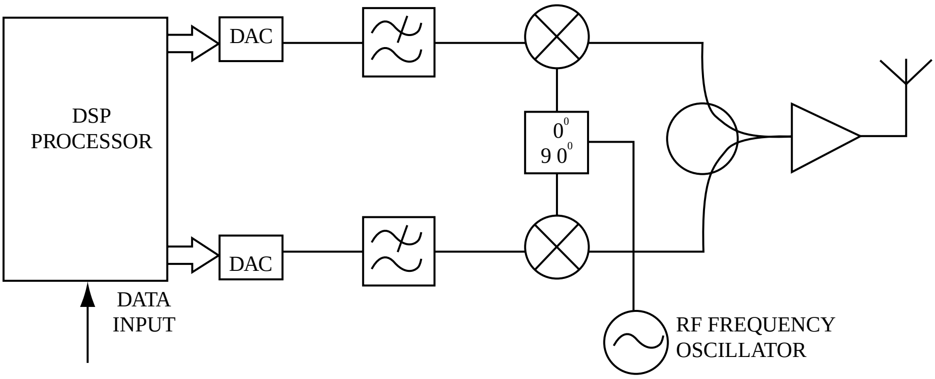

FIGURE 2.18 Transmit section.

For the twin IF chains of a direct conversion receiver, automatic gain control (AGC) is always required due the fact that each IF channel can vary between zero and the envelope peak at much lower rates than the highest signal bandwidth frequency. An additional requirement in newer systems is received signal strength indication (RSSI) to measure the signal or interference level on any given channel.

Moving on to the transmitter architecture (shown in Fig. 2.18 is a typical I-Q system), it is safe to say that the task of generating an RF signal is much simpler than receiving it. A transmitter consists of three main components: a final frequency generator, a modulator, and the power amplifier. These components can all be combined in common circuits, i.e., frequency synthesizer with inbuilt modulator. The problem of generating a carrier at a high frequency is largely one of frequency control. The main approach for accurately generating an output frequency from a crystal reference today is the PLL, and there is considerable literature available on the subject [Gardner, 1979]. In the modulation stage, depending upon the tightness of the phase accuracy specification of a cordless system, it may be necessary to apply tight control on the modulation index to ensure that the phase path of the signal jumps exactly in 90° increments.

Defining Terms

AGC: Automatic gain control.
ARQ: Automatic repeat request.
AWGN: Additive white Gaussian noise.
BABT: British approvals board for telecommunications.
Base Station: The fixed radio component of a cordless link. This may be single-channel (for domestic) or multichannel (for Telepoint and business).
BER: Bit error rate (or ratio).
CCITT: Comitè Consultatif International des Tèlègraphes et Tèlèphones, part of the ITU.
CEPT: Conference of European Posts and Telecommunications Administrations.
CPFSK: Continuous phase frequency shift keying.
CPP: Cordless portable part; the cordless telephone handset carried by he user.
CRC: Cyclic redundancy check.
CT2: Second generation cordless telephone-digital.
D Channel: Control and information data channel (16 kb/s in ISDN).
DCT: Digital cordless telephone.
DECT: Digital European cordless telecommunications.
DLC: Data link control layer, protocol layer in DECT.
DSP: Digital signal processing.
DTMF: Dual tone multiple frequency (audio tone signalling system).

ETSI: European Telecommunications Standards Institute.

FDMA: Frequency division multiple access.

FSK: Frequency shift keying.

GMSK: Gaussian filtered minimum shift keying.

ISDN: Integrated services digital network.

ITU: International Telecommunications Union.

MPT 1375: U.K. standard for common air interface (CAI) digital cordless telephones.

MSK: Minimum shift keying.

PSK: Phase shift keying.

RES 3: Technical subcommittee, radio equipment and systems 3 of ETSI, responsible for the specification of DECT.

RSSI: Received signal strength indication.

SAW: Surface acoustic wave.

TDD: Time division duplex.

TDMA: Time division multiple access.

References

Cheer, A.P. .1985. Architectures for digitally implemented radios, IEE Colloquium on Digitally Implemented Radios, London.

Comité Consultatif International des Télégraphes et Téléphones. 1984, "32 kbits/sec Adaptive Differential Pulse Code Modulation (ADPCM)," CCITT Red Book, Fascicle III.3, Rec. G721.

Comité Consultatif International des Télégraphes et Téléphones, 1984–1985. *General Characteristics of International Telephone Connections and Circuits,* CCITT Red Book, Vol. 3, Fascicle III.1, Rec. G101–G181.

de Buda, R. 1972. Coherent demodulation of frequency shifting with low deviation ratio. *IEEE Trans.* COM-20 (June):466–470.

de Jager, F. and Dekker, C.B. 1978. Tamed frequency modulation. A novel method to achieve spectrum economy in digital transmission, *IEEE Trans. in Comm.* COM-20 (May):534–542.

Dijkstra, S. and Owen, F. 1994. The case for DECT, *Mobile Comms. Int.* 60–65.

European Telecommunications Standards Inst. 1992. RES-3 DECT Ref. Doc. ETS 300 175-1 (Overview). Oct. ETSI Secretariat, Sophia Antipolis Ceder, France.

European Telecommunications Standards Inst. 1992. RES-3 DECT Ref. Doc. ETS 300 175-2 (Physical Layer) Oct. ETSI Secretariat, Sophia Antipolis Ceder, France.

European Telecommunications Standards Inst. 1992. RES-3 DECT Ref. Doc. ETS 300 175-3 (MAC Layer) Oct. ETSI Secretariat, Sophia Antipolis Ceder, France.

European Telecommunications Standards Inst. 1992. RES-3 DECT Ref. Doc. ETS 300 175-4 (Data Link Control Layer) Oct. ETSI Secretariat, Sophia Antipolis Ceder, France.

European Telecommunications Standards Inst. 1992. RES-3 DECT Ref. Doc. ETS 300 175-5 (Network Layer) Oct. ETSI Secretariat, Sophia Antipolis Ceder, France.

European Telecommunications Standards Inst. 1992. RES-3 DECT Ref. Doc. ETS 300 175-6 (Identities and Addressing) Oct. ETSI Secretariat, Sophia Antipolis Ceder, France.

European Telecommunications Standards Inst. 1992. RES-3 DECT Ref. Doc. ETS 300 175-7 (Security Features) Oct. ETSI Secretariat, Sophia Antipolis Ceder, France.

European Telecommunications Standards Inst. 1992. RES-3 DECT Ref. Doc. ETS 300 175-8 (Speech Coding & Transmission) Oct. ETSI Secretariat, Sophia Antipolis Ceder, France.

European Telecommunications Standards Inst. 1992. RES-3 DECT Ref. Doc. ETS 300 175-9 (Public Access Profile) Oct. ETSI Secretariat, Sophia Antipolis Ceder, France.

European Telecommunications Standards Inst. 1992. RES-3 DECT Ref. Doc. ETS 300 176 (Approval Test Spec) Oct. ETSI Secretariat, Sophia Antipolis Ceder, France.

Gardner, F.M. 1979. *Phase Lock Techniques,* Wiley-Interscience, New York.

Bar-Cohen, Avram et al. "Systems Configurations"
The RF and Microwave Handbook
Editor in Chief Mike Golio
Boca Raton: CRC Press LLC,2001

3

Systems Considerations

Avram Bar-Cohen
University of Minnesota

Karl J. Geisler
University of Minnesota

Allan D. Kraus
Allan D. Kraus Associates

John M. Osepchuk
Full Spectrum Consulting

Ronald C. Petersen
Lucent Technologies Inc./Bell Labs

John F. Sevic
UltraRF, Inc.

Leland M. Farrer
Cadence Design Systems, Inc.

Brent A. McDonald
Dell Computer Corp.

George K. Schoneman
Rockwell Collins

Daniel E. Jenkins
Dell Computer Corp.

Mike Golio
Rockwell Collins

Arun Ramakrishnan
University of Maryland

Toby Syrus
University of Maryland

Michael Pecht
University of Maryland

3.1 Thermal Analysis and Design of Electronic Systems

Avram Bar-Cohen, Karl J. Geisler, and Allan D. Kraus

Motivation

In the thermal control of RF devices, it is necessary to provide an acceptable *microclimate* for a diversity of devices and packages that vary widely in size, power dissipation, and sensitivity to temperature.

Although the thermal management of all electronic components is motivated by a common set of concerns, this diversity often leads to the design and development of distinct thermal control systems for different types of electronic equipment. Moreover, due to substantial variations in the performance, cost, and environmental specifications across product categories, the thermal control of similar components may require widely differing thermal management strategies.

The prevention of catastrophic thermal failure (defined as an immediate, thermally induced, total loss of electronic function) must be viewed as the primary and foremost aim of electronics thermal control. Catastrophic failure may result from a significant deterioration in the performance of the component/system or from a loss of structural integrity at the relevant packaging levels. In early microelectronic systems, catastrophic failure was primarily *functional* and thought to result from changes in the bias voltage, *thermal runaway* produced by regenerative heating, and dopant migration, all occurring at elevated transistor junction temperatures. While these failure modes may still occur during the device development process, improved semiconductor simulation tools and thermally compensated devices have largely quieted these concerns and substantially broadened the operating temperature range of today's RF devices.

In microelectronic, microwave, and RF components, the levels of integration and device density on the chips, as well as frequencies of operation, continue to increase. The most critical heat-producing component for most RF systems is the power amplifier (PA) stage. Output power required from these stages ranges from less than 1 watt for some handheld commercial applications to greater than 1 kW (multiple parallel stages) for certain military, avionics, and data link applications. Single transistor output power levels are as high as 100 W to 200 W for applications ranging from commercial base stations to avionics, satellite communications, and military. Amplified efficiencies for the highest output power requirements are typically in the 15 to 35% range. To facilitate effective thermal management for such high power levels, PA operation must be pulsed with low duty cycles (reducing thermal power dissipation requirements). Improved thermal performance can be translated into higher duty cycles and therefore into greater data transfer or more efficient use of bandwidth. For these kinds of applications, performance is already limited primarily by the maximum achievable heat flux. Improvements in that figure of merit automatically and immediately translate into improved system performance.

More generally, however, thermal design is aimed at preventing thermally induced physical failures through reduction of the temperature rise above ambient and minimization of temperature variations within the packaging structure(s). With RF integrated circuits or discrete RF high-performance devices, maximum frequency of operation, noise figure, power saturation levels, and nonlinear behavior are all affected by temperature. The use of many low-temperature materials and the structural complexity of chip packages and printed circuit boards has increased the risk of catastrophic failures associated with the vaporization of organic materials, the melting of solders, and thermal-stress fractures of leads, joints, and seals as well as the fatigue-induced delamination and fracture or creep-induced deformation of encapsulants and laminates. To prevent catastrophic thermal failure, the designer must know the maximum allowable temperatures, acceptable internal temperature differences, and the power consumption/dissipation of the various components. This information can be used to select the appropriate fluid, heat transfer mode, and inlet temperature for the coolant and to thus establish the thermal control strategy early in the design process.

After the selection of an appropriate thermal control strategy, attention can be turned to meeting the desired system-level reliability and the target failure rates of each component and subassembly. Individual solid-state electronic devices are inherently reliable and can typically be expected to operate, at room temperature, for some 100,000 years, i.e., with a base failure rate of 1 FIT (failures in 10^9 h). However, since the number of devices in a typical radio component is rapidly increasing and since an RF system may consist of many tens to several hundreds of such components, achieving a system Mean Time Between Failures of several thousand hours in military equipment and 40,000 to 60,000 hours in commercial systems is a most formidable task.

Many of the failure mechanisms, which are activated by prolonged operation of electronic components, are related to the local temperature and/or temperature gradients, as well as the thermal history of the package.[1] Device-related functional failures often exhibit a strong relationship between failure rate and operating temperature. This dependence can be represented in the form of an exponential Arrhenius relation, with unique, empirically determined coefficients and activation energy for each component type and failure mechanism. In the normal operating range of microelectronic components, a 10 to 20°C increase in chip temperature may double the component failure rate, and even a 1°C decrease may then lower the predicted failure rate associated with such mechanisms by 2 to 4%.[2]

Unfortunately, it is not generally possible to characterize thermally induced structural failures, which develop as a result of differential thermal expansion among the materials constituting a microwave package, in the form of an Arrhenius relation. Although these mechanical stresses may well increase as the temperature of the component is elevated, thermal stress failures are, by their nature, dependent on the details of the local temperature fields, as well as the assembly, attachment, and local operating history of the component. Furthermore, thermal stress generation in packaging materials and structures is exacerbated by power transients, as well as by the periodically varying environmental temperatures, experienced by most electronic systems, during both qualification tests and actual operation. However, stress variations in the elastic domain or in the range below the fatigue limit may have little effect on the component failure rate. Consequently, the minimization of elimination of thermally induced failures often requires careful attention to both the temperature and stress fields in the electronic components and necessitates the empirical validation of any proposed thermostructural design criteria.

Thermal Packaging Options

When the heat flux dissipated by the electronic component, device, or assembly is known and the allowable temperature rise above the local ambient condition is specified, the equations of the following sections can be used to determine which heat transfer process or combination of processes (if any) can be employed to meet the desired performance goals. Figure 3.1 shows the variation of attainable temperature differences with surface heat flux for a variety of heat transfer modes and coolant fluids.

Examination of Fig. 3.1 reveals that for a typical allowable temperature difference of 60°C between the component surface and the ambient, "natural" cooling in air — relying on both free convection and radiation — is effective only for heat fluxes below approximately 0.05 W/cm^2. Although forced convection cooling in air offers approximately an order-of-magnitude improvement in heat transfer coefficient, this thermal configuration is unlikely to provide heat removal capability in excess of 1 W/cm^2 even at an allowable temperature difference of 100°C.

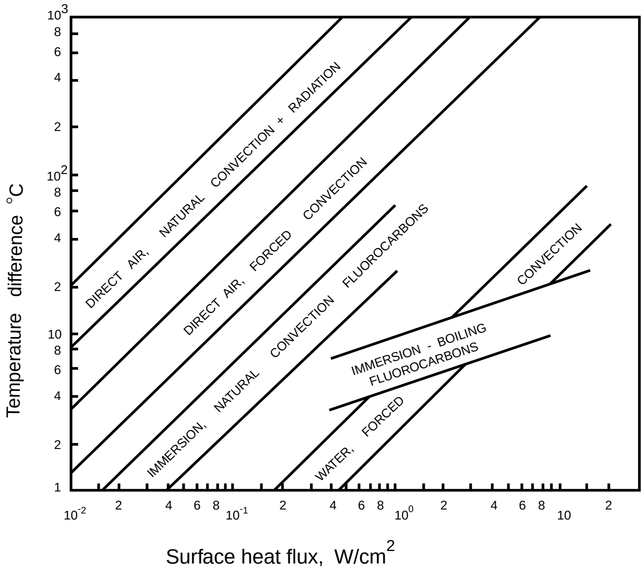

FIGURE 3.1 Temperature differences attainable as a function of heat flux for various heat transfer modes and various coolant fluids. (From Ref. 3, with permission.)

To facilitate the transfer of moderate and high heat fluxes from component surfaces, the thermal designer must choose between the use of finned, air-cooled heat sinks and direct or indirect liquid cooling. Finned arrays and sophisticated techniques for improving convective heat transfer coefficients can extend the effectiveness of air cooling to progressively higher component heat fluxes, but often at ever-increasing weight, cost, and volume penalties. Alternately, reliance on heat transfer to liquids flowing at high velocity through so-called "cold plates" can offer a dramatic improvement in the transferable heat flux even at temperature differences as low as 10°C, when the conduction resistance in the cold plate wall is negligible.

A similar high heat flux capability is offered by boiling heat transfer to perfluorinated (FCs) and hydrofluoroether (HFEs) liquids. The high dielectric strength and low dielectric constant of these liquids make it possible to implement this approach for a wide range of components. Direct liquid contact allows the removal of component heat fluxes in excess of 10 W/cm^2 with saturated pool boiling at temperature differences typically less than 20°C. Natural convection (i.e., non-boiling) immersion cooling can also offer significant advantages and, as seen in Fig. 3.1, serves to bridge the gap between direct air cooling and cold plate technology.

Unfortunately, when addressed within stringent cost targets, the cooling requirements of 21st-century microelectronic, microwave, and RF components cannot be met by today's thermal packaging technology. Rather, ways must be sought to improve on currently available technology, to leverage and combine the best features of existing thermal packaging hardware, and to introduce unconventional, perhaps even radical, thermal solutions into the electronic product family. In so doing, attention must be devoted to three primary issues:

- Highly effective air cooling — removing dissipated power from one or several high-performance components within minimal volumes and with low air-side pressure drops.
- Heat spreading — transporting heat from the relatively small area of the device to the substrate, card, or board, or to a relatively large heat sink or cold plate base.
- Interfacial heat transfer — transferring heat across the thermal resistances between the device and the next level of thermal packaging.

Attention now turns to a detailed discussion of basic heat transfer and the determination of the various types of thermal resistances often encountered in electronic equipment.

Thermal Modeling

To determine the temperature differences encountered in the flow of heat within electronic systems, it is necessary to recognize the relevant heat transfer mechanisms and their governing relations. In a typical system, heat removal from the active regions of the device(s) may require the use of several mechanisms, some operating in series and others in parallel, to transport the generated heat to the coolant or ultimate heat sink. Practitioners of the thermal arts and sciences generally deal with four basic thermal transport modes: conduction, convection, phase change, and radiation.

Conduction Heat Transfer

One-Dimensional Conduction

Steady thermal transport through solids is governed by the Fourier equation, which in one-dimensional form, is expressible as

$$q = -kA\frac{\mathrm{d}T}{\mathrm{d}x} \tag{3.1}$$

where q is the heat flow, k is the thermal conductivity of the medium, A is the cross-sectional area for the heat flow, and $\mathrm{d}T/\mathrm{d}x$ is the temperature gradient. As depicted in Fig. 3.2, heat flow produced by a negative temperature gradient is considered positive. This convention requires the insertion of the minus sign in Eq. (3.1) to assure a positive heat flow, q. The temperature difference resulting from the steady

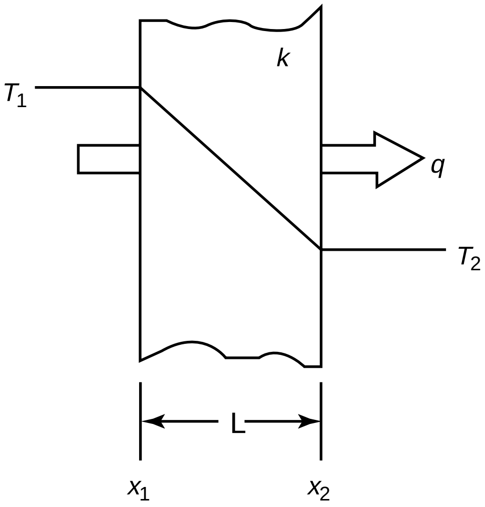

FIGURE 3.2 One-dimensional conduction through a slab. (From Ref. 4, with permission.)

state diffusion of heat is thus related to the thermal conductivity of the material, the cross-sectional area, and the path length, L, according to

$$\left(T_1 - T_2\right)_{\text{cd}} = q\frac{L}{kA} \tag{3.2}$$

The form of Eq. (3.2) suggests that, by analogy to Ohm's Law governing electrical current flow through a resistance, it is possible to define a thermal resistance for conduction, R_{cd}, as

$$R_{\text{cd}} \equiv \frac{\left(T_1 - T_2\right)}{q} = \frac{L}{kA} \tag{3.3}$$

One-Dimensional Conduction with Internal Heat Generation

Situations in which a solid experiences internal heat generation, such as that produced by the flow of an electric current, give rise to more complex governing equations and require greater care in obtaining the appropriate temperature differences. The axial temperature variation in a slim, internally-heated conductor whose edges (ends) are held at a temperature T_o, is found to equal

$$T = T_o + q_g\frac{L^2}{2k}\left[\left(\frac{x}{L}\right) - \left(\frac{x}{L}\right)^2\right] \tag{3.4}$$

When the volumetric heat generation rate, q_g, in W/m^3, is uniform throughout, the peak temperature is developed at the center of the solid and is given by

$$T_{\max} = T_o + q_g\frac{L^2}{8k} \tag{3.5}$$

Alternatively, since q_g is the volumetric heat generation, $q_g = q/LW\delta$, the center-edge temperature difference can be expressed as

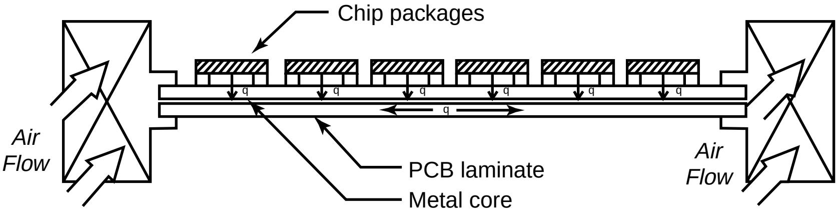

FIGURE 3.3 Edge-cooled printed circuit board populated with components. (From Ref. 4, with permission.)

$$T_{\max} - T_o = q\frac{L^2}{8kLW\delta} = q\frac{L}{8kA} \tag{3.6}$$

where the cross-sectional area, A, is the product of the width, W, and the thickness, δ. An examination of Eq. (3.6) reveals that the thermal resistance of a conductor with a distributed heat input is only one quarter that of a structure in which all of the heat is generated at the center.

In the design of airborne electronic system and equipment to be operated in a corrosive or damaging environment, it is often necessary to conduct the heat dissipated by the components down into the substrate or printed circuit board and, as shown in Fig. 3.3, across the substrate/PCB to a cold plate or sealed heat exchanger. For a symmetrically cooled substrate/PCB with approximately uniform heat dissipation on the surface, a first estimate of the peak temperature at the center of the board, can be obtained using Eq. (3.6).

This relation can be used effectively in the determination of the temperatures experienced by conductively cooled substrates and conventional printed circuit boards, as well as PCBs with copper lattice on the surface, metal cores, or heat sink plates in the center. In each case it is necessary to evaluate or obtain the effective thermal conductivity of the conducting layer. As an example, consider an alumina substrate, 0.20 m long, 0.15 m wide, and 0.005 m thick with a thermal conductivity of 20 W/mK, whose edges are cooled to 35°C by a cold plate. Assuming that the substrate is populated by 15 compounds, each dissipating 2 W, the substrate center temperature will be found to be equal to 85°C when calculated using Eq. (3.6).

Spreading Resistance

In component packages that provide for lateral spreading of the heat generated in the device(s), the increasing cross-sectional area for heat flow at successive "layers" adjacent to the device reduces the internal thermal resistance. Unfortunately, however, there is an additional resistance associated with this lateral flow of heat. This, of course, must be taken into account in the determination of the overall component package temperature difference.

For the circular and square geometries common in many applications, Negus et al.[5] provided an engineering approximation for the spreading resistance of a small heat source on a thick substrate or heat spreader (required to be 3 to 5 times thicker than the square root of the heat source area), which can be expressed as

$$R_{sp} = \frac{0.475 - 0.62\epsilon + 0.13\epsilon^3}{k\sqrt{A_c}} \tag{3.7}$$

where ϵ is the ratio of the heat source area to the substrate area, k is the thermal conductivity of the substrate, and A_c is the area of the heat source.

For relatively thin layers on thicker substrates, such as encountered in the use of thin lead frames, or heat spreaders interposed between the device and substrate, Eq. (3.7) cannot provide an acceptable prediction of R_{sp}. Instead, use can be made of the numerical results plotted in Fig. 3.4 to obtain the requisite value of the spreading resistance.

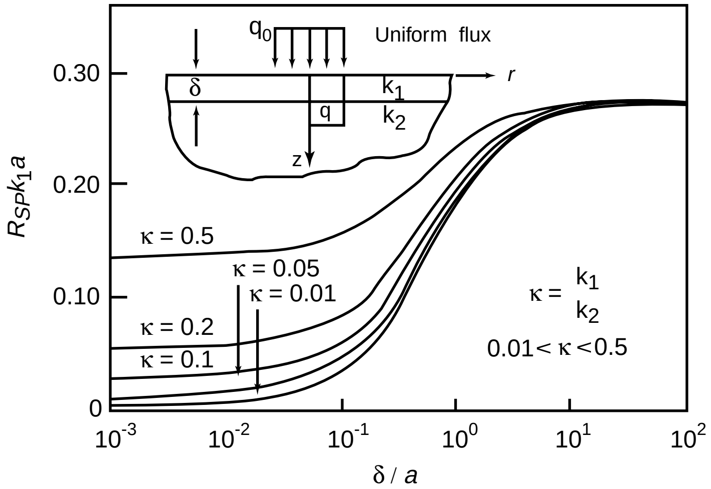

FIGURE 3.4 The thermal resistance for a circular heat source on a two-layer substrate. (From Ref. 6, with permission.)

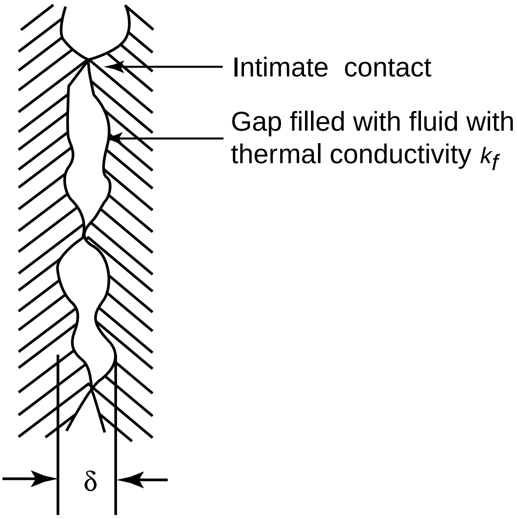

FIGURE 3.5 Physical contact between two nonideal surfaces. (From Ref. 4, with permission.)

Interface/Contact Resistance

Heat transfer across the interface between two solids is generally accompanied by a measurable temperature difference, which can be ascribed to a contact or interface thermal resistance. For perfectly adhering solids, geometrical differences in the crystal structure (lattice mismatch) can impede the flow of photons and electrons across the interface, but this resistance is generally negligible in engineering design. When dealing with real interfaces, the asperities present on each of the surfaces, as shown in an artist's conception in Fig. 3.5, limit actual contact between the two solids to a very small fraction of the apparent interface area. The flow of heat across the gap between two solids in nominal contact is, thus, seen to involve solid conduction in the areas of actual contact and fluid conduction across the "open" spaces. Radiation across the gap can be important in a vacuum environment or when the surface temperatures are high.

The total contact conductance, h_{co}, is taken as the sum of the solid-to-solid conductance, h_c, and the gap conductance, h_g.

$$h_{\mathrm{co}} = h_{\mathrm{c}} + h_{\mathrm{g}} \tag{3.8}$$

The contact resistance based on the apparent contact area, A_{a} may be defined as

$$R_{\mathrm{co}} \equiv \frac{1}{h_{\mathrm{co}} A_{\mathrm{a}}} \tag{3.9}$$

In Eq. (3.8), h_{c} is given by Yovanovich and Antonetti[6] as

$$h_{\mathrm{c}} = 1.25 \mathrm{k}_{\mathrm{s}} \left(\frac{m}{\sigma} \right) \left(\frac{P}{H} \right)^{0.95} \tag{3.10}$$

where P is the contact pressure and H is the micro-hardness of the softer material (both in Pa), k_{s} is the harmonic mean thermal conductivity for the two solids with thermal conductivities, k_1 and k_2,

$$k_{\mathrm{s}} = \frac{2k_1 k_2}{k_1 + k_2}$$

σ is the effective rms surface roughness developed from the surface roughnesses of the two materials, σ_1 and σ_2,

$$\sigma = \sqrt{\sigma_1^2 + \sigma_2^2}$$

and m is the effective absolute surface slope composed of the individual slopes of the two materials, m_1 and m_2,

$$m = \sqrt{m_1^2 + m_2^2}$$

In the absence of detailed information, the σ/m ratio can be assumed to fall into the range of 5 to 9 microns for relatively smooth surfaces.[7]

For normal interstitial gases around atmospheric pressure, h_{g} in Eq. (3.8) is given by

$$h_{\mathrm{g}} = \frac{k_{\mathrm{g}}}{Y} \tag{3.11}$$

where k_{g} is the thermal conductivity of the gap fluid, and Y is the distance between the mean planes given by

$$Y = 1.185 \left[-\ln \left(3.132 \frac{P}{H} \right) \right]^{0.547} \sigma$$

Equations (3.10) and (3.11) can be added, and then in accordance with (3.9), the total contact resistance becomes

$$R_{\mathrm{co}} \equiv \left\{ \left[1.25 k_{\mathrm{s}} \left(\frac{m}{\sigma} \right) \left(\frac{P}{H} \right)^{0.95} + \frac{k_{\mathrm{g}}}{Y} \right] A_{\mathrm{a}} \right\}^{-1} \tag{3.12}$$

Transient Heating or Cooling

An externally heated solid of relatively high thermal conductivity, that is experiencing no external cooling, will undergo a constant rise in temperature according to

$$\frac{\mathrm{d}T}{\mathrm{d}t} = \frac{q}{mc} \tag{3.13}$$

where q is the rate of internal heat generation, m is the mass of the solid, and c is the specific heat of the solid. Equation (3.13) assumes that all of the mass can be represented by a single temperature and this relation is frequently termed the "lumped capacity" solution for transient heating.

Expanding on the analogy between thermal and electrical resistances, the product of mass and specific heat can be viewed as analogous to electrical capacitance and thus to constitute the "thermal capacitance."

When the same solid is externally cooled, the temperature rises asymptotically toward the steady-state temperature, which is itself determined by the external resistance to the heat flow, R_{ex}. Consequently, the time variation of the temperature of the solid is expressible as

$$T(t) = T(t=0) + qR_{\mathrm{ex}}\left[1 - e^{-t/mcR_{\mathrm{ex}}}\right] \tag{3.14}$$

The lump capacitance model is accurate when the ratio of the internal conduction resistance of a solid to the external thermal resistance is small. This ratio is represented by the Biot number, and the criterion for applicability of the lumped capacitance model is given as

$$\mathrm{Bi} = \frac{hL_{\mathrm{c}}}{k} < 0.1 \tag{3.15}$$

where the characteristic length, L_{c}, is typically defined as the ratio of the solid's volume to its surface area. More generally, L_{c} should be taken as the distance over which the solid experiences its maximum temperature difference.[8]

Convective Heat Transfer

The Heat Transfer Coefficient

Convective thermal transport from a surface to a fluid in motion can be related to the heat transfer coefficient, h, the surface-to-fluid temperature difference and the "wetted" surface area, A, in the form

$$q = hA\left(T_{\mathrm{s}} - T_{\mathrm{fl}}\right) \tag{3.16}$$

The differences between convection to a rapidly moving fluid, a slowly flowing or stagnant fluid, as well as variations in the convective heat transfer rate among various fluids, are reflected in the values of h. For a particular geometry and flow regime, h may be found from available empirical correlations and/or theoretical relations. Use of Eq. (3.16) makes it possible to define the convective thermal resistance, as

$$R_{\mathrm{cv}} \equiv \frac{1}{hA} \tag{3.17}$$

Dimensionless Parameters

Common dimensionless quantities that are used in the correlation of heat transfer data are the *Nusselt number,* Nu, which relates the convective heat transfer coefficient to the conduction in the fluid where the subscript, fl, pertains to a fluid property,

$$\mathrm{Nu} \equiv \frac{h}{k_{\mathrm{fl}}/L} = \frac{hL}{k_{\mathrm{fl}}} \tag{3.18}$$

the *Prandtl number,* Pr, which is a fluid property parameter relating the diffusion of momentum to the conduction of heat,

$$\mathrm{Pr} \equiv \frac{c_{\mathrm{p}}\mu}{k_{\mathrm{fl}}} \tag{3.19}$$

the *Grashof number,* Gr, which accounts for the buoyancy effect produced by the volumetric expansion of the fluid,

$$\mathrm{Gr} \equiv \frac{\rho^2 \beta g L^3 \Delta T}{\mu^2} \tag{3.20}$$

and the *Reynolds number,* Re, which relates the momentum in the flow to the viscous dissipation,

$$\mathrm{Re} \equiv \frac{\rho V L}{\mu} \tag{3.21}$$

Natural Convection

Despite increasing performance demands and advances in thermal management technology, direct air-cooling of electronic equipment continues to command substantial attention. Natural convection is the quietest, least expensive, and most reliable implementation of direct fluid cooling. In more demanding systems, natural convection cooling with air is often investigated as a baseline design to justify the application of more sophisticated techniques.

In natural convection, fluid motion is induced by density differences resulting from temperature gradients in the fluid. The heat transfer coefficient for this regime can be related to the buoyancy and the thermal properties of the fluid through the *Rayleigh number,* Ra, which is the product of the Grashof and Prandtl numbers,

$$\mathrm{Ra} = \frac{\rho^2 \beta g c_p}{\mu k_{\mathrm{fl}}} L^3 \Delta T \tag{3.22}$$

where the fluid properties, ρ, β, c_p, μ, and k are evaluated at the fluid bulk temperature, and ΔT is the temperature difference between the surface and the fluid.

Empirical correlations for the natural convection heat transfer coefficient generally take the form

$$h = C\left(\frac{k_{\mathrm{fl}}}{L}\right)\left(\mathrm{Ra}\right)^n \tag{3.23}$$

where n is found to be approximately 0.25 for $10^3 < \mathrm{Ra} < 10^9$, representing laminar flow, 0.33 for $10^9 < \mathrm{Ra} < 10^{12}$, the region associated with the transition to turbulent flow, and 0.4 for $\mathrm{Ra} > 10^{12}$ when strong turbulent flow prevails. The precise value of the correlating coefficient, C, depends on fluid, the geometry of the surface, and the Rayleigh number range. Nevertheless, for natural convection in air from common plate, cylinder, and sphere configurations, it has been found to vary in the relatively narrow range of 0.45 to 0.65 for laminar flow and 0.11 to 0.15 for turbulent flow past the heated surface.[3]

Vertical Channels — Vertical channels formed by parallel printed circuit boards (PCBs) or longitudinal fins are a frequently encountered configuration in natural convection cooling of electronic equipment. The historical work of Elenbaas,[9] a milestone of experimental results and empirical correlations, was the first to document a detailed study of natural convection in smooth, isothermal parallel plate channels. In subsequent years, this work was confirmed and expanded both experimentally and numerically by a number of researchers, including Bodoia[10], Sobel et al.,[11] Aung,[12] Aung et al.,[13] Miyatake and Fujii,[14] and Miyatake et al.[15]

These studies revealed that the value of the Nusselt number lies between two extremes associated with the separation between the plates or the channel width. For wide spacing, the plates appear to have little influence upon one another and the Nusselt number in this case achieves its *isolated plate limit.* On the other hand, for closely spaced plates or for relatively long channels, the fluid attains its *fully developed* velocity profile and the Nusselt number reaches its *fully developed limit.* Intermediate values of the Nusselt number can be obtained from a family of composite expressions developed by Bar-Cohen and Rohsenow[16] and verified by comparison to numerous experimental and numerical studies.

For an isothermal channel, at the fully developed limit, the Nusselt number takes the form

$$Nu = \frac{El}{C_1} \tag{3.24}$$

where *El* is the Elenbaas number, defined as

$$El \equiv \frac{c_p \rho^2 g \beta \left(T_w - T_{amb}\right) b^4}{\mu k L} \tag{3.25}$$

where b is the channel spacing, L is the channel length, and $(T_w - T_{amb})$ is the temperature difference between the channel wall and the ambient, or channel inlet. For an asymmetric channel, or one in which one wall is heated and the other is insulated, the appropriate values of C_1 is 12, while for symmetrically heated channels, $C_1 = 24$.

For an isoflux channel, at the fully developed limit, the Nusselt number has been shown to take the form

$$Nu = \sqrt{\frac{El'}{C_1}} \tag{3.26}$$

where the modified *Elenbaas number*, *El′*, is defined as

$$El' \equiv \frac{c_p \rho^2 g \beta q'' b^5}{\mu k^2 L} \tag{3.27}$$

where q'' is the heat flux leaving the channel wall(s). When this Nusselt number is based on the maximum wall temperature ($x = L$), the appropriate values of C_1 are 24 and 48 for the asymmetric and symmetric cases, respectively. When based on the mid-height ($x = l/2$) wall temperature, the asymmetric and symmetric C_1 values are 6 and 12, respectively.

In the limit where the channel spacing is very large, the opposing channel walls do not influence each other either hydrodynamically or thermally. This situation may be accurately modeled as heat transfer from an isolated vertical surface in an infinite medium. Natural convection from an isothermal plate can be expressed as

$$Nu = C_2 El^{1/4} \tag{3.28}$$

where McAdams[17] suggests a C_2 value of 0.59. However, more recent research suggests that the available data could be better correlated with C_2 = 0.515.[8] Natural convection from an isoflux plate is typically expressed as

$$Nu = C_2 El'^{\,1/5} \tag{3.29}$$

with a leading coefficient of 0.631 when the Nusselt number is based on the maximum ($x = L$) wall temperature and 0.73 when the Nusselt number is based on the mid-height ($x = l/2$) wall temperature.

Composite Equations — When a function is expected to vary smoothly between two limiting expressions, which are themselves well defined, and when intermediate values are difficult to obtain, an approximate composite relation can be obtained by appropriately summing the two limiting expressions. Using the Churchill and Usagi[18] method, Bar-Cohen and Rohsenow[19] developed composite Nusselt number relations for natural convection in parallel plate channels of the form

$$Nu = \left[\left(Nu_{\text{fd}}\right)^{-n} + \left(Nu_{\text{ip}}\right)^{-n} \right]^{-1/n} \tag{3.30}$$

where Nu_{fd} and Nu_{ip} are Nusselt numbers for the fully developed and isolated plate limits, respectively. The correlating exponent n was given a value of 2 to offer good agreement with Elenbaas'[9] experimental results.

For an isothermal channel, combining Eqs. (3.24) and (3.28) yields a composite relation of the form

$$Nu = \left[\frac{C_3}{El^2} + \frac{C_4}{\sqrt{El}} \right]^{-1/2} \tag{3.31}$$

while for an isoflux channel, Eqs. (3.26) and (3.29) yield a result of the form

$$Nu = \left[\frac{C_3}{El'} + \frac{C_4}{El'^{2/5}} \right]^{-1/2} \tag{3.32}$$

Values of the coefficients C_3 and C_4 appropriate to various cases of interest appear in Table 3.1. It is to be noted that the tabulated values reflect a change in the value of the coefficient from 0.59 originally used by Bar-Cohen and Rohsenow[19] in the isolated, isothermal plate limit to the more appropriate 0.515 value.

In electronic cooling applications where volumetric concerns are not an issue, it is desirable to space PCBs far enough apart that the isolated plate Nusselt number prevails along the surface. In lieu of choosing an infinite plate spacing, the composite Nusselt number may be set equal to 99%, or some other high fraction of its associated isolated plate value. The composite Nusselt number relation may then be solved for the appropriate channel spacing.

For an isothermal channel, the channel spacing that maximizes the rate of heat transfer from individual PCBs takes the form

TABLE 3.1 Appropriate Values for the C_i coefficients appearing in Eqs. (3.24)–(3.39).

Case	C_1	C_2	C_3	C_4	C_5	C_6	C_7
			Isothermal				
Symmetric heating	24	0.515	576	3.77	4.43	0.00655	2.60
Asymmetric heating	12	0.515	144	3.77	3.51	0.0262	2.06
			Isoflux				
Symmetric heating							
Maximum temp.	48	0.63	48	2.52	9.79	0.105	2.12
Midheight temp.	12	0.73	12	1.88	6.80	0.313	1.47
Asymmetric heating							
Maximum temp.	24	0.63	24	2.52	7.77	0.210	1.68
Midheight temp.	6	0.73	6	1.88	5.40	0.626	1.17

$$b_{\max} = \frac{C_5}{P^{1/4}} \tag{3.33}$$

where

$$P = \frac{c_p \rho^2 g\beta \left(T_w - T_{amb}\right)}{\mu k L} = \frac{El}{b^4}$$

while for an isoflux channel, the channel spacing that minimizes the PCB temperature for a given heat flux takes the form

$$b_{\max} = \frac{C_5}{R^{1/5}} \tag{3.34}$$

where

$$R = \frac{c_p \rho^2 g\beta q''}{\mu k^2 L} = \frac{El'}{b^5}$$

Values of the coefficient C_5 appropriate to various cases of interest appear in Table 3.1.

Optimum Spacing — In addition to being used to predict heat transfer coefficients, the composite relations presented may be used to optimize the spacing between plates. For isothermal arrays, the optimum spacing maximizes the total heat transfer from a given base area or the volume assigned to an array of plates or printed circuit boards. In the case of isoflux parallel plate arrays, the total array heat transfer for a given base area may be maximized by increasing the number of plates indefinitely, though the plate will experience a commensurate increase in temperature. Thus, it is more appropriate to define the optimum channel spacing for an array of isoflux plates as the spacing that will yield the maximum volumetric heat dissipation rate per unit temperature difference. Despite this distinction, the optimum spacing is found in the same manner.

The total heat transfer rate from an array of vertical, single-sided plates can be written as

$$\frac{Q_T}{LsWk\Delta t} = \left(\frac{Nu}{b\left(b+d\right)}\right) \tag{3.35}$$

where the number of plates, $m = W/(b + d)$, d is the plate thickness, W is the width of the entire array, and s is the depth of the channel. The optimum spacing may be found by substituting the appropriate composite Nusselt number equation into Eq. (3.35), taking the derivative of the resulting expression with respect to b, and setting the result equal to zero. Use of an isothermal composite Nusselt number in Eq. (3.35) yields a relation of the form

$$\left(2b + 3d - C_6 P^{3/2} b^7\right)_{\text{opt}} = 0 \tag{3.36}$$

or

$$b_{\text{opt}} = \frac{C_7}{P^{1/4}} \; (d = 0) \tag{3.37}$$

where d, the plate thickness, is negligible. Use of an isoflux composite Nusselt number yields

$$\left(b + 3d - C_6 R^{3/5} b^4\right)_{\text{opt}} = 0 \tag{3.38}$$

or

$$b_{\text{opt}} = \frac{C_7}{R^{1/5}} \quad \left(d = 0\right) \tag{3.39}$$

Values of the coefficients C_6 and C_7 appropriate to various cases of interest appear in Table 3.1.

Limitations — These smooth-plate relations have proven useful in a wide variety of applications and have been shown to yield very good agreement with measured empirical results for heat transfer from arrays of PCBs. However, when applied to closely spaced printed circuit boards, where the spacing is of the order of the component height, these equations tend to under-predict heat transfer in the channel due to the presence of between-package "wall flow" and the non-smooth nature of the channel surfaces.[20]

Forced Convection

For forced flow in long or very narrow parallel-plate channels, the heat transfer coefficient attains an asymptotic value (a fully developed limit), which for symmetrically heated channel surfaces is approximately equal to

$$h = \frac{4k_{\text{fl}}}{d_{\text{e}}} \tag{3.40}$$

where d_{e} is the *hydraulic diameter* defined in terms of the flow area, A, and the wetted perimeter of the channel, P_{w}

$$d_{\text{e}} \equiv \frac{4A}{P_{\text{w}}}$$

In the inlet zones of such parallel-plate channels and along isolated plates, the heat transfer coefficient varies with the distance from the leading edge. The low-velocity, or laminar flow, average convective heat transfer coefficient for $\text{Re} < 2 \times 10^5$ is given by[3]

$$h = 0.664\left(\frac{k}{L}\right)\text{Re}^{1/2}\,\text{Pr}^{1/3} \tag{3.41}$$

where k is the fluid thermal conductivity and L is the characteristic dimension of the surface. This heat transfer coefficient decreases asymptotically toward the fully developed value given by Eq. (3.40).

A similar relation applies to flow in tubes, pipes, ducts, channels and/or annuli with the equivalent diameter, d_e, serving as the characteristic dimension in both the Nusselt and Reynolds numbers. For laminar flow, Re ≤ 2100

$$\frac{\bar{h} d_e}{k} = 1.86 \left[\mathrm{Re}\,\mathrm{Pr} \left(\frac{d_e}{L} \right) \right]^{1/3} \left(\frac{\mu}{\mu_w} \right)^{0.14} \tag{3.42}$$

which is attributed to Sieder and Tate[21] and where μ_w is the viscosity of the convective medium at the wall temperature. Observe that Eqs. (3.41) and (3.42) show that the heat transfer coefficient from the surface to the fluid is highest for short channels and decreases as L increases.

In higher velocity turbulent flow, the dependence of the convective heat transfer coefficient on the Reynolds number increases and, in the range $\mathrm{Re} \geq 3 \times 10^5$, is typically given by[3]

$$h = 0.036 \left(\frac{k}{L} \right) (\mathrm{Re})^{0.80} (\mathrm{Pr})^{1/3} \tag{3.43}$$

In pipes, tubes, channels, ducts and/or annuli, transition to turbulent flow occurs at an equivalent diameter-based Reynolds number of approximately 10,000. Thus, the flow regime bracketed by

$$2100 \leq \mathrm{Re} \leq 10{,}000$$

is usually referred to as the transition region. Hausen[22] has provided the correlation

$$\frac{h d_e}{k} = 0.116 \left[\mathrm{Re} - 125 \right] (\mathrm{Pr})^{1/3} \left(1 + \frac{d_e}{L} \right)^{2/3} \left(\frac{\mu}{\mu_w} \right) \tag{3.44}$$

and Sieder and Tate[21] give for turbulent flow

$$\frac{h d_e}{k} = 0.23 (\mathrm{Re})^{0.80} (\mathrm{Pr})^{1/3} \left(\frac{\mu}{\mu_w} \right) \tag{3.45}$$

Additional correlations for the coefficient of heat transfer in forced convection for various configurations may be found in the heat transfer textbooks.[8,23–25]

Phase Change Heat Transfer

When heat exchange is accompanied by evaporation of a liquid or condensation of a vapor, the resulting flow of vapor toward or away from the heat transfer surface and the high rates of thermal transport associated with the latent heat of the fluid can provide significantly higher heat transfer rates than single-phase heat transfer alone.

Boiling

Boiling heat transfer displays a complex dependence on the temperature difference between the heated surface and the saturation temperature (boiling point) of the liquid. In nucleate boiling, the primary region of interest, the ebullient heat transfer rate is typically expressed in the form of the Rohsenow[26] equation

$$q = \mu_{\mathrm{f}} h_{\mathrm{fg}} \sqrt{\frac{g\left(\rho_{\mathrm{f}} - \rho_{\mathrm{g}}\right)}{\sigma}} \left[\frac{c_{\mathrm{pf}}}{C_{\mathrm{sf}} Pr_{\mathrm{f}}^{1.7} h_{\mathrm{fg}}}\right]^{1/r} \left(T_{\mathrm{S}} - T_{\mathrm{sat}}\right)^{1/r} \tag{3.46}$$

where $1/r$ is typically correlated with a value of 3, and C_{sf} is a function of characteristics of the surface/fluid combination. Rohsenow recommended that the fluid properties in Eq. (3.46) be evaluated at the liquid saturation temperature.

For pool boiling of the dielectric liquid FC-72 (T_{sat} = 56°C at 101.3 kPa) on a plastic-pin-grid-array (PPGA) chip package, Watwe et al.[27] obtained values of 7.47 for $1/r$ and 0.0075 for C_{sf}. At a surface heat flux of 10 W/cm^2, the wall superheat at 101.3 kPa is nearly 30°C, corresponding to a average surface temperature of approximately 86°C.

The departure from nucleate boiling, or "Critical Heat Flux" (CHF), places an upper limit on the use of the highly efficient boiling heat transfer mechanism. CHF can be significantly influenced by system parameters such as pressure, subcooling, heater thickness and properties, and dissolved gas content. Watwe et al.[27] presented the following equation to predict the pool boiling critical heat flux of dielectric coolants from microelectronic components and under a variety of parametric conditions.

$$\begin{aligned} \mathrm{CHF} = {} & \left\{\frac{\pi}{24} h_{\mathrm{fg}} \sqrt{\rho_{\mathrm{g}}} \left[\sigma_{\mathrm{f}} g\left(\rho_{\mathrm{f}} - \rho_{\mathrm{g}}\right)\right]^{1/4}\right\} \left(\frac{\delta\sqrt{\rho_{\mathrm{h}} c_{\mathrm{ph}} k_{\mathrm{h}}}}{\delta\sqrt{\rho_{\mathrm{h}} c_{\mathrm{ph}} k_{\mathrm{h}}} + 0.1}\right) \\ & \times \left\{1 + \left[0.3014 - 0.01507 L'\left(P\right)\right]\right\} \left\{1 + 0.03\left[\left(\frac{\rho_{\mathrm{f}}}{\rho_{\mathrm{g}}}\right)^{0.75} \frac{c_{\mathrm{pf}}}{h_{\mathrm{fg}}}\right] \Delta T_{\mathrm{sub}}\right\} \end{aligned} \tag{3.47}$$

The first term on the right-hand side of Eq. (3.47) is the classical Kutateladze-Zuber prediction, which is the upper limit on the saturation value of CHF on very large horizontal heaters. The second term represents the effects of heater thickness and thermal properties on the critical heat flux. The third term in Eq. (3.47) accounts for the influence of the heater size, where

$$L' = L\sqrt{\frac{g\left(\rho_{\mathrm{f}} - \rho_{\mathrm{g}}\right)}{\sigma_{\mathrm{f}}}} \tag{3.48}$$

This third term is only to be included when its value is larger than unity (i.e., $0.3014 - 0.01507L' > 0$) as small heaters show an increase in CHF over larger heaters. The last term is an equation representing the best-fit line through the experimental data of Watwe et al.[27] and represents the influence of subcooling on CHF. The pressure effect on CHF is embodied in the Kutateladze-Zuber and the subcooling model predictions, which make up Eq. (3.47), via the thermophysical properties. Thus, Eq. (3.47) can be used to estimate the combined influences of various system and heater parameters on CHF. The critical heat flux, under saturation conditions at atmospheric pressure, for a typical dielectric coolant like FC-72 and for a 1-cm component is approximately 15 W/cm^2. Alternately, at 2 atm and 30°C of subcooling CHF for FC-72 could be expected to reach 22 W/cm^2.

Condensation

Closed systems involving an evaporative process must also include some capability for vapor condensation. Gerstmann and Griffith[28] correlated film condensation on a downward-facing flat plate as

$$\mathrm{Nu} = 0.81 Ra^{0.193} \qquad 10^{10} > Ra > 10^{8} \tag{3.49}$$

$$\mathrm{Nu} = 0.69 Ra^{0.20} \qquad 10^8 > Ra > 10^6 \tag{3.50}$$

where,

$$Nu \equiv \frac{h}{k}\left(\frac{\sigma}{g\left(\rho_\mathrm{f} - \rho_\mathrm{g}\right)}\right)^{1/2} \tag{3.51}$$

$$Ra \equiv \frac{g\rho_\mathrm{f}\left(\rho_\mathrm{f} - \rho_\mathrm{g}\right)h_\mathrm{fg}}{k\mu\Delta T}\left(\frac{\sigma}{g\left(\rho_\mathrm{f} - \rho_\mathrm{g}\right)}\right)^{3/2} \tag{3.52}$$

The Nusselt number for laminar film condensation on vertical surfaces was correlated by Nusselt[29] and later modified by Sadasivan and Lienhard[30] as:

$$\mathrm{Nu} = \frac{hL}{k_\mathrm{f}} = 0.943\left[\frac{g\Delta\rho_\mathrm{fg}L^3h'_\mathrm{fg}}{k_\mathrm{f}\nu_\mathrm{f}\left(T_\mathrm{sat} - T_\mathrm{c}\right)}\right]^{1/4} \tag{3.53}$$

where

$$h'_\mathrm{fg} = h_\mathrm{fg}\left(1 + C_\mathrm{c}Ja\right)$$

$$C_\mathrm{c} = 0.683 - \frac{0.228}{Pr_l}$$

$$Ja = \frac{c_\mathrm{pf}\left(T_\mathrm{sat} - T_\mathrm{c}\right)}{h_\mathrm{fg}}$$

Phase Change Materials

In recent years there has been growing use of solid-liquid phase change materials (PCM) to help mitigate the deleterious effects of transient "spikes" in the power dissipation and/or environmental load imposed on RF modules. This is of particular importance for outdoor modules, where PCMs can serve to smooth diurnal variations in the air temperature and solar radiations. To determine the mass of PCM needed to absorb a specified thermal load at a constant (melting) temperature, it is necessary to obtain the latent heat of fusion of that material and insert it in the following relation

$$m = \frac{Q}{h_{fs}} \tag{3.54}$$

Flow Resistance

The transfer of heat to a flowing gas or liquid that is not undergoing a phase change results in an increase in the coolant temperature from an inlet temperature of T_in to an outlet temperature of T_out, according to

$$T_\mathrm{out} - T_\mathrm{in} = \frac{q}{\dot{m}c_\mathrm{p}} \tag{3.55}$$

Based on this relation, it is possible to define an effective flow resistance, R_{fl}, as

$$R_{\text{fl}} \equiv \frac{1}{\dot{m}c_{\text{p}}} \tag{3.56}$$

where $\dot{m}$, the mass flow rate, is given in kg/s.

In multicomponent systems, determination of individual component temperatures requires knowledge of the fluid temperature adjacent to the component. The rise in fluid temperature relative to the inlet value can be expressed in a flow thermal resistance, as done in Eq. (3.56). When the coolant flow path traverses many individual components, care must be taken to use R_{fl} with the total heat absorbed by the coolant along its path, rather than the heat dissipated by an individual component. For system-level calculations aimed at determining the average component temperature, it is common to base the flow resistance on the average rise in fluid temperature, that is, one-half the value indicated by Eq. (3.56).

Radiative Heat Transfer

Unlike conduction and convection, radiative heat transfer between two surfaces or between a surface and its surroundings is not linearly dependent on the temperature difference and is expressed instead as

$$q = \sigma AF\left(T_1^4 - T_2^4\right) \tag{3.57}$$

where F includes the effects of surface properties and geometry and σ is the Stefan-Boltzman constant, $\sigma = 5.67 \times 10^{-8}$ W/m^{2}K^4. For modest temperature differences, this equation can be linearized to the form

$$q = h_{\text{r}}A\left(T_1 - T_2\right) \tag{3.58}$$

where h_{r} is the effective "radiation" heat transfer coefficient

$$h_{\text{r}} = \sigma F\left(T_1^2 + T_2^2\right)\left(T_1 + T_2\right) \tag{3.59}$$

and, for small $\Delta T = T_1 - T_2$, h_{r} is approximately equal to

$$h_{\text{r}} = 4\sigma F\left(T_1 T_2\right)^{3/2} \tag{3.60}$$

where T_1 and T_2 must be expressed in absolute degrees Kelvin. It is of interest to note that for temperature differences of the order of 10 K with absolute temperatures around room temperature, the radiative heat transfer coefficient, h_{r}, for an ideal (or "black") surface in an absorbing environment is approximately equal to the heat transfer coefficient in natural convection of air.

Noting the form of Eq. (3.58), the radiation thermal resistance, analogous to the convective resistance, is seen to equal

$$R_{\text{r}} \equiv \frac{1}{h_{\text{r}}A} \tag{3.61}$$

Environmental Heat Transfer

In applying the foregoing thermal transport relations to microwave equipment located outdoors, attention must be devoted to properly characterizing the atmospheric conditions and including both incoming solar radiation and outgoing night-sky radiation in the heat balance relations. While best results will be obtained by using precise environmental specifications for the "microclimate" at the relevant location, more general specifications may be of use in early stages of product design. The external environment can vary in temperature from –50°C to +50°C, representing the polar regions at one extreme and the subtropical deserts at the other, and experience a range in air pressure from 76 kPa (11 psi), at high plateaus, to 107 kPa (15.5 psi), in deep rift valleys. Incident solar fluxes at noon can reach 1 kW/m^2 on a horizontal surface, but more typically may average 0.5 kW/m^2, of both direct and diffuse radiation, during the peak solar hours. The outgoing long-wave radiation from an outdoor module exposed to the clear nighttime sky falls in the range of 0.01 to 0.1 kW/m^2.[31] It may be anticipated that convective heat transfer coefficients on large exposed surfaces at sea level will attain values of 6 W/m^{2}K for still air to 75 W/m^{2}K, at wind velocities approaching 100 km/h. To determine the surface temperature of an outdoor module, use can be made of the heat balance relation equating the incoming heat — from the microwave components and solar load — with the outgoing heat — by radiation and convection, as

$$q_{\mathrm{rf}} + q_{\mathrm{solar}} = q_{\mathrm{rad}} + q_{\mathrm{conv}} \tag{3.62}$$

or

$$\begin{aligned} q_{\mathrm{rf}} &= q_{\mathrm{rad}} + q_{\mathrm{conv}} - q_{\mathrm{solar}} \\ &= \sigma A_{\mathrm{surf}} F\left(T_{\mathrm{surf}}^4 - T_{\mathrm{sky}}^4\right) + h_{\mathrm{conv}} A_{\mathrm{surf}}\left(T_{\mathrm{surf}} - T_{\mathrm{amb}}\right) - \alpha A_{\mathrm{surf}} S \end{aligned} \tag{3.63}$$

or

$$T_{\mathrm{surf}} = \frac{\dfrac{q_{\mathrm{rf}}}{A_{\mathrm{surf}}} + \alpha S}{\sigma F\left(T_{\mathrm{surf}}^2 + T_{\mathrm{sky}}^2\right)\left(T_{\mathrm{surf}} + T_{\mathrm{sky}}\right) + h_{\mathrm{conv}}} + T_{\mathrm{sky}} \tag{3.64}$$

where S is the solar incidence (W/m^2) and T_{sky} is the effective sky temperature (K) (typically equal to ambient temperature during the day and up to 20 K below the air temperature on a dry, clear night).

Thermal Resistance Networks

The expression of the governing heat transfer relations in the form of thermal resistances greatly simplifies the first-order thermal analysis of electronic systems. Following the established rules for resistance networks, thermal resistances that occur sequentially along a thermal path can be simply summed to establish the overall thermal resistance for that path. In similar fashion, the reciprocal of the effective overall resistance of several parallel heat transfer paths can be found by summing the reciprocals of the individual resistances. In refining the thermal design of an electronic system, prime attention should be devoted to reducing the largest resistances along a specified thermal path and/or providing parallel paths for heat removal from a critical area.

While the thermal resistances associated with various paths and thermal transport mechanisms constitute the "building blocks" in performing a detailed thermal analysis, they have also found widespread application as "figures-of-merit" in evaluating and comparing the thermal efficacy of various packaging techniques and thermal management strategies.

Chip Module Thermal Resistance

Definition

The thermal performance of alternative chip packaging techniques is commonly compared on the basis of the overall (junction-to-coolant or junction-to-ambient) thermal resistance, R_{ja}. This packaging figure-of-merit is generally defined in a purely empirical fashion,

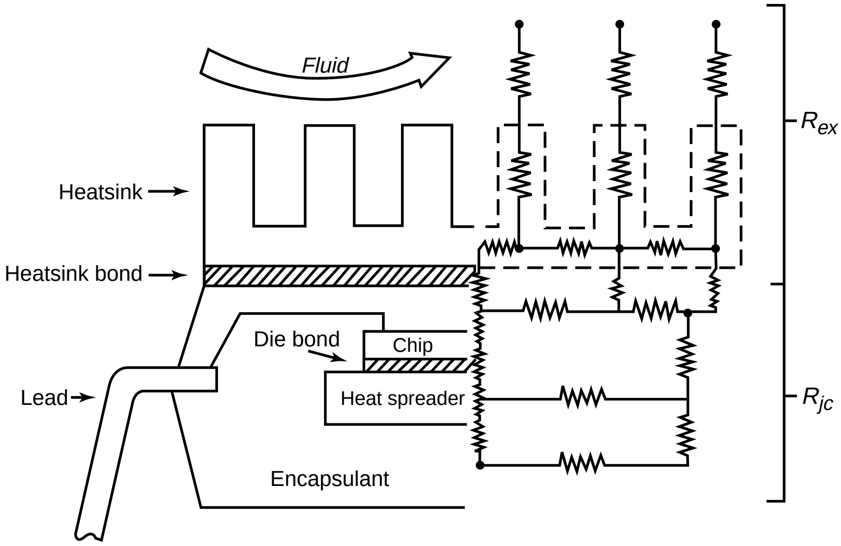

FIGURE 3.6 Primary thermal resistances in a single chip package. (From Ref. 4, with permission.)

$$R_{ja} \equiv \frac{T_j - T_{fl}}{q_c} \tag{3.65}$$

where T_j and T_{fl} are the junction and coolant (fluid) temperatures, respectively, and q_c is the chip heat dissipation.

Unfortunately, however, most measurement techniques are incapable of detecting the actual junction temperature, that is, the temperature of the small volume at the interface of p-type and n-type semiconductors. Hence, this term generally refers to the average temperature or a representative temperature on the chip.

Examination of various packaging techniques reveals that the junction-to-coolant thermal resistance is, in fact, composed of an internal, largely conductive resistance and an external, primarily convective resistance. As shown in Fig. 3.6, the internal resistance, R_{jc}, is encountered in the flow of dissipated heat from the active chip surface through the materials used to support and bond the chip and on to the case of the integrated circuit package. The flow of heat from the case directly to the coolant, or indirectly through a fin structure and then to the coolant, must overcome the external resistance, R_{ex}.

Internal Thermal Resistance

As previously discussed, conductive thermal transport is governed by the Fourier Equation, which can be used to define a conduction thermal resistance, as in Eq. (3.3). In flowing from the chip to the package surface or case, the heat encounters a series of resistances associated with individual layers of materials, starting with the chip (silicon, galium arsenide, indium phosphide, etc.) and continuing thru solder, copper, alumina, and epoxy, as well as the contact resistances that occur at the interfaces between pairs of materials. Although the actual heat flow paths within a chip package are rather complex and may shift to accommodate varying external cooling situations, it is possible to obtain a first-order estimate of the internal resistance by assuming that power is dissipated uniformly across the chip surface and that heat flow is largely one-dimensional. To the accuracy of these assumptions, Eq. (3.67)

$$R_{jc} = \frac{T_j - T_c}{q_c} = \sum \frac{\Delta x}{kA} \tag{3.66}$$

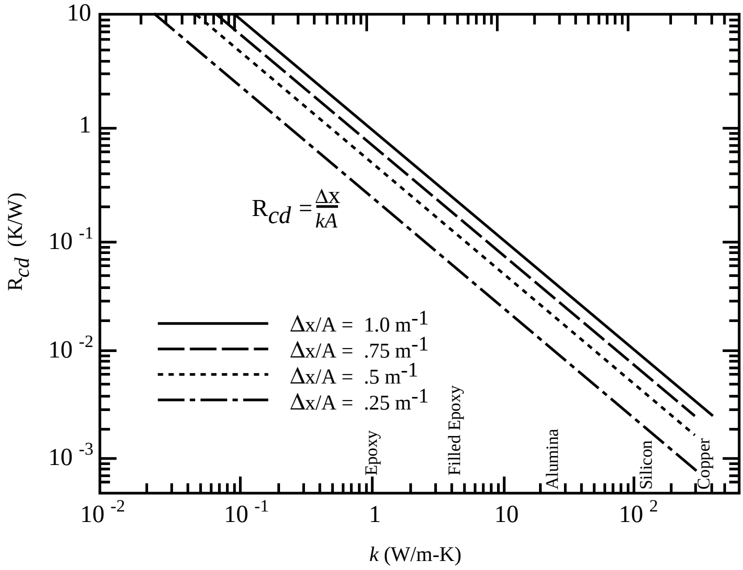

FIGURE 3.7 Conductive thermal resistances for packaging materials. (From Ref. 4, with permission.)

can be used to determine the internal chip module resistance, where the summed terms represent the conduction thermal resistances posed by the individual layers, each with thickness Δ*x*. As the thickness of each layer decreases and/or the thermal conductivity and cross-sectional area increase, the resistance of the individual layers decreases. Values of R_{cd} for packaging materials with typical dimensions can be found via Eq. (3.67) or Fig. 3.7, to range from 2 K/W for a 1000 mm^2 by 1-mm thick layer of epoxy encapsulant to 0.0006 K/W for a 100 mm^2 by 25-micron (1-mil) thick layer of copper. Similarly, the values of conduction resistance for typical "soft" bonding materials are found to lie in the range of approximately 0.1 K/W for solders and 1 to 3 K/W for epoxies and thermal pastes for typical Δ*x*/*A* ratios of 0.25 to 1.0.

Comparison of theoretical and experimental values of R_{jc} reveals that the resistances associated with compliant, low thermal conductivity bonding materials and the spreading resistances, as well as the contact resistances at the lightly loaded interfaces within the package, often dominate the internal thermal resistance of the chip package. It is, thus, not only necessary to correctly determine the bond resistance but to also add the values of R_{sp}, obtained from Eq. (3.7) and/or Fig. 3.4, and R_{co} from Eq. (3.9) or (3.12) to the junction-to-case resistance calculated from Eq. (3.67). Unfortunately, the absence of detailed information on the voidage in the die-bonding and heat-sink attach layers and the present inability to determine, with precision, the contact pressure at the relevant interfaces, conspire to limit the accuracy of this calculation.

External Resistance

An application of Eq. (3.41) or (3.43) to the transfer of heat from the case of a chip module to the coolant shows that the external resistance, $R_{ex} = 1/hA$, is inversely proportional to the wetted surface area and to the coolant velocity to the 0.5 to 0.8 power and directly proportional to the length scale in the flow direction to the 0.5 to 0.2 power. It may, thus, be observed that the external resistance can be strongly influenced by the fluid velocity and package dimensions and that these factors must be addressed in any meaningful evaluation of the external thermal resistances offered by various packaging technologies.

Values of the external resistance for a variety of coolants and heat transfer mechanisms are shown in Fig. 3.8 for a typical component wetted area of 10 cm^2 and a velocity range of 2 to 8 m/s. They are seen to vary from a nominal 100 K/W for natural convection in air, to 33 K/W for forced convection in air, to 1 K/W in fluorocarbon liquid forced convection and to less than 0.5 K/W for boiling in fluorocarbon

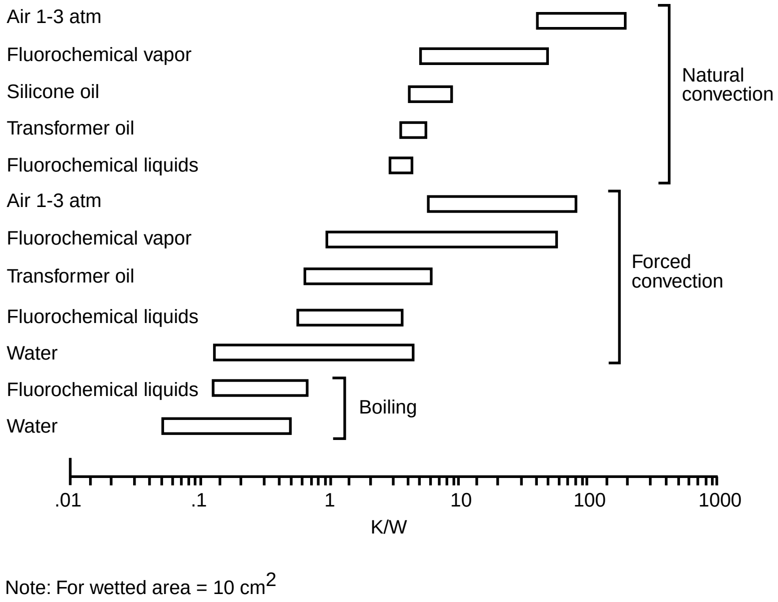

FIGURE 3.8 Typical external (convective) thermal resistances for various coolants and cooling modes. (From Ref. 4, with permission.)

liquids. Clearly, larger chip packages will experience proportionately lower external resistances than the displayed values. Moreover, conduction of heat through the leads and package base into the printed circuit board or substrate will serve to further reduce the effective thermal resistance.

In the event that the direct cooling of the package surface is inadequate to maintain the desired chip temperature, it is common to attach finned heat sinks, or compact heat exchangers, to the chip package. These heat sinks can considerably increase the wetted surface area, but may act to reduce the convective heat transfer coefficient by obstructing the flow channel. Similarly, the attachment of a heat sink to the package can be expected to introduce additional conductive resistances, in the adhesive used to bond the heat sink and in the body of the heat sink. Typical air-cooled heat sinks can reduce the external resistance to approximately 10 to 15 K/W in natural convection and to as low as 3 to 5 K/W for moderate forced convection velocities.

When a heat sink or compact heat exchanger is attached to the package, the external resistance accounting for the bond-layer conduction and the total resistance of the heat sink, R_{hs}, can be expressed as

$$R_{\mathrm{ex}} = \frac{T_{\mathrm{c}} - T_{\mathrm{fl}}}{q_{\mathrm{c}}} = \sum \left(\frac{\Delta x}{kA} \right)_b + R_{\mathrm{hs}} \tag{3.67}$$

where R_{hs}

$$R_{\mathrm{hs}} = \left[\frac{1}{nhA_{\mathrm{f}}\eta} + \frac{1}{h_{\mathrm{b}}A_{\mathrm{b}}} \right]^{-1} \tag{3.68}$$

is the parallel combination of the resistance of the n fins

$$R_f = \frac{1}{nhA_{\mathrm{f}}\eta} \tag{3.69}$$

and the *bare* or base surface not occupied by the fins

$$R_{\mathrm{b}} = \frac{1}{h_{\mathrm{b}} A_{\mathrm{b}}} \tag{3.70}$$

Here, the base surface is $A_{\mathrm{b}} = A - A_{\mathrm{f}}$ and use of the heat transfer coefficient, h_{b}, is meant to recognize that the heat transfer coefficient that is applied to the base surfaces is not necessarily equal to that applied to the fins.

An alternative expression for R_{hs} involves an *overall surface efficiency,* η_{o}, defined by

$$\eta_o = 1 - \frac{nA_{\mathrm{f}}}{A}(1 - \eta) \tag{3.71}$$

where A is the total surface composed of the base surface and the finned surfaces of n fins

$$A = A_{\mathrm{b}} + nA_{\mathrm{f}} \tag{3.72}$$

In this case, it is presumed that $h_{\mathrm{b}} = h$ so that

$$R_{\mathrm{hs}} = \frac{1}{h\eta_{\mathrm{o}} A} \tag{3.73}$$

In an optimally designed fin structure, η can be expected to fall in the range of 0.50 to 0.70.[4] Relatively thick fins in a low velocity flow of gas are likely to yield fin efficiencies approaching unity. This same unity value would be appropriate, as well, for an unfinned surface and, thus, serve to generalize the use of Eq. (3.68) to all package configurations.

Total Resistance — Single Chip Packages

To the accuracy of the assumptions employed in the preceding development, the overall single chip package resistance, relating the chip temperature to the inlet temperature of the coolant, can be found by summing the internal, external, and flow resistances to yield

$$\begin{aligned} R_{\mathrm{jaj}} &= R_{\mathrm{jc}} + R_{\mathrm{ex}} + R_{\mathrm{fl}} \\ &= \sum \frac{\Delta x}{kA} + R_{\mathrm{int}} + R_{\mathrm{sp}} \\ &= \frac{1}{\eta hA} + \left(\frac{Q}{q}\right)\left(\frac{1}{2\rho Q c_{\mathrm{p}}}\right) \end{aligned} \tag{3.74}$$

In evaluating the thermal resistance by this relationship, care must be taken to determine the effective cross-sectional area for heat flow at each layer in the module and to consider possible voidage in any solder and adhesive layers.

As previously noted in the development of the relationships for the external and internal resistances, Eq. (3.75) shows R_{ja} to be a strong function of the convective heat transfer coefficient, the flowing heat capacity of the coolant, and geometric parameters (thickness and cross-sectional area of each layer). Thus, the introduction of a superior coolant, use of thermal enhancement techniques that increase the local heat transfer coefficient, or selection of a heat transfer mode with inherently high heat transfer coefficients (boiling, for example) will all be reflected in appropriately lower external and total thermal resistances. Similarly, improvements in the thermal conductivity and reduction in the thickness of the relatively low conductivity bonding materials (such as soft solder, epoxy, or silicone) would act to reduce the internal and total thermal resistances.

Weighted-Average Modification of R_{jc}

The commonly used junction-to-case thermal resistance, relying on just a single case temperature, can be used with confidence only when the package case is nearly isothermal. In a more typical packaging configuration, when substantial temperature variations are encountered among and along the external surfaces of the package,[32–34] the use of the reported $R_{\rm jc}$ can lead to erroneous chip temperature predictions. This is especially of concern in the analysis and design of plastic chip packages, due to the inherently high thermal resistance of the plastic encapsulant and the package anisotropies introduced by the large differences in the conductivity between the lead frame and/or heat spreader and the plastic encapsulant. Since $R_{\rm jc}$ is strictly valid only for an isothermal package surface, a method must be found to address the individual contributions of the various surface segments according to their influence on the junction temperature.

Following Krueger and Bar-Cohen,[35] it is convenient to introduce the expanded $R_{\rm jc}$ methodology with a thermal model of a chip package that can be approximated by a network of three thermal resistances connected in parallel, from the chip to the top, sides, and bottom of the package, respectively. This type of compact model is commonly referred to as a “star network” and, in this model, the heat flow from the chip is

$$q = q_1 + q_2 + q_3 \tag{3.75}$$

or

$$q = \frac{T_{\rm j} - T_1}{R_1} + \frac{T_{\rm j} - T_2}{R_2} + \frac{T_{\rm j} - T_3}{R_3} \tag{3.76}$$

This compact model of an electronic device is shown schematically in Fig. 3.9.

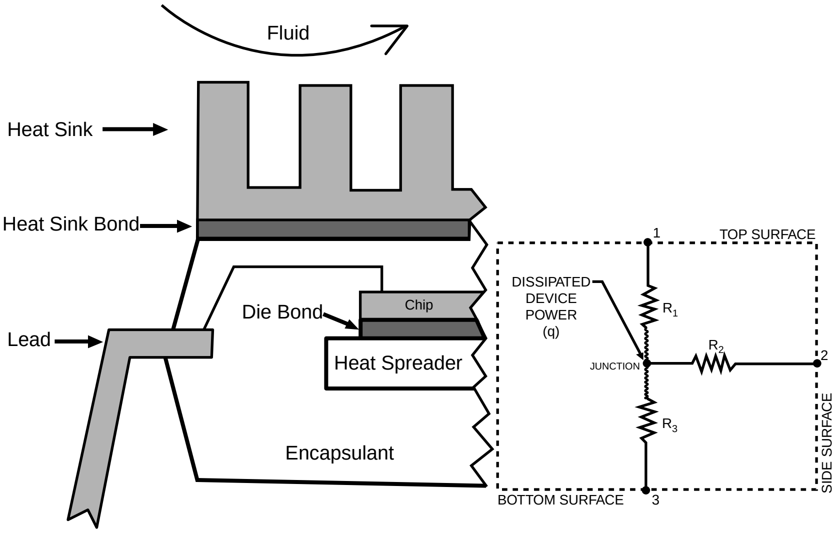

FIGURE 3.9 Geometry of a 28-lead PLCC device. (a) The compact model schematic, and (b) the actual device cross-section.[35]

Equation (3.77) can be rearranged to yield the dependence of the chip (or junction) temperature on the temperature of the three surface segments as

$$T_{\mathrm{j}} = \left(\frac{R_2R_3}{R_s}\right)T_1 + \left(\frac{R_3R_1}{R_{\mathrm{s}}}\right)T_2 + \left(\frac{R_1R_2}{R_{\mathrm{s}}}\right)T_3 + \left(\frac{R_1R_2R_3}{R_{\mathrm{s}}}\right)q \tag{3.77}$$

where $R_s = R_1R_2 + R_1R_3 + R_2R_3$

Equation (3.78) may be generalized to admit n-distinct elements along the package surface, or

$$T_{\mathrm{j}} = \sum_{k=1}^{n} I_kT_k + I_{n+1}q \tag{3.78}$$

A comparison of Eqs. (3.78) and (3.79) shows that the coefficients of the specified surface temperatures, the I_k's are totally determined by the internal resistances of the chip package

$$\begin{aligned} I_1 &= \frac{R_2R_3}{R_{\mathrm{s}}} & I_2 &= \frac{R_3R_1}{R_{\mathrm{s}}} \\ I_3 &= \frac{R_1R_2}{R_{\mathrm{s}}} & I_4 &= \frac{R_1R_2R_3}{R_{\mathrm{s}}} \end{aligned} \tag{3.79}$$

The temperature coefficients needed to generate a junction temperature relation of the form shown in Eq. (3.79) can thus be determined from previously calculated internal resistance or, in the absence of such values, by extraction from empirical data or numerical results for the junction temperature. Furthermore, it is to be noted that the sum of the coefficients of the various surface temperature is equal to unity and that the power dissipation coefficient, $I_{n+1}q$, is, in fact, the familiar R_{jc} isothermal, junction-to-case thermal resistance. Consequently, Eq. (3.79) may be rewritten as

$$T_{\mathrm{j}} = \sum_{k=1}^{n} I_kT_k + R_{\mathrm{jc}}q \tag{3.80}$$

or, returning to R_{jc}

$$R_{\mathrm{jc}} = \frac{T_{\mathrm{j}} - \sum_{k=1}^{n} I_kT_k}{q} = \frac{T_{\mathrm{j}} - \overline{T}_{\mathrm{c}}}{q} \tag{3.81}$$

where $\overline{T}_{\mathrm{c}}$ is the average case temperature

$$\overline{T}_{\mathrm{c}} = \frac{\sum_{k=1}^{n} A_kT_k}{A_{\mathrm{T}}} \tag{3.82}$$

where A_k is the surface area of the k^{th} surface and A_{T} is the surface area of the entire package.

In many applications, chip packages are cooled selectively along particular exposed surfaces. One such example is a package cooled from the top and side surfaces while the bottom surface is insulated. The thermally active surfaces may vary from application, to application and the thermal analyst needs to quantify the effect of thermally insulating one or more areas on a package of known thermal resistance.

For the assumptions used in the development of the expanded R_{jc} model, insulation of surface-*m* results in zero heat flow through resistance, R_m. This causes the temperature of surface-*m* to equal the chip temperature. With this in mind, the junction temperature for a package with a single insulated surface given by Eq. (3.81) is found to equal

$$T_{\mathrm{j}} = \sum_{k \neq m} \left(\frac{I_k}{1 - I_m} \right) T_k + \left(\frac{I_{n+1}}{1 - I_m} \right) q \tag{3.83}$$

The weighted average case temperature for this thermal configuration is found to equal

$$\overline{T}_{\mathrm{c}} = \sum_{k \neq m} \left(\frac{I_k}{1 - I_m} \right) T_k \tag{3.84}$$

and the modified junction to case resistance, R^*_{jc} is

$$R^*_{\mathrm{jc}} = \frac{R_{\mathrm{jc}}}{1 - I_m} \tag{3.85}$$

Multichip Modules

The thermostructural complexity of multichip modules in current use hampers effective thermal characterization and introduces significant uncertainty in any attempt to compare the thermal performance of these packaging configurations. Variations in heat generation patterns across the active chips (reflecting differences in functional requirements and the duty cycle among the macrocells constituting a particular chip), as well as nonuniformities in heat dissipation among the chips assembled in a single module, further complicate this task. While nonthermal issues (e.g., electromagnetic crosstalk) may often be the dominant limiting factors in RF multichip modules, the high power associated with microwave devices makes it essential that the thermal performance of this packaging configuration be analyzed and reported in a consistent manner. To establish a common basis for comparison of multichip modules, it is possible to neglect the on-chip and chip-to-chip variations and consider that the heat generated by each chip flows through a unit cell of the module structure to the external coolant.[36,37] For a given structure, increasing the area of the unit cell allows heat to spread from the chip to a larger cross-section, reducing the heat flux at some of the thermally critical interfaces and at the convectively cooled surfaces. Consequently, the thermal performance of a multichip module can be best represented by the area-specific thermal resistance, i.e., the temperature difference between the chip and the coolant divided by the substrate heat flux, expressed in units of K/(W/cm^2). This figure of merit is equivalent to the inverse of the overall heat transfer coefficient, *U*, commonly used in the compact heat exchanger literature. Despite significant variation in design and fabrication, the leading edge water-cooled and air-cooled modules of the late 1980s provided a specific thermal resistance of approximately 20°C for every watt per square centimeter at the substrate. A decade later, the thermally best multichip modules of the 1990s offered specific thermal resistance values between 5 and 10 K/(W/cm^2).

Radar System Applications

The frequent demand for high radiated power in civilian and military radar systems, for the ranging and detection of remote objects, has led to the development of many high-energy microwave systems. Due to the inefficiencies inherent in electrical-to-microwave energy conversion and the management of radio-frequency (RF) energy, the operation of such radar equipment often results in significant heat dissipation. To avoid catastrophic failures, to achieve the reliability targets of the system, and to satisfy the frequency stability requirements of the RF tubes, system requirements commonly specify temperature control to within several degrees Celsius around 150°C. These thermal requirements necessitate the use of aggressive thermal management techniques, including the use of high flow rate liquid forced convection, pool and flow boiling, and high pressure-drop, air-cooled compact heat exchangers.[3]

In traditional, mechanically steered radar systems, much of the total power dissipation occurs in the power tubes (e.g., klystron, gyrotrons, amplitrons), with secondary dissipation in the rotary joints and wave guides. Heat release along the collector surfaces of the tubes is proportional to the RF power of the system and can range from 1 kW to as much as 20 kW, with a peak local flux of several watts/cm^2 to, perhaps, several thousand watts/cm^2, at operating temperatures of 150°C.[3] Similar, though less severe thermal problems are encountered in the RF rotary joints and waveguides, where heat fluxes of 5 W/cm^2 to 10 W/cm^2, with allowable temperatures of 150°C, may be encountered.

Growing applications of active antenna array elements, utilizing amplifier diodes and solid-state phase shifters to provide electronic steering of the radiated RF beam, have introduced new dimensions into the thermal control of microwave equipment. In such "phased array" radar systems, high power tubes and waveguides can be eliminated with low power RF delivered to each antenna element. The low conversion efficiency of the amplifier diodes results in diode heat dissipation between 1 W and 10 W and local heat fluxes comparable to power transistors. In "phased array" antenna, precise shaping of the radiated wave often requires relatively cool (<90°C) ferrite phase shifters and no significant temperature variations (<10°C) across the elements used in the array.

References

1. M. Pecht, P. Lall, and E. Hakim, The influence of temperature on integrated circuit failure mechanisms, *Advances in Thermal Modeling of Electronic Components and Systems,* vol. 3, A. Bar-Chen and A.D. Kraus, Eds., ASME Press, New York, 1992.
2. R.A. Morrison, Improved avionics reliability through phase change conductive cooling, *Proceedings, IEEE National Telesystems Conference,* 1982, B5.6.1–B5.6.6.
3. A.D. Kraus and A. Bar-Cohen, *Thermal Analysis and Control of Electronic Equipment,* McGraw-Hill, New York, 1983.
4. A.D. Kraus and A. Bar-Cohen, *Design and Analysis of Heat Sinks,* John Wiley & Sons, New York, 1995.
5. K.J. Negus, M.M. Yovanovich, and J.V. Beck, On the non-dimensionalization of constriction resistance for semi-infinite heat flux tubes, *J. Heat Trans.,* 1111, 804–807, 1989.
6. M.M. Yovanovich and V.W. Antonetti, Application of thermal contact resistance theory to electronic packages, in *Advances in Thermal Modeling of Electronic Components and Systems,* A. Bar-Cohen and A.D. Kraus (eds.), Hemisphere Publishing Co, New York, 1988, 79, 28.
7. M.M. Yovanovich, personal communication, 1990.
8. F.P. Incropera and D.P. Dewitt, *Introduction to Heat Transfer,* John Wiley and Sons, New York, 1996.
9. W. Elenbaas, Heat dissipation of parallel plates by free convection, *Physica,* 9, 1, 665–671, 1942.
10. J.R. Bodoia and J.F. Osterle, The development of free convection between heated vertical plates, *J. Heat Transfer,* 84, 40–44, 1964.
11. N. Sobel, F. Landis, and W.K. Mueller, Natural convection heat transfer in short vertical channels including the effect of stagger, *Proc. 3d Int. Heat Transfer Conf.,* Chicago, 2, 1966, 121–125.
12. W. Aung, Fully developed laminar free convection between vertical plates heated asymmetrically, *Int. J. Heat Mass Transfer,* 15, 40–44, 1972.
13. W. Aung, L.S. Fletcher, and V. Sernas, Developing laminar free convection between vertical flat plates with asymmetric heating, *Int. J. Heat Mass Transfer,* 15, 2293–2308, 1972.
14. O. Miyatake and T. Fujii, Free convection heat transfer between vertical parallel plates — one plate isothermally heated and the other thermally insulated, *Heat Transfer Jpn. Res.,* 3, 30–38, 1972.
15. O. Miyatake, T. Fujii, M. Fujii, and H. Tanaka, Natural convection heat transfer between vertical parallel plates — one plate with a uniform heat flux and the other thermally insulated, *Heat Transfer Jpn. Res.,* 4, 25–33, 1973.

16. A. Bar-Cohen and W.M. Rohsenow, Thermal optimum spacing of vertical, natural convection cooled, vertical plates, *J. Heat Trans.,* 106, 116–122, 1984.
17. W.H. McAdams, *Heat Transmission,* McGraw-Hill, New York, 1954.
18. S.W. Churchill and R. Usagi, A. general expression for the correlation of rates of transfer and other phenomena, *AIChE J.,* 18, 6, 1121–1138, 1972.
19. A. Bar-Cohen and W.M. Rohsenow, Thermally optimum spacing of vertical, natural convection cooled, parallel plates, *Heat Transfer in Electronic Equipment, ASME HTD 20, ASME WAM,* Washington, D.C., 11–18, 1981.
20. A. Bar-Cohen, Bounding relations for natural convection heat transfer from vertical printed circuit boards, *Proceedings of the IEEE,* September 1985.
21. E.N. Sieder and G.E. Tate, Heat transfer and pressure drops of liquids in tubes, *Ind. Eng. Chem.,* 28, 1429–1435, 1936.
22. H. Hausen, Darstelling des wärmeuberganges in rohren durch verallgemeinerte potenzbeziehungen, *VDI Z,* 4, 91–98, 1943.
23. A. Bejan, *Heat Transfer,* John Wiley & Sons, New York, 1993.
24. J.P. Holman, *Heat Transfer,* McGraw-Hill, New York, 1990.
25. J.H. Lienhard, *A Heat Transfer Textbook,* Prentice-Hall, Englewood Cliffs, NJ, 1987.
26. W.M. Rohsenow, A method of correlating heat transfer data for surface boiling of liquids, *Transactions of ASME* (reprinted in *3rd ASME/JSME Thermal Engineering Joint Conference,* 1, 503–512), 74, 969–976, 1951.
27. A.A. Watwe, A. Bar-Cohen, and A. McNeil, Combined pressure and subcooling effects on pool boiling from a PPGA chip package, *ASME J. Electronics Packaging,* March 1997.
28. F. Gertsmann and P. Griffith, Laminar film condensation on the underside of horizontal and inclined surfaces, *Int. J. Heat Mass Trans.,* 10, 567–580, 1966.
29. W.Z. Nusselt, Die oberflächencondensation der wasserdamfes, *Z. Ver. Deut. Ing.,* 60, 541–569, 1916.
30. P. Sadasivan and J.H. Lienhard, Sensible heat correction in laminar film boiling and condensation, *J. Heat Trans.,* 109, 545–546, 1987.
31. C. Rambach and A. Bar-Cohen, Nocturnal heat rejection by skyward radiation, in *Future Energy Production Systems,* J.C. Denton and N. Afgan, eds., Hemisphere Publishing, New York, 1976, 713–726.
32. J.A. Andrews, Package thermal resistance model dependency on equipment design, *IEEE CHMT Trans.,* 11, 4, 528–537, 1988.
33. S.S. Furkay, Thermal characterization of plastic and surface mount components, *IEEE CHMT Trans.,* 11, 4, 521–527, 1988.
34. E.A. Wilson, Factors influencing the interdependence of R_{jc} and R_{ca}, *Proceedings of the Second International Electronic Packaging Society Meeting,* 247–255, 1981.
35. W.B. Krueger and A. Bar-Cohen, Thermal characterization of a PLCC — expanded R_{jc} methodology, *IEEE CHMT Trans.,* 15, 5, 691–698, 1992.
36. A. Bar-Cohen, Thermal management of air- and liquid-cooled multichip modules, *IEEE CHMT Trans.,* CHMT-10, 2, 159–175, 1987.
37. A. Bar-Cohen, Addendum and correction to thermal management of air- and liquid-cooled multichip modules, *IEEE CHMT Trans.,* CHMT-11, 3, 333–334, 1988.

3.2 Safety and Environmental Issues

John M. Osepchuk and Ronald C. Petersen

This section is aimed at providing the modern microwave engineer with fundamental facts about the bioeffects and potential hazards of exposure to microwave energy. This subject had a tortured history in the last half of the 20th century and is often characterized by misinformation, especially in the modern media. The research in this field, though very extensive, is often of poor quality and often marred by

TABLE 3.2 Approximate Dielectric Parameters for Muscle Tissue at Various Frequencies[a]

Frequency (MHz)	Relative Dielectric Constant (ε_r)	Conductivity (σ) (S/m)	Penetration Depth (δ) (cm)
0.1	1850	0.56	213
1.0	411	0.59	70
10	131	0.68	13.2
100	79	0.81	7.7
1000	60	1.33	3.4
10,000	42	13.3	0.27
100,000	8	60	0.03

[a] Muscle tissue, field parallel to tissue fibers.[3]

microwave artifacts. Scientists and engineers of all disciplines critically review this literature and derive, by broad consensus and due process of the IEEE (the Institute of Electrical and Electronics Engineers), sound safety standards with reasonable safety factors. The standards literature deals not only with potential effects on the human body but also allied effects on fuel, electro-explosive devices (EEDs), and medical devices. Related subjects are the expanding field of medical applications of microwave energy, as in hyperthermia, and the growing threat of interference between microwave systems — especially between wireless LANs operating in the ISM (Industrial, Scientific, and Medical) band of 2.40 to 2.5 GHz, where many microwave-power systems operate, including roughly 200 million microwave ovens in the world. Although science-based standards are the rational basis for developing safety practices in the presence of microwave energy, there is some confusion presented by recent ideas such as the Precautionary Principle. Thus, there is a need for continuing education on this subject from responsible professional organizations such as the IEEE.

Characteristics of Biological Tissue and RF Absorption Properties

Modern IEEE standards for safe exposure to RF electromagnetic energy cover frequencies up to 300 GHz and down to at least 3 kHz. Although the term "microwaves" usually means frequencies well above 100 or 300 MHz, related bioeffects/hazards exist down to roughly 100 kHz. These are thermal in nature. Below 100 kHz the dominant effects are electrostimulatory in nature. We will confine our attention to thermal effects and refer the reader to an authoritative treatment on the subject of electrostimulation by Reilly.[1]

In order to understand any bioeffect caused by exposure of a biological body to microwave/RF energy one needs to have an idea of the distribution of the internal E and B fields generated by the exposure. In turn one must have some information about the dielectric properties of the tissues in the biological body. Later we will refer to modern computer modeling of the absorption using elaborate anatomically correct models of the body that are heterogeneous in general with muscle, bone, skin, etc. Some simple but important properties of absorption can be gained from simple models.

The dielectric properties of various tissues have been tabulated in a popular reference called the *Radiation Dosimetry Handbook,* edited by Durney et al.[2] In recent years these data, particularly for bone, have been improved by Gabriel et al.[3] From these sources we can tabulate the approximate values for muscle-like tissue as in Table 3.2.

In Table 3.2, the relative dielectric constant is shown as well as the conductivity. The complex permittivity is given by:

$$\varepsilon = \varepsilon_r \varepsilon_o + j\frac{\sigma}{\omega} \tag{3.86}$$

where $\varepsilon_o = 8.86 \times 10^{-12}$ f/m. The penetration depth is that at which a plane wave is attenuated by a factor of e in E-field or 8.69 dB. Its classical derivation is presented in Durney et al.[2] We see that penetration at low RF frequencies is considerably more than 10 cm, but above 6 GHz the penetration depth rapidly decreases to a millimeter or less in the millimeter-wave range of the microwave spectrum. The penetration depth is one basic factor in determining how much energy reaches deep into the body. The other factor is the reflection at the external surface, or at lower frequencies the shunting of the electric field by a conducting body. For a small spherical object, Schwan[4] has shown that at 60 Hz, the internal E field is nearly six orders of magnitude less than the external E field, even though the theoretical penetration depth is quite large at low frequencies. It has been estimated by Osepchuk[5] that only around the "resonance" frequency of man, i.e., around 100 MHz, is the internal E field deep in the body within one order of magnitude of the external field. At very high frequencies, e.g., in the millimeter-wave range, the E field deep in the body is many orders of magnitude below the external field because the penetration depth is only one millimeter or less.

The principles of modern dosimetry have recently been reviewed by Chou et al.[6] The specific absorption rate (SAR), i.e., the mass averaged rate of energy absorption in tissue, is related to E by

$$\mathrm{SAR} = \frac{\sigma|E|^2}{\rho} \ \mathrm{W/kg} \tag{3.87}$$

where σ is the conductivity of the tissue in Siemens per meter, ρ is the density in kg per cubic meter, and E is the rms electric field strength in volts per meter. SAR is thus a measure of the electric field at the point under study and it is also a measure of the local heating rate dT/dt, viz.:

$$\frac{dT}{dt} = \frac{\mathrm{SAR}}{c} \ {}^\circ\mathrm{C/s} \tag{3.88}$$

where c is the specific heat capacity of the tissue in J/kg °C. Thus, a SAR of 1 W/kg is associated with a heating rate less than 0.0003°C per second in muscle tissue ($c \cong 3.5$ kJ/kg°C). Clearly this is a very small heating rate since even without blood or other cooling it would take more than one hour to increase the temperature 1 degree Celsius.

The SAR concept is a key concept in planning and analysis of experiments, both *in vivo* and *in vitro*, as well as the formulation of safe exposure limits for humans. Both the local SAR value and the whole-body average are important in these endeavors. There is an extensive literature on the calculation of whole-body average SAR for various models of animals, including man, especially those based on ellipsoids, which are summarized in the *Dosimetry Handbook*.[2] In Fig. 3.10 we show the calculated SAR for an average man based on such a model, when exposed to a plane wave of power density of 1 mW/cm^2. Shown is the whole-body-averaged SAR vs. frequency for three polarizations; E — in which the E-field is parallel to the main axis, H — in which the H-field is parallel to the main axis, and k — in which the direction of propagation is parallel to the main axis of the body. We see that there is a low-Q resonance at about 70 to 80 MHz for a standard man (and at about half that frequency when standing on a conducting ground plane). The peak absorption is highest for E polarization and is equal to about 0.2 W/kg per mW/cm^2 incident power density. At high frequencies the SAR decreases to an asymptotic "quasi-optical" value 5 to 6 times lower than the SAR peak. At very low frequencies the SAR varies as f^2, as expected. The peak SAR values for animals are higher, e.g., for a mouse at its resonance frequency of about 2 GHz, the peak SAR is somewhat over 1.0 W/kg per mW/cm^2.

The SAR distributions within the body are quite complicated even when resulting from exposure to the simplest plane wave in the far field. Depending upon the body position and frequency, it is possible that there are one or more "hot spots" of SAR peaks within the animal body. Based upon the work of

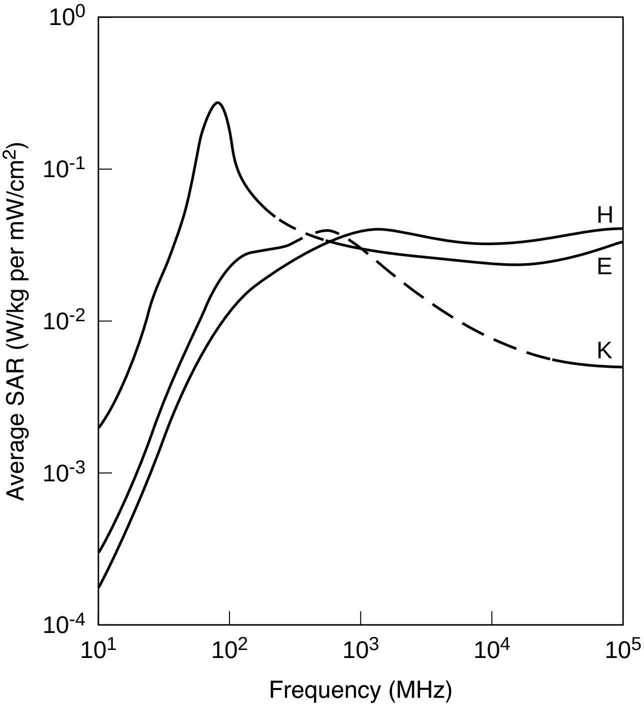

FIGURE 3.10 Calculated whole-body average SAR versus frequency for models of the average man for three standard polarizations. The incident power density is 1 mW/cm^2. (From Durney, et al.[2])

Kritikos and Schwan,[7] however, such internal SAR peaks are very unlikely for man, but are more probable for small animals.

Bioeffects and Hazards of Microwave/RF Energy

More than 20,000 papers have been published in world literature about the bioeffects of microwave/RF energy. Many deal with experiments with animals, i.e., *in vivo*, especially at frequencies between 10 MHz and 60 GHz. The early literature before 1980 showed a major share of these experiments with small animals were done at 2.45 GHz, at which, as the microwave-oven frequency, there is an inexpensive source of power. Substantial literature is also available about *in vitro* experiments in which small samples of tissue or cells are exposed in a variety of exposure systems. These occur more after 1980. Epidemiological studies are few and tend to have been done in recent years. For most, exposure assessment is at best questionable and at worst nonexistent. One should not forget that a large amount of human exposure data exist from the history[8] of diathermy at 27 MHz and at 2.45 GHz. Millions of patients were treated with up to 125 watts of power applied to various parts of the body for 15 to 30 minutes. In recent years, diathermy has been less popular, perhaps because of the growth of electrophobia directed toward the "radiation" aspect of "microwave" energy. In the last few decades, however, this human exposure data has been tremendously expanded in the medical area by the widespread use of MRI (magnetic resonance imaging) in which RF energy at VHF frequencies and of the order of 100 watts is applied to the body. Lastly there are a variety of other medical applications[9] of microwave/RF energy such as hyperthermia for the treatment of cancer.

To better understand experiments in microwave exposure as well as their relation to safety standards, it is useful to refer to the "exposure diagram" of Fig. 3.11. In this diagram, with log-log coordinates of power (or power density or SAR) on the ordinate and time on the abscissa, we can draw the threshold

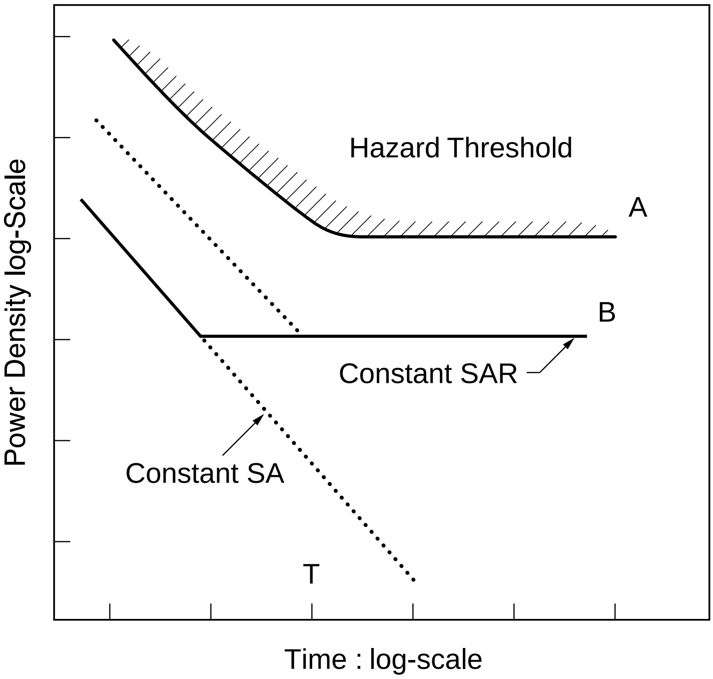

FIGURE 3.11 Thresholds for various effects and hazards expressed as a function of time.

for various effects and hazards. For example, to heat a finite sample to a given temperature, the threshold is a constant SAR for long periods of time while for small periods of time, during which no heat is lost from the sample, the threshold curve is a line of constant SA (specific absorption = SAR × time) which is at 45 degrees from the horizontal in Fig. 3.11. The intersection of the two lines, constant SAR and constant SA, determines the applicable thermal time constant or associated "averaging time" in exposure standards. Similar curves would result for the threshold for burns using the classic data of Henriques and Moritz[10] for threshold temperature for burns, which is around 60°C for 5 seconds but approaching 45°C for long exposure times, where 45°C is also the threshold temperature for pain sensation in man.

Thus, much early data described by such threshold curves described the lethal thresholds of exposure of animals in terms of power density and exposure duration, usually at room temperature. For example, Michaelson[11] found that for a dog the lethal threshold at 2.8 GHz was about 2 to 4 hours at 165 mW/cm^2. On the other hand Addington[12] found that at 200 MHz, for a dog the lethal threshold was only 20 minutes at 220 mW/cm^2. In the Soviet literature[13] the lethal threshold reported for the rat was 40 mW/cm^2 for 90 minutes at 3 GHz but at 70 MHz, the threshold was about 1000 mW/cm^2 for 100 minutes. Although not appreciated at those early times, these results appear quite reasonable in terms of the expected SAR absorption curves and respective resonance frequencies for the various size animals. This physical understanding based on heating was further strengthened when experiments[14] with fruit flies (Drosophilae) showed no effect when exposed at 2.45 GHz with over 6500 mW/cm^2 and 45 minutes exposure duration. This result is eminently reasonable to the engineer well acquainted with the absorption cross-section theory that shows absorption decreasing rapidly as the square of the animal dimension. (It also explains the mystifying — to the layman — observation that small ants are not perturbed in an operating microwave oven). In 1971 Samaras et al.[15] demonstrated the expected, but still dramatic, dependence on environmental temperature. At room temperature the lethal threshold for a rat at 2.45 GHz for a 17-minute exposure was 100 mW/cm^2, but at freezing temperatures below 0°C that same power density was life preserving for the rat.

In 1979 Tell and Harlen[16] analyzed a host of data in the literature demonstrating thermal effects in animals. They showed how all the animal data seemed to form a coherent picture and extrapolated to man so as to suggest that, at least for frequencies above 1 GHz, 100 mW/cm^2 was a conservative estimate of the threshold for a 1°C core temperature rise for exposure durations of more than an hour. Their analysis suggested also that the thermal time constant for whole-body heating of man is an hour or more. In the last decade, however, actual experiments with humans by Adair[17] have shown that exposures at 450 MHz and 2.45 GHz for 45 minutes showed no core temperature rise at power densities corresponding to at least ten times the basis of the current safety limits (expressed as 4 W/kg). Adair is proceeding with further experiments with humans in the resonance frequency range below 100 MHz.

Many endpoints of the health of animals have been studied in the thousands of experiments reported in the literature. We will not specifically review all categories but special mention of "cataracts" is justified in view of the myths that were attached to this subject in the 1970s. Cataracts, i.e., opacities of the lens that interfere with vision, are probably the most studied effect associated with exposure to microwave energy. The hard science on the subject shows that the threshold[18] for cataracts in the rabbit is of the order of 180 mW/cm^2 for an exposure duration of one-half hour or more at 2.45 GHz. This result was obtained when the rabbit was restrained or under anesthesia, and only when the energy was applied locally to the eyes with near-field applicators such as diathermy antennas. At X-band, attempts to produce cataracts resulted in skin burns first around the eyes. Attempts to produce cataracts at UHF resulted in the death of the animal before the cataract could be produced. Long-term exposures of the rabbit by Guy et al.[19] at 2.45 GHz and 10 mW/cm^2 showed no ocular damage. Microwave-induced cataracts have not been demonstrated in primates, but in the last two decades there have been some reports[20] of corneal damage from high peak power pulsed fields at moderate average power densities around 10 mW/cm^2. Attempts to replicate these findings have failed.[21]

The extensive literature on microwave bioeffects has been surveyed often. Some of the classic papers are reproduced, along with extensive bibliographies and commentaries in a reprint volume[22] produced by the IEEE Committee on Man and Radiation (COMAR). Other good reviews of the literature before 1990 include a special issue[23] of the *Proceedings of the IEEE* and an extensive review[24] by the EPA.

Over the years Polson and Heynick[25] have produced critical reviews of the literature, under the sponsorship of the U. S. Air Force. An excellent text was authored by Michaelson and Lin[26] and multi-author books have been edited by Gandhi[27] and Polk and Postow.[28] Although most confirmed bioeffects are associated with significant temperature rise in experimental animals there is one exception, the microwave auditory effect.[29] It has been shown that exposure of the head to microwave pulses results in audible clicks above a threshold of roughly 40 μJ/cm^2 energy density incident on the head at 2.45 GHz. This effect is not believed hazardous but it has been used in some safety guidelines to set limits for exposures to pulsed fields. Special mention should be made of DeLorge's[30] studies of the disruption of food-motivated learned behavior of animals. Thresholds for this effect, which is believed to be the most sensitive and reproducible known effect, have been the principal basis for most modern safety standards beginning with the series of C95 standards produced under IEEE sponsorship. Disruption occurs reliably at whole-body-averaged SARs between 2 to 3 and 9 W/kg across frequency and animal species from mice to baboons (see Table 3.3).[43,48]

TABLE 3.3 Comparison of Power Density and SAR Thresholds for Behavioral Disruption in Trained Laboratory Animals

Species and Conditions	225 MHz (CW)	1.3 GHz (Pulsed)	2.45 GHz (CW)	5.8 GHz (Pulsed)
Norwegian Rat				
Power Density	—	10 mW/cm^2	28 mW/cm^2	20 mW/cm^2
SAR	—	2.5 W/kg	5.0 W/kg	4.9 W/kg
Squirrel Monkey				
Power Density	—	—	45 mW/cm^2	40 mW/cm^2
SAR	—	—	4.5 W/kg	7.2 W/kg
Rhesus Monkey				
Power Density	8 mW/cm^2	57 mW/cm^2	67 mW/cm^2	140 mW/cm^2
SAR	3.2 W/kg	4.5 W/kg	4.7 W/kg	8.4 W/kg

It needs to be said that this field has been fraught with much confusion and much poor quality literature. In 1977 Senator Stevenson[31] stated: "I have never gotten into a subject on which there has been so much disagreement and so much confessed lack of knowledge." He was speaking of the field of microwave bioeffects. Later Foster and Guy[32] and Foster and Pickard[33] wrote critical papers pointing out the prevalence of many papers in the literature that could not be replicated or confirmed. They wondered when such research, which never found robust confirmed effects, would cease. An example of such literature is that of the former Soviet Union, and to some extent Germany, which reports frequency-sensitive effects of millimeter-wave radiation at low levels of around 1 mW/cm^2. These reports led to an extensive practice of mm-wave therapy for medical purposes in Russia and the Ukraine, but neither the research nor the medical practice has been found valid in the West. (See the discussion in Reference 27.) More recently there was a report[34] from Russia of bioeffects at extraordinarily low levels of power density ~10^{-19} W/cm^2 at a millimeter-wave frequency. We[35] have shown, however, that this extraordinary claim is most probably invalid because of the lack of control of significant energy at the harmonic frequencies. This is only one example of the presence of microwave artifacts that mar many of the papers in the literature. Other artifacts include the great nonuniformity of microwave heating of objects, which is often neglected. Thus, it often is reported that the object temperature is of some value when in actuality the object has a wide spatial variation in temperature. Unfortunately these artifacts not only appear in *in vitro* studies but also in *in vivo* studies that have become increasingly prevalent in this field. One recent study[36] of a large number of transgenic mice has implied a connection of low-level microwave exposure with a cancer (lymphoma). Unfortunately the experiment was done in a metal enclosure and it is known that exposures in metal cavities, lightly-loaded, most probably are chaotic and unpredictable.

Some recent reviews of the field have tended to ignore the past bulk of literature on confirmed effects and instead focus on more recent controversial claims of low-level or "athermal" effects, particularly for ELF amplitude-modulated RF/microwave exposures where it is claimed that the modulation frequency is important. These reviews include that by the Royal Scientific Society in Canada[37] and the recent report of a panel in the U.K. chaired by Sir William Stewart. [38] These claims of "athermal" effects in general are characterized by lack of replication and by the presence of artifacts. There are valid scientific considerations that make such claims implausible. The extensive paper by Valberg et al.[39] has shown that claims of low-level mechanisms are implausible at low frequencies. It is worthwhile to recall that similar claims of "specific," rather than "thermal," effects were prevalent during the first half of the 20th century. The challenge presented in the review by Bierman[40] in the 1940s remains as useful today as it was then, viz.: the burden of proof remains on those who claim other than heating as a mechanism for observed microwave bioeffects.

Standards for the Safe Use of Microwave Energy

It is useful, at the outset, to define some terms prevalent in the standards world, especially that of the IEEE.[41] There are three levels of authority in standards documents. First there are *standards* that imply mandatory actions and rules. The word *shall* is used often. Secondly there are *recommended practices*. These describe preferred actions and rules. The word *should* is used often. Lastly there are *guides*. In these documents alternative actions, procedures, policies, and rules are discussed. The word *may* is used and the choice of various options is at the discretion of the user.

In addition it is useful to classify standards by their differing purpose or target for control. The most fundamental type of standard is the *exposure* standard. This sets limits on safe exposure of people in terms of easily measurable quantities such as field strength, power density, and induced current. These limits, usually called maximum permissible exposure (MPE) levels or investigation levels, are expressed as a function of time or exposure duration. The MPEs are derived from the limiting dosimetric quantities such as SAR, energy density or SA, and current density. The key feature of *exposure* standards is that they are rules that apply to people and it is implied, to some extent, that exposure is voluntary or at least the subject is aware of the exposure or acknowledges the exposure. In the IEEE system, exposure limits are presented in standards documents that also contain the definitions and rules necessary for their implementation. Other organizations may apply different names to their documents, such as *guidelines,* and they may not have the strict definitions, background, and guidance for their implementation that an IEEE standard has.

A different type of standard is the *product performance* standard. This applies to a product and it is designed to ensure that potential exposures of people who use the product will be well below the MPEs found in exposure standards. Examples include the laser standards and the microwave oven standard. The laser standards define accessible emission limits per stated class of laser where the classes are based on potential hazard. The microwave oven standard limits the emission of microwave energy as measured at any point 5 cm from the external surface of the oven.

Although not commonly used today, there is another type of standard that may find greater use in the future. This is the *environmental* standard in which limits are set for EM fields in the environment without a specified dependence on an exposure time, except for possible exemptions at sites where passage is transient, e.g., on bridges, etc. The basis for an *environmental* standard would be considerations of possible interference effects, side effects such as arcing at ends of long cables near a transmitting tower, and possible effects on local flora and fauna, e.g., endangered bird species. In addition, consideration would be made of the psychosocial factors deriving from the concerns of the people who live or work in the environment in question.

Because interference with electronic devices and equipment occurs at far lower EM field levels than biological exposure phenomena, there is also the possibility that exposures to EM fields could lead to *hazardous RFI,* e.g., with medical devices like the implanted pacemaker. Although limiting exposure could control this, it is more logical to control such hazards by limiting the *susceptibility* of medical devices. In practice, often there are applied control measures on both the "radiator" and the "victim" even though the preferred (e.g., by the FCC) emphasis should be on limiting susceptibility of the "victim" device or system.

Another class of standard document may be that for prevention of accidental ignition of fuels or electro-explosive devices. This may take the form of limiting the approach of users of EEDs to known high-power transmitters, i.e., safe distances for use of EEDs.

The history of development of microwave exposure standards has been recently presented[42] by the present authors, especially that of the development of the ANSI/IEEE series of C95 standards. In the early 1990s a survey by Petersen[43] showed that exposure limits in the microwave frequency range of various organizations around the world were not greatly different (i.e., within a few dB). In the United States, in addition to the IEEE, safety documents for microwave exposure are also produced[44] by the NCRP (National Council on Radiation Protection and Measurement) as well as the ACGIH (American Conference of Governmental and Industrial Hygienists). In Europe safety documents have been produced by various organizations including CENELEC. In recent years European countries, besides developing national safety documents, have made increasing reference to guidelines published by ICNIRP (International Commission on Non-Ionizing Radiation Protection). The most recent ICNIRP guidelines[45] are in fair agreement with IEEE standards in the microwave range (both are based on the same SAR thresholds) but are far more conservative at low frequencies. Extensive criticism[46] has been leveled at ICNIRP for the excessive safety factor at low frequencies. Finally, the IEC (International Electrotechnical Commission) develops product and measurement standards. Recently a new umbrella committee, TC-106, has been created[47] to oversee activity within the IEC in the area of EM energy safety.

In this review, we discuss in some detail only the requirements in the latest C95.1 standard[48] issued by the IEEE Standards Coordinating Committee 28 (SCC-28). This standard was developed under the due process rules of the IEEE with extensive documentation of all deliberations and with procedures assuring a broad consensus. At present several hundred people of all disciplines are involved in the various subgroups of SCC-28 with about 15% non-U.S. participation, a figure that is growing rapidly. As suggested by the exposure diagram in Fig. 3.12, exposure limits involve an *averaging time.* Thus, the maximum permissible exposures (MPEs) are in terms of field-strength (squared) or power density (or internal SAR), which are time averaged over any contiguous period of time equal to the averaging time. Thus, in the microwave range, and in the controlled environment, all exposures are averaged over six minutes. This

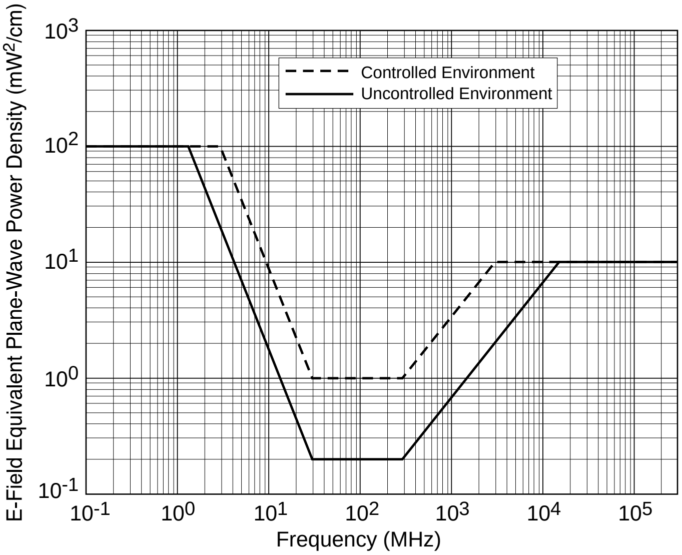

FIGURE 3.12 The IEEE C95.1-1991 MPEs (in terms of the E-field plane-wave equivalent power density). The lower curve is for the uncontrolled environment.

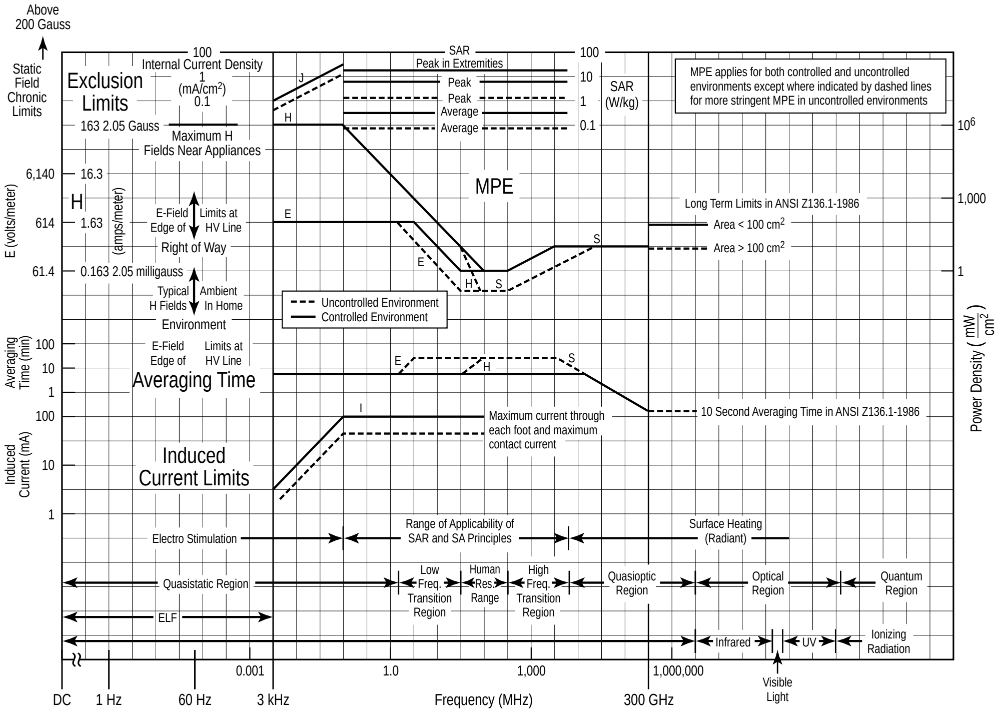

FIGURE 3.13 A capsule guide to the IEEE C95.1-1991 standard showing all of the relevant features.

means that higher exposures are permitted for short periods of time as long as the time average is below the MPE.

The basic rules of the latest C95.1 standard are presented in Figs. 3.12 and 3.13. In Fig. 3.12 the MPEs for the controlled and for the uncontrolled environment are shown in terms of the E-field plain-wave equivalent power as a function of frequency. In Fig. 3.13, a "capsule" presentation of most of the features of the C95.1 standard is shown. Some key observations are:

1. The use of two "tiers," for controlled and uncontrolled environments applies only around the resonance range for man, where there may be maximum concern about exposures. The lower tier applies when the exposed people are unaware of their exposure and are not competent to address safety measures. The use of two tiers originated[49] in an attempt to apply an exposure standard conservatively to the environment. In the future the lower tier may disappear from standards like C95.1.
2. The use of the SAR and SA concepts as basic restrictions applies only between 100 kHz and 6 GHz, in which range there are significant internal fields of RF exposure. Below 100 kHz the limits derive from electrostimulation phenomena. Above 6 GHz there is little penetration (e.g., less than two millimeters) into the body, and surface absorption determines bioeffects and hazards.
3. Averaging times are ramped with frequency in accordance with the thermal time constants of the body. In the last few years, two intensive conferences[50] between the laser and microwave communities have resulted in plans to improve the agreement between laser and microwave standards in the transition range around 300 GHz. This involves tailoring the ramp in averaging time to better fit the dependence of thermal time constants versus frequency.
4. In response to a request from the IEEE MTT Society, a limit on peak exposure levels for very short pulses was introduced. It consists of a value of 100 kV/m maximum as well as an energy limit for short pulses. These are based on studies by the U. S. Air Force that showed that the potential hazards of short pulses were of the "stun" variety and associated with thermal phenomena. The peak limits are well above theoretical thresholds for the auditory effect.
5. Limits on induced or contact currents are included, but these are continually being expanded and refined to include spark-discharge phenomena as well as point contact currents.
6. Relaxation of limits for partial-body exposure is included in an incomplete form and on a tentative basis. Exposure of the testes and eyes poses a risk, but this will likely be eliminated if improved ramps for averaging time at high frequencies eliminate undesirable high energy content in short duration exposures.
7. The basic SAR limits are 0.4 W/kg average and 8 W/kg spatial peak. These were derived from far-field animal exposure studies associated with behavioral disruption. The 8 W/kg (in any 1 g of tissue in the shape of a cube) peak spatial average derives from the 20:1 peak-to-average ratio of the SAR distributions observed in experimental animals under far-field exposure conditions. In C95.1 these have been extended in a doubly conservative manner to the control of localized exposures from sources such as cellular phones, first by invoking the lower tier reduction of 5 and then by assuming that the spatial peak from whole-body experiments should apply to partial-body exposure. In the C95.1 standard, the result is the so-called "low-power" exclusion clauses.

Besides C95.1, important C95 standards include a recently issued revision[52] of the standard on warning symbols and the C95.3 measurement standard,[53] which is presently being revised and balloted.

Product performance standards for microwave technologies arose after the passage of the Radiation Control for Health and Safety Act of 1968 (P. L. 90-602).[53] This led to the emission standard[54] for microwave ovens and to some control of industrial and other microwave sources. All the currently applicable regulations are accessible at Internet site http://www.fda.gov/cdrh/radhlth/index.html. It is unlikely that oven limits will be changed for health reasons. Because of an impending RFI scenario[56] involving microwave ovens and wireless (e.g., Bluetooth) applications operating in the oven (ISM) band there are some pressures to voluntarily limit emissions from ISM equipment.

In the U. S., most civilian applications of microwave/RF energy are now regulated by FCC rules,[57] which are based in large part on the C95.1 standards but also on the NCRP guidelines at higher microwave frequencies. The FCC is concerned not only with regulation of the environment around transmitting towers and antennas, but also the microwave/RF exposure to users of wireless handsets. In this sense the

FCC has taken on the responsibility that normally, under P.L. 90-602, would fall to the FDA. In any case the FCC as well as the FDA support the derivation of product standards through the IEEE system. Although the FDA has the authority to develop performance standards for all microwave equipment including wireless phones, it has instead supported the creation of a new committee to develop such standards, IEEE Standards Coordinating Committee 34.

SCC-34 is a relatively new committee having been established in 1995 for the purpose of developing product performance standards relative to the safe use of electromagnetic energy. The committee uses the exposure criteria and basic restrictions developed by SCC-28, and in some cases, by other committees, to develop standardized assessment procedures, emission limits, etc., to allow manufacturers to readily ensure that their products comply with these criteria. The goal is to develop unambiguous procedures that yield repeatable results, e.g., similar to the procedure for certifying compliance of microwave ovens. So far three subcommittees have been established. The subjects being addressed are pleasure boat radar, protocols for assessing the efficacy of RF protective garments, and protocols for certifying compliance of wireless handsets.

Protocols for assessing the peak spatial average SAR associated with the use of handheld radio transceivers used for personal communications, e.g., cell phones, are especially important. Since 1993, when a guest on a TV talk show alleged that his wife's brain tumor was exacerbated by the use of a cell phone, the media has focused on this issue. Inordinate attention continues to be given to preliminary results of every study reported to even suggest an association between untoward medical effects and the use of cell phones, even when the exposure paradigm is completely different. Recent attention has focused on differences between SAR measurement results reported by different laboratories for the same phone. By a major leap of logic small differences, which are not unexpected in light of the different protocols being used to test cell phones, are translated to a theme of uncertainty about cell phone safety. This seems to occur more in this field than in many others, i.e., a focus on uncertainty related to small differences in analytical or measurement results while completely ignoring the issue of how far below established safety criteria (exposure) the results may be.

Following the 1993 program that first raised the safety issue, a $25 to 27 million research program was established. This program, funded by industry through a blind trust, was to review the literature, develop a research agenda, and fund the studies necessary to address criticisms levied against judgments based on interpretations of the extant literature. One such criticism, unwarranted as it may be, was that there was a lack of studies at exactly the same frequencies, modulations, and exposures as those associated with cell phones. Part of the research program was the establishment of a dosimetry working group to develop uniform protocols for assessing exposure from wireless handsets. When funding was withdrawn for this particular project, the working group, which by then included representatives from most handset manufacturers, a number of test houses, and academia, evolved into Subcommittee 2 of SCC-34.

Two separate recommended practices are being developed by SCC-34. One is based on experimental techniques, the other on numerical techniques. The experimental technique utilizes robot-controlled miniature electric field probes to scan and measure the SAR in a homogeneous tissue-simulating liquid-filled anthropomorphic model of the human head. The numerical technique applies the FDTD method of solving Maxwell's equations in a heterogeneous representation of the human head developed from CT and MRI scans of humans. Models with resolutions of 2 × 2 × 2 mm,[58] 1.1 × 1.1 × 1.4 mm using sub-gridding in some regions,[59] and 0.9 × 0.9 × 1.5 mm[60] have been reported. Both techniques have advantages and disadvantages. For example, the experimental technique uses the actual cell phone as the source, but the homogeneous head model is less than an ideal representation. Head size, the dielectric properties of the tissue simulant, and the thickness of the spacer representing the pinna are standardized to represent a worst case situation that overestimates the SAR induced in the brain. With the numerical technique, the head model is an accurate representation of a human head, but the handset has to be modeled, usually as a simple metal box with an appropriate antenna. CAD files of actual phones complete with some internal structures have been used and differences between these and the results from the simple model are being investigated. An advantage of the computational technique is that it can be applied at the design stage to optimize antenna performance while ensuring that the peak SAR is below the specified limit.

Because most manufacturers are now using the experimental technique to certify their products, mainly because measurement systems are available commercially, the initial effort has been directed to completing this practice. Much of the information needed to complete the document was not available in the literature, e.g., assessment of the uncertainty associated with each component of the system and the overall assessment uncertainty, but was developed in the laboratories of the committee members as the practice developed. This included series of inter-laboratory comparisons of canonical models such as standard half-wave dipoles above a flat phantom or sphere and the development of a generic phone by three of the manufacturers for further inter-laboratory comparisons. The committee has also been working with similar groups, e.g., CENELEC, to ensure international harmonization. Both the FDA and the FCC play an active role on the committee. In fact, the FCC uses the drafts to develop their own requirements with which manufacturers must comply. Future projects will be the extension of the handset protocols to other wireless devices, e.g., wireless modems and body-mounted radio transceivers. Having standard protocols in place should mitigate some of the media-driven concern about wireless devices exemplified by a recent series of TV "specials" calling attention to the uncertainty of cell phone safety — in this case the uncertainty of the peak SAR.

In recent years there has been a trend toward international harmonization of standards in the microwave/RF area. IEEE SCC-28 and SCC-34 are very involved in this activity both by expansion of non-U.S. membership and by closer liaison with other international groups such as the IEC and ICNIRP. In this global activity it is the intent of the IEEE to ensure that the benefits of the IEEE standards process, with due process and broad consensus of all stakeholders, are recognized. The importance of rational science-based standards cannot be overstated. Excessive safety factor, as in the ICNIRP '98 guidelines, can unduly suppress technology, e.g., antitheft and weapons detector systems. Uneven safety factors across the spectrum can give unfair advantage to one technology versus another that uses a different part of the spectrum and, almost as important, convey a sense of uncertainty about the science. In addition, ultra-conservative safety limits can lead to inferior performance and loss of benefit and reliability. This could be important if it involves emergency communications, for example.

Risk Assessment and Public Education

The fears of microwaves along with a generalized electrophobia were promoted, in large measure, by the writings of Paul Brodeur.[61] In succession there have been waves of fear targeted at microwave ovens, radars, microwave relay towers, visual-display terminals, power lines, electric blankets, police radar, cellular phones, and wireless base stations. In the 1980s historian Nicholas Steneck[62] attacked the C95 standards as being too science based. He felt exposure limits should be as low as possible and not based on actual hazard thresholds. When the power line (50 Hz) controversy erupted in the nineties, Nair and Morgan[63] proposed the practice of "prudent avoidance," just in case the weak allegations of a cancer link were true. As documented by Park,[64] however, the power-line scare was baseless and derived from "voodoo science."

Now, in the context of a mushrooming global wireless technology, a plethora of proposals to apply the same caution with a new name has arisen, viz. the Precautionary Principle.[65] It has been endorsed by the Stewart panel[38] in the U.K. for use in processing applications for wireless base stations. Despite the new name this proposal is simply another tool for attacking reliance on science-based standards. The Electromagnetic Energy Association is preparing[66] a formal rebuttal of this concept for application to EM energy. In response to a request from members of a federal interagency committee charged with writing a report at the conclusion of the RAPID program on EMF research, IEEE SCC-28 submitted advice[67] that discussions of cautionary polices and procedures should be done at the lowest level of authority — i.e., in preparing *guides* that present optional alternatives that individuals or organizations can adopt on an ad hoc discretionary basis. In this way there is no acknowledgment of such a cautionary principle as voiding or superseding reliance on standards.

This new principle simply adds to the forces of electrophobia. It raises the level of fear of microwaves and stimulates the sale of a wide variety of allegedly protective devices and services. This amounts to an exploitation of electrophobia and in general is to be discouraged. These devices include measurement devices, shields, books, newsletters, etc. Besides selling oven leakage detectors, discouraged by both the FDA and leading consumer organizations, the exploiting parties give advice on how to minimize exposure including "running" out of the kitchen after turning on the microwave oven. The IEEE COMAR committee[68] continues to fight this phobia and allied misinformation through a series of technical information statements. Other organizations also provide useful information.

A partial list of useful Websites includes:

CTIA:	http://www.WOW-COM.com
EEA:	http://www.elecenergy.com
FCC:	http://www.fcc.gov/oet.rfsafety/cellpcs.html
FDA:	http://www.fda.gov/cdrh/radhlth/index.html
ICNIRP:	http://www.icnirp.de
IEEE/COMAR:	http://homepage.seas.upenn.edu/~kfoster/comar.html
IMPI:	http://www.impi.org
IEEE SCC-28:	http://grouper.IEEE.org/groups/scc28
IEEE SCC-34:	http://grouper.IEEE.org/groups/scc34
Dr. Moulder/FAQ:	http://www.mcw.edu/grcr/cop.html
WHO:	http://www.who.ch/
IEC:	http://www.iec.ch

These are some of the Websites where information useful to microwave engineers can be obtained. The FDA Website also links to an educational site maintained by a professor at the University of Virginia. It contains much useful information, but errs in recommending the use of inexpensive oven leakage detectors and presenting a less than complete explanation of superheating of liquids in microwave ovens. On the Website for the FCC, much detailed information is available including a series of reports, fact sheets, and an interactive database containing the dielectric properties for a number of biological tissues.

The site for IMPI (International Microwave Power Institute) can be useful in exploring power (non-communications) applications of microwave energy. These include medical applications, food heating and processing, microwave discharge lamps for UV curing and lighting, and microwave power transmission, some of it for solar power satellites. Other future applications include the comfort heating of animals and man through microwaves that can contribute toward solving energy crises. The other sites are self-explanatory in their functions.

Conclusions

The modern microwave engineer needs to be knowledgeable about safety standards in general, and in particular, the IEEE C95 series of standards. Microwave engineers, through their professional societies as well as employers, should support and participate in the increasingly global activities of the IEEE in developing standards for the safe use of electromagnetic energy. The financial support of all IEEE activities in global standards and public education will be critical in the future development of microwave technology. With rational standards and an educated public all microwave technologies, both for communications and power applications, can be realized for optimum benefit to mankind.

References

1. Reilly, J. P., *Applied Bioelectricity: From Electrical Stimulation to Electropathology,* Springer Verlag, New York, 1998.
2. Durney, C. H., Massoudi, H., and Iskander, M. F., *Radiofrequency Radiation Dosimetry Handbook,* Fourth Edition, Report USAFSAM-TR-85-73, USAF School of Aerospace Medicine, Brooks AFB, TX, 1986.

3. Gabriel, S., Lau, R. W., and Gabriel, C., The dielectric properties of biological tissues: III Parametric models for the dielectric spectrum of tissues, *Phys. Med. Biol.*, 41, 2271–2293, 1996. These properties can also be downloaded from Internet site: http://www.brooks.af.mil/AFRL/HED/hedr/reports/dielectric/home.html.
4. Schwan, H. P., History of the genesis and development of the study of low energy electromagnetic fields, in Grandolof, M., Michaelson, S., and Rindi, A., (eds.), *Biological Effects and Dosimetry of Non-Ionizing Radiation,* Plenum Publishing Company, New York, 1981, 1–17.
5. Osepchuk, J. M., Basic characteristics of microwaves, *Bull. N. Y. Acad. Med.,* 55, 976–998, 1979.
6. Chou, C. K., Bassen, H., Osepchuk, J., Balzano, Q., Petersen R., Meltz, M., Cleveland, R., Lin, J. C., and Heynick, L., Radio frequency electromagnetic exposure: tutorial review on experimental dosimetry, *Bioelectromagnetics,* 17, 195–206, 1996.
7. Kritikos, H. N. and Schwan, H. P., The distribution of heating potential inside lossy spheres, *IEEE Trans. Bio, Med. Eng.,* BME-22, 457–463, 1975.
8. Guy, A. W., Lehmann, J. F., and Stonebridge, J. B., Therapeutic applications of microwave power, *Proc. IEEE,* 62, 55–75, 1975.
9. Durney, C. H. and Christensen, D. A., Hyperthermia for Cancer Therapy, in Gandhi, O. P., Ed., *Biological Effects and Medical Applications of Electromagnetic Energy,* Prentice-Hall, Englewood Cliffs, NJ, 1990, 436–477.
10. Moritz, A. R. and Henriques, F. C., Jr., Studies of thermal injury II, The relative importance of time and surface temperature in the causation of cutaneous burns, *Am. J. Pathol.,* 23, 695–720, 1947.
11. Michaelson, S.M., Thomson, R. A. E., and Howland, J. W., Physiologic aspects of microwave irradiation of mammals, *Am. J. Physiol.,* 201, 351, 1961.
12. Addington, C. H., Osborn, C., Swartz, G., Fischer, F., Neubauer, R. A., and Sarkees, Y. T., Biological effects of microwave energy at 200 megacycles, in Peyton, M. F., Ed., *Proc. 4th Annual Tri-Service Conf. Biol. Effects of Microwave Radiation,* Plenum Press, New York, 1961, 177.
13. Minin, B. A., *Microwaves and Human Safety,* I. Translation from U. S. Joint Publications Research Service, JPRS 65506-1, U.S. Department of Commerce, 1965.
14. Pay, T.L., Microwave effects on reproductive capacity and genetic transmission in Drosophila melanogaster, *J. Microwave Power,* 7, 175, 1972.
15. Samaras, G. M., Muroff, L. R., and Anderson, G. E., Prolongation of life during high-intensity microwave exposures, *IEEE Trans. on Microwave Theory and Techniques,* MTT-19, 2, 245–247, 1971.
16. Tell, R. A. and Harlen, F., A review of selected biological effects and dosimetric data useful for development of radiofrequency safety standards for human exposure*, J. Microwave Power, 1*4, 4, 405–424, 1979.
17. Adair, E.R., Mylacraine, K. S., and Kelleher, S. A., Human exposure at two radiofrequencies (450 and 2450 MHz): similarities and differences in physiological response, *Bioelectromagnetics*, 20, 12, 1999.
18. Carpenter, R. L., Ocular effects of microwave radiation, *Bull. NY Acad Med.,* 55,1048–1057, 1979.
19. Guy, A. W., Kramar, P. O., Harris, C. A., and Chou, C. K., Long-term 2450 MHz CW microwave irradiation of rabbits: methodology and evaluation of ocular and physiologic effects, *J. Microwave Power*, 15, 37–44, 1980.
20. Kues, H. A., Hirst, L. W., Lutty, G. A., D'Anna, S. A., and Dunkelberger, G. R., Effects of 2.34 GHz microwaves on primate corneal endothelium, *Bioelectromagnetics,* 6, 177–188, 1985.
21. Kamimura, Y., Saito, K-i, Saiga, T., and Amenmiya, Y., Effect of 2.45 GHz microwave irradiation on monkey eyes, *IEICE Trans. Commun.,* E77-B, 762–764, 1994.
22. Osepchuk, J. M. Ed., *Biological Effects of Electromagnetic Radiation,* John Wiley & Sons, New York, 1983.
23. Gandhi, O. P. Ed., Special issue on biological effects and medical applications of electromagnetic energy, *Proc. IEEE,* 68, 1980.
24. Elder, J. A. and Cahill, D. F., *Biological Effects of Radiofrequency Radiation,* Report EPA-600/8-83-026F, 1984.

25. Polson, P. and Heynick, L. N., Overview of the radiofrequency radiation (RFR) bioeffects database, in Klauenberg, B. J., Grandolfo, M., and Erwin, D. N., *Radiofrequency Radiation Standards,* Plenum Press, New York, 337–390, 1995.
26. Michaelson, S. M., and Lin, J. C., *Biological Effects and Health Implications of Radiofrequency Radiation,* Plenum Press, New York, 1987.
27. Gandhi, O. P. Ed., *Biological Effects and Medical Applications of Electromagnetic Energy,* Prentice-Hall, Englewood Cliffs, NJ, 1990.
28. Polk, C. and Postow, E., *CRC Handbook of Biological Effects of Electromagnetic Fields,* CRC Press, Boca Raton, FL, 1995.
29. Lin, J. C., *Microwave Auditory Effects and Applications,* Charles C. Thomas, Springfield, IL, 1978.
30. DeLorge, J. O. and Ezell, C. S., Observing responses of rats exposed to 1.28 GHz and 5.4 GHz microwaves, *Bioelectromagnetics,* 1, 183–198, 1980.
31. Stevenson, Sen. A., U.S. Senate Hearing Record on Oversight of Radiation Health and Safety, June 16–29, 1977.
32. Guy, A. W. and Foster, K. R., The microwave problem, *Scientific American,* 255, 3, 32–39, 1986.
33. Foster, K. R. and Pickard, W. F., The risks of risk research, *Nature* 330, 531–532, 1987.
34. Belyaev, I. Y., Sheheglov, V. S., Alipov, Y. D., and Polunin, V. A., Resonance effect of millimeter waves in the power range of 10^{-19} to 3×10^{-3} W/cm^2 on *Escherichia coli* cells at different concentrations, *Bioelectromagnetics* 17, 4, 312–321, 1996.
35. Osepchuk, J. M. and Petersen, R. C., Comments on Resonance effect of millimeter waves in the power range from 10^{-19} to 3×10^{-3} W/cm^2 on escheria coli cells at different concentrations, Belyaev et al., *Bioelectromagnetics,* 17, 312–321 (1996), *Bioelectromagnetics,* 18, 7, 527–528, 1997.
36. Repacholi, M. H., Basten, A., Gebski, V., Noonan, D., Finnie, J., and Harris, A. W., Lymphomas in Eμ-Pim 1 transgenic mice exposed to pulsed 900 MHz electromagnetic fields, *Radiat. Res.,* 147, 631–647, 1997.
37. Royal Society of Canada Expert Panel Report, *A Review of the Potential Health Risks of Radiofrequency Fields from Wireless Telecommunication Devices,* Royal Society of Canada, RSC.EPR 99-1, 1999.
38. Independent Expert group on Mobile Phones, Stewart, Sir William, Chairman*, Mobile Phones and Health,* NRPB, Chilton, Didcot, Oxon OX11 0RQ, U.K., 2000.
39. Valberg, P., Kavet, R., and Rafferty, C. N., Can low-level 50/60 Hz electric and magnetic fields cause biological effects?, *Radiation Research,* 148, 2–21, 1997.
40. Mortimer, B. and Osborne, S. L., *J. Am. Med. Assoc.* 104, 1413, 1935.
41. IEEE Standards Association, *IEEE Standards Manual,* IEEE, Piscataway, NJ, 2000.
42. Osepchuk, J. M. and Petersen, R. C., Past may help solve electromagnetic issue, *Forum* 9, 2, 99–103, 1994.
43. Petersen, R. C., Radiofrequency/microwave protection guides, *Health Physics* 61, 59–67, 1991.
44. Petersen, R. C., Radiofrequency safety standards-setting in the United States, in *Electricity and Magnetism in Biology and Medicine,* Bersani, F. Ed., Plenum Press, New York, 1999, 761–764.
45. International Commission on Non-Ionizing Radiation Protection (ICNIRP), Guidelines for limiting exposure to time-varying electric, magnetic, and electromagnetic fields (up to 300 GHz), *Health Physics* 74, 4, 494–522, 1998.
46. Various authors, Series of letters commenting on ICNIRP '98 guidelines, *Health Physics* 76–77, 1998–1999.
47. ACEC Task Force on Human Exposure to EM Fields, *ACEC TF EMF (Convenor) 21,* International Electrotechnical Commission (IEC), 1999-05.
48. IEEE, *IEEE Standard for Safety Levels with Respect to Human Exposure to Radio Frequency Electromagnetic Fields, 3 kHz to 300 GHz,* IEEE Std. C95.1, 1999 Edition, Piscataway, NJ, 1999.
49. Osepchuk, J. M., Impact of public concerns about low-level EMF-RFR database, in *Radiofrequency Radiation Standards,* Klauenberg, B. J., Grandolfo, M., and Erwin, D., Eds., Plenum Press, New York, 1995, 425–426.

50. *Digest, Infrared Lasers & Millimeter Waves Workshop: The Links Between Microwaves & Laser Optics,* Air Force research Laboratories, Brooks AFB, TX, January 1997.
51. IEEE, *IEEE C95.2-1999, IEEE Standard for Radio Frequency Energy and Current Flow Symbols,* IEEE-SA, Piscataway, NJ, 1999.
52. IEEE, *IEEE C95.3-1991 (Reaff 1997), IEEE Recommended Practice for the Measurement of Potentially Hazardous Electromagnetic Fields-RF and Microwave,* IEEE-SA, Piscataway, NJ, 1991.
53. Public Law 90-602, *Radiation Control for Health and Safety Act of 1968,* Approved by Congress, October 18, 1968.
54. Osepchuk, J. M., Review of microwave oven safety, *J. Microwave Power* 13, 13–26, 1978.
55. The Internet site for FDA/CDRH is: http://www.fda.gov/cdrh/radhlth/index.html.
56. Osepchuk, J. M., The Bluetooth threat to microwave equipment, *Microwave World,* 20, 1, 4–5, 1999.
57. FCC, *Report and Order FCC 96-326,* In the matter of guidelines for evaluating the environmental effects of radiofrequency radiation, ET Docket No. 93–62, August 1, 1996.
58. Dimbylow, P. J. and Mann, S. M., SAR calculations in an anatomically based realistic model of the head for mobile communication transceivers at 900 MHz and 1.8 GHz, *Physics in Medicine and Biology*, 39, 1537-1553, 1994
59. Okoniewski, M. and Stuchly, M.A., A study of the handset antenna and human body interaction, *IEEE Trans. MTT,* 44, 10, 1855-1864, Oct. 1996.
60. Olley, P. and Excell, P. S., Classification of a high resolution voxel image of a human head, *Voxel Phantom Development*, Proceedings of an International Workshop held at the National Radiological Protection Board, Chilton, U.K., P. J. Dimbylow, Ed., 1995.
61. Brodeur, P., *The Zapping of America,* William Morrow, New York, 1978.
62. Steneck, N. H., *The Microwave Debate,* MIT Press, Cambridge, MA, 1985.
63. Morgan, M. G., Prudent avoidance, *Public Utilities Fortnightly,* 26–29, 1992.
64. Park, R., *Voodoo Science,* Oxford University Press, New York, 2000.
65. Foster, K. R., Vecchia, P., and Repacholi, M. H., Science and the Precautionary Principle, *Science,* 979–981, May 12, 2000.
66. Electromagnetic Energy Association, *Fact Sheet on Cautionary Policies,* Washington, D.C., in press.
67. IEEE SCC-28, *Response of: Institute of Electrical and Electronic Engineers Standards Coordinating Committee 28 to: Interagency Committee re: Advice on Mitigation of Risks Related to EMF Exposure,* December 1999.
68. Osepchuk, J. M., COMAR after 25 years: still a challenge!, *IEEE Eng. in Medicine and Biology,* 15, 3, 120–125, 1996.

3.3 Signal Characterization and Modulation Theory

John F. Sevic

Spectral efficiency is of paramount importance when considering the design of virtually all commercial wireless communication systems, whether for voice, video, or data. Spectral efficiency can be measured by the number of users per unit of spectrum or by the number of bits that can be represented per unit of spectrum. In general, wireless service providers are interested in maximizing both the number of users and the number of bits per unit spectrum, which in both cases results in the maximum revenue.

Spectral efficiency can be increased by using several methods including signal polarization, access method, modulation method, and signal coding technique. The first method is commonly adopted in satellite communication systems, where, for example, the uplink and downlink may be right-hand and left-hand circularly polarized, respectively.

Access method refers to how a common resource, such as frequency, is shared among each of the users of the system. Frequency domain multiple access (FDMA) is the basis for all commercial broadcast and most wireless communication systems. With FDMA, each user is allocated a particular section of spectrum that is devoted to that user only. The first-generation cellular phone system in the United States, called advanced mobile phone system (AMPS) has approximately 600 30-kHz channels, each one of which can be utilized for voice and low data-rate communication [1].

Users can also be allocated a certain segment of time, called a slot, leading to time-domain multiple access (TDMA). With TDMA, users share a common frequency and are assigned one, or in some cases more than one slot out of several available slots. In this fashion spectral efficiency is increased by segregating users in time. Second-generation wireless communication systems based on TDMA include the North American Digital Cellular system (NADC) and the Global Standard for Mobile Communications (GSM), which have three slots and eight slots, respectively [2,3].

Code-division multiple access (CDMA) results when each user is assigned a unique code, which is orthogonal to all the other available codes. The Walsh function has been adopted as the orthogonal code set for first-generation CDMA systems. At the receiver, the signal is correlated with a known Walsh function, and the transmitted information thus extracted. The ability of these systems to improve spectral efficiency relies on the development of robust orthogonal functions, since any cross-correlation results in performance degradation. Many wireless systems are hybrids of two access methods. For example, the first CDMA-based wireless system, developed by Qualcomm, is based on FDMA and CDMA [4].

Modulation is the process of impressing an information source on a carrier signal. Three characteristics of a signal can be modulated: amplitude, frequency, and phase. In many types of modulation, two characteristics are modulated simultaneously. Analog modulation results when the relationship between the information source and the modulated signal is continuous. Digital modulation results when the modulated characteristic assumes certain prescribed discrete states.

Signal coding techniques are many and varied, and require detail beyond what can be presented in this introductory chapter. Coding can impact the characteristics of the signal, as will be examined in more detail with CDMA.

The purpose of this chapter is to provide an introduction to the representation and characterization of signals used in contemporary wireless communication systems. The time domain representation of an information-bearing signal determines uniquely what the impact of nonlinear amplification will be, so the study begins with a review of time domain signal analysis techniques. Since the effects of nonlinear amplification are of most interest in the frequency domain, the signal analysis review will also include frequency domain methods. Random process theory is an integral element of digital modulation theory, and will also be covered. Following this, a review of several types of modulations will be given, with both a time domain and frequency domain complex envelope description. The impact of filtering, for spectral efficiency improvement, will be assessed. A probabilistic time domain method of characterizing the envelope of a signal, called the envelope distribution function (EDF), will be introduced. This function is more useful than the peak-to-average ratio in estimating the impact of a PA on a signal. A complete reference section is given at the end of the chapter.

Complex Envelope Representation of Signals

Using Fourier analysis, any periodic signal can be exactly represented as an infinite summation of harmonic phasors [5]. Most often a signal $x(t)$ is approximated as a finite summation of harmonic phasors, in which case

$$x\left(t\right)=\sum_{k=-\infty}^{\infty}\tilde{a}_k e^{j\omega kt}\approx\sum_{k=-Q}^{Q}\tilde{a}_k d^{j\omega kt} \tag{3.89a}$$

where

$$\tilde{a}_k=\frac{1}{T}\int_{t}^{t+T}x\left(\tau\right)e^{-j2\pi f\tau}d\tau \tag{3.89b}$$

and Q is chosen sufficiently large to accurately represent the signal under consideration. A physical basis for this approximation is that all systems have an essentially low-pass response.

Parsavel's theorem states that average power is invariant with respect to which domain it is calculated in, and is expressed as

$$\overline{P}=\frac{1}{T}\int_{t}^{t+T}\left|x(\tau)\right|^{2}d\tau=\sum_{k=-¢}^{\infty}\left|\tilde{a}_{k}\right|^{2}\approx\sum_{k=-Q}^{Q}\left|\tilde{a}_{k}\right|^{2} \tag{3.90}$$

In many instances, calculation of average power may be easier to evaluate in either the time domain or the frequency domain representation.

The modulation property illustrates the frequency-shifting nature of time domain multiplication. This is expressed as

$$m(t)\cos(2\pi f_{o}t)\Rightarrow\frac{1}{2}\left[M(f-f_{o})+M(f+f_{o})\right] \tag{3.91}$$

where $M(f)$ is the Fourier transform of $m(t)$. Note that both upper and lower sidebands are generated, indicating the presence of a negative frequency component.

In many instances, knowledge of the envelope of a signal is sufficient for its characterization and for assessing the associated impact of a nonlinear PA. An arbitrarily modulated signal can be represented in the time-domain as

$$x(t)=real\left\{m(t)\exp\left[2\pi f_{o}t+\phi(t)\right]\right\} \tag{3.92}$$

where $m(t)$ and $\phi(t)$ describe the time-varying amplitude and phase of the information signal, respectively, and f_o is the carrier frequency [6]. Note that frequency modulation results by differentiation of the phase modulation. The complex envelope of Eq. (3.92) is

$$\tilde{x}(t)=i(t)+jq(t)=m(t)e^{j\phi(t)} \tag{3.93}$$

where $i(t)$ and $q(t)$ are defined as the in-phase and quadrature components of the complex envelope. Although there are other methods available of representing modulated signals, Eq. (3.93) is adopted here due to the elegant geometric interpretation afforded by the complex plane representation. The components of Eq. (3.93) are calculated from

$$i(t)=real\{x(t)e^{-j2\pi f_{0}t} \tag{3.94a}$$

$$q(t)=imag\{\hat{x}(t)e^{-j2\pi f_{0}t} \tag{3.94b}$$

where $\hat{x}(t)$ is the Hilbert transform of $x(t)$ [7]. Since statistically independent signals are orthogonal, calculation of the Hilbert transform is often unnecessary, and instead two statistically independent data sources for i, (t) and $q(t)$ can be used. Figure 3.14 shows the spectrum of an arbitrary complex envelope equivalent power density spectrum. Note that the spectrum is not even-symmetric about the y-axis, with the resultant requirement that the time domain signal Eq. (3.93) is in general complex.

Linear network analysis using the complex envelope is similar to conventional network analysis. Taking the Fourier transform of Eq. (3.93), and denoting the complex transfer function as $\tilde{H}(f)$, we have

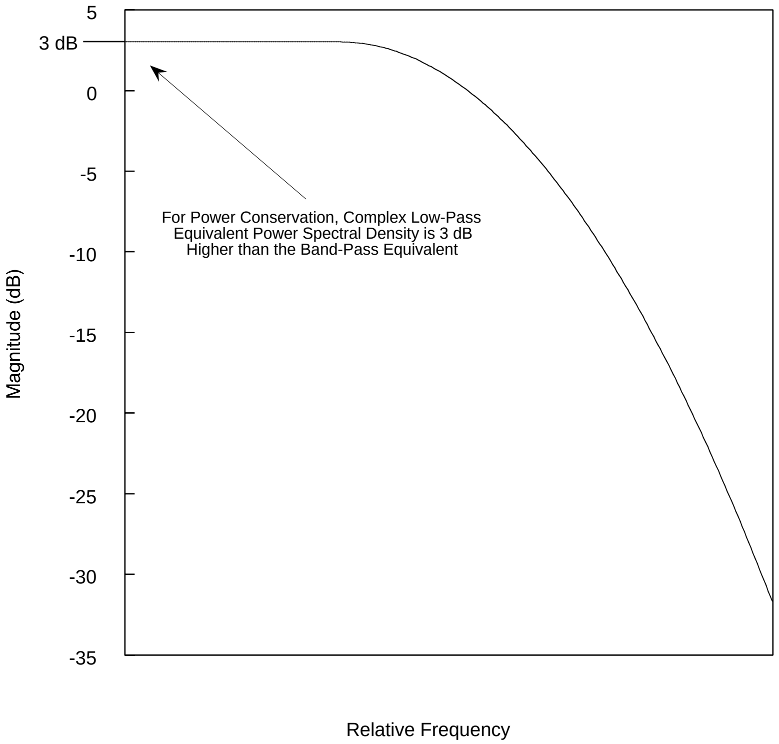

FIGURE 3.14 Power spectral density of an arbitrary complex envelope equivalent signal.

$$\tilde{Y}(f) = \tilde{H}(f)\tilde{X}(f) \tag{3.95a}$$

This response can also be calculated directly in the time domain using the convolution integral

$$\tilde{y}(t) = \int_{-\infty}^{\infty} \tilde{h}(\tau)\tilde{x}(t-\tau)d\tau \tag{3.95b}$$

The equivalent band-pass time domain response is found by

$$y(t) = real\left\{\tilde{v}(t)e^{j2\pi f_0 t}\right. \tag{3.96}$$

Representation and Characterization of Random Signals

Consider a random signal $x(t)$ that could describe either a voltage or current. In general the associated *n-dimensional* joint probability density function is required to describe $x(t)$ over n time instants [8]. Since the expected amplitude and power of a signal are most often of interest, the first- and second-moments are sufficient for representation and characterization of $x(t)$. The first- and second-moments of $x(t)$ are

$$\bar{x}(t) = \int_{-\infty}^{\infty} \tau f(\tau)d\tau = \sqrt{DC\ Power} \tag{3.97a}$$

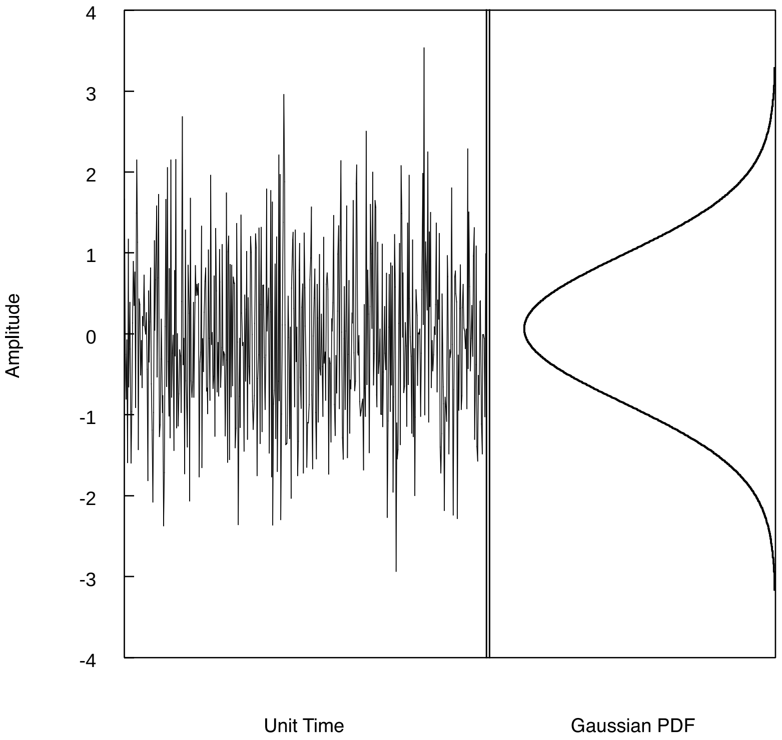

FIGURE 3.15 Illustration of the meaning of random signal having a Gaussian amplitude distribution. In this example the Gaussian pdf represents the probability of the signal amplitude being less than a given value. For example, since the pdf is symmetric about the time axis, this signal has zero mean. Since the noise in this example is uncorrelated, it is defined as white. Similarly, a colored noise process will exhibit correlation.

$$\overline{x^2} = \int_{-\infty}^{\infty} \tau^2 f(\tau) d\tau = Total\ Average\ Power \tag{3.97b}$$

where $f(\tau)$ is the associated probability distribution function (pdf) of $x(t)$. The pdf describes the probability of the instantaneous amplitude of $x(t)$ being less than a specified value. This idea is illustrated with a Gaussian pdf in Fig. 3.15. Note that the amplitude of this signal is concentrated around its mean value, which is zero.

Since the average value and average power of $x(t)$, as determined by Eq. (3.97), are based on ensembles, they are defined as ensemble averages. The average value and average power of a signal can also be calculated with respect to time, which is the method most engineers are familiar with. Signals are said to be ergodic when their ensemble and time averages are the same. All of the signals described in this chapter are ergodic.

Probabilistic characterization of how rapidly a signal changes over time, and hence its spectral distribution, is described by its autocorrelation function

$$R_x(\tau) = \overline{x(t)x(t+\tau)} = \iint_{\infty} \tau_1 \tau_2 f(\tau_1, \tau_2) d\tau_1 d\tau_2 \tag{3.98}$$

The autocorrelation function evaluated at $\tau = 0$ is the total average power in the signal, as Eq. (3.97b) shows. Using Eq. (3.97a) and Eq. (3.97b), which represent average amplitude and total average power, respectively, gives the AC power of the signal

$$P_{AC} = R_x(0) - (\bar{x})^2 = \overline{x^2} - (\bar{x})^2 \tag{3.99}$$

Using the Wiener-Khintchine theorem, the spectral distribution of power of $x(t)$ is evaluated by taking the Fourier transform of the autocorrelation function

$$S_x(f) = \int_{-\infty}^{\infty} R_x(\tau) e^{j2\pi f\tau} d\tau \tag{3.100}$$

where $S_x(f)$ is the power spectral density (PSD) of $x(t)$.

In the case of an arbitrary autocorrelation function, $R_x(\tau)$, the PSD is expressed as

$$S_x(f) = S_{pulse}(f) S_{corr}(f) \tag{3.101}$$

where $S_{pulse}(f)$ is the PSD of the pulse function representing $x(t)$ and $S_{corr}(f)$ is the PSD of the autocorrelation function of the data [9]. From this expression, it is clear that the spectral characteristics of a signal are influenced not only by the pulse characteristics, but also any correlation between adjacent pulses.

Let $x(t)$ be the input to a linear system and let $y(t)$ be the associated output. The impulse response, $h(t)$, is described in the frequency domain as $H(f)$. The average amplitude of $y(t)$ is

$$\bar{y}(t) = \tilde{H}(0)\bar{x}(t) \tag{3.102}$$

and the average power of $y(t)$ is

$$\overline{y^2}(t) = R_y(0) = \int_{-\infty}^{\infty} \left|H(f)\right|^2 df = \int_{-\infty}^{\infty} \left|H(f)\right|^2 S_x(f) df \tag{3.103}$$

The output autocorrelation function is

$$R_y(\tau) = h(\tau) * h(-\tau) * R_x(\tau) \tag{3.104}$$

where * denotes convolution. Taking the Fourier transform gives the output PSD in terms of the input PSD

$$S_y(f) = \left|H(f)\right|^2 S_x(f) \tag{3.105}$$

Complex envelope equivalent analysis is done by replacing all variables with the associated complex envelope representation and restricting the integration of Eq. (3.103) to positive frequency [6]. Note that this analysis gives an example of how choosing the domain in which to carry out an analysis can greatly simplify the effort involved.

Modulation Theory

Modulation theory provides a framework for representing and characterizing the time domain and frequency domain characteristics of an information-bearing signal, and the subsequent impact of nonlinear amplification of the signal. The general analysis method to be followed is to describe the signal in the time domain, using the geometric interpretation of Eq. (3.93), and then determine resultant signal degradation by characterization in the frequency domain.

Access method, modulation, and coding each directly impact the spectral efficiency of a signal. From Fourier analysis it is also clear, therefore, that the time domain characteristics are also impacted, due to the inverse relationship between the time domain and frequency domain. In other words, a signal that varies rapidly in time, due to access method, modulation, or coding, will be wider in extent in the frequency domain than a slowly varying signal. Note here that signal refers to the envelope of the carrier, and the extent of the signal in the frequency domain refers to the associated spectral description of the envelope.

As Eq. (3.93) indicates, modulation can be interpreted geometrically by associating a position in the complex plane with the instantaneous value of the information source. For analog modulation, a continuous range of values is possible; digital modulation allows only certain locations to be occupied. This mapping operation will directly establish the resultant time domain characteristics of the modulation. Many modulations are based on phase since they are relatively impervious to amplitude-related noise disturbances, FM being an example of this. When phase modulation is digital, the characteristics of the digital pulse will influence the signal as well, as Eq. (3.101) shows. Since pulses may be rapidly varying, it is expected that some type of filtering will be necessary to give acceptable spectral efficiency. Thus, to describe a modulation, the mapping method and any associated band-limiting filtering must be considered to provide a complete time domain description of the complex envelope.

Analog Modulation

The simplest modulation is analog double sideband suppressed carrier (DSB-SC). When the information source is a sinusoid, DSB-SC is the classical two-tone intermodulation test signal. The complex envelope representation of DSB-SC is

$$\tilde{x}\left(t\right) = m\left(t\right) \tag{3.106}$$

where $m(t)$ is the information signal. Since the envelope of DSB-SC varies in direct proportion to $m(t)$, it is not a constant envelope modulation. Note also that, from a geometric interpretation using Eq. (3.93), DSB-SC requires only one dimension, meaning there is no phase modulation.

All of the first-generation cellular systems, such as AMPS and ETACS, are based on FM, with a complex envelope representation of

$$\tilde{x}\left(t\right) = \exp\left[jk_f \int_{-\infty}^{t} m\left(\tau\right) d\tau\right] \tag{3.107}$$

where k_f is the frequency-deviation constant and $m(t)$ is the information signal. Since the magnitude of the complex exponential is unity, FM is a constant envelope modulation. A geometric interpretation of FM shows that it would be a unit circle, with the speed in movement about this circle proportional to the instantaneous value of the information signal. Carson's rule shows that the spectral efficiency of FM is less than DSB-SC [6]. In general, constant envelope modulation is not as spectrally efficient as modulation that exhibits a time-varying envelope.

Discontinuous Phase-Shift Keying

Virtually all second- and third-generation wireless communication systems are based on digital modulation, with digital phase modulation being the most common. Digital phase modulation is commonly referred

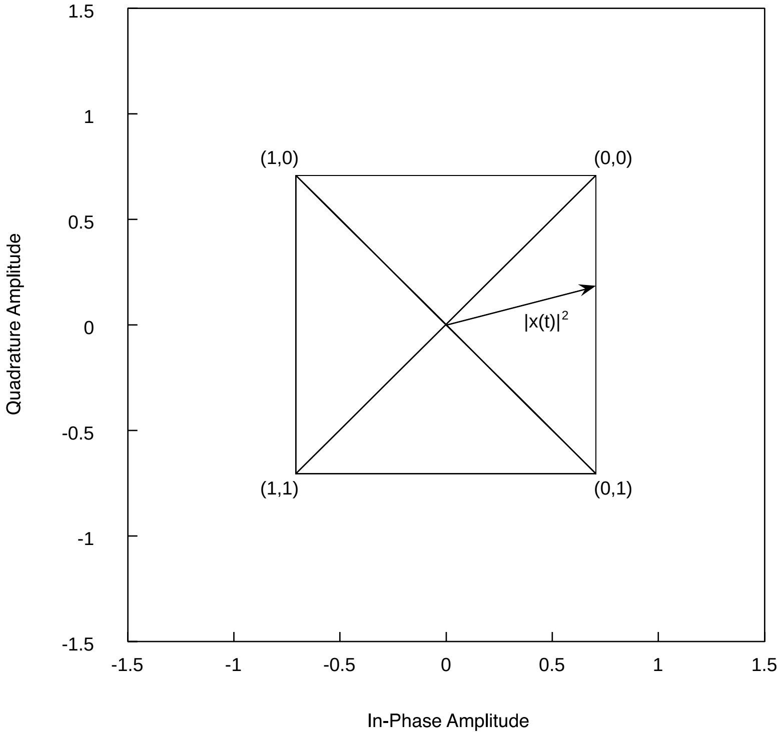

FIGURE 3.16 Complex plane representation of unfiltered quadrature modulation (QPSK). Each corner of the constellation diagram represents two data bits. Depending on the data sequence, each transition goes through a phase change of either ± 90° or ± 180°, which always causes a step change in the signal envelope.

to as phase-shift keying (PSK). PSK consists of two DSB-SC signals in quadrature, and can be represented using Eq. (3.93) with in-phase and quadrature components each generated from a digital data source. Each data source is usually generated by multiplexing a serial data stream, which, if necessary, is already coded, such as with CDMA. Quadrature digital modulation is represented in the complex plane as shown in Fig. 3.16, where the horizontal axis represents the real part of Eq. (3.93) and the vertical axis represents the imaginary part of Eq. (3.93). The trajectory is the instantaneous envelope of the signal and for the constellation given, there are four unique phases, with each phase representing a unique combination of two bits. Each combination of bits is defined as a symbol. Some third-generation wireless systems have adopted PSK with eight unique locations, giving 8-PSK, with the result that each location now represents a unique combination of three bits. Note also from Fig. 3.16 that PSK modulation is constant envelope.

The complex envelope representation of quadrature digital modulation is

$$\tilde{x}\left(kT_b\right) = i\left(kT_b\right) + jq\left(kT_b\right) \tag{3.108}$$

where

$$i(kT_b) = \sum_{k=-\infty}^{\infty} a(kT_b) f(t - kT_b - \tau_f) \tag{3.109a}$$

$$q(kT_b) = \sum_{k=-\infty}^{\infty} b(kT_b) g(t - kT_b - \tau_g) \tag{3.109b}$$

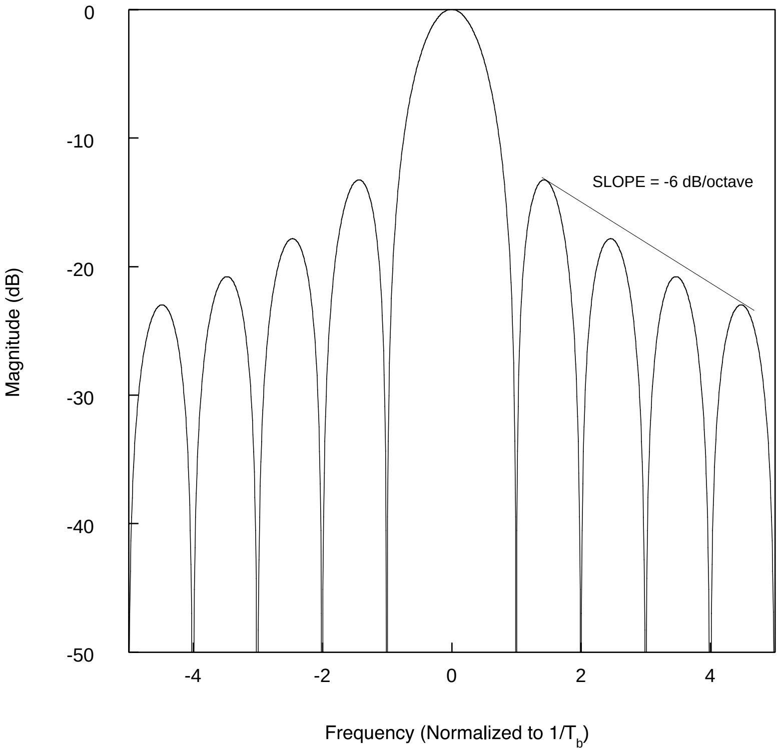

FIGURE 3.17

and $a(kT_b)$ and $a(kT_b)$ represent unit-amplitude data sources, f and g are pulse functions, T_b is the bit rate, and τ_f and τ_g are arbitrary phase offsets. The functions f and g are usually rectangular pulse streams with zero mean and zero correlation between pulses. In this case, the PSD of Eqs. (3.109a) and (3.109b) is given as

$$S_i(f) = T_b \text{sinc}^2(\pi T_b f) \tag{3.109c}$$

$$S_q(f) = T_b \text{sinc}^2(\pi T_b f) \tag{3.109d}$$

In Fig. 3.17 it is shown that Eqs. (3.109c) and (3.109d) exhibit a –6 dB/octave roll off. A communication system based on rectangular pulses would therefore exhibit very poor spectral efficiency due to the relatively large energy present in the spectrum in the neighboring sidelobes. To resolve this problem, band-limiting filtering is used. Although it is possible to use arbitrary band-limiting filters, such as the Chebyshev low-pass response, the Nyquist response is often adopted since it exhibits certain characteristics amenable to demodulation of the signal at the receiver [10-12].

A significant consequence of band-limiting a discontinuous signal, such as that exhibited by PSK with rectangular pulses, is that envelope variations will be introduced. Thus, although PSK modulation is constant envelope, the necessity of band-limiting induces envelope variations, which gives a band-limited PSK signal properties of both phase modulation and amplitude modulation. The degree of amplitude variation is directly proportional to the degree of band limiting. Figure 3.18 illustrates the impact of band limiting on the QPSK constellation of Fig. 3.16, where the amplitude variations are apparent. Band limiting will necessarily require a reduction in the efficiency of a PA, in order to support the peak excursions of the envelope.

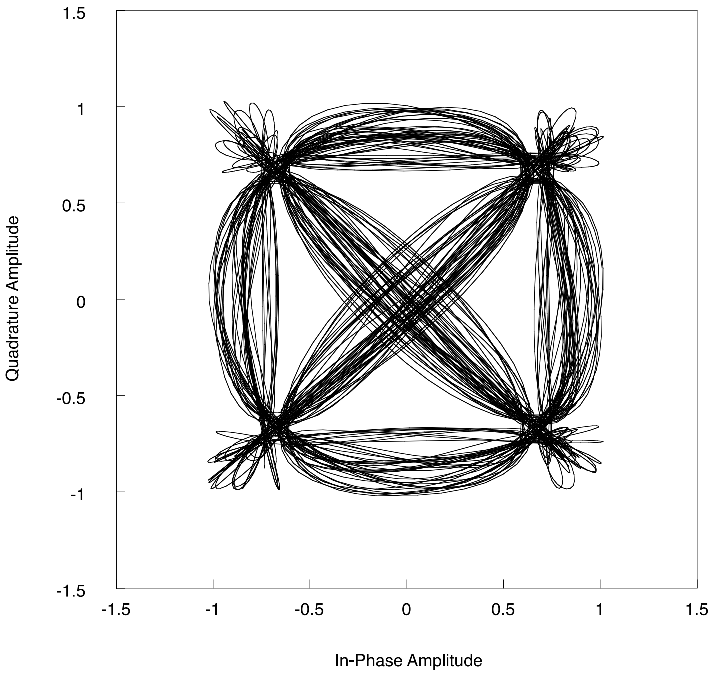

FIGURE 3.18 Constellation diagram of band-limited QPSK. The transient response of the band-limiting filter increases the peak-average ratio of the signal. The more severe the band limiting, yielding increased spectral efficiency, the higher the peak-to-average ratio becomes.

The Nyquist filter response exhibits simultaneous band limiting and zero inter-symbol interference (ISI). Zero ISI is desirable, though not necessary, for a digital communication system to give acceptable performance. To understand the impact of inter-symbol interference, consider the convolution integral Eq. (3.95b), where it is seen that convolution is essentially a summation operation that accounts for the past state of a signal or system at the present time. Use of an arbitrary filter response will result in interference of the present state of a signal due to its past values, leading to the potential for an error in the actual value of the signal at the present time. The impulse response of a Nyquist filter has zero crossings at multiples of the symbol rate, and thus does not cause inter-symbol interference [11,12].

The most common form of Nyquist filter currently adopted is the raised cosine response. The raised-cosine response is expressed in the frequency domain as

$$H(f)=\begin{cases} T_s, & |f|\le \dfrac{1}{2T_s}-\alpha \\ T_s\cos^2\left[\dfrac{\pi}{4\alpha}\left(|f|-\dfrac{1}{2T_s}+\alpha\right)\right], & \dfrac{1}{2T_s}-\alpha\le|f|\le\dfrac{1}{2T_s}+\alpha \\ 0, & |f|>\dfrac{1}{2T_s}+\alpha \end{cases} \tag{3.110}$$

where T_s is the symbol rate in seconds and α is the excess-bandwidth factor [6,13]. By adjusting α, the spectral efficiency of a digitally modulated signal can be controlled, while maintaining zero ISI. Figure 3.19 shows the frequency response of Eq. (3.110) for various values of α. At the Nyquist limit of $\alpha = 0$, all energy above half of the main lobe is removed. This results in maximum spectral efficiency but the largest time domain peak-to-average ratio.

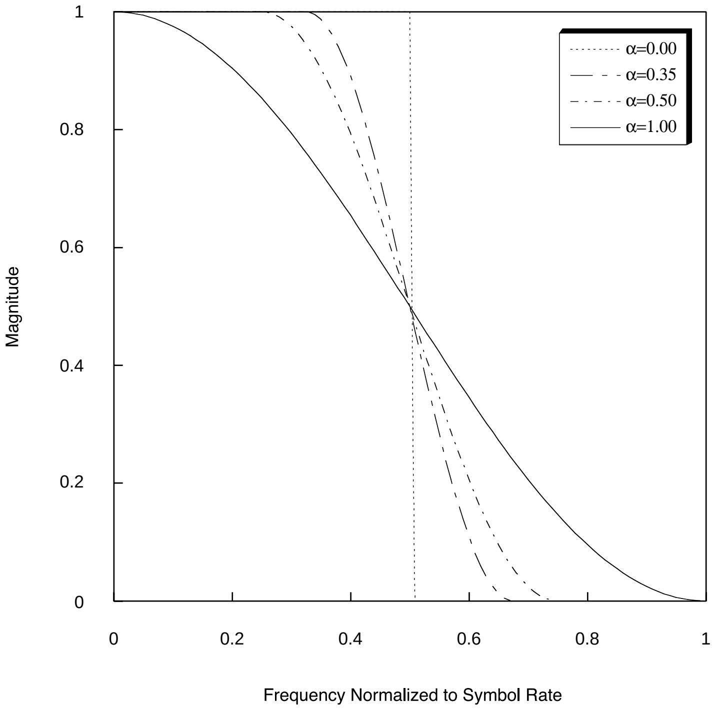

FIGURE 3.19 Raised-cosine filter response for several excess-bandwidth factors. The frequency axis is normalized to the symbol rate. NADC uses an α = 0.35.

To maximize receiver signal-to-noise ratio (SNR), many wireless communication systems split the filter response equally between the transmitter and receiver [9,10]. The resultant response is called the square-root raised-cosine response, which in the time domain is expressed as

$$h(t) = 4\alpha \frac{\cos\left[(1+\alpha)\frac{\pi}{T_s}t\right] + \dfrac{\sin\left[(1-\alpha)\frac{\pi}{T_s}t\right]}{\dfrac{4\alpha}{T_s}t}}{\left(\pi T_s^{0.5}\right)\left[\left(\dfrac{4\alpha}{T_s}t\right)^2 - 1\right]} \tag{3.111}$$

where the variables are defined as above in Eq. (3.110) [11].

Many digital wireless standards specify the symbol rate and excess-bandwidth factor to specify the root-raised cosine filter. This can lead to ambiguity in specifying the filter response insofar as the length of the impulse response is not specified. An impulse response that is too short will exhibit unacceptable band-limiting performance and can lead to incorrect characterization of spectral regrowth. Alternatively, some standards specify a band-limiting impulse response in the form of a digital filter to ensure that the appropriate frequency domain response is used [4,14].

Several wireless communication systems are based on discontinuous PSK modulation. These include the North American Digital Cellular standard (NADC), the Personal Digital Cellular System (PDC), the Personal Handyphone System (PHS), and cdmaOne [2,15,4]. The first three of these systems have adopted π/4-DQPSK modulation with a root-raised cosine filter response. The cdmaOne system has adopted

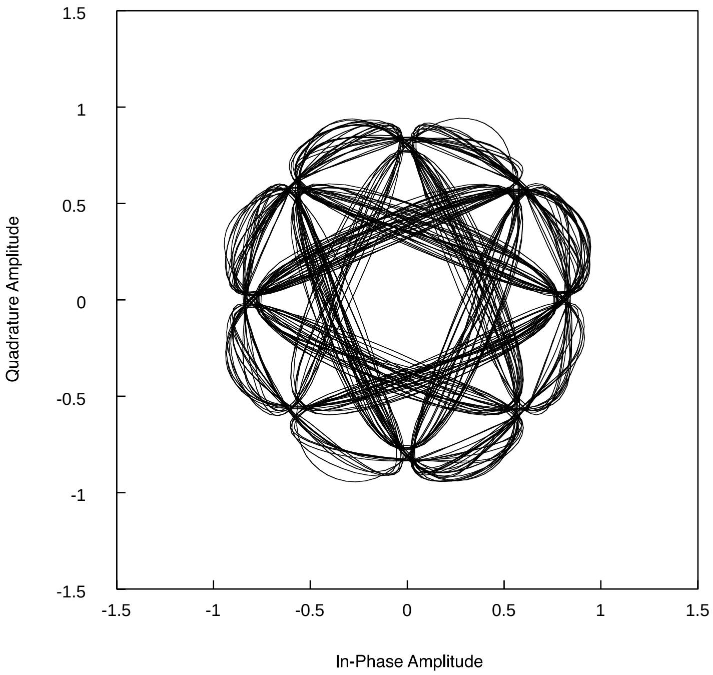

FIGURE 3.20 Constellation diagram for π/4-DQPSK with α = 0.35.This modulation is used for NADC, PDC, and PHS.

QPSK for the forward-link and offset QPSK (O-QPSK) for the reverse link, in both cases using a Chebyshev filter response.

π/4-DQPSK, a derivative of QPSK, differentially encodes the symbols, and adds a π/4 rotation at each symbol instant. This results in an envelope that avoids the origin, thus decreasing the peak-average of the signal. This is done presumably to reduce the PA back-off requirement, but as recent work has illustrated, this is not achieved in practice due to the original assumptions made [16]. Figure 3.20 shows the constellation diagram for π/4-DQPSK with α = 0.35, corresponding to the NADC standard. Note that at each of the constellation points, the trajectories do not overlap; this is inter-symbol interference. At the receiver, this signal will be convolved with the remaining half of the raised-cosine filter, leading to the desired response given by Eq. (3.110). PDC and PHS are also based on π/4-DQPSK, with an excess bandwidth factor of α = 0.50. Their constellation diagrams are similar to the NADC diagram shown in Fig. 3.20.

Figure 3.21 shows the constellation diagram for reverse-link cdmaOne, which is based on O-QPSK. Like π/4-DQPSK, O-QPSK was developed to reduce the peak-to-average ratio of the signal. It has been shown that this approach, while reducing the peak-to-average ratio, does not necessarily reduce the PA linearity requirements [16]. Note also in Fig. 3.21 the significant ISI, due to the fact that a Nyquist filter was not used. The forward link for cdmaOne uses QPSK modulation, which is shown in Fig. 3.18. As with the reverse link, the forward link uses a Chebyshev response specified by the standard.

To increase spectral efficiency, it is possible to add four additional phase locations to QPSK, called 8-PSK, with each location corresponding to a unique combination of three bits. Figure 3.22 shows the constellation diagram for the EDGE standard, which is based on 8-PSK and a specially developed filter that exhibits limited response in both the time domain and frequency domain [17]. EDGE was developed to increase the system capacity of the current GSM system while minimizing the requirements for linearity. In contrast to GSM, which is constant envelope, the EDGE systems provides increased spectral efficiency at the expense of envelope variations. However, EDGE intentionally minimizes the resultant

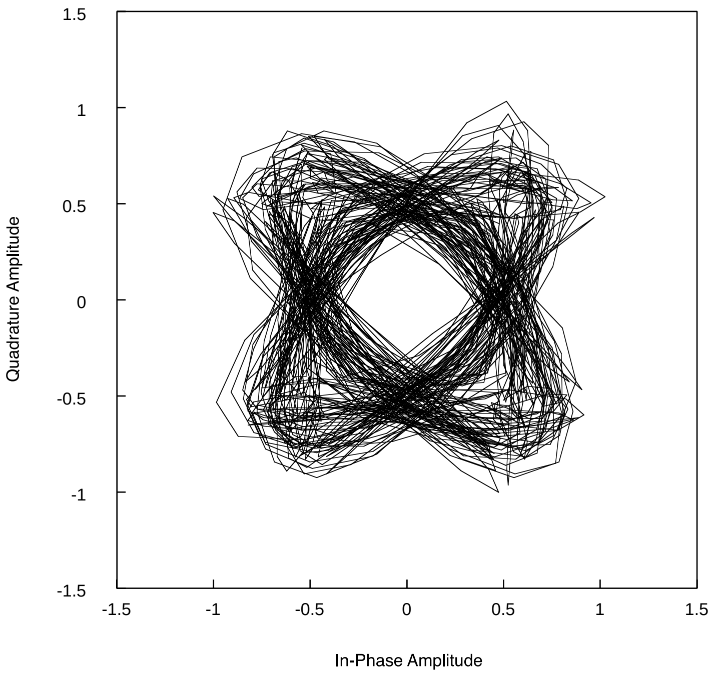

FIGURE 3.21 Constellation diagram for O-QPSK using the filter response specified by the IS-95 standard for cdmaOne.

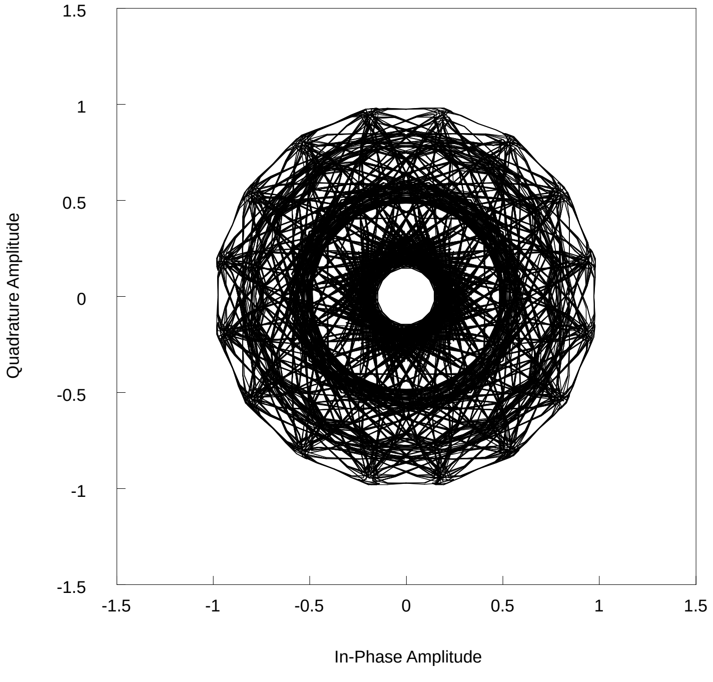

FIGURE 3.22 Constellation diagram for EDGE.

amplitude modulation to ensure that existing GSM amplification systems, optimized for constant envelope modulation, could still be used.

Continuous Phase-Shift Keying

With the exception of EDGE, each of the PSK modulations considered in the previous section exhibited significant out-of-band energy due to the discontinuous transitions. To reduce the out-of-band energy, band limiting was required, which resulted in envelope variations. An alternative modulation process is continuous-phase modulation (CPM), which requires that the phase transitions from one symbol to the next be continuous [9,13]. This results in a signal that is intrinsically band limited while maintaining a constant envelope. The price paid is a potential reduction in spectral efficiency. Two types of CPM will be examined in this section: minimum-shift keying (MSK) and Gaussian MSK (GMSK).

The complex envelope representation of MSK is

$$x\left(t\right)=\cos\left[a\left(kT_b\frac{\pi t}{2T_b}\right)\right]+j\sin\left[b\left(kT_b\right)\frac{\pi t}{2T_b}\right] \tag{3.112}$$

$a(kT_b)$ and $b(kT_b)$ represent unit-amplitude data sources as defined in Eq. (3.109). This modulation is identical to O-QSPK using a half-wave sinusoidal pulse function instead of a rectangular pulse function. Taking the magnitude squared of each term of Eq. (3.112) shows that it is indeed a constant envelope.

GMSK uses Gaussian pulse shaping, and has a complex envelope representation of

$$x\left(t\right)=\exp\left[jk_f\int_{-\infty}^{t}i\left(\tau\right)d\tau\right]=\exp\left[jk_f\int_{-\infty}^{t}\sum_{k=-\infty}^{\infty}a\left(kT_b\right)f\left(\tau-kT_b\right)d\tau\right] \tag{3.113}$$

where $f(\tau - kT_b)$ is a Gaussian pulse function and $a(kT_b)$ is a unit-amplitude data source as defined in Eq. (3.109). Since the Fourier transform of a Gaussian pulse in the time domain is a Gaussian pulse, it is seen that this modulation will exhibit intrinsic band limiting, in contrast to PSK. In Fig. 3.23 the GMSK constellation diagram is illustrated, where it is seen that the envelope is constant. The information is contained in how rapidly the phase function moves from one location on the circle to another, in a fashion similar to FM. GMSK is used in the Global Standard for Mobile Communications (GSM) wireless system [3].

Probabilistic Envelope Characterization

The complex trajectory of a signal, determined by the modulation technique, band limiting, and signal coding used, is a time parametric representation of the instantaneous envelope of the signal. As such, the duration of a particular envelope level in combination with the transfer characteristics of the power amplifier (PA) will establish the resultant instantaneous saturation level. If the average spectral regrowth exhibited by a PA is considered a summation of many instantaneous saturation events, it follows that the more often an envelope induces saturation, the higher the average spectral regrowth will be. It is for this reason that the peak-to-average ratio, though widely used, is ill suited for estimating and comparing the linearity requirements of a PA [16].

This section introduces a method for probabilistically evaluating the time domain characteristics of a an arbitrary signal to establish its associated peak-to-average ratio and instantaneous envelope power distribution. The envelope distribution function (EDF) is introduced to estimate the peak power capability required of the PA and compare different signals. The EDF for many of the wireless systems presently in use are examined.

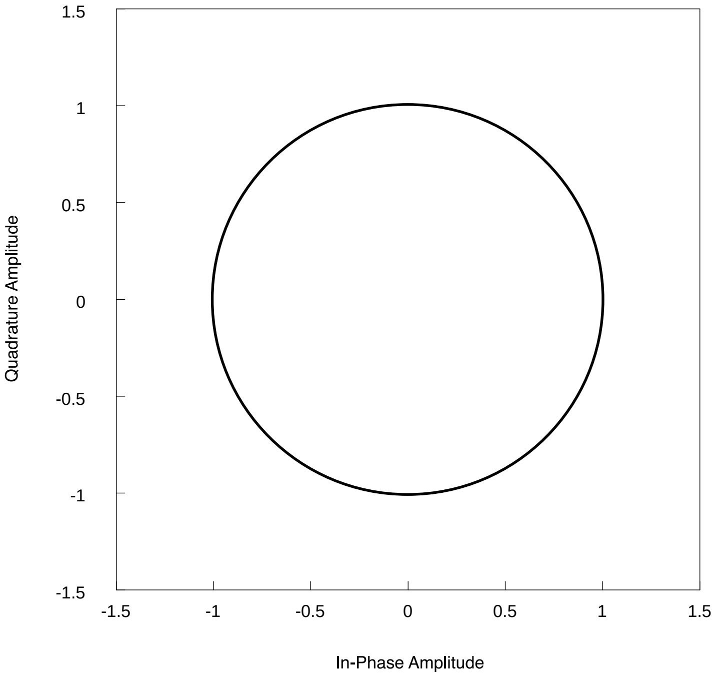

FIGURE 3.23 Constellation diagram for GMSK, which is used in the GSM wireless system.

The Envelope Distribution Function

Let $\tilde{p}(t)$ be the instantaneous power of a signal $\tilde{x}(t)$, with an associated instantaneous power probability distribution function $\varphi(\tilde{p})$. The probability of the instantaneous power exceeding the mean signal power is

$$\Pr\left[\text{instantaneous power} > \text{mean power}\right] = \Psi\left(\tilde{p}\right) = 1 - \int_{E\left[\tilde{p}\right]}^{\infty} \varphi\left(\tilde{p}\right) d\tilde{p} \tag{3.114}$$

where $E[\tilde{p}]$ is the average power of $\tilde{p}(t)$. This function is defined as the envelope distribution function (EDF). In practice, the EDF is evaluated numerically, although it is possible to generate closed-form expressions. A specified probability of the EDF, typically 10^{-6}, is referred to as the peak-to-average ratio, σ. This is defined as

$$\sigma = \frac{\text{EDF @ } 10^{-6}}{E\left[\tilde{p}\left(t\right)\right]} \tag{3.115}$$

A gradual roll off of the EDF indicates the instantaneous power is less likely to be near the mean power of the signal. This characteristic implies enhanced linearity performance to minimize increased distortion associated with the relative increase in the instantaneous clipping of the signal. Alternatively, for a given linearity requirement, the average power of the signal must necessarily decrease, resulting in lower efficiency. The amount that the average power must be reduced is referred to as output back off, and is usually specified in dB normalized to the 1 dB compression point of the PA under single-tone excitation. Finally, note that the EDF only has meaning for signals with a time-varying envelope.

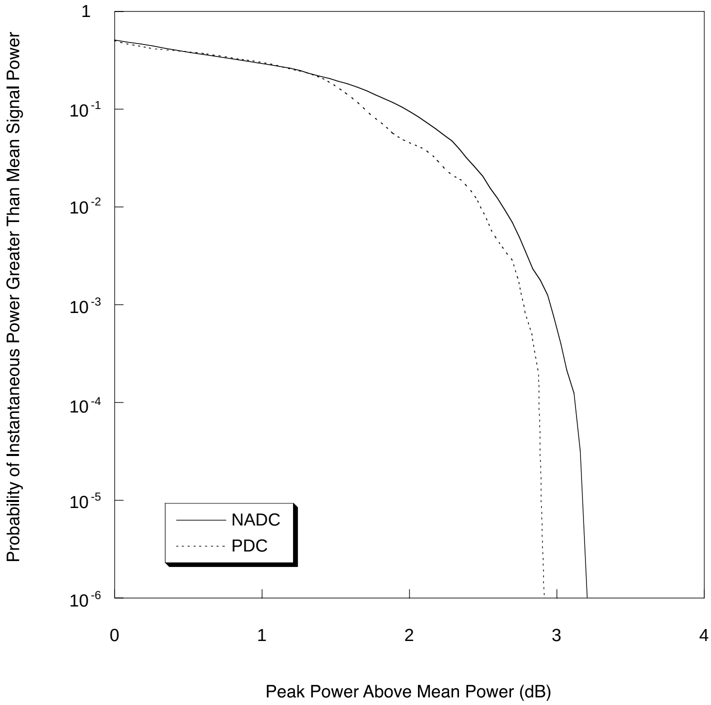

FIGURE 3.24 The EDF for NADC and PDC. NADC uses π/4-DQPSK with α = 0.35 and PDC uses π/4-DQPSK with α = 0.50. Note PDC has a slightly lower peak-to-average ratio due to the more gradual roll off of the filter response.

The EDF for Various Wireless Systems

In this section, Eq. (3.114) is used to examine the EDF for several of the wireless systems described earlier. NADC, PDC, and EDGE are considered first. The EDF for CDMA-FL and CDMA-RL using only a pilot tone is considered next. The impact of traffic channel, synchronization channel, and paging channels on the CDMA-FL EDF is then illustrated, where it will be seen that a significant increase in the peak-to-average ratio results, making this signal difficult to amplify. For comparison purposes, the EDF for a two-tone signal and complex Gaussian noise will also be shown. The EDF for each of these signals is shown in Figs. 3.24 through 3.29.

Summary

Contemporary microwave circuit design requires a basic understanding of digital modulation theory in order to meet the needs of a customer who ultimately speaks in terms of communication theory. This chapter was intended to provide a brief overview of the signal analysis tools necessary for the microwave engineer to understand digital modulation and how it impacts the design and characterization of microwave circuits used in contemporary wireless communication systems.

Complex envelope analysis was introduced as a means to describe arbitrarily modulated signals, leading to a geometric interpretation of modulation. The necessity and subsequent implications of band-limiting PSK signals were discussed. As an alternative to PSK, CPM was also introduced.

Signal analysis methods are often used to simplify the design process. Although the peak-to-average ratio of a signal is widely used to estimate of the linearity requirements of a PA, it was shown that this metric is ill suited in general for this purpose due to the random distribution of instantaneous power of a signal. The envelope distribution function (EDF) was introduced as means to compare various signals and to provide a more accurate estimate of the required linearity performance of a PA.

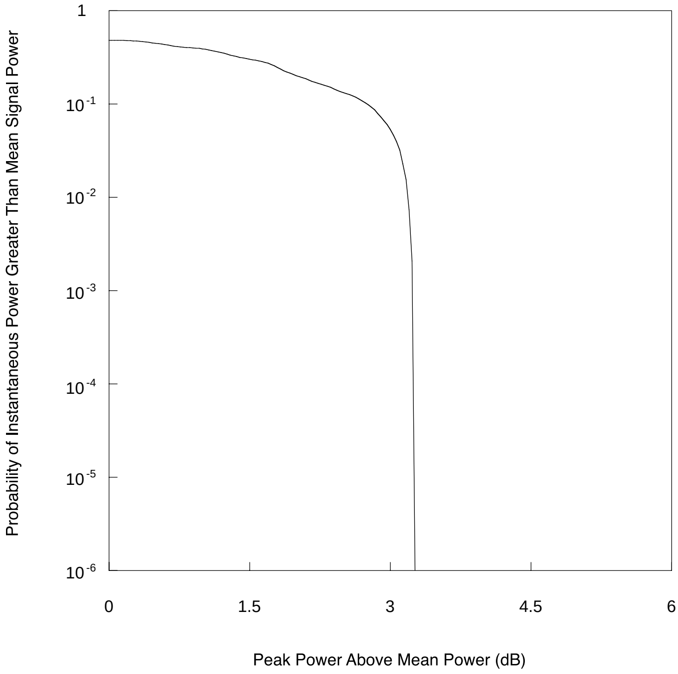

FIGURE 3.25 The EDF for EDGE (with all time slots active). Compare to Fig. 3.28, where the EDF for a two-tone signal is shown.

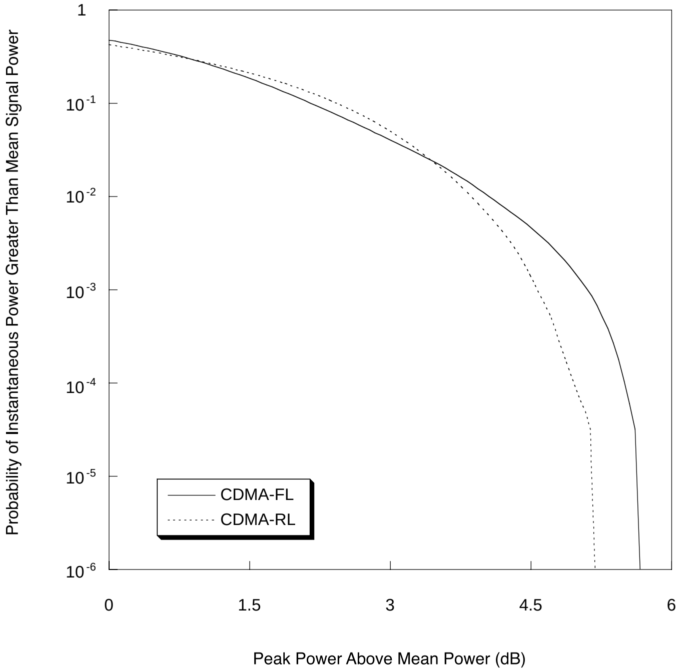

FIGURE 3.26 The EDF for forward-link CDMA and reverse-link CDMA with pilot tone only. Note that although CDMA-RL has a lower peak-to-average ratio, in areas of high probability of occurrence it has a higher peak power and results in higher spectral regrowth than CDMA-FL. This comparison clearly illustrates the advantages of using the EDF over the peak-to-average ratio.

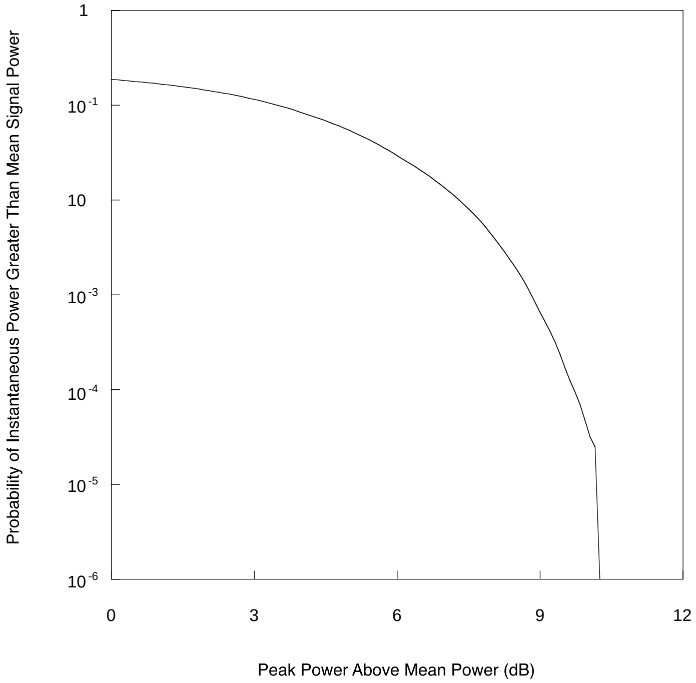

FIGURE 3.27 The EDF for forward-link CDMA with six traffic channels active and synchronization, paging, and pilot also active. Compare to Fig. 3.26 and observe the significant increase in peak-to-average ratio.

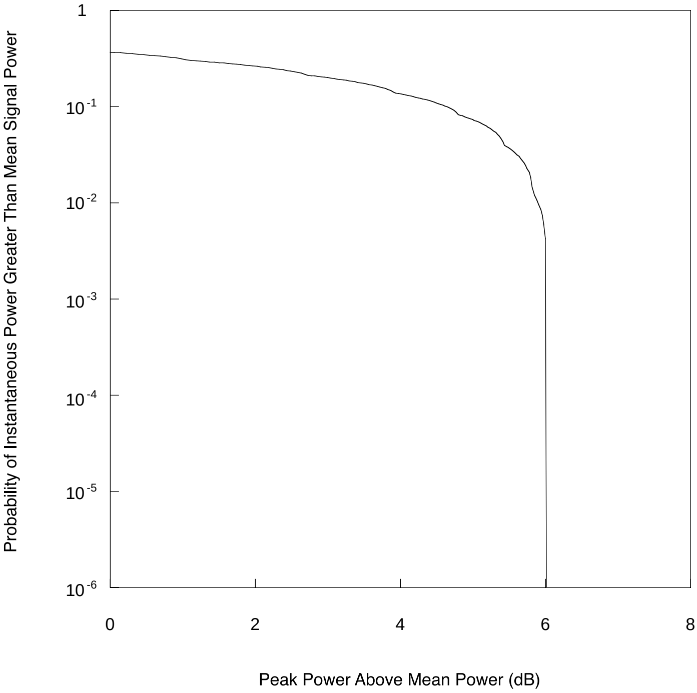

FIGURE 3.28 The EDF for a two-tone signal. Note that like the EDGE signal, the two-tone signal exhibits a gradual roll off, leading to increased distortion with respect to a similar signal with the same peak-to-average ratio but a faster roll off, such as CDMA-FL.

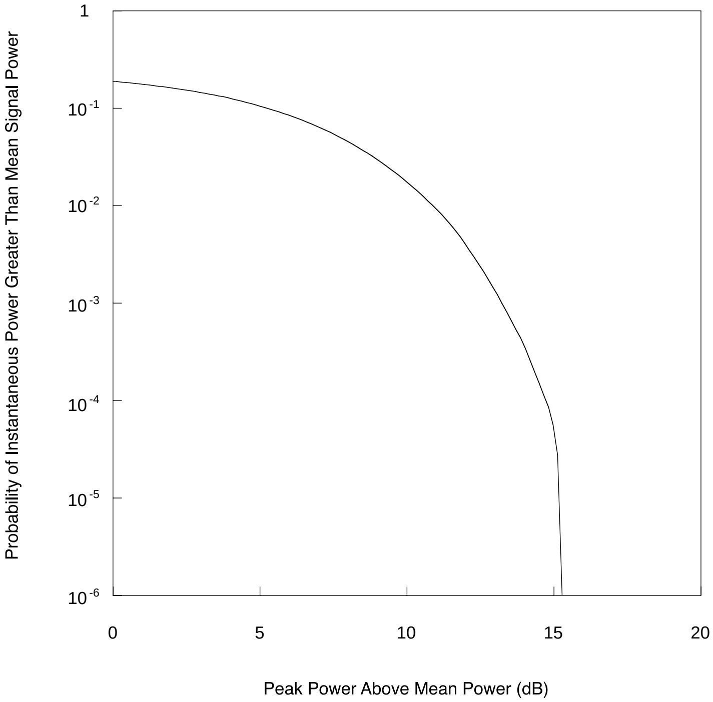

FIGURE 3.29 The EDF for a complex white Gaussian noise signal (commonly used for noise-to-power ratio characterization). The theoretical peak-to-average of this signal is infinite, but in practice is approximately 10 dB to 15 dB, depending on the length the sequence used.

References

1. W. C. Y. Lee, *Mobile Cellular Telecommunications Systems*, New York: McGraw-Hill, 1989.
2. EIA/TIA Interim Standard, Recommended Minimum Performance Standards for 800 MHz Dual-Mode Mobile Stations, EIA/TIA/IS-55, 1991.
3. M. R. L. Hodges, The GSM Radio Interface, *British Telecom. Tech. Journal,* 8, 31–43, January 1990.
4. EIA/TIA Interim Standard, *Mobile Station — Base Station Compatibility Standard for Dual-Mode Wideband Spread Spectrum Cellular System,* TIA/EIA/IS-95, 1993
5. R. N. Bracewell, *The Fourier Transform and Its Application*, New York: McGraw-Hill, 1978.
6. L. W. Couch, *Digital and Analog Communications*, 4th ed. New York: Macmillan, 1994.
7. M. Jeruchim, P. Balaban, and K. Shanmugan, *Simulation of Communication Systems*, New York: Plenum Press, 1992.
8. A. Papuolis, *Probability, Random Variables, and Stochastic Processes*, 3rd ed., New York: McGraw-Hill, 1991.
9. M. K. Simon, S. M. Hinedi, and W. C. Lindsey, *Digital Communication Techniques: Signal Design and Detection*, New York: Prentice-Hall, 1994.
10. M. Schwartz, *Information Transmission, Modulation, and Noise*, 3rd ed., New York: McGraw-Hill, 1980.
11. W. R. Bennett and J. R. Davey, *Data Transmission*, New York: McGraw-Hill, 1965.
12. H. Nyquist, Certain topics in telegraph transmission theory, *Transactions of the AIEE*, 47, 117-141, February 1928.
13. J. G. Proakis, *Digital Communications*, 2nd ed., New York: McGraw-Hill, 1992.
14. R. Schaefer and A. Openheim, *Discrete Time Signal Processing*, New York: McGraw-Hill, 1992.

15. Research and Development Center for Radio Systems (RCR), *Digital Cellular Communication Systems,* RCR STD-27, April 1991.
16. J. F. Sevic and M. B. Steer, On the Significance of Envelope Peak-to-Average Ratio for Estimating the Spectral Regrowth Characteristics of an RF/Microwave Power Amplifier, *IEEE Transactions on Microwave Theory and Techniques*, in press.
17. ETSI Standard GSM 11.21: Digital Cellular Telecommunications System BSS Radio Aspects, ETSI, 1999.

3.4 Cost Modeling

Leland M. Farrer

In the commercial industry, the ability to accurately estimate what a product can be built and sold for at a competitive profit, is a challenging task. Accurate cost modeling will simplify and organize the process into a powerful tool for the person entrusted with the task of quoting a project.

Each time a project manager is asked to quote on a future project, he is tasked with producing a cost for the development and cost for the end product. It does not seem to matter what industry you are in, the process is the same, and in the end, most managers succumb to estimating by experience rather than using a detailed costing model. The costing model is used to minimize the potential error by homing in on a model design that matches the market and, with feedback, can produce very good correlation with the end result.

The three major divisions of models include *product* focused, *service* focused, and *idea* focused. The classification of the three shows that the major emphasis is placed on *material*, *labor*, or *technology*.

1. Product-focused models are those where material costs are highest; where the added labor component has been minimized to the highest yield per hour spent. Examples include any production-line product that is automated.
2. Service-focused models are those where labor cost is highest. An example is a firmware product.
3. Idea- or technology-focused models involve an emerging technology with little track record. Examples are early life cycle inventions.

The cost model for all estimating has the following elements:

Bill of materials + Process time + Yield margin + Overhead + Profit = COST

The elements can be interconnected and developed into a spreadsheet application. Many organizations will have the company database connected to the cost model so that all elements are current and real time. A listing of the elements would be like this:

1. Bill of material (BOM) = Raw material cost (no labor for assembly or test) in $$
2. Process time = Operating cost per hour (labor) x Production cycle time = $$
3. Yield margin = (BOM + Process time)/Yield factor = $$
4. Overhead = (Process time + Yield margin) x Burden = $$. Overhead should also contain marketing costs as well as warranty or field returns as part of the burden element.
5. Profit = (BOM + Process time + Yield margin + Overhead) x Percent of markup = $$
6. Cost = the $$ value is the total of all elements.

Complimentary to the cost model is the risk assessment model. Where the cost model covers everything you know about, risk modeling evaluates and puts a dollar value on the things you don't know about that can surprise you. If risk modeling is done, it can be included with the other elements as a cost consideration.

BOM (Bill of Materials)

The bill of material is usually the total cost of all purchased parts such as resistors, semiconductors, etc., and fabricated cost such as PCB, shields, and outside fabricated parts. Depending on the internal requirement, all of these costs may be listed as raw materials with no handling markup. Some cost models will use this as the cost of goods for a product estimation and have a 20% handling charge on the dollar value as a burden element, independent of the G&A burden burden. This allows a softer reliance on hard yield and overhead elements later, but does mask the true cost. As with any production, the BOM costs will vary greatly with volume numbers. BOM costs at a quantity of 1000 will be much higher than at 1,000,000. Similarly, domestic BOM costs will be different than the same costs offshore.

Process Time

Depending on the item being estimated, the process time might be a resource output from a Gantt chart of all of the labor needed to design, test, and commission a prototype. This gets more difficult for development projects involving design review meetings and where many of the tasks are interrelated with critical path links. In complicated multiphase projects, the estimation of critical paths and margins to accommodate some slippage will become a requirement of the overall labor element of cost modeling. The cost element will be a total of all the individual worker hours at their unburdened individual rates.

Many models are available for setting up the production process. The decision regarding the method used will be based on industry needs and the maturity of the product.

In a manufacturing model, it might be the average cost per hour to operate a machine. The process time would then be the cost per hour times the cycle time to produce the item. Two types of process times must be considered each with a different cost impact. Variable (recurring) costs allow an incremental cost based on quantity changes. Fixed (nonrecurring) process cost is the base cost of holding the doors open (rent, etc.), and must be added. The final process time cost is the result of adding the percentage of use of the fixed cost and the increase due to volume increases.

Yield Margin

Yield margin is the amount of acceptable product vs. the number that failed in the manufacturing process. In the semiconductor industry, it is the percentage or dollar value of good devices vs. those units lost in wafer test, packaging, operational test, etc. In assembly, it is the number of units needed to set up the line, or parts lost in transport, QC, or customer rejection. If you need to deliver 100 units, and experience for like products have a total reject rate of 3%, then you will need a 3% margin (103) for proper yield. The cost, then, is the value of the rejected units spread across the 100 good units delivered.

Overhead

Overhead = Burden = $$(%). There is no easy number here. It must be calculated for each industry, geographical location, and will change as a company grows. For fledgling companies, this cost is shared by just a few individuals and can be quite high. If you are renting a location for $2 to $3 per square foot triple net, and have 5000 ft^2, this can be a significant number for 10 people. "Triple net" is a lease requiring the tenant to pay, in addition to a fixed rental, the expenses of the property leases such as taxes, insurance, maintenance, utilities, cleaning, etc. In this example, that is $10,000 to $15,000 plus capital equipment amortization, insurance, utilities, facilities maintenance, etc., plus the administrative staff, secretaries, sales staffs, etc. These are items that are not directly adding labor to produce the product. If you are quoting on the development of a product and expect it to take 3 months of time and all of your direct labor people, then the overhead cost for the three months will be the number to use. The number can be proportionally less if only some of the resources are used. When commissions are used, it can be added as part of the burden factor, although it is more commonly added after the cost is computed and becomes part of the cost given to the customer. Usually when a company is stable in resources and size, the burden number can be expressed as a percentage of man-hours. If not, it must be computed on an individual basis of labor cost for each direct labor resource used.

Profit

Profit = (BOM + Process time + Yield margin + Overhead) × Percent of markup = $$(%). How much do you want to make? There are many ways to look at this number. If your market is highly variable, you may need a higher number to cover the low-income periods. If you are in the semiconductor industry, the number is part of a strategy for growth. Competition will also force some consideration of how much to charge. Generally the final number is a percentage of the cost of doing business and marketing opportunity based upon the customers' needs and what the market will tolerate. A point to remember for costing is the constant fluctuation of the exchange rates for foreign currency. Where the estimate covers a significant period of time, care must be taken to get professional assistance in this area. This could involve tying the value of the currency to the dollar or buying foreign funds to cover the exposure.

Cost

Now that we have put all of the elements together, the other side of the equation equals *cost*. It is now time to evaluate this number. Does the dollar amount meet the needs of the customer? Will the company be underbid by the competition? Are we leaving money on the table? If the answer to any of these is no, go back and see where the critical element is that will turn them into yeses. Remember, not all quotes are good ones. Some will not be good for you or your business. Most are good ones and it is up to you to find the right balance of value elements for your cost model equation.

Although this is not an exhaustive list of elements, it serves as a basis. Cost modeling is an extremely valuable tool in the quoting process, as well as a monitor of ongoing business health. Let's look at the major differences in the marketplace.

Product-Focused Models

When a technology has matured to the point where a high level of automation is implemented or where the percentage of material cost to labor contribution is high, the model can be very accurate and margins can be predicted to a high level of certainty. The BOM cost can be easily obtained from past purchases or the company's materials resource planning (MRP) database. The process time of the new design can be compared to the existing product and weighted accordingly. The yield and margins applied and the cost to produce can be generated from existing production runs. The chip manufacturing industry is an excellent example of this type of market, as are low-priced consumer market products. The material costs can be very accurately determined and process times are minimized as much as possible. In these markets, the volumes are high and per-unit costs are highly refined and generally low. This market is highly mature and cost models are finely tuned so that extracting the final profitability dollar amount has low risk. One key control for this model is feedback from the production line to confirm yields. Statistical Process Control (SPC) can be employed to measure performance and flag when corrective action is necessary. The run numbers from yield and process time allow confirmation of the model accuracy for future cost model estimating. With the high commitment of capital equipment and process time, cost modeling is necessary to minimize the loading risk. This model is well suited for fixed bid as well as projects with a time and material (T & M) cap.

Service-Focused Models

When the major contribution of the product is labor, the estimation is only as good as the reliability of the workers and their task execution. The elements of the model are the same, but the focus on past experience and more margin is required to compensate for this uncertainty. Examples of this are electronic prototype construction, software development, and warranty service. This model will display a wider swing in uncertainty relative to the product-focused model. Many service industries use this weighted model, and it is also taxed with individual performance estimating as a requirement. It is not helpful when worker substitution and different skill levels are factors, unless added margin is allowed.

Idea-/Technology-Focused Models

These can be the highest risk models. This is where invention is needed or relied upon for success. This can be seen in Gantt charts where the task "something magic happens here" is implied. It is also the area where the Intellectual Property (IP) (the idea) is not fully developed or needs refinement to make it ready for production. An example would be taking a reference design circuit and making an application-specific product. Due to the uncertainty of the elements of this model, the estimation is likely to be on the conservative side unless an investment in market penetration or a strategic alliance exists or is desired, in which case a more aggressive costing might be undertaken to secure the contract against competition.

Here again is the reliance on past experience. Regular reviews are needed of completed project performance to ensure that the model elements are operating properly. Failure to continually review and update the model elements on a daily, weekly, and monthly basis will result in an out-of-control erosion of the margins and profit.

Feedback

Probably the most important and often overlooked feature for accurate cost modeling is the use of feedback in the maintenance of the cost model. This can take several forms and is a featured process in all ISO 9000 documentation. Production feedback is used regularly on the factory floor at QA stations to ensure the quality of the product. No less important is the feedback from a development project to indicate the fiscal health of the team in meeting the milestones with calendar, material, and labor costs on track. This information not only needs to get back to the project managers for online project correction, but, also needs to get back to the contract administrators who generate the quotes to evaluate and adjust the cost model elements as necessary. Examples of corrections are the need for margin in the labor element if a unique skill set is required, or when vendor performance is in the critical path to meet a scheduled milestone and a calendar slip is likely. All feedback that will affect the performance accuracy must be routinely fed back into the cost model for correction.

Refinement of the Cost Model

In conclusion, the cost model is a living tool. Cost model effectiveness is only as good as the accuracy of the information going into each of the elements and the constant feedback to fine-tune it. A model that is good in a bull market may not be the one you need for the downturn era. As your company grows, the model will need to constantly evolve to keep pace with your needs. Putting the cost model into a spreadsheet will allow effective use and permit a lot of "what if" investigation as well as cost model evolution.

References

ECOM, European Space Agency, (ESA) Cost Modeling, A general Description http://www.estec.esa.nl/eawww/ecom/article/ecom.htm.

Barringer and Associates, Life Cycle Cost Modelling, Freeware, http://www.barringer1.com/MC.htm.

Skitmore, M., ed., *Cost Modelling,*

3.5 Power Supply Management

Brent A. McDonald, George K. Schoneman, and Daniel E. Jenkins

Background

A Short History (1970–2000)

1970 — Switching frequencies were normally 50 KHz or less. Bipolar transistors were predominately used as the power switching elements. Royer oscillators were popular during this period.[1]

1980 — Switching frequencies were normally 100 KHz or less. MOSFET transistors were predominately used as the power switching elements. Control ICs were introduced. Constant frequency pulse width modulation became popular. Schottky diodes were introduced.

1990 — Switching frequencies were normally 500 KHz or less. Current mode control became popular (Peak Current Mode Control and Average Current Mode Control). Synchronous rectifiers were introduced. Commercial Off The Shelf (COTS) became popular. Zero-voltage and zero-current switching techniques were introduced.

2000 — Technology trends have not changed much since 1990. Switching frequencies are still 500 KHz or less. Current mode control remains on the forefront of many designs. Synchronous rectifiers are gaining popularity.

Future — Consumer PC voltages are projected to be as low as 0.5 V by the year 2010. These trends are suggesting dense hybridized power supplies co-located with the microprocessor. The automotive industry is going toward the more electric and all electric car.

Power Supply Types

Most power supplies are configured to supply a well-regulated, constant voltage output, however, this does not have to be the case. Theoretically, a power supply can be configured to deliver constant current or power. Since most applications require some type of regulated voltage source, this topic will be addressed from that point of view.

Obviously, a power supply does not produce power for its load. It takes power from a source and reconditions the power so that the load can operate without damage or interference. If a power supply is required, it must be assumed that the power source is in some way not suitable to the device(s) it is powering.

This section will discuss three basic types of power supplies: linear regulators, charge pumps, and switch mode power supplies (SMPS). Each of these has an appropriate range of application and its own unique operational characteristics. A linear regulator takes a DC voltage with a higher magnitude than required by the load and steps it down to the intended level. The linear regulator typically accomplishes this by dropping the excess voltage across some kind of series pass element, commonly known as a series pass regulator. The second most common form of linear regulator is the shunt regulator. This approach often utilizes a fixed series impedance with a variable shunt impedance. Since the source voltage and load may vary, a feedback loop is usually used to minimize these affects on the output voltage. Figure 3.30 illustrates these two types of regulators.

A charge pump is capable of boosting a voltage to a higher level. A simplified charge pump is shown in Fig. 3.31. These voltages may not be as well regulated as the SMPS or linear regulator approaches since their output regulation is dependant on items such as the forward voltage drop of the diodes and the initial tolerance of the power source being used. When turned on, the inrush current may be very high. Essentially, the voltage sources are looking into a capacitor. The currents will be limited by the rate of rise of the source, the impedance of the diodes, and any parasitic resistance and inductance in series with the capacitor.

An SMPS operates by taking a DC voltage and converting it into a square wave and then passing that square wave through a low pass filter. In many applications, this allows for a more efficient transfer of power than can be achieved with a linear.

Figure 3.32 lists a general comparison between these three types of power supplies.

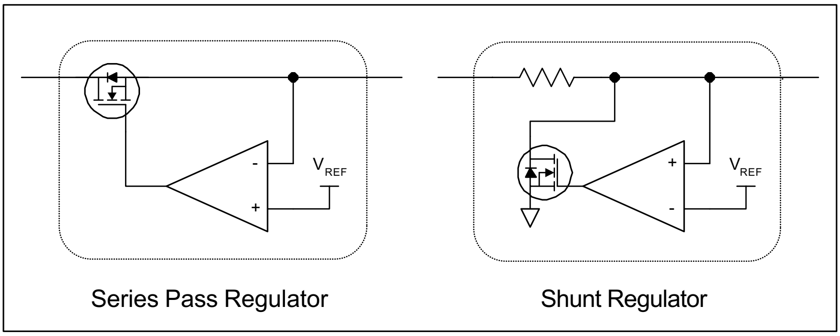

FIGURE 3.30 Two basic types of linear regulators.

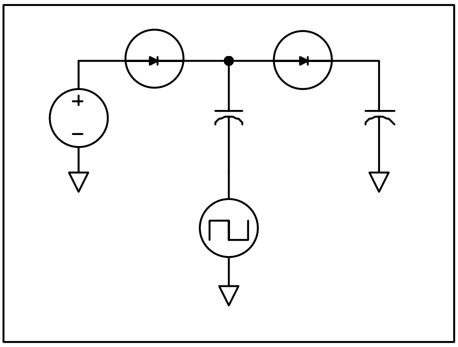

FIGURE 3.31 Typical charge pump.

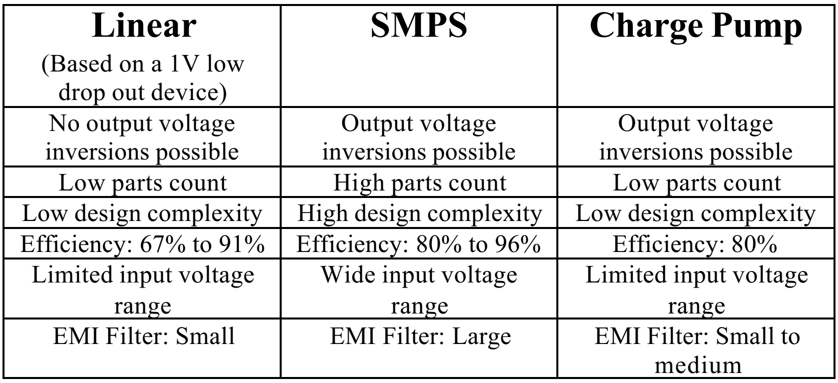

Linear (Based on a 1V low drop out device)	**SMPS**	**Charge Pump**
No output voltage inversions possible	Output voltage inversions possible	Output voltage inversions possible
Low parts count	High parts count	Low parts count
Low design complexity	High design complexity	Low design complexity
Efficiency: 67% to 91%	Efficiency: 80% to 96%	Efficiency: 80%
Limited input voltage range	Wide input voltage range	Limited input voltage range
EMI Filter: Small	EMI Filter: Large	EMI Filter: Small to medium

FIGURE 3.32 Power supply comparison (2V < Vout < 10V, 15W).

Why Use a Power Supply?

Some power sources have voltages that vary 2:1 in normal operation and more than 10:1 during some transient conditions. Very few loads can function properly over these ranges and most will be damaged. A power supply can provide an interface to make these line voltage variations transparent, or at least tolerable to the load's operation.

Some applications such as transmitters, stepper motors, processors, etc., have large step loads. This may require lower output impedance than the source alone can provide. In other words, if the load requires a sudden burst of current, it is desirable that the output voltage remain in regulation. A low impedance capacitor bank can provide this step current. Alternatively, the control loop can sometimes be modified to supply such step loads.

System Issues: Specifications and Requirements

Input Voltage

This is an area where many mistakes are made in the initial design. The input voltage, or source, is rarely as well behaved as the title indicates. As an example, let's examine the average automobile electrical system as it exists in year 2000. The owner's manual will call it a "12 Volt" system, which sounds good, but when the alternator is charging, the voltage is typically ~13.8 Volts (~15% increase). That is "typical," but actual numbers could range as high as 15 Volts (~25% increase). And it gets worse! Those voltages are defined as "steady state" or "normal operation." When heavy loads on the system are removed (headlights, starter motor, cooling/heating fans, air-conditioning, horn, etc.) the voltage on the bus can exceed 60 Volts (500% increase!) for durations > 100 ms.

Standard household power is equally inhospitable. Lightning, power surges, and brownouts can result in a very wide input-voltage range that your design may have to tolerate.

Battery-operated units are somewhat better, but attaching and removing battery chargers can cause large voltage spikes. Due to the internal impedance of the battery, transient step loads will cause degradation in the battery bus voltage.

Output

Power supplies are designed to power a specified load. In other words, there is no such thing as "one size fits all." For example, a supply that powers a 50 W load with 85% efficiency would be totally inappropriate for a 1 kW load.

A reactive load will introduce additional phase shift that a resistive load will not. This additional phase shift can create unstable or marginally stable systems. The module designer will often add significant capacitance to decouple one circuit from another. If this capacitance is large enough and not accounted for in the selection of the power supply, reduced stability margins and/or a compromised transient performance can result. Likewise, if inductors are used to de-couple the circuits, an inductive load can result and a similar detrimental effect on stability and transient performance is possible.

If the load exhibits large/fast step changes, the equivalent series resistance (ESR) of the output capacitors may cause the output voltage to drop below the valid operating range. The control loop will then try to correct for the error and overshoot can result.

A common misconception is that the DC accuracy of the output voltage is primarily a function of the reference. Usually, the output voltage is resistively divided down before being compared to the reference. If this is the case, the tolerance of the divider resistors needs to be accounted for. Offset voltages, offset currents, bias currents, and the location of the gains in the loop relative to the reference voltage can also significantly affect the DC settling point. This is all further complicated by the fact that these are all temperature-dependent terms.

The output ripple voltage waveforms of SMPS are harmonically rich. Generally, they will take the shape of a triangle or trapezoid. The fundamental frequency of these waveforms is at the switching frequency and will usually have harmonic content both above and below the fundamental. The content below the fundamental can be the result of input voltage variations, load variations, or injected noise. The ripple voltage specification listed on a data sheet or in a requirements document will probably give the maximum peak-to-peak voltage at the switching frequency or the RMS voltage. Often, larger spikes can be present for which the ripple voltage specification does not account. Figure 3.33 shows a typical output ripple voltage waveform and the frequency spectrum of that waveform. This particular case is a 20 V input, 3.3 V output, operating at 18 W.

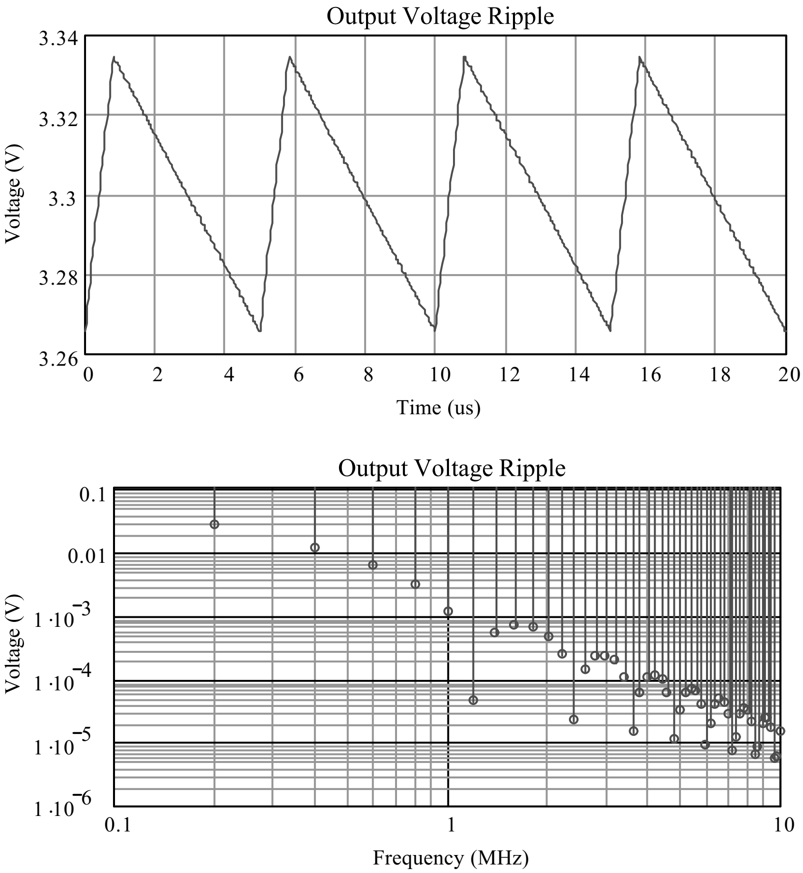

FIGURE 3.33 Waveform and spectrum of the output voltage of a 20 V to 3.3 V power supply at a load of 18 W.

Environment: Thermal, EMI/EMC

Looking at efficiency numbers can be misleading. Attention needs to be given to what the actual systems requirements are. In the case of a battery-operated system, efficiency may be of utmost importance. In this case, maximizing the time between battery replacements (or recharges) is a must. It may be particularly important to have some kind of ultra-low-power, stand-by mode to prevent the needless waste of power when the supply is not being used. A system running off a generator or a low impedance power source probably is not as driven by the actual efficiency, but by the overall power dissipation. For example, it would not be uncommon to see a supply operate at 90% efficiency at the full-specified load. However, if that load drops by a factor of 10, the efficiency may drop into the 60% range. The reason for this is that the power supply usually requires some fixed level of overhead power. The larger the percentage of the actual load that the overhead represents, the lower the efficiency. However, this is usually inconsequential. After all, if the source can provide the full load, it should have no problem powering a lighter load. Therefore, the efficiency at a light load may be irrelevant. The thermal loading of the box is what matters.

EMI/EMC can be divided into several categories: conducted emissions, radiated emissions, conducted susceptibility, and radiated susceptibility. A conducted emissions specification will define how much current can be put on the power lines for a given frequency. Figure 3.34 shows a typical input current waveform for a Buck derived SMPS. This particular case is a 20 V input, 3.3 V output, operating at 18 W.

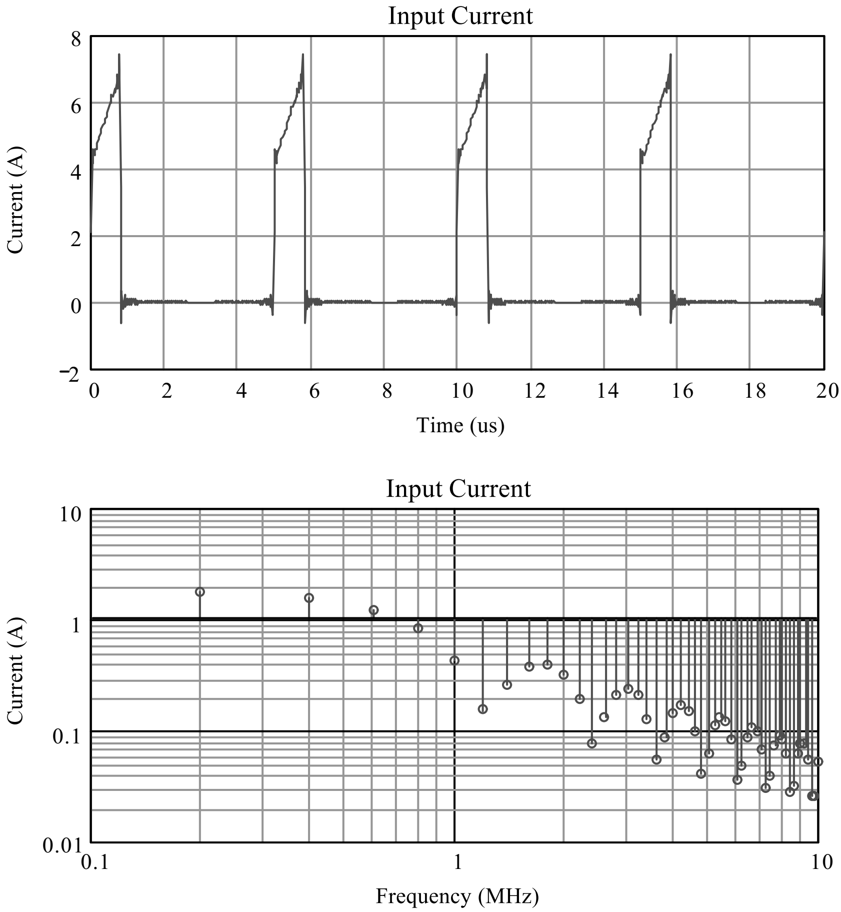

FIGURE 3.34 Waveform and spectrum of the input current of a 20 V to 3.3 V power supply at a load of 18 W.

The EMI filter must attenuate this current spectrum per the system specifications. A two-pole LC filter is often used as a method for controlling emissions, such as those shown in Fig. 3.34.

A radiated emissions requirement will define the level of E and H field that can be radiated from the unit under test. A SMPS can be a significant source of these types of emissions, because of the high $\frac{dV}{dt}$'S and $\frac{dI}{dt}$'S present. Typically speaking, if the conducted emissions are controlled, the radiated emission requirement is usually met. If necessary, shielded magnetics may be used to limit the H fields.

Conducted susceptibility defines the disturbance levels the power lines can be subjected to while the unit under test must continue to operate properly. Figure 3.35 shows an example of this kind of requirement.

In this case, the chart shows the RMS voltage that can be put on the power line for a range of frequencies. For example, the graph may start at 20 Hz, start to roll off at 2 kHz, and end at 50 kHz. (For a specific example see MIL-STD-461C.[2]) Many times, conducted susceptibility can be addressed by using an input-voltage-feed-forward term in the power supply control loop (this will be discussed in greater detail later).

Radiated susceptibility defines how much radiated E and H fields the unit under test can be exposed to and expected to operate properly. Ensuring EMC here is generally a mechanical housing issue.

Cost

Cost considerations are one of the most difficult areas to predict. So much of cost is dependent on the technology of the day. However, it can be safely stated that reducing size will increase both recurring and nonrecurring cost. Increasing efficiency will increase nonrecurring cost and may or may not increase

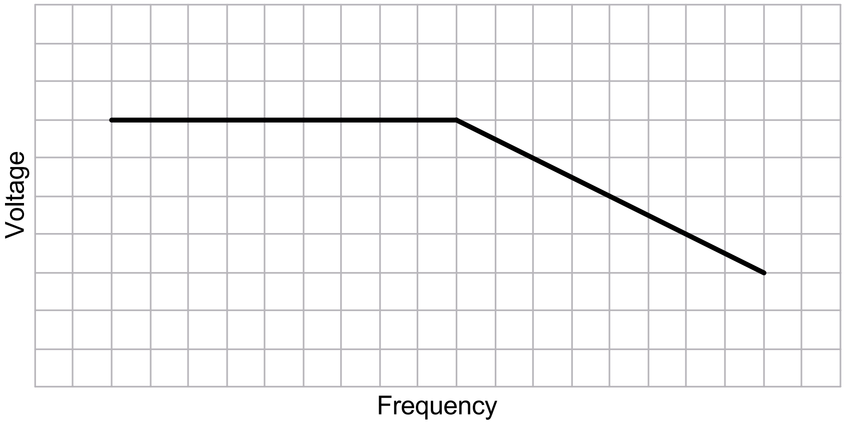

FIGURE 3.35 General conducted susceptibility curve.

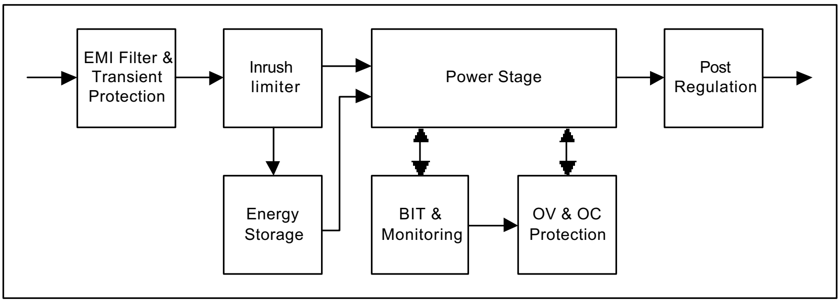

FIGURE 3.36 Power supply block diagram.

recurring cost. Typically speaking, the power inductor, bulk input and output capacitors, integrated circuits, and printed wiring boards will represent the majority of the cost.

Block Diagram

Figure 3.36 shows the basic blocks that make up a power supply. In reality, the blocks may be more integrated or arranged differently to accommodate various system requirements. For example, some systems have no requirement for energy storage or it is done in series with the power stage instead of in parallel.

The EMI (Electro Magnetic Interference) filter and transient protection serve to protect the power supply from excessive line voltages and to ensure EMC (Electro Magnetic Compatibility). Many power lines have short duration, high-voltage spikes (e.g., lightning). Designing a power supply so that all of the relevant components can withstand these elevated voltages is usually unnecessary and will likely result in reduced efficiency and increased size. Normally, the energy contained in such a burst is low enough that a transient suppressor can be used to absorb it.

The inrush limiter serves to limit peak currents that occur due to the rapid charging of the input capacitance during start up or "hot swap." Hot swap is a special start-up condition that occurs when a power supply is removed and reinserted without the removal of power. Once a power source is turned on, it can take several milliseconds before its voltage is up and good. This time reduces the peak current stresses due to the reduced $\frac{dV}{dt}$ that the capacitors see. If a power supply is plugged into a source that is already powered up, significantly higher inrush currents can result.

Some power systems require the output voltages to be unaffected by short duration power outages (less than 200 ms for the purposes of this paper). An energy storage module accomplishes this. If the

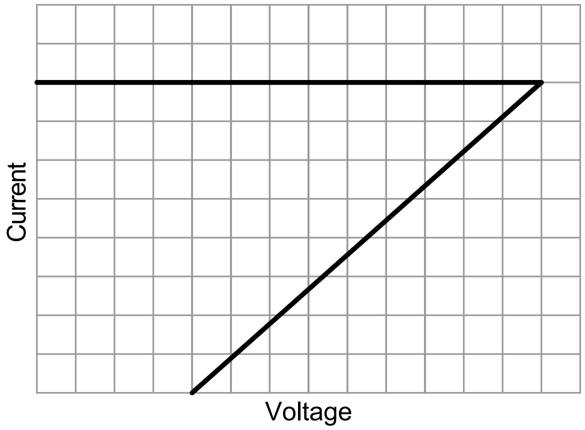

FIGURE 3.37 General fold-back current limit curve.

duration is longer, a UPS (Uninterruptible Power Supply) may be used. In either case, some type of energy storage element (e.g., battery, capacitor bank) is charged and in the event of a loss of primary power, the supply runs off of the stored energy. The power stage will be discussed in detail later.

The BIT and monitoring typically monitors for output overvoltage, under-voltage, and over-current. Overvoltage protection is necessary to limit the propagation of damage in a system. In order to do this, something needs to be done to clear the fault. Sometimes a series switch is used to remove power from the supply. If this is the case, the switch normally latches open and can only be reset by cycling the primary power on and off. Another common method is a crow bar. A fuse is placed in series with the power line. If an overvoltage is detected, a short is placed on the output of the supply that will force the fuse to open. The downside of doing this is that it becomes a maintenance item, however, it does a good job of guaranteeing that the overvoltage will be cleared.

Over-current is also used to prevent the propagation of damage. Two common ways of addressing this are a brick wall current limit or fold back. Limiting the maximum current that the supply can put out makes a brick wall limit. For example, if the current limit is set at 6 A, the supply will never put out more than 6 A, even if a dead short is placed on the output. This works well, but sometimes the thermal loading during current limit can be more than the system can handle. In such a case, a fold-back limit may be more appropriate. A typical characteristic is shown in Fig. 3.37.

Notice that when the current hits the maximum level and the output voltage begins to drop, the current limit point also falls. This works to reduce the power dissipation in the supply. Care needs to be used when working with fold-back limiting. It is possible to get the supply latched in a low voltage state when there is no fault.

Under-voltage is used to prevent erroneous operation. Often a signal is sent out to report an under-voltage condition. This signal can be used to hold a processor in reset or to inhibit another operation. Latching a supply off on an under-voltage is difficult, due to the danger that the supply may never start up!

In an effort to reduce size, many SMPS converters rely on a transformer as an easy way to produce multiple outputs. The basic idea is for one of the outputs to be tightly regulated through a control loop and the auxiliary outputs to track by transformer turns ratio. The problem is variations in the inductor DC Resistance (DCR), diode forward voltage drop, transformer coupling, load, temperature, etc., can all cause the auxiliary voltages to vary. This additional variation appears on top of the initial tolerance established by the control loop. The bottom line is the auxiliary windings may not have sufficient accuracy. If this is the case, there are post-regulation methods that can tighten the output tolerance with a minimal efficiency hit.

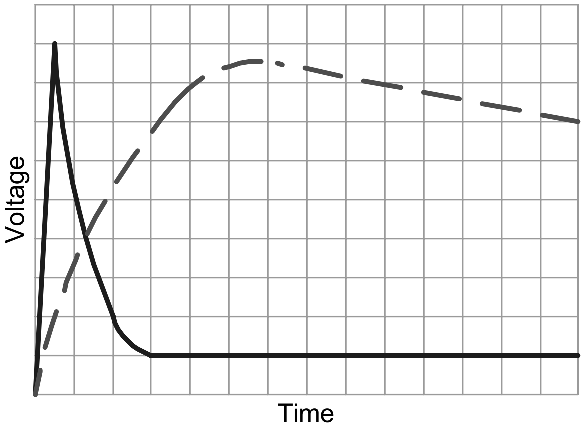

FIGURE 3.38 Typical start-up characteristics without soft start.

Power Supplies

Soft start is an area that can often be a problem. Figure 3.38 illustrates this problem. The solid trace is the error amplifier output voltage. This signal controls the output voltage level. The dashed trace is the output voltage.

When a power supply is commanded to turn on, the error amplifier will attempt to raise the output voltage as quickly as possible. Once the output voltage is in regulation, the error amplifier must slew quickly to avoid overshoot. The problem is compounded by the fact that stability considerations demand that the error amplifier be slowed down. This usually results in an overvoltage.

Active circuitry can be added to force the error amplifier's output to rise slowly to the level required for proper regulation. There are a variety of ways to accomplish this, however, it is essential that it be addressed in most systems.

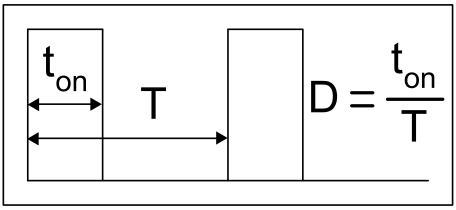

FIGURE 3.39 General duty cycle definition.

When talking about SMPS, it is customary to talk about duty cycle (herein referred to as D). This is the percentage of time that the main switch is on per cycle. The remainder of the cycle is often referred to as 1-D.

SMPS are often categorized according to the state of the inductor current. Figure 3.40 shows the inductor current for a simple buck converter in steady state operation. The first picture shows discontinuous conduction mode (DCM). This condition occurs when the inductor current goes to zero during the 1-D time. A special case exists when the inductor current just reaches zero. This case is shown in the second picture and is called critical conduction. The third picture shows continuous conduction mode (CCM). This condition occurs when the inductor current is greater than zero throughout the cycle.

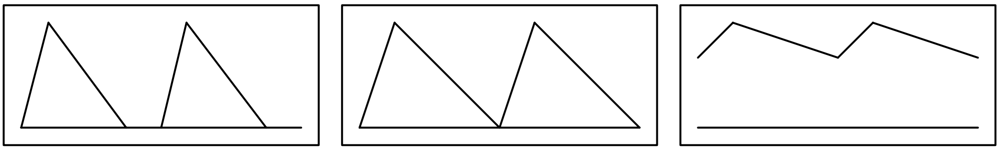

FIGURE 3.40 Basic inductor current waveforms (DCM, Critical, CCM).

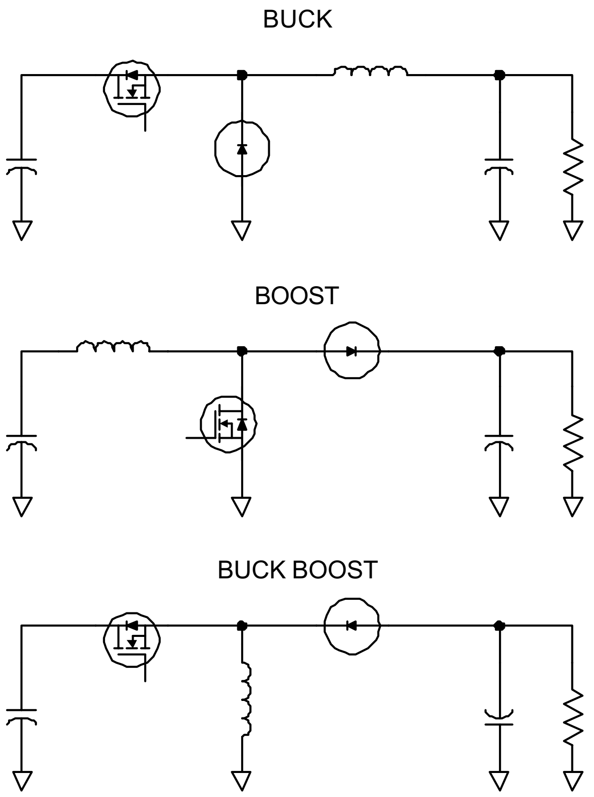

FIGURE 3.41 Basic non-isolated DC-DC converter power stage topologies.

Figure 3.41 shows the power stages for the basic non-isolated DC-to-DC switching power supply topologies. In each case, there are two switches (MOSFET, diode), an inductor, and an output capacitor. The input capacitor is shown to represent the low impedance input required for operation. The resistor on the output models the load, however, the load may not necessarily be resistive.

The CCM buck converter is the simplest to understand of the three approaches. It takes an input voltage and steps it down. Essentially, the MOSFET and diode create a square wave at the input to an LC filter. The high frequency content of the square wave is filtered off by the LC, resulting in a DC voltage across the output capacitor. Since the AC portion of the inductor current is the same as the output capacitor current, it is relatively easy to reduce the output ripple voltage by increasing the inductance. Figures 3.42 and 3.43 show the MOSFET and diode current, respectively. Please note that these waveforms have an identical shape for each of the three topologies.

The CCM boost converter operation is a little more complex. This time the MOSFET shorts the inductor to ground, allowing the inductor current to ramp up (Fig. 3.42 is the MOSFET current). When the MOSFET turns off, the inductor current continues to flow by turning the diode on (Fig. 3.43 is the diode current). In order for the inductor current to continue to flow, the output voltage must rise higher than the input.

The CCM buck-boost (or flyback) operates in an energy transfer mode. When the main MOSFET closes, the inductor charges. This charge action is shown in Fig. 3.42. Once the MOSFET opens, the current in the inductor continues to flow and turns the diode on, transferring charge to the output capacitor. In the non-coupled approach, this always results in a voltage inversion on the output. Figure 3.43 shows the diode current.

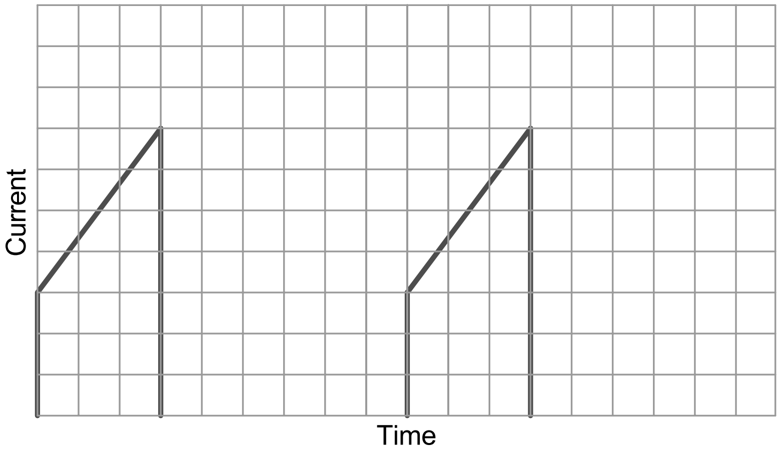

FIGURE 3.42 MOSFET current waveform for a SMPS.

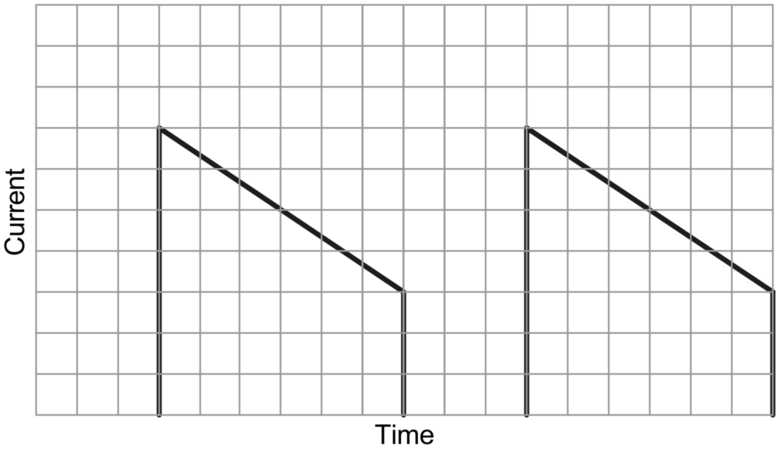

FIGURE 3.43 Diode current waveform for a SMPS.

The duty cycle required to generate a given output voltage is different in each topology and is dependent on the mode of operation. When in CCM, D is defined only in terms of input and output voltage. If in DCM, the relationship is more complex. The main point here is in CCM, the output voltage is independent of load. In DCM, it has the additional dependence on inductance, switch frequency, and load.

Duty Cycle	**Buck**	**Boost**	**Buck-Boost**
CCM	$\frac{V_{out}}{V_{in}}$	$\frac{V_{out} - V_{in}}{V_{out}}$	$\frac{V_{out}}{V_{out} - V_{in}}$
DCM	$V_{out} \cdot \sqrt{\frac{2 \cdot L \cdot f_s}{R \cdot V_{in} \cdot \left(V_{in} - V_{out}\right)}}$	$\frac{1}{V_{in}} \cdot \sqrt{\frac{2 \cdot L \cdot f_s \cdot V_{out} \cdot \left(V_{out} - V_{in}\right)}{R}}$	$\frac{V_{out}}{V_{in}} \cdot \sqrt{\frac{2 \cdot L \cdot f_s}{R}}$

FIGURE 3.44 Duty cycle expressions for Buck, Boost, and Buck-Boost converters.

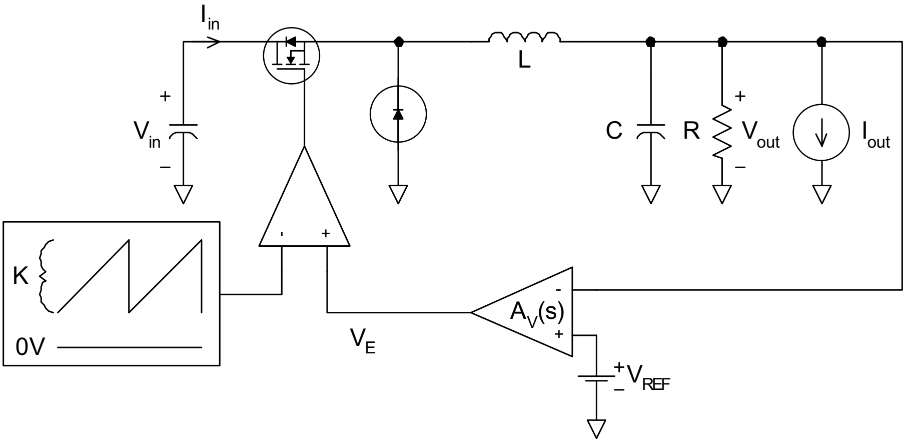

FIGURE 3.45 Basic non-isolated Buck with voltage mode control (VMC).

$$\begin{bmatrix} \frac{V_{in}}{I_{in}} & \frac{I_{in}}{I_{out}} \\ \frac{V_{out}}{V_{in}} & \frac{V_{out}}{I_{out}} \end{bmatrix} = \begin{bmatrix} \dfrac{s^2 + \frac{s}{R\cdot C} + \frac{1}{L\cdot C}\cdot 1 + \frac{v_{in}}{V_{RP}}\cdot A_v(s)}{\frac{d^2}{L}\cdot\left[s + \frac{1}{R\cdot C}\cdot 1 - \frac{v_{in}}{V_{RP}}\cdot A_v(s)\right]} & \dfrac{\frac{d}{L\cdot C\cdot R}\cdot\left[s\cdot L\cdot\frac{v_{in}}{V_{RP}}\cdot A_v(s) + R\cdot 1 + \frac{v_{in}}{V_{RP}}\cdot A_v(s)\right]}{s^2 + \frac{s}{R\cdot C} + \frac{1}{L\cdot C}\cdot 1 + \frac{v_{in}}{V_{RP}}\cdot A_v(s)} \\ \dfrac{\frac{d}{L\cdot C}}{s^2 + \frac{s}{R\cdot C} + \frac{1}{L\cdot C}\cdot 1 + \frac{v_{in}}{V_{RP}}\cdot A_v(s)} & \dfrac{\frac{-s}{C}}{s^2 + \frac{s}{R\cdot C} + \frac{1}{L\cdot C}\cdot 1 + \frac{v_{in}}{V_{RP}}\cdot A_v(s)} \end{bmatrix}$$

FIGURE 3.46 Voltage Mode Control (VMC) transfer functions.

Figure 3.45 shows one of the simplest standard methods for regulating the output voltage of a SMPS, voltage mode control (VCM). For simplicity, the Buck typology in CCM has been chosen.

A constant duty cycle applied to the MOSFET switch will produce a DC output voltage equal to the input voltage multiplied by duty cycle. If the duty cycle goes up, the output voltage will go up. If it goes down, the output voltage will also go down. The device driving the MOSFET is a comparator. The inputs to the comparator are a signal proportional to the output voltage (V_E) and a voltage ramp. If V_E goes up, D goes up and raises the output. Likewise, if V_E goes down, D goes down and the output falls. Some type of compensation is placed between the output and V_E to close the control loop (labeled $A_v(s)$ in the diagram). This compensation will control the stability and transient performance of the supply. Figure 3.46 contains the mathematical definition of several transfer functions for the above system.

These equations are based on a modeling technique called state space averaging.[3] Practically, they only apply to 1/10 to 1/3 of the switch frequency. They are based on an averaged linearized model of the power supply. They do not contain valid information about the large signal response of the system, only the small signal. When this method is applied to a DCM topology, the standard approach may need to be modified to obtain a more accurate result.[4]

If the voltage ramp that is fed into the comparator is proportional to the input voltage (generally referred to as input voltage feedforward), these equations simplify to the following:

$$\begin{bmatrix} \dfrac{V_{in}}{I_{in}} & \dfrac{I_{in}}{I_{out}} \\ \dfrac{V_{out}}{V_{in}} & \dfrac{V_{out}}{I_{out}} \end{bmatrix} = \begin{bmatrix} -\dfrac{R}{d^2} & \dfrac{\dfrac{d}{L\cdot C\cdot R}\cdot\left[s\cdot L\cdot A_V(s)\cdot K + R\cdot\left(1 + A_V(s)\cdot K\right)\right]}{s^2 + \dfrac{s}{R\cdot C} + \dfrac{1}{L\cdot C\cdot R}\cdot\left(1 + A_V(s)\cdot K\right)} \\ 0 & \dfrac{\dfrac{-s}{C}}{s^2 + \dfrac{s}{R\cdot C} + \dfrac{1}{L\cdot C\cdot R}\cdot\left(1 + A_V(s)\cdot K\right)} \end{bmatrix}$$

FIGURE 3.47 Voltage Mode Control (VMC) transfer functions with input voltage feedforward.

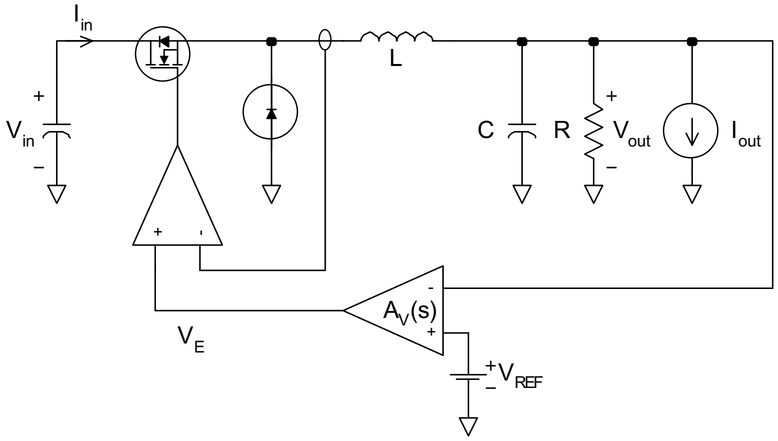

FIGURE 3.48 Basic non-isolated Buck with peak current mode control.

The most practical result of this simplification is that perfect input transient rejection is achieved. In other words, the output will not be perturbed by variations on the input. Please keep in mind that these equations are simplified and idealized. Perfect input voltage transient rejection is not possible. Some input variations will reach the output due to delay times, parasitic effects, etc.

Figure 3.48 shows one of the most popular ways to control a power supply, peak current mode control (CMC). The fundamental difference between CMC and VMC is that the ramp used for comparison to V_E is now directly proportional to the inductor current. This action creates an inherent feedforward term that serves to reject input voltage transients. However, it does not provide the ideal rejection that the VMC with input voltage feedforward does. This can be achieved by adding slope compensation. If a constant slope (exactly equal to ½V_{out}/L, or ½ the down slope) is added to the ramp, derived from the inductor current, the ideal input transient rejection is achieved.[5] Again, this is an ideal approximation. In reality, delay times and circuit parasitics will allow some of the input voltage variations to reach the output.

The following are the linearized state space averaged equations with the slope compensation equal to ½ the downslope of the inductor current. The technique used for modeling the current loop does not model the sub-harmonic oscillation, which is described widely in the literature. Models that are more complex are needed to predict this effect.[6] (Please note: R_s/N is the gain of the inductor current to the input of the comparator, f_s is the switching frequency of the converter.)

$$\begin{bmatrix} \dfrac{V_{in}}{I_{in}} & \dfrac{I_{in}}{I_{out}} \\[2ex] \dfrac{V_{out}}{V_{in}} & \dfrac{V_{out}}{I_{out}} \end{bmatrix} = \begin{bmatrix} -\dfrac{R}{d^2} & \dfrac{\dfrac{d}{R\cdot C}\cdot\dfrac{2\cdot L\cdot A_V(s)\cdot f_s\cdot N}{R_s}+d\cdot s+\dfrac{d}{L\cdot C}\cdot\left[1+d+2\cdot f_s\cdot L\cdot\dfrac{A_V(s)\cdot N}{R_s}-\dfrac{1}{R}\right]}{s^2+\dfrac{1}{R\cdot C}+2\cdot f_s\cdot s+\dfrac{1}{L\cdot C}\cdot\left[1+d+2\cdot f_s\cdot L\cdot\dfrac{A_V(s)\cdot N}{R_s}+\dfrac{1}{R}\right]} \\[4ex] 0 & \dfrac{\dfrac{-1}{C}\cdot s+2\cdot f_s}{s^2+\dfrac{1}{R\cdot C}+2\cdot f_s\cdot s+\dfrac{1}{L\cdot C}\cdot\left[1+d+2\cdot f_s\cdot L\cdot\dfrac{A_V(s)\cdot N}{R_s}+\dfrac{1}{R}\right]} \end{bmatrix}$$

FIGURE 3.49 Transfer functions of a basic non-isolated Buck with peak CMC and optimal slope compensation.

Conclusion

Simply put, a DC-to-DC power supply takes one DC voltage and puts out a different one. However, the process of getting there can be much more complex. Consideration needs to be given to the system and environment in which the supply is expected to operate (e.g., input voltage, EMI/EMC, energy hold up, output ripple, efficiency, thermal management, battery life, temperature, health monitoring, stability, transient response, etc.). These types of issues all impact the type of supply needed (e.g., linear, charge pump, SMPS) and how that supply needs to be configured for a given application.

As stated earlier, the trend for power seems to be toward lower output voltages at higher load currents. This trend is going to demand that power supply efficiency be maximized. This is always important, however, when the required output voltage drops, the detrimental effect of circuit parasitics (e.g., resistance, diode forward voltage drops) on efficiency becomes larger. This coupled with the fact that the load currents are not dropping, but rising, creates a greater thermal load on the system. In the case of microprocessors, this will likely result in dense hybridized power supplies that will be colocated with the processor.

References

1. Pressman, A. I., *Switching Power Supply Design,* McGraw-Hill, New York, 1991, 248–264.
2. MIL-STD-461C, Electromagnetic Emission and Susceptibility Requirements for the Control of Electromagnetic Interference, Department of Defense, The United States of America, August 4, 1986, Part 2, 13.
3. Mitchell, D. M., *Switching Regulator Analysis,* McGraw-Hill, New York, 1988, 51–73.
4. Sun, J., Mitchell, D. M., and Jenkins, D. E., Delay effects in averaged modeling of PWM converters, Power Electronic Specialists Conference, 1999. PESC99. 30th Annual IEEE, 1999.
5. Modeling, Analysis and Compensation of the Current-Mode Converter, Unitrode Application Note, U97, 1997, Section 3, 43–48.
6. Ridley, R. B., A New, Continuous-Time Model For Current-Mode Control, *IEEE Trans. on Power Electr.,* 6, 2, 271-280, April 1991.

3.6 Low Voltage/Low Power Microwave Electronics

Mike Golio

The development and manufacture of low voltage/low power RF and microwave electronics has been the subject of intense focus over the past few decades. The development of active circuits that consume lower power at lower voltage levels is consistent with the general trends of semiconductor scaling. From the simple relationship

$$E = V/d \qquad (3.116)$$

where E is the electric field, V is the voltage, and d is the separation distance, it can be seen that smaller devices (reduced d) require less voltage to achieve the same electric field levels. Since to first order it is electric field in a material that dominates electron transport properties, electric field levels must be preserved when devices are scaled. Therefore, for each reduction in critical dimension (gate length or base width) reductions in operating voltage have been realized.

Because semiconductor physics implies an inverse relationship between device size and required voltage level, and because transistor scaling has been a major driver for integrated circuit (IC) technology since the earliest transistors were introduced, the trend toward reduced power supply voltage has been ongoing since the beginning of the semiconductor industry. The explosive growth of portable wireless products, however, has brought a sense of urgency and technical focus to this issue. Portable product requirements have forced technologists to consider battery drain and methods to extend battery lifetime.

Since the total global volume requirements for digital ICs far exceeds the requirements for RF and microwave ICs, digital applications have been the primary drivers for most IC device technologies. The continuing advances of CMOS technology in particular have supported the low voltage/low power trend. Bipolar, BiCMOS, and more recently SiGe HBT developments have similarly supported this trend. For digital circuitry, the low voltage/low power trend is essentially without negative consequences. Each reduction in device size and power supply requirement has led to significant performance improvements. The reduced device size leads to smaller, lighter, cheaper, and faster circuits while the reduced voltage leads to reduced power consumption and improved reliability. The combination of these advantages provides the potential for higher levels of integration, which leads to the use of more complex and sophisticated architectures and systems.

For RF and microwave circuitry, however, the push toward lower voltage and lower power consumption is counter to many other radio requirements and presents challenges not faced by digital circuit designers. Although smaller, lighter, cheaper, and faster are generally desirable qualities for RF as well as digital applications, reduced voltage can produce negative consequences for RF circuit performance. In particular, reduced voltage leads to reduced dynamic range, which can be especially critical to the development of linear power amplifiers.

An imperative to develop and produce low voltage/low power RF products requires that every aspect of radio component development be considered. The ultimate success of a low voltage/low power RF product strategy is affected by all of the following issues:

- Materials technology (GaAs, Si, epitaxiy, implant, heterojunctions).
- Device technology (BJT, HBT, MESFET, MOSFET, HEMT).
- Circuit technology (matching and topology challenges for low voltage).
- Radio system design issues (impact of system and radio architecture on performance).

Motivations for Reduced Voltage

Commercial handheld products are clearly a significant driver for the low voltage/low power imperative. Reduced power consumption translates into longer battery lifetime and/or smaller, lighter products through reduction of battery size. Consumers value both of these attributes highly, which has led to the widespread acceptance of portable pagers, cell phones, and wireless personal area network products. An additional collateral benefit to reduced voltage operation is improved product reliability.

For vehicle-based products, the low power imperative is less compelling since battery size and lifetime issues are not relevant to these applications. Smaller and lighter electronics, however, are still valued in these applications. Power supplies represent a fixed payload that must be transported throughout the lifetime of the vehicle. In the case of jet aircraft, a single additional pound of payload represents tens of thousands of dollars of jet fuel over the life of the aircraft. A reduction in the size and weight of power supplies also represents payload that can be displaced with additional safety, communication, or navigation equipment. As in the case of handheld equipment, reduced power consumption will contribute to improved product reliability.

Even for many fixed site applications, reduced power consumption can provide benefits. Particularly in urban environments, base stations must be located in high-cost real estate areas (at the top of skyscrapers, for example). Rental of this space is often billed on a per square foot basis, so reduction in size carries some cost advantage. Increased reliability also leads to reduced maintenance costs.

Advantages of low voltage/low power RF circuitry are also significant for military applications. Supply line requirements during a military operation are often a determining factor in the outcome of battle. Transport vehicles are limited in number and capacity, so extended battery lifetime translates directly into decreased battlefield transport capacity requirements for battery resupply. This reduction in battery resupply transport requirements frees up valuable resources to transport additional lifesaving materials. The advantage is also directly felt by the foot soldier who is able to achieve greater mobility and/or additional electronic functionality (communication or navigation equipment).

As mentioned in the introduction, low voltage/low power trends have been almost without negative impact for most digital applications. Since most portable radio products are comprised of both digital ICs and RF parts, manufacturers would prefer to run all of the electronics from a single power supply. RF and microwave circuitry has had to follow the trend to low voltage, even when that trend brings on increasing challenges. This requirement to conform is exacerbated by the fact that the volume of digital circuitry required from semiconductor factories is far higher than the volume of RF circuitry. Applications that would benefit from high voltage operation comprise a nearly insignificant portion of the total semiconductor market so get little attention from most semiconductor manufacturers. The RF designer often has little choice but to use a low voltage IC process.

Semiconductor Materials Technology

Low voltage/low power operation requires improved efficiency, low parasitic resistance, low parasitic capacitance, and precise control of on-voltage. The selection of the semiconductor material impacts all of these characteristics.

Improvements in efficiency and reductions in parasitic resistance can be achieved by using materials that exhibit increased carrier mobility and velocity. Figure 3.50 plots the carrier velocity in bulk

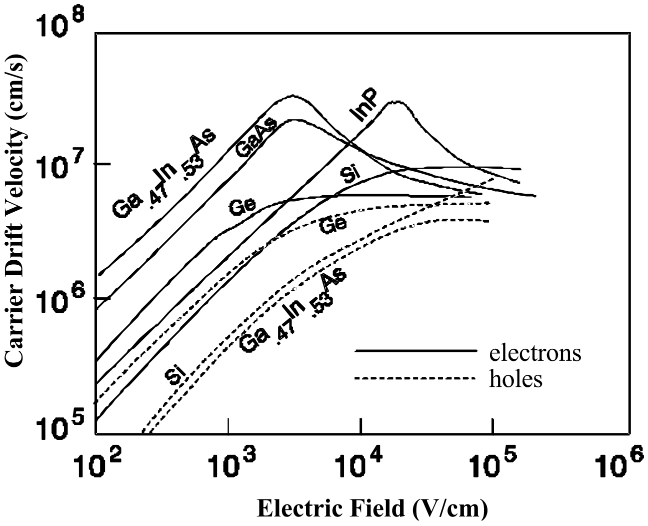

FIGURE 3.50 A plot of the carrier velocity in bulk semiconductor material as a function of the applied electric field for several commonly used semiconductors.

semiconductor material as a function of the applied electric field for several commonly used semiconductors. The carrier (electron or hole) mobility is given by

$$\mu_0 = \frac{v}{E} \qquad \text{for small E} \tag{3.117}$$

where v is the carrier velocity in the material and E is the electric field. The figure illustrates that III-V semiconductor materials such as GaAs, GaInAs, and InP exhibit superior electron velocity and mobility characteristics relative to silicon. For this reason, devices fabricated in III-V materials are expected to exhibit some advantages in achieving high efficiency and low parasitic resistance.

Low parasitic capacitance is also a desirable characteristic to insure low loss and minimal battery drain. Because GaAs and InP offer semi-insulating substrates, they exhibit performance advantages over the much more conductive, and hence poorer performing silicon substrates. Advanced materials strategies such as silicon-on-insulator offer potential advantages even over III-V materials, but at increased cost and complexity.

Precise control of on-voltage becomes increasingly important as supply voltages diminish. Low voltage operation means that the total voltage swing that can be realized by the RF signal is reduced. Bipolar transistors offer clear, significant advantages over FETs with respect to this characteristic since bipolar on-voltage characteristics are determined primarily by material band gaps while FET on-voltage characteristics are determined by material process parameters such as thickness and charge densities. When other considerations indicate that a FET structure is appropriate, however, heterostructure buffer layers improve the on-voltage control of FETs. Within either the FET or bipolar class of semiconductor devices, Silicon process control tends to be superior to Gallium Arsenide or other III-V process control.

Heterostructure semiconductor materials offer other potential advantages for low voltage design. In FET structures, heterostructure buffer layers provide greater carrier confinement. This can reduce substrate parasitics. Similarly, in bipolar transistors, heterostructures provide the potential to reduce unwanted minority carrier concentrations in critical portions of the device. In both the FET and bipolar case improved output conductance and greater linearity results from the use of properly designed heterostructures. Heterostructure technology also offers the potential of realizing high current and high breakdown simultaneously in a device by placing the right material in the right place.

From a purely technical performance perspective, the above discussion argues primarily for the use of III-V heterostructure devices. These arguments are not complete, however. Most commercial wireless products also have requirements for high yield, high volume, low cost, and rapid product development cycles. These requirements can overwhelm the material selection process and they favor mature processes and high volume experience. The silicon high volume manufacturing experience base is far greater than that of any III-V semiconductor facility. Silicon digital parts are routinely produced in volumes that dwarf total global III-V semiconductor device requirements. This digital experience is easily leveraged into the production of silicon RF and microwave parts, giving silicon materials a clear advantage in these areas.

No short cut for the development of experience and maturity with advanced material structures is available. As demand for diminishing power consumption RF products continues to grow, however, experience will be gained and the fundamental physical advantages of III-V heterostructure devices will lead to increasing presence in commercial wireless products.

Semiconductor Device Technology

Device technology decisions influence many of the same performance metrics that are affected by material decisions. Efficiency, parasitic resistance, and on-voltage control are all affected by the choice of device. Additional device considerations may depend on the particular circuit application being considered. For an oscillator application, for example, the 1/f noise characteristics of the transistor are likely to be critical to achieving the required circuit level performance. These same transistor characteristics may be of little interest for many other circuit applications.

TABLE 3.4 Semiconductor Devices are Evaluated against Several Important Device Characteristics for Portable Power Amplifer Applications

	MESFET/HEMT	III-V HBT	Si BJT	Si:Ge HBT	Power MOSFET (LDMOS)
			Low Voltage Related Characteristics		
Parasitic loss	Very good	Very good	Moderate	Moderate	Moderate
Single-polarity supply	No[a]	Yes	Yes	Yes	Yes
Power added efficiency	Excellent	Very good	Moderater	Moderate	Good for f<~2 GHz
Linearity	Excellent[b]	Very good	Moderate	Very good	Moderate
Power density	Moderate	Excellent	Very good	Excellent	Moderate
			General Characteristics		
Cost	Moderate to high	Moderate to high	Low to moderate	Moderate to high	Low to moderate
Maturity	Good	Good	Excellent	Moderate	Very good

[a] e-mode MESFETs and HEMTs do make use of single-polarity supply voltage, but at a cost of more difficult manufacturing and with a more limited dynamic range.

[b] MESFET devices manufactured using epi-taxial material (as opposed to ion-implanted) as well as HEMTs exhibit excellent linearity.

Table 3.4 evaluates most modern transistor technologies against a list of performance characteristics that are of interest for portable power amplifier applications. The performance metrics considered in the table include: parasitic loss, ability to easily use a single polarity power supply, power added efficiency, linearity, cost, and maturity. As is readily seen from the table, no particular device type excels in all areas and all devices exhibit at least some significant disadvantages. The relative values of each of the metrics are not equal and are not identical for all applications. Meeting linearity requirements, for example, is central to the power amplifier (PA) design process for many digitally modulated portable radios, while the linearity requirements for many analog radios is easily achieved and therefore less valued.

Parasitic loss is clearly important to reduce undesirable current drain. The III-V device technologies offer advantages over silicon technologies in this area because of their material advantages.

Single polarity power supplies are desirable since other radio components do not require a negative supply. The generation of a negative voltage required to bias a transistor adds to the parts count, cost, and current drain of the radio. HBTs, BJTs, and LDMOS parts have a clear advantage over conventional MESFETs and HEMTs in this area. Enhancement mode HEMTs offer a potential solution to this problem, but at a cost to manufacturing ability and dynamic range.

Linearity requirements are typically driven by government regulations to keep wireless products from interfering with each other. Linearity specifications are not consistent for all radio architectures and are sometimes the subject of erroneous discussions in the technical literature. The linearity of the Gummel plot [log(I_c) vs. log(I_b)] of a BJT or HBT, for example, is not equivalent or translated into RF linearity. It is also difficult to measure linearity and determine an absolute performance limit for a particular device. RF circuit tuning performed to optimize power, gain, or efficiency is not necessarily optimum for achieving high linearity. MESFETs fabricated using epitaxial material (as opposed to ion-implanted material) and HEMTs exhibit slight advantages in linearity over other devices. HBTs and BJTs have also demonstrated competitive linearity characteristics.

Once power, gain, and linearity specifications are met, efficiency often becomes the key distinguishing figure of merit for modern wireless power amplifiers. Improvements in PA efficiency are translated directly into reduced battery drain and longer battery lifetime. HEMTs hold certain advantages in this area while silicon BJTs have not produced efficiency values that are as competitive. Both LDMOS and HBT parts have also produced competitive efficiencies for certain applications.

High power density is desirable since it leads to reduced part size. Smaller devices not only reduce the size of the final product, but more importantly, reduce the cost of the device since more devices can be processed on a single wafer. HBTs demonstrate the highest power density with adequate breakdown characteristics of any wireless PA devices today. Ion-implanted MESFETs and LDMOS parts exhibit very low power densities compared to HBTs.

As in the case of material considerations, the technical characteristics of devices must be weighed against the cost and maturity requirements for wireless product development. Although cost is a primary driver for many radio applications today, it may be difficult to determine fabrication costs of emerging device technologies. For most parts utilized in high volume commercial applications, the cost of fabrication is not closely related to the purchase price for the part. The market supply and demand forces determine purchase price — the price is set as high as the market will bear. If the fabrication costs can be brought below the market price with a comfortable margin, the part will continue to be manufactured. If not, the part will be discontinued. Large semiconductor manufacturing companies may choose to subsidize new technologies for several years before deciding to discontinue them. Although difficult to quantify, cost is critical to the long-term success of a device. Silicon transistors have historically come with a cost advantage over III-V devices. The high volume experience of silicon fabrication facilities and greater maturity of the processes contribute significantly to the low cost advantage.

Examination of Table 3.4 and the discussion of the preceding paragraphs illustrate the difficulty in choosing the optimum device for low voltage/low power applications. Although important, the low voltage characteristics of the part are not the only characteristics that must be considered. No transistor is optimal for all requirements and each device choice carries implied compromises for the final product.

Although not included Table 3.4, the frequency of the application can also be a critical performance characteristic in the selection of device technology. Figure 3.51 illustrates the relationship between frequency of the application and device technology choice. Because of the fundamental material characteristics illustrated in Fig. 3.50, silicon technologies will always have lower theoretical maximum operation frequencies than III-V technologies. The higher the frequency of the application, the more likely the optimum device choice will be a III-V transistor over a silicon transistor. Above a certain frequency (labeled $f_{III\text{-}V}$ in Fig. 3.51), III-V devices dominate the transistors of choice, with silicon playing no significant role in the RF portion of the product. In contrast, below a certain frequency (labeled f_{Si} in Fig. 3.51) the cost and maturity advantages of silicon provide little opportunity for III-V devices to compete. In the transition spectrum between f_{Si} and $f_{III\text{-}V}$, the device technology is not an either/or choice, but rather silicon and III-V devices coexist. Although silicon devices are capable of operating above frequency f_{Si}, this operation is often gained at the expense of current drain. As frequency is increased above f_{Si} in the transition spectrum, efficiency advantages of gallium arsenide and other III-V devices provide competitive opportunities for these parts. The critical frequencies, f_{Si} and $f_{III\text{-}V}$ are not static frequency values. Rather, they are continually being moved upward by the advances of silicon technologies — primarily by decreasing critical device dimensions.

The process of choosing device technology is compounded further if higher levels of integration are implemented. Table 3.5 is a companion to Table 3.4. Again, several semiconductor device technologies are ranked in terms of desirable device characteristics. In contrast to Table 3.4, Table 3.5 considers characteristics of interest for integrated radio front-end applications. Although some characteristics are common to both tables, many are not. The evaluation of which technology is superior is likely to change when Table 3.5 characteristics are used to make a device technology choice instead of those listed in Table 3.4. The final column of Table 3.5 replaces LDMOS characteristics with those of CMOS. This change in device technologies that are considered for the application is appropriate and indicative of the problem of choosing an optimum device technology. LDMOS is not a likely device technology for most integrated radio applications while CMOS is not a viable power amplifier technology for most portable wireless products.

Circuit Design

RF circuit performance is not generally improved by the reduction of voltage or current. Virtually all types of circuits exhibit degradation in performance with reduced DC power. As an example, when either

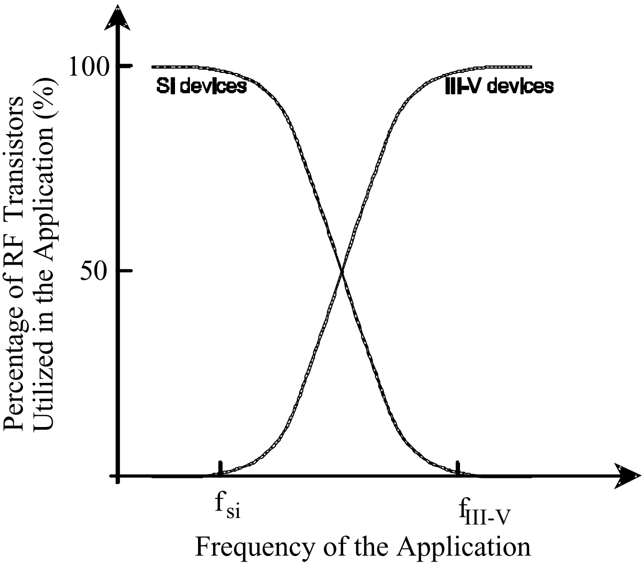

FIGURE 3.51 An illustration of the relationship between frequency of the application and device technology choice.

TABLE 3.5 Semiconductor Devices are Evaluated against Several Important Device Characteristics for Radio Integration Applications

	MESFET/HEMT	III-V HBT	Si BJT	Si:Ge HBT	CMOS
			Low Voltage Related Characteristics		
Single-polarity supply	No[a]	Yes	Yes	Yes	Yes
Turn-on voltage control	Moderate	Very good	Excellent	Excellent	Good
			General Characteristics		
Cost	Moderate to high	Moderate to high	Low to moderate	Moderate to high	Low
Maturity	Good	Good	Excellent	Moderate	Excellent
RF integration capability[b]	Very good	Very good	Excellent for f<3 GHz	Excellent for f<3 GHz	Excellent for f<2 GHz
Noise figure	Excellent	Very good	Good	Very good	Moderate
Phase noise	Poor	Good	Excellent	Excellent	Good

[a] e-mode MESFETs and HEMTs do make use of single-polarity supply voltage, but at a cost of more difficult manufacturing and with a more limited dynamic range.

[b] Comparing Silicon RF integration capability to III-V RF integration capability is difficult. Silicon process maturity allows for far higher levels of integration (in terms of numbers of transistors), but becomes of limited value above a few GHz because of the parasitics of the Si substrate.

current or voltage is reduced, a typical RF amplifier circuit will exhibit degradation of gain, linearity, and dynamic range.

If RF power levels are to be maintained, power amplifier load lines must be altered as supply voltage is reduced. Figure 3.52 illustrates the issue of load line and reduced voltage. The load line labeled “a” represents an optimum, idealized, high-efficiency load line for 6 volt power supply operation. The slope of the load line is determined primarily by the matching characteristics between the device and the load. As voltage is reduced from 6 volts to 3 volts, preservation of the slope of the load line would imply a reduction in power by ~3 dB (load line labeled “b”). Power is estimated to first order as the area underneath the load line and contained by the current-voltage plot. If power is to be maintained, the load line for the 3 volt supply case must be made steeper. This is indicated by load line “c.” With a steeper

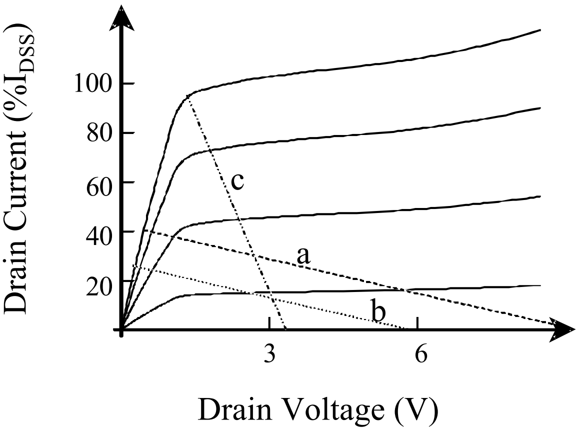

FIGURE 3.52 An illustration of the effect that lowering supply voltage has on power amplifier load line. Load line *a* represents an optimum high efficiency load line for 6-volt supply voltage. Load line *b* results from reducing the supply voltage to 3 volts without modifying the load line slope. The result of using load line *b* is a reduction in output power by more than 3 dB. Load line *c* represents a 3-volt load line where output power level is maintained. The result of using load line *c* is reduced efficiency from the load line *a* case.

load line, the average current along the load line (which represents DC current drain) is increased, while the intersection of the load line and the I-V curve is raised in voltage. When RF power levels are held constant, moving from load line "a" to load line "c" will tend to have the undesirable effect of reducing the amplifier efficiency.

To compensate for this problem, low voltage devices are designed to be larger than their higher voltage counterparts. Increased periphery devices provide higher peak currents required to maintain power level with decreased voltage. Larger devices, however, exhibit lower impedance that must be matched. Thus, low voltage power amplifier parts have high transformation ratios. Typical 1-4 Watt power amplifier parts for commercial portable wireless products exhibit output impedance of less than a few ohms. High Q matching elements provide some advantage in achieving required transformations but come at high cost and reduced integration.

As designers struggle to maintain power, gain, and efficiency with diminishing supply voltage, linearity must also be maintained. This requirement brings increasing importance to the use of linearization circuitry, feedforward, and pre-distortion schemes. Active bias control is also a valuable circuit design technique for many applications. Bias schemes that cause the transistor bias to rise with increased incident RF power help to provide needed maximum power while maintaining efficiency when lower power levels are needed.

Even for low power RF applications, bias control is critical when limited power supply voltage is available. The problem is compounded by device-to-device variability in current-voltage characteristics. Device stacking opportunities are limited and current control bias schemes, as opposed to voltage control schemes, are often preferred.

Radio and System Architecture

The ongoing communication technology revolution continues to demand greater bit transfer rates and higher bandwidths from wireless products. These demands lead to greater required linearity and higher frequencies of operation from the RF portion of these products. Broader bandwidth, higher frequency operation contributes to increases in battery drain creating a greater challenge to reduce operating voltage and power consumption.

Providing access to significantly increased information content also forces requirements for greater functionality causing a need for greater circuit complexity. Increasing functionality of the product is viewed as a potential method for establishing competitive advantage in an otherwise regulated environment. Built-in address books and more sophisticated displays are just two of the features appearing on new products. Since each new function requires power, this trend also works against the low power consumption imperative.

Other radio architecture trends, such as the movement toward digital modulation, can ease the low voltage/low power design issues. The improved signal-to-noise advantages offered by digital modulation results in reduced output power requirements. Digital modulation schemes can also provide the potential for pulsed (versus CW) operation, reducing power consumption even more.

Some proposed and emerging wireless systems will have a dramatic effect on the war on power consumption, which will change the requirements (and the technologies of choice) entirely.

Micro-cell telephone systems and small area Wireless Personal Area Networks (see Chapter 2) will dramatically reduce the battery requirements for these wireless systems. A smaller geographic cell size reduces the required RF output power of both subscriber and base station amplifiers. The required subscriber transmission power is reduced since the total distance that information must be transmitted is reduced. The base station power is also reduced for the same reason and because the total number of users that will be within the smaller cell is reduced. These reductions in required transmission power translate into dramatically reduced power consumption requirements. The power consumption of the RF portion of the radio becomes insignificant compared to the rest of the electronics. The device and material selection process can also become inconsequential. Although from a consumer point of view, this solution offers a significant advantage with no clear downside, the micro-cell infrastructure installation represents a significant investment for the service provider.

In contrast, satellite cellular systems (see Chapter 2) present significant challenges due to the high instantaneous output power requirements of the PA and low minimum noise figure of the front end LNA.

Although the choice of semiconductor material, type of transistor, and circuit topology all affect low voltage design, the radio architecture and system concept can dominate important low voltage performance specifications such as required battery size and battery lifetime.

Limits to Reductions in Voltage

There are some implications to the reduction of battery size and weight and that will impose serious constraints on the minimum useful operating voltage for portable RF products.

As discussed previously in this section, a primary driver for reduced voltage is the successful evolution of low voltage digital IC technologies. The advantage of running digital and RF circuitry from a single power supply is clear. Issues that limit DC power requirements for RF circuits, however, are fundamentally different than those that limit DC power requirements for associated digital circuits. Digital circuitry is required to store and analyze information that is encoded in a binary manner. This can be accomplished theoretically by the presence or absence of a small charge (even a single electron). Although practical considerations make a single electron memory improbable, and movement of even one electron into and out of storage still requires energy, it is clear that binary data can be manipulated with extremely small amounts of energy. The digital system requirements do not impose arbitrary power requirements on the strength of the digital signal.

In contrast to the digital case, minimum RF power requirements are implied by the radio system design. The RF signal must be transmitted and received across a specified distance or range of distances. Because power is lost in the radiation process, RF circuits must be able to handle power levels that are determined by the propagation media and transmitter-to-receiver separation. If 1 W of transmission power is required for the remote receiver to successfully detect the signal, then reductions in RF power below this level will cause the radio to fail. Unlike the digital situation where any discernable bit is as good as any other bit, the minimum RF transmission power must be maintained. For RF circuitry, increased efficiency and/or increased current must accompany a reduction in voltage.

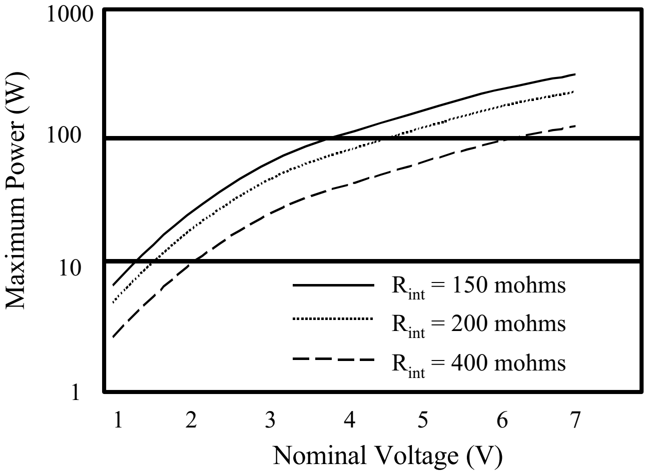

FIGURE 3.53 The maximum power capability for a battery as a function of nominal voltage and internal resistance. Maximum power for this figure is defined as the nominal voltage times the short circuit current.

Most portable units operate at efficiency levels within 2 to 10 percent of the theoretical limits. The implication of near theoretical efficiency is that voltage reductions necessarily involve increased current requirements. If voltage is halved, current must be doubled.

As battery current requirements are increased, the internal resistance becomes a limiting factor in the total power the battery is capable of delivering. For most applications, batteries have been considered ideal voltage sources, but as low voltage electronics trends continue, this assumption will begin to break down.

Figure 3.53 presents the maximum power capability for a battery as a function of nominal voltage and internal resistance. Maximum power for Fig. 3.53 is defined quite optimistically as the nominal voltage times the short circuit current. Although internal resistance is a function of the chemistry as well as the number and size of the battery cells, the values used in Fig. 3.53 are typical for nickel-metal-hydride and Li-ion batteries in common use for portable wireless products today. Further, the trends plotted in the figure will hold for all batteries, regardless of battery chemistry or size. It is clear from the figure that as battery voltages are reduced below approximately 2 volts, the maximum power available from them is reduced to levels on the order of that required from a portable cellular PA alone. When efficiency and other circuit requirements are accounted for, battery power levels are inadequate to support the product.

Summary

Reductions in voltage and power consumption are important to the development of portable wireless products that are smaller, lighter, and have long battery lifetimes. Low voltage supply requirements are also being driven by a need to make RF ICs compatible with digital ICs. Careful consideration and improvement in the choice of semiconductor material, device type, and circuit topology can help to achieve reductions in voltage. System design and choice of radio architecture also has impact on low voltage/low power electronics. These latter issues have potentially the largest impact on low voltage requirements. The ultimate limit to decreasing battery voltage, however, will be determined by transmitter power requirements and achievable internal resistance of batteries.

The discussion in this section has focused on commercial wireless products. These same trends, however, also describe military, satellite, or avionics communications products — both today and over the past several decades. All of these systems are being driven by the demand to move increasing amounts of information between points via a wireless system.

References

M. Golio, Low Voltage Electronics for Portable Wireless Applications: An Industrial Perspective, 1998 IEEE MTT-S International Microwave Symposium Digest, Baltimore, MD, IEEE Press, June 7–12, 1998.

M. Golio, Low Voltage Microwave Electronics, Santa Clara Valley IEEE MTT Short Course, Santa Clara, CA, Santa Clara Chapter IEEE, MTT, April 4, 1998.

M. Golio, Active Devices for Commercial Subscriber Power Amplifier Products, 1996 URSI Conference, Lille, France, 28 August–5 September 1996.

D. Halchin, M. Golio, C. Farley, Issues with Measurements, Design, and Modeling of Devices for Wireless Applications, Wireless Conference, Sedona, AZ, September 30, 1996.

E. Pettenpaul, New Horizons for the Microwave Business in Europe, *Proceedings of the European Microwave Conference*, Madrid, Spain, 1–5, 1993.

Y. Kitahara, Personal Mobile Communications in Microwave Band, *Proceedings of the European Microwave Conference*, Madrid, Spain, 94–95, 1993.

R. C. Dixon, Portable Communications Needs and No-Nos, *GaAs IC Symposium Digest*, 29–32, 1993.

P. Briere, E. Perea, O. de Saint Leger, System and Technology Aspects of Future Digital Cellular Phones in Europe, *GaAs IC Symposium Digest*, Monterey, CA, 33–36, 1991.

E. Pettenpaul, L. Scharf, K.J. Schopf, Enhanced GaAs Device Concepts for the New Digital Mobile Communication Systems, *Proceedings of the European Microwave Conference*, Madrid, Spain, 132–134, 1993.

G. P. Donzelli, GaAs versus Silicon Technology, *Proceedings of the European Microwave Conference*, Madrid, Spain, 110–112, 1993.

C. Kermarrec, G. Dawe, T. Tewksbury, B. Meyerson, D. Harame, M. Gilbert, SiGe Technology: Applications to Wireless Digital Communications, *IEEE Microwave and Millimeter-Wave Monolithic Circuits Symposium Digest,* San Diego, CA, 1–4, 1994.

M. Hirayama, K. Honjo, M. Obara, N. Yokoyama, HBT IC Technologies and Applications in Japan, *GaAs IC Symposium Digest*, 3–6, 1991.

D. Whipple, The CDMA Standard, *Applied Microwave & Wireless,* 6, 24–37, Spring 1994.

M. Sullivan, Wireless LANs, Status and Future, *Applied Microwave & Wireless,* 6, 54–61, Spring 1994.

Low Voltage Silicon Bipolar Transistors, *Microwave Journal,* 37, 126–128, June 1994.

T. Yamaguchi, T. Archer, R. Johnston, J. Lee, Process and Device Optimization of an Analog Complementary Bipolar IC Technology with 5.5-Ghz fT PNP Transistors, *IEEE Trans. Electron. Devices,* 41, 1019–1026, June 1994.

D. Vook, T. Kamins, G. Burton, P. Vande Voorde, H. Wang, R. Coen, J. Lin, D. Pettengill, P. Yu, S. Rosner, J. Turner, S. Laderman, H-S. Fu, A. Wang, Double-Diffused Graded SiGe-Base Bipolar Transistors, *IEEE Trans. Electron. Devices,* 41, 1013–1018, June 1994.

V. Nair, R. Vaitkus, D. Scheitlin, J. Kline, H. Swanson, Low Current GaAs Integrated Down Converter for Portable Communication Applications, *GaAs IC Symposium Digest*, IEEE Press, 41–44, 1993.

V. Nair, Low Current Enhancement Mode MMICs for Portable Communication Applications, *GaAs IC Symposium Digest*, IEEE Press, 67–70, 1989.

K. Kanazawa, M. Kazumura, S. Nambu, G. Kano, I. Teramoto, A GaAs Double-Balanced Dual-Gate FET Mixer IC for UHF Receiver Front-End Applications, *IEEE Trans. Microwave Theory & Techn.*, MTT-33, 1548–1553, December 1985.

O. Ishikawa, Y. Ota, M. Maeda, A. Tezuka, H. Sakai, T. Katoh, J. Itoh, Y. Mori, M. Sagawa, M. Inada, Advanced Technologies of Low-Power GaAs ICs and Power Modules for Cellular Telephones, *GaAs IC Symposium Digest*, IEEE Press, 131–134, 1992.

P. Philippe, M. Pertus, A 2 Ghz Enhancement Mode GaAs Down Converter IC for Satellite TV Tuner, *Proceedings of the European Microwave Conference*, Madrid, Spain, 61–64, 1993.

H. Heaney, F. McGrath, P. O'Sullivan, C. Kermarrec, Ultra Low Power Low Noise Amplifiers for Wireless Communications, *GaAs IC Symposium Digest*, IEEE Press, 49–51, 1993.

J.O. Plouchart, H. Wang, M. Riet, HBT Monolithic Integrated Phase Locked Oscillator for DCS 1800 Mobile Communications, *Proceedings of the European Microwave Conference*, Madrid, Spain, 834–836, 1993.

M. Nakatsugawa, Y. Yamaguchi, M. Muraguchi, An L-Band Ultra Low Power Consumption Monolithic Low Noise Amplifier, *GaAs IC Symposium Digest*, IEEE Press, 45–48, 1993.

K. R. Cioffi, Monolithic L-Band Amplifiers Operating at Milliwatt and Sub-Milliwatt DC Power Consumption, *IEEE Microwave and Millimeter-Wave Monolithic Circuits Symposium Digest,* Albuquerque, NM, 9–12, 1992.

H. Takeuchi, M. Muraoka, T. Hatakeyama, A. Matsuoka, M. Honjo, S. Miyazaki, K. Tanaka, T. Nakata, A Si Wide-Band MMIC Amplifier Family for L-S Band Consumer Product Applications, *IEEE Microwave Theory and Techniques Symposium Digest,* 1283–1284, 1991.

Y. Imai, M. Tokumitsu, A. Minakawa, Design and Performance of Low-Current GaAs MMICs for L-Band Front-End Applications, *IEEE Trans. Microwave Theory & Techn.*, 39, 209–214, February 1991.

Y. Imai, M. Tokumitsu, A. Minakawa, T. Sugeta, M. Aikawa, Very Low-Current and Small-Size GaAs MMICs for L-Band Front-End Applications, *GaAs IC Symposium Digest*, IEEE Press, 71–74, 1989.

W. Baumberger, A Single Chip Rejecting Downconverter for the 2.44 Ghz Band, *GaAs IC Symposium Digest*, 37–40, 1993.

B. Khabbaz, A. Douglas, J. DeAngelis, L. Hongsmatip, V. Pelliccia, W. Fahey, G. Dawe, A High Performance 2.4 Ghz Transceiver Chip-Set for High Volume Commercial Applications, *IEEE Microwave and Millimeter-Wave Monolithic Circuits Symposium Digest,* San Diego, CA, 11–14, 1994.

M. Wang, M. Carriere, P. O'Sullivan, B. Maoz, A Single-Chip MMIC Transceiver for 2.4 Ghz Spread Spectrum Communication, *IEEE Microwave and Millimeter-Wave Monolithic Circuits Symposium Digest,* San Diego, CA, 19–22, 1994.

J. Moniz, B. Maoz, Improving the Dynamic Range of Si MMIC Gilbert Cell Mixers for Homodyne Receivers, *IEEE Microwave and Millimeter-Wave Monolithic Circuits Symposium Digest,* San Diego, CA, 103–106, 1994.

R. Herman, A. Chao, J. Deichsel, C. Mason, A. McKay, Highly Integrated Mixed-Signal L-Band Configurable Receiver Array, *IEEE Microwave and Millimeter-Wave Monolithic Circuits Symposium Digest,* San Diego, CA, 23–26, 1994.

T. Apel, E. Creviston, S. Ludvik, L. Quist, B. Tuch, A GaAs MMIC Transceiver for 2.45 Ghz Wireless Commercial Products, *IEEE Microwave and Millimeter-Wave Monolithic Circuits Symposium Digest,* San Diego, CA, 15–18, 1994.

R. Meyer, W. Mack, A 1-Ghz BiCMOS RF Front-End IC, *IEEE J. of Solid-State Circuits,* 29, 350–355, March 1994.

K. Sakuno, M. Akagi, H. Sato, M. Miyauchi, M. Hasegawa, T. Yoshimasu, S. Hara, A 3.5W HBT MMIC Power Amplifier Module for Mobile Communications, *IEEE Microwave and Millimeter-Wave Monolithic Circuits Symposium Digest,* San Diego, CA, 63–66, 1994.

Y. Ota, M. Yanagihara, T. Yokoyama, C. Azuma, M. Maeda, O. Ishikawa, Highly Efficient, Very Compact GaAs Power Module for Cellular Telephone, *IEEE Microwave Theory and Techniques Symposium Digest,* Albuquerque, NM, 1571–1520, 1992.

M. Maeda, M. Nishijima, H. Takegara, C. Adachi, H. Fujimoto, Y. Ota, O. Ishikawa, A 3.5 V, 1.3 W GaAs Power Multi Chip IC for Cellular Phone, *GaAs IC Symposium Digest*, Atlanta, GA, 53–56, 1993.

A. Herrera, E. Artal, E. Puechberty, D. Masliah, High Efficiency, Highly Compact L-Band Power Amplifier for DECT Applications, *Proceedings of the European Microwave Conference*, Madrid, Spain, 155–157, 1993.

S. Makioka, K. Tateoka, M. Yuri, N. Yoshikawa, K. Kanazawa, A High Efficiency GaAs MCM Power Amplifier for 1.9 Ghz Digital Cordless Telephones, *IEEE Microwave and Millimeter-Wave Monolithic Circuits Symposium Digest,* San Diego, CA, 51–54, 1994.

T. Kunihisa, T. Yooyama, H. Fujimoto, K. Ishida, H. Takehara, O. Ishikawa, High Efficiency, Low Adjacent Channel Leakage GaAs Power MMIC for Digital Cordless Telephone, *IEEE Microwave and Millimeter-Wave Monolithic Circuits Symposium Digest,* San Diego, CA, 55–58, 1994.

T. Yoshimasu, N. Tanaba, S. Hara, An HBT MMIC Linear Power Amplifier for 1.9 Ghz Personal Communications, *IEEE Microwave and Millimeter-Wave Monolithic Circuits Symposium Digest,* San Diego, CA, 59–62, 1994.

P. O'Sullivan, G. St. Onge, E. Heaney, F. McGrath, C. Kermarrec, High Performance Integrated PA, T/R Switch for 1.9 Ghz Personal Communications Handsets, *GaAs IC Symposium Digest*, Albuquerque, NM, 33–35, 1993.

S. Dietsche, C. Duvanaud, G. Pataut, J. Obregon, Design of High Power-Added Efficiency FET Amplifiers Operating with Very Low Drain Bias Voltages for Use in Mobile Telephones at 1.7 Ghz, *Proceedings of the European Microwave Conference*, Madrid, Spain, 252–254, 1993.

J. Griffiths, 3 Volt MMIC Power Amplifier for Wireless Phones, *Applied Microwave & Wireless,* 6, 38–53, Spring 1994.

K. Inosako, K Matsunaga, Y. Okamoto, M. Kuzuhara, Highly Efficient Double-Doped Heterojunction FET's for Battery-Operated Portable Power Applications, *IEEE Electron. Device Letters,* 15, 248–250, July 1994.

M. Golio, Large Signal Microwave Device Modeling Challenges for High Volume Commercial Communications Applications, *Workshop Proceedings of the European Microwave Conference*: *Advanced Microwave Devices, Characterisation and Modelling*, Madrid, Spain, 30–33, 1993.

R. Darling, Subthreshold Conduction in Uniformly Doped Epitaxial GaAs MESFETs, *IEEE Trans. Electron Devices,* 36, 1264–1273, July 1989.

M. Golio, Characterization, Parameter Extraction and Modeling for High Frequency Applications, *Proceedings of the European Microwave Conference*, Madrid, Spain, pp. 69-72, 1993.

J. Pedro, J. Perez, A Novel Non-Linear GaAs FET Model for Intermodulation Analysis in General Purpose Harmonic-Balance Simulators, *Proceedings of the European Microwave Conference*, 714–716, 1993.

T. Yoshimasu, K. Sakuno, N. Matsumoto, E. Suematsu, T. Tsukao, T. Tomita, Low Current GaAs MMIC Family with a Miniaturized Band-Stop Filter for Ku-Band Broadcast Satellite Applications, *GaAs IC Symposium Digest*, 147–150, 1991.

N. Shiga, T. Sekiguchi, S. Nakajima, K. Otobe, N. Kuwata, K. Matsuzaki, H. Hayashi, MMIC Family for DBS Downconverter with Pulse-Doped GaAs MESFETs, *GaAs IC Symposium Digest*, 139–142, 1991.

C. Caux, P. Gamand, M. Pertus, A Cost Effective True European DBS Low Noise Converter, *GaAs IC Symposium Digest*, 143–145, 1991.

K. W. Kobayashi, R. Esfandiari, M. Hafizi, D. Streit, A. Oki, M. Kim, GaAs HBT Wideband and Low Power Consumption Amplifiers to 24 Ghz, *IEEE Microwave and Millimeter-Wave Monolithic Circuits Symposium Digest,* 85–88, 1991.

J. M. Golio, M. Miller, J. Staudinger, W.B. Beckwith, E.N. Arnold, *Microwave MESFETs and HEMTs*, Norwood, MA: Artech House, 1991.

R. A. Pucel, D. Masse, R. Bera, Performance of GaAs FET Mixers at X-band, *IEEE Trans. Microwave Theory & Techn*., MTT-24, 351–360, June 1976.

S. Maas, B. Nelson, D. Tait, Intermodulation in Heterojunction Bipolar Transistors, *IEEE Microwave Theory and Techniques Symposium Digest,* IEEE Press, 91–93, 1991.

M. Kim, A. Oki, J. Camou, P. Chow, B. Nelson, D. Smith, J. Canyon, C. Yang, R. Dixit, B. Allen, 12–40 Ghz Low Harmonic Distortion and Phase Noise Performance of GaAs Heterojunction Bipolar Transistors, *GaAs IC Symposium Digest*, 117–120, 1988.

W. Liu, T. Kim, P. Ikalainen, A. Khatibzadeh, High Linearity Power X-Band GaInP/GaAs Heterojunction Bipolar Transistor, *IEEE Electron. Device Letters,* 15, 190–192, June 1994.

3.7 Productivity Initiatives

Mike Golio

Productivity initiatives have become a significant part of the engineering design system utilized by the RF/microwave industry. There are an abundance of these initiatives that have modified and molded the microwave engineer's methodologies and work habits in the past 10 to 15 years. The popularity of these initiatives is so pervasive among companies that an entire industry of consultant trainers has emerged to help companies launch and implement successful programs to improve corporate efficiency and performance. Popular initiatives include:

- Design for Manufacturability
- Design to Cost
- Total Customer Satisfaction
- Six Sigma
- Just-In-Time Delivery
- Total Cycle Time Reduction
- Total Quality Management
- Lean Electronics
- Best Place to Work

All of the initiatives are designed to improve productivity — and therefore profit. Some initiatives focus primarily on the use of new tools and metrics (such as Six Sigma) to improve manufacturing productivity. Just-In-Time initiatives focus on inventory reduction and procurement efficiency. Initiatives like Lean Electronics represent a collection of productivity techniques coupled together by an underlying theme of efficiency. Finally, some initiatives focus primarily on direct alteration of the attitudes and perceptions of the workforce toward their customers and coworkers (such as Total Customer Satisfaction and Best Place to Work). To some extent, all major productivity initiatives are culture-changing exercises.

Although it is not possible within a single article to discuss (or even list) all of the specific productivity initiatives that have invaded the workplace, it is possible to discuss some of the fundamental engineering principles and tools that lead to efficient engineering practice.

Customizing Initiatives for the Organization

Improved productivity and profit are undeniably compelling reasons for a company to undertake the task of changing its culture. But the successful implementation of a productivity initiative must be tailored to the specific organization. Implementation of any successful initiative must account for: 1) the market and market drivers for the organization undergoing change, and 2) the existing culture of that organization.

Figure 3.54 illustrates how particular microwave/RF markets affect the primary focus and development time constants of the technology development process. The shift of technical focus is dramatic as technologies move from a proof-of-concept to a high volume manufacturing stage. A similarly dramatic shift in the acceptable development time frames is associated with this maturity process.

RF and microwave technology typically travels a maturation path that starts in a university, industry, or government R&D lab with a feasibility demonstration. These proof-of-concept efforts sometimes take decades or even lifetimes to achieve. This type of work is focused primarily on the development of a one-time proof-of-concept demonstration. Although the advocates of the new technology may have visions of high volume manufacturing at a future date, the initial goal is simply to prove that the idea has potential merit.

Promising technologies with demonstrated proof-of-concept merit typically migrate into low volume, high performance applications. Often government/military needs drive these early applications. In this stage of maturity, the research and development is likely to be focused on optimization of performance and on reliability issues. Development time frames often run for several years.

As success is reached at each stage of technology development, new applications emerge with different technical foci and shorter acceptable development times. Communications Satellites and Avionics are example applications that form the center of the technology maturation chart of Fig. 3.54. Manufacturing volumes for these applications are still low enough that nonrecurring engineering costs (NRE) usually dominate the technical focus of the development process, which can still run in time frames of years.

Applications such as automotive, industrial, and wireless base station electronics represent the next stages of typical technology maturation. These applications often support high enough volumes to bring increased focus onto development schedule duration and recurring costs (RE).

Portable wireless products represent an application that is dominated by manufacturability issues and reduced cycle times. Product development cycles are typically measured in months while cost, yield, and factory throughput dominate the focus of the technical workforce.

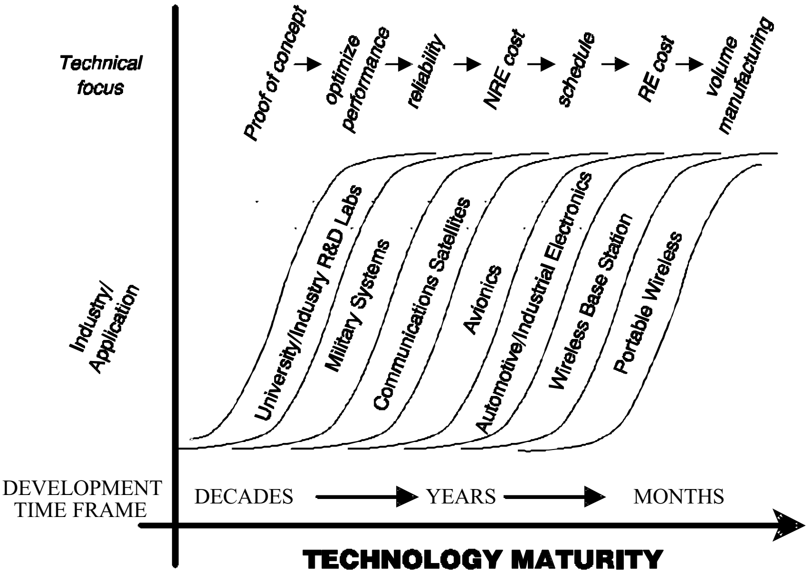

FIGURE 3.54 An illustration of a typical maturation path for emerging RF technologies. At each phase of the maturity process, technical focus and development time frames are radically different. Productivity initiatives should account for these differences if they are to be implemented successfully.

A successful *productivity initiative* needs to address the primary technical focus and development time constants of the industry where it is being applied. From the discussion above, it is clear that any profit-driven productivity initiative needs to account for the unique constraints of the organization's target market. Initiatives with primary focus on statistical process control and high manufacturing yields may be critical to an organization working in the portable wireless industry, but have very little applicability to a research and development lab with a charter to perform long-term, high-risk research of new technologies.

Even within a given market segment, application of productivity initiatives must be customized to specific organizations. Different countries, regions of a country, companies, and even organizations within a large company all have different roles, different cultures, and different levels of productivity awareness and maturity. Since these initiatives are culture-changing processes, it is important that the existing culture is understood so that appropriate steps are taken to mature the culture toward the ultimate goal. An organization that has no quality and productivity metrics in place may not be ready to take the same steps toward a fully integrated, customer-focused, quality manufacturing system that an organization that has already spent several years moving down that path should take.

Productivity and Marketing

For most product development applications, the engineering process begins with marketing. Productivity initiatives that focus on customer awareness and customer relationships (Total Customer Satisfaction, for example) should address some of the marketing issues engineers will be concerned with. Marketing establishes the groundwork for design for manufacturability efforts.

Prior to any significant engineering planning it is important to identify the required sales volumes, cost targets, and acceptable development schedule (i.e., required time-to-market).

As an example, assume that an 18 GHz radio product is scheduled to go into production in 18 months with a cost target of $100/unit at a quantity of 100,000 units per month. The targeted time-to-market dictates that little new technology will be developed. In only 18 months, there will barely be time to identify a design, find components, assemble and align a working breadboard, and develop a production manufacturing and test plan consistent with an existing production facility. The limit placed on the amount of technology development that is feasible in such a project extends not only to the radio components, but also to the manufacturing and test technologies needed in production. An analysis of the quantity requirements (assuming two shifts working 5 days a week) leads to the result that the radio product must be manufactured at the rate of approximately one unit every 12 seconds. Clearly, little tuning or manual alignment will be acceptable. The quantity and cost targets dictate an automated manufacturing and test environment. Locating off-the-shelf parts available in the quantities required will be critical. Assuming a reasonable product life cycle, the recurring cost of manufacturing dominates this engineering effort. Nonrecurring cost of development is likely to be insignificant as compared to the goal of achieving the required development cycle time.

In contrast, if a similar radio product is to be produced in quantity 4 for an R&D demonstration as part of a three-year research project, the entire engineering approach changes. Optimum technical performance may be the primary focus of the effort. A premium is likely to be paid (or even required) for utilizing new technologies, new architectures, or new methodologies. Recurring manufacturing cost has little meaning while nonrecurring cost is the determining factor in the profitability of the program. Delays in schedule of months or years may be acceptable provided the innovation is great enough.

When optimizing for profit, nonrecurring costs, recurring costs, performance, and schedule are all part of the formula. The engineering process must compare the options to the marketing requirements. In consumer applications where time-to-market is critical, a rapidly developed, nonoptimized design may provide enough performance at a low enough cost to succeed. The critical questions for these cases may be, "How long will it take to achieve the minimum performance?" and "How long will it take to achieve the lowest cost?" In general, speed and technology insertions are inversely related.

Planning and Scheduling

Although planning and scheduling are not explicitly addressed in many productivity initiatives, they are the foundation for all engineering efforts. Without good planning, other productivity efforts can produce only modest success at best. Planning and scheduling are also required for the development of important productivity metrics.

Planning and scheduling, are the processes of deciding in advance what work is required and when and where the work will be performed. The scheduling process seeks estimates of the time to do the work, identification of the organizations or people who will perform the work, and identification of the required resources.

Many scheduling tools, methodologies, and representations can be used to perform the planning and scheduling functions. Gantt systems are perhaps the most common scheduling tools used in engineering. Regardless of the methodology, the baseline schedule represents the yardstick against which actual work is measured. If improvements in engineering productivity are to be quantified, it is critical that planning and scheduling be done as accurately as possible.

Table 3.6 lists several desirable characteristics for a good engineering planning and scheduling process.

TABLE 3.6 Desirable Characteristics of a Good Engineering Planning and Scheduling Process

Characteristic of Schedule and Planning Process	Comments
Formal process	Involve representation from all organizations that will be required to release the product
Simple process	Should be simple enough to encourage use by many contributors
Work tasks	Work should be broken down into tasks small enough to establish estimates of the level of effort
Meaningful objectives	Schedule must identify meaningful, measurable milestones that mark the end of each work task

The planning process should be a formal, concise process that involves representation from all organizations that will contribute directly to the final release of the product. This will include not only project managers and engineers, but may also require representation from manufacturing, systems engineering, quality assurance, reliability, marketing, contracts, and sales.

Simplicity is another valued characteristic of a good planning and scheduling process. The scheduling system needs to be used and updated by a large number of people. Complexity or confusion should not discourage use of the system. Unneeded complexity will also add cost to the process. The scheduling system should provide the required information at the lowest cost.

All schedules start from the documentation of clearly identified objectives. A well-defined project plan expressed in a work breakdown structure (WBS) can accomplish this. The WBS should be comprised of work tasks that end with the completion of a meaningful milestone. The work tasks that comprise the WBS must be developed with enough understanding to establish accurate estimates of the time and effort required to complete the task.

Establishing meaningful milestones is a critical task for effective scheduling. A milestone that does not represent a meaningful product, accomplishment, or event to the performer is of very limited value.

Design

The goal of design is to develop a blueprint for successful production. From this perspective, design teams can be viewed as a factory whose product output is a production blueprint. The design factory must develop a road map to convert intellectual property, labor, and/or materials into a competitive product. This description of design is far broader than the conventional view of design as a process that produces an electrical circuit description or demonstration breadboard. Whether the product is a research report or a commercial wireless telephone, this design factory concept can be used to some advantage.

As in the case of other manufacturing facilities, economy and efficiency can be obtained by loading the factory, but this loading will adversely affect the throughput time for a product and the ability to effect change. Since the goal of all productivity initiatives is to bring about cultural change, close examination of the loading of the design factory is required. If every engineer in the design factory is loaded with work accounting for a 110% workload factor, there will be little capacity to learn new concepts and methods. Yet such learning is required to realize successful productivity initiatives. Change will come very slowly for a loaded design factory. If the design factory loading is reduced, new initiative efforts can fill the remaining capacity and change may occur more quickly.

Important parameters to monitor for design factories include speed, cost, and value of the designs produced by the factory. Clearly, as in any other factory, access to required resources and raw materials is required to fuel the factory. For the design factory, these resources include appropriate office environments, office support, computers, design tools, literature access, etc. The efficient design factory must also be maintained with appropriate support organizations. For many engineering applications these organizations include marketing, quality assurance, reliability, and sales. An important concept unique to the design factory, which should be considered when launching productivity initiatives, is that the design factory improves its speed, cost, and value through learning. The design factory machinery (engineers) thrive on learning and teaching. This fact leads to some important concepts related to productivity initiatives.

We learn in many ways, especially by failure. Finding a failure quickly is often critical to ultimate timely success. For the entire design factory to learn from failure, however, requires that failures are identified and made public. There is a natural resistance to this in most engineering cultures, since failures have historically not been rewarded. It is important that the cost and value of failures be understood and that high value/low cost failures be rewarded. Early fast failures often stimulate the design machine to identify and apply appropriate resources to the most critical problems, thus developing successful designs more quickly. Rewarding such failure will create an environment that will favor fast design.

The need for learning also implies a need for intellectual stimulation and creativity. Diversity is a key ingredient to the development of a stimulating engineering culture. Diversity in both training and experience helps to fuel the creative machinery.

Productivity Metrics for Design — Earned Value

A design is only good to the extent that it helps accomplish the cost and schedule targets as well as the technical targets. Meeting performance and missing the cost or schedule can be a failure while relaxed performance at an earlier date and lower cost may provide success. Design metrics should provide a yardstick to measure cost, schedule, and performance variances during the design process. Earned Value Analysis (**EVA**) provides a simple method to develop design performance metrics that indicate how the design factory is performing against its original plan.

To perform EVA, a baseline plan that includes the following is required:

1. Planned budget to execute
2. Planned schedule
   - Detailed work breakdown structure (WBS)
   - Measurable milestones
3. Actual budget to execute
4. Actual schedule required to perform

Figure 3.55 illustrates an initial baseline plan for a design project prior to initiating work on any of the tasks. The example plan is comprised of four separate tasks with estimated levels of effort of 80, 60, 100, and 50 hours. The plan could be quantified in terms of monetary values or other measurable units instead of hours. The example plan is also divided into two distinct work periods. The x-axis on the chart is calendar time. The task hours may not correspond directly with the calendar time since task hours may represent part-time effort of an individual engineer or may represent several engineers' efforts on a full-time basis.

The plan defines the Budgeted Cost of Work Scheduled (**BCWS**). BCWS is simply the budget or plan. The BCWS for an interval of time is the sum of the work of all tasks scheduled to be performed in that period. For the example in Fig. 3.55, the BCWS for period 1 is the sum of 80 hours for task A, plus 60 hours for task B, plus 30 hours for task C. For period 1, BCWS = 170 hours.

The Budget at Completion (**BAC**) is also defined in terms of the plan and is simply the sum of all tasks for the entire project. For the example in Fig. 3.55, BAC = 290 hours.

As work progresses on the project, actual accomplishments and levels of effort can be compared to the baseline schedule. Figure 3.56 illustrates a possible representation of the progress through the end of period 1. In the figure, black bars are used to fill the work tasks to the extent that they have been completed to date.

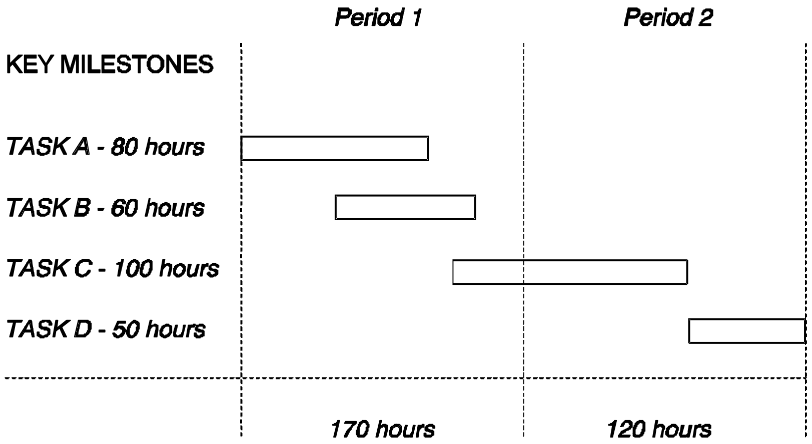

FIGURE 3.55 An illustration of an initial baseline plan for a design project prior to initiating work on any of the tasks.

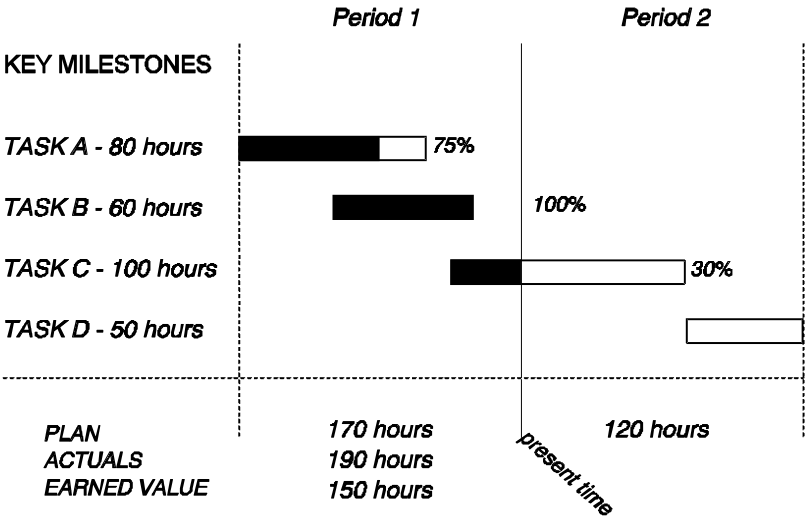

FIGURE 3.56 A representation of the progress completed on the initial baseline plan of Fig. 3.55 through the end of period 1. In the figure, black bars are used to fill the work tasks to the extent that they have been completed to date.

The Actual Cost of Work Performed (**ACWP**) is the actual costs incurred for a task or period. From Fig. 3.56, for period 1, ACWP = 190 hours. This value is noted on the figure, but is not represented in the graphics. Actual hours worked to achieve the progress reported is determined from other charging reports and simply recorded on the graph of Fig. 3.56. The 190 hours ACWP represents a variance from the baseline plan of 20 additional hours.

Figure 3.56 also indicates that the tasks originally planned for period 1 were not completed. Although tasks B and C were completed to the level indicated in the original plan, task A was scheduled for completion before the end of period 1 and is actually only 75% complete. The Budgeted Cost of Work Performed (**BCWP**) captures the earned value of the effort. The BCWP takes actual accomplishments and assigns the value that the original plan indicated it would cost to do this task. In Fig. 3.56, BCWP for period 1 is obtained by summing up the costs identified by the black bars of each task. The earned value for period 1 is 150 hours. This represents a deficiency from the baseline plan of 20 hours.

From Figs. 3.55 and 3.56 and the definitions given above, several important performance metrics can be defined. Figure 3.57 illustrates some of these metrics graphically.

Schedule Variance (**SV**) indicates whether the project is ahead or behind schedule. A schedule variance can exist for several reasons and does not provide any indication about the cost performance. The Schedule Variance is defined as

$$SV = BCWP - BCWS \tag{3.118}$$

The Schedule Performance Index (**SPI**) indicates the schedule efficiency. Schedule Performance Index is the ratio of earned value to planned effort expressed as

$$SPI = \frac{BCWP}{BCWS} \tag{3.119}$$

Cost Variance (**CV**) indicates whether the project is over or below budget. A cost variance can exist for several different reasons and does not provide any indication about the schedule performance. The Cost Variance is defined as

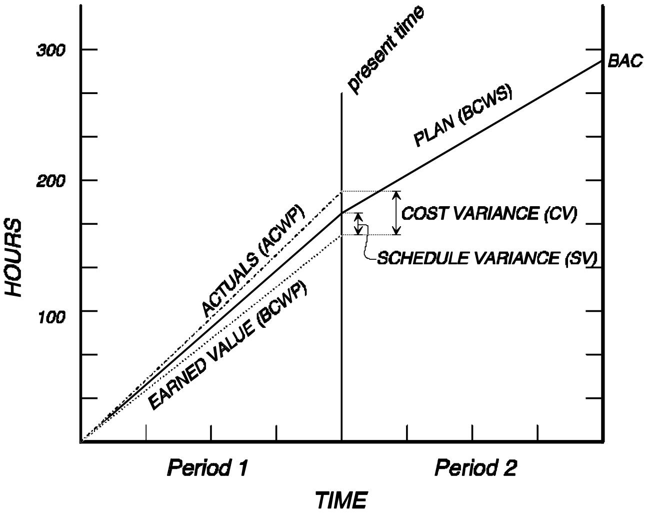

FIGURE 3.57 A graphical illustration of key metrics from an earned value program evaluation.

$$CV = BCWP - ACWP \tag{3.120}$$

Cost Efficiency is quantified with the Cost Performance Index (**CPI**). Cost Performance Index is the ratio of earned value to actual effort expressed as

$$CPI = \frac{BCWP}{ACWP} \tag{3.121}$$

The earned value quantities defined above provide a method to evaluate design performance against the original plan. Evaluation of the cost and schedule variance and efficiency is a first step to improving design performance.

A project that is on schedule and at budget will exhibit CPI and SPI values of unity. A low value for SPI indicates the project is behind schedule while a low value of CPI indicates the project is over budget. Schedule and budget performance variance, however, can have many different root causes, including the use of a poor plan. It is important that the EVA is followed by an effort to determine the root cause of any poor performance metrics before action to remedy the problem is adopted. For example, if schedule metrics are in deficit with the baseline plan while budget metrics are consistent with plan, this is an indication that the level of effort applied to the program is less than planned. Acquisition or identification of additional resources for the remainder of the program could lead to successful completion of the program (both budget and schedule goals met) for this case. If both schedule and budget metrics show a deficit from plan, there is an indication that the work is not on target for successful completion. Careful review of the original plan as well as the execution issues related to each task is required.

Manufacturing

The most widely known productivity initiatives focus on manufacturing metrics and yield analysis tools. These initiatives make extensive use of statistical process control. Statistical process control uses sampling and statistical methods to monitor the quality of an ongoing process such as a production operation.

A graphical display of statistical process variation known as a control chart provides the basis for determining when process variation is due to common causes (random variations) or to assignable,

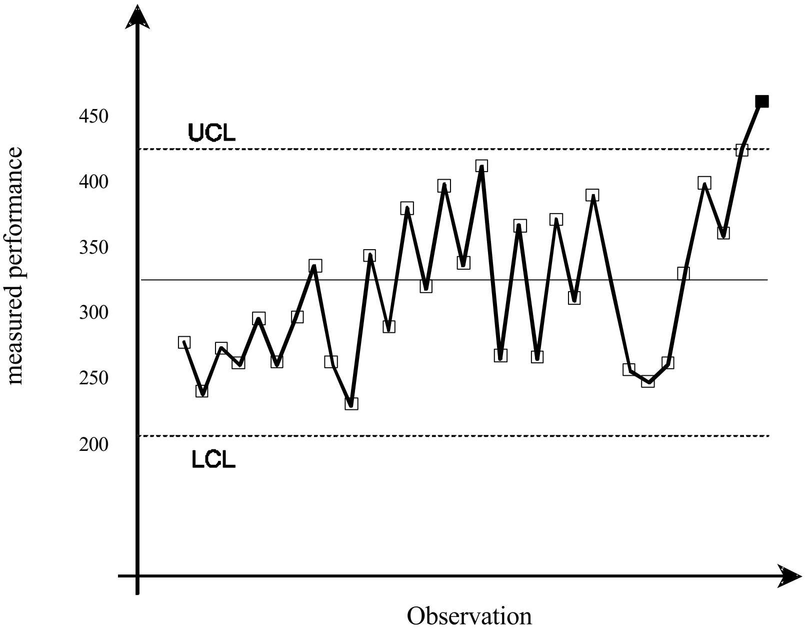

FIGURE 3.58 An example control chart.

preventable causes. If our measurement equipment has enough accuracy, all processes will exhibit variations. The goal of reviewing control charts is to distinguish the variations intrinsic in the process from those that can be assigned a caus and, therefore, can be controlled. An example control chart is presented in Fig. 3.58. Control charts plot sequential evolution of time along the x-axis and the statistic that is being measured along the y-axis. Control limits (random variations inherent in the process) are statistically determined by careful observation of the process. These limits are plotted as bounds of expected process behavior. The mean value of the process is also plotted on the control chart. When variations exceed the control limits, the process is assumed to have shifted and adjustments in the process must be made. Variations within the control limits are assumed to be inherent to the process and do not require process adjustments.

Control limits must represent actual process variability inherent in the process. Customer requirements or goals should never be used to establish control limits. To define control limits requires that an appropriate history of the process be collected.

Six Sigma

Six Sigma is the name applied to the manufacturing initiative that has become by far the most pervasive in the industry. This productivity initiative is a quality improvement and a business strategy that was pioneered at Motorola in 1987. The Greek letter sigma designates the standard deviation from the average in a Gaussian distribution of any process or procedure. The common measurement unit of Six Sigma is "defects per million units." The sigma value of a process indicates how often defects are likely to occur. Three sigma means 66,807 defects per million. Four sigma translates into 6,210 defects. Six Sigma quality implies only 3.4 defects per million. Ideally, product quality increases and cost decreases as sigma rises.

Although Six Sigma programs can be described in elaborate mathematical detail, the attainment of "six sigma quality" is not precisely defined. There are many ways to calculate defects per million units of a process. A unit, for example, can be almost anything: a system, a module, a component within a module, a part within a component, etc. Similarly, a process or procedure can be defined in many ways. The action of soldering a component to a board can be considered to be one single process, or can be

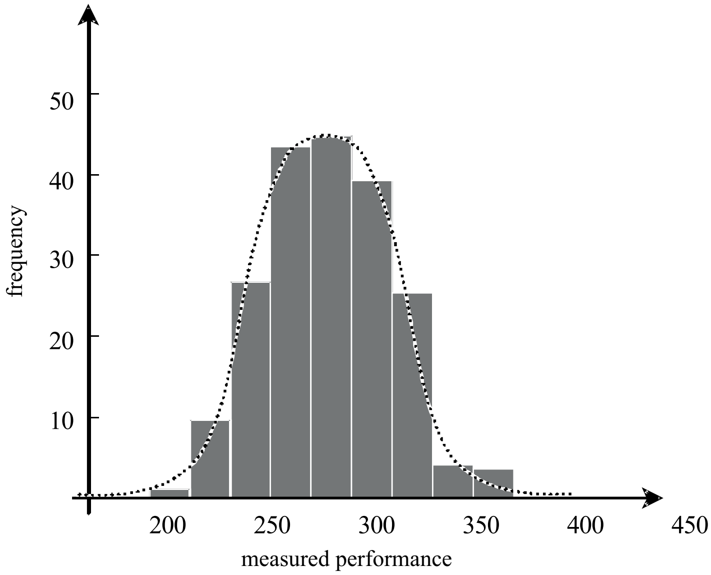

FIGURE 3.59 Example distribution statistics for a process. The observed statistics appear to approximate a normal distribution function.

broken down into several — picking the component, placing it, applying heat, etc. The choice of definition for a unit and a process can have a dramatic effect on the "defects per million" calculation. When an auto manufacturer claims to have achieved six sigma production standards, it does not mean that they produce only 3.4 defective cars per million. The 3.4 figure applies to the number of opportunities for errors. If a car consists of 10,000 different components and each one is assembled using 10 defined procedures, the opportunities for error totals one hundred thousand per auto. Six sigma production quality would imply 3.4 defects for every 10 cars.

Despite these ambiguities, Six Sigma programs have led to dramatic cost savings and competitive advantages to many companies that have embraced the philosophy. The list of companies that credit Six Sigma programs with significant cost and cycle time improvements is nearly endless.

Implementation of a Six Sigma program involves training employees to use statistical process control tools to achieve their defect reduction goals. Figures of merit are defined in terms of the statistical distribution of processed parts and these figures are monitored in an attempt to gain better control of the process.

Figure 3.59 illustrates the distribution statistics for a process. Plotted along the x-axis is the range of measured performance for the process of interest. The performance metric used for the process should be easily and quickly measured. This should be done in order to keep the measurement process from having a significant negative impact on the production cycle. Automation of the measurement and implementation of the measurement as a required part of the manufacturing process flow is important. The metric may not be a direct measurement of the actual desirable result, but it should reflect the quality and variability of the process (i.e., if the metric is controlled, the process should be controlled).

Plotted along the y-axis of Fig. 3.59 is the frequency that a measurement was observed within the sample of process measurements. For a process that is dominated by random variations, the frequency of observation versus measurement value plot is expected to describe a normal distribution. As seen from the figure, the normal distribution peaks at a specific (mean) value and drops off toward zero symmetrically in either direction away from the mean. The mean value of a distribution provides a good description of the central tendency of the process. A second important parameter describing a distribution is the standard deviation. Standard deviation provides a measure of the magnitude of the random variation inherent in a process.

Six Sigma Mathematics

The normal distribution function (also called the Gaussian distribution function after the German mathematician, Carl Friedrich Gauss) is the fundamental mathematical equation for Six Sigma metrics. A normal distribution function is the indefinite integral of the normal density function, the graph of which exhibits a typical bell shape. The normal distribution function can be described by

$$F_N\left(x'\right)=k\int_{-\infty}^{x'}\exp\left[\frac{-\left(x-\mu\right)^2}{2\omega^2}\right]dx \tag{3.122}$$

where the constant *k* is called the normalizing coefficient and adjusts the amplitude of the function so that the integral of the distribution over all possible values of x will give a probability value of unity. The constant *k* can be expressed as

$$k=\frac{1}{\sigma\sqrt{2\pi}} \tag{3.123}$$

In Eqs. (3.122) and (3.123), μ is the mean, or average, of the distribution. For normal distributions, the mean value is also the point where the function reaches its maximum. The quantity σ is the standard deviation and characterizes the width of the distribution. For engineering processes, the mean value is typically the manufacturing target value and the sigma corresponds to the variability in the process. An ideal probability distribution would have a σ value that approached zero.

Two important metrics to analyze relative to Six Sigma performance are the C_p and C_{pk}. The C_p metric is referred to as the Process Capability Index and is given by

$$C_p=\frac{CPU+CPL}{2}=\frac{USL-LSL}{6\sigma} \tag{3.124}$$

where CPU is defined as

$$CPU=\frac{USL-\mu}{3\sigma}=\frac{z_U}{3} \tag{3.125}$$

CPL is defined as

$$CPL=\frac{\mu-LSL}{3\sigma}=\frac{z_L}{3} \tag{3.126}$$

and the quantities LSL and USL represent the lower and upper spec limits. The quantities z_U and z_L that appear in Eqs. (3.125) and (3.126) are derived from normalizing the *x* values of the observed measurement space to the process standard deviation using the transformation

$$z=\frac{x-\mu}{\sigma} \tag{3.127}$$

The C_{pk} metric is called the Process Bias and is similarly given by

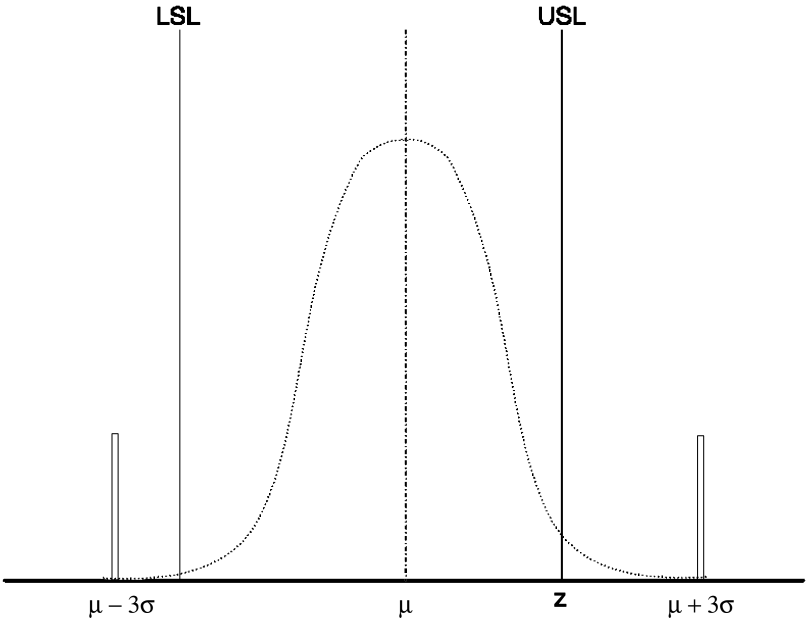

FIGURE 3.60 A process distribution chart with the quantities USL, LSL, μ, and σ illustrated on the plot. In this example, USL and LSL are not symmetric with respect to the mean while both are within the 6σ limits.

$$C_{pk} = \min\left(CPU, CPL\right) \tag{3.128}$$

For a process to be of Six Sigma quality, the following conditions must hold:

$$C_p \geq 2 \tag{3.129}$$

and

$$C_{pk} \geq 1.5 \tag{3.130}$$

A process distribution chart is illustrated in Fig. 3.60 with the quantities USL, LSL, μ, and σ illustrated on the plot. In this example, USL and LSL are not symmetric with respect to the mean while both are within the 6σ limits.

The Six Sigma goal may not be appropriate for every process as applied to every manufacturing task. The initiative to train all of the workers in a factory to monitor process variations and to understand the statistical metrics listed above, however, almost certainly has merit. This training procedure and heightened awareness of yield and process variation issues may be the real value of Six Sigma initiatives.

References

Reinertsen, D., *Managing the Design Factory,* The Free Press, New York, 1997.

Montgomery, D. C., *Introduction to Statistical Quality Control,* John Wiley & Sons, New York, 1991.

Hahn, G. J. and Shapiro, S S., *Statistical Models in Engineering,* John Wiley & Sons, New York, 1967.

Womack, J. P. and Jones, D. T., Beyond Toyota: How to root out waste and pursue perfection, *Harvard Business Review,* Sept.–Oct. 1996.

3.8 Electronic Hardware Reliability

Arun Ramakrishnan, Toby Syrus, and Michael Pecht

Reliability is the ability of a product to perform as intended (i.e., without failure and within specified performance limits) for a specified time, in its life cycle application environment. To achieve product reliability over time demands an approach that consists of a set of tasks, each requiring total engineering and management commitment and enforcement. These tasks impact electronic hardware reliability through the selection of materials, structural geometries and design tolerances, manufacturing processes and tolerances, assembly techniques, shipping and handling methods, operational conditions, and maintenance and maintainability guidelines.[1] The tasks are as follows:

1. Define realistic product requirements and constraints determined by the life cycle application profile, required operating and storage life, performance expectations, size, weight, and cost. The manufacturer and the customer must jointly define the product requirements in the light of both the customer's needs and the manufacturer's capability to meet those needs.
2. Define the product life cycle environment by specifying all relevant assembly, storage, handling, shipping, and operating conditions for the fielded product. This includes all stress and loading conditions.
3. Characterize the materials and the manufacturing and assembly processes. Variabilities in material properties and manufacturing processes can induce failures. A knowledge of the variability is required to assess design margins and possible trade-offs with weight, size, and cost.
4. Select the parts required for the product, using a well-defined assessment procedure that ensures that the parts selected have sufficient quality and integrity, are capable of delivering the expected performance and reliability in the application, and will be available to sustain the product throughout its life cycle.
5. Identify the potential failure sites and failure mechanisms by which the product can be expected to fail. Critical parts, part details, and potential failure modes and mechanisms must be identified early in the design, and appropriate measures must be implemented to assure design control. Potential architectural and stress interactions must also be defined and assessed.
6. Design to the usage and process capability of the product (i.e., the quality level that can be controlled in manufacturing and assembly), considering the potential failure sites and failure mechanisms. The design stress spectra, the part test spectra, and the full-scale test spectra must be based on the anticipated life cycle usage conditions. The proposed product must survive the life cycle environment, be optimized for manufacturability, quality, reliability, and cost-effectiveness, and be available to the market in a timely manner.
7. Qualify the product manufacturing and assembly processes. Key process characteristics in all the manufacturing and assembly processes required to make the part must be identified, measured, and optimized. Tests should be conducted to verify the results for complex products. The goal of this step is to provide a physics-of-failure basis for design decisions, with an assessment of all possible failure mechanisms for the anticipated product. If all the processes are in control and the design is valid, then product testing is not warranted and is therefore not cost effective. This represents a transition from product test, analysis, and screening to process test, analysis, and screening.
8. Monitor and control the manufacturing and assembly processes addressed in the design, so that process shifts do not arise. Each process may involve screens and tests to assess statistical process control.
9. Manage the life cycle usage of the product using closed loop management procedures. This includes realistic inspection and maintenance procedures.

Product Requirements and Constraints

A product's requirements and constraints are defined in terms of customer demands and the company's core competencies, culture, and goals. If the product is for direct sale to end users, marketing usually takes the lead in defining the product's requirements and constraints, through interaction with the customer's marketplace, examination of the current product sales figures, and analysis of the competition. Alternatively, if the product is a subsystem that fits within a larger product, the requirements and constraints are determined by the product into which the subsystem fits. The results of capturing product requirements and constraints allow the design team to choose product parts that conform to product-specific and company objectives.

The definition process begins with the identification of an initial set of requirements and constraints defined by either the marketing activity (or in some cases by a specific customer), or by the product into which the subsystem fits. The initial requirements are formulated into a requirements document, where they are prioritized. The requirements document needs to be approved by several groups of people, ranging from engineers to corporate management to customers (the specific people involved in the approval will vary with the company and the product). Once the requirements are approved, the engineering team prepares a preliminary specification indicating the exact set of requirements that are practical to implement. Disconnects between the requirements document and the preliminary specification become the topic of trade-off analyses (usually cost/performance trade-offs), and if, after analyses and negotiation, all the requirements cannot be implemented, the requirements document may be modified. When the requirements document and the preliminary specifications are agreed upon, a final specification is prepared and the design begins.

The Product Life Cycle Environment

The product life cycle environment goes hand-in-hand with the product requirements. The life cycle environment affects product design and development decisions, qualification and specification processes, parts selection and management, quality assurance, product safety, warranty and support commitments, and regulatory conformance.

The product life cycle environment describes the assembly, storage, handling, and scenario for the use of the product, as well as the expected severity and duration of these environments, and thus contains the necessary load input information for failure assessment and the development of design guidelines, assembly guidelines, screens, and tests. Specific load conditions include absolute temperatures, temperature ranges, temperature cycles, temperature gradients, humidity levels, pressure levels, pressure gradients, vibrational or shock loads and transfer functions, chemically aggressive or inert environments, acoustic levels, sand, dust, and electromagnetic radiation levels. In electrical systems, stresses caused by power, current, and voltage should also be considered. These conditions may influence the reliability of the product either individually or in combination with each other. Since the performance of a product over time is often highly dependent on the magnitude of the stress cycle, the rate of change of the stress, and the variation of the stress with time and space, the interaction between the application profile, and the internal conditions must be specified in the design.

The product life cycle environment can be divided into three parts: the application and life profile conditions, the external conditions under which the product must operate, and the internal product-generated stress conditions. The application and life profile conditions include the application length, the number of applications in the expected life of the product, the product utilization or non-utilization profile (storage, testing, transportation), the deployment operations, and the maintenance concept or plan. This information is used to group usage platforms (whether the product will be installed in a car, boat, airplane, satellite, or underground), to develop duty cycles (on-off cycles, storage cycles, transportation cycles, modes of operation, and repair cycles), to determine design criteria, to develop screens and test guidelines, and to develop support requirements to sustain attainment of reliability and maintainability objectives.

The external operational conditions include the anticipated environment(s) and the associated stresses that the product will be required to survive. These conditions are determined through experimentation and through the use of numerical simulation techniques. Experiments are performed by creating environmental parameter monitoring systems, consisting of sensors placed near and within the product that are capable of monitoring the loads that the product experiences. A sensor's function is to convert a physical variable input into, in most cases, an electrical output that is directly related to the physical variable. Signals can be transmitted to either local or remote output devices, enabling data to be collected in a safe and secure manner. Numerical simulation techniques combine material properties, geometry, and product architecture information with environmental data to determine the life cycle environment based on external stresses. Whenever credible data is not available, the worst-case design load must be estimated. A common cause of failure is the use of design factors related to average loads, without adequate consideration being given to the extreme conditions that may occur during the product's life cycle.[2]

The internal operational conditions are associated with product-generated stresses, such as power consumption and dissipation, internal radiation, and release or outgassing of potential contaminants. If the product is connected to other products or subsystems in a system, the stresses associated with the interfaces (i.e., external power consumption, voltage transients, voltage spikes, electronic noise, and heat dissipation) must also be included.

Life cycle stresses can cause strength degradation in materials, for example, combined stresses can accelerate damage and reduce the fatigue limit. In such cases, protective measures must be taken to mitigate the life cycle environment by the use of packaging, provision of warning labels and instructions, and protective treatment of surfaces. The measures to be taken must be identified as appropriate to assembly, storage, transportation, handling, operation, and maintenance. Protection against extreme loads may not always be possible, but should be considered whenever practicable. When overload protection is provided, a reliability analysis should be performed on the basis of the maximum anticipated load, keeping the tolerances of the protection system in mind.[2] If complete protection is not possible, the design team must specify appropriate maintenance procedures for inspection, cleaning, and replacement.

An example of the scenario for use of a product is a flight application, which can involve engine warm-up, taxi, climb, cruising, maneuvers, rapid descent, and emergency landing. Each part of the application will be associated with a set of load conditions, such as time, cycles, acceleration, velocity, vibration, shocks, temperature, humidity, and electrical power cycles. Together, these loads comprise a load history of the product.

Characterization of Materials, Parts, and Manufacturing Processes

Design is intrinsically linked to the materials, parts, interfaces, and manufacturing processes used to establish and maintain the functional and structural integrity of the product. It is unrealistic and potentially dangerous to assume defect-free and perfect-tolerance materials, parts, and structures. Materials often have naturally occurring defects, and manufacturing processes can introduce additional defects in the materials, parts, and structures. The design team must also recognize that the production lots or vendor sources for parts that comprise the design are subject to change, and variability in parts characteristics is likely to occur during the fielded life of a product.

Design decisions involve the selection of parts, materials, and controllable process techniques using processes appropriate to the scheduled production quantity. Any new parts, materials, and processes must be assessed and tested before being put into practice, so that training for production personnel can be planned, quality control safeguards can be set up, and alternative second sources can be located. Often, the goal is to maximize part and configuration standardization, to increase package modularity for ease in fabrication, assembly, and modification, to increase flexibility of design adaptation to alternate uses, and to utilize common fabrication processes. Design decisions also involve choosing the best material interfaces and the best geometric configurations, given the product requirements and constraints.

Parts Selection and Management

Product differentiation, which determines market share gain and loss, often motivates a company to adopt new technologies and insert them into their mainstream products. However, while technological advances continue to fuel product development, two factors, management decisions regarding when and

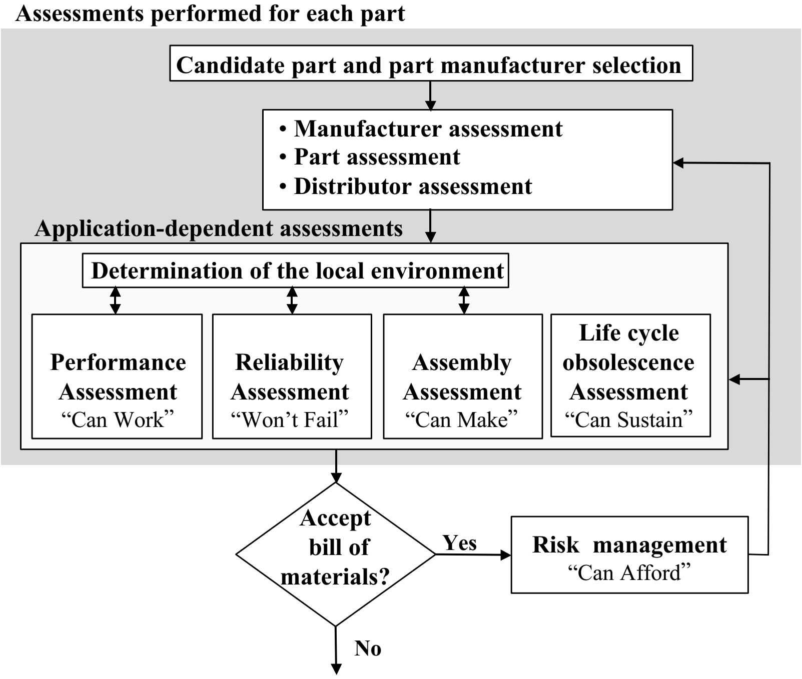
Assessments performed for each part
Candidate part and part manufacturer selection
• Manufacturer assessment
• Part assessment
• Distributor assessment
Application-dependent assessments
Determination of the local environment
Performance Assessment "Can Work"
Reliability Assessment "Won't Fail"
Assembly Assessment "Can Make"
Life cycle obsolescence Assessment "Can Sustain"
Accept bill of materials?
Yes
No
Risk management "Can Afford"

FIGURE 3.61 Parts selection and management methodology.

how a new technology will be used, and accurately assessing risks associated with a technology, differentiate the winners from the losers. Few companies have failed because the right technology was not available; far more have failed when a technology was not effectively managed.

The methodology, shown in Fig. 3.61, provides an "eyes-on, hands-off" approach to parts selection and management, which enables companies to:

- employ risk assessment and mitigation techniques to address technology insertion;
- organize and conduct fact-finding processes to select parts with improved quality, integrity, application-specific reliability, and cost effectiveness;
- make an informed company-wide decision about parts selection and management, based upon company resources, policies, culture, goals, and customer demands;
- understand and evaluate the local environment the part sees within a product's life cycle, and thereby choose the most appropriate technique to fit the part to its intended environmental requirements;
- maximize product supportability by preparing for and meeting the challenge of parts becoming obsolete during product life; and
- improve supply-chain interactions and communications with regulatory agencies in order to minimize time to profit.

Candidate Part and Part Manufacturer Selection

A candidate part is one that conforms to the functional, electrical, and mechanical requirements of the product, considering a company's product requirements, technology direction, and development. In addition, a candidate part must conform to availability and cost constraints. Availability of an electronic part is a measure of the ease with which the part can be procured. Availability is assessed by determining the amount of inventory at hand, the number of parts required for units in production and forecasted, the economic order quantity for the part(s), the lead time(s) between placing an order for the part(s) and receiving the part(s), production schedules and deadlines, and part discontinuation plans. The cost of the part is assessed relative to the product's budget during candidate part selection. In many cases, a part similar to the required one will have already been designed and tested. This "preferred part" is typically mature, in the sense that the variabilities in manufacturing, assembly, and field operation that could cause problems will have already been identified and corrected. Many design groups maintain a list of preferred parts of proven performance, cost, availability, and reliability.

Manufacturer, Part, and Distributor Assessment

In the manufacturer assessment, the part manufacturer's ability to produce parts with consistent quality is evaluated, and in the part assessment, the candidate part's quality and integrity is gauged. The distributor assessment evaluates the distributor's ability to provide parts without affecting the initial quality and integrity, and to provide certain specific services, such as part problem and change notifications. The equipment supplier's parts selection and management team defines the minimum acceptability criteria for this assessment, based on the equipment supplier's requirements. If the part satisfies the minimum acceptability criteria, the candidate part then moves to "application-dependent assessments."

If the part is found unacceptable due to nonconformance with the minimum acceptability criteria, some form of equipment supplier intervention may be considered.[3,4] If equipment supplier intervention is not feasible due to economic or schedule considerations, the candidate part may be rejected. If, however, equipment supplier intervention is considered necessary, then the intervention action items should be identified, and their cost and schedule implications should be analyzed through the "risk management" process step.

Performance Assessment

The goal of performance assessment is to evaluate the part's ability to meet the functional, mechanical, and electrical performance requirements of the product. In order to increase performance, products often incorporate features that tend to make them less reliable than proven, lower-performance products. Increasing the number of parts, although improving performance, also increases product complexity, and may lead to lower reliability unless compensating measures are taken.[5] In such situations, product reliability can be maintained only if part reliability is increased or part redundancy is built into the product. Each of these alternatives, in turn, must be assessed against the incurred cost. The trade-off between performance, reliability, and cost is a subtle issue, involving loads, functionality, system complexity, and the use of new materials and concepts.

In general, there are no distinct stress boundaries for parameters such as voltage, current, temperature, and power dissipation, above which immediate failure will occur and below which a part will operate indefinitely.[6] However, there is often a minimum and a maximum stress limit beyond which the part will not function properly, or at which the increased complexity required will not offer an advantage in cost effectiveness. Part manufacturers' ratings or users' procurement ratings are generally used to determine these limiting values. Equipment manufacturers who integrate such parts into their products need to adapt their design so that the parts do not experience conditions beyond their absolute maximum ratings, even under the worst possible operating conditions (e.g., supply voltage variations, load variations, and signal variations).[7] It is the responsibility of the parts selection and management team to establish that the electrical, mechanical, and functional performance of the part is suitable for the operating conditions of the particular product. If a product must be operated outside the manufacturer-specified operating conditions, then uprating[*] may have to be considered.

Part manufacturers need to assess the capability of a part over its entire intended life cycle environment, based on the local environment that is determined. If the parametric and functional requirements of the

[*] The term uprating was coined by Michael Pecht to distinguish it from *upscreening*, which is a term used to describe the practice of attempting to create a part equivalent to a higher quality by additional screening of a part (e.g., screening a JANTXV part to JANS requirements).

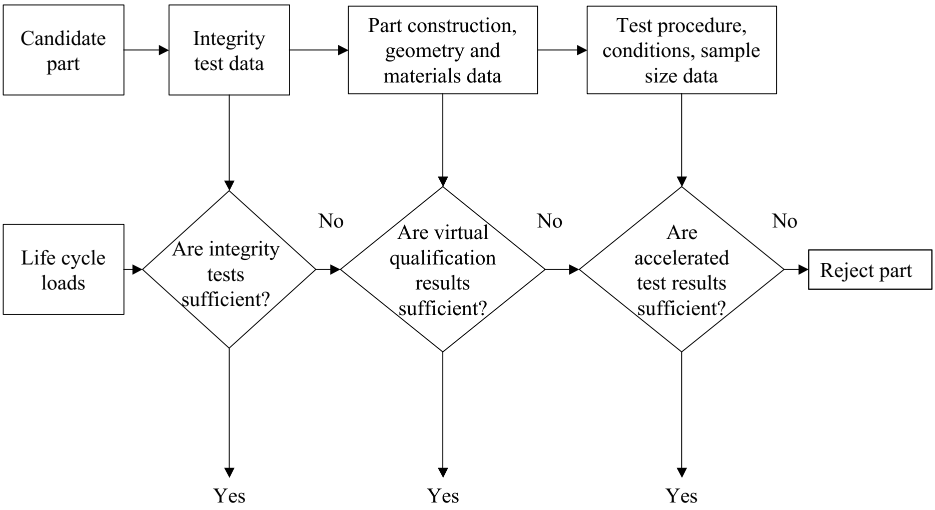
Candidate part
Integrity test data
Part construction, geometry and materials data
Test procedure, conditions, sample size data
Life cycle loads
Are integrity tests sufficient?
No
Are virtual qualification results sufficient?
No
Are accelerated test results sufficient?
No
Reject part
Yes
Yes
Yes

FIGURE 3.62 Reliability assessment process.

system cannot be met within the required local environment, then the local environment may have to be modified, or a different part may have to be used.

Reliability Assessment

Reliability assessment results provide information about the ability of a part to meet the required performance specifications in its life cycle application environment for a specified period of time. Reliability assessment is conducted through the use of integrity test data, virtual qualification results, or accelerated test results. The reliability assessment process is shown in Fig. 3.62.

Integrity is a measure of the appropriateness of the tests conducted by the manufacturer and of the part's ability to survive those tests. Integrity monitoring tests are conducted by the part manufacturer to monitor part/process changes and the ongoing material or process changes specific to the part. Integrity test data (often available from the part manufacturer) is examined in light of the application life cycle stresses and the applicable failure modes and mechanisms. If the magnitude and duration of the application life cycle loads are less severe than those of the integrity tests, and if the test sample size and results are acceptable, then the part reliability is acceptable. However, if the magnitude and duration of the application life cycle loads are not as severe as those of the integrity tests, then integrity test data cannot be used to validate part reliability in the application, and virtual qualification should be considered.

Virtual qualification is a simulation-based methodology used to identify the dominant failure mechanisms associated with the part under the life cycle loads, to determine the acceleration factor for a given set of accelerated test parameters, and to determine the time-to-failures corresponding to the identified failure mechanisms. Virtual qualification allows the operator to optimize the part parameters (e.g., dimensions, materials) so that the minimum time-to-failure of any part is greater than the expected product life.

If virtual qualification proves insufficient to validate part reliability, accelerated testing should be performed. Once the appropriate test procedures, conditions, and sample sizes are determined, accelerated testing can be conducted by either the part manufacturer, the equipment supplier, or third-party test facilities. Accelerated testing results are used to predict the life of a product in its field application by computing an acceleration factor that correlates the accelerated test conditions and the actual field conditions. Whether integrity test data, virtual qualification results, accelerated test results, or a combination thereof are used, each applicable failure mechanism to which the part is susceptible must be addressed.

If part reliability is not ensured through the reliability assessment process, the equipment supplier must consider an alternate part or product redesign. If redesign is not considered a viable option, the part should be rejected, and an alternate part must be selected. If the part must be used in the application, redesign options may include thermal management techniques, vibration damping, and modifying assembly parameters. If product design changes are made, part reliability must be reassessed.

Assembly Issues

A part may be unacceptable from an assembly viewpoint if (1) it is incompatible with the assembly equipment or process; (2) it is impossible or impractical to wire the part into the product (routing compatibility), or (3) it cannot be acceptably tested or reworked. Assembly compatibility addresses whether a product that contains the part can be manufactured (assembled). Routing compatibility assesses if the candidate part can be routed within a specific application on the selected board. Test and rework acceptability assess whether the candidate part can be adequately and economically tested and reworked during assembly.

Assembly Compatibility

Parts must conform to a range of manufacturability constraints associated with their assembly into products. Assembly manufacturability constraints that must be considered when designing a product fall into three categories:

- Assembly process compatibility: involves comparing the part's size, shape, and mounting method to the process that will be used to assemble the boards containing the part.
- Proximity to other structures: involves checking the location of the component relative to other parts assembled on the board and the edge of the board. Proximity checking includes evaluating the orientation (rotation) of the part.
- Artwork verification: involves checking the board layout for the correct orientation and location of fiducials (alignment marks), alignment holes, and other structures necessary to facilitate assembly.

Assembly compatibility and proximity checking can produce three possible outcomes: cannot be assembled, can be assembled with a corresponding cost and yield penalty, and can be assembled with no cost or yield penalties. Artwork verification is decoupled from part selection.

Routing Compatibility

Routing compatibility pertains to the layout and routing of an application. If the selection of a particular part causes significant layout or routing problems within the board, the part may be rejected. Rejection of a part is usually based on its use of routing resources within the board. Two routing issues must be considered:

- How much board area is required to wire the part to the rest of the product?
- How many layers of the board are required to "escape route" the part?

Escape routing is only applicable if the part has an area array format connection to the board, for example, a flip chip or ball grid array package. A component is virtually always "routable," given a sufficient number of board layers. If the rest of the parts on the board are known, routing estimation techniques can be used to determine the effective routing limited footprint of a part under the constraints posed by the board design rules (lines, spaces, via/hole capture pad diameter) and layer count. If a candidate part exceeds the fraction of board wiring resources budgeted to it based on board growth and cost constraints, it may be rejected.

A limiting requirement for some parts is escape routing. If a part's I/Os are in an area array format (as opposed to a peripheral format), the part cannot be wired into the product until all of its I/Os are routed out from under the part. The process of liberating I/Os from an array is called escape routing.

Test and Rework Acceptability

Test and rework costs are important criteria in determining whether a part is acceptable or not. The cost of testing the part (to a specified quality level) prior to assembly and the cost of replacing the part if it needs to be repaired after it is assembled must be considered.

The cost of testing a part is related to what level of testing is performed by the part manufacturer, whether the part is in a package or bare, the function that the part performs, the number of gates or bits contained in the part, and the test equipment. If the part does not come from the manufacturer fully tested (e.g., a bare die), then test costs may need to be assessed. Test costs include the cost of creating the test patterns (or obtaining them from the manufacturer) and the cost of applying the test to the part. Predicting testing costs is of little value unless the corresponding test coverage (fraction of defects detected by the test) is also predicted.

Another key assembly-related cost is the cost of replacing a part that has been identified as defective during the assembly process. The cost of removing a defective part is a function of how the part is mounted to the board, the size of the part, and its proximity to other parts.

Life Cycle Mismatch Assessment

Lengthy design, qualification, and production processes inherent in electronic industries often cause parts to become obsolete before the first product is produced.[8] Furthermore, in order to cater to market demands and remain competitive, part manufacturers often introduce new parts and discontinue older parts. In general, electronic products go through six phases during their life cycles: design, manufacturing, growth, maturity, decline, and discontinuation. A life cycle mismatch occurs between a product and its constituent parts if the parts are not available to support the product throughout its life cycle. When factors such as lead time, risk of part obsolescence, or estimation of the product market are ignored or improperly judged during the design phase, the consequences can be costly. The obsolete part can inhibit the functioning of the product, idle the assembly line, lead to dissatisfied customers, and cause a loss of reputation for the company. The net outcome can be a financial loss for the company.

A successful life cycle mismatch assessment process is one that prevents, if possible, the selection of parts that are already obsolete or soon to be discontinued. This strategy reduces the risk associated with a life cycle mismatch between a product and its parts. The part selection depends on the degree of mismatch and the flexibility to adopt an obsolescence management strategy (e.g., redesign, lifetime buy, buy from aftermarket sources, part substitution). The strategy is intended to mitigate obsolescence risks associated with using the part at some future point in the life cycle of the product. If the equipment supplier finds the life cycle mismatch between part and product unacceptable, the part is unsuitable and should be rejected.

Risk Management

After a part is accepted, resources must be applied to managing the life cycle of the part, including supply chain management, obsolescence assessment, manufacturing and assembly feedback, manufacturer warranties management, and field failure and root-cause analysis. It is important to consider the process of managing the part and all the risks associated with the long-term use of the part throughout its life cycle during the part selection process. The risk management process is characterized using the risks identified in the parts selection process to determine the resources needed to support a part throughout its application life cycle, thus minimizing the probability of a failure. The key metric used to determine whether risks should be managed or not is resources, which include time, data, opportunity, and money.

The risks associated with including a part in the product fall into two categories:

- Managed risks: risks that the product development team chooses to proactively manage by creating a management plan and performing a prescribed regimen of monitoring the part's field performance, manufacturer, and manufacturability.
- Unmanaged risks: risks that the product development team chooses not to proactively manage.

If risk management is considered necessary, a plan should be prepared. The plan should contain details about how the part is monitored (data collection), and how the results of the monitoring feed back into various parts selection and management processes. The feasibility, effort, and cost involved in management processes prior to the final decision to select the part must be considered.

Feedback regarding the part's assembly performance, field performance, and sales history may be essential to ascertain the validity of the predictions made during the part selection process. If the feedback calls for changes in selection criteria, they should be incorporated into the part selection process. Prospective parts should be judged based on the altered part selection criteria. Part monitoring data may also be needed to make changes in parts that are already in use. For example, part monitoring field data might indicate that a change in operating conditions is required for the part to perform satisfactorily.

Failure Modes and Mechanisms

Failure mechanisms are the physical processes by which stresses can damage the materials used to build the product. Investigation of the possible failure modes and mechanisms of the product aids in developing failure-free and reliable designs. The design team must be aware of all possible failure mechanisms in order to design hardware capable of withstanding loads without failing. Failure mechanisms and their related models are also important for planning tests and screens to audit the nominal design and manufacturing specifications, as well as the level of defects introduced by excessive variability in manufacturing and material parameters. Numerous studies focusing on material failure mechanisms and physics-of-failure based damage models and their role in obtaining reliable electronic products have been illustrated in a series of tutorials comprising all relevant wearout and overstress failures.[9-23]

Catastrophic failures occurring due to a single occurrence of a stress event when the intrinsic strength of the material is exceeded are termed overstress failures. Failure mechanisms due to monotonic accumulation of incremental damage beyond the endurance of the material are termed "wearout mechanisms."[24] When the damage exceeds the endurance limit of the component, failure will occur. Unanticipated large stress events can either cause an overstress (catastrophic) failure, or shorten life by causing the accumulation of wearout damage. Examples of such stresses are accidental abuse and acts of God. On the other hand, in well-designed and high-quality hardware, stresses should cause only uniform accumulation of wearout damage; the threshold of damage required to cause eventual failure should not occur within the usage life of the product.

Electrical performance failures can be caused by individual components with improper electrical parameters, such as resistance, impedance, capacitance, or dielectric properties, or by inadequate shielding from electromagnetic interference (EMI) or particle radiation. Failure modes can manifest as reversible drifts in transient and steady-state responses, such as delay time, rise time, attenuation, signal-to-noise ratio, and crosstalk. Electrical failures, common in electronic hardware, include overstress mechanisms due to electrical overstress (EOS) and electrostatic discharge (ESD) such as dielectric breakdown, junction breakdown, hot electron injection, surface and bulk trapping, and surface breakdown and wearout mechanisms such as electromigration and stress-driven diffusive voiding.

Thermal performance failures can arise due to incorrect design of thermal paths in an electronic assembly. This includes incorrect conductivity and surface emissivity of individual components, as well as incorrect convective and conductive paths for heat transfer. Thermal overstress failures are a result of heating a component beyond critical temperatures such as the glass-transition temperature, melting point, fictive point, or flash point. Some examples of thermal wearout failures are aging due to depolymerization, intermetallic growth, and interdiffusion. Failures due to inadequate thermal design may be manifested as components running too hot or too cold and causing operational parameters to drift beyond specifications, although the degradation is often reversible upon cooling. Such failures can be caused either by direct thermal loads or by electrical resistive loads, which in turn generate excessive localized thermal stresses. Adequate design checks require proper analysis for thermal stress, and should include conductive, convective, and radiative heat paths.

Mechanical performance failures include those that may compromise the product performance without necessarily causing any irreversible material damage, such as abnormal elastic deformation in response to mechanical static loads, abnormal transient response (such as natural frequency or damping) to dynamic loads, and abnormal time-dependent reversible (anelastic) response, as well as failures that cause material damage, such as buckling, brittle and/or ductile fracture, interfacial separation, fatigue crack initiation, and propagation, creep, and creep rupture. For example, excessive elastic deformations in slender structures in electronic packages due to overstress loads can sometimes constitute functional failure, such as excessive flexing of interconnection wires, package lids, or flex circuits in electronic devices, causing shorting and/or excessive crosstalk. However, when the load is removed, the deformations (and consequent functional abnormalities) disappear completely without any permanent damage.

Radiation failures are principally caused by uranium and thorium contaminants, and secondary cosmic rays. Radiation can cause wearout, aging, embrittlement of materials, and overstress soft errors in electronic hardware, such as logic chips. Chemical failures occur in adverse chemical environments that result in corrosion, oxidation, or ionic surface dendritic growth. There may also be interactions between different types of stresses. For example, metal migration may be accelerated in the presence of chemical contaminants and composition gradients, and thermal loads can accelerate a failure mechanism due to a thermal expansion mismatch.

Failure modes and effects analysis (FMEA) is an evaluation process for analyzing and assessing the potential failures in a product. Its objectives are to:

1. identify the causes and effects of each failure mode in every part in the product;
2. ascertain the effects of each failure mode on product operation and personnel safety;
3. assess each potential failure according to the effects on other portions of the systems; and,
4. provide a recommendation to eliminate the causes of the failure modes or compensate for their effects.

Failure effects may be considered at subsystem and at overall system levels.

The two approaches to FMEA are functional and hardware. The functional approach, which should be used when the product definition has been identified, begins with the initial product indenture level, and proceeds downward through lower levels. The top level shows the gross operational requirements of the product, while the lower levels represent progressive expansions of the individual functions of the preceding level. This documentation is prepared down to the level necessary to establish the hardware, software, facilities, and personnel and data requirements of the system.

The hardware approach to FMEA should be used when the design team has access to schematics, drawings, and other engineering and design data normally available once the system has matured beyond the functional design stage. This approach begins with obtaining all the information available on the design, including specifications, requirements, constraints, intended applications, drawings, stress data, test results, and so on, to the extent they are available at that time. The approach then proceeds in a part level-up fashion.

Once the approach for the analysis is selected, the product is defined in terms of a functional block diagram and a reliability block diagram. If the product operates in more than one mode in which different functional relationships or part operating modes exist, then these must be considered in the design. FMEA should involve an analysis of possible sneak circuits in the product, that is, an unexpected path or logic flow that can initiate an undesired function or inhibit a desired function. Effects of redundancy must also be considered by evaluating the effects of the failure modes assuming that the redundant system or subsystem is or is not available. The FMEA is then performed using a worksheet, and working to the part or subsystem level considered appropriate, keeping the design data available in mind. A fish-bone diagram of the product, showing all the possible ways in which the product can be expected to fail, is often used in the process. The analysis should take all the failure modes of every part into account, especially when the effects of a failure are serious (e.g., high warranty costs, reliability reputation, safety). FMEA should be started as soon as initial design information is available, and should be performed iteratively as the design evolves, so that the analysis can be used to improve the design and to provide documentation of the eventually completed design.

Design Guidelines and Techniques

Generally, products are replaced with other products, and the replaced product can be used as a baseline for comparisons with products to be introduced. Lessons learned from the baseline comparison product can be used to establish new product parameters, to identify areas of focus in new product designs, and to avoid the mistakes of the past.

Once the parts, materials, processes, and stress conditions are identified, the objective is to design a product using parts and materials that have been sufficiently characterized in terms of how they perform over time when subjected to the manufacturing and application profile conditions. Only through a methodical design approach using physics-of-failure and root-cause analysis can a reliable and cost-effective product be designed. A physics-of-failure based reliability assessment tool must exhibit a diverse array of capabilities:

1. It should be able to predict the reliability of components under a wide range of environmental conditions.
2. It should be able to predict the time-to-failure for fundamental failure mechanisms.
3. It should consider the effect of different manufacturing processes on reliability.

All of these can be accomplished by the use of tools such as virtual qualification and accelerated testing. Design guidelines that are based on physics-of-failure models can also be used to develop tests, screens, and derating factors. Tests based on physics-of-failure models can be designed to measure specific quantities, to detect the presence of unexpected flaws, and to detect manufacturing or maintenance problems. Screens can be designed to precipitate failures in the weak population while not cutting into the design life of the normal population. Derating or safety factors can be determined to lower the stresses for the dominant failure mechanisms.

In using design guidelines, there may not be a unique path to follow. Instead, there is a general flow in the design process. Multiple branches may exist, depending on the input design constraints. The design team should explore an adequate number of these branches to gain confidence that the final design is the best for the prescribed input information. The design team should also assess the use of guidelines for the complete design, and not those limited to specific aspects of an existing design. This does not imply that guidelines cannot be used to address only a specific aspect of an existing design, but the design team may have to trace through the implications that a given guideline suggests.

Protective Architectures

In designs where safety is an issue, it is generally desirable to design in some means for preventing a part, structure, or interconnection from failing, or from causing further damage when it fails. Fuses and circuit breakers are examples of elements used in electronic products to sense excessive current drain and to disconnect power from the concerned part. Fuses within circuits safeguard parts against voltage transients or excessive power dissipation, and protect power supplies from shorted parts. As another example, thermostats can be used to sense critical temperature limiting conditions, and to shut down the product or a part of the system until the temperature returns to normal. In some products, self-checking circuitry can also be incorporated to sense abnormal conditions and operate adjusting means to restore normal conditions, or to activate switching means to compensate for the malfunction.[6]

In some instances, it may be desirable to permit partial operation of the product after a part failure in preference to total product failure. By the same reasoning, degraded performance of a product after failure of a part is often preferable to complete stoppage. An example is the shutting down of a failed circuit whose function is to provide precise trimming adjustment within a deadband[*] of another control

[*] When the input in a control system changes direction, an initial change in the input has no effect on the output. This amount of side-to-side play in the system for which there is no change in the output is referred to as the deadband. The deadband is centered about the output.

product; acceptable performance may thus be achieved, perhaps under emergency conditions, with the deadband control product alone.[6]

Sometimes, the physical removal of a part from a product can harm or cause failure in another part by removing either load, drive, bias, or control. In such cases, the first part should be equipped with some form of interlock mechanism to shut down or otherwise protect the second part. The ultimate design, in addition to its ability to act after a failure, should be capable of sensing and adjusting for parametric drifts to avert failures.

In the use of protective techniques, the basic procedure is to take some form of action, after an initial failure or malfunction, to prevent additional or secondary failures. By reducing the number of failures, techniques such as enhancing product reliability can be considered, although they also affect availability and product effectiveness. Equally important considerations are the impacts of maintenance, repair, and part replacement. For example, if a fuse protecting a circuit is replaced, the following questions need to be answered: What is the impact when the product is reenergized? What protective architectures are appropriate for post-repair operations? What maintenance guidance must be documented and followed when fail-safe protective architectures have or have not been included?

Stress Margins

A properly designed product should be capable of operating satisfactorily with parts that drift or change with variables such as time, temperature, humidity, pressure, altitude, etc., as long as the interconnects and the other parameters of the parts are within their rated tolerances. To guard against out-of-tolerance failures, the design team must consider the combined effects of tolerances on parts to be used in manufacture, of subsequent changes due to the range of expected environmental conditions, of drifts due to aging over the period of time specified in the reliability requirement, and of tolerances in parts used in future repair or maintenance functions. Parts and structures should be designed to operate satisfactorily at the extremes of the parameter ranges, and allowable ranges must be included in the procurement or reprocurement specifications.

Statistical analysis and worst-case analysis are methods of dealing with part and structural parameter variations. In statistical analysis, a functional relationship is established between the output characteristics of the structure and the parameters of one or more of its parts. In worst-case analysis, the effect that a part has on product output is evaluated on the basis of end-of-life performance values or out-of-specification replacement parts.

Derating

Derating is a technique by which either the operational stresses acting on a device or structure are reduced relative to the rated strength, or the strength is increased relative to the allocated operating stress levels. Reducing the stress is achieved by specifying upper limits on the operating loads below the rated capacity of the hardware. For example, manufacturers of electronic hardware often specify limits for supply voltage, output current, power dissipation, junction temperature, and frequency. The equipment design team may decide to select an alternative component or make a design change that ensures that the operational condition for a particular parameter, such as temperature, is always below the rated level. The component is then said to have been derated for thermal stress.

The derating factor, typically defined as the ratio of the rated level of a given stress parameter to its actual operating level, is actually a margin of safety or margin of ignorance, determined by the criticality of any possible failures and by the amount of uncertainty inherent in the reliability model and its inputs. Ideally, this margin should be kept to a minimum to maintain the cost effectiveness of the design. This puts the responsibility on the reliability engineer to identify the rated strength, the relevant operating stresses, and the reliability as unambiguously as possible.

To be effective, derating criteria must target the right stress parameter to address modeling of the relevant failure mechanisms. Field measurements may also be necessary, in conjunction with modeling simulations, to identify the actual operating stresses at the failure site. Once the failure models have been quantified, the impact of derating on the effective reliability of the component for a given load can be determined. Quantitative correlations between derating and reliability enable design teams and users to effectively tailor the margin of safety to the level of criticality of the component, leading to better and more cost-effective use of the functional capacity of the component.

Redundancy

Redundancy permits a product to operate even though certain parts and interconnections have failed, thus increasing its reliability and availability. Redundant configurations can be classified as either active or standby. Elements in active redundancy operate simultaneously in performing the same function. Elements in standby redundancy are designed so that an inactive one will, or can, be switched into service when an active element fails. The reliability of the associated function increases with the number of standby elements (optimistically assuming that the sensing and switching devices of the redundant configuration are working perfectly, and failed redundant components are replaced before their companion components fail). One preferred design alternative is that a failed redundant component can be repaired without adversely impacting the product operation, and without placing the maintenance person or the product at risk.

A design team may often find that redundancy is:

- the quickest way to improve product reliability if there is insufficient time to explore alternatives, or if the part is already designed;
- the cheapest solution, if the cost of redundancy is economical in comparison with the cost of redesign; and/or
- the only solution, if the reliability requirement is beyond the state of the art.

On the other hand, in weighing its disadvantages, the design team may find that redundancy will:

- prove too expensive, if the parts, redundant sensors, and switching devices are costly;
- exceed the limitations on size and weight, (for example, in avionics, missiles, and satellites);
- exceed the power limitations, particularly in active redundancy;
- attenuate the input signal, requiring additional amplifiers (which increase complexity); and/or
- require sensing and switching circuitry so complex as to offset the reliability advantage of redundancy.

Qualification and Accelerated Testing

Qualification includes all activities that ensure that the nominal design and manufacturing specifications will meet or exceed the desired reliability targets. Qualification validates the ability of the nominal design and manufacturing specifications of the product to meet the customer's expectations, and assesses the probability of survival of the product over its complete life cycle. The purpose of qualification is to define the acceptable range of variabilities for all critical product parameters affected by design and manufacturing, such as geometric dimensions, material properties, and operating environmental limits. Product attributes that are outside the acceptable ranges are termed defects, since they have the potential to compromise product reliability.[25]

Qualification tests should be performed only during initial product development, and immediately after any design or manufacturing changes in an existing product. Once the product is qualified, routine lot-to-lot requalification is redundant and an unnecessary cost item. A well-designed qualification procedure provides economic savings and quick turnaround during development of new products or mature products subject to manufacturing and process changes.

Investigating failure mechanisms and assessing the reliability of products where long lives are required may be a challenge, since a very long test period under the actual operating conditions is necessary to obtain sufficient data to determine actual failure characteristics. One approach to the problem of obtaining meaningful qualification data for high-reliability devices in shorter time periods is to use methods such as virtual qualification and accelerated testing to achieve test-time compression. However, when qualifying the reliability of a product for overstress mechanisms, a single cycle of the expected overstress load may be adequate, and acceleration of test parameters may not be necessary. This is sometimes called proof-stress testing.

Virtual Qualification

Virtual qualification is a process that requires significantly less time and money than accelerated testing to qualify a part for its life cycle environment. This simulation-based methodology is used to identify the dominant failure mechanisms associated with the part under life cycle loads, to determine the acceleration factor for a given set of accelerated test parameters, and to determine the time-to-failure corresponding to the identified failure mechanisms. Each failure model comprises a stress analysis model and a damage assessment model. The output is a ranking of different failure mechanisms, based on the time to failure. The stress model captures the product architecture, while the damage model depends on a material's response to the applied stress. This process is therefore applicable to existing as well as new products. The objective of virtual qualification is to optimize the product design in such a way that the minimum time-to-failure of any part of the product is greater than its desired life. Although the data obtained from virtual qualification cannot fully replace that obtained from physical tests, it can increase the efficiency of physical tests by indicating the potential failure modes and mechanisms that the operator can expect to encounter.

Ideally, a virtual qualification process will involve identification of quality suppliers, computer-aided physics-of-failure qualification, and a risk assessment and mitigation program. The process allows qualification to be readily incorporated into the design phase of product development since it allows design, test, and redesign to be conducted promptly and cost effectively. It also allows consumers to qualify off-the-shelf components for use in specific environments without extensive physical tests. Since virtual qualification reduces emphasis on examining a physical sample, it is imperative that the manufacturing technology and quality assurance capability of the manufacturer be taken into account. The manufacturer's design, production, test, and measurement procedures must be evaluated and certified. If the data on which the virtual qualification is performed is inaccurate or unreliable, all results are suspect. In addition, if a reduced quantity of physical tests is performed in the interest of simply verifying virtual results, the operator needs to be confident that the group of parts selected is sufficient to represent the product. Further, it should be remembered that the accuracy of the results using virtual qualification depends on the accuracy of the inputs to the process, i.e., the accuracy of the life cycle loads, the choice of the failure models used, the choice of the analysis domain (e.g., 2D, pseudo-3D, full 3D), the constants in the failure model, the material properties, and so on. Hence, in order to obtain a reliable prediction, the variabilities in the inputs should be specified using distribution functions, and the validity of the failure models should be tested by conducting accelerated tests.

Accelerated Testing

Accelerated testing involves measuring the performance of the test product at loads or stresses that are more severe than would normally be encountered, in order to enhance the damage accumulation rate within a reduced time period. The goal of such testing is to accelerate time-dependent failure mechanisms and the damage accumulation rate to reduce the time to failure. The failure mechanisms and modes in the accelerated environment must be the same as (or quantitatively correlated with) those observed under actual usage conditions, and it must be possible to quantitatively extrapolate from the accelerated environment to the usage environment with some reasonable degree of assurance.

Accelerated testing begins by identifying all the possible overstress and wearout failure mechanisms. The load parameter that directly causes the time-dependent failure is selected as the acceleration parameter, and is commonly called the accelerated load. Common accelerated loads include thermal loads, such as temperature, temperature cycling, and rates of temperature change; chemical loads, such as humidity, corrosives, acid, and salt; electrical loads, such as voltage, or power; and mechanical loads, such as vibration, mechanical load cycles, strain cycles, and shock/impulses. The accelerated environment may include a combination of these loads. Interpretation of results for combined loads requires a quantitative understanding of their relative interactions and the contribution of each load to the overall damage.

Failure due to a particular mechanism can be induced by several acceleration parameters. For example, corrosion can be accelerated by both temperature and humidity; and creep can be accelerated by both mechanical stress and temperature. Furthermore, a single accelerated stress can induce failure by several wearout mechanisms simultaneously. For example, temperature can accelerate wearout damage accumulation not only by electromigration, but also by corrosion, creep, and so on. Failure mechanisms that dominate under usual operating conditions may lose their dominance as the stress is elevated. Conversely, failure mechanisms that are dormant under normal use conditions may contribute to device failure under accelerated conditions. Thus, accelerated tests require careful planning in order to represent the actual usage environments and operating conditions without introducing extraneous failure mechanisms or nonrepresentative physical or material behavior. The degree of stress acceleration is usually controlled by an acceleration factor, defined as the ratio of the life under normal use conditions as compared to that under the accelerated condition. The acceleration factor should be tailored to the hardware in question, and can be estimated from an acceleration transform (i.e., a functional relationship between the accelerated stress and the life cycle stress) in terms of all the hardware parameters.

Once the failure mechanisms are identified, it is necessary to select the appropriate acceleration load; to determine the test procedures and the stress levels; to determine the test method, such as constant stress acceleration or step-stress acceleration; to perform the tests; and to interpret the test data, which includes extrapolating the accelerated test results to normal operating conditions. The test results provide qualitative failure information for improving the hardware through design and/or process changes. Accelerated testing includes:

- Accelerated test planning and development: used to develop a test program that focuses on the potential failure mechanisms and modes that were identified in the first phase as the weak links under life cycle loads. The various issues addressed in this phase include designing the test matrix and test loads, analysis, design and preparation of the test vehicle, setting up the test facilities (e.g., test platforms, stress monitoring schemes, failure monitoring and data acquisition schemes), fixture design, effective sensor placement, and data collection and post-processing schemes.
- Test vehicle characterization: used to identify the contribution of the environment on the test vehicle in the accelerated life tests.
- Accelerated life testing: evaluates the vulnerability of the product to the applied life cycle due to wearout failure mechanisms. This step yields a meaningful assessment of life cycle durability only if it is preceded by the steps discussed above. Without these steps, accelerated life testing can only provide comparisons between alternate designs if the same failure mechanism is precipitated.
- Life assessment: used to provide a scientific and rational method to understand and extrapolate accelerated life testing failure data to estimate the life of the product in the field environment.

Detailed failure analysis of failed samples is a crucial step in the qualification and validation program. Without such analyses and feedback to the design team for corrective action, the purpose of the qualification program is defeated. In other words, it is not adequate simply to collect failure data. The key is to use the test results to provide insights into, and consequent control over, relevant failure mechanisms and to prevent them cost effectively.

Manufacturing Issues

Manufacturing and assembly processes can significantly impact the quality and reliability of hardware. Improper assembly and manufacturing techniques can introduce defects, flaws, and residual stresses that act as potential failure sites or stress raisers later in the life of the product. If these defects and stresses can be identified, the design analyst can proactively account for them during the design and development phase.

Auditing the merits of the manufacturing process involves two crucial steps. First, qualification procedures are required, as in design qualification, to ensure that manufacturing specifications do not compromise the long-term reliability of the hardware. Second, lot-to-lot screening is required to ensure that the variabilities of all manufacturing-related parameters are within specified tolerances.[25,26] In other words, screening ensures the quality of the product by precipitating latent defects before they reach the field.

Process Qualification

Like design qualification, process qualification should be conducted at the prototype development phase. The intent is to ensure that the nominal manufacturing specifications and tolerances produce acceptable reliability in the product. The process needs requalification when process parameters, materials, manufacturing specifications, or human factors change.

Process qualification tests can be the same set of accelerated wearout tests used in design qualification. As in design qualification, overstress tests may be used to qualify a product for anticipated field overstress loads. Overstress tests may also be exploited to ensure that manufacturing processes do not degrade the intrinsic material strength of hardware beyond a specified limit. However, such tests should supplement, not replace, the accelerated wearout test program, unless explicit physics-based correlations are available between overstress test results and wearout field-failure data.

Manufacturability

The control and rectification of manufacturing defects has typically been the concern of production and process-control engineers, but not of the design team. In the spirit and context of concurrent product development, however, hardware design teams must understand material limits, available processes, and manufacturing process capabilities in order to select materials and construct architectures that promote producibility and reduce the occurrence of defects, increasing yield and quality. Therefore, no specification is complete without a clear discussion of manufacturing defects and acceptability limits. The reliability engineer must have clear definitions of the threshold for acceptable quality, and of what constitutes nonconformance. Nonconformance that compromises hardware performance and reliability is considered a defect. Failure mechanism models provide a convenient vehicle for developing such criteria. It is important for the reliability analyst to understand what deviations from specifications can compromise performance or reliability, and what deviations are benign and can be accepted.

A defect is any outcome of a process (manufacturing or assembly) that impairs or has the potential to impair the functionality of the product at any time. The defect may arise during a single process or may be the result of a sequence of processes. The yield of a process is the fraction of products that are acceptable for use in a subsequent process in the manufacturing sequence or product life cycle. The cumulative yield of the process is approximately determined by multiplying the individual yields of each of the individual process steps. The source of defects is not always apparent, because defects resulting from a process can go undetected until the product reaches some downstream point in the process sequence, especially if screening is not employed.

It is often possible to simplify the manufacturing and assembly processes in order to reduce the probability of workmanship defects. As processes become more sophisticated, however, process monitoring and control are necessary to ensure a defect-free product. The bounds that specify whether the process is within tolerance limits, often referred to as the process window, are defined in terms of the independent variables to be controlled within the process and the effects of the process on the product or the dependent product variables. The goal is to understand the effect of each process variable on each product parameter in order to formulate control limits for the process, that is, the points on the variable scale where the defect rate begins to possess a potential for causing failure. In defining the process window, the upper and lower limits of each process variable beyond which it will produce defects must be determined. Manufacturing processes must be contained in the process window by defect testing, analysis of the causes of defects, and elimination of defects by process control, such as closed-loop corrective action systems. The establishment of an effective feedback path to report process-related defect data is critical. Once this is done and the process window is determined, the process window itself becomes a feedback system for the process operator.

Several process parameters may interact to produce a different defect than would have resulted from the individual effects of these parameters acting independently. This complex case may require that the interaction of various process parameters be evaluated in a matrix of experiments. In some cases, a defect cannot be detected until late in the process sequence. Thus, a defect can cause rejection, rework, or failure of the product after considerable value has been added to it. These cost items due to defects can affect return on investments by adding to hidden factory costs. All critical processes require special attention for defect elimination by process control.

Process Verification Testing

Process verification testing is often called screening. Screening involves 100% auditing of all manufactured products to detect or precipitate defects. The aim is to preempt potential quality problems before they reach the field. In principle, this should not be required for a well-controlled process. When uncertainties are likely in process controls, however, screening is often used as a safety net.

Some products exhibit a multimodal probability density function for failures, with a secondary peak during the early period of their service life due to the use of faulty materials, poorly controlled manufacturing and assembly technologies, or mishandling. This type of early-life failure is often called infant mortality. Properly applied screening techniques can successfully detect or precipitate these failures, eliminating or reducing their occurrence in field use. Screening should only be considered for use during the early stages of production, if at all, and only when products are expected to exhibit infant mortality field failures. Screening will be ineffective and costly if there is only one main peak in the failure probability density function. Further, failures arising due to unanticipated events such as acts of God (lightning, earthquakes) may be impossible to screen cost effectively.

Since screening is done on 100% basis, it is important to develop screens that do not harm good components. The best screens, therefore, are nondestructive evaluation techniques, such as microscopic visual exams, X-rays, acoustic scans, nuclear magnetic resonance (NMR), electronic paramagnetic resonance (EPR), and so on. Stress screening involves the application of stresses, possibly above the rated operational limits. If stress screens are unavoidable, overstress tests are preferred to accelerated wearout tests, since the latter are more likely to consume some useful life of good components. If damage to good components is unavoidable during stress screening, then quantitative estimates of the screening damage, based on failure mechanism models must be developed to allow the design team to account for this loss of usable life. The appropriate stress levels for screening must be tailored to the specific hardware. As in qualification testing, quantitative models of failure mechanisms can aid in determining screen parameters.

A stress screen need not necessarily simulate the field environment, or even utilize the same failure mechanism as the one likely to be triggered by this defect in field conditions. Instead, a screen should exploit the most convenient and effective failure mechanism to stimulate the defects that can show up in the field as infant mortality. Obviously, this requires an awareness of the possible defects that may occur in the hardware and extensive familiarity with the associated failure mechanisms.

Unlike qualification testing, the effectiveness of screens is maximized when screens are conducted immediately after the operation believed to be responsible for introducing the defect. Qualification testing is preferably conducted on the finished product or as close to the final operation as possible; on the other hand, screening only at the final stage, when all operations have been completed, is less effective, since failure analysis, defect diagnostics, and troubleshooting are difficult and impair corrective actions. Further, if a defect is introduced early in the manufacturing process, subsequent value added through new materials and processes is wasted, which additionally burdens operating costs and reduces productivity. Admittedly, there are also several disadvantages to such an approach. The cost of screening at every manufacturing station may be prohibitive, especially for small batch jobs. Further, components will experience repeated screening loads as they pass through several manufacturing steps, which increases the risk of accumulating wearout damage in good components due to screening stresses. To arrive at a screening matrix that addresses as many defects and failure mechanisms as feasible with each screen test, an optimum situation must be sought through analysis of cost effectiveness, risk, and the criticality of the defects. All defects must be traced back to the root cause of the variability.

Any commitment to stress screening must include the necessary funding and staff to determine the root cause and appropriate corrective actions for all failed units. The type of stress screening chosen should be derived from the design, manufacturing, and quality teams. Although a stress screen may be necessary during the early stages of production, stress screening carries substantial penalties in capital, operating expense, and cycle time, and its benefits diminish as a product approaches maturity. If almost all of the products fail in a properly designed screen test, the design is probably incorrect. If many products fail, a revision of the manufacturing process is required. If the number of failures in a screen is small, the processes are likely to be within tolerances and the observed faults may be beyond the resources of the design and production process.

Summary

Reliability is not a matter of chance or good fortune; rather, it is a rational consequence of conscious, systematic, rigorous efforts at every stage of design, development, and manufacture. High product reliability can only be assured through robust product designs, capable processes that are known to be within tolerances, and qualified components and materials from vendors whose processes are also capable and within tolerances. Quantitative understanding and modeling of all relevant failure mechanisms provide a convenient vehicle for formulating effective design, process, and test specifications and tolerances.

The physics-of-failure approach is not only a tool to provide better and more effective designs, but it also helps develop cost-effective approaches for improving the entire approach to building electronic products. Proactive improvements can be implemented for defining more realistic performance requirements and environmental conditions, identifying and characterizing key material properties, developing new product architectures and technologies, developing more realistic and effective accelerated stress tests to audit reliability and quality, enhancing manufacturing-for-reliability through mechanistic process modeling and characterization to allow proactive process optimization, increasing first-pass yields, and reducing hidden factory costs associated with inspection, rework, and scrap.

When utilized early in the concept development stage of a product's development, reliability serves as an aid to determine feasibility and risk. In the design stage of product development, reliability analysis involves methods to enhance performance over time through the selection of materials, design of structures, choice of design tolerance, manufacturing processes and tolerances, assembly techniques, shipping and handling methods, and maintenance and maintainability guidelines. Engineering concepts such as strength, fatigue, fracture, creep, tolerances, corrosion, and aging play a role in these design analyses. The use of physics-of-failure concepts coupled with mechanistic and probabilistic techniques is often required to understand the potential problems and trade-offs, and to take corrective actions. The use of factors of safety and worst-case studies as part of the analysis is useful in determining stress screening and burn-in procedures, reliability growth, maintenance modifications, field testing procedures, and various logistics requirements.

Defining Terms

Accelerated testing: Tests conducted at stress levels that are more severe than the normal operating levels, in order to enhance the damage accumulation rate within a reduced time period.

Damage: The failure pattern of an electronic or mechanical product.

Derating: Practice of subjecting parts to lower electrical or mechanical stresses than they can withstand in order to increase the life expectancy of the part.

Failure mode: Any physically observable change caused by a failure mechanism.

Failure mechanism: A process through which a defect nucleates and grows as a function of stresses such as thermal, mechanical, electromagnetic, or chemical loadings, i.e., creep, fatigue, wear, and so on, which results in degradation or failure of a product.

Integrity: A measure of the appropriateness of the tests conducted by the manufacturer and the part's ability to survive those tests.

Overstress failures: Catastrophic sudden failures due to a single occurrence of a stress event that exceeds the intrinsic strength of a material.

Product performance: The ability of a product to perform as required according to specifications.

Qualification: All activities that ensure that the nominal design and manufacturing specifications will meet or exceed the reliability goals.

Quality: A measure of a part's ability to meet the workmanship criteria of the manufacturer.

Reliability: The ability of a product to perform as intended (i.e., without failure and within specified performance limits) for a specified time, in its life cycle application environment.

Wearout failures: Failures due to accumulation of incremental damage, occurring when the accumulated damage exceeds the material endurance limit.

References

1. Pecht, M., *Integrated Circuit, Hybrid, and Mutichip Module Package Design Guidelines — A Focus on Reliability*, John Wiley & Sons, New York, 1994.
2. O'Connor, P., *Practical Reliability Engineering*, John Wiley & Sons, New York, 1991.
3. Jackson, M., Mathur, A., Pecht, M., and Kendall, R., Part Manufacturer Assessment Process, *Quality and Reliability Engineering International*, 15, 457, 1999.
4. Jackson, M., Sandborn, P., Pecht, M., Hemens-Davis, C., and Audette, P., A risk-informed methodology for parts selection and management, *Quality and Reliability Engineering International*, 15, 261, 1999.
5. Lewis, E.E., *Introduction to Reliability Engineering*, John Wiley & Sons, New York, 1996.
6. Sage, A.P. and Rouse, W.B., *Handbook of Systems Engineering and Management*, John Wiley & Sons, New York, 1999.
7. IEC Standard 60134, *Rating systems for electronic tubes and valves and analogous semiconductor devices*, (Last reviewed in July 1994 by the IEC Technical Committee 39 on Semiconductors), 1961.
8. Stogdill, R. C., Dealing with obsolete parts, *IEEE Design & Test of Computers*, 16, 2, 17, 1999.
9. Dasgupta, A. and Pecht, M., Failure mechanisms and damage models, *IEEE Transactions on Reliability*, 40, 5, 531, 1991.
10. Dasgupta, A. and Hu, J.M., Failure mechanism models for brittle fracture, *IEEE Transactions on Reliability*, 41, 3, 328, 1992.
11. Dasgupta, A. and Hu, J.M., Failure mechanism models for ductile fracture, *IEEE Transactions on Reliability*, 41, 4, 489, 1992.
12. Dasgupta, A. and Hu, J.M., Failure mechanism models for excessive elastic deformation, *IEEE Transactions on Reliability*, 41, 1, 149, 1992.
13. Dasgupta, A. and Hu, J.M., Failure mechanism models for plastic deformation, *IEEE Transactions on Reliability*, 41, 2, 168, 1992.
14. Dasgupta, A. and Haslach, H. W., Jr., Mechanical design failure models for buckling, *IEEE Transactions on Reliability*, 42, 1, 9, 1993.
15. Engel, P.A., Failure models for mechanical wear modes and mechanisms, *IEEE Transactions on Reliability*, 42, 2, 262, 1993.
16. Li, J. and Dasgupta, A., Failure mechanism models for material aging due to interdiffusion, *IEEE Transactions on Reliability*, 43, 1, 2, 1994.
17. Li, J. and Dasgupta, A., Failure-mechanism models for creep and creep rupture, *IEEE Transactions on Reliability*, 42, 3, 339, 1994.
18. Dasgupta, A., Failure mechanism models for cyclic fatigue, *IEEE Transactions on Reliability*, 42, 4, 548, 1993.
19. Young, D. and Christou, A., Failure mechanism models for electromigration, *IEEE Transactions on Reliability*, 43, 2, 186, 1994.

20. Rudra, B. and Jennings, D., Failure mechanism models for conductive-filament formation, *IEEE Transactions on Reliability*, 43, 3, 354, 1994.
21. Al-Sheikhly, M. and Christou, A., How radiation affects polymeric materials, *IEEE Transactions on Reliability*, 43, 4, 551, 1994.
22. Diaz, C., Kang, S.M., and Duvvury, C., Electrical overstress and electrostatic discharge, *IEEE Transactions on Reliability*, 44, 1, 2, 1995.
23. Tullmin, M. and Roberge, P.R., Corrosion of metallic materials, *IEEE Transactions on Reliability*, 44, 2, 271, 1995.
24. Upadhyayula, K. and Dasgupta, A., Guidelines for physics-of-failure based accelerated stress testing, *Annual Reliability and Maintainability Symposium 1998 Proceedings, International Symposium on Product Quality and Integrity*, 345, 1998.
25. Pecht, M., Dasgupta, A., Evans, J. W., and Evans, J. Y, *Quality Conformance and Qualification of Microelectronic Packages and Interconnects*, John Wiley & Sons, New York, 1994.
26. Kraus, A., Hannemann, R., Pecht, M., *Semiconductor Packaging: A Multidisciplinary Approach*, John Wiley & Sons, New York, 1994.

Further Information

Microelectronics Reliability: http://www.elsevier.com/locate/microrel
IEEE Transactions on Reliability: http://www.ewh.ieee.org/soc/rs/transactions.htm

Ham, R. E. et al. "Microwave Measurements"
The RF and Microwave Handbook
Editor in Chief Mike Golio
Boca Raton: CRC Press LLC,2001

4

Microwave Measurements

R.E. Ham
Consultant

Joseph Staudinger
Motorola

Alfy Riddle
Macallan Consulting

J. Stevenson Kenney
Georgia Institute of Technology

John F. Sevic
UltraRF, Incorporated

Anthony E. Parker
Macquarie University

James G. Rathmell
University of Sydney

Jonathan B. Scott
Agilent Technologies

Jean-Pierre Lanteri
TycoElectronics

Christopher Jones
TycoElectronics

John R. Mahon
TycoElectronics

4.1 Linear Measurements

R.E. Ham

Microwave and RF measurements can be classified in two distinct but often overlapping categories: signal measurements and network measurements. Signal measurements include observation and determination

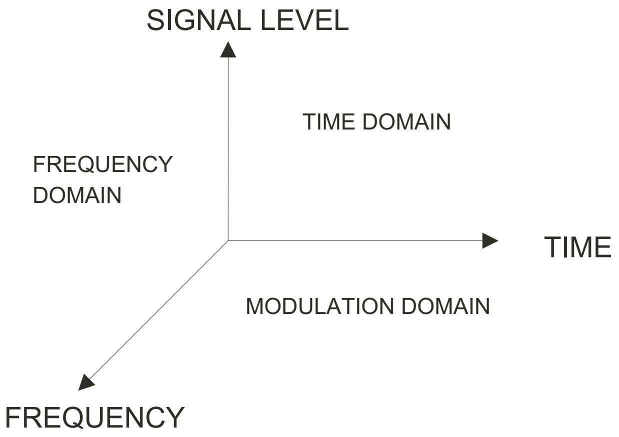

FIGURE 4.1 Signals are characterized by three different types of measurements.

of the characteristics of waves and waveforms. These parameters can be obtained in the time, frequency, or modulation domain. Network measurement determines the terminal and signal transfer characteristics of devices and systems with any number of ports.

Signal Measurements

Signal measurements are taken in any one or more of three measurement planes as illustrated in Fig. 4.1. The most common measurement at low frequencies is in the time domain where the amplitude of a signal waveform is observed with respect to time. The instrument used for this is an oscilloscope. By continuing to observe the amplitude of the signal over a small frequency range, the spectral components of the signal are obtained. This measurement is normally made with a spectrum analyzer. Determining the instantaneous frequency of a signal versus time is a modulation domain measurement.

Time Domain

Observation of RF and microwave signals with an analog oscilloscope is limited by the speed of response of the instrument circuits and of the display. Building such an instrument for operation beyond a few hundred megahertz is very difficult and expensive. For observing very high-speed waveforms signal sampling techniques are incorporated.

A sampling oscilloscope measures the value of a waveform at a particular time and digitally stores the sample data for display. If the sampling can be performed fast enough, the entire waveform shape can be recreated from the sample data. This is done at relatively low frequencies; however, as the frequency increases it is not possible to capture enough points during one waveform occurrence. By delaying subsequent samples to be taken a very short time later during the occurrence of another cycle of the waveform, the recurring waveform shape can ultimately be reconstructed from the stored digital data.

Note the qualification that the waveform shape that can be measured by the high-speed sampling technique must be recurring. This makes capturing a onetime occurrence very difficult and, even if points in a gigahertz waveform can be captured, this does not mean that one cycle of the waveform can be captured.

Frequency Domain

The number of measurements that must be made on a signal over a specified period of time is a function of the stability and modulation placed on the signal. The exact measurement of the frequency of a stable and spectrally pure signal is performed with a frequency counter and measurements are normally made a few times per second. Direct counting circuits are available well into the lower microwave frequency range. At high microwave frequencies counters use conversion oscillators and mixers to heterodyne the signal down in frequency to where it can be directly counted. Microprocessor controllers and knowledge of the exact frequency of the conversion oscillators enables an exact signal frequency to be calculated.

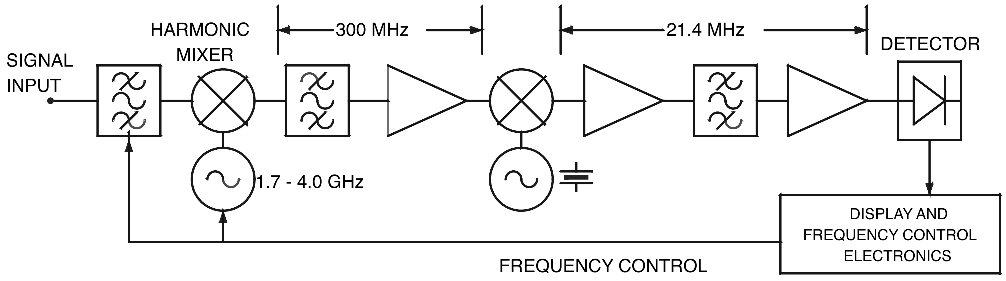

OSCILLATOR HARMONIC NUMBER (n)	EFFECTIVE OSCILLATOR FREQUENCY (GHz)	TUNED RF FREQUENCY (GHz)
1	1.7 - 4.0	2.0 - 4.3
2	3.4 - 8.0	3.7 - 8.3
3	5.1 - 12.0	5.4 - 12.3
4	6.8 - 14.0	7.1 - 14.3
5	8.5 - 20.0	8.8 - 20.3

FIGURE 4.2 Simplified block diagram of a microwave spectrum analyzer.

A spectrum analyzer [1] is used to make frequency domain measurements of complex signals and signals with characteristics that vary with time. This is basically a swept frequency filter with a detector to determine the signal amplitude within the bandwidth of the filter and some means of displaying or storing the measured information. To increase the selectivity and dynamic range of such a basic instrument, heterodyne conversions are used. Figure 4.2 is the block diagram of a typical microwave spectrum analyzer.

The first intermediate frequency is chosen to permit a front-end filter to eliminate the image from the first mixer. In this case, 300 MHz is chosen because the tunable filter, usually a YIG device, will have considerable attenuation at the image frequency 600 MHz away from the desired signal. The second intermediate frequency is chosen because reasonably selective filters can be constructed to enable resolving signal components that are close to each other. Additionally, detector and signal processing components, such as digital signal processors, can be readily constructed at the lower frequency.

Because the normal frequency range required from a microwave spectrum analyzer is many octaves wide, multiple first conversion oscillators are required; however, this is an extremely expensive approach. Spectrum analyzers use a harmonic mixer for the first conversion and the first filter is tuned to eliminate the products that would be received due to the undesired harmonics of the conversion oscillator. Note the list of harmonic numbers (*n*) and the resulting tuned frequency of the example analyzer. As the harmonic number increases the sensitivity of the analyzer decreases because the harmonic mixer efficiency decreases with increasing *n*.

The most important spectrum analyzer specifications are:

1. Frequency tuning range — to include all of the frequency components of the signal to be measured.
2. Frequency accuracy and stability — to be more stable and accurate than the signal to be measured.
3. Sweep width — the band of frequencies over which the unit can sweep without readjustment.
4. Resolution bandwidth — narrow enough to resolve different spectral components of the signal.
5. Sensitivity and/or noise figure — to observe very small signals or small parts of large signals.
6. Sweep rate — maximum sweep rate is established by the settling time of the filter that sets the resolution bandwidth.
7. Dynamic range — the difference between the largest and smallest signal the analyzer can measure without readjustment.
8. Phase noise — a signal with spectral purity greater than that of the analyzer conversion oscillators cannot be characterized.

Spectrum analyzers using other than swept frequency techniques can be made. For example, high speed sampling methods used with digital signal processors (DSP) calculating the Fast Fourier Transform (FFT) are readily implemented; however, the speed of operation of the logic circuits limits the upper frequency of operation. This is a common method of intermediate frequency demodulation and the useable frequency will move upward with semiconductor development.

Modulation Domain

Modulation domain measurements [2] yield the instantaneous frequency of a signal as a function of time. Two examples of useful modulation domain data are the instantaneous frequency of a phase-locked oscillator as the loop settles and the pulse repetition rate of a fire control radar as it goes from search mode (low pulse repetition frequency or PRF) to lock and fire mode (high PRF).

A modulation domain analyzer establishes the exact time at which a desired event occurs and catalogs the time. The event captured in a phase-locked oscillator is the zero crossing of the oscillator output voltage. For a radar it is the leading edge of each pulse. From this information the event frequency is calculated. Various other modulation domain analyzers can be made with instantaneous frequency correlators and frequency discriminators.

Network Measurements

Low frequency circuit design and performance evaluation is based upon the measurement of voltages and currents. Knowing the impedance level at a point in a circuit to be the ratio of voltage to current, a voltage or current measurement can be used to calculate power. By measuring voltage and current as a complex quantity, yielding complex impedances, this method of circuit characterization can be used at relatively high frequencies even with the limitations of nontrivial values of circuit capacitive and inductive parasitics. When the parasitics can no longer be treated as lumped elements, distributed circuit concepts must be used.

A simple transmission line such as the coaxial line in Fig. 4.3a can, if physically very small in all dimensions with respect to a wavelength, be modeled as a lumped element circuit as shown in Fig. 4.3b; however, as the size of the line increases relative to the wavelength, it becomes necessary to use an extremely complex lumped element model or to use the transmission line equations for the distributed line. The concept of a transmission line accounts for the transformation of impedances between circuit points and for the time delay between points that must be considered when the circuit size approaches

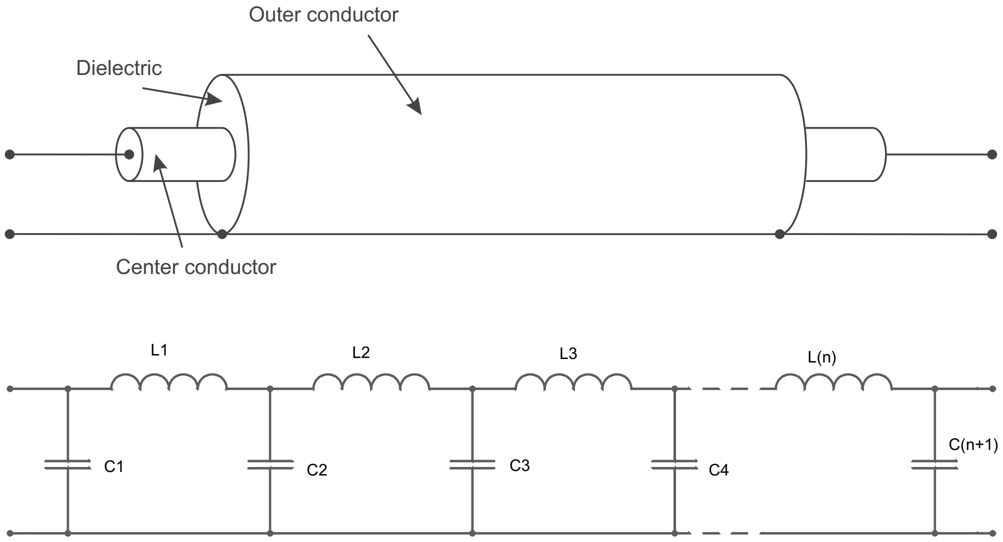

FIGURE 4.3 Examples of transmission lines: (a) coaxial; (b) lumped element.

a significant fraction of a wavelength of the frequency being measured; hence, RF and microwave measurements are primarily based upon transmission line concepts and measurements.

The basic quantities measured in high frequency circuits are power, impedance, port-to-port transfer functions of n-port devices, frequency, and noise [3, 4].

Power

Microwave power cannot be readily detected with equipment used at lower frequencies such as voltmeters and oscilloscopes [5]. The RF and microwave utility of these instruments are limited by circuit parasitics and the resultant limited frequency response. Central to all microwave measurements is the determination of the microwave power available at ports in the measurement circuit. To facilitate measurements, a characteristic impedance or reference resistance is assumed. The instruments used to measure microwave and RF power typically have a 50-ohm input and output impedance at the frequency being measured.

Diode detectors sense the amplitude of a signal. By establishing the input impedance of a diode detector, the power of a signal at a test port can be measured. The diode detector shown in Fig. 4.4 allows current to pass through the diode when the diode is forward biased and prevents current from flowing when the diode is reverse biased. The average of the current flow when forward biased results in a DC output from the lowpass RC filter that is proportional to the amplitude of the input voltage. Note that as the diode junction area must be small to minimize the parasitic junction capacitance that would short the signal

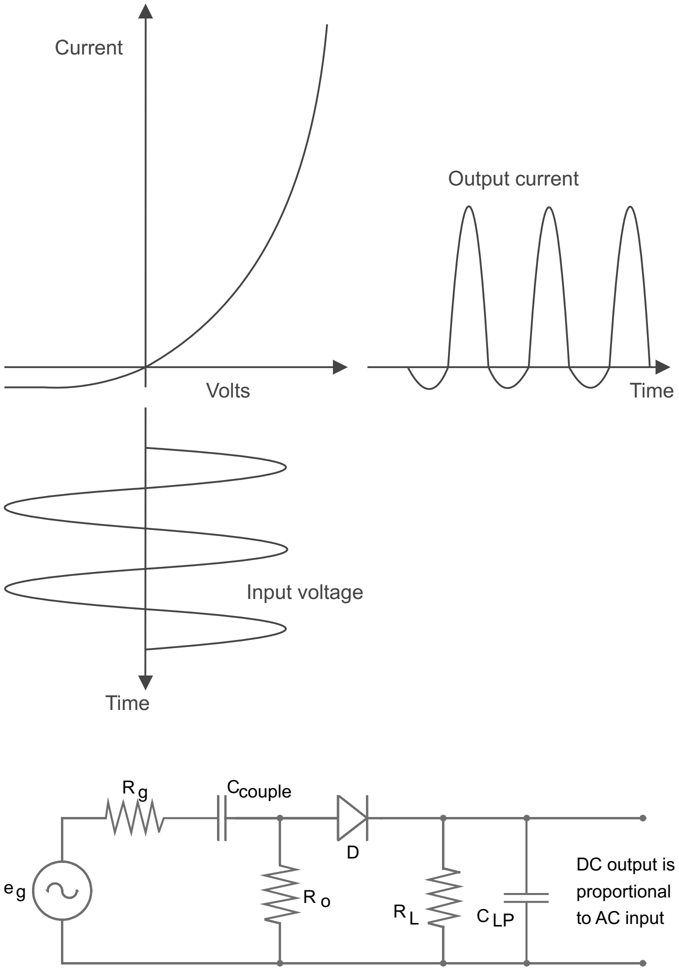

FIGURE 4.4 Diode detector: (a) diode detector waveforms; (b) diode detector circuit.

across the diode, the load resistor must be a relatively large value to minimize the diode current; therefore, the impedance seen looking into the diode detector is established primarily by the resistor placed across the detector input. If the input voltage is less than that where the diode current becomes linearly proportional to the input voltage, the diode is in a predominantly square law region and the voltage out of the detector is proportional to the input power in decibels. This square law range typically extends over a 50-dB range from –60 dBm to –10 dBm in a 50-ohm system. Diodes are used in the linear range up to about 10 dBm. The one significant disadvantage of the diode detector is the temperature sensitivity of the diode. The diode detector response can be very fast, but it cannot easily be used for accurate power measurement.

The most accurate RF and microwave power measuring devices are thermally dependent detectors. These detectors absorb the power and by either measuring the change in the detector temperature or the change in the resistance of the detecting device with a change in temperature, the power absorbed by the detector can be accurately determined.

The primary thermally dependent detectors are the bolometer and the thermistor. They are placed across the transmission media as a matched impedance termination. A bridge as shown in Fig. 4.5(a) can be used to detect a change in the resistance of the bolometer. To increase the detector sensitivity, two units can be placed in parallel for the RF/microwave signal and in series for the change in DC resistance as shown in Fig. 4.5(b). Unfortunately, this circuit can also be used as a thermometer; therefore, an

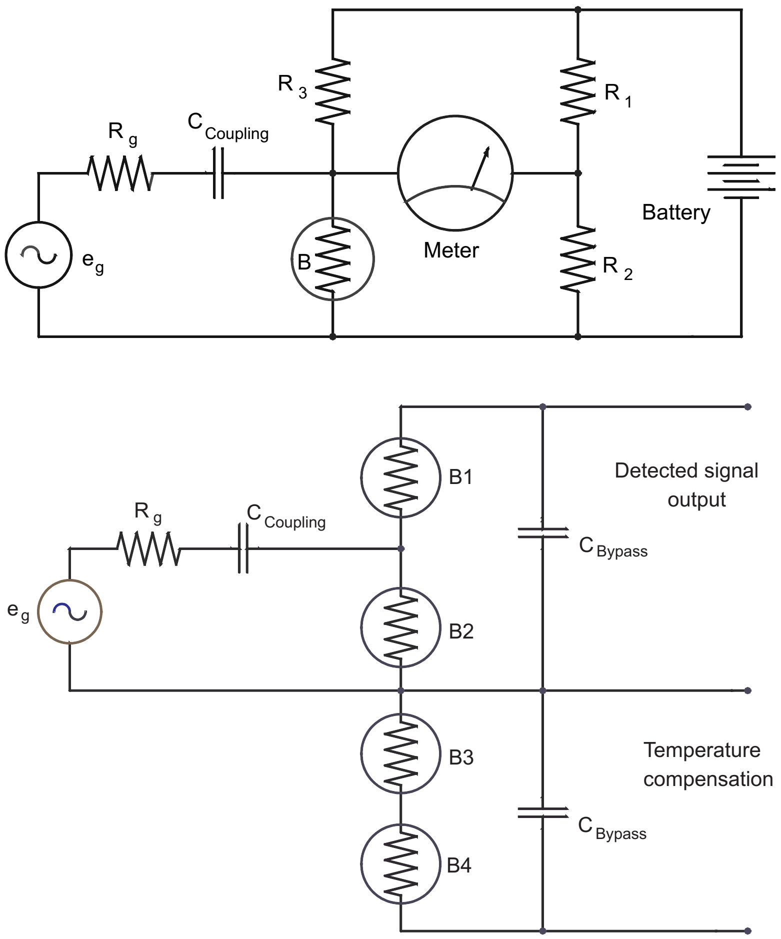

FIGURE 4.5 Thermally dependent detector circuits: (a) bolometer in a bridge circuit; (b) temperature compensated bolometer head; (c) self-balancing bridge circuit.

identical pair of bolometer detectors are normally placed in close thermal proximity but only one of the detectors is used to detect signal power. The other detector is used to detect environmental temperature changes so that the difference in temperature change is due to the signal power absorbed in the upper detector.

To maintain a constant impedance looking into the bolometer elements, a bias current is passed through the elements to increase their temperature above operational ambient. The resistance of the detectors is compared to a fixed resistance in a bridge. The bridge error is used to adjust the bias current in the bolometers. The bias energy that must be removed from the detector to maintain a constant resistance is equal to the amount of signal energy absorbed by the detector; therefore, the meter can be calibrated in power by knowing the amount of bias power applied to the detector. Figure 4.5(c) is a simplified example of a self-balancing bridge circuit.

Impedance

Consider a very simple transmission line, two parallel pieces of wire spaced a uniform distance and in free space, as shown in Fig. 4.6. A DC voltage with a source resistance R_g and series switch is connected to terminal 1 and a resistor R_L is placed across terminal two.

First, let the length of the wires be zero. Close the switch. If the load resistor R_L is equal to the source resistance R_g, the condition necessary for maximum power transfer from a source to a load, then the voltage across the load R_L is $e_g/2$. This is the voltage that will be measured from a signal generator when the output is terminated in its characteristic impedance, commonly called R_o. The signal power from the signal generator, and also the maximum available power from the generator, is then e_g^2/R_g. If R_L is a short circuit the output voltage is zero. If R_L is an open circuit the output voltage is 2 times $e_g/2$ or e_g.

Now let the line have a length, L. When the switch is closed, a traveling wave of voltage moves toward the load resistor at the speed of light, c. At time t, the wave has moved down the line a distance ct. A wave of current travels with the wave of voltage. If the characteristic impedance of this parallel transmission line is Z_o and the load resistance is equal to Z_o, then the current traveling with the voltage wave has a value at any point along the line of the value of the voltage at that point divided by Z_o. For this special case, when the wave reaches the load resistor, all of the energy in the wave is dissipated in the resistor; however, if the resistor is not equal to Z_o there is energy in the wave that must go someplace as it is not dissipated in the load resistor.

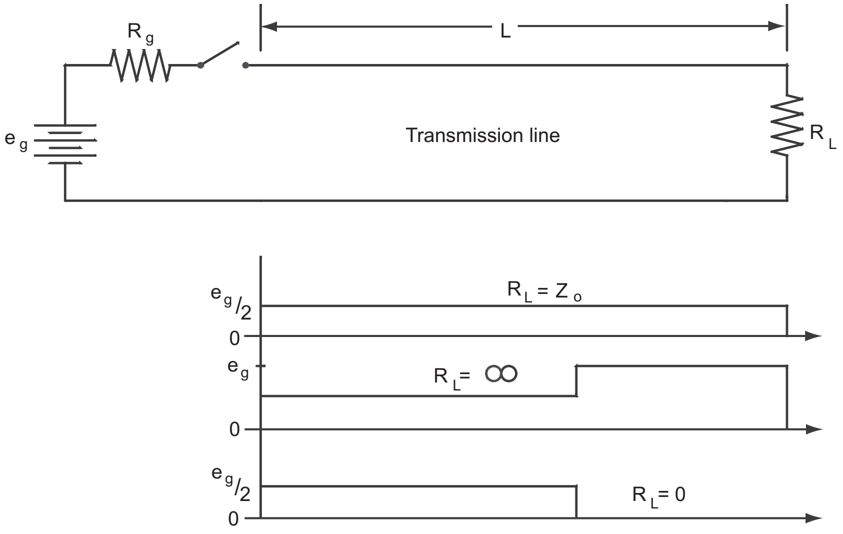

FIGURE 4.6 Switched DC line voltage at time > length/velocity for various impedances at the end of the line.

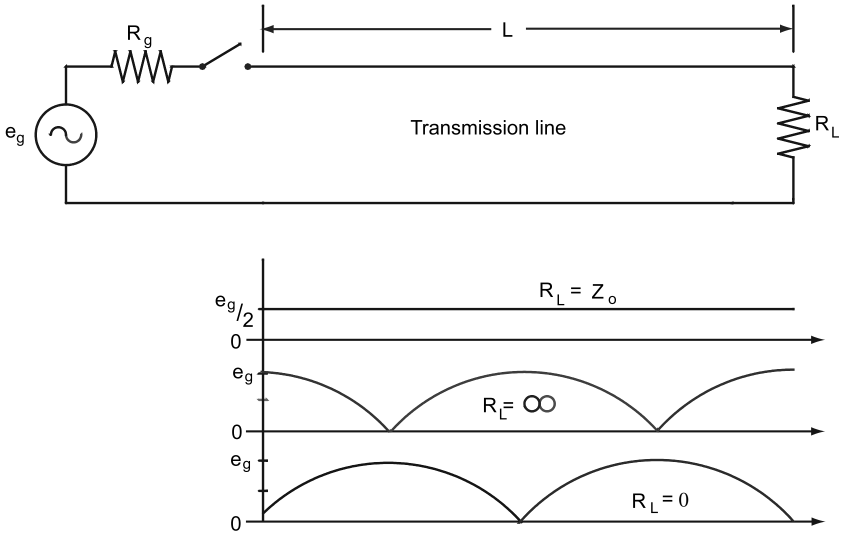

FIGURE 4.7 Waveforms on the line for a sinusoidal source and various impedances at the end of the line.

This mismatch between the characteristic impedance of the line and the terminating load resistor results in a reflected wave that travels back toward the voltage source. If the load resistor is a short circuit, the voltage at the end of the line must equal zero at all times. The only way for this to occur is for the reflected voltage at the end of the wire to be equal to –1 times the incident voltage at that same point. If the load is an open circuit the reflected voltage will be exactly equal to the incident voltage; hence the sum of the incident and reflected voltages will be twice the value of the incident voltage at the end of the line. Note the similarity of these three cases to those of the zero length line.

Now replace the DC voltage source and switch with a sinusoidal voltage source as in Fig. 4.7. The voltages shown are the RMS values of the vector sum of the incident and reflected waves. As the source voltage varies, the instantaneous value of the sinusoidal voltage between the wires travels down the wires. The ratio of the traveling voltage wave to the traveling current wave is the characteristic impedance of the transmission line. If the terminating impedance is equal to the line characteristic impedance, there is no wave reflected back toward the generator; however, if the termination resistance is any value other than Z_o there is a reflected wave. If R_L is a real impedance and greater than Z_o, the reflected wave is 180° out of phase with the incident wave. If R_L is a real impedance and is less than Z_o, the reflected wave is in phase with the incident wave. The amount of variation of R_L from Z_o determines the magnitude of the reflected wave. If the termination is complex, the phase of the reflected wave is neither zero nor 180°.

Assuming the generator impedance R_s is equal to the line characteristic impedance, so that a reflected wave incident on the generator does not cause another reflected wave, sampling the voltage at any point along the transmission line will yield the vector sum of the incident and reflected waves. With a matched impedance ($R_L = Z_o$) termination the magnitude of the AC voltage along the line is a constant. With a short circuit termination, the voltage magnitude at the load will be zero and, moving back toward the generator, the voltage one-half wavelength from the end of the line will also be zero. With an open circuit there is a voltage maxima at the end of the line and a minima on the line one-quarter wavelength back toward the generator.

The complex reflection coefficient Γ is the ratio of the reflected wave to the incident wave; hence it has a magnitude ρ between 0 and 1 and an angle θ between +180° and –180°. The reflection coefficient as a function of the measured impedance Z_L with respect to the measurement system characteristic impedance Z_o is

$$\Gamma = \frac{Z_L - Z_o}{Z_L + Z_o} = \rho\left(\sin\theta + j\cos\theta\right)$$

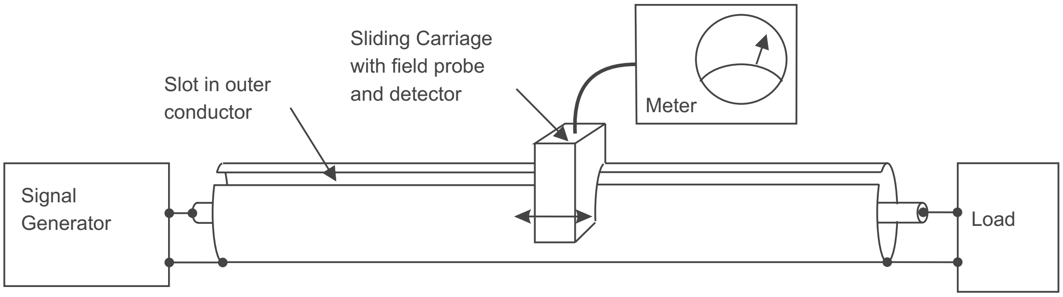

FIGURE 4.8 A slotted line is used to measure the impedance of an unknown load.

Slotted Line

Determination of the relative locations of the minima and maxima along the line, or similarly the determination of the magnitude of waves traveling toward and away from the load resistor, is the basis for the measurement of RF and microwave impedance and the most basic instrument used for making this measurement is the slotted line. The slotted line is a transmission line with a slit in the side that enables a probe to be inserted into the transmission mode electromagnetic field as shown in Fig. 4.8. A diode detector placed within the sliding probe provides a DC voltage that is proportional to the magnitude of the field in the slotted line. As the probe is moved along the line, the minimum and maximum field positions and magnitudes can be determined. The ratio of the maximum field magnitude to the minimum field magnitude is the standing wave ratio (SWR). SWR is normally stated as a scalar quantity and is

$$SWR = \frac{1+\rho}{1-\rho}$$

Before placing an unknown impedance at the measurement terminal of the slotted line, the line is calibrated with a short circuit. This establishes a measurement plane at the short circuit. Any measurement made after calibrating with this reference short is made at the plane of the short circuit. A phase reference is located at the position on the slotted line of a minimum voltage measurement. The distance between two minimum voltage measurement locations is one-half wavelength at the measurement frequency.

If the short circuit is replaced with an open circuit, the minimum voltage locations along the line are shifted by one-quarter wavelength. The difference between the phase of a reflected wave of an open and a short circuit is 180°; hence, the distance between two minimum measurements represents 360° of phase shift in the reflected wave. Note that it is very difficult to use an open circuit for a reference at high frequencies because fringing and radiated fields at the end of the transmission line result in phase and amplitude errors in the reflected wave.

The impedance to be measured now replaces the calibrating short circuit. The new minimum voltage location is found by moving the detector carriage along the slotted line. The distance the minimum voltage measurement moves from the short circuit reference location is ratioed to 180° at a quarter of a wavelength shift (For example, a minimum shift of one-eighth wavelength results from a reflection coefficient phase shift of 90°). This is the phase difference between the forward and reflected waves on the transmission line. Either way the minimum moves from the short circuit calibrated reference point is a shift from 180° back toward 0°. If the shift is toward the load, then the actual phase of the reflection coefficient is –180° plus the shift. If the shift is toward the generator from the reference point, the actual phase of the reflection coefficient is 180° minus the shift.

The best method of visualizing complex impedances as a function of the complex reflection coefficient is the Smith Chart [6, 7, 8]. A simplified Smith Chart is shown in Fig. 4.9. The distance from the center of the chart to the outside of the circle is the reflection coefficient ρ. The minimum value of ρ is 0 and the maximum value is 1. If there is no reflection, the impedance is resistive and equal to the characteristic

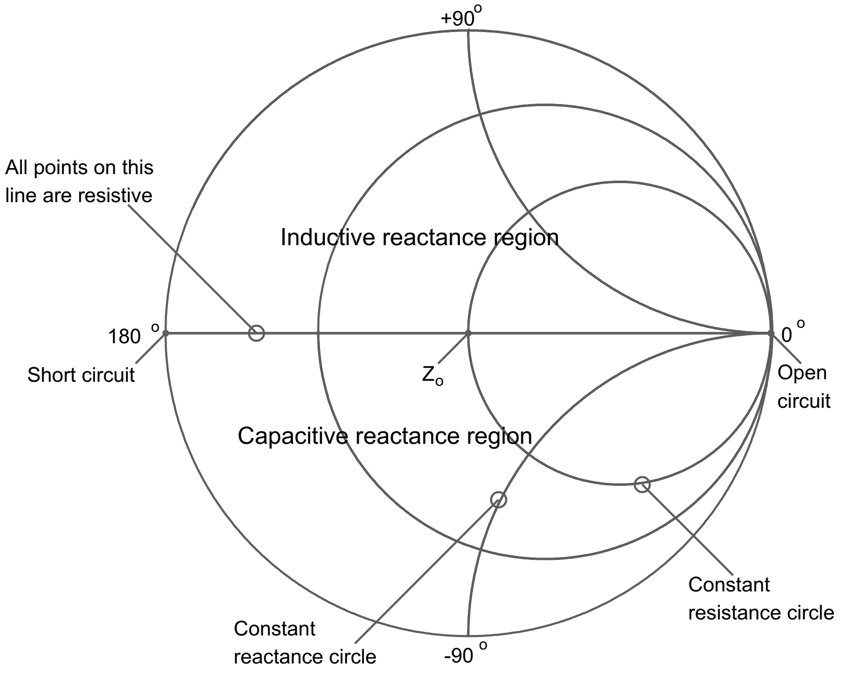
+90°
All points on this line are resistive
Inductive reactance region
180 °
Short circuit
Z$_o$
0 °
Open circuit
Capacitive reactance region
Constant resistance circle
Constant reactance circle
-90 °

FIGURE 4.9 The Smith Chart is a plot of all nonnegative real impedances.

impedance of the transmission line or slotted line. If the reflected wave is equal to the incident wave, the reflection coefficient is one and the impedance lies on the circumference of the circle. If the angle of the reflection coefficient is zero or 180°, the impedance is real and lies along the central axis. Reflection coefficients with negative angles have capacitive components in the impedance and those with positive angles have inductive components.

Directional Coupler

Slotted lines must be on the order of a wavelength long. Additionally, they do not lend themselves to computer-controlled or automatic measurements. Another device for measuring the forward and reflected waves on a transmission line is the directional coupler [9]. Physically this is a pair of open transmission lines that are placed close enough for the fields generated by a propagating wave in one line to couple to the other line, hence inducing a proportional wave in the second line. The coupler is a four-port device. Referencing Fig. 4.10, a wave propagating to the right in line one couples to line 2 and propagates to the left. A wave propagating in line 1 to the left couples to line 2 and propagates to the right; therefore, the outputs from ports 3 and 4 are proportional to the forward and reverse wave propagating in line 1.

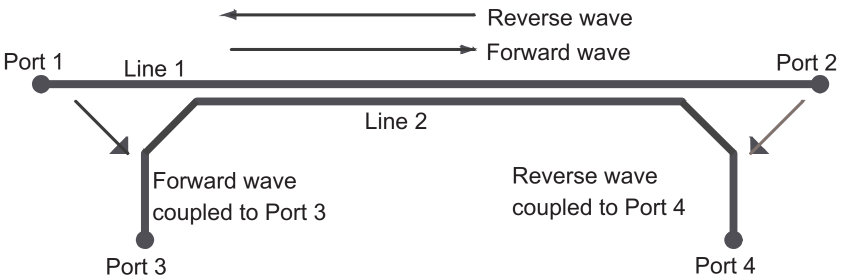
Reverse wave
Forward wave
Port 1
Line 1
Port 2
Line 2
Forward wave coupled to Port 3
Reverse wave coupled to Port 4
Port 3
Port 4

FIGURE 4.10 A directional coupler separates forward and reverse waves on a transmission line.

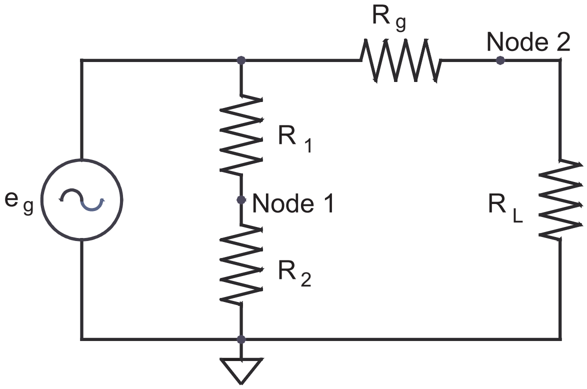

FIGURE 4.11 A resistive bridge can be used to measure the reverse wave on a transmission line.

The primary specifications for a coupler are its useful frequency range, the attenuation of the coupled wave to the coupled ports (coupling), and the attenuation of a signal traveling in the opposite direction to the desired signal at the desired signal's coupled port (directivity). For example, a 10-dB coupler with a 10-dBm signal propagating in the forward direction in line 1 will output a 10-dBm signal at port 3. If the directivity of the coupler is 30 dB there will also be a –40-dBm signal resulting from the forward wave at the reverse wave port, port 4. If the forward wave is properly terminated with the system impedance, there will be no reverse wave on line 1; hence, there will not be an output at port 4 due to a reverse wave.

Note that power must be conserved through the coupler. Therefore, if in the example above, 1.54 dBm is coupled from the forward signal in line 1 to port 3, there will be only a 90-dBm output from port 2. This power must be taken into account in the measurement. The greater the attenuation to the coupled ports, the less the correction will be. Normally 20- or 30-dB couplers are used so the correction is minimal and, in many cases, small enough to be ignored.

By measuring the power from the forward and reverse coupled ports, the magnitude of the reflection coefficient and the SWR can be calculated. Typically the most common indication of the quality of the power match of a device being measured is the attenuation of the reflected wave. This is

$$RL = 10 * \log_{10}\left(\frac{P_{Forward}}{P_{Reverse}}\right)$$

As power is proportional to voltage squared, when the termination resistance is equal on all ports, the return loss can also be expressed as a voltage ratio

$$RL(dB) = 10 * \log_{10}\left(\frac{V_{Forward}^{2}/R_o}{V_{Reverse}^{2}/R_o}\right) = -20 * \log_{10}\left(\frac{V_{Reverse}}{V_{Forward}}\right) = -20 * \log_{10}(\rho)$$

Hence the return loss is the magnitude of the reflection coefficient ρ in decibels.

Resistive Bridge

The directional coupler is functionally equivalent to a bridge circuit, the primary difference being that the only losses in the transmission line coupler are from parasitics and can be designed to be very small. Referencing Fig. 4.11, the voltage drop across R_g when R_L equals R_g is $e_g/2$. For this case, the equivalent reflected wave amplitude is zero. By summing circuit voltages it is found that

$$\Gamma = \frac{e_g - e_g/2}{e_g/2} = \frac{V_{Reverse}}{V_{Forward}}$$

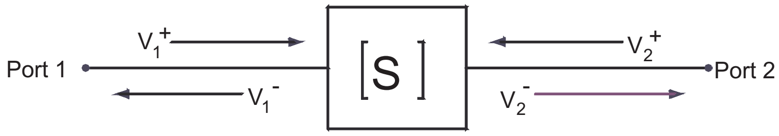

FIGURE 4.12 S-parameters are defined by forward and reverse voltage waves.

By placing a series circuit of two equal resistors across e_g, node 1 has a voltage of $e_g/2$. The voltage between node 1 and node 2 is equal to the reflected wave. Note that this is the standard resistive bridge circuit.

Network Analyzers

General RF and microwave network analyzers (NWA) measure scattering parameters (s-parameters). These measurements use a source with a well-defined impedance equal to the system impedance and all ports of the device under test (DUT) are terminated with the same impedance. The output port being measured is terminated in the test channel of the network analyzer that has an input impedance equal to the system characteristic impedance. Measurement of system parameters with all ports terminated minimizes the problems caused by short-circuit, open-circuit, and test-circuit parasitics that cause considerable difficulty in the measurement of *Y*- and *h*-parameters at very high frequencies. S-parameters can be converted to *Y*- and *h*-parameters.

Figure 4.12 illustrates a two-port device under test. If the generator is connected to port 1 and a matched load to port 2, the incident wave to the DUT is V_1^+. A wave reflected from the device back to port one is V_1^-. A signal traveling through the DUT and toward port 2 is V_2^-. Any reflection from the load (zero if it is truly a matched load) is V_2^+. The s-parameters are defined in terms of these voltage waves:

$s_{11} = V_1^-/V_1^+ =$ Input terminal reflection coefficient, Γ_1
$s_{21} = V_2^-/V_1^+ =$ Forward gain or loss

By moving the signal generator to port 2 and terminating port 1, the other two port s-parameters are measured:

$s_{12} = V_1^-/V_2^+ =$ Reverse gain or loss
$s_{22} = V_2^-/V_2^+ =$ Output terminal reflection coefficient, Γ_2

The s-matrix is then

$$\left[S\right] = \begin{bmatrix} s_{11} & s_{12} \\ s_{21} & s_{22} \end{bmatrix}$$

where

$$\begin{bmatrix} V_1^- \\ V_2^- \end{bmatrix} = \left[S\right] \begin{bmatrix} V_1^+ \\ V_2^+ \end{bmatrix}$$

Scalar Analyzer

A scalar network analyzer, Fig. 4.13, with resistor-loaded diode probes or power meters is used to measure scalar return loss and gain. Diode detectors are either used in the square law range as power detectors or logarithmic amplifiers are used in the analyzer to produce nominally a 50 dB dynamic range of measurement. A spectrum analyzer with a tracking test generator can be used as a scalar analyzer with up to 90 dB of dynamic range.

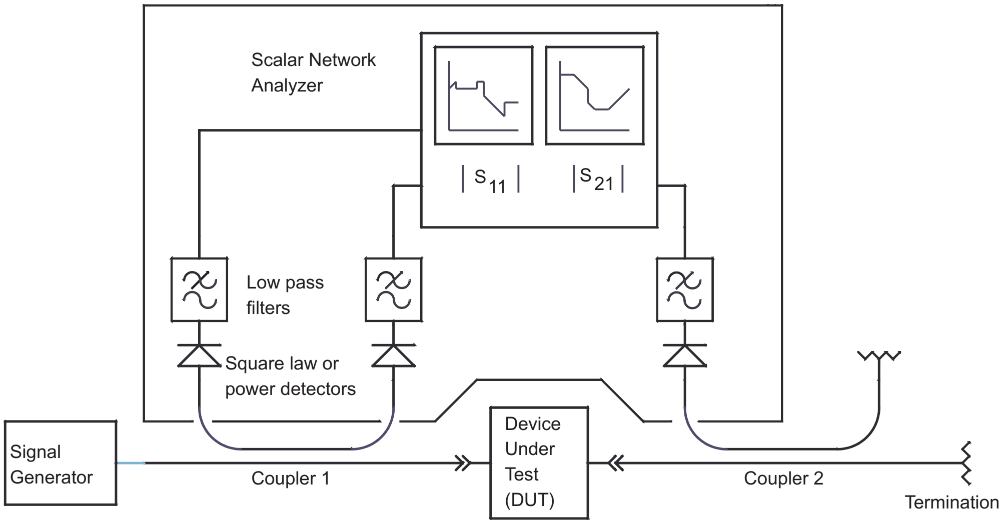

FIGURE 4.13 A scalar network analyzer can measure the magnitude of gain and return loss.

Gains and losses are calculated in scalar analyzers by adding and subtracting relative power levels in decibels. Note that this can only establish the magnitude of the reflection coefficient so that an absolute impedance cannot be measured. To establish the impedance of a device, the phase angle of the reflected wave relative to the incident wave must be known. To measure the phase difference between the forward and reflected wave, a phase meter or vector network analyzer is used.

Vector Heterodyne Analyzer

Accurate direct measurement of the phase angle between two signals at RF and microwave frequencies is difficult; therefore, most vector impedance analyzers downconvert the signals using a common local oscillator. By using a common oscillator the relative phase of the two signals is maintained. The signal is ultimately converted to a frequency where rapid and accurate comparison of the two signals yields their phase difference. In these analyzers the relative amplitude information is maintained so that the amplitude measurements are also made at the low intermediate frequency (IF).

The vector network analyzer (VNA) is a multichannel phase-coherent receiver with a tracking signal source. When interfaced with various power splitters and couplers, the channels can measure forward, reverse, and transmitted waves. As the phase and amplitude information is available on each channel, parameters of the device being measured can be computed. The most common VNA configuration measures the forward and reflected waves to and from a two-port device. From these measurements, the two-port scattering matrix can be computed.

The automatic vector network analyzer performs these operations under the supervision of a computer requiring the operator to input instructions relating to the desired data. The computer performs the routine “housekeeping.”

The use of computers also facilitates extensive improvement in measurement accuracy by measuring known high-quality components, calculating nonideal characteristics of the measurement system, and applying corrections derived from these measurements to data from other devices. In other words, the accuracy of a known component can be transferred to the measurement accuracy of an unknown component.

With the measurement frequency accurately known and the phase and amplitude response measured and corrected, the Fourier transform of the frequency domain yields the time domain response. A very useful measurement of this type transforms the s_{11} frequency domain data to a time domain response

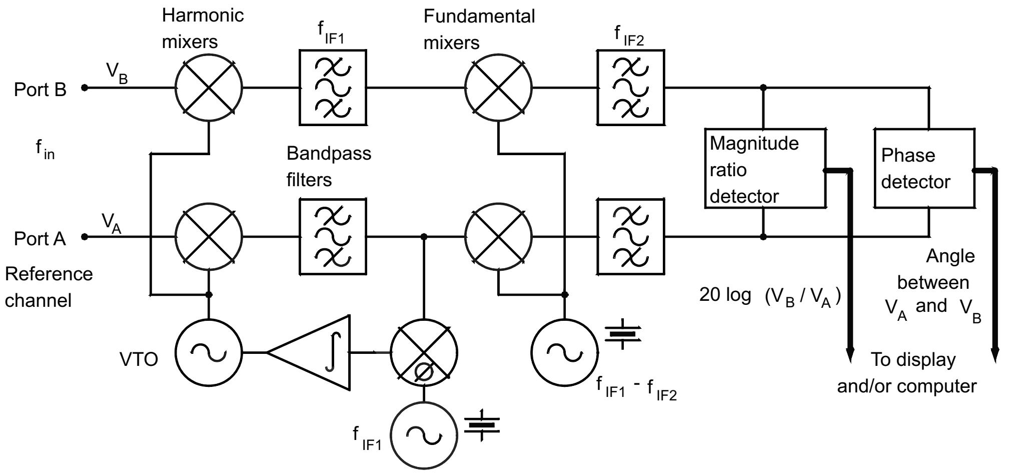

FIGURE 4.14 A vector network analyzer measures complex ratios.

with the same information as time domain reflectometry; that is, deviations from the characteristic impedance can be seen over the length of the measured transmission media.

The simplified block diagram of a typical multichannel VNA is shown in Fig. 4.14. There are two channels fed from the test set. The inputs are converted first to a low intermediate frequency such as 20 MHz and then to 100 kHz before being routed to phase detectors. The first conversion oscillator is followed by a comb generator and the oscillator is phase locked to the mixer output so the unit will frequency track the test source.

Multiple methods of generating the conversion oscillator voltages are used. Low RF frequency analyzer signal generators commonly generate a test signal plus another output that is frequency offset by the desired IF frequency. This can be done with offset synthesizers or by mixing a common oscillator with a stable oscillator at the IF frequency and selecting the desired mixing product using phasing or filtering techniques.

For microwave analyzers, because of the high cost of oscillators and the wide frequency coverage required, a more common method of generating conversion oscillators is to use a low frequency oscillator and a very broadband frequency multiplier. A harmonic of the low frequency conversion oscillator is offset by an oscillator equal to the IF frequency and the conversion oscillator is then phase locked to the reference channel of the NWA. The reference channel signal is normally the forward wave voltage derived from a directional coupler in an impedance measurement.

The outputs of the synchronous detectors supply the raw data to be converted to a format compatible with the computer. Corrections and manipulation of the data to the required output form is then done by the processors.

The test set supplies the first mixer inputs with the sampled signals necessary to make the desired measurement and there are many possible configurations. The most versatile is the two-port scattering matrix test set. This unit enables full two-port measurements to be made without the necessity of changing cable connections to the device. The simplified block diagram of a two-port s-parameter test set is shown in Fig. 4.15. The RF/microwave input is switched between port 1 and port 2 measurements. In each case the RF is split into a reference and test channel. The reference channel is fed directly to a reference channel converter. The test channel feeds the device under test by way of a directional coupler. The coupler output sampling the reflected power is routed to the test channel converter. Sampled components of incident and reflected power to both the input and output of the test device are available for processing.

In a full two-port measurement, multiple error terms can be identified, measured, and then used to translate the accuracy of calibration references to the measured data from the device under test. For

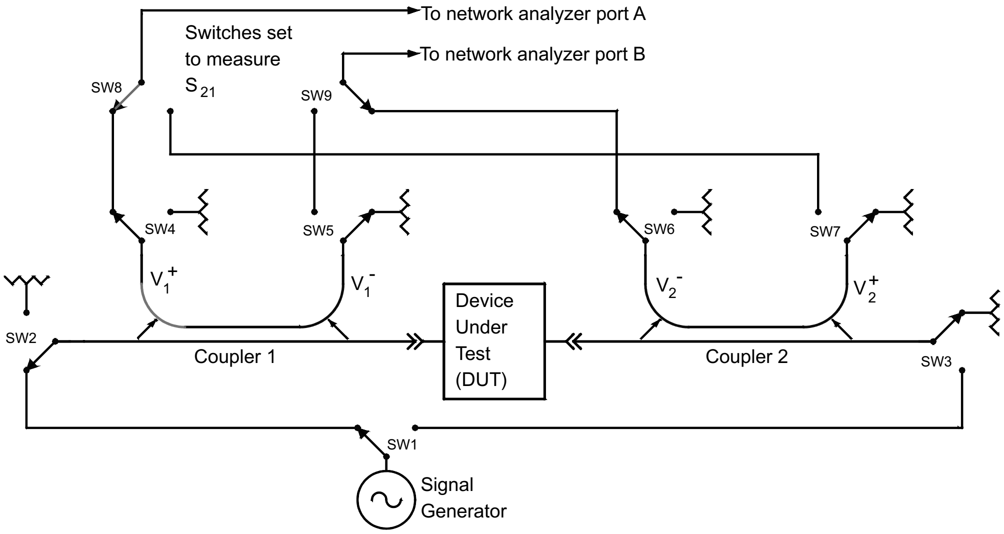

FIGURE 4.15 A two-port s-parameter test set can measure all four s-parameters without moving the DUT.

example, if the load used is not ideal, there will be some reflection back into the DUT. If the source generator impedance is not ideal, any reflections from the input of the DUT back to the generator will result in a further contribution to the incident DUT voltage. The couplers are also nonideal and have phase and amplitude errors.

By measuring the full two-port s-parameters of a set of known references such as opens, shorts, matched loads, known lengths of transmission lines, and through and open circuited paths, a system of equations can be derived that includes the error terms. If 8 error terms are identified, then 8 equations with 8 unknowns can be derived. The error terms can then be solved for and applied to the results of the measurement of an unknown two-port device to correct for measurement system deviations from the ideal.

Vector Six-Port Analyzer

A combination of couplers and power dividers, having 0°, 90°, and 180° differences in their output signals can be used to construct a circuit with multiple outputs where the power from the outputs can be used in a system of *n* equations with *n* unknowns. An example of this circuit is shown in Fig. 4.16. In a properly designed circuit, among the solutions to the system of equations will be the magnitudes and relative phase of the forward and reflected wave. The optimum number of ports for such a device is six; hence, a passive six-port device with diode or power detectors on four of the ports can be used as a vector impedance analyzer [10].

The six-port analyzer has limited bandwidth, usually no more than an octave, because the couplers and power dividers [11] have the same limitation in frequency range to maintain the required amplitude and phase characteristics; however, the low cost of the six-port analyzer makes it attractive for narrowband and built-in test applications.

Typically, measurement test set deviations from the ideal are even more prevalent with the six-port analyzer than for the frequency converting VNA; therefore, use of known calibration elements and the application of the resultant error correction terms is very important for the six-port VNA. The derivation of the error terms and their application to measurement correction is virtually the same for the two analyzers.

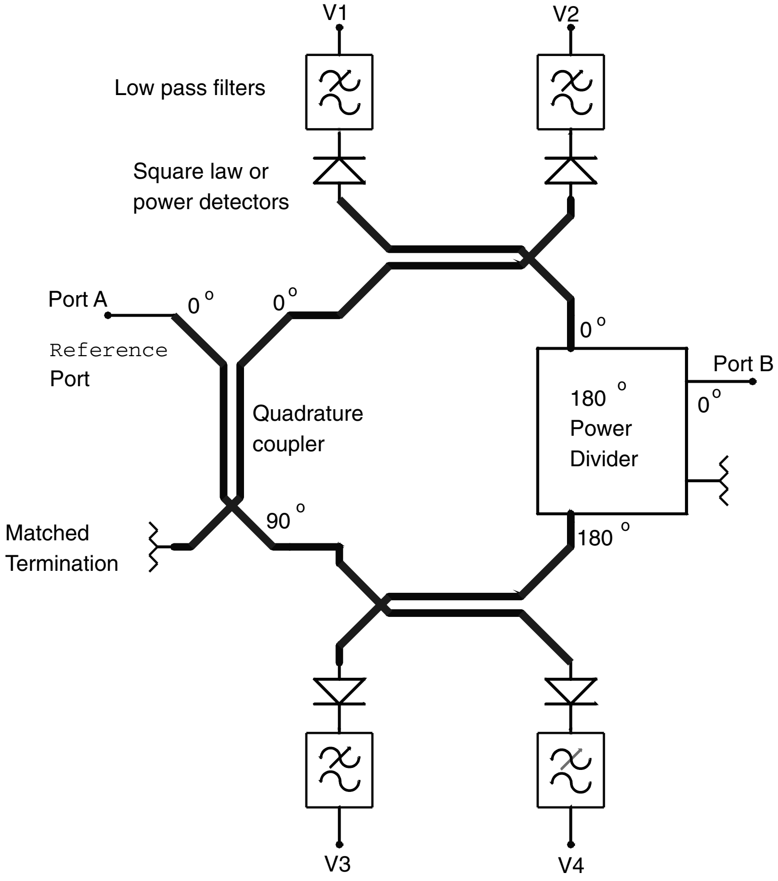

FIGURE 4.16 A six-port network can be used as a narrow band vector analyzer.

References

1. M. Engelson and F. Telewski, *Spectrum Analyzer Theory and Applications*, Artech House, Dedham, MA, 1974.
2. Agilent Technologies, Inc., *Operating Reference Manual for HP 53310A Modulation Domain Analyzer*, Agilent, Santa Clara, CA.
3. S. F. Adam, *Microwave Theory and Applications*, Prentice-Hall, Englewood Cliffs, NJ, 1969.
4. T. S. Laverghetta, *Modern Microwave Measurements and Techniques*, Artech House, Dedham, MA, 1989.
5. J. G. Webster (ed.), *Wiley Encyclopedia of Electrical and Electronics Engineering*, Vol. 13, John Wiley & Sons, New York, 1999, 84–90.
6. P. H. Smith, Transmission line calculator, *Electronics*, 12, 29, January 1939.
7. F. E. Terman, *Electronic and Radio Engineering*, McGraw-Hill, New York, 1955, 100.
8. S. Ramo, J. R. Winnery, and T. Van Duzer, *Fields and Waves in Communications Electronics*, 2nd ed., John Wiley & Sons, New York, 1988, 229–238.
9. G. L. Matthaei, L. Young, and E. M. T. Jones, *Microwave Filters, Impedance-Matching Networks, and Coupling Structures*, Artech House, Dedham, MA, 1980, 775–842.
10. G. F. Engen, A (Historical) Review of the Six-Port Measurement Technique, *IEEE Transactions on Microwave Theory and Technique*, December 1997, 2414–2417.
11. P. A. Rizzi, *Microwave Engineering: Passive Circuits*, Prentice Hall, Englewood Cliffs, NJ, 1988, 367–404.

4.2 Network Analyzer Calibration

Joseph Staudinger

Vector network analyzers (VNA) find very wide application as a primary tool in measuring and characterizing circuits, devices, and components. They are typically applied to measure small signal or linear characteristics of multi-port networks at frequencies ranging from RF to beyond 100 GHz (submillimeter in wavelength). Although current commercial VNA systems can support such measurements at much lower frequencies (a few Hz), higher frequency measurements pose significantly more difficulties in calibrating the instrumentation to yield accurate results with respect to a known or desired electrical reference plane. For example, characterization of many microwave components is difficult since the devices cannot easily be connected directly to VNA-supporting coaxial or waveguide media. Often, the device under test (DUT) is fabricated in a noncoaxial or waveguide medium and thus requires fixturing and additional cabling to enable an electrical connection to the VNA (Fig. 4.17). The point at which the DUT connects with the measurement system is defined as the DUT reference plane. It is generally the point where it is desired that measurements be referenced. However, any measurement includes not only that of the DUT, but contributions from the fixture and cables as well. Note that with increasing frequency, the electrical contribution of the fixture and cables becomes increasingly significant. In addition, practical limitations of the VNA in the form of limited dynamic range, isolation, imperfect source/load match, and other imperfections contribute systematic error to the measurement. To lessen the contribution of systematic error, remove contributions of cabling and fixturing, and therefore enhance measurement accuracy, the VNA must first be calibrated though a process of applying and measuring standards in lieu of the DUT.

Basic measurements consist of applying a stimulus and then determining incident, reflected, and transmitted waves. Ratios of these vector quantities are then computed via post processing yielding network scattering parameters (S-parameters). Most VNAs support measurements on one- and two-port networks, although equipment is commercially available that supports measurements on circuits with more than two ports as well as on differential networks.

VNA Functionality

A highly simplified block diagram illustrating the functionality of a vector network is provided in Fig. 4.18. Generally, a VNA includes an RF switch such that the RF stimulus can be applied to either port 1 or 2, thereby allowing full two-port measurements without necessitating manual disconnection of the DUT and reversing connections. RF couplers attached at the input and output ports allow

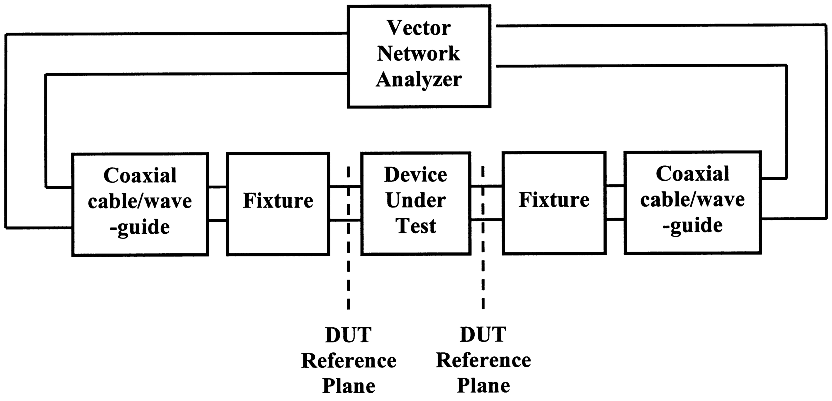

FIGURE 4.17 Typical measurement setup consisting of a device under test embedded in a fixture connected to the vector network analyzer with appropriate cables.

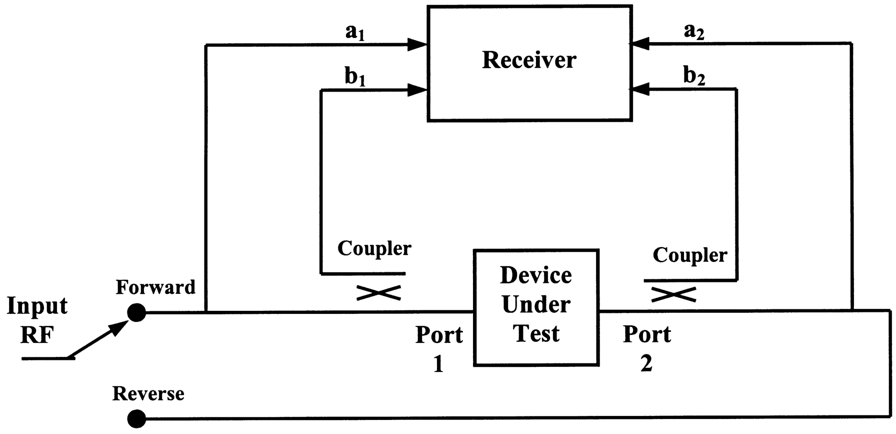

FIGURE 4.18 High simplified VNA block diagram.

measuring reflected voltages. With the RF signal applied in the forward direction (i.e., to port 1), samples of the incident (a_1) and reflected signals at port 1 (b_1) are routed to the receiver. The transmitted signal b_2 reaching port 2 is also directed to the receiver. The receiver functions to downconvert these signals to a lower frequency, which enables digitization and post-processing. Assuming ideal source and load terminations such that a_2 is equal to zero, two scattering parameters can be defined:

$$S_{11} = \frac{b_1}{a_1} \text{ and } S_{21} = \frac{b_2}{a_1}.$$

In reverse operation, the RF signal is directed to port 2 and samples of signals a_2, b_2, and b_1 are directed to the receiver. Assuming ideal source and load terminations such that a_1 is equal to zero, the remaining two scattering parameters are defined:

$$S_{22} = \frac{b_2}{a_2} \text{ and } S_{12} = \frac{b_1}{a_2}.$$

Sources of Measurement Uncertainties

Sources of uncertainty or error in VNA measurements are primarily the result of systematic, random, and drift errors. The latter two effects tend to be unpredictable and therefore cannot be removed from the measurement. They are the results of factors such as system noise, connector repeatability, temperature variations, and physical changes within the VNA. Systematic errors, however, arise from imperfections within the VNA, are repeatable, and can be largely removed through a process of calibration. Of the three, systematic errors are generally the most significant, particularly at RF and microwave frequencies. In calibration, such errors are quantified by measuring characteristics of known devices (standards). Hence, once quantified, systematic errors can be removed from the resulting measurement. The choice of calibration standards is not necessarily unique. Selection of a suitable set of standards is often based on such factors as ease of fabrication in a particular medium, repeatability, and the accuracy to which the characteristics of the standard can be determined.

Modeling VNA Systematic Errors

A mathematical description of systematic errors is accomplished using the concept of error models. The error models are intended to represent the most significant systematic errors of the VNA system up to

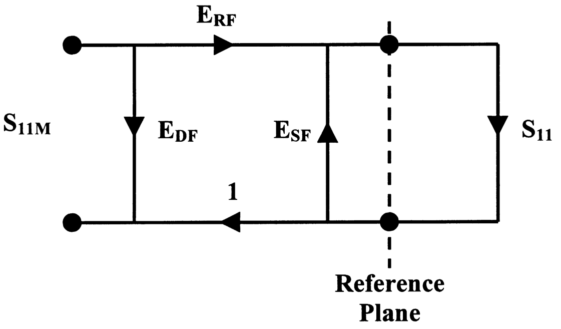

FIGURE 4.19 Typical one-port VNA error model for reflection coefficient measurements.

the reference plane — the electrical plane where standards are connected (Fig. 4.17). Hence, contributions from cables and fixturing in the measurement, up to the reference plane, are accounted for as well.

A flow graph illustrating a typical error model for one-port reflection measurements is depicted in Fig. 4.19. The model consists of three terms, E_{DF}, E_{RF}, and E_{SF}. The term S_{11M} represents the reflection coefficient measured by the receiver within the VNA. The term S_{11} represents the reflection coefficient of the DUT with respect to the reference plane (i.e., the desired quantity).

The three error terms represent various imperfections. Term E_{DF} accounts for directivity in that the measured reflected signal does not consist entirely of reflections caused by the DUT. Limited directivity of the coupler and other signal leakage paths result in other signal components vectorally combining with the DUT reflected signal. Term E_{SF} accounts for source match in that the impedance at the reference plane is not exactly the characteristic impedance (generally 50 ohms). Term E_{RF} describes frequency tracking imperfections between reference and test channels.

A flow graph illustrating a typical error model for two-port measurement, accounting for both reflection and transmission coefficients is depicted in Fig. 4.20. The flow graph consists of both forward (RF signal applied to port 1) and reverse (RF signal applied to port 2) error models. The model consists of twelve terms, six each for forward and reverse paths. Three more error terms are included in addition to those shown in the one-port model, (E_{LF}, E_{TF}, and E_{XF} for the forward path, and similarly E_{LR}, E_{TR}, and E_{XR} for the reverse path). As before, reflection as well as transmission coefficients measured by the receiver within the VNA are denoted with an M subscript (e.g., S_{21M}). The desired two-port S-parameters referenced with respect to port 1/2 reference planes are denoted as S_{11}, S_{21}, S_{12}, and S_{22}. The transmission coefficients are ratios of transmitted and incident signals. Error term E_{LF} accounts for measurement errors resulting from an imperfect load termination. Term E_{TF} describes transmission frequency tracking errors. The term E_{XF} accounts for isolation in that a small component of the transmitted signal reaching the receiver is due to finite isolation where it reaches the receiver without passing through the DUT. The error coefficients for the reverse path are similarly defined.

Calibration

From the above discussion, it is possible to mathematically relate uncorrected scattering parameters measured by the VNA (S_M) to the above-mentioned error terms and the S-Parameters exhibited by the DUT (S). For example, with the VNA modeled for one-port measurements as illustrated in Fig. 4.19, the reflection coefficient of the DUT (S_{11}) is given by:

$$S_{11} = \frac{S_{11M} - E_{DF}}{E_{SF}\left(S_{11M} - E_{DF}\right) + E_{RF}}$$

Similarly, for two-port networks, DUT S-parameters can be mathematically related to the error terms and uncorrected measured S-parameters. DUT parameters S_{11} and S_{21} can be described as functions of

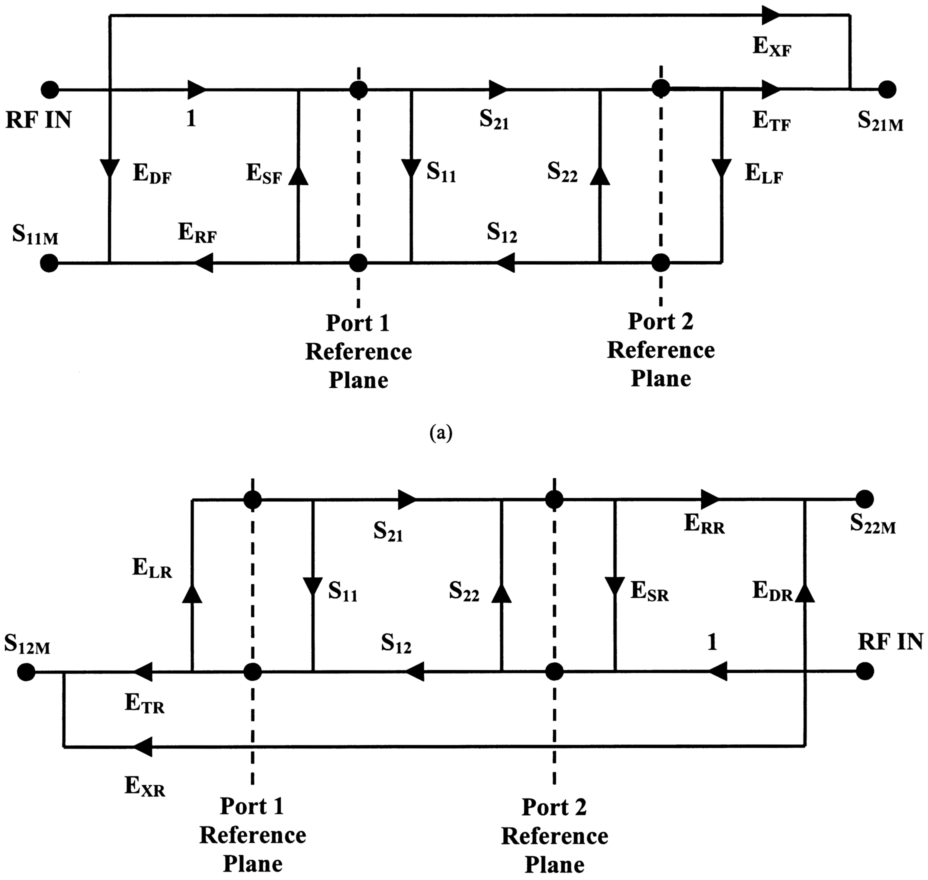

FIGURE 4.20 Typical two-port VNA error model; (a) forward model, and (b) reverse model.

S_{11M}, S_{21M}, S_{12M}, S_{22M} and the six forward error terms. Likewise, S_{12} and S_{22} are functions of the four measured S-parameters and the six reverse error terms. Hence, when each error coefficient is known, the DUT S-parameters can be determined from uncorrected measurement.

Therefore, calibration is essentially the process of determining these error coefficients. This is accomplished by replacing the DUT with a number of standards whose electrical properties are known with respect to the desired reference plane (the reader is referred to [1-5] for additional information). Additionally, since the system is frequency dependent, the process is repeated at each frequency of interest.

Calibration Standards

Determination of the error coefficients requires the use of several standards, although the choice of which standards to use is not necessarily unique. Traditionally, short, open, load, and through (SOLT) standards have been applied, especially in a coaxial medium that facilitates their accurate and repeatable fabrication. Electrical definitions for ideal and lossless SOLT standards (with respect to port 1 and 2 reference planes) are depicted in Fig. 4.21. Obviously, and especially with increasing frequency, it is impossible to fabricate standards such that they are (1) lossless and (2) exhibit the defined reflection and transmission coefficients at these reference planes. Fabrication and physical constants dictate some nonzero length of transmission line must be associated with each (Fig. 4.22). Hence, for completeness, the characteristics of the transmission line must be (1) known, and (2) included in defining the parameters of each standard. Wave propagation is described as

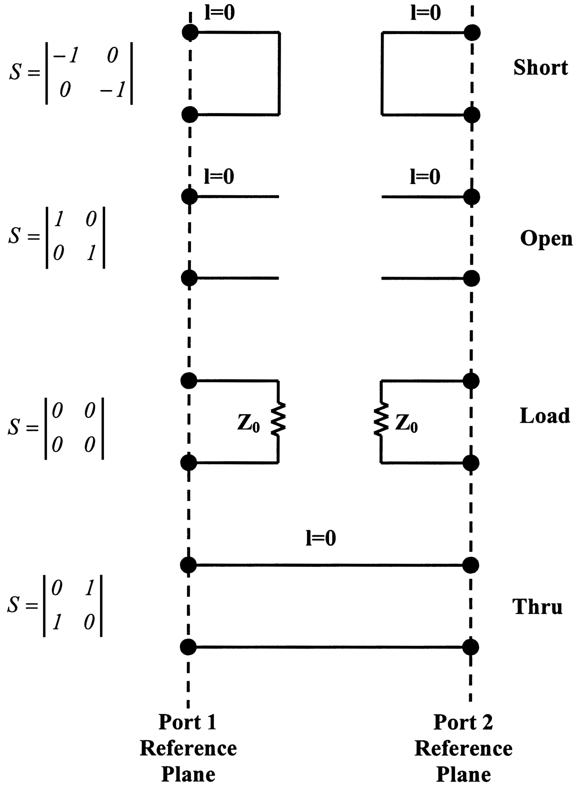

FIGURE 4.21 Electrical definition for lossless and ideal SOLT standards.

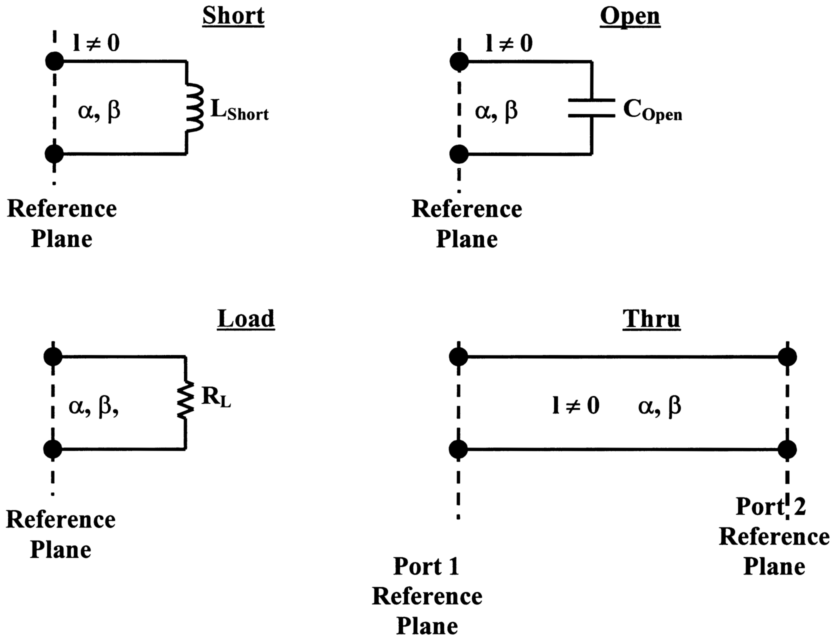

FIGURE 4.22 High frequency descriptions of SOLT standards generally consider nonzero length transmission lines, loss mechanisms, and fringing field effects associated with the open standard.

$$V(z) = Ae^{-\gamma z} + Be^{\gamma z}$$

where γ is the propagation constant defined as

$$\gamma = \alpha + j\beta$$

Assuming the electrical length of the transmission line associated with the standards is short, losses become small and perhaps α can be neglected without significant degradation in accuracy. Alternatively, commercial VNA manufacturers often describe the transmission line in terms of a delay coefficient with a small resistive loss component. The open standard exhibits further imperfections since the electric field pattern at the open end tends to vary with frequency. The open-end effect is often described in terms of a frequency-dependent fringing capacitance (C_{Open}) expressed in terms of a polynomial expansion taking the form:

$$C_{Open} = C_0 + C_1F + C_2F^2 + +C_3F^3 + \ldots$$

where C_0, C_1, … are coefficients and F is frequency.

The load termination largely determines forward and reverse directivity error terms (E_{DF} and E_{DR}). Considering the error models in Figs. 4.19 and 4.20, with the load standard applied on port 1, forward directivity error takes the following form:

$$E_{DF} = S_{11M} - \frac{S_{11Load}\,E_{RF}}{1 - E_{SF}S_{11Load}}$$

where $S_{11\ \mathrm{Load}}$ is the actual reflection coefficient of the load standard. Ideally, the load standard should exhibit an impedance of Z_0 (characteristic impedance) and thus a reflection coefficient of zero (i.e., $S_{11\ \mathrm{Load}} = 0$) in which case E_{DF} becomes the measured value of S_{11} with the load standard connected to port 1. High quality coaxial-based fixed load standards exhibiting high return loss over broad bandwidths are generally commercially available, especially at RF and microwave frequencies. At higher frequencies and/or where the electrical performance of the fixed load terminations is inadequate, sliding terminations are employed. Sliding terminations use mechanical methods to adjust the electrical length of a transmission line associated with the load standard. Neglecting losses in the transmission line, the above expression forms a circle in the S_{11} measurement plane as the length of the transmission line is varied. The center of the circle defines error term E_{DF} (Fig. 4.23).

Often it is desirable to characterize devices in noncoaxial media. For example, measuring the characteristics of devices and circuits at the wafer level by connecting microwave probes directly to the wafer. Other situations arise where components cannot be directly probed but must be placed in packages with coaxial connectors and it is desirable to calibrate the fixture/VNA at the package/fixture interface. Although fabrication techniques favor SOLT standards in coax, it is difficult to realize them precisely in other media such as microstrip and hence non-SOLT standards are more appropriate. Presently, standards based on one or more transmission lines and reflection elements have become popular for RFICs and MMICs. Fundamentally, they are more suitable for MMICs and RFICs since they rely on fabricating transmission lines (in microstrip, for example), where the impedance of the lines can be precisely determined based on physical dimensions, metalization, and substrate properties. The TRL (thru, reflect, line) series of standards have become popular as well as variations of it such as LRM (line, reflect, match), and LRL (line, reflect, line) to name but a few. In general, TRL utilizes a short length thru (sometime assumed zero length), a highly reflective element, and a nonzero length transmission line. One advantage

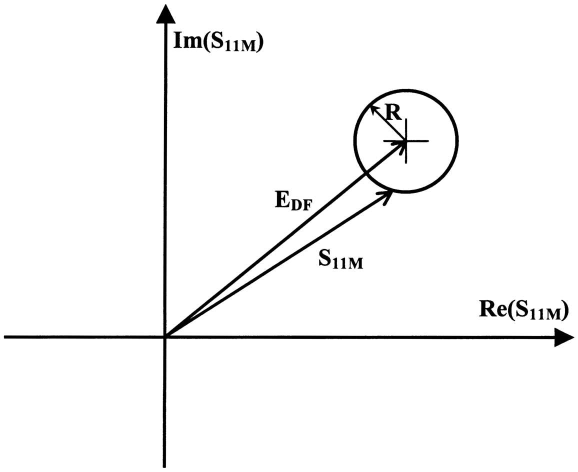

FIGURE 4.23 Characterizing directivity error terms using a sliding load termination.

of this technique is that a complete electrical description of each standard is not necessary. However, each standard is assumed to exhibit certain electrical criteria. For example, the length of the thru generally must be known, or alternatively, the thru may in many cases be fabricated such that its physical dimensions approach zero length at the frequencies of interest and are therefore insignificant. The characteristic impedance of the line standard is particularly important in that it is the major contributor in defining the reference impedance of the measurement. Its length is also important. Lengths approaching either 0° or multiples of 180° (relative to the length of the thru) are problematic and lead to poor calibrations. The phase of the reflection standard is not critical, although its phase generally must be known to within one-quarter of a wavelength.

In the interest of reducing hardware cost, a series of VNAs are commercially available based on a receiver architecture containing three rather than four sampling elements. In four-sampling receiver architecture, independent measurements are made of a_1, b_1, a_2, and b_2. Impedance contributions of the internal switch that routes the RF stimulus to port 1 for forward measurements and to port 2 for reverse measurements can be accounted for during the calibration process. In a three-sampling receiver architecture, independent measurements are made on b_1, b_2 and on a combined a_1 and a_2. This architecture is inherently less accurate than the former in that systematic errors introduced by the internal RF switch are not fully removed via TRL calibration, although mitigating this effect to some extent is possible [5]. However, it should be noted that this architecture provides measurement accuracy that is quite adequate for many applications.

References

1. Staudinger, J., A two-tier method of de-embedding device scattering parameters using novel techniques, Master Thesis, Arizona State University, May 1987.
2. Lane, R., De-Embedding Device Scattering Parameters, *Microwave J.*, Aug. 1984.
3. Fitzpatrick, J., Error Models For Systems Measurement, *Microwave J.*, May 1978.
4. Operating and Programming Manual For the HP8510 Network Analyzer, Hewlett Packard, Inc., Santa Rosa, CA.
5. Metzger, D., Improving TRL* Calibrations of Vector Network Analyzers, *Microwave J.*, May 1995.

4.3 Noise Measurements

Alfy Riddle

Fundamentals of Noise

Statistics

Noise is a random process. There may be nonrandom system disturbances we call noise, but this section will consider noise as a random process. Noise can have many different sources such as thermally generated resistive noise, charge crossing a potential barrier, and generation-recombination (G-R) noise [1]. The different noise sources are described by different statistics, the thermal noise in a resistor is a Gaussian process while the shot noise in a diode is a Poisson process. In the cases considered here, the number of noise "events" will be so large that all noise processes will have essentially Gaussian statistics and so be represented by the probability distribution in Eq. (4.1).

$$p(x) = 1\Big/\left(2\pi\sigma^2\right) e^{-x^2/2\sigma^2} \tag{4.1}$$

The statistics of noise are essential for determining the results of passing noise through nonlinearities because the nonlinearity will change the noise distribution [2]. Noise statistics are useful even in linear networks because multiple noise sources will require correlation between the noise sources to find the total noise power. Linear networks will not change the statistics of a noise signal even if the noise spectrum is changed.

Bandwidth

The noise energy available from a hot resistor is given in Eq. (4.2), where h = 6.62×10^{-34} J s, T is in degrees Kelvin, and k = $1.38\text{x}10^{-23}$ J/degree K [1]. N is in joules, or watt-seconds, or W/Hz, which is noise power spectral density. For most of the microwave spectrum hf << kT so Eq. (4.2) reduces to Eq. (4.3).

$$N = hf\Big/\left(e^{hf/kT} - 1\right) \tag{4.2}$$

$$N \cong kT \qquad\qquad f \ll kT/h \tag{4.3}$$

The noise power available from the hot resistor will be the integration of this energy, or spectral density, over the measuring bandwidth as given in Eq. (4.4).

$$P = {}_{f1}\!\int^{f2} N\, df \tag{4.4}$$

As the frequency increases, *N* reduces so the integration in Eq. (4.4) will be finite even if the frequency range is infinite. Note that for microwave networks using cooled circuits, quantum effects can become important at relatively low frequencies because of the temperature-dependent condition in Eq. (4.3). For a resistor at microwave frequencies and room temperature, *N* is independent of frequency so the total power available is simply $P = kT(f_2 - f_1)$, or $P = kTB$, as shown in Eq. (4.5), where B is the bandwidth. Figure 4.24 shows a resistor with an available thermal power of kTB, which can be represented either as a series voltage source with $e_n^2 = 4\,kTRB$ or a shunt current source with $i_n^2 = 4\,kTB/R$, where the squared value is taken to be the mean-square value. At times it is tempting to represent e_n as $\sqrt{(4\,kTB)}$, but this is a mistake because e_n is a random variable, not a sinusoid. The process of computing the mean-square value of a noise source is important for establishing any possible correlation with any other noise source in the system [1,16]. Representing a noise source as an equivalent sinusoidal voltage can result in an error due to incorrect accounting of correlation.

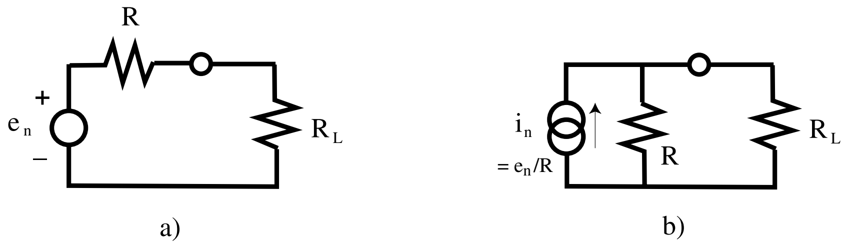

FIGURE 4.24 Equivalent thermal noise sources: (a) voltage and (b) current.

$$P = kT\,B \qquad f \ll kT/h \tag{4.5}$$

When noise passes through a filter we must repeat the integration of Eq. (4.4). Two useful concepts in noise measurement are noise power per hertz and equivalent noise bandwidth. Noise power per hertz is simply the spectral density of the noise, or N in the above equations because it has units of watt-seconds or joules. Spectral densities are also given in V^2/Hz and A^2/Hz. The equivalent noise bandwidth of a noise source can be found by dividing the total power detected by the maximum power detected per hertz, as shown in Eq. (4.6).

$$B_e = P/\mathrm{Max}\{N\} \tag{4.6}$$

The noise equivalent bandwidth of a filter is especially useful when measuring noise sources with a spectrum analyzer. The noise equivalent bandwidth of a filter is defined by integrating its power transfer function, $|H(f)|^2$, over all frequency and dividing by the peak of the power transfer function, as shown in Eq. (4.7).

$$B_e = {}_0\!\int^{\infty} \left|H(f)\right|^2 df \Big/ \mathrm{Max}\left\{\left|H(f)\right|^2\right\} \tag{4.7}$$

Power meters are often used with bandpass filters in noise measurements so that the noise power has a well-defined range. The noise equivalent bandwidth of the filter can be used to convert the noise power back to a power/Hz spectral density that is easier to use in computations and comparisons. As an example, a first-order bandpass filter has a $B_e = \pi/2\ B_{-3}$, where B_{-3} is the –3 dB bandwidth. The noise equivalent bandwidth is greater than the 3 dB bandwidth because of the finite power in the filter skirts.

Detection

The most accurate and traceable measurement of noise power is by comparison with thermal standards [3]. In the everyday lab the second best method for noise measurement is a calibrated power meter preceded by a filter of known noise bandwidth. Because of its convenience, the most common method of noise power measurement is a spectrum analyzer. This most common method is also the most inaccurate because of the inherent inaccuracy of a spectrum analyzer and because of the nonlinear processes used in a spectrum analyzer for power estimation. As mentioned in the section on statistics, nonlinearities change the statistics of a noise source. For example, Gaussian noise run through a linear envelope detector acquires a Rayleigh distribution as shown in Fig. 4.25.

The average of the Rayleigh distribution is not the standard deviation of the Gaussian, so a detector calibrated for sine waves will read about 1 dB high for noise. Spectrum analyzers also use a logarithmic amplifier that further distorts the noise statistics and accounts for another 1.5 dB of error. Many modern spectrum analyzers automatically correct for these nonlinear errors as well as equivalent bandwidth when put in a “Marker Noise” mode [4].

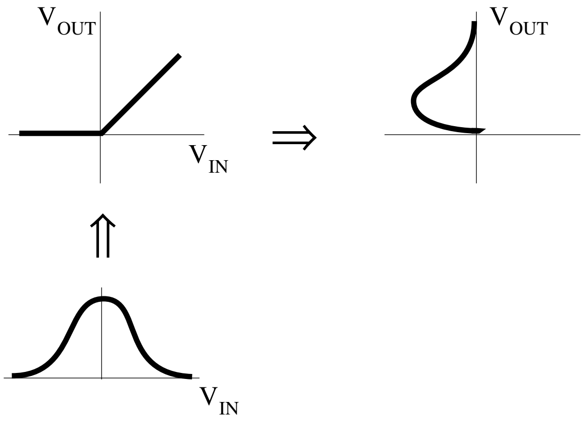

FIGURE 4.25 Nonlinear transformation of Gaussian noise.

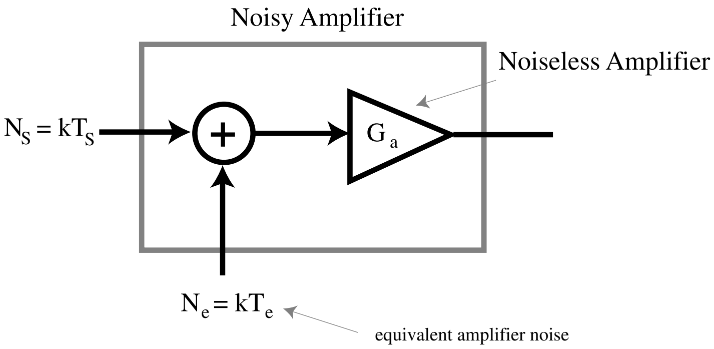

FIGURE 4.26 System view of amplifier noise.

Noise Figure and Y-Factor Method

At high frequencies it is far easier to measure power flow than it is to measure individual voltage and current noise sources. All of a linear device's noise power can be considered as concentrated at its input as shown in Fig. 4.26 [1].

We can lump all of the amplifier noise generators into an equivalent noise temperature with an equivalent input noise power per hertz of $N_a = kT_e$. As shown in Fig. 4.26, the noise power per hertz available from the noise source is $N_S = kT_S$. In system applications the degradation of signal-to-noise ratio (SNR) is a primary concern. We can define a figure of merit for an amplifier, called the noise factor (F), which describes the reduction in SNR of a signal passed through the amplifier shown in Fig. 4.26 [5]. The noise factor for an amplifier is derived in Eq. (4.8).

$$F = SNR_{IN}/SNR_{OUT} = S_{IN}/kT_S/(G_a S_{IN}/(G_a k(T_S + T_e)) = (T_S + T_e)/T_S = 1 + T_e/T \qquad (4.8)$$

Eq. (4.8) is very simple and only contains the amplifier equivalent temperature and the source temperature. F does vary with frequency and so is measured in a narrow bandwidth, or spot. Note that F is not a function of measurement bandwidth. Eq. (4.8) also implies that the network is tuned for maximum available gain, which happens by default if all the components are perfectly matched to 50 ohms and used in a 50-ohm system.

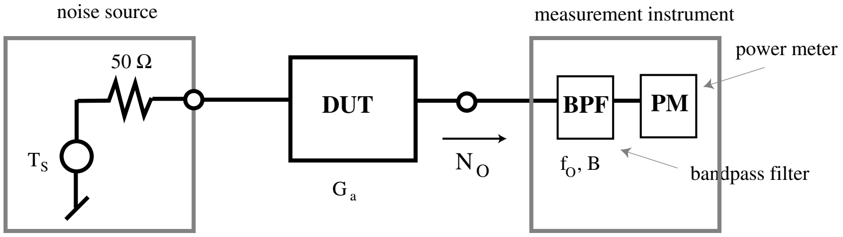

FIGURE 4.27 Test setup for Y-factor method.

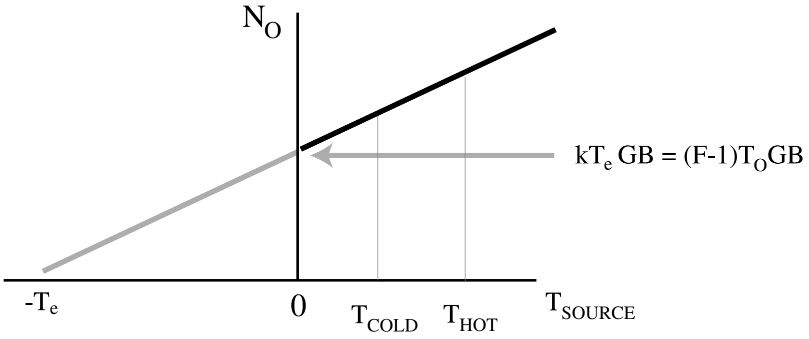

FIGURE 4.28 Output noise power vs. source temperature.

Device noise factor can be measured with the setup shown in Fig. 4.27 [1]. The Y-Factor method takes advantage of the fact that as the source temperature is varied, the device noise output, N_O, varies yet the device noise contribution remains a constant. Figure 4.28 shows that as T_S changes the noise power measured as the power meter changes according to Eq. (4.9).

$$N_O\left(T_S\right) = \left(k\ T_S\ G_a + k\ T_e\ G_a\right)B \tag{4.9}$$

The value of $N_O(T_S = 0)$ gives the noise power of the device alone. By using two known values of T_S, a cold measurement at $T_S = T_{COLD}$, and a hot measurement at $T_S = T_{HOT}$, the slope of the line in Fig. 4.28 can be derived. Once the slope is known, the intercept at $T_S = 0$ can be found by measuring $N_O(T_{COLD})$ and $N_O(T_{HOT})$. The room temperature, T_O, is also needed to serve as a reference temperature for the device noise factor, F. For a room temperature $F = 1 + T_e/T_O$, we can define $T_e = (F - 1)\ T_O$. The following equations derive the Y-Factor method. Equation (4.10) is the basis for the Y-Factor method.

$$Y = \frac{N_O\left(T_{HOT}\right)}{N_O\left(T_{COLD}\right)} = \frac{\left(k\ T_{HOT}\ G_a + \left(F-1\right)k\ T_O\ G_a\right)B}{\left(k\ T_{COLD}\ G_a + \left(F-1\right)k\ T_O\ G_a\right)B} = \frac{T_{HOT} + \left(F-1\right)\ T_O}{T_{COLD} + \left(F-1\right)\ T_O} \tag{4.10}$$

Solving for F we get Eq. (4.11) which can be solved for T_e as shown in Eq. (4.12).

$$F = 1 + \frac{T_{HOT} - Y\ T_{COLD}}{\left(Y-1\right)T_O} = 1 + T_e/T_O \tag{4.11}$$

$$T_e = \frac{T_{HOT} - Y\, T_{COLD}}{\left(Y - 1\right)} \tag{4.12}$$

Equation (4.12) can be rearranged to define another useful parameter known as the equivalent noise ratio, or ENR, of a noise source as shown in Eq. (4.13) [1].

$$F = \frac{\left(T_{HOT}/T_O - 1\right) + Y\left(1 - T_{COLD}/T_O\right)}{\left(Y - 1\right)} = \frac{ENR + Y\left(1 - T_{COLD}/T_O\right)}{\left(Y - 1\right)} = \frac{ENR}{\left(Y - 1\right)}\Bigg|_{T_{COLD} = T_O} \tag{4.13}$$

Note that when T_{COLD} is set to the reference temperature for *F*, which the IEEE gives as T_O = 290° Kelvin, then the device noise factor has a simple relationship to both ENR and Y [1,3].

Practically speaking, the noise factor is usually given in decibels and called the noise figure, $NF = 10 \log F$. While the most accurate noise sources use variable temperature loads, the most convenient variable noise sources use avalanche diodes with calibrated noise power versus bias current [6]. The diode noise sources usually contain an internal pad to reduce the impedance variation between on (hot) and off (cold) states. Also, the diodes come with an ENR versus frequency calibration curve.

Phase Noise and Jitter

Introduction

The noise we have been discussing was broadband noise. When noise is referenced to a carrier frequency it appears to modulate the carrier and so causes amplitude and phase variations in the carrier [7]. Because of the amplitude-limiting mechanism in an oscillator, oscillator phase modulation noise (PM) is much larger than amplitude modulation noise (AM) close enough to the carrier to be within the oscillator loop bandwidth. The phase variations, caused by the noise at different offset, or modulation frequencies create a variance in the zero crossing time of the oscillator. This zero crossing variance in the time domain is called jitter and is critical in digital communication systems. Paradoxically, even though jitter is easily measured in the time domain and often defined in picoseconds it turns out to be better to specify jitter in the frequency domain as demonstrated by the jitter tolerance mask for an OC-48 SONET signal [8]. The jitter plot shown in Fig. 4.29 can be translated into script *L* versus frequency using the equations in the following section [9].

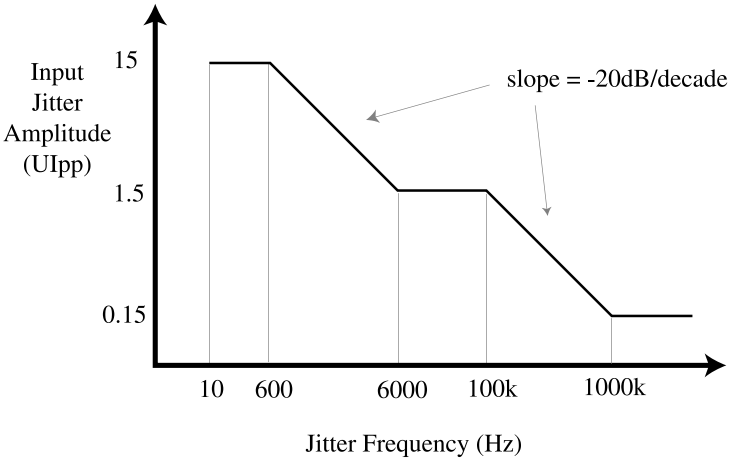

FIGURE 4.29 SONET Category II jitter tolerance mask for OC-48.

Jitter is best specified in the frequency domain because systems are more sensitive to some jitter frequencies than others. Also, jitter attenuators, which are simply narrowband phase-locked loops (PLLs), have well-defined frequency domain transfer functions that can be cascaded with the measured input jitter to derive the output jitter.

$$V_O(t) = V_C\left\{1 + m(t)\right\}\cos\left[\omega_C t + \beta(t)\right] \tag{4.14}$$

Mathematical Basics

Consider the time domain voltage given in Eq. (4.14). This signal contains both amplitude modulation, m(t), and phase modulation, β(t) [10]. If we let $m(t) = m_1(t)\cos(\omega_m t)$, $\beta(t) = \beta_1(t)\sin(\omega_m t)$, and we define $|\beta_1(t)| \ll 1$, then Eq. (4.14) can be expanded into AM and PM sidebands as shown in Eq. (4.15).

$$\begin{aligned} V_O(t) \cong {} & V_C\cos\left[\omega_C t\right] \\ & + V_C m_1(t)/2\left\{\cos\left[\omega_C t + \omega_m t\right] + \cos\left[\omega_C t - \omega_m t\right]\right\} \\ & + V_C\beta_1(t)/2\left\{\cos\left[\omega_C t + \omega_m t\right] - \cos\left[\omega_C t - \omega_m t\right]\right\} \end{aligned} \tag{4.15}$$

We can let $m_1(t)$ and $\beta_1(t)$ be fixed amplitudes as when sinusoidal test signals are used to characterize an oscillator, or we can let $m_1(t)$ and $\beta_1(t)$ be slowly varying, with respect to ω_m, noise signals. The latter case gives us the narrowband Gaussian noise approximation, which can represent an oscillator spectrum when the noise signals are summed over all modulation frequencies, ω_m [7].

Several notes should be made here. First, as $\beta_1(t)$ becomes large the single sidebands of Eq. (4.15) expand into a Bessel series that ultimately generates a flat-topped spectrum close into the average carrier frequency. This flat-topped spectrum is essentially the FM spectrum created by the large phase excursions that result from the $1/f^3$ increase in phase noise at low modulating frequencies. Second, if $|m_1(t)| = |\beta_1(t)|$, and they are fully correlated, then by altering the phases between $m_1(t)$ and $\beta_1(t)$ we can cancel the upper or lower sideband at will. This second point also shows that a single sideband contains equal amounts of AM and PM, which is useful for testing and calibration purposes [11].

Oscillator noise analysis uses several standard terms such as AM spectral density, PM spectral density, FM spectral density, script L, and jitter [10,12]. These terms are defined in Eqs. (4.16) through (4.20). The AM spectral density, or $S_{AM}(f_m)$, shown in Eq. (4.16) is derived by computing the power spectrum of m(t), given in Eq. (4.14), with a 1-hertz-wide filter. S_{AM} is called a spectral density because it is on a 1-hertz basis. Similarly, the PM spectral density, or $S_\phi(f_m)$ in radians^2/Hz, is shown in Eq. (4.17) and is derived by computing the power spectrum of β(t) in Eq. (4.14). The FM spectral density, or $S_{FM}(f_m)$ in *Hz*^{2}*/Hz*, is typically derived by using a frequency discriminator to measure the frequency deviations in a signal. Because frequency is simply the rate of change of phase, FM spectral density can be derived from PM spectral density as shown in Eq. (4.18). Script L is a measured quantity usually given in dBc/Hz and best described by Fig. 4.30. It is important to remember that the definition of script L requires the sidebands to be due to phase noise. Because script L is defined as a measure of phase noise it can be related to the PM spectral density as shown in Eq. (4.19). Two complications arise in using script L. First, most spectrum analyzers do not determine if the sidebands are only due to phase noise. Second, the constant relating script L to S_ϕ is 2 if the sidebands are correlated and √2 if the sidebands are uncorrelated and the spectrum analyzer does not help in telling these two cases apart. Jitter is simply the rms value of the variation in zero crossing times of a signal compared with a reference of the same average frequency. Of course, the jitter of a signal can be derived by accumulating the phase noise as shown in Eq. (4.20). In Eqs. (4.16) through (4.20) $\Im\{x\}$ denotes the Fourier transform of *x* [7]. Most of these terms can also be defined from the Fourier transform of the autocorrelation of m(t) or β(t). The spectral densities are typically given in dB using a 1-Hz measurement bandwidth, abbreviated as dB/Hz.

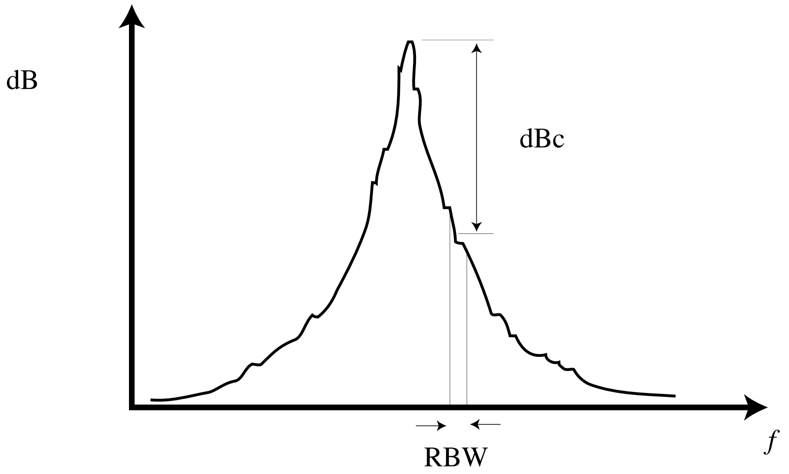

FIGURE 4.30 Typical measured spectrum on a spectrum analyzer.

$$S_{AM}\left(f_m\right) = \Im\left\{m\left(t\right)\right\} \Im\left\{m*\left(t\right)\right\} = m_1^2 \big/ 2\ \delta\left(f_m - f_a\right)\Big|_{m\left(t\right) = m_1 \cos\left(\omega_a t\right)} \tag{4.16}$$

$$S_\phi\left(f_m\right) = \Im\left\{\beta\left(t\right)\right\} \Im\left\{\beta*\left(t\right)\right\} = \beta_1^2 \big/ 2\ \delta\left(f_m - f_a\right)\Big|_{\beta\left(t\right) = \beta_1 \cos\left(\omega_a t\right)} \tag{4.17}$$

$$S_{FM}\left(f_m\right) = f_m^2\ S_\phi\left(f_m\right) \qquad\qquad \text{because } \omega_m = d\phi \big/ dt \tag{4.18}$$

$$\text{script L}\left(f_m\right) = P_{SSB}\left(f_m\right) \big/ Hz \big/ P_C = S_\phi\left(f_m\right) \big/ 2\Big|_{\text{when phase noise has correlated sidebands}} \tag{4.19}$$

$$\text{jitter} = \sqrt{\left({}_0\!\int^\infty S_\phi\left(f_m\right) df_m\right)} = \beta_1 \big/ \sqrt{2}\Big|_{\beta\left(t\right) = \beta_1 \cos\left(\omega_m t\right)} \tag{4.20}$$

In the above equations f_m indicates the offset frequency from the carrier. In Eq. (4.19) P_{SSB} is defined as phase noise, but often is just the noise measured by a spectrum analyzer close to the carrier frequency, and P_C is the total oscillator power. The jitter given in Eq. (4.20) is the total jitter that results from a time domain measurement. Jitter as a function of frequency, f_m, is just the square root of $S_\phi(f_m)$. Jitter as a function of frequency can be translated to various other formats, such as degrees, radians, seconds, and unit intervals (UIs), using Eq. (4.21) [9].

$$\text{jitter} = \begin{Bmatrix} \beta_{RMS} \text{ in radians} \\ UI = \beta_{RMS} \big/ 2\pi \text{ in unit intervals} \\ UI \big/ f_C = \beta_{RMS} \big/ \omega_C \text{ in seconds} \\ 360\ UI = 360\beta_{RMS} \big/ 2\pi \text{ in degrees} \end{Bmatrix} \tag{4.21}$$

For most free-running oscillators the $1/f^3$ region of the phase noise dominates the jitter so integrating the $1/f^3$ slope gives UI ≈ $f_a/2\ 10^{\text{scriptL}(f_a)/10}$ where f_a is any frequency on the $1/f^3$ slope and script L is in dBc/Hz. For PLL-based sources with large noise pedestals, a complete integration should be done.

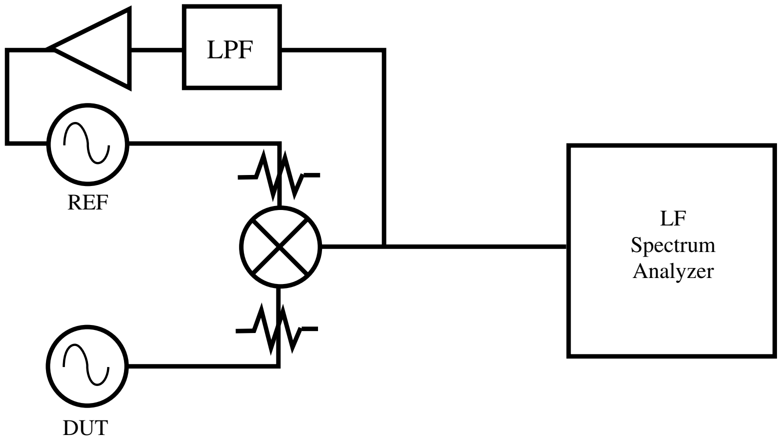

FIGURE 4.31 PLL phase noise measurement.

Phase Noise Measurements

Phase noise is typically measured in one of three ways: spectrum analyzer, PLL, or transmission line discriminator [1,10,13-15]. The spectrum analyzer is the easiest method of measuring script L(f_m) for any oscillator noisier than the spectrum analyzer reference source. Figure 4.30 shows a typical source spectrum. Care must be taken to make the resolution bandwidth, RBW, narrow enough to not cover a significant slope of the measured noise [1]. The spectrum analyzer cannot distinguish between phase and amplitude noise, so reporting the results as script L only holds where $S_\phi > S_{AM}$, which usually means within the $1/f^3$ region of the source. Spectrum analyzer measurements can be very tedious when the oscillator is noisy enough to wander significantly in frequency.

PLL-based phase noise measurement is used in most commercial systems [14]. Figure 4.31 shows a PLL-based phase noise test set. The reference oscillator in Fig. 4.31 is phase locked to the device under test (DUT) through a low pass filter (LPF) with a cutoff frequency well below the lowest desired measurement frequency. This allows the reference oscillator to track the DUT and downconvert the phase noise sidebands without tracking the noise as well. The low frequency spectrum analyzer measures the noise sidebands and arrives at a phase noise spectral density by factoring in the mixer loss or using a calibration tone [11]. A PLL system requires the reference source to be at least as quiet as the DUT. Another DUT can be used as a reference with the resulting noise sidebands increasing by 3 dB, but usually the reference is much quieter than the DUT so fewer corrections have to be made.

A transmission line frequency discriminator can provide accurate and high-resolution phase noise measurements without the need for a reference oscillator [13]. The discriminator resolution is proportional to the delay line delay, τ. The phase shifter is adjusted so that the mixer signals are in quadrature, which means the mixer DC output voltage is set to the internal offset voltage (approximately zero). Transmission line discriminators can be calibrated with an offset source of known amplitude, as discussed previously, or with a source of known modulation sensitivity [11] (see Fig. 4.32). The disadvantages of a transmission line discriminator are that high source output levels are required to drive the system (typically greater than 13 dBm), and the system must be retuned as the DUT drifts. Also, it is important to remember that the discriminator detects FM noise which is related to phase noise as given in Eq. (4.18) and shown in Fig. 4.33.

Summary

Accurate noise measurement and analysis must recognize that noise is a random process. While nonlinear devices will affect the noise statistics, linear networks will not change the noise statistics. Noise statistics are also important for analyzing multiple noise sources because the correlation between the noise sources

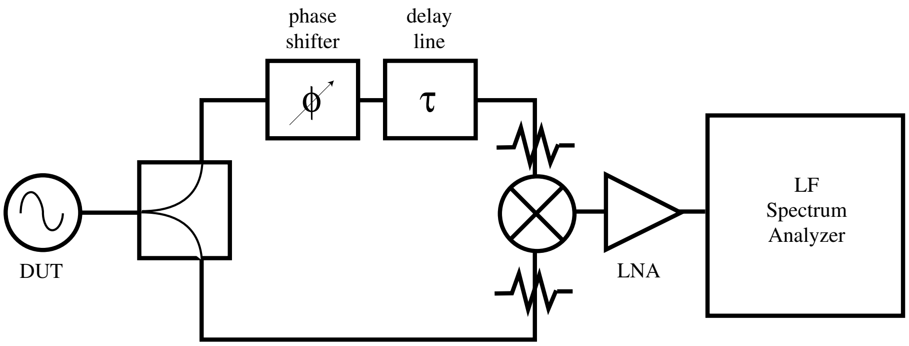

FIGURE 4.32 Transmission line discriminator.

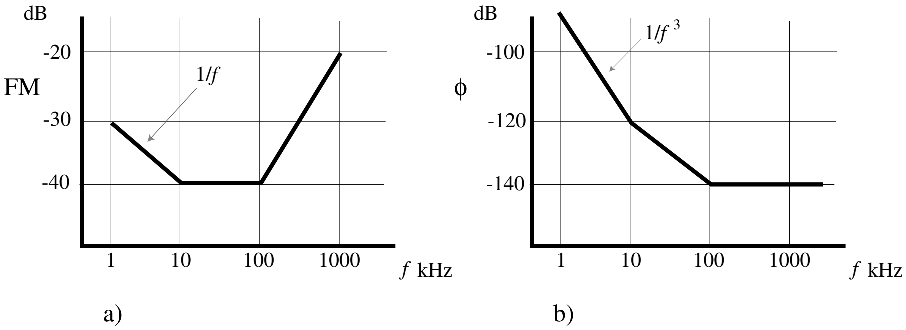

FIGURE 4.33 (a) FM and (b) phase noise spectral densities for the same device.

must be considered. At very high frequencies it is easier to work with noise power flow than individual noise voltage and current sources, so methods such as the Y-Factor technique have been developed for amplifier noise figure measurement. Measuring oscillator noise mostly involves the phase variations of a source. These phase variations can be represented in the frequency domain as script L, or in the time domain as jitter. Several techniques of measuring source phase noise have been developed which trade off accuracy for cost and simplicity.

References

1. Ambrozy, A., *Electronic Noise*, McGraw-Hill, New York, 1982.
2. Papoulis, A., *Probability, Random Variables and Stochastic Processes*, McGraw-Hill, New York, 1965.
3. Haus, H.A., IRE Standards on Methods of Measuring Noise in Linear Twoports, *Proc. IRE*, 60–68, Jan. 1960.
4. Staff, *HP 8560 E-Series Spectrum Analyzer User's Guide*, Hewlett-Packard, Dec. 1997.
5. Friis, H.T., Noise Figures of Radio Receivers, *Proc. IRE*, 419–422, July 1944.
6. Pastori, W.E., A Review of Noise Figure Instrumentation, *Microwave J.,* 50–60, Apr. 1983.
7. Carlson, B.A., *Communication Systems*, McGraw-Hill, New York, 1975.
8. ANSI, Telecommunications-Synchronous Optical Network (SONET)- Jitter at Network Interfaces, *ANSI T1.105.03-1994*, 1994.
9. Adler, J.V., Clock Source Jitter: A Clear Understanding Aids Clock Source Selection, *EDN*, 79–86, Feb. 18, 1999.
10. Ondria, J.G., A Microwave System for Measurement of AM and FM Noise Spectra, *IEEE Trans. MTT*, 767–781, Sept. 1968.

11. Buck, J.R., and Healey, D.J. III, Calibration of Short-Term Frequency Stability Measuring Apparatus, *Proc. IEEE*, 305–306, Feb. 1966.
12. Blair, B.E., *Time and Frequency: Theory and Fundamentals*, U.S. Dept. Commerce, NBS Monograph 140, 1974.
13. Schielbold, C., Theory and Design of the Delay Line Discriminator for Phase Noise Measurement, *Microwave J.,* 103–120, Dec. 1983.
14. Harrison, D.M., Howes, M.J., and Pollard, R.D., The Evaluation of Phase Noise in Low Noise Oscillators, *IEEE MTT-S Digest*, 521–524, 1987.
15. Staff, *Noise Measurements Using the Spectrum Analyzer, Part One: Random Noise*, Tektronix, Beaverton, 1975.
16. Haus, H.A. and Adler, R.B., *Circuit Theory of Linear Noisy Networks*, MIT Press, Cambridge, MA, 1959.

4.4 Nonlinear Microwave Measurement and Characterization

J. Stevenson Kenney

While powerful methods have been developed to analyze complex linear circuits, it is unfortunate that almost all physical systems exhibit some form of nonlinear behavior. Often the nonlinear behavior of a microwave circuit is detrimental to the signals that pass through it. Such is the case with distortion within a microwave power amplifier. In some cases nonlinearities may be exploited to realize useful circuit functions, such as frequency translation or detection. In either case, methods have been devised to characterize and measure nonlinear effects on various signals. These effects are treated in this chapter and include:

- Harmonic Distortion
- Gain Compression
- Intermodulation Distortion
- Phase Distortion
- Adjacent Channel Interference
- Error Vector Magnitude

Many of the above characterizations are different manifestations of nonlinear behavior for different types of signals. For instance, both analog and digital communication systems are affected by *intermodulation distortion.* However, these effects are usually measured in different ways. Nevertheless, some standard measurements are used as figures of merit for comparing the performance to different circuits. These include:

- Output Power at 1 *dB* Gain Compression
- Third Order Intercept Point
- Spurious Free Dynamic Range
- Noise Power Ratio
- Spectral Mask Measurements

This chapter treats the characterization and measurement of nonlinearities in microwave circuits. The concentration will be on standard techniques for analog and digital communication circuits. For more advanced techniques, the reader is advised to consult the references at the end of this section.

Mathematical Characterization of Nonlinear Circuits

To analyze the effects of nonlinearities in microwave circuits, one must be able to describe the input-output relationships of signals that pass through them. Nonlinear circuits are generally characterized by input-output relationships called *transfer characteristics.* In general, any memoryless circuit described by transfer characteristics that does not satisfy the following definition of a *linear* memoryless circuit is said to be *nonlinear.*

$$v_{out}(t) = A v_{in}(t), \tag{4.22}$$

where v_{in} and v_{out} are the input and output time-domain waveforms and A is a constant independent of time. Thus, one form of a nonlinear circuit has a transfer characteristic of the form

$$v_{out}(t) = g\left[v_{in}(t)\right]. \tag{4.23}$$

The form of $g(v)$ will determine all measurable distortion characteristics of a nonlinear circuit. Special cases of nonlinear transfer characteristics include:

- Time Invariant: g does not depend on t
- Memoryless: g is evaluated at time t using only values of v_{in} at time t

Nonlinear Memoryless Circuits

If a transfer characteristic includes no integrals, differentials, or finite time differences, then the instantaneous value at a time t depends only on the input values at time t. Such a transfer characteristic is said to be *memoryless*, and may be expressed in the form of a power series

$$g(v) = g_0 + g_1 v + g_2 v^2 + g_3 v^3 + \ldots \tag{4.24a}$$

where g_n are real-valued, time-invariant coefficients. Frequency domain analysis of the output signal $v_{out}(t)$ where $g(v)$ is expressed by Eq. (4.24a) yields a Fourier series, whereby the harmonic components are governed by the coefficients G_n. If $v_{in}(t)$ is a sinusoidal function at frequency f_c with amplitude V_{in}, then the output signal is a harmonic series of the form

$$v_{out}(t) = G_0 + G_1 V_{in} \cos(2\pi f_c t) + G_2 V_{in}^2 \cos(4\pi f_c t) + G_3 V_{in}^3 \cos(6\pi f_c t) + \ldots \tag{4.24b}$$

The coefficients, G_n are functions of the coefficients g_n, and are all real. The extent that the coefficients g_n are nonzero is called the *order* of the nonlinearity. Thus, from Eq. (4.24b), it is seen that an n^{th} order system will produce harmonics of n^{th} order of amplitude $G_n V_{in}^n$.

Nonlinear Circuits with Memory

As described in Eq. (4.24a), $g(v)$ is said to be *memoryless* because the output signal at a time t depends only on the input signal at time t. If the output depends on the input at times different from time t, the nonlinearity is said to have *memory.* A nonlinear function with a finite memory (i.e., a *finite impulse response*) may be described as

$$v_{out}(t) = g\left[v_{in}(t), v_{in}(t-\tau_1), v_{in}(t-\tau_2), \ldots v_{in}(t-\tau_n)\right]. \tag{4.25}$$

The largest time delay, τ_n, determines the length of the memory of the circuit. *Infinite impulse response* nonlinear systems may be represented as functions of integrals and differentials of the input signal

$$v_{out}(t) = g\left[v_{in}(t), \int_{-\infty}^{t} v_{in}(\tau) d\tau, \frac{\partial^n v_{in}}{\partial t^n}\right]. \tag{4.26}$$

The most general characterization of a nonlinear system is the *Volterra Series.*[1] Consider a linear circuit that is stimulated by an input signal $v_{in}(t)$. The output signal $v_{out}(t)$ is then given by the convolution with the input signal $v_{in}(t)$ and the *impulse response* $h(t)$. Unless the impulse response takes the form of the *delta function* $\delta(t)$, the output $v_{out}(t)$ depends on values of the input $v_{in}(t)$ at times other than t, i.e., the circuit is said to have memory.

$$v_{out}(t) = \int_{-\infty}^{\infty} v_{in}(\tau) h(t-\tau) d\tau. \tag{4.27a}$$

Equivalently, in the frequency domain,

$$V_{out}(f) = V_{in}(f) H(f). \tag{4.27b}$$

In the most general case, a nonlinear circuit with reactive elements can be described using a Volterra series, which is said to be a power series with *memory.*

$$v_{out}(t) = g_0 + \int_{-\infty}^{\infty} v_{in}(\tau) g_1(t-\tau) d\tau + \int_{-\infty}^{\infty}\int_{-\infty}^{\infty} v_{in}(t-\tau_1) v_{in}(t-\tau_2) g_2(\tau_1, \tau_2) d\tau_1 d\tau_2 + \ldots \tag{4.28a}$$

An equivalent representation is obtained by taking the n-fold Fourier transform of Eq. (4.28a)

$$V_{out}(f_1, f_2, \ldots) = G_0 \delta(f_1) + G_1(f_1) V_{in}(f_1) + G_2(f_1, f_2) + \ldots \tag{4.28b}$$

Notice that the Volterra series is applicable to nonlinear effects on signals with discrete spectra (i.e., a signal consisting of a sum of sinusoids). For instance, the DC component of the output signal is given by $g_0 = G_0$, while the fundamental component is given by $G_1(f_1)V_{in}(f_1)$, where G_1 and V_{in} are the Fourier transforms of the impulse response g_1 and v_{in}, respectively, evaluated at frequency f_1. The higher order terms in the Volterra series represent the harmonic responses and intermodulation response of the circuit.

Fortunately, extraction of high order Volterra series representations of nonlinear microwave circuits is rarely required to gain useful information on the deleterious and/or useful effects of distortion on common signals. Such simplifications often involve considering the circuit to be memoryless, as in Eq. (4.24a,b), or having finite order, or having integral representations, as in Eq. (4.26).

Harmonic Distortion

A fundamental result of the distortion of nonlinear circuits is that they generate frequency components in the output signal that are not present in the input signal. For sinusoidal inputs, the salient characteristic is *harmonic distortion,* whereby signal outputs consist of integer multiples of the input frequency.

Harmonic Generation in Nonlinear Circuits

As far as microwave circuits are concerned, the major characteristic of a nonlinear circuit is that the frequency components of the output signal differ from those of the input signal. This is readily seen by examining the output of a sinusoidal input from Eq. (4.29).

$$\begin{aligned} v_{out}(t) &= g_0 + g_1 A\cos(2\pi f_c t) + g_2 A^2 \cos^2(2\pi f_c t) + g_3 A^3 \cos^3(2\pi f_c t) + \cdots \\ &= g_0 + \frac{g_2 A^2}{2} + \left(g_1 A + \frac{3 g_3 A^3}{4}\right)\cos(2\pi f_c t) + \frac{a g_2 A^2}{2}\cos(4\pi f_c t) + \frac{g_3 A^3}{4}\cos(6\pi f_c t) + \cdots \end{aligned} \tag{4.29}$$

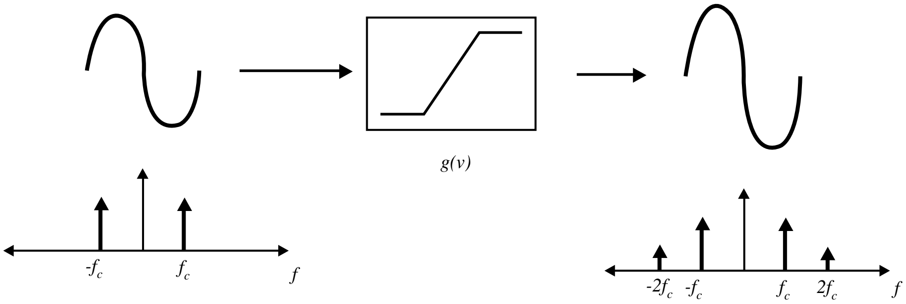

FIGURE 4.34 Effects of a nonlinear transfer characteristic on a sinusoidal input: harmonic distortion.

TABLE 4.1 Effect of Nonlinearities on Carrier Term by Term

Term	Amplitude	Qualitative Effect
DC	$g_0 + g_2A^2/2$	Small offset added due to RF detection
Fundamental	$20\log(g_1A + 3\ g_3A^3/4)$	Amplitude changed due to compression
2nd Harmonic	$40\log(g_2A^2/2)$	2:1 slope on P_{in}/P_{out} curve
3rd Harmonic	$60\log(g_3A^3/4)$	3:1 slope on P_{in}/P_{out} curve

It is readily seen that, along with the *fundamental* component at a frequency of f_c, there exists a DC component, and *harmonic* components at integer multiples of f_c. The output signal is said to have acquired *harmonic distortion* as a result of the nonlinear transfer characteristic. This is illustrated in Fig. 4.34. The function represented by $g(v)$ is that of an ideal limiting amplifier. The net effect of the terms are summarized in Table 4.1.

Measurement of Harmonic Distortion

While instruments are available at low frequencies to measure the *total harmonic distortion* (*THD*), the level of each harmonic is generally measured individually using a spectrum analyzer. Such a setup is shown in Fig. 4.35.

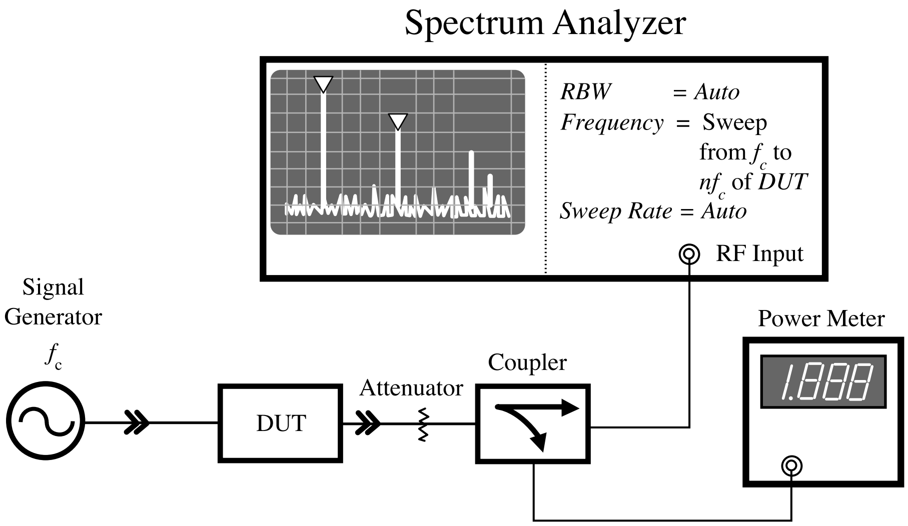

RBW = *Auto*
Frequency = Sweep from f_c to nf_c of *DUT*
Sweep Rate = *Auto*

FIGURE 4.35 Setup used to measure harmonic distortion. Because harmonic levels are a function of output amplitude, a power meter is needed to accurately characterize the harmonic distortion properties.

Harmonic levels are usually measured in a relative manner by placing a marker on the fundamental signal and a delta marker at the n^{th} harmonic frequency. When measured in this mode, the harmonic level is expressed in *dBc*, which designates *dB* relative to carrier (i.e., the fundamental frequency) level. While it is convenient to set the spectrum analyzer sweep to include all harmonics of interest, it may be necessary to center a narrow span at the harmonic frequency in order to reduce the *noise floor* on the spectrum analyzer. An attenuator may be needed to protect the spectrum analyzer from overload. Note that the power level present at the spectrum analyzer input includes all harmonics, not just the ones displayed on the screen. Finally, it is important to note that spectrum analyzers have their own nonlinear characteristics that depend on the level input to the instrument. It is sometimes difficult to ascertain whether measured harmonic distortion is being generated within the device or with the test instrument. One method to do this is to use a step attenuator at the output of the device and step up and down. If distortion is being generated with the spectrum analyzer, the harmonic levels will change with different attenuator settings.

Gain Compression and Phase Distortion

A major result of changing impedances in microwave circuits is signal gain and phase shift that depend on input amplitude level. A change in signal gain between input and output may result from signal clipping due to device current saturation or cutoff. Insertion phase may change because of nonlinear resistances in combination with a reactance. Though there are exceptions, signal gain generally decreases with increasing amplitude or power level. For this reason, the *gain compression* characteristics of microwave components are often characterized. Phase distortion may change either way, so it is often described as *phase deviation* as a function of amplitude or power level.

Gain Compression

Referring back to Eq. (4.29), it is seen that, in addition to harmonic distortion, the level fundamental signal has been modified beyond that dictated by the linear term, g_1. This effect is described as *gain compression* in that the gain of the circuit becomes a function of the input amplitude A. Figure 4.36 illustrates this result. For small values of A, the g_1 term will dominate, giving a 1:1 slope when the output power is plotted against the input power on a *log* (i.e., *dB*) scale. Note that the power level of the n^{th} harmonic plotted in like fashion will have an n:1 slope.

Gain compression is normally measured on a *bandpass* nonlinear circuit.[2] Such a circuit is illustrated in Fig. 4.37. It is interesting to note that an ideal limiting amplifier described by Eq. (4.30) when heavily

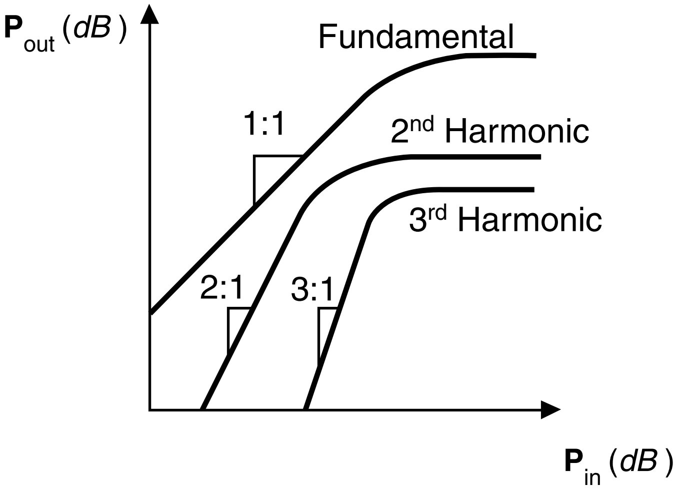

FIGURE 4.36 Output power vs. input power for a nonlinear circuit.

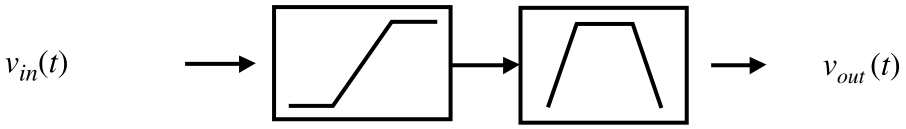

FIGURE 4.37 Bandpass nonlinear circuit.

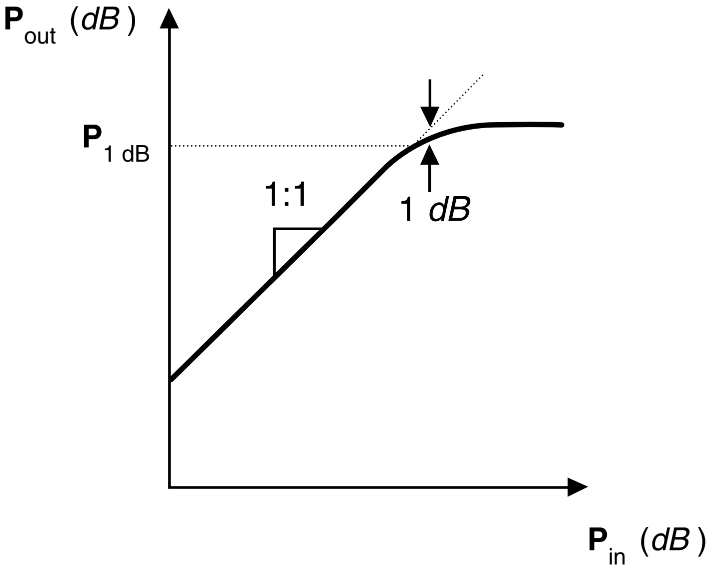

FIGURE 4.38 Gain compression of a bandpass nonlinear circuit. A figure of merit P_{1dB} is the output power at which the gain has been reduced by 1 *dB*.

overdriven at the input will eventually produce a square wave at the output, which is filtered by the bandpass filter. Note that the amplitude of the fundamental component of a square wave is at a level of 4/π times, or 2.1 dB greater than the amplitude of the square wave set by the clipping level.

$$v_{out}(t) = \begin{cases} g_1 v_{in}(t) & v_{out} < v_{\lim} \\ v_{\lim} & otherwise \end{cases} \tag{4.30}$$

For a general third-order nonlinear transfer characteristic driven by a sinusoidal input, the bandpass output is given by

$$v_{out}(t) = \left(g_1 A + \frac{3 g_3 A^3}{4} \right) \cos(2\pi f_c t) \tag{4.31}$$

A bandpass nonlinear circuit may be characterized by the power output at 1 *dB* gain compression, P_{1dB} as illustrated in Fig. 4.38.

Phase Distortion

Nonlinear circuits may also contain reactive elements that give rise to *memory* effects. It is usually unnecessary to extract the entire Volterra representation of a nonlinear circuit with reactive elements if a few assumptions can be made. For bandpass nonlinear circuits with memory effects of time duration of the order of the period of the carrier waveform, a simple model is often used to describe the phase deviation versus amplitude:

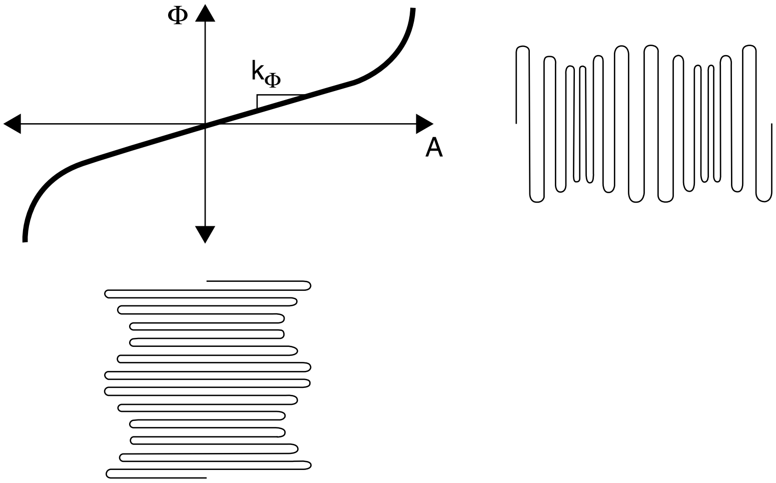

FIGURE 4.39 Effect of *AM-PM* distortion on a modulated signal. Input signal has *AM* component only. Output signal has interrelated *AM* and *FM* components due to the *AM-PM* distortion of the circuit.

$$v_{out}(t) = A(t)\cos\{2\pi f_c t + \Phi[A(t)]\}. \tag{4.32}$$

Equation (4.32) represents the *AM-PM* distortion caused by short-term memory effects (i.e., small capacitances and inductances in microwave circuits). The *effects* of *AM-PM* on an amplitude-modulated signal is illustrated in Fig. 4.39.

For the case of input signals with small deviations of amplitude ΔA, the phase deviation may be considered linear, with a proportionality constant k_ϕ as seen in Fig. 4.39. For a sinusoidally modulated input signal, an approximation for small modulation index FM signals may be utilized. One obtains the following expression for the output signal:

$$\begin{aligned} v_{out}(t) &= [A + \Delta A \sin(2\pi f_m t)]\cos\{2\pi f_c t + k_\phi A + k_\phi \Delta A \sin(2\pi f_m t)\} \\ &\approx A\cos(2\pi f_c t + k_\phi A)\sum_{n=0}^{\infty} J_n(k_\phi \Delta A)\cos(2n\pi f_m t) \end{aligned} \tag{4.33}$$

where J_n is the n^{th} order Bessel function of the first kind.[3] Thus, like amplitude distortion, *AM-PM* distortion creates sidebands at the harmonics of the modulating signal. Unlike amplitude distortion, these sidebands are not limited to the first sideband. Thus, *AM-PM* distortion effects often dominate the out-of-band interference beyond $f_c \pm f_m$ as seen in Fig. 4.40.

The *FM* modulation index k_ϕ may be used as a figure of merit to assess the impact of *AM-PM* on signal with small amplitude deviations. The relative level of the sidebands may be calculated from Eq. (4.33). It must be noted that two sidebands nearest to the carrier may be masked from the *AM* components of the signal, but the out-of-band components are readily identified.

Measurement of Gain Compression and Phase Deviation

For bandpass components where the input frequency is equal to the output frequency, such as amplifiers, gain compression and phase deviation of a nonlinear circuit are readily measured with a *network analyzer* in power sweep mode. Such a setup is shown in Fig. 4.41. P_{1dB} is easily measured using delta markers by placing the reference marker at the beginning of the sweep (i.e., where the DUT is not compressed), and moving the measurement marker where $\Delta Mag(S_{21}) = -1\ dB$. Sweeping at too high a rate may affect the

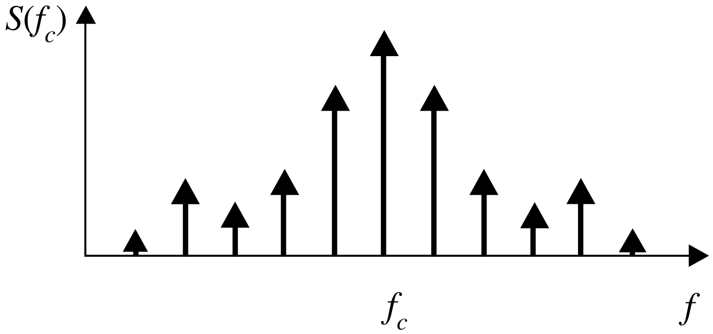

FIGURE 4.40 Output components of an amplitude-modulated signal distorted by *AM-PM* effects.

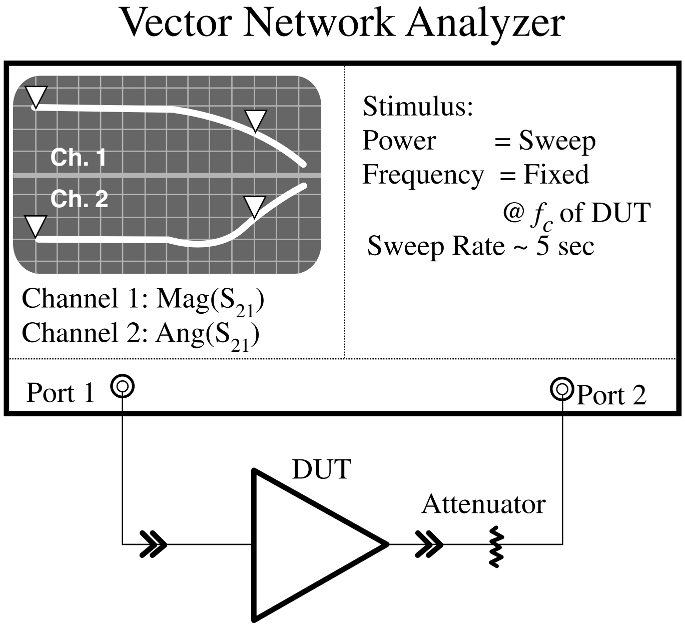

FIGURE 4.41 Setup used to measure gain compression and *AM-PM*.

readings. The sweep must be slow enough so that steady-state conditions exist in both the thermal case and the DC bias network within the circuit. Sweeper retrace may also affect the first few points on the trace. These points must be neglected when setting the reference marker.

The *FM* modulation index is often estimated by measuring the phase deviation at 1 *dB* gain compression $\Delta\Phi(P_{1dB})$

$$k_\phi \approx \frac{\Delta\Phi\left(P_{1dB}\right)}{2Z_0\sqrt{P_{1dB}}}. \tag{4.34}$$

For circuits such as mixers, where the input frequency is not equal to the output frequency, gain compression may be measured using the network analyzer with the measurement mode setup for frequency translation. The operation in this mode is essentially that of a *scalar network analyzer*, and all phase information is lost. *AM-PM* effects may be measured using a *spectrum analyzer* and fitting the sideband levels to Eq. (4.33).

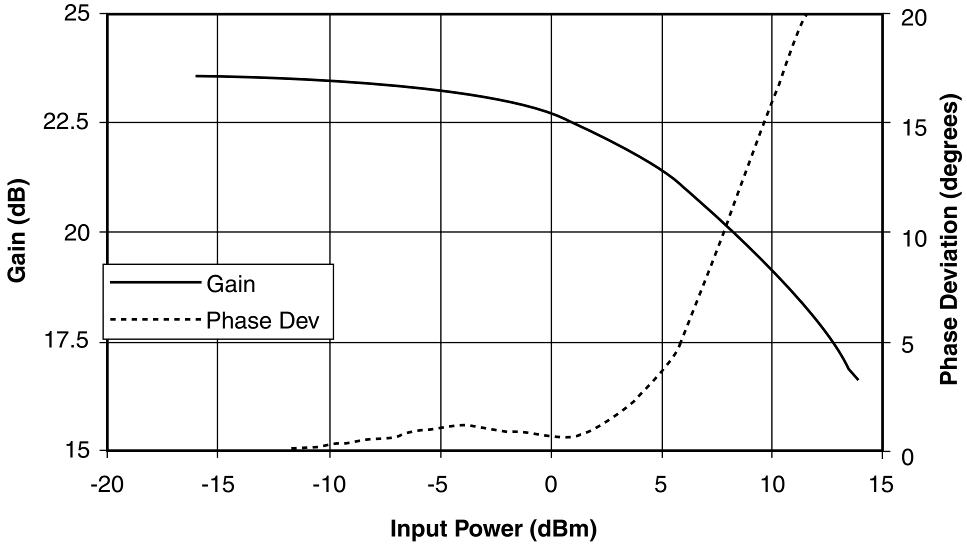

FIGURE 4.42 Measured gain compression and *AM-PM* of a 0.5 W 1960 MHz GaAs MESFET power amplifier IC using an HP8753C Vector Network Analyzer in power sweep mode.

The gain compression and phase deviation of a GaAs power amplifier is shown in Fig. 4.42. P_{1dB} for this amplifier is approximately 23 *dBm* or 0.5 W. The phase deviation $\Delta\Phi$ is not constant from low power to P_{1dB}. Nevertheless, as a figure of merit, the modulation index k_ϕ may be calculated from Eq. (4.34) to be 0.14°/*V*. Notice that for higher power levels, the amplifier is well into compression, and the phase deviation occurs at a much higher slope than k_ϕ would indicate.

Intermodulation Distortion

When more than one frequency component is present in a signal, the distortion from a nonlinear circuit is manifested as *intermodulation distortion* (*IMD*).[4] The *IMD* performance of microwave circuits is important because it can create unwanted interference in adjacent channels. While *bandpass* filtering can eliminate much of the effects of harmonic distortion, intermodulation distortion is difficult to filter out because the IMD components may be very close to the carrier frequency. A common figure of merit is *two-tone* intermodulation distortion.

Two-Tone Intermodulation Distortion

Consider a signal consisting of two sinusoids

$$v_{in}(t) = A\cos(2\pi f_1) + A\cos(2\pi f_2). \tag{4.35}$$

Such a signal may be represented in a different fashion by invoking well-known trigonometric identities.

$$v_{in}(t) = A\cos(2\pi f_c)\cos(2\pi f_m), \tag{4.36a}$$

where

$$f_c = \frac{f_1 + f_2}{2} \quad \text{and} \quad f_m = \left|\frac{f_1 - f_2}{2}\right| \tag{4.36b}$$

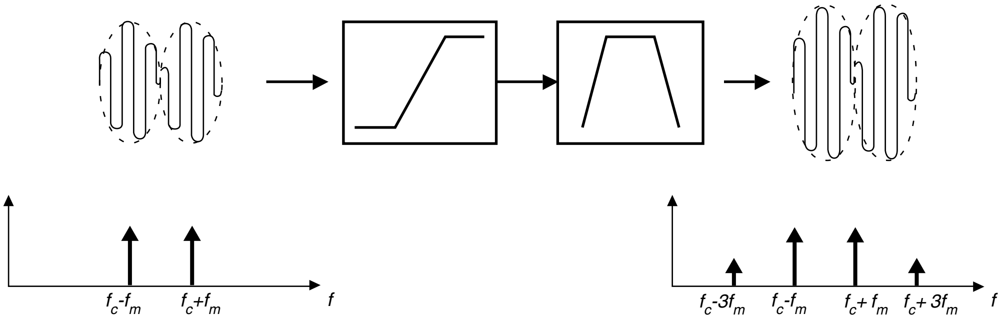

FIGURE 4.43 Intermodulation distortion of a two-tone signal. The output bandpass signal contains the original input signal as well as the harmonics of the envelope at the sum and difference frequencies.

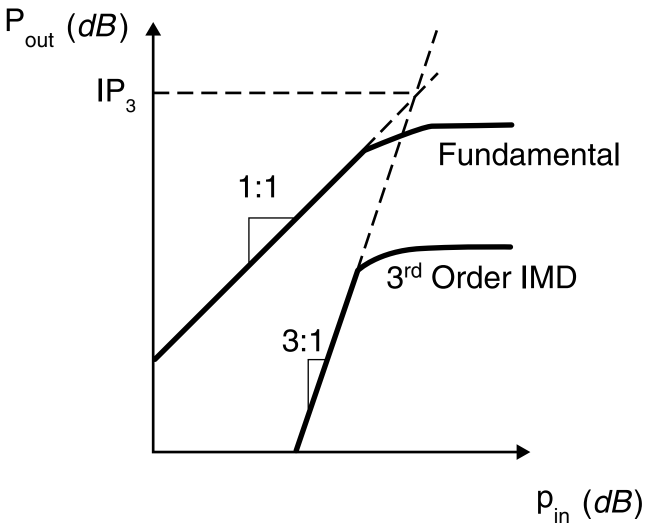

FIGURE 4.44 Relationship between signal output power and intermodulation distortion product power levels. Extrapolating the trends, a figure of merit called the *third order intercept point* (IP_3) is obtained.

Applying such a signal to a memoryless nonlinearity as defined in Eq. (4.24), one obtains the following result:

$$v_{out} = \left[\left(g_1 A + \frac{3g_3A^3}{4}\right)\cos\left(2\pi f_m t\right) + \frac{3g_3A^3}{4}\cos\left(6\pi f_m t\right)\right]\cos\left(2\pi f_c t\right). \tag{4.37}$$

Thus, it is seen that the IMD products near the input carrier frequency are simply the odd-order harmonic distortion products of the modulating *envelope*. This is illustrated in Fig. 4.43.

Third Order Intercept Point

Referring to Fig. 4.44, note that the output signal varies at a 1:1 slope on a *log-log* scale with the input signal, while the IMD products vary at a 3:1 slope. Though both the fundamental and the IMD products saturate at some output power level, if one were to extrapolate the level of each and find the intercept point, the corresponding output power level is called the *third order intercept point* (IP_3). Thus, if the IP_3 of a nonlinear circuit is known, the IMD level relative to the output signal level may be found from

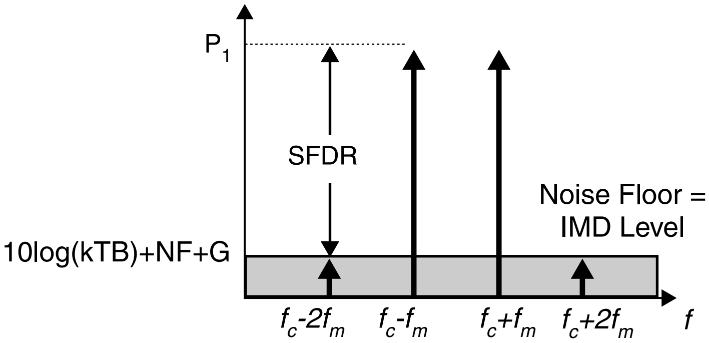

FIGURE 4.45 An illustration of spurious free dynamic range, which defines the range of signal levels where the worst case signal-to-noise ratio is defined by the noise floor of the system, rather than the *IMD* level.

$$IMD_{dBc} = 2\left(P_{out,dBm} - IP_{3,dBm}\right). \tag{4.38}$$

It must be noted that 3rd order *IMD* is only dominant for low levels of distortion (<10 *dB* below P_{1dB}). At higher levels, 5th and higher order *IMD* effects can also produce sidebands at the 3rd order frequency. The net result is that the relative *IMD* level will change at a rate greater than 2:1 compared to carrier level. Care should be taken to avoid extrapolating IP_3 from points where this may be occurring. Another point of caution is *AM-PM* effects. In theory, the sidebands produced by phase modulation are in quadrature with those produced by *AM* distortion, and thus should add directly to the *IMD* power. However, the author's experience has shown that these *AM-PM* products can be rotated in phase and thus vector added to the *AM* sidebands. Since the *FM* sidebands are antiphase, one *FM* sideband adds constructively to the *AM* sidebands, while the other adds destructively. The net effect is an imbalance in the *IMD* levels from lower to higher sideband frequencies. Most specifications of *IMD* level will measure the worst case of the two.

For a limiting amplifier, an often used rule of thumb may be derived that predicts a relationship between P_{1dB} and IP_3.[4]

$$IP_3 = P_{1dB} + 9.6\ dB. \tag{4.39}$$

While this may not be rigorously relied upon for every situation, it is often accurate within ±2 *dB* for small-signal amplifiers and class-A power amplifiers.

Dynamic Range

Because intermodulation distortion generally increases with increasing signal levels, IP_3 may be used to establish the *dynamic range* of a system. The signal level at which the *IMD* level meets the noise floor is defined at the *spurious free dynamic range* (*SFDR*).[5] This is illustrated in Fig. 4.45.

The *SFDR* of a system with gain *G* may be derived from IP_3 and the *noise figure NF*

$$SFDR = \frac{2IP_3 - 2\left[10\log\left(kT_{eq}B\right) + NF + G\right]}{3}, \tag{4.40}$$

where *k* is Boltzman's constant, T_{eq} is the equivalent input noise temperature, and *B* is the bandwidth of the system.

Intermodulation Distortion of Cascaded Components

The question often arises when two components are cascaded of what effect the driving stage *IMD* has on the total *IMD*. This is shown in Fig. 4.46. To the degree that the *IMD* products produced by the n^{th}

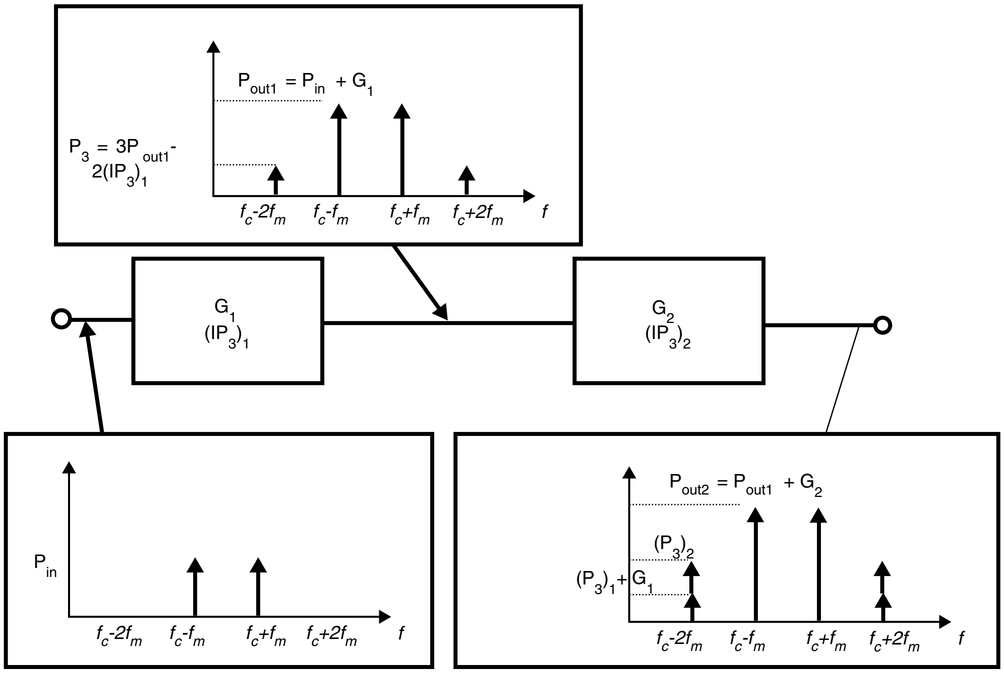

FIGURE 4.46 Effect of cascaded *IMD* levels. The *IMD* from the first stage may be power added to those of the second stage with levels adjusted for the gain of the stage.

stage are uncorrelated with those of the $n + 1$ stage, the output *IMD* may be calculated as the power addition of 3rd order *IMD* levels (P_3) with levels adjusted accordingly for gain.

$$(P_3)_{n+1} = 10\log\left[10^{\left[(P_3)_n + G_1\right]/10} + 10^{\left[3(P_1)_{n+1} - 2(IP_3)_{n+1}/10\right]}\right]. \tag{4.41}$$

Measurement of Intermodulation Distortion

IMD is normally measured with two-signal generators and a *spectrum analyzer*. Such a setup is shown in Fig. 4.47. Care must be taken to isolate the signal generators, as *IMD* may result from one output mixing with signal from the opposing generator. The carrier levels should be within 0.5 *dB* of each other for accurate *IMD* measurements. Also, it is usually recommended that a power meter be used to get an accurate reading of output power level from the DUT. Relative *IMD* level is measured by placing a reference marker on one of the two carrier signals, and placing a delta marker at either sideband. Finally, the input level must be maintained well below the input IP_3 of the spectrum analyzer to insure error-free reading of the DUT.

Multicarrier Intermodulation Distortion and Noise Power Ratio

While two-tone intermodulation distortion serves to compare the linearity of one component to another, in many applications, a component will see more than two carriers in the normal operation of a microwave system. Thus direct measurement of multitone *IMD* is often necessary to insure adequate carrier-to-interference level within a communication system.

Peak-to-Average Ratio of Multicarrier Signals

The major difference between two-tone signals and multitone signals is the *peak-to-average* (*pk/avg*) power ratio.[6] From Eq. (4.35), it is clear that the average power of a two-tone signal is equal to the sum

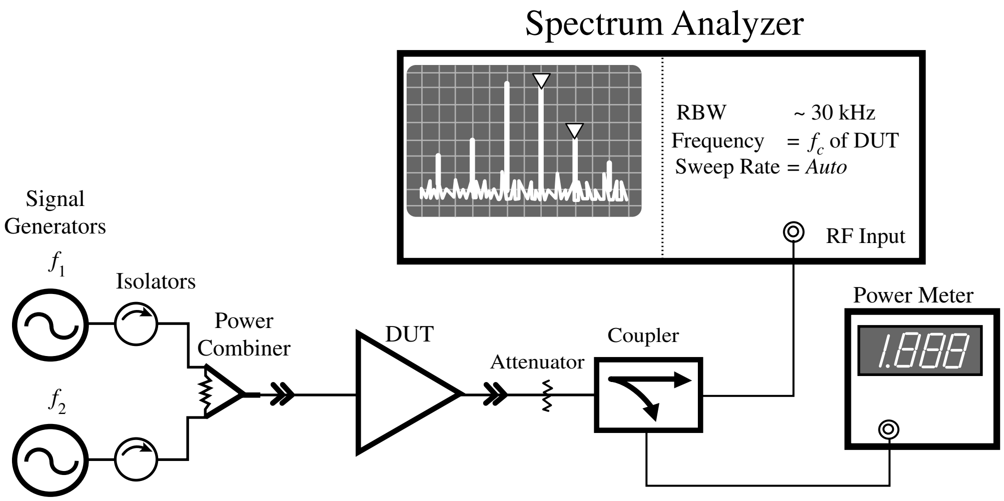

FIGURE 4.47 Setup used to measure two-tone intermodulation distortion (*IMD*).

of powers from the individual carriers. However, from Eq. (4.36), one may derive that the *peak envelope power* (*PEP*) is four times the level of the individual carriers. Thus, it is said that the *pk*/*avg* ratio of a two-tone signal is a factor of 2, or 3 *dB*. From inductive reasoning, it is then clear that the *pk*/*avg* ratio of an *n*-tone signal is

$$pk/avg = 10\log(n). \tag{4.42}$$

While the absolute peak of a multicarrier is dependent only on the number of carriers, the probability distribution of the *pk*/*avg* ratio depends on the modulation. Figure 4.48 shows the difference between 16 phase-aligned tones, and 16 carriers with randomly modulated phases. In general, multiple modulated signals encountered in communication systems will mimic the behavior of random phase modulated sinusoids. Phase aligned sinusoids may be considered a worst case condition. As the number of carriers increases, and if their phases are uncorrelated, the Central Limit Theorem predicts that the distribution of *pk*/*avg* approaches that of white Gaussian random noise.[7] The latter signal is treated in the next section.

Noise Power Ratio

For many systems, including those that process multicarrier signals, white Gaussian noise is a close approximation for the real-world signals. This is a result of the *Central Limit Theorem*, which states that the probability distribution of a sum of a large number of random variables will approach the Gaussian distribution, regardless of the distributions of the individual signals.[7] One metric that has been employed to describe the *IMD* level one would expect in a dense multicarrier environment is the *noise power ratio.* This concept is illustrated in Fig. 4.49.

Measurement of Multitone IMD and Noise Power Ratio

Thus it is clear that power ratings for components must be increased for peak power levels given by Eq. (4.42). Furthermore, two-tone intermodulation distortion may not be indicative of *IMD* of multitone signals. Measurement over various power levels is the only way to accurately predict multitone IMD. Figure 4.50 illustrates a setup that may be used to measure multitone intermodulation.

The challenge in measuring *NPR* is creating the signal. It is clear that, to get an accurate indication of *IMD* performance, the signal bandwidth must not exceed the bandwidth of the device under test. Furthermore, to measure *NPR*, one must notch out the noise power over a bandwidth approximating one channel *BW.* As an example, an *NPR* measurement on a component designed for North American Digital Cellular System (IS-136) ideally would produce a 25-MHz wide noise source with one channel

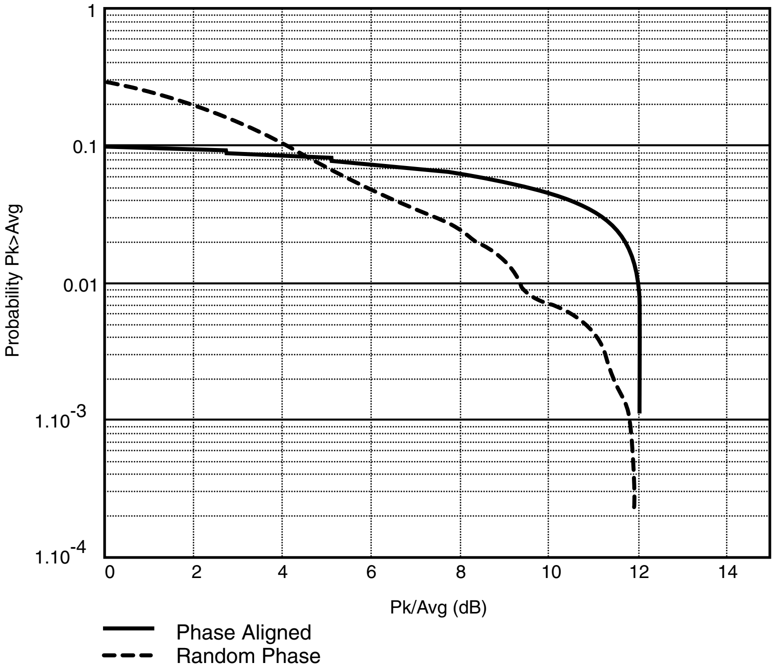

FIGURE 4.48 Distribution of *peak-to-average* ratio of a phase-aligned 16 carrier signal and a random-phase 16 carrier signal. The *y*-axis shows the probability that the signal exceeds a power level above average on the *x*-axis. While both signals ultimately have the same *pk/avg* ratio, their distributions are much different.

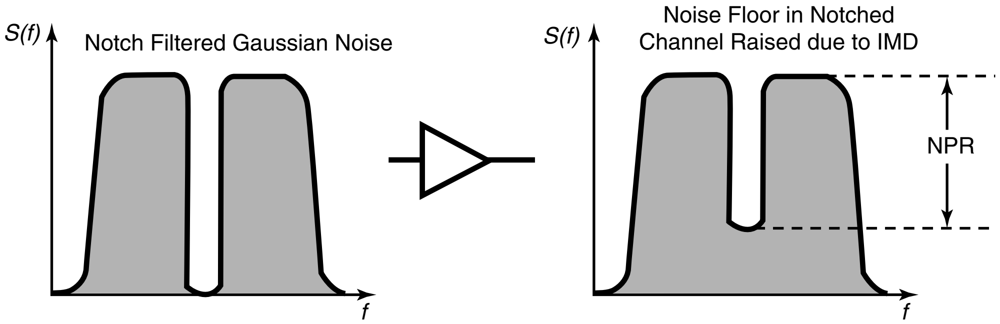

FIGURE 4.49 An illustration of *noise power ratio. NPR* is essentially a measure of the carrier-to-interference level experienced by multiple carriers passing through a nonlinear component.

of bandwidth equal to 30 *kHz*. The *Q* of a notch filter to produce such a signal would be in excess of 25,000. Practical measurements employ filters with *Q*s around 1000, and are able to achieve more than 50 *dB* of measurement range. Such a setup is shown in Fig. 4.51.

Distortion of Digitally Modulated Signals

While standard test signals such as a two-tone or band-limited Gaussian noise provide relative figures of merit of the linearity of a nonlinear component, they cannot generally insure compliance with government or industry system-compatibility standards. For this reason, methods have been developed to measure and characterize the intermodulation distortion of the specific digitally modulated signals used in various systems. Table 4.2 summarizes the modulation formats for North American digital cellular telephone systems.[8,9]

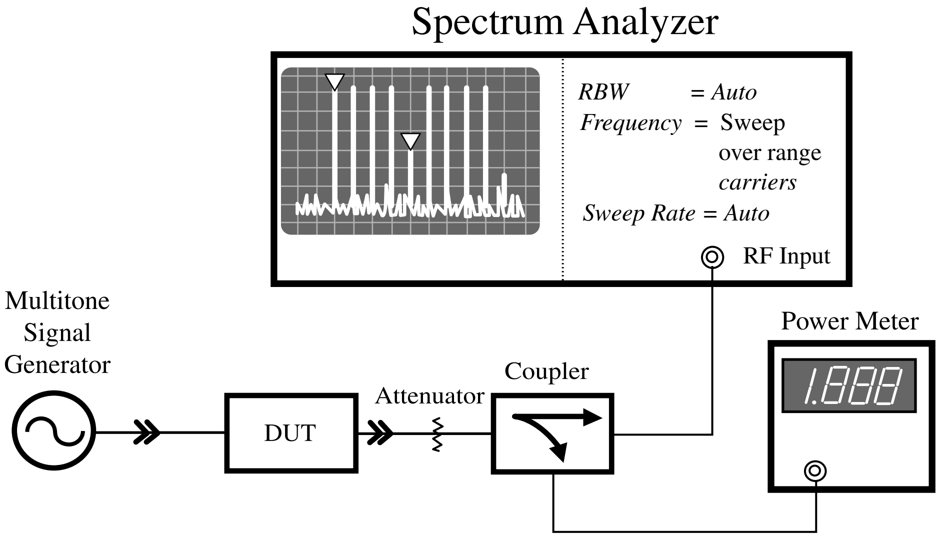

FIGURE 4.50 Measurement setup for multitone *IMD*. Tones are usually spaced equally, with the middle tone deleted to allow measurement of the worst-case *IMD*.

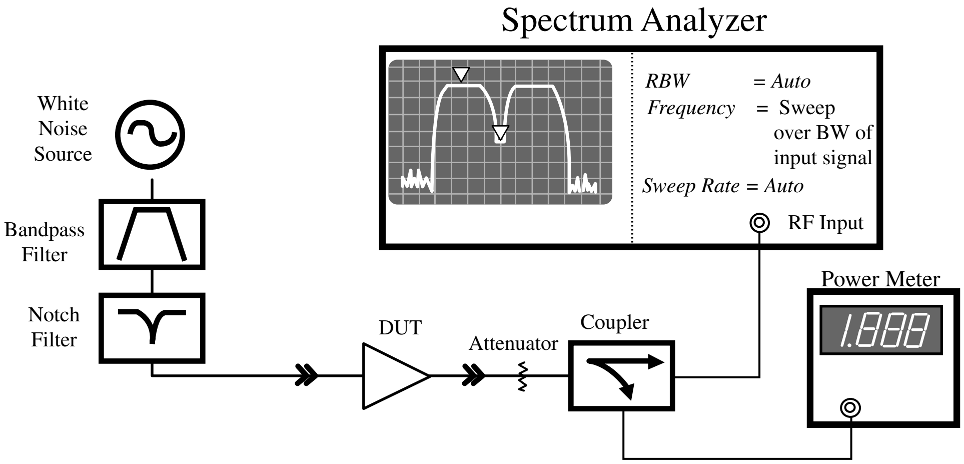

FIGURE 4.51 Noise Power Ratio measurement setup. The rejection of the notch filter should be at least 10 *dB* below the *NPR* level to avoid erroneous measurement.

TABLE 4.2 Modulation Formats for North American Digital Cellular Telephone Systems

Standard	Multiple Access Mode	Channel Power Output	Modulation	Channel Bandwidth
IS-136[8]	TDMA	+28 dBm	π/4-DQPSK	30 kHz
IS-95[9]	CDMA	+28 dBm	OQPSK	1.23 MHz

Intermodulation Distortion of Digitally Modulated Signals

Amplitude and phase distortion affect digitally modulated signals the same way they affect analog modulated signals: gain compression and phase deviation. This is readily seen in Fig. 4.52. Because both amplitude and phase modulation are used to generate digitally modulated signals, they are often expressed

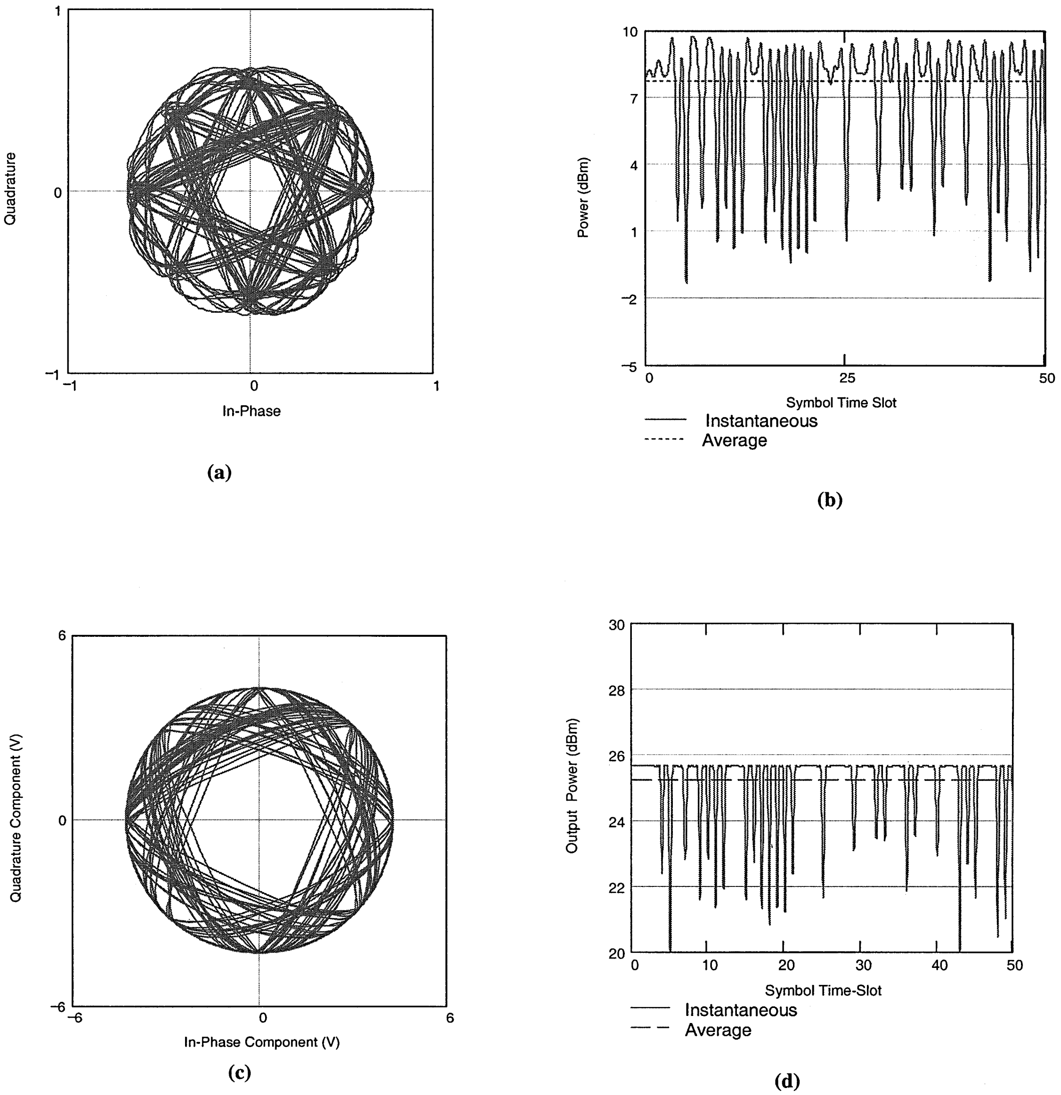

FIGURE 4.52 Effect of amplitude and phase distortion on digitally modulated signals. (a) Shows a π/4 DQPSK signal constellation, and its associated power envelope in (b). When such a signal is passed through a nonlinear amplifier, the resulting envelope is clipped (d), and portions of the constellation are rotated (c).

as a *constellation* plot, with the in-phase component $I = A\cos\phi$ envelope plotted against the quadrature component $Q = A\sin\phi$. The instantaneous power envelope is given by

$$P(t) = I(t)^2 + Q(t)^2 = A(t)^2. \tag{4.43}$$

When the envelope is clipped and/or phase rotated, the resulting *IMD* is referred to as *spectral regrowth.* Figure 4.53 shows the effect of nonlinear distortion on a digitally modulated signal. The out-of-band products may lie in adjacent channels, thus causing interference to other users of the system. For this reason, the *IMD* of digitally modulated signals are often specified as *adjacent channel power ratio* (*ACPR*).[10]

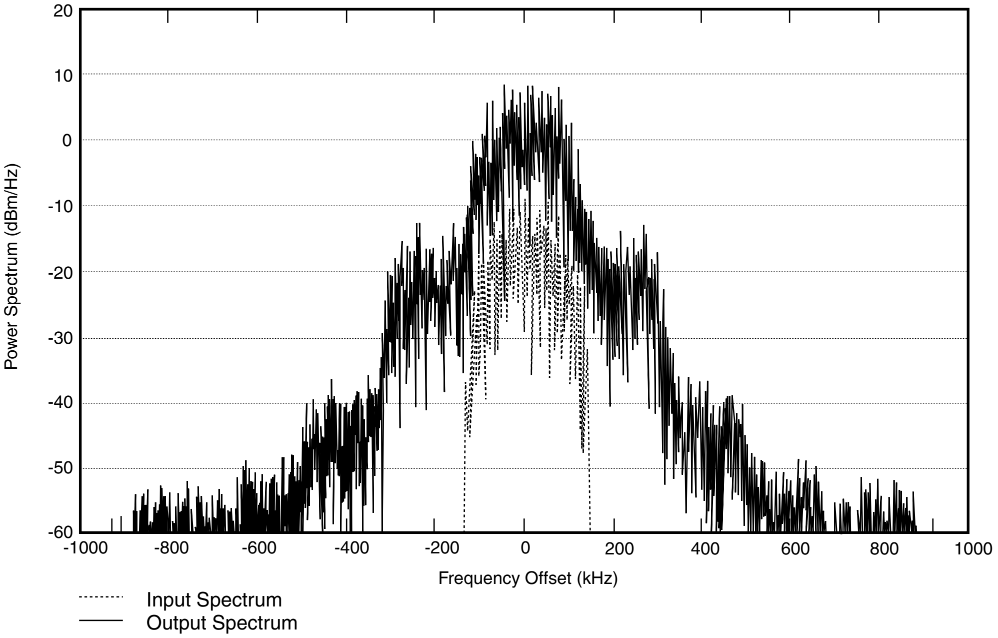

FIGURE 4.53 Effect of nonlinear distortion on a digitally modulated signal. The lower power input signal to a power amplifier has a frequency spectrum that is well contained within a specified channel bandwidth. IMD due to nonlinear distortion creates out-of-band products that may fall within the adjacent channels, causing interference to other users of the system.

ACPR may be specified in a number of ways, depending on the system architecture. In general, *ACPR* is given by

$$ACPR = \frac{I_{adj}}{C_{ch}} = \frac{\int_{f_o - B_{adj}}^{f_o - B_{adj}} S(f)df}{\int_{-B_{ch}/2}^{B_{ch}/2} S(f)df}, \tag{4.44}$$

where I_{adj} is the total interference power in a specified adjacent channel bandwidth, B_{adj} at a given frequency offset f_o from the carrier frequency, and C_{ch} is the channel carrier power in the specified channel bandwidth B_{ch}. Note that the carrier channel bandwidth may be different from the interference channel bandwidth because of regulations enforcing interference limits between different types of systems. Furthermore, the interference level may be specified in more than one adjacent channel. In this case, the specification is referred to as the *alternate channel power ratio*. Table 4.3 shows ACPR specifications for various digital cellular standards.

In addition to the out-of-band interference due to the intermodulation distortion in-band interference will also result from nonlinear distortion. The level of the in-band interference is difficult to measure directly because it is superimposed on the channel spectrum. However, when the signal is demodulated,

TABLE 4.3 ACPR and EVM Specifications for Digital Cellular Subscriber Equipment

Standard	ADJ. CH. PWR	ALT. CH. PWR	EVM
IS-136	–26 dBc/30 kHz @ ± 30 kHz	–45 dBc/30 kHz @ ± 60 kHz	12.5%
IS-95	–42 dBc/30 kHz @ > ± 885 kHz	–54 dBc/30 kHz @ > ± 1.98 MHz	23.7%

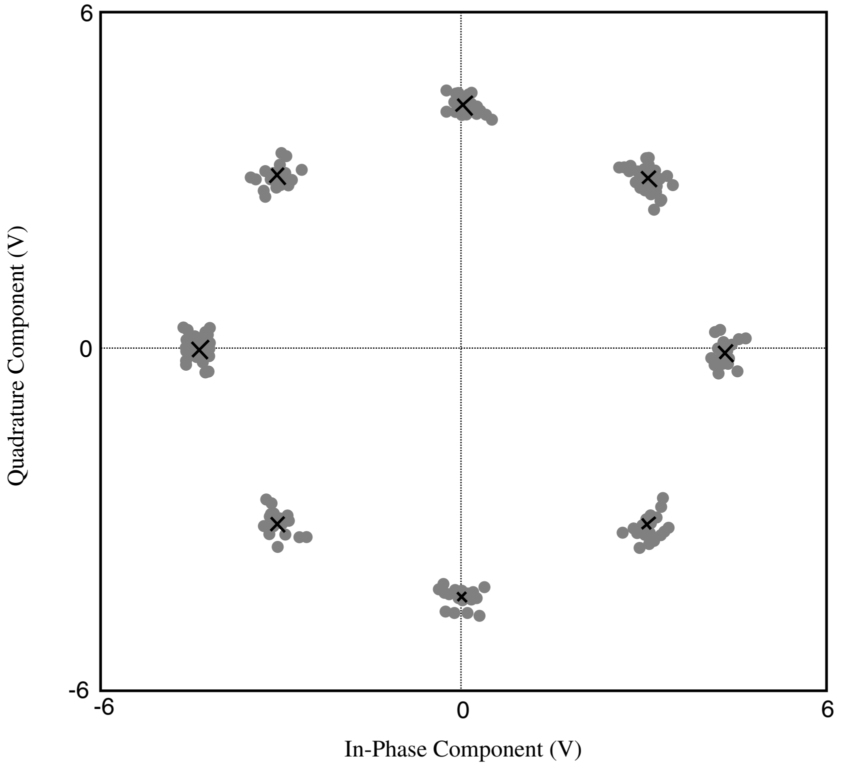

FIGURE 4.54 Errors in the demodulated *I-Q* constellation may result from the in-band *IMD* products. The *rms* summation of errors from the desired location (given by the × markers) give the *error vector magnitude* of the signal distortion.

errors in the output *I-Q* constellation occur at the sample points. This is shown in Fig. 4.54. Because the demodulator must make a decision as to which symbol (i.e., which constellation point) was sent, the resulting errors in the *I-Q* vectors may produce a false decision, and hence cause *bit errors.*

There are two methods to characterize the level *I-Q* vector error: *error vector magnitude* (*EVM*), and a quality factor called the ρ-*factor.*[11] Both *EVM* and ρ-*factor* provide an indication of signal distortion, but they are calculated differently. *EVM* is the *rms* sum of vector errors divided by the number of samples.

$$EVM = \frac{1}{n}\sqrt{\sum_n \left[\left|I\left(t_n\right) - S_{In}\right|^2 + \left|Q\left(t_n\right) - S_{Qn}\right|^2\right]}, \tag{4.45}$$

where the *I-Q* sample points at the n^{th} sample windows are given by $I(t_n)$ and $Q(t_n)$, and the n^{th} symbol location point in-phase and quadrature components are given by S_{In} and S_{Qn} respectively.

Whereas *EVM* provides an indication of *rms* % error of the signal envelope at the sample points, ρ-*factor* is related to the waveform quality of a sig al. It is related to *EVM* by

$$\rho = \frac{1}{1 - EVM^2} \tag{4.46}$$

Measurement of ACPR, EVM, and Rho-Factor

ACPR may be measured using a setup similar to those for measuring *IMD*. The major difference involves generating the test signal. Test signals for digitally modulated signals must be synthesized according to system standards using an *arbitrary waveform generator* (*AWG*), which generates *I*- and *Q*-baseband envelopes. In the most basic form, these are high speed digital-to-analog converters (*DACs*). The files used to generate the envelope waveforms may be created using commonly available mathematics software, and are built in many commercially available *AWGs*. The *I*- and *Q*-baseband envelopes are fed to an *RF* modulator to produce a modulated carrier at the proper center frequency.

In the case of *CDMA* standards, deviations between test setups can arise from different selections of Walsh codes for the traffic channels. While a typical *CDMA* downlink (base station to mobile) signal has a *pk/avg* of approximately 9.5 *dB,* it has been shown that some selections of Walsh codes can result in peak-to-average ratios in excess of 13 *dB*.[12] Measurement of *EVM* is usually done with a *vector signal analyzer* (*VSA*). This instrument is essentially a receiver that is flexible enough to handle a variety of frequencies and modulation formats. Specialized software is often included to directly measure *EVM* or rho-factor for well-known standards used in microwave radio systems.

Summary

This section has treated characterization and measurement techniques for nonlinear microwave components. Figures of merit were developed for such nonlinear effects as harmonic level, gain compression, and intermodulation distortion. While these offer a basis for comparison of the linearity performance between like components, direct measurement of adjacent channel power and error vector magnitude are preferred for newer wireless systems. Measurement setups for the above parameters were suggested in each section. For more advanced treatment, the reader is referred to the references at the end of this section.

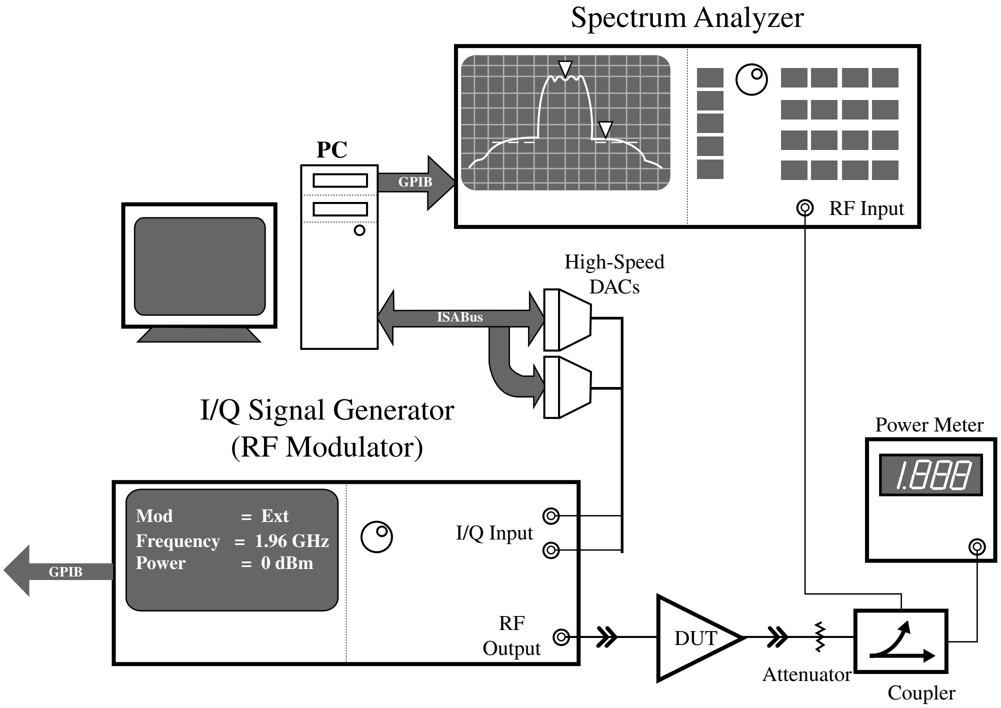

FIGURE 4.55 Measurement setup for ACPR. Waveforms are created using PCs or specialized arbitrary waveform generators. In either case, the baseband waveform must be upconverted to the center frequency of the DUT.

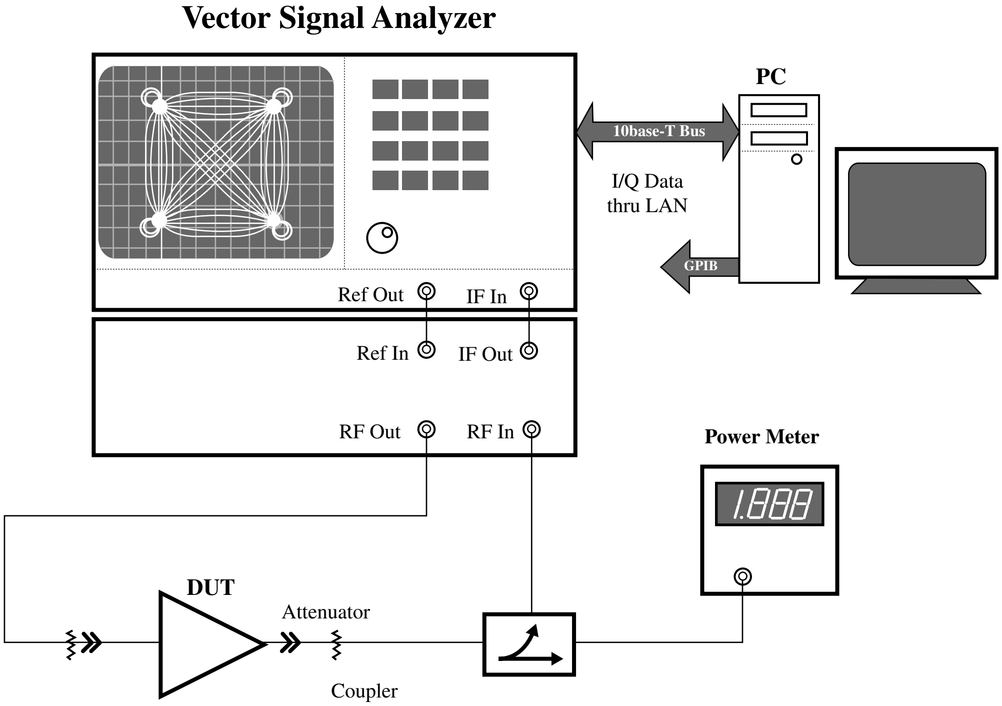

FIGURE 4.56 Setup for measuring *EVM*. The *VSA* demodulates the *I-Q* waveform and calculates the deviation from ideal to calculate *EVM* and ρ-*factor* as given in Eq. (4.45) and Eq. (4.46), respectively.

References

1. Maas, S.A., *Nonlinear Microwave Circuits*, Artech House, Boston, 1988.
2. Blachman, N.M., Band-pass nonlinearities, *IEEE Trans. Information Theory,* IT-10, 162–64, April, 1964.
3. Andrews, L.C., *Special Functions of Mathematics for Engineers,* 2nd ed., McGraw-Hill, New York, 1992, chap. 6.
4. Cripps, S.C., *RF Power Amplifiers for Wireless Communications,* Artech House, Boston, 1999, chap. 7.
5. Carson, R.S., *Radio Concepts: Analog*, John Wiley & Sons, New York, 1990, chap. 10.
6. Kenney, J.S., and Leke, A., Design considerations for multicarrier CDMA base station power amplifiers, *Microwave J.,* 42, 2, 76–86, February, 1999.
7. Papoulis, A., *Probability, Random Variables, and Stochastic Processes,* 3rd ed., McGraw-Hill, New York, 1991, chap. 8.
8. IS-136 Interim Standard, Cellular System Dual-Mode Mobile Station — Base Station Compatibility Standards, Telecommunications Industry Assoc.
9. IS-95 Interim Standard, Mobile Station — Base Station Compatibility Standard for Dual-Mode Wideband Spread Spectrum Cellular Systems, Telecommunications Industry Assoc.
10. Kenney, J.S. and Leke, A., Power amplifier spectral regrowth for digital cellular and PCS applications, *Microwave J.*, 38, 10, 74–92, October 1995.
11. Lindsay, S.A., Equations derive error-vector magnitude, *Microwaves & RF,* April, 1995, 158–67.
12. Braithwaite, R.N., Nonlinear amplification of CDMA waveforms: an analysis of power amplifier gain errors and spectral regrowth, *Proc. 48th Annual IEEE Vehicular Techn. Conf.*, 2160–66, 1998.

Seely, Warren L. et al. "Circuits"
The RF and Microwave Handbook
Editor in Chief Mike Golio
Boca Raton: CRC Press LLC,2001

5

Circuits

Warren L. Seely
Motorola

Jakub Kucera
Infineon Technologies

Urs Lott
Acter AG

Anthony M. Pavio
Motorola

Charles Nelson
California State University

Mark Bloom
Motorola SPS

Alfy Riddle
Macallan Consulting

Robert Newgard
Rockwell Collins

Richard V. Snyder
RS Microwave

Robert J. Trew
U.S. Department of Defense

5.1 Receivers

Warren L. Seely

An electromagnetic signal picked up by an antenna is fed into a receiver. The ideal receiver rejects all unwanted noise including other signals. It does not add any noise or interference to the desired signal. The signal is converted, regardless of form or format, to fit the characteristics required by the detection scheme in the signal processor, which in turn feeds an intelligible user interface (Fig. 5.1). The unit must require no new processes, materials, or devices not readily available. This ideal receiver adds no weight, size, or cost to the overall system. In addition, it requires no power source and generates no heat. It has an infinite operating lifetime in any environment, and will never be obsolete. It will be flexible, fitting all past, present, and future requirements. It will not require any maintenance, and will be transparent to the user, who will not need to know anything about it in order to use it. It will be fabricated in an “environmentally friendly” manner, visually pleasing to all who see it, and when the user is finally finished with this ideal receiver, he will be able to recycle it in such a way that the environment is improved rather than harmed. Above all else, this ideal receiver must be wanted by consumers in very large quantities, and it must be extremely profitable to produce. Fortunately, nobody really expects to achieve all of these “ideal” characteristics, at least not yet! However, each of these characteristics must be addressed by the engineering design team in order to produce the best product for the application at hand.

Frequency

Receivers represent a technology with tremendous variety. They include AM, FM, analog, digital, direct conversion, single and multiple conversions, channelized, frequency agile, spread spectrum, chirp, frequency hopping, and others. The applications are left to the imaginations of the people who create them. Radio, telephones, data links, radar, sonar, TV, astronomical, telemetry, and remote control, are just a few of those applications. Regardless of the application, the selection of the operating frequencies is fundamental to obtaining the desired performance.

The actual receive frequencies are generally beyond the control of the design team, being dictated, controlled, and even licensed by various domestic or foreign government agencies, or by the customer. When a product is targeted for international markets, the allocated frequencies can take on nightmare qualities due to differing allocations, adjacent interfering bands, and neighboring country restrictions or allocations. It will usually prove impossible to get the ideal frequency for any given application, and often the allocated spectrum will be shared with other users and multiple applications. Often the spectrum is

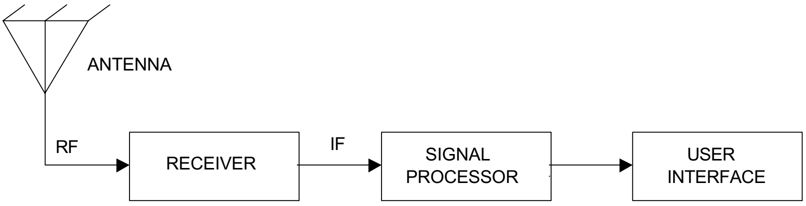

FIGURE 5.1 The receiver.

available for a price, usually to the highest bidder. Failure to utilize the purchased spectrum within a specified time frame may result in forfeiture of what is now an asset; an expensive mistake. This has opened up the opportunity to speculate and make (or lose) large sums of money by purchasing spectrum to either control a market or resell to other users. For some applications where frequency allocation is up to the user, atmospheric or media absorption, multipathing, and background noise are important factors that must be considered. These effects can be detrimental or used to advantage. An example includes cross links for use with communications satellites, where the cross link is unaffected by absorption since it is above the atmosphere. However, the frequency can be selected to use atmospheric absorption to provide isolation between ground signals and the satellite cross links. Sorting out these problems is time consuming and expensive, but represents a fundamental first step in receiver design.

Dynamic Range

The receiver should match the dynamic range of the desired signal at the receiver input to the dynamic range of the signal processor. Dynamic range is defined as the range of desirable signal power levels over which the hardware will operate successfully. It is limited by noise, signal compression, and interfering signals and their power levels.

Power and Gain

The power in any signal(s), whether noise, interference or the desired signal, can be measured and expressed in Watts (W), decibels referenced to 1 Watt (dBW), milliwatts (mW) or decibels referenced to one milliwatt (dBm). The power decibel is 10 times the LOG of the dimensionless power ratio. The power gain of a system is the ratio output signal power to the input signal power expressed in decibels (dB). The gain is positive for components in which the output signal is larger than the input, negative if the output signal is smaller. Negative gain is loss, expressed as attenuation (dB). The power gain of a series component chain is found by simple multiplication of the gain ratios, or by summing the decibel gains of the individual components in the chain. All of these relationships are summarized in Fig. 5.2.

Noise

Thermal noise arises from the random movement of charge carriers. The thermal noise power (n_T) is usually expressed in dBm (N_T), and is the product of Boltzman's constant (k), system temperature in degrees Kelvin (T), and a system noise bandwidth in Hertz (b_n). The system noise bandwidth (b_n) is defined slightly different from system bandwidth. It is determined by measuring or calculating the total system thermal average noise power ($n_{\text{tot-ave}}$) over the entire spectrum and dividing it by the system peak average noise power ($n_{\text{pk-ave}}$) in a 1 Hz bandwidth. This has the effect of creating a system noise bandwidth

$$Decibel = 10LOG\left[\frac{p}{p_{ref}}\right]$$

$$P(dBW) = 10LOG\left[\frac{p(W)}{1W}\right] \qquad g(-) = \frac{p_{out}}{p_{in}}$$

$$G(dB) = 10LOG(g)$$

$$P(dBm) = 10LOG\left[\frac{p(mW)}{1mW}\right] \qquad g_{total}(-) = g_1 * g_2 * .... * g_N = \frac{p_{Nout}}{p_{1in}}$$

$$0dBW = 1Watt \qquad G_{total}(dB) = G_1(dB) + G_2(dB) + ... + G_N(dB) = \Sigma G_i$$

$$0dBm = 1mW \qquad Loss(dB) = -G(dB)$$

$$1000mW = 1W \qquad Loss(dB) = Attenuation(dB)$$

$$30dBm = 0dBW$$

FIGURE 5.2 Power and gain relationships.

$$n_T = kTb_n$$

$$b_n(Hz) = \frac{n_{tot-ave}(W)}{\underline{n}_{pk-ave}(W/Hz)}$$

$$k = 1.38*10^{-23}\frac{W\sec}{K}$$

$$T(K) = T(^0C) + 273.15$$

$$n_T = 1.38*10^{-23}\frac{W\sec}{K}*(25^0C + 273.15)K*1Hz = 4.46*10^{-21}W = 4.46*10^{-18}mW$$

$$N_T = 10LOG(n_T) = -204dBW = -174dBm$$

FIGURE 5.3 Noise power relationships.

in which the noise is all at one level, that of the peak average noise power. For a 1 Hz system noise bandwidth at the input to a system at room temperature (25°C), the thermal noise power is about –174 dBm. These relationships are summarized in Fig. 5.3.

Receiver Noise

The bottom end of the dynamic range is set by the lowest signal level that can reasonably be expected at the receiver input and by the power level of the smallest acceptably discernable signal as determined at the input to the signal processor. This bottom end is limited by thermal noise at the input, and by the gain distribution and addition of noise as the signal progresses through the receiver. Once a signal is below the minimum discernable signal (MDS) level, it will be lost entirely (except for specialized spread spectrum receivers). The driving requirement is determined by the signal clarity needed at the signal processor. For analog systems, the signal starts to get fuzzy or objectionably noisy at about 10 dB above the noise floor. For digital systems, the allowable bit error rate determines the acceptable margin above the noise floor. Thus the signal with margin sets the threshold minimum desirable signal level.

Noise power at the input to the receiver will be amplified and attenuated like any other signal. Each component in the receiver chain will also add noise. Passive devices such as filters, cables, and attenuators will cause a drop in both signal and noise power alike. These passive devices also contribute a small amount of internally generated thermal noise. Thus the actual noise figure of a passive device is slightly higher than the attenuation of that component. This slight difference is ignored in receiver design since the actual noise figures and losses vary by significantly larger amounts. Passive mixers will generally have a noise figure about 1 dB greater than the conversion loss. Active devices can exhibit loss or gain, and signal and noise power at the input will experience the same effect when transferred to the output. However, the internally generated noise of an active device will be substantial and must be accounted for, requiring reasonably accurate noise figures and gain data on each active component.

The bottom end dynamic range of a receiver component cascade is easily described by the noise equations shown in Fig. 5.4. The first three equations for noise factor (f_n), noise figure (NF), and noise temperature (T_n) are equivalent expressions to quantify noise. The noise factor is a dimensionless ratio of the input signal-to-noise ratio and the output signal-to-noise ratio. Replacing the signal ratio with gain results in the final form shown. Noise figure is the decibel form of noise factor, in units of dB. Noise temperature is the conversion of noise factor to an equivalent input temperature that will produce the output noise power, expressed in Kelvin. Convention dictates using noise temperature when discussing antennas and noise figure for receivers and associated electronics. By taking the decibel equivalent of the noise factor, the expression for noise out (N_o) is obtained, where noise in (N_i) is in dBm and noise figure (NF) and gain (G) are in dB. The cascaded noise factor (f_t) is found from the sum of the added noise due to each cascaded component divided by the total gain preceding that element. Use the cascaded noise factor (f_t) followed by the noise out (N_o) equation to determine the noise level at each point in the receiver.

$$f_n = \frac{s_i/n_i}{s_o/n_o} = \frac{n_o}{g n_i}$$

$$NF = 10LOG(f_n)$$

$$T_n = T(f_n - 1) \quad \mathit{whereT\ is\ in\ Kelvin}$$

$$N_o = NF + G + N_i$$

$$f_t = f_1 + \frac{f_2 - 1}{g_1} + \frac{f_3 - 1}{g_1 * g_2} + \cdots + \frac{f_n - 1}{\Pi g_n}$$

$$\Delta f_{n-bandwidth} = \frac{g_1 f_1 + (f_2 - 1)^{b_{n2}}/_{b_{n1}}}{g_1 f_1 + f_2 - 1} \qquad b_{n2} > b_{n1}$$

$$\Delta f_{n-image} = 1 + \frac{l_{ar}}{f_x}$$

$$f_{total} = f_{cascade} * \Delta f_{n-bandwidth} * \Delta f_{n-image}$$

FIGURE 5.4 Receiver noise relationships.

Noise factor is generally computed for a 1 Hz bandwidth and then adjusted for the narrowest filter in the system, which is usually downstream in the signal processor. Occasionally, it will be necessary to account for noise power added to a cascade when components following the narrowest filter have a relatively broad noise bandwidth. The filter will eliminate noise outside its band up to that filter. Broader band components after the filter will add noise back into the system depending on their noise bandwidth. This additional noise can be accounted for using the equation for $\Delta f_{\text{n-bandwidth}}$, where subscript 1 indicates the narrowband component followed by the wideband component (subscript 2). Repeated application of this equation may be necessary if several wideband components are present following the filter. Image noise can be accounted for using the relationship for $\Delta f_{\text{n-image}}$ where l_{ar} is the dimensionless attenuation ratio between the image band and desired signal band and f_x is the noise factor of the system up to the image generator (usually a mixer). Not using an image filter in the system will result in a $\Delta f_{\text{n-image}} = 2$ resulting in a 3 dB increase in noise power. If a filter is used to reject the image by 20 dB, then a substantial reduction in image noise will be achieved. Finally, the corrections for bandwidth and image are easily incorporated using the relationship for the cascaded total noise factor, f_{total}.

A simple single sideband (SSB) receiver example, normalized to a 1 Hz noise bandwidth, is shown in Fig. 5.5. It demonstrates the importance of minimizing the use of lossy components near the receiver front end, as well as the importance of a good LNA. A 10 dB output signal-to-noise margin has been established as part of the design. Using the –174 dBm input thermal noise level and the individual component gains and noise figures, the normalized noise level can be traced through the receiver, resulting in an output noise power of –136.9 dBm. Utilizing each component gain and working backwards from this point with a signal results in the MDS power level in the receiver. Adding the 10 dB signal-to-noise margin to the MDS level results in the signal with margin power level as it progresses through the receiver. The signal and noise levels at the receiver input and output are indicated. The design should minimize the gap between the noise floor and the MDS level. Progressing from the input toward the output, it is readily apparent that the noise floor gets closer to and rapidly converges with the MDS level due to the addition of noise from each component, and that lossy elements near the input hurt system performance. The use of the low noise amplifier as close to the front end of the cascade as possible is critical in order to mask the noise of following components in the cascade and achieve minimum noise figure. The overall cascaded receiver gain is easily determined by the difference in the signal levels from input to output.

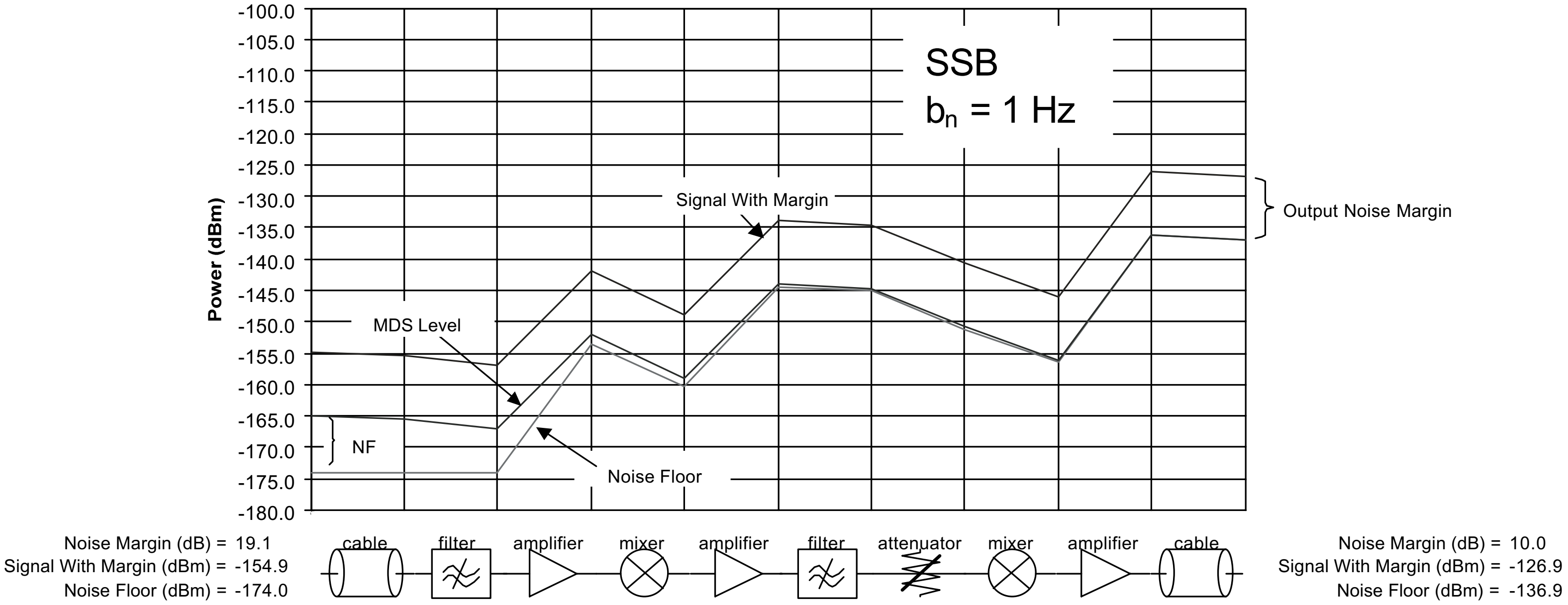

Gain (dB)	-0.5	-1.5	15.0	-7.0	15.0	-0.7	-6.0	-5.5	20.0	-0.8
NF (dB)	0.5	1.5	5.5	8.0	8.0	0.7	6.0	6.5	8.0	0.8
Cumilative Gain (dB)	-0.5	-2.0	13.0	6.0	21.0	20.3	14.3	8.8	28.8	28.0
Cumilative NF (dB)	0.5	2.0	7.5	7.7	8.6	8.6	8.6	8.7	9.1	9.1
Output Signal With Margin (dBm)	-155.4	-156.9	-141.9	-148.9	-133.9	-134.6	-140.6	-146.1	-126.1	-126.9
Output Noise Floor (dBm)	-174.0	-174.0	-153.5	-160.3	-144.4	-145.1	-151.1	-156.5	-136.1	-136.9
Output MDS Level (dBm)	-165.4	-166.9	-151.9	-158.9	-143.9	-144.6	-150.6	-156.1	-136.1	-136.9

FIGURE 5.5 Example SSB receiver noise and signal cascade normalized to b_n = 1.

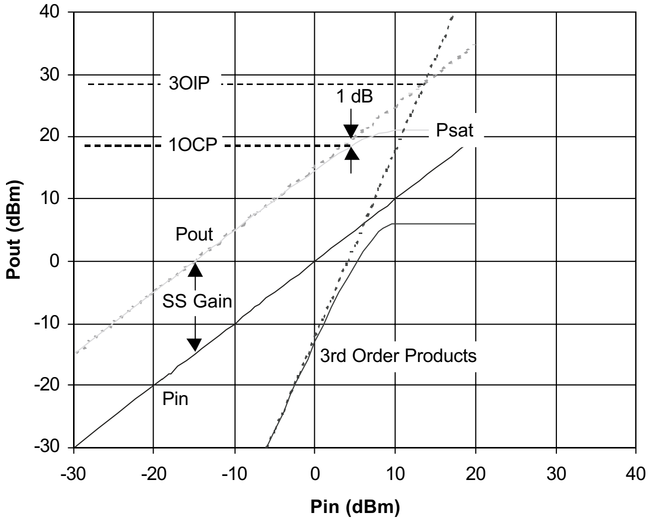

FIGURE 5.6 3OIP, P_{sat}, and 1 dB OCP.

The noise floor margins at both the input and output to the receiver are also easily observed, along with the receiver noise figure. Note also that the actual noise power does not drop below the thermal noise floor, which is always the bottom limit. Finally, the actual normalized signal with margin level of –154.9 dBm at the input to the receiver is easily determined.

Intermodulation

Referring to Fig. 5.6, the upper end of the dynamic range is limited by nonlinearity, compression, and the resulting intermodulation in the presence of interfering signals. The in-band two-tone output 3rd order intercept point (3OIP) is a measure of the nonlinearity of a component. This particular product is important because it can easily result in an undesired signal that is close to the desired signal, which would be impossible to eliminate by filtering. By definition, the 3OIP is found by injecting 2 equal amplitude signals (F_1 and F_2) that are not only close to each other in frequency, but are also both within the passband of the component or system. The 3rd order intermodulation products are then given by $\pm nF_1 \pm mF_2$ where $n + m = 3$. For 3rd order products, n and m must be 1 or 2. Since negative frequencies are not real, this will result in two different 3rd order products which are near each other and within the passband. The power in the intermodulation products is then plotted, and both it and Pout are projected until they intersect, establishing the 3OIP. The desired signal is projected using a 1:1 slope, while the 3rd order products are projected using a 3:1 slope. The output saturation power (P_{sat}) is the maximum power a device will produce. The output 1 dB compression point (1 dB OCP) is the point at which the gain is lowered by 1 dB from small signal conditions due to signal compression on its way to complete saturation. In general, higher values mean better linearity and thus better performance. However, component costs rapidly increase along with these numbers, especially above saturated levels of about +15 dBm, limiting what can be achieved within project constraints. Thus, one generally wants to minimize these parameters in order to produce an affordable receiver. For most components, a beginning assumption of square law operation is reasonable. Under these conditions, the 1 dB OCP is about 3 dB below P_{sat}, and the 3OIP is about 10 dB above the 1 dB OCP. When the input signal is very small (i.e., small signal conditions), Pout increases on a 1:1 slope, and 3rd order products increase on a 3:1 slope. These numbers can vary significantly based on actual component performance and specific loading conditions. This whole process can be reversed, which is where the value of the concept lies. By knowing the small signal gain, Pin or Pout, and the 3OIP, all the remaining parameters, including 1OCP, P_{sat}, and 3rd order IM levels can be estimated. As components are chosen for specific applications, real data should be utilized where possible. Higher order

$$\frac{1}{p_{3iip,tot}} = \frac{1}{p_{3iip,1}} + \frac{g_1}{p_{3iip,2}} + \cdots + \frac{\Pi g_n}{p_{3iip,n}}$$

$$P_{3OIP} = P_{3IIP} + G_{ss}$$

$$SFDP = \frac{2}{3}\left(3IIP - MDS_{input}\right) = \frac{2}{3}\left(3OIP - MDS_{output}\right)$$

$$MSI_{out} = NOISEFLOOR_{out} + SPDR$$

FIGURE 5.7 Receiver 3OIP, P_{sat}, and 1 dB OCP cascade.

products may also cause problems, and should be considered also. Finally, any signal can be jammed if the interfering signal is large enough and within the receiver band. The object is to limit the receiver's susceptibility to interference under reasonable conditions.

Receiver Intermodulation

Analog receiver performance will start to suffer when in-band 3rd order products are within 15 dB of the desired signal at the detector. This level determines the maximum signal of interest (MSI). The margin for digital systems will be determined by acceptable bit error rates. The largest signal that the receiver will pass is determined by the saturated power level of the receiver. Saturating the receiver will result in severe performance problems, and will require a finite time period to recover and return to normal performance. Limiting compression to 1 dB will alleviate recovery.

Analyzing the receiver component cascade for 3OIP, P_{sat}, 1 dB OCP, and MSI will provide insight into the upper limits of the receiver dynamic range, allowing the designer to select components that will perform together at minimum cost and meet the desired performance (Fig. 5.7). The first equation handles the cascading of known components to determine the cumulated input 3rd order input intermod point. After utilizing this equation to determine the cascaded 3OIP up to the component being considered, the second equation can be utilized to determine the associated P_{3OIP} . Successive application will result in completely determining the cascaded performance. The last two equations determine the 3rd order IM spur free dynamic range (SPDR) and the maximum spur-free level or maximum signal of interest (MSI) at the output of the receiver.

An example receiver 3OIP and signal cascade is shown in Fig. 5.8. The results of the cumulative 3OIP are plotted. A gain reference is established by setting and determining the cumulative gain and matching it to the cumulative 3OIP at the output. A design margin of 20 dB is added to set the MSI power level for the cascade.

Receiver Dynamic Range

Combining the results for the noise and intermodulation from the above discussion into one graph results in a graphical representation of the dynamic range of the receiver (Fig. 5.9). Adjusting for the 6 MHz bandwidth moves the noise plots up by 10LOG(6e6) = 67.8 dB. The cumulative 3OIP and gain reference plot remain at the previously determined levels. The SPDR = 2(–5.5 dBm – (–97.1 dBm))/3 = 61.1 dB is calculated and then used to determine the MSI level = –69.1 dBm + 61.1 dB = –8 dBm at the output. The MSI level on the graph is set to this value, backing off to the input by the gain of each component.

The receiver gain, input, and output dynamic ranges, signal levels which can be easily handled, and the appropriate matching signal processing operating range are readily apparent, being between the MSI level and the signal with noise margin. The receiver NF, 3OIP, gain, and SPDR are easily determined from the plot. Weaknesses and choke points, as well as expensive parts are also apparent, and can now be attacked and fixed or improved. In general, components at or near the input to the receiver dominate the noise performance, and thus the lower bounds on dynamic range. Components at or near the output dominate the nonlinear performance, and thus the upper bounds on dynamic range.

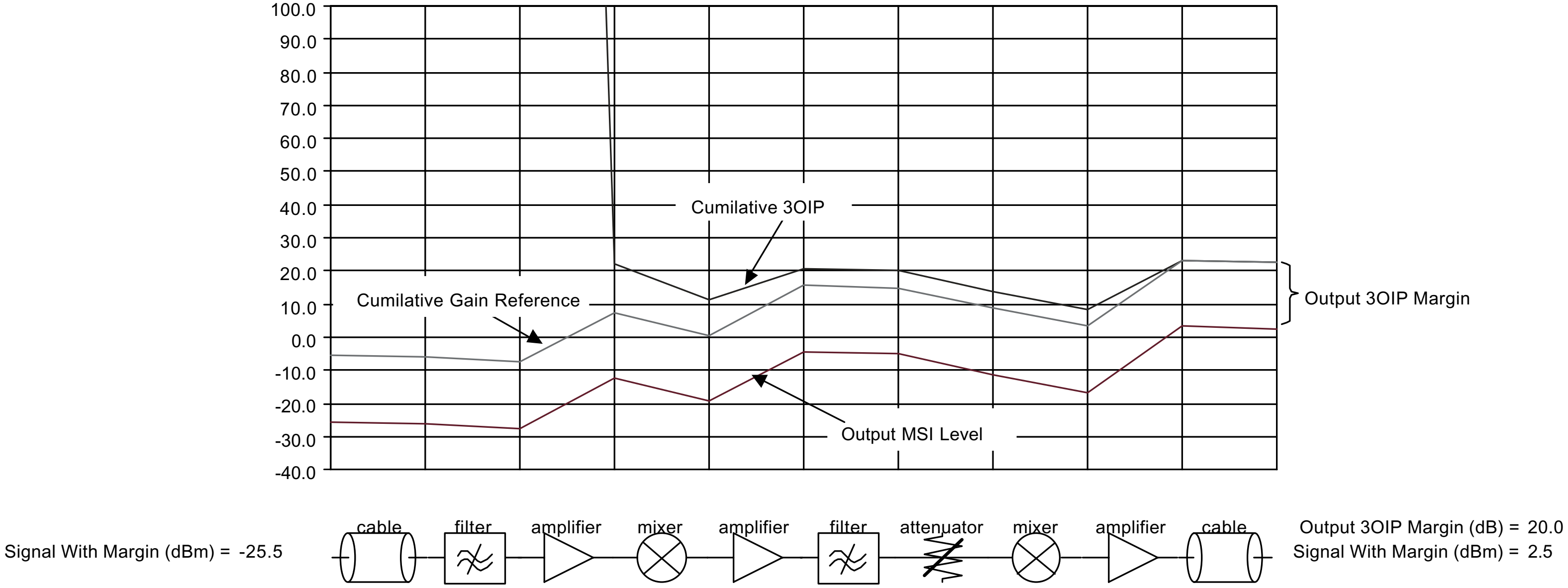

Gain (dB)	-0.5	-1.5	15.0	-7.0	15.0	-0.7	-6.0	-5.5	20.0	-0.8
3IIP (dBm)	999.5	1000.5	7.0	21.0	7.0	999.7	1005.0	28.5	5.0	999.8
3OIP (dBm)	999.0	999.0	22.0	14.0	22.0	999.0	999.0	23.0	25.0	999.0
Cumilative Gain (dB)	-0.5	-2.0	13.0	6.0	21.0	20.3	14.3	8.8	28.8	28.0
Cumilative 3IIP (dBm)	999.5	997.2	9.0	5.5	-0.3	-0.3	-0.3	-0.5	-5.5	-5.5
Cumilative 3OIP (dBm)	999.0	995.2	22.0	11.5	20.7	20.0	14.0	8.3	23.3	22.5
Cumilative Gain Reference (dBm)	-6.0	-7.5	7.5	0.5	15.5	14.8	8.8	3.3	23.3	22.5
Output MSI Level (dBm)	-26.0	-27.5	-12.5	-19.5	-4.5	-5.2	-11.2	-16.7	3.3	2.5

FIGURE 5.8 Example receiver 3OIP and signal cascade.

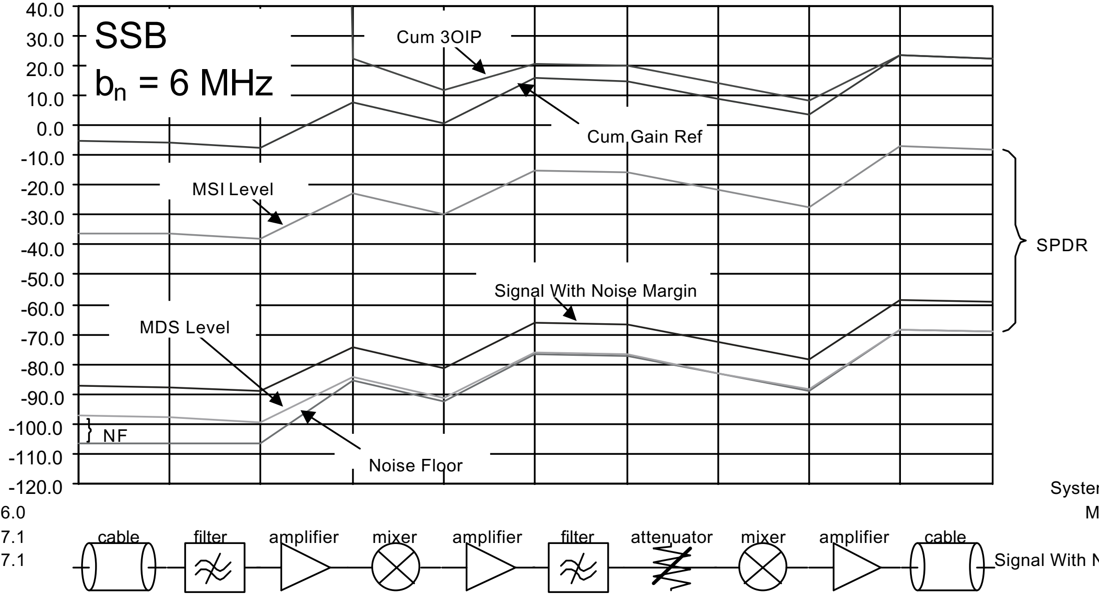

MSI At Input (dBm) = -36.0
Signal With Noise Margin (dBm) = -87.1
MDS At Input (dB) = -97.1

System bandwidth (MHz) = 6.0
MSI At Output (dBm) = -8.0
Noise Margin (dB) = 10.0
Signal With Noise Margin (dBm) = -59.1
Noise Floor (dBm) = 69.1
Calculated SFDR (dB) = 61.1

Gain (dB)	-0.5	-1.5	15.0	-7.0	15.0	-0.7	-6.0	-5.5	20.0	-0.8
NF (dB)	0.5	1.5	5.5	8.0	8.0	0.7	6.0	6.5	8.0	0.8
3IIP (dBm)	999.5	1000.5	7.0	21.0	7.0	999.7	1005.0	28.5	5.0	999.8
3OIP (dBm)	999.0	999.0	22.0	14.0	22.0	999.0	999.0	23.0	25.0	999.0
Cumilative Gain (dB)	-0.5	-2.0	13.0	6.0	21.0	20.3	14.3	8.8	28.8	28.0
Cumilative NF (dB)	0.5	2.0	7.5	7.7	8.6	8.6	8.6	8.7	9.1	9.1
Output Signal With Margin (dBm)	-87.6	-89.1	-74.1	-81.1	-66.1	-66.8	-72.8	-78.3	-58.3	-59.1
Output Noise Floor (dBm)	-106.2	-106.2	-85.7	-92.5	-76.6	-77.3	-83.3	-88.7	-68.3	-69.1
Output MDS Level (dBm)	-97.6	-99.1	-84.1	-91.1	-76.1	-76.8	-82.8	-88.3	-68.3	-69.1
Cumilative 3IIP (dBm)	999.5	997.2	9.0	5.5	-0.3	-0.3	-0.3	-0.5	-5.5	-5.5
Cumilative 3OIP (dBm)	999.0	995.2	22.0	11.5	20.7	20.0	14.0	8.3	23.3	22.5
Cumilative Gain Reference (dBm)	-6.0	-7.5	7.5	0.5	15.5	14.8	8.8	3.3	23.3	22.5
Output MSI Level (dBm)	-36.5	-38.0	-23.0	-30.0	-15.0	-15.7	-21.7	-27.2	-7.2	-8.0

FIGURE 5.9 Example SSB receiver spur free dynamic range normalized to b_n = 6 MHz.

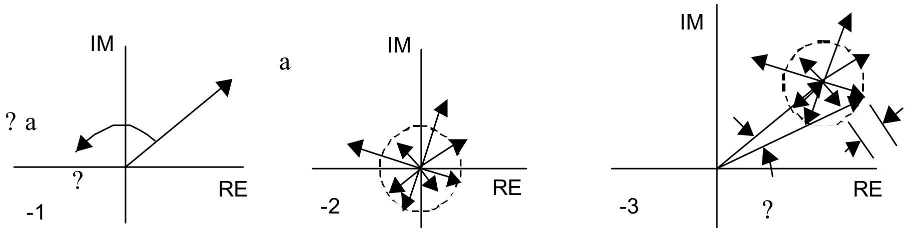

FIGURE 5.10 Phase noise, AM, and PM noise.

The use of 3OIP and noise floors is just one way commonly used to characterize the dynamic range of a receiver. Other methods include determining compression and saturation curves, desensitization, noise power ratios, and intercept analysis for other IM products such as 2OIP up to as high as possibly 15OIP. Specific applications will determine the appropriate analysis required in addition to the main SFDR analysis described above.

The LO Chain

A reference signal or local oscillator (LO) is generally required in order to up- or downconvert the desired signal for further processing. The design of the LO chain is tied to the receiver components by frequency, power level, and phase noise. The LO signal will have both amplitude and phase noise components, both of which will degrade the desired signal. Often, a frequency agile LO is required. The LO can be generated directly by an oscillator, multiplied or divided from another frequency source, created by mixing several signals, injection or phase locked to a reference source, digitally synthesized, or any combination thereof.

Amplitude and Phase Noise

A pure tone can be represented as a vector of a given amplitude (α) rotating with a fixed angular velocity (ω) as shown in Fig. 5.10. A random noise source can be viewed similarly, but has random phase equally distributed over time about 360°, and random amplitude based on a probability distribution. At any given instant in time the vector will change amplitude and angle. A plot of the noise vector positions for a relatively long period of time would appear solid near the origin and slowly fade away at larger radii from the origin (Fig. 5.10). A plot of the number of hits vs. distance from the origin would result in the probability distribution. This random noise is the same noise present in all electronic systems. Combining the pure tone with the random noise results in the vector addition of both signals (Fig. 5.10). At any given instance in time the combined angular velocity will change by $\Delta\omega$, and the amplitude will change by $\Delta\alpha$. The frequency jittering about ω and the amplitude wavering about α result in AM and PM noise components, which distort the signal of interest. Thus, phase noise is a measure of signal stability.

The design of the LO chain usually includes at least one final amplifier stage that is completely saturated. This sets the LO amplitude to a fixed level, minimizes temperature variations, and minimizes or eliminates the AM noise component. Saturation results in a gain reduction of several dB and simultaneously limits the maximum amplitude that can be achieved. Thus as the random noise vector changes the LO amplitude, the saturated amplifier acts to eliminate the output amplitude change. The AM contribution to noise is cleaned up.

The phase noise in the LO chain must be attacked directly at the source. Clean, low phase noise signal generation in oscillators is achieved by the use of very high Q filter components, incorporating bipolar devices as the active oscillator element, maximizing the source power generation, and careful design of the conduction cycle within the oscillator itself. Once a clean signal is created, it must be kept clean.

Frequency multiplying or dividing the signal will also multiply or divide the phase noise by a factor of 20*LOG(N) at any given offset from the base signal. Conversely, if the signal is multiplied or divided, then the spectrum is respectively stretched or contracted by the factor N. The mixing process also mixes the phase noise, but the net result will depend on the mixer types utilized. Injection locking will replicate the injection source modified by the multiplication or division factor N. A phase lock loop exhibits close in noise dependent on the reference source and loop circuitry, but the far out phase noise is set by the source used in the loop itself. Finally, the LO is utilized in the receiver chain to perform frequency conversion. The resulting converted signal will have components of phase noise from the original signal, the LO signal, and from noise in the mixing component.

The Potential for Trouble

Receivers are designed to work with very small signals, transforming these to much larger signals for handling in the signal processor. This inherent process is open to many pitfalls resulting in the vast majority of problems encountered in creating a viable product. It will only take a very small interfering or spurious signal to wreak havoc. Interfering signals generally can be categorized as externally generated, internally generated, conducted, electromagnetically coupled, piezoelectrically induced, electromechanically induced, and optically coupled or injected. Some will be fixed, others may be intermittent, even environmentally dependent. Most of these problem areas can be directly addressed by simple techniques, precluding their appearance altogether. However, ignoring these potential problem areas usually results in disaster, primarily because they are difficult to pinpoint as to cause and effect, and because eliminating them may be difficult or impossible without making major design changes and fabricating new hardware in order to verify the solution. This can easily turn into a long-term iterative nightmare. Additionally, if multiple problems are present, whether or not they are perceived as multiple problems or as a single problem, the amount of actual time involved in solving them will go up exponentially! Oscillator circuits are generally very susceptible to any and all problems, so special consideration should be given in their design and use. Finally, although the various cause, effect, and insight into curing problems are broken down into component parts in the following discussion, it is often the case that several concepts must be combined to correctly interpret and solve any particular problem at hand.

Electromechanical

Vibrations and mechanical shocks will result in physical relative movement of hardware. Printed circuit boards (PCBs), walls, and lids may bow or flutter. Cables and wire can vibrate. Connectors can move. Solder joints can fracture. PCBs, walls, and lids capacitively load the receiver circuitry, interconnects, and cabling. Movement, even very small deflections, will change this parasitic loading, resulting in small changes in circuit performance. In sensitive areas, such as near oscillators and filters, this movement will induce modulation onto the signals present. In phase-dependent systems, the minute changes in physical makeup and hence phase length of coaxial cable will appear as phase modulation. Connector pins sliding around during vibration can introduce both phase and amplitude noise. These problems are generally addressed by proper mechanical design methods, investigating and eliminating mechanical resonance, and minimizing shock susceptibility. Don’t forget that temperature changes will cause expansion and contraction, with similar but slower effects.

Optical Injection

Semiconductor devices are easily affected by electromagnetic energy in the optical region. Photons impinging on the surface of an active semiconductor create extra carriers, which appear as noise. A common occurrence of this happens under fluorescent lighting common in many offices and houses. The 60 Hz “hum” is present in the light given off by these fixtures. The light impinges on the surface of a semiconductor in the receiver, and 60 Hz modulation is introduced into the system. This is easily countered by proper packaging to prevent light from hitting optically sensitive components.

Piezoelectric Effects

Piezoelectric materials are reciprocal, meaning that the application of electric fields or mechanical force changes the electromechanical properties, making devices incorporating these materials highly susceptible to introducing interference. Even properly mounted crystals or SAW devices, such as those utilized in oscillators, will move in frequency or generate modulation sidebands when subjected to mechanical vibration and shock. Special care should therefore be given to any application of these materials in order to minimize these effects. This usually includes working closely with the original equipment manufacturer (OEM) vendors to ensure proper mounting and packaging, followed by extensive testing and evaluation before final part selection and qualification.

Electromagnetic Coupling

Proper design, spacing, shielding, and grounding is essential to eliminate coupled energy between circuits. Improper handling of each can actually be detrimental to achieving performance, adding cost without benefit, or delaying introduction of a product while problems are solved. Proper design techniques will prevent inadvertent detrimental E-M coupling. A simple example is a reject filter intended to minimize LO signal leakage into the receiver, where the filter is capable of the required performance, but the packaging and placement of the filter allow the unwanted LO to bypass the filter and get into the receiver anyway.

It is physically impossible to eliminate all E-M resonant or coupled structures in hardware. A transmission line is created by two or more conductors separated by a dielectric material. A waveguide is created by one or more conductive materials in which a dielectric channel is present, or by two or more nonconductive materials with a large difference in relative dielectric constant. Waveguides do not have to be fully enclosed in order to propagate E-M waves. In order to affect the hardware, the transmission line or waveguide coupling must occur at frequencies that will interfere with operation of the circuits, and a launch into the structure must be provided. Properly sizing the package (a resonant cavity) is only one consideration. Breaking up long, straight edges and introducing interconnecting ground vias on multilayer PCBs can be very effective. Eliminating loops, opens and shorts, sharp bends, and any other "antenna like" structures will help.

E-field coupling usually is associated with high impedance circuits, which allow relatively high E-fields to exist. E-field or capacitive coupling can be eliminated or minimized by any grounded metal shielding. M-field coupling is associated with low impedance circuits in which relatively high currents and the associated magnetic fields are present. M-field or magnetic coupling requires a magnetic shielding material. In either case, the objective is to provide a completely shielded enclosure. Shielding metals must be thick enough to attenuate the interfering signals. This can be determined by E or M skin effect calculations. Alternatively, absorbing materials can also be used. These materials do not eliminate the basic problem, but attempt to mask it, often being very effective, but usually relatively expensive for production environments. Increased spacing of affected circuitry, traces, and wires will reduce coupling. Keeping the E-M fields of necessary but interfering signals orthogonal to each other will add about 20 dB or more to the achieved isolation.

Grounding is a problem that could be considered the "plague" of electronic circuits. Grounding and signal return paths are not always the same, and must be treated accordingly. The subject rates detailed instruction, and indeed entire college level courses are available and recommended for the serious designer. Basically, grounding provides a reference potential, and also prevents an unwanted differential voltage from occurring across either equipment or personnel. In order to accomplish this objective, little or no current must be present. Returns, on the other hand, carry the same current as the circuit, and experience voltage drops accordingly. A return, in order to be effective, must provide the lowest impedance path possible. One way to view this is by considering the area of the circuit loop, and making sure that it is minimized. In addition, the return conductor size should be maximized.

Summary

A good receiver design will match the maximum dynamic range possible to the signal processor. In order to accomplish this goal, careful attention must be given to the front end noise performance of the receiver and the selection of the low noise amplifier. Equally important in achieving this goal is the linearity of the back end receiver components, which will maximize the SFDR. The basic receiver calculations discussed above can be utilized to estimate the attainable performance. Other methods and parameters may be equally important and should be considered in receiver design. These include phase noise, noise power ratio, higher order intercepts, internal spurious, and desensitization.

Further Reading

Sklar, Bernard, Digital Communications Fundamentals and Applications, Prentice-Hall, Englewood Cliffs, NJ, 1988.

Tsui, Dr. James B., *Microwave Receivers and Related Components,* Avionics Laboratory, Air Force Write Aeronautical Laboratories, 1983.

Watkins-Johnson Company Tech-notes, Receiver Dynamic Range: Part 1, Vol. 14, No. 1.

Watkins-Johnson Company Tech-notes, Receiver Dynamic Range: Part 2, Vol. 14, No. 2.

Steinbrecher, D., Achieving Maximum Dynamic Range in a Modern Receiver, *Microwave Journal,* Sept 1985.

5.2 Transmitters

Warren L. Seely

A signal is generated by the frequency synthesizer and amplified by the transmitter (Fig. 5.11), after which it is fed to the antenna for transmission. Modulation and linearization may be included as part of the synthesized signal, or may be added at some point in the transmitter. The transmitter may include frequency conversion or multiplication to the actual transmit band. An ideal transmitter exhibits many of the traits of the ideal receiver described in the previous section of this handbook. Just as with the receiver, the task of creating a radio transmitter begins with defining the critical requirements, including frequencies, modulations, average and peak powers, efficiencies, adjacent channel power or spillover, and phase noise. Additional transmitter parameters that should be considered include harmonic levels, noise powers, spurious levels, linearity, DC power allocations, and thermal dissipations. Nonelectrical, but equally important considerations include reliability, environmentals such as temperature, humidity, and vibration, mechanicals such as size, weight, and packaging or mounting, interfaces, and even appearance, surface textures, and colors. As with most applications today, cost is becoming a primary driver in the design and production of the finished product. For most RF/microwave transmitters, power amplifier considerations dominate the cost and design concerns.

Safety must also be considered, especially when high voltages or high power levels are involved. To paraphrase a popular educational TV show; "be sure to read and understand all safety related materials that are applicable to your design before you begin. And remember, there is nothing more important than shielding yourself and your coworkers (assuming you like them) from high voltages and high levels of RF/microwave power." Another safety issue for portable products concerns the use of multiple lithium batteries connected in parallel. Special care must be taken to insure that the batteries charge and discharge independent of each other in order to prevent excessive I-R heating, which can cause the batteries to explode. It is your life — spend a little time to become familiar with these important issues.

ACP, Modulation, Linearity, and Power

The transmitter average and peak output powers are usually determined from link/margin analysis for the overall system. The transmitter linearity requirements are determined from the transmit power levels, phase noise, modulation type, filtering, and allowed adjacent channel power (ACP) spillover. Linearity

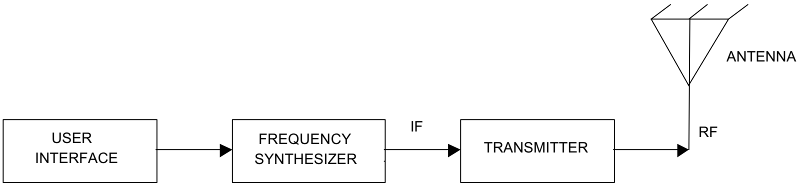

FIGURE 5.11 The transmitter.

is intimately tied to the transmitter saturated power, which in turn is tied to the 1 dB compression point. The need for high linearity is dependent on the maximum acceptable ACP in adjacent channels or bands. This spillover of power will cause interference in adjacent channels or bands, making it difficult or impossible to use that band. The maximum ACP may be regulated by government agencies, or may be left up to the user. Often the actual transmitted power requirement is less stringent than the linearity requirement in determining the necessary power handling capability or saturated power of the transmitter. In order to achieve required linearity, the transmitter may operate significantly backed off from the saturated power capability, even under peak power operation. Since the cost of a transmitter rapidly increases with its power handling capability, and the linearity requirements are translated into additional power requirements, a great deal of the cost of a transmitter may actually be associated with linearity rather than transmit power level. If the added cost to achieve necessary linearity through additional power capability is significant, linearizing the transmitter can be cost effective.

Power

The single most important specification affecting the final system cost is often the transmitter saturated power, which is intimately linked to the transmitter linearity requirements. This parameter drives the power amplifier (PA) device size, packaging, thermal paths and related cooling methods, power supply, and DC interconnect cable sizes, weight, and safety, each of which can rapidly drive costs upward. The power level analysis may include losses in the cables and antenna, transmitter and receiver antenna gains, link conditions such as distance, rain, ice, snow, trees, buildings, walls, windows, atmospherics, mountains, waves, water towers, and other issues that might be pertinent to the specific application. The receiver capabilities are crucial in determining the transmitter power requirements. Once a system analysis has been completed indicating satisfactory performance, then the actual power amplifier (PA) requirements are known. The key parameters to the PA design are frequency, bandwidth, peak and average output power, duty cycle, linearity, gain, bias voltage and current, dissipated power, and reliability mean time to failure (MTBF, usually given as maximum junction temperature). Other factors may also be important, such as power added efficiency (PAE), return losses, isolations, stability, load variations, cost, size, weight, serviceability, manufacturability, etc.

Linearization

Linearity, as previously indicated, is intimately tied to the transmitter power. The need for high linearity is dependent on the maximum acceptable ACP in adjacent channels or bands. This spillover of power will cause interference in those bands, making it difficult or impossible to use that band. The ACP spillover is due to several factors, such as phase noise, modulation type, filtering, and transmit linearity. The basic methods used for linearization include the class A amplifier in back-off, feedforward, Cartesian and polar loops, adaptive predistortion, envelope elimination and recovery (EER), linear amplification using nonlinear components (LINC), combined analog locked-loop universal modulation (CALLUM), I-V trajectory modification, device tailoring, and Dougherty amplification. Each of these methods strives to improve the system linearity while minimizing the overall cost. The methods may be combined for further improvements. Economical use of the methods may require the development of application-specific integrated circuits (ASICs). As demand increases these specialized ICs should become available as building blocks, greatly reducing learning curves, design time, and cost.

Efficiency

Power added efficiency (η_a or *PAE*) is the dimensionless ratio of RF power delivered from a device to the load (p_{out}) minus the input incident RF power ($p_{incident}$) versus the total DC power dissipated in the device (p_{DC}). It is the most commonly used efficiency rating for amplifiers and accounts for both the switching and power gain capabilities of the overall amplifier being considered. High *PAE* is essential to reducing the overall cost of high power transmitter systems, as previously discussed in the power section

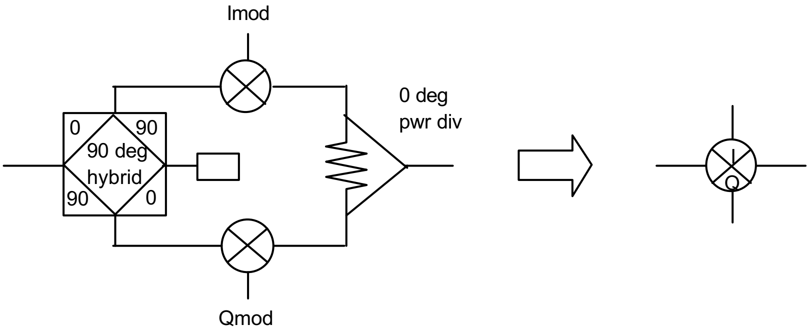

FIGURE 5.12 I-Q modulator block diagram.

above. As with power, *PAE* affects the PA device size, packaging, thermal paths and related cooling methods, power supply, and DC interconnect cable sizes, weight, and safety, each of which can rapidly drive up cost.

$$PAE = \eta_a = \frac{p_{load} - p_{incident}}{p_{DC}}$$

The I-Q Modulator

The I-Q modulator is a basic building block used in numerous applications, and is an essential element of many linearization methods. The basic block diagram is shown in Fig. 5.12, along with the associated symbol that will be used in the following discussions. The modulator consists of two separate mixers that are driven 90° out of phase with each other to generate quadrature (I and Q) signals. The 90° port is usually driven with the high level bias signal, allowing the mixer compression characteristic to minimize amplitude variation from the 90° hybrid. The configuration is reciprocal, allowing either up- or down-conversion.

Class A Amplifier in Back Off

An amplifier is usually required near the output of any transmitter. The linearity of the amplifier is dependent on the saturated power that the amplifier can produce, the amplifier bias and design, and the characteristics of the active device itself. An estimate of the DC power requirements and dissipation for each stage in the PA chain can be made based on the peak or saturated power, duty cycle, and linearity requirements. The maximum or saturated power (P_{sat} in dBW or dBm, depending on whether power is in W or mW) can be estimated (Fig. 5.13) from the product of the RMS voltage and current swings across the RF load, $(V_{sup} - V_{on})/2$ and $I_{on}/2$, and from the loss in the output matching circuits (L_{out} in dB). As previously discussed in the receiver section, the 3OIP is about 6 dB above the saturated power for a square law device, but can vary by as much as 4 dB lower to as much as 10 dB higher for a given actual device. Thus it is very important to determine the actual 3OIP for a given device, using vendor data, simulation, or measurement. One must take into account the effects of transmitter components both prior to and after the PA, utilizing the same analysis technique used for receiver intermodulation. The ACP output intercept point (AOIP) will be closely correlated to the 3OIP, and will act in much the same way, except for the actual value of the AOIP. The delta between the AOIP and 3OIP will be modulation dependent, and must be determined through simulation or measurement at this time. Once this has been determined, it is a relatively easy matter to determine the required back off from P_{sat} for the output amplifier, often as much as 10 to 15 dB. Under these conditions, amplifiers that require a high intercept but in which the required peak power is much lower that the peak power that is available, linearization can be employed to lower the cost.

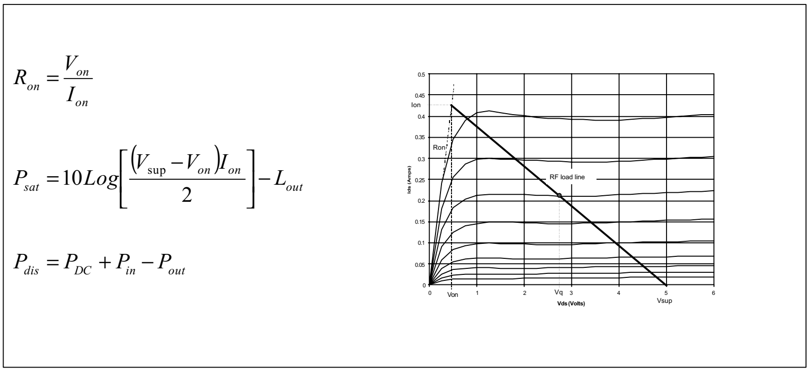

$$R_{on} = \frac{V_{on}}{I_{on}}$$

$$P_{sat} = 10Log\left[\frac{(V_{\sup} - V_{on})I_{on}}{2}\right] - L_{out}$$

$$P_{dis} = P_{DC} + P_{in} - P_{out}$$

FIGURE 5.13 Class A amplifier saturated power estimation.

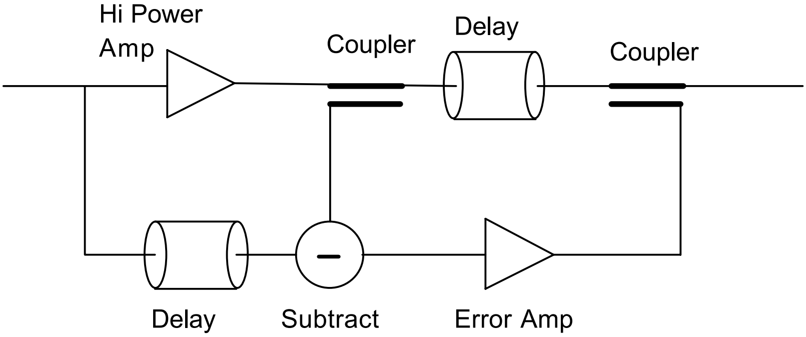

FIGURE 5.14 Feedforward amplifier.

Feed Forward

Although the feedforward amplifier (Fig. 5.14) is a simple concept, it is relatively difficult to implement, especially over temperature and time. The applied signal is amplified to the desired power level by the power amplifier, whose output is sampled. The PA introduces distortion to the system. A portion of the input signal is delayed and then subtracted from the sampled PA signal, nulling out the original signal, leaving only the unwanted distortion created by the PA. This error signal is then adjusted for amplitude and recombined with the distorted signal in the output coupler, canceling out the distortion created by the PA. The resulting linearity improvement is a function of the phase and amplitude balances maintained, especially over temperature and time. The process of generating an error signal will also create nonlinearities, which will limit the ultimate improvements that are attainable, and thus are a critical part of the design.

Cartesian and Polar Loops

The Cartesian loop (CL) (Fig. 5.15) is capable of both good efficiency and high linearity. The efficiency is primarily determined by the amplifier efficiency. The loop action determines the linearity achieved. A carrier signal is generated and applied to the input of the CL, where it is power divided and applied to two separate I-Q mixers. The high power carrier path is quadrature modulated and then amplified by the output PA, after which the distorted modulated signal is sampled by a coupler. The sample distorted signal is then demodulated by mixing it with the original unmodulated carrier, resulting in distorted modulation in quadrature or I-Q form. These distorted I and Q modulations are then subtracted from the original I and Q modulation to generate error I and Q modulation (hence the name Cartesian),

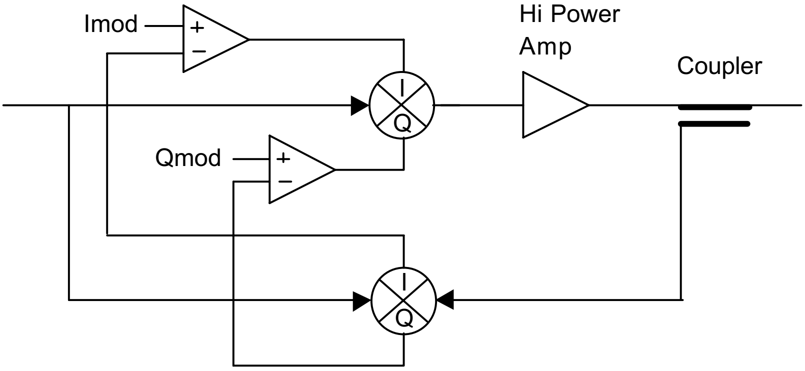

FIGURE 5.15 Cartesian loop.

which will continuously correct the nonlinearity of both the power amplifier and the I-Q modulator. Loop gain and phase relationships are critical to the design, and as with any feedback scheme, care must be taken to prevent loop oscillation. The I-Q modulators and the sampling coupler utilize 90-degree power dividers with limited bandwidth over which satisfactory performance can be attained. The loop delay ultimately will limit the attainable bandwidth to about 10%. Even with these difficulties, the CL is a popular choice. Much of the circuitry is required anyway, and can be easily integrated into ASICs, resulting in low production costs.

Whereas the Cartesian loop depends on quadrature I and Q signals, the related polar loop uses amplitude and phase to achieve higher linearity. The method is much more complex since the modulation correction depends on both frequency modulating the carrier as well as amplitude modulating it. Ultimately the performance will be worse than that of the Cartesian loop, as well as being more costly by a considerable margin. For these reasons, it is not used.

Fixed Predistortion

Fixed predistortion methods are conceptually the simplest form of linearization. A power amplifier will have nonlinearities that distort the original signal. By providing complimentary distortion prior to the PA, the predistorted signal is linearized by the PA. The basic concept can be divided into digital and transfer characteristic methods, both with the same objective. In the digital method (Fig. 5.16), digital signal processing (DSP) is used to provide the required predistortion to the signal. This can be applied at any point in the system, but is usually provided at baseband where it can be cheaply accomplished. The information required for predistortion must be determined and then stored in memory. The DSP then utilizes this information and associated algorithms to predistort the signal, allowing the PA to correct

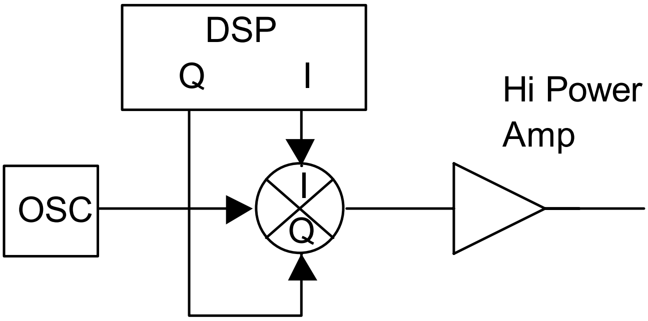

FIGURE 5.16 Fixed digital predistortion.

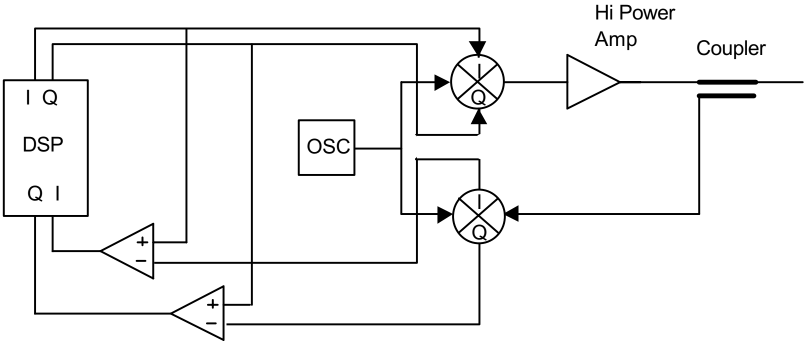

FIGURE 5.17 Adaptive predistortion.

the predistortion, resulting in high linearity. When hardware is used to generate the predistortion, the predistorting transfer characteristic must be determined, and appropriate hardware must be developed. There are no algorithms or methods to accomplish this, so it can be a formidable task. In either case, the improvements in linearity are limited by the lack of any feedback to allow for deviations from the intended operation, and by the ability to actually determine and create the required predistortion. In short, it is cheap, but don't expect dramatic results!

Adaptive Predistortion

Linearization by adaptive predistortion (Fig. 5.17) is very similar to fixed methods, with the introduction of feedback in the form of an error function that can be actively minimized on a continuous basis. The ability to change under operational conditions requires some form of DSP. The error signal is generated in the same way used for Cartesian loop systems, but is then processed by the DSP, allowing the DSP to minimize the error by modifying or adapting the applied predistortion. The disadvantages in this method center on the speed of the DSP and the inability of the system to react due to loop delay. It must see the error before it can correct for it.

Envelope Elimination and Recovery (EER)

The highly efficient envelope elimination and recovery amplifier (Fig. 5.18) accepts a fully modulated signal at its input and power divides the signal. One portion of the signal is amplitude detected and filtered to create the low frequency AM component of the original signal. The other portion of the signal is amplitude limited to strip off or eliminate all of the AM envelope, leaving only the FM component or carrier. Each of these components is then separately amplified using high-efficiency techniques. The amplified AM component is then utilized to control the FM amplifier bias, modulating the amplified FM carrier. Thus the original signal is recovered, only amplified. While this process works very well, an alternative is available that utilizes the DSP capabilities to simplify the whole process, cut costs, and improve performance. In a system, the input half of the EER amplifier can be eliminated and the carrier FM

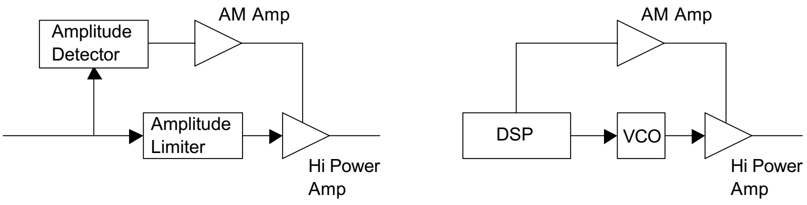

FIGURE 5.18 Envelope elimination and recovery.

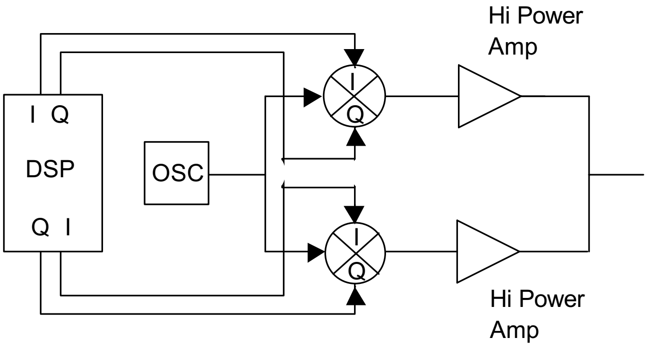

FIGURE 5.19 LINC transmitter.

modulated directly by DSP-generated tuning of a voltage-controlled oscillator (VCO). The DSP-generated AM is amplified and used to control the FM amplifier bias. The result is the desired modulated carrier.

Linear Amplification Using Nonlinear Components (LINC)

The LINC transmitter (Fig. 5.19) concept is quite simple. The DSP creates two separate amplitude and phase-modulated signals, each in quadrature (I-Q) format. These signals are upconverted by I-Q modulators to create two separate phase-modulated signals that are separately applied to high-efficiency output power amplifiers. The amplified FM signals are then combined at the output, the signals being such that all of the unwanted distortion is cancelled by combining 180° out of phase, and all of the desired signal components are added by combining in phase. The challenge in this method is in the DSP generation of the original pair of quadrature signals required for the desired cancellation and combination at the output of the transmitter. Another area of concern with this linearization method is the requirement for amplitude and phase matching of the two channels, which must be tightly controlled in order to achieve optimum performance.

Combined Analog Locked-Loop Universal Modulation (CALLUM)

The CALLUM linearization method is much simpler than it looks at first glance (Fig. 5.20). Basically, the top portion of the transmitter is the LINC transmitter discussed above. An output coupler has been added to allow sampling of the output signal, and the bottom half of the diagram delineates the feedback method that generates the two quadrature pairs of error signals in the same way as used in the Cartesian loop or EER methods. This feedback corrects for channel differences in the basic LINC transmitter, substantially improving performance. Since most of the signal processing is performed at the modulation frequencies, the majority of the circuit is available for ASIC implementation.

I-V Trajectory Modification

In I-V trajectory or cyclic modification, the idea is to create an active I-V characteristic that changes with applied signal level throughout each signal cycle, resulting in improved linear operation (see device tailoring below). A small portion of the signal is tapped off or sampled at the input or output of the amplifier and, based on the continuously sampled signal amplitude, the device bias is continuously modified at each point in the signal cycle. The power range over which high PAE is achieved will be compressed. This method requires a good understanding of the PA device, and excellent modeling. Also, the sampling and bias modification circuitry must be able to react at the same rate or frequencies as the PA itself while providing the required voltage or current to control the PA device. Delay of the sampled signal to the time the bias is modified is critical to obtaining performance. This method is relatively cheap to implement, and can be very effective in improving linearity.

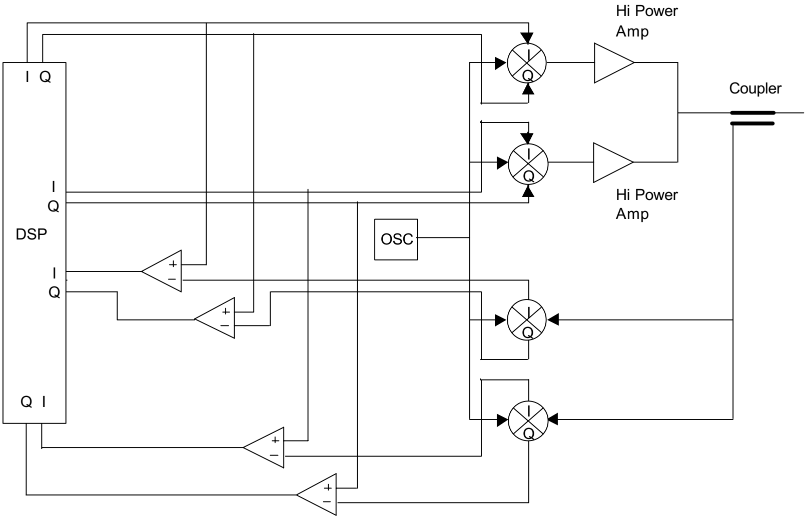

FIGURE 5.20 CALLUM.

Dougherty Amplification

The simplified form of the Dougherty amplifier, which maintains high PAE over a much wider power range than a single amplifier, is shown in Fig. 5.21. In the low power path, a 90° phase shifter is used to compensate for the 90° phase shifter/impedance inverter required in the high power path. The low power amplifier is designed to operate efficiently at a given signal level. The class C high power under low power conditions does not turn on, and thus represents high impedance at the input. The high power 90° phase shifter/impedance inverter provides partial matching for the low power amplifier under these conditions. As the signal level increases, the low power amplifier saturates, the class C high power amplifier turns on, and the power of both amplifiers sum at the output. Under these conditions the high power 90° phase shifter/impedance inverter matches the high power amplifier to the load impedance. Although the modulation bandwidths are not a factor in this technique, the bandwidth is limited by the phase and amplitude transfer characteristics of the 90° elements. This concept can be extended by adding more branches, or by replacing the low power amplifier with a complete Dougherty amplifier in itself.

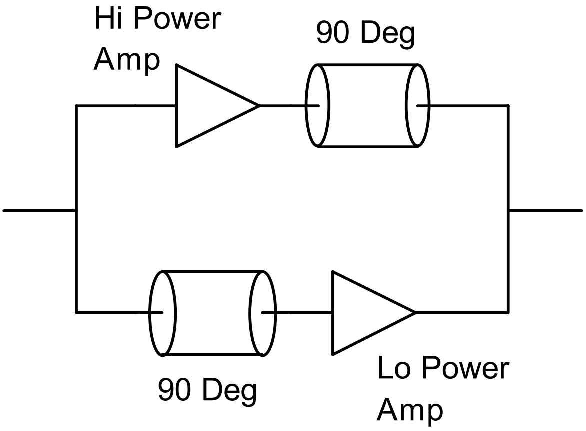

FIGURE 5.21 Dougherty amplifier.

Device Tailoring

For designers with access to a flexible semiconductor foundry service, linearity can be improved directly at the device level. The most obvious way of accomplishing this is by modifying the semiconductor doping to achieve the desired linearity while maintaining other performance parameters. In the ideal device, both the real and reactive device impedance would remain constant and linear (constant derivatives) as the I-V load line or trajectory is traversed for increasing amplitude signals. This linear operation would continue up to the signal amplitude at which both clipping and pinch-off simultaneously occur (ideal biasing). Thus the ideal device would be perfectly linear for any signal below P_{sat}. The objective should be to come as close to this ideal as possible in order to maximize linearity. At best this is a difficult task involving a great deal of device and process engineering. Another strategy might involve trying to minimize the amplitude-dependent parasitic effects such as leakage currents and capacitive or charge-related problems. A third strategy would be to modify the linearity by paralleling two or more devices of varying design together resulting in the desired performance. This is relatively easy to implement through device layout, with best results achieved when this is accomplished at the lowest level of integration (i.e., multiple or tapered gate lengths within a single gate finger, or a stepped or tapered base layer). The results can be quite dramatic with respect to linearity, and best of all the added recurring cost is minimal. As with trajectory modification, the power range for high efficiency operation is compressed.

Summary

The key transmitter parameters of ACP, modulation, linearity, and power are all tightly correlated. These parameters must be determined early in transmitter design so that individual component parameters can be determined and flow-down specifications can be made available to component designers. Linear operation is essential to controlling the power spill-over into adjacent channels (ACP). The basic linearization methods commonly used have been described. These include the class A amplifier in back-off, feedforward, Cartesian and polar loops, adaptive predistortion, envelope elimination and recovery (EER), linear amplification using nonlinear components (LINC), combined analog locked-loop universal modulation (CALLUM), I-V trajectory modification, device tailoring, and Dougherty amplification. Combining methods in such a way as to take advantage of multiple aspects of the nonlinear problem can result in very good performance. An example might be the combination of a Cartesian loop with device tailoring. Unfortunately, it is not yet possible to use simple relationships to calculate ACP directly from linearity requirements, or conversely, required linearity given the ACP. The determination of these requirements is highly dependent on the modulation being used. However, simulators are available that have the capability to design and determine the performance that can be expected.

Further Reading

Casadevall, F., The LINC Transmitter, *RF Design,* Feb. 1990.

Boloorian, M. and McGeeham, J., The Frequency-Hopped Cartesian Feedback Linear Transmitter, *IEEE Transactions on Vehicular Technology,* 45, 4, 1996.

Zavosh, F., Runton, D., and Thron, C., Digital Predistortion Linearizes CDMA LDMOS Amps, *Microwaves & RF,* Mar. 2000.

Kenington, P., Methods Linearize RF Transmitters and Power Amps, Part 1, *Microwaves & RF,* Dec. 1998.

Kenington, P., Methods Linearize RF Transmitters and Power Amps, Part 2, *Microwaves & RF,* Jan. 1999.

Correlation Between P1db and ACP in TDMA Power Amplifiers, *Applied Microwave & Wireless,* Mar. 1999.

Bateman, A., Haines, D., and Wilkinson, R., Linear Transceiver Architectures, Communications Research Group, University of Bristol, England.

Sundstrom, L. and Faulkner, M., Quantization Analysis and Design of a Digital Predistortion Linearizer for RF Power Amplifiers, *IEEE Transactions on Vehicular Technology,* 45, 4, 1996.

5.3 Low Noise Amplifier Design

Jakub Kucera and Urs Lott

Signal amplification is a fundamental function in all wireless communication systems. Amplifiers in the receiving chain that are closest to the antenna receive a weak electric signal. Simultaneously, strong interfering signals may be present. Hence, these low noise amplifiers mainly determine the system noise figure and intermodulation behavior of the overall receiver. The common goals are therefore to minimize the system noise figure, provide enough gain with sufficient linearity, and assure a stable 50 Ω input impedance at a low power consumption.

Definitions

This section introduces some important definitions used in the design theory of linear RF and microwave amplifiers. Further, it develops some basic principles used in the analysis and design of such amplifiers.

Gain Definitions

Several gain definitions are used in the literature for high-frequency amplifier designs.

The transducer gain G_T is defined as the ratio between the effectively delivered power to the load and the power available from the source. The reflection coefficients are shown in Fig. 5.22.

$$G_T = \frac{1-\left|\Gamma_S\right|^2}{\left|1-\Gamma_S \cdot S_{11}\right|^2} \cdot \left|S_{21}\right|^2 \cdot \frac{1-\left|\Gamma_L\right|^2}{\left|1-\Gamma_L \cdot \Gamma_{OUT}\right|^2}$$

The available gain G_{AV} of a two-port is defined as the ratio of the power available from the output of the two-port and the power available from the source.

$$G_{AV} = \frac{1-\left|\Gamma_S\right|^2}{\left|1-\Gamma_S \cdot S_{11}\right|^2} \cdot \left|S_{21}\right|^2 \cdot \frac{1}{\left|1-\Gamma_{OUT}\right|^2} \quad \text{with } \Gamma_{OUT} = S_{22} + \frac{S_{12} \cdot S_{21} \cdot \Gamma_S}{1-\Gamma_S \cdot S_{11}}$$

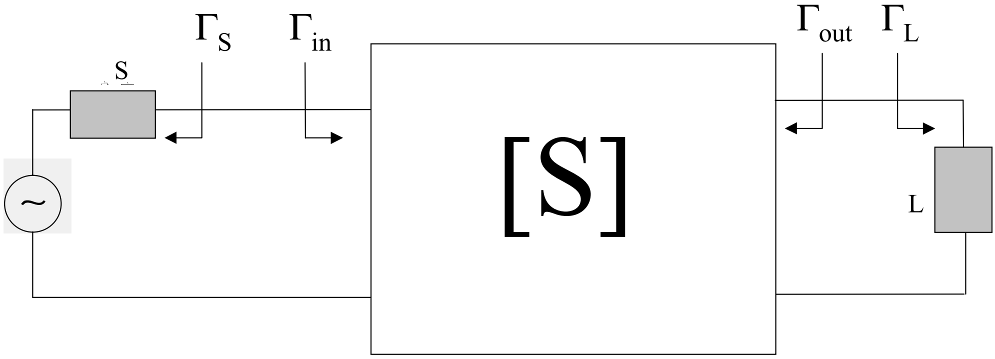

FIGURE 5.22 Amplifier block diagram. Z_S: source impedance, Z_L: load impedance, Γ_S: source reflection coefficient, Γ_{in}: input reflection coefficient, Γ_{out}: output reflection coefficient, Γ_L: load reflection coefficient.

The entire available power at one port can be transferred to the load, if the output is terminated with the complex conjugate load.

The available gain G_{AV} is a function of the two-port scattering parameters and of the source reflection coefficient, but independent of the load reflection coefficient Γ_L. The available gain gives a measure for the maximum gain into a conjugately matched load at a given source admittance.

The associated gain G_{ASS} is defined as the available gain under noise matching conditions.

$$G_{ASS} = \frac{1 - \left|\Gamma_{opt}\right|^2}{\left|1 - \Gamma_{opt} \cdot S_{11}\right|^2} \cdot \left|S_{21}\right|^2 \cdot \frac{1 - \left|\Gamma_L\right|^2}{\left|1 - \Gamma_L \cdot \Gamma_{OUT}\right|^2}$$

Stability and Stability Circles

The stability of an amplifier is a very important consideration in the amplifier design and can be determined from the scattering parameters of the active device, the matching circuits, and the load terminations (see Fig. 5.22). Two stability conditions can be distinguished: unconditional and conditional stability.

Unconditional stability of a two-port means that the two-port remains stable (i.e., does not start to oscillate) for any passive load at the ports. In terms of the reflection coefficients, the conditions for unconditional stability at a given frequency are given by the following equations

$$\left|\Gamma_{IN}\right| = \left|S_{11} + \frac{S_{12} \cdot S_{21} \cdot \Gamma_L}{1 - \Gamma_L \cdot S_{22}}\right| < 1$$

$$\left|\Gamma_{OUT}\right| = \left|S_{22} + \frac{S_{12} \cdot S_{21} \cdot \Gamma_S}{1 - \Gamma_S \cdot S_{11}}\right| < 1$$

$$\left|\Gamma_S\right| < 1 \text{ and } \left|\Gamma_L\right| < 1$$

In terms of the scattering parameters of the two-port, unconditional stability is given, when

$$K = \frac{1 - \left|S_{11}\right|^2 - \left|S_{22}\right|^2 + \left|\Delta\right|^2}{2\left|S_{12} \cdot S_{21}\right|} > 1$$

and

$$\left|\Delta\right| < 1$$

with $\Delta = S_{11} \cdot S_{22} - S_{12} \cdot S_{21}$. K is called the stability factor.[1]

If either $|S_{11}| > 1$ or $|S_{22}| > 1$, the network cannot be unconditionally stable because the termination $\Gamma_L = 0$ or $\Gamma_S = 0$ will produce or $|\Gamma_{IN}| > 1$ or $|\Gamma_{OUT}| > 1$.

The maximum transducer gain is obtained under simultaneous conjugate match conditions $\Gamma_{IN} = \Gamma_S^*$ and $\Gamma_{OUT} = \Gamma_L^*$. Using

$$\Gamma_{IN} = S_{11} + \frac{S_{12} \cdot S_{21} \cdot \Gamma_L}{1 - \Gamma_L \cdot S_{22}} \text{ and } \Gamma_{OUT} = S_{22} + \frac{S_{12} \cdot S_{21} \cdot \Gamma_S}{1 - \Gamma_S \cdot S_{11}}$$

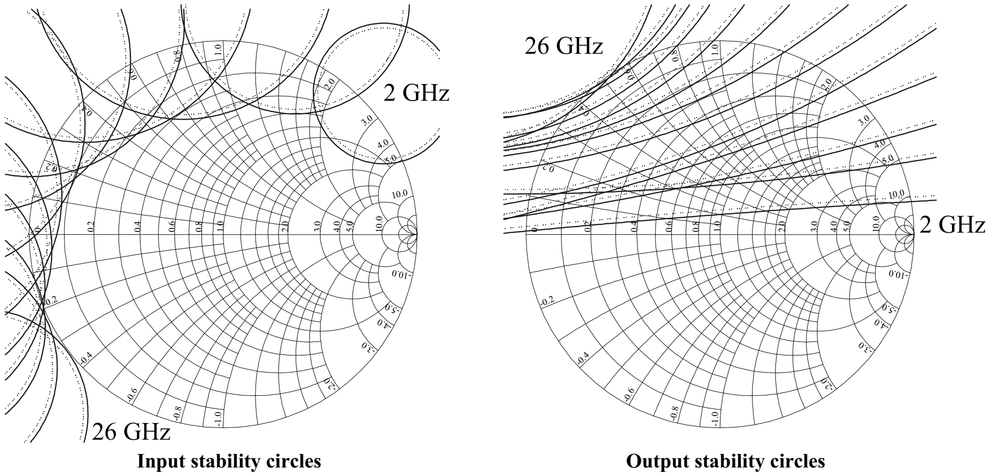

Input stability circles

Output stability circles

FIGURE 5.23 Source (input) and load (output) stability circles in the Smith chart for the MESFET NE710 over the frequency range from 2 to 26 GHz. Unstable region is indicated by the dotted line.

a closed-form solution for the source and load reflection coefficients Γ_S and Γ_L can be found. However, a simultaneous conjugate match having unconditional stability is not always possible if $K < 1$[2].

Conditional stability of a two-port means that for certain passive loads (represented as $\Gamma_L < 1$ or $\Gamma_S < 1$) oscillation may occur. These values of Γ_L and Γ_S can be determined by drawing the stability circles in a Smith chart. The source and load stability circles are defined as

$$\left|\Gamma_{IN}\right| = 1 \text{ and } \left|\Gamma_{OUT}\right| = 1$$

On one side of the stability circle boundary, in the Γ_L plane, $|\Gamma_{IN}| > 1$ and on the other side $|\Gamma_{IN}| < 1$. Similarly, in the Γ_S plane, $|\Gamma_{OUT}| > 1$ and on the other side $|\Gamma_{OUT}| < 1$. The center of the Smith chart ($\Gamma_L = 0$) represents a stable operating point, if $|S_{11}| < 1$, and an unstable operating point, if $|S_{11}| > 1$ (see Fig. 5.23). Based on these observations, the source and load reflection coefficient region for stable operation can be determined.

With unconditional stability, a complex conjugate match of the two-port is possible. The resulting gain then is called the maximum available gain (MAG) and is expressed as

$$MAG = \left|\frac{S_{21}}{S_{12}}\right| \cdot \left(K - \sqrt{K^2 - 1}\right)$$

The maximum stable gain MSG is defined as the maximum transducer gain for which $K = 1$ holds, namely

$$MSG = \left|\frac{S_{21}}{S_{12}}\right|$$

MSG is often used as a figure of merit for potentially unstable devices (see Fig. 5.24).

It must be mentioned, however, that the stability analysis as presented here in its classical form, is applicable only to a single-stage amplifier. In a multistage environment, the above stability conditions are insufficient, because the input or output planes of an intermediate stage may be terminated with active networks. Thus, taking a multistage amplifier as a single two-port and analyzing its K-factor is helpful, but does not guarantee overall stability. Literature on multistage stability analysis is available.[3]

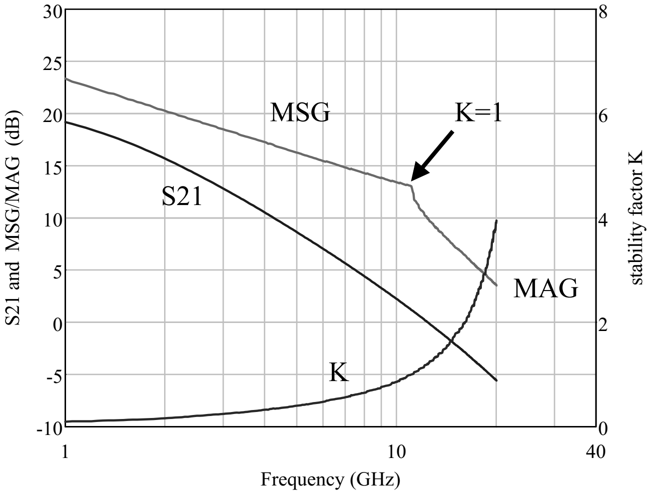

FIGURE 5.24 Maximum stable gain (MSG), maximum available gain (MAG), S_{21}, and stability factor K for a typical MESFET device with 0.6 μm gate length.

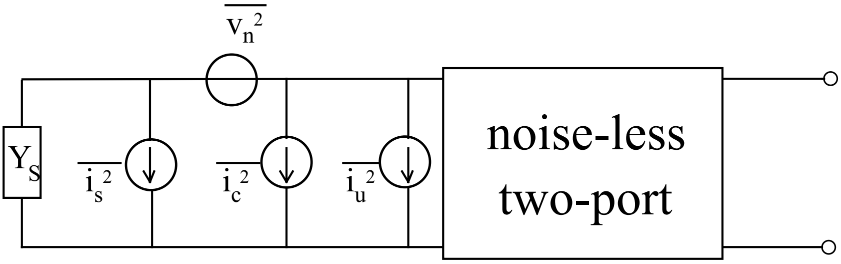

FIGURE 5.25 Representation of noisy two-port as noiseless two-port and two partly correlated noise sources (v_n and $i_c + i_u$) at the input.

Representation of Noise in Two-Ports

The LNA can be represented as a noise-free two-port and two partly correlated input noise sources i_n and v_n as shown in Fig. 5.25. The partial correlation between the noise sources i_n and v_n can be described by splitting i_n into a fully correlated part i_c and a noncorrelated part i_u as

$$i_n = i_c + i_u$$

The fully correlated part i_c is defined by the correlation admittance[4] Y_{cor}

$$i_c = Y_{cor} v_n$$

The source impedance $Z_s = R_s + jB_s$ shows thermal noise i_s which depends on the bandwidth as

$$\overline{i_s^2} = 4kTG_s\Delta f$$

Finally, the noise factor F can be expressed in terms of these equivalent input noise generators as

$$F = 1 + \left|Y_s + Y_{cor}\right|^2 \frac{\overline{v_n^2}}{\overline{i_s^2}} + \frac{\overline{i_u^2}}{\overline{i_s^2}}$$

Details on the use of the correlation matrix and the derivation of the noise factor from the noise sources of the two-port can be found in References 4 and 5.

Noise Parameters

The noise factor *F* of a noisy two-port is defined as the ratio between the available signal-to-noise power ratio at the input to the available signal-to-noise ratio at the output.

$$F = \frac{S_{in}}{N_{in}} \bigg/ \frac{S_{out}}{N_{out}}$$

The noise factor of the two-port can also be expressed in terms of the source admittance $Y_s = G_s + jB_s$ as

$$F = F_{min} + \frac{R_n}{G_s}\left|Y_s - Y_{opt}\right|^2$$

where F_{min} is the minimum achievable noise factor when the optimum source admittance $Y_{opt} = G_{opt} + jB_{opt}$ is presented to the input of the two-port, and R_n is the equivalent noise resistance of the two-port. Sometimes the values Y_s, Y_{opt}, and R_n are given relative to the reference admittance Y_0.

The noise performance of a two-port is fully characterized at a given frequency by the four noise parameters F_{min}, R_n, and real and imaginary parts of Y_{opt}.

Several other equivalent forms of the above equation exist, one of them describing *F* as a function of the source reflection coefficient Γ_s.

$$F = F_{min} + \frac{4R_n}{Z_0} \frac{\left|\Gamma_s - \Gamma_{opt}\right|^2}{\left|1 + \Gamma_{opt}\right|^2 \cdot \left(1 - \left|\Gamma_s\right|^2\right)}$$

When measuring noise, the noise factor is often represented in its logarithmic form as the noise figure *NF*

$$NF = 10 \log F$$

Care must be taken not to mix up the linear noise factor and the logarithmic noise figure in noise calculations.

Noise Circles

Noise circles refer to the contours of constant noise figure for a two-port when plotted in the complex plane of the input admittance of the two-port. The minimum noise figure is presented by a dot, while for any given noise figure higher than the minimum, a circle can be drawn. This procedure is adaptable in the source admittance notation as well as in the source reflection coefficient notation. Fig. 5.26 shows the noise circles in the source reflection plane.

Noise circles in combination with gain circles are efficient aids for circuit designers when optimizing the overall amplifier circuit network for low noise with high associated gain.

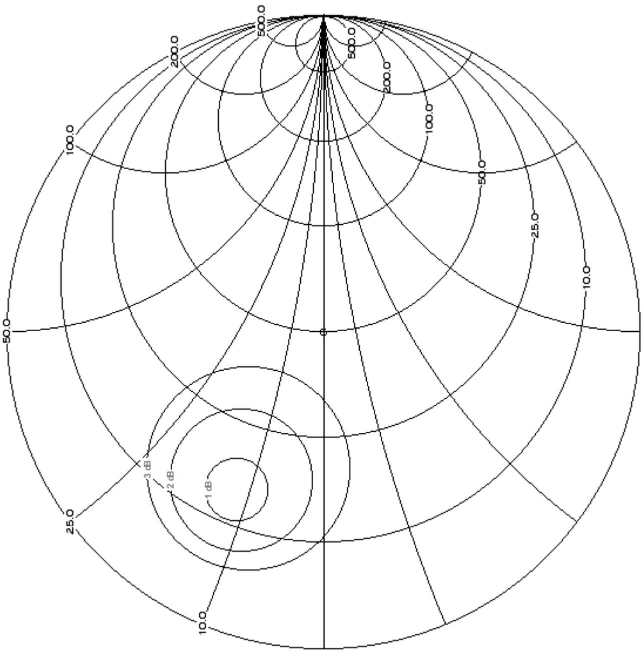

FIGURE 5.26 Noise circles in the input reflection coefficient plane.

Friis Formula: Cascading Noisy Two-Ports

When several noisy two-ports are connected in cascade, the overall noise characteristics are described by[6]

$$F_{tot} = F_1 + \frac{F_2 - 1}{G_1} + \frac{F_3 - 1}{G_1 \cdot G_2} + \ldots + \frac{F_i - 1}{G_1 \cdot G_2 \ldots \cdot G_{i-1}}$$

where F_i and G_i are noise factor and available gain of the ith two-port. The available gain depends on the output admittance of the previous stage.

Noise Measure *M*

The overall noise factor of an infinite number of identical cascaded amplifiers is $F = 1 + M$ with

$$M = \frac{F - 1}{1 - \frac{1}{G}}$$

M is here called the noise measure. The noise measure is useful for comparing the noise performance of devices or LNAs with different power gains.

Design Theory

The apparent structural simplicity of an LNA with its relatively few components is misleading. The design should be easy, but the trade-offs complicate the design. A simultaneous noise and power matching involves a more complicated matching network and the achievable dynamic range is often limited by the given low supply voltage and the maximum allowed current consumption. The LNA must provide enough gain so that the noise contributions from the following components become small. But the maximum tolerable gain is limited by the linearity requirements of the following receiver chain.

The most important design considerations in a high-frequency amplifier are stability, power gain, bandwidth, noise, and DC power consumption requirements.

A systematic mathematical solution, aided by graphical methods, is developed to determine the input and output matching network for a particular noise, gain, stability, and gain criteria. Unconditionally stable designs will not oscillate with any passive termination, while designs with conditional stability require careful analysis of the loading to assure stable operation.

Linear Design Procedure for Single-Stage Amplifiers

1. *Selection of device and circuit topology:* Select the appropriate device based on required gain and noise figure. Also decide on the circuit topology (common-base/gate or common-emitter/source). The most popular circuit topology in the first stage of the LNA is the common-emitter (source) configuration. It is preferred over a common-base (-gate) stage because of its higher power gain and lower noise figure. The common-base (-gate) configuration is a wideband unity-current amplifier with low input impedance ($\approx 1/g_m$) and high predominantly capacitive output impedance. Wideband LNAs requiring good input matching use common-base input stages. At high frequencies the input impedance becomes inductive and can be easily matched.
2. *Sizing and operating point of the active device:* Select a low noise DC operating point and determine scattering and noise parameters of the device. Typically, larger input transistors biased at low current densities are used in low noise designs. At RF frequencies and at a given bias current, unipolar devices such as MOSFET, MESFET, and HEMT are easier to match to 50 Ω when the device width is larger. Both, (hetero-) BJTs and FETs show their lowest intrinsic noise figure when biased at approximately one tenth of the specified maximum current density. Further decreasing the current density will increase the noise figure and reduce the available gain.
3. *Stability and RF feedback:* Evaluate stability of the transistor. If only conditionally stable, either introduce negative feedback (high-resistive DC parallel or inductive series feedback) or draw stability circles to determine loads with stable operation.
4. *Select the source and load impedance:* Based on the available power gain and noise figure circles in the Smith chart, select the load reflection coefficient Γ_L that provides maximum gain, the lowest noise figure (with $\Gamma_S = \Gamma_{opt}$), and good VSWR. In unconditionally stable designs, Γ_L is

$$\Gamma_L = \left(S_{22} + \frac{S_{12} \cdot S_{21} \cdot \Gamma_{opt}}{1 - \Gamma_{opt} \cdot S_{11}} \right)^*$$

   In conditionally stable designs, the optimum reflection coefficient Γ_S may fall into an unstable region in the source reflection coefficient plane. Once Γ_S is selected, Γ_L is selected for the maximum gain $\Gamma_L = \Gamma_{OUT}$, and Γ_L must again be checked to be in the stable region of the load reflection coefficient plane.
5. *Determine the matching circuit:* Based on the required source and load reflection coefficients, the required ideal matching network can be determined. Depending on the center frequency, lumped elements or transmission lines will be applied. In general, there are several different matching circuits available. Based on considerations about insertion loss, simplicity, and reproducibility of each matching circuit, the best selection can be made.
6. *Design the DC bias network:* A suitable DC bias network is crucial for an LNA, which should operate over a wide temperature and supply voltage range and compensate parameter variations of the active device. Further, care must be given that no excessive additional high-frequency noise is injected from the bias network into the signal path, which would degrade the noise figure of the amplifier. High-frequency characteristics including gain, noise figure, and impedance matching are correlated to the device's quiescent current. A resistor bias network is generally avoided because of its poor supply rejection. Active bias networks are capable of compensating temperature effects and rejecting supply voltage variations and are therefore preferred.

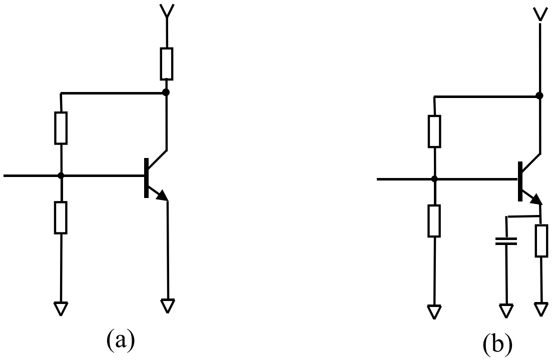

FIGURE 5.27 Passive bias network for bipolar amplifiers.

For bipolar circuits, a simple grounded emitter DC bias network is shown in Fig. 5.27a. The high-resistive bias network uses series feedback to stabilize the current of the active device against device parameter variations. However, the supply rejection of this network is very poor, which limits its applicability. A bypassed emitter resistor is often used at low frequencies to stabilize the DC bias point (Fig. 5.27b). At RF and microwave frequencies, the bypass capacitor can cause unwanted high-frequency instability and must be applied with care. Furthermore, an emitter resistor will degrade the noise figure performance of the amplifier, if the resistor is not fully bypassed at the signal frequency.

More advanced active bias circuits use (temperature compensated) bandgap references and generate a reference current, which is mirrored to the amplifying device through a high value resistor or an RF choke to minimize noise injection. Another popular method is to generate a proportional to absolute temperature (PTAT) current source. The amplifier gain is proportional to the transconductance which itself is proportional to the collector current and inversely proportional to the temperature ($g_m = qI_c/kT$). With the transistor biased with a current proportional to temperature, the gain remains roughly constant over temperature. Combining bandgap circuits with PTAT sources leads to excellent supply and temperature variation suppression.[7]

The implementation of appropriate bias methods for FET amplifiers is generally more involved. The most critical parameter affecting the bias point is the threshold voltage. Stable voltage reference and PTAT current sources are typically based on the Schottky diode barrier height and involve rather sophisticated circuitry.[8]

7. *Optimize entire circuit with lossy matching elements:* The final design optimization of the LNA circuit must include the nonidealities of the matching elements, parasitic components such as bond wire inductance, as well as fabrication tolerance aspects. This last design phase today is usually performed on a computer-aided design (CAD) system.

   The dominant features of an LNA (gain, noise, matching properties) can be simulated with excellent accuracy on a linear CAD tool. The active device is characterized by its scattering parameters in the selected bias point, and the four noise parameters. The passive components are described by empirical or equivalent circuit models built into the linear simulation tool. If good models for elements like millimeter-wave transmission lines are not available, these elements must be described by their measured scattering parameters, too.

   Alternatively, a nonlinear simulator with a full nonlinear device model allows direct performance analysis over varying bias points. The use of nonlinear CAD is mandatory for compression and intermodulation analysis.

   Advanced CAD tools allow for direct numerical optimization of the circuit elements toward user-specified performance goals. However, these optimizers should be used carefully, because it can be very difficult to transform the conflicting design specifications into optimization goals. In many cases, an experienced designer can optimize an LNA faster by using the "tune" tools of a CAD package.

Practical Design of a Low Noise Amplifier

The last section presented a design procedure to design a stable low noise amplifier based on linear design techniques. In practice, there are nonidealities and constraints on component sizing that typically degrade the amplifier performance and complicate the design. In fact, the presented linear design method does not take power consumption versus linearity explicitly into account. Some guidelines are provided in this section that may facilitate the design.

Hybrid vs. Monolithic Integrated LNA

With the current trend to miniaturized wireless devices, LNAs are often fabricated as monolithic integrated circuits, usually referred to as MMIC (monolithic microwave integrated circuit). High volume applications such as cell phones call for even higher integration in the RF front end. Thus the LNA is integrated together with the mixer, local oscillator, and sometimes even parts of the transmitter or the antenna.[9]

Depending on the IC technology, monolithic integration places several additional constraints on the LNA design. The available range of component values may be limited, in particular the maximum inductance and capacitance values are often smaller than required. Integrated passive components in general have lower quality factors Q because of their small size. In some cases, the first inductor of the matching circuit must be realized as an external component.

The electromagnetic and galvanic coupling between adjacent stages is often high due to the close proximity of the components. Furthermore, the lossy and conducting substrate used in many silicon-based technologies increases coupling. At frequencies below about 10 GHz, transmission lines cannot be used for matching because the required chip area would make the IC too expensive, at least for commercial applications.

Finally, monolithic circuits cannot be tuned in production. On the other hand, monolithic integration also has its advantages. The placement of the components is well controlled and repeatable, and the wiring length between components is short. The number of active devices is almost unlimited and adds very little to the cost of the LNA. Each active device can be sized individually.

For applications with low volume where monolithic integration is not cost effective, LNAs can be built as hybrid circuits, sometimes called MIC (microwave integrated circuit). A packaged transistor is mounted on a ceramic or organic substrates. The matching circuit is realized with transmission lines or lumped elements. Substrates such as alumina allow very high quality transmission line structures to be fabricated. Therefore, in LNAs requiring ultimate performance, e.g., for satellite ground stations, hybrid circuit technology is sometimes used even if monolithic circuits are available.

Multistage Designs

Sometimes a single amplifier stage cannot provide the required gain and multiple gain stages must be provided. Multiple gain stages complicate the design considerably. In particular, the interstage matching must be designed carefully (in particular in narrowband designs) to minimize frequency shifts and ensure stability. The ground lines of the different gain stages must often be isolated from each other to avoid positive feedback, which may cause parasitic oscillations. Moreover, some gain stages may need some resistive feedback to enhance stability.

Probably the most widely used multistage topology is the cascode configuration. A low noise amplifier design that uses a bipolar cascode arrangement as shown in Fig. 5.28 offers performance advantages in wireless applications over other configurations. It consists of a common-emitter stage driving a common-base stage. The cascode derives its excellent high-frequency properties from the fact that the collector load of the common-emitter stage is the very low input impedance of the common-base stage. Consequently, the Miller effect is minimal even for higher load impedances and an excellent reverse isolation is achieved. The cascode has high output impedance, which may become difficult to match to 50 Ω. A careful layout of the cascode amplifier is required to avoid instabilities. They mainly arise from parasitic inductive feedback between the emitter of the lower and the base of the upper transistor. Separating the two ground lines will enhance the high-frequency stability considerably.

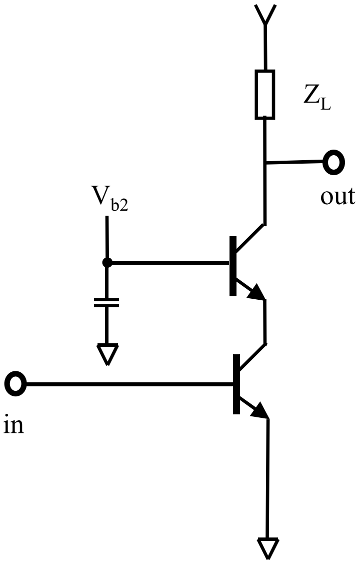

FIGURE 5.28 Cascode amplifier.

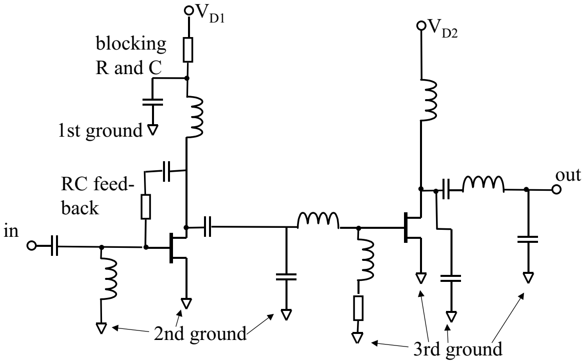

FIGURE 5.29 Design for stability.

Stability Considerations

Figure 5.29 shows a possible strategy for a stable design of a two-stage amplifier. Separated ground and supply lines of the two gain stages minimize positive feedback. RC parallel feedback further enhances in-band stability. Low frequency oscillations caused through unstable bias lines can be attenuated by adding small resistors and blocking capacitors into the supply line.

Feedback

Negative feedback is widely used in amplifier design to stabilize gain against parameter changes in the active device due to supply voltage variations and temperature changes. RF feedback is used in many LNAs to ensure high-frequency stability and make noise and power match coincident. A well-known technique is adding inductance at the emitter (source) of the active device. The inductance L interacts with the base-emitter (gate-source) capacitance C_{IN} and device transconductance g_m to produce a resistive component to the input impedance $g_m \frac{L}{C_{IN}}$, while no additional noise source is introduced (except for the parasitic series resistance of the inductor). Neglecting the Miller capacitance, the input impedance of an inductively degenerated FET stage is

$$Z_{IN} = \frac{1}{j\omega C_{IN}} + j\omega L + g_m \frac{L}{C_{IN}}$$

This method of generating a real term to the input impedance is preferable to resistive methods as only negligible additional noise is introduced. Moreover, the inductance has the helpful side effect of shifting the optimum noise match closer to the complex conjugate power match and reducing the signal distortion. However, the benefits are accompanied by a gain reduction.

Impedance Matching

Following the design procedure in the last section, the conditions for a conjugate match at the input and output ports are satisfied at one frequency. Hence, reactive matching inherently leads to a narrowband design. The input bandwidth is given by

$$BW = \frac{f_0}{Q_{IN}}$$

where f_0 is the center frequency and Q_{IN} is the quality factor of the input matching network. The bandwidth can be increased by increasing the capacitance or decreasing the inductance of the matching network.

Using multistage impedance transformators (lumped element filters or tapers) can broaden the bandwidth, but there is a given limit for the reflection coefficient-bandwidth product using reactive elements.[10] In reality, each matching element will contribute some losses, which directly add to the noise figure.

Select an appropriate matching network based on physical size and quality factor (transmission line length, inductance value): long and high-impedance transmission lines show higher insertion loss. Thus, simple matching typically leads to a lower noise figure.

At higher microwave and millimeter-wave frequencies, balanced amplifiers are sometimes used to provide an appropriate noise and power match over a large bandwidth.

Temperature Effects

Typically, LNAs must operate over a wide temperature range. As transistor transconductance is inversely proportional to the absolute temperature, the gain and amplifier stability may change considerably. When designing LNAs with S-parameters at room temperature, a stability margin should be included to avoid unwanted oscillations at low temperatures, as the stability tends to decrease.

Parasitics

Parasitic capacitance, resistance, or inductance can lead to unwanted frequency shifts, instabilities, or degradation in noise figure and gain and rarely can be neglected. Hence, accurate worst-case simulations with the determined parasitics must be made. Depending on the frequency, the parasitics can be estimated based on simple analytical formulas, or must be determined using suitable electromagnetic field-simulators.

Design Examples

In this section a few design examples of recently implemented low noise amplifiers for frequencies up to 5.8 GHz are presented. They all were manufactured in commercial IC processes.

A Fully Integrated Low Voltage, Low Power LNA at 1.9 GHz[11]

Lowest noise figure can only be achieved when minimizing the number of components contributing to the noise while simultaneously maximizing the gain of the first amplifier stage. Any resistive matching and loading will degrade the noise figure and dynamic behavior and increase power consumption.

In GaAs MESFET processes, the semi-insulating substrate and thick metallization layers allow passive matching components such as spiral inductors and metal-insulator-metal (MIM) capacitors with high

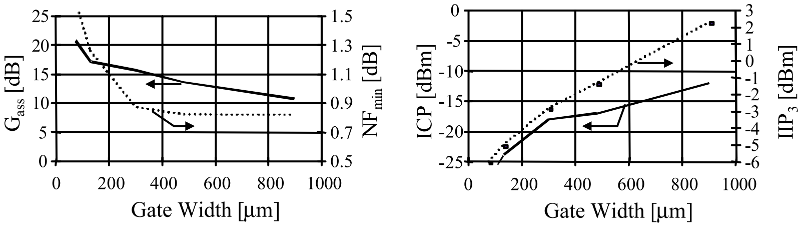

FIGURE 5.30 Simulated performance of an enhancement FET versus device width at a constant power dissipation.

quality factors. These lumped passive components are ideally suited for integrated impedance matching at low GHz frequencies. A fully integrated matching network improves the reproducibility and saves board space while it increases expensive chip area.

It is generally known that GaAs MESFETs have excellent minimum noise figures in the lower GHz frequency range. Still few designs achieve noise figures close to the transistor F_{min}. In fact, several factors prevent F_{min} being attained in practice. If a small input device is employed, a large input impedance transformation involving large inductance values is required. Larger MMIC inductors have higher series resistance and consequently introduce more noise. Further a simultaneous noise and power match often needs additional inductive source degeneration, again introducing noise and reducing gain. For a given maximum power dissipation, very large devices, in contrast, must be biased at very low current densities at which the F_{min} and the gain are degraded. Consequently a trade-off must be made for an optimum design.

The employed GaAs technology features three types of active devices: an enhancement and two depletion MESFETs with different threshold voltages. The enhancement device has a higher maximum available gain, a slightly lower minimum noise figure, but somewhat higher distortion compared to the depletion type. Another advantage of the enhancement FET is that a positive gate bias voltage can be used, which greatly simplifies single-supply operation.

Preliminary simulations are performed using a linear simulator based on measured S- and noise parameters of measured active devices at various bias points and using a scalable large signal model within a harmonic balance simulator in order to investigate the influence of the transistor gate width on the RF performance. The current consumption of the transistor is set at 5.5 mA independent of the gate width. The simulations indicate a good compromise between gain, NF, and intermodulation performance at a gate width of 300 µm (Fig. 5.30).

The LNA schematic is shown in Fig. 5.31. The amplifier consists of a single common-source stage, which uses a weak inductive degeneration at the source (the approximately 0.3 nH are realized with several parallel bondwires to ground). The designed amplifier IC is fabricated in a standard 0.6 µm E/D MESFET foundry process. The matching is done on chip using spiral inductors and MIM capacitors. The complete LNA achieves a measured 50 Ω noise figure of 1.1 dB at 1.9 GHz with an associated gain of 16 dB at a very low supply voltage of $V_{dd} = 1\ V$ and a total current drain of $I_{dd} = 6$ mA. Fig. 5.32 depicts the measured gain and 50 Ω noise figure versus frequency.

The low voltage design with acceptable distortion performance and reasonable power gain can only be achieved using a reactive load with almost no voltage drop.

Figure 5.33 shows, respectively, the supply voltage and supply current dependence of the gain and noise figure. As can be seen, the amplifier still achieves 10 dB gain and a 1.35 dB noise figure at a supply voltage of only 0.3 V and a total current consumption of 2.3 mA. Sweeping the supply voltage from 1 to 5 volts, the gain varies less than 0.5 dB and the noise figure less than 0.15 dB, respectively. IIP_3 and –1 dB compression point are also insensitive to supply voltage variations as shown in Fig. 5.34.

Below 1 V, however, the active device enters the linear region resulting in a much higher distortion.

Finally, the input and output matchings are measured for the LNA. At the nominal 1 V supply, the input and output return loss are –8 dB and –7 dB, respectively.

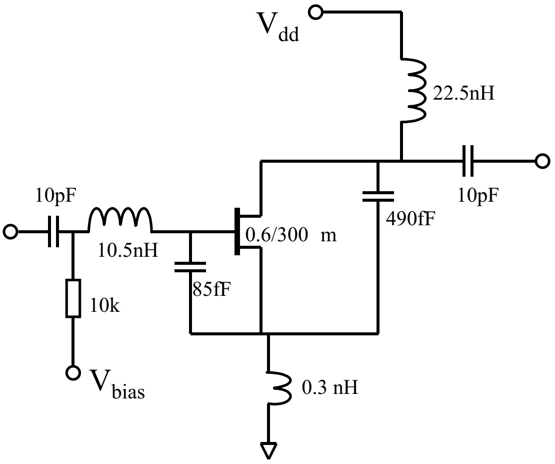

FIGURE 5.31 Schematic diagram of the low voltage GaAs MESFET LNA.

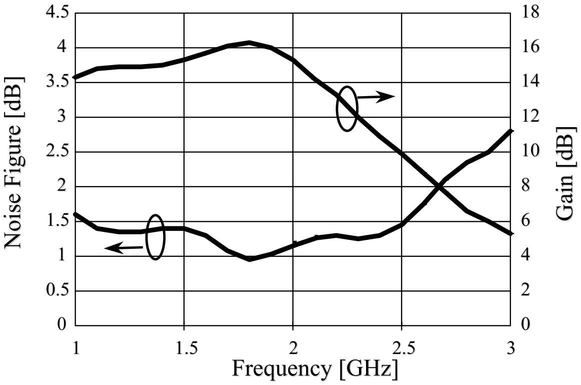

FIGURE 5.32 Measured gain and 50 Ω noise figure vs. frequency.

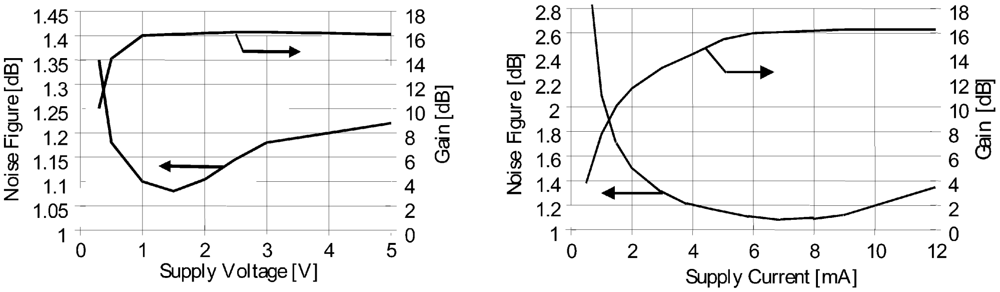

FIGURE 5.33 Measured gain and noise figure vs. supply voltage (I_{dd} = 6 mA) and vs. supply current (V_{dd} = 1 V).

A Fully Matched 800 MHz to 5.2 GHz LNA in SiGe HBT Technology

Bipolar technology is particularly well suited for broadband amplifiers because BJTs typically show low input impedances in the vicinity of 50 Ω and hence can be easily matched. A simplified schematic diagram of the monolithic amplifier is shown in Fig. 5.35. For the active devices of the cascode LNA large emitter

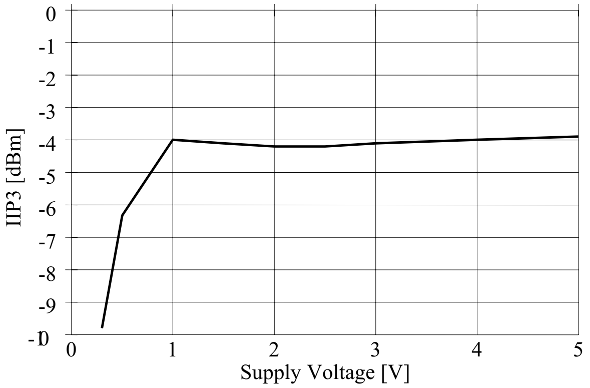

FIGURE 5.34 Measured input IP3 vs. supply voltage.

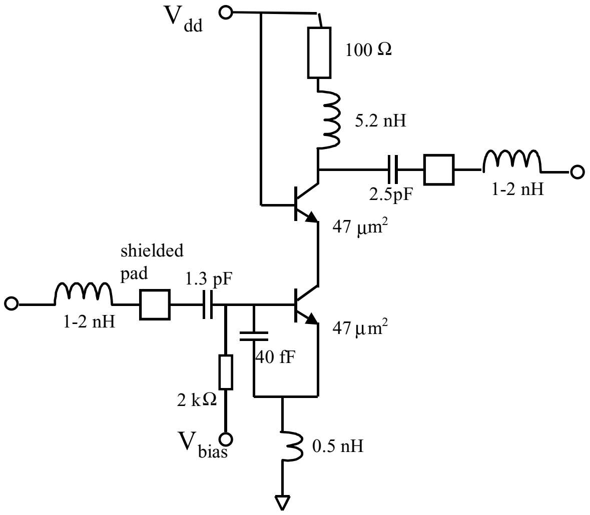

FIGURE 5.35 Schematic diagram of the SiGe HBT LNA.

areas (47 μm^2), biased at low current densities are employed to simplify the simultaneous noise and power match. Input and output matching is consequently obtained simply by the aid of the bondwire inductance at the input and output ports and the chip ground.

The LNA was fabricated with MAXIM's GST-3 SiGe process and subsequently was mounted on a ceramic test package for testing. No additional external components are required for this single-supply LNA.

Figure 5.36 shows the 50 Ω noise figure and associated gain over the frequency range of interest. A relatively flat gain curve is measured from 500 MHz up to 3 GHz. Beyond 3 GHz the gain starts to roll off. The circuit features 14.5 dB of gain along with a 2 dB noise figure at 2 GHz. At 5.2 GHz, the gain is still 10 dB and the noise figure is below 4 dB. The input return loss is less than –10 dB between 2.5 and 6.5 GHz. At 1 GHz it increases to –6 dB.

The distortion performance of the amplifier was measured at the nominal 3 V supply for two frequencies, 2.0 and 5.2 GHz, respectively. At 2 GHz, the –1 dB compression point is +2 dBm at the output. At 5.2 GHz the value degrades to 0 dBm.

The LNA is comprised of two sections: the amplifier core and a PTAT reference. The core is biased with the PTAT to compensate for the gain reduction with increasing temperature. The gain is proportional

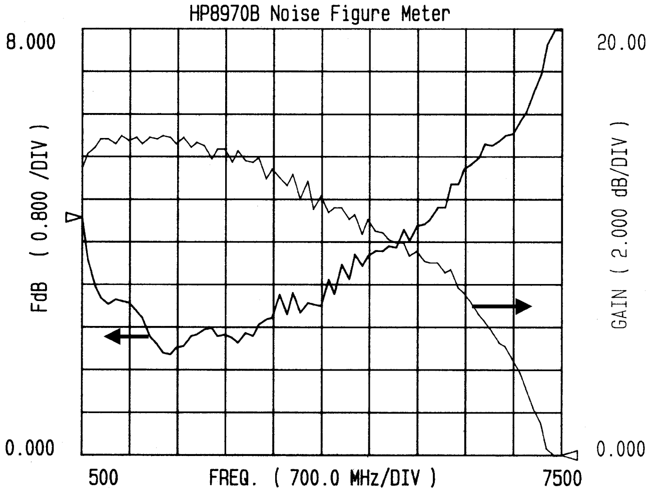

FIGURE 5.36 Measured LNA gain and noise figure vs. frequency (V_{dd} = 3 V, I_{dd} = 8.8 mA).

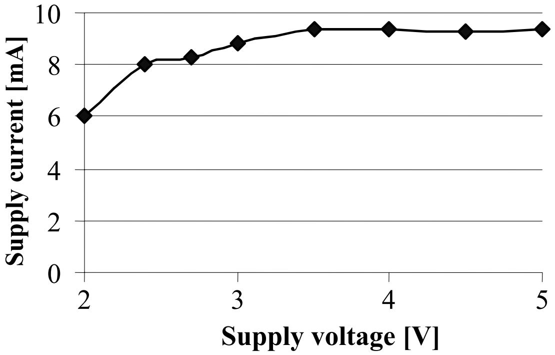

FIGURE 5.37 Supply current vs. supply voltage.

to the transconductance of the transistor, which itself is proportional to collector current and inversely proportional to temperature. The PTAT biasing increases the collector current with temperature to keep the gain roughly constant over temperature. Simultaneously, the biasing shows a good supply rejection as shown in Fig. 5.37.

A chip photograph of the 0.5 × 0.6 mm^2 large LNA is shown in Fig. 5.38.

A Fully Matched Two-Stage Low Power 5.8 GHz LNA[12]

A fully monolithic LNA achieves a noise figure below 2 dB between 4.3 GHz and 5.8 GHz with a gain larger than 15 dB at a DC power consumption of only 6 mW using the enhancement device of a standard 17 GHz f_T 0.6 µm E/D-MESFET process.

A schematic diagram of the integrated LNA core is shown in Fig. 5.39. The circuit consists of two common-source gain stages to provide enough power gain. The first stage uses an on-chip inductive degeneration of the source to achieve a simultaneous noise and power match, and to improve RF stability. Both amplifier stages are biased at the same current. The noise contributions of the biasing resistors are negligible.

The output of each stage is loaded with a band pass LC section to increase the gain at the desired frequency. The load of the first stage, together with the DC block between the stages, is also used for inter-stage matching.

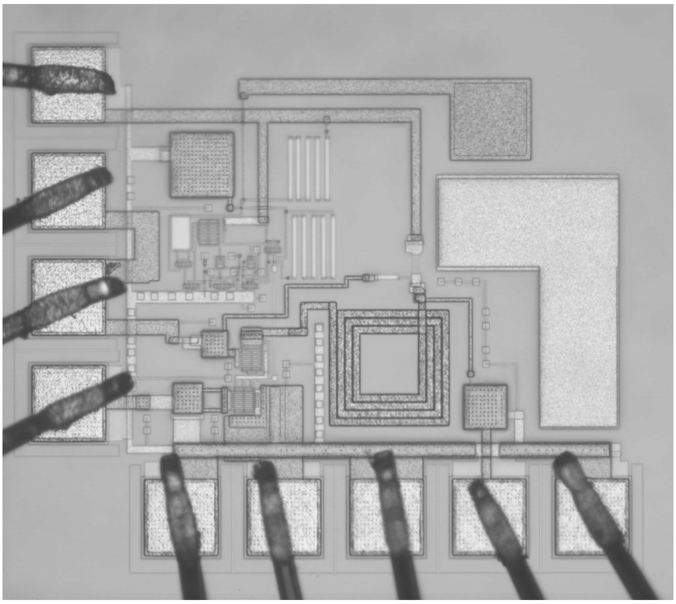

FIGURE 5.38 Chip photograph of the SiGe HBT LNA (0.5 × 0.6 mm^2).

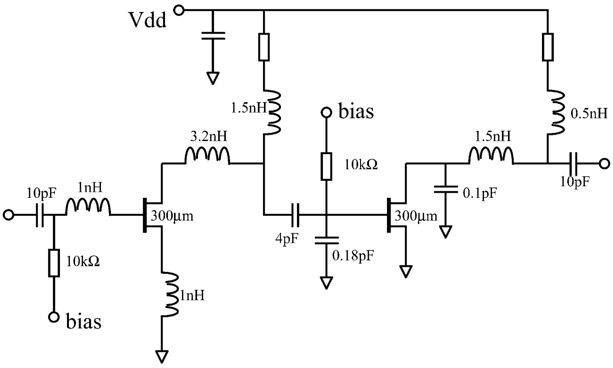

FIGURE 5.39 Schematic diagram of the low noise amplifier.

The DC biasing is done on-chip with a combination of E/D MESFETs (Fig. 5.40). The bias circuit is able to effectively stabilize the bias point for voltages from 1 V to beyond 4 V without any feedback network within the amplifier. It also can accurately compensate for threshold voltage variations.

The correlation of the threshold voltages of enhancement and depletion devices due to simultaneous gate recess etch of both types is used in the bias circuit to reduce the bias current variations over process parameter changes. Figure 5.41 shows the simulated deviation from the nominal current as a function of threshold voltage variations. The device current remains very constant even for extreme threshold voltage shifts.

If the RF input device is small, a large input impedance transformation is required. The third-order intercept point can be degraded and larger inductor values are needed sacrificing chip area and noise figures, due to the additional series resistance of the inductor. If instead a very large device is used, the current consumption is increased, unless the current density is lowered. Below a certain current density the device gain will decrease, the minimum noise figure will increase, and a reliable and reproducible biasing of the device becomes difficult as the device is biased close to the pinch-off voltage. To achieve high quality factors, all inductors are implemented using the two top wiring levels with a total metal

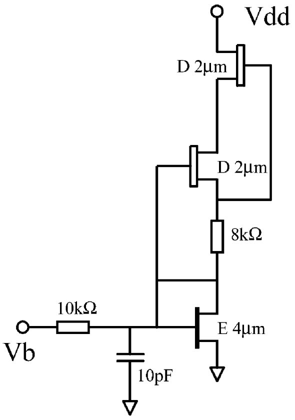

FIGURE 5.40 Schematic diagram of the employed bias circuit.

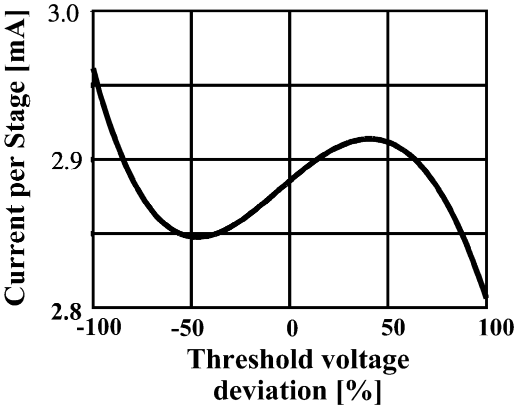

FIGURE 5.41 Simulated current dependence on threshold voltage variations.

thickness of 6 µm. The spiral inductors were analyzed using a 2.5D field simulator in order to accurately determine their equivalent circuit.

Sample test chips were mounted in a ceramic test package (Fig. 5.42) to investigate the influence of the bonding wires and the package parasitics.

In Figs. 5.43 and 5.44 the influence of the bond wires on the input and return loss, gain, and noise figure, respectively, is shown. The optimum input matching is shifted from 5.2 GHz to 5.8 GHz with the bond wire included. In an amplifier stage with moderate feedback one would expect the bond wire to shift the match toward lower frequencies. However, due to the source inductor the inter-stage matching circuit strongly interacts with the input port, causing a frequency shift in the opposite direction.

As expected, the gain curve of the packaged LNA (Fig. 5.44) is flatter and the gain is slightly reduced because of the additional ground inductance arising from the ground bond wires (approx. 40 pH).

At the nominal supply current of 6 mA the measured 50 Ω noise figure is 1.8 dB along with more than 15 dB gain from 5.2 GHz to 5.8 GHz as given in Fig. 5.44. For the packaged LNA the noise figure is slightly degraded due to losses associated with the package and connectors.

At 5.5 GHz the minimum noise figure of the device including the source inductor at the operating bias point is 1.0 dB and the associated gain is 8.5 dB. The minimum noise figure of an amplifier with two identical stages is therefore 1.6 dB. Thus, only a small degradation of the noise figure by the on-chip matching inductor is introduced at the input.

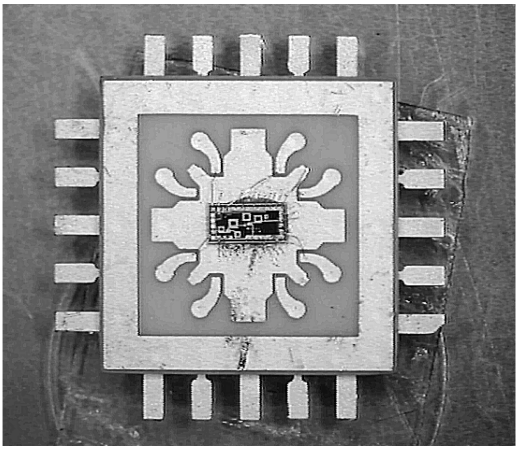

FIGURE 5.42 Photograph of the chip mounted in the test package.

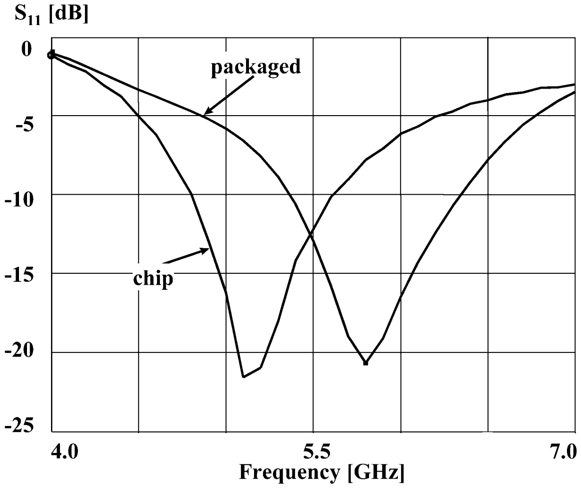

FIGURE 5.43 Input return loss vs. frequency of chip and packaged LNA.

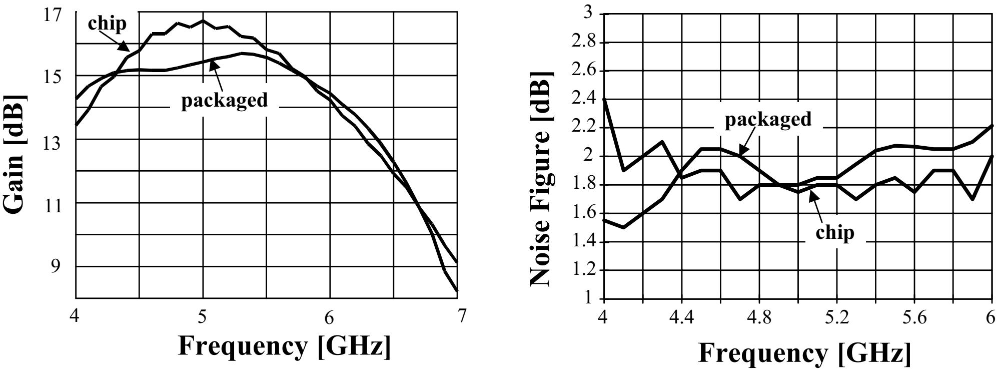

FIGURE 5.44 Gain and noise figure vs. frequency (V_{dd} = 1 V and I_{dd} = 6mA).

At 5.2 GHz a measured –1 dB compression point of 0 dBm at the output confirms the excellent distortion characteristics of GaAs MESFET devices at very low power consumption. The measured input referenced third order intercept point (IIP3) is -6 dBm.

0.25 µm CMOS LNAs for 900 MHz and 1.9 GHz[13,14]

CMOS technology starts to play a significant role in integrated RF transceivers for the low GHz range with effective gate lengths reaching the deep submicron regions. Competitive circuit performance at low power dissipation is becoming possible even for critical building blocks such as the LNA. In fact, quarter-micron CMOS seems to be the threshold where robust designs can be realized with current consumption competitive to BJT implementations. Further downscaling calls for a reduction in supply voltage which will ultimately limit the distortion performance of CMOS-based designs.

Designing a low noise amplifier in CMOS is complicated by the lossy substrate, which requires a careful layout to avoid noise injection from the substrate. The schematic diagrams of two demonstrated 0.25 µm CMOS LNAs for 900 MHz and 1.9 GHz are shown in Figs. 5.45a and 5.45b, respectively. Both circuits use two stages to realize the desired gain.

The first amplifier consisting of an externally matched cascode input stage and a transimpedance output stage consumes 10.8 mA from a 2.5 V supply. The cascode is formed using two 600-µm wide NMOS devices loaded by a 400 Ω resistor. The inductance of approximately 1.2 nH formed by the bondwire at the source of the first stage is used to simplify the matching of an otherwise purely capacitive input impedance. The directly coupled transimpedance output stage isolates the high-gain cascode and provides a good 50 Ω output matching. A simple biasing is included on the chip. At the nominal power dissipation and 900 MHz, the LNA achieves 16 dB gain and a noise figure of below 2 dB. The input and output return losses are –8 dB and –12 dB, respectively. The distortion performance of the LNA can well be estimated by measuring the input referred third order intercept point and the –1 dB compression point. They are –7 dBm and –20 dBm, respectively.

The 1.9 GHz LNA shown in Fig. 5.45b employs a resistively loaded common-source stage followed by a reactively loaded cascode stage. To use inductors to tune out the output capacitance and to realize the 50 Ω output impedance is a viable alternative to using the transimpedance output stage. The circuit employs a self-biasing method by feeding the DC drain voltage of the first stage to the gates. The supply rejection is consequently poor.

The LNA achieves 21 dB gain and a 3 dB noise figure while drawing 10.8 mA from a 2.7 V supply. In Fig. 5.46 the measured gain and noise figure versus frequency are plotted. At the nominal bias the input referred –1 dB compression point is –25 dBm, which corresponds to –4 dBm at the output. The input and output return loss are –5 dB and –13 dB, respectively.

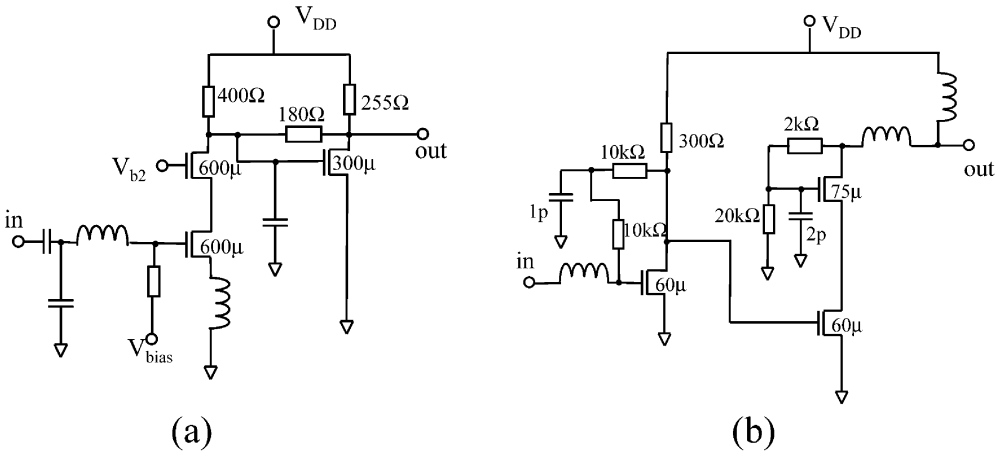

FIGURE 5.45 Schematic diagram of two 0.25 µm CMOS LNAs for 900 MHz (a) and 1900 MHz (b).

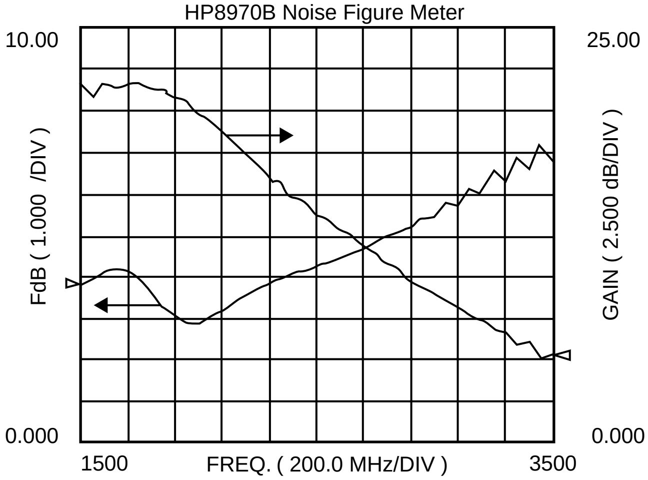

FIGURE 5.46 Measured gain and noise figure of the 1900 MHz CMOS LNA of Figure 5.24(b).

A comparison between the two amplifiers presented reveals some interesting points:

- The 900 MHz LNA explicitly makes use of the bondwire inductance to reduce the (otherwise purely capacitive) input impedance while the fist stage of the 1.9 GHz amplifier is connected to the chip ground. Both amplifiers use an external inductor for the input matching and both achieve a relatively poor input match.
- No explicit inter-stage matching is employed in either of the amplifiers. The 900 MHz amplifier uses the second stage as an impedance transformer.
- The 900 MHz amplifier employs ten times wider devices biased at lower current densities compared to its 1.9 GHz counterpart. As a consequence, the bias current becomes more sensitive to threshold voltage variations due to fabrication.
- At comparable power consumption the two amplifiers show roughly same distortion performance.

A Highly Selective LNA with Electrically Tunable Image Reject Filter for 2 GHz[15]

LNA designs with purely reactive passive components are inherently narrowband. IC technologies on high resistivity substrates allow reproducible passive components (inductors, capacitors, varactors, transmission lines) with excellent quality factors. They are well suited for designs to include a frequency selectivity which goes beyond a simple matching. In particular, amplifiers with adjustable image rejection can be realized. To show the potential of highly frequency selective LNAs as viable alternative to image reject mixers, an LNA for 1.9 GHz is demonstrated, which allows a tunable suppression of the image frequency. The schematic diagram of the circuit is shown in Fig. 5.47. The amplifier consists of two cascaded common-source stages loaded with LC resonant circuits. Undesired frequencies are suppressed using series notch filters as additional loads. Each of the two notch filters is formed by a series connection of a spiral inductor and a varactor diode. The two notches resonate at the same frequencies and must be isolated by the amplifier stages.

A careful design must be done to avoid unwanted resonances and oscillations. In particular, immunity against variations in the ground inductance and appropriate isolation between the supply lines of the two stages must be included. Only the availability of IC technologies with reproducible high-Q, low-tolerance passive components enables the realization of such highly frequency-selective amplifiers.

The LNA draws 9.5 mA from a 3 V supply. At this power dissipation, the input referred –1 dB compression point is measured at –24 dBm.

The measured input and output reflection is plotted in Fig. 5.48. The tuning voltage is set to 0 V. The excellent input match changes only negligibly with varying tuning voltage. The input matching shows a

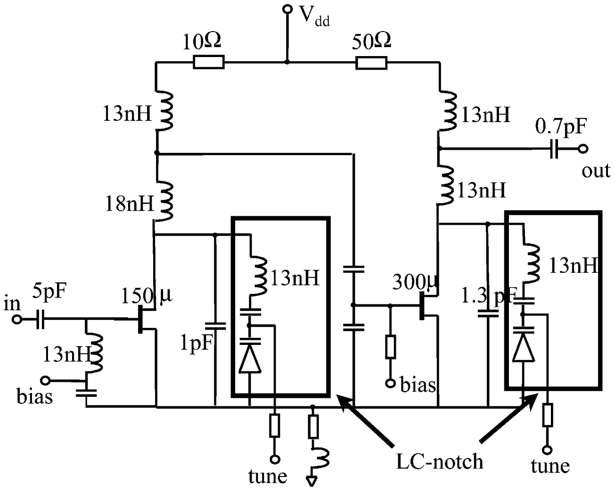

FIGURE 5.47 Schematic diagram of the selective frequency LNA at 2 GHz.

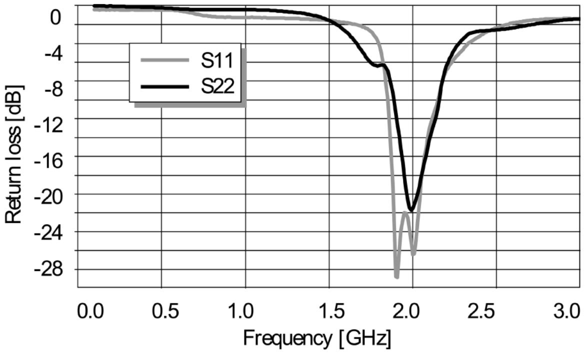

FIGURE 5.48 Measured input and output return loss of the 2 GHz selective LNA.

high-pass characteristic formed by the series C-L combination instead to the commonly used low-pass. So, the inductor can also act as a bias choke and the input matching can contribute to the suppression of lower frequency interferer. Moreover, the employed matching achieves better noise performance than the high-pass matching network.

The power gain vs. frequency for different notch tuning voltages is shown in Fig. 5.49. By varying the tuning voltage from 0.5 V to 1.5 V, the filter center frequency can be adjusted from 1.44 to 1.6 GHz. At all tuning voltages the unwanted signal is suppressed by at least 35 dB.

The temperature dependence of gain and noise figure was measured. The temperature coefficients of the gain and noise figure are –0.03 dB/°C and +0.008 dB/°C, respectively. The noise figure of the LNA at different temperatures is plotted in Fig. 5.50.

A chip photograph of the fabricated 1.6 × 1.0 mm^2 LNA is depicted in Fig. 5.51. More than 50% of the chip area is occupied by the numerous spiral inductors.

Future Trends

RF and microwave functions are increasingly often realized as integrated circuits (ICs) to reduce size and power consumption, enhance reproducibility, minimize costs, and enable mass production.

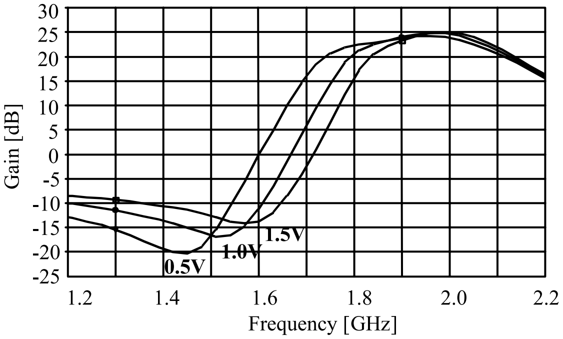

FIGURE 5.49 Selective amplifier gain vs. frequency for different notch filter control voltages.

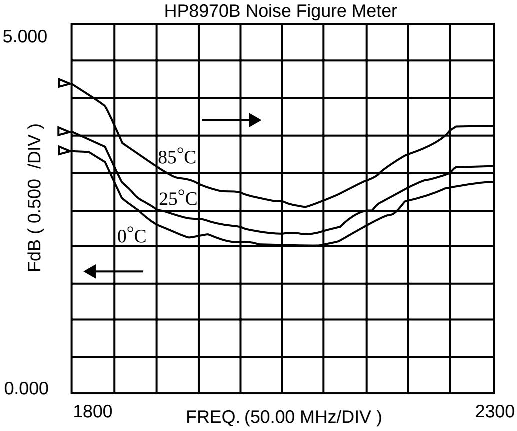

FIGURE 5.50 Amplifier noise figure at various temperatures.

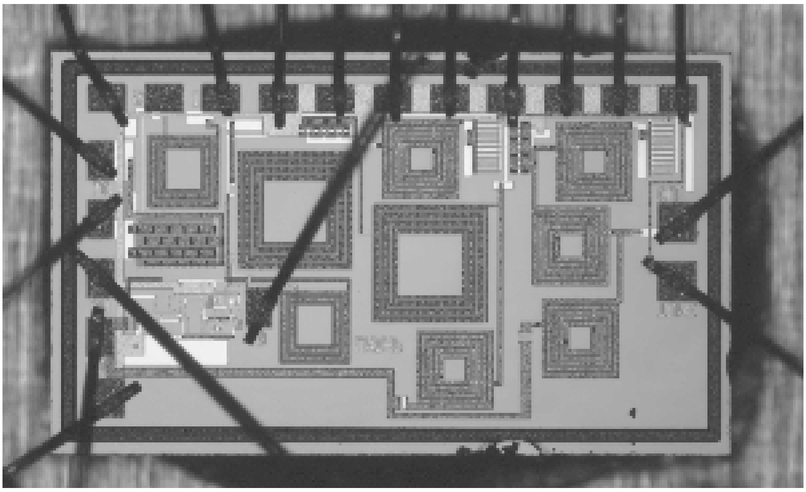

FIGURE 5.51 Chip photograph of the frequency selective LNA.

Design Approach

The classical noise optimization is based on linear methods and does not take power consumption and linearity requirements explicitly into account. Further, these methods offer only little guidance about how to select the active device dimensions. However, LNA circuit design practices are increasingly influenced by the improvements in the device models in terms of accuracy. Powerful optimization tools become available and eases the design procedure. However, a detailed understanding of the basic material will remain necessary for an efficient and robust LNA circuit design.

Device Models

The plurality of bias conditions applied to integrated circuits requires the flexibility of bias-dependent device models. State-of-the-art BJT models (such as Gummel-Poon) already work very well in RF simulations. More recently, sophisticated, semiempirical MOSFET models (such as BSIM3, MM9, or EKV) became suitable for RF simulations. Using accurate models, designs do not need to rely on sample scattering parameters of test devices and tolerance simulations can be implemented.

Circuit Environment

New RF design practices away from the 50 Ω impedance culture will affect the selection of the device size and operation point, but will leave the design procedure basically unchanged. The obstacles in the quest for higher integrated RF radios are the requirements on system noise figure, substrate crosstalk, and parasitic coupling. Trends to alleviate the unwanted coupling involve using fully differential circuit design, which in turn increases the power consumption.

IC Technologies

In recent years, the advances in device shrinking have made silicon devices (BJTs and more recently MOSFETs) become competitive with III-V semiconductors in terms of gain and minimum noise figure at a given power dissipation in the low GHz range.

The introduction of SiGe and SiC layers further enhance the cutoff frequencies and reduce power dissipation of silicon-based transistors. Furthermore, the use of thick (copper) metallization layers allow relatively low-loss passive components such as MIM capacitors and spiral inductors. Silicon-on-insulator (SOI) technologies will further cut substrate losses and parasitic capacitance and reduce bulk crosstalk.

With the scaling toward minimum gate length of below 0.25 μm, the use of CMOS has become a serious option in low-noise amplifier design. In fact, minimum noise figures of 0.5 dB at 2 GHz and cutoff frequencies of above 100 GHz for 0.12 μm devices[16] can easily compete with any other circuit technology. While intrinsic CMOS device F_{min} is becoming excellent for very short gate lengths, there remains the question of how closely amplifier noise figures can approach F_{min} in practice, particularly if there is a constraint on the allowable power consumption.

References

1. J. M. Rollett, Stability and power-gain invariance of linear two ports, *IEEE Trans. on Circuit Theory,* CT-9, 1, 29–32, March 1962, with corrections, CT-10, 1, 107, March 1963.
2. G. Gonzales, *Microwave Transistor Amplifiers Analysis and Design,* 2nd Edition, Prentice Hall, Englewood Cliffs, NJ, 1997.
3. G. Macciarella, et al., Design criteria for multistage microwave amplifiers with match requirements at input and output, *IEEE Trans. Microwave Theory and Techniques,* MTT-41, 1294–98, Aug. 1993.
4. G. D. Vendelin, A. M. Pavio, U. L. Rohde, *Microwave Circuit Design using Linear and Nonlinear Techniques,* 1st Edition, John Wiley & Sons, New York, 1990.
5. H. Hillbrand and P. H. Russer, An efficient method for computer aided noise analysis of linear amplifier networks, *IEEE Trans. on Circuit and Systems,* CAS-23, 4, 235–38, April 1976.
6. H. T. Friis, Noise figure for radio receivers, *Proc. of the IRE,* 419–422, July 1944.
7. H. A. Ainspan, et al., A 5.5 GHz low noise amplifier in SIGe BiCMOS, in *ESSCIRC98 Digest,* 80–83.

8. S. S. Taylor, A GaAs MESFET Schottky diode barrier height reference circuit, *IEEE Journal of Solid-State Circuits,* 32, 12, 2023–29, Dec. 1997.
9. J. J. Kucera, U. Lott, and W. Bächtold, A new antenna switching architecture for mobile handsets, *2000 IEEE Int'l Microwave Symposium Digest,* in press.
10. R. M. Fano, Theoretical limitations on the broad-band matching of arbitrary impedances, *Journal of the Franklin Institute,* 249, 57–83, Jan. 1960, and 139–155, Feb. 1960.
11. J. J. Kucera and W. Bächtold, A 1.9 GHz monolithic 1.1 dB noise figure low power LNA using a standard GaAs MESFET foundry process, *1998 Asia-Pacific Microwave Conference Digest,* 383–386.
12. J. J. Kucera and U. Lott, A 1.8 dB noise figure low DC power MMIC LNA for C-band, *1998 IEEE GaAs IC Symposium Digest,* 221–224.
13. Q. Huang, P. Orsatti and F. Piazza, Broadband, 0.25 µm CMOS LNAs with sub-2dB NF for GSM applications, *IEEE Custom Integrated Circuits Conference,* 67–70, 1998.
14. Ch. Biber, Microwave modeling and circuit design with sub-micron CMOS technologies, PhD thesis, Diss. ETH No. 12505, Zurich, 1998.
15. J. J. Kucera, Highly integrated RF transceivers, PhD thesis, Diss. ETH No. 13361, Zurich, 1999.
16. R. R. J. Vanoppen, et al., RF noise modeling of 0.25μm CMOS and low power LNAs, *1997 IEDM Technical Digest,* 317–320.

5.4 Microwave Mixer Design

Anthony M. Pavio

At the beginning of the 20th century, RF detectors were crude, consisting of a semiconductor crystal contacted by a fine wire ("whisker"), which had to be adjusted periodically so that the detector would keep functioning. With the advent of the triode, a significant improvement in receiver sensitivity was obtained by adding amplification in front of and after the detector. A real advance in performance came with the invention by Edwin Armstrong of the super regenerative receiver. Armstrong was also the first to use a vacuum tube as a frequency converter (mixer) to shift the frequency of an incoming signal to an intermediate frequency (IF), where it could be amplified and detected with good selectivity. The superheterodyne receiver, which is the major advance in receiver architecture to date, is still employed in virtually every receiving system.

The mixer, which can consist of any device capable of exhibiting nonlinear performance, is essentially a multiplier or a chopper. That is, if at least two signals are present, their product will be produced at the output of the mixer. This concept is illustrated in Fig. 5.52. The RF signal applied has a carrier frequency of w_s with modulation $M(t)$, and the local oscillator signal (LO or pump) applied has a pure sinusoidal frequency of w_p. From basic trigonometry we know that the product of two sinusoids produces a sum and difference frequency.

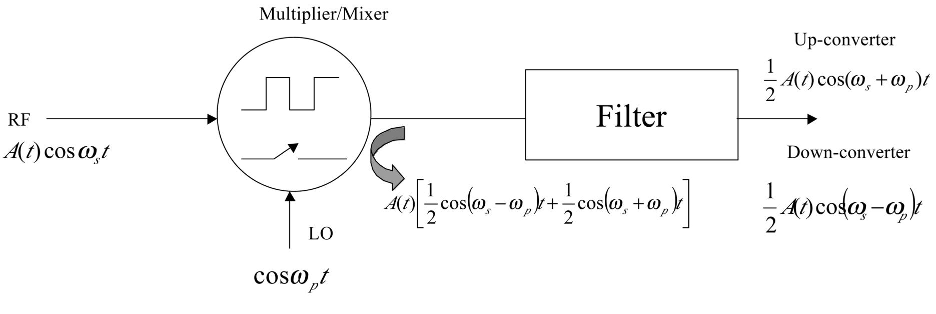
Multiplier/Mixer
RF
$A(t)\cos\omega_s t$
Filter
Up-converter
$\frac{1}{2}A(t)\cos(\omega_s+\omega_p)t$
Down-converter
$A(t)\left[\frac{1}{2}\cos(\omega_s-\omega_p)t+\frac{1}{2}\cos(\omega_s+\omega_p)t\right]$
$\frac{1}{2}A(t)\cos(\omega_s-\omega_p)t$
LO
$\cos\omega_p t$

FIGURE 5.52 Ideal mixer model.

The voltage-current relationship for a diode can be described as an infinite power series, where V is the sum of both input signals and I is the total signal current. If the RF signal is substantially smaller than the LO signal and modulation is ignored, the frequency components of the signal are:

$$w_d = nw_p \pm w_s \tag{5.1}$$

As mentioned above, the desired component is usually the difference frequency ($|w_{p+} w_s|$ or $|f_p - f_s|$), but sometimes the sum frequency ($f_s + f_p$) is desired when building an up-converter, or a product related to a harmonic of the LO can be selected.

A mixer can also be analyzed as a switch that is commutated at a frequency equal to the pump frequency $w_{p.}$ This is a good first-order approximation of the mixing process for a diode since it is driven from the low-resistance state (forward bias) to the high-resistance state (reverse bias) by a high-level LO signal.

The concept of the switching mixer model can also be applied to field-effect transistors used as voltage-controlled resistors. In this mode, the drain-to-source resistance can be changed from a few ohms to many thousands of ohms simply by changing the gate-to-source potential. At frequencies below 1 GHz, virtually no pump power is required to switch the FET, and since no DC drain bias is required, the resulting FET mixer is passive. However, as the operating frequency is raised above 1 GHz, passive FET mixers require LO drive powers comparable to diode or active FET designs.

Mixers can be divided into several classes: (1) single ended, (2) single balanced, or (3) double balanced. Depending on the application and fabrication constraints, one topology can exhibit advantages over the other types. The simplest topology (Fig. 5.53a) consists of a single diode and filter networks. Although there is no isolation inherent in the structure (balance), if the RF, LO, and IF frequencies are sufficiently separated, the filter (or diplexer) networks can provide the necessary isolation. In addition to simplicity, single diode mixers have several advantages over other configurations. Typically, the best conversion loss is possible with a single device, especially at frequencies where balun or transformer construction is difficult or impractical. Local oscillation requirements are also minimal since only a single diode is employed and DC biasing can easily be accomplished to reduce drive requirements. The disadvantages of the topology are: (1) sensitivity to terminations; (2) no spurious response suppression; (3) minimal tolerance to large signals; and (4) narrow bandwidth due to spacing between the RF filter and mixer diode.

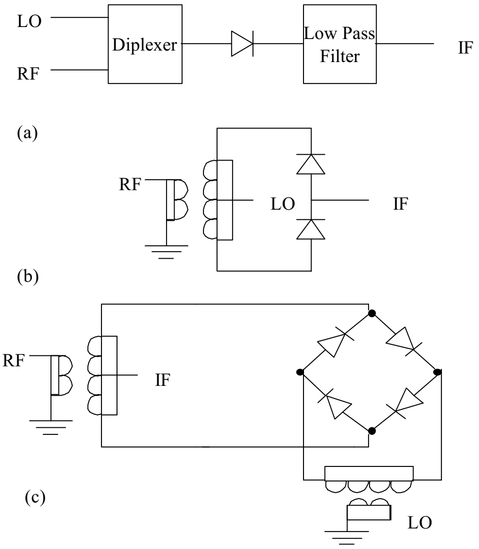

FIGURE 5.53 Typical mixer configurations. (a) Single ended; (b) single balanced; (c) double balanced.

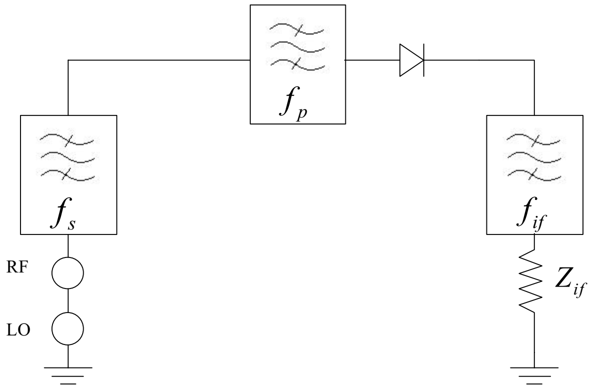

FIGURE 5.54 Filtering requirements for single-diode mixer.

The next topology commonly used is the single balanced structure shown in Fig. 5.53b. These structures tend to exhibit slightly higher conversion loss than that of a single-ended design, but since the RF signal is divided between two diodes, the signal power-handling ability is better. More LO power is required, but the structure does provide balance. The double-balanced mixer (Fig. 5.53c) exhibits the best large signal-handling capability, port-to-port isolation, and spurious rejection. Some high-level mixer designs can employ multiple-diode rings with several diodes per leg in order to achieve the ultimate in large-signal performance. Such designs can easily require hundreds of milliwatts of pump power.

Single-Diode Mixers

The single-diode mixer, although fondly remembered for its use as an AM "crystal" radio or radar detector during World War II, has become less popular due to demanding broadband and high dynamic range requirements encountered at frequencies below 30 GHz. However, there are still many applications at millimeter wave frequencies, as well as consumer applications in the microwave portion of the spectrum, which are adequately served by single-ended designs. The design of single-diode mixers can be approached in the same manner as multi-port network design. The multi-port network contains all mixing product frequencies regardless of whether they are ported to external terminations or terminated internally. With simple mixers, the network's main function is frequency component separation; impedance matching requirements are secondary (Fig. 5.54). Hence, in the simplest approach, the network must be capable of selecting the LO, RF, and IF frequencies (Fig. 5.55).

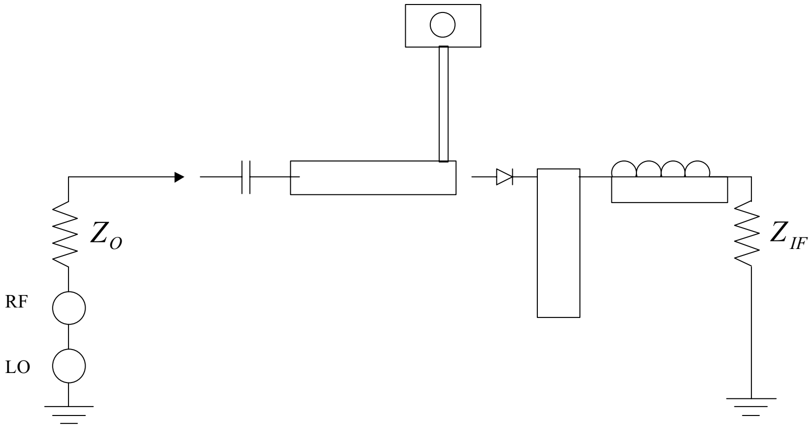

FIGURE 5.55 Typical single-ended mixer.

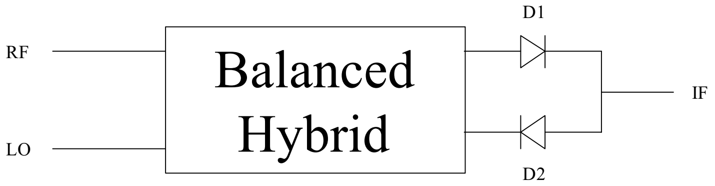

FIGURE 5.56 Single-balanced mixer topology.

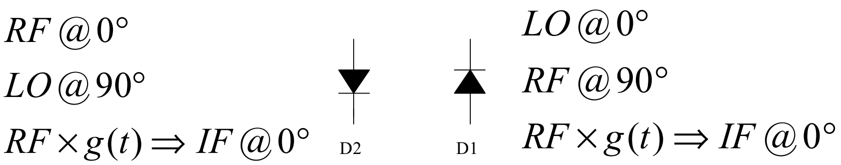
$RF@0°$
$LO@90°$
$RF \times g(t) \Rightarrow IF@0°$
D2
D1
$LO@0°$
$RF@90°$
$RF \times g(t) \Rightarrow IF@0°$

FIGURE 5.57 Signal phase relationships in quadrature coupled hybrid single-balanced mixer.

However, before a network can be designed, the impedance presented to the network by the diode at various frequencies must be determined. Unfortunately, the diode is a nonlinear device; hence, determining its characteristics is more involved than determining an "unknown" impedance with a network analyzer. Since the diode impedance is time varying, it is not readily apparent that a stationary impedance can be found. Stationary impedance values for the RF, LO, and IF frequencies can be measured or determined if sufficient care in analysis or evaluation is taken.

Single-Balanced Mixers

Balanced mixers offer some unique advantages over single-ended designs such as LO noise suppression and rejection of some spurious products. The dynamic range can also be greater because the input RF signal is divided between several diodes, but this advantage is at the expense of increased pump power. Both the increase in complexity and conversion loss can be attributed to the hybrid or balun, and to the fact that perfect balance and lossless operation cannot be achieved.

There are essentially only two design approaches for single-balanced mixers; one employs a 180° hybrid, while the other employs some form of quadrature structure (Fig. 5.56). The numerous variations found in the industry are related to the transmission-line media employed and the ingenuity involved in the design of the hybrid structure. The most common designs for the microwave frequency range employ either a branch-line, Lange, or "rat-race" hybrid structure (Fig. 5.57). At frequencies below about 5 GHz, broadband transformers are very common, while at frequencies above 40 GHz, waveguide and MMIC structures become prevalent.

Double-Balanced Mixers

The most commonly used mixer today is the double-balanced mixer. It usually consists of four diodes and two baluns or hybrids, although a double-ring or double-star design requires eight diodes and three hybrids. The double-balanced mixer has better isolation and spurious performance than the single-balanced designs described previously, but usually requires greater amounts of LO drive power, are more difficult to assemble, and exhibit somewhat higher conversion loss. However, they are usually the mixer of choice because of their spurious performance and isolation characteristics.

A typical single-ring mixer with transformer hybrids is shown in Fig. 5.58. With this configuration the LO voltage is applied across the ring at terminals LO^- and LO^+, and the RF voltage is applied across terminals RF^- and RF^+. As can be seen, if the diodes are identical (matched), nodes RF^- and RF^+ are virtual grounds; thus no LO voltage appears across the secondary of the RF transformer. Similarly, no

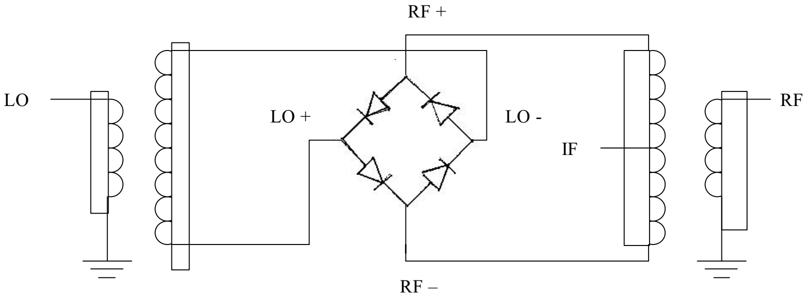

FIGURE 5.58 Transformer coupled double-balanced mixer.

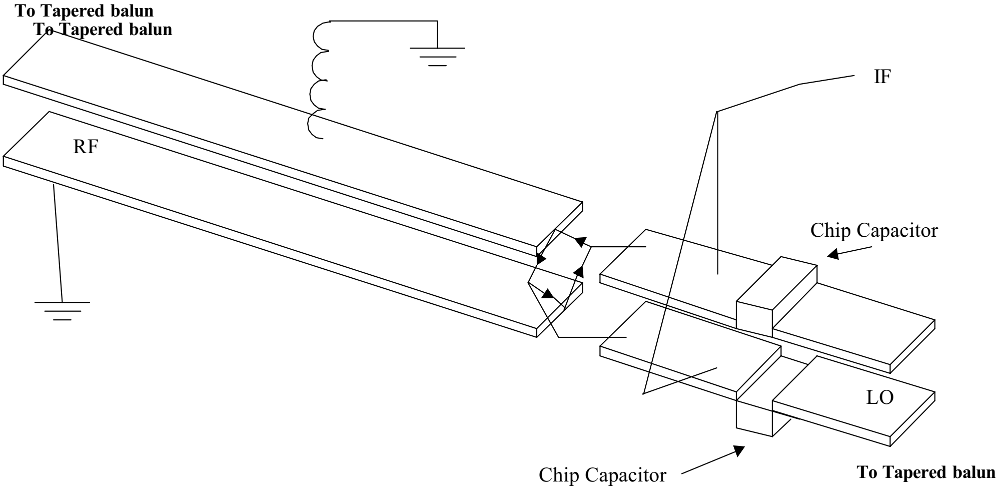

FIGURE 5.59 Double-balanced mixer center section.

RF voltage appears across the secondary of the LO balun. Because of the excellent diode matching that can be obtained with diode rings fabricated on a single chip, the L-to-R isolation of microwave mixers can be quite good, typically 30 to 40 dB.

Transmission-line structures which are naturally balanced, such as slotline and finline, can also be used as balanced feed in mixer design. However, all of the structures above, and the more complex transmission-line structures to follow, exhibit one major drawback compared to a transformer hybrid: There is no true RF center tap. As will be seen, this deficiency in transmission-line structures, extensively complicates the design of microwave-balanced mixers.

The lack of a balun center tap does indeed complicate the extraction of IF energy from the structure, but if the IF frequency is low, diplexing can be employed to ease performance degradation. This concept is illustrated in the following example of the center section of a double-balanced 2 to 12 GHz mixer (Fig. 5.59). It will be assumed that because of the soft-substrate transmission-line media and frequency range, a packaged diode ring with known impedances can be used. For Si diodes in this frequency range, the typical LO impedance range (magnitude) is on the order of 75, while the RF impedance is approximately 50. With these values in mind, microstrip-to-parallel plate transmission-line baluns can be fabricated on soft-substrate material.

As can be seen, both the RF and LO baluns terminate at the diode ring and provide the proper phase excitation. But since there is no center tap, the IF must be summed from the top and bottom of either balun. This summing is accomplished with bond wires that have high reactances at microwave frequencies but negligible inductances in the IF passband. Blocking capacitors form the second element in a high-pass filter, preventing the IF energy to be dissipated externally. An IF return path must also be provided at the terminals of the opposite balun. The top conductor side of the balun is grounded with a bond wire, providing a low-impedance path for the IF return and a sufficiently large impedance in shunt with the RF path. The ground-plane side of the balun provides a sufficiently low impedance for the IF return from the bottom side of the diode ring. The balun inductance and blocking capacitor also form a series resonant circuit shunting the IF output; therefore, this resonant frequency must be kept out of the IF passband.

The upper-frequency limit of mixers fabricated using tapered baluns and low parasitic diode packages, along with a lot of care during assembly, can be extended to 40 GHz. Improved "high-end" performance can be obtained by using beam-lead diodes. Although this design technique is very simple, there is little flexibility in obtaining an optimum port VSWR since the baluns are designed to match the magnitude of the diode impedance. The IF frequency response of using this approach is also limited, due to the lack of a balun center tap, to a frequency range below the RF and IF ports.

FET Mixer Theory

Interest in FET mixers has been very strong due to their excellent conversion gain and intermodulation characteristics. Numerous commercial products employ JFET mixers, but as the frequency of operation approaches 1 GHz, they begin to disappear. At these frequencies and above, the MESFET can easily accomplish the conversion functions that the JFET performs at low frequencies. However, the performance of active FET mixers reported to date by numerous authors has been somewhat disappointing. In short, they have not lived up to expectations, especially concerning noise-figure performance, conversion gain, and circuit-to-circuit repeatability. However, they are simple and low cost, so these sins can be forgiven.

Recently, growing interest is GaAs monolithic circuits is again beginning to heighten interest in active MESFET mixers. This is indeed fortunate, since properly designed FET mixers offer distinct advantages over their passive counterparts. This is especially true in the case of the dual-gate FET mixer; since the additional port allows for some inherent LO-to-RF isolation, it can at times replace single balanced passive approaches. The possibility of conversion gain rather than loss is also an advantage, since the added gain may eliminate the need for excess amplification, thus reducing system complexity.

Unfortunately, there are some drawbacks when designing active mixers. With diode mixers, the design engineer can make excellent first-order performance approximations with linear analysis; also, there is the practical reality that a diode always mixes reasonably well almost independent of the circuit. In active mixer design, these two conditions do not hold. Simulating performance, especially with a dual-gate device, requires some form of nonlinear analysis tool if any circuit information other than small-signal impedance is desired. An analysis of the noise performance is even more difficult.

As we have learned, the dominant nonlinearity of the FET is its transconductance, which is typically (especially with JFETs) a squarelaw function. Hence it makes a very efficient multiplier.

The small-signal circuit [1] shown in Fig. 5.60 denotes the principal elements of the FET that must be considered in the model. The parasitic resistances R_g, R_d, and R_s are small compared to R_{ds} and can be considered constant, but they are important in determining the noise performance of the circuit. The mixing products produced by parametric pumping of the capacitances C_{gs}, C_{dg}, and C_{ds} are typically small and add only second-order effects to the total circuit performance. Time-averaged values of these capacitances can be used in circuit simulation with good results.

This leaves the FET transconductance g_m, which exhibits an extremely strong nonlinear dependence as a function of gate bias. The greatest change is transconductance occurs near pinch off, with the most linear change with respect to gate voltage occurring in the center of the bias range. As the FET is biased toward I_{dss}, the transconductance function again becomes nonlinear. It is in these most nonlinear regions that the FET is most efficient as a mixer.

If we now introduce a second signal, V_c, such that it is substantially smaller than the pump voltage, across the gate-to-source capacitance C_{gs}, the nonlinear action of the transconductance will cause mixing action within the FET producing frequencies $|nw_p \pm w_1|$, where n can be any positive or negative integer. Any practical analysis must include mixing products at both the gate and drain terminal, and at a minimum, allow frequency components in the signal, image, LO, and IF to exist.

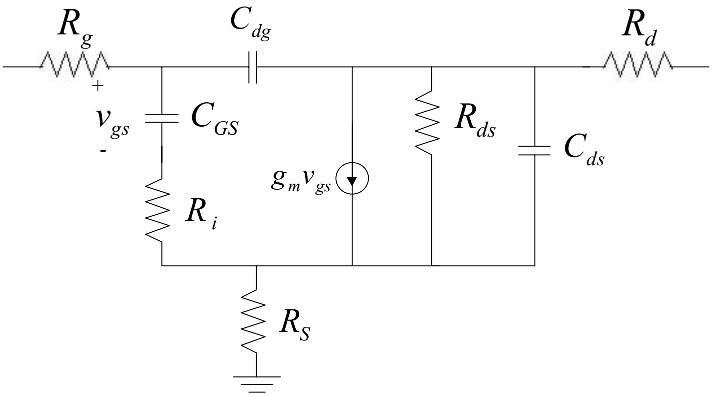

FIGURE 5.60 Typical MESFET model.

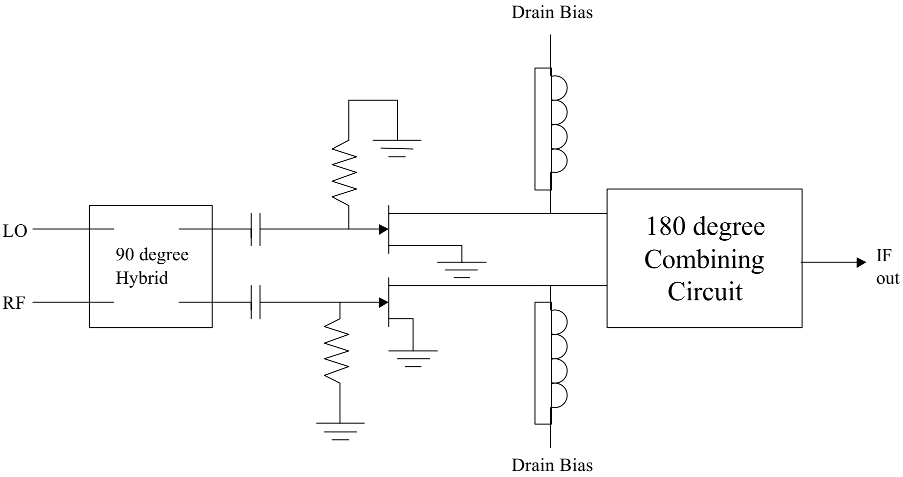

FIGURE 5.61 Typical FET single-balanced mixer.

Double-balanced FET mixers can also be designed using transformer hybrids [1]. Fig. 5.61 shows a typical balanced FET mixer, which can be designed to operate from VHF to SHF. An additional balun is again required because of the phase relationships of the IF signal. This structure is completely balanced and exhibits spurious rejection performance, similar to diode mixers constructed for the same frequency range. However, the intermodulation and noise-figure performance of such structures is superior to those of simple four-diode designs. For example, third-order intercept points in excess of 33 dBm, with associated gains of 6 dB, are common in such structures. High-level multiple-diode ring mixers, which would require substantially more LO power, would exhibit comparable intermodualtion characteristics, but would never exhibit any gain.

There are a variety of interesting mixer topologies in widespread use that perform vital system functions that cannot be simply classified as balanced mixers. Probably the most popular configuration is the image rejection or single-sideband mixer. However, a variety of subharmonically pumped and self-oscillating mixers are in limited use [1].

Reference

1. G. D. Vendelin, A. M. Pavio, and U. L. Rohde, The Design of Amplifiers Mixers and Oscillators Using the S-Parameter Method, John Wiley and Son, New York, 1990.

5.5 Modulation and Demodulation Circuitry

Charles Nelson

Some Fundamentals: Why Modulate?

Because this chapter uses a building block approach, it may seem to be a long succession of setting up straw men and demolishing them. To some extent, this imitates the development of radio and TV, which has been going on for most of the century just ended. A large number of concepts were developed as the technology advanced; each advance made new demands upon the hardware. At first, many of these advances were made by enthusiastic amateurs who had no fear of failure and viewed radio communication the way Hillary viewed Everest — something to be surmounted "because it was there." Since about World War II, there have been increasing numbers of engineers who understood these principles and could propose problem solutions that might have worked the first or second time they were tried. The author fondly hopes this book will help to grow a new cadre of problem solvers for the 21st century.

What probably first motivated the inventors of radio was the need for ships at sea to make distress calls. It may be interesting to note that the signal to be transmitted was a digital kind of thing called Morse Code. Later, the medium became able to transmit equally crucial analog signals, such as a soldier warning, "Watch out!! The woods to your left are full of the abominable enemy!" Eventually, during a period without widespread military conflict, radio became an entertainment medium, with music, comedy, and news, all made possible by businessmen who were convinced you could be persuaded, by a live voice, to buy soap, and later, detergents, cars, cereals not needing cooking, and so on. The essential low and high frequency content of the signal to be transmitted has been very productive for problems to be solved by radio engineers.

The man on radio, urging you to buy a "pre-owned" Cadillac, puts out most of his sound energy below 1000 Hz. A microphone observes pressure fluctuations corresponding to the sound and generates a corresponding voltage. Knowing that all radio broadcasting is done by feeding a voltage to an antenna, the beginning engineer might be tempted to try sending out the microphone signal directly. A big problem with directly broadcasting such a signal is that an antenna miles long would be required to transmit it efficiently. However, if the frequency of the signal is shifted a good deal higher, effective antennas become much shorter and more feasible to fabricate. This upward translation of the original message spectrum is perhaps the most crucial part of what we have come to call "modulation." However, the necessities of retrieving the original message from the modulated signal may dictate other inclusions in the broadcast signal, such as a small or large voltage at the center, or "carrier" frequency of the modulated signal. The need for a carrier signal is dictated by what scheme is used to transmit the modulated signal, which determines important facts of how the signal can be demodulated.

More perspective on the general problem of modulation is often available by looking at the general form of a modulated signal,

$$f(t) = A(t)\cos\theta(t).$$

If the process of modulation causes the multiplier A(t) out front to vary, it is considered to be some type of "amplitude" modulation**.** If one is causing the angle to vary, it is said to be "angle" modulation, but there are two basic types of angle modulation. We may write

$$\theta(t) = \omega_c t + \phi(t).$$

If then our modulation process works directly upon $\omega_c = 2\pi f_c$, we say we have performed "frequency" modulation. If, instead, we directly vary the phase factor $\phi(t)$, we say we have performed "phase" modulation. The two kinds of angle modulation are closely related, so that we may do one kind of operation to get the other result, by proper preprocessing of the modulation signal. Specifically, if we put the modulating signal through an integrating circuit before we feed it to a phase modulator, we come out with frequency modulation. This is, in fact, often done. The dual of this operation is possible but is seldom done in practice. Thus, if the modulating signal is fed through a differentiating circuit before it is fed to a frequency modulator, the result will be phase modulation. However, this process offers no advantages to motivate such efforts.

How to Shift Frequency

Our technique, especially in this chapter, will be to make our proofs as simple as possible; specifically, if trigonometry proves our point, it will be used instead of the convolution theorem of circuit theory. Yet, use of some of the aspects of convolution theory can be enormously enlightening to those who understand. Sometimes, as it will in this first proof, it may also indicate the kind of circuit that will accomplish the task. We will also take liberties with the form of our modulating signal. Sometimes we can be very general, in which case it may be identified as a function m(t). At other times, it may greatly simplify things if we write it very explicitly as a sinusoidal function of time

$$m\left(t\right) = \cos\omega_m t.$$

Sometimes, in the theory, this latter option is called "tone modulation," because, if one listened to the modulating signal through a loudspeaker, it could certainly be heard to have a very well-defined "tone" or pitch. We might justify ourselves by saying that theory certainly allows this, because any particular signal we must deal with could, according the theories of Fourier, be represented as a collection, perhaps infinite, of cosine waves of various phases. We might then assess the maximum capabilities of a communication system by choosing the highest value that the modulating signal might have. In AM radio, the highest modulating frequency is typically about f_m = 5000 Hz. For FM radio, the highest modulation frequency might be f_m = 19 kHz, the frequency of the so-called FM stereo "pilot tone."

In principle, the shifting of a frequency is very simple. This is fairly obvious to those understanding convolution. One theorem of system theory says that multiplication of time functions leads to convolution of the spectra. Let us just multiply the modulating signal by a so-called "carrier" signal. One is allowed to have the mental picture of the carrier signal "carrying" the modulating signal, in the same way that homing pigeons have been used in past wars to carry a light packet containing a message from behind enemy lines to the pigeon's home in friendly territory. So, electronically, for "tone modulation," we need only to accomplish the product

$$\phi\left(t\right) = A\cos\omega_m t\cos\omega_c t.$$

Now, we may enjoy the consequences of our assumption of tone modulation by employing trigonometric identities for the sum or difference of two angles:

$$\cos\left(A + B\right) = \cos A\cos B - \sin A\sin B \text{ and } \cos\left(A - B\right) = \cos A\cos B + \sin A\sin B$$

If we add these two expressions and divide by two, we get the identity we need:

$$\cos A\cos B = 0.5\left[\cos\left(A + B\right) + \cos\left(A - B\right)\right].$$

Stated in words, we might say we got "sum and difference frequencies," but neither of the original frequencies. Let's be just a little more specific and say we started with f_m = 5000 Hz and f_c = 1 MHz, as

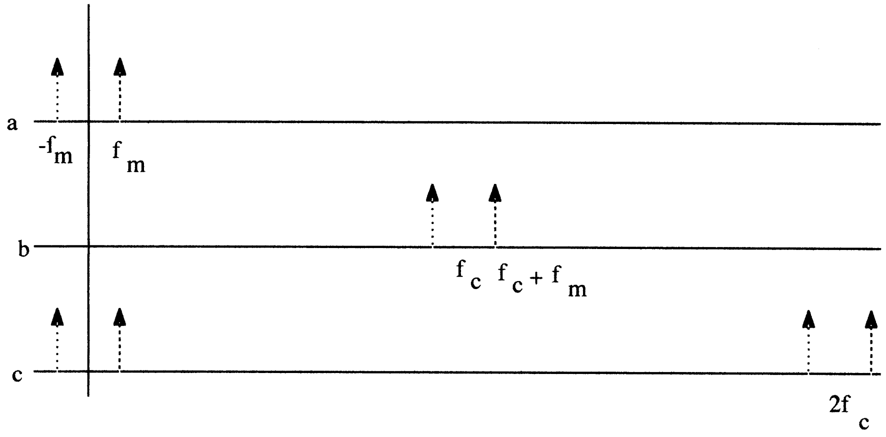

FIGURE 5.62 Unmodulated, modulated, and synchronously demodulated signal spectra. a. Spectrum of tone-modulating signal. b. Spectrum (positive part only) of double sideband suppressed carrier signal. c. Spectrum of synchronously detected DSB–SC signal (except for part near $-2f_c$).

would happen if a radio station whose assigned carrier frequency was 1 MHz were simply transmitting a single tone at 5000 Hz. In "real life," this would not be done very often, but the example serves well to illustrate some definitions and principles. The consequence of the mathematical multiplication is that the new signal has two new frequencies at 995 kHz and 1005 kHz. Let's now just add one modulating tone at 3333 Hz. We would have added two frequencies at 9666.667 kHz and 1003.333 kHz. However, if this multiplication was done purely, *there is no carrier frequency term present.* For this reason, we say we have done a type of "suppressed carrier" modulation. Also, furthermore, we have two *new* frequencies for *each* modulating frequency. We define all of those frequencies above the carrier as the "upper sideband" and all the frequencies below the carrier as the "lower sideband." The whole process we have done here is named "double sideband suppressed carrier" modulation, often known by its initials DSB–SC. Communication theory would tell us that the signal spectrum, before and after modulation with a single tone at a frequency f_m, would appear as in Fig. 5.62. Please note that the theory predicts equal positive and negative frequency components. There is no deep philosophical significance to negative frequencies. They simply make the theory symmetrical and a bit more intuitive.

Analog Multipliers, or "Mixers"

First, there is an unfortunate quirk of terminology; the circuit that multiplies signals together is in communication theory usually called a "mixer." What is unfortunate is that the engineer or technician who produces sound recordings is very apt to feed the outputs of many microphones into potentiometers, the outputs of which are sent in varying amounts to the output of a piece of gear, and *that* component is called a "mixer." Thus, the communication engineer's mixer multiplies and the other adds. Luckily, it will usually be obvious which device one is speaking of.

There are available a number of chips (integrated circuits) designed to serve as analog multipliers. The principle is surprisingly simple, although the chip designers have added circuitry which no doubt optimizes the operation and perhaps makes external factors less influential. The reader might remember that the transconductance g_m for a bipolar transistor is proportional to the collector current; its output is proportional to the g_m *and* the input voltage, so in principle one can replace an emitter resistor with the first transistor, which then controls the collector current of the second transistor. If one seeks to fabricate such a circuit out of discrete transistors, one would do well to expect a need to tweak operating conditions considerably before some approximation of analog multiplication occurs. Recommendation: buy the chip. Best satisfaction will probably occur with a "four-quadrant multiplier." The alternative is a "two-quadrant multiplier," which might embarrass one by being easily driven into cut-off.

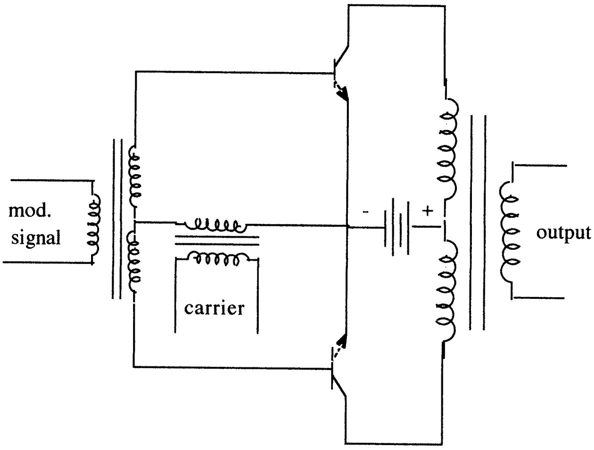

FIGURE 5.63 Balanced modulator.

Another effective analog multiplier is alleged to be the dual-gate FET. The width of the channel in which current flows depends upon the voltage on each of two gates which are insulated from each other. Hence, if different voltages are connected to the two gates, the current that flows is the product of the two voltages. Both devices we have discussed so far have the advantage of having some amplification, so the desired resulting signal has a healthy amplitude. A possible disadvantage may be that spurious signals one does *not* need may also have strong amplitudes.

Actually, the process of multiplication may be the byproduct of any distorting amplifier. One can show this by expressing the output of a distorting amplifier as a Taylor series representing output in terms of input. In principle, such an output would be written

$$V_o = a_0 + a_1\left(v_1 + v_2\right) + a_3\left(v_1 + v_2\right)^2 + \text{ smaller terms.}$$

One can expand $(v_1 + v_2)^2$ as $v_1^2 + 2v_1v_2 + v_2^2$, so this term yields second harmonic terms of each input plus the product of inputs one was seeking. However, the term $a_1(v_1 + v_2)$ also yielded each input, so the carrier here would not be suppressed. If it is fondly desired to suppress the carrier, one must resort to some sort of "balanced modulator." An "active" (meaning there is amplification provided) form of a balanced modulator may be seen in Fig. 5.63; failure to bias the bases of the transistors should assure that the voltage squared term is large.

One will also find purely passive mixers with diodes connected in the shape of a baseball diamond with one signal fed between first and third base, the other from second to home plate. Such an arrangement has the great advantage of not requiring a power supply; the disadvantage is that the amplitude of the sum or difference frequency may be small.

Synchronous Detection of Suppressed Carrier Signals

At this point, the reader without experience in radio may be appreciating the mathematical tricks but wondering, if one can accomplish this multiplication, can it be broadcast and the original signal retrieved by a receiver? A straightforward answer might be that multiplying the received signal by another carrier frequency signal such as cos ω_ct will shift the signal back exactly to where it started and also up to a center frequency of twice the original carrier. This is depicted in part c of Fig. 5.62. The name of this process is "synchronous detection." (In the days when it was apparently felt that communications enjoyed a touch of class if one used words having Greek roots, they called it "homodyne detection." If the reader reads a wide variety of journals, he/she may still encounter the word.) The good/bad news about synchronous detection is that the signal being used in the detector multiplication must have the *exact frequency and phase* of the original carrier, and such a signal is not easy to supply. One method is to send a "pilot" carrier, which is a small amount of the correct signal. The pilot tone is amplified until it is strong enough to accomplish the detection.

Suppose the pilot signal reaches high enough amplitude but is phase-shifted an amount θ with respect to the original carrier. We would then in our synchronous detector be performing the multiplication:

$$m\left(t\right)\cos\omega_c t\cos\left(\omega_c t+\theta\right).$$

To understand what we get, let us expand the second cosine using the identity for the sum of two angles,

$$\cos\left(\omega_c t+\theta\right)=\cos\omega_c t\cos\theta-\sin\omega_c t\sin\theta.$$

Hence, the output of the synchronous detector may be written as

$$m\left(t\right)\cos^2\omega_c t\cos\theta-m\left(t\right)\cos\omega_c t\sin\omega_c t\sin\theta=$$
$$\left(0.5\right)\left[m\left(t\right)\cos\theta\left(1-\cos2\omega_c t\right)-m\left(t\right)\sin\theta\sin2\omega_c t\right].$$

The latter two terms can be eliminated using a low-pass filter, and one is left with the original modulating signal, m(t), attenuated proportionally to the factor cos θ, so major attenuation does not appear until the phase shift approaches 90°, when the signal would vanish completely. Even this is not totally bad news, as it opens up a new technique called "quadrature amplitude modulation."

The principle of QAM, as it is abbreviated, is that entirely different modulating signals are fed to carrier signals that are 90° out of phase; we could call the carrier signals cos $\omega_c t$ and sin $\omega_c t$. The two modulating signals stay perfectly separated if there is no phase shift to the carrier signals fed to the synchronous detectors. The color signals in a color TV system are QAM'ed onto a 3.58 MHz subcarrier to be combined with the black-and-white signals, after they have been demodulated using a carrier generated in synchronism with the "color burst" (several periods of a 3.58 MHz signal), which is cleverly "piggy-backed" onto all the other signals required for driving and synchronizing a color TV receiver.

Single Sideband Suppressed Carrier

The alert engineering student may have heard the words "single sideband" and be led to wonder if we are proposing sending one more sideband than necessary. Of course it is true, and SSB–SC, as it is abbreviated, is the method of choice for "hams," the amateur radio enthusiasts who love to see night fall, when their low wattage signals can bounce between the earth and a layer of ionized atmospheric gasses 100 or so miles up until they have reached halfway around the world. It turns out that a little phase shift is not a really drastic flaw for voice communications, so the "ham" just adjusts the variable frequency oscillator being used to synchronously demodulate incoming signals until the whistles and squeals become coherent, and then he/she listens.

How can one produce single sideband? For many years it was pretty naïve to say, "Well, let's just filter one sideband out!" This would have been very naïve because, of course, one does not have textbook filters with perfectly sharp cut-offs. Recently, however, technology has apparently provided rather good "crystal lattice filters" which are able fairly cleanly to filter the extra sideband. In general,

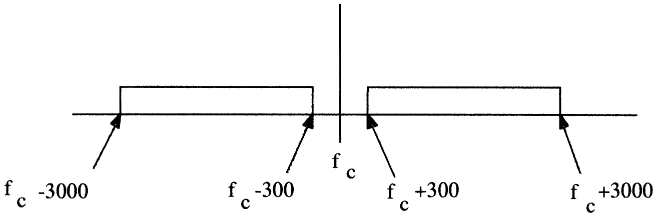

FIGURE 5.64 Double sideband spectrum for modulating signal 300–3000 Hz.

though, the single sideband problem is simplified if the modulating signal does not go to really deep low frequencies; a microphone that does not put out much below 300 Hz might have advantages, as it would leave a transition region of 600 Hz between upper and lower sidebands in which the sideband filter could have its amplitude response "roll off" without letting through much of the sideband to be discarded. Observe Fig. 5.64, showing both sidebands for a baseband signal extending only from 300 Hz to 3.0 kHz.

Another method of producing single sideband, called the "phase-shift method," is suggested if one looks at the mathematical form of just one of the sidebands resulting from tone modulation. Let us just look at a lower sideband. The mathematical form would be

$$v(t) = A\cos(\omega_c - \omega_m)t = A\cos\omega_c t\cos\omega_m t + A\sin\omega_c t\sin\omega_m t$$

Mathematically, one needs to perform DSB–SC with the original carrier and modulating signals (the cosine terms) and also with the two signals each phase shifted 90°; the resulting two signals are then added to obtain the lower sideband. Obtaining a 90° phase shift is not difficult with the carrier, of which there is only one, but we must be prepared to handle a band of modulating signals, and it is not an elementary task to build a circuit that will produce 90° phase shifts over a range of frequency. However, a reasonable job will be done by the circuit of Fig. 5.65 when the frequency range is limited (e.g., from 300 to 3000 Hz). Note that one does *not* modulate directly with the original modulation signal, but that the network uses each input frequency to generate two signals which are attenuated equal amounts and 90° away from each other. These voltages would be designated in the drawing as V_{xz} and V_{yz}. In calculating such voltages, the reader should note that there are two voltage dividers

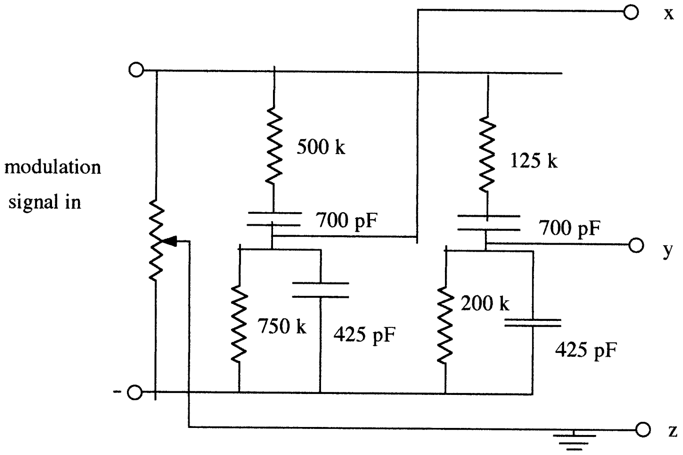

FIGURE 5.65 Audio network for single sideband modulator.

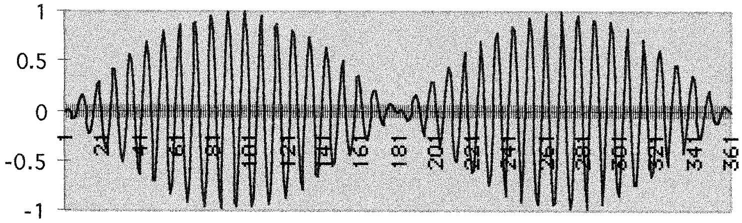

FIGURE 5.66 Double sideband suppressed carrier signal.

connected across the modulating voltage, determining V_x and V_y, and that from both of these voltages is subtracted the voltage from the center-tap to the bottom of the potentiometer. Note also that the resistance of the potentiometer is not relevant as long as it does not load down the source of modulating voltage, and that a good result has been found if the setting of the potentiometer is for 0.224 of the input voltage.

Amplitude Modulation as Double Sideband with Carrier

The budding engineer must understand that synchronous detectors are more expensive than many people can afford, and that a less expensive detection method is needed. What fills this bill much of the time is called the "envelope detector." Let us examine some waveforms, first for DSB–SC and then for a signal having a large carrier component. Figure 5.66 shows a waveform in which not very different carrier and modulating frequencies were chosen so that a spreadsheet plot would show a few details.

An ideal circuit we call an envelope detector would follow the topmost excursion of the waveform sketched here. Now, the original modulating signal was a sine wave, but the topmost excursion would be a *rectified* sinusoid, thus containing large amounts of harmonic distortion. How can one get a waveform that will be detected without distortion by an envelope detector? What was plotted was 1.0 cos ω_{ct}t cos ω_mt. We suspect we must add some amount of carrier B cos ω_ct. The sum will be

$$\phi_{AM}(t) = B\cos\omega_c t + 1.0\cos\omega_{ct} t\cos\omega_m t = \cos\omega_c t\left[B + 1.0\cos\omega_m t\right].$$

This result is what is commonly called "amplitude modulation." Perhaps the most useful way of writing the time function for an amplitude modulation signal having tone modulation at a frequency f_m follows:

$$\phi_{AM}(t) = A\cos\omega_c t\left[1 + a\cos\omega_m t\right].$$

In this expression, we can say that A is the peak amplitude of the carrier signal that would be present if there were no modulation. The total expression inside the [ ] brackets can be called the "envelope" and the factor "a" can be called the "index of modulation." As we have written it, if the index of modulation were >1, the envelope would attempt to go negative; this would make it necessary, for distortion-free detection, to use synchronous detection. "a" is often expressed as a percentage, and when the index of modulation is less than 100%, it is possible to use the simplest of detectors, the envelope detector. We will look at the envelope detector in more detail a bit later.

Modulation Efficiency

It is good news that sending a carrier along with two sidebands makes inexpensive detection using an envelope detector possible. The accompanying bad news is that the presence of carrier does not contribute *at all* to useful signal output; the presence of a carrier only leads after detection to DC, which may be filtered out at the earliest opportunity. Sometimes, as in video, the DC is needed to set the brightness level, in which case DC may need to be added back in at an appropriate level.

To express the effectiveness of a communication system in establishing an output signal-to-noise ratio, it is necessary to define a "modulation efficiency," which, in words, is simply the fraction of output power that is put into sidebands. It is easily figured if the modulation is simply one or two purely sinusoidal tones; for real-life modulation signals, one may have to express it in quantities that are less easy to visualize.

For tone modulation, we can calculate modulation efficiency by simply evaluating the carrier power and the power of all sidebands. For tone modulation, we can write:

$$\phi_{AM}(t) = A\cos\omega_c t\left[1 + a\cos\omega_m t\right] =$$

$$A\cos\omega_c t + (aA)/2\left[\cos(\omega_c + \omega_m)t + \cos(\omega_c - \omega_m t)\right].$$

Now, we have all sinusoids, the carrier, and two sidebands of equal amplitudes, so we can write the average power in terms of peak amplitudes as:

$$P = 0.5\left[A^2 + 2 \times (aA/2)^2\right] = 0.5A^2\left[1 + a^2/2\right].$$

Then modulation efficiency is the ratio of sideband power to total power, for modulation by a single tone with modulation index "a," is:

$$\eta = \frac{(aA/2)^2}{0.5A^2(1 + a^2/2)} = \frac{a^2}{2 + a^2}.$$

Of course, most practical modulation signals are not so simple as sinusoids. It may be necessary to state how close one is to overmodulating, which is to say, how close to negative modulating signals come to driving the envelope negative. Besides this, what is valuable is a quantity we shall just call "m," which is the ratio of average power to peak power for the modulation function. For some familiar waveforms, if the modulation is sinusoidal, m = 1/2. If modulation were a symmetrical square wave, m = 1.0; any kind of symmetrical triangle wave has m = 1/3. In terms of m, the modulation efficiency is

$$\eta = \frac{ma^2}{1 + ma^2}$$

The Envelope Detector

Much of the detection of modulated signals, whether the signals began life as AM or FM broadcast signals or the sound or the video of TV, is done using envelope detectors. Figure 5.68 shows the basic circuit configuration.

The input signal is of course as shown in Fig. 5.67. It is assumed that the forward resistance of the diode is 100 ohms or less. Thus, the capacitor is small enough that it gets charged up to the peak values of the high frequency signal, but then when input drops from the peak, the diode is reverse-biased so the capacitor can only discharge through R. This discharge voltage is of course given by

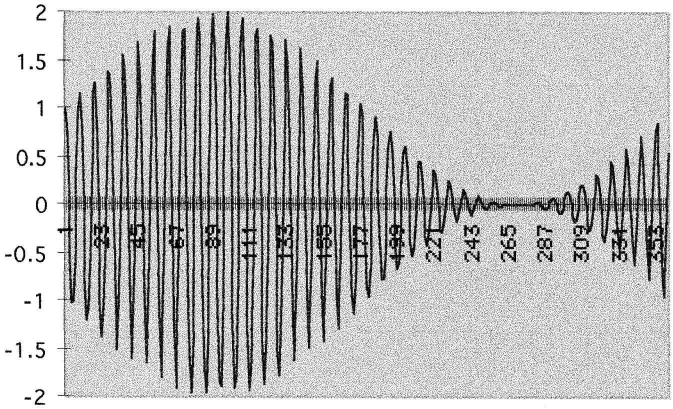

FIGURE 5.67 Amplitude-modulated signal.

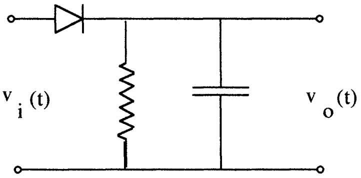

FIGURE 5.68 Simple envelope detector schematic.

$$V(0)\exp(-t/RC).$$

Now the problem in AM detection is that we must have the minimum rate of decay of the voltage be at least the maximum decay of the envelope of the modulated wave. We might write the envelope as a function of time:

$$E(t) = A(1 + a\cos\omega_{mt}t),$$

where A is the amplitude of the carrier before modulation and "a" is the index of modulation, which must be less than one for accurate results with the envelope detector. Then, when we differentiate, we get

$$\frac{dE}{dt} = -\omega_m Aa\sin(\omega_m t).$$

We want this *magnitude* to be less than or equal to the maximum magnitude of the rate of decay of a discharging capacitor, which is E(0)/RC. For what is written as E(0), we will write the instantaneous value of the envelope, and the expression becomes

$$A(1 + a\cos\omega_{mt}t) \geq RC(\omega_m aA\sin(\omega_m t)).$$

The As cancel, and we have

$$\mathrm{RC} \le \frac{1 + a\cos(\omega_m t)}{\omega_m a \sin(\omega_m t)};$$

our major difficulty occurs when the right-hand side has its minimum value.

If we differentiate with respect to $\omega_m t$, we get

$$\frac{\omega_m a \sin\left(\omega_m t \times \left(-\omega_m a \sin(\omega_m t) - \left(1 + a\cos(\omega_m t)(\omega_m)^2 a \cos \omega_m t\right)\right)\right)}{\left(\omega_m a \sin(\omega_m t)\right)^2}.$$

We set the numerator equal to zero to find its maximum. We find we have

$$-(\omega_m a)^2\left[\sin^2(\omega_m t) + \cos^2(\omega_m t)\right] - a(\omega_m)^2 \cos \omega_m t$$
$$= -(\omega_m a)^2 - a(\omega_m)^2 \cos \omega_m t = 0.$$

Hence, the maximum occurs when cos $\omega_m t = -a$, and of course by identity, at that time, sin $\omega_m t = \sqrt{1 - a^2}$.

Inserting these results into our inequality for the time constant RC, we have

$$\mathrm{RC} \le \frac{1 - a^2}{\omega_m a \sqrt{1 - a^2}} = \frac{\sqrt{1 - a^2}}{\omega_m a}.$$

Example 5.1

Suppose we say 2000 Hz is the main problem in our modulation scheme, our modulation index is 0.5, and we choose R = 10k to make it large compared to the diode forward resistance, but not *too* large. What should be the capacitor C?

Solution We use the equality now and get

$$C = \frac{\sqrt{1 - 0.5^2}}{0.5 \times 4000\pi \times 10{,}000} = 13.8 \text{ nF}.$$

Envelope Detection of SSB Using Injected Carrier

Single sideband, it might be said, is a very forgiving medium. Suppose that one were attempting synchronous detection using a carrier that was off by a Hertz or so, compared to the original carrier. Because synchronous detection works by producing sum and difference frequencies, 1 Hz error in carrier frequency would produce 1 Hz error in the detected frequency. Because SSB is mainly used for speech, it would be challenging indeed to find anything wrong with the reception of a voice one has only ever heard over a static-ridden channel. Similar results would also be felt in the following, where we add a carrier to the sideband and find that we have AM, albeit with a small amount of harmonic distortion.

Example 5.2

Starting with just an upper sideband B cos(ω_c + ω_m)t, let us add a carrier term A cos ω_c t, manipulate the total, and prove that we have an envelope to detect. First we expand the sideband term as

$$\Phi_{SSB}(t) = B[\cos\omega_c t \cos\omega_m t - \sin\omega_c t \sin\omega_m t].$$

Adding the carrier term A cos ω_c t and combining like terms, we have

$$\phi(t) = \cos\omega_c t(A + B\cos\omega_m t) - B\sin\omega_c t \sin\omega_m t.$$

In the first circuits class, we see that if we want to write a function of one frequency in the form E(t) cos (ω_c t + phase angle), the amplitude of the multiplier E is the square root of the squares of the coefficients of cos ω_ct and sin ω_ct. Thus,

$$E(t) = \sqrt{(A + B\cos\omega_m t)^2 + (B\sin\omega_m t)^2}$$
$$= \sqrt{A^2 + 2AB\cos\omega_m t + B^2(\cos^2\omega_m t + \sin^2\omega_m t)}.$$

Now, of course, the coefficient of B^2 is unity for all values of ω_mt. We find that best performance occurs if B ≪ A. Then we would have our expression for the envelope (and thus it is detectable using an envelope detector):

$$E(t) = \sqrt{A^2 + B^2 + 2AB\cos\omega_m t} = \sqrt{A^2 + B^2}\sqrt{1 + \frac{2AB}{A^2 + B^2}\cos\omega_m t}.$$

Our condition that B ≪ A allows us to say the coefficient of cos ω_mt is really small compared to unity. We use the binomial theorem to approximate the second square root: $(1 + x)^n \approx 1 + x/2 + (1/2)^2 (-1/2)x^2$ when $x \ll 1$. Using our approximation, $x \approx (2B/A) \cos \omega_m t$. In our expansion, the x term is the modulation term we were seeking, the x^2 term contributes second harmonic distortion. Using the various approximations, and stopping after we find the second harmonic (other harmonics *will* be present, of course, but in decreasing amplitudes), we have

$$\text{Detected } f(t) = B\cos\omega_m t - (1/2)(B^2/A)\cos^2(\omega_m t).$$

When we use trig identities to get the second harmonic, we get another factor of one half; the ratio of detected second harmonic to fundamental is thus (1/4)(B/A). Thus, for example, if B is just 10% of A, second harmonic is only 2.5% of fundamental.

Direct vs. Indirect Means of Generating FM

Let us first remind ourselves of basics regarding FM. We can write the time function in its simplest form as

$$\phi_{FM}(t) = A\cos(\omega_c t + \beta\sin\omega_m t).$$

Now, the alert reader might be saying, "Hold on! That looks a lot like phase modulation. If $\beta = 0$, the phase would increase linearly in time, as an unmodulated signal, but gets advanced or retarded a maximum of β." One needs to remember the definition of instantaneous frequency, which is

$$f_i = \frac{1}{2\pi}\frac{d}{dt}\left(\omega_c t + \beta \sin\omega_m t\right) = \frac{1}{2\pi}\left(2\pi f_c + \beta 2\pi f_m \cos\omega_m t\right) = f_c + \beta f_m \cos\omega_m t.$$

Thus, we can say that instantaneous frequency departs from the carrier frequency by a maximum amount βf_m, which is the so-called "frequency deviation." This has been specified as a maximum of 75 kHz for commercial FM radio but 25 kHz for the sound of TV signals.

Now, certainly, the concept of directly generating FM has an intellectual appeal to it. The problems of direct FM are mainly practical; if the very means of putting information onto a high frequency "carrier" is in varying the frequency, it perhaps stands to reason the center value of the operating frequency will not be well nailed down. Direct FM could be accomplished as in Fig. 5.69(a), but Murphy's law would be very dominant and one might expect center frequency to drift continually in one direction all morning and the other way all afternoon, or the like. This system is sometimes stabilized by having an FM detector called a discriminator tuned to the desired center frequency, so that output would be positive if frequency got high and negative for frequency low. Thus, instantaneous output could be used as an error voltage with a long time constant to push the intended center frequency toward the center, whether the average value is above or below.

The best known method of indirect FM gives credit to the man who, more than any other, saw the possibilities of FM and that its apparent defects could be exploited for superior performance, Edwin Armstrong. He started with a crystal-stabilized oscillator around 100 kHz, from which he obtained also a 90° phase-shifted version. A block diagram of just this early part of the Armstrong modulator is shown in Fig. 5.69(a).

The modulating signal is passed through an integrator before it goes into an analog multiplier, to which is also fed the *phase-shifted* version of the crystal-stabilized signal. Thus, we feed cos $\omega_c t$ and sin $\omega_c t$ sin $\omega_m t$ into a summing amplifier. The phasor diagram shows the two signals with cos $\omega_c t$ as the reference. There is a small phase shift given by $\tan^{-1}(\beta \sin \omega_m t)$ where β here gives the maximum amount of phase shift as a function of time. To see how good a job we have done, we need to expand $\tan^{-1}(x)$ in a Taylor series. We find that

$$\tan^{-1}(x) \approx x - (x)^3 / 3 + (x)^5 / 5 .$$

We see that we have a term proportional to the modulating signal (x) and others that must represent odd-order harmonic distortion, if one accounts for the fact that we have resorted to a subterfuge, using

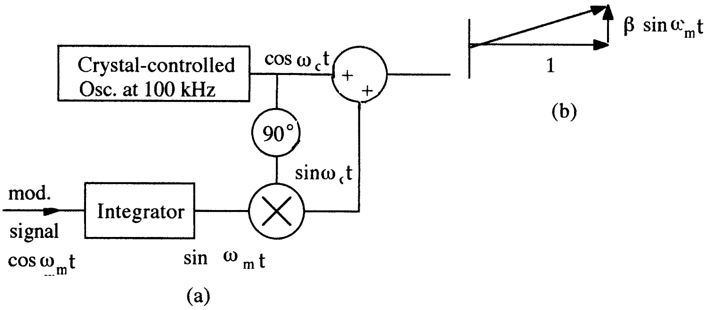

FIGURE 5.69 (a) Crystal-stabilized phase modulator; (b) phasor diagram.

a phase modulator to produce frequency modulation. Assuming that our signal finally goes through a frequency detector, we find that the amount of third harmonic as a fraction of the signal output is $\beta^2/4$. Now, in frequency modulation, the maximum amount of modulation which is permitted is in terms of frequency deviation, an amount of 75 kHz. The relation between frequency deviation and maximum phase shift is

$$\Delta f = \beta f_m,$$

where Δf is the frequency deviation, β is maximum phase shift, and f_m is modulation frequency. Since maximum modulation is defined in terms of Δf, the maximum value of β permitted will correspond to *minimum* modulation frequency. Let us do some numbers to illustrate this problem.

Example 5.3

Suppose we have a high fidelity broadcaster wishing to transmit bass down to 50 Hz with maximum third harmonic distortion of 1%. Find the maximum values of β and Δf.

Solution We have $\beta^2/4 = 0.01$. Solving for β, we get $\beta = 0.2$.

Then, $\Delta f = 0.2 \times 50$ Hz = 10 Hz.

One can recall that the maximum value of frequency deviation allowed in the FM broadcast band is 75 kHz. Thus, use of the indirect modulator has given us much lower frequency deviation than is allowed, and clearly some kind of desperate measures are required. Such are available, but do complicate the process greatly. Suppose we feed the modulated signal into an amplifier which is not biased for low distortion, that is, its Taylor series looks like

$$a_1 x + a_2 x^2 + a_3 x^3, \text{ etc.}$$

Now the squared term leads to second harmonic, the cubed one gives third harmonic, and so on. The phase-modulated signal looks like A $\cos(\omega_c t + \beta \sin \omega_m t)$ and the term a^2 x^2 *not only doubles the carrier frequency, but also the maximum phase shift* β. Thus, starting with the rather low frequency of 100 kHz, we have a fair amount of multiplying room before we arrive in the FM broadcast band 88 to 108 MHz. Unfortunately, we may need different amounts of multiplication for the carrier frequency than we need for the depth of modulation. Let's carry on our example and see the problems that arise. First, if we wish to go from

$$\Delta f = 10 \text{ Hz to } 75{,}000 \text{ Hz},$$

that leads to a total multiplication of 75,000/10 = 7500.

The author likes to say we are limited to frequency doublers and triplers. Let's use as many triplers as possible; we divide the 7500 by 3 until we get close to an even power of 2:

$$7500/3 = 2500;\ \ 2500/3 = 833,\ \ 833/3 = 278;\ \ 278/3 \approx 93,\ \ 93/3 = 31,$$

which is very close to $32 = (2)^5$.

So, to get our maximum modulation index, we need five each triplers and doublers. However, 7500 × 0.1 MHz = 750 MHz, and we have missed the broadcast band by about 7 times. One more thing we need is a mixer, after a certain amount of multiplication. Let's use all the doublers and one tripler to get a multiplication of 32 × 3 = 96, so the carrier arrives at 9.6 MHz. Suppose our final carrier frequency is 90.9 MHz, and because we have remaining to be used a multiplication of $3^4 = 81$, what comes out of the mixer must be

$$90.9/81 - 1.122\ \text{MHz.}$$

To obtain an output of 1.122 MHz from the mixer, with 9.6 MHz going in, we need a local oscillator of either 10.722 or 8.478 MHz. Note that this local oscillator needs a crystal control also, or the eventual carrier frequency will wander about more than is allowed.

Quick-and-Dirty FM Slope Detection

A method of FM detection that is barely respectable, but surprisingly effective, is called "slope detection." The principle is to feed an FM signal into a tuned circuit, not right at the resonant frequency but rather somewhat off the peak. Therefore, the frequency variations due to the modulation will drive the signal up and down the resonant curve, producing simultaneous amplitude variations, which then can be detected using an envelope detector. Let us just take a case of FM and a specific tuned circuit and find the degree of AM.

Example 5.4

We have an FM signal centered at 10.7 MHz, with frequency deviation of 75 kHz. We have a purely parallel resonant circuit with a Q = 30, with resonant frequency such that 10.7 MHz is at the lower half-power frequency. Find the output voltage for Δf = +75 kHz and for –75 kHz.

Solution When we operate close to resonance, adequate accuracy is given by

$$V_o = \frac{V_i}{1 + j2Q\delta'}$$

where δ is the fractional shift of frequency from resonance. If now, 10.7 MHz is the lower half-power point, we can say that $2Q\delta = 1$.

$$\text{Hence, } \delta = 1/(2 \times 30) = (f_o - 10.7\ \text{MHz})/f_o;\ f_o = 10.881\ \text{MHz.}$$

Now, we evaluate the transfer function at 10.7 MHz ± 75.kHz.

We defined it as 0.7071 at 10.7 MHz. For 10.7 + 0.075 MHz, $\delta = (10.881 - 10.775)/\ 10.881 = 9.774 \times 10^{-3}$, and the magnitude of the transfer function is $|1/(1 + j60\delta)| = 0.8626$.

Because the value was 0.7071 for the unmodulated wave, the modulation index in the positive direction would be

$$(0.8624 - 0.7071)/0.7071 = 0.2196 \text{ or } 21.96\%.$$

For (10.7 – 0.075) MHz, $\delta = (10.881 - 10.625)/10.881 = 0.02356$, and the magnitude of the transfer function is $|1/(1 + j60)| = 0.5775$. The modulation index in the negative direction is (0.7071 – 0.5775)/0.7071 = 18.32%. So, modulation index is not the same for positive as for negative indices. The consequence of such asymmetry is that this process will be subject to harmonic distortion, which is why this process is not quite respectable.

Lower Distortion FM Detection

We will assume that the reader has been left wanting an FM detector that has much better performance than the slope detector. A number of more complex circuits have a much lower distortion level than the slope detector. One, called the Balanced FM Discriminator, is shown in Fig. 5.70.

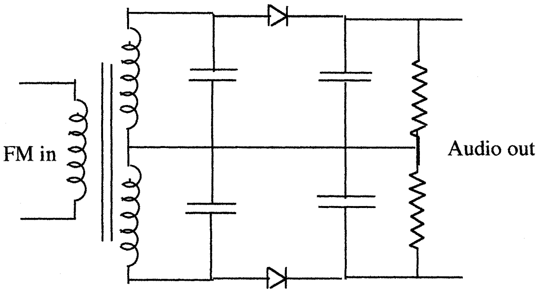

FIGURE 5.70 Balanced FM discriminator.

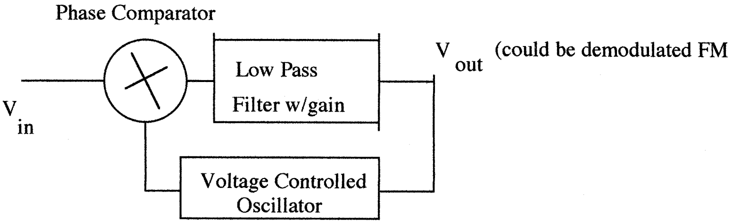

FIGURE 5.71 Basic phase-locked loop.

Basically, we may consider that the circuit contains two "stagger-tuned" resonant circuits, i.e., they are tuned equidistant on opposite sides of the center frequency, connected back to back. The result is that the nonlinearity of the resonant circuits balance each other out, and the FM detection can be very linear. The engineer designing an FM receiving system has a relatively easy job to access such performance; all that he/she must do is to spend the money to obtain high-quality components.

Phase-Locked Loop

The phase-locked loop is an assembly of circuits or systems that perform a number of functions to accomplish several operations, any one or more of the latter, perhaps being useful and to be capitalized upon. If one looks at a simple block diagram, one will see something like Fig. 5.71.

Thus, one function that will always be found is called a "voltage-controlled oscillator;" the linking of these words means that there is an oscillator which would run freely at some frequency, but that if a non-zero DC voltage is fed into a certain input, the frequency of oscillation will shift to one determined by that input voltage. Another function one will always find (although the nomenclature might vary somewhat) is "phase-comparison." The phase "comparator" will usually be followed by some kind of low-pass filter. Of course, if a comparator is to fulfill its function, it requires two inputs — the phases of which to compare. This operation might be accomplished in various ways; however, one method which might be understood from previous discussions is the analog multiplier. Suppose an analog multiplier receives the inputs cos ωt and sin (ωt + ϕ); their product has a sine and a cosine. Now, a trigonometric identity involving these terms is

$$\sin A \cos B = 0.5\left[\sin\left(A+B\right)+\sin\left(A-B\right)\right].$$

Thus, the output of a perfect analog multiplier will be $0.5[\sin(2\omega+\phi)+\sin\phi]$. A low-pass filter following the phase comparator is easily arranged; therefore, one is left with a DC term, which, if it is fed to the VCO in such a polarity as to provide negative feedback, will "lock" the VCO to the frequency of the input signal with a fixed phase shift of 90°.

Phase-locked loops (abbreviated PLL) are used in a wide variety of applications. Many of the applications are demodulators of one sort or another, such as synchronous detectors for AM, basic FM, FM–stereo detectors, and in very precise oscillators known as "frequency synthesizers." One of the early uses seemed to be the detection of weak FM signals, where it can be shown that they extend the threshold of usable weak signals a bit.[1] This latter facet of their usefulness seems not to have made a large impact, but the other aspects of PLL usefulness are very commonly seen.

Digital Means of Modulation

The sections immediately preceding have been concerned with rather traditional analog methods of modulating a carrier. While the beginning engineer can expect to do little or no design in analog communication systems, they serve as an introduction to the digital methods which most certainly will dominate the design work early in the 21st century. Certainly, analog signals will continue to be generated, such as speech, music, and video; however, engineers are finding it so convenient to do digital signal processing that many analog signals are digitized, processed in various performance-enhancing ways, and only restored to analog format shortly before they are fed to a speaker or picture tube. Digital signals can be transmitted in such a way as to use extremely noisy channels. Not long ago, the nightly news brought us video of the Martian landscape. The analog engineer would be appalled to know the number representing traditional signal-to-noise ratio for the Martian signal. The detection problem is greatly simplified because the digital receiver does not need at each instant to try to represent which of an infinite number of possible analog levels is correct; it simply asks, was the signal sent a one or a zero? *That* is simplicity.

Several methods of digital modulation might be considered extreme examples of some kind of analog modulation. Recall amplitude modulation. The digital rendering of AM is called "amplitude shift keying," abbreviated ASK.

What this might look like on an oscilloscope screen is shown in Fig. 5.72. For example, we might say that the larger amplitude signals represent the logic ones and smaller amplitudes represent logic zeroes. Thus, we have illustrated the modulation of the data stream 10101. If the intensity of modulation were carried to the 100% level, the signal would disappear completely during the intervals corresponding to zeroes. The 100% modulation case is sometimes called on–off keying and abbreviated OOK. The latter case has one advantage if this signal were nearly obscured by large amounts of noise; it is easiest for the digital receiver to distinguish between ones and zeroes if the difference between them is maximized. That is, however, only one aspect of the detection problem. It is also often necessary to know the timing of the bits, and for this one may use the signal to synchronize the oscillator in a phase-locked loop; if, for

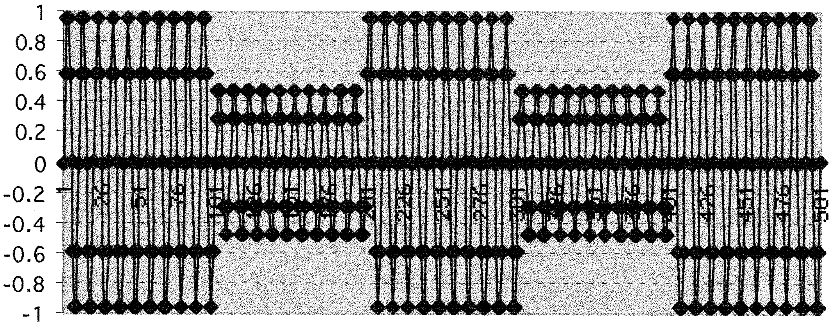

FIGURE 5.72 ASK (amplitude shift keying).

[1] Taub, H. and Schilling, D.L. *Principles of Communication Circuits,* 2nd Edition, McGraw-Hill, New York, 1986, 426–427.

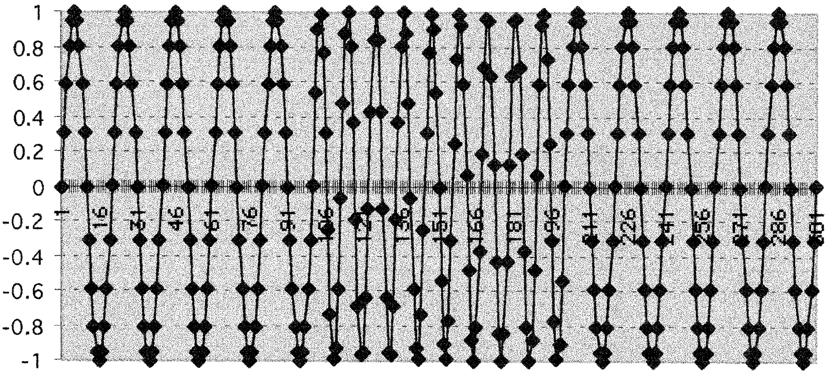

FIGURE 5.73 Frequency shift keying.

50% of the time, there is zero signal by which to be synchronized, the oscillator may drift significantly. In general, a format for digital modulation in which the signal may vanish utterly at intervals is to be adopted with caution and with full cognizance of one's sync problem. Actually, amplitude shift keying is not considered a very high performance means of digital signaling, in much the same was that AM is not greatly valued as a quality means of analog communication. What is mainly used is one or the other of the following methods.

Frequency Shift Keying

Frequency shift keying (abbreviated FSK) can be used in systems having very little to do with high data rate communications; for years it has been the method used in the simple modems one first used to communicate with remote computers. For binary systems, one just sent a pulse of one frequency for a logic one and a second frequency for a logic zero. If one was communicating in a noisy environment, the two signals would be orthogonal, which meant that the two frequencies used were separated by at least the data rate. Now, at first the modem signals were sent over telephone lines which were optimized for voice communications, and were rather limited for data communication. Suppose we consider that for ones we send a 1250 Hz pulse and for zeroes, we send 2250 Hz. In a noisy environment one ought not to attempt sending more than 1000 bits per second (note that 1000 Hz is the exact difference between the two frequencies being used for FSK signaling). Let us instead send at 250 bps. Twelve milliseconds of a 101 bit stream would look as in Figure 5.73.

It is not too difficult to imagine a way to obtain FSK. Assuming one does have access to a VCO, one simply feeds it two different voltage levels for ones and for zeroes. The VCO output is the required output.

Phase Shift Keying

Probably the most commonly used type of digital modulation is some form of phase shift keying. One might simply say there is a carrier frequency f_c and that logic zeroes will be represented by $-\sin 2\pi f_c t$, logic ones by $+\sin 2\pi f_c t$. If the bit rate is 40% of the carrier frequency, the data stream 1010101010 might look as in Fig. 5.74.

In principle, producing binary phase shift keying ought to be fairly straightforward, if one has the polar NRZ (nonreturn to zero, meaning a logic one could be a constant positive voltage for the duration of the bit, zero being an equal negative voltage) bit stream. If then, the bit stream and a carrier signal are fed into an analog multiplier, the output of the multiplier could indeed be considered $\pm\cos \omega_c t$, and the modulation is achieved.

Correlation Detection

Many years ago, the communications theorists came up with the idea that if one could build a "matched filter," that is, a special filter designed with the bit waveform in mind, one would startlingly increase the

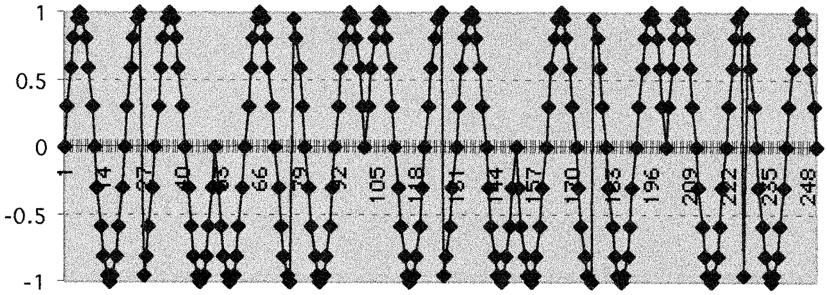

FIGURE 5.74 Phase shift keying.

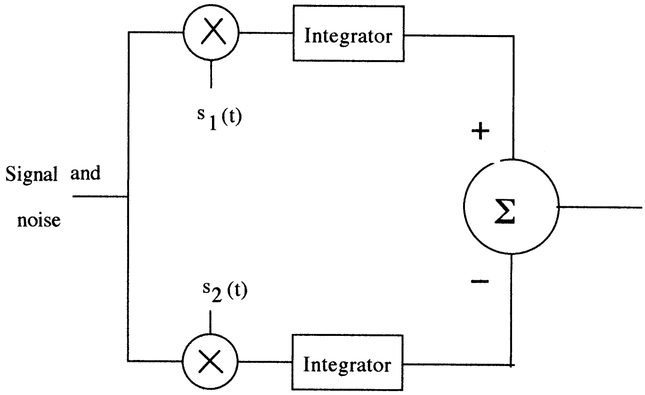

FIGURE 5.75 Correlation detector.

signal-to-noise ratio of the detected signal. Before long, a practically minded communications person had the bright idea that a correlation detector would do the job, at least for rectangular bits. For some reason, as one explains this circuit, one postulates two signals, $s_1(t)$ and $s_2(t)$, which represent, respectively, the signals sent for logic ones and zeroes. The basics of the correlation detector are shown in Fig. 5.75.

Now, a key consideration in the operation of the correlation detector is bit synchronization. It is crucial that the signal $s_1(t)$ be lined up perfectly with the bits being received. Then, the top multiplier "sees" sin $\omega_c t$ coming in one input, and ±sin $\omega_c t$ + noise coming in the other, depending upon whether a one or a zero is being received. If it happens that a one is being received, the multiplier is asked to multiply sin $\omega_c t$(sin $\omega_c t$ + noise). Of course,

$$\sin^2 \omega_c(t) = (1/2)(1 + \cos 2\omega_c t).$$

In the integrator, this is integrated over one bit duration, giving a quantity said to be the energy of one bit. The integrator might also be considered to have been asked to integrate n(t) sin $\omega_c t$, where n is the noise signal. However, the nature of noise is that there is no net area under the curve of its waveform, so considering integration to be a summation, the noise output out of the integrator would simply be the last instantaneous value of the noise voltage at the end of a bit duration, whereas the signal output was bit energy, if the bit synchronization is guaranteed. Meanwhile, the output of the bottom multiplier was the *negative* of the bit energy, so with the signs shown, the output of the summing amplifier is twice the bit energy. Similar reasoning leads to the conclusion that if the instantaneous signal being received were a zero, the summed output would be *minus* twice the bit energy. It takes a rather substantial bit of theory to show that the noise output from the summer is *noise spectral density.* The result may be summarized that the correlation detector can "pull a very noisy signal out of the mud." And, we should

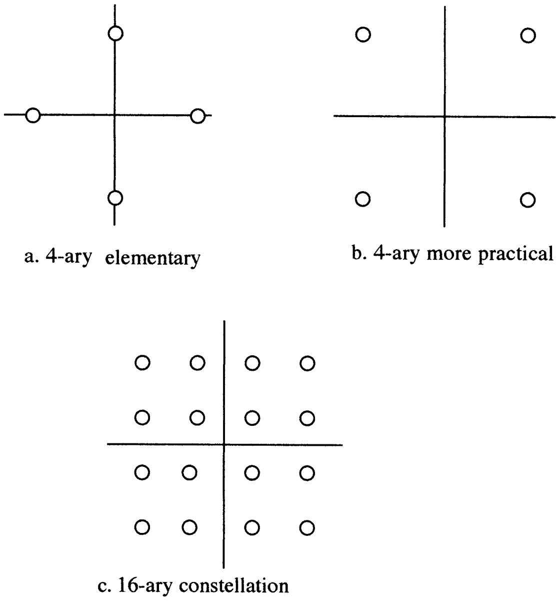

FIGURE 5.76 Constellation showing carrier amplitudes and phase for M'ary signals.

assert at this point that the correlation detector can perform wonders for any one of the methods of digital modulation mentioned up to this point.

Digital QAM

Once the engineer has produced carrier signals that are 90° out of phase with each other, there is no intrinsic specification that the modulation must be analog, as is done for color TV. As a start toward extending the capabilities of PSK, one might consider that one sends bursts of several periods of $\pm\cos \omega_c t$ or $\pm\sin \omega_c t$. This is sometimes called "4-ary" transmission, meaning that there are four different possibilities of what might be sent. Thus, whichever of the possibilities is sent, it may be considered to contain two bits of information. It is a method by which more information may be sent without demanding any more bandwidth, because the duration of the symbol being sent may be no longer or shorter than it was when one was doing binary signaling, sending, for example, simply $\pm\cos \omega_c t$. This idea is sometimes represented in a "constellation," which, for the case we just introduced, would look like part a of Fig. 5.76. However, what is more often done is as shown in Fig. 5.76b, where it could be said that one is sending $\pm\cos(\omega_c t + 45°)$ or $\pm\cos(\omega_c t + 135°)$. It seems as though this may be easier to implement than the case of part a; however, the latter scheme lends itself well to sending 4 bits in a single symbol, as in Fig. 5.76c.

Strictly speaking, one might consider "a" to be the constellation for 4-ary PSK. This leads also to the implication that one could draw a circle with "stars" spaced 45° apart on it and one would have the constellation for 8-ary PSK. The perceptive or well-informed reader might have the strong suspicion that crowding more points on the circle makes it possible to have more errors in distinguishing one symbol from adjacent ones, and would be correct in this suspicion. Hence, M'ary communication probably more commonly uses "b" or "c," which should be considered forms of QAM.

5.6 Power Amplifier Circuits

Mark Bloom

The Power Amplifier (PA) is typically the last stage in a transmitter system. Its role is to provide the final amplification of signal power to a level that is large enough for microwave propagation through an appropriate

Riddle, Alfy et al. "Passive Technologies"
The RF and Microwave Handbook
Editor in Chief Mike Golio
Boca Raton: CRC Press LLC,2001

6

Passive Technologies

Alfy Riddle
Macallan Consulting

Michael B. Steer
North Carolina State University

S. Jerry Fiedziuszko
Space Systems/LORAL

Karl R. Varian
Raytheon

Donald C. Malocha
University of Central Florida

Michael E. Majerus
Motorola

David Anderson
Maury Microwave Corporation

James B. West
Rockwell Collins

Jeanne S. Pavio
Motorola

6.1 Passive Lumped Components

Alfy Riddle

Lumped components such as resistors, capacitors, and inductors make up most of the glue that allows microwave discrete transistors and integrated circuits to work. Lumped components provide impedance matching, attenuation, filtering, DC bypassing, and DC blocking. More advanced lumped components such as chokes, baluns, directional couplers, resonators, and EMI filters are a regular part of RF and microwave circuitry. Figure 6.1 shows examples of lumped resistors, capacitors, inductors, baluns, and directional couplers. Surface mount techniques and ever-shrinking package sizes now allow solderable lumped components useful to 10 GHz.[1]

As lumped components are used at higher and higher frequencies, the intrinsic internal parasitics, as well as the package and mounting parasitics play a key role in determining overall circuit behavior both in and out of the desired frequency range of use. Mounting parasitics come from excess inductance caused by traces between the component soldering pad and a transmission line, and excess capacitance from relatively large mounting pads and the component body.

Resistors

Figure 6.2 shows a typical surface mount resistor. These resistors use a film of resistive material deposited on a ceramic substrate with solderable terminations on the ends of the component. Individual surface mount resistors are available in industry standard sizes from over 2512 to as small as 0201. The package size states the length and width of the package in hundredths of an inch. For example an 0805 package is 8 hundredths long by 5 hundredths wide or 80 mils by 50 mils, where a mil is 1/1000th of an inch. Some manufacturers use metric designations rather than English units, so an 0805 package would be 2 mm by 1.2 mm or a 2012 package. The package size determines the intrinsic component parasitics to the first order, and in the case of resistors determines the allowable dissipation. For resistors the most important specifications are power dissipation and tolerance of value.

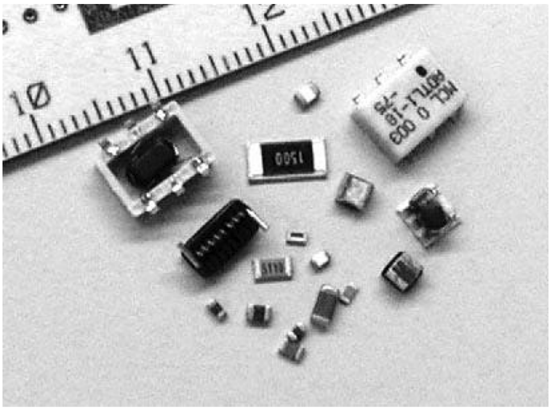

FIGURE 6.1 Assorted surface mount lumped components.

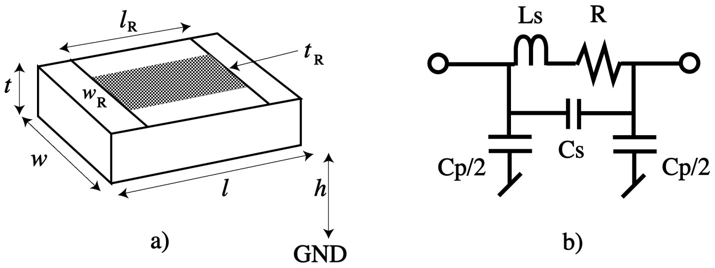

FIGURE 6.2 Surface mount resistor: a) component, b) schematic.

Resistance

Chip resistors have plated, wrap-around end contacts that overlap the resistive material deposited on the top surface of the ceramic carrier. Circuits built from film on alumina can have multiple thin or thick film resistors on one substrate. The same principles for determining resistance, heat dissipation limits, parasitic inductance, and parasitic capacitance apply to both chips and thin film circuits.[2] Standard chip resistors come in 10% and 1% tolerances, with tighter tolerances available.

The resistive material is deposited in a uniform thickness, t_R, and has a finite conductivity, σ_R. The material is almost always in a rectangle that allows the resistance to be calculated by Eq. (6.1).

$$R = l_R \Big/ \left(\sigma_R\, w_R\, t_R\right) = R_p\, l_R \big/ w_R \tag{6.1}$$

Increasing the conductivity, material thickness, or material width lowers the resistance, and the resistance is increased by increasing the resistor length, l_R. Often it is simplest to combine the conductivity and thickness into $R_p = 1/(\sigma_R\, t_R)$, where any square resistor will have resistance R_p. Resistor physical size determines the heat dissipation, parasitic inductance and capacitance, cost, packing density, and mounting difficulty.

Heat Dissipation

Heat dissipation is determined mostly by resistor area, although a large amount of heat can be conducted through the resistor terminations.[3] Generally, the goal is to keep the resistor film below 150 degrees C and the PCB temperature below 100 degrees C. Derating curves are available from individual manufacturers with a typical curve shown in Fig. 6.3. Table 6.1 shows maximum power dissipation versus size for common surface mount resistors.

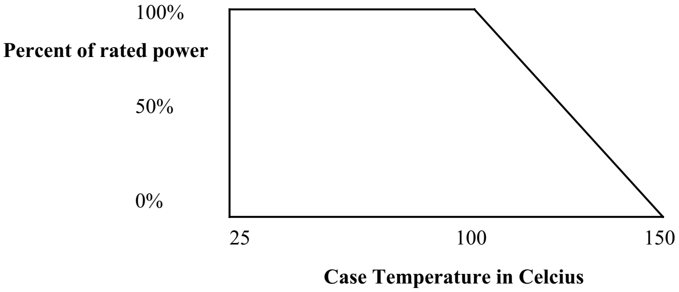

FIGURE 6.3 Surface mount resistor derating curve.

TABLE 6.1 Maximum Resistor Dissipation vs. Size

Resistor Size	P_{Max}(Watts)
2512	1
2510	0.5
1210	0.25
1206	0.125
805	0.1
603	0.0625
402	0.0625

Intrinsic Inductive Parasitics

The resistor length and width determine its effective series inductance. This inductance can be computed from a transmission line model or as a ribbon inductor if the resistor is far enough above the ground plane. The ribbon inductor equation is given in Eq. (6.2), with all units MKS.[20]

$$L_S = 0.125\, l_R \left(\ln\left[2\, l_R / w_R \right] + 0.5 + 2\, w_R / 9\, l_R \right) \mu\text{H} \tag{6.2}$$

For example, an 0805 package has an inductance of about 0.7 nH. If the resistor width equals the transmission line width, then no parasitic inductance will be seen because the resistor appears to be part of the transmission line.

Intrinsic Capacitive Parasitics

There are two types of capacitive parasitics. First, there is the shunt distributed capacitance to the ground plane, C_P. The film resistor essentially forms an RC transmission line and is often modeled as such. In this case, a first order approximation can be based on the parallel plate capacitance plus fringing of the resistor area above the ground plane, as shown in Eq. (6.3). The total permittivity, ε, is a product of the permittivity of free space, ε_O, and the relative permittivity, ε_R. An estimate for effective width, w_E, is $1.4{*}w_R$, but this depends on the ground plane distance, h, and the line width, w. A more accurate method would be to just use the equivalent microstrip line capacitance.

$$C_P = \varepsilon\, w_E\, l_R / h \tag{6.3}$$

For an 0805 resistor on 0.032" FR4 the capacitance will be on the order of 0.2 pF. As with the inductance, when the resistor has the same width as the transmission line, the line C per unit length absorbs the parasitic capacitance. When the resistor is in shunt with the line, the parasitic capacitance will be seen, often limiting the return loss of a discrete pad.

An additional capacitance is the contact-to-contact capacitance, C_S. This capacitance will typically only be noticed with very high resistances. Also, this capacitance can be dominated by mounting parasitics such as microstrip gap capacitances. C_S can be approximated by the contact area, the body length, and the body dielectric constant as in a parallel plate capacitor.

Capacitors

Multilayer chip capacitors are available in the same package styles as chip resistors. Standard values range from 0.5 pF up to microfarads, with some special products available in the tenths of picofarads. Parallel plate capacitors are available with typically lower maximum capacitance for a given size. Many different types of dielectric materials are available, such as NPO, X7R, and Z5U. Low dielectric constant materials, such as NPO, usually have low loss and either very small temperature sensitivity, or well-defined temperature variation for compensation, as shown in Table 6.2. Higher dielectric constant materials, such

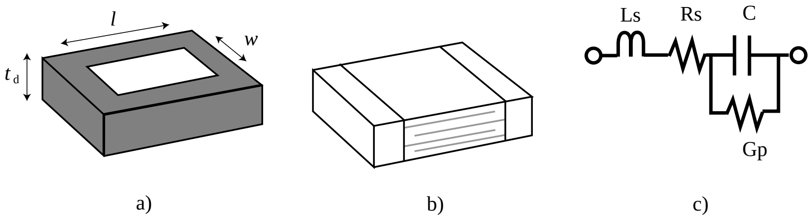

FIGURE 6.4 Capacitor styles and schematic: (a) parallel plate, (b) multilayer, and (c) schematic.

as X7R and Z5U, vary more with temperature than NPO. Z5U will lose almost half its capacitance at very low and very high temperatures. Higher dielectric constant materials, such as X7R and Z5U, also have a reduction in capacitance as voltage is applied.[5,23] The critical specification for these capacitors is the voltage rating. Secondary specifications include temperature stability, Q, tolerance, and equivalent series resistance (ESR).

Parallel Plate

Parallel plate capacitors, as shown in Fig. 6.4a, can use a thin dielectric layer mounted on a low resistance substrate such as silicon, or they can be a thick ceramic with plated terminations on top and bottom. These capacitors can be attached by soldering or bonding with gold wire. Some capacitors come with several pads, each pad typically twice the area of the next smaller, which allows tuning. These capacitors obey the parallel plate capacitance equation below.

$$C = \varepsilon w l / t_d \tag{6.4}$$

Parasitic resistances, R_S, for these capacitors are typically small and well controlled by the contact resistance and the substrate resistance. Parasitic conductances, G_P, are due to dielectric loss. These capacitors have limited maximum values because of using a single plate pair. The voltage ratings are determined by the dielectric thickness, t_d, and the material type. Once the voltage rating and material are chosen, the capacitor area determines the maximum capacitance. The parasitic inductance of these capacitors, which determines their self-resonance frequency, is dominated by the wire connection to the top plate. In some cases these capacitors are mounted with tabs from the top and bottom plate. When this occurs, the parasitic inductance will be the length of the tab from the top plate to the transmission line, as well as the length of the capacitor acting as a coupled transmission line due to the end launch from the tab.

Multilayer Capacitors

Multilayer chip capacitors are a sandwich of many thin electrodes between dielectric layers. The end terminations connect to alternating electrodes, as shown in Fig. 6.4b. A wide variety of dielectric materials are available for these capacitors and a few typical dielectric characteristics are given in Table 6.2.[23]

TABLE 6.2 Chip Capacitor Dielectric Material Comparison

Type	ε_R	Temp. Co. (ppm/degC)	Tol (%)	Range (pF in 805)	Voltage Coeff. (%)
NPO	37	0+/–30	1–20	0.5 p–2200 p	0
4	205	–1500+/–250	1–20	1 p–2200 p	0
7	370	–3300+/–1000	1–20	1 p–2200 p	0
Y	650	–4700+/–1000	1–20	1 p–2200 p	0
X7R	2200	+/–15%	5–20	100 p–1 μ	+0/–25
Z5U	9000	+22/–56%	+80/–20	0.01 μ–0.12 μ	+0/–80

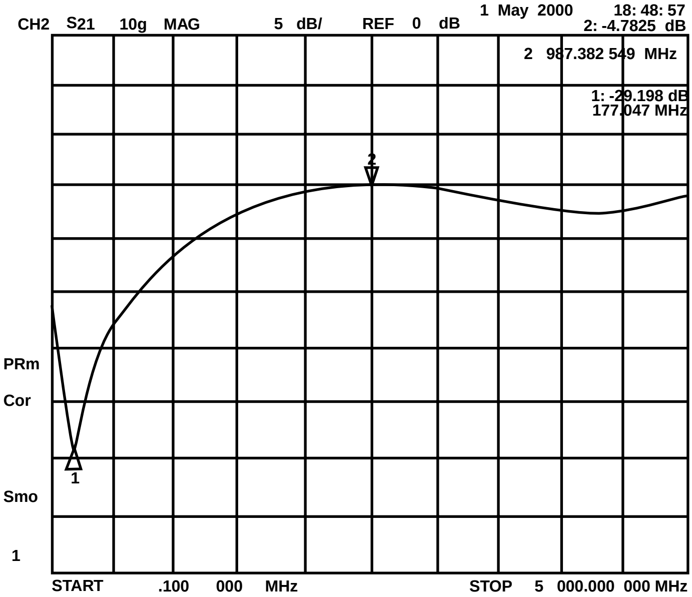

FIGURE 6.5 S21 of a shunt 0805 1000 pF multilayer capacitor, as if used for bypassing.

Table 6.2 shows that critical capacitors will have to use NPO dielectric (or alumina) because of tolerance and stability. DC blocking and bypass capacitors will often use X7R or Z5U dielectrics, but these dielectrics must be used with the knowledge that their capacitance varies significantly with temperature and has a voltage dependent nonlinearity.

$$C_P = \left(n-1\right)\varepsilon w_P l / t_L \tag{6.5}$$

Multilayer capacitors have a more complicated structure than parallel plate capacitors. Their capacitance is given by Eq. (6.5), where t_L is the dielectric layer thickness and w_P is the plate width. The series resistance of the capacitor, Rs, is determined by the parallel combination of all the plate resistance and the conductive loss, Gp, is due to the dielectric loss. Often the series resistance of these capacitors dominates the loss due to the very thin plate electrodes.

By using the package length inductance, as was given in Eq. (6.2), the first series resonance of a capacitor can be estimated. The schematic of Fig. 6.4c only describes the first resonance of a multilayer capacitor. In reality many resonances will be observed as the multilayer transmission line cycles through quarter- and half-wavelength resonances due to the parallel coupled line structure, as shown in Fig. 6.5.[4] The 1000 pF capacitor in Fig. 6.5 has a series inductance of 0.8 nH and a series resistance of 0.8 ohms at the series resonance at 177 MHz. The first parallel resonance for the measured capacitor is at 3 GHz. The equivalent circuit in Fig. 6.4c does not show the shunt capacitance to ground, C_P, caused by mounting the chip capacitor on a PCB. C_P may be calculated just as it was for a chip resistor in the section on Intrinsic Capacitive Parasitics. The Qs for multilayer capacitors can reach 1000 at 1 GHz.

Printed Capacitors

Printed capacitors form very convenient and inexpensive small capacitance values because they are printed directly on the printed circuit board (PCB). Figure 6.6 shows the layout for gap capacitors and interdigital capacitors. The capacitance values for a gap capacitor are very low, typically much less than 1 pF, and estimated by Eq. (6.6).[6] Gap capacitors are best used for very weak coupling and signal sampling because they are not particularly high Q. Equation (6.6) can also be used to estimate coupling between two circuit points to make sure a minimum of coupling is obtained.

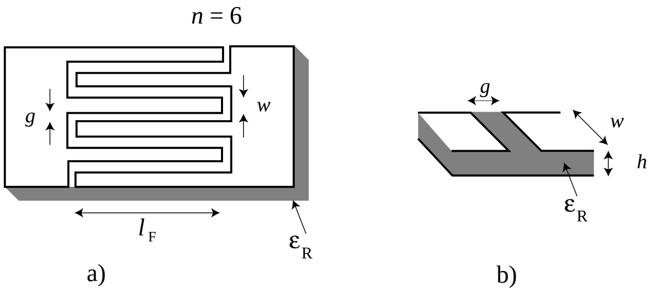

FIGURE 6.6 Printed capacitors: (a) Gap capacitor; (b) interdigital capacitor.

$$C_G = \varepsilon_O \varepsilon_R w \left(\ln\left[0.25 + \left(h/g\right)^2\right] + g/h\,\mathrm{Tan}^{-1}\left[2h/g\right] \right) \Big/ \left(2\pi\right) \qquad (6.6)$$

Interdigital capacitors, shown in Fig. 6.6a are a planar version of the multilayer capacitor. These capacitors have medium Q, are accurate, and are typically less than 1 pF. These capacitors can also be tuned by cutting off fingers. Equation (6.7) gives an estimate of the interdigital capacitance using elliptic functions, K.[7] Because interdigital capacitors have a distributed transmission line structure, they will show multiple resonances as frequency increases. The first resonance occurs when the structure is a quarter wavelength. The Q of this structure is limited by the current crowding at the thin edges of the fingers.

$$C_I = \varepsilon_O \left(1+\varepsilon_R\right)\left(n-1\right) l_F\, K\left[\mathrm{Tan}\left(w\pi \big/ \left(4\left(w+g\right)\right)\right)^4\right] \Big/ K\left[1-\mathrm{Tan}\left(w\pi \big/ \left(4\left(w+g\right)\right)\right)^4\right] \qquad (6.7)$$

Inductors

Inductors are typically printed on the PCB or surface mount chips. Important specifications for these inductors are their Q, their self-resonance frequency, and their maximum current. While wire inductors have their maximum current determined by the ampacity of the wire or trace, inductors made on ferrite or iron cores will saturate the core if too much current is applied. Just as with capacitors, using the largest inductance in a small area means dealing with the parasitics of a nonlinear core material.[8,22]

Chip Inductors

Surface mount inductors come in the same sizes as chip resistors and capacitors, as well as in air-core "springs." "Spring" inductors have the highest Q because they are wound from relatively heavy gauge wire, and they have the highest self-resonance because of their air core. Wound chip inductors, shown in Fig. 6.7a, use a fine gauge wire wrapped on a ceramic or ferrite core. These inductors have a mediocre

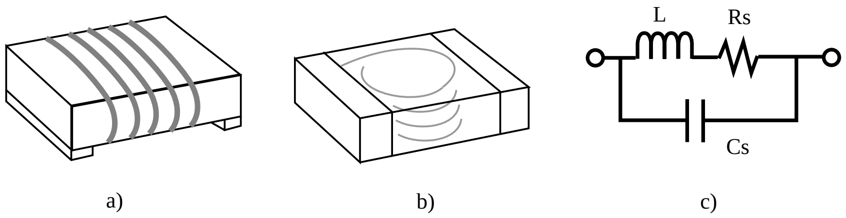

FIGURE 6.7 Chip inductors: (a) wound; (b) multilayer; and (c) schematic.

Q of 10 to 100 and a lowered self-resonance frequency because of the dielectric loading of the ceramic or ferrite core. However, these inductors are available from 1 nH to 1 mH in packages from 402 to 1812. The chip inductors shown in Fig. 6.7b use a multilayer ceramic technology, although some planar spiral inductors are found in chip packages. Either way, these inductors typically have lower Q than wound inductors, but Qs can still reach 100. Multilayer chip inductors use 805 and smaller packages with a maximum inductance of 470 nH. Although the self-resonance frequency of these inductors is high because of the few turns involved, the dielectric loading of the sandwich makes the resonance lower than that of an equivalent "spring" or even a wound inductor, as shown in Table 6.3 and Fig. 6.8. The solenoid formula given in Eq. (6.8) uses MKS units and describes both wound and "spring" inductors.[10] In Eq. (6.8), n is the number of turns, d is the coil diameter, and l is the coil length.

$$L = 9.825\, n^2 d^2 \big/ \left(4.5\, d + 10\, l\right)\ \mu\text{H} \tag{6.8}$$

Figure 6.8 shows an S21 measurement of several series inductors. The inductors are mounted in series to emphasize the various resonances. The 470 nH wound inductor used a 1008 package and had a first parallel resonance at 600 MHz. The 470 nH chip inductor used an 805 package and had a first parallel resonance of 315 MHz. The chip inductor shows a slightly shallower first null, indicating a higher series resistance and lower Q. Both inductors had multiple higher order resonances. The chip inductor also showed less rejection at higher frequencies. Figure 6.8b shows the S21 of a series "spring" inductor with a first parallel resonance of 3 GHz. No higher modes of the "spring" inductor can be seen because of the limited bandwidth of the network analyzer, only a fixture resonance is shown around 4 GHz. Table 6.3 shows a matrix of typical "spring," wound, and chip inductor capability.

Current Capability

Chip inductors have limited current-carrying capability. At the very least, the internal conductor size limits the allowable current. When the inductor core contains ferrite or iron, magnetic core saturation will limit the useful current capability of the inductor, causing the inductance to decrease well before conductor fusing takes place.

$$Q = \omega\, L \big/ Rs \tag{6.9}$$

Parasitic Resistance

The inductor Q is determined by the frequency, inductance, and effective series resistance as shown in Eq. (6.9). The effective series resistance, Rs, comes from the conductor resistance and the core loss when a magnetic core is used. The conductor resistance is due to both DC and skin effect resistance as given by Eqs. (6.1) and (6.10).[9]

$$R_{\text{SKIN}} = l_R \big/ \left(\sigma_R\, \rho_R\, \delta\right), \tag{6.10}$$

where ρ_R is the perimeter of the wire and δ is the skin depth,

$$\delta = \text{Sqrt}\left[\left(2.5\text{ E }6\right) \big/ \left(\sigma_R\, f\, \pi^2\right)\right]. \tag{6.11}$$

When the skin depth is less than half the wire thickness, Eq. (6.10) should be used. For very thin wires the DC resistance is valid up to very high frequencies. For example, 1.4-mil thick copper PCB traces will show skin effect at 14 MHz, while 5 microns of gold on a thin film circuit will not show skin effect until almost 1 GHz.

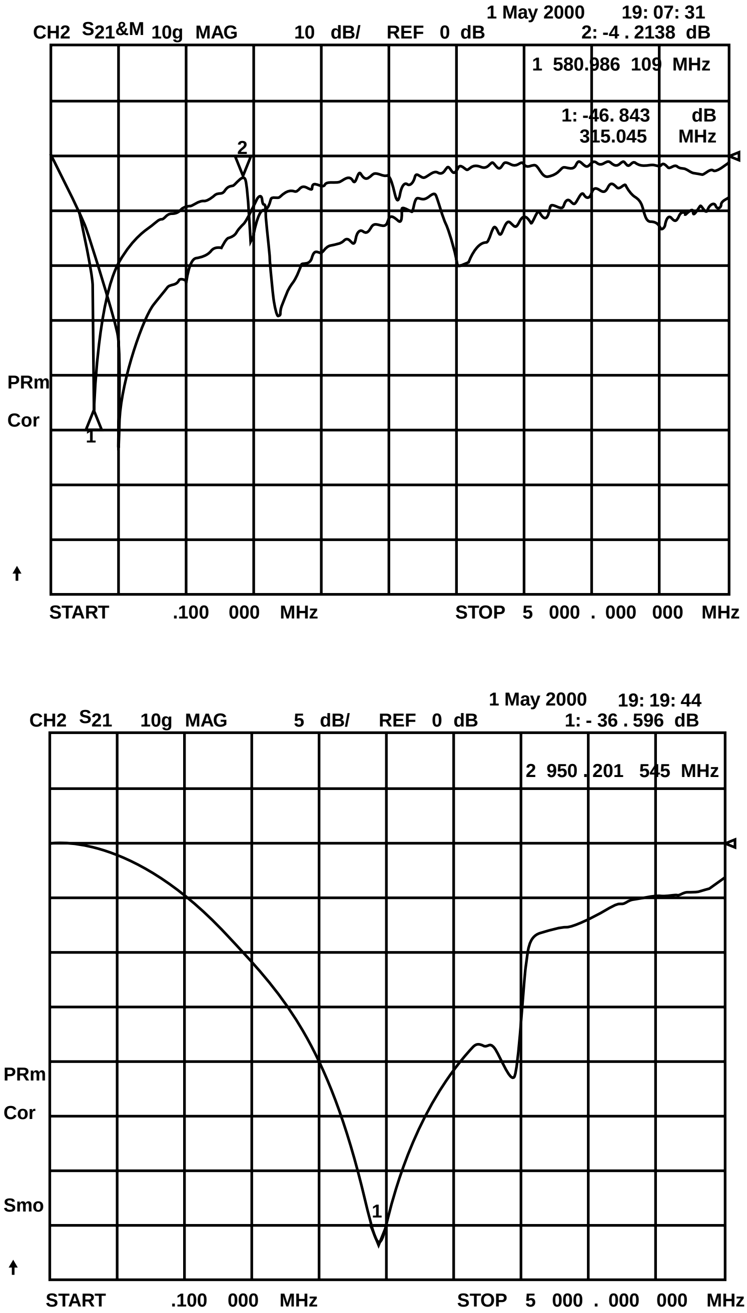

FIGURE 6.8 S21 of series inductors: (a) 470 nH wound and chip inductors; and (b) 19 nH spring inductor.

Parasitic Capacitance

The broadband inductor sweep of Fig. 6.8 shows resonances in wound, chip, and spring inductors. Manufacturers, and the schematic of Fig. 6.7, only show the first parallel resonance. Wound inductors can be modeled as a helical transmission line.[10] The inductance per unit length is the total solenoid inductance divided by the length of the inductor. The capacitance to ground can be modeled as a cylinder

TABLE 6.3 Inductor Matrix

Type	Size	Inductance Range	Q Range	Current Range	Resonance Range
Spring					
	Micro	1.6–13 nH	50–225	NA	4.5–6 GHz
	Mini	2.5–43 nH	90–210	NA	1.5–3 GHz
Wound					
	603	1.8–120 nH	10–90	0.3–0.7 A	1.3–6 GHz
	805	3.3–220 nH	10–90	0.3–0.8 A	0.8–6 GHz
	1008	3.3–10,000 nH	10–100	0.24–1 A	0.06–6 GHz
	1812	1.2–1000 μH	10–60	0.05–0.48 A	1.5–230 MHz
Multilayer					
	402	1–27 nH	10–200	0.3 A	1.6–6 GHz
	603	1.2–100 nH	5–45	0.3 A	0.83–6 GHz
	805	1.5–470 nH	10–70	0.1–0.3 A	0.3–6 GHz

of diameter equal to the coil diameter. The first quarter wave resonance of this helical transmission line is the parallel resonance of the inductor, while the higher resonances follow from transmission line theory. When the inductor is tightly wound, or put on a high dielectric core, the interwinding capacitance increases and lowers the fundamental resonance frequency.

$$L_{WIRE} = 200\, l_W \left(\ln\left[4\, l_W / d\right] + 0.5\, d / l_W - 0.75\right) \text{nH} \tag{6.12}$$

Bond Wires and Vias

The inductance of a length of wire is given by Eq. (6.12).[1] This equation is a useful first order approximation, but rarely accurate because wires usually have other conductors nearby. Parallel conductors such as ground planes or other wires reduce the net inductance because of mutual inductance canceling some of the flux. Perpendicular conductors, such as a ground plane terminating a wire varies the inductance up to a factor of 2 as shown by the Biot-Savart law.[11]

Spiral Inductors

Planar spiral inductors are convenient realizations for PCBs and ICs. They are even implemented in some low-value chip inductors. These inductors tend to have low Q because the spiral blocks the magnetic flux; ground planes, which reduce the inductance tend to be close by; and the current crowds to the wire edges, which increases the resistance. With considerable effort Qs of 20 can be approached in planar spiral inductors.[12] Excellent papers have been written on computing spiral inductance values.[13,14] In some cases, simple formulas can produce reasonable approximations; however, the real challenge is computing the parallel resonance for the spiral. As with the solenoid, the best formulas use the distributed nature of the coil.[14] A first order approximation is to treat the spiral as a microstrip line, compute the total capacitance, and compute the resonance with the coupled wire model of the spiral.

Chokes

Chokes are an important element in almost all broadband RF and microwave circuitry. A choke is essentially a resonance-free high impedance. Generally, chokes are used below 2 GHz, although bias tees are a basic choke application that extends to tens of GHz. Schematically, a choke is an inductor. In the circuit a choke provides a high RF impedance with very little loss to direct current so that supply voltages and resistive losses can be minimized. Most often the choke is an inductor with a ferrite core used in the frequency range where the ferrite is lossy. A ferrite bead on a wire is the most basic form of choke. It is important to remember that direct current will saturate ferrite chokes just as it does ferrite inductors. At higher frequencies, clever winding tricks can yield resonance-free inductance over decades of bandwidth.[15] Ferrite permeability can be approximated by Eq. (6.13).[16]

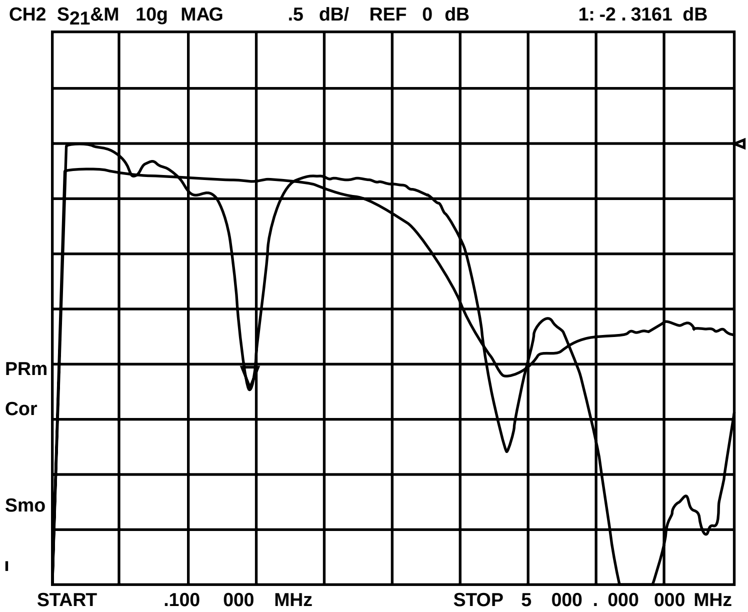

FIGURE 6.9 S21 of shunt 4.7 μH choke and 4.7 μH wound chip inductor, as if used in a DC bias application.

$$\mu\left(f_{\mathrm{MHz}}\right)=1\Big/\left(\mathrm{j}\,f_{\mathrm{MHz}}/2250+1\Big/\left(\mu_{\mathrm{i}}\left(1+\mathrm{j}\,0.8\,\mu_{\mathrm{i}}\;f_{\mathrm{MHz}}/2250\right)\right)\right) \qquad (6.13)$$

For frequencies below 2250 MHz/μ_i, the ferrite makes a low loss inductor, but above this frequency the ferrite becomes lossy and appears resistive.[17] Figure 6.9 shows a comparison of a 4.7 μH choke and a 4.7 μH wound chip inductor. The high frequency resonances present in the wound inductor are absorbed by the ferrite loss. The best model for a ferrite choke is an inductor in parallel with a resistor. The resistance comes from the high frequency core loss, and the inductor comes from the low frequency ferrite permeability, core shape, and wire turns. As can be seen in Eq. (6.13), the real part of the permeability decreases as frequency increases, causing the loss term to dominate.

Ferrite Baluns

Ferrite baluns are a cross between transmission lines and chokes. While transmission line baluns can be used at any frequency, ferrite baluns are most useful between 10 kHz and 2 GHz. Basically, the balun is made from twisted or bifilar wire with the desired differential mode impedance, such as 50 or 75 ohms. The wire is wound on a ferrite core so any common mode currents see the full choke impedance, as shown in Fig. 6.10a. Two-hole balun cores are used because they provide the most efficient inductance per turn in a small size. The ferrite core allows the balun to work over decades of frequency, for example 10 MHz to 1000 MHz is a typical balun bandwidth. Also, the ferrite allows the baluns to be small enough to fit into T0-8 cans on a 0.25-in. square SMT substrate as shown in Fig. 6.1. Extremely high performance baluns are made from miniature coax surrounded by ferrite beads.[18]

Manufacturers design baluns for specific impedance levels and bandwidths. In order to understand the performance trade-offs and limitations, some discussion will be given. Figure 6.10a shows a typical ferrite and wire balun. Figure 6.10b shows a schematic representation of the balun in Fig. 6.10a. The balun is easiest to analyze using the equivalent circuit of Fig. 6.10c. The equivalent circuit shows that the inverting output is loaded with the even-mode choke impedance, Zoe. For low frequency symmetry in output impedance and gain, a choke is often added to the non-inverting output as shown in Fig. 6.10d.

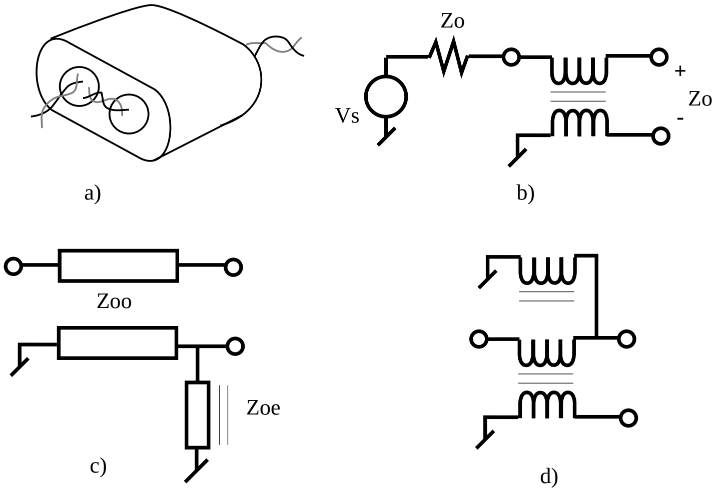

FIGURE 6.10 Ferrite balun (a), with schematic (b), equivalent circuit (c), and symmetric version *(d).

The configuration of Fig. 6.10d is especially useful when coaxial cable is used instead of twisted pair wire. This is because the coax shields the center conductor from the ferrite so the center conductor has infinite even-mode impedance to ground. For twisted pair baluns, the even-mode impedance to ground is finite and creates a lossy transmission line on the ferrite that attenuates the high frequencies. For broadest band operation, ferrite and wire baluns use the configuration of Fig. 6.10b because Fig. 6.10d causes excessive high frequency attenuation. Finally, transitions into and out of the balun, as well as imperfect wire impedance contribute to excess series inductance for the differential-mode impedance. The inductive S11 increases with frequency and is often tuned out with small capacitors across the twisted pair.[19]

References

1. Bahl, I, and Bhartia, P., *Microwave Solid State Circuit Design*, John Wiley & Sons, New York, 1988.
2. Chin, S., RLC Components, *Electronic Products*, 31–33, July 1989.
3. Florida RF Labs, *Component Reference Catalog*, Florida RF Labs, Stuart, FL, 2000.
4. ATC, *The RF Capacitor Handbook*, ATC, Huntington Station, NY, 1979.
5. Ingalls, M.W., Perspectives on Ceramic Chip Capacitors, *RF Design*, 45–53, Nov. 1989.
6. Pavlov, V.I., Gap Capacity in Microstrip, *Radioelectronica and Communication Systems*, 85–87, 1981.
7. Wolff, I., and Kibuuka, G., Computer Models for MMIC Capacitors and Inductors, *14th Euorpean Microwave Conference*, 853–859, 1984.
8. Grover, F.W., *Inductance Calculations*, Dover, New York, 1962.
9. Ramo, S., Whinnery, J.R., and van Duzer, T., *Fields and Waves in Communication Electronics*, John Wiley & Sons, New York, 1984.
10. Rhea, R.W., A Multimode High-Frequency Inductor Model, *Applied Microwaves and Wireless*, 70–80, Nov/Dec 1997.
11. Goldfard, M.E., and Pucel, R.A., Modeling Via Hole Grounds in Microstrip, *IEEE Microwave Guided Letters*, 135–137, June 1991.
12. Gecorgyan, S., Aval, O., Hansson, B., Jaconsson, H., and Lewin, T., Loss Considerations for Lumped Inductors in Silicon MMICs, *IEEE MTT-S Digest*, 859–862, 1999.
13. Remke, R.L., and Burdick, G.A., Spiral Inductors for Hybrid and Microwave Applications, *24th Electronic Components Conference*, 152–161, May 1974.
14. Lang, D., Broadband Model Predicts S-Parameters of Spiral Inductors, *Microwaves & RF*, 107–110, Jan. 1988.
15. Piconics, *Inductive Components for Microelectronic Circuits*, Piconics, Tyngsboro, 1998.

16. Riddle, A., Ferrite and Wire Baluns with under 1 dB Loss to 2.5 GHz, *IEEE MTT-S Digest*, 617–620, 1998.
17. Trans-Tech, *Microwave Magnetic and Dielectric Materials*, Trans-Tech, Adamstown, MD, 1998.
18. Barabas, U., On an Ultrabroadband Hybrid Tee, *IEEE Trans MTT*, 58-64, Jan. 1979.
19. Hilbers, A.H., High-Frequency Wideband Power Transformers, *Electronic Applications*, Philips, 30, 2, 65–73, 1970.
20. Boser, O., and Newsome, V., High Frequency Behavior of Ceramic Multilayer Capacitors, *IEEE Trans CHMT*, 437–439, Sept. 1987.
21. Ingalls, M., and Kent, G., Monolithic Capacitors as Transmission Lines, *IEEE Trans MTT*, 964–970, Nov. 1989.
22. Grossner, N.R., *Transformers for Electronic Circuits*, McGraw Hill, New York, 1983.
23. AVX, RF Microwave/Thin-Film Products, AVX, Kyocera, 2000.

6.2 Passive Microwave Devices

Michael B. Steer

Wavelengths in air at microwave and millimeter-wave frequencies range from 1 m at 300 MHz to 1 mm at 300 GHz. These dimensions are comparable to those of fabricated electrical components. For this reason circuit components commonly used at lower frequencies, such as resistors, capacitors, and inductors, are not readily available. The relationship between the wavelength and physical dimensions enables new classes of distributed components to be constructed that have no analogy at lower frequencies. Components are realized by disturbing the field structure on a transmission line, which results in energy storage and thus reactive effects. Electric (E) field disturbances have a capacitive effect and the magnetic (H) field disturbances appear inductive. Microwave components are fabricated in waveguide, coaxial lines, and strip lines. The majority of circuits are constructed using strip lines as the cost is relatively low since they are produced using photolithography techniques. Fabrication of waveguide components requires precision machining, but they can tolerate higher power levels and are more easily realized at millimeter-wave frequencies (30 to 300 GHz) than can either coaxial or microstrip components.

Characterization of Passive Elements

Passive microwave elements are defined in terms of their reflection and transmission properties for an incident wave of electric field or voltage. In Fig. 6.11(a) a traveling voltage wave with phasor $\mathbf{V}_1^+$ is incident at port 1 of a two-port passive element. A voltage $\mathbf{V}_1^-$ is reflected and $\mathbf{V}_2^-$ is transmitted. In the absence of an incident voltage wave at port 2 (the voltage wave $\mathbf{V}_2^-$ is totally absorbed by Z_0), at port 1 the element has a voltage reflection coefficient

$$\Gamma_1 = \mathbf{V}_1^- \big/ \mathbf{V}_1^+$$

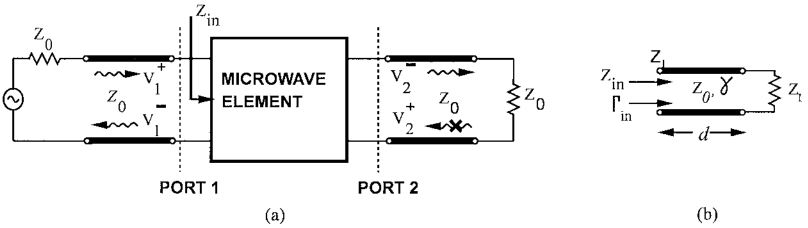

FIGURE 6.11 Incident, reflected and transmitted traveling voltage waves at (a) a passive microwave element, and (b) a transmission line.

and transmission coefficient

$$T = \mathbf{V}_2^- \big/ \mathbf{V}_1^+ .$$

More convenient measures of reflection and transmission performance are the return loss and insertion loss as they are relative measures of power in transmitted and reflected signals. In decibels

$$\text{RETURN LOSS} = -20\,\log\Gamma\,(\text{dB}) \;\text{ and }\; \text{RETURN LOSS} = -20\log T\,(\text{dB})$$

The input impedance at port 1, Z_{in}, is related to Γ by

$$Z_{\text{in}} = Z_0 \frac{1+\Gamma_1}{1-\Gamma_1} \text{ or by } \ldots\; \Gamma = \frac{Z_L - Z_0}{Z_L + Z_0} \tag{6.14}$$

The reflection characteristics are also described by the voltage standing wave ratio (VSWR), a quantity that is more easily measured. The VSWR is the ratio of the maximum voltage amplitude e$|V_1^+| + |V_1^-|$ on the input transmission line to the minimum voltage amplitude e$|V_1^+| - |V_1^-|$. Thus

$$\text{VSWR} = \frac{1+|\Gamma|}{1-|\Gamma|}$$

These quantities will change if the loading conditions are changed. For this reason scattering (S) parameters are used that are defined as the reflection and transmission coefficients with a specific load referred to as the reference impedance. Thus

$$S_{11} = \gamma_1 \;\text{ and }\; S_{21} = T$$

S_{22} and S_{12} are similarly defined when a voltage wave is incident at port 2. For a multiport $S_{pq} = \mathbf{V}_q^-/\mathbf{V}_p^+$ with all of the ports terminated in the reference impedance. Simple formulas relate the S parameters to other network parameters [1] (pp. 16–17), [2]. S parameters are the most convenient network parameters to use with distributed circuits as a change in line length results in a phase change. As well they are the only network parameters that can be measured directly at microwave and millimeter-wave frequencies. Most passive devices, with the notable exception of ferrite devices, are reciprocal and so $S_{pq} = S_{qp}$. A lossless passive device also satisfies the unitary condition: $\sum_p |S_{pq}|^2$ which is a statement of power conservation indicating that all power is either reflected or transmitted. A passive element is fully defined by its S parameters together with its reference impedance, here Z_0. In general the reference impedance at each port can be different.

Circuits are designed to minimize the reflected energy and maximize transmission at least over the frequency range of operation. Thus the return loss is high and the VSWR ≈ 1 for well-designed circuits. However, individual elements may have high reflections.

A terminated transmission line such as that in Fig. 6.11b has an input impedance

$$Z_{in} = Z_0 \frac{Z_L + jZ_0 \tanh\gamma d}{Z_0 + jZ_L \tanh\gamma d}$$

Thus a short section ($\gamma d \ll 1$) of short circuited ($Z_L = 0$) transmission line looks like an inductor, and looks like a capacitor if it is open circuited ($Z_L = \infty$). When the line is a quarter wavelength long, an open circuit is presented at the input to the line if the other end is short circuited.

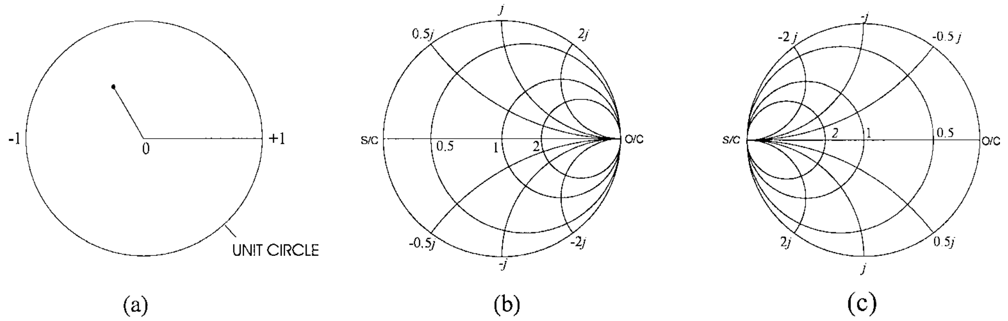

FIGURE 6.12 Smith charts: (a) polar plot of reflection coefficient; (b) normalized impedance Smith chart; and (c) normalized admittance Smith chart.

The Smith Chart

Scattering parameters can be conveniently displayed on a polar plot as shown in Fig. 6.12a. For passive devices $|S_{pq}| \leq 1$ and only for active devices can a scattering parameter be greater than 1. Thus the location of a scattering parameter, plotted as a complex number on the polar plot with respect to the unit circle indicates a basic physical property. As shown earlier in Eq. (6.14), there is a simple relationship between load impedance and reflection coefficient. With the reactance of a load held constant and the load resistance varied, the locus of the reflection coefficent is a circle as shown. Similarly, arcs of circles result when the resistance is held constant and the reactance varied. These lines result in the normalized impedance Smith chart of Fig. 6.12b.

Transmission Line Sections

The simplest microwave circuit element is a uniform section of transmission line that can be used to introduce a time delay or a frequency-dependent phase shift. More commonly it is used to interconnect other components. Other line segments used for interconnections include bends, corners, twists, and transitions between lines of different dimensions (see Fig. 6.13).

The dimensions and shapes are designed to minimize reflections and so maximize return loss and minimize insertion loss.

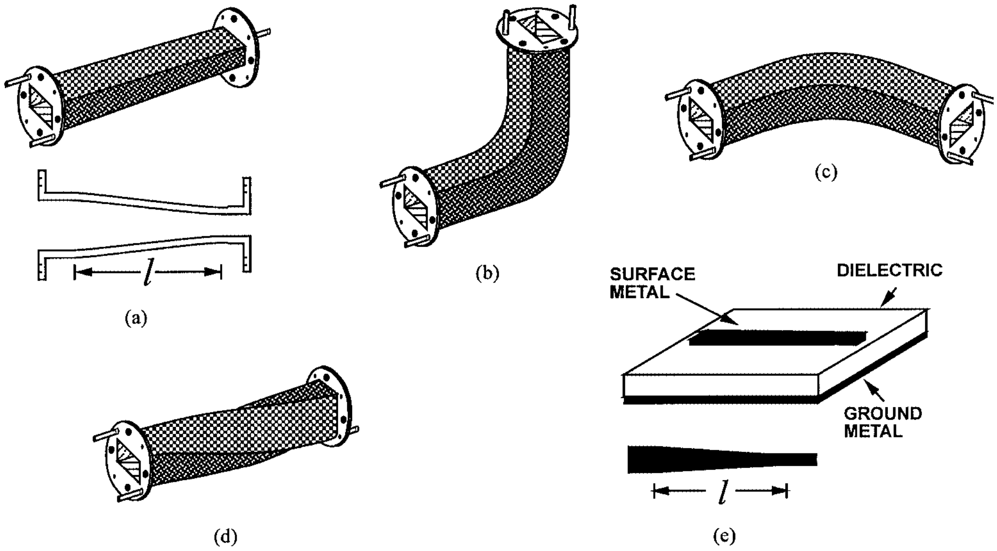

FIGURE 6.13 Sections of transmission lines used for interconnecting components: (a) waveguide tapered section, (b) waveguide E-plane bend, (c) waveguide H-plane bend, (d) waveguide twist, and (e) microstrip tapered line.

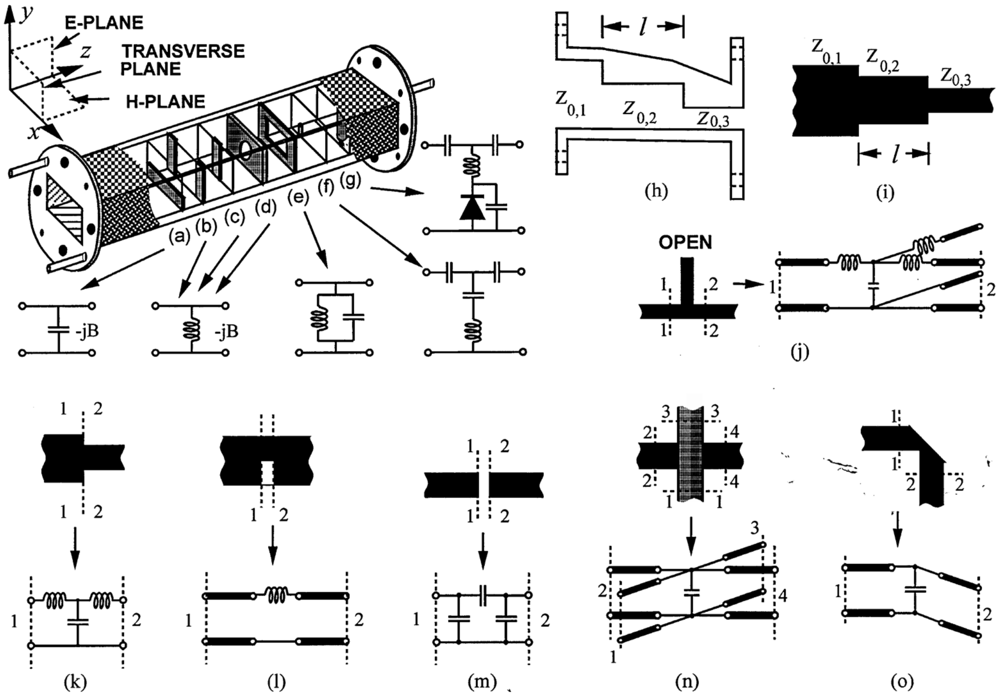

FIGURE 6.14 Discontinuities. Waveguide discontinuities:(a) capacitive E-plane discontinuity, (b) inductive H-plane discontinuity, (c) symmetrical inductive H-plane discontinuity, (d) inductive post discontinuity, (e) resonant window discontinuity, (f) capacitive post discontinuity, (g) diode post mount, and (h) quarter-wave impedance transformer; microstrip discontinuities: (i) quarter-wave impedance transformer, (j) open microstrip stub, (k) step, (l) notch, (m) gap, (n) crossover, and (o) bend.

Discontinuities

The waveguide discontinuities shown in Fig. 6.14a–f illustrate most clearly the use of E and H field disturbances to realize capacitive and inductive components. An E plane discontinuity, Fig. 6.14a, is modeled approximately by a frequency-dependent capacitor. H plane discontinuities (Figs. 6.14b and 6.14c) resemble inductors as does the circular iris of Fig. 6.14d. The resonant waveguide iris of Fig. 6.14e disturbs both the E and H fields and can be modeled by a parallel LC resonant circuit near the frequency of resonance. Posts in waveguide are used both as reactive elements (Fig. 6.14f), and to mount active devices (Fig. 6.14g). The equivalent circuits of microstrip discontinuities (Figs. 6.14j–o), are again modeled by capacitive elements if the E-field is interrupted and by inductive elements if the H field (or current) is disturbed. The stub shown in Fig. 6.14j presents a short circuit to the through transmission line when the length of the stubs is $\lambda_g/4$. When the stub is electrically short $\ll\lambda_g/4$ it introduces a shunt capacitance in the through transmission line.

Impedance Transformers

Impedance transformers interface two sections of line of different characteristic impedance. The smoothest transistion and the one with the broadest bandwidth is a tapered line as shown in Figs. 6.13a and 6.13e. This element tends to be very long as $l > \lambda_g$ and so step terminations called quarter-wave impedance transformers (see Fig. 6.14h) are sometimes used, although their bandwidth is relatively small centered on the frequency at which $l = \lambda_g$. Ideally $Z_{0,2} = \sqrt{Z_{0,1}Z_{0,3}}$.

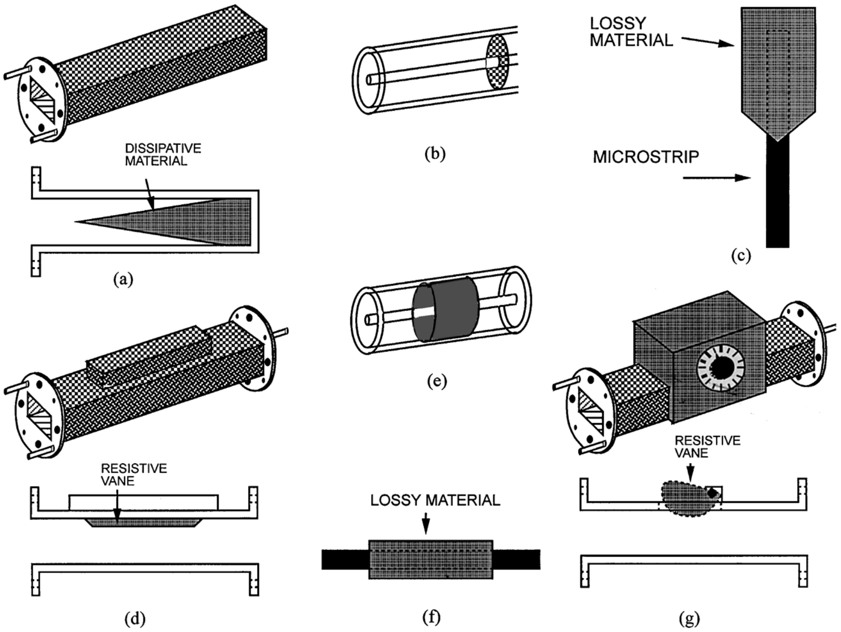

FIGURE 6.15 Terminations and attenuators: (a) waveguide matched load, (b) coaxial line resistive termination, (c) microstrip matched load, (d) waveguide fixed attenuator, (e) coaxial fixed attenuator, (f) microstrip attenuator, and (g) waveguide variable attenuator.

Terminations

In a termination, power is absorbed by a length of lossy material at the end of a shorted piece of transmission line (Figs. 6.15a and 6.15c). This type of termination is called a matched load as power is absorbed and reflections are small irrespective of the characteristic impedance of the transmission line. This is generally preferred as the characteristic impedance of transmission lines varies with frequency — particularly so for waveguides. When the characteristic impedance of a line does not vary much with frequency, as is the case with a coaxial line or microstrip, a simpler and smaller termination can be realized by placing a resistor to ground (Fig. 6.15b).

Attenuators

Attenuators reduce the signal level traveling along a transmission line. The basic design is to make the line lossy but with characteristic impedance approximating that of the connecting lines so as to reduce reflections. The line is made lossy by introducing a resistive vane in the case of a waveguide, Fig. 6.15d, replacing part of the outer conductor of a coaxial line by resistive material, Fig. 6.5e, or covering the line by resistive material in the case of a microstrip line Fig. 6.15f. If the amount of lossy material introduced into the transmission line is controlled, a variable attenuator is obtained, e.g., Fig. 6.15g.

Microwave Resonators

In a lumped element resonant circuit, stored energy is transfered between an inductor, which stores magnetic energy, and a capacitor, which stores electric energy, and back again every period. Microwave resonators function the same way, exchanging energy stored in electric and magnetic forms but with the energy stored spatially. Resonators are described in terms of their quality factor

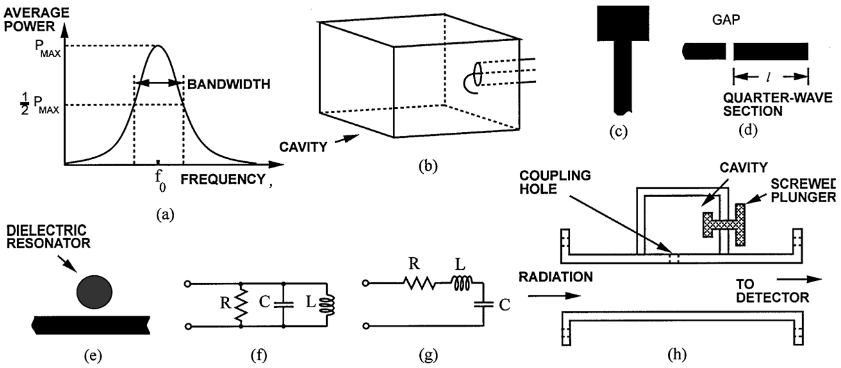

FIGURE 6.16 Microwave resonators: (a) resonator response, (b) rectangular cavity resonator, (c) microstrip patch resonator (d) microstrip gap-coupled reflection resonator, (e) transmission dielectric transmission resonator in microstrip, (f) parallel equivalent circuits, (g) series equivalent circuits, and (h) waveguide wavemeter.

$$Q = 2\pi f_0 \left| \frac{\text{Maximum energy stored in the cavity at } f_0}{\text{Power lost in the cavity}} \right|$$

where f_0 is the resonant frequency. The Q is reduced and thus the resonator bandwidth is increased by the power lost to the external circuit so that the loaded Q

$$Q_L = 2\pi f_0 \left| \frac{\text{Maximum energy stored in the resonator at } f_0}{\text{Power lost in the cavity and to the external circuit}} \right| = \frac{1}{1/Q + 1/Q_{\text{ext}}}$$

where Q_{ext} is called the external Q, Q_L accounts for the power extracted from the resonant circuit and is typically large. For the simple response shown in Fig. 6.16a the half power (3 dB) bandwidth is f_0/Q_L.

Near resonance, the response of a microwave resonator is very similar to the resonance response of a parallel or series *RLC* resonant circuit, Figs. 6.16f and 6.16g. These equivalent circuits can be used over a narrow frequency range.

Several types of resonators are shown in Fig. 6.16. Figure 6.16b is a rectangular cavity resonator coupled to an external coaxial line by a small coupling loop. Figure 6.16c is a microstrip patch reflection resonator. This resonator has large coupling to the external circuit. The coupling can be reduced and photolithographically controlled by introducing a gap as shown in Fig. 6.16d for a microstrip gap-coupled transmission line reflection resonator. The Q of a resonator can be dramatically increased by using a high dielectric constant material as shown in Fig. 6.16e for a dielectric transmission resonator in microstrip.

One simple application of cavity resonator is the waveguide wavemeter, Fig. 6.16h. Here the resonant frequency of a rectangular cavity is varied by changing the the physical dimensions of the cavity with a null of the detector indicating that the frequency corresponds to the cavity resonant frequency.

Tuning Elements

In rectangular waveguide the basic adjustable tuning element is the sliding short shown in Fig. 6.17a. Varying the position of the short will change resonance frequencies of cavities. It can be combined with hybrid tees to achieve a variety of tuning functions. The post in Fig. 6.19f can be replaced by a screw to obtain a screw tuner, which is commonly used in waveguide filters.

Sliding short circuits can be used in coaxial lines and in conjunction with branching elements to obtain stub tuners. Coaxial slug tuners are also used to provide matching at the input and output of active circuits. The slug is movable and changes the characteristic impedance of the transmission line. It is more

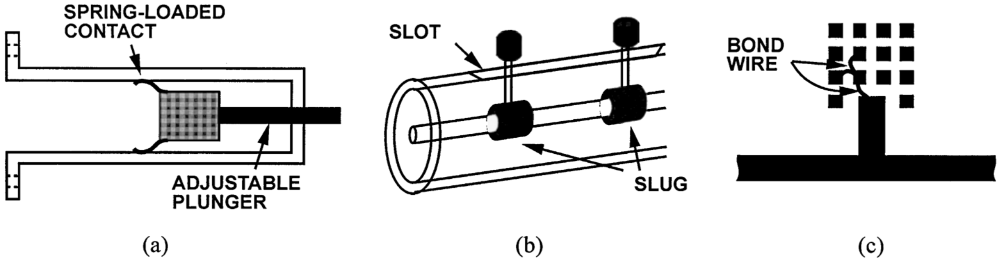

FIGURE 6.17 Tuning elements: (a) waveguide sliding short circuit, (b) coaxial line slug tuner, (c) microstrip stub with tuning pads.

difficult to achieve variable tuning in passive microstrip circuits. One solution is to provide a number of pads as shown in Fig. 6.15c which, in this case, can be bonded to the stub to obtain an adjustable stub length.

Variable amounts of phase shift can be inserted by using a variable length of line called a line stretcher, or by a line with a variable propagation constant. One type of waveguide variable phase shifter is similar to the variable attenuator of Fig. 6.15g with the resistive material replaced by a low-loss dielectric.

Hybrid Circuits and Directional Couplers

Hybrid circuits are multiport components that preferentially route a signal incident at one port to the other ports. This property is called directivity. One type of hybrid is called a directional coupler the schematic of which is shown in Fig. 6.18a. Here the signal incident at port 1 is coupled to ports 2 and 4 while very little is coupled to port 3. Similarly a signal incident at port 2 is coupled to ports 1 and 3, but very little power appears at port 4. The feature that distinguishes a directional coupler from other types of hybrids is that the power at the output ports are different. The performance of a directional coupler is specified by two parameters:

$$\begin{aligned}\text{Coupling Factor} &= P_1/P_4\\ \text{Directivity} &= P_4/P_3\end{aligned}$$

Microstrip and waveguide realizations of directional couplers are shown in Figs. 6.18b and 6.18c.

The power at the output ports of the hybrids shown in Figs. 6.19 and 6.20 are equal and so the hybrids serve to split a signal in half as well having directional sensitivity.

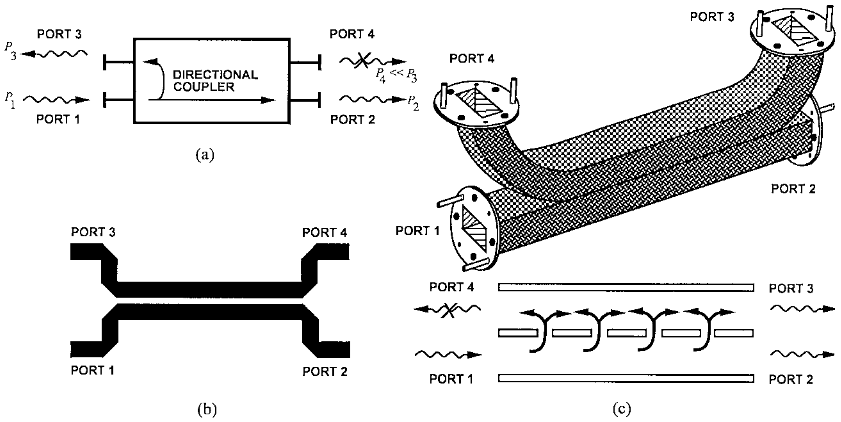

FIGURE 6.18 Directional couplers: (a) schematic, (b) microstrip directional coupler, (c) waveguide directional coupler.

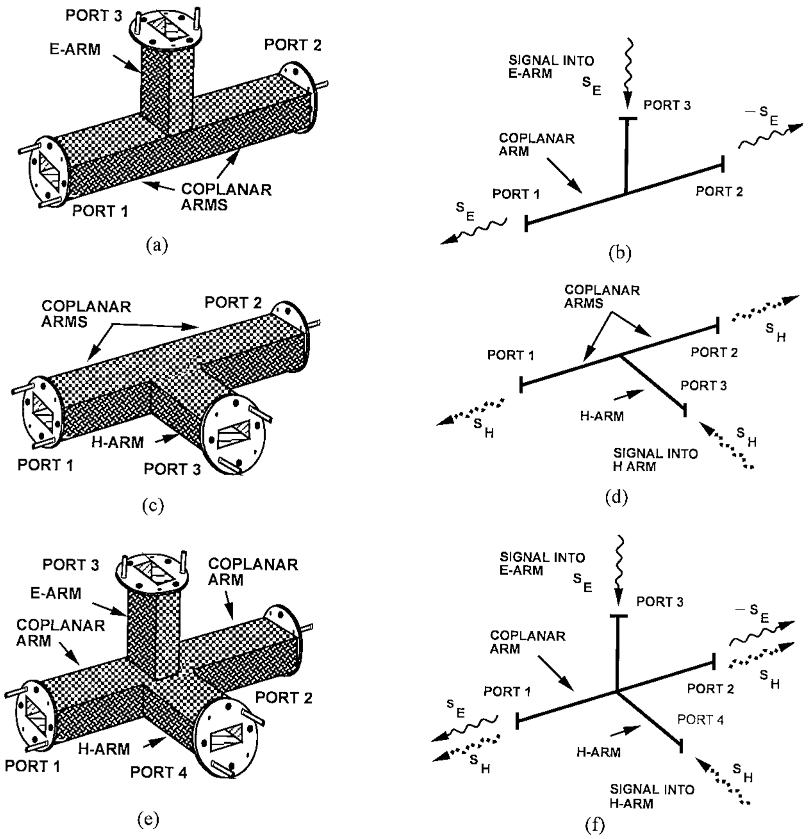

FIGURE 6.19 Waveguide hybrids:(a) E-plane tee and (b) its signal flow; (c) H-plane tee and (d) its signal flow; and (e) magic tee and (f) its signal flow. The negative sign indicates 180° phase reversal.

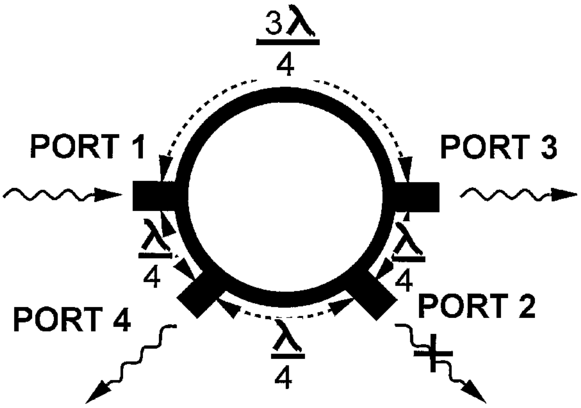

FIGURE 6.20 Microstrip rat race hybrid.

Ferrite Components

Ferrite components are nonreciprocal in that the insertion loss for a wave traveling from port A to port B is not the same as that from port B to port A.

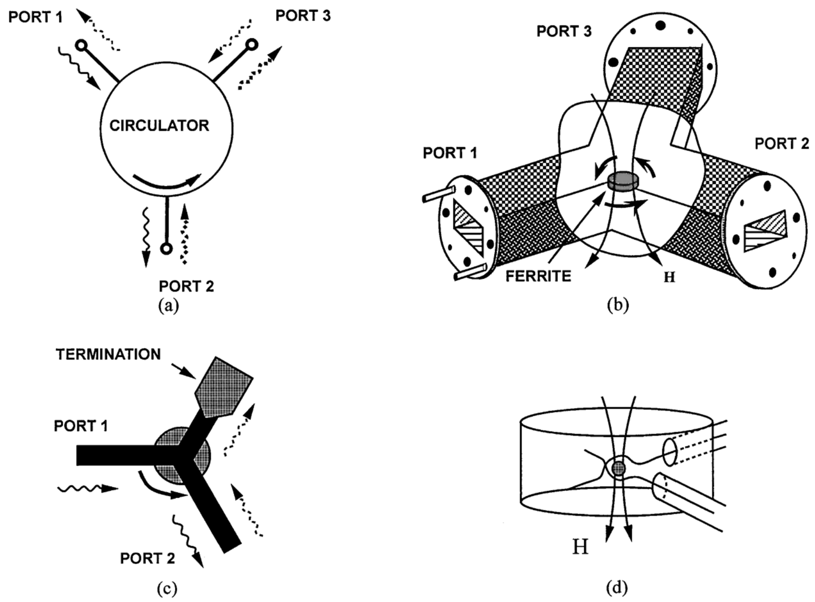

FIGURE 6.21 Ferrite Components: (a) Schematic of a circulator, (b) a waveguide circulator, (c) a microstrip isolator, and (d) a YIG tuned band-pass filter.

Circulators and Isolators

The most important ferrite component is a circulator, Figs. 6.21a and 6.21b. The essential element of a circulator is a piece of ferrite which, when magnetized, becomes nonreciprocal preferring progression of electromagnetic fields in one circular direction. An ideal circulator has the scattering matrix

$$S = \begin{vmatrix} 0 & 0 & S_{13} \\ S_{21} & 0 & 0 \\ & S_{32} & 0 \end{vmatrix}$$

In addition to the insertion and return losses, the performance of a circulator is described by its isolation, which is its insertion loss in the undesired direction. An isolator is just a three-port circulator with one of the ports terminated in a matched load as shown in the microstip realization of Fig. 6.21c. It is used in a transmission line to pass power in one direction but not in the reverse direction. It is commonly used to protect the output of equipment from high reflected signals. A four-port version is called a duplexer and is used in radar systems and to separate the received and transmitted signals in a transciever.

YIG Tuned Resonator

A magnetized YIG (Yttrium Iron Garnet) sphere shown in Fig. 6.21d, provides coupling between two lines over a very narrow band. The center frequency of this bandpass filter can be adjusted by varying the magnetizing field.

Filters and Matching Networks

Filters are combinations of microwave passive elements designed to have a specified frequency response. Typically a topology of a filter is chosen based on established lumped element filter design theory. Then computer-aided design techniques are used to optimize the response of the circuit to the desired response. Matching networks contain reactive elements and have the essential purpose of realizing maximum power transfer. They often interface a complex impedance termination to a resistance source. On a chip, and

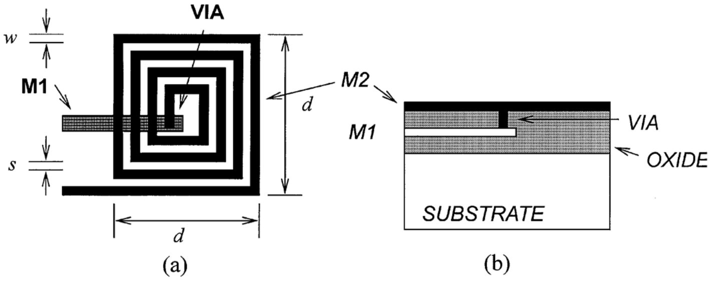

FIGURE 6.22 A spiral inductor fabricated ona monolithic integrated circuit: (a) top view; and (b) cross-section.

at RF frequencies, the matching network consists of parallel plate capacitors and spiral inductors such as that shown in Fig. 6.22.

Passive Semiconductor Devices

A semiconductor diode is modeled by a voltage dependent resistor and capacitor in shunt. Thus an applied DC voltage can be used to change the value of a passive circuit element. Diodes optimized to produce a voltage variable capacitor are called varactors. In detector circuits, a diode's voltage variable resistance is used to achieve rectification and, through design, produce a DC voltage proportional to the power of an incident microwave signal. The controllable variable resistance is used in a PIN diode to realize an electronically controllable switch.

Defining Terms

Characteristic impedance: Ratio of the voltage and current on a transmission line when there are no reflections.

Insertion loss: Power lost when a signal passes through a device.

Reference impedance: Impedance to which scattering parameters are referenced.

Return loss: Power lost upon reflection from a device.

References

1. G.D. Vendelin, A.M. Pavio, and U.L. Rohde, *Microwave Circuit Design Using Linear and Nonlinear Techniques*, Wiley: New York, 1990.
2. T.C. Edwards and M.B. Steer, *Foundations of Interconnect and Microstrip Design*, 3rd edition, Wiley: Chichester, 2000.

Further Information

The following books provide good overviews of passive microwave components: *Foundations of Interconnect and Microstrip Design* by T.C. Edwards and M.B. Steer, 3rd edition, Wiley, Chichester, 2000, *Microwave Engineering Passive Circuits* by P.A. Rizzi, Prentice Hall, Englewood Cliffs, N.J., 1988; *Microwave Devices and Circuits* by S.Y. Liao, 3rd edition, Prentice Hall, Englewood Cliffs, N.J., 1990; *Microwave Theory, Components and Devices* by J.A. Seeger, Prentice Hall, Englewood Cliffs, N.J., 1986; *Microwave Technology* by E. Pehl, Artech House, Dedham, MA, 1985; *Microwave Engineering and Systems Applications* by E.A. Wolff and R. Kaul, Wiley, New York, 1988; and Microwave Engineering by T.K. Ishii, 2 nd edition, Harcourt Brace Jovanovich, Orlando, Florida, 1989. *Microwave Circuit Design Using Linear and Nonlinear Techniques* by G.D. Vendelin, A.M. Pavio and U.L. Rohde, Wiley, New York, 1990, also provides a comphrensive treatment of computer-aided design techniques for both passive and active microwave circuits.

The monthly journals, *IEEE Transactions on Microwave Theory and Techniques*, *IEEE Microwave and Guided Wave Letters*, and *IEEE Transactions on Antennas and Propagation* publish articles on modeling and design of microwave passive circuit components. Articles in the first two journals are more circuit and component oriented while the third focuses on field theoretic analysis. These are published by The Institute of Electrical and Electronics Engineers, Inc. For subscription or ordering contact: IEEE Service Center, 445 Hoes Lane, PO Box 1331, Piscataway, New Jersey 08855-1331, U.S.A.

Articles can also be found in the biweekly magazine, *Electronics Letters*, and the bimonthly magazine, *IEE Proceedings Part H — Microwave, Optics and Antennas*. Both are published by the Institute of Electrical Engineers and subscription enquiries should be sent to IEE Publication Sales, PO Box 96, Stenage, Herts. SG1 2SD, United Kingdom. Telephone number (0438) 313311.

The *International Journal of Microwave and Millimeter-Wave Computer-Aided Engineering* is a quarterly journal devoted to the computer-aided design aspects of microwave circuits and has articles on component modeling and computer-aided design techniques. It has a large number of review-type articles. For subscription information contact John Wiley & Sons, Inc., Periodicals Division, PO Box 7247-8491, Philadelphia, Pennsylvania 19170-8491, U.S.A.

6.3 Dielectric Resonators

S. Jerry Fiedziuszko

Resonating elements are key to the function of most microwave circuits and systems. They are fundamental to the operation of filters and oscillators, and the quality of these circuits is basically limited by the resonator quality factor. Traditionally, microwave circuits have been encumbered by large, heavy, and mechanically complex waveguide structures that are expensive and difficult to adjust and maintain. Dielectric resonators, which can be made to perform the same functions as waveguide filters and resonant cavities, are, in contrast very small, stable, and lightweight. The popularization of advanced dielectric resonators roughly coincides with the miniaturization of many of the other associated elements of most microwave circuits. When taken together, these technologies permit the realization of small, reliable, lightweight, and stable microwave circuits.

Historically, guided electromagnetic wave propagation in dielectric media received widespread attention in the early days of microwaves. Surprisingly, substantial effort in this area predates 1920 and includes such famous scientists as Rayleigh, Sommerfeld, J.C. Bose, and Debye.[1] The term "dielectric resonator" first appeared in 1939 when R.D. Richtmyer of Stanford University showed that unmetalized dielectric objects (sphere and toroid) can function as microwave resonators.[2] However, his theoretical work failed to generate significant interest, and practically nothing happened in this area for more than 25 years. In 1953, a paper by Schlicke[3] reported on super high dielectric constant materials (~1,000 or more) and their applications at relatively low RF frequencies. In the early 1960s, researchers from Columbia University, Okaya and Barash, rediscovered dielectric resonators during their work on high dielectric materials (rutile), paramagnetic resonance and masers. Their papers[4,5] provided the first analysis of modes and resonator design. Nevertheless, the dielectric resonator was still far from practical applications. High dielectric constant materials such as rutile exhibited poor temperature stability causing correspondingly large resonant frequency changes. For this reason, in spite of high Q factor and small size, dielectric resonators were not considered for use in microwave devices.

In the mid-1960s, S. Cohn and his co-workers at Rantec Corporation performed the first extensive theoretical and experimental evaluation of the dielectric resonator.[6] Rutile ceramics were used for experiments that had an isotropic dielectric constant in the order of 100. Again, poor temperature stability prevented development of practical components.

A real breakthrough in ceramic technology occurred in the early 1970s when the first temperature stable, low-loss, Barium Tetratitanate ceramics were developed by Raytheon.[7] Later, a modified Barium Tetratitanate with improved performance was reported by Bell Labs.[8] These positive results led to the actual implementations of dielectric resonators as microwave components. The materials, however, were in scarce supply and not commercially available.

The next major breakthrough came from Japan when Murata Mfg. Co. produced (Zr-Sn)TiO_4 ceramics.[9] They offered adjustable compositions so that the temperature coefficient could be varied between +10 and –12 ppm/degree C. These devices became commercially available at reasonable prices. Afterward, the theoretical work and use of dielectric resonators expanded rapidly.

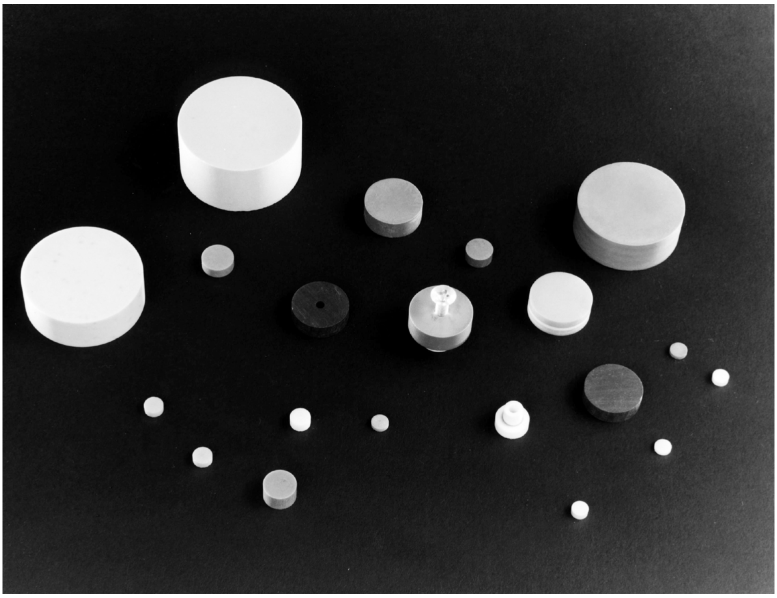

FIGURE 6.23 Dielectric resonators.

Microwave Dielectric Resonator

What is it? A dielectric resonator is a piece of high dielectric constant material usually in the shape of a disc that functions as a miniature microwave resonator (Fig. 6.23).

How does it work? The dielectric element functions as a resonator because of the internal reflections of electromagnetic waves at the high dielectric constant material/air boundary. This results in confinement of energy within, and in the vicinity of, the dielectric material which, therefore forms a resonant structure.

Why use it? Dielectric resonators can replace traditional waveguide cavity resonators in most applications, especially in MIC structures. The resonator is small, lightweight, high Q, temperature stable, low cost, and easy to use. A typical Q exceeds 10,000 at 4 GHz.

Theory of Operation

A conventional metal wall microwave cavity resonates at certain frequencies due to the internal reflections of electromagnetic waves at the air (vacuum)/metal boundary. These multiple reflections from this highly conductive boundary (electrical short) form a standing wave in a cavity with a specific electromagnetic field distribution at a unique frequency. This is called a "mode." A standard nomenclature for cavity modes is based on this specific electromagnetic field distribution of each mode. Since a metal wall cavity has a very well-defined boundary (short) and there is no field leaking through the wall, the associated electromagnetic field problem can be easily solved through exact mathematical analysis and modes for various cavity shapes (e.g., rectangular cavity or circular cavity) are precisely defined.

The TE (transverse electric) and TM (transverse magnetic) mode definitions are widely used. Mode indices e.g., TE_{113} (rectangular cavity analyzed in Cartesian coordinates) indicate how many of the electromagnetic field variations we have along each coordinate (in this case 1 along x and y, and 3 along z). The case of a dielectric resonator situation is more complicated. An electromagnetic wave propagating in a high dielectric medium and impinging on a high dielectric constant medium/air boundary will be reflected. However, contrary to a perfectly conducting boundary (e.g., highly conductive metal) this is a partial reflection and some of the wave will leak through the boundary to the other, low dielectric constant medium (e.g., air or vacuum). The higher the dielectric constant is of the dielectric medium, more of

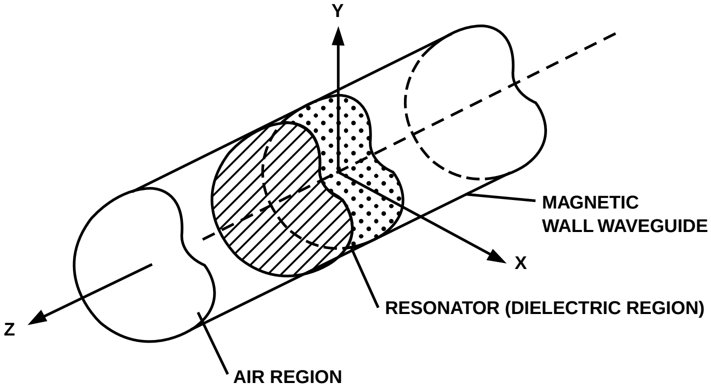

FIGURE 6.24 Magnetic wall waveguide below cut-off model of a dielectric resonator.

the electromagnetic wave is reflected and this boundary can be modeled not as a short (metal) but as an "open." As in a metal wall cavity, these internal reflections form a resonant structure called a dielectric resonator.

As in a conventional metal wall cavity, an infinite number of modes can exist in a dielectric resonator. To a first approximation, a dielectric resonator can be explained as a hypothetical magnetic wall cavity, which is the dual case of a metal (electric) wall cavity. The magnetic wall concept (on which the normal component of the electric field and tangential component of a magnetic field vanish at the boundary) is well known and widely used as a theoretical tool in electromagnetic field theory. In a very crude approximation, the air/high dielectric constant material interface can be modeled as such a magnetic wall (open circuit). Hence, the field distribution and resonant frequencies for such a resonator can be calculated analytically.

To modify this model we have to take into consideration that in actuality some of the electromagnetic field leaks out of the resonator and eventually decays exponentially in its vicinity. This leaking field portion is described by a mode subscript δ. Mode subscript δ is always smaller than one and varies with the field confinement in a resonator. If the dielectric constant of the resonator increases, more of the electromagnetic field is confined in the resonator and the mode subscript δ starts approaching one. The first modification of the magnetic wall model to improve accuracy was to remove two xy plane magnetic walls (Fig. 6.24), and to create a magnetic wall waveguide below cut off filled with the dielectric.[5,6,10]

This gave a calculated frequency accuracy for the $TE_{01\delta}$ mode of about 6%. Figure 6.24 shows the magnetic wall waveguide below cutoff with a dielectric resonator inside. Later, the circular wall was also removed (dielectric waveguide model) and the accuracy of calculations of resonant frequency was improved to 1 to 2%.[11,12] In an actual resonator configuration, usually some sort of metal wall cavity or housing is necessary to prevent radiation of the electromagnetic field and resulting degradation of resonator Q. This is illustrated in Fig. 6.25. Taking this into consideration, the model of the dielectric resonator assembly was modified, and accurate formulas for resonant frequency and electromagnetic field distribution in the structure were obtained through the mode matching method.[13]

In advanced models, additional factors such as dielectric supports, tuning plate, and microstrip substrate, can also be taken into account. The resonant frequency of the dielectric resonator in these configurations can be calculated using mode matching methods with accuracy much better than 1%.

The most commonly used mode in a dielectric resonator is the $TE_{01\delta}$ (in cylindrical resonator) or the $TE_{11\delta}$ (in rectangular resonator). The $TE_{01\delta}$ mode for certain Diameter/Length (D/L) ratios has the lowest resonant frequency, and therefore is classified as the fundamental mode. In general, mode nomenclature in a dielectric resonator is not as well defined as for a metal cavity (TE and TM modes). Many mode designations exist[14-16] and this matter is quite confusing as is true for the dielectric waveguide. In the authors opinion, the mode designation proposed by Y. Kobayashi[14] is the most promising and should be

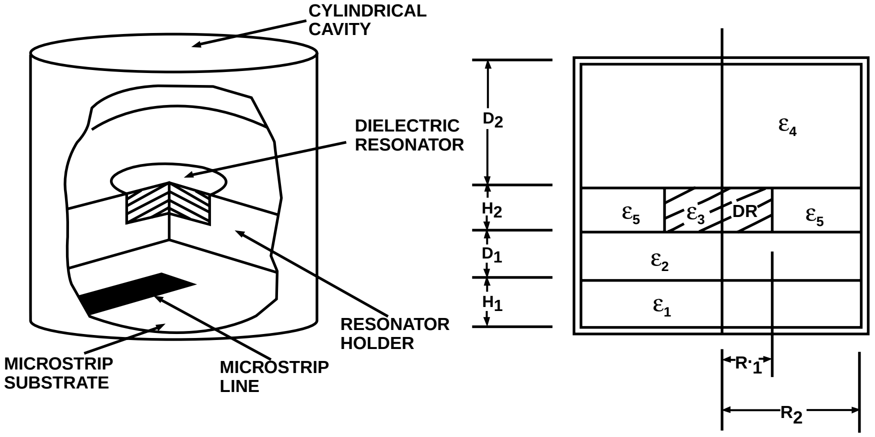

FIGURE 6.25 Practical configurations of a dielectric resonator and corresponding theoretical model.

adopted as a standard (this was addressed by MTT Standards Committee and presently two designations including Kobayashi's are recommended). Some of the modes and their field distributions are presented in Fig. 6.26.

The $TE_{01\delta}$ mode is the most popular and is used in single mode filters and oscillators. $HE_{11\delta}$ (HE indicates a hybrid mode) is used in high performance, dual mode filters,[17] directional filters and oscillators. TM mode is being used in cavity combiners and filters. Hybrid modes have all six components of the electromagnetic field. Also, low frequency filters (~800 MHz) for cellular telephone base stations were designed using the triple mode TM_{010}.[18]

Very high order modes called "whispering gallery modes" are finding applications at millimeter wave frequencies. These modes were first observed by Rayleigh in a study of acoustic waves.

Analogous propagation is possible in dielectric cylinders. Since these modes are well confined near the surface of the dielectric resonator, very high Q values at millimeter frequencies are posssible.

Coupling to Microwave Structures

An advantage of dielectric resonators is the ease with which these devices couple to common transmission lines such as waveguides and microstrip. A typical dielectric resonator in the TE $_{01\delta}$ mode can be transversely inserted into a rectangular waveguide. It couples strongly to the magnetic field, and acts as a simple bandstop filter. Figure 6.27 illustrates the magnetic field coupling into the microstrip. Coupling to a magnetic field in the waveguide can be adjusted by either rotating/tilting the resonator or moving a resonator toward the side of the waveguide. In microstrip line applications, a dielectric $TE_{11\delta}$ resonator couples magnetically and forms a bandstop filter. This is shown in Fig. 6.27. The coupling can be easily adjusted by either moving the resonator away (or toward center) from the microstrip or by lifting the resonator on a special support above the microstrip.

The resonant frequency of a dielectric resonator in this very practical case can be calculated using an equation derived in Reference 13. The resonant frequency in this topology can be adjusted to higher frequency with a metal screw or plate located above the resonator and perturbing the magnetic field, or down in frequency by lifting the resonator (moving it away from the ground plane). A typical range is in the order of 10%. Extra care must be taken, however, not to degrade the Q factor or temperature performance of the resonator by the closely positioned metal plate.

An interesting modification of the dielectric resonator is the so-called double resonator. This configuration is shown in Fig. 6.28. In this configuration, two halves of the ceramic disc or plate act as one resonator. Adjustment of the separation between the two halves of the resonator results in changes of the resonant frequency of the structure (Fig. 6.28). A much wider linear tuning range can be obtained in this configuration without degradation of the Q factor.[19-21]

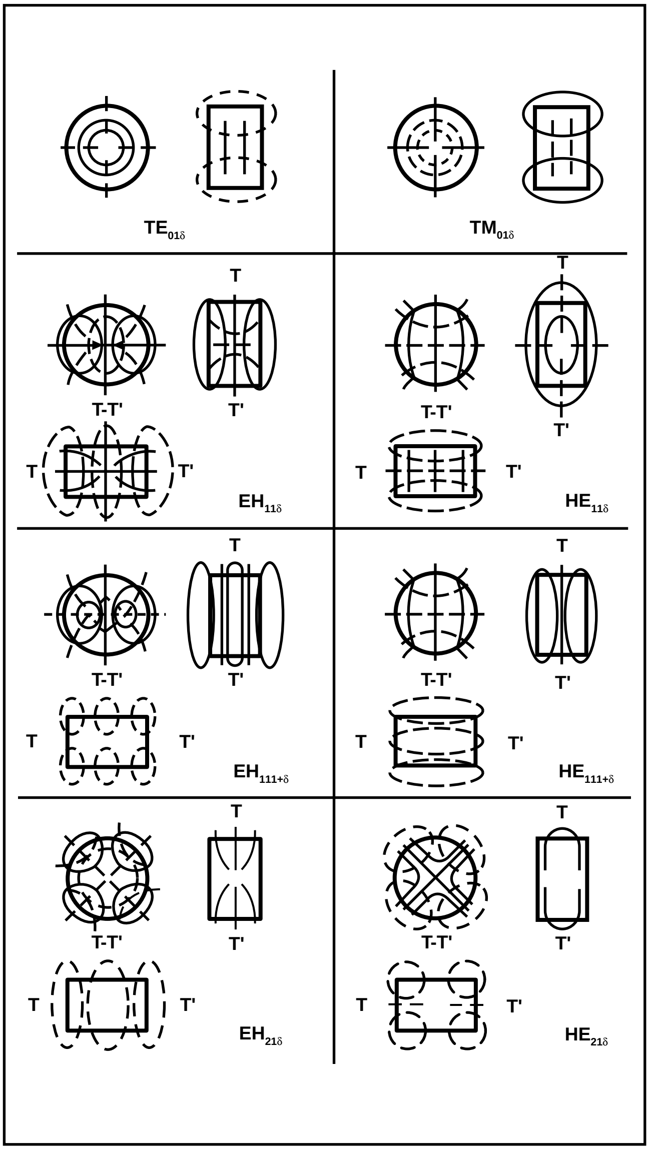

FIGURE 6.26 Modes in a dielectric resonator.

Ceramic Materials

The major problem with previously available high Q materials, such as rutile or rutile ceramics, was the poor temperature stability of the dielectric constant and the resulting instability of the resonant frequency of the dielectric resonators. Newly developed high Q Ceramics, however, have excellent temperature stability and an almost zero temperature coefficient is possible. The most popular materials are composed of a few basic, high Q compounds capable of providing negative and positive temperature coefficients. By adjusting proportions of the compounds and allowing for the linear expansion of the ceramic, perfect temperature compensation is possible. Basic properties of high quality ceramics developed for dielectric resonator applications are presented below in Table 6.4.[22-23]

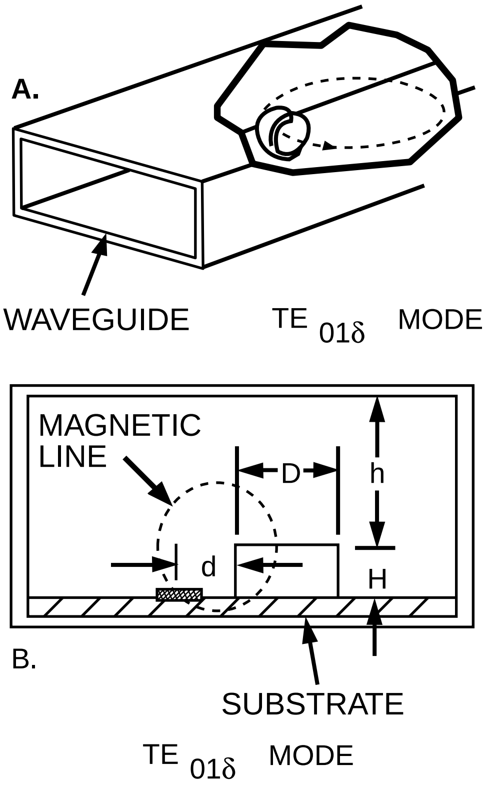

FIGURE 6.27 Magnetic field coupling of a dielectric to rectangular waveguide (top) and Microstrip line (bottom).

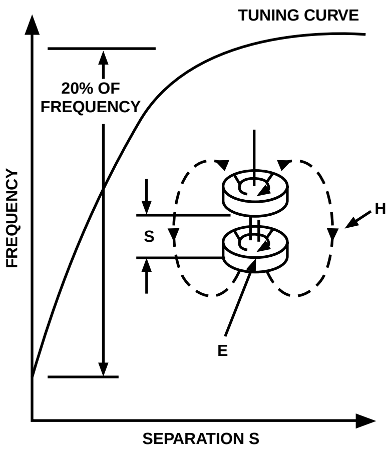

FIGURE 6.28 Double dielectric resonator configuration and tuning curve showing 20% tuning range.

Applications

The miniaturization of microwave components began with the introduction of microwave integrated circuits (MIC) and general advances in semiconductor technology, especially gallium arsenide. MIC components have become very common and presently more advanced, monolithic circuits (MMICs) are

TABLE 6.4 Basic Properties of High Quality Ceramics

Material Composition	Manufacturer	ε	Loss Tangent @ 4 GHz	Temp. Coeff. ppm/degree C
Ba Ti_4O_9	Raytheon, Transtech	38	0.0001	+4
$Ba_2Ti_9O_{20}$	Bell Labs	40	0.0001	+2
(Zr-Sn) TiO_4	Murata Tekelec Siemens Transtech	38	0.0001	−4 to +10 adj.
$Ba(Zn_{1/3}Nb_{2/3})O_2$– $Ba(Zn_{1/3}Ta_{2/3})O_2$	Murata	30	0.00004	0 to +10 adj.

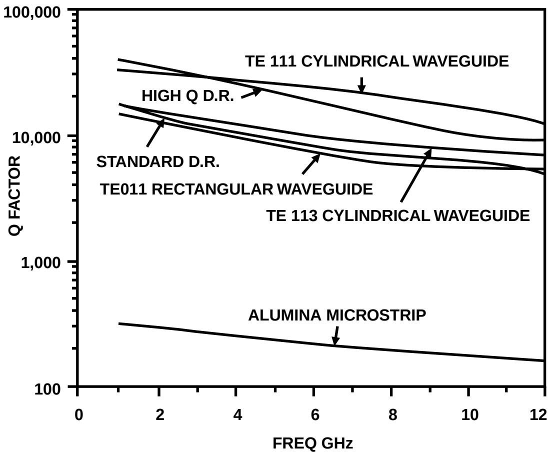

FIGURE 6.29 Achievable quality factor (Q) of various microwave resonator types (copper waveguide — 60 to 70% of theoretical Q is assumed).

being used in many applications. MIC/MMIC structures have suffered, however, from a lack of high Q miniature elements that are required to construct high performance, narrowband filters, and highly stable, fundamental frequency oscillators.Expensive and bulky coaxial and waveguide resonators made out of temperature-stable materials such as INVAR or graphite composites were the only solution in the past (Fig. 6.29). With the dielectric resonator described above, a very economical alternative, which also satisfies very stringent performance requirements, was introduced. Dielectric resonators find use as probing devices to measure dielectric properties of materials as well as the surface resistance of metals, and more recently high temperature superconductors (HTS). Additional applications include miniature antennas, where strongly radiating lower order resonator modes are successfully used.[24]

Filters

Simultaneously with advances in dielectric resonator technology, significant advances were made in microwave filter technology. More sophisticated, high performance designs (such as elliptic function filters) are now fairly common. Application of dielectric resonators in high quality filters is most evident in bandpass and bandstop filters. There are some applications in directional filters and group delay equalizers, but bandpass and bandstop applications using dielectric resonators dominate the filter field.

Bandpass and bandstop filter fields can be subdivided according to the dielectric resonator mode being used. The most commonly used mode is the $TE_{01\delta}$. The $HE_{11\delta}$ (degenerate) hybrid mode finds applications in sophisticated elliptic function filters and high frequency oscillators. This particular mode offers the

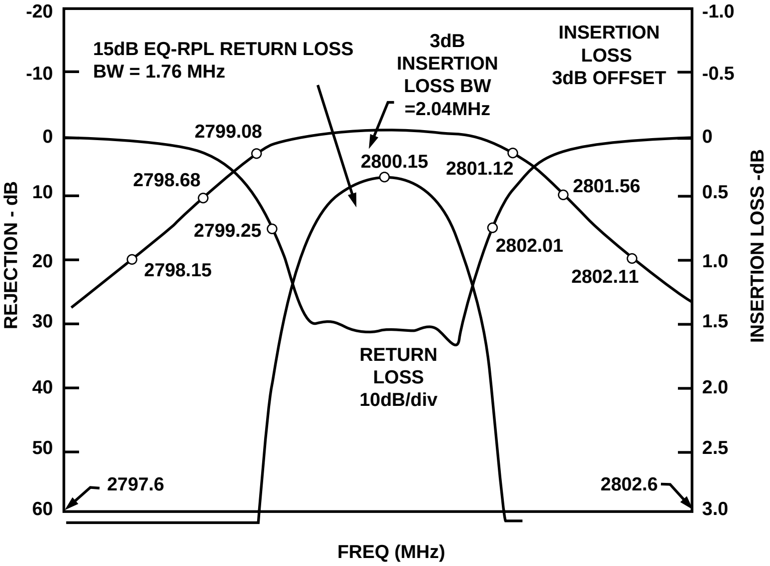

FIGURE 6.30 Typical performance of a four-pole, single made dielectric resonator filter showing insertion loss corresponding to Q factor of 9000.

advantage of smaller volume and weight (approximately $^1/_2$) when compared to a single mode device. This is possible since each resonator resonates in two orthogonal, independent modes.

Single Mode Bandpass Filters

The basic bandpass filter topology element generally can be described as a section of an evanescent-mode waveguide (waveguide below cutoff) in which the dielectric resonators are housed. This particular configuration was originally proposed by Okaya and Barash[5] and later expanded by Cohn[6] and Harrison.[25] The orientation of dielectric resonators can be either transverse or coaxial.

The transverse configuration yields a larger filter, but is presently preferred in practical designs because these can be more conveniently tuned with screws concentric with the resonators. Typical configurations of such filters are presented in Fig. 6.31. Actual performance of one of the filters is shown in Fig. 6.30. This particular design suffers from spurious responses on the high frequency side of the filter and suppressing techniques for these frequencies are necessary. The situation is worse when a microstrip transmission line is used to couple between the resonators.

The equivalent Q-factor of the filter is degraded and mounting of the dielectric resonator on special supports is usually necessary. Also, extra care must be taken to select proper dimensions of the dielectric resonator (e.g., D/L ratio) to place spurious modes as far as possible from the operating frequency. Sufficient spacing from metal walls of the housing is also important since close proximity of conductive walls degrades the high intrinsic Q of the dielectric resonator.

Dual Mode Filters

After reviewing literature in the dielectric resonator area, it is obvious that most attention has been directed toward analysis and applications of the fundamental $TE_{01\delta}$ mode. Higher order modes and the $HE_{11\delta}$ mode, which for certain ratios of diameter/length has a lower resonant frequency than that of the $TE_{01\delta}$ mode, are considered spurious and hard to eliminate. Even for a radially symmetrical mode like $TE_{01\delta}$, which has only 3 components of the electromagnetic field, rigorous analysis is still a problem, and various simplifying assumptions are required. The situation is much more complex for higher modes that are generally hybrid, are usually degenerate, and have all six components of the electromagnetic field.

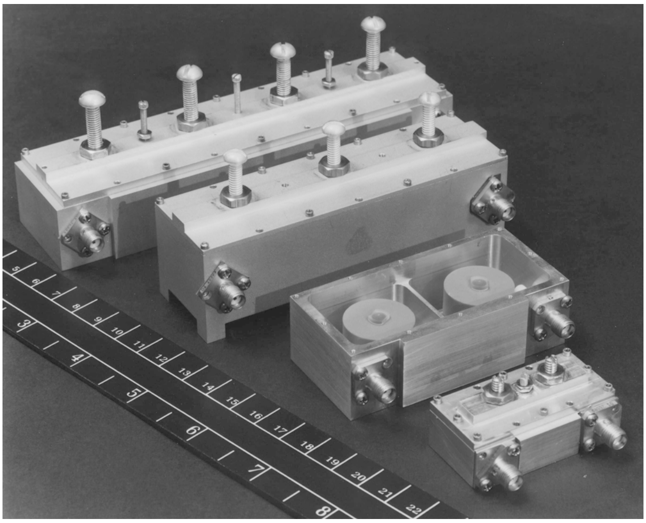

FIGURE 6.31 Single mode dielectric resonator filters (2.8 GHz and 5.6 GHz).

A typical filter configuration using the $HE_{11\delta}$ mode (in line) is presented in Fig. 6.32.[26] Coupling between modes within a single cavity is achieved via a mode-coupling screw with an angular location of 45 degrees with respect to orthogonal tuning screws.

Intercavity coupling is provided by polarization-sensitive coupling slots. This arrangement is similar to that presently used in metal-cavity filters. The design is identical and the standard filter synthesis method can be used. Dielectric resonators are mounted axially in the center of each evanescent, circular cavity. A low-loss stable mounting is required to ensure good electrical and temperature performance.

Size comparison between traditional cavity filters and a dielectric resonator filter is shown in Fig. 6.33. Weight reduction by a factor of five and volume reduction by a factor of > 20 can be achieved. Spurious response performance of the 8-pole filters is similar to the TE_{111} mode cavity filter.

It was found that selection of diameter/length ratios greater than two yields optimum spacing of spurious responses. The TE $_{01\delta}$ mode is not excited because of the axial orientation of the resonator in the center of a circular waveguide.

One of the factors in evaluating a filter design, that is equal in importance to its bandpass characteristics, is its temperature stability. Since most of the electromagnetic field of a dielectric resonator is contained in the material forming the resonator, temperature properties of the filter are basically determined by properties of the ceramics. Typical temperature performance of the filters is in the order of ±1ppm/°C with almost perfect temperature compensation possible.[28]

Dielectric Resonator Probe

The dielectric resonator probe configuration illustrated in Fig. 6.34 employs a dielectric resonator sandwiched between two conductive metal plates in a "post resonator" configuration. The "post resonator" is a special configuration of the dielectric resonator. In a "post resonator," the xy surfaces of the resonator are conductive (e.g., metalized).

The measured Q factor from this configuration is dominated by the losses from the conductive plates directly above and below the dielectric resonator and the dielectric loss (loss tangent) of the dielectric resonator materials. Either one of these two loss contributors can be calibrated out and the other one can be determined with a great accuracy. If we calibrate out the conductive loss (in metal plates) the dielectric loss can be determined.[27,28] In the other case, the loss tangent of the dielectric resonator is known and the conductivity of the nearby metal or superconductor is unknown.[29] As in the case of the other measurement, surface resistance is calculated from a measured Q value.

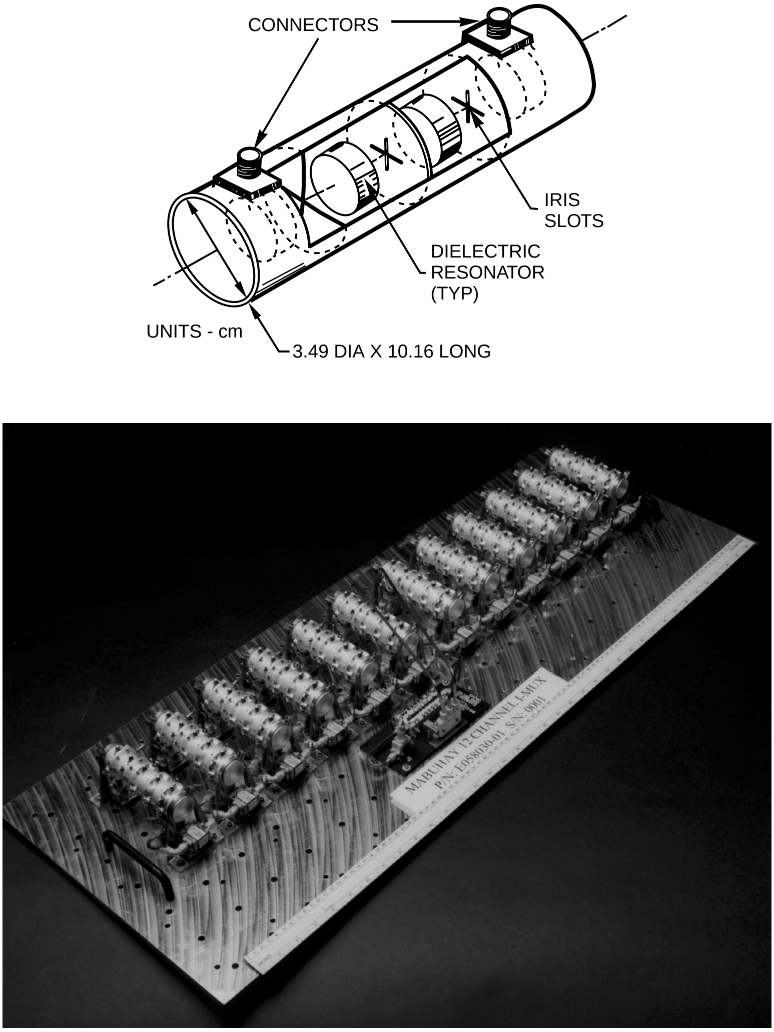

FIGURE 6.32 Dual mode bandpass filter configuration and multiplexer assembly using dual mode dielectric resonator filters.

The TE_{011} mode (post resonator) is used for these measurements since it is easily identified, relatively insensitive to small gaps between the dielectric and the test sample, and has no axial currents across any possible discontinuities in the probe fixture**.**

Diode Oscillators

Dielectric resonators have been used with Gunn diode oscillators to reduce frequency variations resulting from temperature or bias changes and to lower the oscillator phase noise. A typical configuration of such an oscillator is shown in Fig. 6.35. Stability in order of 0.5 ppm/degree C is achievable at 10 GHz.[30]

Gunn diode oscillators exhibit lower phase noise at higher frequencies when compared to FET oscillators. Their performance is inferior, however, when factors such as efficiency and required bias levels are taken into consideration. An interesting application of dielectric resonators, which were used for stabilization of a 4 GHz high power IMPATT oscillator, is shown in Fig. 6.36.[31] The novel oscillator configuration uses two dielectric resonators. This technique allows independent control of fundamental and harmonic frequencies of the oscillator.

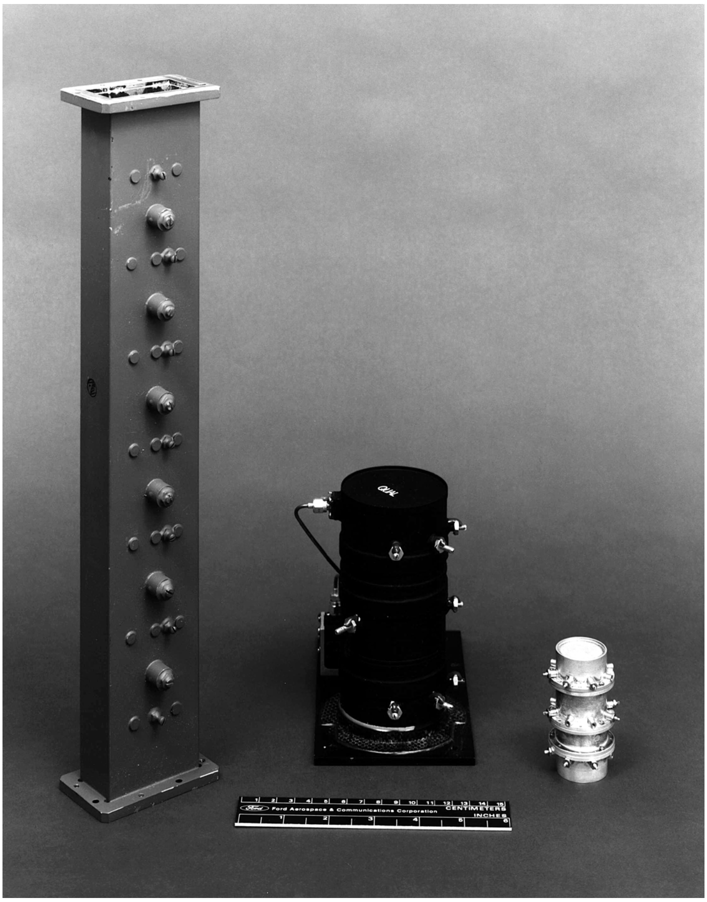

FIGURE 6.33 Size comparisons between traditional cavity filters and dielectric resonator filter (single mode rectangular waveguide filter, dual mode circular cavity filter, and dual mode dielectric resonator filter are shown).

At very high millimeter wave frequencies, dielectric resonators are too small to be effectively controlled. Therefore, much larger resonators utilizing whispering gallery dielectric resonator modes are preferred.[32-38] An additional advantage of these resonators (higher order modes) is better confinement of the electromagnetic field inside the dielectric resonator and consequently, the higher Q factor.

Field Effect Transistor and Bipolar Transistor Oscillators

FET (or bipolar) oscillators using dielectric resonators are classified as reflection or feedback oscillators (Fig. 6.37).

For a reflection oscillator, initial design starts with either an unstable device or external feedback (low Q) to obtain negative resistance and reflection gain at the desired frequency. Next, a properly designed dielectric resonator is placed approximately one-half wavelength away from the FET or bipolar device. In this configuration, the dielectric resonator acts as a weakly coupled bandstop filter with a high external Q. Part of the output energy is reflected toward the device and such a self-injected oscillator will generate a signal at the resonant frequency of the dielectric resonator.

Typical reflection oscillators exhibit very good phase noise characteristics and frequency stability of approximately 1.5 ppm/degree C. Because of the reflective mode of operation, however, these designs are sensitive to load changes and require an output isolator or buffer amplifier.

Feedback oscillators can be divided into two classes: shunt feedback and series feedback (see Fig. 6.37). In these examples, a dielectric resonator actually forms the feedback circuit of the amplifying element,

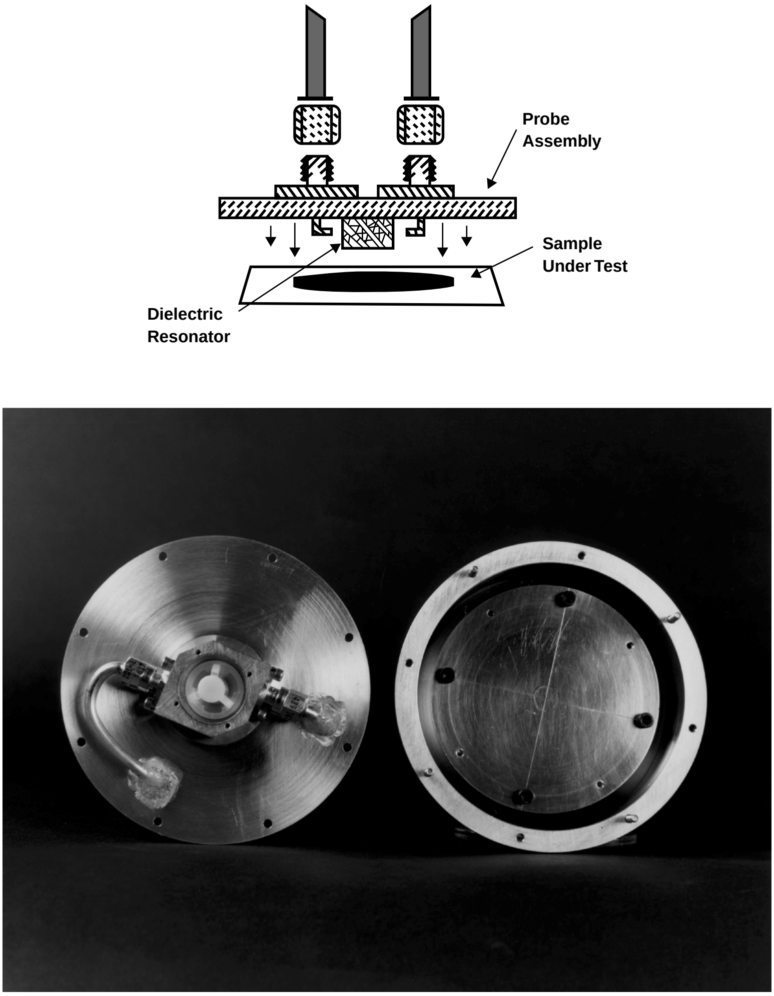

FIGURE 6.34 Illustration and photograph of the dielectric resonator probe.

usually a FET or bipolar transistor. In the shunt feedback arrangement, the resonator is placed between the output and input of the device (e.g., between gate and source, or gate and drain circuits). The conditions for oscillations are met at the resonant frequency of the dielectric resonator. In the shunt feedback scheme, however, the resonator is strongly coupled to the drain and gate transmission lines. Therefore, the loaded Q of the circuit is quite low and phase noise performance is degraded.

Another circuit that yields high stability and low phase noise is the series feedback oscillator.[39] This circuit consists of a high-gain, low-noise FET or bipolar transistor, a 50 ohm transmission line connected to the FET gate (bipolar-base) terminated with a 50 ohm resistor for out-of-band stability, a dielectric resonator coupled to the line and located at the specific distance from the gate (base), a shunt reactance connected to the FET source or drain (collector), and matching output impedance. Critical to the performance of this circuit is the placement of the dielectric resonator on the gate port, where it is isolated from the output circuits by the very low drain to gate capacitance inherent in the device. This isolation minimizes interaction between the output and input ports, which allows the resonator to be lightly coupled to the gate, resulting in a very high loaded Q, and therefore, minimum phase noise. A photograph of the typical dielectric resonator oscillator is shown in Fig. 6.37. The phase noise performance, which demonstrates suitability of such oscillators for stringent communication systems is presented in Fig. 6.38.

Stake, Jan et al. "Active Device Technologies"
The RF and Microwave Handbook
Editor in Chief Mike Golio
Boca Raton: CRC Press LLC,2001

Jan Stake
Chalmers University of Technology

Jack East
University of Michigan

Robert J. Trew
U.S. Department of Defense

John C. Cowles
Analog Devices — Northwest Laboratories

William Liu
Texas Instruments

Leonard MacEachern
Carleton University

Tajinder Manku
University of Waterloo

Michael S. Shur
Rensselaer Polytechnic Institute

Prashant Chavarkar
CREE Lighting Company

Umesh Mishra
University of California

Karen E. Moore
Motorola

Jerry C. Whitaker
Technical Press

Lawrence P. Dunleavy
University of South Florida

7 Active Device Technologies

7.1 Semiconductor Diodes

7.1.1 Varactors

Jan Stake

A varactor is a nonlinear reactive device used for harmonic generation, parametric amplification, mixing, detection, and voltage-variable tuning.[1] However, present applications of varactors are mostly for harmonic generation at millimeter and submillimeter wave frequencies, and as tuning elements in various microwave applications. Varactors normally exhibit a voltage-dependent capacitance and can be fabricated from a variety of semiconductor materials.[2] A common varactor is the reverse biased Schottky diode. Advantages of varactors are low loss and low noise. The maximum frequency of operation is mainly limited by a parasitic series resistance (see Fig. 7.1).

Basic Concepts

Many frequencies may interact in a varactor, and of those, some may be useful inputs or outputs, while the others are *idlers* that, although they are necessary for the operation of the device, are not part of any

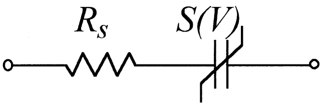

FIGURE 7.1 Equivalent circuit of a pure varactor.[4]

input or output. For instance, to generate high harmonics in a frequency multiplier it is more or less necessary to allow current at intermediate harmonics (idlers) to flow. Such idler circuits are usually realized as short-circuit resonators, which maximize the current at idler frequencies.

Manley-Rowe Formulas

The Manley-Rowe formulas[3] for *lossless* nonlinear reactances are useful for intuitive understanding of multipliers, frequency converters, and dividers. Consider a varactor excited at two frequencies f_p and f_s; the corresponding general Manley-Rowe formulas are

$$\sum_{m=1}^{\infty}\sum_{n=-\infty}^{\infty}\frac{mP_{m,n}}{nf_p+mf_s}=0$$

$$\sum_{m=-\infty}^{\infty}\sum_{n=1}^{\infty}\frac{nP_{m,n}}{nf_p+mf_s}=0$$

where m and n are integers representing different harmonics and $P_{m,n}$ is the average power flowing into the nonlinear reactance at the frequencies nf_p and mf_s.

- Frequency multiplier (m = 0): if the circuit is designed so that only real power can flow at the input frequency, f_p, and at the output frequency, nf_p, the above equations predict a theoretical efficiency of 100%. The Manley-Rowe equation is $P_1 + P_n = 0$.
- Parametric amplifier and frequency converter: assume that the RF-signal at the frequency f_s is small compared to the pump signal at the frequency f_p. Then, the powers exchanged at sidebands of the frequencies nf_p and mf_s for m different from 1 and 0 are negligible. Furthermore, one of the Manley-Rowe formulas only involves the small-signal power as

$$\sum_{n=-\infty}^{\infty}\frac{P_{1,n}}{nf_p+f_s}=0$$

Hence, the nonlinear reactance can act as an amplifying upconverter for the input signal at frequency f_s and output signal extracted at $f_u = f_s + f_p$ with a gain of

$$\frac{P_u}{P_s}=\frac{P_{1,1}}{P_{1,0}}=-\left(1+\frac{f_p}{f_s}\right)=-\frac{f_u}{f_s}$$

Varactor Model

The intrinsic varactor model in Fig. 7.1 has a constant series resistance, R_s, and a nonlinear differential elastance, $S(V) = dV/dQ = 1/C(V)$, where V is the voltage across the diode junction. This simple model is used to describe the basic properties of a varactor and is adequate as long as the displacement current is much larger than any conduction current across the junction. A rigorous analysis should also include the effect of a frequency- and voltage-dependent series resistance, and the equivalent circuit of parasitic elements due to packaging and contacting. The differential elastance is the slope of the voltage-charge

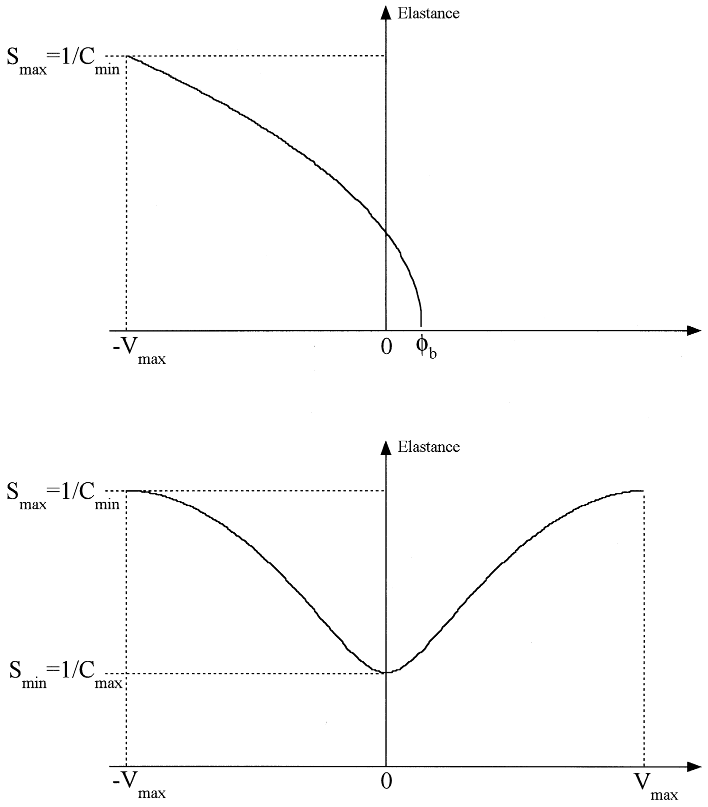

FIGURE 7.2 Elastance as a function of voltage for (top) one side junction diodes and (bottom) symmetric diodes.

relation of the diode and the reciprocal of the differential capacitance, $C(V)$. Since the standard varactor model consists of a resistance in series with a nonlinear capacitance, the elastance is used rather than the capacitance. This simplifies the analysis and gives, generally, a better understanding of the varactor. The differential elastance can be measured directly and is used rather than the ratio of voltage to charge.

The elastance versus voltage for a conventional varactor and a symmetric varactor are shown in Fig. 7.2. In both cases, the maximum available elastance is achieved at the breakdown voltage. The conventional varactor is reverse biased in order to allow maximum elastance swing and avoid any forward conduction current. A symmetric varactor will only produce odd harmonics when a sinusoidal signal is applied. This means that a varactor frequency tripler can be realized without any second harmonic idler circuit or DC bias. This simplifies the design of such circuits and, hence, many novel symmetric varactors have been proposed. Among these, the Heterostructure Barrier Varactor (HBV)[5] has so far shown the best performance.

Pumping

The pumping of a varactor is the process of passing a large current at frequency f_p through the varactor. The nonlinear varactor then behaves as a time-varying elastance, $S(t)$, and the series resistance dissipates power due to the large-signal current. The allowable swing in elastance is limited by the maximum elastance of the device used. Hence, the time domain equation describing the varactor model in Fig. 7.1 is given by:

$$V(t) = R_s i(t) + \int S(t) i(t) dt$$

The above equation, which describes the varactor in the time domain, must be solved together with equations describing the termination of the varactor. How the varactor is terminated at the input, output, and idler frequencies has a strong effect on the performance. The network has to terminate the varactor at some frequencies and couple the varactor to sources and loads at other frequencies. Since this embedding circuit is best described in the frequency domain, the above time domain equation is converted to the frequency domain. Moreover, the varactor is usually pumped strongly at one frequency, f_p, by a local oscillator. If there are, in addition, other small signals present, the varactor can be analyzed in two steps: (1) a large signal simulation of the pumped varactor at the frequency f_p, and (2) the varactor behaves like a time-varying linear elastance at the signal frequency, f_s. For the large signal analysis, the voltage, current, and differential elastance can be written in the forms

$$i(t) = \sum_{k=-\infty}^{\infty} I_k e^{jk\omega_p t},\ I_{-k} = I_k^*$$

$$V(t) = \sum_{k=-\infty}^{\infty} V_k e^{jk\omega_p t},\ V_{-k} = V_k^*$$

$$S(t) = \sum_{k=-\infty}^{\infty} S_k e^{jk\omega_p t},\ S_{-k} = S_k^*$$

Hence, the time domain equation that governs the above varactor model can be converted to the frequency domain and the relation between the Fourier coefficients, I_k, V_k, S_k, reads

$$V_k = R_s I_k + \frac{1}{jk\omega_p} i(t) = \sum_{l=-\infty}^{\infty} I_l S_{k-1}$$

The above equation is the general starting point for analyzing varactors. Since there is a relation between the Fourier coefficients S_k and I_k, the above equation is nonlinear and hard to solve for the general case. Today, the large signal response is usually calculated with a technique called harmonic balance.[6] This type of nonlinear circuit solver is available in most commercial microwave CAD tools.

Assume that the varactor is fully pumped and terminated so that the voltage across the diode junction becomes sinusoidal. The corresponding elastance waveforms for the conventional and symmetrical varactor in Fig. 7.2 are shown in Fig. 7.3. It is important to note that the fundamental frequency of the symmetric elastance device is twice the pump frequency.

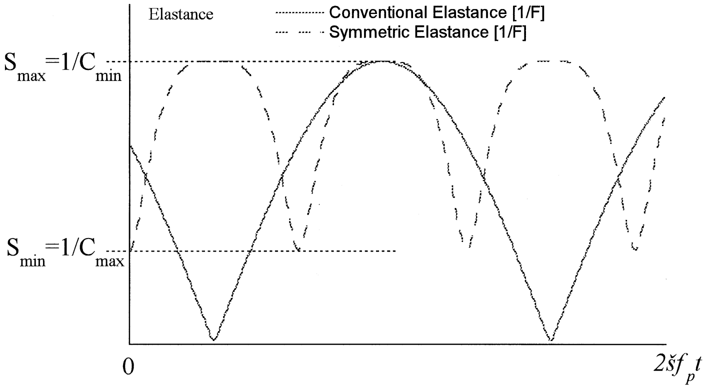

FIGURE 7.3 Elastance waveform $S(t)$ during full pumping with a sinusoidal voltage across the diode junction.

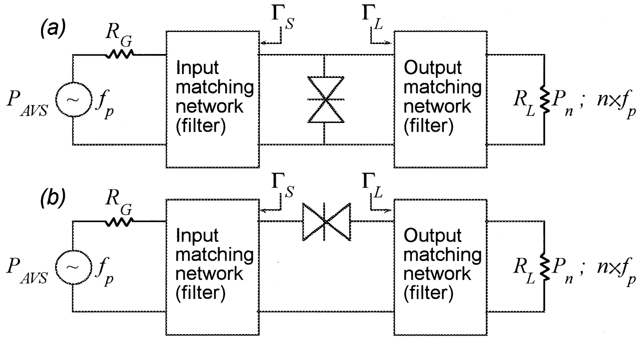

FIGURE 7.4 Block scheme of n^th^-order frequency multiplier circuit with (a) shunt-mounted and (b) series-mounted diodes.

The nonlinear part of the elastance, $S(t) - S_{\min}$, creates harmonics and its impedance should be large compared to the series resistance, R_s, for a good varactor. The impedance ratio of the series resistance and the nonlinear part of the elastance at the fundamental frequency can be written as

$$\frac{R_s}{\dfrac{S_{\max} - S_{\min}}{2\pi f_p}} = \frac{f_p}{f_c}$$

and the dynamic cutoff frequency is introduced as

$$f_c = \frac{S_{\max} - S_{\min}}{2\pi R_s}$$

The dynamic cutoff frequency is an important figure of merit for many varactor applications and a typical value for a state-of-the-art varactor is more than 1 THz. The starting point for a varactor design is, hence, to maximize the elastance swing, $S_{\max} - S_{\min}$, and minimize any losses, R_s. For semiconductor varactors, the maximum elastance swing is limited by at least one of the following conditions:

- depletion layer punch-through,
- large electron conduction from impact ionization or forward conduction current,
- current saturation. The saturated electron velocity in the material determines the maximum length an electron can travel during a quarter of a pump cycle.[7]

Increasing the pump power beyond any of the above conditions will result in reduced performance and probably introduce extra noise.

Varactor Applications

Frequency Multipliers

Varactor frequency multipliers are extensively used to provide LO power to sensitive millimeter- and submillimeter-wavelength receivers. Today, frequency multipliers are the main application of varactors. Solid-state multipliers are relatively inexpensive, compact, lightweight, and reliable compared to vacuum tube technology, which makes them suitable for space applications at these frequencies. State-of-the-art balanced Schottky doublers can deliver 55 mW at 174 GHz[8] and state-of-the-art four-barrier HBV triplers deliver about 9 mW at 248 GHz.[9]

Frequency multiplication or harmonic generation in devices occur due to their nonlinearity. Based on whether the multiplication is due to a nonlinear resistance or a nonlinear reactance, one can differentiate between the varistor and varactor type of multipliers. Varactor type multipliers have a high potential conversion efficiency, but exhibit a narrow bandwidth and a high sensitivity to operating conditions. According to the Page-Pantell inequality, multipliers that depend upon a nonlinear resistance have at most an efficiency of $1/n^2$, where n is the order of multiplication.[10,11] The absence of reactive energy storage in varistor frequency multipliers ensures a large bandwidth. For the ideal varactor multiplier, i.e., a lossless nonlinear reactance, the theoretical limit is a conversion efficiency of 100% according to the Manley-Rowe formula. However, real devices exhibit properties and parameters that are a mixture of the ideal varistor and the ideal varactor multiplier. The following set of parameters is used to describe and compare properties of frequency multipliers:

- Conversion loss, L_n, is defined as the ratio of the available source power, P_{AVS}, to the output harmonic power, P_n, delivered to the load resistance. It is usually expressed in decibels. The inverted value of L_n, i.e., the conversion efficiency, η_n, is often expressed as a percent.
- In order to minimize the conversion loss, the optimum source and load embedding impedances, Z_S and Z_L, should be provided to the diode. Optimum source and load impedances are found from maximizing, e.g., the conversion efficiency, and they depend on each other and on the input signal level. In a nonlinear circuit, such as a multiplier, it is not possible to define a true impedance. However, a "quasi-impedance", Z_n, can be defined for periodic signals as

$$Z_n = \frac{V_n}{I_n}$$

where V_n and I_n are the voltage and the current, respectively, at the n^{th} harmonic.

Basic Principles of Single Diode Frequency Multipliers — Single diode frequency multipliers can either be shunt or series mounted. In both cases the input and the output filter should provide optimum embedding impedances at the input and output frequencies, respectively. The output filter should also provide an open circuit for the shunt-mounted varactor and a short circuit for the series-mounted varactor at the pump frequency. The same arguments apply to the input filter at the output frequency. Analysis and design of conventional doublers and high order varactor multipliers are described well in the book by Penfield et al.[1] and in Reference 12.

In addition to the above conditions, the correct impedances must be provided at the idler frequencies for a high order multiplier (e.g., a quintupler). In general, it is hard to achieve optimum impedances at the different harmonics simultaneously. Therefore, a compromise has to be found.

Performance of Symmetric Varactor Frequency Multipliers — In Fig. 7.5 a calculation of the minimum conversion loss for a tripler and a quintupler is shown. To systematically investigate how the tripler and quintupler performance depends on the shape of the S-V characteristic, a fifth degree polynomial model was employed by Dillner et al.[13] The best efficiency is obtained for a S-V characteristic with a large nonlinearity at zero volts or a large average elastance during a pump cycle. The optimum idler circuit for the quintupler is an inductance in resonance with the diode capacitance (i.e., maximized third harmonic current).

Practical Multipliers — Since frequency multipliers find applications mostly as sources at higher millimeter and submillimeter wave frequencies, they are often realized in waveguide mounts[14,15] (see Fig. 7.6). A classic design is the arrangement of crossed rectangular waveguides of widths specific for the input and output frequency bands. The advantages are:

- The input signal does not excite the output waveguide, which is cut off at the input frequency.
- Low losses.
- The height of the waveguide in the diode mounting plane may be chosen to provide the electrical matching conditions. Assuming a thin planar probe, the output embedding impedance is given by analytical expressions.[16]
- Movable short circuits provide input/output tunability.

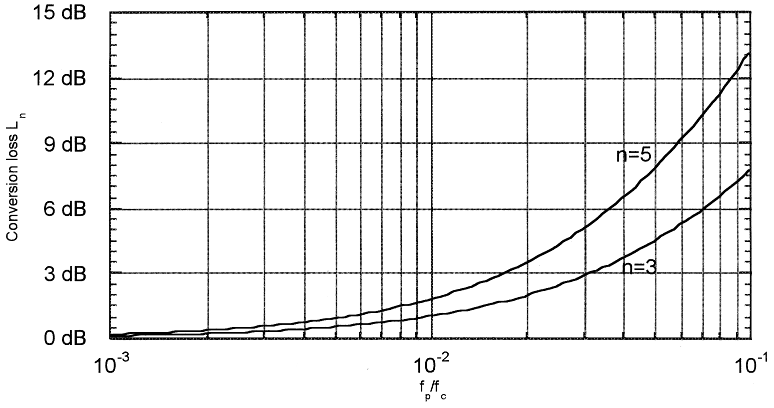

FIGURE 7.5 The minimum conversion loss for a tripler and a quintupler for the symmetric *S-V* characteristic shown in Fig. 7.2. The pump frequency is normalized to the dynamic cutoff frequency. For the quintupler case, the idler circuit is an inductance in resonance with the diode capacitance.

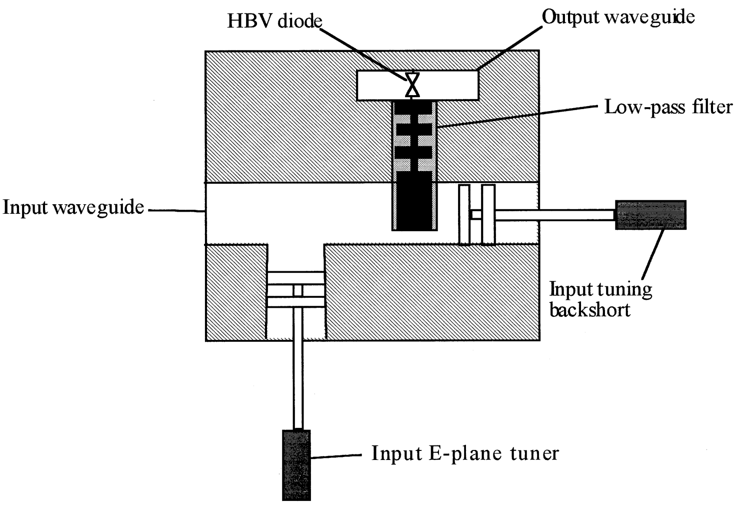

FIGURE 7.6 Schematic diagram of a crossed waveguide frequency multiplier. The output signal is isolated from the input waveguide with a low pass filter.

Today, whole waveguide mounts can be analyzed and designed using commercially available high frequency electromagnetic CAD tools. They either solve Maxwell's equations in the frequency domain or in the time domain using the FDTD method.

The inherently limited bandwidth of varactors can be improved by employing a transmission line periodically loaded with varactors.[17,18] These NonLinear Transmission Lines (NLTLs) can currently provide the largest bandwidth and still achieve a reasonable conversion efficiency as a frequency multiplier. Simultaneous effects of nonlinearity and dispersion may also be used for pulse compression (soliton propagation).

Frequency Converters

The varactor is useful as a frequency converter because of its good noise properties, and because gain can be achieved. The nonlinear reactance is pumped at a frequency f_p, and a small signal is introduced at a frequency f_s. Power will exchange at frequencies of the form $nf_p + f_s$ (n can be negative). If the output frequency is higher than the input frequency, the varactor acts as an upconverter, otherwise it is a downconverter. Furthermore, one differ between lower (n = –1) and upper sideband (n = 1) converters, and according to whether or not power is dissipated at any other sidebands (idlers).

Assume that the elastance is pumped sinusoidally (i.e., $S_k = 0$ for $|k| > 1$), the varactor is open-circuited at all frequencies except $f_s, f_p, f_u = f_p + f_s$, and that the varactor termination tunes out the average elastance. The source resistance is then adjusted to give optimum gain or optimum noise temperature. For the upper sideband upconverter, the minimal noise temperature is

$$T_{\min} = T_d \frac{2f_s}{m_1 f_c}\left[\frac{f_s}{m_1 f_c} + \sqrt{1 + \left(\frac{f_s}{m_1 f_c}\right)^2}\right]$$

when the source resistance is

$$R_o^T = R_s \sqrt{1 + \left(\frac{m_1 f_c}{f_s}\right)^2}$$

where T_d is the diode temperature, f_c is the dynamic cutoff frequency, and m_1 is the modulation ratio defined as

$$m_1 = \frac{|S_1|}{S_{\max} - S_{\min}}$$

It can be shown that there is gain under optimum noise termination conditions only for signal frequencies smaller than $0.455 m_1 f_c$.[1] A different source resistance will result in maximum gain

$$R_o^G = R_s \sqrt{1 + \frac{m_1^2 f_c^2}{f_s f_u}}$$

The corresponding optimum gain is

$$G_{MAX} = \left(\frac{\dfrac{m_1 f_c}{f_s}}{1 + \sqrt{1 + \dfrac{m_1^2 f_c^2}{f_s f_u}}}\right)^2$$

As predicted by the Manley-Rowe formula for a lossless varactor, the gain increases as the output frequency, f_u, increases. The effect of an idler termination at $f_I = f_p - f_s$ can further increase the gain and reduce the noise temperature.

The above expressions for optimum noise and the corresponding source impedance are valid for the lower sideband upconverter as well. However, the lower sideband upconverter may have negative input and output resistances and an infinite gain causing stability problems and spurious oscillations. All pumped varactors may have such problems. With a proper choice of source impedance and pump frequency, it is possible to simultaneously minimize the noise and make the exchangeable gain infinite. This occurs for an "optimum" pump frequency of $f_p = \sqrt{m_1^2 f_c^2 + f_s^2}$ or approximately $m_1 f_c$ if the signal frequency is small. Further information on how to analyze, design, and optimize frequency converters can be found in the book by Penfield et al.[1]

Parametric Amplifiers

The parametric amplifier is a varactor pumped strongly at frequency f_p, with a signal introduced at frequency f_s. If the generated sidebands are terminated properly, the varactor can behave as a negative resistance at f_s. Especially the termination of the idler frequency, $f_p - f_s$, determines the real part of the impedance at the signal frequency. Hence, the varactor can operate as a negative resistance amplifier at the signal frequency, f_s. The series resistance limits the frequencies f_p and f_c for which amplification can be achieved and it also introduces noise.

The explanation of the effective negative resistance can be described as follows: The application of signal plus pump power to the nonlinear capacitance causes frequency mixing to occur. When current is allowed to flow at the idler frequency $f_p - f_s$, further frequency mixing occurs at the pump and idler frequencies. This latter mixing creates harmonics of f_p and $f_p - f_s$, and power at f_s is generated. When the power generated through mixing exceeds that being supplied at the signal frequency f_s, the varactor appears to have a negative resistance. If idler current is not allowed to flow, the negative resistance vanishes. Assuming that the elastance is pumped sinusoidally (i.e., $S_k = 0$ for $|k| > 1$), and the varactor is open circuited at all frequencies except f_s, f_p, $f_i = f_p - f_s$, and that the varactor termination tunes out the average elastance, gain can only be achieved if

$$f_s f_i \left(R_s + R_i\right) < R_s m_1^2 f_c^2$$

where R_i is the idler resistance. By terminating the varactor reactively at the idler frequency, it can be shown that a parametric amplifier attains a minimum noise temperature when pumped at the optimum pump frequency, which is exactly the same as for the simple frequency converter. This is true for nondegenerated amplifiers where the frequencies are well separated. The degenerate parametric amplifier operates with f_i close to f_s, and can use the same physical circuit for idler and signal frequencies. The degenerate amplifier is easier to build, but ordinary concepts of noise figure, noise temperature, and noise measure do not apply.

Voltage Tuning

One important application of varactors is voltage tuning. The variable capacitance is used to tune a resonant circuit with an externally applied voltage. This can be used to implement a Voltage Controlled Oscillator (VCO), since changing the varactor capacitance changes the frequency of oscillation within a certain range. As the bias is increased, the resonant frequency f_o increases from $f_{o,\min}$ to $f_{o,\max}$ as the elastance changes from $S_{\min}$ to $S_{\max}$. If the present RF power is low, the main limitations are the finite tuning range implied by the minimum and maximum elastance and the fact that the series resistance degrades the quality factor, Q, of the tuned circuit. The ratio of the maximum and minimum resonant frequency gives a good indication of the tunability

$$\frac{f_{o,\max}}{f_{o,\min}} \le \sqrt{\frac{S_{\max}}{S_{\min}}}$$

However, if the present RF power level is large, the average elastance, which determines the resonant frequency, depends upon drive level as well as bias. Second, the allowed variation of voltage is reduced for large RF power levels.

Since the varactor elastance is nonlinear, quite steep at low voltages, and almost flat at high voltages, the VCO tuning range is not naturally linear. However, an external bias circuit can improve the linearity of the VCO tuning range. It is also possible to optimize the doping profile of the varactor in terms of linearity, Q-value, or elastance ratio.

Varactor Devices

Conventional Diodes

Common conventional varactors at lower frequencies are reverse biased semiconductor abrupt p^+-n junction diodes made from GaAs or silicon.[2] However, metal-semiconductor junction diodes (Schottky diodes) are superior at high frequencies since the carrier transport only relies on electrons (unipolar device). The effective mass is lower and the mobility is higher for electrons compared to holes. Furthermore, the metal-semiconductor junction can be made very precisely even at a submicron level. A reverse biased Schottky diode exhibits a nonlinear capacitance with a very low leakage current. High frequency diodes are made from GaAs since the electron mobility is much higher than for silicon.

The hyperabrupt p^+-n junction varactor diode has a nonuniform n-doping profile and is often used for voltage tuning. The n-doping concentration is very high close to the junction and the doping profile is tailored to improve elastance ratio and sensitivity. Such doping profiles can be achieved with epitaxial growth or by ion implantation.

The Heterostructure Barrier Varactor Diode

The Heterostructure Barrier Varactor (HBV), first introduced in 1989 by Kollberg et al.,[5] is a symmetric varactor. The main advantage compared to the Schottky diode is that several barriers can be stacked epitaxially. Hence, an HBV diode can be tailored for a certain application in terms of both frequency and power handling capability. Moreover, the HBV operates unbiased and is a symmetric device, thus generating only odd harmonics. This greatly simplifies the design of high order and broadband multipliers.

The HBV diode is an unipolar device and consists of a symmetric layer structure. An undoped high band gap material (barrier) is sandwiched between two moderately n-doped, low band gap materials. The barrier prevents electron transport through the structure. Hence, the barrier should be undoped (no carriers), high and thick enough to minimize thermionic emission and tunnelling of carriers. When the diode is biased a depleted region builds up (Fig. 7.7), causing a nonlinear CV curve.

Contrary to the Schottky diode, where the barrier is formed at the interface between a metallic contact and a semiconductor, the HBV uses a heterojunction as the blocking element. A heterojunction, i.e., two adjacent epitaxial semiconductor layers with different band gaps, exhibits band discontinuities both in the valence and in the conduction band. Since the distance between the barriers (>1000 Å) is large compared to the de Broglie wavelength of the electron, it is possible to understand the stacked barrier structure as a series connection of N individual barriers. A generic layer structure of an HBV is shown in Table 7.1.

The HBV Capacitance — The parallel plate capacitor model, where the plate separation should be replaced with the sum of the barrier thickness, b, the spacer layer thickness, s, and the length of the depleted region, w, is normally an adequate description of the (differential) capacitance. The depletion

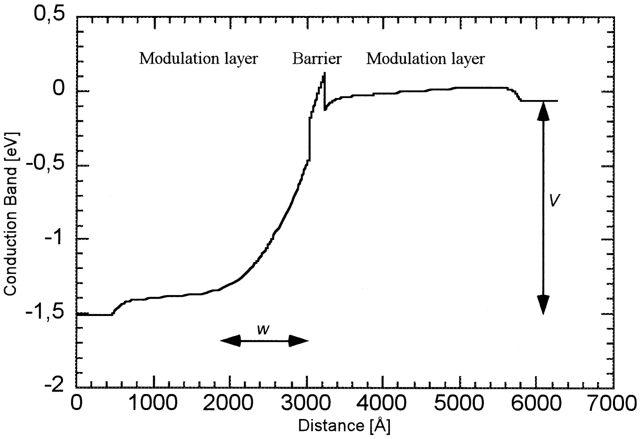

FIGURE 7.7 Conduction band of a biased GaAs/Al$_{0.7}$GaAs HBV.

TABLE 7.1 Generic Layer Structure of an HBV

Layer		Thickness [Å]	Doping Level [cm^{-3}]	
7	Contact	~3000	n^{++}	
6	Modulation	l = 3000	$N_d \sim 10^{17}$	
5	Spacer	s = 50	undoped	
4	Barrier	$b \geq 100$	undoped	xN
3	Spacer	s = 50	undoped	
2	Modulation	l = 3000	$N_d \sim 10^{17}$	
1	Buffer	—	n^{++}	
0	Substrate		n^{++} or SI	

Note: For N epitaxially stacked barriers, the layer sequence 2–5 is repeated N times.

length is bias dependent and the layer structure is symmetric, therefore the elastance is an even function of applied voltage and is given by

$$S = \frac{1}{C} = \frac{N}{A}\left(\frac{b}{\varepsilon_b} + \frac{s}{\varepsilon_d} + \frac{w}{\varepsilon_d}\right)$$

$$w = \sqrt{\frac{2\varepsilon_d \left|V_d\right|}{qN_d}}$$

where V_d is the voltage across the depleted region, N_d is the doping concentration in the modulation layers, b is the barrier thickness, s is the undoped spacer layer thickness, A is the device area, and ε_b and ε_d are the dielectric constants in the barrier material and modulation layers, respectively. The maximum capacitance or the minimum elastance, $S_{\min}$, occurs at zero bias. However, due to screening effects, the minimum elastance, $S_{\min}$, must include the extrinsic Debye length, L_D, as:

$$S_{\min} = \frac{1}{C_{\max}} = \frac{N}{A}\left(\frac{b}{\varepsilon_b} + \frac{2s}{\varepsilon_d} + \frac{2L_D}{\varepsilon_d}\right)$$

$$L_D \equiv \sqrt{\frac{\varepsilon_d kT}{q^2 N_d}}$$

To achieve a high $C_{\max}/C_{\min}$ ratio, the screening length can be minimized with a sheet doping, N_s, at the spacer/depletion layer interface. The minimum capacitance, $C_{\min}$, is normally obtained for punch through condition, i.e., $w = l$, or when the breakdown voltage, $V_{\max}$, is reached.

An accurate quasi-empirical expression for the C-V characteristic of homogeneously doped HBVs has been derived by Dillner et al.[19] The voltage across the nonlinear capacitor is expressed as a function of its charge as

$$V(Q) = N\left(\frac{bQ}{\varepsilon_b A} + 2\frac{sQ}{\varepsilon_d A} + Sign(Q)\left(\frac{Q^2}{2qN_d\varepsilon_d A^2} + \frac{4kT}{q}\left(1 - e^{\frac{|Q|}{2L_D AqN_d}}\right)\right)\right)$$

where T is the device temperature, q is the elementary charge, and Q is the charge stored in the HBV.

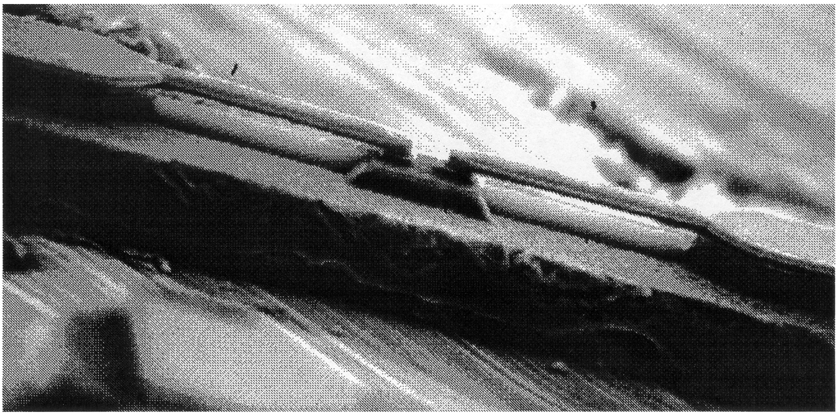

FIGURE 7.8 Planar four-barrier HBV (37 μm²/CTH-NU2003J).

The substrate is either highly doped or semi-insulating (SI), depending on how the device is intended to be mounted. The contact layers (Nos. 1 and 7) should be optimized for low losses. Therefore, the buffer layer (No. 1) must be relatively thick ($\delta \sim 3$ μm) and highly doped for planar HBVs (see Fig. 7.8). The barrier itself can consist of different layers to further improve the blocking characteristic. The spacer prevents diffusion of dopants into the barrier layer and increases the effective barrier height. The thickness of the barrier layer will not influence the cutoff frequency, but it has some influence on the optimum embedding impedances. Hence, the thickness is chosen to be thick enough to avoid tunneling of carriers. Several III-V semiconductor material systems have been employed for HBVs. The best choices to date for HBVs are the lattice matched $In_{0,53}Ga_{0,47}As/In_{0,52}Al_{0,48}As$ system grown on InP substrate and the lattice matched GaAs/AlGaAs system grown on GaAs substrate. High dynamic cutoff frequencies are achieved in both systems. However, the GaAs/AlGaAs system is well characterized and relatively easy to process, which increases the probability of reproducible results. The $In_{0,53}GaAs/In_{0,52}AlAs$ system exhibits a higher electron barrier and is therefore advantageous from a leakage current point of view. The thickness and doping concentration of the modulation layers should be optimized for maximal dynamic cutoff frequency.[20]

In the future, research on wide bandgap semiconductors (e.g., InGaN) could provide solutions for very high power HBVs, a combination of a II-VI barrier for low leakage current and a III-V modulation layer for high mobility and peak velocity. Today, narrow bandgap semiconductors from the III-V groups (e.g., $In_xGa_{1-x}As$) seem to be the most suitable for submillimeter wave applications.

The Si/SiO$_2$/Si Varactor

By bonding two thin silicon wafers, each with a thin layer of silicon dioxide, it is possible to form a structure similar to HBV diodes from III-V compounds. The SiO_2 layer blocks the conduction current very efficiently, but the drawback is the relatively low mobility of silicon. If a method to stack several barriers can be developed, this material system may be interesting for lower frequencies where the series resistance is less critical.

The Ferroelectric Varactor

Ferroelectrics are dielectric materials characterized by an electric field and temperature-dependent dielectric constant. Thin films of $Ba_xSr_{1-x}TiO_3$ have been proposed to be used for various microwave applications. Parallel plate capacitors made from such films can be used in varactor applications. However, the loss mechanisms at strong pump levels and high frequencies have not yet been fully investigated.

References

1. P. Penfield and R. P. Rafuse, *Varactor Applications.* Cambridge: M.I.T. Press, 1962.
2. S. M. Sze, *Physics of Semiconductor Devices,* 2nd ed. Singapore: John Wiley & Sons, 1981.

3. J. M. Manley and H. E. Rowe, Some General Properties of Nonlinear Elements, *IRE Proc.,* 44, 78, 904–913, 1956.
4. A. Uhlir, The potential of semiconductor diodes in high frequency communications, *Proc. IRE,* 46, 1099–1115, 1958.
5. E. L. Kollberg and A. Rydberg, Quantum-barrier-varactor diode for high efficiency millimeter-wave multipliers, *Electron. Lett.,* 25, 1696–1697, 1989.
6. S. A. Maas, Harmonic Balance and Large-Signal-Small-Signal Analysis, in *Nonlinear Microwave Circuits.* Artech House, Norwood, MA, 1988.
7. E. L. Kollberg, T. J. Tolmunen, M. A. Frerking, and J. R. East, Current saturation in submillimeter wave varactors, *IEEE Trans. Microwave Theory and Techniques,* 40, 5, 831–838, 1992.
8. B. J. Rizzi, T. W. Crowe, and N. R. Erickson, A high-power millimeter-wave frequency doubler using a planar diode array, *IEEE Microwave and Guided Wave Letters,* 3, 6, 188–190, 1993.
9. X. Mélique, A. Maestrini, E. Lheurette, P. Mounaix, M. Favreau, O. Vanbésien, J. M. Goutoule, G. Beaudin, T. Nähri, and D. Lippens, 12% Efficiency and 9.5 dBm Output Power from InP-based Heterostructure Barrier Varactor Triplers at 250 GHz, presented at IEEE-MTT Int. Microwave Symposium, Anaheim, CA, 1999.
10. R. H. Pantell, General power relationship for positive and negative nonlinear resistive elements, *Proceedings IRE,* 46, 1910–1913, December 1958.
11. C. H. Page, Harmonic generation with ideal rectifiers, *Proceedings IRE,* 46, 1738–1740, October 1958.
12. C. B. Burckhardt, Analysis of varactor frequency multipliers for arbitrary capacitance variation and drive level, *The Bell System Technical Journal,* 675–692, April 1965.
13. L. Dillner, J. Stake, and E. L. Kollberg, Analysis of symmetric varactor frequency multipliers, *Microwave Opt. Technol. Lett.,* 15, 1, 26–29, 1997.
14. J. W. Archer, Millimeter wavelength frequency multipliers, *IEEE Trans. on Microwave Theory and Techniques,* 29, 6, 552–557, 1981.
15. J. Thornton, C. M. Mann, and P. D. Maagt, Optimization of a 250-GHz Schottky tripler using novel fabrication and design techniques, *IEEE Trans. on Microwave Theory and Techniques,* 46, 8, 1055–1061, 1998.
16. E. L. Eisenhart and P. J. Khan, Theoretical and experimental analysis for a waveguide mounting structure, *IEEE Trans. on Microwave Theory and Techniques,* 19, 8, 1971.
17. S. Hollung, J. Stake, L. Dillner, M. Ingvarson, and E. L. Kollberg, A distributed heterostructure barrier varactor frequency tripler, *IEEE Microwave and Guided Wave Letters,* 10, 1, 24–26, 2000.
18. E. Carman, M. Case, M. Kamegawa, R. Yu, K. Giboney, and M. J. Rodwell, V-band and W-band broadband, monolithic distributed frequency multipliers, *IEEE Microwave and Guided Wave Letters,* 2, 6, 253–254, 1992.
19. L. Dillner, J. Stake, and E. L. Kollberg, Modeling of the Heterostructure Barrier Varactor Diode, presented at 1997 International Semiconductor Device Research Symposium, Charlottesville, SC, 1997.
20. J. Stake, S. H. Jones, L. Dillner, S. Hollung, and E. Kollberg, Heterostructure barrier varactor design, *IEEE Trans. on Microwave Theory and Techniques,* 48, 4, Part 2, 2000.

Further Information

M. T. Faber, J. Chramiec, and M. E. Adamski, *Microwave and Millimeter-Wave Diode Frequency Multipliers.* Artech House Publishers, Norwood, MA, 1995.

S. A. Maas, *Nonlinear Microwave Circuits.* Artech House, Norwood, MA, 1988.

P. Penfield and R. P. Rafuse, *Varactor Applications.* M.I.T. Press, Cambridge, 1962.

S. Yngvesson, *Microwave Semiconductor Devices.* Kluwer Academic Publishers, Boston, 1991.

7.1.2 Schottky Diode Frequency Multipliers

Jack East

Heterodyne receivers are an important component of most high frequency communications systems and other receivers. In its simplest form a receiver consists of a mixer being pumped by a local oscillator. At lower frequencies a variety of local oscillator sources are available, but as the desired frequency of operation increases, the local oscillator source options become more limited. The "lower frequencies" limit has increased with time. Early transistor oscillators were available in the MHz and low GHz range. Two terminal transit time devices such as IMPATT and Gunn diodes were developed for operation in X and Ka band in the early 1970s. However, higher frequency heterodyne receivers were needed for a variety of communications and science applications, so alternative local oscillator sources were needed. One option was vacuum tubes. A variety of vacuum tubes such as klystrons and backward wave oscillators grew out of the radar effort during the Second World War. These devices were able to produce large amounts of power over most of the desired frequency range. However, they were large, bulky, expensive, and suffered from modest lifetimes. They were also difficult to use in small science packages.

An alternative solid state source was needed and the technology of the diode frequency multiplier was developed beginning in the 1950s. These devices use the nonlinear reactance or resistance of a simple semiconductor or diode to produce high frequency signals by frequency multiplication. These multipliers have been a part of many high frequency communications and science applications since that time. As time passed the operating frequencies of both transistors and two-terminal devices increased. Silicon and GaAs transistors have been replaced by much higher frequency HFETs and HBTs with f_{max} values of hundreds of GHz. Two-terminal IMPATT and Gunn diodes can produce more than 100 milliwatts at frequencies above 100 GHz. However, the desired operating frequencies of communications and scientific applications have also increased. The most pressing needs are for a variety of science applications in the frequency range between several hundred GHz and several THz. Applications include space-based remote sensing of the earth's upper atmosphere to better understand the chemistry of ozone depletion and basic astrophysics to investigate the early history of the universe. Both missions will require space-based heterodyne receivers with near THz local oscillators. Size, weight, and prime power will be important parameters. Alternative approaches include mixing of infrared lasers to produce the desired local oscillator frequency from higher frequencies, and a multiplier chain to produce the desired frequency from lower frequencies. Laser-based systems with the desired output frequencies and powers are available, but not with the desired size and weight. Semiconductor diode-based frequency multipliers have the modest size and weight needed, but as of now cannot supply the required powers, on the order of hundreds of microwatts, needed for the missions. This is the subject of ongoing research.

The goal of this chapter is to briefly described the performance of diode frequency multipliers in order to better understand their performance and limitations. The chapter is organized as follows. The next section will describe the properties of Schottky barrier diodes, the most useful form of a varactor multiplier. The following section will describe the analytic tools developed to predict multiplier operation. Two limitations, the reactive multiplier described by Manley and Rowe and the resistive multiplier discussed by Page will be discussed. The results of these two descriptions can be used to understand the basic limits of multiplier operation. However, these analytic results do not provide enough information to design operating circuits. A more realistic computer-based design approach is needed. This will be discussed in the next section. Limitations on realistic devices and some alternative structures will then be described followed by a look at one future application and a brief summary.

Schottky Diode Characteristics

Multiplier operation depends on the nonlinear properties of Schottky diodes. The diode has both a capacitive and a resistive nonlinearity. Consider the simple representation of a uniformly Schottky diode shown in Fig. 7.9. Figure 7.11(a) shows a semiconductor with a Schottky barrier contact on the right and an ohmic contact on the left. The semiconductor has a depletion layer width *w*, with the remaining portion of the structure undepleted. The depletion layer can be represented as a capacitor and the

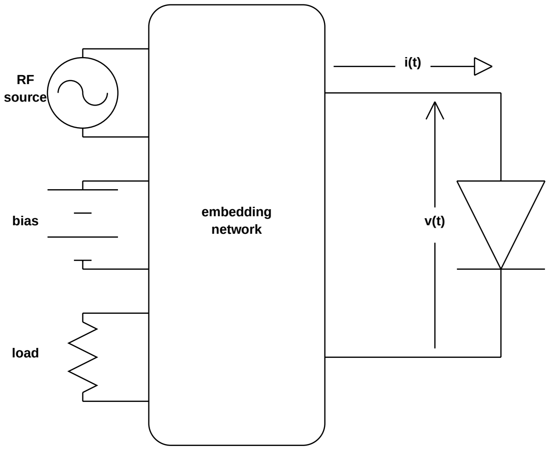

FIGURE 7.9 Schottky diodes (a) structure, (b) electric field, (c) capacitance vs. voltage, and (d) equivalent circuit.

undepleted portion can be represented as a resistor. The depletion layer will act as a parallel plate capacitor with a capacitance of

$$C = \frac{\epsilon A}{w}, \tag{7.1}$$

where C is the capacitance, ϵ is the dielectric constant, A is the area, and W is the depletion width w from Fig. 7.9(a). The electric field vs. distance for this structure is shown in Fig. 7.9(b). For reasonable conditions the electric field in the undepleted region is small. The field in the depletion regions extends over the width of the depletion region and depends linearly on x. The area under the electric field curve in Fig. 7.9(b) is the depletion layer voltage, the sum of the applied voltage V_b and the built-in potential ϕ_{bi}. The resulting depletion width vs. applied reverse voltage is

$$w = \sqrt{\frac{2\epsilon\left(\phi_{bi} + V_{bios}\right)}{qN_d}}, \tag{7.2}$$

where ϕ_{bi} is the built-in potential of the metal semiconductor or junction, V_{bios} is the applied reverse bias, q is the electronic charge, and N_d is the uniform semiconductor doping. This width vs. applied bias will result in the capacitance vs. applied voltage of the form

$$C\left(V\right) = \frac{C_{i0}}{\sqrt{\phi_{bi} + V_{bios}}} \tag{7.3}$$

where C_{i0} is the capacitance at zero applied bias. The resulting capacitance vs. bias voltage is shown in Fig. 7.9(c). This capacitance characteristic is the starting point for the analytic models in the next section. However, other effects are also present. Under realistic pumping conditions, the diode can also be forward biased allowing forward conduction current flow. This can be approximated with a nonlinear voltage-dependent resistance. The resulting equivalent circuit then becomes the right 2 nonlinear elements in Fig. 7.9(c). There are also parasitic elements. The undepleted region of the device and various contact and package resistance will appear in series with the nonlinear junction. Although the undepleted region width is voltage dependent, this series resistance is usually modeled with a constant value. However, at very high frequencies the current through the undepleted region can crowd to the outside edge of the material due to the skin effect, increasing the resistance. This frequency-dependent resistance is sometimes included in multiplier simulations [9]. The varactor diode must be connected to the external circuit. This resulting physical connection usually results in a parasitic shunt capacitance associated with the connection and a parasitic series inductance associated with the current flow through the wire connection. A major part of multiplier research over the past decade has involved attempts to reduce these parasitic effects.

This nonlinear capacitance vs. voltage characteristic can be used as a frequency multiplier. Consider the charge Q in the nonlinear capacitance as a function of voltage

$$Q(v) = \sqrt{a(\phi_{bi} - V)}, \tag{7.4}$$

where a is a constant. This function can be expanded in a series

$$Q(V) = a_0 + a_1 V + a_2 V^2 + a_3 V^3 + \dots, \tag{7.5}$$

The current $I(t)$ is the time derivative of the charge,

$$I(t) = \frac{dQ}{dt} = \left[a_1 + 2a_2 V + 3a_3 V^2 + \dots\right]\frac{dV}{dt} \tag{7.6}$$

If $V(t)$ is of the form $V_{rf}\, sin\ \omega t$, then the higher order V terms will produce harmonics of the input pump frequency.

Analytic Descriptions of Diode Multipliers

Equation (7.6) shows that we can get higher order frequencies out of a nonlinear element. However, it is not clear what the output power or efficiency will be. The earliest research on frequency multipliers were based on closed form descriptions of multiplier operation to investigate this question. This section will discuss the ideal performance of reactive and resistive frequency multipliers.

A nonlinear resistor or capacitor, when driven by a pump source, can generate a series of harmonic frequencies. This is the basic form of a harmonic multiplier. The Manley-Rowe relations are a general description of power and frequency conversion relations in nonlinear reactive elements [1, 2]. They describe the properties of frequency conversion and general in nonlinear reactances. The earliest work on these devices sometimes used nonlinear inductances, but all present work involves the nonlinear capacitance vs. voltage characteristic of a reverse-biased Schottky barrier diode. Although the Manley Rowe equations describe frequency multiplication, mixer operation, and parametric amplification, they are also useful as an upper limit on multiplier operation. If an ideal nonlinear capacitance is a pump with a local oscillator at frequency f_0, and an embedding circuit allows power flow at harmonic frequencies, then the sum of the powers into and out of the capacitor is zero,

$$\sum_{m=0}^{\infty} P_m = 0. \tag{7.7}$$

This expression shows that we can have an ideal frequency multiplier at 100% efficiency converting input power to higher frequency output power if we properly terminate all the other frequencies. Nonlinear resistors can also be used as frequency multipliers [3, 4]. For a nonlinear resistor pumped with a local oscillator at frequency f_0, the sum of the power is

$$\sum_{m=0}^{\infty} m^2 P_m \geq 0. \tag{7.8}$$

For an m^{th} order resistive harmonic generator with only an input and output signal, the efficiency is at best $\frac{1}{m^2}$, 25% for a doubler and 11% for a tripler.

Although Eqs. (7.7) and (7.8) give upper limits on the efficiency to be expected from a multiplier, they provide little design information for real multipliers. The next step in multiplier development was the development of closed form expressions for design based on varactor characteristics [5, 6]. Burckardt [6] gives design tables for linear and abrupt junction multipliers based on closed form expressions for the charge in the diode. These expressions form the starting point for waveform calculations. Computer simulations based on the Fourier components of these waveforms give efficiency and impedance information from 2nd to 8th order. However, these approximations limit the amount of design information available. A detailed set of information on multiplier design and optimization requires a computer-based analysis.

Computer-Based Design Approaches

The analytic tools discussed in the last section are useful to predict the ideal performance of various frequency multipliers. However, more exact techniques are needed for useful designs. Important information such as input and output impedances, the effects of series resistance, and the effect of harmonic terminations at other harmonic frequencies are all important in multiplier design. This information requires detailed knowledge of the current and voltage information at the nonlinear device. Computer-based simulations are needed to provide this information. The general problem can be described with the help of Fig. 7.10. The multiplier consists of a nonlinear microwave diode, an embedding network that provides coupling between the local oscillator source and the output load, provisions for DC bias and terminations for all other non-input or output frequencies. Looking toward the embedding network from the diode, the device sees embedding impedances at the fundamental frequency and each of the harmonic frequencies. The local oscillator power available is usually specified along with the load impedances and the other harmonic frequencies under consideration. The goal is to obtain the operating conditions, the output power and efficiency, and the input and output impedances of the overall circuit. The nonlinear nature of the problem makes the solution more difficult. Within the context of Fig. 7.10, the current as a function of time is a nonlinear function of the voltage. Device impedances can be obtained from ratios of the Fourier components of the voltage and current. The impedances of the diode must match the embedding impedances at the corresponding frequency. A "harmonic balance" is required for the correct situation. Many commercial software tools use nonlinear optimization techniques to solve

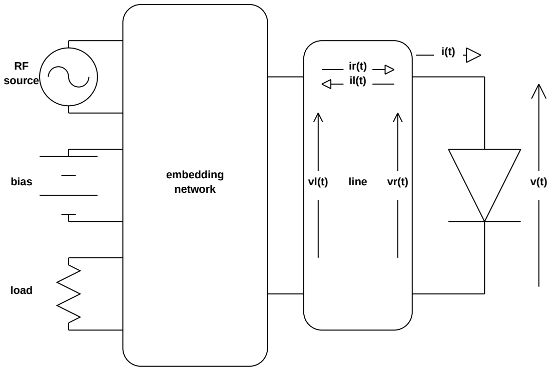

FIGURE 7.10 Generalized frequency multiplier.

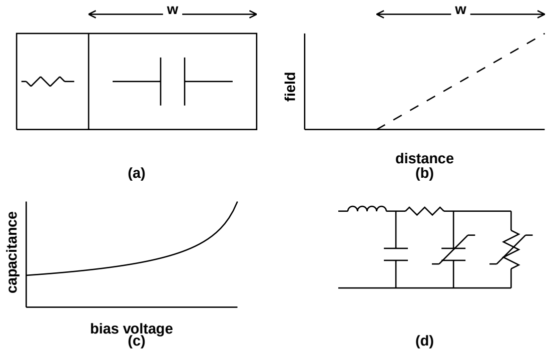

FIGURE 7.11 Multiple reflection circuit.

this "harmonic balance" optimization problem. An alternative approach is the multiple reflection algorithm. This solution has the advantage of a very physical representation of the actual transient response of the circuit. This technique is discussed in References 7, 8, and 9 and will be described here.

The basic problem is to calculate the diode current and voltage waveforms when the device is embedded in an external linear circuit. The diode waveforms are best represented in the time domain. However, the embedding circuit consists of linear elements and is best represented in the frequency or impedance domain. One approach is the multiple reflection technique [7, 8, 9]. This technique splits the simulation into two parts, a nonlinear time domain description of the diode multiplier and a linear frequency domain description of the embedding network. The solution goal is to match the frequency domain impedances of the embedding circuit with the time domain impedances of the nonlinear device. The circuit is shown in Fig. 7.11. The initial circuit is modified by including a long transmission line with a length l equal to an integral number of pump frequency wavelengths and an arbitrary characteristic impedance Z_0 between the diode and the embedding network. Waves will propagate in both directions on this transmission line depending on the conditions at the ends. When steady-state conditions are reached, the waveforms at the circuit and the diode will be the same, with or without the transmission line. This transmission line allows us to determine the waveforms across the diode as a series of reflections from the circuit. The signals on the transmission line are composed of left- and right-traveling current and voltage waves. The voltage at the diode is the sum of the right- and left-traveling wave voltages,

$$v(x) = v_r(x) + v_l(x) \tag{7.9}$$

and the current at the diode is the difference

$$i(x) = i_r(x) - i_l(x) = \frac{v_r(x) - v_l(x)}{Z_0} \tag{7.10}$$

Since the transmission line is an integral number of pump frequency wavelengths long, the conditions are the same at each end under steady-state conditions,

$$v(x=0) = v(x=l) \tag{7.11}$$

$$i(x=0) = i(x=l) \tag{7.12}$$

At the start of the simulation, we assume that there is a right-traveling wave associated with the DC bias at frequency 0 and the pump at frequency 1. This wave with a DC component and a component at the local oscillator frequency will arrive at the diode at $x = 0$ as a $V_r(t)$. The resulting voltage across the diode will produce a diode current. This current driving the transmission line will produce a first reflected voltage,

$$v^1_{reflected} = v^1_l = \left(v^1_{diode} - i^1_{diode}\left(t\right)Z_0\right)\Big/2 \tag{7.13}$$

This time domain reflected or left-traveling wave will then propagate to the embedding network. Here is can be converted into the frequency domain with a Fourier transform. The resulting signal will contain harmonics of the local oscillator signal due to the nonlinear nature of the diode current vs. voltage and charge vs. voltage characteristic. The resulting frequency domain information can then be used to construct a new reflected voltage wave from the embedding network. This process of reflections from the diode and the circuit or "multiple reflections" continues until a steady-state solution is reached.

This computer-based solution has several advantages over the simpler analysis-based solutions. It can handle combinations of resistive and reactive nonlinearities. Most high-efficiency multipliers are pumped into forward conduction during a portion of the RF cycle so this is an important advantage for accurate performance predictions. In practice the varactor diode will also have series resistance, parasitic capacitances, and series inductances. These additional elements are easily included in the multiplier simulation. At very high frequencies the series resistance can be frequency dependent, due to current crowding in the semiconductor associated with the skin effect. This frequency dependence loss can also be included in simulations. Computer programs with these features are widely used to design high performance frequency multipliers.

An alternative solution technique is the fixed point method [10]. This technique uses a circuit similar to Fig. 7.11, with a nonlinear device and an embedding network connected with a transmission line. However, this approach uses a fixed point iteration to arrive at a converged solution. The solution starts with arbitrary voltages at the local oscillator frequency at the harmonics. With these starting conditions, a new voltage is obtained from the existing conditions using

$$V_{n,k+1} = \frac{Z_0 V_{rf}}{Z^L_n + Z_0} + \frac{Z^L_n\left(V_{n,k} - I_{n,k}Z_0\right)}{Z^L_n + Z_0} \tag{7.14}$$

for the driven local oscillator frequency and

$$V_{n,k+1} = \frac{Z_0}{Z^L_n + Z_0}\left(V_{n,k} - I_{n,k}Z_0\right) \tag{7.15}$$

for the remaining frequencies, where Z^L_n are the embedding impedances at frequency n, Z_0 is the same line characteristic impedance used in the multiple reflection simulation, $Z^{NL}_{n,k}$ is the nonlinear device impedance at frequency n and iteration number k, $V_{n,k}$, and $I_{n,k}$ are the frequency domain voltage and current at iteration k, and V^S_n is the RF voltage at the pump source. These two equations provide an iterative solution of the nonlinear problem. They are particularly useful when a simple equivalent circuit for the nonlinear device is not available. We now have the numerical tools to investigate the nonlinear operation of multipliers. However, there are some operating conditions where this equivalent circuit approach breaks down. Some of these limitations will be discussed in the next section.

Device Limitations and Alternative Device Structures

The simulation tools and simple device model do a good job of predicting the performance of low frequency diode multipliers. However, many multiplier applications require very high frequency output signals with reasonable output power levels. Under these conditions, the output powers and efficiencies predicted are always higher than the experimental results. There are several possible reasons. Circuit loss increases with frequency, so the loss between the diode and the external connection should be higher. Measurements are less accurate at these frequencies, so the differences between the desired designed circuit embedding impedances and the actual values may be different. Parasitic effects are also more important, degrading the performance. However, even when all these effects are taken into account, the experimental powers and efficiencies are still low. The problem is with the equivalent circuit of the diode in Fig. 7.9(d). It does not correctly represent the high frequency device physics [11]. The difficulty can be explained by referring back to Fig. 7.9(a). The device is a series connection of the depletion layer capacitance and a bulk series resistance. The displacement current flowing through the capacitor must be equal to the conduction current flowing through the undepleted resistive region. The capacitor displacement current is

$$I(t) = \frac{dC(V)V(t)}{dt} \tag{7.16}$$

If we approximate $V(t)$ with V_{rf} cos (ωt), then the current becomes

$$I(t) = V_{rf}\omega C(V)\sin\omega t + V(t)\frac{dC(V)}{dt} \tag{7.17}$$

For a given device, the displacement current and the resulting current through the resistor increase with the frequency and the RF voltage. At modest drive levels and frequencies the undepleted region can support this current and the equivalent resistance remains constant. However, the current density through the undepleted region is

$$J_{dep} = qN_d v(E), \tag{7.18}$$

where J_{dep} is the conduction current density in the undepleted region and $v(E)$ is the carrier velocity vs. electric field. At low electric fields the slope of the velocity field curve is constant with a value equal to the carrier mobility μ. However at higher electric fields, the velocity begins to saturate at a constant value. Additional increases in the electric field do not increase the conduction current through the varactor. This current saturation is a fundamental limit on the multiplier performance. A more physical explanation also uses Fig. 7.9(a). A nonlinear capacitor implies a change in the depletion layer width with voltage. However, changing the depletion layer width involves moving electrons from the depletion layer edge. These electrons are limited by their saturated velocity, so the time rate of change of the capacitance is also unlimited.

This simple theory allows a modified device design. Equations (7.18) and (7.17) are the starting point. Our goal is usually to optimize the power or efficiency available from a multiplier circuit. Clearly one option is to increase the doping N_d in Eq. (7.18) to increase the available J_{dep}. However, increasing the doping decreases the breakdown voltage and thus the maximum RF voltage that can be present across the reverse biased depletion layer. The device doping design becomes a parameter in the overall multiplier design. The optimum efficiency and optimum power operating points for the same input and output frequency are usually different. Although this simple description provides useful information, a detailed physical model is usually needed for best results [12].

The discussion so far has been based on a uniformly doped abrupt junction varactor. However, other doping or material layer combinations are possible [13]. One option is to tailor the doping or material profile to obtain a capacitance vs. voltage that is more nonlinear than the $1/\sqrt{V_{bios}}$ dependence in Eq. (7.2). Two options are the hyperabrupt varactor and the BNN structure. These devices are shown in Fig. 7.12.

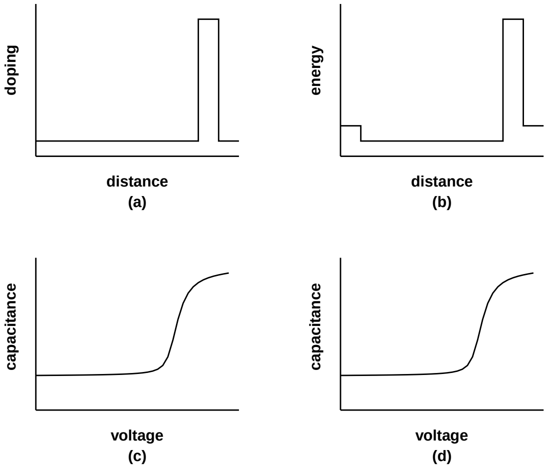

FIGURE 7.12 Alternative structures (a) hyperabrupt doping, (b) BNN energy, (c) hyperabrupt capacitance, and (d) BNN capacitance.

The doping profile of a hyperabrupt varactor is shown in Fig. 7.12(a). Instead of a uniform doping, this structure has a much smaller doping over most of the structure with a high doping or doping spike near the metal semiconductor junction. The corresponding capacitance vs. voltage characteristic is shown in Fig. 7.12(c). At modest reverse biases the depletion layer extends from the metal contact to the doping spike. The resulting narrow depletion layer produces a high capacitance. Higher applied voltages begin to deplete the charge in the doping spike. When the spike charge is depleted, there is a rapid increase in the depletion layer width through the second lightly doped region and a corresponding decrease in the capacitance. This structure can produce a more nonlinear capacitance variation than a uniformly doped device. However, the structure combines both lightly doped and heavily doped regions, so saturation effects can occur in the lightly doped portion. An alternative structure is the BNN or BIN device. This structure uses combinations of **B**arriers **I**ntrinsic and **N** doped regions formed with combinations of different epitaxial materials and doping to produce optimized capacitance structures. This structure can have either ohmic or Schottky contacts. A typical structure is shown in Fig. 7.12(b). Notice that conduction band energy rather than doping is being plotted. The structure consists of an $n+$ ohmic contact on the right followed by an n region that can be depleted, a wide bandgap barrier region, and a second $n+$ ohmic contact on the left. This structure can have a highly nonlinear capacitance characteristics as shown in Fig. 7.12(d), depending on the choice of layer doping and energy band offsets. These BNN structures have potential advantages in monolithic integration and can be fabricated in a stacked or series configuration for higher output powers.

Since the major application of frequency multipliers is for high frequency local oscillator sources, it would be reasonable to try to fabricate higher order multipliers, triplers for example, instead of doublers. Although based on Eq. (7.7), this is possible, there are some problems. Efficient higher order multiplication requires currents and voltages at intermediate frequencies, at the second harmonic in a tripler for example. This is an “idler” frequency or circuit. However, in order to avoid loss, this frequency must have the correct reactive termination. This adds to the complexity of the circuit design. Some details of doublers and triplers are given in Reference 14. An alternative that avoids the idlers is an even or symmetrical capacitance voltage characteristic. One possibility is the single barrier or quantum barrier varactor [15]. The structure and associated capacitance voltage characteristic are shown in Fig. 7.13. This structure, shown in Fig. 7.13(a), is similar to the BNN expect the barrier is the middle with lightly doped regions on either side. This will be a series connection of a depletion layer, a barrier and a depletion region, with ohmic contacts on each end. The capacitance is maximum at zero applied bias, with a built-in depletion layer on each side of the barrier. When a voltage is applied, one to the depletion layers will become forward biased and shrink and the other one will be reverse biased and expand. The series

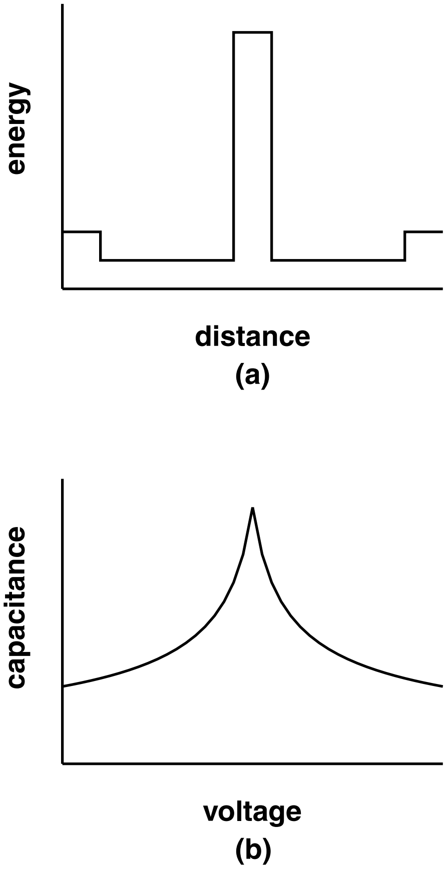

FIGURE 7.13 Structure and associated capacitance voltage characteristic.

combination capacitance will become smaller. Reversing the applied voltage will produce the same capacitance. The resulting symmetrical capacitance is shown in Fig. 7.13(b). This capacitance characteristic is a useful starting point for odd order multipliers.

Summary and Conclusions

This chapter has briefly discussed the properties of Schottky barrier diodes that are useful for frequency multipliers. Although a variety of other solid state sources are available for lower frequency sources, these devices are a critical component of future space-based applications.

References

1. J.M. Manley and H.E. Rowe, Some General Properties of Nonlinear Elements, I: General Energy Relations, *Proceedings of the IRE,* 44, 904, 1956.
2. H.A. Watson, *Microwave Semiconductor Devices and Their Circuit Applications,* McGraw-Hill, New York, 1969, chap. 8.
3. C.H. Page, Frequency Conversion With Positive Nonlinear Resistors, *Journal of Research of the National Bureau of Standards,* 56, 4, 179–182, April 1956.
4. R.H. Pantell, General Power Relationships for Positive and Negative Nonlinear Resistive Elements, *Proceedings of the IRE,* 46, 12, 1910–1913, December 1958.
5. J.A. Morrison, Maximization of the Fundamental Power in Nonlinear Capacitance Diodes, *Bell System Technical Journal,* 41, 677–721, 1962.

6. C.B. Burckardt, Analysis of Varactor Frequency Multipliers for Arbitrary Capacitance Variation and Drive Level, *Bell System Technical Journal,* 44, 675–692, 1965.
7. D.N. Held and A.R. Kerr, Conversion Loss and Noise of Microwave and Millimeter Wave Mixers: Part 1-Theory; Part 2 Experiment, *IEEE Transactions on Microwave Theory and Techniques,* MTT-26, 49, 1978.
8. S.A. Maas, *Microwave Mixers,* Artech House, Norwood, MA, 1986.
9. P. Siegel, A. Kerr and W. Hwang, Topics in the Optimization of Millimeter Wave Mixers, NASA Technical Paper 2287, March 1984.
10. G.B. Tait, Efficient Solution Method Unified Nonlinear Microwave Circuit and Numerical Solid-State Device Simulation, *IEEE Microwave and Guided Wave Letters,* 4, 12, 420–422, December 1994.
11. E.L. Kollberg, T.J. Tolmunen, M.A. Frerking, and J.R. East, Current Saturation in Submillimeter Wave Varactors, *IEEE Transactions on Microwave Theory and Techniques,* MTT-40, 5, 831–838, May 1992.
12. J.R. East, E.L. Kollberg and M.A. Frerking, Performance Limitations of Varactor Multipliers, Fourth International Conference on Space Terahertz Technology, Ann Arbor, MI, March 1993.
13. M. Frerking and J.R. East, Novel Heterojunction Varactors, *Proceedings of the IEEE Special Issue on Terahertz Technology,* 80, 11, 1853–1860, November 1992.
14. A. Raisanen, Frequency Multipliers for Millimeter and Submillimeter Wavelengths, *Proceedings of the IEEE Special Issue on Terahertz Technology,* 80, 11, 1842–1852, November 1992.
15. E. Kollberg and A. Rydberg, Quantum Barrier Varactor Diodes for High-Efficiency Millimeter-Wave Multipliers, *Electronics Letters,* 25, 1696–1697, December 1989.

7.1.3 Transit Time Microwave Devices

Robert J. Trew

There are several types of active two-terminal diodes that can oscillate or supply gain at microwave and millimeter-wave frequencies. These devices can be fabricated from a variety of semiconductor materials, but Si, GaAs, and InP are generally used. The most common types of active diodes are the IMPATT (an acronym for IMPact Avalanche Transit-Time) diode, and the Transferred Electron Device (generally called a Gunn diode). Tunnel diodes are also capable of producing active characteristics at microwave and millimeter-wave frequencies, but have been replaced in most applications by three-terminal transistors (such as GaAs MESFETs and AlGaAs/GaAs HEMTs), which have superior RF and noise performance, and are also much easier to use in systems applications. The IMPATT and Gunn diodes make use of a combination of internal feedback mechanisms and transit-time effects to create a phase delay between the RF current and voltage that is more than 90°, thereby generating active characteristics. These devices have high frequency capability since the saturated velocity of an electron in a semiconductor is high (generally on the order of ~10^7 cm/sec) and the transit time is short since the length of the region over which the electron transits can be made on the order of a micron (i.e., 10^{-4} cm) or less. The ability to fabricate devices with layer thicknesses on this scale permits these devices to operate at frequencies well into the millimeter-wave region. Oscillation frequency on the order of 400 GHz has been achieved with IMPATT diodes, and Gunn devices have produced oscillations up to about 150 GHz. These devices have been in practical use since the 1960s and their availability enabled a wide variety of solid-state system components to be designed and fabricated.

Semiconductor Material Properties

Active device operation is strongly dependent upon the charge transport, thermal, electronic breakdown, and mechanical characteristics of the semiconductor material from which the device is fabricated. The charge transport properties describe the ease with which free charge can flow through the material. This is described by the charge velocity-electric field characteristic, as shown in Fig. 7.14 for several commonly used semiconductors. At low values of electric field, the charge transport is ohmic and the charge velocity

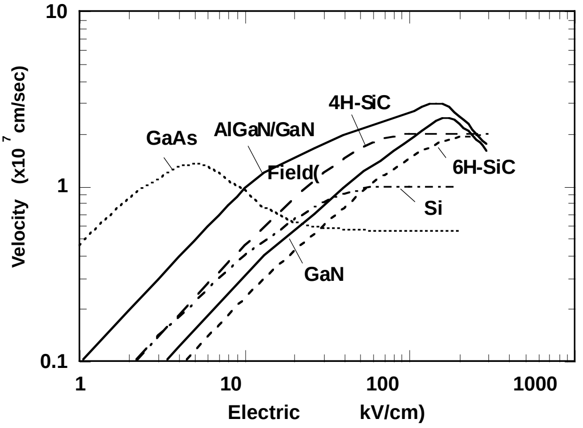

FIGURE 7.14 Electron velocity versus electric field characteristics for several semiconductors.

is directly proportional to the magnitude of the electric field. The proportionality constant is called the mobility and has units of cm^2/V-sec. Above a critical value for the electric field, the charge velocity (units of cm/sec) saturates and either becomes constant (e.g., Si) or decreases with increasing field (e.g., GaAs). Both of these behaviors have implications for device fabrication, especially for devices intended for high frequency operation. Generally, for transit time devices, a high velocity is desired since current is directly proportional to velocity. The greatest saturated velocity is demonstrated for electrons in the wide bandgap semiconductors, SiC and GaN. Both of these materials have saturated electron velocities on the order of $v_s \sim 2 \times 10^7$ cm/sec. This is one of the main reasons these materials are being developed for high frequency electronic devices. Also, a low value for the magnitude of the electric field at which velocity saturation occurs is desirable since this implies high charge mobility. High mobility produces low resistivity, and therefore low values for parasitic and access resistances for semiconductor devices.

The decreasing electron velocity with electric field characteristic for compound semiconductors such as GaAs and InP makes active two-terminal devices called Transferred Electron Devices (TED's) or Gunn diodes possible. The negative slope of the velocity versus electric field characteristic implies a decreasing current with increasing voltage. That is, the device has a negative resistance. When a properly sized piece of these materials is biased in the region of decreasing current with voltage, and placed in a resonant cavity, the device will be unstable up to very high frequencies. By proper selection of embedding impedances, oscillators or amplifiers can be constructed.

Other semiconductor material parameters of interest include thermal conductivity, dielectric constant, energy bandgap, electric breakdown critical field, and minority carrier lifetime. The thermal conductivity of the material is important because it describes how easily heat can be extracted from the device. The thermal conductivity has units of W/cm-°K, and in general, high thermal conductivity is desirable. Compound semiconductors, such as GaAs and InP, have relatively poor thermal conductivity compared to elemental semiconductors such as Si. Materials such as SiC have excellent thermal conductivity and are used in high power electronic devices. The dielectric constant is important since it represents capacitive loading and, therefore, affects the size of the semiconductor device. Low values of dielectric constant are desirable since this permits larger device area, which in turn results in increased RF current and increased RF power that can be developed. Electric breakdown characteristics are important since electronic breakdown limits the magnitudes of the DC and RF voltages that can be applied to the device. A low magnitude for electric field breakdown limits the DC bias that can be applied to a device, and thereby limits the RF power that can be handled or generated by the device. The electric breakdown for the material is generally described by the critical value of electric field that produces avalanche ionization. Minority carrier lifetime is important for bipolar devices, such as pn junction diodes, rectifiers, and

TABLE 7.2 Material Parameters for Several Semiconductors

Material	E_g(eV)	ε_r	κ(W/K-cm) @ 300°K	E_c(V/cm)	τ_{minority} (sec)
Si	1.12	11.9	1.5	3×10^5	2.5×10^{-3}
GaAs	1.42	12.5	0.54	4×10^5	$\sim 10^{-8}$
InP	1.34	12.4	0.67	4.5×10^5	$\sim 10^{-8}$
6H-SiC	2.86	10.0	4.9	3.8×10^6	$\sim(10\text{–}100) \times 10^{-9}$
4H-SiC	3.2	10.0	4.9	3.5×10^6	$\sim(10\text{–}100) \times 10^{-9}$
3C-SiC	2.2	9.7	3.3	$(1\text{–}5) \times 10^6$	$\sim(10\text{–}100) \times 10^{-9}$
GaN	3.4	9.5	1.3	2×10^6	$\sim(1\text{–}100) \times 10^{-9}$

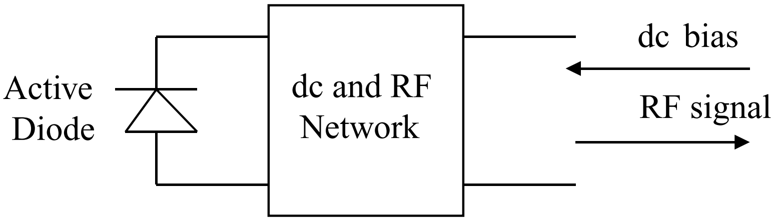

FIGURE 7.15 One-port network.

bipolar junction transistors (BJTs). A low value for minority carrier lifetime is desirable for devices such as diode temperature sensors and switches where low reverse bias leakage current is desirable. A long minority carrier lifetime is desirable for devices such as bipolar transistors. For materials such as Si and SiC the minority carrier lifetime can be varied by controlled impurity doping. A comparison of some of the important material parameters for several common semiconductors is presented in Table 7.2. The large variation for minority lifetime shown in Table 7.2 for SiC and GaN is due to relatively immature materials growth technology for these wide bandgap semiconductors.

Two-Terminal Active Microwave Devices

The IMPATT diode, transferred electron device (often called a Gunn diode), and tunnel diode are the most commonly used two-terminal active devices. These devices can operate from the low microwave through high mm-wave frequencies, extending to several hundred GHz. They were the first semiconductor devices that could provide useful RF power levels at microwave and mm-wave frequencies and were extensively used in early systems as solid-state replacements for vacuum tubes. The three devices are similar in that they are fabricated from diode or diode-like semiconductor structures. DC bias is applied through two metal contacts that form the anode and cathode electrodes. The same electrodes are used for both the DC and RF ports and since only two electrodes are available, the devices must be operated as a one-port RF network, as shown in Fig. 7.15. This causes little difficulty for oscillator circuits, but is problematic for amplifiers since a means of separating the input RF signal from the output RF signal must be devised. The use of a nonreciprocal device, such as a circulator can be used to accomplish the task. Circulators, however, are large, bulky, and their performance is sensitive to thermal variations. In general, circulators are difficult to use for integrated circuit applications. The one-port character of diodes has limited their use in modern microwave systems, particularly for amplifiers, since transistors, which have three terminals and are two-port networks, can be designed to operate with comparable RF performance, and are much easier to integrate. Diodes, however, are often used in oscillator circuits since these components are by nature one-port networks.

IMPATT and Gunn diodes require a combination of charge injection and transit time effects to generate active characteristics and they operate as negative immittance components (the term “immittance” is a

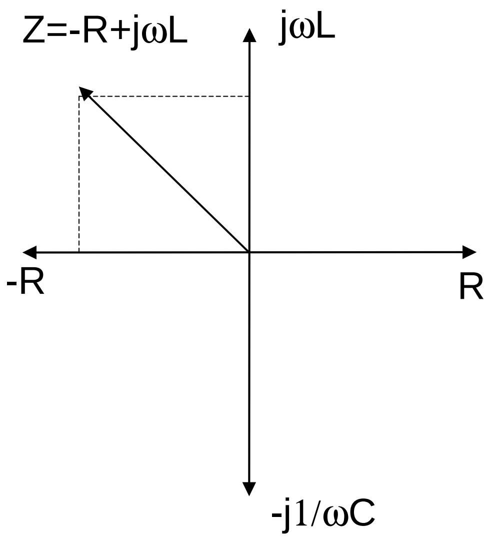

FIGURE 7.16 Complex impedance plane showing active characteristic.

general reference that includes both "impedance" and "admittance"). When properly designed and biased, the active characteristics of the diodes can be described as either a negative resistance or a negative conductance. Which description to use is determined by the physical operating principles of the particular device, and the two descriptions are, in general, not interchangeable. Bias and RF circuits for the two active characteristics must satisfy different stability and impedance matching criteria.

Transit time effects alone cannot generate active characteristics. This is illustrated in Fig. 7.16, which shows a general impedance plane. All passive circuits, no matter how complex or how many circuit elements are included, when arranged into a one-port network as shown in Fig. 7.15, and viewed from an external vantage point, will have an input impedance that lies in the right-hand plane of Fig. 7.16. The network resistance will be positive and real, and the reactance will be inductive or capacitive. This type of network is not capable of active performance and cannot add energy to a signal. Transit time effects can only produce terminal impedances with inductive or capacitive reactive effects, depending upon the magnitude of the delay relative to the RF period of the signal. In order to generate active characteristics it is necessary to develop an additional delay that will result in a phase delay between the terminal RF voltage and current that is greater than 90° and less than 270°. The additional delay can be generated by feedback that can be developed by physical phenomena internal to the device structure, or created by circuit design external to the device. The IMPATT and Gunn diodes make use of internal feedback resulting from electronic charge transfer within the semiconductor structure. The internal feedback generally produces a phase delay of ~90°, which when added to the transit time delay will produce a negative real component to the terminal immittance.

Tunnel Diodes

Tunnel diodes [1] generate active characteristics by an internal feedback mechanism involving the physical tunneling of electrons between energy bands in highly doped semiconductors, as illustrated in the energy band diagram shown in Fig. 7.17. The illustration shows a p^+n junction diode with heavily doped conduction and valence bands located in close proximity. When a bias is applied, charge carriers can tunnel through the electrostatic barrier separating the p-type and n-type regions, rather than be thermionically emitted over the barrier, as generally occurs in most diodes. When the diode is biased (either forward or reverse bias) current immediately flows and ohmic conduction characteristics are obtained. In the forward bias direction conduction occurs until the applied bias forces the conduction and valence

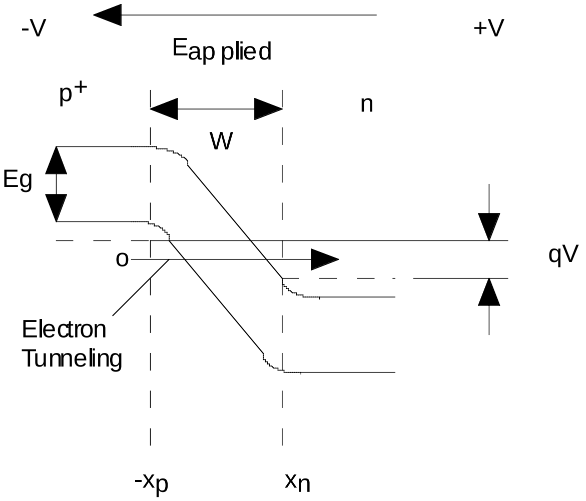

FIGURE 7.17 Energy-band diagram for a p$^+$n semiconductor junction showing electron tunneling behavior.

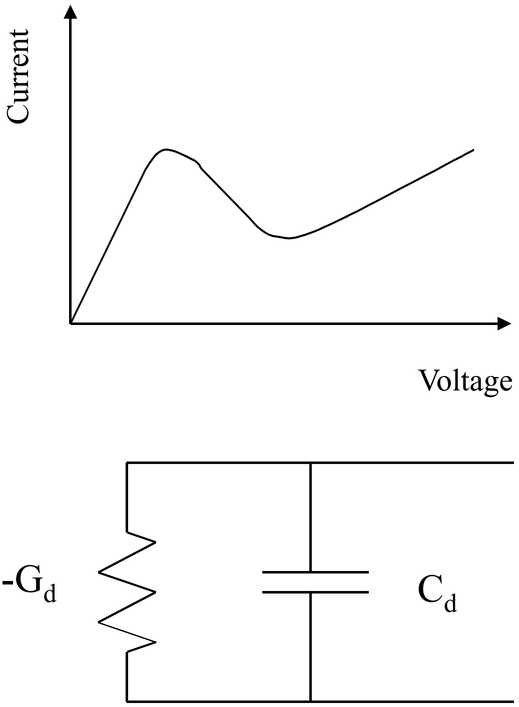

FIGURE 7.18 (a) Current-voltage characteristic for an N-type active device. (b) Small-signal RF equivalent circuit for an N-type active device.

bands to separate. The tunnel current then decreases and normal, thermionic junction conduction occurs. In the forward bias region where the tunnel current is decreasing with increasing bias voltage an N-type negative immittance characteristic is generated, as shown in Fig. 7.18a. The immittance is called "N-type" because the I-V characteristic looks like the letter N. This type of active element is current driven and is short-circuit stable. It is described by a negative conductance in shunt with a capacitance, as shown in

Fig. 7.18b. Tunnel diodes are limited in operation frequency by the time it takes for charge carriers to tunnel through the junction. Since this time is very short (on the order of 10^{-12} s) operation frequency can be very high, approaching 1000 GHz.

Tunnel diodes have been operated at 100s of GHz, and are primarily limited in frequency response by practical packaging and parasitic impedance considerations. The RF power available from a tunnel diode is limited (~100s of mW level) since the maximum RF voltage swing that can be developed across the junction is limited by the forward turn-on characteristics of the device (typically 0.6 to 0.9 v). Increased RF power can only be obtained by increasing device area to increase RF current. However, increases in diode area will limit operation frequency due to increased diode capacitance. Tunnel diodes have moderate DC-to-RF conversion efficiency (<10%) and very low noise figures and have been used in low noise systems applications, such as microwave and mm-wave receivers used for radioastronomy.

Transferred Electron Devices

Transferred electron devices (i.e., Gunn diodes) [2] also have N-type active characteristics and can be modeled as a negative conductance in parallel with a capacitance, as shown in Fig. 7.18b. Device operation, however, is based upon a fundamentally different principle. The negative conductance derives from the complex conduction band structure of certain compound semiconductors, such as GaAs and InP. In these direct bandgap materials the lower valley central (or Γ) conduction band is in close energy-momentum proximity to secondary, higher order conduction bands (i.e., the X and L) valleys (illustrated schematically as the L upper valley in Fig. 7.19). The electron effective mass is determined by the shape of the conduction bands and the effective mass is "light" in the Γ valley, but "heavy" in the higher order X and L upper valleys. When the crystal is biased, current flow is initially due to electrons in the light effective mass Γ valley and conduction is ohmic. However, as the bias field is increased, an increasing proportion of the free electrons are transferred into the X and L valleys where the electrons have heavier effective mass. The increased effective mass slows down the electrons, with a corresponding decrease in conduction current through the crystal. The net result is that the crystal displays a region of applied bias voltages where current decreases with increasing voltage. That is, a negative resistance is generated. A charge dipole domain is formed in the device, and this domain will travel through the device generating a transit time effect. The combination of the transferred electron effect and the transit time delay will produce a phase shift between the terminal RF current and voltage that is greater than 90°. The device is unstable and when placed in an RF circuit or resonant cavity, oscillators or amplifiers can be fabricated.

The Gunn device is not actually a diode since no pn or Schottky junction is used. The transferred electron phenomenon is a characteristic of the bulk material and the special structure of the conduction bands in certain compound semiconductors. In order to generate a transferred electron effect, a semiconductor must have Γ, X, and L valleys in the conduction bands in close proximity so that charge can be transferred from the lower Γ valley to the upper valleys at reasonable magnitude of applied electric field. It is desirable that the charge transfer occur at low values of applied bias voltage in order for the device to operate with good DC-to-RF conversion efficiency. Most semiconductors do not have the conduction band structure necessary for the transferred electron effect, and in practical use, Gunn diodes have only been fabricated from GaAs and InP. It should be noted that the name "Gunn diode" is actually a misnomer since the device is not actually a diode, but rather a piece of bulk semiconductor.

TEDs are widely used in oscillators from the microwave through high mm-wave frequency bands. They can be fabricated at low cost and provide an excellent price-to-performance ratio. They are, for example, the most common oscillator device used in police automotive radars. They have good RF output power capability (mW to W level), moderate efficiency (< 20%), and excellent noise and bandwidth capability. Octave or multi-octave band tunable oscillators are easily fabricated using devices such as YIG (yttrium iron garnet) resonators. High tuning speed can be achieved by using varactors as the tuning element. Many commercially available solid-state sources for 60 to 100 GHz operation (for example, automotive collision-avoidance radars) often use InP TEDs.

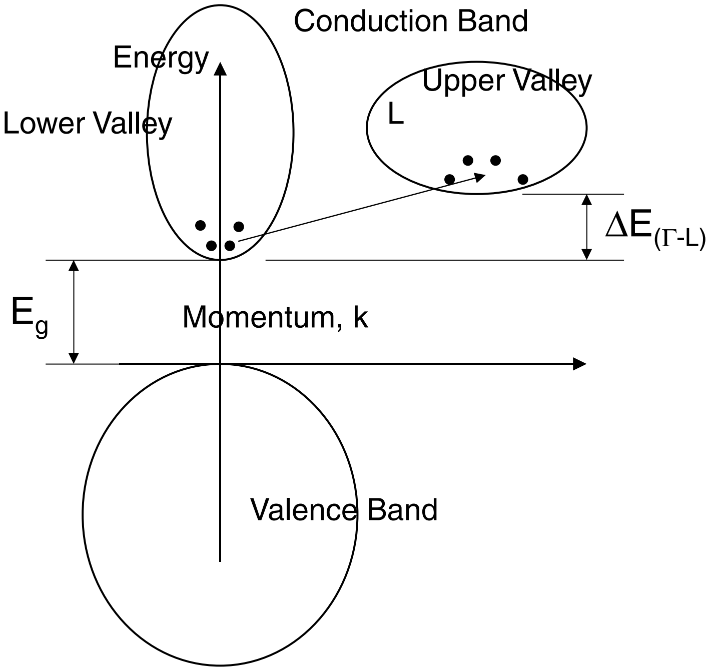

FIGURE 7.19 Energy band diagram for a semiconductor that demonstrates the transferred electron effect.

IMPATT Diodes

IMPATT (IMPact Avalanche Transit Time) diodes [3] are fabricated from pn or Schottky junctions. The doping profile in the device is generally tailored for optimum performance and a typical p^+nn^+ junction device structure as shown in Fig. 7.20. The diode is designed so that when it is reverse biased, the n-region is depleted of free electrons. The electric field at the p^+n junction exceeds the critical magnitude for avalanche breakdown, and the electric field exceeds the magnitude required to maintain electron velocity saturation throughout the n-region. Saturated charge carrier velocity must be maintained throughout the RF cycle in order for the device to operate with maximum efficiency. In operation, the high electric field region at the p^+n interface will generate charge when the sum of the RF and DC bias voltage produces an electric field that exceeds the critical value. A pulse of free charge (electrons and holes) will be generated. The holes will be swept into the p^+ region and the electrons will be injected into the depleted n-region, where they will drift through the diode, inducing a current in the external circuit as shown in Fig. 7.21. Due to the avalanche process, the RF current across the avalanche region lags the RF voltage by 90°. This inductive delay is not sufficient, by itself, to produce active characteristics. However, when the 90° phase shift is added to that arising from an additional inductive delay caused by the transit time of the carriers drifting through the remainder of the diode external to the avalanche region, a phase shift between the terminal RF voltage and current greater than 90° is obtained. A Fourier analysis of the resulting waveforms reveals a device impedance with a negative real part. That is, the device is active and can be used to generate or amplify RF signals. The device impedance has an "S-type" active i-v characteristic, as shown in Fig. 7.22a, and the device equivalent circuit consists of a negative resistance in series with an inductor, as shown in Fig. 7.22b. An S-Type active device is voltage driven and is open-circuit stable. For IMPATT diodes, the active characteristics only exist under RF conditions. That is, there is a lower frequency below which the diode does not generate a negative resistance. Also, the negative resistance is generally small in magnitude, and on the order of –1 Ω to –10 Ω. Therefore, it is necessary

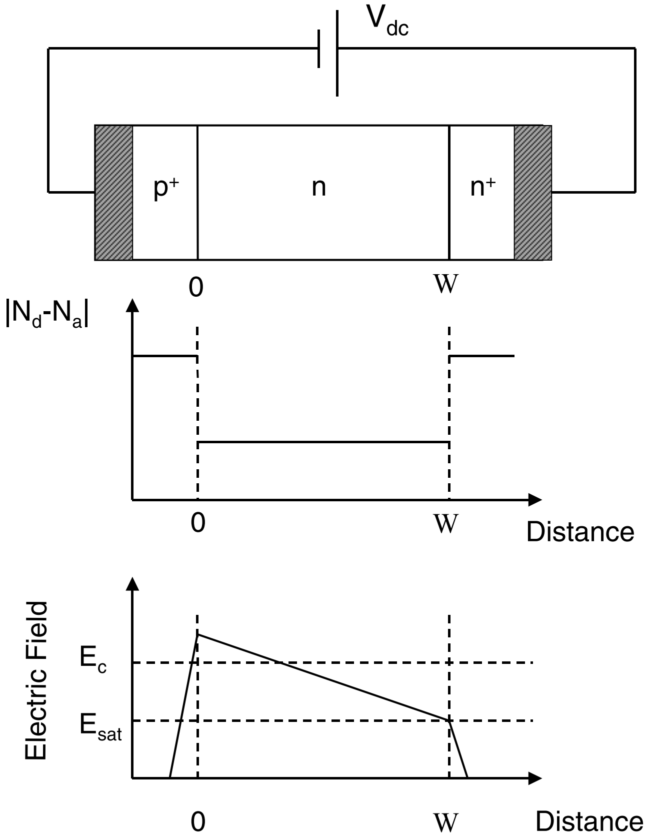

FIGURE 7.20 Diode structure, doping profile, and internal electric field for a p^+nn^+ IMPATT diode.

to reduce all parasitic resistances in external circuits to the maximum extent possible since parasitic series resistance will degrade the device's negative resistance, thereby limiting device performance. An IMPATT diode has significant pn junction capacitance that must be considered and a complete equivalent circuit includes the device capacitance in parallel with the series negative resistance-inductance elements, as shown in Fig. 7.22b.

For optimum performance the drift region is designed so that the electric field throughout the RF cycle is sufficiently high to produce velocity saturation for the charge carriers. In order to achieve this it is common to design complex structures consisting of alternating layers of highly doped and lightly doped semiconductor regions. These structures are called "high-low," "low-high-low," or "Read" diodes, after the man who first proposed their use [1]. They can also be fabricated in a back-to-back arrangement to form double-drift structures [4]. These devices are particularly attractive for mm-wave applications since the back-to-back arrangement permits the device to generate RF power from series-connected diodes, but each diode acts independently with regard to frequency response.

IMPATT diodes can be fabricated from most semiconductors, but are generally fabricated from Si or GaAs. The devices are capable of good RF output power (mW to tens of W) and good DC-to-RF conversion efficiency (~10 to 20%). They operate well into the mm-wave region and have been operated at frequencies in excess of 400 GHz. They have moderate bandwidth capability, but have relatively poor noise performance due to the impact ionization process associated with avalanche breakdown. The power-frequency performance of IMPATT diodes fabricated from Si, GaAs, and SiC is shown in Fig. 7.23. The Si and GaAs data are experimental, and the SiC data are predicted from simulation. The numbers associated with the data points are the conversion efficiencies for each point.

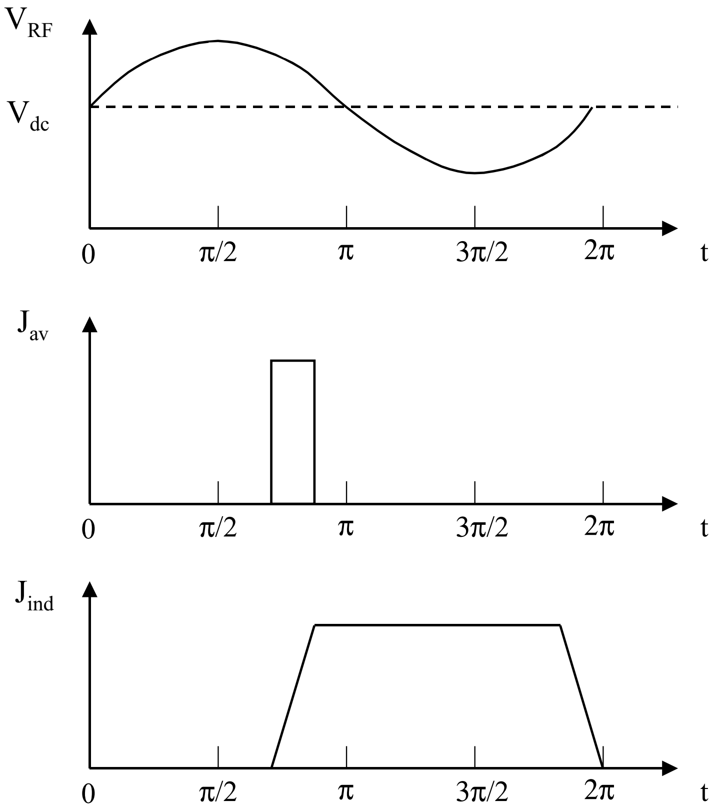

FIGURE 7.21 Terminal voltage, avalanche current, and induced current for an IMPATT oscillator.

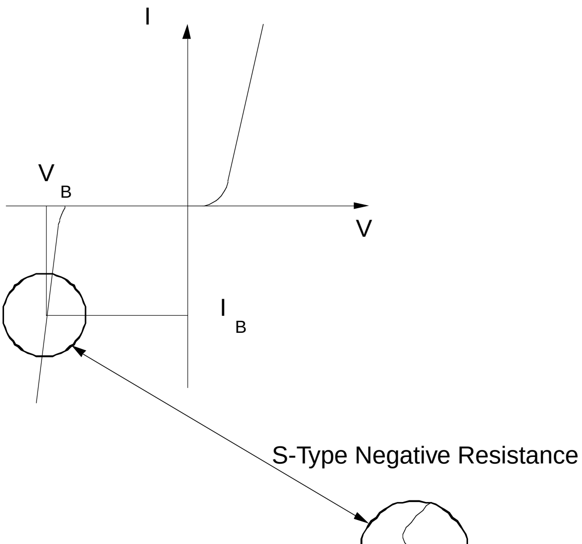

FIGURE 7.22 (a) Current-voltage characteristic for an S-type active device. The S-characteristic behavior does not exist under DC conditions for an IMPATT diode. The inset shows the dynamic i-v behavior that would exist about the DC operation point under RF conditions. (b) Small-signal RF equivalent circuit for an S-type active device.

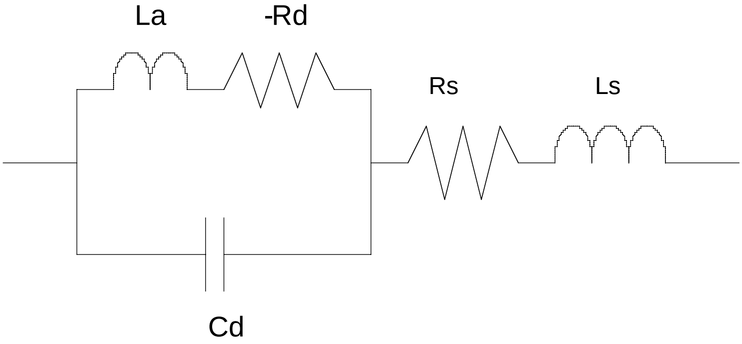

FIGURE 7.22 (continued)

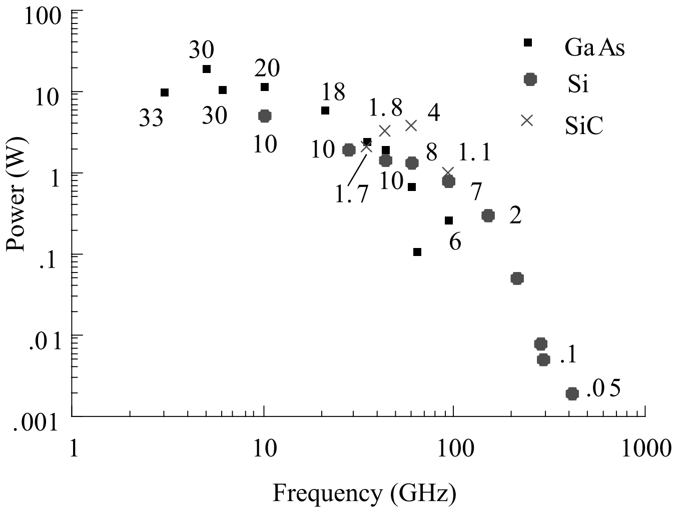

FIGURE 7.23 RF power-frequency performance for IMPATT oscillators (numbers associated with data points are DC-to-RF conversion efficiency).

Defining Terms

Immittance: A general term that refers to both impedance and admittance.

Active device: A device that can convert energy from a DC bias source to a signal at an RF frequency. Active devices are required in oscillators and amplifiers.

Two-terminal device: An electronic device, such as a diode, that has two contacts. The contacts are usually termed the cathode and anode.

One-port network: An electrical network that has only one RF port. This port must be used as both the input and output to the network. Two-terminal devices result in one-port networks.

Charge carriers: Units of electrical charge that produce current flow when moving. In a semiconductor two types of charge carriers exist: electrons and holes. Electrons carry unit negative charge and have an effective mass that is determined by the shape of the conduction band in energy-momentum space. The effective mass of an electron in a semiconductor is generally significantly less than an electron in free space. Holes have unit positive charge. Holes have an effective mass that is determined by the shape of the valence band in energy-momentum space. The effective mass of a hole is generally significantly larger than that for an electron. For this reason electrons generally move much faster than holes when an electric field is applied to the semiconductor.

References

1. Sze, S.M., 1981. *Physics of Semiconductor Devices*, 2nd Edition, Wiley-Interscience, New York.
2. Bosch, B.G., Engelmann, R.W. 1975. *Gunn-Effect Electronics*, Halsted Press, New York.
3. S.M. Sze, 1998. *Modern Semiconductor Device Physics*, Wiley-Interscience, New York.
4. P. Bhartia and I.J. Bahl, 1984. *Millimeter Wave Engineering and Applications*, Wiley-Interscience, New York.

7.2 Transistors

7.2.1 Bipolar Junction Transistors (BJTs)

John C. Cowles

The topic of bipolar junction transistors (BJTs) is obviously quite broad and a full treatment would consume volumes. This work focuses on basic principles to develop an intuitive feel for the transistor behavior and its application in contemporary high-speed integrated circuits (IC). The exponential growth in high bandwidth wired, wireless, and fiber communication systems coupled with advanced IC technologies has created an interesting convergence of two disparate worlds: the microwave and analog domains. The traditional microwave IC consists of a few transistors in discrete form or in low levels of integration surrounded by a sea of transmission lines and passive components. The modern high-speed analog IC usually involves 10s to 1000s of transistors with few passive components. The analog designer finds it a more cost-effective solution to use extra transistors rather than passive components to resolve performance issues. The microwave designer speaks in terms of noise figure, IP3, power gain, stability factor, VSWR, and s-parameters while the analog designer prefers noise voltages, harmonic distortion, voltage gain, phase margin, and impedance levels. Present BJT IC technologies fall exactly in this divide and thus force the two worlds together. Since parasitics within an IC are significantly lower than those associated with packages and external interconnects, analog techniques can be applied well into the microwave region and traditional microwave techniques such as impedance matching are only necessary when interfacing with the external world where reference impedances are the rule. This symbiosis has evolved into what is now termed radio frequency IC (RFIC) design. With this in mind, both analog and microwave aspects of bipolar transistors will be addressed. Throughout the discussion, the major differences between BJTs and field-effect transistors (FETs) will be mentioned.

A Brief History

The origin of the BJT was more a fortuitous discovery rather than an invention. The team of Shockley, Brattain, and Bardeen at Bell Labs had been pursuing a field effect device in the 1940s to replace vacuum tubes in telephony applications when they stumbled upon bipolar transistor action in their experimental point-contact structure. The point contact transistor consisted of a slab of n-type germanium sitting on a metal "base" with two metal contacts on either side. With proper applied bias, the "emitter" contact would inject current into the bulk and then the "collector" contact would sweep it up. They announced their discovery in 1948 for which they later received the Nobel Prize in 1956. At that point, the device was described as a current-controlled voltage source. This misinterpretation of the device as a transresistor led to coining of the universal term transistor that today applies to both BJTs and their field-effect brethren.

Within a few years of the discovery of the transistor, its theory of operation was developed and refined. The decade of the 1950s was a race toward the development of a practical technique to fabricate them. Research into various aspects of the material sciences led to the development of the planar process with silicon as the cornerstone element. Substrate and epitaxial growth, dopant diffusion, ion-implantation, metalization, lithography, and oxidation had to be perfected and integrated into a manufacturable process flow. These efforts culminated with Robert Noyce's patent application for the planar silicon BJT IC concept that he invented while at Fairchild. In the 1960s, the first commercial ICs appeared on the market, launching the modern age of electronics. Since then, transistor performance and integration levels have skyrocketed driven primarily by advances in materials, metrology, and process technology as well as competition, cost, and opportunity.

Basic Operation

The basic structure of the bipolar transistor given in Fig. 7.24a consists of two back-to-back intimately coupled p-n junctions. While the npn transistor will be chosen as the example, note that the pnp structure operates identically, albeit in complementary fashion. Bipolar transistor action is based on the injection of minority carrier electrons from the emitter into the base as dictated by the base-emitter voltage. These carriers diffuse across the thin base region and are swept by the collector, which is normally reverse biased. In high speed ICs, BJTs are nearly always biased in this way, which is known as the forward active mode. The net effect is that an input signal voltage presented across the base-emitter terminals causes a current to flow into the collector terminal. The relationship between collector current, I_c, and base-emitter voltage, V_{be}, originates from fundamental thermodynamic arguments via the statistical Boltzmann distribution of electrons and holes in solids. It is given by,

$$I_c = I_s \exp\left(V_{be}/V_t\right) \tag{7.19}$$

where I_s is called the saturation current and V_t is Boltzmann's thermal voltage kT/q, which is 26 mV at room temperature (RT). This expression plotted in Fig. 7.24b is valid over many decades of current and

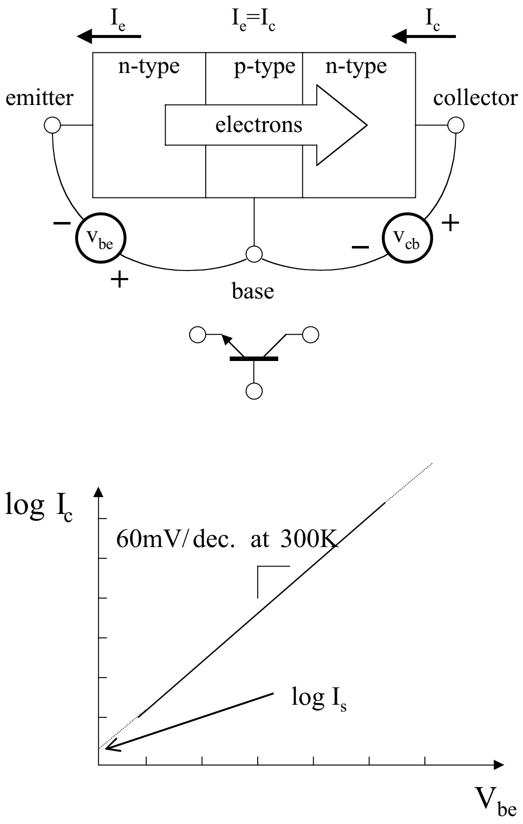

FIGURE 7.24 (a) BJT action involves carrier injection across the base from emitter to collector; (b) the ideal BJT exhibits a perfectly exponential input-output transfer function.

its implications are far reaching in BJT IC design. Consider the small-signal transfer characteristics relating the output current to input voltage at a given bias current, I_c, i.e., the transconductance, g_m. It is given by the remarkably simple expression,

$$\delta I_c / \delta V_{be} \big| I_c = g_m = I_c / V_t . \tag{7.20}$$

The notion that transconductance is precisely and linearly proportional to the bias current, I_c and inversely proportional to temperature through V_t is known as translinearity. Notice that I_s, which has a strong dependence on temperature, base-width, and other physical device parameters, has dropped out of the picture. This view of bipolar transistors as a voltage-controlled current source suggests that it should have been named the transductor rather than the transistor. Although bipolar transistors are usually considered hopelessly nonlinear because of the exponential law in Eq. (7.19), extremely precise and robust linear and nonlinear functions can be realized at very high frequencies by proper circuit techniques that exploit the translinear property embodied in Eq. (7.20).

The intrinsic bandwidth of high frequency BJTs is ultimately limited by minority carrier storage primarily in the base region. Current is conveyed from the emitter to the collector by the relatively slow process of diffusion resulting from the gradient in the distribution of stored minority carriers in the base. In contrast, current in FETs is transported by the faster process of majority carrier drift in response to an electric field. By invoking the quasi-static approximation, which assumes that signals of interest change on a much longer time scale than the device time constants, carrier storage can be modeled as a lumped diffusion capacitance, C_d given by,

$$C_d = \delta Q_d / \delta V_{be} = \delta\left(I_c \tau_f\right) / \delta V_{be} = g_m \tau_f \tag{7.21}$$

where Q_d is the stored charge and τ_f is the forward transit time. The parameter τ_f can be viewed as the average time an electron spends diffusing across the base and can be expressed as a function of basic material and device parameters,

$$\tau_f = W_B^2 / 2\eta D_n \tag{7.22}$$

where W_B is the physical base width, D_n is the electron diffusion coefficient, and η is a dimensionless factor that accounts for any aiding fields in the base. Despite the limitations associated with carrier storage and diffusion, BJTs have demonstrated excellent high frequency performance. This is partly due to their vertical nature where dimensions such as W_B can be significantly less than 100 nm. In contrast, FETs are laterally arranged devices where the critical dimension through which carriers drift is determined by lithography and is typically larger than 100 nm even in the most advanced technologies. Furthermore, the fundamental limit contained in τ_f is never achieved in practice since other factors, both device and circuit-related, conspire to reduce the actual bandwidth.

A first order model of BJTs is illustrated in Fig. 7.25 consisting of a diode at the base-emitter junction whose current is conveyed entirely to the collector according to Eq. (7.19) and a diffusion capacitance that models the carrier storage. From this simplistic model, the transistor f_t, defined as the frequency at which the common-emitter short-circuit current gain, h_{21}, reaches unity, can be calculated from,

$$h_{21} = i_c / i_b = f_t / f . \tag{7.23a}$$

$$f_t = g_m / 2\pi C_d = 1 / 2\pi\tau_f . \tag{7.23b}$$

Note that f_t is independent of current and is solely a function of material parameters and device design details. Pushing this figure of merit to higher frequencies has dominated industrial and academic research

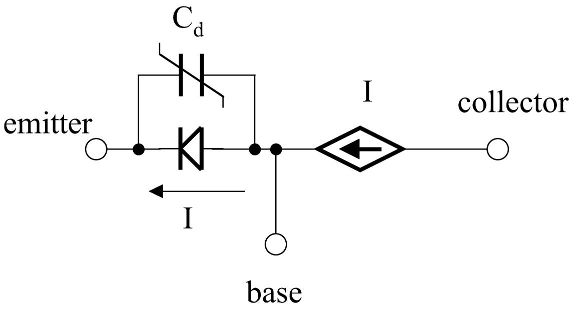

FIGURE 7.25 First order BJT model includes the nonlinear carrier injection and storage.

for years. Polysilicon emitter BJTs, Si/SiGe heterojunction BJTs (HBTs), and III-V-based HBTs are all attempts to craft the active layers in order to maximize f_t without significantly compromising other device aspects.

Parasitics and Refinements

The first order model captures the essential operation of the BJT. However, actual devices deviate from that ideal in many aspects. As electrons diffuse across the base, some are lost to the process of recombination with holes as illustrated in Fig. 7.26a. Excess holes are also parasitically injected into the emitter. This overall loss of holes must originate at the base terminal and represents a finite base current, I_b, which is related to I_c via the parameter, β, known as the common emitter current gain,

$$\beta = I_c / I_b . \tag{7.24}$$

The effect of finite β is to modify the emitter-base diode current by a correction factor, α, known as the common-base current gain, that accounts for the extra base current. Since $I_e = I_b + I_c$, it is easy to show that,

$$\alpha = \beta / \beta + 1 < 1 \tag{7.25}$$

so that the emitter-base diode current now becomes I_s/α. Many factors figure into determining β, including W_B and the highly variable recombination lifetime τ_r. Since β is a poorly controlled parameter with potential variations of ±50%, it is inadvisable to design circuits that depend on its exact value. Fortunately, it is usually possible to design ICs that are insensitive to β as long as β is large, say >50, thanks to matching of co-integrated devices. Figure 7.26b illustrates the well-known BJT Gummel plot, which shows the translinearity of I_c as well as the finite I_b in response to V_{be}. The separation between the two curves represents β. As shown in Fig. 7.27, β represents a low frequency asymptote of h_{21} that exhibits a single pole roll off toward f_t at a frequency, f_β given by f_t/β. Since RFICs most often operate well above f_β, the useful measure of current gain is actually f_t/f rather than β, although high DC β is still important for low noise and ease of biasing.

Traditionally, BJTs have been characterized as current-controlled devices where a forced I_b drives an I_c into an load impedance, consistent with Shockley's trans-resistor description. Now if I_b is considered a parasitic nuisance rather than a fundamental aspect, it becomes even more appropriate to view the BJT as a voltage-controlled device that behaves as a transconductor, albeit with exponential characteristics. In fact, contemporary analog IC design avoids operating the BJT as a current-controlled device due to the unpredictability of β. Instead, the designer takes advantage of device matching in an IC environment and translinearity to provide the appropriate voltage drive. This approach can be shown to be robust against device, process, temperature, and supply voltage variations.

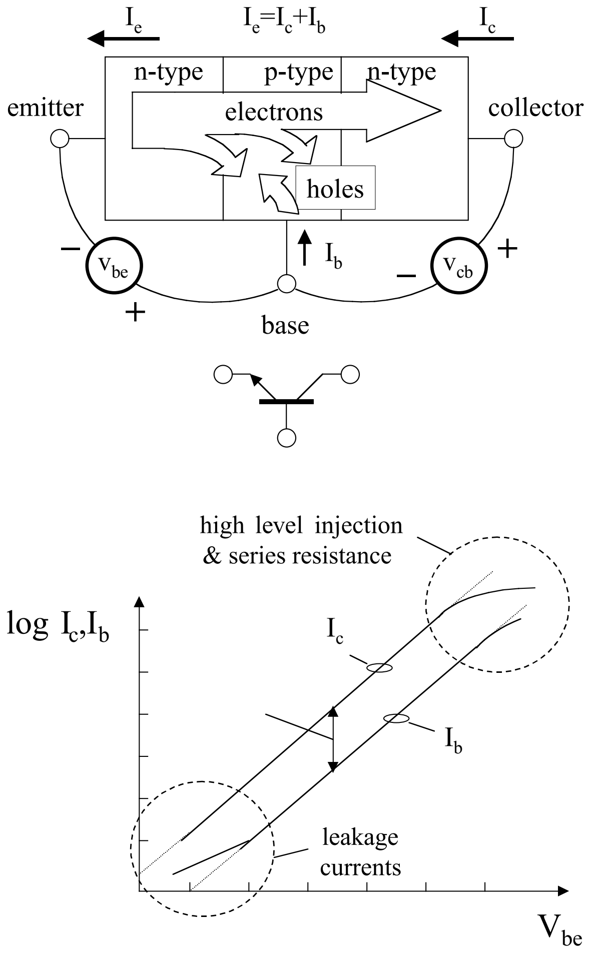

FIGURE 7.26 (a) Recombination of electrons and holes leads to finite current gain, β; (b) the Gummel plot illustrates the effects of finite β and other nonidealities.

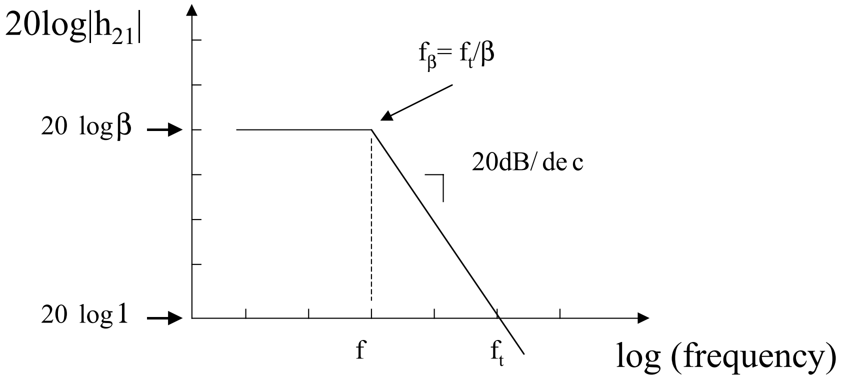

FIGURE 7.27 The frequency dependence of h_{21} captures finite β and f_t.

Superimposed on the basic model are parasitic ohmic resistances in series with each active terminal (R_b, R_e, R_c) and parasitic capacitances associated with all pn junction depletion regions (C_{jc}, C_{je}, C_{js}), including the collector-substrate junction present to some extent in all technologies. Since parasitics degrade the idealized DC and RF characteristics captured in Eqs. (7.19) and (7.23), a major effort is focused on minimizing them through aggressive scaling and process engineering. Their values and bias dependencies can be estimated from the physical device structure and layout.

In particular, the base and emitter resistance, R_b and R_e, soften the elegant exponential characteristics in Eq. (7.19) by essentially de-biasing the junction since

$$I_c = I_s \exp\left(\left[V_{be} - I_b R_b - I_e R_e\right] / V_t\right). \tag{7.26}$$

This effect is also illustrated in Fig. 7.26b at high values of V_{be} where both curves appear to saturate. This departure from ideal translinearity can introduce unwelcome distortion into many otherwise linear ICs. Furthermore, these resistances add unwelcome noise and degeneration (voltage drops) as will be discussed later.

The idealized formulation for f_t given in Eq. (7.23) also needs to be modified to account for parasitics. A more comprehensive expression for f_t based on a more complex equivalent circuit results in,

$$f_t = \left(2\pi^* \left[\tau_f + \left(C_{je} + C_{jc}\right) / g_m + C_{jc}\left(R_c + R_e\right)\right]\right)^{-1} \tag{7.27}$$

where now f_t is dependent on current through g_m charging of C_{je} and C_{jc}. To achieve peak f_t, high currents are required to overcome the capacitances. As the intrinsic device τ_f has been reduced, the parasitics have become a dominant part of the BJTs' high frequency performance requiring even higher currents to reach the lofty peak values of f_t. It should also be kept in mind that f_t only captures a snapshot of the device high frequency performance. In circuits, transistors are rarely current driven and short circuited at the output. The base resistance and substrate capacitance that do not appear in Eq. (7.27) can have significant impact on high frequency IC performance. While various other figures of merit such as f_{max} have been proposed, none can capture the complex effects of device interactions with source and load impedances in a compact form. The moral of the story is that ideal BJTs should have low inertia all around, i.e., not only high peak f_t but also low parasitic capacitances and resistances, so that time constants in general can be minimized at the lowest possible currents.

At the high currents required for high f_t, second order phenomena known in general as high level injection begin to corrupt the DC and RF characteristics. Essentially, the electron concentration responsible for carrying the current becomes comparable to the background doping levels in the device causing deviations from the basic theory that assumes low level injection. The dominant phenomenon known as the Kirk effect or base-pushout manifests itself as a sudden widening of the base width at the expense of the collector. This translates into a departure from translinearity with dramatic drops in both β and f_t. A number of other effects have been identified over the years such as Webster effect, base conductivity modulation, and current crowding. High level injection sets a practical maximum current at which peak f_t can be realized. Figure 7.28 illustrates the typical behavior of f_t with I_c. To counteract high level injection, doping levels throughout the device have increased at a cost of higher depletion capacitances and lower breakdown voltages. Since modeling of these effects is very complex and not necessarily included in many models, it is dangerous to design in this regime.

So far, the transistor output has been considered a perfect current source with infinite output resistance. In reality, as the output voltage swings, the base width is modulated, causing I_s and thus I_c to vary for a fixed V_{be}. This is exactly the effect of an output resistance and is modeled by a parameter V_a, the Early voltage,

$$r_o = \delta V_{ce} / \delta I_c = V_a / I_c. \tag{7.28}$$

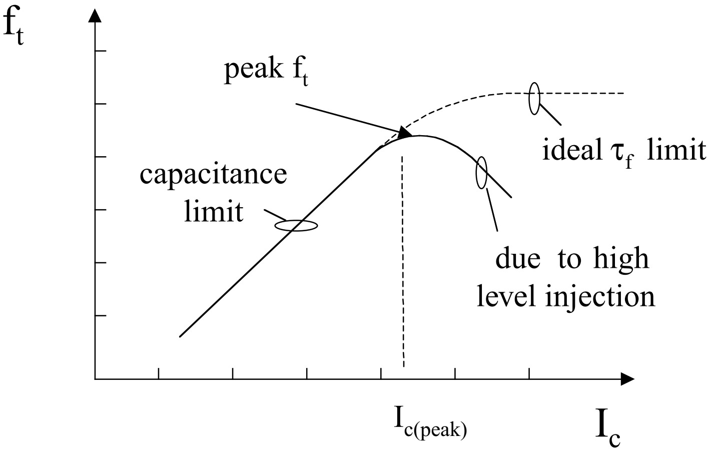

FIGURE 7.28 The f_t peaks at a particular current when high level injection occurs.

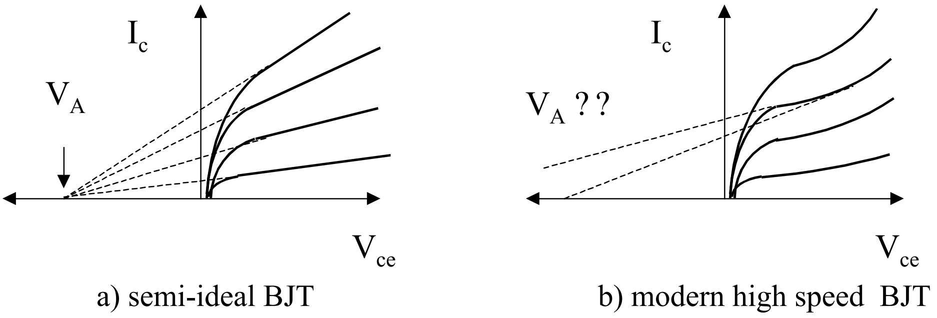

a) semi-ideal BJT

b) modern high speed BJT

FIGURE 7.29 (a) The traditional interpretation of V_A is not unique in modern BJTs as shown in (b).

As illustrated in the output common-emitter characteristics, I_c vs. V_{ce}, shown in Fig. 7.29a, V_a represents the common extrapolation point where all tangents intersect the V_{ce} axis. The effect of r_o is to set the maximum small-signal unloaded voltage gain since

$$A_v = \delta V_o / \delta V_i = \left(\delta I_c / \delta V_i\right)\left(\delta V_o / \delta I_c\right) = -g_m r_o = -V_a / V_t \tag{7.29}$$

For typical values of V_a = 50 V, A_v = 2000 (66 dB) at room temperature. Note that this gain is independent of I_c and is quite high for a single device, representing one of the main advantages of BJTs over FETs where the maximum gain is usually limited to < 40 dB for reasonable gate lengths. In modern devices, however, V_a is not constant due to complex interactions between flowing electrons and internal electric fields. The net effect illustrated in Fig. 7.29b indicates a varying V_a depending on I_c and V_{ce}. This is often termed soft breakdown or weak avalanche in contrast to actual breakdown which will be discussed shortly. The effect of a varying V_a is to introduce another form of distortion since the gain will vary according to bias point. Figure 7.30 shows a more complete model that includes the fundamental parameters as well as the parasitics and refinements considered so far. It resembles a simplified version of the popular Gummel-Poon model found in many simulators.

Another form of pseudo-breakdown occurs in ultra-narrow base BJTs operating at high voltages. If the Early effect or base-width modulation is taken to an extreme, the base eventually becomes completely depleted. After this point, a further change in collector voltage directly modulates the emitter-base junction leading to an exponential increase in current flow. This phenomenon known as punchthrough

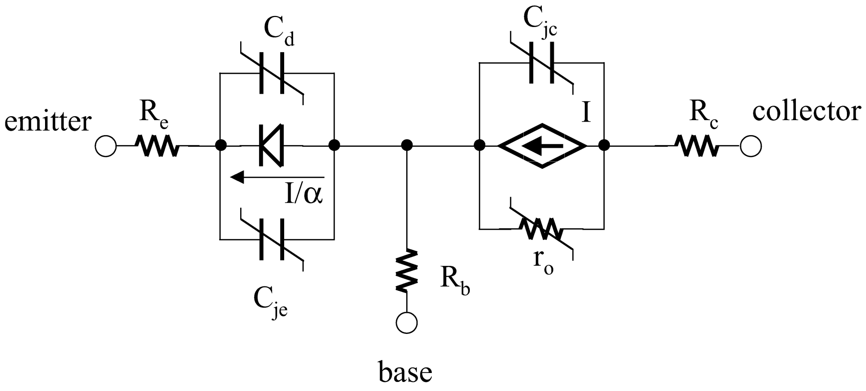

FIGURE 7.30 Augmented BJT model with parasitic resistances and finite base current.

fortunately has been mitigated by the fact that as base widths have narrowed, the base doping has been forced to increase so as to maintain a reasonable base resistance. Furthermore, since higher collector doping levels have been necessary to fight high level injection, true breakdown has become the voltage limiting mechanism rather than punchthrough.

Just as high level injection limits the maximum operating current, junction breakdown restricts the maximum operating voltage. When the collector voltage is raised, the collector base junction is reverse biased. The resulting electric field reaches a critical point where valence electrons are literally ripped out of their energy band and promoted to the conduction band while leaving holes in the valence band. The observed effect known as avalanche breakdown is a dramatic increase in current. The breakdown of the collector-base junction in isolation, i.e., with the emitter open circuited, is termed the BV_{cbo} where the "o" refers to the emitter open. Another limiting case of interest is when the base is open while a collector-emitter voltage is applied. In this case, an initial avalanche current acts as base current that induces more current flow, which further drives the avalanche process. The resulting positive feedback process causes the BV_{ceo} to be significantly lower than BV_{cbo}. The relationship clearly depends on β and is empirically modeled as,

$$BV_{ceo} = BV_{cbo} / \beta^{1/n} \tag{7.30}$$

where n is a fit parameter. A third limit occurs when the base is AC shorted to ground via a low impedance. In this scenario, avalanche currents are shunted to ground before becoming base current and BV_{ces} ("s" means shorted) would be expected to be $BV_{cbo} + V_{be}$. Therefore, BV_{ces} represents an absolute maximum value for V_{ce} while BV_{ceo} represents a pessimistic limit since the base is rarely open. Operating in the intermediate region requires care in setting the base impedance to ground and knowing its effect on breakdown. Figure 7.31 illustrates the transition from BV_{ceo} to BV_{ces}. The base-emitter junction is also

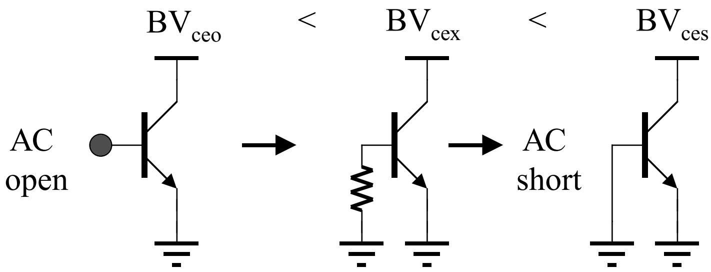

FIGURE 7.31 The AC base impedance helps determine the effective breakdown voltage.

sensitive to reverse bias. In this case, the breakdown is usually related to Zener tunneling and is represented by BV_{ebo}. Excessive excursions toward BV_{ebo} can cause injection of energetic carriers into surrounding dielectrics, leading to leakage currents, degraded reliability, and possibly device failure. Since these breakdown mechanisms in general are poorly modeled, it is recommended to operate well below BV_{ceo} and BV_{ebo}.

Even when these guidelines are followed, there are still situations where peak voltages might exceed breakdown limits. For instance, modern ICs in portable products often require a disable mode in which the part consumes virtually no current so as to conserve battery life. When disabled, it is common for transistors that are normally in a safe operating condition to find themselves with reverse-biased junctions in excess of BV_{ceo} and BV_{ebo}. The resulting leakage currents can lead to expectedly high disable currents, accidental activation of certain circuit blocks, and again to potential reliability failures. A second situation is when output stages drive variable reactive loads. It is possible (and likely) that certain conditions will cause 2 to 3 times the supply voltage to appear directly across a transistor leading to certain catastrophic breakdown.

As devices have been scaled down in size, isolated in dielectrics, and driven with higher current densities, self-heating has become increasingly problematic. The thermal resistance, R_{th}, and capacitance, C_{th}, model the change in junction temperature with power and the time constant of its response. The DC and AC variations in the junction temperature induce global variations in nearly all model parameters causing bias shifts, distortion, and even potentially catastrophic thermal runaway. Furthermore, local heating in one part of a circuit, say an ouput power stage, can start affecting neighboring areas such as bias circuits creating havoc. It is essential to selectively model thermal hotspots and ensure that they are within maximum temperature limits and that their effect on other circuit blocks is minimized by proper layout.

Dynamic Range

The limits on signal integrity are bounded on the low end by noise and on the high end by distortion. It is not appropriate to claim a certain dynamic range for BJTs since the circuit topology has a large impact on it. However, the fundamental noise sources and nonlinearities in BJTs can be quantified and then manipulated by circuit design. It is customary to refer the effects of noise and nonlinearity to either the input or the output of the device or circuit to allow fair comparisons and to facilitate cascaded system-level analyses. Here, all effects will be referred to the input, noting that the output quantity is simply scaled up by the appropriate gain.

There are three fundamental noise mechanisms that are manifested in BJTs. Figure 7.32 presents a linearized small-signal model that includes the noise sources. The objective will be to refer all noise sources to equivalent voltage and current noise sources, e_n and i_n, respectively, at the input. Shot noise is associated with fluctuations in current caused by the discrete nature of electronic charge overcoming the junction potential. The presence of the forward biased base-emitter junction results in collector and base shot noise, i_{cn}, and i_{bn}, which are given by,

$$i_{cn}^2 = 2qI_c;\ i_{bn}^2 = 2qI_b \tag{7.31}$$

where q is the electronic charge. This is a major disadvantage of BJTs with respect to FETs, which are free of shot noise due to the absence of potential barriers that determine current flow. Each physical resistance carries an associated Johnson noise represented as

$$e_{Rx}^2 = 4kTR_x \tag{7.32}$$

where R_x is the appropriate resistance and k is Boltzmann's constant. Finally, a 1/f noise source, $i_{1/f}^2$ associated primarily with recombination at semiconductor surfaces appears at the input. The 1/f noise component decreases with increasing frequency, as expected. A corner frequency is often quoted as the

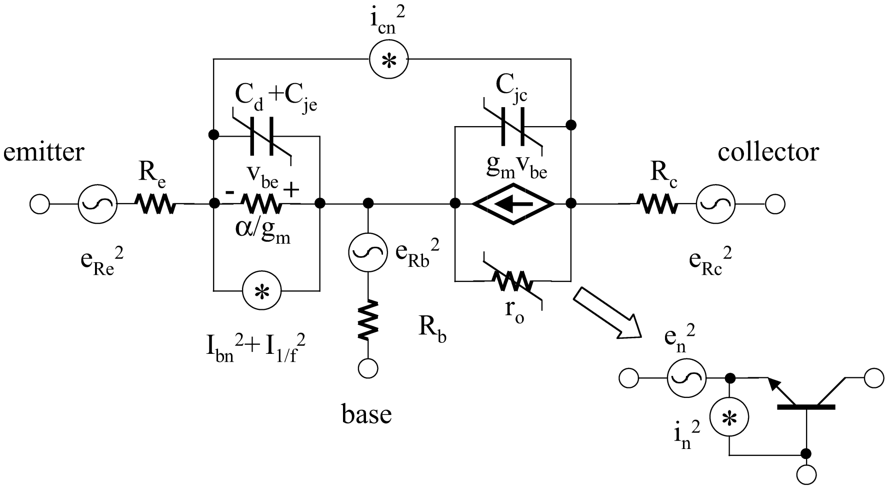

FIGURE 7.32 The fundamental noise sources can be transformed to equivalent input-referred sources.

point where the 1/f noise and the white thermal and shot noise cross over. It is an empirical value that varies from device to device and depends on bias conditions and source impedance. BJTs typically offer lower 1/f corner frequency than FETs since surfaces play a lesser role in BJTs. Except for broadband DC-coupled circuits and strongly nonlinear circuits such as oscillators and mixers that perform frequency conversion, 1/f noise is insignificant at high frequencies and will be ignored for simplicity. Note that treating noise in nonlinear systems is quite complex and remains an active research topic.

Once the noise sources are input referred, e_n and i_n are approximately given by

$$e_n^2 = 4kT\left(R_b + R_e + 1/2g_m\right) \tag{7.33a}$$

$$i_n^2 = 2q\left(I_b + I_c \Big/ \left|h_{21}(f)\right|^2\right). \tag{7.33b}$$

An arbitrarily higher I_c reduces e_n through the larger g_m but has mixed effects on i_n depending on how $h_{21}(f)$ varies with current. An arbitrarily larger device reduces e_n by lowering R_b and R_e but the commensurate increase in capacitance might degrade $h_{21}(f)$ and thus i_n. The moral here is that minimization of noise requires a trade-off in I_c and device size given an f_t equation and parasitic scaling rules with device geometry.

Distortion originates in nonlinearities within the device. For simplicity, distortion will be described in terms of a power series to derive expressions for harmonic distortion, intermodulation distortion, and compression. It is assumed that linearities up to only third order are considered, limiting the accuracy of the results as compression is approached. While this approach is valid at low frequencies, capacitive effects at higher frequencies greatly complicate nonlinear analysis and more generalized Volterra series must be invoked. However, the general idea is still valid. Note that not all systems can be mathematically modeled by power or Volterra series; for example, a hard limiting amplifier that shows sudden changes in characteristics.

In BJTs, the fundamental transfer function given in Eq. (7.19) represents one of strongest nonlinearities. As shown in Fig. 7.33, by expanding Eq. (7.19) in its power series up to 3rd order, the following measures of input-referred figures of merit are derived in dBV (mV),

$$P_{1db} = 0.933\ V_t = 24.3\ \text{mV} = -32.3\ \text{dBV} \tag{7.34a}$$

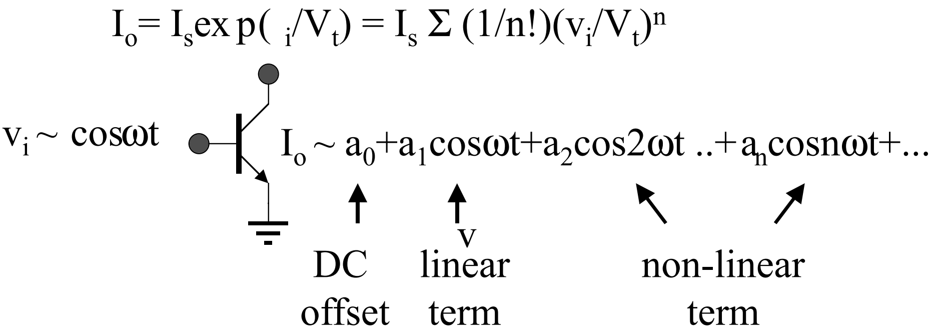
$I_o = I_s \exp(_i/V_t) = I_s \Sigma (1/n!)(v_i/V_t)^n$
$v_i \sim \cos\omega t$
$I_o \sim a_0 + a_1\cos\omega t + a_2\cos 2\omega t .. + a_n\cos n\omega t + ...$
v
DC offset
linear term
non-linear term

FIGURE 7.33 A power series expansion of the exponential junction nonlinearity can be used to quantify distortion.

$$\text{IIP3} = 2.83\ V_t = 73.5\text{ mV} = -22.7\text{ dBV} \tag{7.34b}$$

$$\text{P3OI} = 4.89\ V_t = 127\text{ mV} = -17.9\text{ dBV} \tag{7.34c}$$

where P_{1db} is the 1-dB gain compression point, IIP3 is the third order intercept point, and P3OI is the third harmonic intercept point. Note that the conversion from dBV to dBm referenced to 50 Ω is + 10 dB. From the analysis, it can be inferred that P_{1db} occurs for peak input swings of about V_t while a third order intermodulation level of 40 dBc is achieved for an input swing of only 0.0283 V_t or 0.73 mV at room temperature. These values are quite low, indicating that circuit linearization techniques must be invoked to exceed these limits. FETs on the other hand possess a more benign input nonlinearity that ranges from square law in long channel devices to nearly linear in short channels. While this is not the sole source of nonlinear behavior, FETs are expected to have superior linearity as compared to BJTs from this perspective. It is interesting to observe that the commonly used rule of thumb stating that IIP3 is approximately 10 dB higher than P_{1db} is true in this case. As mentioned earlier, higher order terms, parasitics, and reactive effects modify the results in Eq. (7.34) but they do provide a useful order of magnitude.

A common technique for extending overall dynamic range is emitter degeneration, which as illustrated in Fig. 7.34, essentially amounts to series-series feedback. The impedance in series with the emitter reduces the signal that appears directly across the emitter base leading to lower input-referred distortion. Note that the gain is proportionately reduced so that output-referred distortion is not improved to the same

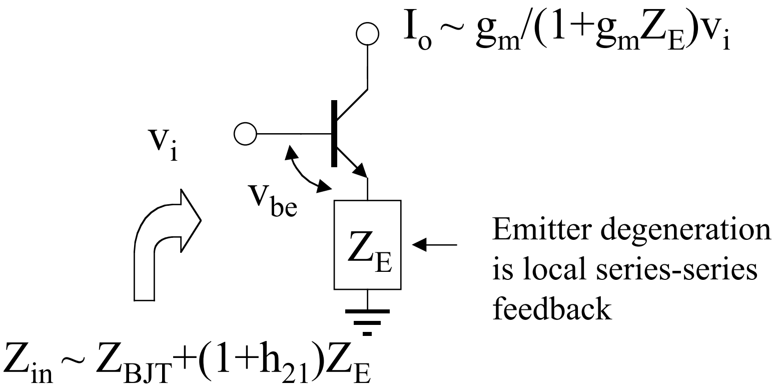
$I_o \sim g_m/(1+g_m Z_E)v_i$
v_i
v_{be}
Z_E
Emitter degeneration is local series-series feedback
$Z_{in} \sim Z_{BJT} + (1+h_{21})Z_E$

FIGURE 7.34 Emitter degeneration can improve dynamic range and change impedance levels.

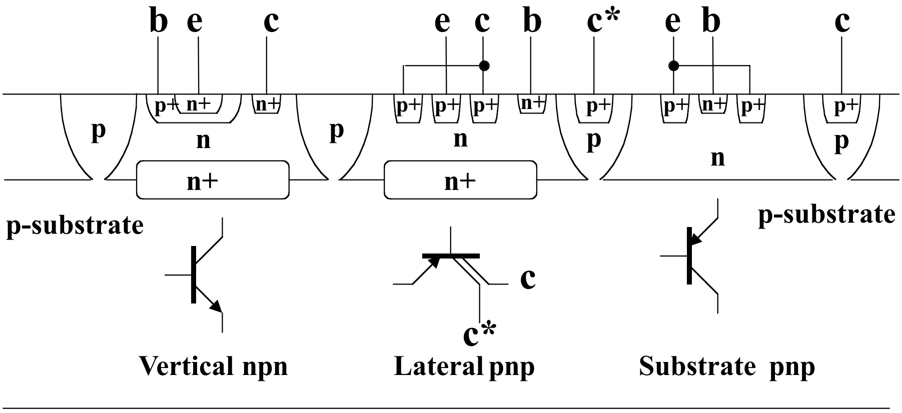

FIGURE 7.35 Both lateral and substrate pnp BJTs can be generated in a typical npn process.

degree. The potentially superior distortion performance of FETs is analogous to a strongly degenerated BJT with the accompanying lower gain. Since this degenerating impedance is directly in the signal path, it also affects noise. If the impedance is a resistor, it will contribute noise as if it were an extra R_e in Eq. (7.33a). If R_e is not a dominant noise contributor, this approach can extend dynamic range significantly. Another option is to use a degenerating inductor, which at high frequencies provides adequate degeneration while only contributing noise associated with its finite quality factor, Q. Other feedback techniques are also possible to improve dynamic range, but care must be taken to ensure stability particularly around longer feedback loops. Additional benefits of using local feedback are desensitization of input impedance and gain to device parameters.

Complementary Pnp

The availability of a pnp device to complement the npn offers numerous advantages, particularly at lower supply voltages. For example, pnp active loads can provide more voltage gain at a given supply voltage; signals can be "folded" up and down to avoid hitting the rails and balanced complementary push-pull topologies can operate near rail-to-rail. In general, the p-type device is slower than the n-type device across most technologies due to the fundamentally lower hole mobility with respect to electron mobility. Furthermore, in practice, the pnp transistor is often implemented as a parasitic device, i.e., the fabrication process is optimized for the npn and the pnp shares the available layers. Figure 7.35 illustrates how two different pnp's can be constructed in an npn process (p-type substrate). The so-called substrate pnp has the substrate double as its collector and thus only appears in a grounded collector arrangement. The lateral pnp frees the collector terminal, but carries along a parasitic substrate pnp of its own that injects large currents into the substrate and degrades f_t and β. In some cases, true complementary technologies are available in which both the npn's and pnp's are synthesized and optimized separately.

When only lateral and substrate pnp's are available, they are usually used outside of the high-speed signal path due to their compromised RF performance. They appear prominently in bias generation and distribution as well as in low and intermediate frequency blocks. When using either pnp, care must be taken to account for current injection into the substrate, which acts locally as a collector. This current can induce noise and signal coupling as well as unintentional voltage drops along the substrate. It is customary to add substrate contacts around the pnp's to bring this current to the surface before it disperses throughout the IC. If true high-quality vertical pnp's are available that are balanced in performance with respect to the npn's, they can be used for high-frequency signal processing, enabling a number of circuit concepts commonly used at lower frequencies to be applied at RF.

Topologies

Several basic single-transistor and composite transistor configurations are commonly encountered in RFICs. Figure 7.36 shows the three basic single-transistor connections known as common-emitter (CE),

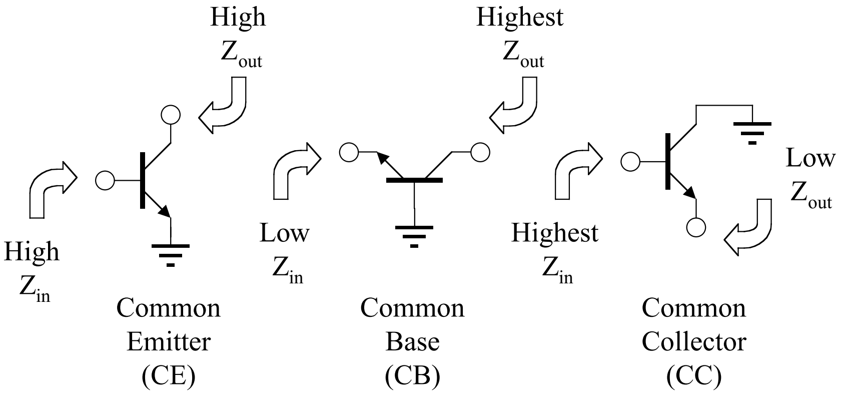

FIGURE 7.36 The three basic single BJT stages offer different features.

common-base (CB), and common-collector (CC). The name refers to the fact that the common terminal is AC grounded. Their properties are well covered in numerous texts and only a brief discussion on their general properties and applications will be presented here.

The CE stage is the most commonly considered configuration since it provides a fairly high input impedance, high output impedance, and both current gain, $h_{21}(f)$, and voltage gain, g_mR_L. The noise and distortion properties are the same as considered earlier for the BJT. It is commonly used in single-ended, low noise amplifiers (LNA) and power amplifiers (PA). A well-known drawback of the CE stage at high frequencies is the feedback C_{jc}, which degrades gain via Miller multiplication and couples input and output networks leading to detuning of matching networks and possible instability.

As noted earlier, emitter degeneration can be used not only to improve dynamic range but also to help set impedance levels. It is sometimes necessary for the IC to present a standard impedance level at its input and output terminals to provide proper terminations. The use of emitter inductive degeneration has the fortuitous property of generating a synthetic resistive input impedance at high frequencies without contributing noise. As illustrated in Fig. 7.34 earlier, the transformed value is given by

$$R_{eff} = h_{21}(f)Z_E = (f_t/f)(2\pi f L_E) = 2\pi\ f_t\ L_E \tag{7.35}$$

which now appears in series with the input terminal.

The CB stage provides a well-predicted low input impedance given by $1/g_m$, high output impedance and voltage gain, g_mR_L, but has near unity current gain, α. It acts as an excellent current buffer and is often used to isolate circuit nodes. The CB appears most often in tight synergy with other transistors arranged in composite configurations. Although it lacks the capacitive feedback present in the CE that degrades gain and destabilizes operation, any series feedback at the grounded base node can lead to instability. The feedback element might be due to metallization, package parastics, or even the actual device base resistance. Extreme care must be exercised when grounding the CB stage. Another difference is that with a grounded base, the larger BV_{cbo} sets the voltage limit. The noise and distortion properties are identical to the CE.

The CC stage is often known as an emitter follower. It is predominantly used as a level shifter and as a voltage buffer to isolate stages and provide extra drive. It offers high input impedance, low output impedance, and near unity voltage gain. The impedance buffering factor is roughly $h_{21}(f)$ and at frequencies approaching f_t, its effectiveness is diminished as $h_{21}(f)$ nears unity. In this case it is common to see several stages of cascaded followers to provide adequate drive and buffering. The CC stage is a very wideband stage since direct capacitive feedthrough via C_d and C_{je} cancels the dominant pole to first order. However, this same capacitive coupling from input to output can cause destabilization, particularly with capacitive loads. In fact, this is the basis of operation of the Colpitts oscillator. From a noise point of

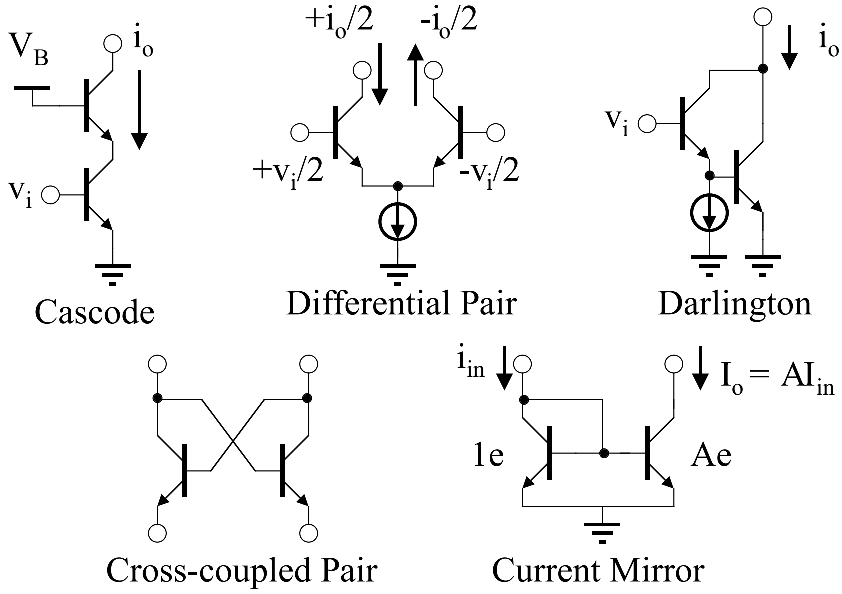

FIGURE 7.37 These common two-transistor configurations are used extensively in BJT ICs.

view, the CC simply transfers noise at its output directly back to its input and then adds on its own noise; therefore it is not used where low noise is essential. From a distortion perspective, the CC can be fairly linear as long as the impedance that it is driving is significantly higher than its own output impedance $1/g_m$. For minimal added shot noise and low distortion, CC stages must run at high bias currents.

The strength of IC technology is the ability to use transistors at will at practically no extra cost. Figure 7.37 illustrates five very common composite transistor configurations, namely the cascode, the differential pair, the Darlington, the cross-coupled pair, and the current mirror. These ubiquitous forms are common enough to be considered in more detail. Discussion of the current mirror appears later.

The cascode topology is a CE-CB connection. The CB provides a low impedance to the output of the CE stage, eliminating Miller multiplication of its C_{jc} and increasing the overall bandwidth. It also raises the output impedance of the single transistor by a factor of approximately β, which is useful in current sources. More importantly at RF, it improves input-output isolation, minimizing interactions that reduce the gain. The cascode configuration is common in LNAs since higher tuned power gain is achievable with minimal degradation in noise. Note that the CB transistor can be significantly smaller than the CE transistor, minimizing the parasitic capacitance at its output. The cascode requires a higher supply voltage than a stand-alone CE stage by at least a $V_{ce(sat)}$ to keep the lower BJT in its active region.

The differential pair (also known as a long-tailed pair) can be thought of as a CC-CB connection when driven in a single-ended fashion or as parallel CE stages when driven differentially. A tail current source or a current setting resistance is required to establish the operating point. This ubiquitous, cannonical form has a long, distinguished history in operational amplifiers, mixers, IF/RF amplifiers, digital ECL/CML gates, and even oscillators and latches when cross-coupled. The basic operation relies on the controlled steering of current from one branch to the other. Notice that the dynamic range is modified by the fact that noise sources from two transistors contribute to the total noise while the signal is divided across two junctions. The noise associated with the tail current source appears as common mode noise and does not affect the input noise if differential signaling is used. The structure can be enhanced with the addition of emitter degeneration, cascoding CB stages, and buffering CC stages.

The Darlington connection is a CE stage buffered at the input by CC stage. This configuration behaves essentially like a super-transistor with greater impedance buffering capability and higher $h_{21}(f)$. It typically appears at input and output interfaces where drive and buffering requirements are most severe. The

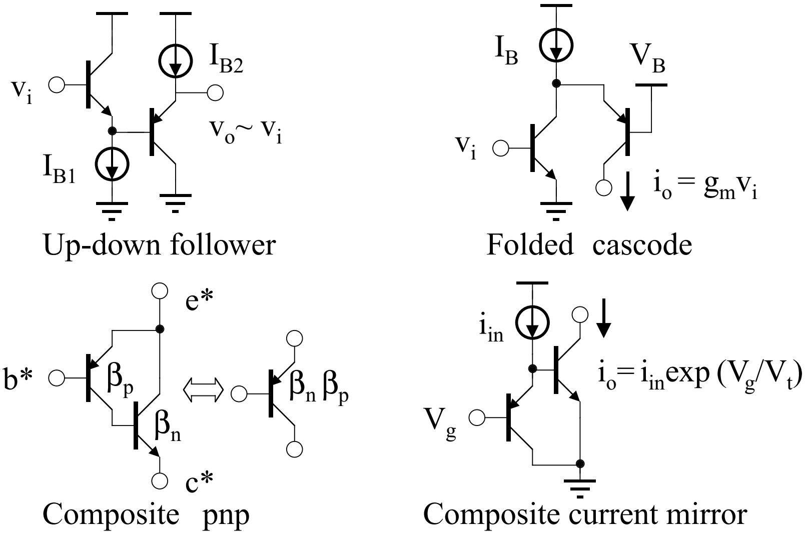

FIGURE 7.38 Composite npn-pnp combinations add functionality at lower supply voltages.

Darlington and the differential pair are sometimes called f_t multipliers since the input signal appears across two transistor junctions in series while the output signal is a parallel combination of currents. For a fixed input bias current per device, the effective input capacitance is $C_d/2$ while the effective transconductance is still g_m, giving from Eq. (7.23) an $f_t^{eff} = 2f_{tBJT}$. This of course ignores additional higher order poles and requires twice the current of a single BJT. In analogy to the differential pair, noise and distortion occur across two junctions in series.

The cross-coupled connection is derived from the differential pair. Following the signals around the loops leads to a positive feedback condition that can be used to induce regeneration for Schmidt triggers, multivibrators, and latches or negative resistance for tuned VCOs and gain peaking. It has also been used to synthesize voltage-to-current converters, bias cells, multipliers, and other functions. Since positive feedback is inevitably invoked in cross-coupled devices, care must be taken to avoid instability when it is undesired.

Note that npn-pnp composite structures are also possible creating many permutations that might offer certain advantages. These are illustrated in Fig. 7.38 in the form of the double up-down emitter-follower, the folded cascode, the composite pnp, and complementary mirror. The first two examples reduce the supply voltage requirements over their npn-only embodiment, the third transforms a poor quality pnp into a nearly ideal device, and the fourth provides a voltage controlled mirror ratio.

Translinear Circuits

The concept of translinearity was observed in deriving the basic properties of BJTs and its usefulness was alluded to in general terms. In particular, if the signals of interest are conveyed as currents rather than voltages, a large class of linear and nonlinear functions can be synthesized. When current-mode signals are used, extremely large dynamic ranges are possible since the junction essentially compresses the current signal logarithmically to a voltage; i.e., a 60 dB (1000x) signal current range corresponds to 180 mV of voltage swing at room temperature. The relatively small voltage swings represent a low impedance through which capacitances charge and discharge and thus the bandwidth of these circuits achieves broadband operation out to near the device limits represented by f_t. Furthermore, reduced internal voltage swings are consistent with lower supply voltages.

The simplest example of a translinear circuit is the well-known current mirror shown in Fig. 7.37. The input current, I_{in}, is mirrored to the output, I_{out} according to a scaling factor associated with the ratio of device sizes. Inherent in this process is a nonlinear conversion from I_{in} to the common V_{be} and then a second related nonlinear conversion from V_{be} to I_{out}. The impedance at the common base node is

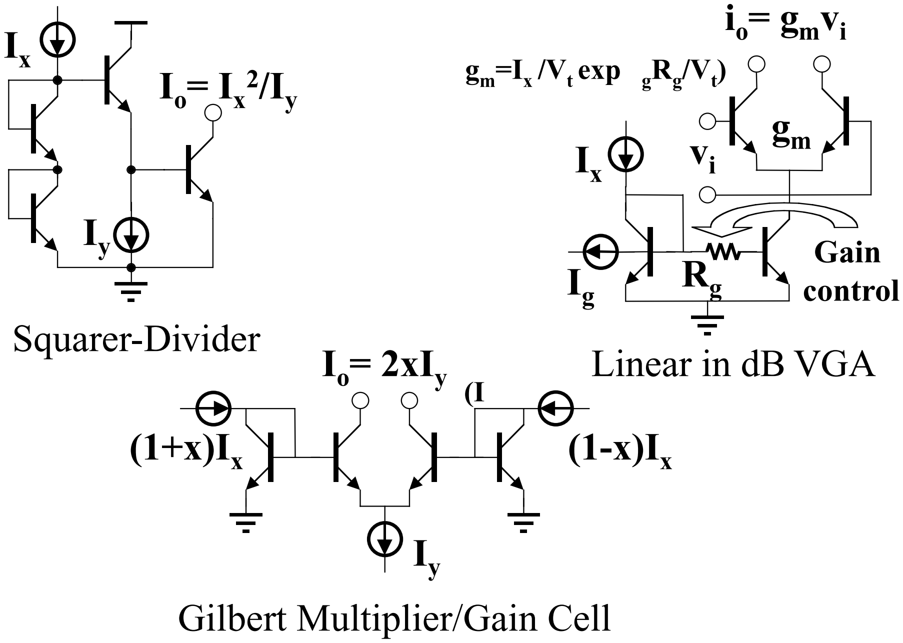

FIGURE 7.39 Numerous functions can be implemented using translinear principles.

nominally a parallel combination of $1/g_m$ and $(1 + A)C_d$, which results in a low time constant on the order of τ_f.

A large family of translinear circuits has been synthesized by applying the translinear principle stated as: *In a closed loop containing only junctions, the product of current densities flowing in the clockwise direction is equal to the product of current densities flowing in the counterclockwise direction.*

The principle has a corollary when voltage sources are inserted into the loop, namely that the products are equal to within a factor $\exp(V_a/V_t)$, where V_a is the applied voltage. It is merely a restatement that logarithmic multiplication and division, i.e., addition and subtraction of V_{be}'s, is tantamount to products and quotients of currents. In this sense, the BJT can be thought of as the mathematical transistor. Note that since the signals are in current form, the distortion is not caused by the exponential characteristics but is actually due to *departure* from it, i.e., series resistances, high level injection, and Early voltage effects conspire to distort the signals.

Fig. 7.39 illustrates three examples of translinear IC design. The first example is an analog squarer/divider with input signals I_x, I_y and output, I_o. By following the translinear principle, it can be shown that the mathematical operation

$$I_o = I_x^2 \big/ I_y \tag{7.36a}$$

is performed. The second example is the well-known Gilbert-cell multiplier/gain cell with predistortion. Again, by following the rules, the differential output currents have the same form as the two inputs. The third example is a linear in dB variable gain amplifier. In this case a voltage $V_g = R_g I_g$ is inserted into the loop and Eq. (7.36a) is modified so that

$$i_o = I_x \big/ V_t \exp\left(V_g \big/ V_t\right) V_i = I_x \big/ V_t G_o 10^{Vg/Vt} \tag{7.36b}$$

Note that if V_g and I_x are engineered to be proportional to temperature, then the gain control becomes stable with temperature. In all cases, the operating frequency of these circuits approaches the technology f_t.

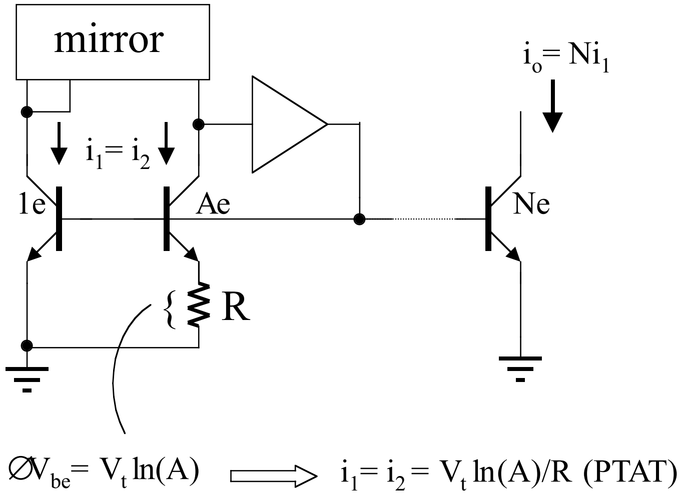
mirror
$i_o = Ni_1$
$i_1 = i_2$
1e
Ae
Ne
R
$\varnothing V_{be} = V_t \ln(A)$
$i_1 = i_2 = V_t \ln(A)/R$ (PTAT)

FIGURE 7.40 The ΔV_{be} cell that generates a PTAT current is ubiquitous in BJT biasing.

Biasing Techniques

Microwave IC designers have historically focused on the signal path with biasing treated as an afterthought. Analog IC designers, on the other hand, have placed a strong emphasis on biasing since it usually determines the sensitivity and robustness of a circuit. In particular, as was already seen in the variable gain amplifier, it is often necessary to generate a current that is proportional to absolute temperature, PTAT. Other times it is necessary to generate a current that is complementary to absolute temperature, CTAT. Finally sometimes a zero temperature coefficient current, ZTAT, is desired. The choice on temperature shaping depends on what is needed. In differential amplifiers where the gain is given by $g_m R_L = I_o R_L / 2V_t$, it is appropriate to choose a PTAT bias current for a stable gain; however, if the amplifier is actually a limiter, then a stable limited voltage swing requires a ZTAT shaping. By far the most common and fundamental bias current shape for BJTs turns out to be PTAT. From the PTAT form, other shapes can be derived.

The fundamental way to synthesize a bias sub-circuit is to start with a ΔV_{be} cell that generates a PTAT current. This cell, illustrated in Fig. 7.40, is a modified translinear loop. Two area ratioed BJTs each forced to carry the same current generate a difference in V_{be} given by

$$\Delta V_{be} = V_t \ln\left(A\right) \tag{7.37}$$

where A is the area ratio. This voltage develops a current in R that is PTAT and can now be mirrored throughout the IC by adding a driver that buffers the ΔV_{be} cell.

In some cases, a stable voltage reference is desired for scaling and it is beneficial to derive the various currents from this reference. To achieve a stable reference, the bandgap principle is invoked. As illustrated in Fig. 7.41, the idea is to add a CTAT voltage to a PTAT voltage so that the sum is a constant with temperature. It can be shown that the desired reference voltage V_g nearly corresponds to the bandgap energy, E_g of silicon, a very fundamental property. Intuitively, this is expected since at the extreme temperature of 0 K, it takes an energy equivalent to E_g to promote an electron into conduction. It so happens that a transistor V_{be} at a fixed I_c can be shown to be CTAT while a PTAT voltage can be generated from the ΔV_{be} cell. With this in mind, the PTAT component should be scaled such that it adds to the CTAT component to synthesize V_g. A physical realization of this principle known as a bandgap reference is illustrated in its simplest form in Fig. 7.42. It consists of a ΔV_{be} cell to generate a PTAT current and a resistor that converts it to the required PTAT voltage. Transistor Q1 plays a double role as part of the

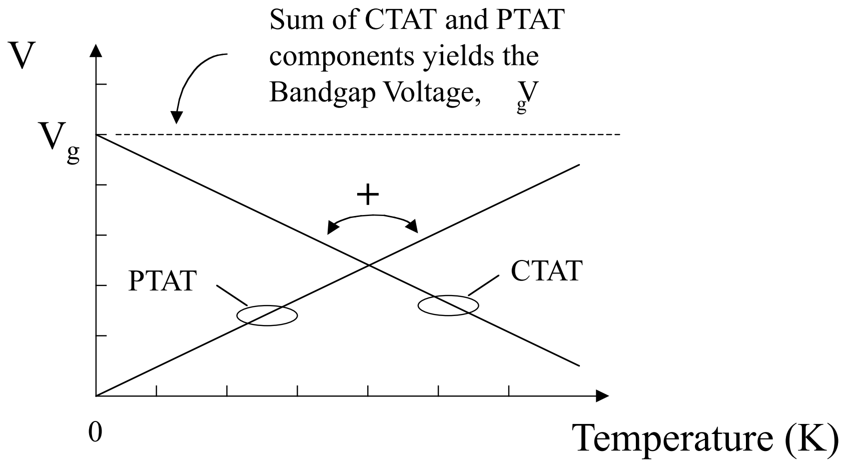

FIGURE 7.41 V_g is generated from properly proportioned PTAT and CTAT voltages.

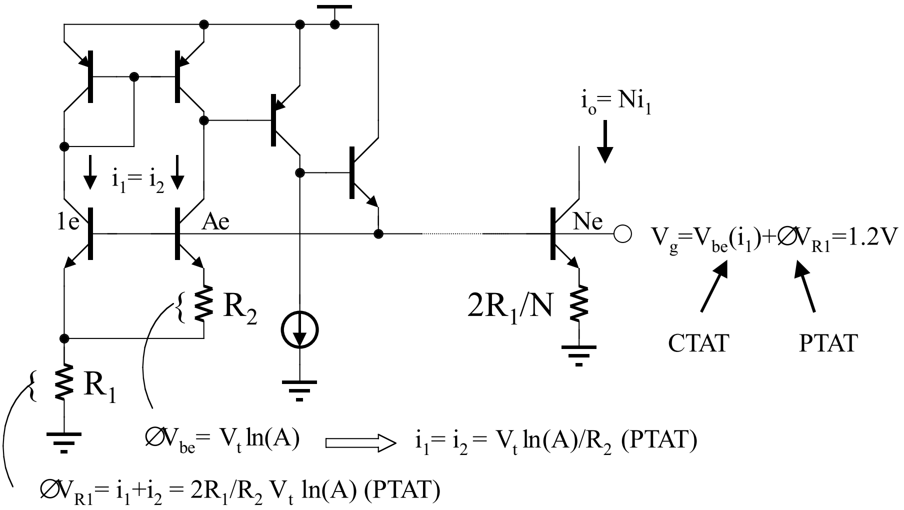
i_o= Ni_1
i_1= i_2
1e
Ae
Ne
V_g=$V_{be}(i_1)$+∅V_{R1}=1.2V
CTAT
PTAT
R_2
$2R_1/N$
R_1
∅V_{be}= V_t ln(A)
i_1= i_2 = V_t ln(A)/R_2 (PTAT)
∅V_{R1}= i_1+i_2 = $2R_1/R_2$ V_t ln(A) (PTAT)

FIGURE 7.42 The Brokaw cell provides PTAT currents and a stable voltage reference.

ΔV_{be} cell and as the V_{be} responsible for the CTAT voltage. The current mirror above ensures that both currents are the same and the buffer provides drive to the reference output. This output can be used to generate PTAT currents elsewhere in the circuit as shown in Fig. 7.42. The target transistor and resistor scaling are necessary to preserve the PTAT shape. This topology can be made insensitive to supply voltage, temperature, and process variations by the use of more sophisticated cells and by the prudent choice of component sizes and layout.

Fabrication Technology

The technology for fabricating BJTs has been performance and cost driven toward smaller transistor geometries, lower device and interconnect parasitics, higher yield/integration, and greater functionality. Silicon-based BJT technology has benefited greatly from the synergy with CMOS processes targeting VLSI/ULSI digital applications. Several variants of the simple npn process have evolved over the years that feature better npn's and/or addition of other transistor types. Examples include BiCMOS, which integrates BJTs with CMOS; fully complementary bipolar with true vertical npn's and pnp's; SiGe/Si HBT,

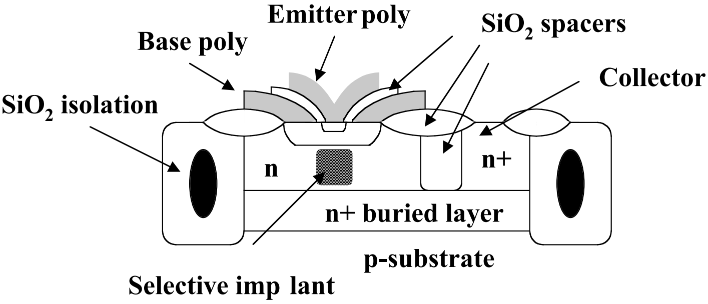

FIGURE 7.43 Modern processes feature double-poly, SiO_2 trenches and sub-μm lithography.

which offers higher f_t and lower R_b than traditional BJTs; and silicon-on-insulator (SOI) processes that rely on an insulating substrate to isolate devices and reduce substrate parasitics. III-V based HBTs have developed in a different direction since raw device speed has been more than adequate, but integration levels and process complexity have limited their availability. Process features can be grouped into two general categories: the active device, which determines the transistor performance, and the back-end process, which defines the interconnect metallization, dielectric isolation, passive components, and through-vias. The back-end process is particularly critical in RFICs since they set limits to IC parasitics and are responsible for the quality of resistors, capacitors, and inductors.

The silicon BJT process has evolved from the junction isolated buried collector process shown in Fig. 7.35 to the oxide trench isolated double-poly (emitter and base) process diagrammed in Fig. 7.43. The double poly structure with self-aligned spacers allows ultra-small emitter-base structures to be defined while simultaneously providing low extrinsic base resistance and low emitter charge storage. A selective collector implant under the active emitter helps delay the Kirk effect without significantly increasing the depletion capacitance. In general, the devices are defined by diffusions into the substrate with interconnects and passives constructed over dielectrics above the substrate. Standard aluminum metals have been silicided for improved reliability. Overall, this has led to significantly reduced device footprints and feature sizes with emitter geometries down to < 0.35 μm and f_t ranging from 30 GHz for standard BJTs to > 100 GHz for SiGe HBTs. Refinements such as silicided base handles and optimized epitaxially deposited bases promise even further improvements in device performance. On the back-end side, thin-film resistors and metal-metal capacitors are replacing their polysilicon and diffused versions bringing lower temperature coefficients, reduced parasitics and coupling to the substrate, trimming capability, and bias insensitivity. Furthermore, advanced multiple level interconnect modules and planarization techniques have been adopted from CMOS processes in the form of copper metalization, chemical-mechanical polishing, tungsten plugs, and low dielectric insulators. For RFICs, advanced interconnects are desirable not for high packing density, but for defining high quality passives away from the lossy substrate, particularly inductors, which are essential in certain applications.

The fabrication technology for the III-V HBTs is significantly different from that of silicon BJTs. The main difference stems from the fact that the starting material must be grown by advanced epitaxial techniques such as molecular beam epitaxy (MBE) or metallo-organic chemical vapor deposition (MOCVD). Each layer in the stack is individually optimized as needed. As a result of the predefined layers as well as thermal limits that disallow high temperature diffusion, the device is literally carved into the substrate leading to the wedding-cake triple mesa structure depicted in Fig. 7.44. The nature of the process limits minimum emitter geometries to about 1 μm, although self-aligned structures are used to minimize extrinsic areas. Values of f_t range from 30 GHz for power devices to 200 GHz for the highest speed structures. Interestingly, the improvements being made to silicon BJTs such as epitaxial bases, polysilicon emitters, and silicided bases, make use of deposited active layers, which is reminiscent of III-V technologies based on epitaxy. The back-end process inevitably consists of thin film resistors and metal-metal capacitors. Since the substrate is semi-insulating by definition, high-Q monolithic inductors are

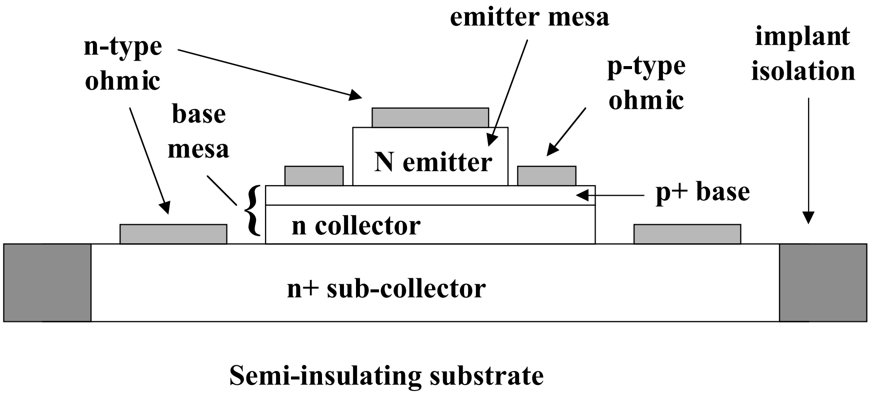

FIGURE 7.44 III-V HBTs are fabricated with mesa structures and relaxed lithography.

already available. Some processes offer backside vias that literally provide a direct connection from the front-side to the back-side of the wafer enabling easy and effective grounding at any point on the circuit.

7.2.2 Heterostructure Bipolar Transistors (HBTs)

William Liu

Basic Device Principle

Heterojunction bipolar transistors (HBTs) differ from conventional bipolar junction transistors (BJTs) in their use of hetero-structures, particularly in the base-emitter junction. In a uniform material, an electric field exerts the same amount of force on an electron and a hole, producing movements in opposite directions as shown in Fig. 7.45a. With appropriate modifications in the semiconductor energy gap, the forces on an electron and a hole may differ, and at an extreme, drive the carriers along the same direction as shown in Fig. 7.45b.[1] The ability to modify the material composition to independently control the movement of carriers is the key advantage of adopting hetero-structures for transistor design.

Figure Fig. 7.46 illustrates the band diagram of a *npn* BJT under normal operation, wherein the base-emitter bias (V_{BE}) is positive and the base-collector bias (V_{BC}) is negative. The bipolar transistor was

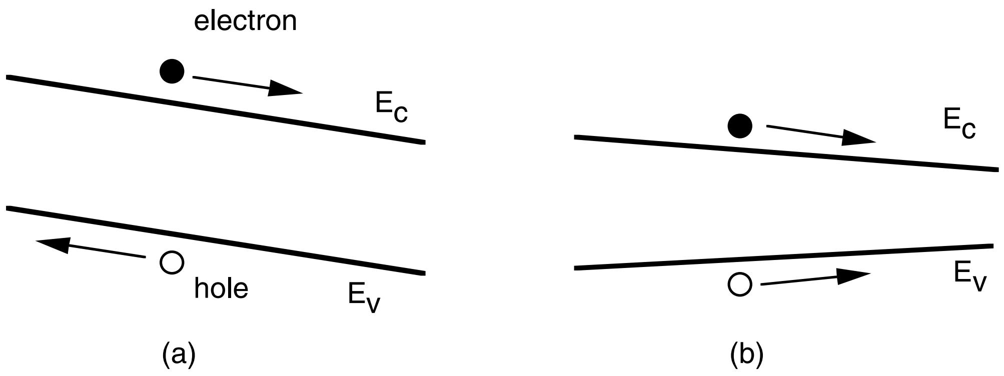

FIGURE 7.45 (a) An electric field exerts the same amount of force (but in opposite directions) on an electron and a hole. (b) Electron and hole can move in the same direction in a hetero-structure. (After Ref. [1], with permission.)

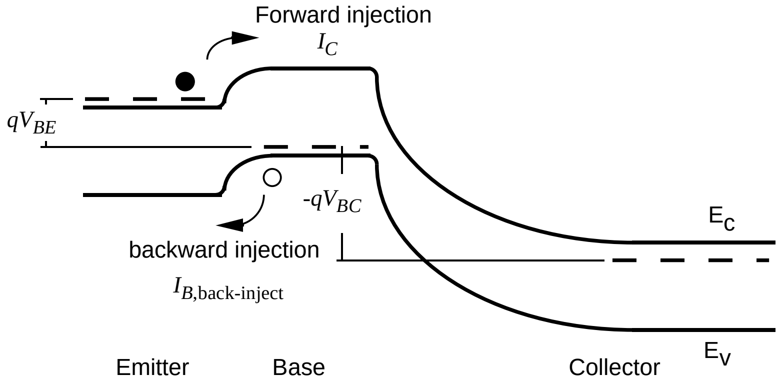

FIGURE 7.46 Band diagram of a *npn* bipolar junction transistor.

detailed in the previous section. Here we use Fig. 7.46 to emphasize that the energy gap is the same throughout the entire transistor structure. The Fermi levels and the depletion regions of the band diagram reflect the BJT design constraint that the doping level is highest in the emitter, and lowest in the collector. The Fermi level in the emitter is above the conduction band, signifying that the emitter is degenerately doped.

A BJT has two key current components. The first is the forward-injection current conducted by the electrons. These electrons are emitted at the emitter, crossing the base-emitter potential barrier with the help of the V_{BE} bias, diffusing through the thin base layer as minority carriers, and then are swept by the large electric field in the reverse-biased base-collector junction. The carriers finally leave the collector, forming the collector current (I_C). In their journey, only a few electrons are lost through recombinations with the majority holes in the base. We therefore denote the electron current as I_C in Fig. 7.46, even though the current magnitude in the emitter is slightly larger than that which finally exits the collector terminal. Of the three phases of the journey, the diffusion through the base layer is the rate-limiting step. Hence, a quantitative expression of I_C, to be developed shortly, relates intimately to the base layer parameters.

By varying V_{BE}, we control the amount of the electron injection from the emitter to the base, and subsequently, the amount of electrons collected at the collector. This current flow, however, is independent of V_{BC}, as long as the base-collector junction is reverse biased. The property that the desired signal (I_C) is modified by the input bias (V_{BE}) but unaffected by the output bias (V_{BC}) fulfills the requirement of a sound three-terminal device. As the input and output ports are decoupled from one another, complicated circuits based on the transistors can be easily designed.

The second current component is composed of holes that are back-injected from the base to the emitter. This current does not get collected at the collector terminal and does not contribute to the desired output signal. However, the moment a V_{BE} is applied so that the desired electrons are emitted from the emitter to the base, these holes are back-injected from the base to the emitter. The bipolar transistor is so named to emphasize that both electron and hole play significant roles in the device operation. A good design of a bipolar transistor maximizes the electron current transfer while minimizing the hole current. As indicated on Fig. 7.46, we refer the hole current as $I_{B,\text{back-inject}}$. It is a base current because the holes come from the base layer where they are the majority carriers.

We mentioned that I_C is limited by the diffusion process in the base, wherein the electrons are minority carriers. Likewise, $I_{B,\text{back-inject}}$ is limited by the diffusion in the emitter, wherein the holes are minority carriers. Fisk's law states that a diffusion current density across a layer is equal to the diffusion coefficient times the carrier concentration gradient.[2] (From the Einstein relationship, the diffusion coefficient can be taken to be kT/q times the carrier mobility.) The carrier concentrations at one end of the base layer (for the calculation of I_C) and the emitter layer (for the calculation of $I_{B,\text{back-inject}}$) are both proportional to $\exp(qV_{BE}/kT)$, and are 0 at the other end. An application of Fisk's Law leads to:[3,4]

$$I_C = \frac{qA_{\text{emit}} D_{n,\text{base}}}{X_{\text{base}}} \frac{n_{i,\text{base}}^2}{N_{\text{base}}} \exp\left(\frac{qV_{BE}}{kT}\right) \tag{7.38}$$

$$I_{B,\text{back-inject}} = \frac{qA_{\text{emit}} D_{p,\text{emit}}}{X_{\text{emit}}} \frac{n_{i,\text{emit}}^2}{N_{\text{emit}}} \exp\left(\frac{qV_{BE}}{kT}\right) \tag{7.39}$$

where, for example, A_{emit} is the emitter area; $D_{n,\text{base}}$ is the electron diffusion coefficient in the base layer; N_{base} is the base doping; X_{base} is the base thickness; and $n_{i,\text{base}}$ is the intrinsic carrier concentration in the base layer. I_C is proportional to the emitter area rather than the collector area because I_C is composed of the electrons injected from the emitter. For homojunction BJTs, $n_{i,\text{base}}$ is identical to $n_{i,\text{emit}}$. The ratio of the desired I_C to the undesired $I_{B,\text{back-inject}}$ is,

$$\frac{I_C}{I_{B,\text{back-inject}}} = \frac{X_{\text{emit}}}{X_{\text{base}}} \frac{D_{n,\text{base}}}{D_{p,\text{emit}}} \times \frac{N_{\text{emit}}}{N_{\text{base}}} \quad \left(\text{homojunction BJT}\right) \tag{7.40}$$

Because the diffusion coefficients and layer thicknesses are roughly equal on the first order, Eq. (7.40) demonstrates that the emitter doping of a BJT must exceed the base doping in order for I_C to exceed $I_{B,\text{back-inject}}$. For most applications, we would actually prefer the base doping be high and the emitter doping, low. A high base doping results in a small base resistance and a low emitter doping reduces the base-emitter junction capacitance, both factors leading to improved high frequency performance. Unfortunately, these advantages must be compromised in the interest of minimizing $I_{B,\text{back-inject}}$ in homojunction transistors.

A heterojunction bipolar transistor (HBT), formed by a replacement of the homojunction emitter by a larger energy gap material, enables the design freedom of independently optimizing the $I_C/I_{B,\text{back-inject}}$ ratio and the doping levels. Figure 7.47 illustrates the band diagrams of *Npn* HBTs. The capital *N* in "*Npn*" rather than a small letter *n* emphasizes that the emitter is made of a larger energy gap material than the rest. It is implicit that the base-collector junction of an HBT is a homojunction. An HBT whose base-collector junction is also a heterojunction is called a double heterojunction bipolar transistor (DHBT), typically found in the InP/InGaAs material system.

The energy gap difference in the base-emitter heterojunction of an HBT burdens the holes from the base to experience a much larger energy barrier than the electrons from the emitter. With the same application of V_{BE}, the forces acting on the electrons and holes differ, favoring the electron injection from

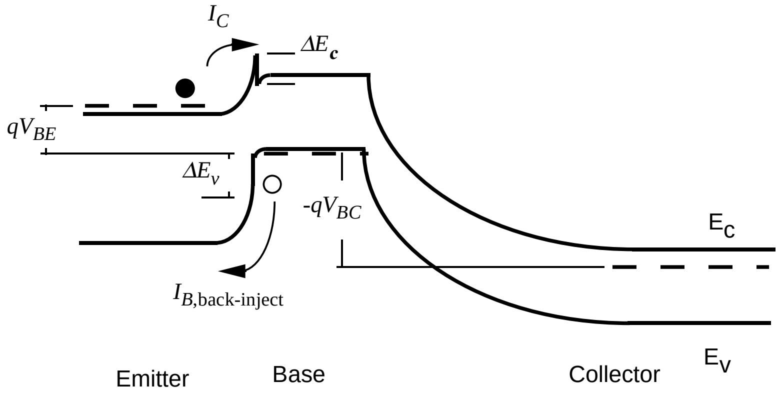

FIGURE 7.47 Band diagram of a *Npn* abrupt heterojunction bipolar transistor.

the emitter into the base to the hole back-injection from the base into the emitter. Figure 7.47 shows that the difference in the electron and hole barriers is ΔE_v, the valence band discontinuity. The $I_C/I_{B,\text{back-inject}}$ ratio of Eq. (7.40) can be extended to the HBT as:[1]

$$\frac{I_C}{I_{B,\text{back-inject}}} = \frac{X_{\text{emit}}}{X_{\text{base}}}\frac{D_{n,\text{base}}}{D_{p,\text{emit}}} \times \frac{N_{\text{emit}}}{N_{\text{base}}} \exp\left(\frac{\Delta E_v}{kT}\right) \quad (\text{abrupt HBT}) \tag{7.41}$$

The exponential factor is the key to the fact that base doping can be made larger than the emitter doping without adversely affecting the HBT performance.

We qualify the expression in Eq. (7.41): that is for an *abrupt* HBT. This means that an abrupt change of material composition exists between the emitter and the base. An example is an InP/$In_{0.53}Ga_{0.47}As$ HBT. The indium and gallium compositions form a fixed ratio so that the resulting $In_{0.53}Ga_{0.47}As$ layer has the same lattice constant as InP, the starting substrate material. Otherwise, the dislocations due to lattice mismatch prevent the device from being functional. In fact, although the idea of HBT is as old as the homojunction transistor itself,[5] HBTs have emerged as practical transistors only after molecular beam epitaxy (MBE) and metal-organic chemical vapor deposition (MOCVD) were developed to grow high-quality epitaxial layers in the 1980s.[6] Another example of an abrupt HBT is the $Al_{0.3}Ga_{0.7}As$/GaAs HBT, in which the entire emitter layer consists of $Al_{0.3}Ga_{0.7}As$, while the base and collector are GaAs. When the AlGaAs/GaAs material system is used, we can take advantage of the material property that AlAs and GaAs have nearly the same lattice constants. It is therefore possible to grow an $Al_xGa_{1-x}As$ layer with any composition *x* and still be lattice-matched to GaAs. When the aluminum composition of an intermediate AlGaAs layer is graded from 0 at the GaAs base to 30% at the $Al_{0.3}Ga_{0.7}As$ emitter, then the resulting structure is called a *graded* HBT.

The band diagram of a graded HBT is shown in Fig. 7.48. A graded HBT has the advantage that the hole barrier is larger than the electron barrier by ΔE_g, the energy-gap discontinuity between the emitter and the base materials. Previously, in an abrupt HBT, the difference in the hole and electron barriers was only ΔE_v. The additional barrier brings forth an even larger $I_C/I_{B,\text{back-inject}}$ ratio for the graded HBT:

$$\frac{I_C}{I_{B,\text{back-inject}}} = \frac{X_{\text{emit}}}{X_{\text{base}}}\frac{D_{n,\text{base}}}{D_{p,\text{emit}}} \times \frac{N_{\text{emit}}}{N_{\text{base}}} \exp\left(\frac{\Delta E_g}{kT}\right) \quad (\text{Graded HBT}) \tag{7.42}$$

Equation (7.42) is obtained from the inspection of the band diagram. It is also derivable from Eqs. (7.38) and (7.39) by noting that $n_{i,\text{base}}^2 = n_{i,\text{emit}}^2 \times \exp(\Delta E_g/kT)$.

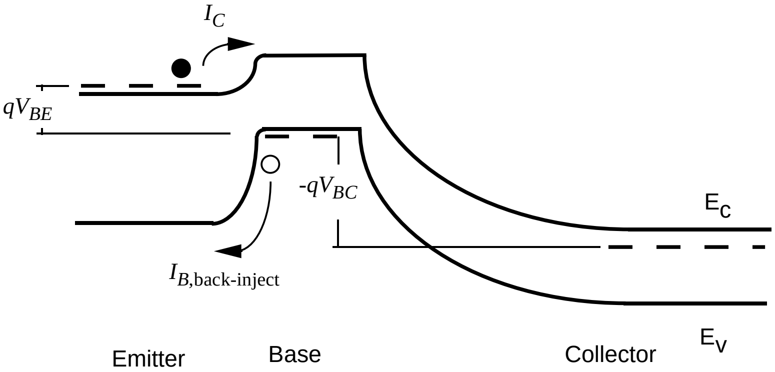

FIGURE 7.48 Band diagram of a *Npn* graded heterojunction bipolar transistor.

TABLE 7.3 Heterojunction Parameters at Room Temperature

	$Al_xGa_{1-x}As/GaAs$ ($x \leq 0.45$)	$Ga_{0.51}In_{0.49}P/GaAs$	$InP/In_{0.53}Ga_{0.47}As$	$In_{0.52}Al_{0.48}As/In_{0.53}Ga_{0.47}As$	$Si/Si_{0.8}Ge_{0.2}$
ΔE_g (eV)	$1.247 \cdot x$	Ordered: 0.43 Disordered: 0.46	0.60	0.71	0.165
ΔE_c (eV)	$0.697 \cdot x$	Ordered: 0.03 Disordered: 0.22	0.23	0.50	
ΔE_v (eV)	$0.55 \cdot x$	Ordered: 0.40 Disordered: 0.24	0.37	0.21	
E_g (eV)	GaAs: 1.424	Ordered: 1.424	InP: 1.35	InGaAs: 0.75	Si: 1.12

The amount of improvement from a homojunction to a heterojunction depends on the band alignment properties of the two hetero-materials. Table 7.3 lists the conduction band discontinuity (ΔE_c), valence band discontinuity (ΔE_v), and their sum which is the energy-gap discontinuity (ΔE_g), for several material systems used for HBTs. The energy gap of a semiconductor in the system is also given for convenience. The values shown in Table 7.3 are room temperature values.

The most popular III-V material system is $Al_xGa_{1-x}As/GaAs$. The table lists its band alignment parameters for $x \leq 0.45$. At these aluminum mole fractions, the AlGaAs layer is a direct energy-gap material, in which the electron wave function's wave vectors **k** at both the conduction band minimum and the valence band maximum are along the same crystal direction.[2] Since nearly all semiconductor valence band maximums take place when **k** is [000], the conduction band minimum in a direct energy-gap material is also at **k** = [000]. The conduction band structure surrounding this **k** direction is called the Γ valley. There are two other **k** directions of interest because the energy band structures in such directions can have either the minimum or a local minimum in the conduction band. When **k** is in the [100] direction, the band structure surrounding it is called the X valley, and when **k** is in the [111] direction, the L valley. As the aluminum mole fraction of $Al_xGa_{1-x}As$ exceeds 0.45, it becomes an indirect energy-gap material, with its conduction band minimum residing in the X valley. The band alignment parameters at $x > 0.45$ are found elsewhere.[3] SiGe is an indirect energy-gap material; its conduction band minimum is also located in the X valley. Electron-hole generation or recombination in indirect energy-gap materials requires a change of momentum ($\mathbf{p} = \hbar\mathbf{k}$), a condition that generally precludes them from being useful for laser or light-emitting applications.

Particularly due to the perceived advantage in improved reliability, HBTs made with the GaInP/GaAs system have gained considerable interest.[7] The band alignment of GaInP/GaAs depends on whether the grown GaInP layer is ordered or disordered, as noted in Table 7.3. The crystalline structure in an *ordered* GaInP layer is such that sheets of pure Ga, P, In, and P atoms alternate on the (001) planes of the basic unit cell, without the intermixing of the Ga and In atoms on the same lattice plane.[8] When the Ga, In and P atoms randomly distribute themselves on a plane, the GaInP layer is termed *disordered*.

The processing of AlGaAs/GaAs and GaInP/GaAs HBTs is fairly simple. Both wet and dry etching are used in production environments, and ion implantation is an effective technique to isolate the active devices from the rest. The processing of InP/InGaAs and InAlAs/InGaAs materials, in contrast, is not straightforward. Because of the narrow energy-gap of the InGaAs layer, achieving an effective device isolation often requires a complete removal of the inactive area surrounding the device, literally digging out trenches to form islands of devices. Further, the dry-etching, and its associated advantages such as directionality of etching, is not readily/easily available for InGaAs.[9] However, the material advantages intrinsic to InP/InGaAs and InAlAs/InGaAs make them the choice for applications above 40 GHz. In addition, the turn-on voltage, the applied V_{BE} giving rise to a certain collector current, is smaller for HBTs formed with InGaAs base compared to GaAs base (due to the energy-gap difference). The turn-on characteristics of various HBTs are shown in Fig. 7.49.

A calculation illustrates the advantage of an HBT. Consider an AlGaAs/GaAs HBT structure designed for power amplifier applications, as shown in Fig. 7.50.[10] The emitter and the base layers of the transistor are: $N_{\text{emit}} = 5 \times 10^{17}$ cm^{-3}; $N_{\text{base}} = 4 \times 10^{19}$ cm^{-3}; $X_{\text{emit}} \approx 1300$ Å; and $X_{\text{base}} = 1000$ Å. We shall use the

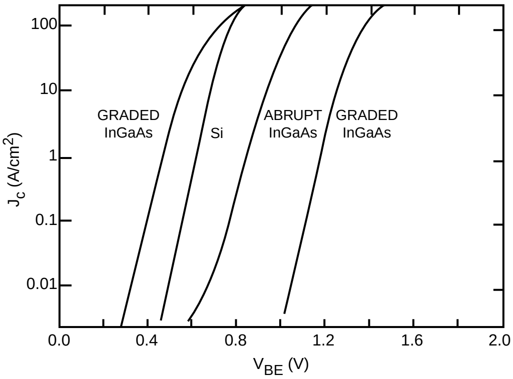

FIGURE 7.49 Turn-on characteristics of bipolar transistors based on various material systems. (After Ref. [6], with permission.)

Material	Thickness (Å)	Composition x	Doping (cm^{-3})	
n-In$_x$Ga$_{1-x}$As	800	$0 \rightarrow 0.6$	$> 3 \times 10^{19}$	
n-GaAs	2000		5×10^{18}	
N-Al$_x$Ga$_{1-x}$As	300	$0.3 \rightarrow 0$	1×10^{18}	
N-Al$_x$Ga$_{1-x}$As	1000	0.3	5×10^{17}	Emitter
N-Al$_x$Ga$_{1-x}$As	300	$0 \rightarrow 0.3$	5×10^{17}	
	(The above grading layer is absent in abrupt HBT)			
p-GaAs	1000		4×10^{19}	Base
n-GaAs	7000		3×10^{16}	Collector
n-GaAs	6000		5×10^{18}	Subcollector
	Semi-insulating GaAs Substrate			

FIGURE 7.50 Typical HBT epitaxial structure designed for power amplifier applications. (After Ref. [10], with permission.)

following diffusion coefficients for the calculation: $D_{n,\text{base}} = 20$ and $D_{p,\text{emit}} = 2.0$ cm^2/V-s. For a graded Al$_{0.3}$Ga$_{0.7}$As/GaAs heterojunction, ΔE_g is calculated from Table 7.3 to be 0.3 × 1.247 = 0.374 eV. The ratio for the graded HBT, according to Eq. (7.42), is,

$$\frac{I_C}{I_{B,\text{back-inject}}} = \frac{1300}{1000}\,\frac{20}{2.0} \times \frac{5 \times 10^{17}}{4 \times 10^{19}} \exp\left(\frac{0.374}{0.0258}\right) = 2.5 \times 10^5$$

For an abrupt Al$_{0.3}$Ga$_{0.7}$As/GaAs HBT, ΔE_v is the parameter of interest. According to the table, ΔE_v at $x =$ 0.3 is 0.55 × 0.3 = 0.165 eV. Therefore, Eq. (7.41) leads to:

$$\frac{I_C}{I_{B,\text{back-inject}}} = \frac{1300}{1000}\,\frac{20}{2.0} \times \frac{5 \times 10^{17}}{4 \times 10^{19}} \exp\left(\frac{0.165}{0.0258}\right) = 97$$

Consider a Si BJT with identical doping levels, layer thicknesses, and diffusion coefficients, except that it is a homojunction transistor so that $\Delta E_g = 0$. Using Eq. (7.40), we find the $I_C/I_{B,\text{back-inject}}$ ratio to be:

$$\frac{I_C}{I_{B,\text{back-inject}}} = \frac{1300}{1000}\,\frac{20}{2.0} \times \frac{5 \times 10^{17}}{4 \times 10^{19}} = 0.16.$$

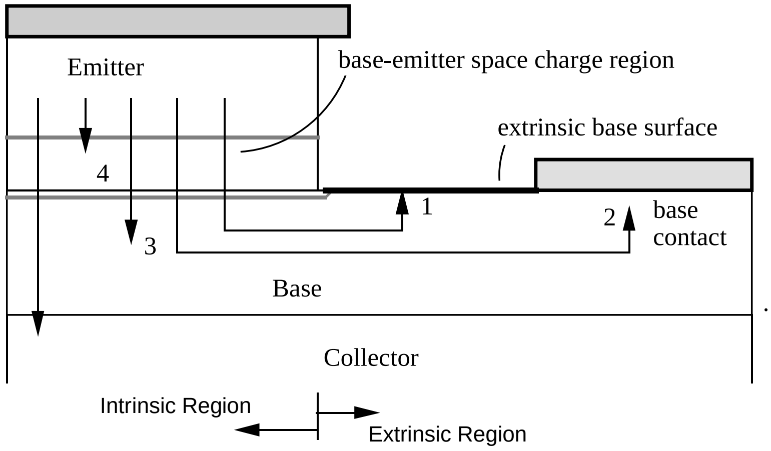

FIGURE 7.51 Locations of the four base recombination currents. The fifth base current component, not a recombination current, is $I_{B\text{,back-inject}}$ shown in Figure 7.46. (After Liu, W., Microwave and DC characterizations of Npn and Pnp HBTs, PhD. Dissertation, Stanford University, Stanford, CA, 1991.)

The useful collector current in the homojunction transistor is only 1/6 of the undesirable back-injection current. This means the device is useless. In contrast, both the graded and the abrupt HBTs remain functional, despite the higher base doping in comparison to the emitter.

Base Current Components

$I_{B\text{,back-inject}}$ is only one of the five dominant base current components in a bipolar transistor. We have thus far considered only $I_{B\text{,back-inject}}$ because it is the distinguishing component between a HBT and a BJT. Once $I_{B\text{,back-inject}}$ is made small in a HBT through the use of a heterojunction, the remaining four components become noteworthy. All of these components are recombination currents; they differ only in the locations where the recombinations take place, as shown in Fig. 7.51. They are: (1) extrinsic base surface recombination current, $I_{B\text{,surf}}$; (2) base contact surface recombination current, $I_{B\text{,cont}}$; (3) bulk recombination current in the base layer, $I_{B\text{,bulk}}$; and (4) space-charge recombination current in the base-emitter junction depletion region, $I_{B\text{,scr}}$. In the discussion of bipolar transistors, an easily measurable quantity of prime importance is the current gain (β), defined as the ratio of I_C to the total base current I_B:

$$\beta = \frac{I_C}{I_B} = \frac{I_C}{I_{B\text{,back-inject}} + I_{B\text{,surf}} + I_{B\text{,cont}} + I_{B\text{,bulk}} + I_{B\text{,scr}}} \tag{7.43}$$

Depending on the transistor geometrical layout, epitaxial layer design, and the processing details that shape each of the five base current components, the current gain can have various bias and temperature dependencies. In the following, the characteristics of each of the five base components are described, so that we can better interpret the current gain from measurement and establish some insight about the measured device.

Figure 7.52a illustrates a schematic cross-section of an HBT. Without special consideration, a conventional fabrication process results in an exposed base surface at the extrinsic base regions. (*Intrinsic region* is that underneath the emitter, and *extrinsic region* is outside the emitter mesa, as shown in Fig. 7.51.) Because the exposed surface is near the emitter mesa where the minority carrier concentration is large, and because the surface recombination velocity in GaAs is high (on the order of 10^6 cm/s), $I_{B\text{,surf}}$ is significant in these unpassivated devices. Various surface passivation techniques have been tested. The most effective method is *ledge passivation*,[11,12] formed with, for example, an AlGaAs layer on top of the GaAs base. The AlGaAs ledge must be thin enough so that it is fully depleted by a combination of the free surface Fermi level pinning above and the base-emitter junction below. If the passivation ledge is

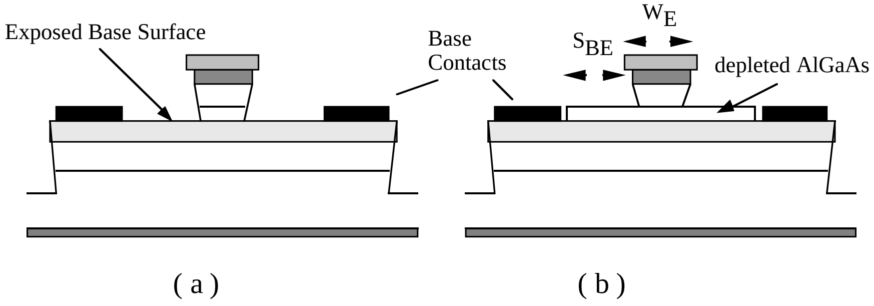

FIGURE 7.52 Schematic cross-sections of HBTs: (a) unpassivated HBTs, and (b) passivated HBTs. (After Liu, W., Microwave and DC characterizations of Npn and Pnp HBTs, PhD. Dissertation, Stanford University, Stanford, CA, 1991.)

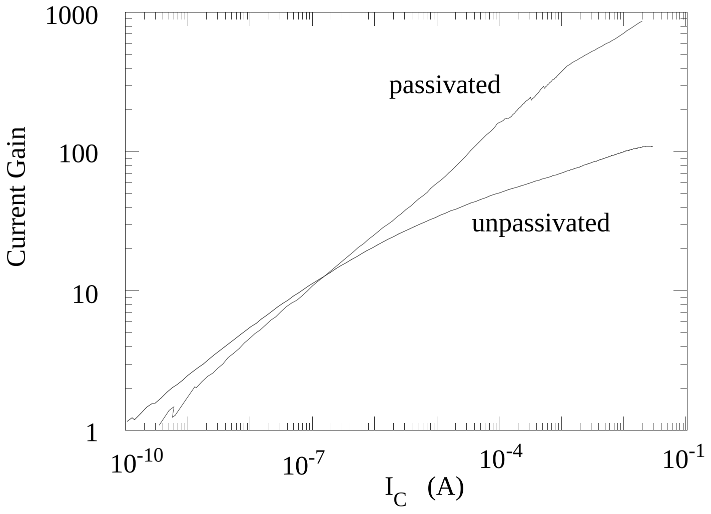

FIGURE 7.53 Measured current gain as a function of collector current for both passivated and unpassivated HBTs. (After Liu, W. et al., Diode ideality factor for surface recombination current in AlGaAs/GaAs heterojunction bipolar transistors, *IEEE Trans. Electron Devices*, 39, 2726–2732, 1992, with permission.)

not fully depleted, the active device area would be much larger than the designed emitter. The requirement for the AlGaAs layer to be fully depleted limits the AlGaAs thickness to the order of 1000 Å, and emitter doping to low to mid 10^{17} cm^{-3}. Although the ledge passivation was originally designed to minimize $I_{B,\text{surf}}$, it is also crucial to long-term reliability.[3,7]

Unlike I_C, $I_{B,\text{surf}}$ is proportional to the emitter periphery rather than the emitter area. For high frequency devices whose emitter is in a strip form (thus the perimeter-to-area ratio is large), $I_{B,\text{surf}}$ is a major component to the overall base current. The current gain is substantially reduced from that of a large squarish device whose perimeter-to-area ratio is small. The discrepancy in β due to emitter geometry is termed the *emitter-size effect*. Figure 7.53 displays β vs. I_C for both passivated and unpassivated devices with $A_{\text{emit}} = 4 \times 10$ µm^2. The emitter area is small enough to demonstrate the benefit of the surface passivation. A large device has negligible surface recombination current and the current gain does not depend on whether the surface is passivated or not. Because the two devices are fabricated simultaneously and physically adjacent to each other, the difference between the measured βs is attributed to the additional $I_{B,\text{surf}}$ of the unpassivated device.

The second base recombination current, $I_{B,\text{cont}}$, is in principle the same as $I_{B,\text{surf}}$. Both are surface recombination currents, except $I_{B,\text{cont}}$ takes place on the base contacts whereas $I_{B,\text{surf}}$, on the extrinsic base surfaces. Because the contacts are located further away from the intrinsic emitter than the extrinsic base surface, $I_{B,\mathrm{cont}}$ is generally smaller than $I_{B,\mathrm{surf}}$ when the surface is unpassivated. However, it may replace $I_{B,\mathrm{surf}}$ in significance in passivated devices (or in Si BJTs whose silicon dioxide is famous in passivating silicon). There is a characteristic distance for the minority carrier concentration to decrease exponentially from the emitter edge toward the extrinsic base region.[3] As long as the base contact is placed at roughly 3 times this characteristic length away from the intrinsic emitter, $I_{B,\mathrm{cont}}$ can be made small. The base contact cannot be placed too far from the emitter, however. An excessively wide separation increases the resistance in the extrinsic base region and degrades the transistor's high frequency performance.

The above two recombination currents occur in the extrinsic base region. Developing analytical expressions for them requires a solution of the two-dimensional carrier profile. Although this is possible without a full-blown numerical analysis,[3] the resulting analytical equations are quite complicated. The base bulk recombination current, in contrast, can be accurately determined from a one-dimensional analysis since most of the base minority carriers reside in the intrinsic region. It is convenient to express $I_{B,\mathrm{bulk}}$ through its ratio with I_C:

$$\frac{I_C}{I_{B,\mathrm{bulk}}} = \frac{\tau_n}{\tau_b} \tag{7.44}$$

where τ_n is the minority carrier lifetime in the base, and τ_b, the minority carrier transit time across the base. In a typical Si BJT design, an electron spends about 10 ns diffusing through the base layer while in every 1 μs an electron is lost through recombination. The transistor then has a current gain of 1 μs/10 ns = 100. The recombination lifetime in the GaAs base material is significantly shorter than in Si, at about 1 ns. However, the transit time through the GaAs is also much shorter than in Si due to the higher carrier mobility in GaAs. A well-designed HBT has a τ_b of 0.01 ns; therefore, a $\beta = 100$ is also routinely obtainable in III-V HBTs.

Equation (7.44) indicates that $I_{B,\mathrm{bulk}}$ is large if τ_n is small. The recombination lifetime of a semiconductor, a material property, is found to be inversely proportional to the doping level. When the base doping in an AlGaAs/GaAs (or GaInP/GaAs) HBT is 5×10^{18} cm^{-3}, the current gain easily exceeds 1000 when proper device passivation is made and the base contacts are placed far from the emitter. As the base doping increases to 10^{20} cm^{-3}, $I_{B,\mathrm{bulk}}$ dominates all other base current components, and the current gain decreases to only about 10, independent of whether the extrinsic surface is passivated or not. The base doping in III-V HBTs for power applications, as shown in Fig. 7.50, is around $3 - 5 \times 10^{19}$ cm^{-3}. It is a compromise between achieving a reasonable current gain (between 40 and 200) and minimizing the intrinsic base resistance to boost the high frequency performance.

Equation (7.44) also reveals that $I_{B,\mathrm{bulk}}$ is large when the base transit time is long. This is the time that a base minority carrier injected from the emitter takes to diffuse through the base. Unlike the carrier lifetime, which is mostly a material constant, the base transit time is a strong function of the base layer design:

$$\tau_b = \frac{X_{\mathrm{base}}^2}{2D_{n,\mathrm{base}}} \tag{7.45}$$

Because τ_b is proportional to the square of X_{base}, the base thickness is designed to be thin. Making the base too thin, however, degrades high frequency performance due to increased base resistance. A compromise between these two considerations results in a X_{base} at around 800 – 1000 Å, as shown in Fig. 7.50.

The derivation of Eq. (7.45) assumes that the minority carriers traverse through the base purely by diffusion. This is certainly the scenario in a bipolar transistor whose base layer is uniformly doped and of the same material composition. With energy-gap engineering, however, it is possible to shorten the base transit time (often by a factor of 3) by providing a drift field. In a Si/SiGe HBT for example, the Ge

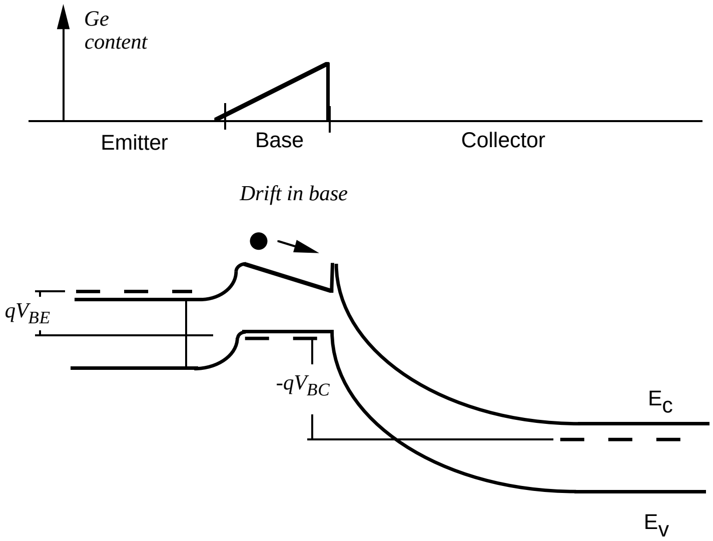

FIGURE 7.54 Band diagram of a SiGe HBT with a base quasi-electric field established by grading the germanium content.

content can be linearly graded from 0 to 8% across a 300 Å base to result a *quasi-electric field* on the order of 30 to 50 kV/cm.[13] We used the term quasi-electric field to describe the electric field generated by grading the energy gap, or more specifically, the gradient of the electron affinity (χ_e). In a conventional bipolar transistor, an electric field can be established only in the presence of space charges (such as the depletion region in a *p-n* junction). In an HBT with a graded base, the overall electric field in the base layer is nonzero even though the entire base region remains charge neutral. A SiGe HBT band diagram, shown in Fig. 7.54, illustrates how a minority carrier can speed up in the presence of the band grading. The figure shows that the energy gap becomes narrower as the Ge content increases. Because the base layer is heavily doped, the quasi-Fermi level in the base is pinned to be relatively flat with respect to position. The entire energy gap difference appears in the conduction band. The base quasi-electric field, being proportional to the slope of the band bending, propels the electrons to drift from the emitter toward the collector. As the carrier movement is enhanced by the drift motion, in addition to the diffusion, the base transit time decreases.

Figure 7.54 is characteristic of the SiGe HBT pioneered by a U.S. company,[14] in which the Ge content is placed nearly entirely in the base and graded in a way to create a base quasi-electric field. The base-emitter junction is practically a homojunction; therefore, it perhaps does not strictly fit the definition of being a heterojunction bipolar transistor and the base must be doped somewhat lighter than the emitter. This type of transistor resembles a drift homojunction transistor,[15] in which a base electric field is established by grading the base doping level. A drift transistor made with dopant grading suffers from the fact that part of the base must be lightly doped (at the collector side), thus bearing a large base resistance. An alternative school of SiGe HBT places a fixed Ge content in the base, mostly promoted by European companies.[16] Transistors fabricated with the latter approach do not have a base quasi-electric field. However, the existence of the base-emitter heterojunction allows the emitter to be more lightly doped than the base, just as in III-V HBTs. In either type of SiGe HBTs, there can be a conduction band discontinuity between the base and collector layers. This base-collector junction spike (Fig. 7.54), also notable in InP-based DHBT, has been known to cause current gain fall off.[3] The spike can be eliminated by grading the Ge content from the base to inside the collector layer.

Likely due to reliability concerns or for purely historical reasons, most commercial III-V HBTs have a uniformly doped base without a base quasi-electric field. If a base electric field is desired, in

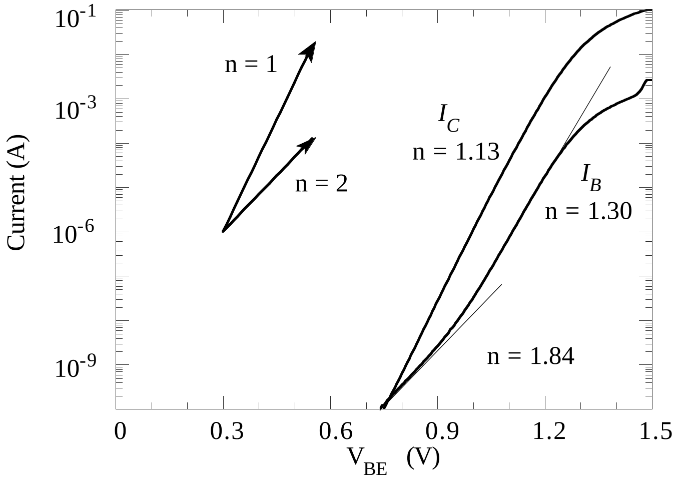

FIGURE 7.55 Measured Gummel plot of an abrupt AlGaAs/GaAs HBT. (After Liu, W., Experimental comparison of base recombination currents in abrupt and graded AlGaAs/GaAs heterojunction bipolar transistors, *Electronic Letters*, 27, 2115–2116, 1991, with permission.)

AlGaAs/"GaAs" HBTs in particular, the field can be established by grading of the aluminum concentration in the AlGaAs base layer.

The fourth recombination current is the space-charge recombination current in the base-emitter depletion region. $I_{B,\text{scr}}$ differs from the other base current components in its bias dependency. Equations (7.38) and (7.39) show that I_C and $I_{B,\text{back-inject}}$ are proportional to $\exp(qV_{BE}/nkT)$ with n, the *ideality factor*, being equal to 1. Equation (7.44) also shows that $I_{B,\text{bulk}}$ is directly proportional to I_C. Hence, $I_{B,\text{bulk}}$ has a unity ideality factor as well. Extensive measurement experiments and theoretical calculations indicate that $I_{B,\text{surf}}$ and hence, $I_{B,\text{cont}}$, have an ideality factor closer to 1 than 2.[3,17] The ideality factor of $I_{B,\text{scr}}$, in contrast, is nearly 2 because the electron and hole concentrations in the forward-biased base-emitter junction are both proportional to $\exp(qV_{BE}/2kT)$.[2] This means $I_{B,\text{scr}}$ is most significant when V_{BE} is small, at which operating region I_C is also small. A *Gummel plot*, I_B and I_C as a function of V_{BE} taken at $V_{BC} = 0$, illustrates dominance of $I_{B,\text{scr}}$ in low-current regions, as shown in Fig. 7.55. There are times when $I_{B,\text{scr}}$ dominates other base current components even at high I_C levels, particularly in graded HBTs.[3]

The previous four base current components are all recombination current. The fifth component is the back-injection current, $I_{B,\text{back-inject}}$. This component is made small in a heterojunction transistor, at least at room temperature. However, as temperature increases, the extra energy barrier provided to the hole carriers becomes less effective in impeding the back injection. When the HBT is biased with a high I_C and a certain amount of V_{BC}, the power dissipated in the device can heat up the device itself (called *self-heating*). As the HBTs junction temperature rises, $I_{B,\text{back-inject}}$ increases and the current gain decreases. This β's temperature dependency is to be contrasted with silicon BJTs current gain, which increases with temperature.[18]

Kirk Effects

Understanding the properties of the various base current components facilitates the description of the measured device characteristics, such as the β vs. I_C curve of Fig. 7.53. The previous analysis of the transistor currents implicitly assumes that the transistor operates in the normal bias condition, under which the transistor gain is seen to increase steadily with the collector current. However, I_C cannot increase indefinitely without adverse effects. Figure 7.53 reveals that, after a certain critical I_C is reached while V_{BC} is kept constant, the current gain plummets, rendering the device useless. For high-power applications, such as a power amplifier for wireless communications, HBTs are biased at a large current (with a current density on the order of 10^4 A/cm^2), not only because the output power is directly proportional to I_C, but also because the high frequency performance is superior at large I_C (but before the current gain falls). Therefore, it is imperative to understand the factor setting the maximum I_C level, below which the current gain is maintained at some finite values.

The Poisson equation relates charges to the spatial variations of the electric field (ε).[2] It is a fundamental equation, applicable to any region at any time in a semiconductor:

$$\frac{d\varepsilon}{dx} = \frac{q}{\epsilon_s}\left(p - n + N_d - N_a\right) \tag{7.46}$$

ϵ_s is the dielectric constant of the semiconductor; N_d and N_a are the donor and acceptor doping levels, respectively; and n and p are the mobile electron and hole carrier concentrations, respectively. We apply this equation to the base-collector junction of HBTs, which is typically a homojunction. Since the base doping greatly exceeds the collector doping, most of the depletion region of the base-collector junction is at the collector side. In the depleted collector region where it is doped n-type, N_d in Eq. (7.46) is the collector doping level, N_{coll}, and N_a is 0. The collector current flowing through the junction consists of electrons. If the field inside the depletion region was small, then these electrons would move at a speed equal to the product of the mobility and the electric field: $\mu_n \cdot \varepsilon$. It is a fundamental semiconductor property that, once the electric field exceeds a certain critical value ($\varepsilon_{\text{crit}} \sim 10^3$ V/cm for GaAs), the carrier travels at a constant velocity called the saturation velocity (v_{sat}). Because the electric field inside most of the depletion region exceeds 10^4 V/cm, practically all of these electrons travel at a constant speed of v_{sat}. The electron carrier concentration inside the collector can be related to the collector current density (J_C; equal to I_C/A_{emit}) as:

$$n(x) = \frac{J_C}{qv_{sat}} = \text{constant inside the base-collector junction} \tag{7.47}$$

Lastly, because there is no hole current, p in Eq. (7.46) is zero.

Equation (7.46), when applied to the base-collector junction of a HBT, is simplified to:

$$\frac{d\varepsilon}{dx} = \frac{q}{\epsilon_s}\left(-\frac{J_C}{qv_{sat}} + N_{\text{coll}}\right) \tag{7.48}$$

When J_C is small, the slope of the electric field is completely determined by the collector doping, N_{coll}. Because the doping is constant with position, solving Eq. (7.48) at negligible J_C gives rise to a field profile that varies linearly with position, as shown in Fig. 7.56a. As the current density increases, the mobile electron concentration constituting the current partially cancels the positive donor charge concentration N_{coll}. As the net charge concentration decreases, the slope of the field decreases, as shown in Fig. 7.56b. While the current density increases, the base-collector bias V_{BC} remains unchanged. Therefore, the enclosed area of the electric field profile, which is basically the junction voltage, is the same before and after the current increase. The simultaneous requirements of having a decreasing field slope and a constant enclosed area imply that the depletion region extends toward the subcollector layer and the maximum electric field decreases. The depletion thickness continues to increase until the collector is fully depleted, as shown in Fig. 7.56c. The depletion thickness does not extend beyond the collector layer because the subcollector is a heavily doped layer. Afterwards, further increase of current results in a quadrangle field profile, as shown in Fig. 7.56d, replacing the previous triangular profile. As the current density increases to a level such that $J_C = qN_{\text{coll}} \cdot v_{sat}$, the term inside the parentheses of Eq. (7.48) becomes zero. A field gradient of zero means that the field profile stays constant with the position inside the junction (slope = 0). This situation, depicted in Fig. 7.56e, marks the beginning the *field reversal*. When J_C increases further such that $J_C > qN_{\text{coll}} \cdot v_{sat}$, the mobile electrons brought about by the collector current more than

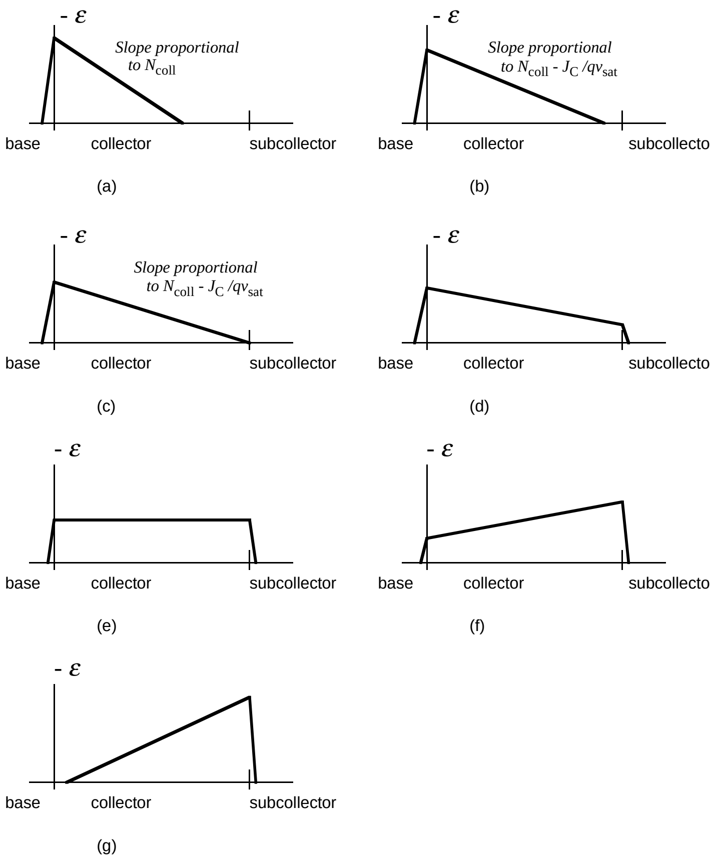

FIGURE 7.56 Electric field profile inside the base-collector junction of HBT during normal operation. (a) $J_C = 0$; (b) J_C is small; (c) J_C further increases so the entire collector is depleted; (d) further increase in J_C; (e) J_C reaches $qN_{\text{coll}} \cdot v_{sat}$; (f)$J_C > qN_{\text{coll}} \cdot v_{sat}$ and field reversal occurs; (g) further increase in J_C results in base push out as the electric field at the base-collector boundary decreases to zero.

compensates the fixed charges inside the collector. The net charge concentration for the first time becomes negative and the electric field takes on a negative slope (Fig. 7.56f), with a smaller magnitude at the base side of the junction than at the subcollector side. As the trend progresses, the magnitude of the field base-collector junction eventually diminishes to zero (Fig. 7.56g). When there is no more field to block the holes from "spilling" into the collector, the *base pushout* is said to occur and the current gain falls. The device characteristics as a result of the base pushout are referred to as *Kirk effects*.[19] The above description suggests that the threshold current due to Kirk effects increases if the collector doping increases. However, in many applications where the collector doping may not be increased arbitrarily (so the operating voltage is greater than a certain value), Kirk effects then become an important mechanism affecting the current gain falloff in HBTs. For an HBT with a collector doping of 3×10^{16} cm^{-3} (Fig. 7.50), the threshold current density is roughly $J_C = qN_{\text{coll}} \cdot v_{sat} = 3.9 \times 10^4$ A/cm^2 (v_{sat} is ~ 8×10^6 cm/s). Clearly, the value of such threshold current density depends on the magnitude of the saturation velocity. Since the saturation velocity decreases with the ambient temperature, the threshold density due to Kirk effects is lower at higher temperatures.

Kirk effects confine the operating collector current to some values. Similarly, the collector-to-emitter bias (V_{CE}) has its limit, set by two physical phenomena. The first one, well analyzed in elementary device physics, is the avalanche breakdown in the base-collector junction. The base-collector junction is a reverse-biased junction with a finite electric field. The mobile electrons comprised of J_C, while moving through the junction, quickly accelerate and pick up energy from the field. When V_{CE} is small, the magnitude of the field is not too large. The energy the carriers acquired is small and is quickly dissipated in the lattice as the carriers impact upon the lattice atoms. The distance within which a carrier travels between successive impacts with the lattice atoms is called a *mean free path*. As V_{CE} increases such that the electric field approaches $10^5 - 10^6$ V/cm, the energy gained by a carrier within one mean free path can exceed the energy gap of the collector material. As the highly energetic carrier impacts the lattice atoms, the atoms are ionized. The act of a carrier impacting the lattice and thereby creating electron-hole pairs is called *impact ionization*. One single impact ionization creates an electron-hole pair, which leads to further impact ionization as the recently generated carriers also pick up enough energy to ionize the lattice. The net result of this positive feedback mechanism is a rapid rise of I_C, which puts the transistor out of useful (or controllable) range of operation. The V_{CE} corresponding the rapid rise in I_C is called the *breakdown voltage*.

Collapse of Current Gain

The breakdown voltage represents the absolute maximum bias that can be applied to a bipolar transistor. There is, in addition, one more physical phenomenon that further restricts V_{CE} to values smaller than the breakdown voltage. This phenomenon occurs in multi-finger HBTs, having roots in the thermal-electrical interaction in the device. It is termed the *collapse of current gain* (or *gain collapse*) to emphasize the abrupt decrease of current gain observed in measured I-V characteristics when V_{CE} increases past certain values. Figure 7.57 is one such example, measured from a 2-finger HBT. The figure reveals two distinct operating regions, separated by a dotted curve. When V_{CE} is small, I_C decreases gradually with V_{CE}, exhibiting a negative differential resistance (NDR). We briefly describe the cause of NDR, as it relates to the understanding of the gain collapse. The band diagrams in Figs. 7.47 and 7.48 showed that the back-injected holes from the base into the emitter experience a larger energy barrier than the emitter electrons forward injected into the base. The ratio of the desirable I_C to the undesirable $I_{B,\text{back-inject}}$ is proportional to $\exp(\Delta E_g/kT)$ in a graded HBT, and $\exp(\Delta E_v/kT)$ in an abrupt HBT. At room temperature, this ratio is large in either HBT. However, as V_{CE} increases, the power dissipation in the HBT increases, gradually elevating the device temperature above the ambient temperature. $I_C/I_{B,\text{back-inject}}$, and hence the current gain, gradually decrease with increasing V_{CE}. Since Fig. 7.57 is measured I_C for several constant I_B, the decreasing β directly translates to the gradual decrease of I_C.

As V_{CE} crosses the dotted curve, NDR gives in to the collapse phenomenon, as marked by a dramatic lowering of I_C. The *collapse locus*, the dotted curve, is the collection of I_C as a function of V_{CE} at which the gain collapse occurs. When several identical transistors are connected together to common emitter, base, and collector electrodes, we tend to expect each transistor to conduct the same amount of collector current for any biases. Contrary to our intuition, equal conduction takes place only when the power dissipation is low to moderate, such that the junction temperature rise above the ambient temperature is small. At high V_{CE} and/or high I_C operation where the transistor is operated at elevated temperatures, one transistor spontaneously starts to conduct more current than the others (even if all the transistors are ideal and identical). Eventually, one transistor conducts all the current while the others become electrically inactive. This current imbalance originates from a universal bipolar transistor property that as the junction temperature increases, the bias required to turn on some arbitrary current level decreases. Quantitatively, this property is expressed by an empirical expression relating I_C, V_{BE}, and T:

$$I_C = I_{C,\text{sat}} \cdot \exp\left[\frac{q}{kT_0} \cdot \left(V_{BE,\text{junction}} - \phi \cdot \left(T - T_0\right)\right)\right] \tag{7.49}$$

where $I_{C,\text{sat}}$ is the collector saturation current; $V_{BE,\text{junction}}$ is the bias across the base-emitter junction; T_0 is the ambient temperature; and T is the actual device temperature. The degree of the turn-on voltage change in response to a junction temperature change is characterized by ϕ, which is called the *thermal-electrical feedback coefficient*. ϕ decreases logarithmically with I_C^3, and can be approximately as 1.1 mV/°C.

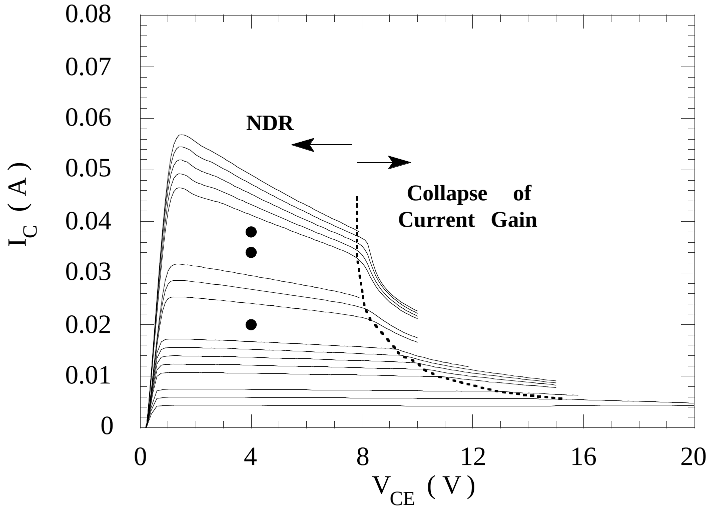

FIGURE 7.57 Measured I-V characteristics of a 2-finger AlGaAs/GaAs HBT showing two distinct regions of operation.

This means that when the junction temperature exceeds the ambient temperature by 1°C, turning on the same amount of I_C requires 1.1 mV less of $V_{BE,\text{junction}}$.

A multi-finger HBT can be viewed as consisting of several identical sub-HBTs, with their respective emitter, base, and collector leads connected together. If one finger (i.e., one sub-HBT) becomes slightly warmer than the others, its base-emitter junction turn-on voltage becomes slightly lower. Consequently, this particular finger conducts more current for a given fixed base-emitter voltage. The increased collector current, in turn, increases the power dissipation in the junction, raising the junction temperature even further. The gain collapse occurs when the junction temperature in one finger of the entire device becomes much hotter than the rest of the fingers, so that the feedback action of increased collector current with junction temperature quickly leads to the fact that just one particular finger conducts the entire device current. Since the transition from uniform current conduction to one finger domination occurs suddenly, the surge in junction temperature in the conducting finger quickly lowers the overall device current gain. The fundamental cause of both NDR and collapse is the current gain lowering at elevated temperatures. Their difference, however, lies in the degree of temperature increase as V_{CE} increases. In the NDR region, all fingers share relatively the same amount of current and the junction temperatures increase gradually with V_{CE}. In contrast, in the collapse region, as the device power is entirely dissipated in one finger and the junction temperature rises sharply, the current gain suddenly plummets.

The equation governing the collapse locus (per unit finger) is given by:[3,20]

$$I_{C,\text{collapse}} = \frac{kT_0}{q} \frac{1}{R_{th} \cdot \phi \cdot V_{CE} - R_E} \tag{7.50}$$

where R_{th} is the thermal resistance per finger and R_E is the emitter resistance per finger. When the individual finger current is below this critical current level (or when $I_{C,\text{collapse}}$ is negative), all fingers share the same amount of current. Above this critical current level, one finger conducts most of the current, whereas the rest of the fingers share the remaining current equally. Equation (7.50) shows that an effective method to increase $I_{C,\text{collapse}}$ is to increase R_E. The portion of the resistance that is intentionally introduced into device fabrication (such as by connecting a TaN thin-film resistor in series with the emitter electrode) is called the *ballasting resistance*. Alternatively, $I_{C,\text{collapse}}$ can be increased by reducing the thermal resistance, a goal often requiring more elaborate processes.[21]

Equation (7.50) neglects the contribution from the base resistance, R_B. For III-V HBTs, it is actually advantageous to use base ballasting; i.e., with the ballasting resistance placed in the base terminal.[22] The reason why the base ballasting approach is undesirable for Si BJT has been analyzed.[3]

The collapse of current gain occurring in III-V HBTs, closely relates to the thermal runaway in Si BJTs. HBTs suffering from gain collapse remain functional and can be biased out of the collapse region by reducing V_{CE}. Si BJTs suffering from thermal runaway, however, die instantly. The bias conditions triggering the thermal runaway in Si BJTs are identically given by the collapse locus equation [Eq. (7.50)]. The main cause of the difference between the collapse in HBTs and thermal runaway in Si BJTs is that the current gain increases with temperature in Si BJTs whereas it decreases with temperature in HBTs.[3]

High Frequency Performance

Current gain is the most important DC parameter characterizing a bipolar transistor. The high frequency properties are generally measured by two figures of merit: f_T, the cutoff frequency, and $f_{\max}$, the maximum oscillation frequency. The cutoff frequency is the frequency at which the magnitude of the AC current gain (small-signal collector current divided by small-signal base current) decreases to unity. As far as analytical expression is concerned, it is easier to work with the related emitter-collector transit time (τ_{ec}), which is inversely proportional to f_T:

$$f_T = \frac{1}{2\pi\,\tau_{ec}}. \tag{7.51}$$

The emitter-collector transit time can be broken up into several components. The emitter charging time, τ_e, is the time required to change the base potential by charging up the capacitances through the differential base-emitter junction resistance:

$$\tau_e = \frac{kT}{q\,I_C}\cdot\left(C_{j,\mathrm{BE}} + C_{j,\mathrm{BC}}\right). \tag{7.52}$$

$C_{j,\mathrm{BE}}$ and $C_{j,\mathrm{BC}}$ denote the junction capacitances of the base-emitter and the base-collector junctions, respectively. The inverse dependence of τ_e on I_C is the primary reason why BJTs and HBTs are biased at high current levels. When the current density is below 10^4 A/cm^2, this term often dominates the overall collector-emitter transit time.

The second component is the base transit time, the time required for the forward-injected charges to diffuse/drift through base. It is given by,

$$\tau_b = \frac{X_{\mathrm{base}}^2}{\nu\cdot D_{n,\mathrm{base}}} \tag{7.53}$$

The value of ν depends on the magnitude of the base quasi-electric field. In a uniform base without a base field, ν is 2, as suggested by Eq. (7.45). Depending on the amount of energy-gap grading, ν can easily increase to 6 to 10.[3]

The space-charge transit time, τ_{sc}, is the time required for the electrons to drift through the depletion region of the base-collector junction. It is given by,

$$\tau_{sc} = \frac{X_{dep}}{2\,v_{sat}} \tag{7.54}$$

where X_{dep} is the depletion thickness of the base-collector junction. The factor of 2 results from averaging the sinusoidal of carriers current over a time period.[3] It is assumed in the derivation that, because the electric field is large throughout the entire reverse-biased base-collector junction, the carriers travel at a constant saturation velocity, v_{sat}. With a p^- collector layer placed adjacent to the p^+ base of an otherwise conventional *Npn* HBT,[23] the electric field near the base can be made smaller than $\varepsilon_{\text{crit}}$. Consequently, the electrons travel at the velocity determined completely by the $\boldsymbol{\Gamma}$ valley. Without scattering to the *L* valley, the electrons continue to travel at a velocity that is much larger than v_{sat}, and τ_{sc} is significantly reduced. When carriers travel faster than v_{sat} under an off-equilibrium condition, *velocity overshoot* is said to occur.

The last term, the collector charging time, τ_c, is given by,

$$\tau_c = \left(R_E + R_C\right) \cdot C_{j,\text{BC}}, \tag{7.55}$$

where R_E and R_C are the device emitter and collector resistances, respectively. The value of this charging time depends greatly on the parasitic resistances. This is the term that degrades the HBT's high frequency performance when the contacts are poorly fabricated.

The overall transit time is a sum of the four time constants:

$$\tau_{ec} = \frac{kT}{q\,I_C} \cdot \left(C_{j,\text{BE}} + C_{j,\text{BC}}\right) + \frac{X_{\text{base}}^2}{\nu \cdot D_{n,\text{base}}} + \frac{X_{dep}}{2\,v_{sat}} + \left(R_E + R_C\right) \cdot C_{j,\text{BC}} \tag{7.56}$$

In most HBTs, R_E and R_C are dominated by the electrode resistances; the epitaxial resistances in the emitter and collector layers are insignificant. The cutoff frequency relates to τ_{ec} through Eq. (7.51).

The maximum oscillation frequency is the frequency at which the unilateral power gain is equal to 1. The derivation is quite involved,[3] but the final result is elegant:

$$f_{\max} = \sqrt{\frac{f_T}{8\pi\, R_B C_{j,\text{BC}}}}. \tag{7.57}$$

The base resistance has three components that are roughly equal in magnitude. They are base electrode resistance ($R_{B,\text{eltd}}$); intrinsic base resistance ($R_{B,\text{intrinsic}}$); and extrinsic base resistance ($R_{B,\text{extrinsic}}$). $R_{B,\text{eltd}}$ is intimately related to processing, depending on the contact metal and the alloying recipe used to form the contact. The other two base resistance components, in contrast, depend purely on the designed base layer and the geometrical details. The HBT cross-sections illustrated in Fig. 7.52 show two base contacts placed symmetrically beside the central emitter mesa. For this popular transistor geometry, the intrinsic base resistance is given by,

$$R_{B,\text{intrinsic}} = \frac{1}{12} \times R_{SH,\text{base}} \frac{W_E}{L_E} \tag{7.58}$$

where W_E and L_E are the emitter width and length, respectively; and $R_{SH,\text{base}}$ is the base sheet resistance in Ω/square. Where does the 1/12 factor come from? If all of the base current that goes into one of the base contacts in Fig. 7.52 leaves from the other contact, the intrinsic base resistance would follow our intuitive formula of simple resistance, equal to $R_{SH,\text{base}} \times W_E/L_E$. However, during the actual transistor operation, the base current enters through both contacts, but no current flows out at the other end. The holes constituting the base current gradually decrease in number as they are recombined at the extrinsic base surface, in the base bulk layer, and in the base-emitter space-charge region. Some base current carriers remain in the base layer for a longer portion of the width before getting recombined. Other carriers get recombined sooner. The factor 1/12 accounts for the distributed nature of the current conduction, as derived elsewhere.[3] Because of the way the current flows in the base layer, the intrinsic base resistance is called a *distributed resistance*. If instead there is only one base contact, the factor 1/12 is replaced by 1/3 (not 1/6!).[24] The distributed resistance also exists in the gate of MOS transistors,[25] or III-V field-effect transistors.[4]

The extrinsic base resistance is the resistance associated with the base epitaxial layer between the emitter and the base contacts. It is given by,

$$R_{B,\text{extrinsic}} = \frac{1}{2} \times R_{SH,\text{base}} \frac{S_{BE}}{L_E} \tag{7.59}$$

where S_{BE} is the separation between the base and emitter contacts. The factor 1/2 appears in the transistor shown in Fig. 7.52, which has two base contacts. The presence of $R_{B,\text{extrinsic}}$ is the reason why most transistors are fabricated with self-aligned base-emitter contacts, and that the base contacts are deposited right next to the emitter contacts, regardless of the finite alignment tolerance between the base and emitter contact photolithographical steps. (A detailed fabrication process will be described shortly.) With self-alignment, the distance S_{BE} is minimized, to around 3000 Å.

A detailed calculation of f_T and $f_{\max}$ has been performed for a $W_E \times L_E = 2 \times 30\ \mu\text{m}^2$ HBT,[4] with a S_{BE} of 0.2 μm, a base thickness of 800 Å, a base sheet resistance of 280 Ω/square, and a base diffusion coefficient of 25.5 cm^2/s. Although device parameters will have different values in other HBT structures and geometries, the exemplar calculation gives a good estimation of the relative magnitudes of various terms that determine a HBTs high frequency performance. We briefly list the key results here. The HBT has: $R_E = 0.45\ \Omega$; $R_{B,\text{eltd}} = 7\ \Omega$; $R_{B,\text{extrinsic}} = 0.94\ \Omega$; $R_{B,\text{intrinsic}} = 1.56\ \Omega$; $C_{j,\text{BE}} = 0.224$ pF; $C_{j,\text{BC}} = 0.026$ pF. It was further determined at the bias condition of $J_C = 10^4$ A/cm^2 and $V_{BC} = -4$ V, that the collector depletion thickness $X_{dep} = 0.59$ μm. Therefore,

$$\tau_e = \frac{kT}{q\,I_C} \cdot \left(C_{j,\text{BE}} + C_{j,\text{BC}}\right) = \frac{0.0258\left(2.24 \times 10^{-13} + 2.59 \times 10^{-14}\right)}{1 \times 10^4 \cdot 2 \times 10^{-4} \cdot 3 \times 10^{-4}} = 1.08 \text{ ps.}$$

$$\tau_b = \frac{X^2 base}{\nu \cdot D_{n,\text{base}}} = \frac{\left(800 \times 10^{-8}\right)^2}{2 \cdot 25.5} = 1.25 \text{ ps.}$$

$$\tau_{\text{sc}} = \frac{X_{dep}}{2\,v_{sat}} = \frac{0.591 \times 10^{-4}}{2 \cdot 8 \times 10^6} = 3.69 \text{ ps.}$$

$$\tau_c = \left(R_E + R_C\right) C_{j,\text{BC}} = \left(0.453 + 4.32\right) \cdot 2.59 \times 10^{-14} = 0.124 \text{ ps.}$$

Summing up these four components, we find the emitter-collector transit time to be 6.14 ps. The cutoff frequency is therefore 1/(2π·6.14 ps) = 26 GHz. As mentioned, although this calculation is specific to a particular power HBT design, the relative magnitudes of the four time constants are quite representative. Generally, the space-charge transit time is the major component of the overall transit time. This is unlike silicon BJTs, whose τ_b and τ_e usually dominate, because of the low base diffusion coefficient in the silicon material and the high base-emitter junction capacitance associated with high emitter doping. HBT design places a great emphasis on the collector design, while the Si BJT design concentrates on the base and emitter layers.

The total base resistance is $R_B = 7 + 0.96 + 1.95 = 9.91\ \Omega$. The maximum oscillation frequency, calculated with Eq. (7.57), is 65 GHz.

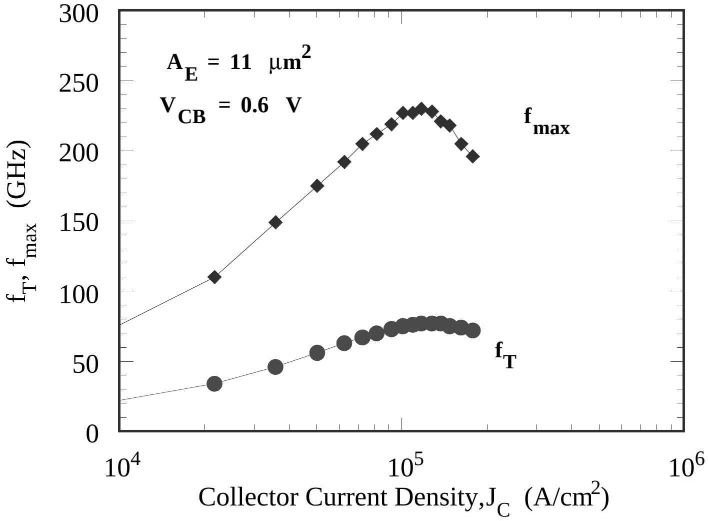

FIGURE 7.58 High-frequency performance of a state-of-the-art InAlAs/InGaAs HBT. (After Chau, H. and Kao, Y., High f_{max} InAlAs/InGaAs heterojunction bipolar transistors, IEEE IEDM, 783–786, 1993, with permission.)

Figure 7.58 illustrates the cutoff and maximum oscillation frequencies of a state-of-art InAlAs/InGaAs HBT. The frequency responses are plotted as a function of the collector current to facilitate the circuit design at the proper bias condition. When the current is small, the cutoff frequency is small because the emitter charging time is large. As the current increases, f_T increases because the emitter charging time decreases. When the current density exceeds roughly 10^5 A/cm^2, Kirk effects take place and the transistor performance degrades rapidly. $f_{\max}$'s current dependence follows f_T's, as governed by the relationship of Eq. (7.57).

The high frequency transistor of the calculated example has a narrow width of 2 μm. What happens if W_E increases to a large value, such as 200 μm? A direct application of Eq. (7.56) would still lead to a cutoff frequency in the GHz range. In practice, such a 200 μm wide device will have a cutoff frequency much smaller than 1 GHz. The reason for the discrepancy is simple; the time constants appearing in Eq. (7.56), which all roughly scale with the emitter area, are based on the assumption that the current conduction is uniform within the entire emitter mesa. In HBTs, and more so in Si BJTs, the base resistance is significant. As the base current flows horizontally from the base contacts to the center of the emitter region, some finite voltage is developed, with a increasingly larger magnitude toward the center of the mesa. The effective base-emitter junction voltage is larger at the edge than at the center. Since the amount of carrier injection depends exponentially on the junction voltage at the given position, most of the injection takes place near the emitter edges, hence the term *emitter crowding*. Sometimes this phenomenon of nonuniform current conduction is referred to as the *base crowding*. Both terms are acceptable, depending on whether the focus is on the crowding of the emitter current or the base current. A figure of merit quantifying the severity of emitter crowding is the effective emitter width (W_{eff}). It is defined as the emitter width that would result in the same current level if current crowding were absent and the emitter current density were uniform at its edge value. Figure 7.59 illustrates the effective emitter width (normalized by the defined emitter width) as a function of base doping and collector current.

Because of the emitter crowding, all high-frequency III-V HBTs capable of GHz performance have a narrow emitter width on the order of 2 μm. For wireless applications in the 2 GHz range, 2 to 3 μm W_E is often used,[26] but a 6.4 μm W_E has also been reported.[27] The choice of the emitter width is a trade-off between the ease (cost) of device fabrication versus the transistor performance. We intuitively expected

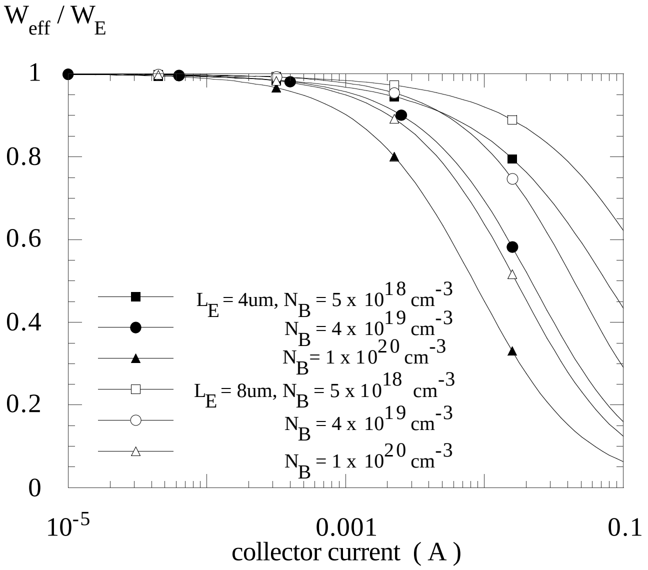

FIGURE 7.59 Calculated W_{eff}/W_E ratio. (After Liu, W. and Harris, J., Dependence of base crowding effect on base doping and thickness for Npn AlGaAs/GaAs heterojunction bipolar transistors, *Electronic Letters*, 27, 2048–2050, 1991, with permission.)

the W_{eff}/W_E ratio to increase as the doping increased (since the base resistance decreased). However, an increase in base doping was accompanied by shortened minority lifetime. The large increase in $I_{B,\text{bulk}}$ causes the emitter crowding to be more pronounced as N_{base} increases, as shown in Fig. 7.59. Due to differences in material properties, the emitter width in Si BJT or SiGe HBTs tends to be on the order of 0.5 µm.

Device Fabrication

An HBT mask layout suitable for high-frequency applications is shown in Fig. 7.60, and a corresponding fabrication process is delineated in Fig. 7.61. The following discussion of processing steps assumes the AlGaAs/GaAs HBT epitaxial structure shown in Fig. 7.50. The first step is to deposit ~7000 Å of silicon dioxide, onto which the first-mask pattern "ISOL" is defined, and 1.5 µm of aluminum, evaporated and lifted off. The aluminum protects the silicon dioxide underneath during the subsequent reactive ion etch (RIE), resulting in the profile shown in Fig. 7.61a. Oxygen atoms or protons are then implanted everywhere on the wafer. This implantation is designed to make the region outside of "ISOL" pattern electrically inactive. A shallow etching is applied right after the implantation so that a trail mark of the active device area is preserved. This facilitates the alignment of future mask levels to the first mask. Afterward, both aluminum and oxide are removed with wet etching solutions, reexposing the fresh InGaAs top surface onto which a refractory metal (such as W) is sputtered. The "EMIT" mask level is used to define the emitter mesas, and Ti/Al, a conventional contact metal used in III-V technologies, is evaporated and lifted off. If a refractory metal is not inserted between the InGaAs semiconductor and the Ti/Al metal, long-term reliability problems can arise as titanium reacts with indium. During the ensuing RIE, the refractory metal not protected by the emitter metal is removed.

The resulting transistor profile is shown in Fig. 7.61b. Wet or dry etching techniques are applied to remove the exposed GaAs cap and the AlGaAs active emitter layer, and eventually reach the top of the base layer. Silicon nitride is deposited by plasma enhanced chemical vapor deposition (PECVD). This deposition is conformal, forming a nitride layer everywhere, including the vertical edges. Immediately

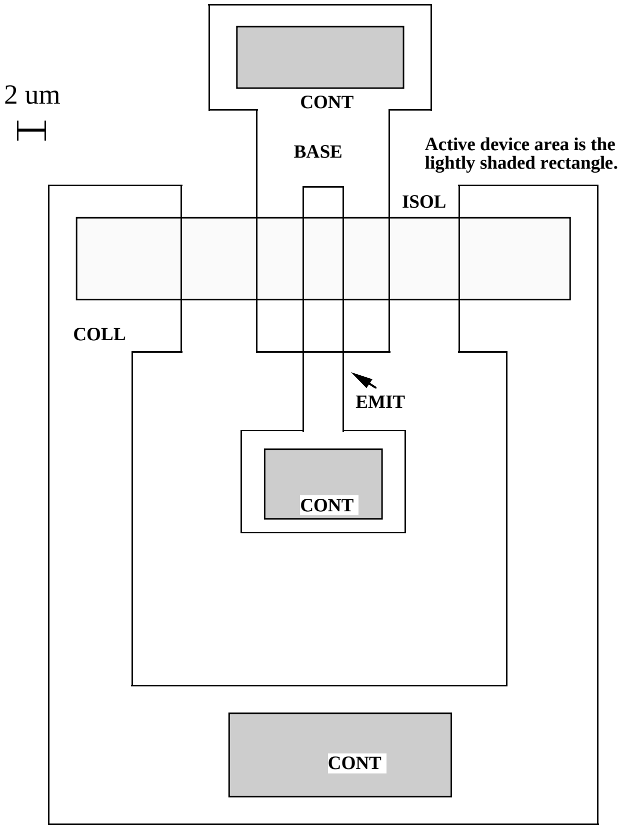

FIGURE 7.60 A HBT mask layout suitable for high-frequency applications. (After Liu, W., Microwave and DC Characterizations of Npn and Pnp HBTs, PhD. Dissertation, Stanford University, Stanford, CA, 1991.)

after the nitride deposition, the whole wafer is etched by RIE. Because a vertical electric field is set up in the RIE chamber to propel the chemical species in the vertical direction, the sidewall nitride covering the sides of the emitter mesas remains untouched while the nitride layer lying on a flat surface is etched away (Fig. 7.61c). The nitride sidewall improves the device yield by cutting down the possible electrical short between the emitter contact and the soon-to-be-deposited base contacts.

The step after the nitride sidewall formation is the "BASE" lithography. As shown in the layout of Fig. 7.60, there is no separation between the "BASE" and the "EMIT" levels. The base metal during the evaporation partly lands on the emitter mesa, and some of it lands on the base layer as desired (Fig. 7.61d). The process has the desired feature that, even if the "BASE" level is somewhat misaligned with the "EMIT" level, the distance S_{BE} between the emitter and base contacts is unchanged, and is at the minimum value determined by the thickness of the nitride sidewall. In this manner, the base contact is said to be *self-aligned* to the emitter. Self-alignment reduces $R_{B,\text{extrinsic}}$ [Eq. 7.59)] and $C_{j,\text{BC}}$, hence improving the high-frequency performance. Typically, Ti/Pt/Au is the choice for the base metal.

Following the base metal formation, the collector is defined and contact metal of Au/Ge/Ni/Au is deposited (Fig. 7.61e). After the contact is alloyed at ~450°C for ~1 minute, a polyimide layer is spun to planarize the device as shown in Fig. 7.61f. The contact holes are then defined and Ti/Au is evaporated to contact various electrodes. The final device cross-section after the entire process is shown in Fig. 7.61g.

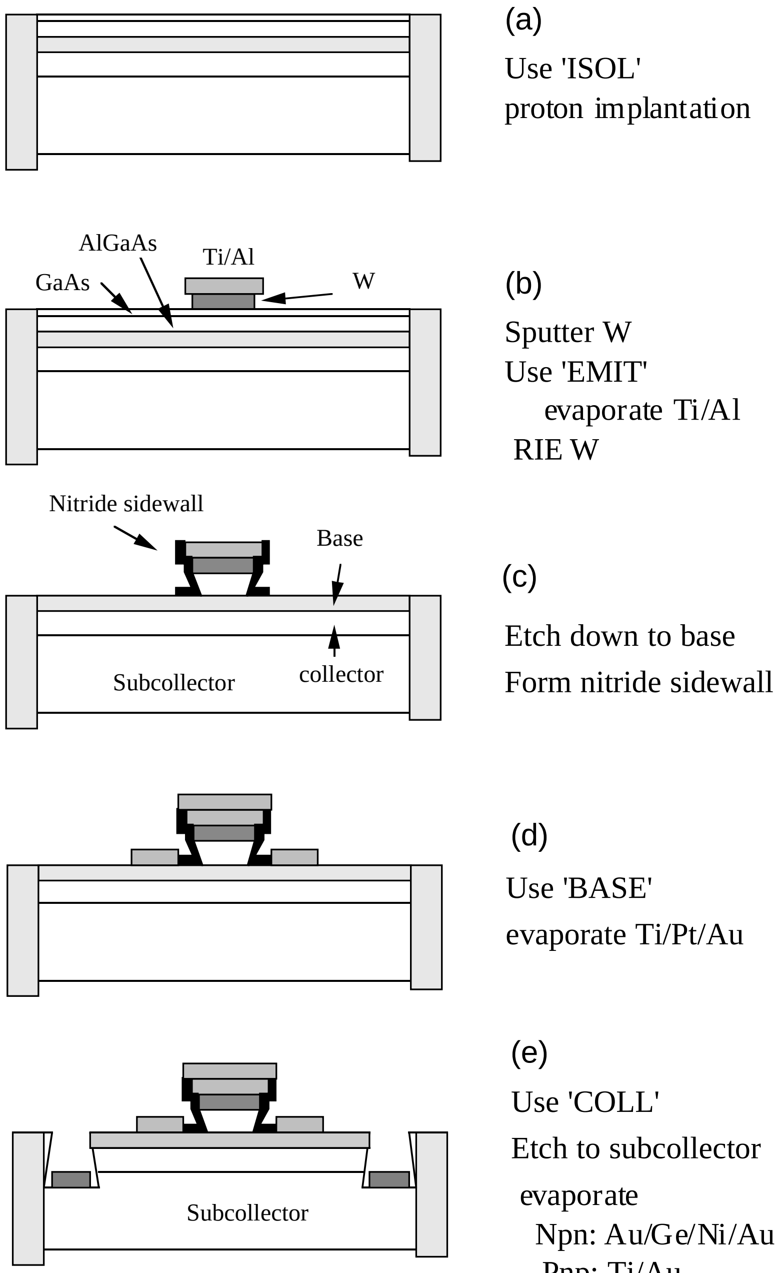

(a)
Use 'ISOL'
proton implantation

(b)
Sputter W
Use 'EMIT'
evaporate Ti/Al
RIE W

(c)
Etch down to base
Form nitride sidewall

(d)
Use 'BASE'
evaporate Ti/Pt/Au

(e)
Use 'COLL'
Etch to subcollector
evaporate
Npn: Au/Ge/Ni/Au
Pnp: Ti/Au

FIGURE 7.61 A high-frequency HBT process flow. (After Liu, W., Microwave and DC Characterizations of Npn and Pnp HBTs, PhD. Dissertation, Stanford University, Stanford, CA, 1991.)

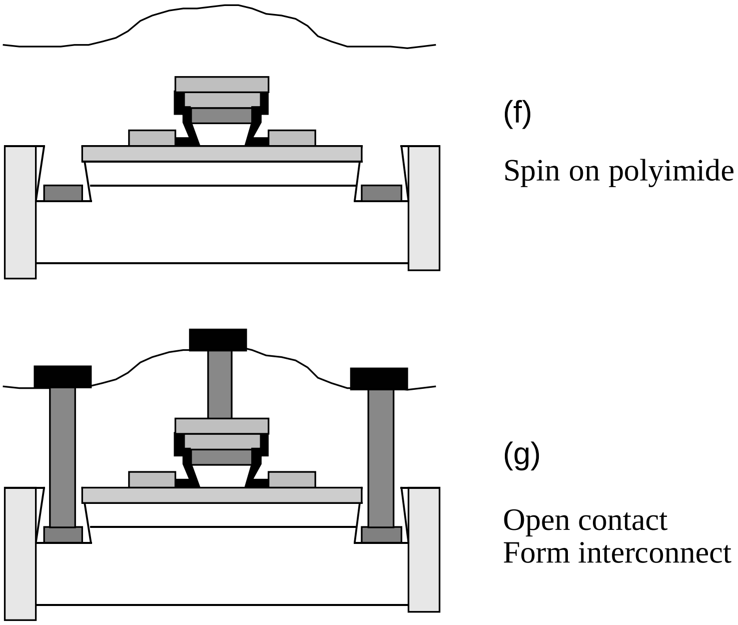

FIGURE 7.61 (continued)

References

1. Kroemer, H, Heterostructure bipolar transistors and integrated circuits, *Proc. IEEE*, 70, 13, 1982.
2. Sah, C.T., *Fundamentals of Solid-State Electronics*, World Scientific, Singapore, 1991.
3. Liu, W., *Handbook of III-V Heterojunction Bipolar Transistors*, Wiley & Sons, New York, 1998. An in-depth discussion of several topics can be found in this handbook.
4. Liu, W., *Fundamentals of III-V Devices: HBTs, MESFETs, and HFETs/HEMTs*, Wiley & Sons, New York, 1999.
5. Kroemer, H., Theory of wide gap emitter for transistors, *Proc. IRE*, 45, 1535, 1957.
6. For pioneering HBT papers, see for example, Asbeck, P., Chang, M., Higgins, J., Sheng, N., Sullivan, G., and Wang, K., GaAlAs/GaAs heterojunction bipolar transistors: issues and prospects for application, *IEEE Trans. Electron Devices*, 36, 2032–2041, 1989. For introduction to MBE and MOCVD growth techniques, see References 3 and 4.
7. Henderson, T., Physics of degradation in GaAs-based heterojunction bipolar transistors, *Microelectronics Reliability*, 39, 1033–1042, 1999. See also, Low, T., et al., Migration from an AlGaAs to an InGaP emitter HBT IC process for improved reliability, *IEEE GaAs IC Symposium*, 153–156, 1998.
8. Liu, W. et al., Recent developments in GaInP/GaAs heterojunction bipolar transistors, in *Current Trends in Heterojunction Bipolar Transistors*, Chang, M.F., Ed., World Scientific, Singapore, 1996.
9. Chau, H. and Liu, W., Heterojunction bipolar transistors and circuit applications, in *InP-Based Material and Devices: Physics and Technology*, Wada, O. and Hasegawa, H., Eds., Wiley & Sons, New York, 1999.
10. Ali, F., Gupta, A. and Higgins, A., Advances in GaAs HBT power amplifiers for cellular phones and military applications, *IEEE Microwave and Millimeter-Wave Monolithic Circuits Symposium*, 61–66, 1996.
11. Lin, H. and Lee, S., Super-gain AlGaAs/GaAs heterojunction bipolar transistor using an emitter edge-thinning design, *Appl. Phys. Lett.*, 47, 839–841, 1985.

12. Lee, W., Ueda, D., Ma, T., Pao, Y. and Harris, J., Effect of emitter-base spacing on the current gain of AlGaAs/GaAs heterojunction bipolar transistors, *IEEE Electron Device Lett.*, 10, 200–202, 1989.
13. Patton, G., 75-GHz fr SiGe-base heterojunction bipolar transitors, *IEEE Electron Devices Lett.*, 11, 171–173, 1990.
14. Meyerson, B. et al., Silicon:Germanium heterojunction bipolar transistors; from experiment to technology, in *Current Trends in Heterojunction Bipolar Transistors*, Chang, M., Ed., World Scientific, Singapore, 1996.
15. Pritchard, R., *Electrical Characteristics of Transistors*, McGraw-Hill, New York, 1967.
16. Konig, U., SiGe & GaAs as competitive technologies for RF applications, *IEEE Bipolar Circuit Technology Meeting*, 87–92, 1998.
17. Tiwari, S., Frank, D. and Wright, S., Surface recombination current in GaAlAs/GaAs heterostructure bipolar transistors, *J. Appl. Phys.*, 64, 5009–5012, 1988.
18. Buhanan, D., Investigation of current-gain temperature dependence in silicon transistors, *IEEE Trans. Electron Devices*, 16, 117–124, 1969.
19. Kirk, C., A theory of transistor cutoff frequency falloff at high current densities, *IRE Trans. Electron Devices*, 9, 164–174, 1962.
20. Winkler, R., Thermal properties of high-power transistors, *IEEE Trans. Electron Devices*, 14, 1305–1306, 1958.
21. Hill, D., Katibzadeh, A., Liu, W., Kim, T. and Ikalainen, P., Novel HBT with reduced thermal impedance, *IEEE Microwave and Guided Wave Lett.*, 5, 373–375, 1995.
22. Khatibzadeh, A. and Liu, W., *Base Ballasting*, U.S. Patent Number 5,321,279, issued on June 14, 1994.
23. Maziar, C., Klausmeier-Brown, M. and Lundstrom, M., Proposed structure for collector transit time reduction in AlGaAs/GaAs bipolar transistors, *IEEE Electron Device Lett.*, 7, 483–385, 1986.
24. Hauser, J., The effects of distributed base potential on emitter-current injection density and effective base resistance for stripe transistor geometries, *IEEE Trans. Electron Devices*, 11, 238–242, 1964.
25. Liu, W., *MOSFET Models for SPICE Simulation, Including BSIM3v3 and BSIM4*, Wiley & Sons, New York, in press.
26. RF Microdevices Inc., A high efficiency HBT analog cellular power amplifier, *Microwave Journal*, 168–172, January 1996.
27. Yoshimasu, T., Tanba, N. and Hara, S., High-efficiency HBT MMIC linear power amplifier for L-band personal communication systems, *IEEE Microwave and Guided Wave Lett.*, 4, 65–67, 1994.

7.2.3 Metal-Oxide-Semiconductor Field-Effect Transistors (MOSFETs)

Leonard MacEachern and Tajinder Manku

The insulated-gate field-effect transistor was conceived in the 1930s by Lilienfeld and Heil. An insulated-gate transistor is distinguished by the presence of an insulator between the main control terminal and the remainder of the device. Ideally, the transistor draws no current through its gate (in practice a small leakage current on the order of 10^{-18} A to 10^{-16} A exists). This is in sharp contrast to bipolar junction transistors that require a significant base current to operate. Unfortunately, the **M**etal-**O**xide-**S**emiconductor **F**ield-**E**ffect **T**ransistor (**MOSFET**) had to wait nearly 30 years until the 1960s when manufacturing advances made the device a practical reality. Since then, the explosive growth of MOSFET utilization in every aspect of electronics has been phenomenal. The use of MOSFETs in electronics became ever more prevalent when "complementary" types of MOSFET devices were combined by Wanlass in the early 1960s to produce logic that required virtually no power except when changing state. MOSFET processes that offer complementary types of transistors are known as **C**omplementary **M**etal **O**xide **S**emiconductor (**CMOS**) processes, and are the foundation of the modern commodity electronics industry. The MOSFET's primary advantages over other types of integrated devices are its mature fabrication technology, its high integration levels, its mixed analog/digital compatibility, its capability for low voltage operation,

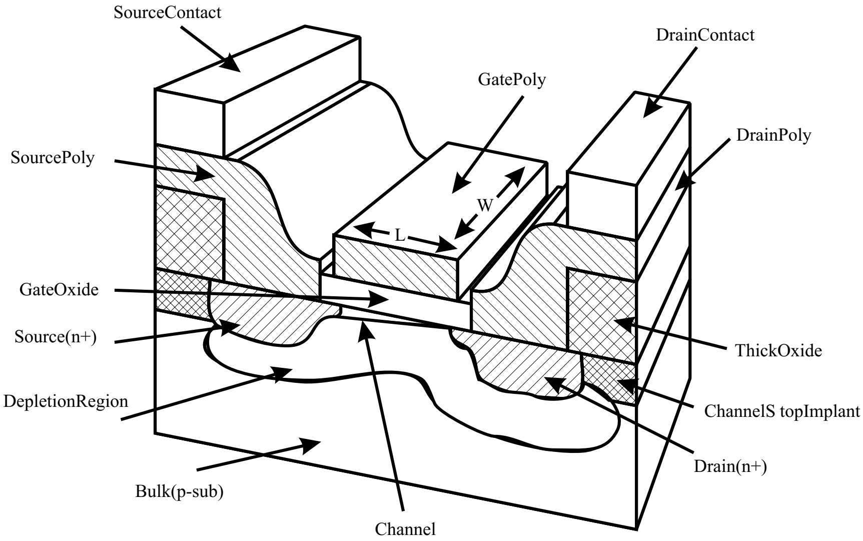

FIGURE 7.62 MOSFET physical structure.

its successful scaling characteristics, and the combination of complementary MOSFETs yielding low power CMOS circuits.

In this section, basic material concerning the MOSFET physical structure and operation is first presented. Nonideal effects are briefly discussed, as are important parasitics and distributed effects found in MOSFETs. Once the important parasitics and distributed effects are understood, the operation of MOSFETs at radio frequencies is examined, and important MOSFET operating parameters are given. Following this, MOSFET noise sources relevant to radio frequency designs are discussed. This section concludes with a discussion of MOSFET design and physical layout appropriate for radio frequency implementations.

MOSFET Fundamentals

Today, each of the tens of millions of MOSFETs that can occupy mere square centimetres of silicon area shares the same basic physical structure. The physical structure of the MOSFET is deceptively simple, as illustrated by the MOSFET cross-section appearing in Fig. 7.62. Visible in the figure are the various materials used to construct a MOSFET. These materials appear in layers when the MOSFET cross-section is viewed; this is a direct consequence of the processes of "doping," deposition, growth, and etching which are fundamental in conventional processing facilities.

The fabrication process of silicon MOSFET devices has evolved over the last 30 years into a reliable integrated circuit manufacturing technology. Silicon has emerged as the material of choice for MOSFETs, largely because of its stable oxide, SiO_2, which is used as a general insulator, as a surface passivation layer, and as an excellent gate dielectric.

Full appreciation of the MOSFET structure and operation requires some knowledge of silicon semiconductor properties and "doping." These topics are briefly reviewed next.

On the scale of conductivity that exists between pure insulators and perfect conductors, semiconductors fall between the extremes. The semiconductor material commonly used to make MOSFETs is silicon. Pure, or "intrinsic" silicon exists as an orderly three-dimensional array of atoms, arranged in a crystal lattice. The atoms of the lattice are bound together by covalent bonds containing silicon valence electrons. At absolute-zero temperature, all valence electrons are locked into these covalent bonds and are unavailable for current conduction, but as the temperature is increased, it is possible for an electron to gain enough thermal energy to escape its covalent bond, and in the process leave behind a covalent bond with a missing electron, or "hole." When that happens the electron that escaped is free to move about the crystal lattice. At the same time, another electron, which is still trapped in nearby covalent bonds because of its lower energy state, can move into the hole left by the escaping electron. The mechanism of current conduction in intrinsic silicon is therefore by hole-electron pair generation, and the subsequent motion of free electrons and holes throughout the lattice.

At normal temperatures intrinsic silicon behaves as an insulator because the number of free electron-hole pairs available for conducting current is very low, only about 14.5 hole-electron pairs per 1000 μm^3 of silicon. The conductivity of silicon can be adjusted by adding foreign atoms to the silicon crystal. This process is called "doping," and a "doped" semiconductor is referred to as an "extrinsic" semiconductor. Depending on what type of material is added to the pure silicon, the resulting crystal structure can either have more electrons than the normal number needed for perfect bonding within the silicon structure, or less electrons than needed for perfect bonding. When the dopant material increases the number of free electrons in the silicon crystal, the dopant is called a "donor." The donor materials commonly used to dope silicon are phosphorus, arsenic, and antimony. In a donor-doped semiconductor the number of free electrons is much larger than the number of holes, and so the free electrons are called the "majority carriers" and the holes are called the "minority carriers." Since electrons carry a negative charge and they are the majority carriers in a donor-doped silicon semiconductor; any semiconductor that is predominantly doped with donor impurities is known as "n-type." Semiconductors with extremely high donor doping concentrations are often denoted "n+ type."

Dopant atoms that accept electrons from the silicon lattice are also used to alter the electrical characteristics of silicon semiconductors. These types of dopants are known as "acceptors." The introduction of the acceptor impurity atoms creates the situation in which the dopant atoms have one less valence electron than necessary for complete bonding with neighboring silicon atoms. The number of holes in the lattice therefore increases. The holes are therefore the majority carriers and the electrons are the minority carriers. Semiconductors doped with acceptor impurities are known as "p-type," since the majority carriers effectively carry a positive charge. Semiconductors with extremely high acceptor doping concentrations are called "p+ type." Typical acceptor materials used to dope silicon are boron, gallium, and indium.

A general point that can be made concerning doping of semiconductor materials is that the greater the dopant concentration, the greater the conductivity of the doped semiconductor. A second general point that can be made about semiconductor doping is that n-type material exhibits a greater conductivity than p-type material of the same doping level. The reason for this is that electron mobility within the crystal lattice is greater than hole mobility, for the same doping concentration.

MOSFET Physical Structure and Operation

A cross-section through a typical n-type MOSFET, or "NFET," is shown in Fig. 7.63(a). The MOSFET consists of two highly conductive regions (the "source" and the "drain") separated by a semiconducting channel. The channel is typically rectangular, with an associated length (L) and width (W). The ratio of the channel width to the channel length, W/L, is an important determining factor for MOSFET performance.

As shown in Fig. 7.63(a), the MOSFET is considered a four-terminal device. These terminals are known as the gate (G), the bulk (B), the drain (D), and the source (S), and the voltages present at these terminals collectively control the current that flows within the device. For most circuit designs, the current flow from drain to source is the desired controlled quantity.

The operation of field-effect transistors (FETs) is based upon the principal of capacitively controlled conductivity in a channel. The MOSFET gate terminal sits on top of the channel, and is separated from the channel by an insulating layer of SiO_2. The controlling capacitance in a MOSFET device is therefore due to the insulating oxide layer between the gate and the semiconductor surface of the channel. The conductivity of the channel region is controlled by the voltage applied across the gate oxide and channel region to the bulk material under the channel. The resulting electric field causes the redistribution of holes and electrons within the channel. For example, when a positive voltage is applied to the gate, it is possible that enough electrons are attracted to the region under the gate oxide, that this region experiences a local inversion of the majority carrier type. Although the bulk material is p-type (the majority carriers

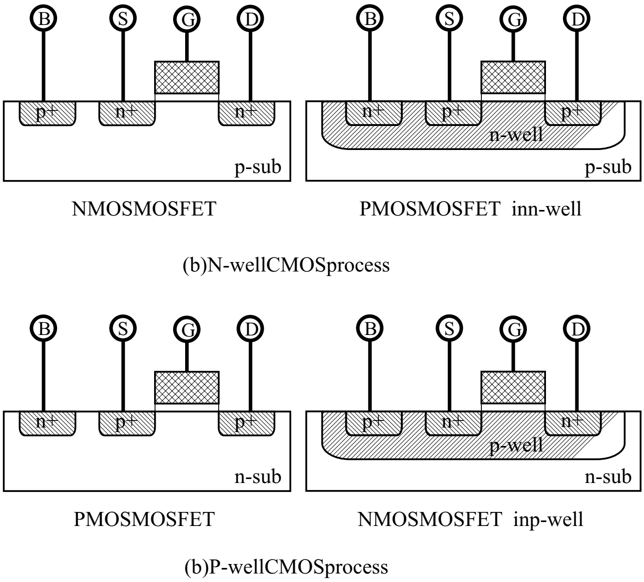

(b)N-wellCMOSprocess

(b)P-wellCMOSprocess

FIGURE 7.63 MOSFET terminals and active regions. (a) MOSFETs constructed on p-type substrate, (b) MOSFETs constructed on n-type substrate.

are holes and minority carriers are electrons), if enough electrons are attracted to the same region within the semiconductor material, the region becomes effectively n-type. Then the electrons are the majority carriers and the holes are the minority carriers. Under this condition electrons can flow from the n+ type drain to the n+ type source if a sufficient potential difference exists between the drain and source.

When the gate-to-source voltage exceeds a certain threshold, called V_T, the conductivity of the channel increases to the point where current may easily flow between the drain and the source. The value of V_T required for this to happen is determined largely by the dopant concentrations in the channel, but it also depends in part upon the voltage present on the bulk. This dependence of the threshold voltage upon the bulk voltage is known as the "body effect" and is discussed further in another section.

In MOSFETs, both holes and electrons can be used for conduction. As shown in Fig. 7.63, both n-type and p-type MOSFETs are possible. If, for an n-type MOSFET, all the n-type regions are replaced with p-type regions and all the p-type regions are replaced with n-type regions, the result is a p-type MOSFET. Since both the n-type and p-type MOSFETs require substrate material of the opposite type of doping, two distinct CMOS technologies exist, defined by whether the bulk is n-type or p-type. If the bulk material is p-type substrate, then n-type MOSFETs can be built directly on the substrate while p-type MOSFETs must be placed in an n-well. This type of process is illustrated in Fig. 7.63(a). Another possibility is that the bulk is composed of n-type substrate material, and in this case the p-type MOSFETs can be constructed directly on the bulk, while the n-type MOSFETs must be placed in an p-well, as in Fig. 7.63(b). A third type of process known as twin-well or twin-tub CMOS requires that both the p-type and n-type MOSFETs be placed in wells of the opposite type of doping. Other combinations of substrate doping and well types are in common use. For example, some processes offer a "deep-well" capability, which is useful for threshold adjustments and circuitry isolation.

Modern MOSFETs differ in an important respect from their counterparts developed in the 1960s. While the gate material used in the field effect transistors produced thirty years ago was made of metal, the use of this material was problematic for several reasons. At that time, the gate material was typically aluminium and was normally deposited by evaporating an aluminium wire by placing it in contact with a heated tungsten filament. Unfortunately, this method led to sodium ion contamination in the gate oxide, which caused the MOSFET's threshold voltage to be both high and unstable. A second problem with the earlier methods of gate deposition was that the gate was not necessarily correctly aligned with the source and drain regions. Matching between transistors was then problematic because of variability in the gate location with respect to source and drain for the various devices. Parasitics also varied greatly between devices because of this variability in gate location with respect to the source and drain regions. In the worst case, a nonfunctional device was produced because of the errors associated with the gate placement.

Devices manufactured today employ a different gate material, namely "polysilicon," and the processing stages used to produce a field-effect transistor with a poly gate are different than the processing stages required to produce a field-effect transistor with a metal gate. In particular, the drain and source wells are patterned using the gate and field oxide as a mask during the doping stage. Since the drain and source regions are defined in terms of the gate region, the source and drain are automatically aligned with the gate. CMOS manufacturing processes are referred to as self-aligning processes when this technique is used. Certain parasitics, such as the overlap parasitics considered later in this chapter, are minimized using this method. The use of a polysilicon gate tends to simplify the manufacturing process, reduces the variability in the threshold voltage, and has the additional benefit of automatically aligning the gate material with the edges of the source and drain regions.

The use of polysilicon for the gate material has one important drawback: the sheet resistance of polysilicon is much larger than that of aluminium and so the resistance of the gate is larger when polysilicon is used as the gate material. High-speed digital processes require fast switching time from the MOSFETs used in the digital circuitry, yet a large gate resistance hampers the switching speed of a MOSFET. One method commonly used to lower the gate resistance is to add a layer of silicide on top of the gate material. A silicide is a compound formed using silicon and a refractory metal, for example $TiSi_2$. Later in this chapter the importance of the gate resistance upon the radio frequency performance of the MOSFET is examined. In general, the use of silicided gates is required for reasonable radio frequency MOSFET performance.

Although the metal-oxide-semiconductor sandwich is no longer regularly used at the gate, the devices are still called MOSFETs. The term **I**nsulated-**G**ate **F**ield-**E**ffect **T**ransistor (**IGFET**) is also in common usage.

MOSFET Large Signal Current-Voltage Characteristics

When a bias voltage in excess of the threshold voltage is applied to the gate material, a sufficient number of charge carriers are concentrated under the gate oxide such that conduction between the source and drain is possible. Recall that the majority carrier component of the channel current is composed of charge carriers of the type opposite that of the substrate. If the substrate is p-type silicon then the majority carriers are electrons. For n-type silicon substrates, holes are the majority carriers.

The threshold voltage of a MOSFET depends on several transistor properties such as the gate material, the oxide thickness, and the silicon doping levels. The threshold voltage is also dependent upon any fixed charge present between the gate material and the gate oxides. MOSFETs used in most commodity products are normally the "enhancement mode" type. Enhancement mode n-type MOSFETs have a positive threshold voltage and do not conduct appreciable charge between the source and the drain unless the threshold voltage is exceeded. In contrast, "depletion mode" MOSFETs exhibit a negative threshold voltage and are normally conductive. Similarly, there exists enhancement mode and depletion mode p-type MOSFETs. For p-type MOSFETs the sign of the threshold voltage is reversed.

Equations that describe how MOSFET threshold voltage is affected by substrate doping, source and substrate biasing, oxide thickness, gate material, and surface charge density have been derived in the literature.[1–4] Of particular importance is the increase in the threshold voltage associated with a nonzero source-to-bulk voltage. This is known as the "body effect" and is quantified by the equation,

$$V_T = V_{T0} + \gamma\left(\sqrt{\left|2\phi_F\right| + V_{SB}} - \sqrt{\left|2\phi_F\right|}\right) \tag{7.60}$$

where V_{T0} is the zero-bias threshold voltage, γ is the body effect coefficient or body factor, ϕ_F is the bulk surface potential, and V_{SB} is the bulk-to-source voltage. Details on the calculation of each of the terms in Eq. (7.60) is discussed extensively in the literature.[5]

Operating Regions

MOSFETs exhibit fairly distinct regions of operation depending upon their biasing conditions. In the simplest treatments of MOSFETs, the three operating regions considered are subthreshold, triode, and saturation.

Subthreshold — When the applied gate-to-source voltage is below the device's threshold voltage, the MOSFET is said to be operating in the subthreshold region. For gate voltages below the threshold voltage, the current decreases exponentially toward zero according to the equation

$$i_{DS} = I_{DS0}\frac{W}{L}\exp\left(\frac{v_{GS}}{nkT/q}\right) \tag{7.61}$$

where n is given by

$$n = 1 + \frac{\gamma}{2\sqrt{\phi_j - v_{BS}}} \tag{7.62}$$

in which γ is the body factor, ϕ_j is the channel junction built-in voltage, and v_{BS} is the source-to-bulk voltage.

For radio frequency applications, the MOSFET is normally operated in its saturation region. The reasons for this will become clear later in this section. It should be noted, however, that some researchers feel that it may be advantageous to operate deep-submicron radio frequency MOSFETs in the moderate inversion (subthreshold) region.[6]

Triode — A MOSFET operates in its triode, also called "linear" region, when bias conditions cause the induced channel to extend from the source to the drain. When $V_{GS} > V_T$ the surface under the oxide is inverted and if $V_{DS} > 0$ a drift current will flow from the drain to the source. The drain-to-source voltage is assumed small so that the depletion layer is approximately constant along the length of the channel. Under these conditions, the drain source current for an NMOS device is given by the relation,

$$I_D = \mu_n C'_{ox}\frac{W}{L}\left(\left(V_{GS} - V_T\right)V_{DS} - \frac{V_{DS}^2}{2}\right)\Bigg|_{\substack{V_{GS} \geq V_T \\ V_{DS} \leq V_{GS} - V_T}} \tag{7.63}$$

where μ_n is the electron mobility in the channel and C'_{ox} is the per unit area capacitance over the gate area. Similarly, for PMOS transistors the current relationship is given as,

$$I_D = \mu_p C'_{ox}\frac{W}{L}\left(\left(V_{SG} - V_T\right)V_{SD} - \frac{V_{SD}^2}{2}\right)\Bigg|_{\substack{V_{SG} \geq V_T \\ V_{SD} \leq V_{SG} - V_T}} \tag{7.64}$$

in which the threshold voltage of the p-type MOSFET is assumed to be positive and μ_p is the hole mobility.

Saturation — The conditions $V_{DS} \leq V_{GS} - V_T$ in Eq. (7.63) and $V_{SD} \leq V_{SG} - V_T$ in Eq. (7.64) ensure that the inversion charge is never zero for any point along the channel's length. However, when $V_{DS} = V_{GS} - V_T$ (or $V_{SD} = V_{SG} - V_T$ in PMOS devices) the inversion charge under the gate at the channel-drain junction is zero. The required drain-to-source voltage is called $V_{DS,sat}$ for NMOS and $V_{SD,sat}$ for PMOS.

For $V_{DS} > V_{DS,sat}$ ($V_{SD} > V_{SD,sat}$ for PMOS), the channel charge becomes "pinched off," and any increase in V_{DS} increases the drain current only slightly. The reason that the drain currents will increase for increasing V_{DS} is because the depletion layer width increases for increasing V_{DS}. This effect is called channel length modulation and is accounted for by λ, the channel length modulation parameter. The channel length modulation parameter ranges from approximately 0.1 for short channel devices to 0.01 for long channel devices. Since MOSFETs designed for radio frequency operation normally use minimum channel lengths, channel length modulation is an important concern for radio frequency implementations in CMOS.

When a MOSFET is operated with its channel pinched off, in other words $V_{DS} > V_{GS} - V_T$ and $V_{GS} \geq V_T$ for NMOS (or $V_{SD} > V_{SG} - V_T$ and $V_{SG} \geq V_T$ for PMOS), the device is said to be operating in the saturation region. The corresponding equations for the drain current are given by,

$$I_D = \frac{1}{2}\mu_n C'_{ox}\frac{W}{L}\left(V_{GS} - V_T\right)^2\left(1 + \lambda\left(V_{DS} - V_{DS,sat}\right)\right) \qquad (7.65)$$

for long-channel NMOS devices and by,

$$I_D = \frac{1}{2}\mu_p C'_{ox}\frac{W}{L}\left(V_{SG} - V_T\right)^2\left(1 + \lambda\left(V_{SD} - V_{SD,sat}\right)\right) \qquad (7.66)$$

for long-channel PMOS devices.

Figure 7.64 illustrates a family of curves typically used to visualize a MOSFET's drain current as a function of its terminal voltages. The drain-to-source voltage spans the operating region while the gate-to-source voltage is fixed at several values. The bulk-to-source voltage has been taken as zero. As shown in Fig. 7.64, when the MOSFET enters the saturation region the drain current is essentially independent of the drain-to-source voltage and so the curve is flat. The slope is not identically zero however, as the drain-to-source voltage does have some effect upon the channel current due to channel modulation effects.

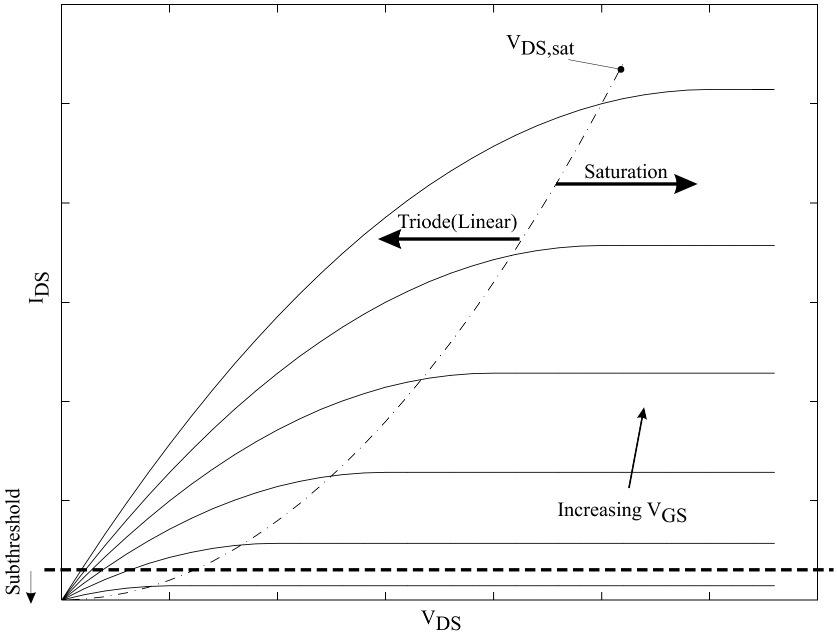

FIGURE 7.64 Characteristic drain-current versus terminal-voltage curves for a MOSFET.

Three simplifying assumptions are advantageous when one is trying to gain an intuitive understanding of the low-frequency operation of a circuit containing MOSFETs. When operated in the linear region, the MOSFET can be treated much like a resistor with terminal voltage V_{DS}. When operated in the saturation region, the MOSFET may be considered a voltage-controlled current source where the controlling voltage is present at the gate. Finally, when operated below the voltage threshold, the MOSFET can be considered an open circuit from the drain to the source.

Nonideal and Short Channel Effects

The equations presented for the subthreshold, triode, and saturation regions of the MOSFET operating characteristic curves do not include the many nonidealities exhibited by MOSFETs. Most of these nonideal behaviors are more pronounced in deep submicron devices such as those employed in radio frequency designs, and so it is important for a designer to be aware of them.

Velocity saturation — Electron and hole mobility are not constants; they are a function of the applied electric field. Above a certain critical electric field strength the mobility starts to decrease, and the drift velocity of carriers does not increase in proportion to the applied electric field. Under these conditions the device is said to be velocity saturated. Velocity saturation has important practical consequences in terms of the current-voltage characteristics of a MOSFET acting in the saturation region. In particular, the drain current of a velocity saturated MOSFET operating in the saturation region is a linear function of V_{GS}. This is in contrast to the results given in Eqs. (7.65) and (7.66). The drain current for a short channel device operating under velocity saturation conditions is given by

$$I_D = \mu_{crit} C'_{ox} W \left(V_{GS} - V_T \right) \tag{7.67}$$

where μ_{crit} is the carrier mobility at the critical electric field strength.

Drain-induced barrier lowering — A positive voltage applied to the drain terminal helps to attract electrons under the gate oxide region. This increases the surface potential and causes a threshold voltage reduction. Since the threshold decreases with increasing V_{DS}, the result is an increase in drain current and therefore an effective decrease in the MOSFET's output resistance. The effects of drain-induced barrier lowering are reduced in modern CMOS processes by using lightly doped drain (LDD) structures.

Hot carriers — Velocity saturated charge carriers are often called hot carriers. Hot carriers can potentially tunnel through the gate oxide and cause a gate current, or they may become trapped in the gate oxide. Hot carriers that become trapped in the gate oxide change the device threshold voltage. Over time, if enough hot carriers accumulate in the gate oxide, the threshold voltage is adjusted to the point that analog circuitry performance is severely degraded. Therefore, depending upon the application, it may be unwise to operate a device so that the carriers are velocity saturated since the reliability and lifespan of the circuit is degraded.

Small Signal Models

Small signal equivalent circuits are useful when the voltage and current waveforms in a circuit can be decomposed into a constant level plus a small time-varying offset. Under these conditions, a circuit can be linearized about its DC operating point. Nonlinear components are replaced with linear components that reflect the bias conditions.

The low-frequency small signal model for a MOSFET is shown in Fig. 7.65. Only the intrinsic portion of the transistor is considered for simplicity. As shown, the small signal model consists of three components: the small signal gate transconductance, g_m; the small signal substrate transconductance, g_{mb}; and the small signal drain conductance, g_d. Mathematically, these three components are defined by

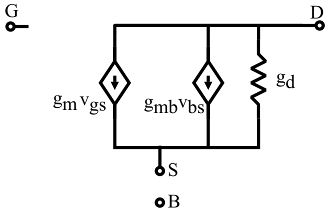

FIGURE 7.65 Low-frequency small signal MOSFET model.

$$g_m = \left.\frac{\partial I_D}{\partial V_{GS}}\right|_{V_{BS}, V_{DS} \text{ constant}} \tag{7.68}$$

$$g_{mb} = \left.\frac{\partial I_D}{\partial V_{BS}}\right|_{V_{GS}, V_{DS} \text{ constant}} \tag{7.69}$$

and

$$g_d = \left.\frac{\partial I_D}{\partial V_{DS}}\right|_{V_{GS}, V_{BS} \text{ constant}} \tag{7.70}$$

Equations (7.68), (7.69), and (7.70) can be evaluated using the relationships given earlier. For the saturation region, the small signal transconductances and the drain conductance are given by,

$$g_m = \mu C'_{ox} \frac{W}{L}\left(V_{GS} - V_T\right) \tag{7.71}$$

$$g_{mb} = g_m \eta \tag{7.72}$$

and

$$g_d = \frac{1}{2}\mu C'_{ox} \frac{W}{L}\left(V_{GS} - V_T\right)^2 \lambda \tag{7.73}$$

where η in Eq. (7.72) is a factor that describes how the threshold voltages changes with reverse body bias. For small V_{BS}, $\eta \approx 0$.

The small signal model shown in Fig. 7.65 is only valid at very low frequencies. At higher frequencies capacitances present in the MOSFET must be included in the small signal model, and at radio frequencies distributed effects must be taken into account. In the next section these two factors are explored and the small signal model is revised.

CMOS at Radio Frequencies

Integrated radio frequency transceiver design is an evolving field, particularly in terms of understanding device performance and maximizing integration level. Typical commercial implementations of highly-integrated high-performance wireless transceivers use a mixture of technologies, including CMOS, BiCMOS, BJTs, GaAs FETs, and HBTs. Regardless of the technology, all radio frequency integrated circuits contend with the same issues of noise, linearity, gain, and efficiency.

The best technology choice for an integrated radio frequency application must weigh the consequences of wafer cost, level of integration, performance, economics, and time to market. These requirements often lead designers into using several technologies within one transceiver system. Partitioning of transceiver functionality according to technology implies that the signal must go on-chip and off-chip at several locations. Bringing the signal off-chip and then on-chip again complicates the transceiver design because proper matching at the output and input terminals is required. Also, bringing the signal off-chip implies that power requirements are increased because it takes more power to drive an off-chip load than to keep the signal completely on the same integrated circuit. Generally, taking the signal off and then on-chip results in signal power loss accompanied by an undesirable increase in noise figure.

Recent trends apply CMOS to virtually the entire transceiver design, since CMOS excels in its level of integration. The level of integration offered by a particular technology determines the required die size, which in turn affects both the cost and the physical size of the final packaged circuitry. CMOS technology currently has the performance levels necessary to operate in the 900 MHz to 2.4 GHz frequency range, which is important for existing cellular and wireless network applications. Upcoming technologies should be able to operate in the 5 GHz ISM band, which is seen as the next important commodity frequency. CMOS devices manufactured with gate lengths of 0.18 μm will function at these frequencies, albeit with generous biasing currents. Future generations of CMOS scaled below the 100 nm gate length range are anticipated to provide the performance required to operate beyond the 5 GHz frequency range for receiver applications.

High Frequency Modeling

The majority of existing analog MOSFET models predate the use of CMOS in radio frequency designs and generally are unable to predict the performance of MOSFETs operating at microwave frequencies with the accuracy required and expected of modern simulators. These modeling shortcomings occur on two fronts. In the first case, existing models do not properly account for the distributed nature of the MOSFET, meaning that at high frequencies, geometry-related effects are ignored. In the second case, existing models do not properly model MOSFET noise at high frequencies. Typical problems with noise modeling include:

- not accounting for velocity-saturated carriers within the channel and the associated noise;
- discounting the significant thermal noise generated by the distributed gate resistance;
- ignoring the correlation between the induced gate noise and the MOSFET drain noise.

Accurate noise modeling is extremely important when low noise operation is essential, such as in a front-end low noise amplifier.

High Frequency Operation

MOSFET dimensions and physical layout are important determining factors for high frequency performance. As MOSFET operating frequencies approach several hundred MHz, the MOSFET can no longer be considered a lumped device. The intrinsic and extrinsic capacitance, conductance, and resistance are all distributed according to the geometry and physical layout of the MOSFET. The distributed nature of the MOSFET operating at high frequencies is particularly important for the front-end circuitry in a receiver, such as in the low noise amplifier and first stage mixer input MOSFETs. The devices used in these portions of the input circuitry are normally large, with high W/L ratios. Large W/L ratios are required because of the inherently low transconductance offered by CMOS, and in order to realize reasonable gain, the devices are therefore relatively wide compared to more conventional analog circuit layouts. Additionally, minimum gate lengths are preferred because the maximum operating frequency of the MOSFET scales as $1/L^2$. Shorter channels imply higher frequency because the time it takes the carriers to move from drain to source is inversely proportional to the length of the channel. Also, the mobility of the carriers is proportional to the electric field strength. Since the electric field strength along the length of the channel is inversely proportional to the distance between the source and the drain, the carrier mobility is inversely proportional to the length of the channel. Combined, these two effects have traditionally allowed the maximum operating frequency of the MOSFET to scale as $1/L^2$. It must be noted that in modern deep submicrometer MOSFETs experiencing velocity saturation, the maximum operating frequency no longer scales as $1/L^2$, but more closely to $1/L$. In any event, for maximum operating frequency, the device channel length should be the minimum allowable.

Since the gate width in RF front-end MOSFET devices is typically on the order of several hundred microns, the gate acts as a transmission line along its width. The gate acting as a transmission line is modeled similarly to a microstrip transmission line and can be analyzed by utilizing a distributed circuit model for transmission lines. Normally a transmission line is viewed as a two-port network in which the transmission line receives power from the source at the input port (source end) and delivers the power

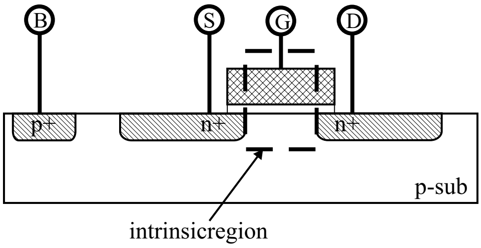

FIGURE 7.66 MOSFET intrinsic and extrinsic capacitance boundary.

to the load of the output port (load end). In order to apply transmission line analysis to the gate of a MOSFET along its width, the width of the MOSFET gate is divided into many identical sections of incremental width Δx. Each portion of the transmission line with the width Δx is modeled by a resistance "R" per unit width, an inductance "L" per unit width, a capacitance "C" per unit width, and a conductance "G" per unit width. Normally the transmission line is assumed to be uniform, so that these parameters are constants along the transmission line's width. When analyzing signal propagation along the MOSFET gate width, it is important to note that there is no single output node. The transmission line cannot be treated as a two-port, since the gate couples to the channel in a distributed fashion.

Important Parasitics and Distributed Effects

Parasitic capacitances — At high operating frequencies the effects of parasitic capacitances on the operation of the MOSFET cannot be ignored. Transistor parasitic capacitances are subdivided into two general categories; extrinsic capacitances and intrinsic capacitances. The extrinsic capacitances are associated with regions of the transistor outside the dashed line shown in Fig. 7.66, while the intrinsic capacitances are all those capacitances located within the region illustrated in Fig. 7.66.

Extrinsic capacitances — Extrinsic capacitances are modeled by using small-signal lumped capacitances, each of which is associated with a region of the transistor's geometry. Seven small-signal capacitances are used, one capacitor between each pair of transistor terminals, plus an additional capacitor between the well and the bulk if the transistor is fabricated in a well. Figure 7.67(a) illustrates the seven extrinsic transistor capacitances added to an intrinsic small signal model, and Fig. 7.67(b) assigns a location to each capacitance within the transistor structure. In order of importance to high frequency performance, the extrinsic capacitances are as follows:

Gate overlap capacitances —Although MOSFETs are manufactured using a self-aligned process, there is still some overlap between the gate and the source and the gate and the drain. This overlapped area gives rise to the gate overlap capacitances denoted by C_{GSO} and C_{GDO} for the gate-to-source overlap capacitance and the gate-to-drain overlap capacitance, respectively. Both capacitances C_{GSO} and C_{GDO} are proportional to the width, W, of the device and the amount that the gate overlaps the source and the drain, typically denoted as "LD" in SPICE parameter files. The overlap capacitances of the source and the drain are often modeled as linear parallel plate capacitors, since the high dopant concentration in the source and drain regions and the gate material implies that the resulting capacitance is largely bias independent. However, for MOSFETs constructed with a lightly doped drain (LDD-MOSFET), the overlap capacitances can be highly bias dependent and therefore nonlinear. For a treatment of overlap capacitances in LDD-MOSFETs, refer to Klein.[7] For non-lightly doped drain MOSFETs, the gate-drain and gate-source overlap capacitances are given by the expression $C_{GSO} = C_{GDO} = W\ LD\ C_{ox}$, where C_{ox} is the thin oxide field capacitance per unit area under the gate region.

When the overlap distances are small, fringing field lines add significantly to the total capacitance. Since the exact calculation of the fringing capacitance requires an accurate knowledge of the drain and source region geometry, estimates of the fringing field capacitances based on measurements are normally used.

Extrinsic junction capacitances —The bias-dependent junction capacitances that must be considered when evaluating the extrinsic lumped-capacitance values are illustrated in Fig. 7.67(a) and summarized

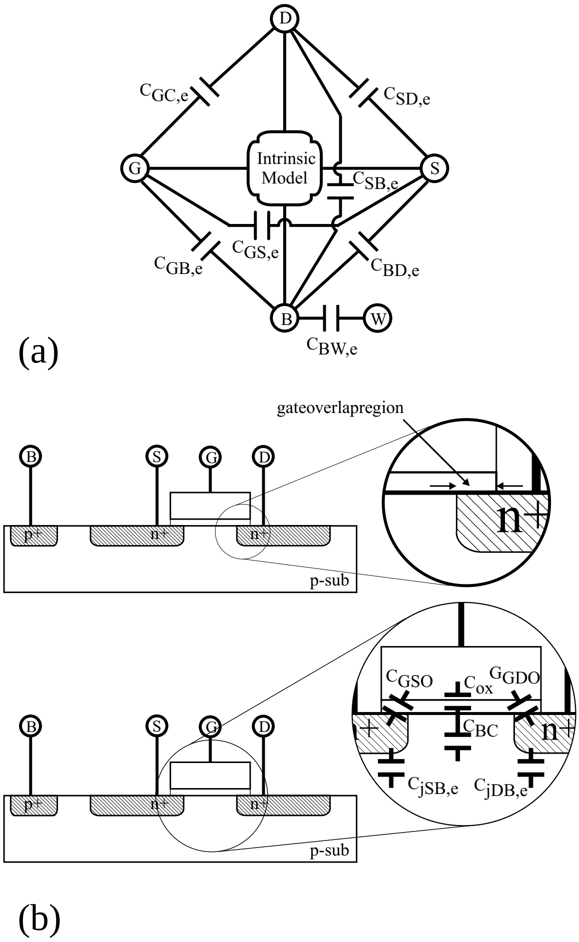

FIGURE 7.67 Extrinsic capacitances. (a) Lumped terminal capacitances added to the intrinsic model, (b) physical location of extrinsic capacitances.

in Table 7.4. At the source region there is a source-to-bulk junction capacitance, $C_{jBS,e}$, and at the drain region there is a drain-to-bulk junction capacitance, $C_{jBD,e}$. These capacitances can be calculated by splitting the drain and source regions into a "side wall" portion and a "bottom wall" portion. The capacitance associated with the side wall portion is found by multiplying the length of the side wall perimeter (excluding the side contacting the channel) by the effective side wall capacitance per unit length. Similarly, the capacitance for the bottom wall portion is found by multiplying the area of the bottom wall by the bottom wall capacitance per unit area. Additionally, if the MOSFET is in a well, a well-to-bulk junction capacitance, $C_{jBW,e}$, must be added. The well-bulk junction capacitance is calculated similar to the source and drain junction capacitances, by dividing the total well-bulk junction capacitance into side wall and bottom wall components. If more than one transistor is placed in a well, the well-bulk junction capacitance should only be included once in the total model.

Both the effective side wall capacitance and the effective bottom wall capacitance are bias dependent. Normally the per unit length zero-bias, side wall capacitance and the per unit area zero-bias, bottom wall capacitance are estimated from measured data. The values of these parameters for nonzero reverse-bias conditions are then calculated using the formulas given in Table 7.4.

Extrinsic source-drain capacitance — Accurate models of short channel devices may include the capacitance that exists between the source and drain region of the MOSFET. As shown in Fig. 7.67(a), the source-drain capacitance is denoted as $C_{sd,e}$. Although the source-drain capacitance originates in the

TABLE 7.4 MOSFET Extrinsic Junction Capacitances

Extrinsic Source Capacitance	$C_{jBS,e} = C'_{jBS}A_S + C''_{jswBS}P_S$	$C'_{jBS} = \dfrac{C'_j}{\left(1-\dfrac{V_{BS}}{\phi_j}\right)^{m_j}}$	$C''_{jswBS} = \dfrac{C''_{jsw}}{\left(1-\dfrac{V_{BS}}{\phi_{jsw}}\right)^{m_{jsw}}}$
Extrinsic Drain Capacitance	$C_{jBD,e} = C'_{jBD}A_D + C''_{jswBD}P_D$	$C'_{jBD} = \dfrac{C'_j}{\left(1-\dfrac{V_{BD}}{\phi_j}\right)^{m_j}}$	$C''_{jswBD} = \dfrac{C''_{jsw}}{\left(1-\dfrac{V_{BD}}{\phi_{jsw}}\right)^{m_{jsw}}}$
Extrinsic Well Capacitance	$C_{jBW,e} = C'_{jBW}A_W + C''_{jswBW}P_W$	$C'_{jBW} = \dfrac{C'_j}{\left(1-\dfrac{V_{BW}}{\phi_j}\right)^{m_j}}$	$C''_{jswBW} = \dfrac{C''_{jsw}}{\left(1-\dfrac{V_{BW}}{\phi_{jsw}}\right)^{m_{jsw}}}$

Notes: m_j and m_{jsw} are process dependent, typically 1/3 … 1/2.

$$C'_j = \sqrt{\frac{\varepsilon_{si} q N_B}{2\phi_j}}$$

Where: ϕ_j and ϕ_{jsw} are the built-in junction potential and side wall junction potentials, respectively. ε_{si} is the dielectric constant of silicon, q is the electronic charge constant, and N_B is the bulk dopant concentration.

$$C''_{jsw} = \sqrt{\frac{\varepsilon_{si} q N_B}{2\phi_{jsw}}}$$

A_S, A_D, and A_W are the source, drain, and well areas, respectively.
P_s, P_d, and P_w are the source, drain, and well perimeters, respectively. The source and drain perimeters do not include the channel boundary.

region within the dashed line in Fig. 7.66, it is still referred to as an extrinsic capacitance.[1] The value of this capacitance is difficult to calculate because its value is highly dependent upon the source and drain geometries. For longer channel devices, $C_{sd,e}$ is very small in comparison to the other extrinsic capacitances, and is therefore normally ignored.

Extrinsic gate-bulk capacitance — As with the gate-to-source and gate-to-drain overlap capacitances, there is a gate-to-bulk overlap capacitance caused by imperfect processing of the MOSFET. The parasitic gate-bulk capacitance, $C_{GB,e}$, is located in the overlap region between the gate and the substrate (or well) material outside the channel region. The parasitic extrinsic gate-bulk capacitance is extremely small in comparison to the other parasitic capacitances. In particular, it is negligible in comparison to the intrinsic gate-bulk capacitance. The parasitic extrinsic gate-bulk capacitance has little effect on the gate input impedance and is therefore generally ignored in most models.

Intrinsic capacitances — Intrinsic MOSFET capacitances are significantly more complicated than extrinsic capacitances because they are a strong function of the voltages at the terminals and the field distributions within the device. Although intrinsic MOSFET capacitances are distributed throughout the device, for the purposes of simpler modeling and simulation, the distributed capacitances are normally represented by lumped terminal capacitances. The terminal capacitances are derived by considering the change in charge associated with each terminal with respect to a change in voltage at another terminal, under the condition that the voltage at all other terminals is constant. The five intrinsic small signal capacitances are therefore expressed as,

$$C_{gd,i} = \left.\frac{\partial Q_G}{\partial V_D}\right|_{V_G, V_S, V_B} \tag{7.74}$$

$$C_{gs,i} = \left.\frac{\partial Q_G}{\partial V_S}\right|_{V_G, V_D, V_B} \tag{7.75}$$

TABLE 7.5 Intrinsic MOSFET Capacitances

Operating Region	$C_{gs,i}$	$C_{gd,i}$	$C_{gb,i}$	$C_{bs,i}$	$C_{bd,i}$
Triode	$\approx \frac{1}{2} C_{ox}$	$\approx \frac{1}{2} C_{ox}$	≈ 0	$k_0 C_{ox}$	$k_0 C_{ox}$
Saturation	$\approx \frac{2}{3} C_{ox}$	≈ 0	$K_1 C_{ox}$	$K_2 C_{ox}$	≈ 0

Notes: Triode region approximations are for $V_{DS} = 0$.
k_0, k_1, and k_2 are bias dependent. See [1].

$$C_{bd,i} = \left. \frac{\partial Q_B}{\partial V_D} \right|_{V_G, V_S, V_B} \tag{7.76}$$

$$C_{bs,i} = \left. \frac{\partial Q_B}{\partial V_D} \right|_{V_G, V_D, V_B} \tag{7.77}$$

and

$$C_{gb,i} = \left. \frac{\partial Q_G}{\partial V_B} \right|_{V_G, V_S, V_D} \tag{7.78}$$

These capacitances are evaluated in terms of the region of operation of the MOSFET, which is a function of the terminal voltages. Detailed models for each region of operation were investigated by Cobbold.[8] Simplified expressions are given in Table 7.5, for the triode and saturation operating regions. The total terminal capacitances are then given by combining the extrinsic capacitances and intrinsic capacitances according to,

$$\begin{aligned}
C_{gs} &= C_{gs,i} + C_{gs,e} = C_{gs,i} + C_{gso} \\
C_{gd} &= C_{gd,i} + C_{gd,e} = C_{gd,i} + C_{gdo} \\
C_{gb} &= C_{gb,i} + C_{gb,e} = C_{gb,i} + C_{gbo} \\
C_{sb} &= C_{bs,i} + C_{sb,e} = C_{bs,i} + C_{jsb} \\
C_{db} &= C_{bd,i} + C_{db,e} = C_{bd,i} + C_{jdb}
\end{aligned} \tag{7.79}$$

in which the small-signal form of each capacitance has been used.

The contribution of the total gate-to-channel capacitance, C_{GC}, to the gate-to-drain and gate-to-source capacitances is dependent upon the operating region of the MOSFET. The total value of the gate-to-channel capacitance is determined by the per unit area capacitance C_{ox} and the effective area over which the capacitance is taken. Since the extrinsic overlap capacitances include some of the region under the gate, this region must be removed when calculating the gate-to-channel capacitance. The effective channel length, L_{eff}, is given by $L_{eff} = L - 2LD$ so that the gate-to-channel capacitance can be calculated by the formula $C_{GC} = C_{ox} W L_{eff}$. The total value of the gate-to-channel capacitance is apportioned to both the drain and source terminals according to the operating region of the device. When the device is in the triode region, the capacitance exists solely between the gate and the channel and extends from the drain to the source. Its value is therefore evenly split between the terminal capacitances C_{gs} and C_{gd} as shown in Table 7.5. When the device operates in the saturation region, the channel does not extend all the way from the source to the drain. No portion of C_{GC} is added to the drain terminal capacitance under these circumstances. Again, as shown in Table 7.5, analytical calculations demonstrated that an appropriate amount of C_{GS} to include in the source terminal capacitance is 2/3 of the total.[1]

Finally, the channel to bulk junction capacitance, C_{BC}, should be considered. This particular capacitance is calculated in the same manner as the gate-to-channel capacitance. Also similar to the gate-to-channel capacitance proportioning between the drain in the source when calculating the terminal capacitances, the channel-to-bulk junction capacitance is also proportioned between the source-to-bulk and drain-to-bulk terminal capacitances, depending on the region of operation of the MOSFET.

Wiring capacitances — Referring to Fig. 7.62, one can see that the drain contact interconnect overlapping the field oxide and substrate body forms a capacitor. The value of this overlap capacitance is determined by the overlapping area, the fringing field, and the oxide thickness. Reduction of the overlapping area will decrease the capacitance to a point, but with an undesirable increase in the parasitic resistance at the interconnect to MOSFET drain juncture. The parasitic capacitance occurring at the drain is particularly troublesome due to the Miller effect, which effectively magnifies the parasitic capacitance value by the gain of the device. The interconnects between MOSFET devices also add parasitic capacitive loads to the each device. These interconnects may extend across the width of the IC in the worst case, and must be considered when determining the overall circuit performance.

Modern CMOS processes employ thick field-oxides that reduce the parasitic capacitance that exists at the drain and source contacts, and between interconnect wiring and the substrate. The thick field-oxide also aids in reducing the possibility of unintentional MOSFET operation in the field region.

Distributed gate resistance — Low-frequency MOSFET models treat the gate as purely capacitive. This assumption is invalid for frequencies beyond approximately 1 GHz, because the distributed gate resistance is typically larger than the capacitive reactance present at the gate input for frequencies beyond 1 GHz.

The impact of the distributed gate resistance upon the high frequency performance of MOSFETs has been investigated both experimentally and analytically by several researchers.[1,6,9–15] The distributed gate resistance affects the radio frequency performance of the MOSFET in three primary ways. In the first case, discounting the gate resistance causes nonoptimal power matching to off-chip source impedances. In the second case, discounting the distributed gate resistance in noise figure calculations causes an underestimation of the noise figure of the transistor. Finally, in the third case, since the power gain of the MOS transistor is strongly governed by the gate resistance, discounting the gate resistance causes an overestimation of the MOSFET's available power gain and maximum oscillation frequency. The gate resistance of MOSFET transistors therefore deserves important consideration during the design phase of integrated RF CMOS receivers.

Nonzero gate resistances have been factored into recent successful designs. Rofougaran et al.[16] noted that matching, input noise, and voltage gain are all ultimately limited by transistor imperfections such as gate resistance. The effects were most recently quantified by Enz.[6]

Channel charging resistance — Charge carriers located in the channel cannot instantaneously respond to changes in the MOSFET gate-to-source voltage. The channel charging resistance is used to account for this non-quasi-static behavior along the channel length. In Bagheri et al.,[15] the channel charging resistance was shown to be inversely proportional to the MOSFET transconductance, $r_i \approx (kg_m)^{-1}$. For long channel devices, with the distributed nature of the channel resistance between the source and drain taken into account, the constant of proportionality, k, was shown to equal five. Measurements of short channel devices indicate that the proportionality constant can go as low as one.

The channel charging resistance of a MOSFET is important because it strongly influences the input conductance and the forward transconductance parameters of the device. Both the input conductance and the forward transconductance are monotonically decreasing functions of the channel charging resistance. Since the transconductance of even a large MOSFET is small, on the order of 10 mS, the charging resistance of typical front-end transistors is large, potentially on the order of hundreds of ohms.

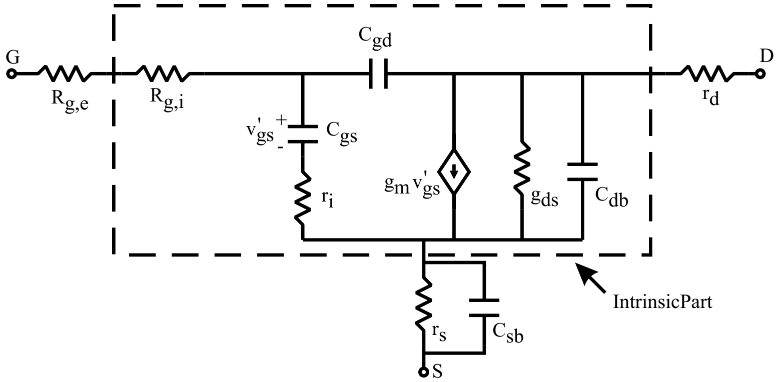

FIGURE 7.68 MOSFET small-signal high-frequency model.

Transconductance delay — MOSFET transconductance does not respond instantaneously to changes in gate voltage. The time it takes for the charge in the channel to be redistributed after an excitation of the gate voltage is dictated by the time constant due to the gate-to-source capacitance and the channel charging resistance. This time constant is denoted as τ, and is given by the expression $\tau \approx r_i C_{gs}$. The transconductance delay is generally ignored for frequencies less than $2\pi/\tau$.

Small Signal Models

Several high frequency small signal models incorporating the effects described in the previous sections have been proposed in the literature. The small signal model presented in Fig. 7.68 is useful for MOSFETs operating in saturation in a common-source configuration. Evident in the figure are the various lumped terminal capacitances, the drain conductance, and the output transconductance. Note that the transconductance g_{mb} is taken as zero because $V_{SB} = 0$ is assumed. Also evident in the model are the high-frequency related elements, namely the charging resistance, the transconductance delay, and the extrinsic and intrinsic gate resistances.

MOSFET Small Signal Y-parameters

Small-signal y-parameters are useful in radio frequency design work involving MOSFETs. As discussed later in this section, radio frequency MOSFETs are typically laid out in a "fingered" style, and if the y-parameters are found for a single finger, they are easily combined for the complete device.

The y-parameters corresponding to the small signal equivalent circuit shown in Fig. 7.68 have been evaluated and appear in Table 7.6. These y-parameters cannot accurately portray the distributed nature of the MOSFET at high frequencies because the model presented in Fig. 7.68 is composed of lumped elements. Recall that the gate resistance in MOS transistors operating at GHz frequencies in conjunction with intrinsic and extrinsic device capacitances acts as a distributed RC network. This is shown schematically in Fig. 7.69, where a MOSFET is represented as a network of smaller MOSFETs, interconnected by gate material.

Several models developed over the last three decades incorporate high frequency and distributed effects. Noise arising from the distributed gate was modeled by Jindal,[12] but high frequency effects were not incorporated in this model. Distributed geometry effects were recognized as important,[14,15] but the distributed nature of the gate was not fully explored analytically.[10] As the viability of CMOS in RF transceiver applications improved, significant progress in modeling wide devices, such as those required for RF applications, was made by Kim et al.[11] and Razavi et al.,[9] in which wide transistors were treated as arrays of smaller transistors interconnected by resistors representing the gate. Recently in a paper by Abou-Allam,[17,18] a closed-form, small signal model incorporating the distributed gate for wide transistors was derived, taking into account the distributed nature of the gate resistance and intrinsic capacitances. The y-parameters developed in Abou-Allam's paper[17] appear here in Table 7.6.

TABLE 7.6 MOSFET Small-Signal Y-Parameters

Parameter	Y-Parameters for the Intrinsic MOSFET Model of Fig. 7.68	Distributed MOSFET Y-Parameters*
y_{11}	$\frac{s(\kappa+C_{gd})}{1+s(\kappa+C_{gd})R_{g,i}}$	$\frac{s(C_{gs}+C_{gd})+s^2C_{gs}C_{gd}r_i}{1+sC_{gs}r_i}\,\frac{\tanh(\gamma W)}{\gamma W}$
y_{12}	$\frac{-sC_{gd}}{1+s(\kappa+C_{gd})R_{g,i}}$	$-sC_{gd}\frac{\tanh(\gamma W)}{\gamma W}$
y_{21}	$\frac{g_m-sC_{gd}}{1+s(\kappa+C_{gd})R_{g,i}}$	$\left(\frac{g_m}{1+sC_{gs}r_i}-sC_{gd}\right)\frac{\tanh(\gamma W)}{\gamma W}$
y_{22}	$g_d+sC_{gd}+\frac{(g_m-s(\kappa-C_{gd}))sC_{gd}R_{g,i}}{1+s(\kappa+C_{gd})R_{g,i}}$	$g_d+sC_{gd}+\frac{\left(\frac{g_m}{1+sC_{gs}r_i}-sC_{gd}\right)C_{gd}}{C_{gd}+\frac{C_{gs}}{1+sC_{gs}r_i}}\left(1-\frac{\tanh(\gamma W)}{\gamma W}\right)$
Notes:	$\kappa=\frac{C_{gs}}{1+sC_{gs}r_i}$	$\gamma=\frac{\sqrt{sC_{gd}r_i\frac{sC_{gs}r_i}{1+sC_{gs}r_i}}}{W}$

*Source: Abou-Allam, E. and Manku, T., An Improved Transmission-Line Model for MOS Transistors, *IEEE Transactions on Circuits and Systems II: Analog and Digital Signal Processing,* 46, 1380–1387, Nov. 1999.

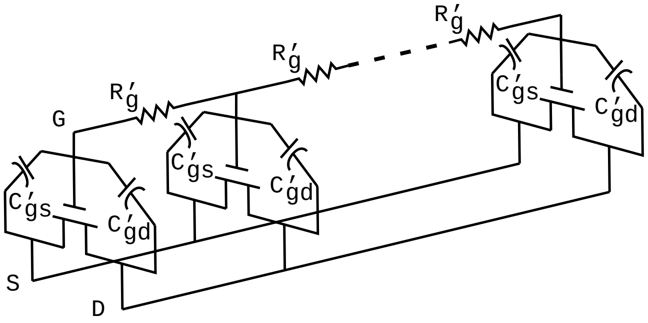

FIGURE 7.69 Illustration of distributed MOSFET network model.

A parallel between the results presented by Razavi et al.[9] and Abou-Allam[18] was drawn in a paper by Tin et al.,[19] in which a useful small signal lumped circuit model was presented and leads to the model here in Fig. 7.70. The lumped model shown in Fig. 7.70 incorporates the distributed effects represented by the $\tanh(\gamma W)/\gamma W$ factor within the expressions for the y-parameters presented in Table 7.6.

The distributed gate resistance appears as a lumped resistor of value $R_g/3$ and the distributed intrinsic capacitances appear as a lumped capacitor with value $C_g/5$. It is important to note that these expressions were derived for a gate connected from one end only. For example, when the gate is connected from both ends, the equivalent resistor changes to $R_g/12$.

The performance limitations imposed by distributed effects at radio frequencies was summarized by Manku.[20] Analysis of a two-port constructed from the y-parameters as given in Table 7.6 for a traditional MOSFET yields several important device performance metrics, as now discussed.

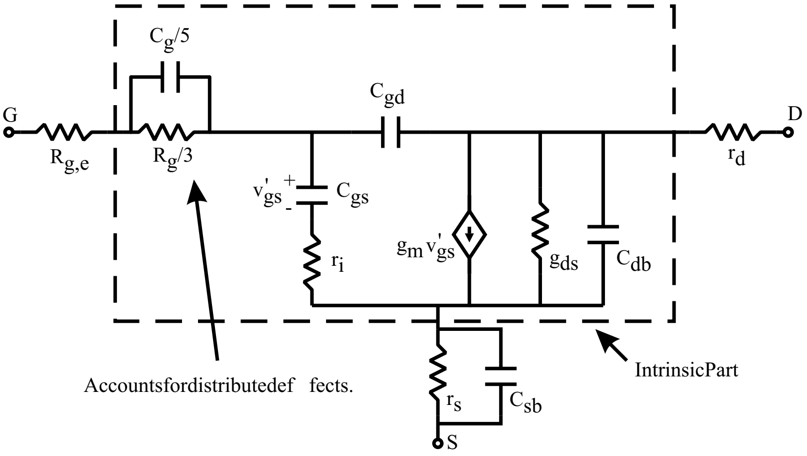

FIGURE 7.70 A lumped small-signal MOSFET model that accounts for distributed gate resistance effects.

Unity Current Gain Frequency: f_t

The unity current gain frequency is defined as the signal input frequency at which the extrapolated small-signal current gain of the MOSFET equals one. The small-signal current gain is defined as the amplitude of the small-signal drain current to the small-signal gate current. The symbol used in the literature to denote the unity current gain frequency is f_t and is read as the "transit frequency."

The unity current gain frequency, or transit frequency, is used as a benchmark to describe the speed of the intrinsic device. The performance of the complete device, which includes the additional effects of the extrinsic parasitics, is always lower. For linear amplifier configurations, the small-signal unity current gain is of primary concern since it determines the maximum achievable gain-bandwidth product of the amplifier. Small signal linear two-port models are useful for estimating the unity current gain frequency. The value of f_t is most easily found from the y-parameters using the relation,[13]

$$\left|\frac{y_{21}}{y_{11}}\right| = 1 \tag{7.80}$$

which holds when the current gain is unity. From y-parameters given in Table 7.6, the value of f_t is found as,

$$f_t = \frac{g_m}{2\pi\sqrt{C_g^2 - \left(g_m R_{gi} C_{gs} - C_{gs}\right)^2}} \approx \left.\frac{g_m}{2\pi C_g}\right|_{C_g = C_{gs} + C_{gd}} \tag{7.81}$$

where $C_g^2 \gg (g_m R_{gi} C_{gs} - C_{gs})^2$ is assumed.

Note that the unity current gain frequency is independent of the distributed gate resistance. The most important determining factors of the unity current gain frequency are the device transconductance and the gate-to-source and gate-to-drain capacitances. Since the device f_t is directly proportional to g_m, the analog circuit designer can trade power for speed by increasing the device bias current and therefore g_m. Note that f_t cannot be arbitrarily increased by an increase in drain-source bias current; eventually g_m becomes independent of I_{DS}, and therefore f_t becomes independent of the bias current. MOSFETs used at radio frequencies are normally operated in saturation, because g_m is maximum for a given device in the saturation region. Recall that g_m can also be increased by increasing the width of the transistor, but this will not increase f_t because the parasitic capacitance C_g is proportional to the width of the device.

The transit frequency must not be confused with another often used performance metric, the "intrinsic cutoff frequency," f_τ. While both the "t" in f_t and the "τ" in f_τ refer to the carrier transit time along the length of the device channel, the two symbols have decidedly different meanings. The intrinsic cutoff frequency is given by $f_{\tau = (2\pi\tau)^{-1}}$ where τ is the mean transit time of the carriers along the channel length. Typically, f_τ is five or six times larger than f_t.[6]

Maximum Available Power Gain: G_{max}

Maximum port-to-port power gain within a device occurs when both the input and the output ports are matched to the impedance of the source and the load, respectively. The maximum available power gain of a device, G_{max}, provides a fundamental limit on how much power gain can be achieved with the device. The maximum available power gain achievable within a linear two-port network can be described in terms of the two-port y-parameters as,[13]

$$G_{\text{max}} = \frac{1}{4} \frac{\left|y_{21} - y_{12}\right|^2}{\text{Re}\left(y_{11}\right)\text{Re}\left(y_{22}\right) - \text{Re}\left(y_{21}\right)\text{Re}\left(y_{12}\right)} \tag{7.82}$$

where the two-port system is assumed to be unconditionally stable. Treating a common-source MOSFET as a two-port and using the y-parameters shown in Table 7.6 and the relation for f_t given in Eq. (7.81), the MOSFET G_{max} is derived in terms of the intrinsic device parameters as,

$$\begin{aligned} G_{\text{max}} &\approx \frac{\left(f_t/f\right)^2}{4R_{g,i}\left(g_{ds} + g_m C_{gd}/C_g\right) + 4r_i g_{ds}} \\ &\approx \frac{f_t}{8\pi R_{g,i} C_{gd} f^2} \end{aligned} \tag{7.83}$$

in which the simplifying assumption $(R_{g,i} + r_i)g_{ds} \ll g_m R_{g,i} C_{gd}/C_g$ is made. To first order, the maximum achievable power gain of a MOSFET is proportional to the device's f_t, and the maximum achievable power gain is inversely proportional to the device's intrinsic gate resistance, $R_{g,i}$. Note that linear amplification is assumed in Eqs. (7.82) and (7.83). Equation (7.83) therefore applies to small-signal analyses such as for a receiver front-end, and would possibly be inadequate for describing the maximum power gain achievable using a nonlinear power amplifier in the transmitter portion of a transceiver.

Unity Power Gain Frequency: f_{max}

The third important figure of merit for MOSFET transistors operating at radio frequencies is the maximum frequency of oscillation, f_{max}. This is the frequency at which the maximum available power gain of the transistor is equal to one. An estimate of f_{max} for MOSFET transistors operating in saturation is found from Eq. (7.83) by setting $G_{\text{max}} = 1$ and is given by,

$$f_{\text{max}} = \sqrt{\frac{f_t}{8\pi R_{g,i} C_{gd}}} \tag{7.84}$$

From a designer's perspective, f_{max} can be optimized by a combination of proper device layout and careful choice of the operating bias point. From Eq. (7.81) $f_t \propto g_m$, therefore $f_{\text{max}} \propto \sqrt{g_m}$, and hence g_m should be maximized. Maximizing g_m requires some combination of increasing the gate-source overdrive, increasing device bias current I_{DS}, or increasing the device width. Note that increasing the device width will increase $R_{g,i}$ and reduce f_{max} unless a fingered layout is used.

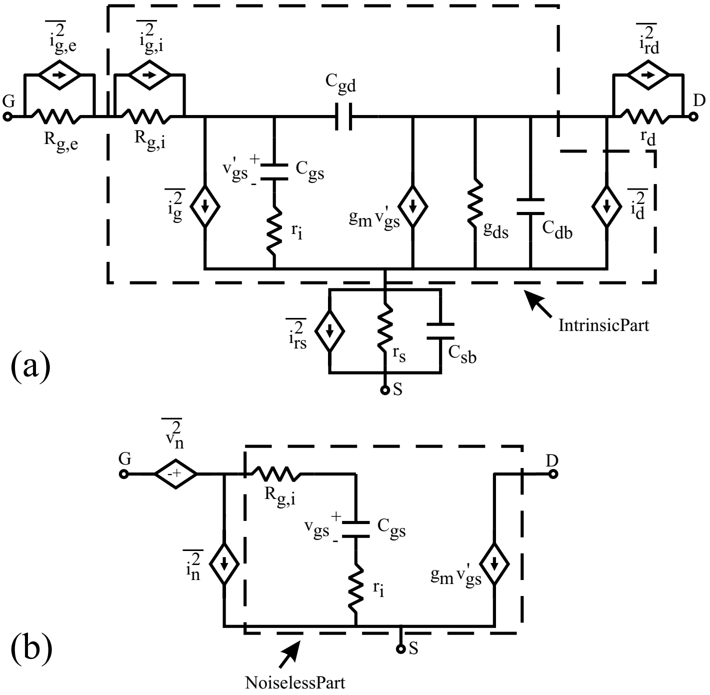

FIGURE 7.71 MOSFET small-signal noise model. (a) High-frequency small-signal model augmented with noise sources, (b) input-referred noise model.

MOSFET Noise Sources

The intrinsic and extrinsic noise sources in a MOSFET operating at microwave frequencies are predominantly thermal in origin. The extrinsic noise arises from the parasitic resistances found at the MOSFET terminal connections, and the metal to semiconductor junctions found at the contacts at these terminals. The intrinsic noise arises from three important sources:

- Drain channel noise, $\overline{i_d^2}$, which is the noise generated by the carriers in the channel region and appears as a noise current;
- Gate resistance noise, $\overline{v_{rg}^2}$, which is the thermal noise due to the resistance of the distributed gate material;
- Induced gate noise, $\overline{i_g^2}$, which is a gate noise current that is capacitively coupled onto the gate from the distributed noise generated by the carriers in the channel and the distributed channel charging resistance. Induced gate noise is one of the main components of noise within the intrinsic portion of a MOSFET transistor.

MOSFET Noise Models

The noise sources discussed previously can be added to an appropriate lumped network model of a MOSFET transistor. The small-signal equivalent circuit shown in Fig. 7.71(a) incorporates the noise sources that are important at radio frequencies. The model is essentially the same model as presented in Fig. 7.68 except for the inclusion of the thermally generated noise. It is possible to refer all of the internal MOSFET noise sources to the gate input as shown in Fig. 7.71(b). This procedure is discussed in a later section for optimum noise matching. The various noise sources are now described.

Gate Resistance Noise

The resistance of the gate material, given by $R_g = (W \times R_\square)/(N \times L)$, where $R_\square$ is the sheet resistance of the gate material, contributes to the thermal noise present in the device. The lumped resistor shown at the gate of the MOSFET in Figs. 7.68 and 7.71(a) is intended to represent the thermal noise resistance of the distributed gate material. The value of this resistor is dependent upon whether the gate is connected from one end or both ends, and can be approximated analytically by treating the gate as a transmission line along its width, since for practical radio frequency MOSFET dimensions $W \gg L$. In the case of the gate connected from one end only, $R_{g,i} = R_g/3$. When the gate is connected from both ends, $R_{g,i} = R_g/12$. In terms of the equivalent gate resistance and the transistor's dimensions, the gate resistance noise is given by,

$$\overline{v_{g,i}^2} = 4kTR_{g,i}\Delta f \tag{7.85}$$

where k is Boltzmann's constant and T is the temperature in Kelvin. Note that the gate resistance noise is proportional to the width, inversely proportional to the length of the device, and scales in inverse proportion to the number of fingers used in the transistor layout.

Thermal Channel Noise

Thermal noise within the channel produces both drain channel noise and induced gate noise. Since both the channel drain noise and the induced gate noise are generated by the same physical noise sources, they exhibit a degree of correlation. The normalized correlation coefficient between the drain current noise and the gate current noise is in general a complex quantity given by the expression,[21]

$$c = \frac{\overline{i_g i_d^*}}{\sqrt{\overline{i_g i_g^*} \cdot \overline{i_d i_d^*}}} \tag{7.86}$$

Simulations and experimental measurements indicate that the real part of "c" in Eq. (7.86) is approximately equal to zero. Intuitively this makes sense because the gate noise is induced from the channel current noise capacitively. There is, therefore, a 90° phase shift between the induced gate current noise and the source of this noise, which is the channel current noise.

The value of "c" has been found for low frequencies and longer gate lengths as c = –j0.395.[21] For submicron MOSFETs, and as the frequency of operation increases, c approaches –j0.3.

Channel noise — The drain channel noise is a complicated function of the transistor bias conditions. For radio frequency applications, the MOSFET is assumed to operate in the saturation region and the drain channel noise is given approximately by

$$\overline{i_d^2} = 4kT\gamma g_{do}\Delta f \tag{7.87}$$

where γ is a bias dependent parameter and g_{do} is the zero drain voltage conductance of the channel. Usually $g_{do} = g_m$ is assumed. The factor γ is an increasing function of V_{DS}, but a value of 2/3 is often used for hand calculations and simple simulations. For quasi-static MOSFET operation, $\overline{i_d^2}$ is essentially independent of frequency.

Induced gate noise — Fluctuations in the channel are coupled to the transistor gate via the oxide capacitance. This produces a weak noise current at the gate terminal. The mean square value of this noise current was evaluated by van der Ziel[21] and is approximated by,

$$\overline{i_g^2} = 4kT\beta g_{do}\frac{\left(\omega C_{gs}\right)^2}{k_{gs}g_{do}}\Delta f \tag{7.88}$$

where β is a bias-dependent parameter typically greater than or equal to 4/3. The factor $1/k_{gs}$ arises from a first-order expansion that gives $k_{gs} = 5$ for long channel devices. Interestingly, the induced gate noise is proportional to the square of the frequency. Clearly this expression cannot hold as the frequency becomes extremely large. The expression given in Eq. (7.88) is valid up to approximately $\frac{2}{3}f_t$.

1/f-Noise

Experimental measurements of the noise spectral density in MOSFETs demonstrate that the noise increases with decreasing frequency. The noise spectral density at very low frequencies exceeds the noise levels predicted for purely thermally generated noise. This excess noise is evident up to a corner frequency of approximately 100 kHz to 1 MHz for MOSFETs. The low-frequency excess noise is generally known as a flicker noise, and its spectral density is inversely proportional to the frequency raised to some power. Due to this inverse relationship to frequency, flicker noise is also called 1/f-noise or "pink" noise.

There are two dominant theories on the origins of 1/f-noise in MOSFETs. First, there is the carrier density fluctuation theory in which flicker noise is taken as a direct result of the random trapping and release of charges by the oxide traps near the Si-SiO$_2$ interface beneath the gate. The channel surface potential fluctuates because of this charge fluctuation, and the channel carrier density is in turn modulated by the channel surface potential fluctuation. The carrier density fluctuation theory predicts that the input-referred flicker noise is independent of the gate bias voltage and the noise power is proportional to the interface trap density. The carrier density fluctuation model is supported by experimental measurements that demonstrate the correlation between the flicker noise power and the interface trap density.

The second major theory on the origins of flicker noise is the mobility fluctuation theory. This theory treats flicker noise as arising from the fluctuation in bulk mobility based on Hooge's empirical relation for the spectral density of flicker noise in a homogenous medium. In contrast with the charge density fluctuation theory, the mobility fluctuation theory does predict that the power spectral density of 1/f-noise is dependent upon the gate bias voltage.

Neither of these two main theories satisfactorily accounts for the observed 1/f-noise power spectral density in MOSFETs under all conditions. Current thinking applies both models for an overall understanding of 1/f-noise in MOSFETs. Expressions for the MOSFET 1/f-noise have been derived by various researchers and normally some amount of "fitting" is required to agree with theory. Common expressions for the 1/f-noise of a MOSFET operating in saturation include

$$\overline{di_f^2} = K_f \frac{g_m^2}{C'_{ox} W L} \frac{df}{f^a} \tag{7.89}$$

for the flicker-noise current, and

$$\overline{dv_{in,f}^2} = K_f \frac{1}{C'_{ox} W L} \frac{df}{f^a} \tag{7.90}$$

for the equivalent input noise voltage. The value of α is typically close to unity, and K_f is in general a bias-dependent parameter, on the order of 10^{-14} C/m^2 for PMOS devices and 10^{-15} C/m^2 for NMOS devices.

Although 1/f-noise is negligible at radio frequencies, it is still an important consideration for transceiver design. For example, 1/f-noise can be a limiting factor in direct conversion receivers. Since the direct conversion receiver directly translates the signal channel of interest to base band, the 1/f-noise corrupts the desired information content. Modern modulation formats place important information signal content near the center of a channel. When such a channel is directly downconverted to DC, this important central region experiences the worst of the 1/f-noise contamination. If the 1/f-noise degrades the signal-to-noise ratio sufficiently, reception becomes impossible.

A second area of transceiver design in which 1/f-noise can create problems and cannot be ignored involves oxillator design. The close-in phase noise of an oscillator is normally dominated by 1/f-noise. At frequencies close to the oscillator center frequency, the phase noise fall off is typically –30 dB per decade, while further from the center frequency the phase noise fall off is normally –20 dB per decade. The additional phase noise close to the center frequency can be attributed to flicker noise present in the active devices comprising the oscillator circuitry.

Designers seeking to minimize 1/f-noise have four options. First, the choice of technology and process is important since the flicker noise exhibited by devices of equal sizes across different processes can vary significantly. Second, a designer can opt to use PMOS devices instead of NMOS devices since PMOS devices typically exhibit one tenth the amount of flicker noise a comparable NMOS device produces. Thirdly, devices operating in weak inversion exhibit markedly lower 1/f-noise than devices operated in saturation. However, operating in weak inversion is normally not an option for devices working at radio frequencies, since the device f_t is too low in the weak inversion region. Finally, as shown in Eqs. (7.89) and (7.90), the area of the device plays an important role in determining the flicker noise produced by the device, and so the area should be maximized. Unfortunately, for radio frequency designs there are constraints on the maximum practical width and length of the MOSFETs. Both the width and length determine the highest usable operating frequency of the device and so they are normally kept small. Small width and length implies that the flicker noise of devices designed for operation at radio frequencies is comparatively large.

Extrinsic Noise

The primary extrinsic noise sources of concern are due to the parasitic resistances at the MOSFETs terminals. The corresponding mean-square noise currents due to these parasitic resistances are given by,

$$\begin{aligned}
\overline{i_{D,e}^2} &= \frac{4kT}{R_{D,e}}\Delta f \\
\overline{i_{S,e}^2} &= \frac{4kT}{R_{S,e}}\Delta f \\
\overline{i_{G,e}^2} &= \frac{4kT}{R_{G,e}}\Delta f \\
\overline{i_{B,e}^2} &= \frac{4kT}{R_{B,e}}\Delta f
\end{aligned} \tag{7.91}$$

where $R_{D,e}$, $R_{S,e}$, $R_{G,e}$ and $R_{B,e}$, are the extrinsic parasitic resistances at the drain, source, gate, and bulk, respectively.

MOSFET Design for RF Operation

Radio frequency integrated circuit design with CMOS requires numerous choices regarding device dimensions and bias voltages and currents. A combination of microwave theory and analog design fundamentals must be pooled with a firm knowledge of the overall system-level functional requirements. System-level calculations will normally dictate the allowable gain, linearity, and noise of the basic circuitry. Two important aspects of radio frequency design in CMOS involve MOSFET input impedance matching for power gain, and impedance matching for minimum noise figure. These two important topics are discussed next.

MOSFET Impedance Matching

Circuitry that accepts a signal from off-chip, such as the input to a receiver's low noise amplifier, must be conjugately matched to the source impedance. The concept of conjugate matching is often unfamiliar to digital designers of CMOS, but is a common theme in microwave design. When a source and load are conjugately matched, maximum power transfer from the source to the load occurs. Input impedance matching is also important because pre-select filters preceding the low noise amplifier may be sensitive to the quality of their terminating impedances.

A load is conjugately matched to its driving impedance when the input impedance of the load equals the complex conjugate of the driving impedance. Since the input impedance of any two-port network is given by,

$$Z_{in} = \frac{y_{22}}{y_{11}y_{22} - y_{21}y_{12}} \tag{7.92}$$

the y-parameters given in Table 7.6 can be used in conjunction with circuit analysis to give the total circuit input impedance. Note that a linear system has been tacitly assumed in Eq. (7.92). For small-signal applications, such as in the receiver portion of a transceiver, linearity is a reasonable assumption. However, for some applications, such as a nonlinear power amplifier, conjugate matching is not possible and so a resistive load line is used instead.

While matching can be augmented by a high-Q matching network constructed off-chip, this method adds expense to mass-market products, in which commodity radio frequency ICs may terminate an unknown length of transmission line. It is therefore desirable to provide as close to a stable 50 Ω input impedance as possible within the integrated circuit. The quality of the external matching network can then be relaxed.

As an example of input impedance matching, consider the common source low noise amplifier configuration shown in Fig. 7.72. The matching components include L_1, which is typically implemented as a bond wire having a value of 1 to 2 nH. Inductor L_1 is used for producing the real part of the input impedance for matching. For simplicity, the bonding pad capacitance is ignored. The LNA is assumed to be operating in a cascode configuration and so the Miller capacitance of the MOSFET is ignored. Conjugate matching to the source resistance R_S requires that the approximate matching condition $R_g + \frac{g_m}{C_{gs}} L_1 = R_S$ is satisfied. Proper choice of the device width, biasing, and number of fingers used for construction allow this relation to be met. Note that $2\pi f_t \approx g_m/C_{gs}$, and as discussed in the section on Maximum Available Power Gain, the maximum achievable power gain of a MOSFET is proportional to the device's f_t. Also, as shown in the next section, the device noise figure is inversely proportional to f_t. Hence the MOSFET biasing should be designed such that the resulting f_t is adequate for the application.

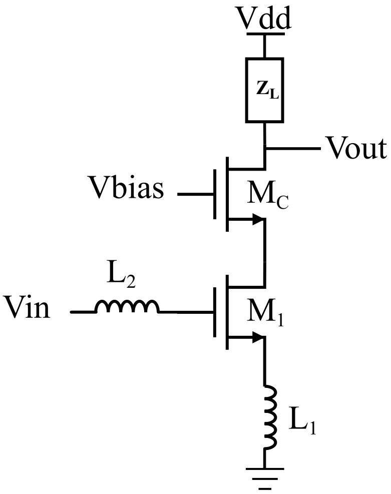

FIGURE 7.72 Common-source low-noise amplifier configuration.

Matching for Noise

Classical noise matching analysis is applicable to the MOSFET shown in Fig. 7.71(b). Classical methods are directly applicable when all MOSFET internal noise sources are referred to the input. For the common source MOSFET configuration shown in Fig. 7.71(b), the input referred noise sources v_n and i_n are given by,

$$v_n = v_{g,i} - \frac{i_d}{g_m} + \left(R_{g,i} + r_i\right)i_g - j\frac{f}{f_t}\left(R_{g,i} + r_i\right)i_d \tag{7.93}$$

and

$$i_n = i_g - j\frac{f}{f_t}i_d \tag{7.94}$$

Recall from the section on Thermal Channel Noise that the two noise sources in Eqs. (7.93) and (7.94) are correlated since i_d and i_g arise from the same physical process.

The noise performance of a transistor with driving impedance $Z_{SS} = R_{SS} + jX_{SS}$ is fully described in terms of four noise parameters: the minimum noise figure ($F_{\min}$), the noise conductance (G_n), and the optimum driving impedance (Z_{opt}), which consists of a resistance (R_{opt}) and a reactance (X_{opt}). Following the procedure of Gonzalez[13] the noise parameters are found as,

$$G_n \approx \left(\frac{f}{f_t}\right)^2 \gamma g_{do} F_1 \tag{7.95}$$

$$R_{opt} \approx \sqrt{\left(R_{g,i} + r_i\right)^2 + \left(\frac{f_t}{f}\right)^2 \frac{R_{g,i}F_4}{\gamma g_{do}} + \left(\frac{f_t}{f}\right)^2 \frac{F_2^{\,2} F_5}{\gamma g_{do}^{\,2} F_1}} \tag{7.96}$$

$$X_{opt} \approx \frac{F_2}{2\pi f C_{gs}} \approx -F_2 X_{in} \tag{7.97}$$

and

$$\begin{aligned} F_{\min} &\approx 1 + 2G_n\left(R_{opt} + R_{g,i} + r_i\right) \\ &\approx 1 + 2F_3 \frac{f}{f_t}\sqrt{\gamma g_{do} R_{g,i}} \end{aligned} \tag{7.98}$$

The factors $\{F_1, F_2, F_3, F_4, F_5\}$ result from algebraic manipulations of Eqs. (7.93) and (7.94). If induced gate noise is ignored, then $\{F_1, F_2, F_3, F_4\}$ are all equal to one, otherwise they are less than one. The fifth factor, F_5, is equal to zero if induced gate noise is ignored, and equal to one if induced gate noise is included. From Eq. (7.98) the minimum noise figure is proportional to $\sqrt{R_{g,i}}$. Therefore to realize a low noise figure the intrinsic gate resistance must be made as small as practical. Noting that g_{do} in Eq. (7.98) is approximately equal to g_m, and using the results for f_t from Eq. (7.81), the minimum noise figure is shown to be inversely proportional to $\sqrt{g_m}$. Hence, increasing the g_m of the device decreases the minimum noise figure. Since both g_m and γ are functions of the transistor bias conditions, an optimum biasing point can be found that gives the lowest minimum noise figure.[20]

For optimum noise matching, the optimum noise resistance should equal the driving source resistance. For MOSFETs, near-optimum noise matching is possible by correctly choosing the number of gate fingers used to construct the MOSFET. In Fig. 7.71(b), the equivalent input noise current i_{eq} and noise voltage v_{eq}, yield a transistor noise figure given by

$$F = F_{\min} + \frac{G_n}{R_S}\left|R_S - Z_{opt}\right|^2 \tag{7.99}$$

where R_S is the driving source resistance, G_n is the noise conductance of a single finger, and Z_{opt} is the optimum noise impedance. Neglecting interconnect parasitics, if N MOSFETs are placed in parallel, the equivalent noise current is $i_{eq}^{(N)} = i_{eq}\sqrt{N}$ and the equivalent noise voltage is $v_{eq}^{(N)} = v_{eq} = v_{eq}/\sqrt{N}$. The noise figure for the complete MOSFET consisting of N fingers is then given by

$$F = F_{\min} + \frac{NG_n}{R_S}\left|R_S - \frac{Z_{opt}}{N}\right|^2 \tag{7.100}$$

TABLE 7.7 MOSFET Scaling Rules for the Saturation Region

	Parameter	Number of Fingers N	Finger Width W	Bias Current	
				$I_{DS} < I_{DS,sat}$	$I_{DS} > I_{DS,sat}$
Performance	g_m	N	W	Increases with I_{DS}	~constant
	f_t	Independent	Independent	Increases with I_{DS}	~constant
	$f_{\max}$	Independent	~$1/W$	Increases with I_{DS}	~constant
Parasitics	C_{gs}, C_{gd}	N	W	~constant	~constant
	r_d, r_s, r_i	$1/N$	$1/W$	Independent	Independent
	$R_{g,i}$	$1/N$	W	Independent	Independent
Noise	$F_{\min}$	Independent	~$1/W$	Decreases with I_{DS}	Increases with I_{DS}
	G_n	N	W	Increases with I_{DS}	~constant
	R_{opt}	$1/N$	~$1/W$	Decreases with I_{DS}	~constant
	X_{opt}	$1/N$	$1/W$	Independent	Independent

in which the minimum noise finger is independent of the number of fingers, but the noise conductance scales as N, and the optimum noise impedance scales as 1/N. Therefore, by using fingered MOSFETs, the transistor can be matched for noise using the number of fingers as a design parameter.

MOSFET Layout

Radio frequency MOSFET layout is a nontrivial task. A poor transistor layout adversely affects every aspect of the transistor's radio frequency performance. Recall that a MOSFET's $f_{\max}$, $NF_{\min}$, and input impedance-matching characteristics are all determined by the transistor's W/L ratio and the number of fingers used to construct the device. Additionally, both matching and flicker noise are affected by the area of the gate. Devices with a large gate area will match better and have lower flicker noise.

The various scaling rules for MOSFETs operating in saturation appear in Table 7.7. The MOSFET length is assumed to be the minimum allowed. Also shown in Table 7.7 is the effect of biasing upon the MOSFET. A typical design trade-off is between maximum gain and maximum $f_{\max}$, assuming power requirements are a secondary concern. Using multiple MOSFET fingers is a convenient way of improving the device performance.

Fingered Layout

MOSFETs designed for radio frequency applications normally have large W/L ratios. This is primarily so that the MOSFET has a large transconductance and therefore has a large f_t so that its noise figure is minimal. As shown in Table 7.7, increasing the MOSFET width causes a decrease in $f_{\max}$. To counteract this effect, the MOSFET is laid out as a parallel connection of narrower MOSFETs. The resulting fingered structure is shown in Fig. 7.73. Neglecting the interconnect resistance between fingers, the intrinsic gate resistance scales as $1/N$, where N is the number of fingers.

Substrate Connections

Parasitic resistance to the substrate affects both the impedance matching and the noise figure of MOSFETs. The substrate resistance is in general bias dependent. Local variations in threshold voltage are therefore possible, and matching between devices is reduced. This may affect the performance of differential pairs and differential circuitry. Voltage fluctuations induced in the substrate, especially by digital clocks and switching circuitry, will raise the noise figure of radio frequency analog MOSFETs. Adequate substrate connections are therefore important for low-noise, precision MOSFET design. A substrate connection method is shown in Fig. 7.73.

The Future of CMOS

CMOS has definite potential for applications in commodity radio frequency electronics, and is expected to find increased use in radio frequency integrated circuits. Although this section has considered CMOS operating at radio frequencies mostly in terms of analog small-signal performance, it is important to note that existing implementations of digital logic are also operating at radio frequencies. Microprocessors

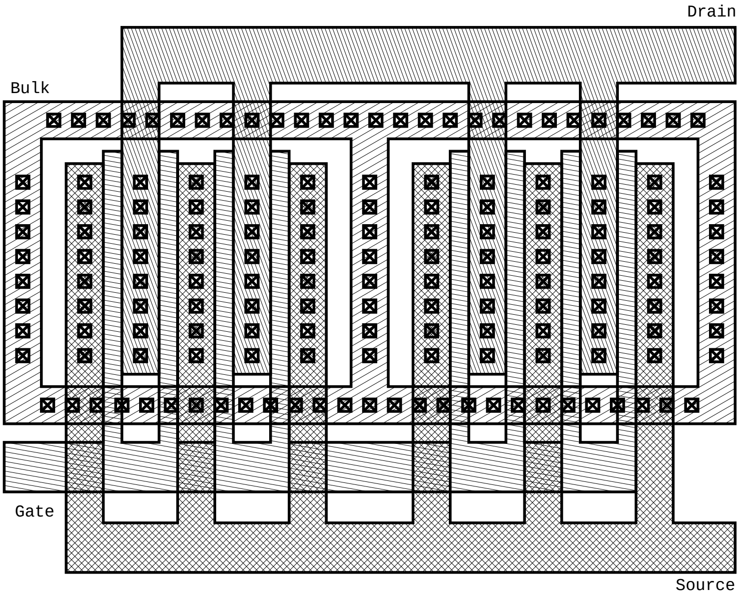

FIGURE 7.73 MOSFET finger layout style for high frequency applications.

operating above 1 GHz are now commonplace. The modeling of radio frequency logic (RFL) and the study of radio frequency digital design will be important contributing factors for future high-speed microprocessors, digital signal processors, and ASICs. Additionally, as the demand for extremely high-speed digital microprocessors increases, the base-level digital CMOS processes will improve to accommodate the performance expectations of designers. Exotic process features that were once considered purely for analog design use are now appearing in digital designs.

CMOS is not the ideal radio frequency technology, but it does compare favorably with bipolar and BiCMOS. For example, although not discussed in this section, communications circuits constructed with CMOS devices often exhibit higher linearity than their counterparts do when constructed with other technologies such as bipolar. Furthermore, in applications where the MOSFET's square-law characteristic applies, differential circuitry can effectively reduce second-order distortion. For an LNA constructed using deep submicron MOSFETs operating in velocity saturation, the device transconductance is essentially constant with v_{gs}, which implies an increased level of linearity.

CMOS may become the technology of choice in the near term for consumer radio frequency applications in the sub-10 GHz bands. The extent to which this becomes possible is dependent on the ability of the device performance to improve as the technology scales and improves. With this in mind, this section concludes with a brief examination of scaling issues in radio frequency CMOS, and recent advances in MOSFET manufacture.

The Impact of Technology Scaling and Process Improvements

A common measure for the gain efficiency of a MOSFET is its transconductance per drain current g_m/I_{DS}. MOSFETs require a large W/L ratio and a high DC biasing current to offer a transconductance comparable to that of other RF device technologies, such as bipolar. In bipolar transistors, the transconductance-to-bias current ratio equals kT/q, which was proved by Johnson[22] to be the maximum transconductance for both MOSFET and bipolar devices. As MOSFET processing improves and the minimum gate length decreases, the g_m/I_{DS} ratio has been found to tend toward the maximum value of kT/q.

Continual reduction in MOSFET minimum gate length has enabled commensurate increases in device f_t and $f_{\max}$. Existing 0.18 µm devices have demonstrated f_t's in excess of 60 GHz, and experimental processes with gate lengths less than 0.1 µm have demonstrated f_t values in the order of 150 GHz. These increases in device f_t also mean that the overall device noise performance improves as the gate length scales down.

Although the radio frequency performance of MOSFETs has traditionally scaled in accordance with a decreasing minimum gate length, this trend will probably not continue along its present path. For example, the gate oxide thickness scales approximately linearly with the minimum gate length. The gate source capacitance therefore remains roughly constant per unit width of the gate for minimum channel length devices. As shown in Eq. (7.81), the MOSFET f_t is inversely proportional to the gate source capacitance, and if the gate source capacitance does not scale in inverse proportion to the gate length, it becomes a limiting factor. Other limitations for increased radio frequency performance of MOSFETs are found in the extrinsic parasitics, such as the gate overlap capacitances. For example, the gate-source overlap capacitance does not scale as 1/L for submicron devices, and C_{gso} becomes an increasingly large proportion of the total gate-to-source terminal capacitance, therefore limiting the high frequency gain of the device.

Certain process enhancements have a profound effect upon the performance of integrated MOSFET circuitry. The use of copper interconnects between MOSFETs is expected to increase the operating frequency of both digital and analog circuitry when used in place of aluminum. Copper has two primary advantages over aluminum when used as an interconnect material. First, the resistivity of copper is approximately 40% lower than that of aluminum. Second, electromigration effects are lower in copper interconnects implying that copper interconnects will exhibit higher reliability, longer life spans, and greater current-handling capability.

Since copper has a lower resistivity than aluminum, interconnect lines can be thinner and yet still allow for the same circuit performance. Alternatively, maintaining the same interconnect thickness gives a lower series resistance. Decreasing the series resistance of metal lines improves the quality factor of integrated inductors and capacitors.

Recent CMOS processes have given designers six or more interconnect metal layers. The increased number of metal layers has important consequences for radio frequency design. For example, several metal layers can be linked in parallel in order to decrease the series resistance of metal lines used to create inductors. Additionally, the top-level metal layers may be used so that the metal-to-substrate capacitance is reduced and therefore the quality factor of the integrated circuit is improved.

While not yet offered on any commodity CMOS processes, substrate etching has been used to increase the quality factor of integrated inductors by removing a section of substrate below the metal lines. Isolation between lower-level metal lines and substrate has also been achieved using patterned ground shields and spun-on thick dielectrics. Future process enhancements will increase the applicability of CMOS to radio frequency applications. Sub-micron mixed-signal processes featuring six metal layers, metal-insulator-metal capacitors, deep n-wells, and threshold voltage-adjust capability are available now, and hint at what will become available in the near future.

To conclude, CMOS is a mature, easily sourced, and reliable technology. If the performance of CMOS can be improved via scaling to within that of bipolar, BiCMOS, and GaAs, there is no reason why it will not supplant those technologies in commodity radio frequency integrated circuit applications.

References

1. Tsividis, Y. P., *Operation and Modeling of the MOS Transistor*, New York: McGraw-Hill, 1987.
2. Sze, S. *Physics of Semiconductor Devices*, New York: Wiley and Sons, 1981.
3. Grove, A. *Physics and Technology of Semiconductor Devices*, New York: Wiley and Sons, 1967.
4. Muller, R. and Kamins, T. *Device Electronics for Integrated Circuits*, New York: Wiley and Sons, 1986.
5. Laker, K. R. and Sansen, W. M. C. *Design of Analog Integrated Circuits and Systems*, New York: McGraw-Hill, 1994.
6. Enz, C. C. and Cheng, Y., MOS Transistor Modeling for RF IC Design, *IEEE Journal of Solid-State Circuits*, 35, 186–201, Feb. 2000.

Staudinger, Joseph et al. "CAD, Simulation, and Modeling"
The RF and Microwave Handbook
Editor in Chief Mike Golio
Boca Raton: CRC Press LLC,2001

8

CAD, Simulation, and Modeling

Joseph Staudinger
Motorola

Manos M. Tentzeris
Georgia Institute of Technology

Daniel G. Swanson, Jr.
Bartley R.F. Systems

Michael B. Steer
North Carolina State University

John F. Sevic
Ultra RF, Inc.

Michael Lightner
University of Colorado

Ron Kielmeyer
Motorola

Walter R. Curtice
W. R. Curtice Consulting

Peter A. Blakey
Motorola

8.1 System Simulation

Joseph Staudinger

The concept of system simulation is an exceptionally broad topic. The term itself, system, does not have a rigid definition and in practice the term is applied to represent dramatically differing levels of circuit integration, complexity, and interaction. In a simple sense, the term is applied to represent the interconnection and interaction of several electrical circuits. In a broader sense, such as in communication systems, the term may be applied to represent a much higher level of complexity including part of, or the composite mobile radio, base unit, and the transmission medium (channel). Regardless of complexity of the level, the issue of simulation is of critical importance in the area of design and optimization.

As one might expect, the techniques and methods available in the engineering environment to simulate system level performance are quite diverse in technique and complexity [1–3]. Techniques include mathematically simple formula-based methods based upon simplified models of electrical elements. Such methods tend to be useful in the early design phase and are applied with the intent of providing insight into performance level and trade-off issues. While such methods tend to be computationally efficient allowing simulations to be performed rapidly, accuracy is limited in large part due to the use of simplified models representing electrical elements. Other techniques tend to be computationally intensive CAD-based where waveforms are generated and calculated throughout the system. The waveform level technique is more versatile and can accommodate describing electrical elements to almost any level of detail required, thereby exploring the system design and performance space in fine detail. The models may be simple or complex in mathematical form. In addition, it is possible to use measured component data (e.g., scattering parameters) or results from other simulators (e.g., small- and large-signal circuit simulations using harmonic balance where the active device is represented by a large-signal electrical model). The price for the improvement in accuracy is significantly longer, perhaps much longer simulation times and the requirement to very accurately describe the characteristics of the electrical components.

The intent of this section is to examine fundamental issues relative to simulating and evaluating performance of microwave/RF related system components. A number of terms describing system level performance characteristics will be examined and defined. In addition, first order methods for calculating the performance of systems consisting of cascaded electrical circuits will be examined. To begin, consider three parameters of interest in nearly all systems: gain, noise figure (*NF*), and intermodulation distortion (*IMD*).

Gain

A usual parameter of interest in all systems is the small signal (linear) gain relationship describing signal characteristics at the output port relative to the input port and/or source for a series of cascaded circuits. Numerous definitions of gain have been defined in relationship to voltage, current, and power (e.g., power gain can be defined in terms of transducer, available, maximum stable, etc.) [1]. In general for system analysis, the concept of transducer power gain (G_T) is often applied to approximate the small signal gain response of a series of cascaded elements. Transducer power gain (G_T) is defined as the magnitude of the forward scattering parameter (S_{21}) squared (i.e., $G_T = |S_{21}|^2$, the ratio of power delivered to the load to that available from the source). This assumes the source (Γ_S) and load (Γ_L) voltage reflection coefficient are equal to zero, or alternatively defined as a terminating impedance equal to characteristic impedance Z_0 (typically 50 ohms).

Consider several two-port networks cascaded together as illustrated in Fig. 8.1 where the transducer power gain of the ith element is represented as G_{Ti}. The transducer power gain of the cascaded network is:

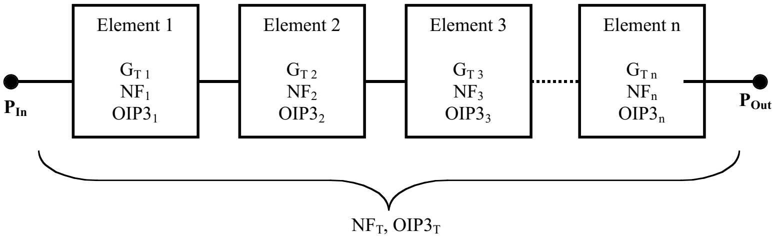

FIGURE 8.1 System formed by cascading three electrical elements.

$$G_{T_T} = G_{T1}\left(dB\right) + G_{T2}\left(dB\right) + G_{T3}\left(dB\right) + \ldots G_{Tn}\left(dB\right) \tag{8.1}$$

The accuracy of Eq. (8.1) relies on the assumption that that ith two port network is terminated by characteristic impedance Z_0 per the above definition. In practice, the source and load termination provided to the ith element is defined by the ith – 1 and ith + 1 elements, respectively. Even though in a well-designed subsystem, each two-port network is designed such that the input (S_{11}) and output (S_{22}) scattering parameters are near zero in magnitude, they cannot be exactly zero resulting in impedance mismatch effects. Hence, Eq. (8.1) is approximate and its accuracy dependent on each element satisfying the above criteria. A more thorough analysis accounting for impedance mismatches can be performed at the expense of more complexity. In general this requires a more precise description of each element using perhaps some form of network parameters. For example, the T and scattering parameters (T_T and S_T, respectively) for two networks, A and B, cascaded together are given by [3,7]

$$T_T = \begin{bmatrix} T_{11}^A & T_{12}^A \\ T_{21}^A & T_{22}^A \end{bmatrix} \begin{bmatrix} T_{11}^B & T_{12}^B \\ T_{21}^B & T_{22}^B \end{bmatrix} \tag{8.2}$$

$$S_T = \begin{bmatrix} S_{11}^A & 0 \\ 0 & S_{22}^B \end{bmatrix} + \begin{bmatrix} S_{12}^A & 0 \\ 0 & S_{21}^B \end{bmatrix} \begin{bmatrix} -S_{22}^A & 1 \\ 1 & -S_{11}^B \end{bmatrix}^{-1} \begin{bmatrix} S_{21}^A & 0 \\ 0 & S_{12}^B \end{bmatrix} \tag{8.3}$$

While the above methods allow an exact analysis for cascaded linear circuits, it is often difficult to apply them to practical systems since the network parameters for each of the elements comprising the system are usually not known precisely. For example, in systems consisting of interconnected circuits, board layout effects (e.g., coupling between elements) and interconnecting structures (board traces) must also be included in applying the network analysis techniques shown in Eqs. (8.2) and (8.3). This, of course, requires accurate knowledge of the electrical nature of these structures, which is often unknown. In critical situations, the network parameters for these elements can be determined by measurement or through the use of electromagnetic simulations assuming the geometrical and physical nature of these structures are known.

Noise

A second parameter of interest important to all systems is noise. In receivers, noise performance is often specified by noise figure, defined as

$$NF\left(dB\right) = \frac{S_i/N_i}{S_o/N_o} \tag{8.4}$$

where S_i/N_i and S_o/N_o are the signal-to-noise ratio at the input and output ports, respectively. Note that *NF* is always greater than or equal to unity (0 dB). When several circuits are cascaded together as illustrated in Fig. 8.1, the cascaded noise figure (NF_T) is given by

$$NF_T = NF_1 + \frac{NF_2 - 1}{G_1} + \frac{NF_3 - 1}{G_1 G_2} + \frac{NF_4 - 1}{G_1 G_2 G_3} + \ldots \frac{NF_n - 1}{G_1 G_2 G_3 \ldots G_n} \tag{8.5}$$

where G_i and NF_i are the gain and noise figure of the ith element, respectively. Note the importance of the contribution of the first element's noise figure to the total cascaded noise figure. Hence, the noise figure of the low noise amplifier contained in a receiver is a major contributor in setting the noise performance of the receiver.

Intermodulation Distortion

Intermodulation distortion (IMD) has been a traditional spectral measure (frequency domain) of linearity applied to both receiver and transmitter elements. The basis of *IMD* is formed around the concept that the input-output signal relationship of an electrical circuit can be expressed in terms of a series expansion taking the form:

$$E_o = a_1 E_{in} + a_2 E_{in}^2 + a_3 E_{in}^3 + a_4 E_{in}^4 + a_5 E_{in}^5 + \ldots \tag{8.6}$$

where E_{in} and E_o are instantaneous signal levels at the input and output ports of the electrical circuit, respectively. If the circuit is exactly linear, all terms in the expansion are zero except for a_1 (i.e., gain). In practice, all circuits exhibit some nonlinear behavior and hence higher order coefficients are nonzero. Of particular interest is the spectral content of the output signal when the circuit is driven by an input consisting of two sinusoids separated slightly in frequency taking the form

$$E_{in}(t) = \cos(\omega_1 t) + \cos(\omega_2 t) \tag{8.7}$$

where ω_1 and ω_2 are the angular frequencies of the input stimuli and where ω_2 is slightly greater than ω_1. The output signal will exhibit spectral components at frequencies $m\omega_1 \pm n\omega_2$, m = 0,1,2, … and n = 0,1,2, … as illustrated in Fig. 8.2. Notice that the third series term (a_3 Ein^3) generates spectral tones at $2\omega_1 - \omega_2$ and $2\omega_2 - \omega_1$. These spectral components are termed third order intermodulation distortion (*IM*3). It can also be shown that series terms greater than three also produce spectral components at these frequencies and hence the total *IM*3 is the vector sum from Ein^3, Ein^4…. In a similar manner, higher order IMD products exist (e.g., *IM*5 @ $3\omega_1 - 2\omega_2$ and $3\omega_2 - 2\omega_1$) due to the higher order series terms. Notice however, that all IMD products are close in frequency to ω_1 and ω_2, fall within the desired frequency

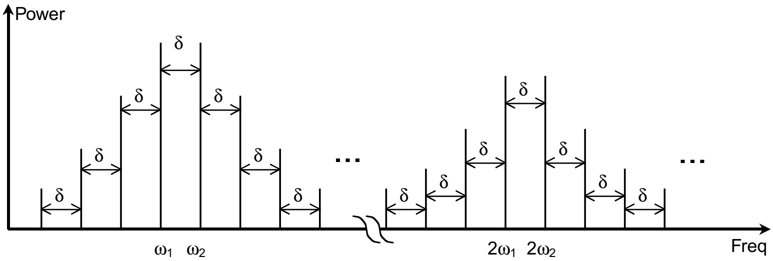

FIGURE 8.2 Resultant spectrum representing the nonlinear amplification of two equal amplitude sinusoidal stimuli at frequencies ω_1 and ω_2 ($\delta = \omega_2 - \omega_1$).

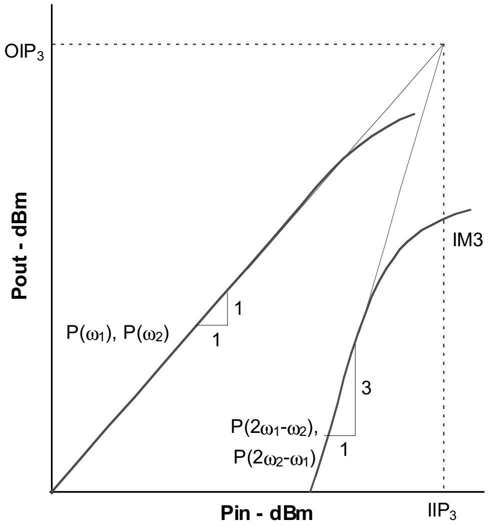

FIGURE 8.3 Expected relationship between fundamental frequency components and third order intermodulation distortion products neglecting effects due to higher order series coefficients.

band of the circuit, and hence cannot be removed by external filtering. In practice, third order products are often the highest in magnitude and thus of greatest concern, although in some cases 5th and higher order products may also be of interest. Spectral analysis of the circuit can be greatly simplified if the input signal is assumed small in magnitude such that the dominant contributor to *IM3* is from *Ein*³.

Intermodulation distortion products (*IM3*, *IM5*,…) can be expressed in terms of power, either absolute (dBm) or relative to the carrier (dBc), or by a fictitious intercept point. For certain circuits where the input stimulus is small in magnitude (e.g., low noise amplifier and certain receiver components), an intercept point distortion specification is useful. Consider the nonlinear response of a circuit represented by Eq. (8.6) and driven with an equal amplitude two-tone sinusoidal stimuli as given in Eq. (8.7). Assume further than only a_1 and a_3 in Eq. (8.6) are nonzero. A plot of the circuit's output power spectrum as a function of input power is illustrated in Fig. 8.3. The output spectral tones at ω_1 and ω_2 increase on a 1:1 (dB) basis with input power. The *IM3* products ($2\omega_1 - \omega_2$, $2\omega_2 - \omega_1$) increase on a 3:1 (dB) basis with input power (due to E_{in}^3). The intersection of the fundamental tones with the third order products is defined as the third order intercept point. Note that the intercept point can be specified relative to input or output power of each tone, IIP_3 and OIP_3, respectively. Given this linear relationship, the output intercept point can easily be calculated based on the power of the fundamental and third order terms present at the output port [2,6]

$$OIP3(dBm) = P_{out}(\omega_1) + \frac{P_{out}(\omega_1) - P_{out}(2\omega_1 - \omega_2)}{2} \tag{8.8}$$

where $P_{out}(\omega_1)$ and $P_{out}(2\omega_2 - \omega_1)$ is the power (dBm) in the fundamental and third order products referenced to the output port. Notice that since the input stimuli is an equal amplitude two-tone sinusoidal stimulus, like order spectra products are assumed equal in magnitude (i.e., $P_{out}(\omega_1) = P_{out}(\omega_2)$, $P_{out}(2\omega_2 - \omega_1) = P_{out}(2\omega_1 - \omega_2)$, …).

The relationship between input and output intercept points is given by

$$IIP3(dBm) = OIP3(dBm) - G(dBm) \tag{8.9}$$

In a similar manner, the fifth order output intercept point can be defined as [5]

$$OIP5(dBm) = P_{out}(\omega_1) + \frac{P_{out}(\omega_1) - P_{out}(3\omega_1 - 2\omega_2)}{4} \tag{8.10}$$

where $P_{out}(3\omega_2 - 2\omega_1)$ is power (dBm) of fifth order products referenced to the output port.

Similarly,

$$IIP5(dBm) = OIP5(dBm) - G(dBm) \tag{8.11}$$

In system analysis, it is often desirable to consider the linearity performance for a series of cascaded two-port circuits and the contribution of each circuit's nonlinearity to the total. The IM3 distortion of the complete cascaded network can be approximated based on the third order intercept point of each element. Consider the two-tone sinusoidal stimulus [Eq. (8.7)] applied to the input of the cascaded circuits shown in Fig. 8.1. The magnitude of the fundamental and IM3 products (i.e., $\omega_{1,}$ $\omega_{2,}$ $2\omega_1 - \omega_2$, and $2\omega_2 - \omega$) at the output port of the 1st element can be calculated based on knowledge of the input power level of tones ω_1 and ω_2, transducer gain, and the third order intercept point of element one using Eq. (8.8). Next, consider the second element where the input stimulus now consists of spectral components at $2\omega_1 - \omega_2$ and $2\omega_2 - \omega_1$ in addition to those at ω_1 and ω_2. The IM3 spectral products at the second element's output port will be the result of contributions from two sources, (1) those due to intermodulation distortion of ω_1 and ω_2 in element 2, and (2) those due to amplifying spectral products $2\omega_1 - \omega_2$, and $2\omega_2 - \omega$ present at the input port of element 2. The IM3 products due to the former are, again, calculated from Eq. (8.8). The IM3 products at the output of element 2 due to the latter will be the IM3 products at the input amplified by G_2. Hence, the total *IM*3 spectral products are the vector sum from each. Both a minimum and maximum value is possible depending on the vector relationship between the various signals. A worst case (lowest *OIP*3) results when they combine in phase and are given by [2]

$$\frac{1}{IIP3_T} = \frac{1}{IIP3_1} + \frac{G_1}{IIP3_2} + \frac{G_1 G_2}{IIP3_3} \ldots \tag{8.12}$$

with *IIP*3 expressed in Watts.

Or alternatively from [6]

$$OIP3_{T\,\min} = \left(\sum_{i=1}^{n} \frac{1}{OIP3_i g_i} \right)^{-1} \tag{8.13}$$

with *OIP*3 expressed in Watts and where g_i is the cascaded gain from the output of the i^{th} element to the system output, including impedance mismatch effects. A best case scenario (highest *OIP*3) results when they combine out of phase with the results given by [6]:

$$OIP3_{T\,\max} = \left(\sum_{i=1}^{n} \frac{1}{OIP3_i^2\, g_i^2} - 2 \sum_{i=2}^{n} \sum_{j=1}^{n} \frac{1}{OIP3_i OIP3_j g_i gj} \right)^{-1/2} \tag{8.14}$$

$$i > j$$

Hence, Eqs. (8.13) and (8.14) specify bounds for intercept performance of cascaded networks.

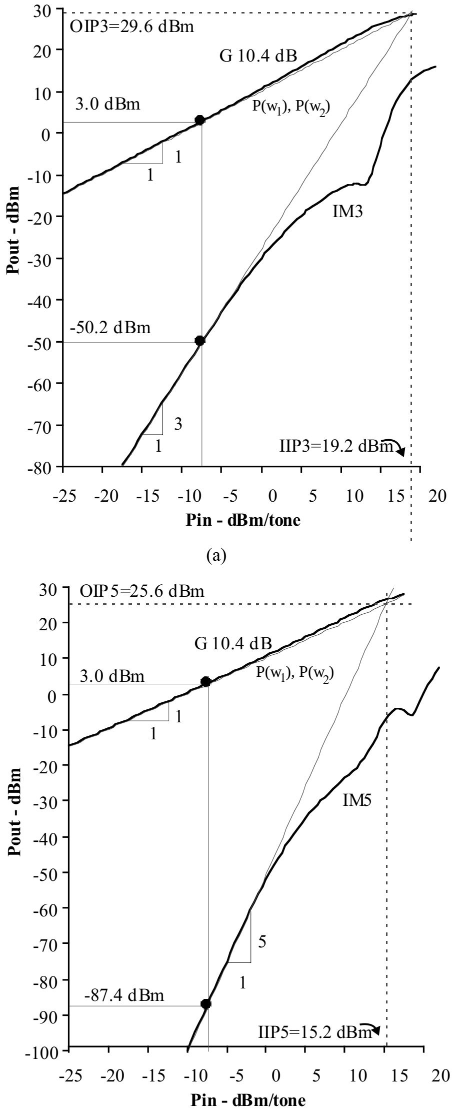

(a)

(b)

FIGURE 8.4 Typical relationship between fundamental frequency components and 3rd and 5th order intermodulation distortion products including effects due to higher order series coefficients. a) Third order IMD, and b) Fifth order IMD.

An illustration of the measured spectral content of an amplifier driven with a two-tone sinusoidal stimuli is shown in Fig. 8.4. At low power levels, third and fifth order IM products closely follow a 3:1 and 5:1 (dB) relationship with input power. Hence, per the previous discussion, *OIP*3 and *OIP*5 can be calculated based on measurements of the output spectral products at a given input power level. In this example, the spectral content is $P_{out}(3\omega_2 - 2\omega_1) = -87.4$ dBm, $P_{out}(2\omega_2 - \omega_1) = -50.2$ dBm, $P_{out}(\omega_1) = +3.0$ dBm and G = 10.4 dB for the input level shown. Applying Eqs. (8.8) and (8.10) yield *OIP3* = 29.6 dBm and *OIP5* = 25.6 dBm, respectively. The input intercept points are determined from Eqs. (8.9) and (8.11).

Limitations rooted in the approximations in deriving intercept points become more apparent at higher power levels where the relationship between input power and spectral products deviates dramatically from their assumed values. At some increased power level, the effects due to the higher order series coefficients in Eq. (8.6) become significant and cannot be ignored. Hence, for certain circuits, such as power amplifiers for example, the concept of intercept point is meaningless. A more meaningful measure of nonlinearity is the relative power in the IMD products (dBc) referenced to the fundamental tones, with the reference generally made to output rather than input power.

System Simulation with a Digitally Modulated RF Stimuli

Many modern communications systems, including 2nd and 3rd generation cellular, satellite communications, and wireless local area networks (W-LAN), to name but a few, utilize some form of digital modulation to encode information onto an RF carrier. As discussed earlier in this chapter, these signals are complex in that the RF carrier's phase, amplitude, or both are modulated in some manner to represent digital information. An extensive examination of the mathematical techniques and available methods to simulate the system response of passing such signals through various RF circuits is well beyond the scope of this section. The reader is referred to [1] for a more detailed discussion of simulation techniques. Nevertheless, some of the fundamental RF-related aspects of system simulation will be examined in the context of a mobile wireless radio. Consider the architecture illustrated in Fig. 8.5 which is intended to represent major elements of wireless radio such as presently utilized in 2G and 3G cellular systems. The radio utilizes frequency division multiplexing whereby a diplexer confines RX and TX signals to the respective receiver and transmitter paths.

To begin, consider the TX path where digital information is first generated by a DSP. This data is modulated onto an RF carrier whereby the information is encoded and modulated onto a carrier conforming to a particular modulation format. From this point, the signal is injected into a mixer where it is raised in frequency to coincide with the TX frequency band. The signal is then amplified by a power amplifier and passed to the antenna via a diplexer.

Simulation of the TX signal path begins by considering the digital information present at the modulator. In a cellular system, this information corresponds to a digital sequence representing voice information and/or data. The precise structure of the sequence (i.e., patterns of zeros and ones) is important in that it is a major contributor in defining the envelope characteristics of the RF signal to be transmitted. Also note for simulation purposes, the RF stimulus is generally formed by repeating this sequence and modulating it onto an RF carrier. Hence, the resultant RF signal is periodic per the digital bit sequence. The effect of a particular digital bit sequence in defining the RF signal is illustrated by considering the two randomly generated NRZ bit patterns shown in Fig. 8.6. The amplitude modulated RF envelope voltage developed by utilizing these sequences in a $\pi/4$ DQPSK modulator is also shown in Fig. 8.6. While the two envelope signals are nearly identical in their average power levels, they are substantially different, especially in their peak voltage excursions. Hence, the digital bit sequence and the resultant modulated

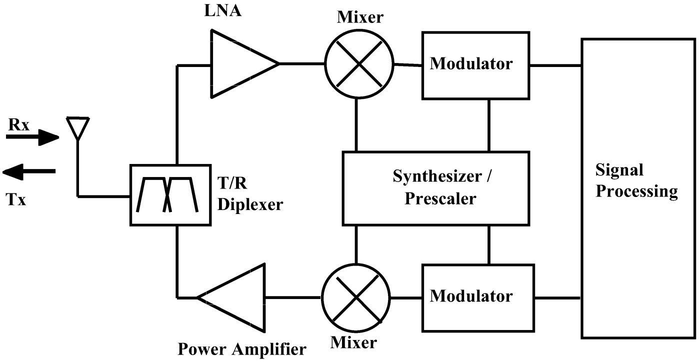

FIGURE 8.5 Block diagram representing major elements in mobile cellular radio.

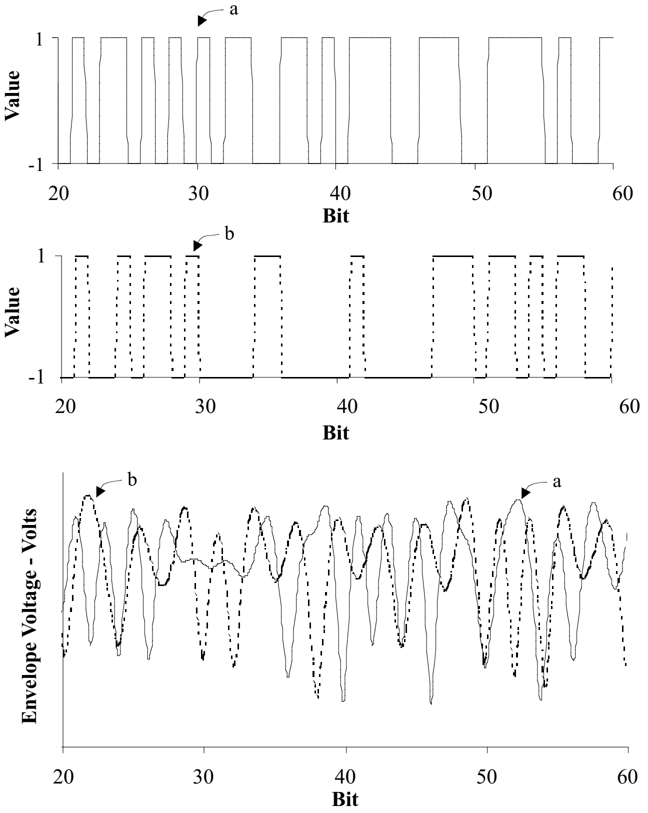

FIGURE 8.6 The RF modulated envelope formed by considering two randomly generated bit sequences.

RF waveform can be particularly important when evaluating the performance of nonlinear circuits such as power amplifiers in that the bit sequence can affect spectral distortion. Nevertheless for simulation purposes, it is necessary to choose a suitable sequence to represent the digital information to be transmitted. In general, either a predefined binary NRZ sequence, a randomly generated one, or a pseudonoise (PN) sequence is generally chosen. Often the latter is considered a more desirable choice due to its statistical properties. For example, a maximal length PN sequence of length 2^m-1 contains all but one m bit combinations of 1s and 0s. This property is particularly important in that it allows all possible bit patterns (except for the all zeros pattern) to be utilized in generating the RF modulated waveform. In contrast, a much longer random sequence would be needed with no guarantee of this property. Further, the autocorrelation function of a PN sequence is similar to a random one [1]. A potentially significant disadvantage of applying a random sequence in evaluating nonlinear circuit blocks is that the simulation results will change from evaluation to evaluation as the randomly generated sequence is not identical for each simulation.

Once a sequence is chosen, the performance of the modulator can be evaluated. The modulator can be modeled and simulated at the component level using time-based methods such as SPICE. However, in the early system design phase, such detail and the time required to perform a full circuit level simulation may be unattractive. On the other hand, it may be more appropriate to model the modulator at a higher level (e.g., behavioral model) and only consider selected first order effects. For example, the simplified diagram in Fig. 8.7 depicts the functionality of a quadrature modulator (in this case to represent a QPSK modulator). Starting with a data steam, every two bits are grouped into separate binary streams representing even and odd bits as indicated by X_K and Y_K. These signals (X_K and Y_K) are encoded in some manner (e.g., as relative changes in phase for IS-136 cellular) and are now represented as I_K and Q_K with

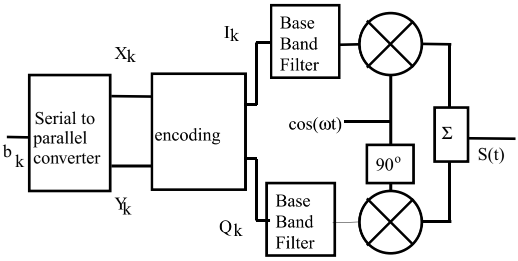

FIGURE 8.7 The process of generating modulated signal *S*(*t*) in a QPSK system.

each symbol extending over two bit time intervals. These signals now pass though a baseband filter, often implemented as a finite impulse response filter with impulse response h(t). The filtered signal can be calculated based upon the convolution theorem for time sampled signals. These signals are then modulated onto a carrier (IF) with the output modulated signal taking the form

$$S(t) = \sum_n g(t - nT)\cos(\Phi_n)\cos(\omega_c t) - \sum_n g(t - nT)\sin(\Phi_n)\sin(\omega_c t) \tag{8.15}$$

where ω_c is the radian carrier frequency, Φ_n represents phase, $g(t)$ is a pulse shaping factor, and n = 0, 1, 2, … are discrete time samples.

At this point, some first order effects can be evaluated by considering the mathematical nature of Eq. (8.15). For example, phase imbalance (Φ_{imb}) within the modulator can be modeled as:

$$S(t) = \sum_n g(t - nT)\cos(\Phi_n)\cos(\omega_c t) - \sum_n g(t - nT)\sin(\Phi_n)\sin(\omega_c t + \Phi_{imb}) \tag{8.16}$$

Given a higher level model, the modulated envelope can be simulated using time-based methods to determine *S*(*t*).

The power amplifier represents an element in the transmitter chain where linearity is of concern, especially in those RF systems employing modulation methods resulting in a nonconstant amplitude envelope. These cases, which incidentally include a number of cellular and PCS systems, require a linear power amplifier to preserve the amplitude/phase characteristics of the signal. The nonlinear characteristics of the amplifier can be simulated at the circuit level using time- and/or frequency-based methods. However, circuit-based simulations require accurate and detailed knowledge of all circuit components within the amplifier, including an appropriate large signal model for all active devices as well as highly accurate models for all passive structures. Such knowledge is often unavailable at the system level with sufficient detail and accuracy to perform such a simulation. In addition, circuit level nonlinear simulations of the amplifier driven by digitally modulated RF stimulus are generally quite computationally intensive resulting in long simulation times, making this approach even more unattractive.

A more common approach to modeling the nonlinearity of a power amplifier at the system level is through the use of behavioral models [1,7,8]. While a number of behavioral models have been proposed with varying levels of complexity and sophistication, all of them rely to some extent on certain approximations regarding the circuit nonlinearity. A common assumption in many of the behavioral models is that the nonlinear circuit/RF-modulated stimulus can be represented in terms of a memoryless and bandpass nonlinearity [1]. Although the active device within the amplifier generally exhibits some memory behavior, and additional memory-like effects can be caused by bias networks, these assumptions are generally not too limiting for power amplifiers utilized in cellular communications systems. Further, when the above-noted assumptions are met or nearly met, the simulation results are very accurate and the needed simulation time is very short.

In general, an input-output complex envelope voltage relationship is assumed with the complex output envelope voltage v_{out}(t) taking the form

$$v_{out}\left(t\right) = RE\left\{G\left(V\left(t\right)\right)e^{j\left\{\Phi\left(t\right)+\varphi\left(V\left(t\right)\right)+\omega_c t\right\}}\right\} \tag{8.17}$$

where $G(V(\mathrm{t}))$ and $\varphi(V(\mathrm{t}))$ describe the instantaneous input-output envelope voltage gain and phase. Note that functions $G(V)$ and $\varphi(V)$ represent the amplifier's am-am and am-pm response, respectively. The term ω_c represents the carrier frequency.

An inspection of Eq. (8.17) suggests the output envelope voltage can be calculated in a time-based method by selecting time samples with respect to the modulation rate rather than at the RF carrier frequency. This feature is particularly advantageous in digitally modulated systems where the bit rate and modulation bandwidth are small in comparison to the carrier frequency. Significantly long and arbitrary bit sequences can be simulated very quickly since the time steps are at the envelope rate. For example, consider an NRZ bit sequence on the order of several mS which is filtered at baseband and modulated onto an RF carrier with a 1nS period (i.e., 1 GHz). Time-based simulation at the RF frequency would likely require time samples significantly less than 0.1 nS and the overall number of sample points would easily exceed 10^7. Alternatively, simulating the output envelope voltage by choosing time steps relative to the modulation rate would result in several orders of magnitude fewer time samples.

A particular advantage of the above model is that the entire power amplifier nonlinearity is described in terms of its am-am (gain) and am-pm (insertion phase) response. The am-am response is equivalent to RF gain and the am-pm characteristics are equivalent to the insertion phase — both measured from input to output ports with each expressed as a function of input RF power. For simplicity, both characteristics are often determined using a single tone CW stimulus, although modulated RF signals can be used at the expense of more complexity. The nature of the behavioral model allows it to be characterized based on the results from another simulator (e.g., harmonic balance simulations of the amplifier circuit), an idealized or assumed response represented in terms of mathematical functions describing am-am and am-pm characteristics, or from measurements made on an actual amplifier.

Computation of the output envelope voltage from Eq. (8.17) allows evaluation of many critical system characteristics, including ACPR (Adjacent and/or Alternate Channel Power Ratio), Error Vector Magnitude (EVM), and Bit Error Rate (BER) to name but a few. For example, using Fourier methods, the spectral properties of the output signal expressed in Eq. (8.17) can be calculated. Nonlinear distortion mechanisms are manifested in spectral regrowth or equivalently a widening of the spectral properties. This regrowth is quantified by figure of merit ACPR, which is defined as a ratio of power in the adjacent (or in some cases alternative) transmit channel to that in the main channel. In some systems (e.g., IS-136), the measurement is reference to the receiver (i.e., the transmitted signal must be downconverted in frequency and filtered at base band). An illustration of spectral distortion for a π/4 DQPSK stimulus compliant to the IS-136 cellular standard is shown in Fig. 8.8. In this system the channel bandwidth is 30 KHz. Hence, using the specified root raised cosine baseband filter with excess bandwidth ratio α = 0.35, a 24.3 KS/s data sequence will result in a non-distorted modulated RF stimulus band limited to 32.805 KHz (i.e., 1.35 * 24.3 KS/s) as illustrated in Fig. 8.8. Nonlinear distortion mechanisms cause regrowth as illustrated. Note the substantial increase in power in adjacent and alternate channels.

Another measure of nonlinear distortions involves examining the envelope characteristics of $S(t)$ in time as measured by the receiver. Consider an input π/4 DPSK modulated RF signal which is developed from a 256 length randomly selected NRZ symbol sequence and passed through both linear and nonlinear amplifiers. Figure 8.9 illustrates the constellation diagram for both signals as measured at the receiver. Note that both signals represent the I and Q components of the envelope where $S(t)$ has been passed through a root-raised-cosine receiver filter. The constellation plot only shows the values of the I and Q components at the appropriate time sample intervals. The non-distorted signal exhibits expected values of ± 1, $\pm\sqrt{1/2} \pm i\sqrt{1/2}$, and $\pm i$. The distorted signal is in error from these expected values in terms of both amplitude and phase.

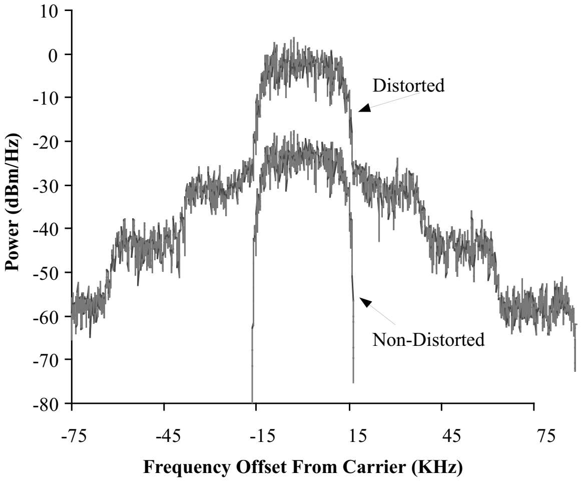

FIGURE 8.8 Nonlinear distortions due to a power amplifier result in a widening of the spectral properties of the RF signal.

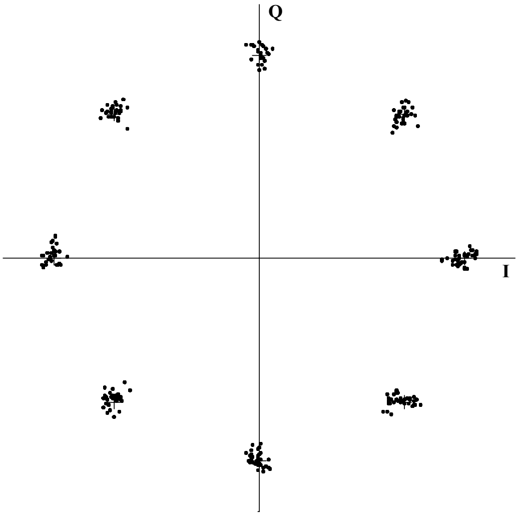

FIGURE 8.9 Constellation plot for both a non-distorted and distorted π/4 DPSK stimulus.

References

1. Michel C. Jeruchim, Philip Balaban, and K. Sam Shanmugan, *Simulation of Communication Systems,* Plenum Press, New York, 1992.
2. J. Tsui, *Microwave Receivers and Related Components,* Air Force Avionics Lab., Wright-Patterson AFB, OH, 1983.
3. G. Gonzalez, *Microwave Transistor Amplifiers,* Prentice-Hall, Inc., Englewood Cliffs, N.J., 1984.
4. J. Sevice, Nonlinear Analysis Methods for the Simulation of Digital Wireless Communication Systems, *Int. Journal of Microwave and Millimeter-Wave Computer-Aided Eng.,* 6, 1997, 197–216.
5. H. Xiao, Q. Wu, F. Li, Measure a Power Amplifier's Fifth-Order Intercept Point, *RF Design,* April 1999, 54–56.
6. N. Kanaglekar, R. Mcintosh, and W. Bryant, Analysis of Two-Tone, Third-Order Distortion in Cascaded Two-Ports, *IEEE Transactions on Microwave Theory and Techniques,* April 1988, 701–705.

7. System Theory of Operation, OmniSys Manual, Hewlett-Packard Co.
8. J. Staudinger, Applying the Quadrature Modeling Technique to Wireless Power Amplifiers, *Microwave Journal,* Nov. 1997, 66–86.

8.2 Numerical Techniques for the Analysis and Design of RF/Microwave Structures

Manos M. Tentzeris

Recent advances in wireless and microwave communication systems (higher operation frequency bands, more compact topologies containing MMICs and MEMS) have increased the necessity of fast and accurate numerical simulation techniques [1–20]. Unlike hybrid microwave integrated circuits at low frequencies, it is extremely difficult and essentially impossible to adjust the circuit and radiation characteristics of communication modules once they are fabricated. The starting point for the development of efficient numerical algorithms is an accurate characterization of the passive and active structures involved in the topologies. Although most commercial CAD programs are based on curve-fitting formulas and lookup tables and not on accurate numerical characterization, the latter can be used if it is fast enough. In addition, it can be used to generate lookup tables and to check the accuracy of empirical formulas.

Any numerical method for characterization needs to be as efficient and economical as possible in both CPU time and temporary storage requirement, although recent rapid advances in computers impose less severe restrictions on the efficiency and economy of the method. Another important aspect in the development of numerical methods has been the versatility of the method. In reality, however, numerical methods are chosen on the basis of trade-offs between accuracy, speed, storage requirements, versatility, etc. and are often structure dependent. Among these techniques, the most popular ones include the Moment Method (MoM), Integral Equation Based Techniques, Mode-Matching (MM), the Finite-Difference Time-Domain (FDTD), the Transmission Line Matrix method (TLM) and the Finite Element (FEM) method.

Integral Equation Based Techniques

Method of Moments (MoM) — Integral Equation

The term "Moment Method" was introduced in electromagnetics by R. Harrington [3] in 1968 in order to specify a certain general method for reducing linear operator equations to finite matrix solutions [4–7]. MoM computations invariably reduce the physical problem, specified by the Maxwell's equations and the boundary conditions, into integral equations having finite, and preferably small, domains. In this small domain, the discretization is performed through the expansion of unknowns as a series of basis functions. An example is the Magnetic Field Integral Equation (MFIE) for the scattering of a perfectly conducting body illuminated by an incident field H^i [21],

$$\hat{n} \times \mathbf{H}\left(\mathbf{r}\right) = 2\hat{n} \times \mathbf{H}^{\mathbf{i}}\left(\mathbf{r}\right) + 2\hat{n} \times \int_S \left[\hat{n}' \times \mathbf{H}\left(\mathbf{r}'\right)\right] \times \nabla' G\left(r, r'\right) ds' \quad on \;\; S \tag{8.18}$$

where $\mathbf{H}^{\mathbf{i}}$ is defined as the field due to the source in the absence of the scattering body S, and

$$G\left(r, r'\right) = \frac{e^{-jk\left|r - r'\right|}}{4\pi\left|r - r'\right|} \tag{8.19}$$

where r and r' are the position vectors for the field and source positions, respectively. A continuous integral, such as the one above, can be written in an abbreviated form as

$$L(f) = g \tag{8.20}$$

where f denotes the unknown, which is **H** above, and g denotes the given excitation, which is $\mathbf{H}^i$. Also, L is a linear operator. Let f be expanded in a series of functions $f_1, f_2, f_3, \ldots$ in the domain S of L, as

$$f = \sum_n a_n f_n \tag{8.21}$$

where a_n are constants and f_n are called expansion (basis) functions. For exact solutions, the above summation is infinite and f_n forms a complete set of basis functions. For approximate solutions, this solution is truncated to

$$\sum_n a_n L(f_n) = g \tag{8.22}$$

Assume that a suitable inner product $\langle f, g\rangle = \int f(x)g(x)dx$ has been determined for the problem. Defining a set of weighting (testing) functions, $w_1, w_2, w_3, \ldots$ in the range of L, and taking the inner product of the above summation with each w_m leads to the result

$$\sum_n a_n \langle w_m, L(f_n)\rangle = \langle w_m, g\rangle, \quad m = 1, 2, 3, \ldots \tag{8.23}$$

which can be written in matrix form as

$$[l_{mn}][a_n] = [g_m], \tag{8.24}$$

where

$$[l_{mn}] = \begin{bmatrix} \langle w_1, L(f_1)\rangle & \langle w_1, L(f_2)\rangle & \cdots \\ \langle w_2, L(f_1)\rangle & \langle w_2, L(f_2)\rangle & \cdots \\ \cdots & \cdots & \cdots \end{bmatrix}, \quad [a_n] = \begin{bmatrix} a_1 \\ a_2 \\ \vdots \end{bmatrix}, \quad [g_m] = \begin{bmatrix} \langle w_1, g\rangle \\ \langle w_2, g\rangle \\ \vdots \end{bmatrix}. \tag{8.25}$$

If the matrix $[l]$ is nonsingular, its inverse $[l]^{-1}$ exists and the a_n are given by

$$[a_n] = [l_{mn}]^{-1}[g_m] \tag{8.26}$$

and the unknown f is given from the weighted summation [Eq. (8.21)]. Assuming that the finite expansion basis is defined by $[\tilde{f}_n] = [f_1\ f_2\ f_3\ \ldots]$, the approximate solution for f is

$$f = [\tilde{f}_n][a_n] = [\tilde{f}_n][l_{mn}]^{-1}[g_m] \tag{8.27}$$

Depending upon the choice of f_n and w_n this solution could be exact or approximate [22]. The most important aspect of MoM is the choice of expansion and testing functions. The f_n should be linearly independent and chosen such that a finite-term superposition approximates f quite well. The w_n should also be linearly independent. In addition, this choice is affected by the size of the matrix that has to be

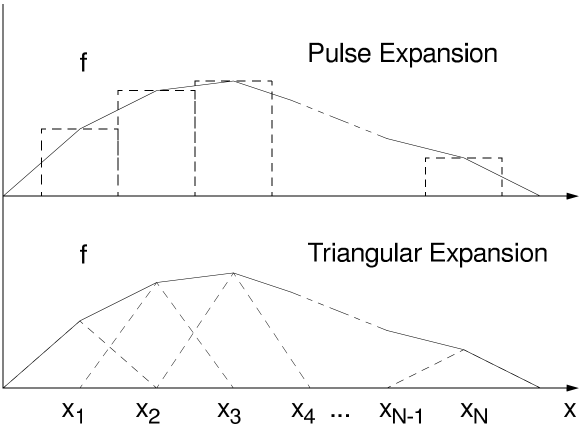

FIGURE 8.10 Moment method expansion in pulse and triangular basis.

inverted (should be minimal), the ease of evaluation of the matrix elements, the accuracy of the desired solution, and the realization of a well-conditioned matrix $[l]$. The special choice $w_n = f_n$ gives Galerkin's method. The two most popular subsectional bases are the pulse function (step approximation) and the triangle function (piecewise linear approximation), as shown in Fig. 8.10. The numerical Gaussian Quadrature rule [7] is used when the integrations involved in the evaluation of $l_{mn} = \langle w_m, Lf_n \rangle$ are difficult to perform for common w_m's for a specific problem or when a more complex expansion basis is used. An alternative approach makes use of the Dirac delta functions for testing. This technique is called point-matching and effectively satisfies Eq. (8.19) at discrete points in the region of interest. When the basis functions f_n exist only over subsections of the domain of f, each a_n affects the approximation of f only over a subsection of the region of interest (method of subsections). In this way, the evaluation of l_{mn} is simplified and the form of the matrix $[l]$ is stripped and easier to invert.

The Method of Moments (MoM) involves setting up and solving dense, full, complex-valued systems. For a one-dimensional structure (e.g., a wire) of length L wavelengths, the size of the matrix is typically on the value of 10 L; for a 3D structure with surface area S square wavelengths, the size is typically on the order of 100 S. Consequently, there are applications such as radar scattering from aircraft when the system of equations has order in excess of one million. Though MoM has been proven to be a very robust technique, it is plagued by the significant computational burden of having to solve a dense matrix equation of large order. In addition, modeling of a new structure requires the reformulation of the integral equation, a task that may require the very difficult derivation of a geometry-specific Green's function. MoM is used for the solution of various integral equations such as the Electric Field Integral Equation (EFIE) and the Magnetic Field Integral Equation (MFIE). The integral equation approach has the advantage that it rigorously takes into account the radiation conditions of any open structure and therefore it is not necessary to implement absorbing boundary conditions. The kernel of the integral equation is the Green's function that accurately describes all possible wave propagation effects, such as radiation, leakage, anisotropy, stratification, etc.

The Method of Moments has been used in many scattering problems [23–25], microstrip lines on multilayered dielectrics [26], microstrip antennas [27, 28], integrated waveguides in microwave [29, 30], and optical frequencies [31] even on anisotropical substrates [32]. In addition, results have been derived for the characterization of junctions [33], high-speed interconnects [34], viaholes [35], couplers [36], and infinite aperture arrays [37]. It should be emphasized that the discretization may be nonuniform, something that has been demonstrated in the application of MoM to planar circuits in [38].

Spectral Domain Approach

Electromagnetic analysis in the spectral (Fourier transform) domain is preferable to many spatial domain numerical techniques, especially for planar transmission lines, microstrip antennas, and other planar layered structures. If applied to an equation describing EM fields in planar media, a Fourier transform reduces a fully coupled, three-dimensional equation to a one-dimensional equation that depends on two parameters (the transform variables), but is uncoupled and can be solved independently at any values of those parameters. After solving the one-dimensional equation, the inverse Fourier transform performs a superposition of the uncoupled one-dimensional solutions to obtain the three-dimensional solution. Thus, the process offers substantial savings since it effectively converts a 3D problem into a series of 1D problems.

Yamashita and Mittra [39] introduced the Fourier domain analysis for the calculation of the phase velocity and the characteristic impedance of a microstrip line. Using the quasi-TEM approximation (negligible longitudinal E- and H-fields), the line capacitance is determined by the assumed charge density through the application of the Fourier domain variational method. Denlinger [40] extended this approach to the full wave analysis of the same line. However, his solution depends strongly to the assumed current strip distributions. Itoh and Mittra [41] introduced a new technique, the Spectral Domain Approach (SDA) that allows for the systematic improvement of the solution accuracy to a desired degree. In SDA, the transformed equations are discretized using MoM, yielding a homogeneous system of equations to determine the propagation constant and the amplitude of current distributions from which the characteristic impedance is derived.

For metallic strip problems, the Fourier transform is performed along the direction parallel to the substrate interface and perpendicular to the strip. The first step is the formulation of the integral equation that correlates the E-field and the current distribution J along the strip and the application of the boundary conditions for E- and H-fields. Then, the Fourier transform is applied over E and J and the MoM technique produces a system of algebraic equations that can be solved. Different choices of expansion and testing functions have been discussed in [42]. SDA is applicable to most planar transmission lines (microstrips, finlines, CPWs) [43–48], microstrip antennas and arrays [49, 50], interconnects [51], junctions [52], dielectric waveguides [53], resonators of planar configurations [54], and micromachined devices [55] on single or multilayered dielectric substrates. This method requires significant analytical preprocessing, something that improves its numerical efficiency, but also restricts its applicability especially for structures with finite conductivity strips and arbitrary dielectric discontinuities.

Mode Matching Technique

This technique is usually applied to the analysis of waveguiding/packaging discontinuities that involve numerous field modes. The fields on both sides of the discontinuity are expanded in summations of the modes in the respective regions with unknown coefficients [56] and appropriate continuity conditions are imposed at the interface to yield a system of equations. As an example, to analyze a waveguide step discontinuity with TE_{n0} excitation, E_y and H_x fields are written as the superposition of the modal functions $\phi_{an}(x)$ and $\phi_{bn}(x)$ for $n = 1, 2, \ldots$, respectively for the left waveguide (waveguide A) and the right waveguide (waveguide B), as it is displayed in Fig. 8.11. Both of these fields should be continuous at the interface z = 0. Thus:

$$\sum_{n=1}^{\infty}\left(A_n^+ + A_n^-\right)\phi_{an} = \begin{cases} \sum_{n=1}^{\infty}\left(B_n^+ + B_n^-\right)\phi_{bn}, & 0 < x < b \\ 0, & b < x < a \end{cases} \tag{8.28}$$

$$\sum_{n=1}^{\infty}\left(A_n^+ - A_n^-\right)Y_{an}\,\phi_{an} = \begin{cases} \sum_{n=1}^{\infty}\left(B_n^+ - B_n^-\right)Y_{bn}\,\phi_{bn}, & 0 < x < b \\ 0, & b < x < a \end{cases} \tag{8.29}$$

where (+) and (–) indicate the modal waves propagating to the positive and negative z direction and Y_{an}, Y_{bn} are the mode impedances. Sampling these equations with ϕ_{bm} (m-mode in waveguide B) and making use of the mode orthogonality in waveguide B,

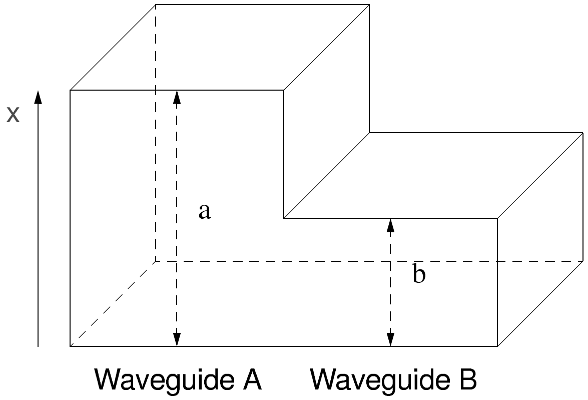

FIGURE 8.11 Rectangular waveguide discontinuity.

$$\sum_{n=1}^{\infty} H_{nm}\left(A_n^+ + A_n^-\right) = B_m^+ + B_m^- \tag{8.30}$$

$$\sum_{n=1}^{\infty} H_{nm} Y_{an}\left(A_n^+ - A_n^-\right) = Y_{bm}\left(B_m^+ - B_m^-\right) \tag{8.31}$$

with: $H_{nm} = \int_0^b \phi_{an}(x)\phi_{bm}(x)dx$. Similarly, sampling Eqs. (8.28) and (8.29) with ϕ_{am} (m-mode in waveguide A) and making use of mode orthogonality in waveguide A, we have

$$A_m^+ + A_m^- = \sum_{n=1}^{\infty} H_{mn}\left(B_n^+ + B_n^-\right) \tag{8.32}$$

$$Y_{am}\left(A_m^+ - A_m^-\right) = \sum_{n=1}^{\infty} H_{mn} Y_{an}\left(B_n^+ - B_n^-\right) \tag{8.33}$$

Assuming that the structure is excited through A_n^+ terms, the calculation of A_n^- (reflected modes in A) and B_m^+ (transmitted modes in B) will provide the scattering parameters for the analyzed structure through a procedure that involves matrix inversions.

The foundation of this technique is the expansion of an electromagnetic field in terms of an infinite series of normal modes. Because a computer's capacity for numerical calculation is finite, these summations have to be truncated, something that could lead to incorrect solutions if not performed efficiently. The main criterion for this truncation is the convergence of the summation. A natural way to check it is to plot the numerical values of some desired parameters versus the number of retained terms. The truncation is considered sufficient when the change in the parameters is smaller than prespecified criteria. The procedure becomes more complicated where there is a need for the truncation of two or more infinite series (bifurcated waveguide, step junction). The numerical results appear to converge to different values depending on the manner of the truncation, a phenomenon that is called relative convergence. It has been found that relative convergence is related to the violation of field distributions at the edge of a conductor at the boundary [9] and to the ill-conditioned situation of the linear system of the computation process [57]. Thus, either the edge condition or the condition number of the linear system can be used as a criterion to ensure the validity of modal analyses. Another common criterion is to plot the field distributions on both sides of the boundary and observe their matching conditions. The mode matching method has been applied to analyze various discontinuities in waveguides [58, 59], finlines [60, 61], microstrip lines [62, 63], and coplanar waveguides [64, 65]. In addition, it is used for closed-region scattering geometries involving a discrete set of modes, such as E-plane filters [66, 67], waveguide impedance transformers [68], power dividers [69], and microstrip filters [70]. Moreover, this technique has been implemented for the solution of eigenvalue problems, such as the resonant frequency of a cavity [71] and the performance of evanescent mode filters [72], since it can efficiently model both evanescent and propagating modes.

PDE-Based Techniques FDTD, MRTD, FEM

In contrast to the previous techniques, numerical methods based on the partial differential equation (PDE) solutions of Maxwell's equations yield either sparse matrices (frequency domain, finite-element methods) or no matrices at all (time domain, finite-difference or finite-volume methods). In addition, specifying a new geometry is reduced to a problem of mesh generation only. Thus, PDE solvers could provide a framework for a space/time (frequency) microscope permitting the EM designer to visualize with submicron/subpicosecond resolution the dynamics of electromagnetic wave phenomena propagating at light speed within proposed geometries.

Finite-Difference Time Domain (FDTD) Technique

The Finite-Difference Time-Domain (FDTD) [10–13] is an explicit solution method for Maxwell's time-dependent curl equations. It is based upon volumetric sampling of the electric and magnetic field distribution within and around the structure of interest over a period of time. The sampling is set below the Nyquist limit and typically more than 10 samples per wavelength are required. The time step has to satisfy a stability condition. For simulations of open geometries, absorbing boundary conditions (ABC) are employed at the outer grid truncation planes in order to reduce spurious numerical reflections from the grid termination.

In 1966, Yee [73] suggested the solution of the first-order Maxwell equations in time and space instead of solving the second order wave equation. In this way, the solution is more robust and more accurate for a wider class of structures. In Yee's discretization cell, E- and H-fields are interlaced by half space and time gridding steps, as shown in Fig. 8.12. The spatial displacement is very useful in specifying field boundary conditions and singularities and leads to finite-difference expressions for the space derivatives that are central in nature and second-order accurate. The time displacement (leapfrog) is fully explicit, completely avoiding the problems involved with simultaneous equations and matrix inversion. The

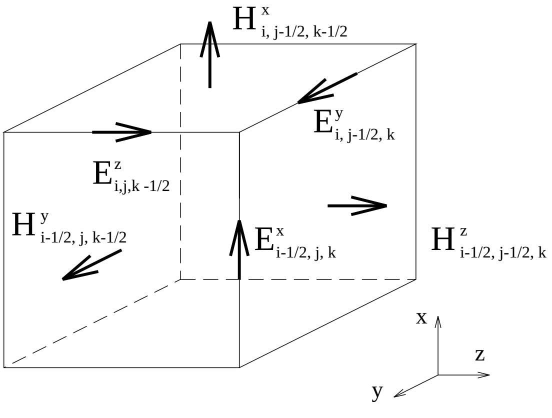

FIGURE 8.12 FDTD Yee cell.

resulting scheme is non-dissipative; numerical wave modes propagating in the mesh do not spuriously decay due to a nonphysical artifact of the time-stepping algorithm. Denoting any function u of space and time evaluated at a discrete point in the grid and at a discrete point in time as $u(i\Delta x, j\Delta y, k\Delta z, l\Delta t) = {}_{l}u_{i,j,k}$, where Δt is the time step and Δx, Δy, Δz the cell size along the x-, y- and z-direction, the first partial space derivative of u in the x-direction and the first time derivative of u are approximated with the following central differences, respectively

$$\begin{aligned}
\frac{\partial u}{\partial x}\left(i\Delta x, j\Delta y, k\Delta z, l\Delta t\right) &= \frac{{}_{l}u_{i+1/2,j,k} - {}_{l}u_{i-1/2,j,k}}{\Delta x} + O\left[\left(\Delta x\right)^{2}\right] \\
\frac{\partial u}{\partial t}\left(i\Delta x, j\Delta y, k\Delta z, l\Delta t\right) &= \frac{{}_{l+1/2}u_{i,j,k} - {}_{l-1/2}u_{i,j,k}}{\Delta t} + O\left[\left(\Delta t\right)^{2}\right]
\end{aligned} \tag{8.34}$$

Applying the above notation, the FDTD equations are derived for all field components. For example,

$$\begin{aligned}
{}_{l+0.5}H^{x}_{i,j-0.5,k-0.5} &= \left(\frac{1-\dfrac{\rho'_{i,j,k}\Delta t}{2\mu_{i,j,k}}}{1+\dfrac{\rho'_{i,j,k}\Delta t}{2\mu_{i,j,k}}}\right){}_{l-0.5}H^{x}_{i,j-0.5,k-0.5} \\
&+\left(\frac{\dfrac{\Delta t}{\mu_{i,j,k}}}{1+\dfrac{\rho'_{i,j,k}\Delta t}{2\mu_{i,j,k}}}\right)\left(\frac{{}_{l}E^{y}_{i,j-0.5,k} - {}_{l}E^{y}_{i,j-0.5,k-1}}{\Delta z} - \frac{{}_{l}E^{z}_{i,j,k-0.5} - {}_{l}E^{z}_{i,j-1,k-0.5}}{\Delta y}\right)
\end{aligned} \tag{8.35}$$

where $\rho'_{i,j,k}$ is the magnetic loss coefficient for the (i, j, k) cell. It can be observed that a new value of a field vector component at any space lattice point depends only on its previous value and the previous values of the components of the other field vectors at adjacent points. Therefore, at any given time step, the value of a field vector component at p different lattice points can be calculated simultaneously if p parallel processors are employed, demonstrating that the FDTD algorithm is highly parallelizable. Holland [74] suggested an exponential time stepping to model the exponential decay of propagating waves in certain highly lossy media that the standard Yee time-stepping algorithm fails to describe. Stability analysis [75] has shown that the upper bound for the FDTD time step for a homogeneous region of space (ϵ_r, μ_r) is given by

$$\Delta t \le \frac{\sqrt{\epsilon_r \mu_r}}{c\sqrt{\dfrac{1}{\left(\Delta x\right)^{2}} + \dfrac{1}{\left(\Delta y\right)^{2}} + \dfrac{1}{\left(\Delta z\right)^{2}}}}\left(3D\ simulations\right), \quad \Delta t \le \frac{\sqrt{\epsilon_r \mu_r}}{c\sqrt{\dfrac{1}{\left(\Delta x\right)^{2}} + \dfrac{1}{\left(\Delta y\right)^{2}}}}\left(2D\ simulations\right)$$

Lower values of upper bounds are used in case a highly lossy material or a variable grid is employed. Discretization with at least 10 to 20 cells/wavelength almost guarantees that the FDTD algorithm will have satisfactory dispersion characteristics (phase error smaller than 5°/λ for time step close to the upper bound value).

The computational domain must be large enough to enclose the structure of interest, and a suitable absorbing boundary condition (ABC) on the outer perimeter of the domain must be used to simulate its extension to infinity to minimize numerical reflections for a wide range of incidence angles and frequencies. Central differences cannot be implemented at the outermost lattice planes, since by definition no information exists concerning the fields at points one-half space cell outside of these planes. The perfectly matched layer (PML) ABC, introduced in 2D by Berenger in 1994 [76] and extended to 3D by Katz et al. [77], provides numerical reflection comparable to the reflection of anechoic chambers with values –40 dB lower than the previous absorbers. A new ABC based on Green's functions that absorbs efficiently propagating and evanescent modes has also been demonstrated [78, 79] for waveguide and RF packaging structures.

An incoming plane wave source [73] is very useful in modeling radar scattering problems, since in most cases of this type the target of interest is in the near field of the radiating antenna, and the incident illumination can be considered to be a plane wave. The hard source [80] is another common FDTD source implementation. It is set up simply by superimposing a desired time function onto specific electric or magnetic field components in the FDTD space lattice that are regularly updated by the FDTD equations. Collinear arrays of hard-source field vector components in 3D can be useful for exciting waveguides and strip lines. In the FDTD simulations of microstrip and stripline structures, the Gaussian pulse (nonzero DC content) is used as the excitation of the microstrip and stripline structures. The Gabor function

$$s\left(t\right)=e^{-\left(\left(t-t_o\right)/\left(pw\right)\right)^2}\sin\left(wt\right) \tag{8.36}$$

where $pw = 2 \cdot \frac{\sqrt{6}}{\pi(f_{\max}-f_{\min})}$, $t_o = 2pw$, $w = \pi(f_{\min} + f_{\max})$, is used as the excitation of the waveguide structures, since it has zero DC content. By modifying the parameters pw and w, the frequency spectrum of the Gabor function can be practically restricted to the interval $[f_{\min}, f_{\max}]$. As a result, the envelope of the Gabor function represents a Gaussian function in both time and frequency domain. Monochromatic simulations are performed through the use of continuous-wave (sinusoidal) excitations.

It is very common, especially for high-speed circuit structures, to use a cell size Δ that is dictated by the very fine dimensions of the circuit and is almost always much finer than needed to resolve the smallest spectral wavelength propagating in the circuit. As a result, with the time step Δt bound to Δ by numerical stability considerations, FDTD simulations have to run for tens of thousands of time steps in order to fully evolve the impulse responses needed for calculating impedances, S-parameters, or resonant frequencies. One popular way to avoid virtually prohibitive execution time has been to apply contemporary analysis techniques from the discipline of digital signal processing and spectrum estimation. The strategy is to extrapolate the electromagnetic field time waveform by 10:1 or more beyond the actual FDTD time window, allowing a very good estimate of the complete system response with 90% or greater reduction in computation time. This extrapolation can be performed using forward-backward predictors [81] or autoregressive (AR) models [82].

The FDTD technique has found numerous applications in modeling microwave devices such as waveguides, resonators, transmissions lines, vias, antennas, and active and passive elements. In 1985, DePourcq [83] used FDTD to analyze various 3D waveguide devices. Navarro et al. [84] investigated rectangular, circular, and T junctions in square coaxial waveguides and narrow-wall, multiple-slot couplers. Wang et al. [85] studied the Q factors of resonators using FDTD. Liang et al. [86] used FDTD to analyze coplanar waveguides and slotlines and Sheen et al. [87] presented FDTD results for various microstrip structures including a rectangular patch antenna, a low-pass filter, and a branch-line coupler. Cangellaris estimated the effect of the staircasing approximation of conductors of arbitrary orientation in [88].

The characterization of interconnect transitions in multichip and microwave circuit modules has also been investigated using FDTD. Lam et al. [89] used a nonuniform mesh to model microstrip-to-via-to-stripline connections. Piket-May et al. [90] studied pulse propagation and crosstalk in a computer module with more than ten metal-dielectric-metal layers and numerous vias. Luebbers et al. [91] and Shlager and Smith [92] developed and described in detail efficient three-dimensional, time domain, near-to-far-field transformations. In 1990, Maloney et al. [93] presented accurate results for the radiation from rotationally symmetric simple antennas such as cylindrical and conical monopoles, while Luebbers and coworkers [94, 95] presented mutual coupling and gain computations for a pair of wire dipoles and Tirkas and Balanis [96] modeled three-dimensional horn antennas. Uehara and Kagoshima [97] analyzed microstrip phased-array antennas and Jensen and Rahmat-Samii [98] presented results for the input impedance and gain of monopoles, planar inverted-F antennas (PIFAs) and loop antennas on handheld transceivers. In addition, Taflove [99] used FDTD to model scattering and compute near/far fields and radar cross-section (RCS) for 2D and 3D structures. Britt [100] calculated the RCS of both two- and three-dimensional perfectly conducting and dielectric scatterers.

Another area of FDTD applications is active and passive device modeling. Two different approaches are used. In the first, analytical device models are coupled directly with FDTD. In the second, lumped-element subgrid models are used with the device behavior being determined by other software, something that may be preferable in the modeling of active devices with complicated equivalent circuits. In 1992, Sui et al. [101] reported a 2D FDTD model with lumped circuit elements, including nonlinear devices, such as diodes and transistors and this approach was extended to 3D by Piket-May et al. [90] and Ciampollini et al. [102]. Kuo et al. [103] presented a large-signal analysis of packaged nonlinear active microwave circuits. Alsunaidi et al. [104] developed an active device model that couples the Yee update equations with the solution of the current continuity equation, the energy-conservation equation, and the momentum-conservation equations. Thomas et al. [105] developed an approach for coupling SPICE lumped elements into the FDTD method.

Transmission Line Matrix Method (TLM)

The TLM method [106–108] is similar to FDTD. The main difference is that the electromagnetic problem is analyzed through the use of a three-dimensional equivalent network problem [109]. It is a very versatile time domain technique and discretizes the computational domain using cubic cells with a period Δl. Boundaries corresponding to perfect electric (magnetic) conductors are represented by short-circuited (open-circuited) parallel nodes on the boundary. Variations of dielectric and diamagnetic constant [110] are introduced by adding short-circuited series stubs of length $\Delta l/2$ at the series (H-field) nodes and open-circuited $\Delta l/2$ stubs at the shunt (E-field) nodes. Losses can be introduced by resistively loading the shunt nodes. After the time domain response is obtained, the frequency response is calculated using the Fourier transform. Due to the introduction of periodic lattice structures, a typical passband-stopband phenomenon appears in the frequency domain data. The frequency range must be below the upper bound of the lowest passband and is determined by the mesh size Δl. The TLM technique has been used in the analysis of waveguiding structures [111] making use of the Diakoptics Theorem [112] and has been extensively compared to the FDTD technique [113]. Effective numerical absorbers [114, 115] including the FDTD-popular PML absorber have been derived and implemented in the modeling of radiating structures [116]. In addition, TLM has been employed in the analysis of Bondwire Packaging [117] and MEMS switches [118].

Finite Element Method (FEM)

In the finite element method [14–20], instead of partial differential equations with boundary conditions, corresponding functionals (e.g., power) are set up and variational expressions are applied to each cell (element) of the area of interest. Most of the time the elements are rectangles or triangles for two-dimensional problems and parallelepiped (bricks) or tetrahedra for three-dimensional problems, something that allows for the efficient representation of most arbitrary shapes.

Assume that the two-dimensional (x-y) Laplace equation is to be solved

$$\frac{\partial^2 \phi}{\partial x^2} + \frac{\partial^2 \phi}{\partial y^2} = 0 \tag{8.37}$$

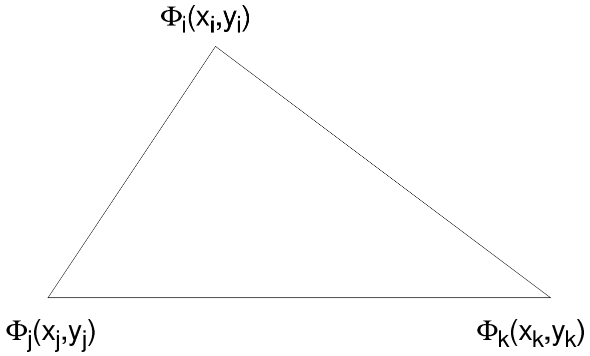

FIGURE 8.13 FEM triangular (2D) element.

The solution is equivalent to the minimization of the functional

$$I(\phi) = \langle \phi, \nabla^2 \phi \rangle = \iint_S \phi \left(\frac{\partial^2 \phi}{\partial x^2} + \frac{\partial^2 \phi}{\partial y^2} \right) dx\, dy = -\iint_S \left[\left(\frac{\partial \phi}{\partial x} \right)^2 + \left(\frac{\partial \phi}{\partial y} \right)^2 \right] dx\, dy. \tag{8.38}$$

The last integral is the superposition of each element's contribution. In each 2D element ϕ can be approximated as polynomial of variables *x* and *y*. For example, for a triangular element *p* (Fig. 8.13),

$$\phi = a + a_x x + a_y y, \tag{8.39}$$

where the constants a, a_x, a_y depend on the ϕ values at the three vertices of the triangle

$$\phi_p = a + a_x x_p + a_y y_p, \tag{8.40}$$

where $p = i, j, k$ are the three triangle vertices. Due to the first derivatives of Eq. (8.39), only a_x, a_y are needed for the calculation of $I(\phi)$, thus

$$\begin{bmatrix} a_x \\ a_y \end{bmatrix} = A \begin{bmatrix} \phi_i \\ \phi_j \\ \phi_k \end{bmatrix} \tag{8.41}$$

For each (i, j, k) element, $I(\phi)$ gets the value

$$I_{i,j,k}(\phi) = \left[\phi_i, \phi_j, \phi_k \right] A^T A \begin{bmatrix} \phi_i \\ \phi_j \\ \phi_k \end{bmatrix} \cdot |\Delta S|, \tag{8.42}$$

where A^T is the transpose of A and ΔS is the area of the triangle (element) calculated by

$$\Delta S = \frac{1}{2} \begin{vmatrix} 1 & x_i & y_i \\ 1 & x_j & y_j \\ 1 & x_k & y_k \end{vmatrix}. \tag{8.43}$$

The Rayleigh-Ritz technique is used for the minimization of $I_{i,j,k}$

$$\frac{\partial I_{i,j,k}}{\partial \phi_i} = \frac{\partial I_{i,j,k}}{\partial \phi_j} = \frac{\partial I_{i,j,k}}{\partial \phi_k} = 0 \tag{8.44}$$

As a result, for each (i, j, k) element

$$A^T A \begin{bmatrix} \phi_i \\ \phi_j \\ \phi_k \end{bmatrix} = 0 \tag{8.45}$$

After iterating this procedure to all elements of the computational domain S and using a connection matrix to account for points that are vertices common to more than one element, the following matrix equation is derived

$$\mathbf{B} \begin{bmatrix} \phi_1 \\ \phi_2 \\ \vdots \\ \phi_N \end{bmatrix} = 0 \tag{8.46}$$

After plugging in the known values of the ϕ_i's that are located on the boundaries, the rest of the ϕ's are calculated through the inversion of matrix **B**. In this way, the potentials of all interior points can be given by Eq. (8.39).

Various element forms [119–123] have been used in order to minimize the memory requirements and facilitate the gridding procedure and the modeling of boundary conditions (PECs, dielectric interfaces). The effect of discretization error on the numerical dispersion has been extensively studied and gridding guidelines have been derived in References 124 and 125. In addition, the analysis of radiating (antennas) and scattering problems have led to the development of numerical absorbers [126–128] with very low numerical reflection coefficients. Due to the shape of the finite elements, the FEM technique can accurately represent very complex geometries and is one of the most popular techniques for scattering problems [129], discontinuities and transitions [130], packaging [131], interconnects [132], and MMIC modeling [133].

The boundary element technique (BE) [134, 135] is a combination of the boundary integral equation and a finite-element discretization applied to the boundary. In essence, it is a form of the integral equation — MoM approach discussed previously. The wave equation for the volume is converted to the surface integral equation through Green's identity. The surface integrals are discretized into N elements, and the evaluation is performed for each element after E- and H-fields are approximated by polynomials. Due to the reduction of the number of dimensions, there is a significant reduction in memory and CPU time requirements. The BE technique has been utilized in the analysis of cavities [136], of planar layered media [137], and in the incorporation of lumped elements in the FEM analysis [138].

Hybrid Techniques

As has become clear from the previous discussion, all numerical techniques have advantages and disadvantages depending on the geometry to be modeled. Integral equation techniques allow for the quick and efficient modeling of radiation phenomena, but derivation of Green's function for complex structures is tedious. The MM method is more appropriate for waveguiding structures where modes are easily determined. The FDTD (and TLM) technique is quite general and requires no preprocessing, though it must often to be run for medium to large execution times. The FEM technique is adaptive due to the shape of the elements, but gridding and functional optimization demands significant computational effort. Thus, there have been numerous efforts for the development of hybrid simulation approaches that use different techniques for different subgeometries and utilize connection relationships for the areas of numerical interfaces. Jin [139] and Gedney [140] proposed a hybrid FEM/MoM method for the modeling of wave scattering by 3D apertures and wave diffraction in gratings. Wu [142] and Monorchio [143] suggested an FEM/FDTD approach for the multifrequency modeling of complex geometries. The MM technique has been coupled with Integral Equation [144], spectral domain [145], and FEM [146] to analyze complicated waveguiding problems including inductive loading and wave scattering. Lindenmeier [147] introduced a hybrid TLM/MIE for thin wire modeling and Pierantoni [148] analyzed numerical aspects of MoM-FDTD and TLM-Integral Equation used in EMC Modeling.

Wavelets: A Memory-Efficient Adaptive Approach?

The term “wavelet” [149–153] has a very broad meaning, ranging from singular integral operators in harmonic approach to sub-band coding algorithms in signal processing, from coherent states in quantum analysis to spline analysis in approximation theory, from multi-resolution transform in computer vision to a multilevel approach in the numerical solution of partial differential equations, and so on. Most of the time wavelets could be considered mathematical tools for waveform representations and segmentations, time-frequency analysis, and fast and efficient algorithms for easy implementation in both time and frequency domains. One of the most important characteristics of expansion to scaling and wavelet functions is the time (domain)-frequency (Fourier-transformed domain) localization. Another very salient feature of these new expansions is that the entire set of basis functions is generated by the dilation and shifting of a single function, called the mother wavelet. The standard approach in ideal lowpass (“scaling,” Fig. 8.14) and bandpass (“wavelet,” Fig. 8.15) filtering for separating an analog signal into different frequency bands emphasizes the importance of time localization. Multiresolution Analysis (MRA), introduced by Mallat and Meyer [154, 155], provides a very powerful tool for the construction of wavelets and implementation of the wavelet decomposition/reconstruction algorithms. In the case of cardinal B-splines [156], an orthonormalization process is used to produce an orthonormal scaling function and, hence, its corresponding orthonormal wavelet by a suitable modification of the two-scale

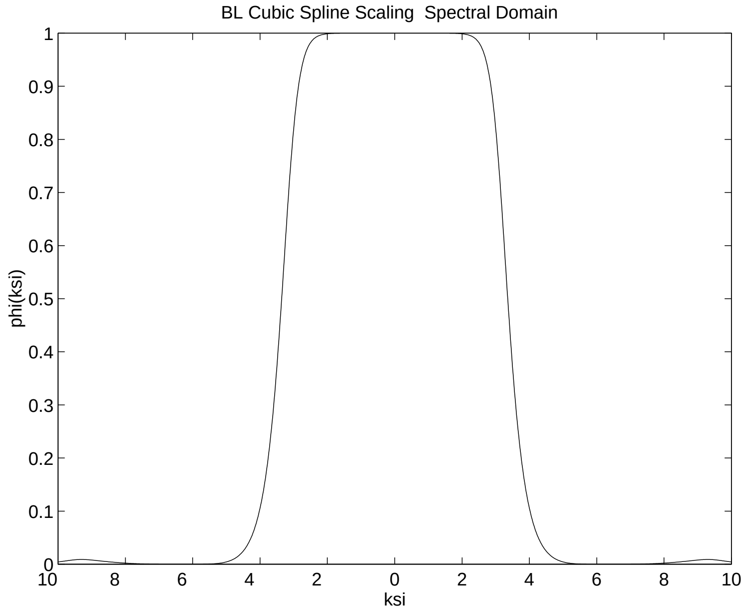

FIGURE 8.14 Battle-Lemarie scaling-spectral (“lowpass”) domain.

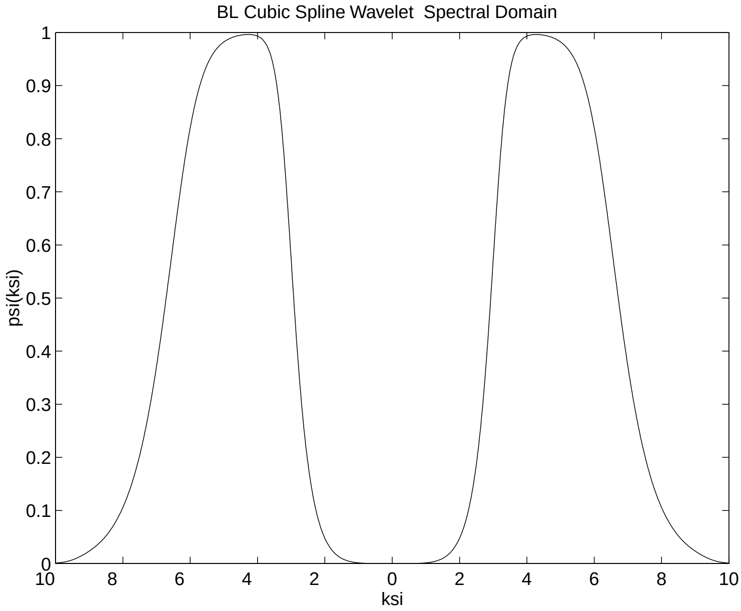

FIGURE 8.15 Battle-Lemarie wavelet-spectral ("bandpass") domain.

sequence. The orthonormalization process was introduced by Schweinler and Wigner [157] and the resulting wavelets are the Battle-Lemarie wavelets, obtained independently by Battle [158] and Lemarie [159] using different methods. The only orthonormal wavelet that is symmetric or antisymmetric and has compact support (to give finite decomposition and reconstruction series) is the Haar [160] wavelet. Nevertheless, these wavelets exhibit poor time-frequency localization. Another set of orthonormal basis is the Daubechies wavelets [161]. At present, MRA has been applied to alleviate the numerical disadvantages mainly of Integral Equation and FDTD methods, though preliminary efforts for FEM are currently being investigated.

It is well known that the Integral Equation method described in previous sections offers a straightforward and efficient numerical solution when applied to small- to medium-scale problems. Difficulties arise when the complexity of the geometry and subsequently the number of the unknowns increases, resulting in very large matrices. All conventional basis functions traditionally used in MoM generate full moment matrices. The computational problems associated with the storage and manipulation of large, densely populated matrices easily rules out the practicality of the integral equation techniques. The potential application of wavelet theory in the numerical solution of integral equations led to the finding that wavelet expansion of certain types of integral operators generates highly sparse linear systems [162]. This proposition was used [163–165] in the moment method formulation of one-dimensional electromagnetic scattering problems and by in the analysis of integrated millimeter-wave and submillimeter-wave waveguides with a Battle-Lemarie orthonormal basis [166]. Sparsity results above 90% allowed for the accurate modeling of structures that could not be analyzed with IE using conventional expansions.

As far as it concerns FDTD, despite its numerous applications, many practical geometries, especially in microwave and millimeter-wave integrated circuits (MMIC), packaging, interconnects, subnanosecond digital electronic circuits [such as multichip modules (MCM)], and antennas used in wireless and microwave communication systems, have been left untreated due to their complexity and the inability of the existing techniques to deal with requirements for large size and high resolution. Krumpholz has shown that Yee's FDTD scheme can be derived by applying the method of moments for the discretization of Maxwell's equations using pulse basis functions for the expansion of the unknown fields. The use of scaling and wavelet functions as a complete expansion basis of the fields demonstrates that MultiResolution Time Domain (MRTD) [167] schemes are generalizations of Yee's FDTD and can extend this

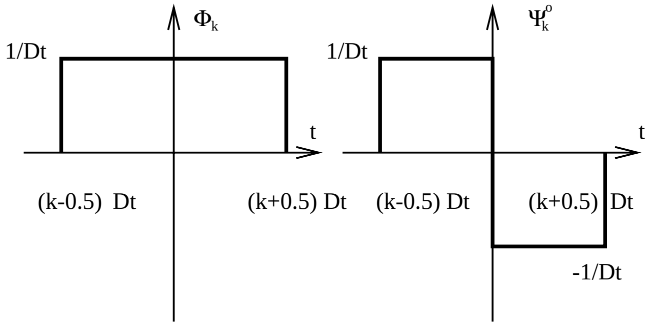

FIGURE 8.16 Haar expansion basis.

technique's capabilities by improving computational efficiency and substantially reducing computer resources. In an MRTD scheme the fields are represented by a twofold expansion in scaling and wavelet functions with respect to time/space. Scaling functions ("lowpass") guarantee a correct modeling of smoothly varying fields. In regions characterized by strong field variations or field singularities, higher resolution is enhanced by incorporating wavelets in the field expansions. The major advantage of the use of MRTD in the time domain is the capability to develop time and space adaptive grids through the thresholding of the wavelet coefficients for each time step throughout the grid. MRTD schemes based on cubic spline Battle-Lemarie scaling and wavelet functions have been used for the derivation of time/space-adaptive schemes [168, 169] in real time. They have been successfully applied to the simulation of 2.5D transmission lines [170] and 3D dielectric cavities [171], filters [172], and mixers [173] offering economies in memory and execution time of order(s) of magnitude with respect to FDTD. Dispersion analysis [174] shows the capability of excellent accuracy with up to 2 points/wavelength (Nyquist limit)! Nevertheless, the functions of this family do not have compact support; thus the MRTD schemes have to be truncated with respect to space, something that requires the use of image theory for the modeling of hard boundaries (e.g., PECs). Thus, specific problems may require the use of functions with compact support (e.g., Haar, Fig. 8.16) especially for the approximation of time derivatives. In this way, the modeling of boundary conditions is most straightforward, though the computational economies are not so dramatic [175–177].

Conclusions

This chapter has briefly presented various numerical techniques that are commonly used for the analysis and design of RF and microwave circuits. Their fundamental features as well as their advantages and disadvantages have been discussed and representative references have been reported. It must be emphasized that there is no numerical scheme that can achieve optimal performance for all types of structures. Thus, the hybridization of these techniques or the implementation of novel approaches (e.g., wavelets), successfully applied in other research areas, would be better candidates for the generalized, efficient, and accurate modeling of modern complex devices used in telecommunication, radar, and computing applications.

References

1. T. Itoh, *Numerical Techniques for Microwave and Millimeter-Wave Passive Structures*, John Wiley & Sons, New York, 1989.
2. R.C. Booton, *Computational Methods for Electromagnetics and Microwaves*, John Wiley & Sons, New York, 1992.
3. R.F. Harrington, *Field Computation by Moment Methods*, The Macmillan Company, New York, 1968.
4. R.C. Hansen, *Moment Methods in Antennas and Scattering*, Artech House, Norwood, MA, 1990.

5. J.H. Wang, *Generalized Moment Methods in Electromagnetics,* John Wiley & Sons, New York, 1991.
6. R. Bancroft, *Understanding Electromagnetic Scattering Using the Moment Method: A Practical Approach,* Artech House, Norwood, MA, 1996.
7. A.F. Peterson, S.L. Ray, and R. Mittra, *Computational Methods for EM,* IEEE Press, 1998.
8. C.R. Scott, *The Spectral Domain Method in Electromagnetics*, Artech House, Norwood, MA, 1989.
9. R. Mittra and W.W. Lee, *Analytical Techniques in the Theory of Guided Waves,* Macmillan, New York, 1971.
10. K.S. Kunz and R.J. Luebbers, *The Finite Difference Time-Domain Method for Electromagnetics,* CRC Press, Boca Raton, FL, 1993.
11. A. Taflove, *Computational Electrodynamics: The Finite-Difference Time-Domain Technique,* Artech House, Norwood, MA, 1995.
12. A. Taflove, *Advances in Computational Electrodynamics,* Artech House, Norwood, MA, 1998.
13. T. Itoh and B. Housmand, *Time-Domain Methods for Microwave Structures: Analysis and Design,* IEEE Press, 1998.
14. G. Strang and G.J. Fix, *An Analysis of the Finite Element Method,* Prentice-Hall, Englewood Cliffs, NJ, 1973.
15. P.P. Silvester and R.L. Ferrari, *Finite Elements for Electrical Engineers,* Cambridge University Press, Cambridge, 1983.
16. J.N. Reddy, *An Introduction to the Finite Element Method,* McGraw Hill, New York, 1984.
17. J.-C. Sabonnadiere and J.-L. Coulomb, *Finite Element Methods in CAD: Electric and Magnetic Fields,* Springer-Verlag, New York, 1987.
18. O.C. Zienkiewicz and R.L. Taylor, *The Finite Element Method,* McGraw Hill, London, 1988.
19. T. Itoh, G. Pelosi, and P.P. Silvester, *Finite Element Software for Microwave Engineering,* John Wiley and Sons, New York, 1996.
20. J.L. Volakis, A Chaterjee, and L.C. Kempel, *Finite Elements Method for Electromagnetics,* IEEE Press, 1998.
21. A.W. Glisson and D.R. Wilton, Simple and efficient methods for problems of radiation and scattering from surfaces, *IEEE Trans. Antennas and Propagation*, 28, 593–603, 1980.
22. T.K. Sarkar, A.R. Djordjevic, and E. Arvas, On the choice of expansion and weighting functions in the numerical solution of operator equations, *IEEE Trans. Antennas and Propagation,* 33, 988–996, 1985.
23. J.R. Mossig and F.E. Gardiol, Analytical and numerical techniques in the Green's function treatment of microstrip antennas and scatterers, *IEE Proc.,* Part H, 130, 175–182, 1983.
24. A.J. Poggio and E.K. Miller, Integral equation solutions of 3D scattering problems, in *Computer Techniques for Electromagnetics,* R. Mittra, Ed., Hemisphere, New York, 1987.
25. A.F. Peterson and P.W. Klock, An improved MFIE formulation for TE-wave scattering from lossy, inhomogeneous dielectric cylinders, *IEEE Trans. Antennas and Propagation,* 25, 518–524, 1987.
26. F. Ling, D. Jiao, and J.M. Jin, Efficient EM modeling of microstrip structures in multilayer media, *IEEE Trans. Microwave Theory Tech.,* 47, 1810–1818, 1999.
27. D.M. Pozar, Input impedance and mutual coupling of rectangular microstrip antennas, *IEEE Trans. Antennas and Propagation,* 30, 1191–1196, 1982.
28. W.-T. Chen and H.-R. Chuang, Numerical computation of the EM coupling between a circular loop antenna and a full-scale human-body model, *IEEE Trans. Microwave Theory Tech.,* 1516–1520, 1998.
29. G. Athanasoulias and N.K. Uzunoglu, An accurate and efficient entire-domain basis Galerkin's method for the integral equation analysis of integrated rectangular dielectric waveguides, *IEEE Trans. Microwave Theory Tech.,* 43, 2794–2804, 1995.
30. M. Swaminathan, T.K. Sarkar, and A.T. Adams, Computation of TM and TE modes in waveguides based on surface integral formulation, *IEEE Trans. Microwave Theory Tech.,* 40, 285–297, 1992.
31. S.J. Polychronopoulos and N.K. Uzunoglu, Propagation and coupling properties of integrated optical waveguides — an integral equation formulation, *IEEE Trans. Microwave Theory Tech.,* 44, 641–650, 1996.

32. P. Cottis and N. Uzunoglu, Integral equation approach for the analysis of anisotropic channel waveguides, *J. Opt. Soc. A. A,* 8, 4, 608–614, 1991.
33. P. Guillot, P. Couffignal, H. Baudrand, and B. Theron, Improvement in calculation of some surface integrals: application to junction characterization in cavity filter design, *IEEE Trans. Microwave Theory Tech.,* 41, 2156–2160, 1993.
34. T.E. van Deventer, L.P.B. Katehi, and A.C. Cangellaris, Analysis of conductor losses in high-speed interconnects, *IEEE Trans. Microwave Theory Tech.,* 42, 78–83, 1994.
35. A.W. Mathis and A.F. Peterson, Efficient electromagnetic analysis of a doubly infinite array of rectangular apertures, *IEEE Trans. Microwave Theory Tech.,* 46–54, 1998.
36. S-G. Hsu and R.-B. Wu, Full-wave characterization of a through hole via in multi-layered packaging, *IEEE Trans. Microwave Theory Tech.,* 1073–1081, 1995.
37. A.M. Rajeek and A. Chakraborty, Analysis of a wide compound slot-coupled parallel waveguide coupler and radiator, *IEEE Trans. Microwave Theory Tech.,* 43, 802–809, 1995.
38. G.V. Eleftheriades, J.R. Mosig, and M. Guglielmi, A fast integral equation technique for shielded planar circuits defined on nonuniform meshes, *IEEE Trans. Microwave Theory, Tech.,* 44, 2293–2296, 1996.
39. E. Yamashita and R. Mittra, Variational method for the analysis of microstrip line, *IEEE Trans. Microwave Theory, Tech.,* 16, 251–256, 1968.
40. E.J. Denlinger, A frequency dependent solution for microstrip transmission lines, *IEEE Trans. Microwave Theory, Tech.,* 19, 30–39, 1971.
41. T. Itoh and R. Mittra, Spectral-domain approach for calculating the dispersion characteristics of microstrip lines, *IEEE Trans. Microwave Theory, Tech.,* 21, 496–499, 1973.
42. M.I. Aksun and R. Mittra, Choices of expansion and testing functions for MoM applied to a class of EM problems, *IEEE Trans. Microwave Theory, Tech.,* 41, 503–509, 1993.
43. R.H. Jansen, Unified user-oriented computation of shielded, covered and open planar microwave and millimeter wave transmission-line characteristics, *IEE J. Microwave Opt. Acoust.,* 3, 14–22, 1979.
44. T. Itoh, Spectral domain immitance approach for dispersion characteristics of generalized printed transmission lines, *IEEE Trans. Microwave Theory Tech.,* 28, 733–736, 1980.
45. J. Sercu, N. Fache, F. Libbrecht, and D. De Zutter, Full-wave space-domain analysis of open microstrip discontinuities including the singular current-edge behavior, *IEEE Trans. Microwave Theory Tech.,* 41, 1581–1588, 1993.
46. F. Olyslager, D. De Zutter, and K. Blomme, Rigorous full-wave analysis of propagation characteristics of general lossless and lossy multiconductor transmission lines in multilayered media, *IEEE Trans. Microwave Theory Tech.,* 41, 79–88, 1993.
47. K.K.M. Cheng and J.K.A. Everard, A new technique for the quasi-TEM analysis of conductor-backed coplanar waveguide structures, *IEEE Trans. Microwave Theory Tech.,* 41, 1589–1592, 1993.
48. N. Gupta and M. Singh, Investigation of periodic structures in a fin line: A space-spectral domain approach, *IEEE Trans. Microwave Theory Tech.,* 43, 2708–2710, 1995.
49. Y. Imaizumi, M. Shinagawa, and H. Ogawa, Electric field distribution measurement of microstrip antennas and arrays using electro-optic sampling, *IEEE Trans. Microwave Theory Tech.,* 43, 2402–2407, 1995.
50. Y.-D. Lin, J.-W. Sheen, and C.-K.C. Tzuang, Analysis and design of feeding structures for microstrip leaky wave antenna, *IEEE Trans. Microwave Theory Tech.,* 44, 1540–1547, 1996.
51. P. Petre and M. Swaminathan, Spectral domain technique using surface wave excitation for the analysis of interconnects, *IEEE Trans. Microwave Theory Tech.,* 42, 1744–1749, 1994.
52. B.L. Ooi, M.S. Leong, P.S. Kooi, and T.S. Yeo, Enhancements of the spectral-domain approach for analysis of microstrip Y-junction, *IEEE Trans. Microwave Theory Tech.,* 45, 1800–1805, 1997.
53. K. Sabetfakhri and L.P.B. Katehi, Analysis of general class of open dielectric waveguides by spectral-domain technique, *Proc. IEEE-MTT Symposium,* 3, 1523–1526, 1993.
54. T. Itoh, Analysis of microstrip resonators, *IEEE Trans. Microwave Theory Tech.,* MTT-22, 946–952, 1974.

55. T.M. Weller, K.J. Herrick, and L.P.B. Katehi, Quasi-static design technique for mm-wave micromachined filters with lumped elements and series stubs, *IEEE Trans. Microwave Theory Tech.,* 45, 931–938, 1997.
56. Y.C. Shih and K.G. Gray, Convergence of numerical solutions of step-type waveguide discontinuity problems by modal analysis, *Proc. IEEE-MTT Symposium,* 233–235, 1983.
57. M. Leroy, On the convergence of numerical results in modal analysis, *IEEE Trans. Antennas and Propagation,* 31, 655–659, 1983.
58. A. Wexler, Solution of waveguide discontinuities by modal analysis, *IEEE Trans. Microwave Theory Tech.,* 15, 508–517, 1967.
59. W. Wessel, T. Sieverding, and F. Arndt, Mode-matching analysis of general waveguide multiport junctions, *Proc. IEEE-MTT Symposium,* 1273–1276, 1999.
60. A.S. Omar and K. Schunemann, Transmission matrix representation of finite discontinuity, *IEEE Trans. Microwave Theory Tech.,* 33, 830–835, 1985.
61. R. Vahldieck and W.J.R. Hoefer, Finline and metal insert filters with improved passband separation and increased stopband attenuation, *IEEE Trans. Microwave Theory Tech.,* 33, 1333–1339, 1985.
62. W. Menzel and I. Wolff, A method for calculating the frequency-dependent properties of microstrip discontinuities, *IEEE Trans. Microwave Theory Tech.,* 25, 107–112, 1977.
63. T.S. Chu, T. Itoh, and Y.-C. Shih, Comparative study of mode-matching formulations for microstrip discontinuity problems, *IEEE Trans. Microwave Theory Tech.,* 33, 1018–1023, 1985.
64. F. Alessandri, G. Baini, M. Mongiardo, and R. Sorrentino, A 3D mode matching technique for the efficient analysis of coplanar MMIC discontinuities with finite metallization thickness, *IEEE Trans. Microwave Theory Tech.,* 41, 1625–1629, 1993.
65. R. Schmidt and P. Russer, Modeling of cascaded coplanar waveguide discontinuities by the mode-matching approach, *IEEE Trans. Microwave Theory Tech.,* 43, 2910–2917, 1995.
66. Y.C. Shih, Design of waveguide E-plane filters with all metal insert, *IEEE Trans. Microwave Theory Tech.,* 32, 695–704, 1984.
67. F. Arndt et al., E-plane integrated filters with improved stopband attenuation, *IEEE Trans. Microwave Theory Tech.,* 32, 1391–1394, 1984.
68. F. Arndt et al., Computer-optimized multisection transforms between rectangular waveguides of adjacent frequency bands, *IEEE Trans. Microwave Theory Tech.,* 32, 1479–1484, 1984.
69. F. Arndt et al., Optimized E-plane T-junction series power divider, *IEEE Trans. Microwave Theory Tech.,* 35, 1052–1059, 1987.
70. R. Mehran, Computer-aided design of microstrip filters considering dispersion, loss and discontinuity effects, *IEEE Trans. Microwave Theory Tech.,* 27, 239–245, 1979.
71. L. Accatino, G. Bertin, and M. Mongiardo, Elliptical cavity resonators for dual-mode narrow-band filters, *IEEE Trans. Microwave Theory Tech.,* 45, 2393–2401, 1997.
72. J. Bornemann and F. Arndt, Rigorous design of evanescent-mode E-plane finned waveguide band-pass filters, *Proc. IEEE-MTT Symposium,* 603–606, 1989.
73. K.S. Yee, Numerical solution of initial boundary value problems involving Maxwell's equations in isotropic media, *IEEE Trans. Antennas and Propagation,* 14, 302–307, 1966.
74. R. Holland, THREDE: A free-field EMP coupling and scattering code, *IEEE Trans. Nuclear Science,* 24, 2416–2421, 1977.
75. A. Taflove and M.E. Brodwin, Numerical solution of steady-state electromagnetic scattering problems using the time-dependent Maxwell's equations, *IEEE Trans. Microwave Theory Tech.,* 23, 623–630, 1975.
76. J.-P. Berenger, A perfectly matched layer for the absorption of electromagnetic waves, *Computational Physics,* 114, 185–200, 1994.
77. D.S. Katz, E.T. Thiele, and A. Taflove, Validation and extension to three dimensions of the Berenger PML absorbing boundary conditions for FDTD meshes, *IEEE Microwave and Guided Wave Letters,* 4, 344–346, 1994.

78. E. Tentzeris, M. Krumpholz, N. Dib, J.-G. Yook, and L.P.B. Katehi, FDTD characterization of waveguide probe structures, *IEEE Trans. Microwave Theory Tech.,* 46, 10, 1452–1460, 1998.

79. M. Werthen, M. Rittweger, and I. Wolff, FDTD simulation of waveguide junctions using a new boundary condition for rectangular waveguides, *Proc. 24th European Microwave Conf.,* Cannes, France, 1715–1719, 1994.

80. A. Taflove, Computation of the electromagnetic fields and induced temperatures within a model of the microwave-irradiated human eye, Ph.D. Dissertation, Department of Electrical Engineering, Northwestern University, Evanston, IL, June 1975.

81. J. Chen, C. Wu, T.K. Lo, K.-L. Wu, and J. Litva, Using linear and nonlinear predictors to improve the computational efficiency of the FDTD algorithm, *IEEE Trans. Microwave Theory Tech.,* 42, 1992–1997, 1994.

82. V. Jandhyala, E. Michielssen, and R. Mittra, On the performance of different AR methods in the spectral estimation of FDTD waveforms, *Microwave and Optical Technology Letters,* 7, 690–692, 1994.

83. M. DePourcq, Field and power density calculations in closed microwave systems by 3D finite differences, *IEE Proc. H: Microwaves, Antennas and Propagation,* 132, 360–368, 1985.

84. E.A. Navarro, V. Such, B. Gimeno, and J.L. Cruz, T-junctions in square coaxial waveguide: an FDTD approach, *IEEE Trans. Microwave Theory Tech.,* 42, 347–350, 1994.

85. C. Wang, B.-Q. Gao, and C.-P. Ding, Q factor of a resonator by the FDTD method incorporating perturbation techniques, *Electronics Letters,* 29, 1866–1867, 1993.

86. G.-C. Liang, Y.-W. Liu, and K.K. Mei, Full-wave analysis of coplanar waveguide and slotline using FDTD, *IEEE Trans. Microwave Theory Tech.,* 37, 1949–1957, 1989.

87. D.M. Sheen, S.M. Ali, M.D. Abouzahra, and J.A. Kong, Application of the 3D FDTD method to the analysis of planar microstrip circuits, *IEEE Trans. Microwave Theory Tech.,* 38, 849–857, 1990.

88. A.C. Cangellaris and D.B. Wright, Analysis of the numerical error caused by the stair-stepped approximation of a conducting boundary in FDTD simulations of electromagnetic phenomena, *IEEE Trans. Antennas and Propagation,* 39, 1518–1525, 1991.

89. C.-W. Lam, S.M. Ali, and P. Nuytkens, Three-dimensional modeling of multichip module interconnects, *IEEE Trans. Components, Hybrids and Manufacturing Technology,* 16, 699–704, 1993.

90. M. Piket-May, A. Taflove, and J. Baron, FDTD modeling of digital signal propagation in 3D circuits with passive and active loads, *IEEE Trans. Microwave Theory Tech.,* 42, 1514–1523, 1994.

91. R.J. Luebbers, K.S. Kunz, M. Schneider, and F. Hunsberger, An FDTD near zone to far zone transformation, *IEEE Trans. Antennas and Propagation,* 39, 429–433, 1991.

92. K.L. Shlager and G.S. Smith, Comparison of two FDTD near-field to near-field transformations applied to pulsed antenna problems, *Electronics Letters,* 31, 936–938, 1995.

93. J.G. Maloney, G.S. Smith, and W.R. Scott, Jr., Accurate computation of the radiation from simple antennas using the FDTD method, *IEEE Trans. Antennas and Propagation,* 38, 1059–1069, 1990.

94. R. Luebbers and K. Kunz, FDTD calculations of antenna mutual coupling, *IEEE Trans. Electromagnetic Compatibility,* 34, 357–359, 1992.

95. R.J. Luebbers and J. Beggs, FDTD calculation of wideband antenna gain and efficiency, *IEEE Trans. Antennas and Propagation,* 40, 1403–1407, 1992.

96. P.A. Tirkas and C.A. Balanis, FDTD method for antenna radiation, *IEEE Trans. Antenna and Propagation,* 40, 334–340, 1992.

97. K. Uehara and K. Kagoshima, Rigorous analysis of microstrip phased array antennas using a new FDTD method, *Electronics Letters,* 30, 100–101, 1994.

98. M.A. Jensen and Y. Rahmat-Samii, Performance analysis of antennas for hand-held transceivers using FDTD, *IEEE Trans. Antennas and Propagation,* 42, 1106–1113, 1994.

99. A Taflove and K.R. Umashankar, Radar cross section of general three-dimensional scatterers, *IEEE Trans. Electromagnetic Compatibility,* 25, 433–440, 1983.

100. C.L. Britt, Solution of electromagnetic scattering problems using time-domain techniques, *IEEE Trans. Antennas and Propagation,* 37, 1181–1192, 1989.

101. W. Sui, D.A. Christensen, and C.H. Durney, Extending the 2D FDTD method to hybrid electromagnetic systems with active and passive lumped elements, *IEEE Trans. Microwave Theory Tech.,* 40, 724–730, 1992.
102. P. Ciampolini, P. Mezzanotte, L. Roselli, and R. Sorrentino, Accurate and efficient circuit simulation with lumped-element FDTD, *IEEE Trans. Microwave Theory Tech.,* 44, 2207–2215, 1996.
103. C.-N. Kuo, B. Housmand, and T. Itoh, Full-wave analysis of packaged microwave circuits with active and nonlinear devices: an FDTD approach, *IEEE Trans. Microwave Theory Tech.,* 45, 819–826, 1997.
104. M.A. Alsunaidi, S.M. Sohel Imtiaz, and S.M. El-Ghazaly, Electromagnetic wave effects on microwave transistors using a full-wave time-domain model, *IEEE Trans. Microwave Theory Tech.,* 44, 799–808, 1996.
105. V.A. Thomas, M.E. Jones, M. Piket-May, A. Taflove, and E. Harrigan, The use of SPICE lumped circuits as sub-grid models for FDTD analysis, *IEEE Microwave and Guided Wave Letters,* 4, 141–143, 1994.
106. S. Akhtarzad and P.B. Johns, Three-dimensional transmission-line matrix computer analysis of microstrip resonators, *IEEE Trans. Microwave Theory Tech.,* MTT-23, 990–997, 1975.
107. W.J.R. Hoefer, The transmission-line matrix method-theory and applications, *IEEE Trans. Microwave Theory Tech.,* MTT-33, 882–893, 1985.
108. C. Christopoulos, *The Transmission-Line Modeling Method,* IEEE/OUP, 1995.
109. P.B. Johns, A symmetrical condensed node for the TLM-method, *IEEE Trans. Microwave Theory Tech.,* 35, 370–377, 1987.
110. L.R.A.X. de Menezes and W.J.R. Hoefer, Modeling of general (nonlinear) constitutive relationships in SCN TLM, *IEEE Trans. Microwave Theory Tech.,* MTT-44, 854–861, 1996.
111. M. Krumpholz and P. Russer, Discrete time-domain Green's functions for three-dimensional TLM modeling of the radiating boundary conditions, *9th Annual Review of Progress in ACES Digest,* 458–466, 1993.
112. M. Righi and W.J.R. Hoefer, Efficient 3D-SCN-TLM diakoptics for waveguide components, *IEEE Trans. Microwave Theory Tech.,* 42, 2381–2384, 1994.
113. M. Krumpholz, C. Huber, and P. Russer, A field theoretical comparison of FDTD and TLM, *IEEE Trans. Microwave Theory Tech.,* 43, 1935–1950, 1995.
114. C. Eswarappa and W.J.R. Hoefer, One-way equation absorbing boundary condition for 3D TLM analysis of planar and quasi-planar structures, *IEEE Trans. Microwave Theory Tech.,* 42, 1669–1677, 1994.
115. J.L. Dubard and D. Pompei, A modified 3D-TLM variable node for the Berenger's perfectly matched layer implementation, *13th Annual Review of Progress in ACES Digest,* 661–665, 1997.
116. M.I. Sobhy, M.W.R. Ng, R.J. Langley, and J.C. Batchelor, TLM simulation of patch antenna on magnetized ferrite substrate, *16th Annual Review of Progress in ACES Digest,* 562–569, 2000.
117. A.P. Duffy, J.L. Herring, T.M. Benson, and C. Christopoulos, Improved wire modeling in TLM, *IEEE Trans. Microwave Theory Tech.,* 42, 1978–1983, 1994.
118. F. Coccetti, L. Vietzorreck, V. Chtchekatourov, and P. Russer, A numerical study of MEMS capacitive switches using TLM, *16th Annual Review of Progress in ACES Digest,* 580–587, 2000.
119. D.H. Schaubert, D.R. Wilton, and A.W. Glisson, A tetrahedral method for electromagnetic scattering by arbitrarily shaped inhomogeneous dielectric bodies, *IEEE Trans. Antennas and Propagation,* 32, 77–85, 1984.
120. Z.J. Cendes, Vector finite elements for electromagnetic field computation, *IEEE Trans. Magnetics,* 27, 3958–3966, 1991.
121. A. Chatterjee, J.M. Jin, and J.L. Volakis, Edge-based finite elements and vector ABC's applied to 3D scattering, *IEEE Trans Antennas and Propagation,* 41, 221–226, 1993.
122. A.F. Peterson and D.R. Wilton, Curl-conforming mixed-order edge elements for discretizing the 2D and 3D vector Helmholtz equation, in *Finite Element Software for Microwave Engineering,* T. Itoh, G. Pelosi, and P.P. Silvester, Eds., Wiley, New York, 1996.

123. Z. Pantic-Tanner, J.S. Savage, D.R. Tanner, and A.F. Peterson, Two-dimensional singular vector elements for finite-element analysis, *IEEE Trans. Microwave Theory Tech.,* 46, 178–184, 1998.
124. R. Lee and A.C. Cangellaris, A study of discretization error in the finite element approximation of wave solutions, *IEEE Trans. Antennas and Propagation,* 40, 542–549, 1992.
125. G.S. Warren and W.R. Scott, An investigation of numerical dispersion in the vector finite element method, *IEEE Trans. Antennas and Propagation,* 42, 1502–1508, 1994.
126. L.W. Pearson, R.A. Whitaker, and L.J. Bahrmasel, An exact radiation boundary condition for the finite-element solution of electromagnetic scattering on an open domain, *IEEE Trans. Magnet.,* 25, 3046–3048, 1989.
127. J.P. Webb and V.N. Kanellopoulos, A numerical study of vector absorbing boundary conditions for the finite element solution of Maxwell's equations, *IEEE Microwave Guided Wave Letters,* 1, 325–327, 1991.
128. W. Sun and C.A. Balanis, Vector one-way absorbing boundary conditions for FEM applications, *IEEE Trans. Antennas and Propagation,* 42, 872–878, 1994.
129. J.M. Jin and V.V. Liepa, A note on hybrid finite element for solving scattering problems, *IEEE Trans. Antennas and Propagation,* 36, 1486–1490, 1988.
130. J.S. Wang, Analysis of microstrip discontinuities based on edge-element 3D FEM formulation and absorbing boundary conditions, *Proc. IEEE-MTT Symposium,* 2, 745–748, 1993.
131. J.-S. Wang and R. Mittra, Finite element analysis of MMIC structures and electronic packages using absorbing boundary conditions, *IEEE Trans. Microwave Theory Tech.,* 42, 441–449, 1994.
132. J.-G. Yook, N.I. Dib, and L.P.B. Katehi, Characterization of high frequency interconnects using finite difference time-domain and finite element methods, *IEEE Trans. Microwave Theory Tech.,* 42, 1727–1736, 1994.
133. A.C. Polycarpou, M.R. Lyons, and C.A. Balanis, Finite element analysis of MMIC waveguide structures with anisotropic substrates, *IEEE Trans. Microwave Theory Tech.,* 44, 1650–1663, 1996.
134. C.A. Brebbia, *The Boundary Element Method for Engineers,* Pentech Press, London, 1978.
135. S. Kagami and I. Fukai, Application of boundary element method to EM field problems, *IEEE Trans. Microwave Theory Tech.,* 32, 455–461, 1984.
136. H. Cam, S. Toutain, P. Gelin, and G. Landrac, Study of Fabry-Perot cavity in the microwave frequency range by the boundary element method, *IEEE Trans. Microwave Theory Tech.,* 40, 298–304, 1992.
137. T.F. Eibert and V. Hansen, 3-D FEM/BEM-hybrid approach based on a general formulation of Huygen's principle for planar layered media, *IEEE Trans. Microwave Theory Tech.,* 45, 1105–1112, 1997.
138. K. Guillouard, M.F. Wong, and V. Fouad Hanna, A new global time domain electromagnetic simulator of microwave circuits including lumped elements based on finite element method, *Proc. IEEE-MTT Symposium,* 1239–1242, 1997.
139. J.M. Jin, J.L. Volakis, A FE-boundary integral formulation for scattering by 3D cavity-blocked apertures, *IEEE Trans. Antennas and Propagation,* 39, 97–104, 1991.
140. S.D. Gedney, J.F. Lee, and R. Mittra, A combined FEM/MoM approach to analyze the plane wave diffraction by arbitrary gratings, *IEEE Trans. Antenna and Propagation,* 40, 363–370, 1992.
141. R.D. Graglia, D.R. Wilton, and A.F. Peterson, Higher order interpolatory vector bases for computational EM, *IEEE Trans. Antennas and Propagation,* 45, 329–342, 1997.
142. R.-B. Wu and T. Itoh, Hybridizing FDTD analysis with unconditionally stable FEM for objects of curved boundary, *Proc. IEEE-MTT Symposium,* 833–836, 1995.
143. A. Monorchio and R. Mittra, A hybrid FE/FDTD technique for solving complex electromagnetic problems, *IEEE Microwave Guided Wire Letters,* 8, 93–95, 1998.
144. A.G. Engel and L.P.B. Katehi, Frequency and time domain characterization of microstrip-ridge structures, *IEEE Trans. Microwave Theory Tech.,* 1251–1262, 1993.
145. H. Esteban et al., A new hybrid mode-matching method for the analysis of inductive obstacles and discontinuities, *Proc. IEEE-AP Symposium,* 966–969, 1999.

146. D.C. Ross, J.L. Volakis, and H. Anastasiu, Hybrid FE-modal analysis of jet engine inlet scattering, *IEEE Trans. Antennas and Propagation,* 43, 1995.

147. S. Lindenmeier, C. Christopoulos, and P. Russer, Thin wire modeling with TLM/MIE method, *16th Annual Review of Progress in ACES Digest,* 587–594, 2000.

148. L. Pierantoni, G. Cerri, S. Lindemeier, and P. Russer, Theoretical and numerical aspects of the hybrid MoM-FDTD, TLM-IE and ARB methods for the efficient modeling of EMC problems, *Proc. 29 EuMC,* 2, 313–316, 1999.

149. I. Daubechies, *Ten Lectures on Wavelets,* SIAM, 1992.

150. G. Kaiser, *A Friendly Guide to Wavelets,* Springer Verlag, Berlin, 1994.

151. C. Burrus, R.A. Gopinath, and H. Guo, *Introduction to Wavelets and Wavelet Transforms: A Primer,* Prentice Hall, Englewood Cliffs, NJ, 1997.

152. J. Goswami and A. Chan, *Fundamentals on Wavelets: Theory, Algorithms and Applications,* John Wiley & Sons, New York, 1999.

153. W. Dahmen, A.J. Kurdila, and P. Oswald, *Multiscale Wavelet Methods for Partial Differential Equations,* Academic Press, New York, 1997.

154. S. Mallat, Multiresolution representation and wavelets, Ph.D. Thesis, University of Pennsylvania, Philadelphia, 1988.

155. Y. Meyer, Ondelettes et Fonctions Splines, Seminaire EDP, Ecole Polytechnique, Paris, December 1986.

156. L.L. Schumaker, *Spline Functions: Basic Theory,* Wiley-Interscience, New York, 1981.

157. H.C. Schweinler and E.P. Wigner, Orthogonalization methods, *J. Math. Phys.,* 11, 1693–1694, 1970.

158. G. Battle, A block spin construction of ondelettes, Part I: Lemarie functions, *Comm. Math. Phys.,* 110, 601–615, 1987.

159. P.G. Lemarie, Ondelettes a localization exponentielles, *J. Math. Pures Appl.,* 67, 227–236, 1988.

160. A. Haar, Zur theorie der orthogonalen funktionsysteme, *Math. Ann.,* 69, 331–371, 1910.

161. I. Daubechies, Orthonormal bases of compactly supported wavelets, *Comm. Pure Appl. Math.,* 41, 909–996, 1988.

162. G. Beylkin, R. Coifman, and V. Rokhlin, Fast wavelet transforms and numerical algorithms I, *Commun. Pure Appl. Math., 44, 141–183, 1991.*

163. B.Z. Steinberg and Y. Leviatan, On the use of wavelet expansions in the method of moments, *IEEE Trans. Antennas and Propagation,* 41, 610–619, 1993.

164. G. Wang, On the utilization of periodic wavelet expansions in the moment methods, *IEEE Trans. Microwave Theory Tech.,* 43, 2495–2498, 1995.

165. J.C. Goswami, A.K. Chan, and C.K. Chui, On solving first-kind integral equations using wavelets on a bounded interval, *IEEE Trans. Antennas and Propagation,* 43, 614–622, 1995.

166. K. Sabetfakhri and L.P.B. Katehi, Analysis of integrated millimeter-wave and submillimeter-wave waveguides using orthonormal wavelet expansions, *IEEE Trans. Microwave Theory Tech.,* 42, 2412–2422, 1994.

167. M. Krumpholz and L.P.B. Katehi, MRTD: New time domain schemes based on multiresolution analysis, *IEEE Trans. Microwave Theory Tech.,* 44, 4, 555–561, April 1996.

168. M.M. Tentzeris, J. Harvey, and L.P.B. Katehi, Time adaptive time-domain techniques for the design of microwave circuits, *IEEE Microwave Guided Wave Letters,* 9, 96–98, 1999.

169. M. Tentzeris, R. Robertson, A. Cangellaris, and L.P.B. Katehi, Space- and time-adaptive gridding using MRTD, *Proc. IEEE-MTT Symposium,* 337–340, 1997.

170. M. Tentzeris, M. Krumpholz, and L.P.B. Katehi, Applications of MRTD to printed transmission lines, *Proc. IEEE-MTT Symposium,* 573–576, 1996.

171. R.L. Robertson, M. Tentzeris, and L.P.B. Katehi, Modelling of dielectric-loaded cavities using MRTD, *Int. Journal of Numerical Modeling, Special Issue on Wavelets in Electromagnetics,* 11, 55–68, 1998.

172. M. Tentzeris and L.P.B. Katehi, Space adaptive analysis of evanescent waveguide filters, *Proc. IEEE-MTT Symposium,* 481–484, 1998.

173. L. Roselli, M. Tentzeris, and L.P.B. Katehi, Nonlinear circuit characterization using a multiresolution time domain technique, *Proc. IEEE-MTT Symposium,* 1387–1390, 1998.
174. M. Tentzeris, R. Robertson, J. Harvey, and L.P.B. Katehi, Stability and dispersion analysis of Battle-Lemarie based MRTD schemes, *IEEE Trans. Microwave Theory Tech.,* 47, 7, 1004–1013, 1999.
175. K. Goverdhanam, M. Tentzeris, M. Krumpholz, and L.P.B. Katehi, An FDTD multigrid based on multiresolution analysis, *Proc. IEEE-AP Symposium,* 352–355, 1996.
176. M. Fujii and W.J.R. Hoefer, Formulation of a Haar-wavelet based multiresolution analysis similar to 3D FDTD method, *Proc. IEEE-MTT Symposium,* 1393–1396, 1998.
177. C. Sarris and L.P.B. Katehi, Multiresolution time-domain (MRTD) schemes with space-time Haar wavelets, *Proc. IEEE-MTT Symposium,* 1459–1462, 1999.

8.3 Computer Aided Design of Passive Components

Daniel G. Swanson, Jr.

Computer-aided design (CAD) of passive RF and microwave components has advanced slowly but steadily over the past four decades. The 1960s and 1970s were the decades of the mainframe computer. In the early years, CAD tools were proprietary, in-house efforts running on text-only terminals. The few graphics terminals available were large, expensive, and required a short, direct connection to the mainframe. Later in this period, commercial tools became available for use on in-house machines or through time sharing services. A simulation of a RF or microwave network was based on a combination of lumped and distributed elements. The elements were connected in cascade using ABCD parameters or in a nodal network using admittance- or Y-parameters. The connection between elements and the control parameters for the simulation were stored in a text file called a netlist. The netlist syntax was similar but unique for each software tool. The mathematical foundations for a more sophisticated analysis based on Maxwell's equations were being laid down in this same time period.[1-4] However, the computer technology of the day could not support effective commercial implementation of these more advanced codes.

The 1980s brought the development of the microprocessor and UNIX workstations. The UNIX workstation played a large role in the development of more sophisticated CAD tools. For the first time there was a common operating system and computer language (the C language) to support the development of cross-platform applications. UNIX workstations also featured large, bit mapped graphics displays for interaction with the user. The same microprocessor technology that launched the workstation also made the personal computer possible. Although the workstation architecture was initially more sophisticated, personal computer hardware and software has grown steadily more elaborate. Today, the choice between a workstation and a personal computer is largely a personal one. CAD tools in this time period were still based on lumped and distributed concepts. The innovations brought about by the cheaper, graphics-based hardware had largely to do with schematic capture and layout. Schematic capture replaced the netlist on the input side of the analysis and automatic or semi-automatic layout provided a quicker path to the finished circuit after analysis and optimization.

The greatest innovation in the 1990s was the emergence of CAD tools based on the direct solution of Maxwell's equations. Finally, there was enough computer horsepower to support commercial versions of the codes that had been in development since the late 1960s and early 1970s. These codes are in general labeled electromagnetic field-solvers although any one code may be based on one of several different numerical methods. Sonnet ***em***,[5] based on the Method of Moments (MoM), was the first commercially viable tool designed for RF and microwave engineers. Only a few months later, Hewlett-Packard HFSS,[6] a Finite Element Method (FEM) code co-developed with Ansoft Corp., was released to the design community. All of these tools approximate the true fields or currents in the problem space by subdividing the problem into basic "cells" or "elements" that are roughly one tenth to one twentieth of a guide wavelength in size. For any guided electromagnetic wave, the guide wavelength is the distance spanned by one full cycle of the electric or magnetic field. The problem is to find the magnitude of the assumed current on each cell or the field at the junction of elements. The final solution is then just the sum of

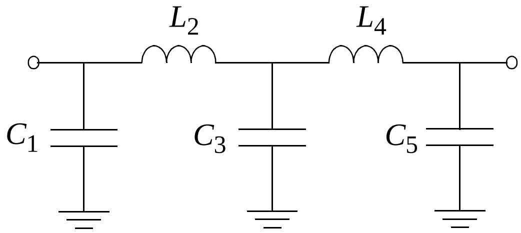

FIGURE 8.17 Lumped element lowpass filter or matching network.

each small contribution from each basic unit. Most of these codes first appeared on UNIX workstations and then migrated to the personal computer, as that hardware became more powerful. In the later years of the 1990s, field-solver codes appeared that were developed on and for the personal computer. In the early years, the typical field-solver problem was a single discontinuity or some other structure that was small in terms of wavelengths. Today, groups of discontinuities, complete matching networks, or small parts of a multilayer printed circuit (PC) board are all suitable problems for a field-solver. Field-solver data in S-parameter form is typically imported into a circuit simulator and combined with lumped and distributed models to complete the analysis of the structure.

Circuit Theory Based CAD

CAD of low frequency circuits is at least 30 years old and microwave circuits have been analyzed by computer for at least 20 years. At very low frequencies, we can connect inductors, capacitors, resistors, and active devices in a very arbitrary way. The lumped lowpass filter shown in Fig. 8.17 is a simple example. This very simple circuit has only three nodes. Most network analysis programs will form an admittance matrix (Y-matrix) internally and invert the matrix to find a solution. The Y-matrix is filled using some fairly simple rules. A shunt element connected to node two generates an entry at Y_{22}. A series element connected between nodes two and three generates entries at Y_{22}, Y_{23}, Y_{32}, and Y_{33}. A large ladder network with sequential node numbering results in a large tri-diagonal matrix with many zeros off axis.

$$\mathbf{Y} = \begin{bmatrix} j\omega C_1 - j\dfrac{1}{\omega L_2} & j\dfrac{1}{\omega L_2} & 0 \\ j\dfrac{1}{\omega L_2} & j\omega C_3 - j\dfrac{1}{\omega L_2} - j\dfrac{1}{\omega L_4} & j\dfrac{1}{\omega L_4} \\ 0 & j\dfrac{1}{\omega L_4} & j\omega C_5 - j\dfrac{1}{\omega L_4} \end{bmatrix}$$

The Y-matrix links the known source currents to the unknown node voltages. **I** is a vector of source currents. Typically the input node is excited with a one amp source and the rest of the nodes are set to zero. **V** is the vector of unknown node voltages. To find **V**, we invert the matrix **Y** and multiply by the known source currents.

$$\mathbf{I} = \mathbf{YV}$$

$$\mathbf{V} = \mathbf{Y}^{-1}\mathbf{I}$$

The time needed to invert an N × N matrix is roughly proportional to N^3. Filling and inverting the Y-matrix for each frequency of interest will be very fast, in this case, so fast it will be difficult to measure the computation time unless we specify a very large number of frequencies. This very simple approach might be good up to 1 MHz or so.

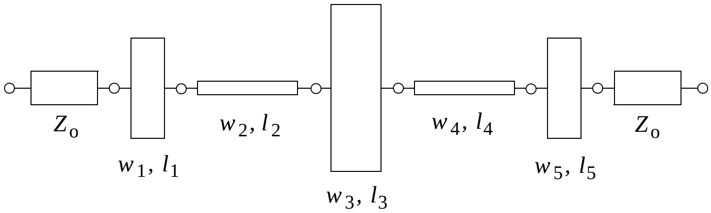

FIGURE 8.18 Distributed lowpass filter circuit. Step discontinuities are ignored.

In our low-frequency model there is no concept of wavelength or even physical size. Any phase shift we compute is strictly due to the reactance of the component, not its physical size. There is also no concept of radiation; power can only be dissipated in resistive components. As we move into the HF frequency range (1 to 30 MHz) the real components we buy will have significant parasitics. Lead lengths and proximity to the ground plane become very important and our physical construction techniques will have a big impact on the results achieved.

By the time we reach VHF frequencies (50 to 150 MHz) we are forced to adopt distributed concepts in the physical construction and analysis of our circuits. The connections between components become transmission lines and many components themselves are based on transmission line models. Our simple lowpass circuit might become a cascade of low and high impedance transmission lines, as seen in Fig. 8.18.

If this was a microstrip circuit, we would typically specify the substrate parameters and the width and length of each transmission line. We have ignored the step discontinuities due to changes in line width in this simplified example. Internally, the software would use analytical equations to convert our physical dimensions to impedances and electrical lengths. The software might use a Y-matrix, a cascade of ABCD parameter blocks, or a cascade of scattering-parameter (S-parameter) blocks for the actual analysis. At the ports, we typically ask for S-parameters referenced to the system impedance.

Notice that we still have a small number of nodes to consider. Our circuit is clearly distributed but the solution time does not depend on its size in terms of wavelengths. Any phase shift we compute is directly related to the physical size of the network. Although we can include conductor and substrate losses, there is still no radiation loss mechanism. It is also difficult to include enclosure effects; there may be box resonances or waveguide modes in our physical implementation. There is also no mechanism for parasitic coupling between our various circuit models.

The boundary between a lumped circuit point of view and a distributed point of view can be somewhat fuzzy. A quick review of some rules of thumb and terminology might be helpful. One common rule of thumb says that the boundary between lumped and distributed behavior is somewhere between a tenth and an eighth of a guide wavelength. Remember that wavelength in inches is defined by

$$\lambda = \frac{11.803}{\sqrt{\varepsilon_{eff} \cdot f}}$$

where ε_{eff} is the effective dielectric constant of the medium and f is in GHz. At 1 GHz, $\lambda = 11.803$ inches in air and $\lambda = 6.465$ inches for a 50 ohm line on 0.014-inch thick FR4. FR4 is a common, low cost printed circuit board material for digital and RF circuits. In Fig. 8.19 we can relate the physical size of our structure to the concept of wavelength and to some common terminology. Again, the boundary between purely lumped and purely distributed behavior is not always distinct.

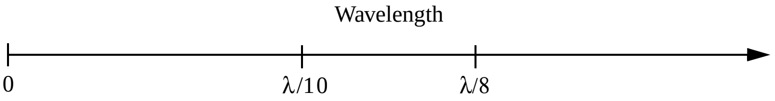

Less than λ/10	Grey Area	λ/8 or Greater
Lumped		Distributed
L, C, R, G		Transmission lines
Voltage, Current		[S], [Z], [Y]
No radiation		Radiation possible
Only reactance can shift phase of V or I		Physical distance can shift phase of V or I
Fields rise and fall at same time all through the structure		There is phase shift in the fields across the structure

FIGURE 8.19 The transition between lumped and distributed behavior and some common terminology.

Field Theory Based CAD

A field-solver based solution is an alternative to the previous distributed, circuit theory based approach. The field-solver takes a more microscopic view of any distributed geometry. Any field-solver we might employ must subdivide the geometry based on guide wavelength. Typically we need 10 to 30 elements or cells per guide wavelength to capture the fields or currents in our structure. Figure 8.20 shows a typical mesh generated by Agilent Momentum[7] for our microstrip lowpass filter example. Narrow cells are used on the edges of the strip to capture the spatial wavelength, or highly nonuniform current distribution across the width of the strips. This Method of Moments code has subdivided the microstrip metal and will solve for the current on each small rectangular or triangular patch. The default settings for mesh generation were used.

For this type of field-solver there is a strong analogy between the Y-matrix description we discussed for our lumped element circuit and what the field-solver must do internally. Imagine a lumped capacitor to ground at the center of each "cell" in our field-solver description. Series inductors connect these capacitors to each other. Coupling between non-adjacent cells can be represented by mutual inductances. So we have to fill and invert a matrix, but this matrix is now large and dense compared to our simple, lumped element circuit Y-matrix. For the mesh in Figure 8.20, N = 474 and we must fill and invert an N × N matrix.

One reason we turn to the field-solver is because it can potentially include all electromagnetic effects from first principles. We can include all loss mechanisms including surface waves and

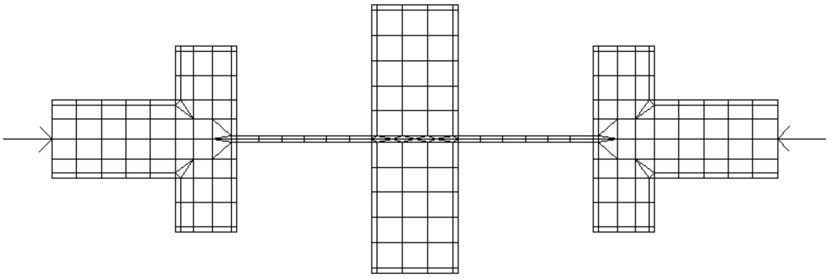

FIGURE 8.20 A typical model mesh fo rthe distributed lowpass filter circuit. The number of unknowns, N is 474. *Agilent Momentum, ADS 1.3.*

radiation. We can also include parasitic coupling between elements and the effects of compacting a circuit into a small space. The effects of the package or housing on our circuit performance can also be included in the field-solver analysis. However, the size of the numerical problem is now proportional to the structure size in wavelengths. The details of how enclosures are included in our analysis will vary from solver to solver. In some tools an enclosure is part of the basic formulation. In other tools, the analysis environment is "laterally open"; there are no sidewalls, although there may be a cover. One of the exciting aspects of field-solvers is the ability to observe fields and currents in the circuit, which sometimes leads to a deeper understanding of how the circuit actually operates. However, the size of the numerical problem will also be greater using a field-solver versus circuit theory, so we must carefully choose which pieces of global problem we will attack with the field-solver.

Although our discussion so far has focused on planar, distributed circuits there are actually three broad classes of field-solver codes. The 2D cross-section codes solve for the modal impedance and phase velocity of 1 to N strips with a uniform cross-section. This class of problem includes coupled microstrips, coupled slots, and conductors of arbitrary cross-section buried in a multilayer PC board. These tools use a variety of numerical methods including Method of Moments, the Finite Element Method, and the Spectral Domain Method. Field-solver engines that solve for multiple strips in a layered environment are built into several linear and nonlinear simulators. A multistrip model of this type is a building block for more complicated geometries like Lange couplers, spiral inductors, baluns, and many distributed filters. The advantage of this approach is speed; only the 2D cross-section must be discretized and solved.

The second general class of codes mesh or subdivide the surfaces of planar metals. The assumed environment for these surface meshing codes is a set of homogeneous dielectric layers with patterned metal conductors at the layer interfaces. Vertical vias are available to form connections between metal layers. There are two fundamental formulations for these codes, closed box and laterally open. In the closed box formulation the boundaries of the problem space are perfectly conducting walls. In the laterally open formulation, the dielectric layers extend to infinity. The numerical method for this class of tool is generally Method of Moments (MoM). Surface meshing codes can solve a broad range of strip- and slot-based planar circuits and antennas. Compared to the 2D cross-section solvers, the numerical effort is considerably higher.

The third general class of codes meshes or subdivides a 3D volume. These volume meshing codes can handle virtually any three-dimensional object, with some restrictions on where ports can be located. Typical problems are waveguide discontinuities, various coaxial junctions, and transitions between different guiding systems, such as transitions from coax to waveguide. These codes can also be quite efficient for computing transitions between layers in multilayer PC boards and connector transitions between boards or off the board. The more popular volume meshing codes employ the Finite Element Method, the Finite Difference Time Domain (FDTD) method, and the Transmission Line Matrix (TLM) method. Although the volume meshing codes can solve a very broad range of problems, the penalty for this generality is total solution time. It typically takes longer to set up and run a 3D problem compared to a surface meshing or cross-section problem. Sadiku[8] has compiled a very thorough introduction to many of these numerical methods.

Solution Time for Circuit Theory and Field Theory

When we use circuit theory to analyze a RF or microwave network, we are building a Y-matrix of dimension N, where N is the number of nodes. A typical amplifier or oscillator design may have only a couple of dozen nodes. Depending on the solution method, the solution time is proportional to a factor between N^2 and N^3. When we talk about a "solution" we really mean matrix inversion. In Fig. 8.21 we have plotted solution time as a function of matrix size N. The vertical time scale is somewhat arbitrary but should be typical of workstations and personal computers today.

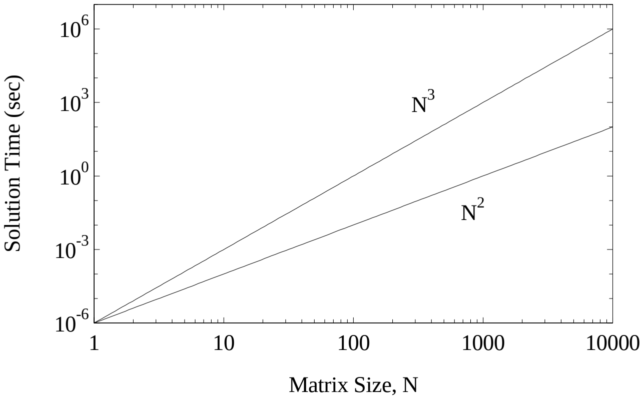

FIGURE 8.21 Solution time as a function of matrix size, N. Solution time for circuit simulators, MoM field-solvers, and FEM field-solvers is roughly proportional to N^3.

When we use a MoM field-solver, a “small” problem has a matrix dimension of N = 300–600. Medium size problems may be around N = 1500 and large problems quickly get into the N = 2000–3000 range. Because of the N^2/N^3 effect, the solution time is impacted dramatically as the problem size grows. In this case we can identify two processes, filling the matrix with all the couplings between cells and inverting or solving that matrix. So we are motivated to keep our problem size as small as possible. The FEM codes also must fill and invert a matrix. Compared to MoM, the matrix tends to be larger but more sparse.

The time domain solvers using FDTD or TLM are exceptions to the N^2/N^3 rule. The solution process for these codes is iterative; there is no matrix to fill or invert with these solvers. Thus the memory required and the solution time grow more linearly with problem size in terms of wavelengths. This is one reason these tools have been very popular for radar cross-section (RCS) analysis of ships and airplanes. However, because these are time stepping codes, we must perform a Fast Fourier Transform (FFT) on the time domain solution to get the frequency domain solution. Closely spaced resonances in the frequency domain require a large number of time samples in the time domain. Therefore, time stepping codes may not be the most efficient choice for structures like filters, although there are techniques available to speed up convergence. Veidt[9] presents a good summary of how solution time scales for various numerical methods.

A Hybrid Approach to Circuit Analysis

If long solution times prevent us from analyzing complete circuits with a field-solver, what is the best strategy for integrating these tools into the design process? I believe the best approach is to identify the key pieces of the problem that need the field-solver, and to do the rest with circuit theory. Thus the final result is a “hybrid solution” using different techniques, and even different tools from different vendors. As computer power grows and software techniques improve, we can do larger and larger pieces of the problem with a field-solver. A simple example will help to demonstrate this approach. The circuit in Fig. 8.22 is part of a larger RF printed circuit board. In one corner of the board we have a branchline coupler, a resistive termination, and several mitered bends.

Using the library of elements in our favorite linear simulator, there are several possible ways to subdivide this network for analysis (see Fig. 8.23). In this case we get about 21 nodes in our circuit. Solution time is roughly proportional to N^3, so if we ignore the overhead of computing any of the individual models, we would expect the solution to come back very quickly. But we have clearly neglected several things in our analysis. Parasitic coupling between the arms of the coupler, interaction between the discontinuities, and any potential interaction with the package have all been ignored. Some of our analytical models may not be as accurate as we would like, and in some cases a combination of models

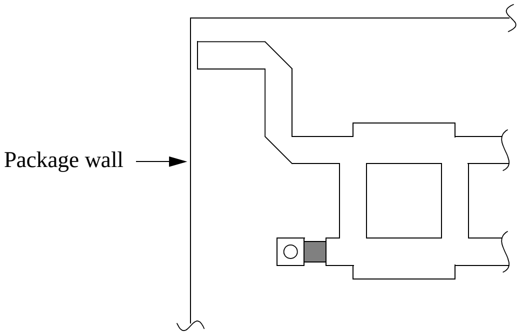

FIGURE 8.22 Part of an RF printed circuit board which includes a branchline coupler, a resistive termination to ground, and several mitered bends.

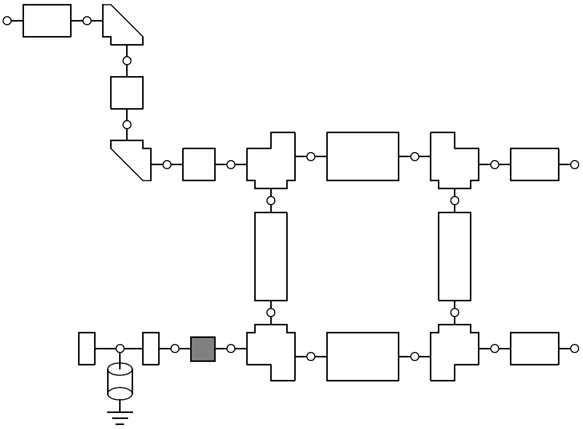

FIGURE 8.23 The layout in Fig. 8.22 has been subdivided for analysis using the standard library elements found in many circuit-theory-based simulations.

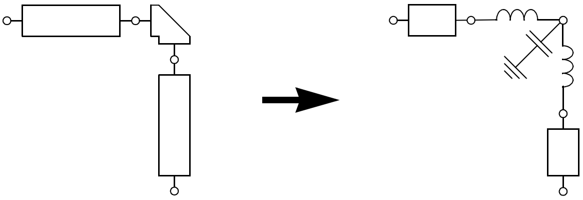

FIGURE 8.24 The equivalent circuit of a microstrip mitered bend. The physical dimensions are mapped to an equivalent lumped element circuit.

may not accurately describe our actual circuit. If this circuit were compacted into a much denser layout, all of the effects mentioned above would become more pronounced.

Each one of the circuit elements in our schematic has some kind of analytic model inside the software. For a transmission line, the model would relate physical width and length to impedance and electrical length through a set of closed form equations. For a discontinuity like the mitered bend, the physical parameters might be mapped to an equivalent lumped element circuit (Fig. 8.24), again through a set of closed form equations. The field-solver will take a more microscopic view of the same mitered bend discontinuity. Any tool we use will subdivide the metal pattern using 10 to 30 elements per guide wavelength. The sharp inside corner where current changes direction rapidly will force an even finer subdivision. If we want to solve the

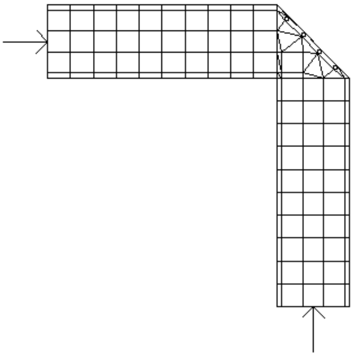

FIGURE 8.25 A typical MoM mesh for the microstrip mitered bend. The number of unknowns, N, is 221. *Agilent Momentum, ADS 1.3.*

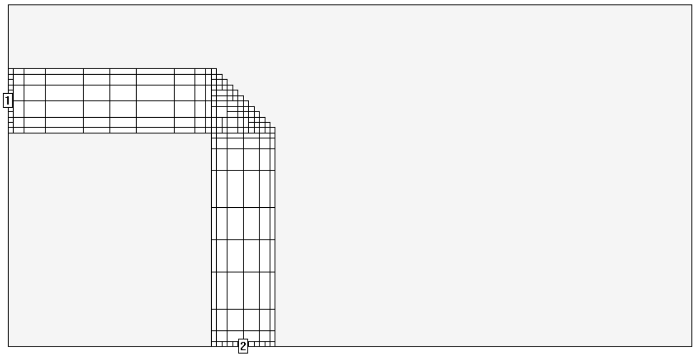

FIGURE 8.26 An analysis of the input line and the mitered bend in the presence of the package walls. The number of unknowns, N, is 360. *Sonnet **em** 6.0.*

bend discontinuity individually, we must also connect a short length of series line to each port. Agilent Momentum generated the mesh in Fig. 8.25. The number of unknowns is 221. If the line widths are not variable in our design, we could compute this bend once, and use it over and over again in our circuit design.

Another potential field-solver problem is in the corner of the package near the input trace. You might be able to include the box wall effect on the series line, but wall effects are generally not included in discontinuity models. However, it is quite easy to set up a field-solver problem that would include the microstrip line, the mitered bend, and the influence of the walls. The project in Fig. 8.26 was drawn using Sonnet ***em***. The box walls to the left and top in the electromagnetic simulation mimic the true location of the package walls in the real hardware. There are 360 unknowns in this simulation.

One of the more interesting ways to use a field-solver is to analyze groups of discontinuities rather than single discontinuities. A good example of this is the termination resistor and via[10,11] in our example circuit. A field-solver analysis of this group may be much more accurate than a combination of individual analytical models. We could also optimize the termination, then use the analysis data and the optimized geometry over and over again in this project or other projects. The mesh for the resistor via combination (Fig. 8.27) was generated using Sonnet ***em*** and represents a problem with 452 unknowns.

Our original analysis scheme based on circuit theory models alone is shown in Fig. 8.23. Although this will give us the fastest analysis, there may be room for improvement. We can substitute results in our field-solver for the elements near the package walls and for the resistor/via combination (Fig. 8.28).

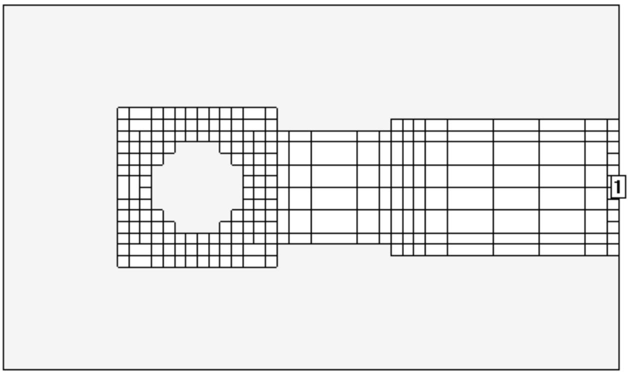

FIGURE 8.27 A MoM analysis of a group of discontinuities including a thin-film resistor, two steps in width, and a via hole to ground. The number of unknowns, N, is 452. *Sonnet **em** 6.0.*

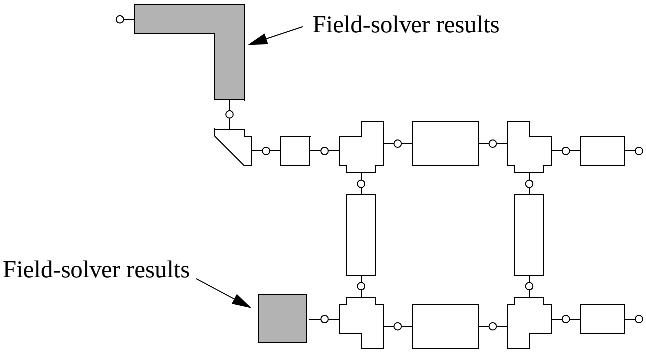

FIGURE 8.28 Substituting field-solver results into the original solution scheme mixes field-theory and circuit theory in a cost effective way.

The data from the field-solver would typically be S-parameter files. This "hybrid" solution mixes field theory and circuit theory in a cost-effective way.[12] The challenge for the design engineer is to identify the critical components that should be addressed using the field-solver.

The hybrid solution philosophy is not limited to planar components; three-dimensional problems can be solved and cascaded as well. The right angle coax bend shown in Fig. 8.29 is one example of a 3D component that was analyzed and optimized using Ansoft HFSS.[13] In this case we have taken advantage of a symmetry plane down the center of the problem in order to reduce solution time. This component includes a large step in inner conductor diameter and a Teflon sleeve to support the larger inner conductor. After optimizing two dimensions, the computed return loss is greater than –30 dB. The coax bend is only one of several problems taken from a larger assembly that included a lowpass filter, coupler, amplifier, and bandpass filter.

Optimization

Optimization is a key component of modern linear and nonlinear circuit design. Many optimization schemes require gradient information, which is often computed by taking simple forward or central differences. The extra computations required to find gradients become very costly if there is a field-solver inside the optimization loop. So it is important to minimize the number of field-solver analysis runs. It is also necessary to capture the desired changes in the geometry and pass this information to the field-solver. Bandler et al.[14,15] developed an elegant solution to both of these problems in 1993. The key concept was a "data pipe" program sitting between the simulator and the field-solver (see Fig. 8.30). When the

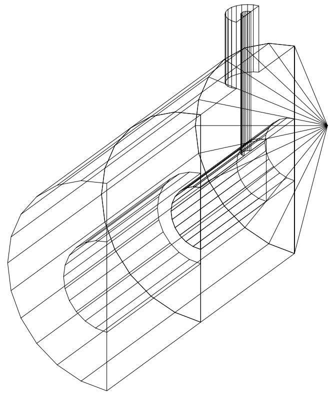

FIGURE 8.29 A right angle coax-to-coax transition that was optimized for return loss. The number of unknowns, N, is 8172. *An soft HFSS 7.0.*

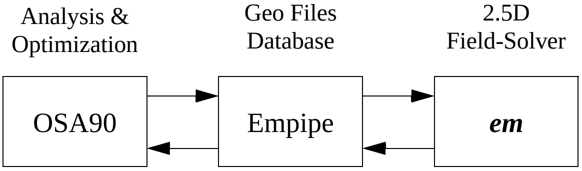

FIGURE 8.30 The first commercially successful optimization scheme which included a field-solver inside the optimization loop.

linear simulator calls for a field-solver analysis, the data pipe generates a new geometry file and passes it to the field-solver. In the reverse direction, the data pipe stores the analysis results and interpolates between data sets if possible. The final iterations of the optimization operate entirely on interpolated data without requiring any new field-solver runs. This concept was applied quite successfully to both surface meshing[16] and volume meshing solvers. The same basic rules that lead to successful circuit theory based optimization apply when a field-solver is in the loop as well. First, a good starting point leads to more rapid and consistent convergence. Second, it is important to limit the number of variables.

The Next Decade

The need for inexpensive wireless systems has forced the RF community to rapidly adopt low cost, multilayer PC board technology. In the simpler examples, most circuitry and components are mounted on the top layer while inner layers are used for routing of RF signals and DC bias. However, more complex examples can be found where printed passive components and discontinuities are located in one or more buried layers. Given the large number of variables in PC board construction it will be difficult for vendors of linear and nonlinear circuit simulators to support large libraries of passive models that cover all possible scenarios. However, a field-solver can be used to generate new models as needed for any novel layer stack up. Of course the user is also free to use the field-solver data to develop custom, proprietary models for his or her particular technology.

The traditional hierarchy of construction for RF systems has been a chip device, mounted to leaded package, mounted to printed circuit board located in system cabinet or housing. Today however, the "package" may be a multilayer Low Temperature Co-fired Ceramic (LTCC) substrate or a multilayer PC board using Ball Grid Array (BGA) interconnects. Thus the boundary between package and PC board has blurred somewhat. No matter what the technology details, the problem remains to transfer a signal from the outside world into the system, onto the main system board, through the package, and into the chip. And of course there is an analogous connection from the chip back to the outside world. From this point of view, the problem becomes a complex, multilevel passive interconnect that must support not only the signal currents but also the ground currents in the return path. It is often the ground return path that limits package isolation or causes unexpected oscillations in active circuits.[17] The high-speed digital community is faced with very similar passive interconnect challenges at similar, if not higher frequencies and typically much higher signal densities. Again, there is ample opportunity to apply field-solver technology to these problems, although practical problem size is still somewhat limited. The challenge to the practitioner is to identify and correct problems at multiple points in the signal path.

Conclusion

At very low frequencies we can use lumped element models to describe our circuits. Connection lengths and device parasitics are not issues. At higher frequencies we use distributed models to capture the effects of guide wavelength, but spurious couplings between elements and other effects due to circuit compaction are typically not captured. A field-solver can potentially capture all the macro and micro aspects of our circuit. It should capture spatial wavelength effects, guide wavelength, spurious couplings among elements, and interference among elements due to dense packing. Although the size of a practical field-solver problem is still somewhat small, there are many useful and cost effective problems that can be identified and solved using a combination of circuit theory based and field theory based CAD.

References

1. K. S. Yee, Numerical solution of initial boundary-value problems involving Maxwell's equations in isotropic media, *IEEE Trans. Ant. Prop.*, AP-14, 302–207, May 1966.
2. R. F. Harrington, *Field Computation by Moment Methods*, Macmillan, New York, 1968.
3. P. B. Johns and R. L. Beurle, Numerical solution of 2-dimensional scattering problems using a transmission-line matrix, *Proc. Inst. Electr. Eng.*, 118, 1203–1208, Sept. 1971.
4. P. Silvester, Finite element analysis of planar microwave networks, *IEEE Trans. Microwave Theory Tech.*, MTT-21, 104–108, Feb. 1973.
5. ***em***™, Sonnet Software, Liverpool, NY.
6. HFSS, Hewlett-Packard, Santa Rosa, CA and Ansoft, Pittsburgh, PA.
7. Momentum, Agilent EEsof EDA, Santa Rosa, CA.
8. M. Sadiku, *Numerical Techniques in Electromagnetics*, CRC Press, Boca Raton, 1992.
9. B. Veidt, Selecting 3D electromagnetic software, *Microwave Journal*, 126–137, Sept. 1998.
10. M. Goldfarb and R. Pucel, Modeling via hole grounds in microstrip, *IEEE Microwave and Guided Wave Letters*, 1, 135–137, June 1991.
11. D. Swanson, Grounding microstrip lines with via holes, *IEEE Trans. Microwave Theory Tech.*, MTT-40, 1719–1721, Aug. 1992.
12. D. Swanson, Using a microstrip bandpass filter to compare different circuit analysis techniques, *Int. J. MIMICAE*, 5, 4–12, Jan. 1995.
13. HFSS, Ansoft Corp., Pittsburgh, PA.
14. J. W. Bandler, S. Ye, R. M. Biernacki, S. H. Chen, and D. G. Swanson, Jr., Minimax microstrip filter design using direct em field simulation, *IEEE MTT-S Int. Microwave Symposium Digest*, 889–892, 1993.
15. J. W. Bandler, R. M. Biernacki, S. H. Chen, D. G. Swanson, Jr., and S. Ye, Microstrip filter design using direct em field simulation, *IEEE Trans. Microwave Theory Tech.*, MTT-42, 1353–1359, July 1994.
16. D. Swanson, Optimizing a microstrip bandpass filter using electromagnetics, *Int. J. MIMICAE*, 5, 344–351, Sept. 1995.
17. D. Swanson, D. Baker, and M. O'Mahoney, Connecting MMIC chips to ground in a microstrip environment, *Microwave Journal*, 58–64, Dec. 1993.

8.4 Nonlinear RF and Microwave Circuit Analysis

Michael B. Steer and John F. Sevic

The two most popular circuit-level simulation technologies are embodied in SPICE-like simulators, operating entirely in the time domain, and in Harmonic Balance (HB) simulators, which are hybrid time and frequency domain simulators. Neither is ideal for modeling RF and microwave circuits and in this chapter their concepts and bases of operation will be explored with the aim of illuminating the limitations and advantages of each. All of the technologies considered here have been implemented in commercial microwave simulators. An effort is made to provide sufficient background for these to be used to full advantage.

Simulation of digital and low frequency analog circuits at the component level is performed using SPICE, or commercial equivalents, and this has proved to be very robust. The operation of SPICE will be considered in detail later, but in essence SPICE solves for the state of the circuit at a time point and then uses this state to estimate the state of the circuit at the next time point (and so is referred to as a time-marching technique). The state of the circuit at the new time point is iterated to minimize error. This process captures the transient response of a circuit and the algorithm obtains the best waveform estimate. That is, the best estimate of the current and voltages in the circuit at each time point are obtained. The accurate calculation of the waveform in a circuit is what we want in low pass circuits such as digital and low frequency analog circuits. However with RF and microwave circuits, especially in communications, it is more critical to accurately determine the spectrum of a signal (i.e., the frequency components and their amplitudes) than the precise waveform. In part this is because regulations require strict control of spurious spectral emissions so as not to interfere with other wireless systems, and also because the generation of extraneous emissions compromises the demodulation and detection of communication signals by other radios in the same system. The primary distortion concern in radio is spectrum spreading or more specifically, adjacent channel interference. In-band distortion is also important especially with base station amplifiers where filtering can be used to eliminate spectral components outside the main channel. Distortion is largely the result of the nonlinear behavior of transmitters and so characterization of this phenomenon is important in RF design. In addition, provided that the designer has confidence in the stability and well-behaved transient response of a circuit, it is only necessary to determine its steady-state response. In order to determine the steady-state response using a time-marching approach, it is necessary to determine the RF waveform for perhaps millions of RF cycles, including the full transient interval, so as to extract the superimposed modulated signal. The essential feature of HB is that a solution form is assumed, in particular, a sum of sinusoids and the unknowns to be solved for are the amplitudes and phases of these sinusoids. The form of the solution then allows simplification of the equations and determination of the unknown coefficients. HB procedures work well when the signal can be described by a simple spectrum. However, it does not enable the transient response to be determined exactly.

In the following sections we will first look at the types of signals that must be characterized and identify the information that must be extracted from a circuit simulation. We will then look at transient SPICE-like simulation and HB simulation. Both types of analyses have restrictions and neither provides a complete characterization of an RF or microwave circuit. However, there are extensions to each that improve their basic capabilities and increase applicability. We will also review frequency domain analysis techniques as this is also an important technique and forms the basis of behavioral modeling approaches.

Modeling RF and Microwave Signals

The way nonlinear effects are modeled and characterized depends on the properties of the input signal. Signals having frequency components above a few hundred megahertz are generally regarded as RF or microwave signals. However, the distinguishing features that identify RF and microwave circuits are the design methodologies used with them. Communication systems generally have a a small operating fractional bandwidth — rarely is it much higher than 10%. Generated or monitored signals in sensing systems (including radar and imaging systems) generally have small bandwidths. Even broadband systems including instrumentation circuits and octave (and more) bandwidth amplifiers have passband characteristics. Thus RF and microwave design and modeling technology has developed specifically for narrowband systems.

The signals to be characterized in RF and microwave circuits are either correlated, in the case of communication and radar systems, or uncorrelated noise in the case of many imaging systems. We are principally interested in handling correlated signals as uncorrelated noise is nearly always very small and can be handled using relatively straightforward linear circuit analysis techniques. There are two families of correlated signals, one being discrete tone and the other being digitally modulated. In the following, three types of signals will be examined and their response to nonlinearities described.

Discrete Tone Signals

Single tone signals, i.e., a single sinewave, are found in frequency sources but such tones do not transmit information and must be modulated. Until recently, communication and radar systems used amplitude, phase, or frequency modulation (AM, PM, and FM, respectively) to put information on a carrier and transmission of the carrier was usually suppressed. These modulation formats are called analog modulation and the resulting frequency components can be considered as being sums of sinusoids. The signal and its response are then deterministic and a well-defined design methodology has been developed to characterize nonlinear effects. With multifrequency sinusoidal excitation consisting possibly of nonharmonically related (or non-commensurable) frequency components, the waveforms in the circuit are not periodic yet the nonlinear circuit does have a steady-state response. Even considering a single-tone signal (a single sinewave) yields directly usable design information. However, being able to model the response of a circuit to a multitone stimulus increases the likelihood that the fabricated circuit will have the desired performance.

In an FM modulated scheme the transmitted signal can be represented as

$$x(t) = \cos\left\{\left[\omega_c + \omega_i(t)\right]t\right\} + \sin\left\{\left[\omega_c + \omega_q(t)\right]t\right\} \tag{8.47}$$

where the signal information is contained in $\omega_i(t)$ and can be adequately represented as a sum of sinewaves. The term $\omega_q(t)$ is the quadrature of $\omega_i(t)$, meaning that it is 90° out of phase. The net result is that $x(t)$ can also be represented as a sum of sinusoids. Other forms of analog modulation can be represented in a similar way. The consequence of this is that all signals in a circuit with analog modulation can be adequately represented as comprising discrete tones.

With discrete tones input to a nonlinear circuit, the output will also consist of discrete tones but will have components at frequencies that were not part of the input signal. Power series expansion analysis of a nonlinear subsystem illustrates the nonlinear process involved. When a single frequency sinusoidal signal excites a nonlinear circuit, the response "usually" includes the original signal and harmonics of the input sinewave. We say "usually," because if the circuit contains nonlinear reactive elements, subharmonics and autonomous oscillation could also be present. The process is more complicated when the excitation includes more than one sinusoid, as the circuit response may then include all sum and difference frequencies of the original signals. The term *intermodulation* is generally used to describe this process, in which power at one frequency, or group of frequencies, is transferred to power at other frequencies. The term intermodulation is also used to describe the production of sum and difference frequency components, or intermodulation frequencies, in the output of a system with multiple input sinewaves. This is a macroscopic definition of intermodulation as the generation of each intermodulation frequency component derives from many separate intermodulation processes. Here a treatment of intermodulation is developed at the microscopic level.

To begin with, consider a nonlinear system with output $y(t)$ described by the power series

$$y(t)=\sum_{l=1}^{\infty}a_l x(t)^l \tag{8.48}$$

where $x(t)$ is the input and is the sum of three sinusoids:

$$x(t)=c_1\cos(\omega_1 t)+c_2\cos(\omega_2 t)+c_3\cos(\omega_3 t). \tag{8.49}$$

Thus

$$x(t)^l=\left[c_1\cos(\omega_1 t)+c_2\cos(\omega_2 t)+c_3\cos(\omega_3 t)\right]^l. \tag{8.50}$$

This equation includes a large number of components the radian frequencies of which are the sum and differences of ω_1, ω_2, and ω_3. These result from multiplying out the term $[\cos(\omega_1 t)]^k$ $[\cos(\omega_3 t)]^{l-p}$. For example

$$\begin{aligned}\cos(\omega_1 t)\cos(\omega_2 t)\cos(\omega_3 t)=\Big[&\cos(\omega_1+\omega_2+\omega_3)t+\cos(\omega_1+\omega_2-\omega_3)t+\cos(\omega_1-\omega_2+\omega_3)t\\&+\cos(\omega_1-\omega_2-\omega_3)t\Big]\Big/4\end{aligned} \tag{8.51}$$

where the (radian) frequencies of the components are, in order, $(\omega_1+\omega_2+\omega_3)$, $(\omega_1+\omega_2-\omega_3)$, $(\omega_1-\omega_2+\omega_3)$, and $(\omega_1-\omega_2-\omega_3)$. This mixing process is called intermodulation and the additional tones are called intermodulation frequencies with each separate component of the intermodulation process called an intermodulation product or IP. Thus when a sum of sinusoids is input to a nonlinear element additional frequency components are generated. In order to make the analysis tractable, the number of frequency components considered must be limited. With a two-tone input, the frequencies generated are integer combinations of the two inputs, e.g., $f = mf_1 + nf_2$. One way of limiting the number of frequencies is to consider only the combinations of m and p such that

$$|m|+|n|\le p_{\mathrm{MAX}} \tag{8.52}$$

assuming that all products of order greater than p_{MAX} are negligible. This is called a triangular truncation scheme and is depicted as shown in Fig. 8.31. The alternative rectangular truncation scheme is shown in Fig. 8.32 and is defined by

$$|m|\le m_{\mathrm{MAX}}\quad\text{and}\quad|n|\le n_{\mathrm{MAX}}. \tag{8.53}$$

With one-tone excitation, the spectra of the input and output of a nonlinear circuit consists of a single tone at the input and the original, fundamental tone, and its harmonics. Here intermodulation converts power at f_1 to power at DC (this intermodulation is commonly referred to as rectification), and to power at the harmonics ($2f_1$,$3f_1$, …), as well as to power at f_1. Simply squaring a sinusoidal signal will give rise to a second harmonic component. The measured and simulated responses of a class A amplifier operating at 2 GHz are shown in Fig. 8.33. This exhibits classic responses. At low signal levels the fundamental response has a slope of 1:1 with respect to the input signal level — corresponding to the linear response.

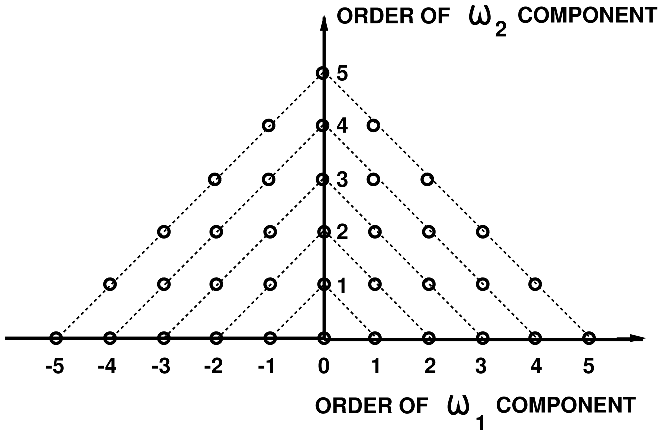

FIGURE 8.31 A triangular scheme for truncating higher order tones.

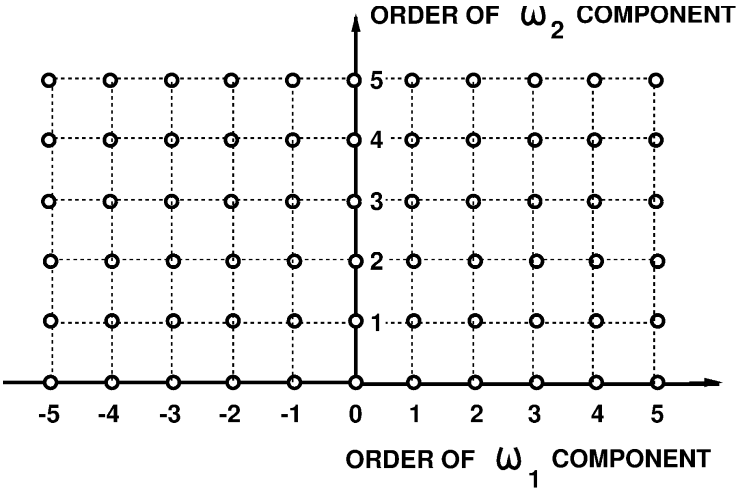

FIGURE 8.32 A rectangular scheme for truncating higher order tones. Here $m_{\text{max}} = 5 = n_{\text{max}}$.

Initially the second harmonic varies as the square of the input fundamental level and so has a 2:1 slope on the log-log plot. This is because the dominant IP contributing to the second harmonic level at low input powers is second order. Similarly the third harmonic response has a 3:1 slope because the dominant IP here is third order. As the input power increases, the second harmonic exhibits classic nonlinear behavior which is observed with many intermodulation tones and results from the production of a second, or more significant IP tone, which is due to higher order intermodulation than the dominant IP. In this situation, the dominant and additional IPs vectorially combine, with the result that the tone almost cancels out.

It is much more complicated to describe the nonlinear response to multifrequency sinusoidal excitation. If the excitation of an analog circuit is sinusoidal, then specifications of circuit performance are generally in terms of frequency domain phenomena, e.g., intermodulation levels, gain, and the 1 dB gain compression point. However, with multi-frequency excitation by signals that are not harmonically related, the waveforms in the circuit are not periodic, although there is a steady-state response often called quasi-periodic.

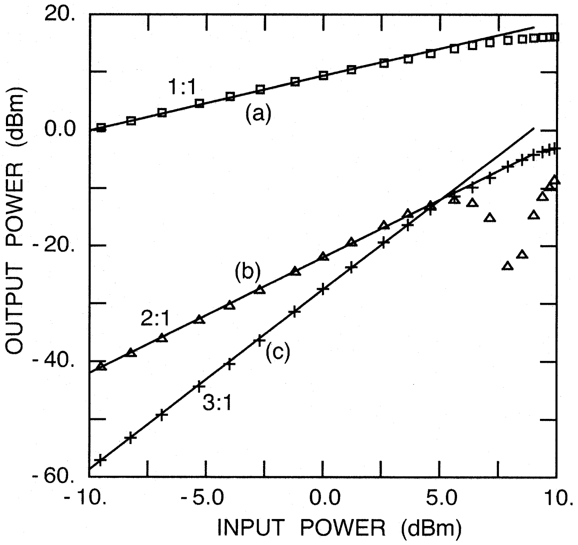

FIGURE 8.33 Measured (markers) and simulated (lines) response of a class A MESFET amplifier to a single tone input: (a) is the fundamental output; (b) is the second harmonic response; and (c) is the third harmonic response.

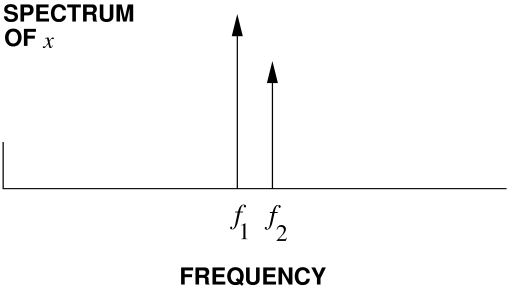

FIGURE 8.34 The spectrum of a two-tone signal.

Consider the nonlinear response of a system to the two-tone excitation shown in Fig. 8.34. The frequencies f_1 and f_2 are, in general, nonharmonically related and components at all sum and difference frequencies $mf_1 + nf_2$, ($m, n = -\infty,\ldots,-1,0,1,\ldots,\infty$) of f_1 and f_2 will appear at the output of the system. If the nonlinear system has a quadratic nonlinearity, the spectrum of the output of the system is that of Fig. 8.35. With a general nonlinearity, the spectrum of the output will contain a very large number of components. An approximate output spectrum is given in Fig. 8.36. Also shown is a truncated spectrum that will be used in the following discussion. Most of the frequency components in the truncated spectrum of Fig. 8.36 have names: DC (f_6) results from rectification; f_3, f_4, f_5, f_8, f_9, f_{10}, and f_{11} are called intermodulation frequency components; f_4, f_5 are commonly called image frequencies, or "third order" intermods, as well; f_1, f_2 are the input frequencies; and f_7, f_8 are harmonics.

All of the frequencies in the steady-state output of the nonlinear system result from intermodulation — the process of frequency mixing. A classification of nonlinear behavior that closely parallels the way in which nonlinear responses are observed and specified is given below.

Gain Compression/Enhancement: Gain compression can be conveniently described in the time domain or in the frequency domain. Time domain descriptions refer to limited power availability or to limitations on voltage or current swings. At low signal levels, moderately nonlinear devices such as class

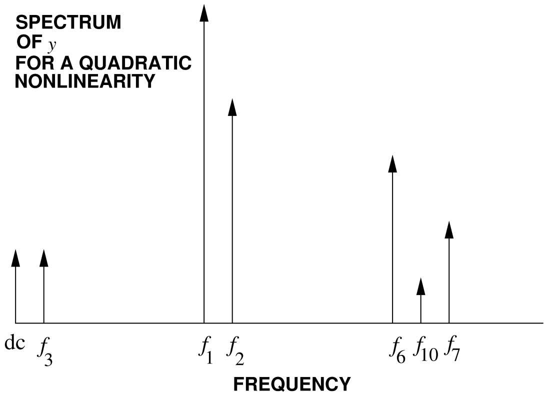

FIGURE 8.35 The spectrum at the output of a quadratic nonlinear system with a two-tone input.

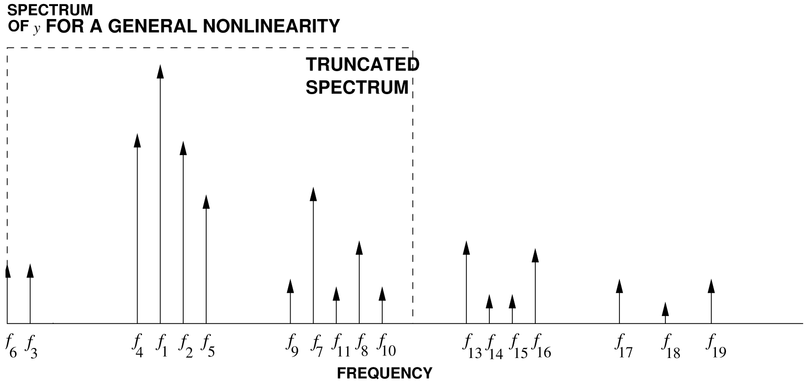

FIGURE 8.36 The approximate spectrum for a general nonlinearity with a two-tone input.

A amplifiers behave linearly so that there is one dominant IP with a zero saturation term. As signal levels increase, other IPs become important as harmonic levels increase. Depending on the harmonic loading condition, these IPs could be in phase with the original IP contributing to gain enhancement or out of phase contributing to gain compression.

Desensitization: Desensitization is the variation of the amplitude of one of the desired components due to the presence of another noncommensurable signal. This is an over-riding saturation effect affecting all output tones and comes out of the power series expansion.

Harmonic Generation: Harmonic generation is the most obvious result of nonlinear distortion and is identical to the process with a single-tone input.

Intermodulation: Intermodulation is the generation of spurious frequency components at the sum and difference frequencies of the input frequencies. In the truncated spectrum f_3, f_4, f_5, f_9, f_{10}, and f_{11} are intermodulation frequencies. Numerically $f_4 = 2f_1 - f_2$ and so this intermodulation tone is commonly called the lower third order intermod. There are other IPs that can contribute to the "third order" intermod that are not due to third order intermodulation. A particularly important intermodulation process begins with the generation of the difference frequency component $f_3 = f_2 - f_1$ as a second order IP. This is also referred to as the baseband component, envelope frequency, intermediate frequency, or difference frequency. This component then mixes with one of the original tones to contribute to the level of the "third order" intermod, e.g., $f_4 = f_1 - f_3$, again a second order process. The corresponding contribution to the upper third order intermod f_5, i.e., $f_5 = f_2 + f_3$, can (depending on the baseband impedance) have a phase that differs from the phase of the f_4 contribution and, in general, the result is that there can be asymmetry in the lower and upper third order intermod levels as the various IPs, at their respective frequencies, add vectorially.

Cross-modulation: Cross-modulation is modulation of one component by another noncommensurable component. Here it would be modulation of f_1 by f_2 or modulation of f_2 by f_1. However, with cross-modulation, information contained in the sidebands of one non-commensurable tone can be transferred to the other non-commensurable tone.

Detuning: Detuning is the generation of DC charge or DC current resulting in change of an active device's operating point. The generation of DC current with a large signal is commonly referred to as rectification. The effect of rectification can often be reduced by biasing using voltage and current sources. However, DC charge generation in nonlinear reactances is more troublesome as it can neither be detected nor effectively reduced.

AM-PM Conversion: The conversion of amplitude modulation to phase modulation (AM-PM conversion) is a troublesome nonlinear phenomenon in high frequency analog circuits and results from the amplitude of a signal affecting the delay through a system. Alternatively, the process can be understood by considering that at higher input levels, additional IPs are generated at the fundamental frequency and when these vectorially contribute to the fundamental response, phase rotation occurs.

Subharmonic Generation and Chaos: In systems with memory effects, i.e., with reactive elements, subharmonic generation is possible. The intermodulation products for subharmonics cannot be expressed in terms of the input non-commensurable components. (Components are non-commensurable if they cannot be expressed as integer multiples of each other.) Subharmonics are initiated by noise, possibly a turn-on transient, and so in a steady-state simulation must be explicitly incorporated into the assumed set of steady-state frequency components. The lowest common denominator of the subharmonic frequencies then becomes the basis non-commensurable component. Chaotic behavior can only be simulated in the time domain. The nonlinear frequency domain methods as well as the conventional harmonic balance methods simplify a nonlinear problem by imposing an assumed steady-state on the nonlinear circuit solution problem. Chaotic behavior is not periodic and so the simplification is not valid in this case. Together with the ability to simulate transient behavior, the capability to simulate chaotic behavior is the unrivaled realm of time domain methods.

Except for chaotic behavior, all nonlinear behavior with discrete tones can be viewed as an intermodulation process with IPs (the number of significant ones increasing with increasing signal level) adding vectorially. Understanding this process provides valuable design insight and is also the basis of frequency domain nonlinear analysis.

Digitally Modulated Signals

A digitally modulated signal cannot be represented by discrete tones and so nonlinear behavior cannot be adequately characterized by considering the response to a sum of sinusoids. Nonlinear effects with digital are difficult to describe as the signals themselves appear to be random, but there is an underlying correlation. It is more appropriate to characterize a digitally modulated signal by its statistics, such as power spectral density, than by its component tones. Most current (and future) wireless communication systems use digital modulation, in contrast to first-generation radio systems, which were based on analog modulation. Digital modulation offers increased channel capacity, improved transmission quality, secure channels, and the ability to provide other value-added services. These systems present significant challenges to the RF and microwave engineer with respect to representation and characterization of digitally modulated signals, and also with respect to nonlinear analysis of digital wireless communication systems.

Amplifier linearity in the context of digital modulation is therefore most suitably characterized by measuring the degree of spectrum regeneration. This is done by comparing the power in the upper and lower adjacent channels to the power in the main channel: the adjacent-channel power ratio (ACPR). The spectrum of a digitally modulated signal is shown in Fig. 8.37. This is the spectrum of a finite bit length digitally modulated signal and not the smooth spectrum of an infinitely long sequence often depicted.

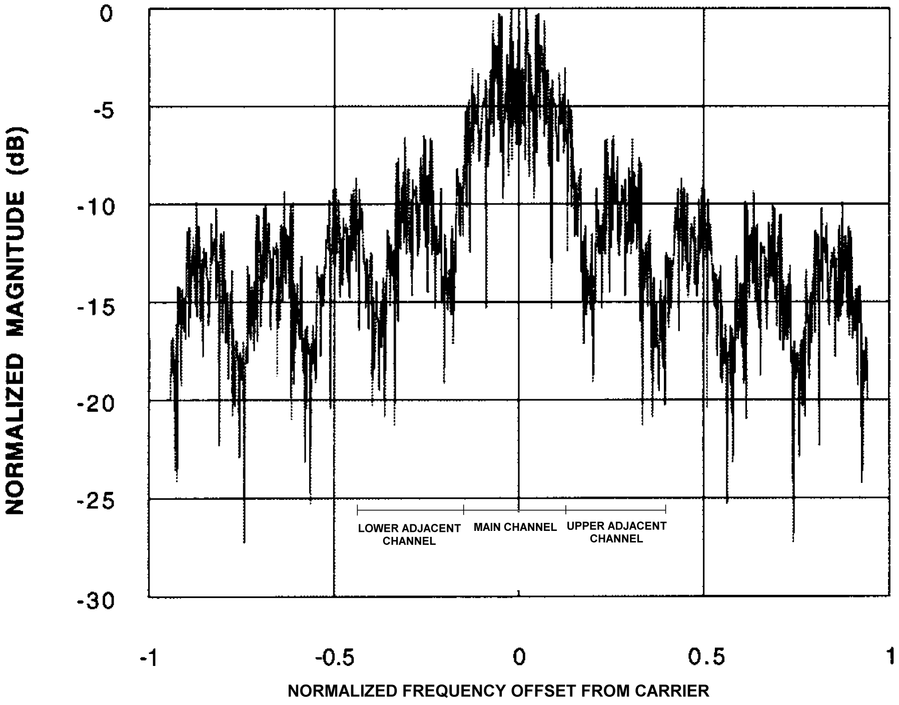

FIGURE 8.37 Spectrum of a digitally modulated signal.

Basics of Circuit Modeling

The solution, or simulation, of a circuit is obtained by solving a number of network equations developed by applying Kirchoff's current law (KCL) and Kirchoff's voltage law (KVL). There are two basic methods for developing the network equations for DC analysis, or steady-state analysis of linear circuits with sinusoidal excitation, based on Kirchoff's laws. These are the nodal formulation and mesh formulation of the network equations. The nodal formulation is best for electronic circuits as there are many fewer nodes than there are elements connecting the nodes. The nodal formulation, specifically node-voltage analysis, requires that the current in an element be expressed as a function of voltage. Some elements cannot be so described and so there is not a node-voltage description for them. Then the modified nodal approach is most commonly used wherein every element that can be described by an equation for current in terms of voltages is described in this way, and only for the exceptional elements are other constitutive relations considered. However, the general formulation approach can be illustrated by considering node-voltage analysis.

The nodal formulation of the network equations is based on the application of KCL, which in its general form states that if a circuit is partitioned, then the total instantaneous current flowing into a partition is zero. This is an instantaneous requirement — physically it is only necessary that the net current flow be zero on average to ensure charge conservation. So this is an artificial constraint imposed by circuit analysis technology. The approach used in overcoming this restriction is to cast this issue as a modeling problem: it is the responsibility of the device modeler to ensure that a model satisfies KCL instantaneously. This results in many of the modeling limitations that are encountered. A general network is shown in Fig. 8.38. The concept here is that every node of the circuit is pulled to the outside of the main body of the network. The main body contains only the constitutive relations and the required external nodes have the connectivity information to implement Kirchoff's laws. The result is that the

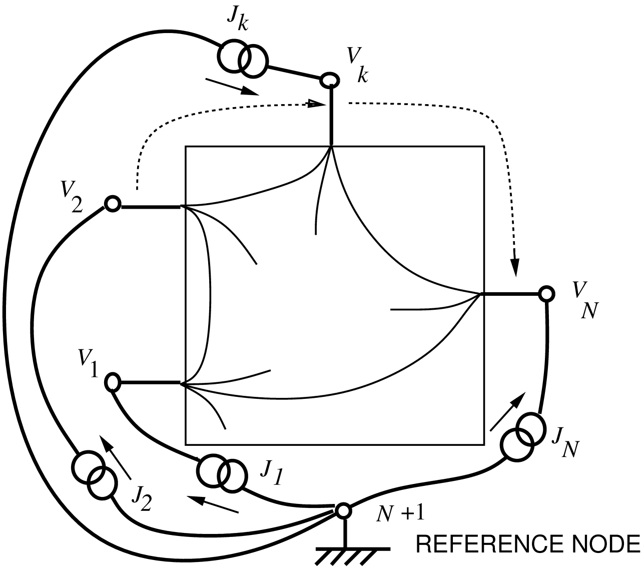

FIGURE 8.38 General network.

constitutive relations are contained in the main body, but the variables, the node-voltages, and the external currents are clearly separated. This representation of a network enables as uniform a treatment as possible. It makes it very easy to add one element at a time to the network as variables are already defined. Indeed this is how all general purpose simulators work and the network equations are built up by inspection. Initially the network is defined with nothing in the main body and only the variables defined. Then each element is considered in turn and the describing relations added to the evolving network equation matrix. This representation serves us well when it comes to harmonic balance. Applying KCL to each of the nodes of the network the following matrix network equation is obtained:

$$\mathbf{YV} = \mathbf{J}. \tag{8.54}$$

Here **Y** is the nodal admittance matrix of the network, **V** is the vector of node voltages (i.e., voltages at the nodes each referred to the reference node), and **J** is the vector of external current sources at each node. Expanding the matrix equation:

$$\begin{bmatrix} y_{11} & y_{12} & \cdots & y_{1N} \\ y_{21} & y_{22} & \cdots & y_{2N} \\ \vdots & \vdots & \ddots & \vdots \\ y_{N1} & y_{N2} & \cdots & y_{NN} \end{bmatrix} \begin{bmatrix} V_1 \\ V_2 \\ \vdots \\ V_N \end{bmatrix} = \begin{bmatrix} J_1 \\ J_2 \\ \vdots \\ J_N \end{bmatrix}. \tag{8.55}$$

We will see this utilized in the formulation of SPICE and HB analyses.

Time-Domain Circuit Simulation

The principal advantage of simulating circuits in the time domain is that it most closely resembles the real world. Phenomena such as chaos, instability, subharmonic generation, and parametric effects can be accurately simulated without the *a priori* knowledge of the spectral components of the signals in a circuit.

Direct Integration of the State Equations

The most direct method for analyzing nonlinear circuits is numerical integration of the differential equations describing the network. By applying Kirchoff's voltage and current laws and using the characteristic equations for the circuit elements (generally using the modified nodal formulation), the state equations can be written as a set of coupled first-order differential equations:

$$\dot{\mathbf{X}} = f(\mathbf{X}, t) \tag{8.56}$$

where, for example, the time derivative of a quantity such as voltage or current is a function of time and of the voltages and currents in the circuit. More generally the state equations are rearranged and written in the implicit form

$$g(\dot{\mathbf{X}}, \mathbf{X}, t) = 0 \tag{8.57}$$

where $\mathbf{X} = [X_1, X_2, \ldots, X_N]^{\mathrm{T}}$ is a set of voltages and currents, typically at different nodes and different time instants. The general formulation of Eq. (8.57) is discretized in time and solved using a numerical integration procedure. This modeling approach can be used with many systems as well as circuits and was the only approach considered in the early days of circuit simulation (in the 1960s). Unfortunately, it was not robust except for the simplest of circuits. SPICE-like analysis, considered next, solves the same problem but in a much more robust way.

SPICE: Associated Discrete Circuit Modeling

SPICE is the most common of the time domain methods used for nonlinear circuit analysis. This method is fundamentally the same as that just described in that the state equations are integrated numerically, however the order of operations is changed. The time discretization step is applied directly to the equations describing the circuit element characteristics. The nonlinear differential equations are thereby converted to nonlinear algebraic equations. Kirchoff's voltage and current laws are then applied to form a set of algebraic equations solved iteratively at each time point.

Converting the differential equations describing the element characteristics into algebraic equations changes the network from a nonlinear dynamic circuit to a nonlinear resistive circuit. In effect, the differential equations describing the capacitors and inductors, for example, are approximated by resistive circuits associated with the numerical integration algorithm. This modeling approach is called associated discrete modeling or just companion modeling. The term "associated" refers to the model's dependence upon the integration method while "discrete" refers to the model's dependence on the discrete time value.

The numerical integration algorithm is the means by which the element characteristics are turned into difference equations. Three low order numerical integration formulas are commonly used: the Forward Euler formula, the Backward Euler formula, and the Trapezoidal Rule. A generalization of these to higher order is called the weighted integration formula from which the Gear Two method, available in some SPICE simulators, is derived. In all methods the aim is to estimate the state of a circuit at the next time instant from the current state of the circuit and derivative information. In one dimension and denoting the current state by x_0 and the next state by x_1, the basic integration step is

$$x_1 = x_0 + hx'. \tag{8.58}$$

The formulas differ by the method used to estimate x'.

In the Forward Euler Formula, $x' = x'_\phi$ is used and the basic numerical integration step [Eq. (8.58)] becomes

$$x_1 = x_0 + hx'_0. \tag{8.59}$$

Numerical integration using the forward Euler formula is called a predictor method as information about the behavior of the waveform at time t_0, x_0', is used to predict the waveform at t_1.

In the Backward Euler Formula, $x' = x_1'$ is used and the discretized numerical integration equation becomes

$$x_1 = x_0 + hx_1'. \tag{8.60}$$

The obvious problem here is how to determine x_1' when x_1 is not known. The solution is to iterate as follows: (1) assume some initial value for x_1 (e.g., using the Forward Euler formula); and (2) iterate to satisfy the requirement $x_1' = f(x_1, t)$. Discretization using the Backward Euler formula is therefore called a predictor-corrector method.

In the Trapezoidal Rule, $x' = (x_0' + x_1')/2$ is used and the discretized numerical integration equation becomes

$$x_1 = x_0 + h\left(x_0' + x_1'\right)\Big/2. \tag{8.61}$$

So the essence of the trapezoidal rule is that the slope of the waveform is taken as the average of the slope at the beginning of the time step and the slope at the end of the time step determined using the Backward Euler formula.

There is a significant difference in the numerical stability, accuracy, and run times of these methods, although all will be stable with a small enough step size. Note that stability is a different issue than whether or not the correct answer is obtained. The Backward Euler and Trapezoidal Rules will always be stable and these are the preferred integration methods. The Forward Euler method of discretization does not always result in a numerically stable method. This can be understood by considering that the Forward Euler method always predicts the response into the future and does not improve on the guess using other information that can be obtained. The Backward Euler and Trapezoidal Rule approaches use a prediction of the future state of a waveform, but then require iteration to correct any error and use derivative information as well as instantaneous information to achieve this. Generally, when any simulation strategy is first developed, predictor methods are used. However, in the long run, predictor-corrector methods are always adopted as these have much better overall performance in terms of stability and accuracy but do require much more development effort. Except for the Forward Euler method, none of the other methods are clearly the best choice in all circumstances, and experimentation should occur. Generally, we can say that for RF and microwave circuits that have resonant bandpass-pass characteristics, the Trapezoidal Rule tends to result in an over-damped response and the Backward Euler method results in an under-damped response. The effect of this on accuracy, the prime requirement, is not consistent and must be investigated for a specific circuit.

Associated Discrete Model of a Linear Element

The development of the associated discrete model (ADM) of an element begins with a time discretization of the constitutive relation of the element. The development for a linear capacitor is presented here as an example. The simplest algorithm to use in developing this discretization is the Backward Euler integration formula. The Backward Euler algorithm for solving the differential equation

$$\dot{x} = f\left(x\right) \tag{8.62}$$

with step size $h = t_{n+1} - t_n$ is

$$x_{n+1} = x_n + hf\left(x_{n+1}\right) = x_n + h\dot{x}_{n+1} \tag{8.63}$$

where the subscript n refers to the nth time sample. The discretization is performed for each and every element independently by replacing the differential equation of Eq. (8.62) by the constitutive relation of the particular elements.

For a linear capacitor, the charge on the capacitor is linearly proportional to the voltage across it so that $q = Cv$. Thus

$$i(t) = \frac{dq}{dt} = C\frac{dv}{dt} = C\dot{v}$$

or

$$v_{n+1} = \frac{1}{C} i_{n+1} \tag{8.64}$$

where the reference convention for the circuit quantities are defined in Fig. 8.39.

Substituting Eq. (8.64) into Eq. (8.65) and rearranging leads to the discretized Backward Euler model of the linear capacitor:

$$i_{n+1} = \frac{C}{h} v_{n+1} - \frac{C}{h} v_n. \tag{8.65}$$

This equation has the form

$$i_{n+1} = g_{eq} v_{n+1} - i_{eq} \tag{8.66}$$

and so is modeled by a constant conductance $g_{eq} = C/h$ in parallel with a current source $i_{eq} = -C/hv_n$ that depends on the previous time step, as shown in Fig. 8.40. The associated discrete circuit models for all other elements are developed in the same way, but of course the development is usually much more complicated, especially for nonlinear and multiterminal elements, but the approach is the same. The final circuit combining the ADM of all of the elements is linear with resistors and current sources, as well as a few special elements such as voltage sources. This circuit is especially compatible with the nodal-formulation described by Eq. (8.55). The linear circuit is then solved repeatedly with the circuit elements updated at each step and, if the circuit voltage and current quantities change by less than a specified tolerance, the time step advanced.

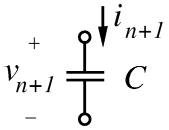

FIGURE 8.39 Reference direction for the circuit quantities of a capacitor.

The feature that distinguishes the associated discrete modeling approach from integration of the state equations for the system is that the discretization and particularly the Newton iteration is performed at the individual element level rather than at the top system level. The most important aspect of this is that special convergence treatments can be applied locally. For example, a diode has an exponential relationship between current and voltage and is the most difficult characteristic to handle. With the top-level systems-of-equations approach, any convergence scheme developed would need to be applied to all elements in a circuit, not just to the problem elements. In the associated discrete modeling, many local steps can be taken to improve convergence properties. This can include limiting the voltage and current changes from one iteration step to another. The scheme adopted depends on the characteristics of a particular element and heuristics developed in using it. It is this focus on local convergence control and embedding specific element knowledge in the element code that makes the SPICE approach so successful.

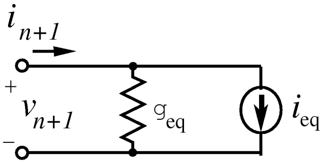

FIGURE 8.40 The associated discrete model of a two-terminal element.

The Shooting Method

As has been mentioned, time-marching simulation has problems in determining the steady-state response because of the long simulation times that are involved. There is one elegant solution when the excitation is a sinusoid so that the response is known to be periodic. For strictly periodic excitation, shooting methods are often used to bypass the transient response altogether. This is advantageous in situations that would require many iterations for the transient components to die out. It is assumed that the nonlinear circuit has a periodic solution and that the solution can be determined by finding an initial state such that transients are not excited. If $\mathbf{x}(t)$ is the set of state variables obtained by a time-domain analysis, the boundary value constraint for periodicity is that $\mathbf{x}(t) = \mathbf{x}(t + T)$, where T is the known period. A series of iterations at time points between t and $t + T$ can be performed for a given set of initial conditions, and the condition for periodicity checked. Thus, in the shooting method, the problem of solving the state equations is converted into the two-point boundary value problem

$$\begin{aligned} \mathbf{x}(0) &= \mathbf{x}(T) \\ \mathbf{x}(T) &= \int_0^T \mathbf{f}(\mathbf{x},\tau)\,d\tau + \mathbf{x}(0). \end{aligned} \tag{8.67}$$

If $\mathbf{x}(t) \neq \mathbf{x}(t + T)$ then a new set of initial conditions can then be determined using a gradient method based upon the error in achieving a periodic solution. Once the sensitivity of the circuit to the choice of initial conditions is established in this way, a set of initial conditions that establishes steady-state operation can be determined; this set is, of course, the desired solution. This iterative procedure can be implemented using the Newton's method iteration

$$\mathbf{x}^{k+1} = \mathbf{x}^k - \left[\mathbf{I} - \frac{\partial \mathbf{x}^k(T)}{\partial \mathbf{x}^k(0)}\right]^{-1} \left[\mathbf{x}^k(0) - \mathbf{x}^k(T)\right] \tag{8.68}$$

where the superscripts refer to iteration numbers and $\mathbf{x}^k(T)$ is found by integrating the circuit equations over one period from the initial state $\mathbf{x}^k(0)$.

To begin the analysis, the period (T) is determined and the initial state $(\mathbf{x}^k(0))$ is estimated. Using these values, the circuit equations are numerically integrated from $t = 0$ to $t = T$ and the necessary derivatives calculated. Then, the estimate of the initial state is updated using the Newton iteration [Eq. (8.68)]. This process is repeated until $\mathbf{x}(0) = \mathbf{x}(T)$ is satisfied within a reasonable tolerance.

Shooting methods are attractive for problems that have small periods. Unlike the direct integration methods, the circuit equations are only integrated over one period (per iteration). They are therefore more efficient, provided that the initial state can be found in a number of iterations that is smaller than the number of periods that must be simulated before steady-state is reached in the direct methods. Unfortunately, shooting methods can only be applied to find periodic solutions. Also, shooting methods become less attractive for cases where the circuit has a large approximate period, for example, when several nonharmonic signals are present. The computation becomes further complicated when transmission lines are present, because functional initial conditions are then required to establish the initial conditions at every point along the line (corresponding to the delayed instants in time seen at the ports of the line).

In multitone situations when only one signal is large and when operating frequencies are not so high that distributed effects are important, the large tone response can be captured using the shooting method and then the frequency conversion method described in the next section can be used to determine the response with the additional small signals present.

Frequency Conversion Matrix Methods

In many multitone situations, one of two or more impressed non-commensurate tones is large while the others are much smaller. In a mixer, a large local oscillator, LO, (which is generally 20 dB or more larger than the other signals) pumps a nonlinearity, while the effect of the other signals on the waveforms at the nonlinearities is negligible. The pumped time-invariant nonlinearity can be replaced by a linear time-varying circuit without an LO signal. The electrical properties of the time-varying circuit are described by a frequency domain conversion matrix. This conversion matrix relates the current and voltage phasors of the first order sidebands with each other. In other words, by performing a fast, single-tone shooting method or harmonic balance analysis with only the LO impressed upon it, the AC operating point of the mixer may be determined and linearized with respect to small-signal perturbations about this point. This information is already available in the Jacobian, which is essentially a gradient matrix relating the sensitivity of one dependent variable to another independent variable. A two-tone signal can be rewritten to group the LO waveform, $x_{LO}(t)$ terms and the first order sidebands as

$$x(t,j) = x_{LO}(t) + \mathrm{Re}\left\{\sum_{p=0}^{N_A} \mathbf{X}_{p,1} e^{j(p\omega_{LO}+\omega_{RF})} + \sum_{p=0}^{N_A} \mathbf{X}_{p,-1} e^{j(p\omega_{LO}-\omega_{RF})}\right\} \tag{8.69}$$

where $\mathbf{X}_{p,1}$ and $\mathbf{X}_{p,-1}$ are vectors of the spectral components at the first order sidebands of the pth harmonic of the LO. For voltage controlled nonlinearities, the output quantities (the $\mathbf{X}$'s) are current phasors so that the expression relating the IF current to the RF voltage is

$$\left[\mathbf{I}_{p,1}, \mathbf{I}_{p,-1}\right]^{\mathrm{T}} = \mathbf{Y}_C\left[\mathbf{V}_{0,1}, \mathbf{V}_{0,-1}\right]^{\mathrm{T}}. \tag{8.70}$$

Here $\mathbf{Y}_C$ is the admittance conversion matrix and can be used in much the same manner as a nodal admittance matrix. Alternatively, for current-controlled nonlinearities the following could be used:

$$\left[\mathbf{V}_{0,1}, \mathbf{V}_{0,-1}\right]^{\mathrm{T}} = \mathbf{Z}_C\left[\mathbf{I}_{0,1}, \mathbf{I}_{0,-1}\right]^{\mathrm{T}} \tag{8.71}$$

where $\mathbf{Z}_C$ is the impedance conversion matrix. Nonlinearities with state variable descriptions or mixed voltage-controlled and current-controlled descriptions require a combination of Eqs. (8.70) and (8.71) to derive a modified nodal admittance formulation.

Convolution Techniques

The fundamental difficulty encountered in integrating RF and microwave circuits in a transient circuit simulator arises because circuits containing nonlinear devices or time dependent characteristics must be characterized in the time domain while distributed elements such as transmission lines with loss, dispersion, and interconnect discontinuities are best simulated in the frequency domain. Convolution techniques are directed at the simulation of these circuits.

The procedure begins by partitioning the network into linear and nonlinear subcircuits as shown in Fig. 8.41. In a typical approach the frequency domain admittance (y) parameter description of the distributed network is converted to a time domain description using a Fourier transform. This time domain description is then the Dirac delta impulse response of the distributed system. Using the method of Green's function, the system response is found by convolving the impulse response with the transient response of the terminating nonlinear load. Normally this requires that the impulse response be extended in time to include many reflections. While this technique can handle arbitrary distributed networks, a difficulty arises as the y parameters of a typical multiconductor array have a wide dynamic range. For a low loss, closely matched, strongly coupled system, the y parameters describing the coupling mechanism

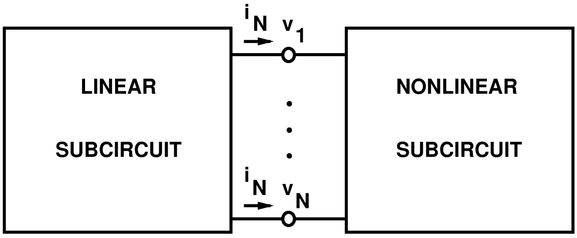

FIGURE 8.41 Circuit partitioned into linear and nonlinear sub-circuits.

approach zero at low frequencies and become very large at high frequencies. Conversely, the transmission and self-admittance *y* parameters approach infinity at DC and zero at resonance frequencies. Both numerical extremes are important in describing the physical process of reflections and crosstalk. The dynamic range of the time domain solution is similarly large and values close to zero are significant in determining reflections and crosstalk. Consequently, aliasing in the frequency domain to time domain transformation can cause appreciable errors in the simulated transient response. The problem is considerably reduced by using resistive padding at the linear-nonlinear circuit interface to reduce the dynamic range of the variables being transformed. The effect of the padding can then be removed in subsequent iteration.

Harmonic Balance: Mixed Frequency and Time Domain Simulation

The Harmonic Balance (HB) procedure has emerged as a practical and efficient tool for the design and analysis of nonlinear circuits in steady-state with sinusoidal excitation. The harmonic balance method is a technique that allows efficient solution of the steady-state response of a nonlinear circuit. For example, the steady-state response of a circuit driven by one or more sinusoidal signals is also a sum of sinusoids and includes tones at frequencies other than those of the input sinusoids (e.g., harmonics and difference frequencies). The response does not need to be periodic to be steady-state and with narrowband systems it is common to call the response to a complicated narrowband input as being quasi-periodic. Usually we are not interested in the transient response of the circuit such as when the power supply is turned on or when a signal is first applied. Thus much of the behavior of the circuit is not of interest. The harmonic balance procedure is a technique to extract just the information that is required to describe the steady-state response. The method may also be compared to the solution of a homogeneous, ordinary differential equation. A solution that is the sum of sinusoids of unknown amplitudes is substituted into the differential equation. Using the orthogonality of the sinusoids, the resulting problem simplifies to solving a set of nonlinear algebraic equations for the amplitudes of the sinusoids. There are several methods of solving for (complex) amplitudes, which will be discussed later in this section.

The HB method formulates the system of nonlinear equations in either domain (although more typically the time domain), with the linear contributions calculated in the frequency domain and the nonlinear contributions in the time domain. This is a distinct advantage for microwave circuits, in that distributed and dispersive elements are then much more readily modeled analytically or using alternative electromagnetic techniques based in the frequency domain.

While it is common to refer to the nonlinear calculations as being in the time domain, the most usual HB implementations require that the nonlinear elements be described algebraically, that is without derivatives or other memory effects. Thus a nonlinear resistor is described, for example, as a current as a nonlinear function of instantaneous voltage. So given the voltage across the nonlinear resistor at a particular time, the current that flows at the same instant can be calculated. A nonlinear capacitive element must be expressed as a charge which is a nonlinear function of instantaneous voltage. Then a sequence of charge values in time is Fourier transformed so that phasors of charge are obtained. Each phasor of charge is then multiplied by the appropriate $j\omega$ to yield current phasors.

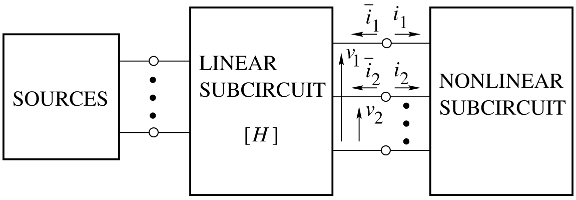

FIGURE 8.42 Circuit partitioned into linear, nonlinear, and source sub-circuits.

Problem Formulation

The harmonic balance method seeks to match the frequency components (harmonics) of current at the interface of two sub-circuits — one linear and one nonlinear. The sub-circuits are chosen in such a way that nonlinear elements are partitioned into one sub-circuit, linear elements into another, and (in some approaches) sources into a third (see Fig. 8.42). The edges at the linear/nonlinear interface connect the two circuits and define corresponding nodes; current flowing out of one circuit must equal that flowing into the other. Every node in the nonlinear circuit is "pulled out" of the nonlinear sub-circuit so that it is at the interface and becomes part of the error function formulation. Matching the frequency components in each edge satisfies the continuity equation for current. The current at each edge is obtained by a process of iteration so that dependencies are satisfied for both the linear and nonlinear sides of the circuit.

The unknowns are found by forming an error function — typically the Kirchoff's Current Law (KCL) error at the linear/nonlinear interface. This error function is minimized by adjusting the voltages at the interface. Every node in the nonlinear sub-circuit is therefore considered to be connected to the linear sub-circuit. If the total circuit has N nodes, and if $\mathbf{v}$ is the vector of node voltage waveforms, then applying KCL to each node yields a system of equations

$$f\left(\mathbf{v},t\right)=\mathbf{i}\left[\mathbf{v}\left(t\right)\right]+\frac{\mathrm{d}}{\mathrm{d}t}\mathbf{q}\left[\mathbf{v}\left(t\right)\right]+\int_{-\infty}^{t} y\left(t-\tau\right)\mathbf{v}\left(\tau\right)\mathrm{d}\tau+\mathbf{i}_S\left(t\right)=0 \tag{8.72}$$

where the nonlinear circuit is chosen to contain only voltage-controlled resistors and capacitors for representational ease. The quantities $\mathbf{i}$ and $\mathbf{q}$ are the sum of the currents and charges entering the nodes from the nonlinearities, $\mathbf{y}$ is the matrix impulse response of the linear circuit with all the nonlinear devices removed, and $\mathbf{i}_S$ are the external source currents.

In the frequency domain, the convolution integral maps into **YV**, where **V** contains the Fourier coefficients of the voltages at each node and at each harmonic, and **Y** is a block node admittance matrix for the linear portion of the circuit. The system of Eq. (8.72) then becomes, on transforming into the frequency domain

$$\mathbf{F}\left(\mathbf{V}\right)=\mathbf{IV}+\mathbf{\Omega QV}+\mathbf{YV}+\mathbf{I}_S=0 \tag{8.73}$$

where $\mathbf{\Omega}$ is a matrix with frequency coefficients (terms such as $j\Omega_k$) representing the differentiation step. The notation here uses small letters to represent the time domain waveforms and capital letters for the frequency domain spectra. This equation is, then, just KCL in the frequency domain for a nonlinear circuit. HB seeks a solution to Eq. (8.73) by matching harmonic quantities at the linear-nonlinear interface. The first two terms are spectra of waveforms calculated in the time domain via the nonlinear model, i.e.,

$$\mathbf{F}\left(\mathbf{V}\right)=\Im i\left(\Im^{-1}\mathbf{V}\right)+\Omega\Im q\left(\Im^{-1}\mathbf{V}\right)+\mathbf{YV}+\mathbf{I}_S=0 \tag{8.74}$$

where $\Im$ is the Fourier transform and $\Im^{-1}$ is the inverse Fourier transform.

The solution of Eq. (8.74) can be obtained by several methods. One method, known as relaxation, uses no derivative information and is relatively simple and fast, but is not robust. In a relaxation method the error function is taken to zero by adjusting current phasors or voltage phasors on successive iterations using what is in effect very limited derivative information. Alternatively, gradient methods can be used to solve either a system of equations (e.g., using a quasi-Newton method) or to minimize an objective function using a quasi-Newton or search method.

The Newton and quasi-Newton methods require derivative information to guide the error minimization process. Calculation of these derivatives is computationally intensive and generally the equations for these require considerable development. As with all the harmonic balance methods, the number of nodes used can be reduced by "burying" internal nodes within the linear network, which then becomes a single multiterminal sub-circuit as far as harmonic balance is concerned. The system of equations is then reduced accordingly. Once the "interfacial" node voltages are known, any internal node voltage can be found by using simple linear analysis and the full y matrix for the linear circuit.

Multitone Analysis

The problem with multitone analysis reduces to implementing a method to perform the multifrequency Fourier transform operations required in solving Eq. (8.74). This also requires developing the multifrequency Jacobian required in a Newton-like procedure. Time-frequency conversion for multitone signals can be achieved using nested Fourier transform operations. This is implemented using the multidimensional Fast Fourier Transform, or MFFT. Application of the multidimensional Fourier transform (MFFT), in which the Fourier coefficients are themselves periodic in the other dimensions, requires that the multiple tones (in each dimension) be truly orthogonal, i.e., not integer multiples of each other. If the two tones are frequency degenerate, then the method fails because orthogonality of the bases is a requirement for determining the Fourier coefficients in that basis. In such a case, one of the tones is slightly shifted to ensure that the technique can be applied.

The most general and easily programmed of the Fourier transform techniques applied to the HB method is the Almost-Periodic Discrete Fourier Transform (APDFT) algorithm. After truncation, consider the K arbitrarily spaced frequencies 0, ω_1, ω_2, …, ω_{K-1} generated by the nonlinearity. Then $\sum_{k=0}^{K-1} X_k^C \cos\omega_1 t_1 + X_k^2 \sin\omega_1 t_1 = x(t)$ may be sampled at S time points, resulting in a set of S equations and $2K$–1 unknowns:

$$\begin{bmatrix} 1 & \cos\omega_1 t_1 & \sin\omega_1 t_1 & \cdots & \cos\omega_{K-1} t_1 & \sin\omega_{K-1} t_1 \\ 1 & \cos\omega_2 t_2 & \sin\omega_2 t_2 & \cdots & \cos\omega_{K-1} t_2 & \sin\omega_{K-1} t_2 \\ \vdots & \vdots & \vdots & \ddots & \vdots & \vdots \\ 1 & \cos\omega_1 t_S & \sin\omega_2 t_S & \cdots & \cos\omega_{K-1} t_S & \sin\omega_{K-1} t_S \end{bmatrix} \begin{bmatrix} X_0 \\ X_1^C \\ X_1^S \\ \vdots \\ X_{K-1}^C \\ X_{K-1}^S \end{bmatrix} = \begin{bmatrix} x(t_1) \\ x(t_1) \\ \vdots \\ x(t_S) \end{bmatrix}. \tag{8.75}$$

The number of samples S must be at least $2K$–1 to uniquely determine the coefficients. This equation may compactly be written as

$$\Gamma^{-1}\mathbf{X} = x \text{ or } \Gamma x = \mathbf{X} \tag{8.76}$$

where Γ and Γ^{-1} are known as an almost-periodic Fourier transform pair. Thus the multifrequency transform can be performed as a matrix operation but spectrum mapping and Fast Fourier transformation is much faster.

Combining the above procedures yields the time invariant form of Harmonic Balance. This is referred to as just Harmonic Balance. This technique is very efficient for simulating circuits with just a few active devices and a few tones, as then there are only a few unknowns. Problems arise as the number of active devices increases or the number of tones becomes large as the size of the problem increases significantly. Still, digitally modulated signals can be reasonably modeled by considering a very large number of tones.

Method of Time-varying Phasors

Harmonic balance using time-variant phasors is ideally suited to the representation and characterization of circuits with digitally modulated signals. In contrast to time-variant harmonic balance, where the assumed phasor solution was time invariant, we instead assume a solution of the form

$$\mathbf{V}_k\left(j\omega\right) = \text{real}\left\{\sum_{m=0}^{n} V_m\left(t\right)\exp\left[jm\omega\left(t\right)+\phi_m\left(t\right)\right]\right\} \tag{8.77}$$

where in general the amplitude, frequency, and phase of each term are allowed to vary with respect to time. If $V_m(t)$ varies slowly with respect to the carrier frequency, we are in essence solving for the envelope of the signal at each node without the requisite memory requirements of time-invariant harmonic balance, or the frequency domain dynamic range and resolution problems of time domain methods. Taking the Fourier transform of each summation term in Eq. (8.77) results in a highly resolved power spectral density distribution approximation of the digitally modulated signal, not an ill-conditioned approximation, as with time-invariant harmonic balance.

Frequency Domain Analysis of Nonlinear Circuits

Frequency domain characterization of RF and microwave circuits directly provides the types of performance parameters required in communication systems as well as many other applications of RF and microwave circuits. The Harmonic Balance (HB) method uses Fourier transformation to relate sequence of instantaneous current, voltage, and charge to their (frequency domain) phasor forms. In frequency domain nonlinear analysis techniques alternative mappings are used. There are many types of mappings for arriving at a set of (say, current) phasors as a nonlinear function of another set of (say, voltage) phasors.

The common underlying principle of frequency domain nonlinear analysis techniques is that the spectrum of the output of a broad class of nonlinear circuits and systems can be calculated directly given the input spectrum input to the nonlinear system. The mapping operation is depicted in Fig. 8.43 and is the concept behind most RF and microwave behavioral modeling approaches. Some techniques determine

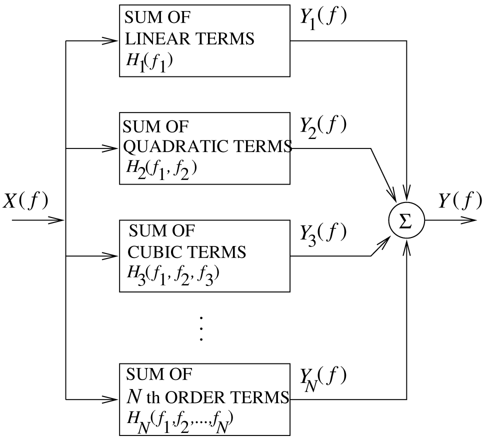
SUM OF LINEAR TERMS $H_1(f_1)$
$Y_1(f)$
SUM OF QUADRATIC TERMS $H_2(f_1, f_2)$
$Y_2(f)$
$X(f)$
SUM OF CUBIC TERMS $H_3(f_1, f_2, f_3)$
$Y_3(f)$
Σ
$Y(f)$
SUM OF N th ORDER TERMS $H_N(f_1, f_2, ..., f_N)$
$Y_N(f)$

FIGURE 8.43 Mapping concept of frequency domain analysis.

an output frequency component by summing calculations of individual intermodulation products. For example, the product of two tones is, in the time domain, the product of two sinusoids. The trigonometric expansion of this yields two intermodulation products with frequencies that are the sum and difference, respectively, of the frequencies of the tones. Power series techniques use trigonometric identities to expand the power series and calculate each intermodulation product individually. Algorithms sum these by frequency to yield the output spectrum. At the coarse end of the scale are Volterra series-based techniques that evaluate groups of intermodulation products at a single frequency. Some frequency-domain nonlinear analysis techniques are noniterative, although these are restricted to unilateral systems. Others, known as frequency domain spectral balance techniques, are iterative, being the frequency domain equivalent of the harmonic balance techniques. The term spectral balance is used to distinguish the frequency domain techniques from the harmonic balance techniques as the latter term has come to be solely applied to mixed time and frequency domain methods in which Fourier transformation is used. Intermediate between these extremes are techniques that operate by converting a nonlinear element into a linear element shunted by a number of controlled current sources. This process is iterative and at each iteration a residual nonlinear element is left that reduces from one iteration to another. This is the basis of one of the Volterra series analysis techniques called the method of nonlinear currents, which is also discussed in the next section.

Volterra Analysis

Expanding on Volterra analysis illustrates the concepts behind functional analysis of circuits in the frequency domain. Volterra series have the form

$$G\left(x\right)=\sum_{n=0}^{\infty}F_n\left(x\right) \tag{8.78}$$

where $F_n(x)$ is a regular homogeneous functional such that

$$F_n\left(x\right)=\int_a^b\cdots\int_a^b h_n\left(\chi_1,\chi_2,\ldots,\chi_n\right)x\left(\chi_1\right)x\left(\chi_2\right)\cdots x\left(\chi_n\right)\mathrm{d}\chi_1\mathrm{d}\chi_2\cdots\mathrm{d}\chi_n \tag{8.79}$$

and the functions $h_n(\chi_1, \chi_2,\ldots, \chi_n)$ are known as the nth order Volterra kernels. It can be used as a time domain description (with the χ's replaced by t) of many nonlinear systems including nonlinear microwave circuits that do not exhibit hysteresis. In this case, the nth order kernel, h_n, is called the nonlinear impulse response of the circuit of order n. Equation (8.79) is then interpreted as an n dimensional convolution of an nth order impulse response (h_n) and the input signal (x). The total response $G(x)$ is the summation of the different order responses $F_n(x)$. Note that for a linear system there is only a first order response so that the total response of the system is the conventional convolution integral

$$G\left(x\right)=F_0+\int_a^b h_1\left(\tau\right)\mathrm{d}\tau \tag{8.80}$$

where F_0 is just a DC offset.

The important concept here is that the total response of a signal is the summation of a number of responses of different order. This scheme only works if, as the order n increases, the contribution to the response gets smaller and eventually insignificant. The reason this works for many RF and microwave circuits is that the response is close to linear and nonlinear behavior is a departure from linearity. A weak nonlinearity could be represented with just the first few terms of such a series.

In analyzing nonlinear circuits it is not necessary to deal with the Volterra series which, here, is in the time domain. Mostly the frequency domain form is used, which is expressed in terms of Volterra nonlinear transfer functions. Mathematically these are obtained by taking the *n*-fold Fourier transform of h_n:

$$H_n\left(f_1, f_2, \ldots, f_n\right) = \int_{-\infty}^{\infty} \cdots \int_{-\infty}^{\infty} h_n\left(\tau_1, \tau_2, \ldots, \tau_n\right) e^{-j2\left(f_1 \tau_{1+\ldots} \tau_n\right)} \mathrm{d}\tau_1 \mathrm{d}\tau_2 \cdots \mathrm{d}\tau_\mathrm{n} \tag{8.81}$$

where H_n is called the nonlinear transfer function of order *n*. The time-domain input-output relation $y(t) = f[x(t)]$ can be put in the form

$$y\left(t\right) = \sum_{n=1}^{\infty} y_n\left(t\right) \tag{8.82}$$

where

$$y_n\left(t\right) = \int_{-\infty}^{\infty} \cdots \int_{-\infty}^{\infty} h_n\left(\tau_1, \ldots, \tau_n\right) x\left(t - \tau_1\right) \cdots x\left(t - \tau_n\right) \mathrm{d}\tau_1 \cdots \mathrm{d}\tau_\mathrm{n} \tag{8.83}$$

and $x(t)$ is the input. Taking the *n*-fold Fourier transform of both sides we have an expression for the spectrum of the *n*th order component of the output

$$\mathbf{Y}_n = \int_{-\infty}^{\infty} \cdots \int_{-\infty}^{\infty} H_n\left(f_1, \ldots, f_n\right) \delta\left(f - f_1 - \cdots - f_n\right) \prod_{i=1}^{n} X\left(f_i\right) \mathrm{d}f_i \tag{8.84}$$

where $\mathbf{X}_n(f)$ is the Fourier transform of $x(t)$, $\mathbf{Y}_n(f)$ is the Fourier transform of $y_n(t)$, and $\delta(\cdot)$ is the delta function. This expresses the *n*th order terms of the output as a function of the input spectrum. The order of the terms refers to the fact that multiplication of the input by a constant *A* results in multiplication of the *n*th order terms by A^n. Then a frequency domain series for the output can be written as

$$Y\left(f\right) = \sum_{n=1}^{\infty} Y_n\left(f\right) \tag{8.85}$$

in terms of the input spectrum and the nonlinear transfer functions. $\mathbf{Y}_n(f)$ is the *n*th order response and corresponds to the response of the *n*th order term in the power series description of the nonlinearity.

The method of nonlinear currents enables the direct calculation of the response of a circuit with nonlinear elements that are described by a power series. Here a circuit is first solved for its linearized response described by zero and first order Volterra nonlinear transfer functions. Considering only the linearized response allows standard linear circuit nodal admittance matrix techniques to be used. The second order response, described by the second order Volterra nonlinear transfer functions can then be represented by controlled current sources. Thus the second order sources are used as excitations again enabling linear nodal admittance techniques to be used. The process is repeated for the third- and higher-order node voltages and is easily automated in a general purpose microwave simulator. The process is terminated at some specified order of the Volterra nonlinear transfer functions. This is a noniterative technique, but relies on rapid convergence of the Volterra series restricting its use to moderately strong nonlinear circuits.

Summary

SPICE is at its best when simulating large circuits as memory and computation time increase a little more than linearly after a circuit reaches a certain size. However, to determine the response to sinusoidal excitation requires simulation over a great many cycles until the transient response has died down. A major problem in itself is determining when the steady state has been achieved. A similar problem occurs with narrowband modulated signals, which can have many millions of RF cycles before the response appears to be steady state. For example, a typical sequence length for the (digitally modulated) DAMPS format is 10 ms, although the time step would be on the order of 100 ps to capture the fundamental and harmonics of the 850 MHz carrier. This results in 10^8 time-points and hence the same order discrete Fourier transforms. Fourier transformation, e.g., using a fast Fourier transform, of the simulated waveform is required to determine its spectral content. This is not too complex a task if the exciting signal is a single frequency, but if the signal driving the nonlinear circuit has non-commensurable frequency components or is digitally modulated, then the procedure is more difficult and the effect of numerical noise is exaggerated. Even low-level numerical noise may make it impossible to extract a low-level tone in the presence of a large tone. The ability to detect a small tone defines the dynamic range of a simulator in RF and microwave applications and SPICE-analysis has poor performance in this case.

There is also a fundamental approximation error present in the SPICE algorithm due to what amounts to a *z*-domain approximation to the frequency domain characteristics of the circuit. The consequence is that time steps must be short for reasonable dynamic range. This also makes it particularly difficult to represent circuits with strongly varying narrowband frequency response. Recent extensions to SPICE — the shooting method with the frequency conversion method and convolution techniques — increase the applicability of SPICE to RF and microwave circuits. In spite of the difficulties, SPICE remains the only method of determining the transient response of a circuit.

Harmonic Balance analysis of circuits achieves significant computation savings by assuming that the signals in a circuit are steady state, described by a sum of sinusoids. The coefficients and phases of these sinusoids are solved for and not the transient response. Harmonic balance has a significant computation time advantage over SPICE for small to medium RF and microwave circuits. However, the time increases rapidly as circuit size increases. HB lends itself well to optimization and to analysis of multifunction circuits including amplifiers, oscillators, mixers, frequency converters, and numerous types of control circuits such as limiters and switches, if transient effects are not of concern. Another major advantage of the harmonic balance method is that linear circuits can be of practically any size, with no significant decrease in speed if additional internal nodes are added, or if elements of widely varying time constants are used (such is not the case with time domain simulators). Two extensions, separately implemented, also increase the usefulness of Harmonic Balance. The method of time-variant phasors enables digitally modulated signals to be handled. The second extension using matrix-free methods enables Harmonic Balance to handle very rich spectra and thus also approximately treat digitally modulated signals.

All of the techniques discussed here have been implemented in circuit simulators developed for RF and microwave circuit modeling. Many other simulator technologies exist, but these are within the overall framework of the discussion here. The reader is directed to the Further Information list for exploration of other technologies and for greater detail on those treated here.

Further Information

The bases of circuit simulation are described in J. Vlach and K. Singhal, *Computer Methods for Circuit Analysis and Design*, Van Nostrand Reinhold, 1983, ISBN 0442281080; and L. T. Pillage, R. A. Rohrer, and C. Visweswariah, *Electronic Circuit and System Simulation Methods*, McGraw-Hill, 1995, ISBN 0070501696. These two books are oriented toward SPICE-like analysis. Details on the algorithms used in SPICE are given in A. Vladimirescu, *The SPICE Book*, J. Wiley, 1994, ISBN 0471609269, and the techniques used in developing the associated discrete models used in SPICE in P. Antognetti and G. Massobrio**,** *Semiconductor Device Modeling with SPICE***,** McGraw-Hill, 1988, ISBN 0070021538. In addition to the above, a short discussion of SPICE errors relevant to modeling RF and microwave circuits is contained in A. Brambilla and D. D'Amore, The simulation errors introduced by the SPICE transient analysis, *IEEE Trans. on Circuits and Systems-I: Fundamental Theory and Application,* 40, 57–60, January 1993. Circuit simulations oriented toward microwave circuit simulation are described in J. Dobrowolski, *Computer-Aided Analysis, Modeling, and Design of Microwave Networks: the Wave Approach,* Artech House, 1996, ISBN 0890066698; P. J. C. Rodrigues, *Computer-Aided Analysis of Nonlinear Microwave Circuits,* Artech House, 1998, ISBN 0890066906; and G. D. Vendelin, A. M. Pavio, and U L. Rohde, *Microwave Circuit Design Using Linear and Nonlinear Techniques,* Wiley, 1990, ISBN 0471602760. As well as providing a treatment of microwave circuit simulation, the following book provides a good treatment of Volterra analysis: S. A. Maas, *Nonlinear Microwave Circuits*, IEEE Press, 1997, ISBN 0780334035. Simulation of microwave circuits with digitally modulated signals is given in J. F. Sevic, M. B. Steer and A. M. Pavio, Nonlinear analysis methods for the simulation of digital wireless communication systems, *Int. J. on Microwave and Millimeter Wave Computer Aided Engineering*, 197–216, May 1996. A review of frequency domain techniques for microwave circuit simulation is given in M. B. Steer, C. R. Chang and G. W. Rhyne, Computer aided analysis of nonlinear microwave circuits using frequency domain spectral balance techniques: the state of the art, *Int. J. on Microwave and Millimeter Wave Computer Aided Engineering*, 1, 181–200, April 1991.

8.5 Time Domain Computer-Aided Circuit Simulation

Michael Lightner

The simulation of circuits at the electrical level has been the primary CAD activity of many designers. Electrical level simulation is used in both digital and analog system design. Its main use for RF and microwave circuits is to study waveform behavior and distortion characteristics of circuits under various environmental and parameter variations. Electrical level simulation is also one of the most costly CAD activities involved in the design of circuits. Because of the importance and expense of electrical simulation it has been widely studied and a huge literature exists of exact and approximate techniques. In this section we will consider the transient solution of nonlinear circuits, as this is the most important area of electrical simulation.

Before we begin the discussion of the details it is useful to see the big picture of how a program such as SPICE operates when solving for the transient response of a circuit. First the program must read in the description of the circuit and form the equations that will be solved. Actually, what SPICE does is read in the data associated with the circuit, the elements and values, the transistor models, and the element interconnections. In addition, controls such as the time range over which to solve the equations, the accuracy requirements, initial conditions, etc. are obtained from the user. Since we assume that the program will be solving nonlinear differential equations there is a set procedure (Table 8.2). These steps are common to solving for the transient response of any circuit. It is these steps that are built into the SPICE program. In fact, any program that produces exact solutions will use a procedure basically similar to this one. It is these steps which we will study in this chapter. Notice that the equations that are written and solved are linear equations. Since this forms the heart of the program we will begin with equation formulation and linear equation solution and follow that with the approximations used to deal with nonlinear and differential elements.

TABLE 8.2 Standard Steps in Solving Circuit Equations

```
Find the initial operating point (DC solution).
Choose a first time step (use the default).
  Discretize the derivatives (C's and L's) forming approximate models.
    Linearize the nonlinear elements forming approximate models.
      Form the linear equations associated with the approximate circuit.
      Solve the linear equations.
    Iterate until have solution or reduce the time step and try again.
  Check for accuracy.
If accurate continue forward in time else reduce time step and try again.
```

Hierarchy of Modeling and Simulation

Modern RF integrated circuits are becoming increasingly complex. Radio-on-a-chip and system-on-a-chip applications lead to extremely large circuits. In some cases. it is not possible to perform circuit simulation on the entire chip; indeed, besides taking much too much time and memory the data generated would overload any engineer's ability to assimilate information. In order to deal with the complexity of modern designs a hierarchy of models and associated simulators is used.

At the highest level, a behavioral model of the entire circuit is written, often in a standard programming language, and the large-scale input/output behavior of the system is studied. This level of modeling is done for both analog and digital circuits. Depending on the type of circuit, i.e., analog or digital, other more complex levels of modeling and simulation are used in the design process. At the lowest level typically dealt with by designers we find interconnections of individual transistors.

The transistor level is what concerns us in this section. We will assume that the higher levels of modeling and simulation have already been done. In addition, we will assume that the integrated circuit process that will be used in building the chip is well characterized and that models for the individual transistors and the interconnect are available. Thus the task that we face is the simulation of a collection of transistors in order to study the details of the voltage and current waveforms and their timing.

Typically microwave and RF transistor level simulation is used to characterize key circuit performance characteristics such as gain, phase, power saturation, and harmonic distortion. Section 8.6 of this handbook describes the application of time domain simulations in greater detail. Circuit size can range from a single transistor with input and output matching elements to dozens or hundreds of transistors for full RF radio-on-a-chip applications. For some mixed-mode circuit applications, transistor counts can get into the thousands. Each of these situations can be addressed using the methods in this section.

Modeling and Basic Circuit Equations

It is clear that no matter how accurate and efficient a simulation program is, the most important factor is the models that are used to represent the circuit. These include models for transistors, interconnects, passive components, and process and temperature dependencies. We will concentrate on the solution of network equations given the basic models. For detailed discussion of modeling the reader is referred to Section 8.7 in this handbook.

Equation Formulation

There are two common methods that are used to write circuit equations for simulators, the tableau approach [Hachtel et al., 1971] and the modified nodal method [Ho et al., 1975]. Both methods will be discussed briefly in this section.

The Tableau Approach

The simplest way to write the equations associated with a circuit is to use the tableau approach. In this technique the Kirchhoff voltage and current laws (**KVL** and **KCL**) and the individual branch/element equations are written in one large matrix. Although there are several ways of writing the KVL and KCL equations we will concentrate on one.

To begin we will assume that we are using the **associated reference direction** to align current and voltage for each element. This reference scheme is shown in Fig. 8.44.

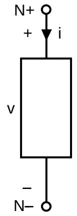

FIGURE 8.44 Associated reference directions.

We will further assume that each element has an orientation of + and – associated with it. In SPICE the first node is the + node and the second the –, for a two-terminal element. Finally, we assume that each node in the network has a unique identifier (we will use numbers) and that the ground node has been identified and has reference number 0. For convenience, let n be the number of nodes including the ground node and b be the number of branches (assuming two terminal branches). With these assumptions we can now form the node-branch incidence matrix A. This matrix, A, is $(n - 1) \times b$ with entries:

$$\begin{aligned} A_{ij} &= 1 \text{ if the } + \text{ of element } j \text{ is connected to node } i \\ &= -1 \text{ if the } - \text{ of element } j \text{ is connected to node } i \\ &= 0 \text{ otherwise} \end{aligned}$$

Now if we let i_b be the vector of branch currents, then KCL can be expressed as:

$$A\, i_b = 0$$

Further, if v_b is the vector of branch voltages and v_n is the vector of node voltages, not including the reference node, then KVL can be expressed:

$$v_b = A^T v_n$$

Finally, we need to express the **branch relationships.** For complete generality in dealing with two-terminal elements, including independent and dependent sources, we need a form of the branch equations such as:

$$R\, i_b + G\, v_b = s$$

where R is a matrix of resistances, G is a matrix of conductances, and s is a vector of source values. For example, if the kth element was a resistor, R_2, then $R_{kk} = R_2$, $G_{kk} = -1$, and $s_k = 0$. Further, if the nth component was a voltage source of value V_n, then $R_{nn} = 0$, $G_{nn} = 1$, and s_n and V_n. If we arrange these equations in one large matrix, we have the **tableau formulation** which has the form:

$$\begin{bmatrix} A & 0 & 0 \\ 0 & -I & A^T \\ R & G & 0 \end{bmatrix} \begin{bmatrix} i_b \\ v_b \\ v_n \end{bmatrix} = \begin{bmatrix} 0 \\ 0 \\ s \end{bmatrix}$$

A simple example is given in Fig. 8.45. For Fig. 8.45 the entries to the tableau are:

$$A = \begin{bmatrix} 1 & 1 & 0 & 0 \\ 0 & -1 & 1 & 1 \end{bmatrix}$$

$$R = \begin{bmatrix} 0 & & & \\ & R_1 & & \\ & & -1 & \\ & & & R_2 \end{bmatrix} \quad G = \begin{bmatrix} 1 & & & \\ & -1 & & \\ & & G_1 & \\ & & & -1 \end{bmatrix} \quad s = \begin{bmatrix} V \\ 0 \\ 0 \\ 0 \end{bmatrix}$$

This method of formulating equations is quite easy to implement. The one drawback is that the set of equations tends to be quite large. For example, if a small chip had 1000 nodes, not including ground, and there were 2500 branches, and an average of 2.5 branches per node, then the tableau equations would be a system of equations 6000 by 6000. In addition, most of the entries would be zero; thus sparse matrix techniques would be required to solve the equations. However, note that any element can be modeled

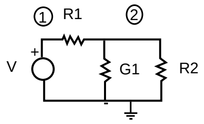

FIGURE 8.45 Example circuit for tableau equations.

using this approach and there are no limitations as there are with the standard nodal and loop analysis methods.

The Modified Nodal Approach

Another method of writing circuit equations that is less demanding of space and almost as flexible is called the **modified nodal approach.** In this approach, the typical nodal equations are written. However, for elements that are a function of current, e.g., inductors and certain controlled sources, extra variables and equations are added. This approach allows a broad range of elements to be modeled and yet keeps the size of the matrix relatively small. In order to describe, in a simple way, the modified nodal method we will consider networks with two terminal elements only (this is not a restriction of the method, but simply a convenience). We will label the elements as either being current controlled or voltage controlled. For example, a resistor, inductor, and independent voltage source will be considered current controlled, while conductors, capacitors, and independent current sources will be considered voltage controlled. Specifically, if the branch relation is written

$$i = f\left(v\right)$$

the element is considered voltage controlled. If the branch relation is written

$$v = g\left(i\right)$$

the element is considered current controlled. Note that the standard nodal equation approach only deals with voltage controlled elements. Consider S_I to be the set of current controlled elements and S_V to be the set of voltage controlled elements. Now we label each current controlled element, $l \in S_I$ with a new unknown I_l, the current through the element and we write the KCL at node k in the following way:

$$\sum_{j \in S_V,\ j \text{ connected to node } k} f_j\left(v\right) + \sum_{j \in S_I,\ j \text{ connected to node } k} I_j = -\sum_{j \in S_V,\ \text{current source currents connected to } k} I_j$$

The summations are all algebraic sums taking the reference directions of the current into account with current flow leaving the node considered positive. This is, of course, the normal way to write a nodal equation except that the unknown currents through current controlled elements have been added as unknowns. This generates a set of equations with more unknowns than equations. In order to provide the necessary additional equations we add the branch relations for each element in S_I to the previous set of equations. There are methods for easily generating these sets of equations. For our purposes a simple example will illustrate the important principles.

For the circuit in Fig. 8.46 the modified nodal equations are given by

$$\begin{bmatrix} 0 & 0 & 0 & 1 & 1 & 0 \\ 0 & G_1 & -G_1 & 0 & -1 & 1 \\ 0 & -G_1 & G_1 & 0 & 0 & 0 \\ 1 & 0 & 0 & 0 & 0 & 0 \\ 1 & -1 & 0 & 0 & -R_1 & 0 \\ 0 & 1 & 0 & 0 & 0 & -L_1 \dfrac{d}{dt} \end{bmatrix} \begin{bmatrix} V_1 \\ V_2 \\ V_3 \\ I_V \\ I_R \\ I_L \end{bmatrix} = \begin{bmatrix} 0 \\ 0 \\ I \\ V \\ 0 \\ 0 \end{bmatrix}$$

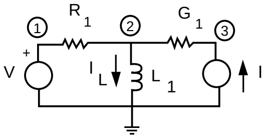

FIGURE 8.46 Example circuit for modified nodal equations.

Solving Linear Equations

The general form of the equations we generated in the previous section is

$$Ax = b$$

This is a set of linear algebraic equations and for our applications the system is completely specified with a unique solution. The goal of our discussion in this section is to explore some of the methods for solving this type of system of equations.

In general, for a system of linear equations we distinguish between direct and iterative methods of solution. Direct methods, the ones we shall examine in this section, are concerned with the calculation of the exact solution of the equation in a single computational step. In contrast, the iterative techniques, sometimes called relaxation techniques, use a sequence of steps to solve the equations and have to specify the conditions under which the computational sequence will converge to the correct answer (or indeed, converge at all).

We will not be concerned to any great extent with accuracy, however, the reader should know that there is a tremendous amount of literature on all facets of these methods.

Direct Methods for Full Systems

We will now consider the classical **Gaussian elimination** scheme for solving

$$Ax = b$$

We will assume that the matrix is relatively full and that whenever we choose a matrix location to use as a divisor that the entry in that location will be nonzero. Methods to deal with relaxing these assumptions are discussed later and in detail in the references.

For an *n* by *n* system of equations the standard Gaussian elimination procedure is given in Table 8.3.

A simple example of this procedure is given below. Forward elimination produces the sequence of matrices given below.

$$\begin{bmatrix} 2 & 2 & 1 \\ 3 & 1 & 0 \\ 0 & 1 & 2 \end{bmatrix} \begin{bmatrix} x_1 \\ x_2 \\ x_3 \end{bmatrix} = \begin{bmatrix} 1 \\ 2 \\ 1 \end{bmatrix}$$

$$\begin{bmatrix} 2 & 2 & 1 \\ 0 & -2 & -3/2 \\ 0 & 1 & 2 \end{bmatrix} \begin{bmatrix} x_1 \\ x_2 \\ x_3 \end{bmatrix} = \begin{bmatrix} 1 \\ 1/2 \\ 1 \end{bmatrix}$$

$$\begin{bmatrix} 2 & 2 & 1 \\ 0 & -2 & -3/2 \\ 0 & 0 & 5/4 \end{bmatrix} \begin{bmatrix} x_1 \\ x_2 \\ x_3 \end{bmatrix} = \begin{bmatrix} 1 \\ 1/2 \\ 5/4 \end{bmatrix}$$

Backward substitution yields:

$$x_3 = 1$$

$$x_2 = \left(\tfrac{1}{2} + \tfrac{3}{2}\,1\right)/2 = -1$$

$$x_1 = \left(1 - 1 - 2(-1)\right)/2 = 1$$

TABLE 8.3 Gaussan Elimination

Forward Elimination	Backward Substitution
For i = 1 to n – 1	For i = n to 1
For j = i + 1 to n	
For k = i to n	$x_i = b_i - \sum_{j=i+1}^{n} a_{ij} x_j$
$a_{jk} = a_{jk} - \frac{a_{ji}}{a_{ii}} a_{ik}$	where
End for	$\sum_{k=n+1}^{n} = 0$
$b_j = b_j - \frac{b_i}{a_{ii}} a_{ji}$	End for
End for	
End for	

This is the simple procedure that you may have seen before. The element that is used as the divisor in the forward elimination is called the *pivot element.* The procedure obviously depends on the pivot elements being nonzero. Furthermore, there is unnecessary work that is done. In particular, there is no need to zero out the column underneath the pivot element. Modifications based upon these observations are common. We note that the complexity of Gaussian elimination is $O(n^3)$ and that this complexity comes from the three nested loops in the forward elimination portion of the algorithm.

In solving linear systems it is often the case that the same equation will be solved with several right-hand sides. In this case, there is a procedure that can result in considerable savings. This procedure is known as *LU factorization* and also incorporates the savings from not zeroing out the column below the pivot element.

In LU factorization, the A matrix is decomposed into the product of a lower triangular matrix, I, and an upper triangular matrix, U. Thus

$$Ax = b$$

becomes

$$LUx = b$$

With this decomposition we can perform a forward substitution and a backward substitution to solve the system of equations. Specifically, we solve

$$Ly = b$$

using a forward substitution and

$$Ux = y$$

using a backward substitution. Both of these systems are triangular and are easy to solve requiring $O(n^2)$ operations each. Furthermore, if the right-hand-side vector is changed it is a simple task to perform the substitutions to find the new answer.

Thus the question becomes: How do we decompose the A matrix into LU? Although we will not analyze this carefully it will turn out that the steps required for the decomposition are the same as those for the forward elimination portion of Gaussian elimination except that we will not zero out the elements below the diagonal. In fact, the procedure given in Table 8.4 will write the LU matrices on top of the A matrix. Also, because the substitution process is straightforward we will only give the procedure for generating the LU decomposition.

TABLE 8.4 LU Decomposition

```
For $i = 1$ to $n$
    For $j = i$ to $n$
        $u_{ij} = a_{ij} - \sum_{p=1}^{i-1} l_{ip} u_{pj}$
        $I_{ji} = a_{ji} - \sum_{p=1}^{j-1} l_{jp} u_{pi} / u_{ii}$
    End for
End for
where
        $\sum_{p=1}^{0} = 0$
```

For illustration purposes we present a matrix A and its LU factors. If

$$A = \begin{bmatrix} 3 & 5 & 1 \\ 1 & 4 & 3 \\ 2 & 2 & 3 \end{bmatrix}$$

then

$$L = \begin{bmatrix} 3 & 0 & 0 \\ 1/3 & 1 & 0 \\ 2/3 & -4/7 & 1 \end{bmatrix}, \quad U = \begin{bmatrix} 3 & 0 & 1 \\ 0 & 7/3 & 5/3 \\ 0 & 0 & 69/21 \end{bmatrix}$$

Pivoting for Accuracy

One subject that we have ignored in our discussion of Gaussian elimination and LU factorization is what to do when the element on the diagonal is zero or very small. In that case we cannot simply divide by the diagonal element without incurring significant numerical error. The choice of which element to use as the divisor in each row is known as *pivot selection* and the element chosen is known as a *pivot element.*

Significant research has gone into the subject of pivot selection, which we will not discuss in this section. However, we do wish to point out that the discussion of **pivoting** in most references will leave a suggestion that after the pivot element is selected there will be a row and column permutation of the matrix to bring that element to the diagonal. In point of fact this is not necessary. In an efficient implementation there would be no data movement, merely a keeping track of the proper order in which to perform the operations. This extra bookkeeping is much cheaper than repeated data motion.

Finally, note that moving columns causes the order of the variables to change and moving rows causes the right-hand side to move. This information should be part of the bookkeeping involved in the solution process.

Solving Sparse Linear Systems

As pointed out earlier, most of the entries in the matrices associated with circuit equations are zero. That is, the matrices are very **sparse.** There are two issues of importance in dealing with sparse matrices: the storage scheme and the pivot strategy.

If proper care is taken in solving sparse systems, the computational cost can, in practice, be reduced from $O(n^3)$ to $O(n^{1.3})$. This is a significant savings and well worth the programming investment when we are solving the systems repeatedly as is the case in circuit simulation.

Storage Scheme for Sparse Matrices

If the matrix is very sparse, it is wasteful of space to store using a n^2 array. In fact, for circuit equations there tends to be a small constant number of nonzeros per row independent of the size of the system. Typically, this is between 3 and 10. Thus in a medium-sized circuit having 1000 nodes there will be about 1% nonzeros.

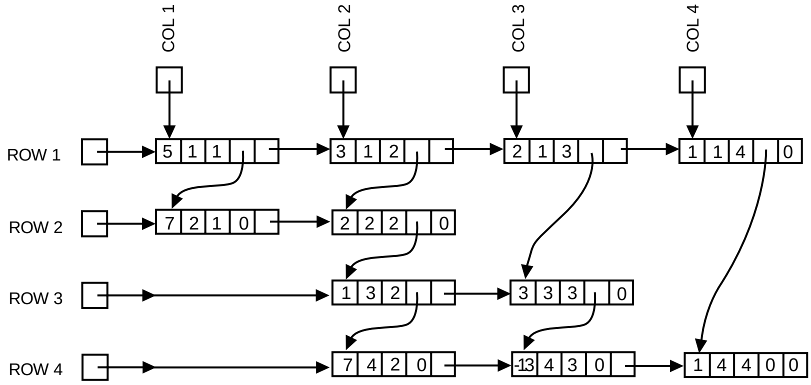

FIGURE 8.47 Bidirectional doubly linked list pivoting for sparsity.

Many storage schemes have been proposed for sparse matrices. The general trade-off is space versus ease of operation. Remember that we still have to search the rows and columns of the matrix during the elimination process. A bidirectional doubly linked list is a very easy data structure to traverse and modify and is a common one for use in storing sparse matrices. Note that this data structure has a relatively high degree of overhead and thus requires a very sparse system to make viable.

Figure 8.47 illustrates the bidirectional doubly linked list structure used to store a sparse matrix.

It is quite possible in the course of the Gaussian elimination process for an entry in the matrix that was zero to become nonzero. This is known as **fill-in.** The example shown below is an extreme case. For an array with the zero/nonzero structure given by

$$A = \begin{bmatrix} x & x & x & x \\ x & x & & \\ x & & x & \\ x & & & x \end{bmatrix}$$

after the first step of Gaussian elimination the zero/nonzero structure becomes

$$\begin{bmatrix} x & x & x & x \\ x & x & x & x \\ x & x & x & x \\ x & x & x & x \end{bmatrix}$$

All of the zeros have become nonzero. In this case there will be $O(n^3)$ operations. This was not necessary. If the matrix had been pivoted to the following form:

$$\begin{bmatrix} x & & & x \\ & x & & x \\ & & x & x \\ x & x & x & x \end{bmatrix}$$

there would have been no fill-in during the elimination process. Clearly there is a requirement that the solution order be chosen to preserve the sparse structure of the equations to the extent possible.

Significant research has been done to find the best pivoting strategy to preserve sparseness. However, of all the methods available, one of the earliest is still robust and used widely. The *Markowitz criteria* is a simple method used to determine the pivot order.

In describing the Markowitz criteria, remember that we are always working on a portion of the matrix, the whole matrix at the first step and reduced portions thereafter. Markowitz looks at each nonzero, a_{ij} in the reduced matrix and counts the number of nonzeros in the associated row, r_i, and column, c_j, and forms the quantity, $(r_i - 1)(c_j - 1)$ (known as the Markowitz count). Then the pivot element is chosen as that nonzero with the smallest Markowitz count (ties are broken arbitrarily).

To illustrate this process we take the arrow head matrix shown above and attach the Markowitz count as superscripts to each of the nonzeros.

$$A = \begin{bmatrix} x^9 & x^3 & x^3 & x^3 \\ x^3 & x^1 & & \\ x^3 & & x^1 & \\ x^3 & & & x^1 \end{bmatrix}$$

Clearly, the (1,1) position would be the last chosen or, in other words, is the worst possible choice. Note that the count has to be recalculated at every step of the elimination process, which emphasizes the need for easy traversal of the data structure.

Solving Nonlinear Equations

Obviously we must deal with nonlinear elements when simulating integrated circuits. These elements arise from the nonlinearities in transistor device models. For the sake of simplicity we will first consider two terminal nonlinearities.

For a simple nonlinear equation

$$f(x) = 0$$

the usual method of solution is some variant on the **Newton-Raphson** (NR) procedure.

In order to understand the NR procedure we must realize that the entire procedure is based upon a linear approximation to the function at the current point, x_c. Thus, if we expand the function in a Taylor series about the current point we have

$$f(x_+) = f(x_c) + \left.\frac{\partial f}{\partial x}\right|_{x=x_c} (x_+ - x_c)$$

Of course, we are ignoring the error involved in the approximation. Now, if we further assume that the x_+ is the solution, i.e.,

$$f(x_+) = 0$$

then we have

$$x_+ = x_c - f(x_c) \Big/ \left.(\partial f / \partial x)\right|_{x=x_c}$$

which is the basic NR step.

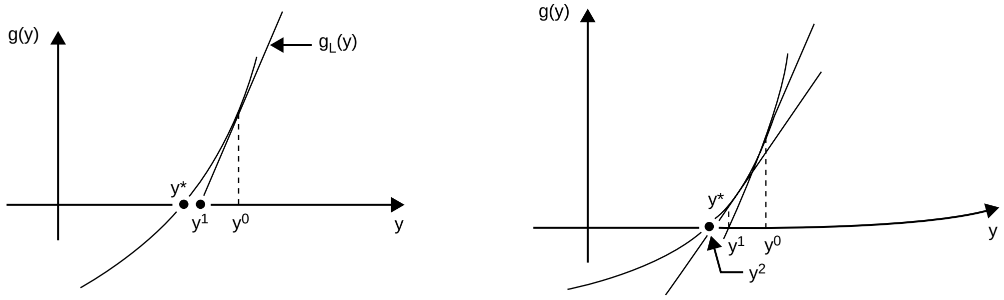

FIGURE 8.48 Newton-Raphson example.

The process of repeated calculation of linear approximations and their solution is illustrated in Fig. 8.48.

The difficulties associated with this scheme are numerous. For example, if the partial derivative (the normal derivative in the single variable case) is zero, then the step fails. Further, we have no guarantee of convergence for the general case. In addition, with the applications to electrical circuits with exponential nonlinearities, numerical accuracy can be a tremendous problem. Significant research has been done to deal with all of these cases, and more. Yet the nonlinear solution problem, especially the initial DC solution, continues to be the least robust portion of the electrical level simulation package.

The question of convergence of the NR algorithm is answered by the following theorem.

Theorem: If f is twice continuously differentiable, $[\partial f(x)/\partial x]|_{x=x^*} \neq 0$, i.e., the derivative is nonzero at the solution, x^*, and the initial guess x_0 is close enough to the solution, then the NR method always converges to the solution. Furthermore, letting

$$\varepsilon_k = |x_k - x^*|$$

be the error at the kth iteration, then

$$\varepsilon_{k+1} \leq C\varepsilon_k^2$$

where C is a positive constant, i.e., the NR methods have quadratic convergence.

Notice that there is no mechanism for determining how close is close enough in the previous theorem. This type of convergence is known as *local convergence;* if the iteration converges from *any* starting point, the algorithm is said to possess *global convergence.* In addition, the quadratic convergence property is

TABLE 8.5 Newton-Raphson

```
Error = $\infty$
Accuracy = $\varepsilon$ (user supplied)
$X_c$ = current estimate of the solution, initially provided by user
While (Error $\geq$ Accuracy)
        calculate an update of the estimated solution
                $x_+ = x_c - f(x_c)/(\partial f/\partial x)|_{x=x_c}$
        calculate the new error
                Error = $|x_+ - x_c|$
        update the estimate of the solution
                $x_c = x_+$
End While
```

very important because it shows that if the error is ever less than one that it will be driven to zero very quickly. In fact, once the error is below one, the number of significant decimal places effectively doubles at each iteration.

Newton-Raphson Applied to Circuit Simulation

Given the general picture of the NR scheme, how is this applied to circuits? The first difficulty is that nonlinear circuit equations are not just a function of a single variable. Further, there is a set of equations and not just a single one. This problem is easily handled by extending the one-dimensional NR scheme to multidimensions using vector calculus. The update formula now becomes

$$x_+ = x_c + \left[\frac{\partial f}{\partial x}\right]^{-1}_{x=x_c} f(x_c)$$

were $\partial f/\partial x$ is known is the *Jacobian* of the set of circuit equations and is the matrix of partial derivatives.

$$\frac{\partial f}{\partial x} = \begin{bmatrix} \frac{\partial f_1}{\partial x_1} & \cdots & \frac{\partial f_1}{\partial x_n} \\ \vdots & \ddots & \vdots \\ \frac{\partial f_n}{\partial x_1} & \cdots & \frac{\partial f_n}{\partial x_n} \end{bmatrix}$$

Rewriting this set of equations we have

$$\left.\frac{\partial f}{\partial x}\right|_{x=x_c} (x_+ - x_c) = f(x_c)$$

This is precisely in the form

$$Ax = b$$

which we studied in the previous section. A similar convergence condition applies and the reader is referred to the literature. Most importantly, we note that local convergence and a quadratic rate of convergence apply in the multidimensional case as well as the single-dimensional case.

The final difficulty we face is how to generate the equations in the first place and then how to take the partial derivative of this large set of equations. What can be shown without too much difficulty, although we will skip the demonstration, is that the individual elements can be linearized and the equations written for this linear network and we still have the same set of equations required for NR.

To illustrate this we will consider the network in Fig. 8.49 with two diodes. We will assume a simple form for the diode equation

$$i = f(v)$$

The linearized form of this becomes

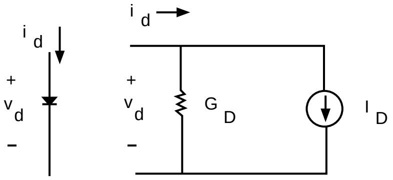

FIGURE 8.49 Diode linearized model.

$$i_+ = i_c + \left.\frac{\partial f}{\partial v}\right|_{v=v_c} (v_+ - v_c)$$

If we rewrite this grouping the known and unknown quantities we have

$$i_+ = \left[i_c - \left.\frac{\partial f}{\partial v}\right|_{v=v_c} v_c \right] + \left.\frac{\partial f}{\partial v}\right|_{v=v_c} v_+$$

This can be interpreted as an electrical model of the linearized diode that has a current source of value

$$I_D = \left[i_c - \left.\frac{\partial f}{\partial v}\right|_{v=v_c} v_c \right]$$

in parallel with a conductance of value

$$G_D = \left.\frac{\partial f}{\partial v}\right|_{v=v_c}$$

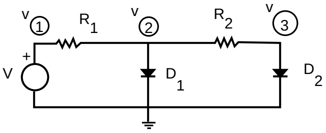

FIGURE 8.50 Nonlinear network used for NR example.

This model is illustrated in Fig. 8.50.

With this model the original circuit can be transformed into a linearized model as shown in Fig. 8.51.

Now we can use the normal equation formulation techniques to generate the set of linear circuit equations that represent the Jacobian of the nonlinear network equations. This is the process used in most circuit simulation programs.

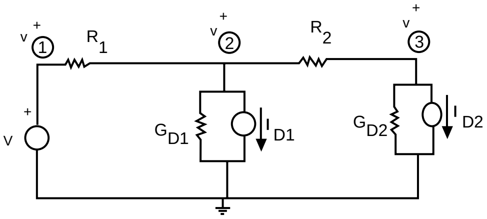

FIGURE 8.51 Linearized network.

Accuracy Control in Circuit Simulation with NR

Two major areas of concern in using NR for solving circuit equations are

- Numerical overflow during the iterations
- Nonconvergence of the iterations

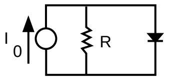

FIGURE 8.52 Circuit example with numerical overflow problems.

The first problem is primarily due to the nature of the nonlinearities in the circuit itself. This is especially a problem with the exponential nonlinearity associated with pn junction and Schottky barrier models. For example, in the circuit shown in Fig. 8.52 if the initial guess is v_0, then the result of the first iteration is v_1 and to continue the iteration we have to evaluate the diode current for a voltage of 10 V; this requires evaluating e^{400} (these iterations are shown in Fig. 8.53). Clearly overflow can be a problem.

Two classes of methods have been proposed to alleviate this problem. Both limit the step in voltage that is actually taken and are known as *limiting methods.* The first group of methods, which we will not discuss in detail, require some arbitrary limitation of the NR step. Although some of these can work well, they are quite heuristic.

The second class of limiting methods, which are used more often in solving circuit equations, involve the changing of the variable of iteration. We have been writing the diode equation as

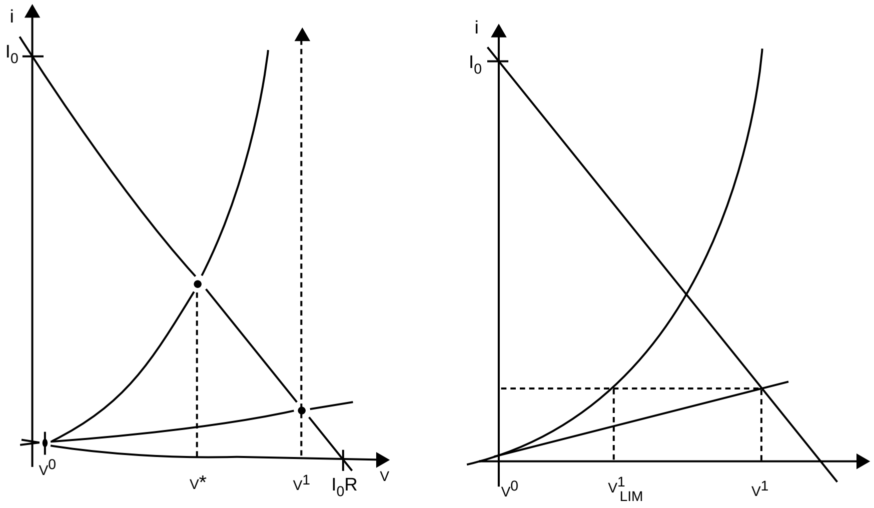

FIGURE 8.53 Alternating *V* and *I* as unknowns in NR.

$$i = f(v)$$

but we could have just as well written

$$v = g(i)$$

As we know, the function *g* is a logarithmic function and so is much less prone to numerical difficulties than the exponential function *f.* The decision on which form to represent the function can be made during the iterations and can change from step to step. The difference between these two steps is illustrated in Fig. 8.53.

The second class of difficulties, nonconvergence, can have several causes:

- The equations may not have a solution due to error in their formulation.
- The first derivatives of the elements' branch relationships lead to a singular Jacobian.
- The initial guess is not sufficiently close to the solution.
- The branch relationships may not have continuous derivatives.

Difficulties with model equations can only be solved with a refinement of the equations themselves and so this is out of our range of discussion.

There are two broad classes of methods to attempt to force convergence of the NR equations:

- Optimization-based methods
- Continuation methods

We will not discuss the first class of methods. The second class of methods is best characterized in circuit simulators as *source stepping methods.* Source stepping methods are generally used to help find the initial DC solution of the circuit. First we note that if all the DC sources are set to zero, then we know the solution to the network — zero. So if we increase the source values slightly from zero to their final value, we have a very good guess at the solution — zero. This process is continued until the sources reach their final value.

There is much known on how to improve the numerical behavior of NR in circuit simulation. Unfortunately, it is mostly known to practitioners and is not in the public domain. This is primarily because good nonlinear solution techniques (especially for the DC solution) are valuable and are not lightly shared from one company to the next.

Solving Differential Equations

The last task we face in constructing and understanding electrical level simulation is how to deal with elements with memory such as capacitors and inductors. For these problems we could write the tableau equations in the following general form

$$F\left(\dot{x}, x, T\right) = 0 \quad x\left(0\right) = X_0 \text{ for } 0 \le t \le T$$

This is known as an initial value problem and has no closed form solution in general.

In attempting to solve this problem we will find approximate solutions at a finite set of points over the time interval of interest

$$t_0 = 0, t_N = T, t_{n+1} = t_n + h_{n+1} \quad n = 0, 1, \ldots, N$$

The h_{n+1} are called *time steps* and their values are called **step sizes.** At each point, t_n, we are going to compute an approximation, x_n, to the exact solution, $x(t_n)$.

A large number of methods are available for solving this problem. The class of methods known as **linear multistep methods** are the ones most widely used in circuit simulation programs and we shall concentrate on this class. For sake of simplicity we will first examine these methods in terms of general, first-order, ordinary scalar differential equations of the form

$$\dot{y} = f\left(y, t\right)$$

A linear multistep method is a numerical method that computes y_{n+1} based on the values of y and $\dot{y}$ at the previous p + 1 time points. Specifically,

$$y_{n+1} = \sum_{i=0}^{p} a_i y_{n-i} + \sum_{i=-1}^{p} h_{n-1} b_i \dot{y}_{n-1}$$

or written using the definition of $\dot{y}$ we have

$$y_{n+1} = \sum_{i=0}^{p} a_i y_{n-1} + \sum_{i=-1}^{p} h_{n-i} b_i f\left(y_{n-i}, t_{n-i}\right)$$

A simple example of a multistep method is the forward Euler method (FE) which is given by

$$y_{n+1} = y_n + h_{n+1} \dot{y}_n$$

Where $p = 0$, $a_0 = 1$, $b_0 = 1$ and all other coefficients are zero. This method can also be considered as a Taylor series expansion about t_n truncated at its first term.

Other well-known multistep methods with $p = 0$, also called single-step methods, are

$$\text{Backward Euler } \left(\text{BE}\right) \quad y_{n+1} = y_n + h_{n+1} \dot{y}_{n+1}$$

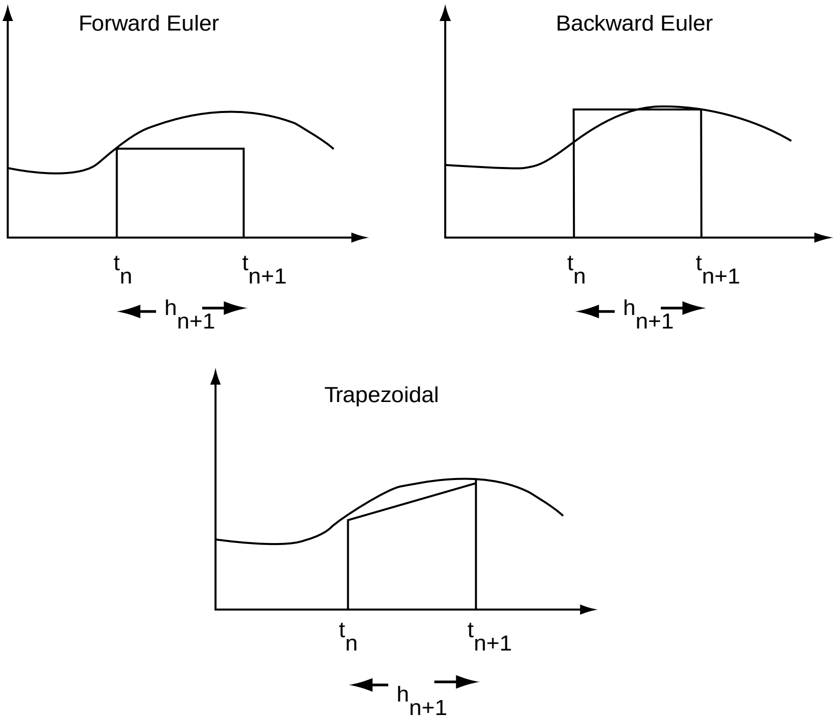

FIGURE 8.54 Geometrical interpretation of integration methods.

and

$$\text{Trapezoidal}\left(\text{TR}\right)\quad y_{n+1} = y_n = \left(\frac{h_{n+1}}{2}\right)\left(\dot{y}_{n+1} + \dot{y}_n\right)$$

Each of these three methods has a simple interpretation. First, note that the solution we are calculating is really the integral of $\dot{y}$. So that if we plot $f(y, t)$ and then look at estimating the area under the curve between t_n and t_{n+1} we generate a simple graphical interpretation of the methods given in Fig. 8.54.

Truncation Error for Linear Multistep Methods

A major concern in solving systems of differential equations is the accuracy of the computed solution. In particular, what is the difference between the computed solution at t_n, y_n, and the exact solution, $y(t_n)$? This particular type of error is known as the **truncation error.**

There are two types of truncation error, local and global. Local truncation error (LTE) of a method at t_{n+1} is the difference between the computed value y_{n+1} and the exact value, $y(t_{n+1})$ *assuming that no previous error has been made,* that is, that

$$y\left(t_i\right) = y_i, \quad i = 0, 1, 2, \ldots, n$$

Stability of Linear Multistep Methods

In order to study the global behavior of multistep methods we must examine how any errors made accumulate. This allows us to gain an understanding of the global truncation error. This type of study addresses the **stability** of the method.

To illustrate that there might be a problem consider the differential equation

$$\dot{y} = -y, \quad y(0) = 1$$

If we apply FE to this equation with step size $h = 1$, we generate the sequence

$$0,\ 0,\ 0,\ \ldots$$

Although not a very accurate answer for the beginning, at least it does not blow up and, indeed, the difference between this sequence and the correct answer goes to zero as time increases. However, if we apply FE with a step size of $h = 3$, we generate the sequence

$$-2,\ 4,\ -8,\ 16,\ -32,\ \ldots$$

which shows a growing oscillation. So whatever error is being made in the calculation accumulates in a disastrous manner.

Applying BE to the same equation with $h = 3$ yields a well-behaved sequence.

Stiff Systems

Especially for microwave and millimeter wave circuits, it is important to include parasitic elements for an accurate model. These parasitics are modeled as very small capacitors and inductors. This results in a system of equations that have very widely separated time constants. This type of system is said to be **stiff.**

The solution of stiff systems poses some severe problems. For example, consider

$$\dot{y} = -\lambda_1\big(y - s(t)\big) + ds/dt, \quad y(0) = y_0$$

where $s(t) = 1 - e^{-\lambda^2 t}$. The exact solution is

$$y(t) = y_0 e^{-\lambda_1 t} + \left(1 - e^{-\lambda_2 t}\right)$$

and is shown in Fig. 8.55.

Suppose that λ_1 and λ_2 are widely separated, with, for example, $\lambda_1 = 10^6$ and $\lambda_2 = 1$ yielding a stiff system. For a good picture of the waveform we have to integrate at least 5 s. But note that the first exponential waveform dies out in 5 µs.

We now are faced with a dilemma: to get an accurate solution of the fast waveform we need a small time step and to have an efficient simulation of the slow waveform we need a large time step. The obvious solution is to use a variable time step, small at the beginning of the simulation and large at the end.

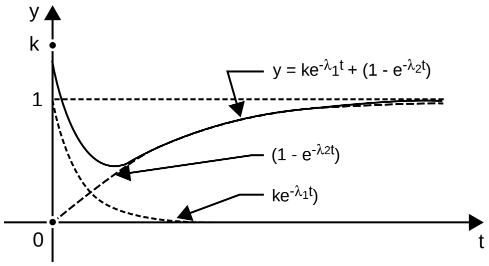

FIGURE 8.55 Exact solution to stiff system.

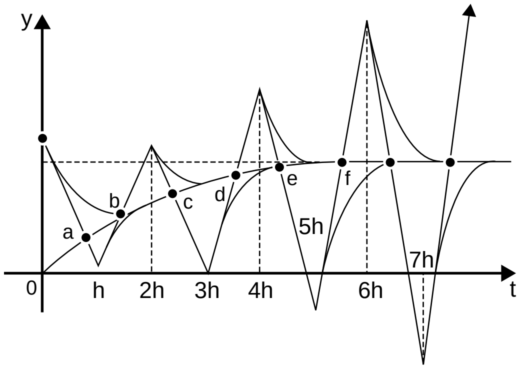

FIGURE 8.56 Numerical instability in FE applied to stiff system.

However, varying the time step changes the analysis of the regions of stability of the linear multistep methods (recall that we assume a constant step size in our analysis). If we apply the FE method to the previous example with an initial step size of 10^{-6} and after five steps we change to a step size of 10^{-4}, the behavior shown in Fig. 8.56 is obtained.

It turns out that the region of absolute stability for FE can be found by looking at the fastest time constant. In Fig. 8.56 y_{n+1} computed by FE is based upon the first derivative of the solution *passing through* y_n. If y_n is not very close to the exact solution, then FE picks up a spurious fast transient which causes instability if h is not chosen small enough.

Thus we see that

- The analysis of stiff systems requires variable time step.
- Not all linear multistep methods can be efficiently used to integrate stiff equations.

Clearly, to be useful for stiff systems the integration methods have to have a region of absolute stability which allows for a large step size for large time constants without being constrained by the small time constants. Thus *A*-stable methods are fine (remember that FE is not *A*-stable).

Time Step Control for Multistep Methods

Now that we know that the time step must be changed for efficiency and we are aware of the importance of different orders of integration schemes, how can we control these in a circuit simulator?

If we let E_{n+1} be a bound on the absolute value of the LTE at t_{n+1}, we know for a multistep method of order k that

$$\left|LTE_{n+1}\right| = \left|\left[C_{k+1}h_{n+1}^{k+1}\big/(k+1)!\right]y^{(k+1)}\left(t_{n+1}\right)\right|$$

Thus we must have

$$h_{n+1} \le \left|\frac{(k+1)!\,E_{n+1}}{C_{k+1}h^{(k+1)}\left(t_{n+1}\right)}\right|^{\frac{1}{k+1}}$$

in order to meet the error requirement. Since the $(k+1)^{st}$ derivative of y is not available we will have to form some approximation of it.

The scheme used in SPICE is the method of *divided differences* (DD). The DD are defined recursively as

$$\mathrm{DD}_1\left(t_{n+1}\right)=\frac{y_{n+1}-y_n}{h_{n+1}}$$

$$\mathrm{DD}_2\left(t_{n+1}\right)=\frac{\mathrm{DD}_1\left(t_{n+1}\right)-\mathrm{DD}_1\left(t_n\right)}{h_{n+1}-h_n}$$

$$\vdots$$

$$\mathrm{DD}_{k+1}\left(t_{n+1}\right)=\frac{\mathrm{DD}_k\left(t_{n+1}\right)-\mathrm{DD}_k\left(t_n\right)}{\sum_{i=-1}^{k-1}h_{n-1}}$$

It is relatively easy to show that

$$y^{(k+1)}\left(t_{n+1}\right)\cong\left(k+1\right)!\mathrm{DD}_{k+1}\left(t_{n+1}\right)$$

Thus we have an algorithm for time step control.

Given a step h_{n+1}, y_{n+1} is computed according to the method chosen for integration. Then, y_{n+1} and h_{n+1} are used to compute $\mathrm{DD}_{k+1}(t_{n+1})$ and h_{n+1} is checked using

$$h_{n+1}\le\left[\frac{E_{n+1}}{C_{k+1}\mathrm{DD}_{k+1}\left(t_{n+1}\right)}\right]^{\frac{1}{k+1}}$$

If h_{n+1} satisfies the test, it is accepted: otherwise it is rejected and a new h_{n+1} given by the right-hand side is used.

After h_{n+1} is accepted h_{n+2} must be chosen. A common strategy is to use the right-hand side of the error checking equation as the new step size.

An important factor in the selection of the step size is the choice of E_{n+1}. In general, a circuit designer has a rough idea of the precision that is required in the simulation. This is generally related to the GTE and not the LTE. Thus a mechanism to transfer the GTE estimate to the LTE is required.

It is often assumed that the LTE accumulates linearly thus giving the following estimate

$$\left|\mathrm{GTE}_{n+1}\right|\le\sum_{i=1}^{n+1}\left|\mathrm{LTE}_i\right|$$

This is quite conservative in practice and so E_{n+1} is often obtained from

$$E_{n+1}=\varepsilon_u h_{n+1}$$

where ε_u is the maximum allowed error per unit step.

There is a large practice, theory, and lore about the choice of step size and integration method. To construct a useful, efficient, and robust circuit simulation package this information must be tapped and utilized. The interested reader is referred to the literature for further information.

Techniques for Large Circuits

The techniques that we have been discussing are used in most standard time-domain circuit simulation, e.g., SPICE in all its various forms. Although very common, these techniques have limitations when solving very large circuits. We have indicated that circuit size may vary from one transistor with matching elements to several hundred or even thousands for high levels of radio and system integration. When very large circuits must be simulated special techniques must be used.

There are three types of specialized techniques that have been used: techniques for partitioning large circuits into smaller ones and combining the solutions, techniques that exploit special characteristics of certain classes of circuits (see the next section), and techniques that utilize parallel and vector high-speed computers.

All of these techniques are beyond the scope of this chapter. However, the reader is referred to the references for further information.

Defining Terms

Associated reference directions: A method of assigning the current and voltage directions to an electrical element so that a positive current-voltage product always means that the element is absorbing power from the network and a negative product always means that the element is delivering power to the network. This method of assigning directions is used in most circuit simulation programs.

Branch relation: The relationship between voltage and current for electrical components. Common branch relations are Ohm's law and the lumped equations for capacitors and inductors. More complex branch relationships would be transistor models.

CAD: Computer-aided design for the electronics industry is concerned with producing new algorithms/programs that aid the designer in the complex tasks associated with designing and building an integrated circuit. There are many subfields of electrical CAD: simulation, synthesis, physical design, testing, packaging, and semiconductor process support.

Circuit simulation: Constructing a mathematical model of an electrical circuit and then solving that model to find the behavior of the model. Since the model usually cannot be solved in closed form, the equations are evaluated for a specific set of input conditions to produce a sequence of voltages and currents that approximates the true solution.

Fill-in: When solving a set of sparse linear equations using Gaussian elimination it is possible for a zero location to become nonzero. This new nonzero is termed a fill-in.

Gaussian elimination: The standard direct method for solving a set of linear equations. It is termed direct because it does not involve iterative solutions. Variations of this scheme are used in most circuit simulators.

KVL, KCL: Kirchhoff voltage and current laws provide the basic physical constraints on voltage and current in an electrical circuit.

Linear multistep method: This is a class of techniques for solving ordinary differential equations that is widely used in circuit simulators.

Modified nodal formulation: A modification of the classical nodal formulation that allows any network to be described. The modification consists of adding extra equations and unknowns when an element not normally modeled in classical nodal analysis is encountered.

Newton-Raphson: A numerical method for finding the solution to a set of simultaneous nonlinear equations. Variations of this method are commonly used in circuit simulation programs.

Pivoting: When applying Gaussian elimination to solve a set of simultaneous linear equations the natural solution order is sometimes varied. The process of varying the natural solution order is termed pivoting. Pivoting is used to avoid fill-in and to maintain the accuracy of a solution.

Sparse equations: When a set of linear simultaneous equations has very few nonzeros in any row the system is said to be sparse. Normally for a system to be considered sparse less than 10% of the possible entries should be nonzero. For large integrated circuits less than 1% of the possible entries are nonzero.

SPICE: The most widely used circuit simulation program. Originally developed at the University of California, Berkeley, this program is available from several commercial sources. SPICE is an acronym for Simulation Program with Integrated Circuit Emphasis.

Stability: In the context of circuit simulation the main stability concern is in the solution of differential equations. Specifically, if small errors made by the integration methods — such as a linear multistep method — are amplified as the solution progresses, the integration method is exhibiting unstable behavior. Controlling the step size is one of the primary mechanisms for maintaining stability.

Step size: When solving for the transient behavior of an electrical circuit the associated differential equations are solved at specific points in time. The difference between two adjacent solution time points is known as the step size.

Stiff system: When an electrical circuit has widely separated time constants the circuit is said to be stiff. The system of equations associated with the circuit is known as a stiff system and special numerical methods must be used to maintain stability and accuracy when simulating a stiff system.

Tableau formulation: A method for formulating the equations governing the behavior of electrical networks. The tableau method simply groups the KVL, KCL, and branch relationships into one huge set of equations.

Truncation error: When numerically solving the differential equations associated with electrical circuits, approximation techniques are used. The errors associated with the use of these methods are termed truncation error. Controlling the local and global truncation error is an important part of a circuit simulator's task. Limits on these errors are often given by the user of the program.

References

W. Banzhaf, *Computer-Aided Circuit Analysis Using PSpice,* Englewood Cliffs, N.J.: Prentice-Hall, 1992.

R. E. Bryant, A survey of switch-level algorithms, *IEEE Design and Test of Computers,* 4, 4, 26–40, 1987.

L. O. Chua and P.-M. Lin, *Computer-Aided Analysis of Electronic Circuits: Algorithms and Computational Techniques,* Englewood Cliffs, N.J.: Prentice-Hall, 1975.

S. W. Director, *Circuit Theory: A Computational Approach,* New York: John Wiley & Sons, 1975.

G. F. Forsythe, M. A. Malcom, and C. B. Moler, *Computer Methods for Mathematical Computations,* Englewood Cliffs, N.J.: Prentice-Hall, 1977.

G. D. Hachtel, R. K. Brayton, and F. G. Gustavson, The sparse tableau approach to network analysis and design, *IEEE Trans. Circuit Theory,* CT-18, 1, 101–113, 1971.

C. H. Ho, A. E. Ruehli, and P. A. Brennan, The modified nodal approach to network analysis, *IEEE Trans. Circuits and Systems,* CAS-22, 6, 504–509, 1975.

A. Jennings, *Matrix Computation for Engineers and Scientists,* New York: John Wiley & Sons, 1977.

J. D. Lambert, *Computational Methods in Ordinary Differential Equations,* New York: John Wiley & Sons, 1973.

J. M. Ortega and W. C. Rheinboldt, *Iterative Solutions of Nonlinear Equations in Several Variables,* New York: Academic Press, 1970.

V. B. Rao, D. V. Overhauser, T. N. Trick, and I. B. Hajj, *Switch-Level Timing Simulation of MOS VLSI Circuits,* Dordrecht, Netherlands: Kluwer Academic Publishers, 1989.

R. A. Saleh and A. R. Newton, *Mixed-Mode Simulation,* Dordrecht, Netherlands: Kluwer Academic Publishers, 1990.

A. F. Schwarz, *Computer-Aided Design of Microelectronic Circuits and Systems* (two volumes), New York: Academic Press, 1987.

R. Spence and J. P. Burgess, *Circuit Analysis by Computer — From Algorithms to Package,* Englewood Cliffs, N.J.: Prentice-Hall, 1986.

J. Vlach and K. Singhal, *Computer Methods for Circuit Analysis and Design,* New York: Van Nostrand Reinhold, 1983.

Further Information

Simulation of circuits at all levels of abstraction is an active research area. The interested reader is encouraged to examine the *IEEE Transactions on Computer-Aided Design*, the *IEEE Transactions on Circuits and Systems*, and the *IEEE Transactions on Computers*. In addition to journal articles there are a number of conferences held each year at which the latest results on circuit simulation are presented. The proceedings of the following conferences have a wealth of information on circuit simulation developments: *Proceedings of the Design Automation Conference (DAC), Proceedings of the International Conference on Computer-Aided Design (ICCAD), Proceeding of the International Conference on Computer Design (ICCD), Proceedings of the European Design Automation Conference (EDAC),* and the *Proceedings of Euro-DAC*. Finally, there are a large number of numerical analysis, computer science, and applied mathematics conferences and journals in which results related to circuit simulation are published.

8.6 Computer Aided Design of Microwave Circuitry

Ron Kielmeyer

The growth of personal communication and Internet industries along with the need for portability has resulted in an ever-increasing demand for low cost, high volume microwave circuitry. The commercialization of GaAs wafer processing and the simultaneous reduction in the physical size of silicon devices has enable the development of complex microwave circuitry which can no longer be designed without the aid of sophisticated CAD circuit simulators. This article will discuss the typical steps involved in a design cycle, some basic requirements for a CAD program, a look at the theory behind the most popular CAD programs in use today, and some emerging CAD technologies.

Initial Design

The design cycle shown in Fig. 8.57 starts with a circuit and/or system function such as an amplifier, a mixer, or a whole receiver along with appropriate specifications for that function. Then active devices such as transistors or diodes, if required to achieve the function, are chosen. Circuit topologies may be explored simultaneously with device selection. With these active devices will come a computer representation for the device, usually from the device vendor. This computer representation is in the form of a mathematical model or measured S-parameters.

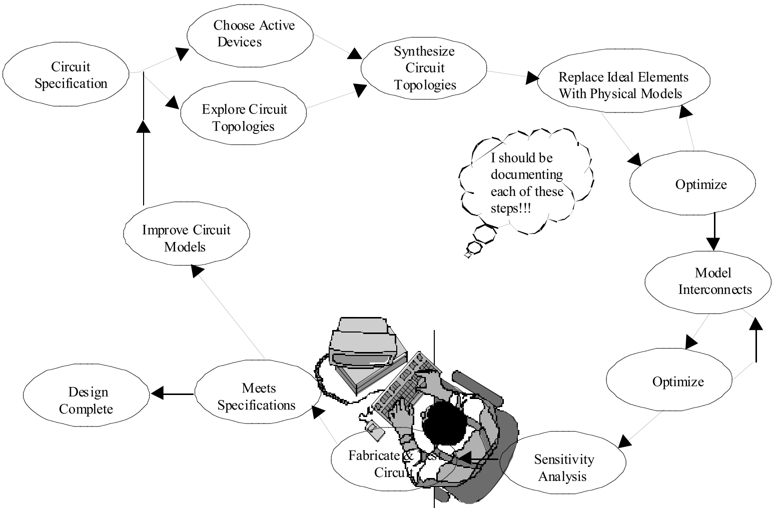

FIGURE 8.57 The design cycle.

Synthesis programs, if available, are used to determine the best possible performance. Many different topologies can be explored or identified as possible candidates for realizing the function. The ideal topologies generated by the synthesis program must exceed the design specifications since performance will only deteriorate from the idealized case.

Physical Element Models

Ideal elements must be replaced by models of the physical devices. These models are typically sub-circuits made up of ideal elements. For example, an ideal capacitor, physically realized by a chip capacitor, must have a model that can account for the finite inductance of the terminals and the finite resistive loss inherent in the physical device. For example, Fig. 8.58 shows a model for a physical capacitor mounted on a printed circuit board. In this model, C is the desired or ideal capacitance while Cpad represents the shunt capacitance of the metal pads on the circuit board to which the capacitor is soldered. Rs and Ls take into account the inductance and conductivity of the metal plates that form the capacitance. Rpar and Cpar account for the parallel resonant characteristics of the capacitor. It is common to refer to the extra elements Rs, Rpar, Cpar, Cpad, and Ls as "parasitic" elements. By replacing the ideal elements with nonideal models one at a time, the designer can accomplish two important practicalities. First, the sensitivity of the circuit to the nonideal element can be evaluated. Second, an optimization step can be performed on the remaining ideal elements in order to bring the circuit back within the design specifications. The actual value of the nonideal elements can also be optimized as long as the resulting optimized values do not change significantly from the pre-optimized values.

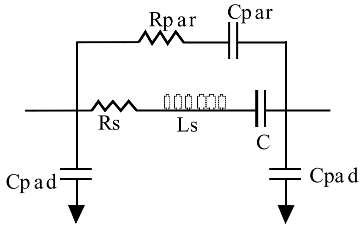

FIGURE 8.58 Physical model of a chip capacitor.

Layout Effects

As the process of replacing the idealized elements continues, the physical layout of the circuit must be introduced into the analysis. Two physical elements cannot be connected with zero length metal patterns. How close the elements can be placed is usually determined by how close the manufacturing process can place them. The metal patterns used to interconnect the physical devices must be introduced in the form of transmission lines and/or transmission line junctions. Figure 8.59 illustrates a simple PI resistive attenuator as might be realized using MMIC or MIC technology. The metal interconnects are modeled as a microstrip transmission line, followed by a Tee junction model. The resistors in this model are modeled as ideal resistors. The ground vias are represented as inductors. As each of these physical effects are introduced, an optimization step is performed in an attempt to meet or exceed the design specifications.

Sensitivity to Process Variation

After transforming many possible design topologies, sensitivity of the circuit to the nonideal or parasitic elements of the circuits as well as to the actual element values must be determined. One measure of the sensitivity of a circuit is the percent yield. To determine the percent yield of a circuit, the element values, parasitic elements, and/or known physical tolerances are treated as independent random variables. A range for each random variable is given and the computer analysis program iterates through random samples of the variables with their given ranges. This process is called a Monte Carlo analysis. The ideal outcome of the Monte Carlo analysis would be that the circuit passes all specifications under any combination of the random variable values. The percent yield can be improved by performing an optimization on the circuit. The optimization includes the ranges assigned to the random variables in the analysis. At each step in the optimization process, the mean values of the random variables are varied. The end result is an overall increase in the percent yield.

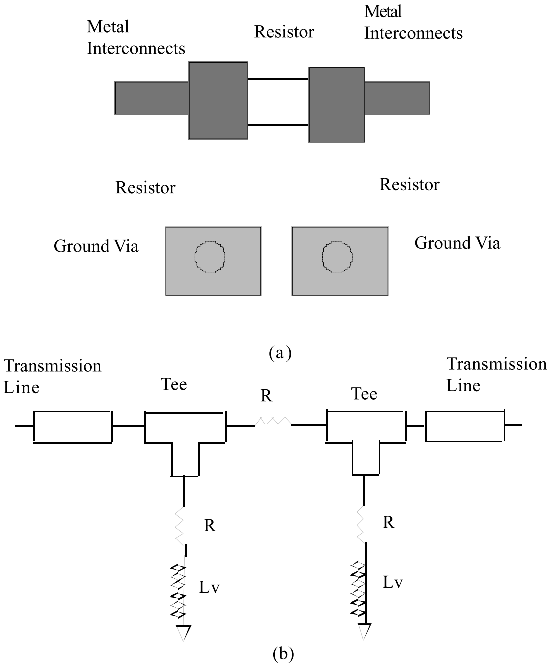

FIGURE 8.59 Simple PI pad resistive attenuator; (a) physical layout, (b) CAD model.

Design of Experiments (DOE) is another way to measure the sensitivity of the circuit to the random variables. In performing the DOE, each of the random variable values are independently incremented from their mean values. The computer keeps track of the analyzed responses and does the tedious bookkeeping task of incrementing all of the variables. Once this process is complete, statistical techniques are used to determine the sensitivity of each of the random variables to each of the specifications.

Design Tool Requirements

There are certain features that a microwave CAD tool must have in order to improve the productivity of the microwave designer. The most important is that it must be accurate. Once a circuit has been simulated, it must be fabricated and tested against the specifications for that circuit. If the computer simulation is inaccurate, the reasons for this must be determined. The fabrication of the circuit and the debugging of the circuit are by far the most time consuming part of the design cycle. Therefore, the goal of any CAD design is to model the circuit so that only one fabrication cycle needs to be implemented.

Inaccurate simulations that are tool dependent can result from numerical difficulties, model inaccuracies, or a lack of acceptable models. Inaccurate simulations that are directly caused by the user usually result from failure to model the circuit correctly or the misuse of models by using them outside the range for which they are valid. The designer has little control over the numerical problems. In some cases, the designer can overcome model accuracy by knowing the limitations of the models being used and if possible compensating for them. However, since model accuracy and availability usually are the features that distinguish one program from the other, companies tend to treat the models as proprietary and therefore do not want to release information about the models and how they are implemented. This can be a great disadvantage since the designer has no way of knowing how the model is implemented and when the range of validity for the model has been exceeded.

Programs usually provide a way to implement custom models. For example, many programs will allow the user to import S-parameter data files to represent a part of the circuit that cannot be accurately represented by standard transmission line discontinuity models. These S-parameter files can be generated from a measurement of the actual discontinuity. Likewise, active device S-parameters can be measured

TABLE 8.6 Summary of Desirable CAD Features

Analysis Features	Synthesis Features	User Interface Features
Accurate models	Filter/impedance matching	Schematic input
Optimization	Constant noise circles	Text and graphical output
Import/export data	Constant gain circles	Easy documentation
Robust model library	Stability circles	Drawing complex shapes

at a specific bias point and imported for use in the design process. Measured data is usually limited to two-port networks since multiport network analyzers are not typically available to the designer. For multiport passive networks, electromagnetic simulators are often used to create data file representations of the passive network. In some cases, programs will allow the designer access to the code or hooks into the code that can be used to implement custom models.

Ease of use is a program feature that can greatly increase the productivity of a designer. Early implementations of circuit analysis programs used a descriptive language called a netlist to describe the circuit to be analyzed. Most modern programs however, use a graphical interface to create a schematic representation of the circuit. Schematics are much easier to create and are less prone to error than netlists. For electromagnetic simulators, a drawing package is used to draw the geometric shapes. These drawing packages, at a minimum, must provide a means to implement complex, difficult-to-draw structures from basic shapes that are easy for a designer to draw. In addition to this, the ability to change dimensions without the need to redraw the shape can greatly decrease the time it takes to perform tolerance studies or to modify the structure in order to meet the desired performance criteria.

Because microwave circuit performance specifications can be both time and frequency domain quantities, the circuit analysis program must provide an easy means to display the resulting data in both the time and frequency domains. The program must also be able to export the results into standard text or graphic formats for importation into word processors or view cell generating programs for documentation and presentation purposes.

Electromagnetic simulators need to be able to display field quantities such as current density on the conductors, E and H field intensity and direction, as well as outputting S, Z, or Y parameters for importation into circuit simulators. Data must be displayed in either graphical or text format.

Synthesis programs are available that provide impedance matching network topologies for amplifier/mixer design and filter response functions. These programs could be simple spreadsheet implementations of well-known design equations, an electronic Smith chart, or sophisticated implementations of impedance matching theory or filter design. The most sophisticated programs can provide networks based on both ideal and nonideal elements. The ability to display constant gain, noise circles, and stability circles can also be considered part of the synthesis capability since these are often used to determine the matching network impedances [1].

Time Domain vs. Frequency Domain Simulation

A circuit can be analyzed in either the frequency domain or the time domain. SPICE is a program developed at the University of California at Berkeley that analyzes a circuit in the time domain. Harmonic balance programs solve the circuit equations partially in the frequency domain and partially in the time domain. The choice of which program is used depends on the parameters that are specified. Since SPICE does the computations in the time domain, it is quite naturally used when the design parameters involve time-dependent quantities. SPICE is used for transient parameters such as the turn-on time of an oscillator or amplifier, the switching time of a switch, or perhaps the impulse response of a circuit. SPICE can also solve for the DC bias point of the circuit and then perform a small-signal, frequency domain analysis of the circuit about this bias point. By adding some special circuit elements to the file description, S-parameters can be computed from the results of this small-signal analysis. However, many SPICE based programs have added direct S-parameter output capability in order to accommodate the needs of microwave designers.

SPICE can be used to predict the effects of noise and distortion within the circuit. Using small-signal, frequency domain analysis, the linear noise parameters of a circuit can be predicted. However, the noise due to mixing effects of nonlinearities within the circuit can not be predicted. Likewise the up- or downconversion noise and phase noise of an oscillator are not analyzed. Distortion analysis using SPICE is usually performed through the use of a transient analysis followed by conversion of a part of the time waveform into the frequency domain using a Discrete Fourier Transform (DFT). The microwave designer is typically interested in two types of distortions — the harmonic content of the time waveform and the intermodulation products caused by the excitation of the circuit by two signals typically close to each other in frequency.

Harmonic balance is used when the circuit is driven by periodic sources and when the design parameters, input and output, are specified in the frequency domain. The assumed periodicity of the circuit response avoids the need to compute the circuit response from time zero until the steady-state response is obtained. Therefore, much less computer time is required to predict the circuit response. Since the harmonic balance techniques were developed specifically to aid the microwave designer in the design of nonlinear circuits, the available programs are custom tailored to provide the results in a format familiar to the designer. For example, the input source for an amplifier can be swept in both frequency and power, and nonlinear parameters such as gain, 1 db compression point, saturated power output, power-added efficiency, and harmonic levels can all be displayed in a graphical or text form. Indeed these parameters are all natural artifacts of the computations. Other parameters that can easily be computed are intermodulation products, third order intercept point, noise side bands, and mixer conversion.

The harmonic balance method is a hybrid of the small-signal, frequency domain analysis and a nonlinear time domain analysis. The circuit is divided into two subcircuits. One sub-circuit contains only those circuit elements that can be modeled in the small signal frequency domain. This sub-circuit results in a Y matrix representation that relates the frequency domain currents to the frequency domain voltages. At this point, the matrix can be reduced in size by eliminating voltages and currents for the nodes that are not connected to the nonlinear devices or the input and output nodes. These matrix computations need only be performed once for each frequency and harmonic frequency of interest. The second subcircuit includes all of the active or nonlinear elements that are modeled in the time domain. These circuit models relate the instantaneous branch currents to the instantaneous voltages across the device nodes. These models are the same models used in SPICE programs.

The two sub-circuits make up two systems of equations having equal node voltages whose branch currents must obey Kirchhoff's current law. The system of equations corresponding to the linear sub-circuit is now solved by making an initial guess at the frequency spectrum of the node voltages. The node voltage frequency spectrum is then used to solve for the frequency spectrum of the branch currents of the linear sub-circuit. In addition to this, the node voltage frequency spectrum is transformed into the time domain using a FFT algorithm. The result of this operation is a sampling of the periodic time voltage waveform. The sample voltages are applied to the time domain sub-circuit resulting in time domain current waveforms, which are then transformed into the frequency domain again using a FFT algorithm. The two frequency domain current spectrums are compared, and based on the error between them, the voltage spectrums are updated. This process is repeated until the error is sufficiently small.

Early implementations of harmonic balance programs used either an optimization routine to solve for the node voltage spectrums [2] or Newton's method [3]. The main advantage of Newton's method is that it uses the derivatives of the nonlinear device currents with respect to the node voltages to predict the next increment in the node voltages. By taking advantage of these derivatives, convergence can be achieved for a relatively large number of nonlinear devices. This method appears to work well as long as the nonlinearity of the system is not too severe.

Emerging Simulation Developments

Current research directed toward improving the implementation of harmonic balance programs is concentrating on techniques that can handle the large number of nonlinear devices typically found in integrated circuits. Currently, Krylov-subspace solutions have been implemented [4]. When Krylov subspace techniques are used, the harmonic balance method can be used to solve circuit problems containing hundreds of transistors.

When the excitation of a circuit consists of multiple sinusoids, closed spaced in frequency, both SPICE and conventional harmonic balance methods tax computer hardware resources as they require large amounts of memory and computer time. A program must be able to efficiently handle this type of excitation in order to be able to predict the effects of spectral reqrowth in digitally modulated circuits, as well as noise-power ratio simulations for these circuits. For these types of circuit analysis, the excitation consists of multiple sinusoids, closely spaced in frequency. Borich [5] has proposed a means of overcoming these problems for harmonic balance programs by adjusting the sampling rate and the spacing between excitation carriers in order to reduce the computations of the multitone distorted spectra to an efficient one-dimensional FFT operation.

Envelope following methods [6] have been implemented to solve for circuits in which the excitation consists of a high frequency carrier modulated by a much slower information signal. The method performs a transient analysis consistent with the time scales of the information signal. At each time step, a harmonic balance analysis is performed at the harmonic frequencies of the carrier. This method can be used to study PPL phase noise, oscillator turn-on time, and mixer spectral regrowth due to digital modulation on the RF carrier [7].

References

1. George D. Vendelin, *Design of Amplifiers & Oscillators by the S-Parameter Method.* John Wiley & Sons, New York, 1982.
2. M. Nakhla and J. Vlach, A Piecewise Harmonic Balance Technique for Determination of Periodic Response of Nonlinear Systems, *IEEE Transactions on Circuits and Systems,* CAS-23, 2, February 1976.
3. K. Kundert and A. Sangiovanni-Vincentelli, Simulation of Nonlinear Circuits in the Frequency Domain, *IEEE Transactions Computer-Aided Design,* CAD-5, 4, October 1986.
4. R. Telichevesky, K. Kundert, I. Elfadel, and J. White, Fast Simulation Algorithms for RF Circuits, IEEE 1996 Custom Integrated Circuits Conference.
5. V. Borich, J. East, and G. Haddad. An Efficient Fourier Transform Algorithm for Multitone Harmonic Balance, *IEEE Transactions Microwave Theory and Techniques,* 47, 2, February 1999.
6. P. Feldmann and J. Roychowdhury, Computation of Circuit Waveform Envelopes Using an Efficient, Matrix-Decomposed Harmonic Balance Algorithm, in *Proc. IC-CAD,* November 1996.
7. K. Mayaram, D.C. Lee, S. Moinian, D. Rich, and J. Roychowdhury, Overview of Computer-Aided Analysis Tools for RFIC Simulation: Algorithms, Features, and Limitations, IEEE 1997 Custom Integrated Circuits Conference.

8.7 Nonlinear Transistor Modeling for Circuit Simulation

Walter R. Curtice

Modeling in General

By definition, a transistor model is a simplified representation of the physical entity, constructed to enable analysis to be made in a relatively simple manner. It follows that models, although useful, may be wrong or inaccurate for some application. Designers must learn the useful range of application for each model.

It is interesting to note that all transistors are fundamentally nonlinear. That is, under any bias condition, one can always measure harmonic output power or intermodulation products at any input RF power level, as long as the power is above the noise threshold of the measurement equipment. In that sense, the nonlinear model is more physical than the linear model.

The purpose of this work is give a tutorial presentation of nonlinear transistor modeling. After reviewing the types of models, we will concentrate on equivalent circuit models, of the type used in

SPICE.[1] Recent improvements in models will be described and the modeling of temperature effects and the effects of traps will be discussed. Finally, parameter extraction and model verification is described.

Two-Dimensional Models

The models constructed for describing the nonlinear behavior of transistors fall into several distinctly different categories, as depicted in Table 8.7. The most complex is the "physics-based" model. Here electron and hole transport is described by fundamental transport and current continuity relationships and the physical geometry may be described in one-, two-, or even three-dimensional space. The electric field is found by solution of Poisson's equation consistent with the distribution of charge and boundary conditions. Such a model may use macro-physics, such as drift-diffusion equations,[2-4] or more detailed descriptions, such as a particle-mesh model with scattering implemented using Monte-Carlo methods.[5,6] Two- and three-dimensional models must be used if geometrical effects are to be included. The matter of how much detail to put into the model is often decided by the time it takes for the available computer to run a useful simulation using the model. In fact, as computers have increased their speed, modelers have increased the complexity of the model simulated.

TABLE 8.7 Types of Large-Signal Transistor Models

I. Physical or "Physics-Based" Device Models
II. Measurement-Based Models
    1 - Anaytical Models, such as SPICE Models
    2 - Black Box Models
        Table-Based Models
        Artificial Neural Network (ANN) Models

The lengthy execution time required for Monte-Carlo analysis can be reduced by using electron temperature[7] as a measure of electron energy. Electron temperature is determined by the standard deviation of the energy distribution function and is well defined in the case of the displaced Maxwellian distribution function. Electron and hole transport coefficients are developed as a function of electron temperature, and nonequilibrium effects, such as velocity overshoot in GaAs, may be simulated in a more efficient manner. However, the solution of Poisson's equation still require appreciable computational time.

BLAZE[8] is a good example of a commercial, physically-based device simulator that uses electron temperature models. BLAZE is efficient enough to model interaction of a device with simple circuits.

The physics-based model would be constructed with all known parameters and simulations of current control for DC and transient or RF operation, then compared with measured data. Using the data, some transport coefficients or physical parameters would be fine-tuned for best agreement between the model and the data. This is the process of calibration of the model.[9] After calibration, simulations can be trusted to be of good accuracy as long as the model is not asked to produce effects that are not part of its construction. That is, if trapping effects[10] have not been incorporated into the model, the model will disagree with data when such effects are important. With the physics-based model, as with all others, a range of validity must be established.

Present physics-based models still require too much computational time to be used to any extent in circuit design work. Optimization of a circuit design will involve invoking the device model frequently enough to be impractical with physics-based models. These models can be used if only one or two nonlinear transistors are used in a specific circuit, but typically, the circuit designer has a larger number of nonlinear devices.

Several quasi two-dimensional models[11,12] have been developed that execute more efficiently. Initial results look good, but accuracy may depend upon the simplifications made in the development of the code and will vary with the application.

Measurement-Based Models

The next general category is that of "measurements-based" models. These are empirical models either constructed using analytical equations and called "analytical models" or based upon a lookup table developed from the measured data. The latter are called "table-based" models. Multidimensional spline functions are used to fit the data in some of these models[13] and only the coefficients need be stored.

In the case of analytical models, the coefficients of the equations serve as fitting parameters to permit the equations to approximate the measured data. Functions are usually chosen with functional behavior similar to measured data so that the number of fitting parameters is reduced.

The advantages of analytical models are: computational efficiency, automatic data smoothing, accommodation of device statistics, physical insight, and the ability to be modified in a systematic manner. Disadvantages are: restriction of behavior often due to use of over-simplified expressions, difficulty in parameter extraction, and guaranteed nonphysical behavior in some operating condition. The nonphysical behavior is often associated with the use of a function, such as a polynomial, to fit data over a specific range of voltages and subsequent application of the model to voltages outside this range. The function may not behave well outside the fitting range. The best example of analytical models is the set of transistor models used in the various forms of the SPICE program. A major advantage of analytical models is that all the microwave nonlinear simulators provide some sort of user-defined model interface for analytical model insertion.

Table-based models have some properties of black-box models. The equations used result from fitting to the data, using splines, or other such functions. These models can therefore "learn" the behavior of the nonlinear device and are ideal for applications where the functional form of the behavior is unknown. Table-based models are efficient but do not provide the user with any insight, since there is a minimal "circuit model." They have difficulty incorporating dispersive effects, such as "parasitic gating" due to traps (see the section on Modeling the Effects Due to Traps) and do not accommodate self-heating effects.

The model cannot be accurately extrapolated into regions where data was not taken, and the models are often limited in their application due to the particular coding used by their author. This means that the model cannot be tailored by users other than the author. Customization of models is important to improve the "performance" of a model. The first table-based model that has been widely used is the Root model.[13]

Physical Parameter Models

One may argue that there is a class of models between physics-based and analytic models, namely, physical-parameter models. A good example would be the Gummel-Poon model.[14] Here, analytical equations are used but the fitting parameters or equation coefficients have physical significance. For example, NF, the ideality factor of the emitter-base junction, is one model parameter. This model is an analytical model but more useful device information may be gleaned from the value of the coefficients. This is often the case and the model is widely used for various forms of bipolar devices.

A useful physical parameter model for the AlGaAs/InGaAs/GaAs PHEMT has been published and verified by Daniel and Tayrani.[15] No information has been given on the range of validity of the analytical model, and it is expected that such a simple model will have inaccuracy when two-dimensional effects or nonequilibrium effects are important. It is interesting that the HEMT structure has less two-dimensional effects than the MESFET because of the sheet current layer produced in the HEMT.

There are many analytical models for which the coefficient has the name and dimensions of a physical parameter but the coefficient is only a fitting parameter and is not strongly related to the physical parameter. Khatibzadeh and Trew[16] have presented one commonly called the Trew model and Ladbrooke[17] has presented a second model commonly called the Ladbrooke model. Ladbrooke's model is an extension of the much earlier Lehovec and Zuleeg[18] model and it is more empirical than physical, as Bandler has shown.[19] Such models must be tested to see how strong the relationship is between the model parameter and the physical parameter. It is a matter of the degree of correlation between the two quantities. It is dangerous to attach too much physical significance to these coefficients. One should verify the relationship before doing so.

There is a unique case where physical parameters have been installed in a previously developed analytical model. The Statz-Pucel (analytical) GaAs MESFET model[20] has been converted to a physical parameter model by D'Agostino et al.[21]

Neural Network Modeling

Rather recently, a new approach has been developed for the modeling of nonlinear devices and networks. It utilizes artificial neural networks, or ANN. ANN models are similar to table-based or black-box models in that there is no assumption of particular analytical functions. As with table-based models, the ANN model "learns" the relationship between current and voltage from the data, and model currents are efficiently calculated after application of voltages. ANN analysis can treat linear or nonlinear operation of devices or complex circuits. ANN models have many of the advantages and deficiencies of table-based models. An excellent special issue of *RF and Microwave Computer-Aided Engineering*[22] has been devoted to this modeling method. Unfortunately, discussion of this approach is beyond the scope of this work.

Scope of This Work

The purpose of this work is to present a tutorial on the modeling of the nonlinear behavior of transistors. The scope is limited to nonlinear models useful for the development of circuit designs. It would not be possible to cover all the important material on other types of models, such as physical models, in this article. This paper will deal primarily with nonlinear analytical models for MESFETs, (P)HEMTs and HBTs. The emphasis is on GaAs device models, although many of these models are also used for transistors fabricated in InP, silicon, and other materials. The RF LDMOS power device is also discussed because it can be treated as a three-terminal device, much like a MESFET.

We address the concerns of analog and digital circuit designers who must choose between a wide variety of nonlinear models for transistors. Of particular concern here is the MMIC designer who must select the proper model to use for his GaAs microwave transistor. Even with very complex models presently supplied in circuit simulators, some specific behaviors are not modeled and new model features are required. We will spend much time on SPICE models and SPICE-type models. We will inspect some of the recent models that incorporate important device effects, omitted in previous models. We will discuss the modeling of gate charge as a function of local and remote voltages, the modeling of self-heating effects, the modeling of trapping effects, and model verification.

Unfortunately, the references presented will only be representative of prior work because there is a wealth of papers in each area of transistor modeling. I apologize to any author not included, as there are now and have been many people working in this area. I do recommend some modeling tutorial articles, previously published. Trew[23] and Snowden[24] and Dortu et al.[25] have presented excellent reviews of SPICE type transistor models and are recommended reading.

Equivalent Circuit Models

We concern ourselves here with equivalent circuit models because they are formulated to be efficiently exercised in a circuit simulator, and thus are efficient for circuit design and optimization. This is because the simulator is accustomed to dealing with resistors, capacitors, inductors, and voltage or current-controlled sources.

One problem is that "de facto" standard models have evolved in the industry, and often these models are inadequate to describe the device behavior. This is even true for small-signal equivalent-circuit models. Still, all circuit simulators utilize standard model topologies for small-signal and large-signal MESFET and PHEMT models. These models represent a minimum number of elements and are efficient for evaluation of transistor characteristics. Figures 8.60 and 8.61 show the conventional topologies for small-signal and large-signal simulation, respectively. It is conventional to separate the extrinsic parameters from the intrinsic device parameters, as shown in Fig. 8.60. The intrinsic parameters are assumed to contain all the bias-dependent behavior and the extrinsic parameters are assumed to be of constant values.

Curtice and Camisa[26] and Viakus[27] have discussed the trade-offs that exist between simple models with a small number of parameters, and complex models with a large number of parameters. A primary concern is the significant increase in the uncertainty for each model parameter in a complex model.

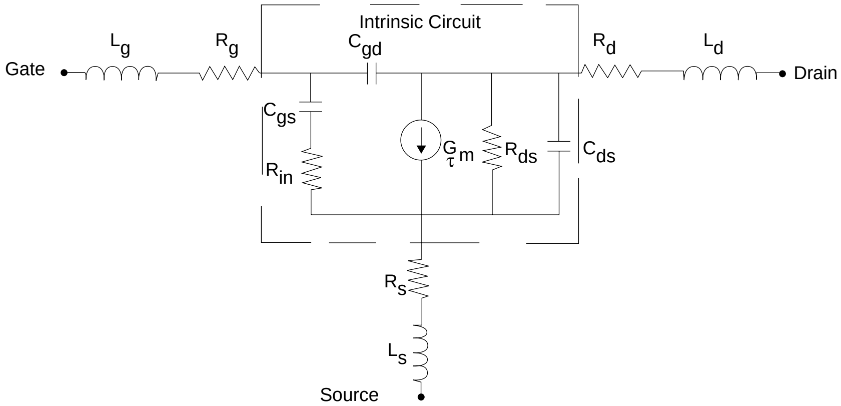

FIGURE 8.60 The conventional small-signal model for a MESFET, showing intrinsic and extrinsic elements.

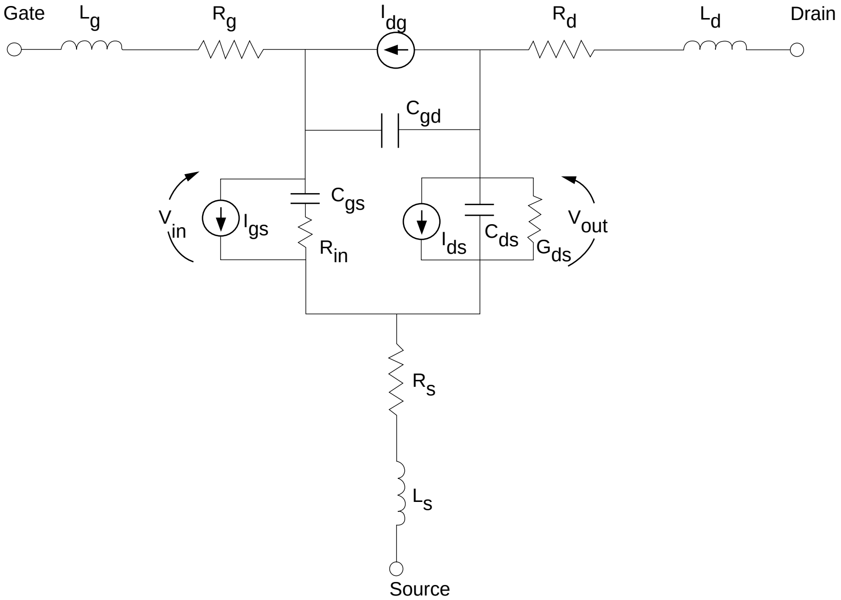

FIGURE 8.61 The conventional large-signal model for MESFET.

Viakus showed that a small increase in the number of elements in a small-signal model could easily increase the uncertainty of critical elements beyond the standard deviation of the element value resulting from the fabrication process.

Byun[28] and others assert that source resistance should be taken as bias dependent. This decision is actually a choice made by the modeler. If source and drain resistance are taken as constant, then the reference planes defining these resistances are taken as being close to the metal ohmic contacts and not too close to the Schottky contact. That is, no region that may become depleted of change is included. All bias-dependent behavior is then lumped into the intrinsic elements. This is the convention followed by most modelers. It results in a simpler model, with fewer parameters.

Unfortunately, many of the published nonlinear device models have inconsistencies with the conventional small-signal model. Some of the inconsistencies may go unnoticed but can cause design errors. A good example that will be described later is the modeling of capacitance as a function of two independent voltages. The small-signal model must contain "transcapacitance" elements to be consistent with the large-signal model.

The large-signal model should agree with the small-signal model, but is not expected to be as efficient. Because transconductance and some resistances and capacitances must be evaluated from functions of voltages, numerical evaluation will take more computational time. However, the behavior of the large-signal model will gracefully go from small-signal to large-signal in a good model.

SPICE Models and Application-Specific Models

SPICE was developed to help in the design of switching circuits. Thus, the SPICE transistor models were developed to model the time domain behavior of devices in such circuits. However, transistors operating in RF analog circuits have a different locus of operation. For example, a simple class A amplifier will have locus of operation around its quiescent bias point. This should be compared with a logic circuit where the transistors go from a biased-off condition (high voltage, low current) to a strongly turned on condition (low voltage, high current). If the same transistor is used in these two applications, one would expect the SPICE model would approximate both behaviors, but not be optimum for either. In fact, if the model is fine-tuned to be more accurate for one of these applications, it will by default, be less accurate for the other.

For these reasons, accurate nonlinear transistor models will be application specific. In order to make the model more general, the model can be made more complex and more model parameters will be added. This may result in poorer execution efficiency.

Clearly one goal of transistor modeling should be to keep the model simple and to keep the number of model parameters small so that the extraction of these parameters is more efficient. My experience is that designers like simple models for initial work and are willing to work with more complicated models for difficult design specifications. The SPICE transistor models serve the function of the initial, simple models. These models are also universally known by name and have history and familiarity associated with them. A designer attempting to use a new GaAs foundry would not be intimidated by obscure nonlinear models if SPICE transistor models are used in that foundry.

Many modelers have attempted to extend or enhance the SPICE models so that their accuracy is improved, particularly in microwave analog applications. Usually, the default model is the original SPICE model and the designer will feel comfortable with this approach. There are many examples. The Gummel-Poon BJT model has been extended by Samelis and Pavlidis[29] and others[30] for application to heterojunction bipolar devices. The JFET SPICE model was extended by Curtice[31] in 1980 for better application to GaAs MESFET logic circuits.

Because of the increasing use of harmonic-balance simulators for microwave applications, many new equivalent circuit models have been developed specifically for these simulators. Nevertheless, these models are "SPICE-type" models, and can also be executed in a time domain simulation. The requirements of a model for SPICE are the same as for harmonic balance since the device is operated in the time domain in both simulators.

The producers of commercial harmonic balance (HB) software recognized the need of users to customize their transistor models. All commercial packages now contain user-defined modeling interfaces that permit the installation of customized models into the transistor model library. The process of installing or customizing a model in SPICE is much more difficult and not available to the average user. However, the ease of installation of models into HB software has produced a rash of new models for many transistor types.

Table 8.8 shows the typical array of SPICE equivalent circuit models available as part of a commercial simulator software package. The models are categorized, in general, as diode models, GaAs MESFET or (P)HEMT models, MOS models, and bipolar device models. The list is not complete for any specific product but representative of the models available. The models listed in Table 8.8 are in most commercial simulator products whether a version of SPICE or a harmonic balance simulator.

TABLE 8.8 SPICE Models

GaAs MESFET/HEMT	MOS Models
Curtice (Cubic and quadratic)	BSIM 1,2,3 3v3
STATZ (Raytheon)	UC Berkeley 2 and 3
JFET (N & P)	HSPICE
TOM (TriQuint's Own Model)	MOSFET (various levels)
Materka	
Diode Models	**BJT Models**
P/N diode	Gummel-Poon
PIN diode	METRAM
	VBIC

Improved Transistor Models for Circuit Simulation

Early SPICE models have shown a number of deficiencies. One problem is that the models developed before 1980 were developed for silicon devices and they do not reflect the behavior of GaAs devices. Most SPICE models need to be customized to be accurate enough for present design requirements. With regard to GaAs MESFET and PHEMT modeling, the strong dependency of gate-source capacitance upon drain-source voltage as well as gate-source voltage is not modeled in the early SPICE models. None of the standard SPICE models accommodate self-heating effects. These effects are more important in GaAs applications due to the poorer thermal conductivity of GaAs compared to silicon. Some GaAs transistors exhibit important dispersion effects in transconductance as well as in drain admittance. All the GaAs models in Table 8.8 were added during the 1980s. These models represented major improvements; however, deficiencies remain. These deficiencies are summarized below for SPICE large-signal models:

- Insufficient accuracy for GaAs applications.
- Poor modeling of nonlinear capacitance.
- Poor modeling of self-heating effects.
- No modeling of dispersion of transconductance.
- Model parameter extraction not defined.
- Poor modeling of nonlinear effects dependent upon higher order derivatives.

The improved large-signal models of the 1990s exhibit some common features. It is quite popular to utilize analytical functions that have an infinite number of derivatives. For example, in the modeling of PHEMTs, Angelov et al.[32] have relied heavily on the hyperbolic tangent function for current because its derivative with respect to gate-source voltage is a bell-shaped curve, much like transconductance in PHEMTs. All further derivatives also exit. The Parker[33] model also utilizes higher order continuity in the drain current description and its derivatives.

Some SPICE models do have continuous derivatives but may not be accurate. The differences between the COBRA[34] model and the previous Materka[35] model are more evident when the derivatives of current (first through third) are compared. Since the COBRA model has derivatives closer to the data, Cojocaru and Brazil[34] show that the model predicts intermodulation products more accurately.

Many SPICE models use a simple expression for junction capacitance in MESFETs and PHEMTs. However, capacitance values extracted from data show that the gate-source and gate-drain capacitance depends strongly on the remote voltage as well as the local voltage (or capacitance terminal voltage). The Statz (Raytheon), the TOM, and the EEFET3 SPICE models[36] all have detailed equations for the gate, drain, and source charge as a function of local and remote voltages. Extraction of coefficients for these expressions is not simple and this will be discussed in the next section.

Modeling Gate Charge as a Function of Local and Remote Voltages in MESFETS and PHEMTS

Small-signal modeling of GaAs and InP MESFETs and PHEMT show that both C_{gd}, the gate-drain capacitance, and C_{gs}, the gate-source capacitance, vary with change of both V_{gs}, the gate-source voltage, and V_{ds}, the drain-source voltage. Thus, these capacitances are dependent upon the local, or terminal voltage, and a remote voltage. The dependency upon the local voltage is expected for capacitances, but the dependency upon the remote voltage leads to a term called "transcapacitance." The modeling of these capacitances can lead to nonphysical effects if not handled properly, as Calvo et al.[37] have shown.

Harmonic balance simulators work with charge functions whose derivatives are capacitive terms. The conventional approach is to find some charge function for total gate charge, such as Q_g (V_{gs}, V_{ds}). Then,

$$C_{11} = \text{Partial Derivative of } Q_g \text{ with respect to } V_{gs}$$

$$C_{12} = \text{Partial Derivative of } Q_g \text{ with respect to } V_{ds}$$

For consistency with small-signal models:

$$C_{11} = C_{gs} + C_{gd}$$

$$C_{12} = -C_{gd}$$

The problem remaining is to partition the total gate charge Q_g into charge associated with the gate-source region, Q_{gs}, and charge associated with the gate-drain region, Q_{gd}. Then, for large signal modeling, the gate node has charge Q_g, the source node has charge $-Q_{gs}$, and the drain node has charge $-Q_{gd}$, and

$$Q_g = Q_{gs} + Q_{gd}.$$

One scheme for partitioning the charge is used in the EEFET model and described in the HP-EEsof Manual.[36] One advantage of this approach is that the model becomes symmetrical, meaning that drain and source may be interchanged and the expressions are still valid.

A simpler approach is presented by Jansen et al.[38] Jansen assumes that all of the gate charge is associated with the gate source region and:

$$Q_{gd} = 0$$

$$Q_g = Q_{gs}.$$

The topology for this approach is different than the conventional model. There is no drain-gate capacitance element. Instead, the transcapacitance term accounts for the conventional drain-to-gate capacitive effects. That is, a change in V_{ds} produces current in the gate source region through the transcapacitance term. Figure 8.62 shows the new topology for the intrinsic circuit.

The procedure for modeling the capacitive effects is the same for both approaches and is the following:

1. Measure small-signal values of C_{gs} and C_{gd} as a function of V_{gs} and V_{ds}
2. Choose a Q_g function and optimize the coefficients of the Q_g expression for best fit of

$$C_{11} = C_{gs} + C_{gd}$$

$$C_{12} = -C_{gd}$$

A good example of the fitting functions and the type of fit obtained is given by Mallavarpu, Teeter, and Snow[39] for a PHEMT.

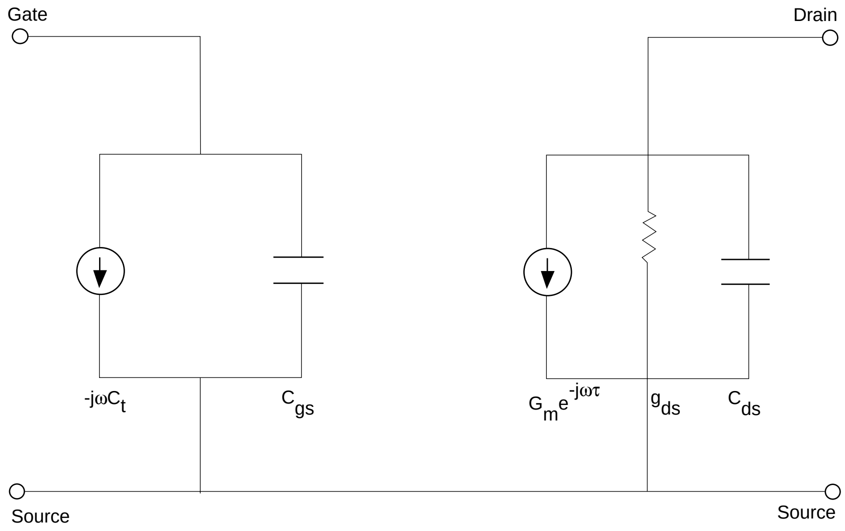

FIGURE 8.62 Jansen's topology for the intrinsic circuit.

In summary, large-signal capacitive effects are modeled by constructing a total gate charge function, $Q_g(V_{gs}, V_{ds})$, whose partial derivative approximates the measured capacitance functions. If device symmetry is important, the EEFET charge partitioning scheme may be used. For amplifier applications, the Jansen model is simplest to code and implement because there is no charge partitioning expression. However, the Jansen model uses a topology that is not conventional.

Modeling the Effects Due to Traps

Electron and hole traps exist in GaAs materials and cause numerous effects during operation of a GaAs MESFET or PHEMT transistor. The following is a brief listing of these effects:

- Dispersion in transconductance and output admittance
- Backgating
- Parasitic bipolar effects
- "Kinks" in the I/V relationship
- Surface gating
- Gate and drain lag effects during switching
- Light sensitivity
- Substrate current or lack of current pinchoff

These effects have been studied and circuit-level models developed to simulate the effects. In many cases, the details of the behavior have been made clear using two-dimensional simulation modeling. For example, Li and Dutton[10] used PISCES-IIB to show that the common EL2 trap causes dispersion in the output conductance of a GaAs MESFET up to several hundred Hz.

The circuit-level modeling of dispersion is described by Cojocaru and Brazil.[34] They extend the previous conventional modeling of dispersion of the output conductance to include dispersion of the transconductance. The circuit is very simple. A second voltage-control current source in parallel with a resistance is capacitively coupled to the internal drain-source terminals. This enables the model's transconductance and drain-source conductance to be tailed for high frequencies using these new elements.

Horio and Usarni[40] use two-dimensional simulation to show that a small amount of avalanche breakdown in the presence of traps causes excess hole charge in the substrate that produces "kinks" in the low-frequency I/V data. Since the traps cannot be easily eliminated, the kinks may be removed by removing the conditions initiating avalanche breakdown.

Upon switching the gate voltage, the drain current of a MESFET will have lag effects in the microsecond and millisecond regions that are produced by traps. Curtice et al.[41] have shown the circuit-level modeling of such gate lag effects as well as drain lag effects. Others, such as Kunihiro and Ohno[42] have also presented circuits for the modeling of drain lag effects.

The transistor model with such circuits may then be used to determine if the lag effects interfere with proper operation of the circuit. The work of Curtice et al. was directed toward GaAs digital circuits where the switching waveform must be of high quality. Using the new transistor model, one may determine not only if the circuit will perform, but also circuit changes that will permit operation in the presence of strong lag effects.

Light sensitivity has been described and modeled by Chakrubarti et al.[43] and by Madjar et al.[44] Some circuit-level models are presented in their discussions.

In the microwave application arena, the principal difficulty with traps is that they cause difficulty in determining an accurate microwave model for the transistor. An excellent experimental study of surface gating effects is given by Teyssier et al.[45] Surface gating means that the charge stored in surface states and traps influences the I/V behavior by acting as a second gate. The amount of charge stored in the traps will vary, depending upon the applied voltages, the ambient light, the temperature, and trapping time constants. Teyssier et al. show that measured trap capture time constants are quite different than trap emission time constants. They show how they are able to accurately characterize the I/V behavior for RF operation by using 150 ns bias pulse width. They also describe how they characterize the thermal behavior using longer pulse width.

Many others have published data showing surface gating effects (see, for example, Platzker et al.[46]). The approach a modeler should use is to first determine how important such trapping effects are in the transistor operation. In many transistor designs, the active region is shielded sufficiently from surface charge so that negligible surface gating occurs. In that case, low-frequency I/V data and the resulting transconductance may be very predictive of microwave-frequency behavior. If the trapping effects are found to be of importance, then short-pulsed characterization is required and low-frequency I/V data will not suffice.

In any case, device characterization must include the behavior changes due to self-heating and ambient temperature effects. The modeling of heating effects will be discussed next.

Modeling Temperature Effects and Self-Heating

Anholt and Swirhun[47] and others have documented the changes of GaAs MESFETs and HEMTs at elevated temperatures. However, the modeling of a device over a temperature range is often accomplished using temperature coefficients. With regard to drain current and DC transconductance, the effects of elevated temperature is quite different at large channel current as compared to operation near pinch off. At large channel current, the electron mobility decrease with temperature increase is most important, whereas at low current, the decrease in the pinch-off voltage with temperature is most important. This produces the interesting effect that transconductance decreases with temperature at large current but increases with temperature at very low currents. This behavior is best modeled using a temperature analog circuit that will be described later.

Figure 8.63 shows the behavior of DC drain current for a 0.25-μm PHEMT at four different ambient temperatures. Heating effects are obvious in Fig. 8.63 where current (and transconductance) near positive V_{gs} is reduced and current (and transconductance) near pinch off is increased.

The effects of temperature upon drain current in MESFETs and PHEMTs may be considered second order but they are of first order in bipolar devices. The reason is due to the current exponential dependence upon temperature in a bipolar device. The gate current effects due to temperature in MESFETs and PHEMTs are of first order for the same reason. First order and even some second order changes with temperature may be modeled using linear temperature coefficients if the changes are reasonably linear.

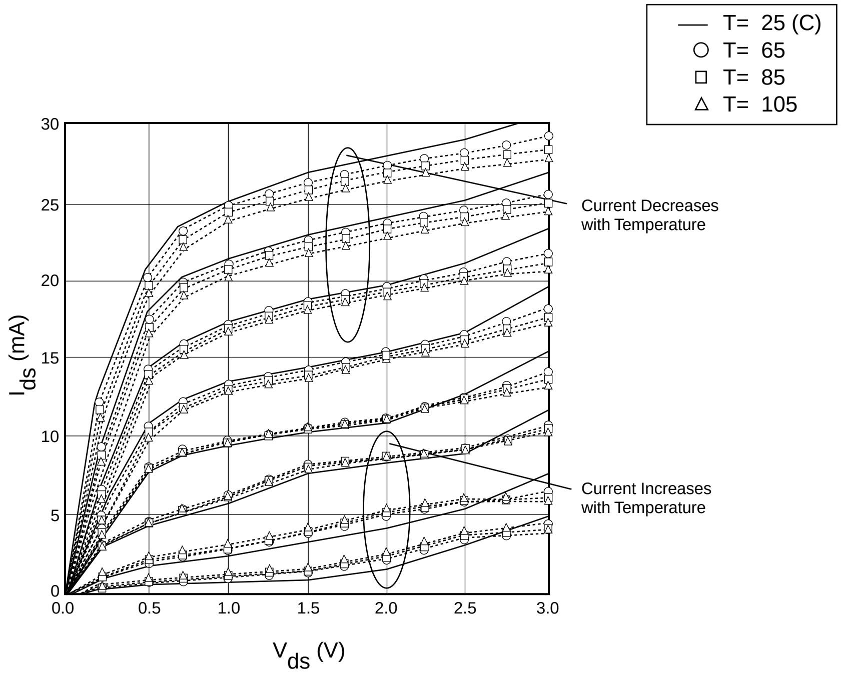

FIGURE 8.63 The behavior of DC drain current for a 0.25-µm PHEMT at four different temperatures.

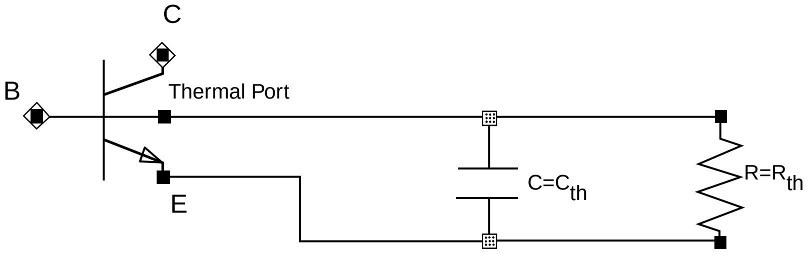

FIGURE 8.64 The HBT transistor model with the thermal analog circuit.

Many devices are operated such that their self-heating effects are quite important. This can occur, for example, in a power amplifier design where the standby biasing current is low, but the advent of input RF power turns on the drain current and output RF power. The ambient temperature may not change but the device will operate with more elevated temperature with the application of the RF power. The use of temperature coefficients may not be accurate for such simulations.

More accurate modeling of self-heating effects in transistors circuits simulators has been done for about ten years using a thermal analog circuit, first used in SPICE applications. It has been found to work well for bipolar simulation as well as for MESFET and PHEMT simulations. The early studies were reported by Grossman and Oki,[48] F. Q. Ye,[49] and others.[50-52] The main differences in these early studies relate to the description of temperature effects in the transistor and not to the CAD model used for simulation in SPICE.

Figure 8.64 shows an HBT transistor model with the additional thermal analog circuit. The device can be of any type but must have well-defined descriptions of the model coefficients as a function of temperature. The analog circuit consists of a current source, a resistor, and a capacitor. R_{th} is the value of thermal resistance and the R_{th}*C_{th} time constant is the thermal time constant of the device. The current source to the thermal circuit, I_{th}, is equal in magnitude to the instantaneous internal dissipated power

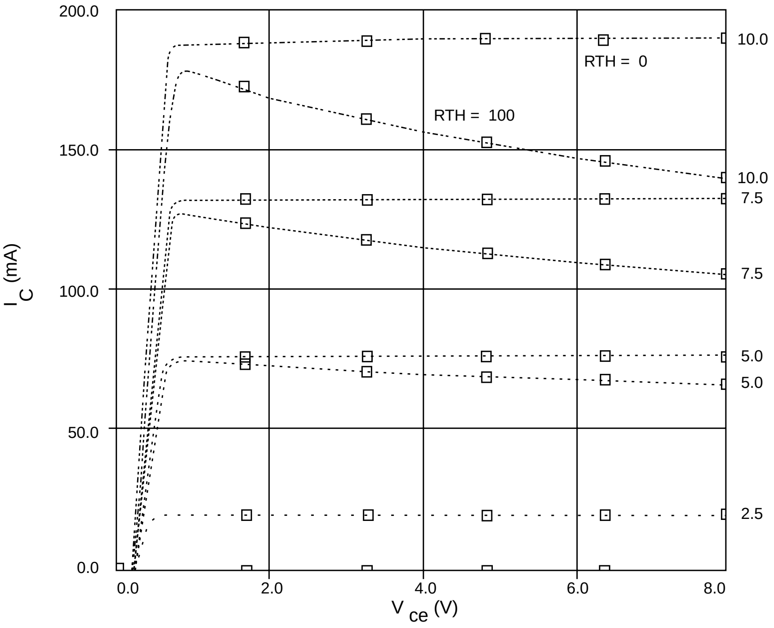

FIGURE 8.65 The collector I-V relationship for an HBT with and without self-heating effects.

to the device. For DC biasing, I_{th} to the thermal circuit would be equal to the total biasing power to the device and the temperature rise would be numerically equal to I_{th} times R_{th}. For RF or transient conditions, the average temperature rise would be that evaluated over some period of time including the effects of the thermal time constant. Thus, for an RF amplifier application, I_{th} would be equal to the DC biasing power plus the RF heating effects less the net RF power leaving the device. Convergence in a simulator is not assured since the value of the model coefficients must be consistent for the temperature of the device.

Harmonic balance simulators usually find the steady-state RF condition efficiently. Using this method, the simulator must find the solution with temperature rise consistent with the device parameters producing the temperature rise. Surprisingly, the harmonic balance simulators do not seem to be much less efficient when the thermal circuit is used, unless a thermal runaway condition exists. In that case, no solution will be found.

Figure 8.65 shows the collector I-V relationship for an HBT exhibiting self-heating effects. The current curves without heating effects are flat in the saturation region. Heating of the lattice reduces the electron mobility, and thus reduces the collector current.

Enhancing the Gummel-Poon Model for Use with GaAs and InP HBTs

The Gummel-Poon model, or the GP model,[14] is a complex, physical parameter model with 55 parameters, and is widely used. It was developed early for SPICE, and all colleges and universities teach their electrical engineering students to use this model. Although the GP model has many parameters, the current expressions are relatively simple. In addition, the current parameters are more closely tied to material parameters rather than manufacturing tolerances, so that there is less variation in current control characteristics than with MESFETs and PHEMTs. The standard bipolar device has less two-dimensional effects than do MESFETs and PHEMTs.

Much effort has been expended to improve the accuracy of compact BJT circuit models for silicon devices. Fossum[53] has reviewed the effort to 1989 and it continues to this day.

Whether the bipolar device is all silicon or a heterojunction device made with SiGe on Si, AlGaAs on GaAs, GaInP on GaAs, or InP on InGaAs, the bipolar action with current gain is the same physical process. So one expects some similarities in the analysis and modeling of the device. However, the heterojunction with the wide bandgap emitter causes the details of the analysis and model to have significant differences from a homojunction device.

The standard SPICE GP model has a number of major deficiencies that must be addressed before it can be used to accurately model a GaAs-based HBT in a large-signal microwave application. First of all, the SPICE code has silicon bandgap parameters hard coded into it and this must be changed to produce the correct temperature effects upon the bandgap. Next, collector-to-base avalanche breakdown must be added because it is important to most GaAs applications. The GP model uses PTF, a phase function, to accommodate the time delay associated with transconductance. It is more convenient for microwave engineers to use the time delay term TAU, as used in MESFET models.

The parameter "Early Voltage" is not as important in GaAs modeling, as it is usually very large. This is because the base doping can be made an order of magnitude larger than for silicon devices, because of the wide bandgap emitter. The large base doping reduces the importance of collector biasing upon the base region, and thus upon the collector current.

There may be dispersion in the collector admittance in HBTs, so some RF conductive element may be needed between collector and emitter.

The manner in which F_t, the frequency for unity current gain, changes with voltage and current is quite different in GaAs devices than with silicon devices. Therefore, a new functional form is need here. Most of the behavior of F_t with respect to collector voltage is related to the electron velocity-electric field (v-E) curve for the material. In the case of silicon devices, F_t generally increases with collector voltage and saturates until heating effects cause a decrease. Figure 8.66 shows such behavior for a SiGe HBT. The I/V characteristic of the device is given in Fig. 8.67.

In the case of GaAs HBTs, F_t peaks at a low voltage and monotonically decrease with further increase of collector voltage. Figure 8.68 shows such data and the devices I/V characteristics are given in Fig. 8.69. This difference in behavior reflects the striking differences between silicon and GaAs v-E curves in the high field region.

There are a multitude of new CAD models formulated to model the behavior of GaAs and InP HBTs. Two examples are the VBIC model[54] and the MEXTRAM model[55] and these are installed on a number

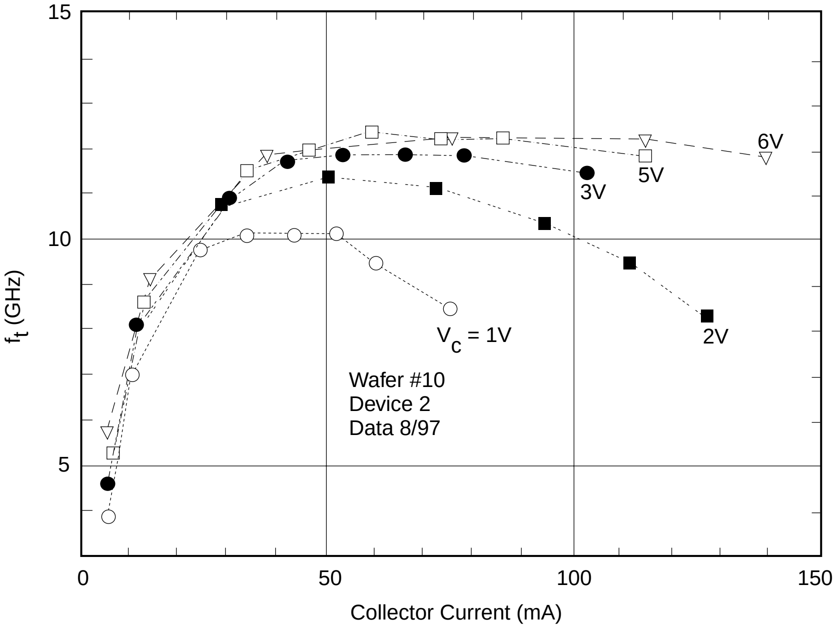

FIGURE 8.66 The behavior of F_t with biasing for a SiGe HBT.

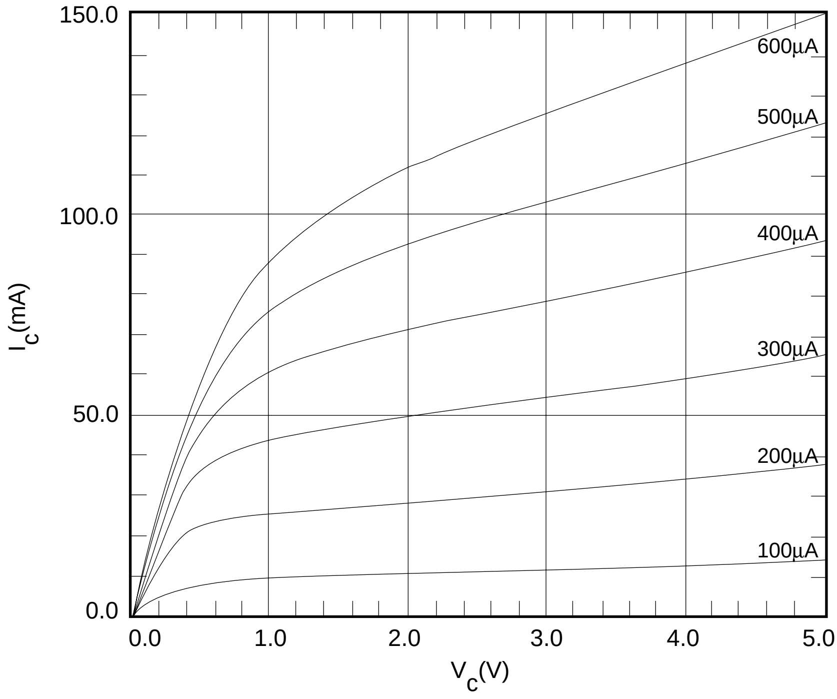

FIGURE 8.67 The I-V relationship for the device of Fig. 8.66.

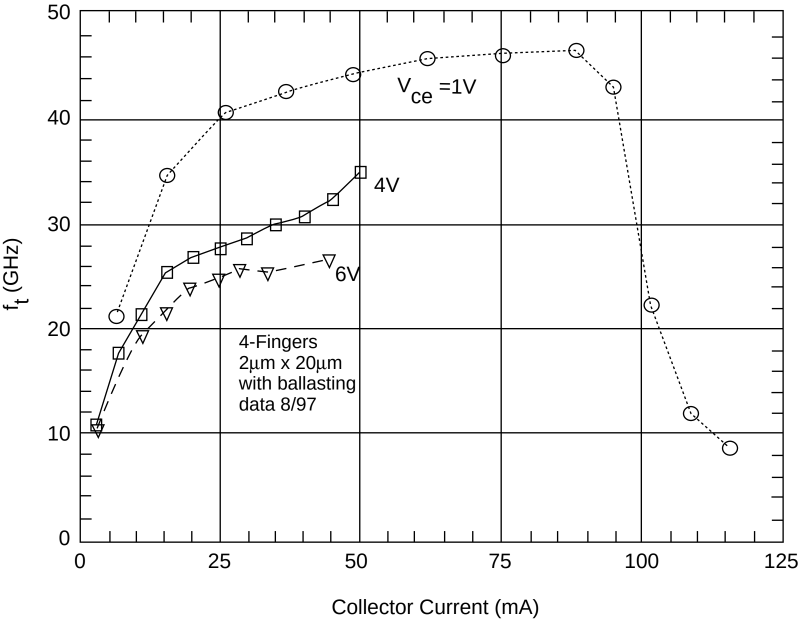

FIGURE 8.68 The behavior of F_t with biasing for GaAs HBT.

of circuit simulators. Most of the new models include self-heating effects because of their importance to device operation and accurate modeling. Because of the significantly poorer thermal conductivity in GaAs compared to silicon and because of the higher power density for best operation in GaAs, self-heating effects are usually important to the operation of the GaAs-based HBTs.

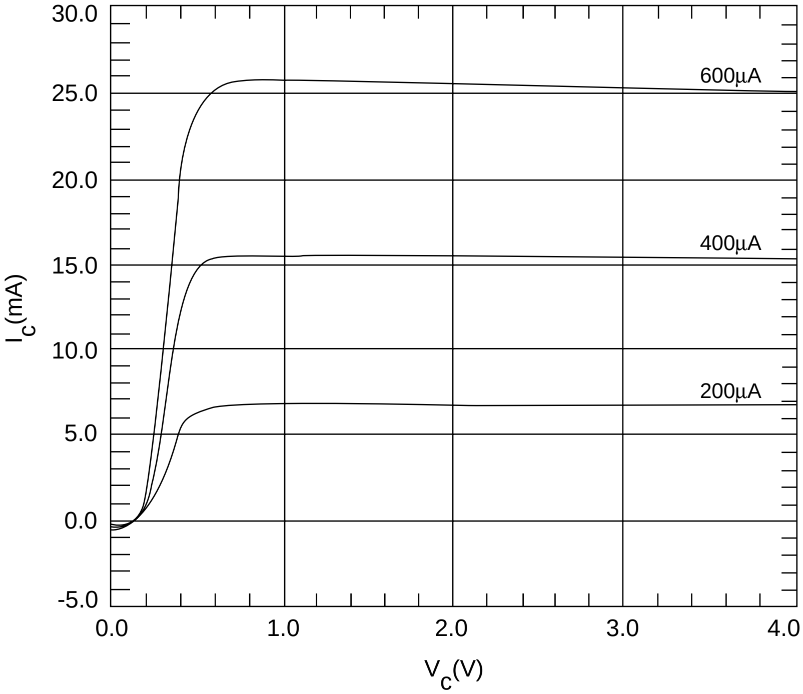

FIGURE 8.69 The I-V relationship for the device of Fig. 8.68.

Modeling the RF LDMOS Power Transistor

There are numerous silicon MOS models available for DC and RF modeling of silicon transistors. Because the silicon LDMOS transistor has become important for cost-effective consumer applications, many companies have developed nonlinear models specifically for this device. The device incorporates a p-type sinker diffusion to ground the source to the substrate, and thus can be treated as a three-terminal device. This makes it possible to construct a much simpler model, one very similar to the SPICE models developed for the GaAs MESFET.

Perugupalli et al.[56] have used a SPICE circuit network incorporating the standard NMOS SPICE element. Motorola uses the Root model developed for GaAs MESFETs for characterizing the device. However, self-heating effects, important for power applications, cannot be incorporated into this model. The Ho, Green, and Culbertson model[57] based upon the SPICE BSIM3v3 model suffers from the same problem.

Miller, Dinh, and Shumate[58] developed analytical current equations for the device, which led to the development of a new, simpler SPICE model by Curtice, Pla, Bridges, Liang, and Shumate.[59] The model includes self-heating effects, is accurate for both small and large-signal simulations, and operates in transient or harmonic balance simulators. Figure 8.70 shows the model predicts power-added efficiency in excellent agreement with the data for an RF power sweep. A similar model based upon the same equations has been developed and verified by Heo et al.[60]

Parameter Extraction for Analytical Models

The extraction of parameters for a device model has become less laborious since the advent of new extraction and equipment control programs, such as IC-CAP by Hewlett Parkard and UTMOST by Sylvaco International. These programs provide data acquisition and parameter extraction. Such software first enables the engineer to collect I/V and RF data in a systematic fashion on each device tested. This

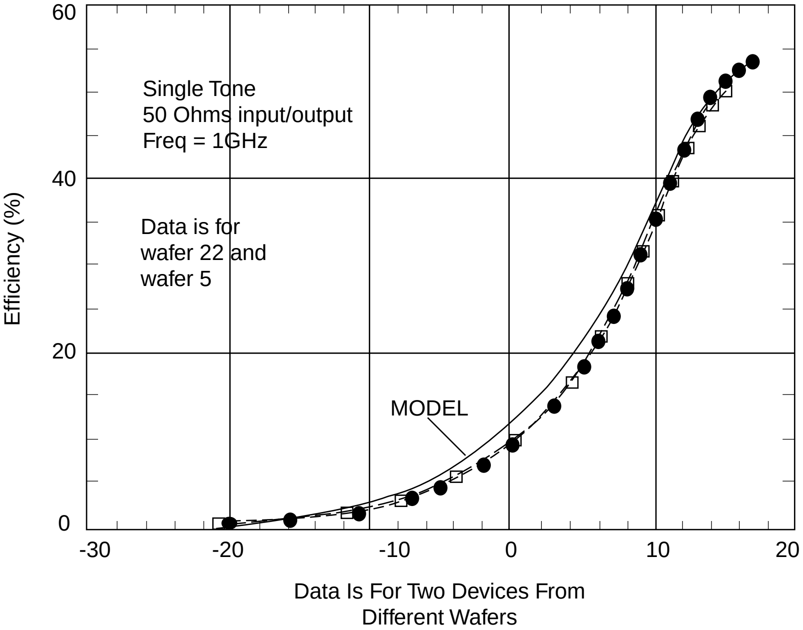

FIGURE 8.70 Efficiency prediction by the model and data for two RF LDMOS devices.

provides consistency between I/V and RF data. The parameter extraction routines then permit the extraction to specific, standard (SPICE) models, such as the Gunnel-Poon, or to new models for which equations may be user defined. Optimizers are used to provide the best fit between the data and the model. Testing can be with pulsed biasing or DC. Heating effects can be separately studied using thermal chucks during testing. Teyssier et al.[45] have discussed the merits of long- and short-pulse testing.

It is usually necessary to use devices of small sizes for characterization and then scale the model to devices actually used in the circuit design. Most SPICE models provide scaling with device area. However, the scaling laws for devices should be verified. It is usually possible to scale MESFETs and HEMTs accurately for a larger number of fingers of the same size. Golio[61] shows the scaling rules if the finger width is different. Because the biasing power may not be uniform on large devices and because the interelectrode capacitance does not scale simply, more complicated scale rules may be found for relatively large devices at high frequencies, i.e., above 5 GHz.

The Vector Nonlinear Network Analyzer

A large-signal, waveform measurement system has been used by many researchers to measure device characteristics dynamically. The equipment provides time domain voltage and current waveforms during RF excitation of the transistor. The equipment is often called the Vectorial Nonlinear Network Analyzer, or VNNA.

Demmler and Tasker[62] have shown that it is possible to accurately determine the drain current relationship to gate voltage for RF excitation at 2 GHz of a MODFET. The characteristic time delay is found by adding delay until "looping" is minimized. Furthermore, the drain-source I-V relationship can also be evaluated at 2 GHz. There is some difference from that obtained from the DC data. Thus the VNNA provides large-signal transfer characteristics from which more accurate model extraction can be done. Wei et al.[63] have also utilized this techniques to provide the data used for device model parameter extraction for a GaAs HBT.

Model Verification

The usual approach to verification of a large-signal model is to compare measured device performance with simulations under the same conditions. Initial verification should be comparison of a power sweep of the transistor at the application frequency and with no matching at the input and the output. For this test, we know that all harmonics at the input and output see 50-ohm impedance.

One should measure not only the output power at the fundamental, but also the power at second and third harmonics. If the model is not fully optimized, it will usually agree well with fundamental output power, gain, and efficiency, but not agree with the harmonic power production. The usual cause is due to poor modeling of the I/V relationship; however, in some cases, the nonlinear capacitive modeling may be the problem. After this problem is fixed, testing of third- and fifth-order IMD (intermodulation distortion) should be made, again in a 50-ohm system. If the harmonics now agree, the third-order IMD should agree and some further work may be required to get agreement for the fifth-order IMD.

In the previous test, it is important that the large-signal model be reasonably accurate at small-signal levels. It need not be as accurate as the best small-signal model for most applications.

Further verification work would involve power sweeps under tuned conditions. That is, the transistor may be tuned for best efficiency and the tuner impedance measured. It is important to measure the tuner impedance for fundamental, second, and third harmonics and to use these values in the simulation. The effects of the second harmonic voltage at either input[64] or output can be extremely important.

Testing of the load-pull characteristics should be made and compared with the model's behavior. Here, again, one has to be careful about the effects of harmonics. There are load-pull systems that operate separately on fundamentals and harmonics.

Further tests that may be important to the application may be testing with various ambient temperatures, noise testing, switch-on testing, and others. The specific application of the transistor will dictate the importance of the agreement for each test as well as the RF frequencies, power, and modulation to use for testing.

Foundry Models and Statistics

GaAs chip foundries provide design manuals that utilize small-signal as well as large-signal models. These are developed from measurements and statistical analysis of the data. However, these are guidelines for the designer, and often the best procedure is to obtain foundry test devices and develop more accurate models based upon new data. Device uniformity has improved greatly and yield prediction is becoming more accurate.

In addition, software programs such as IC-CAP and others provide statistical analysis of models extracted from test wafers. Both corner models and standard statistical patterns are available.

There is the fundamental problem that most foundries continue to tune their processes. It is often the case that the process has been changed and previous statistics are no longer valid. However, the design engineer is better off with approximate guidelines as to statistical patterns or corner models, than none at all.

Future Nonlinear Transistor Models

One can expect that with the ever-increasing speed of computers, circuit simulators will be able to utilize more physics-based models. This will aid in determining the effect of device design parameters upon chip yield and performance.

Improvements will be made in nonlinear model extraction software. The extraction parameters will be much less dependent upon the expertise of the tester. There will be improved collection schemes for transistor model statistics.

Finally, one expects that the nonlinear models will be made to be more easily tailored for adaptation to specific device behaviors. One often would like to start with a template for one of the standard nonlinear models and then tailor its behavior. Future simulators should make this procedure simpler than present procedures.

References

1. Nagle, L. W., SPICE 2: A computer program to simulate semiconductor circuits, Electronics Research Laboratory, College of Engineering, University of California, Berkeley, Memo, ERL-M520, 1975.
2. Pinto, M. R., Conor, R. S., and Dutton, R. W., PIECES2 - Poisson and continuity equation solver, Stanford Electronics Laboratory, Technical Report, Stanford University, 1984.
3. Wada, T. and Frey, J., Physical basis of short-channel MESFET operation, *IEEE Trans. on Electron Devices*, ED-26, 476, 1979.
4. Curtice, W. R., Analysis of the properties of three-terminal transferred electron logic gates, *IEEE Trans. on Electron. Devices*, ED-24, 1553, 1977.
5. Warriner, R. A., Computer simulation of gallium arsenide field-effect transistors using Monte-Carlo methods, *Solid-State Electron Devices*, 1, 105, 1977.
6. Moglestue, C., A self-consistent Monte Carlo particle model to analyze semiconductor microcomponents of any geometry, *IEEE Trans. on CAD*, CAD-5, 326, 1986.
7. Curtice, W. R. and Yun, Y-H, A temperature model for the GaAs MESFET, *IEEE Trans. on Electron Devices*, ED-28, 954, 1981.
8. *ATLAS User's Manual*, Silvaco International, Santa Clara, CA, Version 4.0, 1995.
9. Curtice, W. R., Direct comparison of the electron-temperature model with the particle-mesh (Monte-Carlo) model for the GaAs MESFET, *IEEE Trans. on Electron Devices*, ED-29, 1942, Dec. 1982.
10. Li, Q. and Dutton, R. W., Numerical small-signal AC modeling of deep-level-trap related frequency-dependent output conductance and capacitance for GaAs MESFETs on semi-insulating substrates, *IEEE Trans. on Electron Devices*, 38, 1285, 1991.
11. Snowden, D. M. and Pantoia, R. R., Quasi-two-dimensional MESFET simulation for CAD, *IEEE Trans. on Electron Devices*, 36, 1989.
12. Morton, C. G., Atherton, J. S., Snowden, C. M., Pollard, R. D., and Howes. M. J., A large-signal physical HEMT model, 1996 *International Micrwave Symposium Digest*, 1759, 1996.
13. Root, D. E. et al., Technology independent large-signal non quasi-static FET models by direct construction from automatically characterized device data, 21*st European Microwave Conference Proceedings*, 927, 1991.
14. Gummel and Poon, An integral charge-control relationship for bipolar transistors, *Bell System Tech. Journal*, 49, 115, 1970.
15. Daniel, T. T. and Tayrani, R., Fast bias dependent device models for CAD of MMICs, *Microwave Journal*, 74, 1995.
16. Khatibzadeh, M. A. and Trew, R. J., A large-signal analytical model for the GaAs MESFET, *IEEE Trans. on Microwave Theory and Tech.*, 36, 231, 1988.
17. Ladbrooke, P. H., *MMIC Design: GaAs FETs and HEMTs*, Artech House, Inc., Boston, 1989, chap. 6.
18. Lehovec, K. and Zuleeg, R., Voltage-current characteristics of GaAs JFETs in the hot electron range, *Solid State Electron.*, 13, 1415, 1970.
19. Bandler, J. W. et al., Statistical modeling of GaAs MESFETs, 1991 *IEEE MTT-S International Microwave Symposium Digest,* 1, 87, 1991.
20. Statz, H, Newman, P., Smith, I. W., Pucel, R. A., and Haus, H. A., GaAs FET device and circuit simulation in SPICE, *IEEE Trans. Electron Devices*, 34, 160, 1987.
21. D'Agostino, S. et al., Analytic physics-based expressions for the empirical parameters of the Statz-Pucel MESFET model, *IEEE Trans. on MTT*, MTT-40, 1576, 1992.
22. *International Journal of Microwave and Millimeter-Wave CAE*, 9, No. 3, 1999.
23. Trew, R. J., MESFET models for microwave CAD applications, *Internation Journal of Microwave and Millimeter-Wave CAE*, 1, 143, 1991.
24. Snowden, C. M., Nonlinear modeling of power FETs and HBTs, *International Journal of Microwave and Millimeter-Wave CAE*, 6, 219, 1996.

25. Dortu, J-M, Muller, J-E, Pirola, M., and Ghione, G. Accurate large-signal GaAs MESFET and HEMT modeling for power MMIC amplifier design, *International Journal of Microwave and Millimeter-Wave CAE*, 5, 195, 1995.
26. W. R. Curtice and R. L. Camisa, Self-consistent GaAs FET models for amplifier design and device diagnostics, *IEEE Trans. on Microwave Theory and Tech.*, MTT-32, 1573, 1984.
27. R. L. Vaitkus, Uncertainty in the Values of GaAS MESFET Equivalent Circuit Elements Extracted from Measured Two-Port Scattering Parameters, Presented at 1983 IEEE Cornell Conference on High Speed Semiconductor Devices and Circuits, Cornell University, Ithaca, NY, 1983.
28. Byun, Y. H., Shur, M. S., Peczalski, A., and Schuermeyer, F. L., Gate voltage dependence of source and drain resistances, *IEEE Trans. on Electron Devices*, 35, 1241, 1998.
29. Samelis, A. and Pavlidis, D., Modeling HBT self-heating, *Applied Microwave & Wireless*, Summer Issue, 56, 1995.
30. Teeter, D. A. and Curtice, W. R., Comparison of hybrid pi and tee HBT circuit topologies and their relationship to large-signal modeling, 1997 *IEEE MTT-S International Microwave Symposium Digest*, 2, 375, 1997.
31. Curtice, W. R., A MESFET model for use in the design of GaAs integrated circuits, *IEEE Trans. on Microwave Theory and Techniques*, 23, 448, 1980.
32. Angelov, I., Zirath, H., and Rorsman, N., New empirical nonlinear model for HEMT and MESFET and devices, *IEEE Trans. on Microwave Theory and Techniques*, 40, 2258, 1992.
33. Qu, G. and Parker, A. E., Continuous HEMT model for SPICE, *IEE Electronic Letters,* 32, 1321, 1996.
34. Cojocaru, V. I. and Brazil, T. J., A scalable general-purpose model for microwave FETs including the DC/AC dispersion effects, *IEEE Trans. on Microwave Theory and Techniques*, 12, 2248, 1997.
35. Materka, A. and Kacprzak, T., Computer calculation of large-signal GaAs FET amplifier characteristics, *IEEE Trans. on Microwave Theory and Tech.*, 33, 129, 1985.
36. Circuit Network Items, Series IV, Hewlett Packard, HP Part. No. E4605-90038, 1161, 1995.
37. Calvo, M. V., Snider, A. D., and Dunleavy, L. P., Resolving Capacitor Discrepancies Between Large and Small Signal FET Models, 1995 IEEE MTT-S International Microwave Symposium, 1251, 1995.
38. Jansen, P. et al., Consistent small-signal and large-signal extraction techniques for heterojunction FET's, *IEEE Transaction on Microwave Theory and Tech.*, 43, 1, 87, 1995.
39. Mallavarpu, R., Teeter. D., and Snow, M., The importance of gate charge formulation in large-signal PHEMT modeling, *GaAs IC Symposium Technical Digest*, 87, 1998.
40. Horio, K. and Usarni, K., Analysis of kink-related backgating effect in GaAs MESFETs, *IEEE Electron Devices Letters*, 537, 16, 1995.
41. Curtice, W. R., Bennett, J. H., Suda, D., and Syrett, B. A., Modeling of current lag effects in GaAs IC's, 1998 *IEEE MTT-S International Microwave Symposium Digest*, 2, 603, 1998.
42. K. Kunihiro and Y. Ohno, An equivalent circuit model for deep trap induced drain current transient behavior in HJFETs, *1994 GaAs IC Symposium Digest*, 267, 1994.
43. Chakrabarti, P., Shrestha, S. K., Srivastava, A., and Skxena, D., Switching characteristics of an optically controlled GaAs-MESFET, *IEEE Trans. on Microwave Theory and Techniques,* 42, 365, 1994.
44. Madjar, K., Paolella, A., and Herczfeld, P. R., Modeling the optical switching of MESFET's considering the external and internal photovoltaic effects, *IEEE Trans. on Microwave Theory and Tech.,* 42, 62, 1994.
45. Teyssier, J-P, Bouysse, P., Ouarch, A., Barataud, D., Peyretaillade, T., and Quere, R., 40-GHz/150-ns versatile pulsed measurement system for microwave transistor isothermal characterization, *IEEE Trans. on Microwave Theory and Tech.,* 46, 2043, 1998.
46. A. Platzker et al., Characterization of GaAs devices by a versatile pulsed I-V measurement system, *1990 IEEE MTT Symposium Digest,* 1137.
47. Anlholt and Swirhun, Experimental characterization of the temperature dependence of GaAs FET equivalent circuits, *IEEE Trans. on Electron Devices*, 39, 2029, 1992.
48. Grossman, P. C. and Oki, A., A large signal DC model for GaAs/GaAlAs heterojunction bipolar transistors, *Proc. IEEE BCTM*, 258, 1989.

49. Ye, F. Q., A BJT model with self-heating for WATAND computer simuation, M. S. Thesis, Youngstown State University, Youngstown, OH, 1990.
50. McAndrew, C. C., A complete and consistent electrical/thermal HBT model, *Proc. IEEE BCTM*, 200, 1992.
51. Corcoran, J., Poulton, K. and Knudsen, K., GaAs HBTs: an analog circuit design perspective, *Proc. IEEE BCTM*, 245, 1991.
52. Fox, R. M. and Lee, S-G, Predictive modeling of thermal effects in BJTs, *Proc. IEEE BCTM*, 89, 1991.
53. Fossum, J. G., Modeling issues for advanced bipolar device/circuit simulation, *Proc.* 1989 *IEEE BCTM,* 234, 1989.
54. McAndrew, C. C., Seitchik, J., Bowers, D., Dunn, M., Foisy, M., Getreu, I., Moinian, S., Parker, J., van Wijnen, P., and Wagner, L., VBIC95: An improved vertical IC bipolar transistor model, *Proc.* 1995 *BCTM*, 170, 1995.
55. de Graaff, H. C. and Kloosterman, W. J., New formulation of the current and charge relations in bipolar transistor modeling for CACD purposes, *IEEE Trans. on Electron Devices*, ED-32, 2415, 1986.
56. Perugupalli, P., Trivedi, M., Shenai, K., and Leong, S. K., Modeling and characterization of 80v LDMOSFET for RF communications, *1997 IEEE BCTM*, 92, 1997.
57. Ho, M. C., Green, K., Culbertson, R., Yang, J. Y., Ladwig, D., and Ehnis, P., A physical large signal Si model for RF circuit design, *1997 MTT-S International Microwave Symposium Digest*, 1997.
58. Miller, M., Dinh, T., and Shumate, E., A new empirical large signal model for silicon RF LDMOS FET's, *1997 IEEE MTT Symposium on Technologies for Wireless Applications Digest,* Vancouver, Canada, 19, 1997.
59. Curtice, W. R., Pla, J. A., Bridges, D., Liang, T., and Shumate, E., A new dynamic electro-thermal model for silicon RF LDMOS FET's, *1999 IEEE MTT-S International Microwave Symposium Digest,* 1999.
60. Heo, D., Chen, E., Gebara, E., Yoo, S., Lasker, J., and Anderson, T., Temperature dependent MOSFET RF large signal model incorporating self-heating effects, *1999 MTT-S International Microwave Symposium Digest,* 1999.
61. Golio, J. M., *Microwave MESFETs and HEMTs,* Artech House, Boston, 1991.
62. Demmler, M. and Tasker, P. J., A vector corrected on-wafer large-signal waveform system for novel characterization and onlinear modeling techniques for transistors, Presented at the workshop on New Direction in Nonlinear RF and Microwave Characterization, 1996 International Microwave Symposium, 1996.
63. Wei, C.-J., Lan, Y. E., Hwang, J. C. M., Ho, W.-J., and Higgins, J. A. Waveform-based modeling and characterization of microwave power heterojunction transistors, *IEEE Trans. on Microwave Theory and Techniques,* 43, 2898, 1995.
64. Watanabe, S, Takatuka, S., Takagi, K., Kukoda, H., and Oda, Y., Simulation and experimental results of source harmonic tuning on linearity of power GaAs FET, 1996 MTT-S International Microwave Symposium, 1996.

8.8 Technology Computer Aided Design

Peter A. Blakey

Computer-aided design (CAD) is used in response to complexity in engineering problems. The complexity may be associated with the manipulation and storage of large amounts of relatively simple information; or it may be associated with the interactions of complicated nonlinear physical phenomena. Both types of complexity are encountered in the field of microelectronics. Electronics CAD (ECAD) is used to design new products using an *existing* semiconductor technology, and technology CAD (TCAD) is used to accelerate the development of *new* semiconductor technologies. ECAD is able to manage large amounts of relatively simple information, such as the number, size, and locations of the polygons used to define lithographic masks. TCAD predicts the way in which nonlinear process and device physics would impact the performance of proposed technologies. The subject matter of this chapter is TCAD and its application to the development of RF, microwave, and millimeter-wave semiconductor technologies.

An Overview of TCAD

The core tools of technology CAD (TCAD) are process simulators and device simulators. Process simulators predict the structures that result from applying a sequence of processing steps to an initial structure. Device simulators predict the electrical characteristics of specified structures. Process and device simulators are often used in combination to predict the impact of process variations on electrical behavior. The basic flow of information is indicated in Fig. 8.71.

Process and device simulators use numerical techniques to solve mathematical equations that describe the underlying physics of an experiment. They are able to predict the result of experiments, without requiring the experiments to be run. Predictive simulation is useful whenever it is time consuming, expensive, dangerous, or otherwise difficult to run real experiments. In the case of microelectronics development, it is both time consuming and expensive to run real experiments in a semiconductor fab. As a result, it can be cost effective to substitute simulated experiments for some of the real experiments that would otherwise be required by purely empirical development procedures.

Process simulators incorporate physical models for phenomena such as diffusion, oxidation, ion implantation, deposition, and etching. Device simulators solve equations that express charge continuity and the dependency of the electrostatic potential on the distribution of charge. In order to solve the charge continuity equations, device simulators need models for charge transport and for the generation and recombination of charge carriers. Implementing process and device simulators is a challenging task that requires knowledge of physics, numerical methods, visualization techniques, user interfaces, and software engineering. Research groups in universities and in industry were the first to develop this type of software. However, these groups were not well suited to the task of maintaining the software and providing long-term support to users. General-purpose process and device simulation software is now available from several commercial vendors who provide maintenance and support. Most microelectronics companies use commercial software as the foundation of their TCAD capabilities.

Commercial TCAD systems also include tool integration utilities that make it convenient to use the core tools in combination, and task integration environments that automate large-scale simulation-based experimentation. The tool integration utilities include run time environments, visualization tools, structure editors, layout editors and interfaces, and optimization capabilities. Task integration usually supports a "Virtual Wafer Fab" paradigm that makes it convenient to define and run simulated split lot experiments. After a simulated experiment is defined, the system automatically generates all of the associated jobs, farms out the jobs across a computer network, and collects the results. It may also provide modeling capabilities that make it easy to analyze the simulated results.

Predictive, physics-based simulation is different from data modeling. Simulation predicts the data that an experiment would yield if it were run. Modeling provides a compact description of existing data that

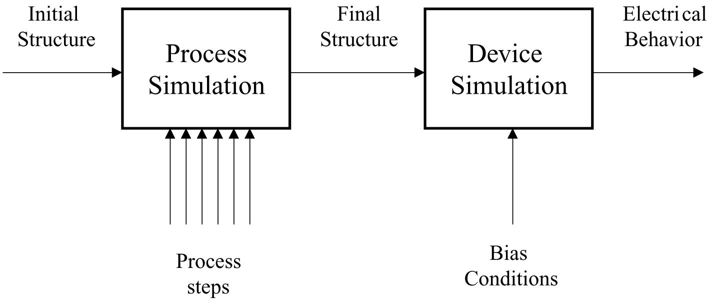

FIGURE 8.71 The basic flow of TCAD information.

may come from either real or simulated experiments. Data models are used to interpolate, but cannot be used to extrapolate. Expectations regarding "accuracy" are quite different for data models and for physics-based simulators. The agreement between modeled and experimental data is normally very good. The agreement between simulated data and experimental data is subject to several sources of uncertainty that can lead to significant discrepancies between simulated data and experimental data. These sources of uncertainty are discussed in a later section.

Process and device simulators were implemented initially to assist the development of digital Si VLSI technologies. In recent years the capabilities of TCAD software have been extended to cover a range of different material systems, and to provide convenient RF-oriented analysis capabilities. The widespread use of epitaxially grown materials and low thermal budget processing means that process simulation for III-V hetero-structure technologies can often be reduced to the definition of material layers and doping densities, with geometric specification of deposition and etch steps. This avoids difficult problems associated with process simulation of silicon technologies, which must account for moving boundaries during oxidation, complicated diffusion mechanisms, and so forth. Device simulation for advanced material systems often requires advanced models for charge transport, and it is usually necessary to account for the impact of deep level traps. The appropriate models have been incorporated into some of the commercially available device simulators.

In principle, device simulators can predict any electrical behavior that can be measured. Simulators targeted toward the development of digital silicon VLSI technologies are primarily concerned with the calculation of DC I-V characteristics, but they also provide basic capabilities for calculating small-signal AC behavior and large-signal transient behavior. Mixed-mode device-and-circuit simulation capabilities are also available. Mixed-mode simulation is basically SPICE-like circuit simulation that uses numerical device simulation to model the behavior of one or more of the active devices in a circuit. Other types of analysis are feasible, but are not available in commercial simulators. One example is the prediction of noise behavior. Another example is harmonic balance analysis of device operation that is implemented at the level of the underlying physics, rather than at the circuit level. Computational load-pull systems seek to mirror the functionality of experimental load-pull systems. These systems predict RF output power, power-added efficiency, gain, linearity, and tunability, and present the results as a function of load (or source) impedance plotted on a Smith chart. Such systems have been implemented in industry, but are not yet offered by commercial vendors.

Benefits of TCAD

Simulated experiments can replace a significant fraction of the real experiments that are otherwise required by traditional, empirical development procedures. Simulated experiments are almost always performed more rapidly and more cheaply than real experiments. The use of TCAD can therefore yield significant reductions in both cycle times and development costs. Reduced development times lead in turn to a faster time to market, and this normally translates into higher profits. The magnitude of the financial benefits depends both on the skill with which TCAD is deployed and on the characteristics of the market for a given technology. TCAD is most useful when the market is high volume, and both performance and cost driven. Until recently, this meant that TCAD was applied primarily to the development of silicon VLSI technologies. As a result of the wireless revolution, TCAD is now being used to accelerate the development of analog, RF, microwave, and millimeter-wave technologies.

The high costs of semiconductor fabs, material, and personnel mean that reducing development costs by even a few percent is enough to justify significant investments in TCAD capabilities. When TCAD is used effectively it can yield direct savings in development times and development costs of around 50%, and can result in enhanced profits (due to faster time to market) that are much greater than the direct cost savings. Savings of this magnitude can, in principle, justify investments of tens or even hundreds of millions of dollars in TCAD capabilities. The investments that companies make in TCAD have traditionally been much smaller than this.

Simulation can predict all of the quantities that are measured routinely. It can also predict the values of quantities that are either very difficult or impossible to measure. Examples of such quantities are the doping profiles, carrier profiles, and electrostatic potential distributions within a semiconductor device. By examining these quantities, engineers gain insight into the subtleties of device operation. This insight can guide the direction of future development, and it can lead to the development of simple analytic theories that capture the essence of device operation. Although the enhanced physical insight is very useful, it is difficult to quantify the value in monetary terms.

Process and device simulators encapsulate and integrate the knowledge of experts in a way that makes detailed knowledge and experience accessible on demand to less expert process and device engineers. For example, it is possible for a device engineer to account for the impact of complicated transport phenomena on device performance, without having any knowledge of the associated physics. This function of encapsulation and integration helps to ameliorate both the shortage of experienced technical personnel and the comparatively narrow technical span of most experts. Once again, it is difficult to quantify the value in monetary terms.

Limitations of TCAD

For certain widely used types of simulation, the underlying physics is well established and, for practical purposes, "exact." For example, electromagnetic simulation is based on Maxwell's equations, thermal simulation is based on the heat flow equation, and circuit simulation is based on Kirchoff's Current and Voltage Laws. The underlying physics of process and device simulation is less well defined. For each physical phenomenon (e.g., ion implantation, or electron transport) there is a hierarchy of models of varying complexity. All of these models introduce approximations. In general, the more complicated models provide a more complete description, but are more difficult to implement and involve longer (often much longer) computation times. The need to select appropriate accuracy-efficiency trade-offs can make it difficult for nonexperts to utilize TCAD effectively.

After a physical model has been selected, it is necessary to define values for the parameters associated with the model. These parameters must usually be defined over a range of different conditions (e.g., for different temperatures, doping concentrations, or electric fields.) The values of the parameters may be obtained from experiments or from theory. In either case, there is often considerable uncertainty in the accuracy of the model parameters.

Process and device simulators solve systems of coupled, nonlinear equations that do not have general analytic solutions. The equations are therefore solved using numerical techniques that are implemented in computer software. Numerical techniques provide an approximate solution that is defined on a discrete "mesh" of points. The choice of mesh and numerical techniques has a major impact on the accuracy and efficiency with which solutions are obtained. Using a finer mesh provides solutions that have higher accuracy but are calculated more slowly. Numerical techniques for solving nonlinear equations employ sequences of approximations that are expected to converge to a solution. In some cases the sequence of approximations fails to converge. Because of these issues, users of TCAD need some expertise in defining meshes and numerical techniques that provide acceptable trade-offs between accuracy, efficiency, and stability.

Discrepancies between measured and simulated results arise because of difficulties in specifying equivalent experiments. For example, a real diffusion step may specify a thermal ramp in terms of the times and temperatures that are dialed in as input to a controller. Process simulation will normally use the same times and temperatures. However, in the real experiment the temperature of the wafer as a function of time is different from the nominally specified ramp. The temperature as a function of time may also vary from wafer to wafer within a lot, and from point to point on a given wafer. Another example is provided by device simulation. The lattice temperature used in device simulation is often assumed to be 300 K, but the real lattice temperature is a function of both the true ambient temperature and any self-heating that occurs. Other sources of uncertainty are systematic measurement and repeatability.

In order to apply TCAD effectively, users need technical skills that encompass physics, numerical techniques, and the application domain. They need to understand and employ effective application methodologies, and they need good judgment to assess the validity and usefulness of TCAD predictions that are impacted by several sources of uncertainty. They also need to be able to "sell" their insights to process and device engineers who do not understand the role of simulation and are skeptical of its value, and they need to be comfortable with having a secondary support role within a technology development organization.

The Role of Calibration

By calibrating simulated results to experimental results, it is possible to ameliorate some of the issues that were outlined in the previous section. The existence of high-quality calibration is a prerequisite for using TCAD for certain applications. Achieving a good calibration involves a considerable amount of effort, and poor calibration can exacerbate the problems outlined previously. In view of the importance of calibration to the effective use of TCAD, a review of the associated issues is presented in this section.

Calibration attempts to reduce some of the errors associated with simulation. The measure of the errors is taken as the differences between simulated and measured results. Calibration seeks to reduce these errors by adjusting the values of the model parameters used by the simulators. In essence, it is assumed that the various sources of errors can be partially compensated for by using appropriate "effective" values of model parameters. A good calibration must use a sufficiently complete set of output variables, i.e., quantities for which the predicted and measured results are to be brought into better agreement. It must also use an appropriate set of input variables, i.e., model parameters whose values are adjusted to improve the agreement between predicted and measured values. A good calibration must not allow the adjusted values of the model parameters to assume implausible values.

Calibration is often performed using ad hoc procedures that lead to unsatisfactory results. A very common error is to adjust too few input variables, or the wrong input variables. A related error is to allow input variables to assume values that are implausible or nonphysical. Another common problem is that some key output variables are neglected, and the associated errors diverge as a result of the calibration attempt. Calibration should be set up as a clearly defined optimization problem and the techniques used for calibration should draw on known methods for nonlinear optimization involving multiple constrained input variables. Black-box optimization can be performed, using small-change parameter sensitivity matrices calculated using TCAD. However, it is usually more efficient to use a sequential, step-by-step calibration procedure in which only a subset of the input and output variables are varied at each step. For example, in the case of a very simple calibration of a GaAs MESFET simulation, the threshold voltage could be matched by adjusting the channel charge. The low-field mobility could then be adjusted to fit the on-resistance in the linear region, and the saturated carrier velocity could be adjusted to fit the saturated current.

Performing a good calibration takes a lot of effort, but certain applications of TCAD only become viable after a good calibration has been achieved. Regardless of the amount of effort expended on calibration, there will still be residual errors. This is because calibration does not remove approximations in the underlying physics; it simply allows a portion of their impact to be absorbed into the values of the model parameters. No set of model parameters can correct for an underlying physical model that is inadequate. The converse of this observation is that the degree to which a calibration is successful provides insight into the adequacy of the underlying physics.

Applications of TCAD

The block diagram shown in Fig. 8.72 provides a high-level view of the activities associated with traditional, empirical development of semiconductor technologies. The development process involves a make-and-measure cycle that is repeated until acceptable results are obtained. The process recipe is then transferred to a fab; and layout rules and electrical models for active and passive components are

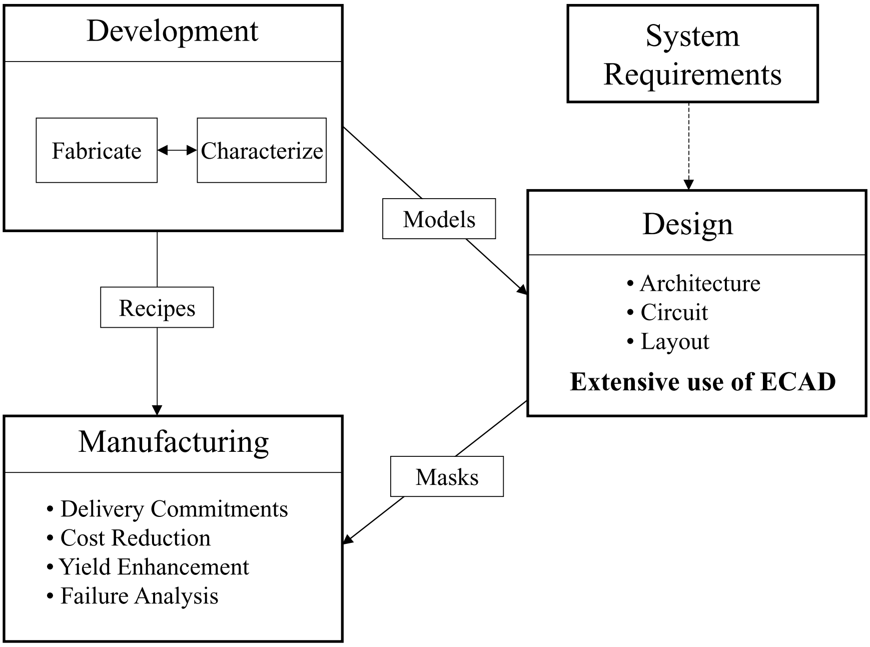

FIGURE 8.72 A high-level view of the traditional development methodology.

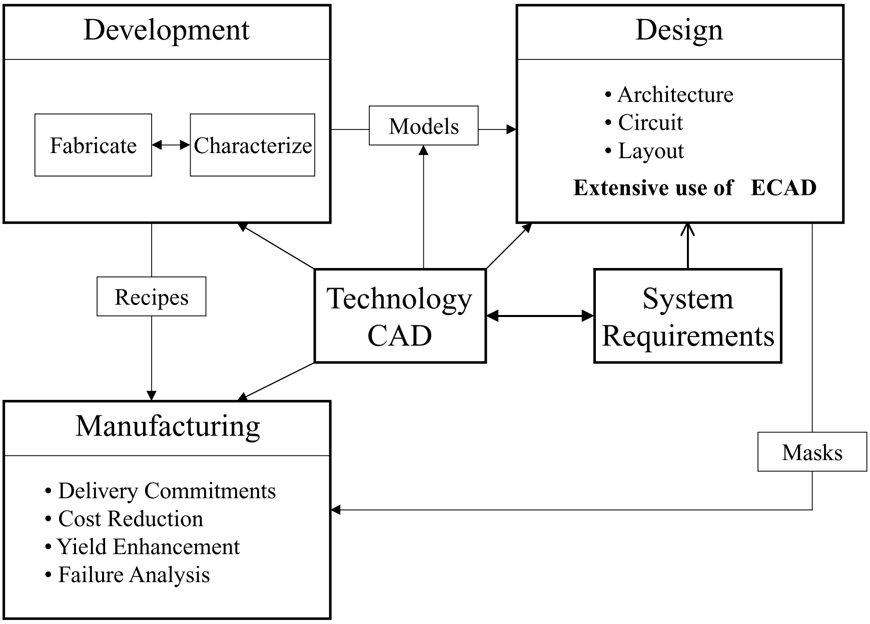

FIGURE 8.73 A high-level of modern development methodologies.

transferred to the circuit design community. Circuits are designed, masks are made, and the circuits are fabricated.

The block diagram shown in Fig. 8.73 provides a high-level view of the activities that are associated with more modern simulation-oriented development strategies. Depending on the ways in which TCAD is used, modern development methodologies may be viewed as being "TCAD influenced," "TCAD driven," or "system driven via TCAD." TCAD-influenced development uses process and device simulation to accelerate the make-and-measure phase of technology development. TCAD-driven development makes more extensive use of process and device simulation in the areas of modeling, characterization, and manufacturing. System-driven development supplements TCAD-driven development by adding explicit bidirectional links to system requirements and basic architectural choices. Much of modern development is TCAD influenced. Some companies use TCAD-driven methodologies, and a few companies are implementing system-driven methodologies.

It is useful to order individual TCAD activities by the amount of calibration required to achieve useful results. One such list, ordered by increasing calibration requirements, is as follows:

- Concept evaluation
- Technology discrimination
- Technology development
- Simulation-based model development
- Simulation-assisted characterization
- Statistical process design
- Technology transfer
- Process control
- Yield enhancement and failure analysis

Prior to the availability of TCAD, there was considerable reliance on simplified analytic models. Gross oversimplification of these models would lead to unrealistic performance projections, e.g., to the prediction of useful transistor performance at THz frequencies. TCAD is now used to perform rapid evaluations of proposed new concepts. Accounting for Poisson's equation, one or more carrier continuity equations, the coupling between these equations, and the need for device contacts ensures more realistic estimates of device performance. Projections of wildly overoptimistic device performance have been substantially eradicated by the widespread availability of TCAD. Concept evaluation usually requires little calibration effort, since all that is required is a go/no-go assessment.

At the initial stages of technology development, it is sometimes necessary to select between two or more competing approaches. TCAD is well suited to this purpose. Calibration is usually not very critical because the errors that are introduced by simulation tend to affect both technologies approximately equally, and are unlikely to cause a simulation-based ranking to be different from an experimentally determined ranking.

Once an overall approach has been selected, TCAD is used to explore different sub-options, and to assist process optimization. This is presently the single most important application of TCAD. Simulation-based design and optimization can and should be done systematically, but in practice it is often done using inefficient ad hoc techniques. Application methodologies associated with simulation-based technology development are discussed in the next section. As the results of real experiments become available they should be fed back to refine the simulator calibrations, in order to improve the usefulness of simulation at each stage of design and optimization. A general goal is for the calibration achieved for one generation of a technology to provide a solid starting point for the simulation-based design and optimization of the next generation of the technology.

TCAD can also be used to assist modeling and characterization activities. In the area of device modeling, TCAD can be used as a reference standard that enables careful testing of assumptions made in the course of developing device models, and supports systematic assessments of the global accuracy of a device model. TCAD is especially useful for assessing the accuracy of large-signal models that are constructed from DC and small-signal AC data. The large-signal behavior predicted by the model is compared to the large-signal behavior predicted directly using TCAD. The development and characterization of charge-based models is also facilitated by the use of TCAD, since the calculated charge distributions within a device can easily be integrated and partitioned in accordance with charge-based modeling approaches. TCAD can also be used to assist in device characterization. For example, it is quite straightforward to predict the values of bias- and temperature-dependent source and drain access resistances. Simulation can also assist in the interpretation of pulsed I-V measurements that are used to characterize thermal effects and low-frequency dispersive effects associated with deep-level traps.

When there is sufficiently high confidence in the quality of an underling calibration, the uses of TCAD can be expanded further. Calculation of process sensitivities provides a foundation for statistical process design, design centering, and yield modeling. Information concerning process sensitivity is also a useful input for process control. Simulation of the impact of large-change variations (e.g., the impact on electrical behavior of skipping a process step) can provide "signature" information that assists failure analysis. The ideal situation is when a comprehensive set of simulated data, together with an associated set of input data, forms an integral part of the technology transfer package that is supplied by a development organization to a manufacturing organization.

Application Protocols

TCAD is often deployed using inefficient ad hoc techniques. In order to use TCAD efficiently, it is helpful to develop, refine, and document sets of useful simulation-based procedures. The details of these procedures often vary considerably from one application (e.g., technology discrimination) to another (e.g., failure analysis.) A description of a simulation-based procedure that is used for a particular application is referred to as an application protocol. From a high-level perspective, the development of simulation-based application protocols is often a two-stage procedure. In the first stage, the simulation-based procedures are set up to mirror the existing experimental procedures associated with traditional, empirical technology development. In the second stage, there is explicit consideration of the additional possibilities that can be exploited due to the use of simulated rather than real experiments.

Since technology development is presently the most important application of TCAD, an example of an application protocol for technology development will be outlined. The first step is to mirror traditional, empirical development procedures that use split-lot experiments. This is the underlying idea of Virtual Wafer Fab (VWF) methodology, variants of which have been implemented by several commercial vendors of TCAD software. VWF methodology makes it convenient to define and run large-scale simulated split-lot experiments. Users select from a broad range of built-in experimental designs, define split variables among input quantities, and specify the output quantities to be extracted. Once these variables have been specified, all of the input descriptions associated with the simulated experiment are generated automatically, and farmed out automatically within a networked computing environment. The results are collected automatically, stored in a database, and are conveniently viewed and analyzed using built-in tools.

The next step is to define ways in which a simulation-based approach can go beyond traditional development procedures. When using TCAD it is possible to use sophisticated "black box" optimization techniques that require the ability to calculate accurate derivatives in a multidimensional search space. Due to long cycle times, high costs, and noisy experimental data, this approach is not feasible in the real world. However, it is quite suitable for use in the simulation world, where results can be obtained quickly and reproducibly. The use of black-box optimization focuses explicit attention on the need to define an objective function, and also on the need to define all of the constraints on the input variables. Split-lot experimentation also involves objective functions and constraints, but they are usually defined and implemented less formally.

A focus on objective functions and constraints leads to a useful high-level view of technology development in general and the role of simulation in particular. Technology development can be viewed as a search, within a multidimensional design space, for the point corresponding to an optimum design. Various techniques are available for narrowing down the regions of the design space that need to be searched. These techniques include analytic theory and scaling arguments, numerical simulation, and real experiments. Each of these techniques has its advantages and limitations. Analytic theory and scaling arguments are quick and easy to apply, and can eliminate large regions of the design space, but their absolute accuracy is poor. Simulation can provide much better accuracy, and is relatively fast and

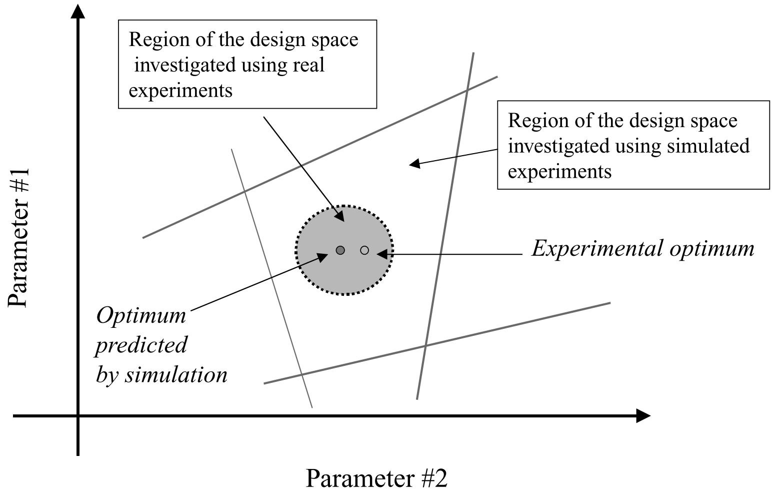
Region of the design space investigated using real experiments
Region of the design space investigated using simulated experiments
Parameter #1
Experimental optimum
Optimum predicted by simulation
Parameter #2

FIGURE 8.74 A simplified view of the search process.

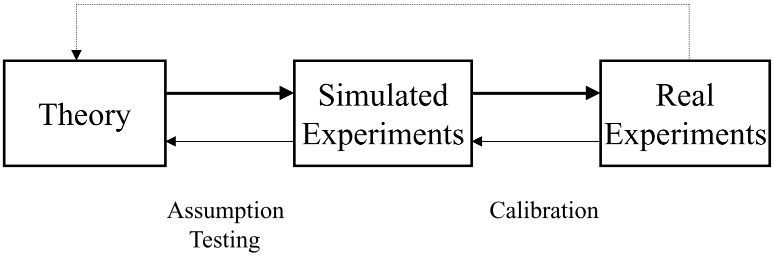

FIGURE 8.75 A three-level hierarchical approach to technology development.

inexpensive, but is subject to model errors and numerical error. Experiments provide "real" data, but are expensive, time consuming, and subject to experimental error. Analytic theory, simulation, and experiments can be viewed as a hierarchy of search techniques that can be applied sequentially and iteratively to maximize the efficiency of the search process.

A simplified view of the search for an optimum design in a two-dimensional space is presented in Fig. 8.74. Analytic theories and scaling arguments are used to establish the boundaries of the region of the design space that needs to be searched. Simulation is then used to predict the optimum point in the design space. Due to modeling and numerical errors, this predicted optimum (indicated by the closed circle) is not exactly coincident with the true optimum point. The region around the predicted optimum is therefore searched experimentally, to determine the location of the true optimum (the open circle). According to this view, the goal of simulation is to predict an optimum design with sufficient accuracy that the true optimum can be found using only a small number of real experiments. Thus, simulation does not eliminate the need for experiments, but it is realistic to expect a reduction of 50 to 80% in the number of real experiments that would be required if simulation is not used.

Figure 8.75 provides another view that indicates how theory, simulated experiments, and real experiments are linked in modern development procedures. The forward arrows indicate the basic sequence of development activities as outlined in the previous paragraph. The reverse arrows indicate that information is fed back to allow simulator calibration and assumption testing. Subsets of this view correspond to other development methodologies. For example, eliminating simulation results in a "traditional" development methodology, in which analytic theory and scaling arguments are used to bracket a design space that is then searched experimentally. Eliminating theory results in a black-box-simulation-reliant development methodology that will usually be inefficient in its search of an unconstrained design space.

Similar approaches can be used to develop application protocols for the other uses of TCAD.

Conclusions

Technology CAD provides benefits associated with faster development times, lower development costs, enhanced physical insight, and the encapsulation and integration of expert knowledge. These benefits are especially important in the context of high-performance, high-volume, consumer-oriented applications. Technology CAD is very well established as an integral part of the procedures used to develop silicon VLSI technologies, and is assuming an important role in the development of semiconductor technologies for RF, microwave, and millimeter-wave applications.

Although the benefits of using TCAD can be very great, achieving the benefits is not easy. Some of the challenges, such as the definition of physical models, model parameters, calibration procedures, and application protocols, are primarily technical in nature. Other challenges, such as a shortage of trained manpower able to apply TCAD effectively, are associated with economic and social factors. Companies that are able to overcome these challenges can obtain a competitive advantage. Conversely, companies that do not deploy TCAD effectively can expect to find themselves at a competitive disadvantage.

Buris, Nicholas E. et al. "Underlying Physics"
The RF and Microwave Handbook
Editor in Chief Mike Golio
Boca Raton: CRC Press LLC,2001

9

Underlying Physics

Nicholas E. Buris
Motorola Labs

Matthew Sadiku
Avaya Inc.

W.R. Deal
Malibu Networks, Inc.

Vesna Radisic
HRL Laboratories, LLC

Y. Qian
University of California

T. Itoh
University of California

Wayne E. Stark
University of Michigan

Alfy Riddle
Macallan Consulting

Mike Golio
Rockwell Collins

K.F. Etzold
IBM Thomas J. Watson Research Center

Mike Harris
Georgia Tech Research Institute

9.1 Maxwell's Equations

Nicholas E. Buris

Microwaves and RF is a branch of electrical engineering that deals ultimately with special cases of the physics of electrically charged particles and their interactions via electromagnetic waves. The fundamental branch of science describing the physics of electrically charged particles is electromagnetism. Electromagnetism deals with the electromagnetic force and is based on the concept of electric and magnetic vector fields, $\boldsymbol{E}(\boldsymbol{r}, t)$ and $\boldsymbol{H}(\boldsymbol{r}, t)$, respectively. The fields $\boldsymbol{E}(\boldsymbol{r}, t)$ and $\boldsymbol{H}(\boldsymbol{r}, t)$ were first introduced to resolve the issues of the "action at a distance" experienced between charges. Maxwell's equations are four coupled partial differential equations describing the electromagnetic field in terms of its sources, the charges, and their associated currents (charges in motion). Electromagnetic waves are one special solution of Maxwell's equations that microwave engineering is built upon. In engineering, of course, depending on the technology of interest, we deal with a full range of special circumstances of electromagnetism. At one end of the spectrum are applications such as solid state devices where electromagnetics is applied to just a few charges, albeit in a phenomenological sense and in conjunction with quantum mechanics. In this realm the forces on individual charges are important. At the other end we have applications where the wavelength of the electromagnetic waves is much smaller than the dimensions of the problem and electromagnetics is reduced to optics where only simple, plane wave phenomena are at play. In the middle of the spectrum, we deal with structures whose size is comparable to the wavelength and electromagnetics is treated as a rigorous mathematical boundary value problem. The majority of microwave applications is somewhat in the middle of this spectrum with some having connections to either end. When studying time harmonic events in microwaves, the frequency domain version of Maxwell's equations is very convenient. In the frequency domain, we have developed a number of high level descriptions of electromagnetic phenomena and several specialized disciplines such as circuits, filtering, antennas, and others have been created to efficiently address the engineering problems at hand. This section of the handbook will describe Maxwell's equations and their solution in order to establish the connection between the various microwave and RF topics and their basic physics, electromagnetism.

Time Domain Differential Form of Maxwell's Equations

As implied earlier, the fundamental description of the physics involved in the study of microwaves and RF is based on the concept of electric and magnetic vector fields, $\boldsymbol{E}(\boldsymbol{r}, t)$ and $\boldsymbol{H}(\boldsymbol{r}, t)$, respectively. According to the well-known Helmholtz's theorem, any vector field can be uniquely specified in terms of its rotation (curl) and divergence components [3]. Maxwell's equations in vacuum essentially define the sources of the curl and divergence of $\boldsymbol{E}$ and $\boldsymbol{H}$. in the International System of units (SI) these equations take the following form:

$$\nabla \times \mathbf{E} = -\mathbf{J}_m - \mu_o \frac{\partial \mathbf{H}}{\partial t} \tag{9.1}$$

$$\nabla \cdot \mathbf{E} = \frac{\rho_e}{\varepsilon_o} \tag{9.2}$$

$$\nabla \times \mathbf{H} = \mathbf{J}_e + \varepsilon_o \frac{\partial \mathbf{E}}{\partial t} \tag{9.3}$$

$$\nabla \cdot \mathbf{H} = \frac{\rho_m}{\mu_o} \tag{9.4}$$

where the constants ε_o and μ_o are the permittivity and permeability of vacuum, ρ_e and $\boldsymbol{J}_e$ are the electric charge and current densities, and ρ_m and $\boldsymbol{J}_m$ are the magnetic charge and current densities.

Equations (9.1) through (9.4) indicate that, in addition to the charges and the currents, time variation in one field serves as a source to the other. In that sense, in microwaves, dealing with high frequency harmonic time variations, the electric and magnetic fields are always coupled and we refer to them combined as the electromagnetic field. It is interesting to note that Maxwell developed his equations by abstraction and generalization from a number of experimental laws that had been discovered previously. Up to Maxwell's time, electromagnetism was a collection of interesting experimental and theoretical laws from Coulomb, Gauss, Faraday, and others. Maxwell, in 1864, combined and extended all these into a remarkably complete system of equations thus founding the science of electromagnetism. Maxwell's generalizations helped start and propel work in electromagnetic waves, and also facilitated the introduced of the special theory of relativity. Interestingly, Maxwell's equations were not covariant under a Galilean transformation (observer moving with respect to the environment). However, after the postulates of the special theory of relativity, no modification of any kind was needed to Maxwell's equations. The speed of light, derived from the wave solutions to Maxwell's equations, is a constant for all inertial frames of reference.

As mentioned above, the electromagnetic fields are a conceptual contraption, the result of an effort to systematically describe how electrically charged particles move. Maxwell's equations describe the field in terms of its sources but they do not describe how the charges move. The motion of charges is governed by Coulomb's law. The force, ***F***, on an electric charge, q, moving with velocity v inside an electromagnetic field is

$$\mathbf{F} = q\mathbf{E} + q\mu_o \mathbf{v} \times \mathbf{H}$$

A very important assumption made here is that the charge q is a test charge. That is, small enough that it does not alter the field in which it exists. The problem of the self fields of charges cannot be solved by classical means, but only through quantum electrodynamics [12]. The fields themselves cannot be measured directly. It is through their effects on charges particles that they are experienced. In most microwave applications we do not see Coulomb's force because we seldom deal with just a few particles. Instead, we devised complicated quantities such as voltage, impedance, and others to arrive at efficient engineering designs.

Some Comments on Maxwell's Equations

Because the divergence of the curl of any vector is identically equal to zero, combining Eqs. (9.2) and (9.3) results in the current continuity equation (charges conservation), i.e.,

$$\nabla \cdot \mathbf{J}_e + \frac{\partial \rho_e}{\partial t} = 0 \tag{9.5a}$$

Similarly,

$$\nabla \cdot \mathbf{J}_m + \frac{\partial \rho_m}{\partial t} = 0 \tag{9.5b}$$

This is a peculiar fact, as the continuity equation is somewhat of a statement on the nature of the field sources, and as such, one would not expect it to be an intrinsic property of Maxwell's equations.

Another peculiar property of Maxwell's equations is that they are covariant under a duality transformation (see part on duality later in this section). Critical quantities quadratic in the fields, remain invariant under such a transformation. Under the proper choice of a duality transformation, Eqs. (9.1) through (9.4) can be made to have only electric, or only magnetic sources. Therefore, the question of whether magnetic sources exist is equivalent to whether the ratio of electric to magnetic sources is the same for all charged particles [6]. Again, this is another statement related to the structure of the field sources and it is rather peculiar that it should be contained in Maxwell's equations. In microwaves, we frequently analyze problems where we consider both electric and magnetic sources to be present. The concept of duality is used extensively to simplify certain problems where apertures are significant parts of the geometry at hand.

Frequency Domain Differential Form of Maxwell's Equations

It is customary to restrict investigation of Maxwell equations to the case where the time variations are harmonic, adopting the phasor convention $e^{j\omega t}$ where ω represents the angular frequency. According to this convention, $\boldsymbol{E}(\boldsymbol{r}, t) = \text{Re}\{\mathbf{E}(\mathbf{r},\omega)\, e^{j\omega t}\}$. Similar expressions hold for all scalar and vector quantities. We say that $\boldsymbol{E}(\boldsymbol{r}, t)$ is the time domain representation of the field while $\mathbf{E}(\mathbf{r},\omega)$ is the phasor, or frequency domain representation. This convention simplifies the mathematics of the partial differential equations with respect to time, reducing time derivatives to simple multiplication by $j\omega$. It should be noted, however, that the product of two harmonic signals in the time domain does not correspond to the product of their phasors.

To effectively treat complicated materials such as dielectrics, ferrites, and others, the electric and magnetic flux density vector fields are introduced, $\mathbf{D}(\mathbf{r},\omega)$ and $\mathbf{B}(\mathbf{r},\omega)$, respectively. These fields essentially account for complicated material mechanisms such as losses and memory (dispersion), in a phenomenological way. They represent average field quantities when large quantities of particles are present. In fact, in the Gaussian system of units, **E** and **D** have the same units and so do **H** and **B**. To 1st order approximation, for example, $\mathbf{D}(\mathbf{r},\omega)$, the electric flux density field in a dielectric equals the externally applied electric field plus the field due to the dipole moment, created by the atoms being "stretched" by the external field. Similar arguments could be made for the magnetic field flux density, although to be correct, quantum mechanical considerations are needed for a more satisfying explanation. Additional discussions on materials will be made in the sections to follow. Maxwell's equations in complicated media and in the frequency domain become

$$\nabla \times \mathbf{E} = -\mathbf{J}_m - j\omega\mathbf{B} \tag{9.6a}$$

$$\nabla \cdot \mathbf{D} = \rho_e \tag{9.6b}$$

$$\nabla \times \mathbf{H} = \mathbf{J}_e + j\omega\mathbf{D} \tag{9.6c}$$

$$\nabla \cdot \mathbf{B} = \rho_m \tag{9.6d}$$

with the constitutive relations

$$\mathbf{D} = \bar{\bar{\varepsilon}} \cdot \mathbf{E} \tag{9.7}$$

and

$$\mathbf{B} = \bar{\bar{\mu}} \cdot \mathbf{H} \tag{9.8}$$

and with the continuity equations

$$\nabla \cdot \mathbf{J}_e + j\omega\rho_e = 0 \tag{9.9}$$

$$\nabla \cdot \mathbf{J}_m + j\omega\rho_m = 0 \tag{9.10}$$

In this formulation, $\bar{\bar{\mu}}$ and $\bar{\bar{\varepsilon}}$ are the generalizations of the parameters ε_o and μ_o and they can be complex, tensorial functions of frequency. There are also some rare materials for which the constitutive relations are even more general. For a simplified, molecular level derivation of ε for dielectrics, see the text by Jackson [5].

To study inhomogeneous materials, we need proper boundary conditions to govern the behavior of the fields across the interface between two media. Consider such an interface as depicted in Fig. 9.1.

Equations (9.1) through (9.4) are associated with the following boundary conditions (derivable from Maxwell's equations themselves).

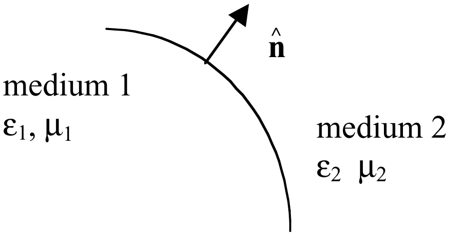

FIGURE 9.1 Geometry for the boundary conditions at the interface between two media.

$$\hat{n}\cdot\left(\mathbf{D}_2-\mathbf{D}_1\right)=\rho_{es} \tag{9.11a}$$

$$\hat{n}\cdot\left(\mathbf{B}_2-\mathbf{B}_1\right)=\rho_{ms} \tag{9.11b}$$

$$-\hat{n}\times\left(\mathbf{E}_2-\mathbf{E}_1\right)=\mathbf{J}_{ms} \tag{9.11c}$$

$$-\hat{n}\times\left(\mathbf{H}_2-\mathbf{H}_1\right)=\mathbf{J}_{es} \tag{9.11d}$$

where $\hat{n}$ is the unit vector normal to the interface pointing from medium 1 to medium 2. The quantities ρ_{es}, $\mathbf{J}_{es}$, ρ_{ms}, and $\mathbf{J}_{ms}$, represent the free electric and magnetic charge and current surface densities on the interface, respectively. Note that these are free sources, and as such, only exist on conductors and are equal to zero on the interface between two dielectric media. There are bound (polarization) charges on dielectric interfaces, but they are accounted for by Eq. (9.11a) and the constitutive relation in Eq. (9.7).

General Solution to Maxwell's Equations (the Stratton–Chu Formulation)

One of the most comprehensive solutions to Maxwell's equations in a general homogeneous and isotropic domain is given by Stratton and Chu [1] and is also further discussed by Silver [2]. Consider a volume V with a boundary consisting of a collection of closed surfaces, S_1, S_2, …, S_n. Next consider the unit vectors, $\hat{n}$, normal to the boundary surface with direction pointing inside the volume of interest as depicted in Fig. 9.2. The volume V is occupied uniformly by a material with dielectric constant ε, and magnetic permeability μ. Inside V there exist electric and magnetic charge and current density distributions, ρ_e, $\mathbf{J}_e$, ρ_m, and $\mathbf{J}_m$, respectively.

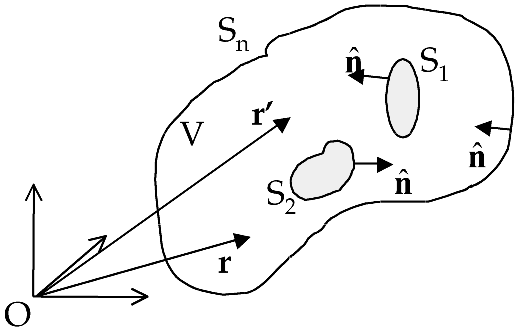

FIGURE 9.2 The volume of interest and its boundary surface consisting of $S_1 + S_2 + \ldots + S_n$.

The electric and magnetic fields at an arbitrary point, **r**, inside V are then given in terms of the sources and the values of the fields at the boundary by the following equations.

$$\begin{aligned}\mathbf{E}(\mathbf{r}) = &-\int_V \left[j\omega\mu G(\mathbf{r},\mathbf{r}')\mathbf{J}_e(\mathbf{r}') + \mathbf{J}_m(\mathbf{r}') \times \nabla' G - \frac{\rho_e(\mathbf{r}')}{\varepsilon}\nabla' G \right] dV' \\ &- \int_{S_1+S_2+\cdots+S_n} \left[j\omega\mu G(\mathbf{r},\mathbf{r}')\left(\hat{n}' \times \mathbf{H}(\mathbf{r}')\right) + \left(-\hat{n}' \times \mathbf{E}(\mathbf{r}')\right) \times \nabla' G - \left(\hat{n}' \cdot \mathbf{E}(\mathbf{r}')\right)\nabla' G \right] dS'\end{aligned} \tag{9.12}$$

and

$$\begin{aligned}\mathbf{H}(\mathbf{r}) = &-\int_V \left[j\omega\varepsilon G(\mathbf{r},\mathbf{r}')\mathbf{J}_m(\mathbf{r}') - \mathbf{J}_e(\mathbf{r}') \times \nabla' G - \frac{\rho_m(\mathbf{r}')}{\mu}\nabla' G \right] dV' \\ &- \int_{S_1+S_2+\cdots+S_n} \left[j\omega\varepsilon G(\mathbf{r},\mathbf{r}')\left(-\hat{n}' \times \mathbf{E}(\mathbf{r}')\right) - \left(\hat{n}' \times \mathbf{H}(\mathbf{r}')\right) \times \nabla' G - \left(\hat{n}' \cdot \mathbf{H}(\mathbf{r}')\right)\nabla' G \right] dS'\end{aligned} \tag{9.13}$$

where

$$G(\mathbf{r},\mathbf{r}') = \frac{e^{-jk\left|\mathbf{r}-\mathbf{r}'\right|}}{4\pi\left|\mathbf{r}-\mathbf{r}'\right|} \tag{9.14}$$

is called the free space Green's function and

$$k = \sqrt{\omega^2\mu\varepsilon} \tag{9.15}$$

is called the wavenumber with ω representing the angular frequency.

When the surface S_n is at infinity, it can be shown that the fields there satisfy the radiation conditions (**E** and **H** attenuate at least as fast as 1/r, they are perpendicular to each other, and to **r**, and their magnitudes are related by the wave impedance, $\sqrt{\mu/\varepsilon}$). Moreover, the continuity equations can be employed to eliminate ρ_e and ρ_m from the field solution. When the volume V is unbounded ($S_n \to$ infinity) and the charges are substituted by their current density expressions, the solution of Maxwell's equations becomes

$$\mathbf{E}(\mathbf{r}) = -\frac{j}{\omega\varepsilon}\int_V \left[\left(\mathbf{J}_e(\mathbf{r}') \cdot \nabla'\right)\nabla' + k^2\,\mathbf{J}_e(\mathbf{r}') - j\omega\varepsilon\,\mathbf{J}_m(\mathbf{r}') \times \nabla' \right] G(\mathbf{r},\mathbf{r}')\,dV' \tag{9.16}$$

and

$$\mathbf{H}(\mathbf{r}) = -\frac{j}{\omega\mu}\int_V \left[\left(\mathbf{J}_m(\mathbf{r}') \cdot \nabla'\right)\nabla' + k^2\,\mathbf{J}_m(\mathbf{r}') + j\omega\mu\,\mathbf{J}_e(\mathbf{r}') \times \nabla' \right] G(\mathbf{r},\mathbf{r}')\,dV'. \tag{9.17}$$

These forms of the fields are used routinely for the numerical solution to Maxwell's equations, particularly using the method of moments.

It should be noted here that in the special case where the boundary surfaces $S_1, S_2, \ldots, S_{n-1}$ are perfect electric conductors, the field solution can be expressed by Eqs. (9.12) and (9.13), or their unbounded counterparts, Eqs. (9.16) and (9.17) provided one recognizes that the free currents on an electric conductor are $\hat{n} \times \mathbf{H}$ and the charges are $\hat{n} \cdot \mathbf{D}$. From the materials point of view (also discussed later in this chapter) a perfect conductor has unlimited capacity to provide free charges that distribute themselves on its surface in such a way as to effectively eliminate their internal fields regardless of the external field they are in. Therefore, since the fields vanish inside, perfect conductors have no energy in them. They simple shape and guide the energy in the space around them. Thus, a coil has no energy inside its metal, it simply stores energy inside and outside its windings. In this light, electromagnetic design of especially small, densely populated electronic structures is very difficult and suffers from potential ElectroMagnetic Interference (EMI) problems.

Far Field Approximation

At the limit where the observation point is at infinity (r → ∞, far field) it can be shown that Eqs. (9.16) and (9.17) simplify to

$$\mathbf{E}(\mathbf{r}) = -j\omega\mu \frac{e^{-jkr}}{4\pi r} \int_V \left[\mathbf{J}_e(\mathbf{r}') - \left(\hat{\mathbf{r}} \cdot \mathbf{J}_e(\mathbf{r}')\right)\hat{\mathbf{r}} + \sqrt{\frac{\varepsilon}{\mu}}\, \mathbf{J}_m(\mathbf{r}') \times \hat{\mathbf{r}}' \right] e^{jk\hat{\mathbf{r}}\cdot\mathbf{r}'}\, d \tag{9.18}$$

with

$$\mathbf{H}(\mathbf{r}) = \sqrt{\frac{\varepsilon}{\mu}}\, \hat{\mathbf{r}} \times \mathbf{E}(\mathbf{r}). \tag{9.19}$$

$\mathbf{E}(\mathbf{r})$ and, consequently, $\mathbf{H}(\mathbf{r})$ in Eqs. (9.18) and (9.19) have zero radial components and can be found often in the following, more practical forms.

$$\mathbf{E}_\theta(\mathbf{r}) = -j\omega\mu \frac{e^{-jkr}}{4\pi r} \int_V \left[\mathbf{J}_\theta(\hat{\mathbf{r}}') + \sqrt{\frac{\varepsilon}{\mu}}\, \mathbf{J}_{m_\phi}(\mathbf{r}') \right] e^{jk\hat{\mathbf{r}}\cdot\mathbf{r}'}\, dV' \tag{9.20}$$

and

$$\mathbf{E}_\phi(\mathbf{r}) = -j\omega\mu \frac{e^{-jkr}}{4\pi r} \int_V \left[\mathbf{J}_\phi(\mathbf{r}') - \sqrt{\frac{\varepsilon}{\mu}}\, \mathbf{J}_{m_\theta}(\mathbf{r}') \right] e^{jk\hat{\mathbf{r}}\cdot\mathbf{r}'}\, dV' \tag{9.21}$$

or, equivalently,

$$\mathbf{E}_\theta(\mathbf{r}) = -j\omega\mu \frac{e^{-jkr}}{4\pi r} \int_V \left[\mathbf{J}_x \cos\theta\cos\phi + \mathbf{J}_y \cos\theta\sin\phi - \mathbf{J}_z \sin\theta + \sqrt{\frac{\varepsilon}{\mu}} \left(-\mathbf{J}_{m_x} \sin\phi + \mathbf{J}_{m_y} \cos\phi \right) \right] e^{jk\hat{\mathbf{r}}\cdot\mathbf{r}'}\, dV' \tag{9.22}$$

and

$$\mathbf{E}_\phi(\mathbf{r}) = -j\omega\mu \frac{e^{-jkr}}{4\pi r} \int_V \left[-\mathbf{J}_x \sin\phi + \mathbf{J}_y \cos\phi - \sqrt{\frac{\varepsilon}{\mu}} \left(\mathbf{J}_{m_x} \cos\theta\cos\phi + \mathbf{J}_{m_y} \cos\theta\sin\phi - \mathbf{J}_{m_z} \sin\theta \right) \right] e^{jk\hat{\mathbf{r}}\cdot\mathbf{r}'}\, dV' \tag{9.23}$$

where it also holds that

$$H_\phi = \sqrt{\frac{\varepsilon}{\mu}}\, E_\theta \tag{9.24}$$

and

$$H_\theta = \sqrt{\frac{\varepsilon}{\mu}}\, E_\phi . \tag{9.25}$$

These solutions to Maxwell's equations can also be derived via a potential field formulation. The interested reader can refer to the treatment in Harrington [10] and Balanis [7].

General Theorems in Electromagnetics

Uniqueness of Solution

It can be shown that the field in the volume V, depicted in Fig. 9.2, is uniquely defined by the source distributions in it and the values of the tangential electric field, or tangential magnetic field on all the boundary surfaces, S_1, S_2, …, S_n. Uniqueness is also guaranteed when the tangential **E** is specified for part of the boundary while tangential **H** is specified for the remaining part. A detailed discussion of the uniqueness of the solution can be found in Stratton [9].

Duality

As briefly mentioned earlier, Maxwell's equations are covariant under duality transformations. Consider the transformation,

$$\begin{pmatrix} \mathbf{E} \\ \mathbf{H} \end{pmatrix} = \begin{bmatrix} \cos\xi & \sin\xi \\ -\sin\xi & \cos\xi \end{bmatrix} \cdot \begin{pmatrix} \mathbf{E}' \\ \mathbf{H}' \end{pmatrix} \tag{9.26}$$

$$\begin{pmatrix} \mathbf{D} \\ \mathbf{B} \end{pmatrix} = \begin{bmatrix} \cos\xi & \sin\xi \\ -\sin\xi & \cos\xi \end{bmatrix} \cdot \begin{pmatrix} \mathbf{D}' \\ \mathbf{B}' \end{pmatrix} \tag{9.27}$$

$$\begin{pmatrix} \mathbf{J}_e \\ \mathbf{J}_m \end{pmatrix} = \begin{bmatrix} \cos\xi & \sin\xi \\ -\sin\xi & \cos\xi \end{bmatrix} \cdot \begin{pmatrix} \mathbf{J}'_e \\ \mathbf{J}'_m \end{pmatrix} \tag{9.28}$$

and

$$\begin{pmatrix} \rho_e \\ \rho_m \end{pmatrix} = \begin{bmatrix} \cos\xi & \sin\xi \\ -\sin\xi & \cos\xi \end{bmatrix} \cdot \begin{pmatrix} \rho'_e \\ \rho'_m \end{pmatrix} \tag{9.29}$$

It can be easily shown that under this duality transformation, Maxwell's equations are covariant. That is, if the primed fields satisfy Maxwell's equations with the primed sources, the non-primed fields satisfy Maxwell's equations with the non-primed sources. Moreover, critical quantities quadratic in the fields, such as $\mathbf{E} \times \mathbf{H}$ and $\mathbf{E} \cdot \mathbf{D} + \mathbf{B} \cdot \mathbf{H}$ remain invariant under this duality transformation (for real ξ). That is, for example, $\mathbf{E} \times \mathbf{H} = \mathbf{E}' \times \mathbf{H}'$ [6]. As a special case of this property, $\xi = -\pi/2$, we have the following correspondence.

$$\begin{aligned} \mathbf{E} &\leftrightarrow -\mathbf{H} \\ \mathbf{H} &\leftrightarrow \mathbf{E} \\ \mathbf{J}_m &\leftrightarrow \mathbf{J}_e \\ \rho_m &\leftrightarrow \rho_e \\ \mu &\leftrightarrow \varepsilon \\ \varepsilon &\leftrightarrow \mu \end{aligned}$$

It is worth mentioning here that, since the fields themselves cannot be measured, and since all the important quantities (such as the power and energy terms, $\mathbf{E} \times \mathbf{H}$ and $\mathbf{E} \cdot \mathbf{D} + \mathbf{B} \cdot \mathbf{H}$) remain invariant under duality, it is just a matter of convenience which of several possible dual solutions to an electromagnetic problem we consider. This is precisely the reason why in some antenna problems, for example, one can formulate them with electric currents on the conductors, or with magnetic currents on the apertures and obtain the same detectable (measurable) results.

Lorentz Reciprocity Theorem

Consider the fields $\mathbf{E}_1$ and $\mathbf{H}_1$, generated by the system of sources $\mathbf{J}_{e1}$ and $\mathbf{J}_{m1}$ and the fields $\mathbf{E}_2$ and $\mathbf{H}_2$, generated by the system of sources $\mathbf{J}_{e2}$ and $\mathbf{J}_{m2}$. Then it can be shown that [8]

$$\oiint_S \left(\mathbf{E}_1 \times \mathbf{H}_2 - \mathbf{E}_2 \times \mathbf{H}_1\right) \cdot d\mathbf{S} = \int_V \left(\mathbf{H}_1 \cdot \mathbf{J}_{m2} - \mathbf{E}_1 \cdot \mathbf{J}_{m2} - \mathbf{H}_2 \cdot \mathbf{J}_{m1} + \mathbf{E}_2 \cdot \mathbf{J}_{e1}\right) dV \tag{9.30}$$

As a special case of this theorem, consider the open volume of interest V and two sources in it, $\mathbf{J}_{e1}$ and $\mathbf{J}_{e2}$. When $\mathbf{J}_{e1}$ is present alone, it generates the field $\mathbf{E}_1$. When $\mathbf{J}_{e2}$ is present alone, it generates the field $\mathbf{E}_2$. Lorentz' reciprocity theorem as stated by Eq. (9.30) implies that

$$\mathbf{E}_1 \cdot \mathbf{J}_{e2} = \mathbf{E}_2 \cdot \mathbf{J}_{e1} \tag{9.31}$$

The reciprocity theorem is used frequently in electromagnetic problem studies to facilitate solution of complicated problems. One well-known application of reciprocity has been in the expressions of the mutual and self-impedance of simple radiators. Reciprocity also manifests itself in some linear circuits so that Eq. (9.13) above holds when the electric fields and the current densities are replaced by voltages and currents, respectively. For details of this property see the text by Valkenburg [13].

Equivalent Principles (Theory of Images)

Equivalent principles are used to describe the electromagnetic field problem in a volume of interest in more than one configuration of sources. While the volume of interest is the same in all the equivalent configurations (materials, geometry, and source distributions), the geometry outside the volume of interest is different for each equivalent configuration. A detailed discussion of field equivalence principles can be found in Collin [8]. Here only the method of images is mentioned. The method of images is based on the uniqueness of the field. Namely, as long as the sources inside the volume of interest, V, and the boundary conditions on S_1, S_2, … remain the same, the fields inside V are unique regardless of what sources exist outside V.

The method of images is based on this principle. Its applicability is limited to just a few canonical geometries. Consider for example, a current-carrying wire over an infinite perfect electric conductor, as shown in Fig. 9.3(a). The tangential electric field is zero on the pec ground plane. Next consider the configuration (b) where the ground plane has been removed and the volume below it has a second current-carrying wire, shaped in the mirror image of the original and with an opposite direction for the

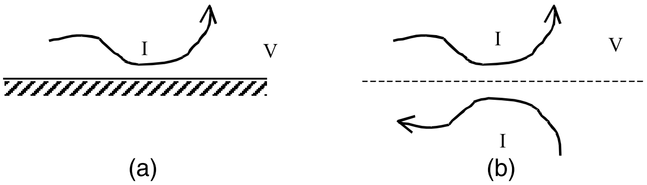

FIGURE 9.3 The fields in V are identical for both configurations, (a) and (b). The fields outside V vanish in (a) while they are certainly nonzero in (b).

current. It can be shown with simple symmetry arguments that the tangential electric field on the dashed line (where the ground plane used to be) in configuration (b) vanishes. Therefore, since (a) and (b) are identical within V and they have the same boundary conditions (zero tangential electric field) on the boundary, the fields inside V are the same.

Clearly, it is much easier to numerically evaluate the solution in configuration (b) than that of configuration (a). Images are very often used in electromagnetic problems when appropriate. It is often easy to extend the theory of images to current-carrying wires in the presence of corners of ground planes. Moreover, there have been several studies to extend the theory of images to more complex geometries [11]. However, the complexity of the images quickly escalates diminishing the benefits of removing the ground planes.

Simple Solution to Maxwell's Equations I (Unbounded Plane Waves)

In electromagnetics, a homogeneous and isotropic region of space with no sources in it is called free space. In free space, $\bar{\bar{\mu}} = \mu_o$, $\bar{\bar{\varepsilon}} = \varepsilon_o$ and Eqs. (9.6a) through (9.6d) decouple giving rise to the following second order wave equations.

$$\nabla^2 \mathbf{E} + \omega^2 \mu_o \varepsilon_o \mathbf{E} = 0 \tag{9.32}$$

$$\nabla^2 \mathbf{H} + \omega^2 \mu_o \varepsilon_o \mathbf{H} = 0 \tag{9.33}$$

Applying separation of variables, Eqs. (9.32) and (9.33) are found to have plane wave solutions of the form

$$\mathbf{E} = \mathbf{E}_o^+ e^{-j\mathbf{k}\cdot\mathbf{r}} + \mathbf{E}_o^- e^{+j\mathbf{k}\cdot\mathbf{r}} \tag{9.34}$$

$$\mathbf{H} = \mathbf{H}_o^+ e^{-j\mathbf{k}\cdot\mathbf{r}} + \mathbf{H}_o^- e^{+j\mathbf{k}\cdot\mathbf{r}} \tag{9.35}$$

The electromagnetic wave propagating in the +**k** direction ($e^{-j\mathbf{k}\cdot\mathbf{r}}$) travels with the speed of light, $1/(\mu_o\varepsilon_o)^{1/2}$ and has a wave impedance,

$$\left|\frac{\mathbf{E}_o^+}{\mathbf{H}_o^+}\right| = \sqrt{\frac{\mu_o}{\varepsilon_o}}. \tag{9.36}$$

The wave number, k, obeys the relation

$$k = \frac{\omega}{c} = \omega\sqrt{\mu_o \varepsilon_o} \tag{9.37}$$

where c is the speed of light. It can be shown that the power density carried by the plane wave is along the direction of propagation, k, and its average value over one period is given by the Poynting vector

$$\mathbf{S}^{+} = \frac{1}{2}\mathbf{E}_{o}^{+} \times \mathbf{H}_{o}^{+} \tag{9.38}$$

where the fields **E** and **H** are represented by their amplitude values in the phasor convention. It is worth noting that the Poynting vector itself is not a phasor. Being the product of two harmonic signals, the power density represented by the Poynting vector has a steady (DC) component and a harmonic component of twice the frequency of the electromagnetic field. The DC component of the Poynting vector is exactly given by Eq. (9.38). Similar discussions hold for the wave propagating in the –**k** direction. These wave solutions obey all the usual wave phenomena of reflection and refraction when incident on interfaces between two different media. For detailed discussions on these phenomena and more general cases of wave solutions to Maxwell's equations, the reader is referred to the following sections of this chapter and the text by Collin [8].

Simple Solution to Maxwell's Equations II (Guided Plane Waves)

It is possible to have electromagnetic waves inside cavities and waveguides. A waveguide is any structure that supports waves traveling in one direction and confined in the transverse plane by its boundaries. A rectangular duct made out of a conductor and a coaxial cable are waveguides with closed boundaries. A twin lead transmission line, or a dielectric plated conductor are among the many open boundary waveguides. Waves supported by waveguides are special solutions to Maxwell's equations.

Let us consider a waveguide along the z axis. We are looking for solutions to Maxwell's equations that represent waves traveling along z. That is, we are looking for solutions in the form:

$$\mathbf{E} = \mathbf{E}(x,y)e^{-j\beta z} = \left(\mathbf{E}_t(x,y) + \hat{\mathbf{z}}E_z(x,y)\right)e^{-j\beta z} \tag{9.39}$$

and

$$\mathbf{H} = \mathbf{H}(x,y)e^{-j\beta z} = \left(\mathbf{H}_t(x,y) + \hat{\mathbf{z}}\mathbf{H}_z(x,y)\right)e^{-j\beta z} \tag{9.40}$$

where $\mathbf{E}_t$ and $\mathbf{H}_t$ are vectors in the transverse, (x,y) plane. Solving Eq. (9.6) in a region of space free from any sources and looking specifically for solutions in the form of Eqs. (9.39) and (9.40) reduces the problem to the following wave equations:

$$\nabla_t^2 E_z + \left(\omega^2\mu\varepsilon - \beta^2\right)E_z = 0 \tag{9.41}$$

and

$$\nabla_t^2 H_z + \left(\omega^2\mu\varepsilon - \beta^2\right)H_z = 0 \tag{9.42}$$

The transverse fields are given in terms of the axial components of the waves as

$$E_t(x,y) = \frac{1}{k^2 - \beta^2}\left(-j\beta\nabla_t E_z(x,y) + j\omega\mu\,\hat{\mathbf{z}} \times \nabla H_z(x,y)\right) \tag{9.43}$$

and

$$\mathbf{H}_t\left(x,y\right)=\frac{1}{k^2-\beta^2}\left(-j\beta\nabla_t H_z\left(x,y\right)-j\omega\varepsilon\,\hat{\mathbf{z}}\times\nabla E_z\left(x,y\right)\right) \tag{9.44}$$

∇_t in the above equations stands for the transverse del operator, i.e., $\nabla_t = \hat{\mathbf{x}}\ \partial/\partial x + \hat{\mathbf{y}}\ \partial/\partial y$.

The wave number of the guided wave, β, is, in general, different from the wave number in the medium ($k^2 = \omega^2\mu\varepsilon$). The wave number is determined when the boundary condition specific to the waveguide are applied. There are some special cases of these guided wave solutions that are examined at a later section in this chapter in much more detail for practical microwave waveguides.

TEM Modes

$$E_z = H_z = 0$$

$$\nabla_t \times \mathbf{E}_t = 0 \quad \beta^2 = k^2 = \omega^2\mu\varepsilon \quad \text{and} \quad \mathbf{H} = \sqrt{\frac{\varepsilon}{\mu}}\left(\hat{\mathbf{z}}\times\mathbf{E}_t\right)$$

TM Modes

$$E_z \neq 0; \quad H_z = 0$$

$$\nabla_t^2 E_z + \left(\omega^2\mu\varepsilon - \beta^2\right)E_z = 0 \quad \mathbf{E}_t\left(x,y\right) = \frac{-j\beta}{k^2-\beta^2}\nabla_t E_z\left(x,y\right) \quad \text{and} \quad \mathbf{H}_t = -\frac{\omega\varepsilon}{\beta}\mathbf{E}_t \times \hat{\mathbf{z}}$$

TE Modes

$$H_z \neq 0; \quad E_z = 0$$

$$\nabla_t^2 H_z + \left(\omega^2\mu\varepsilon - \beta^2\right)H_z = 0 \quad \mathbf{H}_t(x,y) = \frac{-j\beta}{k^2-\beta^2}\nabla_t H_z(x,y) \quad \text{and} \quad \mathbf{E}_t = \frac{\omega\mu}{\beta}\mathbf{H}_t \times \hat{\mathbf{z}}$$

References

1. J.A. Stratton and L.J. Chu, *Phys. Res.,* 56, 99, 1939.
2. S. Silver, Ed., *Microwave Antenna Theory and Design,* McGraw-Hill, New York, 1949, chap. 3.
3. G. Arfken, *Mathematical Methods for Physicists,* 2nd ed., Academic Press, 1970, 66–70.
4. W. Pauli, *Theory of Relativity,* Dover, New York, 1981.
5. J.D. Jackson, *Classical Electrodynamics,* 2nd ed., John Wiley & Sons, New York, 1975, 226–235.
6. J.D. Jackson, *Classical Electrodynamics,* 2nd ed., John Wiley & Sons, New York, 1975, 251–260.
7. C. Balanis, *Advanced Engineering Electromagnetics,* John Wiley & Sons, New York, 1989.
8. R.E. Collin, *Field Theory of Guided Waves,* 2nd ed., *IEEE Press,* 1991.
9. J.A. Stratton, *Electromagnetic Theory,* McGraw-Hill, New York, 1941.
10. R.F. Harrington, *Time-Harmonic Electromagnetic Fields,* McGraw-Hill, New York, 1961.
11. I.V. Lindel, Image Theory for the Soft and Hard Surface, *IEEE Trans. Antenn. Propagat.,* 43, 1, January 1995.
12. R.P. Feynman, R.B. Leighton, and M. Sands, Electromagnetic Mass, in *The Feynman Lectures on Physics,* Addison Wesley, New York, 1964.
13. M.E. Valkenburg, *Network Analysis,* 3rd ed., Prentice-Hall, Englewood Cliffs, NJ, 1974, 255–259.

9.2 Wave Propagation in Free Space

Matthew Sadiku

The concept of propagation refers to the various ways by which an electromagnetic (EM) wave travels from the transmitting antenna to the receiving antenna. Propagation of EM wave may also be regarded as a means of transferring energy or information from one point (a transmitter) to another (a receiver). The transmission of analog or digital information from one point to another is the largest application of microwave frequencies. Therefore, understanding the principles of wave propagation is of practical interest to microwave engineers. Engineers cannot completely apply formulas or models for microwave system design without an adequate knowledge of the propagation issue.

Wave propagation at microwave frequencies has a number of advantages (Veley, 1987). First, microwaves can accommodate very wide bandwidth without causing interference problems because microwave frequencies are so high. Consequently, a huge amount of information can be handled by a single microwave carrier. Second, microwaves propagate along a straight line like light rays and are not bent by the ionosphere as are lower frequency signals. This straight-line propagation makes communication satellites possible. In essence, a communication satellite is a microwave relay station that is used in linking two or more grounded-based transmitters and receivers. Third, it is feasible to design highly directive antenna systems of a reasonable size at microwave frequencies. Fourth, compared with low-frequency electromagnetic waves, microwave energy is more easily controlled, concentrated, and directed. This makes it useful for cooking, drying, and physical diathermy. Moreover, the microwave spectrum provides more communication channels than the radio and TV bands. With the ever-increasing demand for channel allocation, microwave communication has become more common.

EM wave propagation is achieved through guided structures such as transmission lines and waveguides or through space. In this chapter, our major focus is on EM wave propagation in free space and the power resident in the wave.

EM wave propagation can be described by two complimentary models. The physicist attempts a theoretical model based on universal laws, which extends the field of application more widely than currently known. The engineer prefers an empirical model based on measurements, which can be used immediately. This chapter presents the complimentary standpoints by discussing theoretical factors affecting wave propagation and the semiempirical rules allowing handy engineering calculations. First, we consider wave propagation in idealistic simple media, with no obstacles. We later consider the more realistic case of wave propagation around the earth, as influenced by its curvature and by atmospheric conditions.

Wave Equation

The conventional propagation models, on which the basic calculation of microwave links is based, result directly from Maxwell's equations (Sadiku, 2001):

$$\nabla \cdot \mathbf{D} = \rho_v \tag{9.45}$$

$$\nabla \cdot \mathbf{B} = 0 \tag{9.46}$$

$$\nabla \times \mathbf{E} = -\frac{\partial \mathbf{B}}{\partial t} \tag{9.47}$$

$$\nabla \times \mathbf{H} = \mathbf{J} + \frac{\partial \mathbf{D}}{\partial t} \tag{9.48}$$

In these equations, **E** is electric field strength in volts per meter, **H** is magnetic field strength in amperes per meter, **D** is electric flux density in coulombs per square meter, **B** is magnetic flux density in webers per square meter, **J** is conduction current density in ampere per square meter, and ρ_v is electric charge density in coulombs per cubic meter. These equations go hand in hand with the constitutive equations for the medium:

$$\mathbf{D} = \epsilon \mathbf{E} \tag{9.49}$$

$$\mathbf{B} = \mu \mathbf{H} \tag{9.50}$$

$$\mathbf{J} = \sigma \mathbf{E} \tag{9.51}$$

where $\epsilon = \epsilon_o \epsilon_r$, $\mu = \mu_o \mu_r$, and σ are the permittivity, the permeability, and the conductivity of the medium, respectively.

Consider the general case of a lossy medium that is charge-free ($\rho_v = 0$). Assuming time-harmonic fields and suppressing the time factor $e^{j\omega t}$, Eqs. (9.45) to (9.51) can be manipulated to yield Helmholtz's wave equations

$$\nabla^2 \mathbf{E} - \gamma^2 \mathbf{E} = 0 \tag{9.52}$$

$$\nabla^2 \mathbf{H} - \gamma^2 \mathbf{H} = 0 \tag{9.53}$$

where $\gamma = \alpha + j\beta$ is the *propagation constant,* α is the *attenuation constant* in nepers per meter or decibels per meter, and β is the *phase constant* in radians per meter. Constants α and β are given by

$$\alpha = \omega \sqrt{\frac{\mu\epsilon}{2}\left[\sqrt{1 + \left(\frac{\sigma}{\omega\epsilon}\right)^2} - 1\right]} \tag{9.54}$$

$$\beta = \omega \sqrt{\frac{\mu\epsilon}{2}\left[\sqrt{1 + \left(\frac{\sigma}{\omega\epsilon}\right)^2} + 1\right]} \tag{9.55}$$

where $\omega = 2\pi f$ is the frequency of the wave. The wavelength λ and wave velocity u are given in terms of β as

$$\lambda = \frac{2\pi}{\beta} \tag{9.56}$$

$$u = \frac{\omega}{\beta} = f\lambda \tag{9.57}$$

Without loss of generality, if we assume that wave propagates in the z direction and the wave is polarized in the x direction, solving the wave equations (9.52) and (9.53) results in

$$\mathbf{E} = E_o e^{-\alpha z} \cos(\omega t - \beta z)\,\mathbf{a}_x \tag{9.58}$$

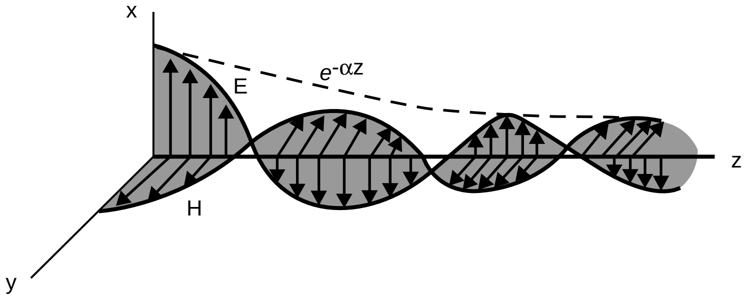

FIGURE 9.4 The magnetic and electric field components of a plane wave in a lossy medium.

$$\mathbf{H} = \frac{E_o}{|\eta|} e^{-\alpha z} \cos\left(\omega t - \beta z - \theta_\eta\right) \mathbf{a}_y \tag{9.59}$$

where $\eta = |\eta| \underline{/\theta_\eta}$ is the *intrinsic impedance* of the medium and is given by

$$|\eta| = \frac{\sqrt{\frac{\mu}{\epsilon}}}{\sqrt[4]{\left[1 + \left(\frac{\sigma}{\omega\epsilon}\right)^2\right]}}, \quad \tan 2\theta_\eta = \frac{\sigma}{\omega\epsilon}, \quad 0 \le \theta_\eta \le 45° \tag{9.60}$$

Equations (9.58) and (9.59) show that as the EM wave propagates in the medium, its amplitude is attenuated according to $e^{-\alpha z}$, as illustrated in Fig. 9.4. The distance δ through which the wave amplitude is reduced by a factor of e^{-1} (about 37%) is called the *skin depth* or *penetration depth* of the medium, i.e.,

$$\delta = \frac{1}{\alpha} \tag{9.61}$$

The power density of the EM wave is obtained from the Poynting vector

$$\mathbf{P} = \mathbf{E} \times \mathbf{H} \tag{9.62}$$

with the time-average value of

$$\begin{aligned} P_{\text{ave}} &= \text{Re}\left(\mathbf{E} \times \mathbf{H}^*\right) \\ &= \frac{E_o^2}{2|\eta|} e^{-2\alpha z} \cos\theta_\eta \mathbf{a}_z \end{aligned} \tag{9.63}$$

It should be noted from Eqs. (9.58) and (9.59) that **E** and **H** are everywhere perpendicular to each other and also to the direction of wave propagation. Thus, the wave described by Eqs. (9.58) and (9.59) is said to be *plane polarized,* implying that the electric field is always parallel to the same plane (the *xz* plane in this case) and is perpendicular to the direction of propagation. Also, as mentioned earlier, the wave decays as it travels in the *z* direction because of loss. This loss is expressed in the *complex relative permittivity* of the medium.

$$\epsilon_c = \epsilon_r' - \epsilon_r'' = \epsilon_r\left(1 - \frac{\sigma}{\omega\epsilon}\right) \tag{9.64}$$

and measured by the *loss tangent,* defined by

$$\tan\delta = \frac{\epsilon_\mathrm{r}''}{\epsilon_\mathrm{r}'} = \frac{\sigma}{\omega\epsilon} \tag{9.65}$$

The imaginary part $\epsilon_r'' = \sigma/\omega\epsilon_o$ corresponds to the losses in the medium. The refractive index of the medium n is given by

$$n = \sqrt{\epsilon_r} \tag{9.66}$$

Having considered the general case of wave propagation through a lossy medium, we now consider wave propagation in other types of media. A medium is said to be a good conductor if the loss tangent is large ($\sigma \gg \omega\epsilon$) or a lossless or good dielectric if the loss tangent is very small ($\sigma \ll \omega\epsilon$). Thus, the characteristics of wave propagation through other types of media can be obtained as special cases of wave propagation in a lossy medium as follows:

1. Good conductors: $\sigma \gg \omega\epsilon$, $\epsilon = \epsilon_o$, $\mu = \mu_o\mu_r$
2. Good dielectrics: $\sigma \ll \omega\epsilon$, $\epsilon = \epsilon_o$, $\mu = \mu_o\mu_r$
3. Free space: $\sigma = 0$, $\epsilon = \epsilon_o$, $\mu = \mu_o$

where $\epsilon_o = 8.854 \times 10^{-11}$ F/m is the free-space permittivity, and $\mu_o = 4\pi \times 10^{-7}$ H/m is the free-space permeability. The conditions for each medium type are merely substituted in Eqs. (9.54) to (9.65) to obtain the wave properties for that medium.

The classical model of wave propagation presented in this section helps us understand some basic concepts of EM wave propagation and the various parameters that play a part in determining the progress of the wave from the transmitter to the receiver. We will apply the ideas to the particular case of wave propagation in free space or the atmosphere in the section on Propagation in the Atmosphere. Before then, we digress a little and consider the important issue of wave polarization.

Wave Polarization

The concept of polarization is an important property of an EM wave that has been developed to described the various types of electric field variation and orientation. It is therefore a common practice to describe an EM wave by its polarization. The polarization of an EM wave depends on the transmitting antenna or source. It is determined by the direction of the electric field. It is regarded as the locus of the tip of the electric field (in a plane perpendicular to the direction of propagation) at a given point in space as a function of time. For this reason, there are four types of polarization: linear or plane, circular, elliptic, and random.

In linear or plane polarized waves, the orientation of the field is constant in space and time. For a plane traveling in the $+z$ direction, the electric field may be written as

$$\mathbf{E}(z,t) = E_x(z,t)\mathbf{a}_x + E_y(z,t)\mathbf{a}_y \tag{9.67}$$

where

$$E_x = \mathrm{Re}\left[E_{ox}e^{j(\omega t - kz + \phi_x)}\right] = E_{ox}\cos(\omega t - kz + \phi_x) \tag{9.68a}$$

$$E_y = \mathrm{Re}\left[E_{oy} e^{j(\omega t - kz + \phi_x)}\right] = E_{oy} \cos(\omega t - kz + \phi_y) \tag{9.68b}$$

For linear polarization, the phase difference between the x and y components must be

$$\Delta\phi = \phi_y - \phi_x = n\pi, \quad n = 0, 1, 2, \dots \tag{9.69}$$

This allows the two components to maintain the same ratio at all times, which implies that the electric field always lies along a straight line in a constant $-z$ plane. In other words, if we observe the wave in the direction of propagation (z in this case), we will notice that the tip of the electric field follows a line. Hence, the term *linear polarization.* Linearly polarized plane waves can be generated by simple antennas (such as dipole antennas) or lasers.

Circular polarized waves are characterized by an electric field with constant magnitude and orientation rotating in a plane transverse to the direction of propagation. Circular polarization takes place when the x and y components are the same in magnitude ($E_x = E_y$) and the phase difference between them is an odd multiple of $\pi/2$, i.e.,

$$\Delta\phi = \phi_y - \phi_x = \pm\left(\frac{1}{2} + 2n\right)\pi, \quad n = 0, 1, 2, \dots \tag{9.70}$$

The two components of the electric field rotate around the axis of propagation as a function of time and space. Circularly polarized waves can be generated by a helically wound wire antenna or by two linear sources that are oriented perpendicular to each other and fed with currents that are out of phase by 90°.

Linear and circular polarizations are special cases of the more general case of the elliptical polarization. An elliptically polarized wave is one in which the tip of the field traces an elliptic locus in a fixed transverse plane as the field changes with time. Elliptical polarization is achieved when the x and y components are not equal in magnitude ($E_x \neq E_y$) and the phase difference between them is an odd multiple of $\pi/2$, i.e.,

$$\Delta\phi = \phi_y - \phi_x = \pm\left(\frac{1}{2} + 2n\right)\pi, \quad n = 0, 1, 2, \dots \tag{9.71}$$

This allows the tip of the electric field to trace an ellipse in the $x - y$ plane.

The polarized waves described so far are illustrated in Fig. 9.5. They are deterministic meaning that the field is a predictable function of space and time. If the field is completely random, the wave is said to be randomly polarized. Typical examples of such waves are radiation from the sun and radio stars.

Propagation in the Atmosphere

Wave propagation hardly occurs under the idealized conditions assumed in previously. For most communication links, the previous analysis must be modified to account for the presence of the earth, the ionosphere, and atmospheric precipitates such as fog, raindrops, snow, and hail. This is done in this section.

The major regions of the earth's atmosphere that are of importance in radio wave propagation are the troposphere and the ionosphere. At radar frequencies (approximately 100 MHz to 300 GHz), the troposphere is by far the most important. It is the lower atmosphere comprised of a nonionized region extending from the earth's surface up to about 15 km. The ionosphere is the earth's upper atmosphere in the altitude region from 50 km to one earth radius (6370 km). Sufficient ionization exists in this region to influence wave propagation.

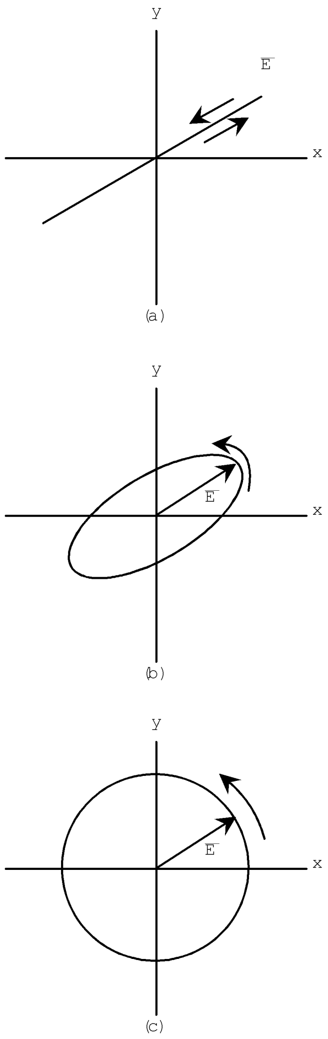

FIGURE 9.5 Wave polarizations: (a) linear, (b) elliptic, (c) circular.

Wave propagation over the surface of the earth may assume any of the following three principal modes:

- Surface wave propagation along the surface of the earth;
- Space wave propagation through the lower atmosphere;
- Sky wave propagation by reflection from the upper atmosphere.

These modes are portrayed in Fig. 9.6. The sky wave is directed toward the ionosphere, which bends the propagation path back toward the earth under certain conditions in a limited frequency range (0 to 50 MHz approximately). This is highly dependent on the condition of the ionosphere (its level of ionization) and the signal frequency. The surface (or ground) wave takes effect at the low-frequency end of the spectrum (2 to 5 MHz approximately) and is directed along the surface over which the wave is propagated. Since the propagation of the ground wave depends on the conductivity of the earth's surface, the wave is attenuated more than if it were propagation through free space. The space wave consists of the direct wave and the reflected wave. The direct wave travels from the transmitter to the receiver in nearly a straight path while the reflected wave is due to ground reflection. The space wave obeys the optical laws in that direct and reflected wave components contribute to the total wave component.

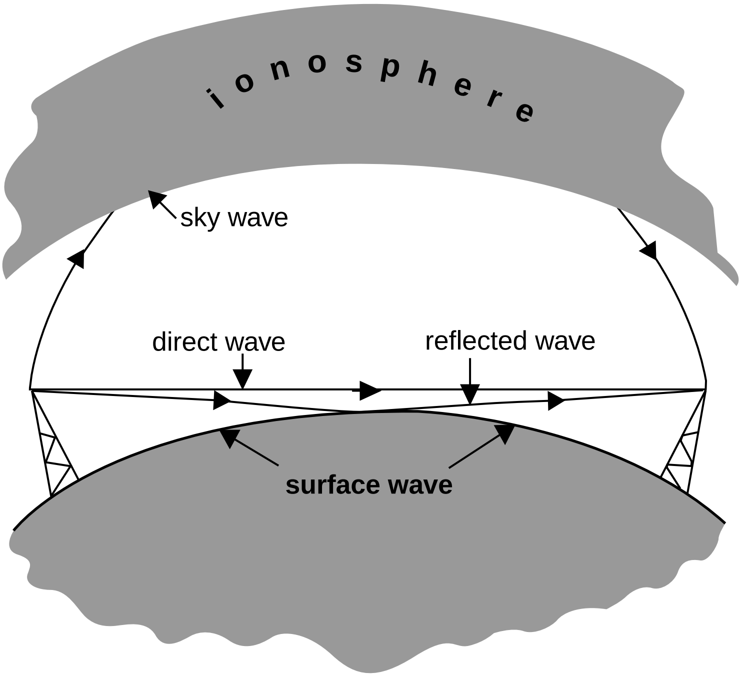

FIGURE 9.6 Modes of wave propagation.

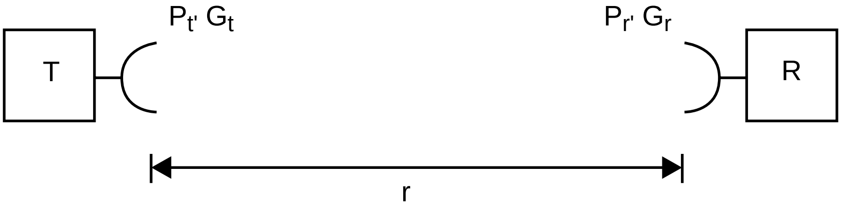

FIGURE 9.7 Transmitting and receiving antennas in free space.

Although the sky and surface waves are important in many applications, we will only consider the space wave in this chapter.

Figure 9.7 depicts the electromagnetic energy transmission between two antennas in space. As a wave radiates from the transmitting antenna and propagates in space, its power density decreases, as expressed ideally in Eq. (9.63). Assuming that the antennas are in a lossless medium or free space, the power received by the receiving antenna is given by the *Friis transmission equation* (Liu and Fang, 1988):

$$P_r = G_r G_t \left(\frac{\lambda}{4\pi r} \right)^2 P_t \tag{9.72}$$

where the subscripts t and r respectively refer to transmitting and receiving antennas. In Eq. (9.72), P = power in watts, G = antenna gain (dimensionless), r = distance between the antennas in meters, and λ = wavelength in meters. The Friis equation relates the power received by one antenna to the power transmitted by the other, provided that the two antennae are separated by $r > 2D^2/\lambda$, and D is the largest dimension of either antenna. Thus, the Friis equation applies only when the two antennas are in the far field of each other. It shows that the received power decays at a rate of 20 dB/decade with distance. In case the propagation path is not in free space, a correction factor F is included to account for the effect of the medium. This factor, known as the *propagation factor,* is simply the ratio of the electric field intensity E_m in the medium to the electric field intensity E_o in free space, i.e.,

$$F = \frac{E_m}{E_o} \tag{9.73}$$

The magnitude of F is always less than unity since E_m is always less than E_o. Thus, for a lossy medium, Eq. (9.72) becomes

$$P_r = G_r G_t \left(\frac{\lambda}{4\pi r}\right)^2 P_t |F|^2 \tag{9.74}$$

For practical reasons, Eqs. (9.72) or (9.73) are commonly expressed in logarithmic form. If the all the terms are expressed in decibels (dB), Eq. (9.74) can be written in logarithmic form as

$$P_r = P_t + G_r + G_t - L_o - L_m \tag{9.75}$$

where P = power in dB referred to 1 W (or simply dBW), G = gain in dB, L_o = free-space loss in dB, and L_m = loss in dB due to the medium. The free-space loss is obtained from standard nomograph or directly from

$$L_o = 20 \log\left(\frac{4\pi r}{\lambda}\right) \tag{9.76}$$

while the loss due to the medium is given by

$$L_m = -20 \log |F| \tag{9.77}$$

Our major concern in the rest of this section is to determine L_o and L_m for two important cases of space propagation that differ considerably from the free-space conditions.

Effect on the Earth

The phenomenon of multipath propagation causes significant departures from free-space conditions. The term *multipath* denotes the possibility of an EM wave propagating along various paths from the transmitter to the receiver. In multipath propagation of an EM wave over the earth's surface, two such paths exist: a direct path and a path via reflection and diffractions from the interface between the atmosphere and the earth. A simplified geometry of the multipath situation is shown in Fig. 9.8. The reflected and diffracted component is commonly separated into two parts: one *specular* (or coherent) and the other *diffuse* (or incoherent), that can be separately analyzed. The specular component is well defined in terms of its amplitude, phase, and incident direction. Its main characteristic is its conformance to Snell's law for reflection, which requires that the angles of incidence and reflection be equal and coplanar. It is a plane wave, and as such, is uniquely specified by its direction. The diffuse component, however, arises out of the random nature of the scattering surface, and as such, is nondeterministic. It is not a plane wave and does not obey Snell's law for reflection. It does not come from a given direction but from a continuum.

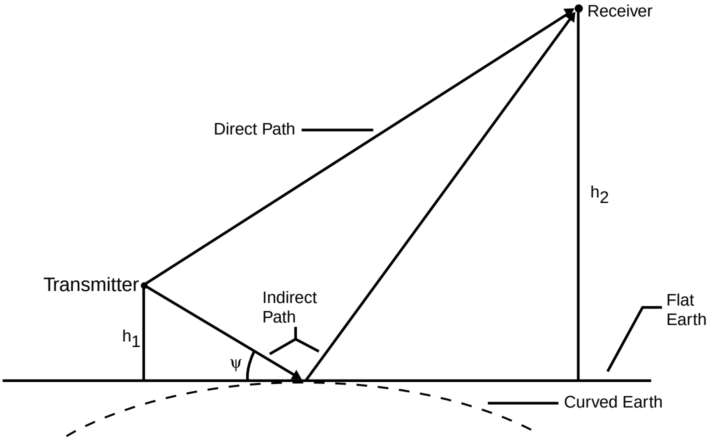

FIGURE 9.8 Multipath geometry.

The loss factor F that accounts for the departures from free-space conditions is given by

$$F = 1 + \Gamma\,\rho_s\,D\,S(\theta)\,e^{-j\Delta} \tag{9.78}$$

where Γ = Fresnel reflection coefficient,
ρ_s = roughness coefficient,
D = divergence factor,
$S(\theta)$ = shadowing function,
Δ = is the phase angle corresponding to the path difference

The Fresnel reflection coefficient Γ accounts for the electrical properties of the earth's surface. Since the earth is a lossy medium, the value of the reflection coefficient depends on the complex relative permittivity ϵ_c of the surface, the grazing angle ψ, and the wave polarization. It is given by

$$\Gamma = \frac{\sin\psi - z}{\sin\psi + z} \tag{9.79}$$

where

$$z = \sqrt{\epsilon_c - \cos^2\psi} \quad \text{for horizontal polarization,} \tag{9.80}$$

$$z = \frac{\sqrt{\epsilon_c - \cos^2\psi}}{\epsilon_c} \quad \text{for vertical polarization,} \tag{9.81}$$

$$\epsilon_c = \epsilon_r - j\frac{\sigma}{\omega\epsilon_o} = \epsilon_r - j60\sigma\lambda \tag{9.82}$$

ϵ_r and σ are the dielectric constant and conductivity of the surface; ω and λ are the frequency and wavelength of the incident wave; and ψ is the grazing angle. It is apparent that $0 < |\Gamma| < 1$.

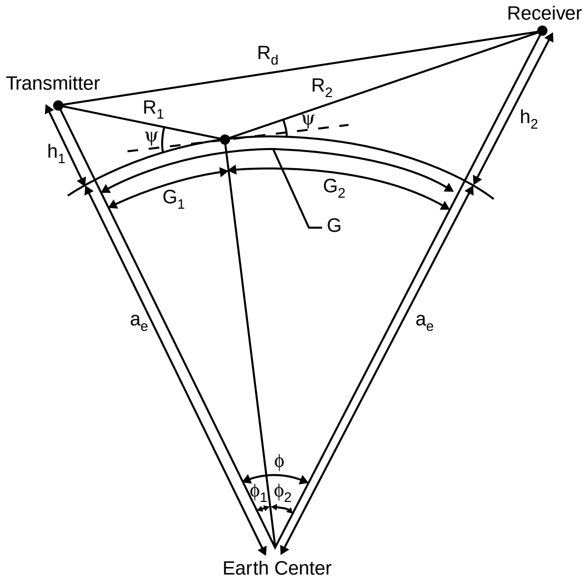

FIGURE 9.9 Geometry of spherical earth reflection.

To account for the spreading (or divergence) of the reflected rays due to earth curvature, we introduce the divergence factor D. The curvature has a tendency to spread out the reflected energy more than a corresponding flat surface. The divergence factor is defined as the ratio of the reflected field from a curved surface to the reflected field from a flat surface (Kerr, 1951). Using the geometry of Fig. 9.9, D is given by

$$D \simeq \left(1 + \frac{2G_1G_2}{a_e G \sin\psi}\right)^{-1/2} \tag{9.83}$$

where $G = G_1 + G_2$ is the total ground range and $a_e = 6370$ km is the effective earth radius. Given the transmitter height h_1, the receiver height h_2, and the total ground range G, we can determine G_1, G_2, and ψ. If we define

$$p = \frac{2}{\sqrt{3}}\left[a_e\left(h_1 + h_2\right) + \frac{G^2}{4}\right]^{1/2} \tag{9.84}$$

$$\alpha = \cos^{-1}\left[\frac{2a_e\left(h_1 - h_2\right)G}{p^3}\right] \tag{9.85}$$

and assume $h_1 \le h_2$, $G_1 \le G_2$, using small angle approximation yields

$$G_1 = \frac{G}{2} + p\cos\left(\frac{\pi + \alpha}{3}\right) \tag{9.86}$$

$$G_2 = G - G_1 \tag{9.87}$$

$$\phi_i = \frac{G_i}{a_e}, \quad i = 1, 2 \tag{9.88}$$

$$R_i = \left[h_i^2 + 4a_e\left(a_e + h_i\right)\sin^2\left(\phi_i/2\right)\right]^{1/2} \quad i = 1, 2 \tag{9.89}$$

The grazing angle is given by

$$\psi = \sin^{-1}\left[\frac{2a_e h_1 + h_1^2 - R_1^2}{2a_e R_1}\right] \tag{9.90}$$

or

$$\psi = \sin^{-1}\left[\frac{2a_e h_1 + h_1^2 + R_1^2}{2\left(a_e + h_1\right)R_1}\right] - \phi_1 \tag{9.91}$$

Although D varies from 0 to 1, in practice D is a significant factor at low grazing angle ψ (less than 0.1%).

The phase angle corresponding to the path difference between direct and reflected waves is given by

$$\Delta = \frac{2\pi}{\lambda}\left(R_1 + R_2 - R_d\right) \tag{9.92}$$

The roughness coefficient ρ_s takes care of the fact that the earth's surface is not sufficiently smooth to produce specular (mirror-like) reflection except at a very low grazing angle. The earth's surface has a height distribution that is random in nature. The randomness arises out of the hills, structures, vegetation, and ocean waves. It is found that the distribution of the different heights on the earth's surface is usually the Gaussian or normal distribution of probability theory. If σ_h is the standard deviation of the normal distribution of heights, we define the roughness parameters as

$$g = \frac{\sigma_h \sin\psi}{\lambda} \tag{9.93}$$

If $g < 1/8$, specular reflection is dominant; if $g > 1/8$, diffuse scattering results. This criterion, known as the *Rayleigh criterion,* should only be used as a guideline since the dividing line between a specular and a diffuse reflection or between a smooth and a rough surface is not well defined. The roughness is taken into account by the roughness coefficient ($0 < \rho_s < 1$), which is the ratio of the field strength after reflection with roughness taken into account to that which would be received if the surface were smooth. The roughness coefficient is given by

$$\rho_s = \exp\left[-2\left(2\pi g\right)^2\right] \tag{9.94}$$

The shadowing function $S(\theta)$ is important at a low grazing angle. It considers the effect of geometric shadowing — the fact that the incident wave cannot illuminate parts of the earth's surface shadowed by higher parts. In a geometric approach, where diffraction and multiple scattering effects are neglected, the reflecting surface will consist of well-defined zones of illumination and shadow. As there will be no

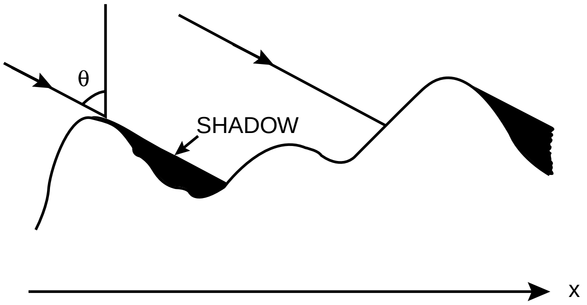

FIGURE 9.10 Rough surface illuminated at an angle of incidence θ.

field on a shadowed portion of the surface, the analysis should include only the illuminated portions of the surface. The phenomenon of shadowing of a stationary surface was first investigated by Beckman in 1965 and subsequently refined by Smith (1967) and others. A pictorial representation of rough surfaces illuminated at the angle of incidence θ (= 90° – ψ) is shown in Fig. 9.10. It is evident from the figure that the shadowing function $S(\theta)$ equals unity when θ = 0 and zero when θ = π/2. According to Smith (1967),

$$S(\theta) \simeq \frac{\left[1-\tfrac{1}{2}\,\mathrm{erfc}(a)\right]}{1+2B} \tag{9.95}$$

where erfc(x) is the complementary error function,

$$\mathrm{erfc}(x) = 1-\mathrm{erf}(x) = \frac{2}{\sqrt{\pi}}\int_x^\infty e^{-t^2}\,dt \tag{9.96}$$

and

$$B = \frac{1}{4a}\left[\frac{1}{\sqrt{\pi}}e^{a^2} - a\,\mathrm{erfc}(a)\right], \tag{9.97}$$

$$a = \frac{\cot\theta}{2s}, \tag{9.98}$$

$$s = \frac{\sigma_h}{\sigma_l} = \text{rms surface slope} \tag{9.99}$$

In Eq. (9.99), σ_h is the rms roughness height and σ_l is the correlation length. Alternative models for $S(\theta)$ are available in the literature. Using Eqs. (9.79) to (9.99), the loss factor in Eq. (9.78) can be calculated. Thus

$$L_o = 20\log\left(\frac{4\pi R_d}{\lambda}\right) \tag{9.100}$$

$$L_m = -20\log\left(1+\Gamma\,\rho_s\,D\,S(\theta)\,e^{-j\Delta}\right) \tag{9.101}$$

Effect of Atmospheric Hydrometeors

The effect of atmospheric hydrometeors on satellite-earth propagation is of major concern at microwave frequencies. The problem of scattering of electromagnetic waves by atmospheric hydrometeors has attracted much interest since the late 1940s. The main hydrometeors that exist for long duration, and have the greatest interaction with microwaves are rain, snow, and dust particles. At frequencies above 10 GHz, rain has been recognized as the most fundamental obstacle in the earth-space path. Rain has been known to cause attenuation, phase difference, and depolarization of radio waves. For analog signals, the effect of rain is more significant above 10 GHz while for digital signals, rain effects can be significant down to 3 GHz. Attenuation of microwaves due to precipitation becomes severe owing to increased scattering and beam energy absorption by raindrops thus impairing terrestrial as well as earth-satellite communication links. Cross-polarization distortion due to rain has also been engaging the attention of researchers. This is particularly of interest when frequency reuse employing signals with orthogonal polarizations are used for doubling the capacity of a communication system. Thorough reviews on the interaction of microwaves with hydrometeors have been done by Oguchi (1983).

The loss due to rain-filled medium is given by

$$L_m = \gamma(R)\,\ell_e(R)\,p(R) \tag{9.102}$$

where γ = attenuation per unit length at rain rate R,
ℓ_e = equivalent path length at rain rate R, and
$p(R)$ = probability in percentage of rainfall rate R.

The attenuation is a function of the cumulative rain-rate distribution, drop-size distribution, refractive index of water, temperature, and other variables. A rigorous calculation of $\gamma(R)$ using various numerical modeling tools and incorporating raindrop size distribution, velocity of raindrops, and the refractive index of water can be found in Sadiku (2001). For practical engineering purposes, what is needed is a simple formula relating attenuation to rain parameters. Such is found in the aR^b empirical relationship, which has been employed to calculate rain attenuation directly (Collin, 1985), i.e.,

$$\gamma(R) = aR^b \quad \text{dB/km} \tag{9.103}$$

where R is the rain rate and a and b are constants. At 0° C, the values of a and b are related to frequency f in gigahertz as follows:

$$a = G_a f^{E_a} \tag{9.104}$$

where

$$\begin{aligned}
&G_a = 6.39\times10^{-5}, && E_a = 2.03, && \text{for } f < 2.9 \text{ GHz}\\
&\mathrm{G_a} = 4.21\times10^{-5}, && E_a = 2.42, && \text{for } 2.9 \text{ GHz} \le f \le 54 \text{ GHz}\\
&G_a = 4.09\times10^{-2}, && E_a = 0.699, && \text{for } 54 \text{ GHz} \le f < 100 \text{ GHz}\\
&G_a = 3.38, && E_a = -0.151, && \text{for } 180 \text{ GHz} < f
\end{aligned}$$

and

$$b = G_b f^{E_b} \tag{9.105}$$

where

$$\begin{aligned}
G_b &= 0.851, & E_b &= 0.158, & &\text{for } f < 8.5\text{ GHz}\\
G_b &= 1.41, & E_b &= -0.0779, & &\text{for } 8.5\text{ GHz} \le f < 25\text{ GHz}\\
G_b &= 2.63, & E_b &= -0.272, & &\text{for } 25\text{ GHz} \le f < 164\text{ GHz}\\
G_b &= 0.616, & E_b &= 0.0126, & &\text{for } 164\text{ GHz} \le f.
\end{aligned}$$

The effective length $\ell_e(R)$ through the medium is needed since rain intensity is not uniform over the path. Its actual value depends on the particular area of interest and therefore has a number of representations (Liu and Fang, 1988). Based on data collected in western Europe and eastern North America, the effective path length has been approximated as (Hyde, 1984)

$$\ell_e(R) = \left[0.00741R^{0.766} + (0.232 - 0.00018R)\sin\theta\right]^{-1} \tag{9.106}$$

where θ is the elevation angle.

The cumulative probability in percentage of rainfall rate R is given by (Hyde, 1984)

$$p(R) = \frac{M}{87.66}\left[0.03\beta e^{-0.03R} + 0.2(1-\beta)\left(e^{-0.258R} + 1.86e^{-1.63R}\right)\right] \tag{9.107}$$

where M is mean the annual rainfall accumulation in mm and β is the Rice–Holmberg thunderstorm ratio.

The effect of other hydrometeors such as vapor, fog, hail, snow, and ice is governed by fundamental principles similar to the effect of rain (Collin, 1985). However, their effects are at least an order of magnitude less than the effect of rain in most cases.

Other Effects

Besides hydrometeors, the atmosphere has the composition given in Table 9.1. While attenuation of EM waves by hydrometeors may result from both absorption and scattering, gases act only as absorbers. Although some of these gases do not absorb microwaves, some possess permanent electric and/or magnetic dipole moment and play some part in microwave absorption. For example, nitrogen molecules do not possess permanent electric or magnetic dipole moment and therefore play no part in microwave absorption. Oxygen has a small magnetic moment that enables it to display weak absorption lines in the

TABLE 9.1 Composition of Dry Atmosphere from Sea Level to about 90 km (Livingston, 1970)

Constituent	Percent by Volume	Percent by Weight
Nitrogen	78.088	75.527
Oxygen	20.949	23.143
Argon	0.93	1.282
Carbon dioxide	0.03	0.0456
Neon	1.8×10^{-3}	1.25×10^{-3}
Helium	5.24×10^{-4}	7.24×10^{-5}
Methane	1.4×10^{-4}	7.75×10^{-5}
Krypton	1.14×10^{-4}	3.30×10^{-4}
Nitrous oxide	5×10^{-5}	7.6×10^{-5}
Xenon	8.6×10^{-6}	3.90×10^{-5}
Hydrogen	5×10^{-5}	3.48×10^{-6}

centimeter- and millimeter-wave regions. Water vapor is a molecular gas with a permanent electric dipole moment. It is more responsive to excitation by an EM field than is oxygen.

Other mechanisms that can affect EM wave propagation in free space, not discussed in this chapter, include clouds, dust, and the ionosphere. The effect of the ionosphere is discussed in detail in standard texts.

References

Collin, R. E., 1985. *Antennas and Radiowave Propagation,* McGraw-Hill, New York, 339–456.

Freeman, R. L., 1994. *Reference Manual for Telecommunications Engineering,* 2nd ed., John Wiley & Sons, New York, 711–768.

Hyde, G., 1984. Microwave propagation, in R. C. Johnson and H. Jasik (eds.), *Antenna Engineering Handbook,* 2nd ed., McGraw-Hill, New York, 45.1–45.17.

Kerr, D. E., 1951. *Propagation of Short Radio Waves,* McGraw-Hill, New York, (Republished by Peter Peregrinus, London, U.K., 1987), 396–444.

Liu, C. H. and D. J. Fang, 1988. Propagation, in Y. T. Lo and S. W. Lee, *Antenna Handbook: Theory, Applications, and Design,* Van Nostrand Reinhold, New York, 29.1–29.56.

Livingston, D. C., 1970. *The Physics of Microwave Propagation,* Prentice-Hall, Englewood Cliffs, NJ, 11.

Oguchi, T., 1983. Electromagnetic Wave Propagation and Scattering in Rain and Other Hydrometeors, *Proc. IEEE,* 71, 1029–1078.

Sadiku, M. N. O., 2001. *Numerical Techniques in Electromagnetics,* 2nd ed., CRC Press, Boca Raton, FL, 95–105.

Sadiku, M. N. O., 2001. *Elements of Electromagnetics,* 3rd ed. Oxford University Press, New York, 410–472.

Smith, B. G., 1967. Geometrical shadowing of a random rough surface, *IEEE Trans. Ant. Prog.,* 15, 668–671.

Veley, V. F., *Modern Microwave Technology,* Prentice-Hall, Englewood Cliffs, NJ, 1987, 23–33.

Further Information

The subject of wave propagation could easily fill many chapters, and here it has only been possible to point out some of the main points of concern to microwave systems engineer. There are several sources of information dealing with the theory and practice of wave propagation in space. Some of these are in the references section. Journals such as *Radio Science, IEE Proceedings Part H, IEEE Transactions on Antenna and Propagation* are devoted to EM wave propagation. *Radio Science* is available at American Geophysical Union, 2000 Florida Avenue, NW, Washington DC 20009; *IEE Proceedings Part H* at IEE Publishing Department, Michael Faraday House, 6 Hills Way, Stevenage, Herts SG1 2AY, U.K.; and *IEEE Transactions on Antenna and Propagation* at IEEE, 445 Hoes Lane, P. O. Box 1331, Piscataway, NJ 08855-1331.

9.3 Guided Wave Propagation and Transmission Lines

W.R. Deal, V. Radisic, Y. Qian, and T. Itoh

At higher frequencies where wavelength becomes small with respect to feature size, it is often necessary to consider an electronic signal as an electromagnetic wave and the structure where this signal exists as a waveguide. A variety of different concepts can be used to examine this wave behavior. The most simplistic view is transmission line theory, where propagation is considered in a simplistic 1-D manner and the cross-sectional variation of the guided wave is entirely represented in terms of distributed transmission parameters in an equivalent circuit. This is the starting point for transmission line theory that is commonly used to design microwave circuits. In other guided wave structures, such as enclosed waveguides, it is more appropriate to examine the concepts of wave propagation from the perspective of Maxwell’s equations, the solutions of which will explicitly demonstrate the cross-sectional dependence of the guided wave structure.

Most practical wave guiding structures rely on single-mode propagation, which is restricted to a single direction. This allows the propagating wave to be categorized according to its polarization properties. A convenient method is classifying the modes as TEM, TE, or TM. TEM modes have both the electric and magnetic field transverse in the direction of propagation. Only the magnetic field transverses in the direction of propagation in TM modes, and only the electric field transverses in the direction of propagation in TE modes.

In this chapter, we first briefly examine the telegrapher's equation, which is the starting point for transmission line theory. The simple transmission line model accurately describes a number of guided wave structures and is the starting point for transmission line theory. In the next section, enclosed waveguides including rectangular and circular waveguides will be discussed. Relevant concepts such as cutoff frequency and modes will be given. In the final section, four common planar guided wave structures will be discussed. These inexpensive and compact structures are the foundation for the modern commercial RF front end.

TEM Transmission Lines, Telegrapher's Equations, and Transmission Line Theory

In this section, the concept of guided waves in simple TEM-guiding structures will be explored in terms of the simple model provided by Telegrapher's Equations, also referred to as transmission line equations. Telegrapher's equations demonstrate guided wave properties in terms of lumped equivalent circuit parameters available for many types of simple two-conductor transmission lines, and are valid for all types of TEM waveguides if their corresponding equivalent circuit parameters are known. These parameters must be found from Maxwell's equations in their fundamental form. Finally, properties and parameters for several types of two-wire TEM transmission line structures are introduced.

A transmission line or waveguide is used to transmit power and information from one point to another in an efficient manner. Three common types of transmission lines that support TEM guided waves are shown in Figure 9.11(a–c), including the parallel-plate transmission line, two-wire line, and coaxial transmission line. The parallel-plate transmission line consists of a dielectric slab sandwiched between two parallel conducting plates of width w. More practical, commonly used variations of this structure at microwave and millimeter-wave frequencies include microstrip and stripline, which will be briefly discussed in the final part of Section 9.3. A two-wire transmission line, consisting of two parallel conducting lines separated by a distance d is shown in Fig. 9.11b. This is commonly used for power distribution at low frequencies. Finally, the coaxial transmission line consists of two concentric conductors separated by a dielectric layer. This structure is well shielded and commonly used at high frequencies well into the microwave range.

The telegrapher's equations form a simple and intuitive starting point for the physics of guided wave propagation in these structures. An equivalent circuit model is shown in Fig. 9.12 for a two-conductor transmission line of differential length Δz in terms of the following four parameters:

R, resistance per unit length of both conductors (Ω/m).
L, inductance per unit length of both conductors (H/m).
G, conductance per unit length (S/m).
C, capacitance per unit length of both conductors (F/m).

These parameters represent physical quantities for each of the relevant transmission lines. For each of the structures shown in Fig. 9.11(a–c), R represents conductor losses, L represents inductance, G represents dielectric losses, and C represents the capacitance between the two lines.

Returning to Fig. 9.12, the quantities $v(z,t)$ and $v(z + \Delta z,t)$ represent change in voltage along the differential length of transmission line, while $i(z,t)$ and $i(z + \Delta z,t)$ represent the change in current. Writing Kirchoff's voltage law and current laws for the structure, dividing by Δz, and applying the fundamental

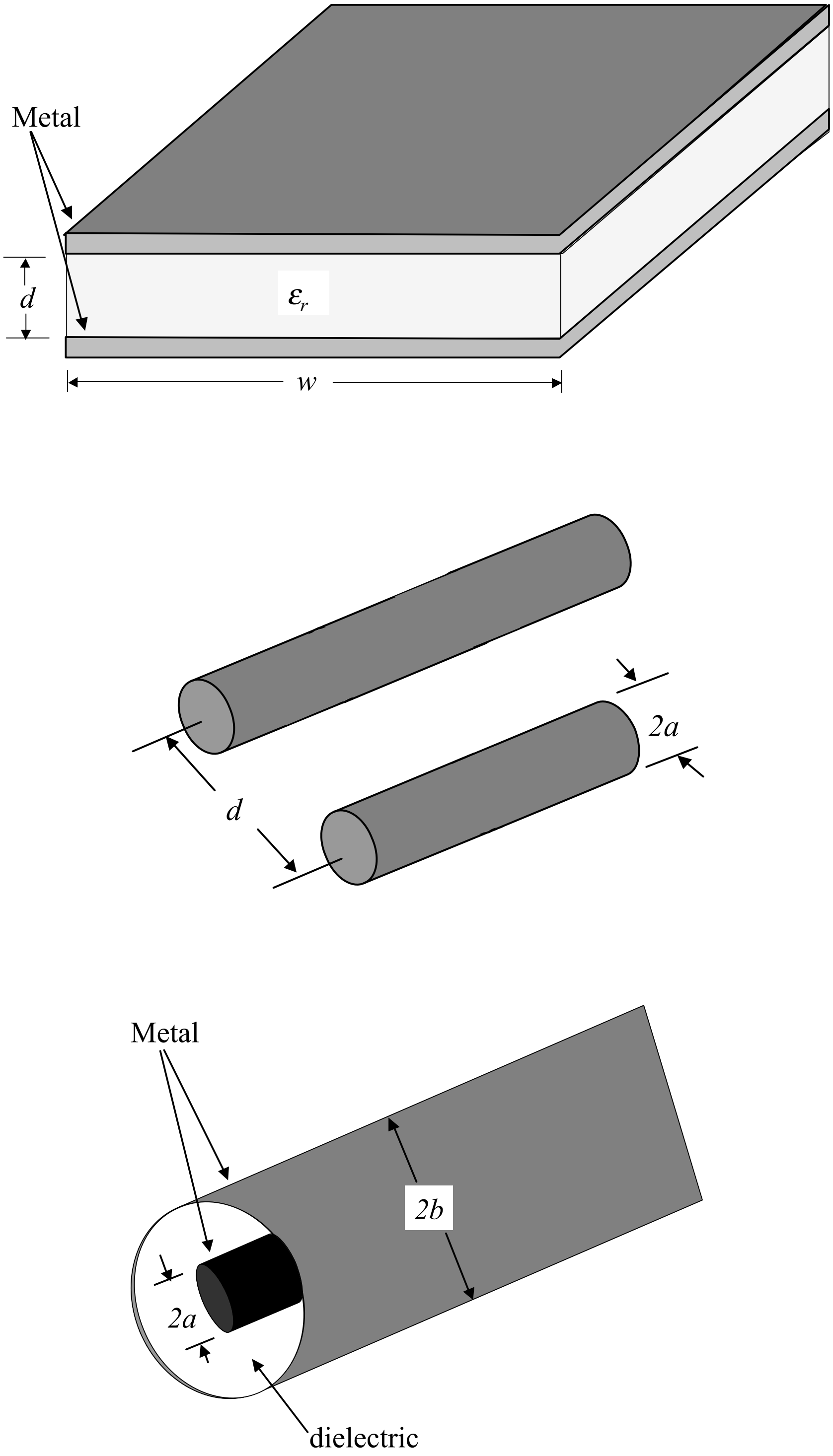

FIGURE 9.11 Three simple TEM-type transmission line geometries including (a) parallel-plate transmission line, (b) two-wire line, and (c) coaxial line.

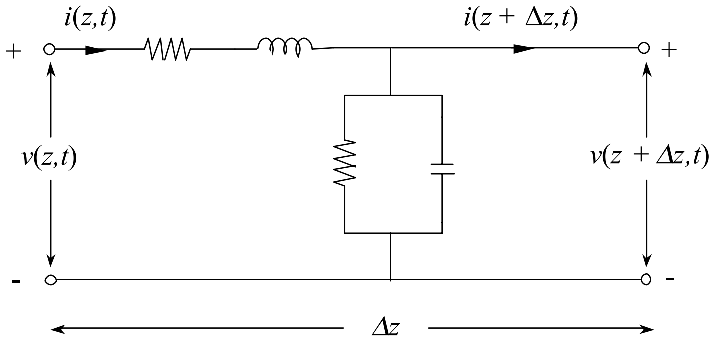

FIGURE 9.12 Distributed equivalent circuit model for a transmission line.

theorem of calculus as $\Delta z \rightarrow 0$, two coupled differential equations known as the telegrapher's equations are obtained:

$$-\frac{\partial v(z,t)}{\partial z} = Ri(z,t) + L\frac{\partial i(z,t)}{\partial t} \tag{9.108}$$

$$-\frac{\partial i(z,t)}{\partial z} = Gi(z,t) + D\frac{\partial v(z,t)}{\partial t} \tag{9.109}$$

However, typically we are interested in signals with harmonic time dependence ($e^{j\omega t}$). In this case, the time harmonic forms of the telegrapher's equations are given by

$$-\frac{dV(z)}{dz} = (R + j\omega L)I(z) \tag{9.110}$$

$$-\frac{dI(z)}{dz} = (G + j\omega C)V(z) \tag{9.111}$$

The constant γ is defined as the propagation constant with real and imaginary parts, α and β, corresponding to the attenuation constant (Np/m) and phase constant (rad/m) in the following manner

$$\gamma = \alpha + j\beta = \sqrt{(R + j\omega L)(G + j\omega C)} \tag{9.112}$$

This may then be substituted into the telegrapher's equations, which may then be solved for $V(z)$ and $I(z)$ to yield the following one-dimensional wave equations:

$$\frac{d^2V(z)}{dz^2} - \gamma^2 V(z) = 0 \tag{9.113}$$

$$\frac{d^2I(z)}{dz^2} - \gamma^2 I(z) = 0 \tag{9.114}$$

The form of this equation is the well-known wave equation. This indicates that the transmission line will support a guided electromagnetic wave traveling in the *z*-direction. The telegrapher's equations use a physical equivalent circuit and basic circuit theory to demonstrate the wave behavior of an electromagnetic signal on a transmission line. Alternatively, the same result can be obtained by starting directly with Maxwell's equations in their fundamental form, which may be used to derive the wave equation for a propagating electromagnetic wave. In this case, the solution of the wave equation will be governed by the boundary conditions. Similarly, the parameters *R*, *L*, *G*, and *C* are determined by the geometry of the transmission line structures.

Returning to the telegrapher's equations, several important facts may be noted. First, the characteristic impedance of the transmission line may be found by taking the ratio of the forward traveling voltage and current wave amplitudes, and is given in terms of the equivalent circuit parameters as

$$Z_0 = \sqrt{\frac{R + j\omega L}{G + j\omega C}} \tag{9.115}$$

In the case of a lossless transmission line, this reduces to $Z_o = \sqrt{L/C}$. The phase velocity, also known as the propagation velocity, is the velocity of the wave as it moves along the waveguide. It is defined as

$$v_p = \frac{\omega}{\beta} \tag{9.116}$$

In the lossless case, this reduces to:

$$v_p = \frac{1}{\sqrt{LC}} = \frac{1}{\sqrt{\mu\varepsilon}} \tag{9.117}$$

This shows that the velocity of the signal is directly related to the medium. In the case of an air-filled, purely TEM mode, the wave will propagate at the familiar value $c = 3 \times 10^8$ m/s. Additionally, it provides the relationship between *L*, *C* and the medium in which the wave is guided. Therefore, if the properties of the medium are known, it is only necessary to determine either *L* or *C*. Once *C* is known, *G* may be determined by the following relationship:

$$\frac{G}{C} = \frac{\sigma}{\varepsilon} \tag{9.118}$$

Note that σ is the conductivity of the medium, not of the metal conductors. The final parameter, the series resistance *R*, is determined by the power loss in the conductors. Simple approximations for the transmission line parameters *R*, *L*, *G*, and *C* for the three types of transmission lines shown in Figs. 9.11(a–c) are well known and are shown in Table 9.2. Note that μ, ε, and σ relate to the medium separating the conductors, and σ_c refers to the conductor. Once the equivalent circuit parameters are determined, the characteristic impedance and propagation constant of the transmission line may be determined. Note that R_s represents the surface resistance of the conductors, given as

$$R_s = \sqrt{\frac{\pi f \mu_c}{\sigma_c}} \tag{9.119}$$

TABLE 9.2 Transmission Line Parameters for Parallel-Plate, Two-Wire Line and Coaxial Transmission Lines

	Parallel-Plate Waveguide	Two-Wire Line	Coaxial Line
R (Ω/m)	$\frac{2}{w}R_s$	$\frac{R_s}{\pi a}$	$\frac{R_s}{2\pi}\left(\frac{1}{a}+\frac{1}{b}\right)$
L (H/m)	$\mu\frac{d}{w}$	$\frac{\mu}{\pi}\cosh^{-1}\left(\frac{D}{2a}\right)$	$\frac{\mu}{2\pi}\ln\left(\frac{b}{a}\right)$
G (S/m)	$\sigma\frac{w}{d}$	$\frac{\pi\sigma}{\cosh^{-1}(D/2a)}$	$\frac{2\pi\sigma}{\ln(b/a)}$
C (F/m)	$\varepsilon\frac{w}{d}$	$\frac{\pi\varepsilon}{\cosh^{-1}(D/2a)}$	$\frac{2\pi\varepsilon}{\ln(b/a)}$

Guided Wave Solution from Maxwell's Equations, Rectangular Waveguide, and Circular Waveguide

A waveguide is any structure that guides an electromagnetic wave. In the preceding section, several simple TEM transmission structures were discussed. While these structures do support a guided wave, the term waveguide more commonly refers to a closed metallic structure with a fixed cross-section within which a guided wave propagates, as shown for the arbitrary cross-section in Fig. 9.13. The guide is filled with a material of permittivity ε and permeability μ, and is defined by its metallic wall parallel to the z-axis. These structures demonstrate lower losses than the simple transmission line structures of the first section, and are used to transport power in the microwave and millimeter-wave frequency range. Ohmic losses are low and the waveguide is capable of carrying large power levels. Disadvantages are bulk, weight, and limited bandwidth, which cause planar transmission lines to be used wherever possible in modern communications circuits. However, a wide variety of components are available in this technology, including high performance filters, couplers, isolators, attenuators, and detectors.

Inside this type of enclosed waveguide, an infinite number of distinct solutions exist, each of which is referred to as a *waveguide mode*. At a given operating frequency, the cross-section of the waveguide

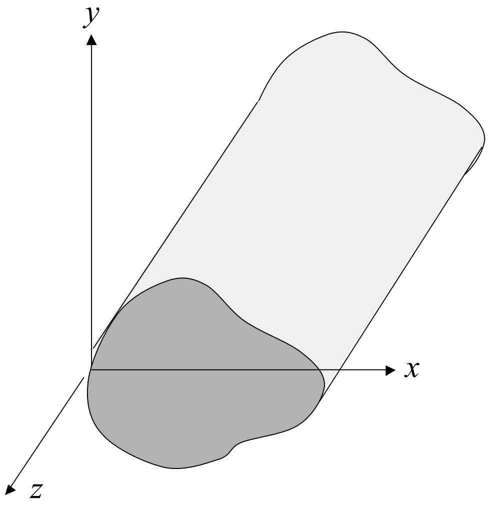

FIGURE 9.13 Geometry of enclosed waveguide with arbitrary cross-section. Propagation is in the z direction.

and the type of material in the waveguide determine the characteristics of these modes. These modes are usually classified by the longitudinal components of the electric and magnetic fields, E_z and H_z, where propagation is in the z direction. The most common classifications are TE (Transverse Electric), TM (Transverse Magnetic), EH, and HE modes. The basic characteristics are described in the next two paragraphs. The TEM modes that were discussed in the previous section do not propagate in this type of metallic enclosed waveguide. This is because a TEM mode requires two conductors to propagate, where a conventional enclosed waveguide has only a single enclosing conductor.

The two most common waveguide modes are the TE and TM modes. TE modes have no component of E in the z direction, which means that E is completely transverse to the direction of propagation. Similarly, TM modes have no component of H in the z direction.

EH and HE modes are hybrid modes that may be present under certain conditions, such as a waveguide partially filled with dielectric. In this case, pure TE and TM are unable to satisfy all of the necessary boundary conditions and a more complex type of modal solution is required. With both EH and HE, neither E nor H are zero in the direction of propagation. In EH modes, the characteristics of the transverse fields are controlled more by H_z than by E_z. HE modes are controlled more by E_z than by H_z. These types of hybrid modes may also be referred to as LSE (Longitudinal Section Electric) and LSM (Longitudinal Section Magnetic). It should be noted that most commonly used waveguides are homogenous, being entirely filled with material of a single permittivity (which may of course be air) and these types of modes will not be present.

Inside a homogenous waveguide, E_z and H_z satisfy the scalar wave equation inside the waveguide:

$$\left(\frac{\partial^2}{\partial x^2}+\frac{\partial^2}{\partial y^2}\right)E_z+h^2E_z=0 \tag{9.120}$$

$$\left(\frac{\partial^2}{\partial x^2}+\frac{\partial^2}{\partial y^2}\right)H_z+h^2H_z=0 \tag{9.121}$$

Note that h is given as:

$$h^2=\omega^2\mu\varepsilon+\gamma^2=k^2+\gamma^2 \tag{9.122}$$

The wavenumber, k, is for the material filling the waveguide. For several simple homogenous waveguides with commonly used waveguide geometries, applying boundary equations on the walls of the waveguide may be used to solve these equations to obtain closed form solutions. The resulting modal solution will possess distinct eigenvalues determined by the cross-section of the waveguide. One important result obtained from this procedure is that waveguide modes, unlike the fundamental TEM mode that propagates in two-wire structures at any frequency, will have a distinct cutoff frequency. It may be shown that the propagation constant varies with frequency as

$$\gamma=\alpha+j\beta=h\sqrt{1-\left(\frac{f}{f_c}\right)^2} \tag{9.123}$$

where the cutoff frequency, f_c is given by:

$$f_c=\frac{h}{2\pi\sqrt{\mu\varepsilon}} \tag{9.124}$$

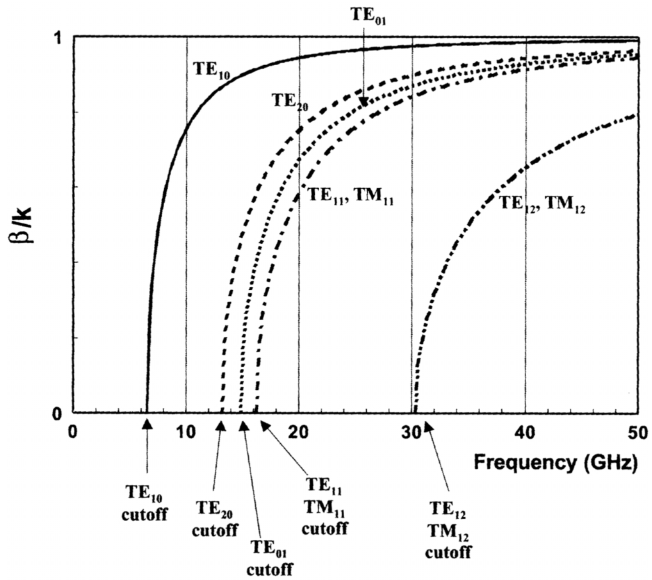

FIGURE 9.14 β/*k* diagram for WR-90 waveguide illustrating the concept of higher mode propagation and cutoff frequency.

By inspection of Eq. (9.133), and recalling the exp($j\omega t - \gamma z$) dependence of the wave propagating in the +*z* direction (for propagation in the –*z* direction, replace *z* with –*z*), the physical significance of the cutoff frequency is clear. For a given mode, when $f > f_c$, the propagation constant γ is imaginary and the wave is propagating. Alternatively, when $f < f_c$, the propagation constant γ is real and the wave decays exponentially. In this case, modes operated below the cutoff frequency attenuate rapidly and are therefore referred to as evanescent modes. In practice, a given waveguide geometry is seldom operated at a frequency where more than one mode will propagate. This fixes the bandwidth of the waveguide to operate at some point above the cutoff frequency of the fundamental mode and below the cutoff frequency of the second order mode, although in some rare instances higher order modes may be used for specialized applications.

The guided wavelength is also a function of the cross-section geometry of the waveguide structure. The guided wavelength is given as:

$$\lambda_g = \frac{\lambda_0}{\sqrt{1-\left(\frac{f_c}{f}\right)^2}} \tag{9.125}$$

Note that λ_0 is the wavelength of a plane wave propagating in an infinite medium of the same material as the waveguide. Two important facts may be noted about this expression. First, at frequencies well above the cutoff frequency, $\lambda_g \approx \lambda$. Secondly, as $f \to f_c$, $\lambda \to \infty$, further illustrating that the mode does not propagate. This is another reason that the operating frequency is always chosen above the cutoff frequency. This concept is graphically depicted in Fig. 9.14, a β/*k* diagram for a standard WR-90 waveguide. At the cutoff frequency, the phase constant goes to zero, indicating that the wave does not propagate. At high frequencies, β approaches the phase constant in an infinite region of the same medium. Therefore, β/*k* approaches one.

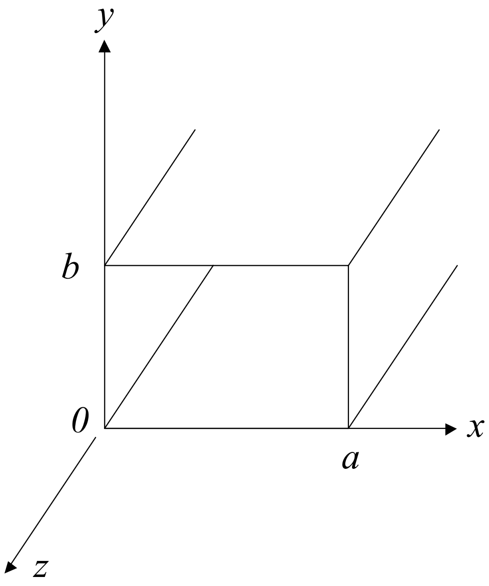

FIGURE 9.15 Geometry of a rectangular waveguide.

The wave impedance of the waveguide is given by the ratio of the magnitudes of the transverse electric and magnetic field components, which will be constant across the cross-section of the waveguide. For a given mode, the wave impedance for the TE and TM modes are given as:

$$Z_{TE} = \frac{E_T}{H_T} = \frac{j\omega\mu}{\mu} \tag{9.126}$$

$$Z_{TM} = \frac{E_T}{H_T} = \frac{\gamma}{j\omega\varepsilon} \tag{9.127}$$

E_T and H_T represent the transverse electric and magnetic fields. Note that at frequencies well above cutoff, the wave impedance for both the TE and TM modes approaches $\sqrt{\mu/\varepsilon}$, the characteristic impedance of a plane wave propagating in an infinite medium of the same material as the waveguide. Further, as $f \to f_c$, then $Z_{TE} \to \infty$ and $Z_{TM} \to 0$, again demonstrating the necessity of choosing an operating point well above cutoff.

A variety of geometries are used for waveguides, the most common being the rectangular waveguide, which is used in the microwave and well into the millimeter-wave frequency regime. Shown in Fig. 9.15, it is a rectangular metallic guide of width a and height b. Rectangular waveguide propagate both TE and TM modes. For conciseness, the field components of the TE_{mn} and TM_{mn} modes are presented in Table 9.3. From the basic form of the equations, we see that the effect of the rectangular cross-section is a standing wave dependence determined by the dimensions of the cross-section, a and b. Further, h (and therefore the propagation constant, γ) are determined by a and b. The dimensions of the waveguide are chosen so that only a single mode propagates at the desired frequency, with all other modes cut off. By convention, $a > b$ and a ratio of $a/b = 2.1$ is typical for commercial waveguide types.

The dominant mode in rectangular waveguide is the TE_{10} mode, which has a cutoff frequency of:

$$f_{c_{10}} = \frac{1}{2a\sqrt{\mu\varepsilon}} = \frac{c}{2a} \tag{9.128}$$

TABLE 9.3 Field Components for Rectangular Waveguide

	TE	TM
E_z	0	$E_0 \sin\left(\frac{m\pi x}{a}\right)\sin\left(\frac{n\pi y}{b}\right)e^{-\gamma_{mn}z}$
H_z	$H_0 \cos\left(\frac{m\pi x}{a}\right)\cos\left(\frac{n\pi y}{b}\right)e^{-\gamma_{mn}z}$	0
E_x	$H_0 \frac{j\omega\mu n\pi}{h_{mn}^2 b}\cos\left(\frac{m\pi x}{a}\right)\sin\left(\frac{n\pi y}{b}\right)e^{-\gamma_{mn}z}$	$-E_0 \frac{\gamma_{mn} m\pi}{h_{mn}^2 a}\cos\left(\frac{m\pi x}{a}\right)\sin\left(\frac{n\pi y}{b}\right)e^{-\gamma_{mn}z}$
H_x	$H_0 \frac{\gamma_{mn} m\pi}{h_{mn}^2 a}\sin\left(\frac{m\pi x}{a}\right)\cos\left(\frac{n\pi y}{b}\right)e^{-\gamma_{mn}z}$	$H_0 \frac{j\omega\varepsilon n\pi}{h_{mn}^2 b}\sin\left(\frac{m\pi x}{a}\right)\cos\left(\frac{n\pi y}{b}\right)e^{-\gamma_{mn}z}$
E_y	$-H_0 \frac{j\omega\mu m\pi}{h_{mn}^2 a}\sin\left(\frac{m\pi x}{a}\right)\cos\left(\frac{n\pi y}{b}\right)e^{-\gamma_{mn}z}$	$-E_0 \frac{\gamma_{mn} n\pi}{h_{mn}^2 b}\sin\left(\frac{m\pi x}{a}\right)\cos\left(\frac{n\pi y}{b}\right)e^{-\gamma_{mn}z}$
H_y	$H_0 \frac{\gamma_{mn} n\pi}{h_{mn}^2 b}\cos\left(\frac{m\pi x}{a}\right)\sin\left(\frac{n\pi y}{b}\right)e^{-\gamma_{mn}z}$	$-E_0 \frac{j\omega\varepsilon m\pi}{h_{mn}^2 a}\cos\left(\frac{m\pi x}{a}\right)\sin\left(\frac{n\pi y}{b}\right)e^{-\gamma_{mn}z}$
h_{mn}	$\sqrt{\left(\frac{m\pi x}{a}\right)^2+\left(\frac{n\pi y}{b}\right)^2} = 2\pi f_c\sqrt{\mu\varepsilon}$	$\sqrt{\left(\frac{m\pi x}{a}\right)^2+\left(\frac{n\pi y}{b}\right)^2} = 2\pi f_c\sqrt{\mu\varepsilon}$

The concept of cutoff frequency is further illustrated in Fig. 9.14, a β/k diagram for a lossless WR-90 waveguide (note that in the lossless case, the propagation constant will be equal to $j\beta$). It is apparent that higher order modes may propagate as the operating frequency increases. At the cutoff frequency, β is zero because the guided wavelength is infinity. At high frequencies, the ratio β/k approaches one.

A number of variations of the rectangular waveguide are available, including single and double-ridged waveguides, which are desirable because of increased bandwidth. However, closed solutions for the fields in these structures do not exist and numerical techniques must be used to solve for the field distributions, as well as essential design information such as guided wavelength and characteristic impedance. Additionally, losses are typically higher than standard waveguides.

The circular waveguide is also used in some applications, although not nearly as often as rectangular geometry guides. Closed form solutions for the fields in a circular geometry, perfectly conducting waveguide with an inside diameter of $2a$ are given in Table 9.4. Note that these equations use a standard cylindrical coordinate system with ρ the radial distance from the z-axis, and ϕ is the angular distance measured from the y-axis. The axis of the waveguide is aligned along the z-axis. For both the TE$_{mn}$ and TM$_{mn}$ modes, any integer value of $n \geq 0$ is allowed, and $J_n(x)$ and $J_n'(x)$ are Bessel functions of order n and its first derivative. As with the rectangular waveguide, only certain values of h are allowed. For the TE$_{mn}$ modes, the allowed values of the modal eigenvalues must satisfy the roots of $J_n'(h_{mn}a) = 0$, where m signifies the root number and may range from one to infinity with $m = 1$ the smallest root. Similarly, for the TM$_{nm}$ modes, the values of the modal eigenvalues are the solutions of $J_n(h_{mn}a) = 0$. The dominant mode in the circular waveguide is the TE$_{11}$ mode, with a cutoff frequency given by:

$$f_{c_{11}} = \frac{0.293}{a\sqrt{\mu\varepsilon}} \tag{9.129}$$

The cutoff frequencies for several of the lowest order modes are given in Table 9.5, referenced to the cutoff frequency of the dominant mode.

TABLE 9.4 Field Components for Circular Waveguide

	TE	TM
E_z	0	$E_0 J_n\left(h_{nm}\rho\right)\cos\left(n\phi\right)e^{-\gamma_{nm}z}$
H_z	$H_0 J_n\left(h_{nm}\rho\right)\cos\left(n\phi\right)e^{-\gamma_{nm}z}$	0
E_ρ	$H_0 \frac{j\omega\mu n}{h_{nm}^2\rho} J_n\left(h_{nm}\rho\right)\sin\left(n\phi\right)e^{-\gamma_{nm}z}$	$-E_0 \frac{\gamma_{nm}}{h_{nm}} J'_n\left(h_{nm}\rho\right)\cos\left(n\phi\right)e^{-\gamma_{nm}z}$
H_ρ	$-H_0 \frac{\gamma_{nm}}{h_{nm}} J'_n\left(h_{nm}\rho\right)\cos\left(n\phi\right)e^{-\gamma_{nm}z}$	$-E_0 \frac{j\omega\varepsilon n}{h_{nm}^2\rho} J'_n\left(h_{nm}\rho\right)\sin\left(n\phi\right)e^{-\gamma_{nm}z}$
E_φ	$-H_0 \frac{j\omega\mu}{h_{nm}} J'_n\left(h_{nm}\rho\right)\cos\left(n\phi\right)e^{-\gamma_{nm}z}$	$E_0 \frac{\gamma_{nm}}{h_{nm}^2\rho} J'_n\left(h_{nm}\rho\right)\sin\left(n\phi\right)e^{-\gamma_{nm}z}$
H_φ	$H_0 \frac{\gamma_{nm}}{h_{nm}^2} J_n\left(h_{nm}\rho\right)\sin\left(n\phi\right)e^{-\gamma_{nm}z}$	$-E_0 \frac{j\omega\varepsilon}{h_{nm}} J'_n\left(h_{nm}\rho\right)\cos\left(n\phi\right)e^{-\gamma_{nm}z}$

TABLE 9.5 Cutoff Frequencies for Several Lower Order Waveguide Modes for Circular Waveguide

$f_c/f_{c_{10}}$	Modes
1.0	TE_{11}
1.307	TM_{01}
1.66	TE_{21}
2.083	TE_{01}, TM_{11}
2.283	TE_{31}
2.791	TE_{21}
2.89	TE_{41}
3.0	TE_{12}

Note: Frequencies have been normalized to the cutoff frequency of the TE_{10} mode.

Planar Guiding Structures

Planar guiding structures are composed of a comparatively thin dielectric substrate with metallization on one or both planes. By controlling the dimensions of the metallization, a variety of passive components, transmission lines, and matching circuits can be constructed using photolithography and photoetching. Further, active devices are readily integrated into planar guiding structures. This provides a low-cost and compact way of realizing complicated microwave and millimeter-wave circuits. Microwave integrated circuits (MICs) and monolithic microwave integrated circuits (MMICs) based on this concept are commonly available.

A variety of planar transmission lines have been demonstrated, including microstrip, coplanar waveguide (CPW), slotline, and coplanar stripline. The cross-section of each of these planar transmission lines is shown in Figs. 9.16(a–d). Once the dielectric substrate is chosen, characteristics of these transmission lines are controlled by the width of the conductors and/or gaps on the top planes of the geometry. Of these, the microstrip is by far the most commonly used planar transmission line. CPW is also often used, with slotlines and coplanar striplines being the least common at microwave frequencies, for a variety of reasons that will briefly be discussed later. In this section, we will describe the basic properties of planar transmission lines. Because of its prevalence, the microstrip will be described in detail and closed form expressions for the design of the microstrip will be given.

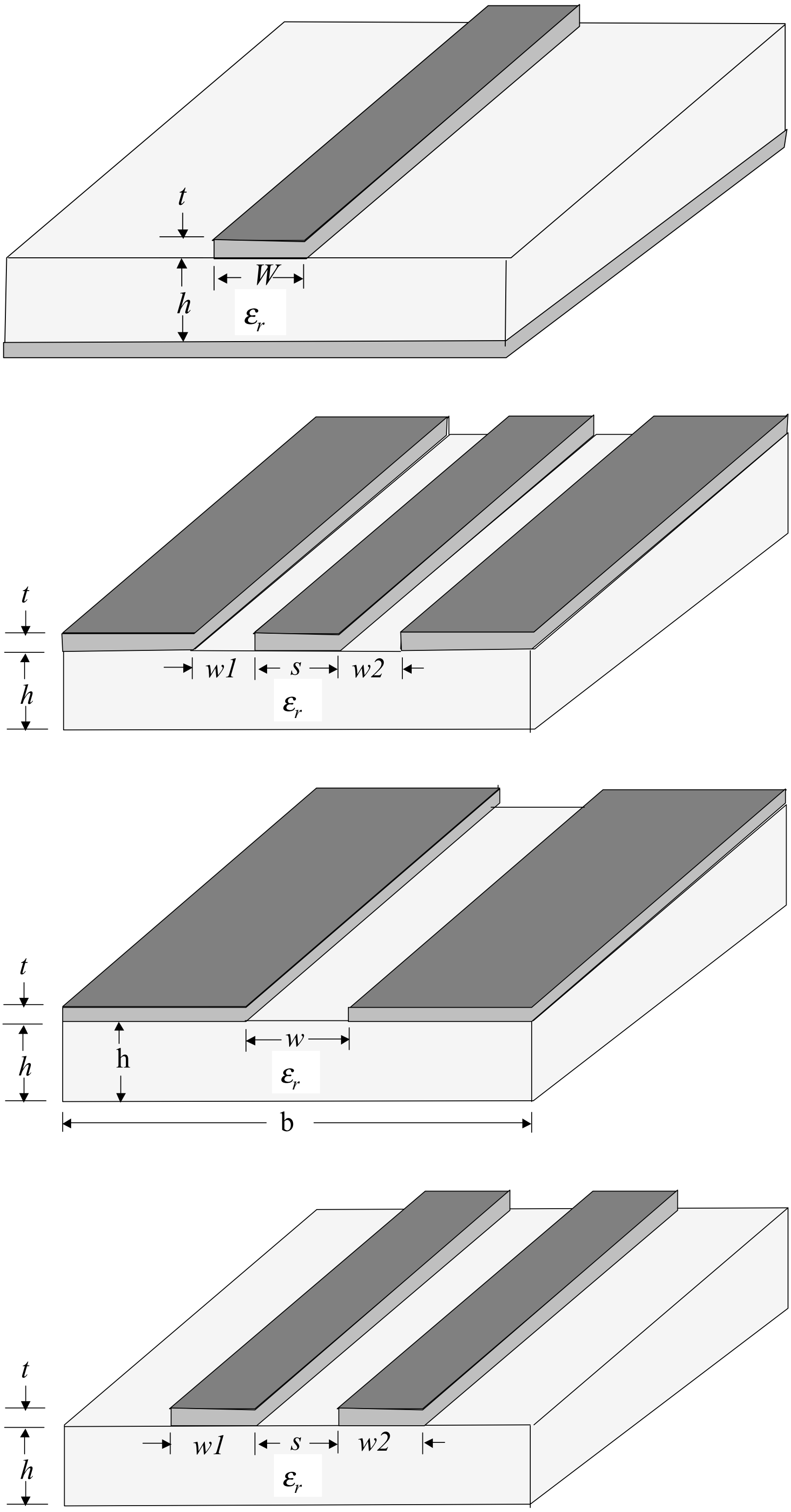

FIGURE 9.16 Cross-section of four of the most popular types of planar guiding structures, including (a) microstrip, (b) coplanar waveguide, (c) slotline, and (d) coplanar stripline.

Microstrip

As seen in Fig. 9.16(a), the simplest form of microstrip consists of a single conductor on a grounded dielectric slab. Microstrip is the most common type of planar transmission line used in microwave and millimeter-wave circuits, with a great deal of design data freely available. A broad range of passive components may be designed with the microstrip, including filters, resonators, diplexers, distribution networks, and matching components. Additionally, three terminal active components can be integrated by using vias to ground. However, this may introduce considerable inductances at high frequencies.

The fundamental mode of propagation for this type of planar waveguide is often referred to as quasi-TEM, because of its close resemblance to pure TEM modes. In fact, noting that the majority of the power is confined in the region bounded by the width of the microstrip, the basic characteristics of microstrip are quite similar to the parallel-strip transmission line of Fig. 9.11(a). Because of the presence of the air-dielectric interface, it is not a true TEM mode. The use of the dielectric between the ground and top conductor confines the majority of the fields in this region, but some energy may radiate from the structures. Using a high permittivity substrate and shielding the structure helps to minimize this factor. Microstrip is capable of carrying moderate power levels (a 50 Ω microstrip line on 25 mil alumina can handle several kW of power), is broadband, and enables realization of a variety of circuit topologies, both active and passive.

To design the basic microstrip line, it is necessary to be able to determine characteristic impedance and effective permittivity, preferably as a function of frequency. A wide variety of approximations have been presented in the literature, with most techniques using a quasi-static approximation for the characteristic impedance, Z_0, at low frequencies, and a dispersion model for the characteristic impedance as a function of frequency, $Z_0(f)$ in terms of Z_0. One fairly accurate and simple model commonly used to obtain Z_0 and the effective permittivity, ε_{re}, neglecting the effect of conductor thickness is given as[1]:

$$Z_0 = \frac{\eta}{2\pi\sqrt{\varepsilon_{re}}} \ln\left(\frac{8h}{W} + 0.25\frac{W}{h}\right) \quad \text{for} \left(\frac{W}{h} \le 1\right) \tag{9.130}$$

$$Z_0 = \frac{\eta}{\sqrt{\varepsilon_{re}}} \left\{\frac{W}{h} + 1.393 + 0.667 \ln\left(\frac{W}{h} + 1.444\right)\right\}^{-1} \quad \text{for} \left(\frac{W}{h} \ge 1\right) \tag{9.131}$$

Note that η is 120π-Ω, by definition. The effective permittivity is given as:

$$\varepsilon_{re} = \frac{\varepsilon_r + 1}{2} + \frac{\varepsilon_r - 1}{2} F(W/h) \tag{9.132}$$

$$F(W/h) = (1 + 12h/W)^{-1/2} + 0.04(1 - W/h)^2 \quad \text{for} \left(\frac{W}{h} \le 1\right)$$

$$F(W/h) = (1 + 12h/W)^{-1/2} \quad \text{for} \left(\frac{W}{h} \ge 1\right)$$

With these equations, one can determine the characteristic impedance in terms of the geometry. For a desired characteristic impedance, the line width can be determined from:

$$W/h = \frac{8\exp(A)}{\exp(2A) - 2} \quad \text{for } A > 1.52 \tag{9.133}$$

$$W/h = \frac{2}{\pi}\left\{B - 1 - \ln(2B-1) + \frac{\varepsilon_r - 1}{2\varepsilon_r}\left[\ln(B-1) + 0.39 - \frac{0.61}{\varepsilon_r}\right]\right\} \quad \text{for } A > 1.52 \tag{9.134}$$

where

$$A = \frac{Z_0}{60}\left\{\frac{\varepsilon_r + 1}{2}\right\}^{1/2} + \frac{\varepsilon_r - 1}{\varepsilon_r + 1}\left\{0.23 + \frac{0.11}{\varepsilon_r}\right\}$$

$$B = \frac{60\pi^2}{Z_0\sqrt{\varepsilon_r}}$$

Once Z_0 and ε_{re} have been determined, effects of dispersion may also be determined using expressions from Hammerstad[2] and Jensen for $Z_0(f)$ and Kobayashi[3] for $\varepsilon_{re}(f)$. To illustrate the effects of dispersion, the characteristic impedance and effective permittivity of several microstrip lines on various substrates are plotted in Figs. 9.17(a–b) using the formulas from the previously mentioned papers. The substrates indicated by the solid (ε_r = 2.33, h = 31 mils, W = 90 mils) and dashed (ε_r = 10.2, h = 25 mils, W = 23 mils) lines in these figures are typical for those that might be used in a hybrid circuit at microwave frequencies. We can see in Fig. 9.17(a) that the characteristic impedance is fairly flat until X-band, above which it may be necessary to consider the effects of dispersion for accurate design. The third line in the figure is an alumina substrate (ε_r = 9, h = 2.464 mils, W = 2.5 mils) on a thin substrate. The characteristic impedance is flat until about 70 GHz, indicating that this thin substrate is useful at higher frequency operation. The effective permittivity as a function of frequency is shown in Fig. 9.17a. Frequency variation for this parameter is more dramatic. However, it must be remembered that guided wavelength is inversely proportional to the square root of the effective permittivity. Therefore, variation in electrical length will be less pronounced than the plot suggests.

In addition to dispersion, higher frequency operation is complicated by a number of issues, including decreased Q-factor, radiation losses, surface wave losses, and higher order mode propagation. The designer must be aware of the limitations of both the substrate on which he is designing and the characteristic impedance of the lines he is working with. In terms of the substrate, a considerable amount of energy can couple between the desired quasi-TEM mode of the microstrip and the lowest order surface wave mode of the substrate. In terms of the substrate thickness and permittivity, an approximation for determining the frequency where this coupling becomes significant is given by the following expression.[4]

$$f_T = \frac{150}{\pi h}\sqrt{\frac{2}{\varepsilon_r - 1}\arctan(\varepsilon_r)} \tag{9.135}$$

Note that f_T is in gigahertz and h is in millimeters. In addition to the quasi-TEM mode, microstrip will propagate undesired higher order TE and TM-type modes with cutoff frequency roughly determined by the cross-section of the microstrip. The excitation of the first mode is approximately given by the following expression.[4]

$$f_c = \frac{300}{\sqrt{\varepsilon_r}(2W + 0.8h)} \tag{9.136}$$

Again, note that f_c is in gigahertz, and h and W are both in millimeters. This expression is useful in determining the lowest impedance that may be reliably used for a given substrate and operating frequency. As a rule of thumb, the maximum operating frequency should be chosen somewhat lower. A good choice for maximum frequency may be 90% of this value or lower.

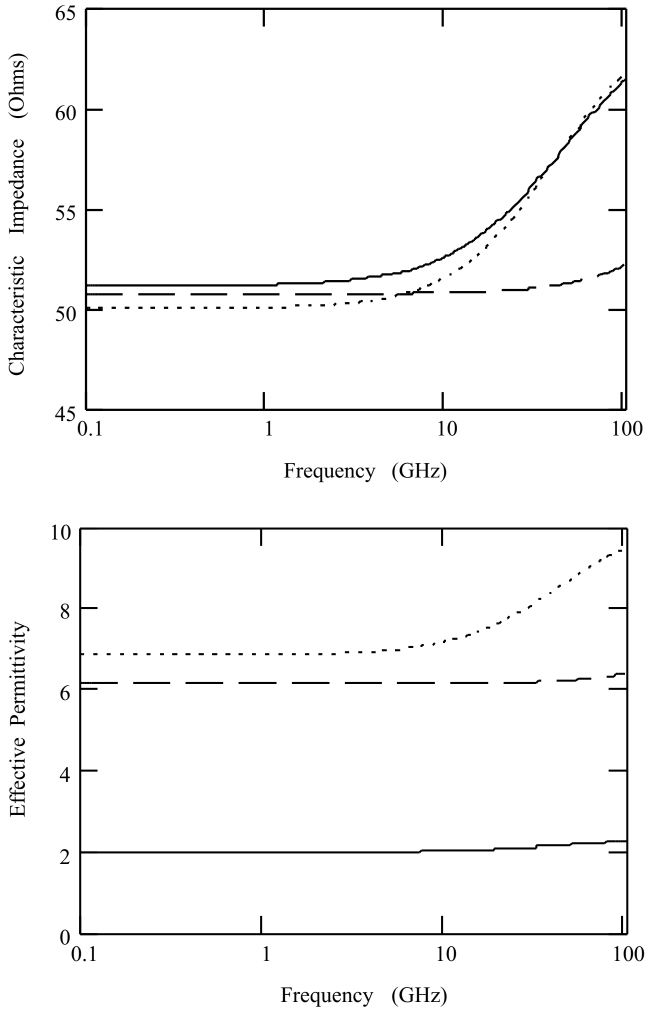

FIGURE 9.17 Dispersion characteristics of 50 Ω line on three substrates (solid line is ε_r = 2.33, *h* = 31 mils, *W* = 90 mils, dotted line is ε_r = 10.2, *h* = 25 mils, *W* = 23 mils and the dashed line is ε_r = 9, h = 2.464 mils, W = 2.5 mils). Shown in (a), the impedance changes significantly at high frequencies for the thicker substrates as does the effective permittivity shown in (b).

A variety of techniques have also been developed to minimize or characterize the effects of discontinuities in microstrip circuits, a variety of which are shown in Figs. 9.18(a,b) including a microstrip bend and a T-junction. Another common effect is the fringing capacitance found at impedance steps or open-circuited microstrip stubs.

The microstrip bend allows flexibility in microstrip circuit layouts and may be at an arbitrary angle with different line widths at either end. However, by far the most common is the 90° bend with equal widths at either end, shown on the left of Fig. 9.18a. Due to the geometry of the bend, excess capacitance is formed causing a discontinuity. A variety of techniques have been used to reduce the discontinuity by eliminating a sufficient amount of capacitance, including the mitered bend shown on the right. Note that another way of reducing this effect is to use a curved microstrip line with sufficiently large radius to minimize the effect. A second type of discontinuity commonly encountered by necessity in layouts is the T-junction, shown in Fig. 9.18b, which is formed at a junction of two lines. As with the bend, excess capacitance is formed, degrading performance. The mitered T-junction below is used to reduce this problem. Again, a variety of other simple techniques have also been developed.

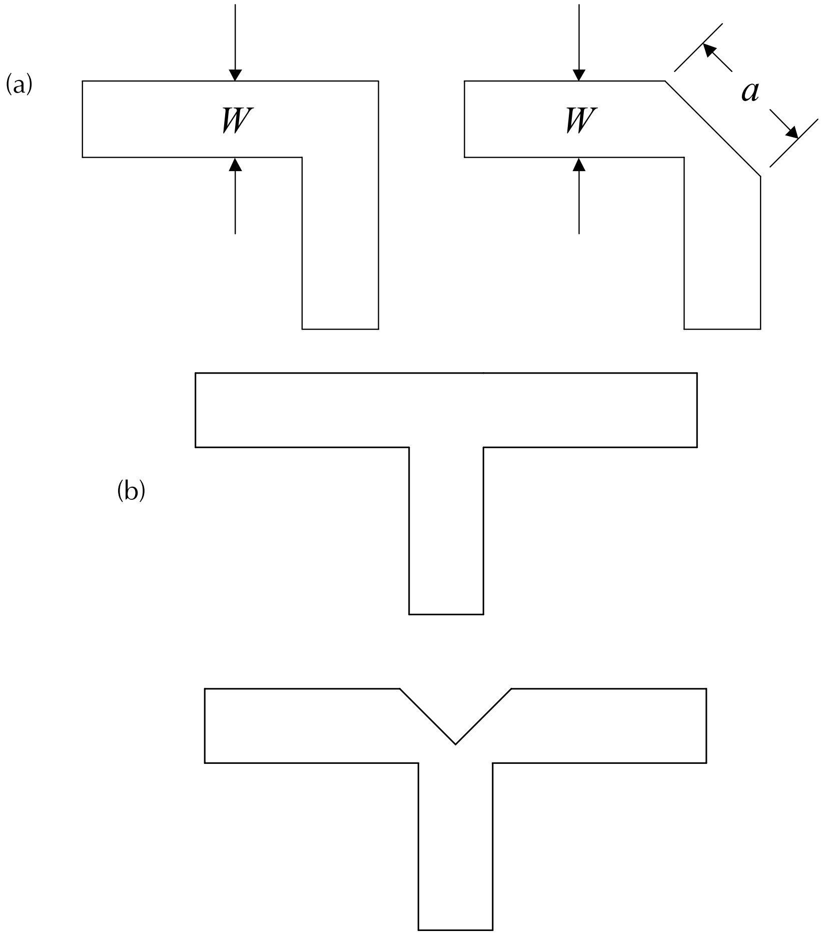

FIGURE 9.18 Two common microstrip discontinuities encountered in layout, including (a) the microstrip bend and (b) the T-junction.

Fringing capacitance will be present with microstrip open-circuited stubs and at impedance steps. With the open-circuited stub, this causes the electrical length of the structure to be somewhat longer. For an impedance step, the lower impedance line will also appear to be electrically longer. The simplest way of compensating for this problem is by modeling the capacitance and effective length of the fringing fields. Again, a variety of simple models have been developed to perform this task, most based on quasi-static approximations. A commonly used expression for the length extension of an open end based on empirical data is given by the following expression.[5]

$$\frac{\Delta l_{oc}}{h} = 0.412 \frac{\varepsilon_{re} + 0.3}{\varepsilon_{re} - 0.258} \left[\frac{W/h + 0.264}{W/h + 0.8} \right] \tag{9.137}$$

This expression is reported to yield relatively accurate results for substrates with permittivity in the range of 2 to 50, but is not as accurate for wide microstrip lines. For the impedance step, a first order approximation for determining the excess length of the impedance step is to multiply the open-end extension, $\Delta l_{oc}/h$ by an appropriate factor to obtain a useful value, i.e., $\Delta l_{step}/h \approx \Delta l_{oc}\,(w_1/w_2 - 1)/h$.

Because of the prevalence of microstrip, modern microwave CAD tools typically have extensive libraries for microstrip components, including discontinuities effects.

Coplanar Waveguide (CPW)

Coplanar Waveguide (CPW), shown in Fig. 9.16b, consists of a signal line and two ground planes on a dielectric slab with metallization on one side. For a given substrate, characteristic impedance is determined by the signal line width, s, and the two gaps, w_1 and w_2. This structure often demonstrates better dispersion characteristics than microstrip. Additionally, three terminal devices are easily integrated into this uniplanar transmission line that requires no vias for grounding. For this reason, parasitics are lower than microstrip making CPW a good choice for high frequency operation where this is a primary design concern.

The three-conductor line shown in Fig. 9.16b supports two fundamental modes, including the desired CPW-mode and an undesired coupled slotline mode if the two ground planes separating the signal line are not kept at the same potential. For this reason, wires or metal strips referred to as *air bridges* are placed at discontinuities where mode conversion may occur.

Packaging may be a problem for this type of structure, because the bottom plane of the dielectric may come in close proximity with other materials, causing perturbations of the transmission line characteristics. In practice, this is remedied by using *grounded* or *conductor-backed* CPW (CB-CPW) where a ground plane is placed on the backside for electrical isolation. At high frequencies, this may present a problem with additional losses through coupling to the parallel-plate waveguide mode. These losses can be minimized using vias in the region around the transmission line to suppress this problem.

Although CPW was first proposed by Wen[6] in 1969, acceptance of CPW has been much slower than microstrip. For this reason, simple and reliable models for CPW are not as readily available as for microstrip. A compilation of some of the more useful data can be found in Reference 6.

Slotline and Coplanar Stripline

Two other types of planar transmission lines are slotline and coplanar stripline (CPS). These structures are used less often than either microstrip or CPW, but do find some applications. Both of these structures consist of a dielectric slab with metallization on one side. Slotline has a slot of width w etched into the ground plane. CPS consists of two metal strips of width w_1 and w_2 separated by a distance s on the dielectric slab. Due to their geometry, both of these structures are balanced transmission line structures, and are useful in balanced circuits such as mixers and modulators. Only limited design information is available for these types of transmission lines.

The slotline mode is non-TEM and is almost entirely TE. However, no cutoff frequency exists as with the waveguide TE modes discussed previously in this section. Microwave circuits designed solely in slotline are seldom used. However, slotline is sometimes used in conjunction with other transmission line types such as microstrip or CPW for increased versatility. Examples of these include filters, hybrids, and resonators. Additionally, slotline is sometimes used in planar antennas, such as the slot antenna or some kinds of multilayer patch antennas.

The CPS transmission line has two conductors on the top plane of the circuit, allowing series or shunt elements to be readily integrated into CPS circuits. CPS is often used in electro-optic circuits such as optic traveling wave modulators, as well as in high-speed digital circuits. Due to its balanced nature, CPS also makes an ideal feed for printed dipoles. Difficulties (or benefits, depending on the application) with CPS include high characteristic impedances.

References

1. E. Hammerstad, Equations for microstrip circuit design, *Proc. European Microwave Conf.*, 1975, 268–272.
2. E. Hammerstad and O. Jensen, Accurate models for microstrip computer-aided design, *IEEE MTT-S Int. Microwave Symp. Dig.*, 1980, 407–409.
3. M. Kobayashi, A dispersion formula satisfying recent requirements in microstrip CAD, *IEEE Trans.*, MTT-36, August 1988, 1246–1250.
4. G.D. Vendelin, Limitations on stripline Q, *Microwave J.*, 13, May 1970, 63–69.

5. R. Garg and I.J. Bahl, Microstrip discontinuities, *Int. J. Electron.*, 45, July 1978, 81–87.
6. C.P. Wen, Coplanar waveguide: A surface strip transmission line suitable for non-reciprocal gyromagnetic device applications, *IEEE Trans.*, MTT-23, 1975, 541–548.
7. K.C. Gupta, R. Garg, I. Bahl, and R. Bhartia, *Microstrip Lines and Slotlines*, Artech House, Inc., Norwood MA, 1996.

9.4 Effects of Multipath Fading in Wireless Communication Systems

Wayne E. Stark

The performance of a wireless communication system is heavily dependent on the channel over which the transmitted signal propagates. Typically in a wireless communication system the channel consists of multiple paths between the transmitter and receiver with different attenuation and delay. The paths have different attenuation and delays because of the different distances between transmitter and receiver along different paths. For certain transmitted signals the entire transmitted signal may experience a deep fade (large attenuation) due to destructive multipath cancellation. The multipath signals may also add constructively giving a larger amplitude. In addition to the multipath effect of the channel on the transmitted signal there are other effects on the transmitted signal due to the channel. One of these is distance related and is called the propagation loss. The larger the distance between the transmitter and receiver the smaller the received power. Another effect is known as shadowing. Shadowing occurs due to buildings and other obstacles obstructing the line-of-sight path between the transmitter and receiver. This causes the received signal amplitude to vary as the receiver moves out from behind buildings or moves behind buildings.

In this chapter we examine models of fading channels and methods of mitigating the degradation in performance due to fading. We first discuss in detail models for the multipath fading effects of wireless channels. We then briefly discuss the models for propagation loss as a function of distance and shadowing. Next we show an example of how diversity in receiving over multiple, independent faded paths can significantly improve performance. We conclude by discussing the fundamental limits on reliable communication in the presence of fading.

Multipath Fading

In this section we discuss the effects of multiple paths between the transmitter and receiver. These effects depend not only on the delays and amplitudes of the paths but also on the transmitted signal. We give examples of frequency selective fading and time selective fading.

Consider a sinusoidal signal transmitted over a multipath channel. If there are two paths between the transmitter and receiver with the same delay and amplitude but opposite phase (180 degree phase shift), the channel will cause the received signal amplitude to be zero. This can be viewed as destructive interference. However, if there is no phase shift, the received signal amplitude will be twice as large as the signal amplitude on each of the individual paths. This is constructive interference.

In a digital communication system data is modulated onto a carrier. The data modulation causes variations in the amplitude and phase of the carrier. These variations occur at a rate proportional to the bandwidth of the modulating signal. As an example, in a cellular system the data rates are on the order of 25 kbps and carrier frequency is about 900 MHz. So the amplitude and phase of the carrier is changing at a rate on the order of 25 kHz. Equivalently, the envelope and phase of the carrier might change significantly every 1/25 KHz = 0.04 ms = 40 µs. If this signal is transmitted over a channel with two paths with differential delay of 1 µs, the modulation part of the signal would not differ significantly. However, if this signal was received on two paths with a differential delay of 40 µs, then there would be a significant difference in the modulated part of the signal. If the data rate of the signal was increased to 250 kbps then the modulated signal would change significantly in a 4 µs time frame and thus the effect of multipath would be different.

Thus the type of fading depends on various parameters of the channel and the transmitted signal. Fading can be considered as a filtering operation on the transmitted signal. The filter characteristics are time varying due to the motion of the transmitter/receiver. The faster the motion the faster the change in the filter characteristics operation. Fading channels are typically characterized in the following ways.

1. *Frequency Selective Fading:* If the transfer function of the filter has significant variations within the frequency band of the transmitted signal, the fading is called frequency selective.
2. *Time Selective Fading:* If the fading changes relatively quickly (compared to the duration of a data bit), the fading is said to be time selective.

If the channel is both time and frequency selective, it is said to be doubly selective.

To illustrate these types of fading we consider some special cases. Consider a simple model for fading where there are a finite number, k, of paths from the transmitter to the receiver. The transmitted signal is denoted by $s(t)$. The signal can be represented as a baseband signal modulated onto a carrier as

$$s(t) = \mathrm{Re}\left[s_0(t)\exp\left\{j2\pi f_c t\right\}\right]$$

where f_c is the carrier frequency and $s_0(t)$ is the baseband signal or the envelope of the signal $s(t)$. The paths between the transmitter and receiver have delays τ_k and amplitudes α_k. The received signal can thus be expressed as

$$r(t) = \mathrm{Re}\left[\sum_k \alpha_k s_0(t-\tau_k)\exp\left\{j2\pi f_c(t-\tau_k) + j\phi_k\right\}\right]$$

where ϕ_k is a phase term added due the kth path that might be due to a reflection off an object. The baseband received signal is given by

$$r_0(t) = \sum_k \alpha_k s_0(t-\tau_k)\exp\left\{j\phi_k - j2\pi f_c \tau_k\right\}.$$

To understand the effects of multipath we will consider a couple different examples.

Frequency/Time Nonselective (Flat) Fading

First we consider a frequency and time nonselective fading model. In this case the multipath components are assumed to have independent phases. If we let W denote the bandwidth of the transmitted signal, the envelope of the signal does not change significantly in time smaller than $1/W$. Thus if the maximum delay satisfies $\tau_{\max} \ll 1/W$, that is

$$\frac{1}{f_c} \ll \tau_k \ll T = W^{-1}$$

Then $s_0(t - \tau_k) \approx s_0(t)$. In this case

$$\begin{aligned} r_0(t) &= s_0(t)\left(\sum_k \alpha_k \exp\left\{j\theta_k\right\}\right) \\ &= Xs_0(t) \end{aligned}$$

where $\theta_k = \phi_k - 2\pi f_c \tau_k$. The factor $X = \sum_k \alpha_k \exp\{j\theta_k\}$ by which the signal is attenuated/phase shifted is usually modeled by a complex Gaussian distributed random variable. The magnitude of X is a Rayleigh distributed random variable. The phase of X is uniformly distributed. The fading occurs because the random phases sometimes add destructively and sometimes add constructively. Thus for narrow enough signal bandwidths ($\tau_k \ll W^{-1}$) the multipath results in an amplitude attenuation by a Rayleigh distributed random variable. It is important to note that the transmitted signal in this example has not been distorted. The only effect on the transmitted signal is an amplitude and phase change. This will not be true in a frequency selective channel.

Usually the path lengths change with time due to motion of the transmitter or receiver. Here we have assumed that the motion is slow enough relative to the symbol duration so that $\alpha_k(t)$ and $\phi_k(t)$ are constants. In this model the transmitted signal is simply attenuated by a slowly varying random variable. This is called a flat fading model or frequency and time nonselective fading.

Frequency Selective/Time Nonselective Fading

Now consider the case where the bandwidth of the modulating signal $s_0(t)$ is W and the delays satisfy

$$\tau_k \gg T = W^{-1}.$$

In this case we say the channel exhibits frequency selective fading. For example, consider a discrete multipath model. That is,

$$r_0(t) = \alpha_1 e^{j\theta_1} s_0(t-\tau_1) + \cdots \alpha_M s_0(t-\tau_M) e^{j\theta_M}.$$

The impulse response of this channel is

$$h(t) = \sum_{k=1}^{M} \alpha_k e^{j\theta_k} \delta(t-\tau_k)$$

and the transfer function is

$$H(f) = \sum_{k=1}^{M} \alpha_k \exp\{j\theta_k - j2\pi f \tau_k\}.$$

More specifically, assume $M = 2$ and that the receiver is synchronized to the first path (so that we assume $\tau_1 = \phi_1 = \theta_1 = 0$). Then

$$H(f) = 1 + \alpha_2 \exp\{j\theta_k - j2\pi f \tau_k\}$$

At frequencies where $2\pi f\tau_2 = \theta_2 + 2n\pi$ or $f = (\theta_2 + 2n\pi)/2\pi\tau_2$ the transfer function will be $H(f) = 1 + \alpha_2$. If $\alpha_2 > 0$, the amplitude of the received signal will be larger because of the second path. This is called constructive interference. At frequencies where $2\pi f\tau_2 = \theta_2 + (2n + 1)\pi$ or $f = (\theta_2 + (2n + 1)\pi)/2\pi\tau_2$, the transfer will be $H(f) = 1 - \alpha_2$. Again, for $\alpha_2 > 0$ the amplitude of the received signal will be smaller due to the second path. This is called destructive interference. The frequency range between successive nulls (destructive interference) is $1/\tau$. Thus if $\tau \gg \frac{1}{W}, \frac{1}{\tau} \ll W$ there will be multiple nulls in the spectrum of the received signal. In Fig. 9.19 we show the transfer function of a multipath channel with two equal strength paths with differential delay of 1 microsecond. In Fig. 9.20 we show the transfer function of a channel with eight equal strength paths with delays from 0 to 7 μs. The frequency selectivity of the channel is seen in the fact that the transfer function varies as a function of frequency. Narrowband systems

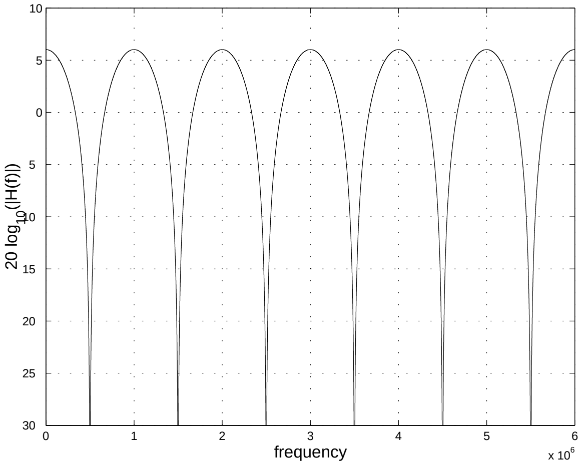

FIGURE 9.19 Transfer function of multipath channel with two equal strength paths and relative delay of 1 µs.

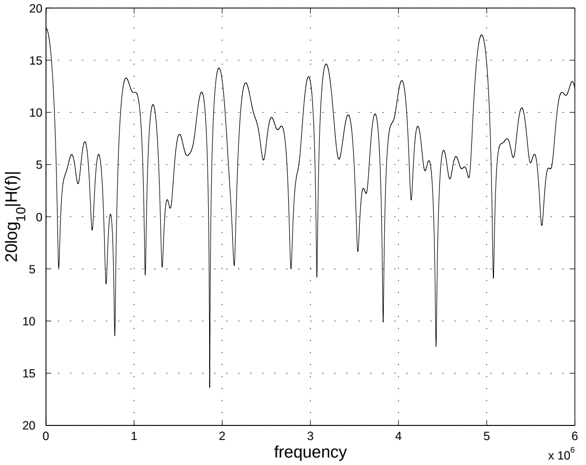

FIGURE 9.20 Transfer function of multipath channel with eight equal strength paths.

have the potential for the whole signal band to experience a deep fade while in wideband systems the transfer function of the channel varies within the band of the transmitted signal and thus the channel causes distortion of the transmitted signal.

Time Selectivity

The dual concept to frequency selectivity is time selectivity. In this case the path strength is changing as a function of time (e.g., due to vehicle motion) and the envelope of the received signal (as the vehicle moves) undergoes time-dependent fading. A model for this would be that of a time-varying impulse response (without frequency selectivity):

$$h\left(t;t-\beta\right)=\alpha_k\left(t\right)e^{j\theta\left(t\right)}\delta\left(t-\beta-\tau\left(t\right)\right)$$

where $\tau(t)$ is the time-varying delay between the transmitter and receiver. The output $r_0(t)$ of the channel is related to the input $s_0(t)$ via

$$r_0(t) = \int_{-\infty}^{\infty} h(t;t-\beta)\, s_0(\beta)\, d\beta$$

$$= \int_{-\infty}^{\infty} \alpha_k(t) e^{j\theta(t)}\, \delta(t-\beta-\tau(t))\, s_0(\beta)\, d\beta$$

$$= \alpha_k(t) e^{j\theta(t)} s_0(t-\tau(t))$$

Because the impulse response is time varying, the fading at different time instances is correlated if the time instances are very close and uncorrelated if they are very far apart. Consider the simple case of a sinusoidal at frequency f_c as the signal transmitted. In this case, the baseband component of the transmitted signal, $s_0(t)$, is a constant DC term. However the output of the channel is given by

$$r_0(t) = \alpha_k(t) e^{j\theta(t)} s_0.$$

The frequency content of the baseband representation of the received signal is no longer just a DC component, but has components at other frequencies due to the time-varying nature of α and θ. If we consider just a single direct path between the transmitter and receiver and assume that the receiver is moving away from the transmitter, then because of the motion there will be a Doppler shift in the received spectrum. That is the received frequency will be shifted down in frequency. Similarly if the receiver is moving toward the transmitter, there will be a shift up in the frequency of the received signal. Because there can be paths between the transmitter and receiver that are direct and paths that are reflected, some paths will be shifted up in frequency and some paths will be shifted down in frequency. The overall received signal will be spread out in the frequency domain due to these different frequency shifts on different paths. The spread in the spectrum of the transmitted signal is known as the Doppler spread. If the data duration is much shorter than the time variation of the fading process, the fading can be considered a constant or a slowly changing random process. In Fig. 9.21 we plot the fading amplitude for a single path as a function of time for a vehicle traveling at 10 miles per hour. In Fig. 9.22 a similar plot is done for a vehicle at 30 mph. It is clear that the faster a vehicle is moving the more quickly the fading amplitude varies. Fading amplitude variations with time can be compensated for by power control at low vehicle velocities. At high velocities the changes in amplitude can be averaged out by proper use of error control coding.

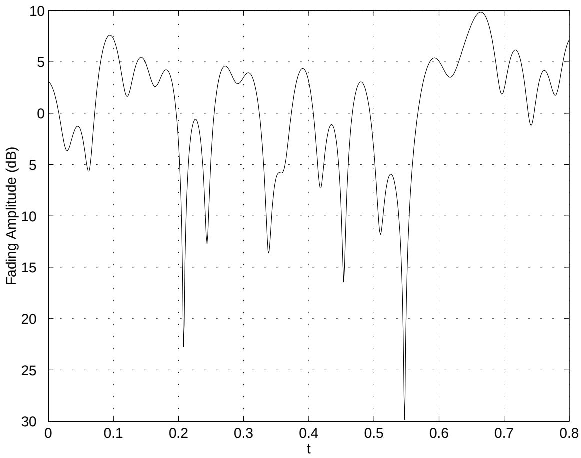

FIGURE 9.21 Received signal strength as a function of time for vehicle velocity 10 mph.

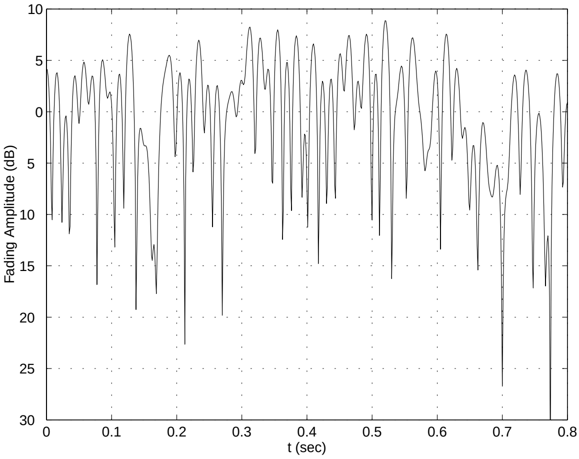

FIGURE 9.22 Received signal strength as a function of time for vehicle velocity 30 mph.

General Model

In this section we describe a general mode for fading channels and discuss the relevant parameters that characterize a fading channel. The most widely used general model for fading channels is the wide-sense stationary, uncorrelated scattering (WSSUS) fading model. In this model the received signal is modeled as a time-varying filter operation on the transmitted signal. That is

$$r_0(t) = \int_{-\infty}^{\infty} h(t; t-\alpha) s_0(\alpha) d\alpha$$

where $h(t; t - \tau)$ is the response due to an impulse at time τ and is modeled as a zero mean complex Gaussian random process. Note that it depends not only on the time difference between the output and the input, but also on the time directly. The first variable in h accounts for the time-varying nature of the channel while the second variable accounts for the delay between the input and output. This is the result of the assumption that there are a large number of (possibly time-varying) paths at a given delay with independent phases. If there is no direct (unfaded) path, then the impulse response will have zero mean. In this case the channel is known as a Rayleigh faded channel. If there is a (strong) direct path between the transmitter and receiver, then the filter $h(t, \tau)$ will have nonzero mean. This case is called a Rican faded channel. In the following we will assume the mean of the channel is zero.

The assumption for WSSUS is that the impulse response, $h(t, \tau)$, is uncorrelated for different delays and the correlation at different times depends only on the time difference. Mathematically we write the correlation of the impulse response at different delays and times as an expectation;

$$E\left[h(t; \tau_1) h^*(t + \Delta t; \tau_2)\right] = \phi(\tau_1; \Delta t) \delta(\tau_2 - \tau_1)$$

where $E[h(t; \tau_1)h^*(t + \Delta t; \tau_2)]$ denotes the expected (average) value of the impulse response at two different delays and times. The function $\phi(\tau; \Delta t)$ is the intensity delay profile and $\delta(\tau)$ is the usual Dirac delta function.

For a wide-sense stationary uncorrelated scattering (WSSUS) model the correlation between the responses at two different times depends only on the difference between times. This is indicated by the Dirac delta function. Also, the response at two different delays are uncorrelated. The amount of power received at a given delay τ is $\gamma(\tau; 0)$. This is called the intensity delay profile or the delay power spectrum. The mean excess delay, μ_m is defined to be the average excess delay above the delay of the first path

$$\mu = \frac{\int_{\tau_{\min}}^{\tau_{\max}} \tau\phi\left(\tau;0\right)d\tau}{\int_{\tau_{\min}}^{\tau_{\max}} \phi\left(\tau;0\right)d\tau} - \tau_{\min}$$

The rms delay spread is defined as

$$s = \left[\frac{\int_{\tau_{\min}}^{\tau_{\max}} \left(\tau - \mu - \tau_{\min}\right)^2 \phi\left(\tau;0\right)d\tau}{\int_{\tau_{\min}}^{\tau_{\max}} \phi\left(\tau;0\right)d\tau}\right]^{1/2}$$

The largest value $\tau_{\max}$ of τ such that $\phi(\tau; 0)$ is nonzero is called the multipath spread of the channel. The importance of the rms delay spread is that it is a good indicator of the performance of a communication system with frequency selective fading. The larger the rms delay spread the more inter-symbol interference. In the general model the delays cause distortion in the received signal.

Now consider the frequency domain representation of the channel response. The time-varying function of the channel $H(f; t)$ is given by the Fourier transform of the impulse response with respect to the delay variable. That is,

$$H\left(f;t\right) = \int_{-\infty}^{\infty} h\left(t;\tau\right)e^{-j2\pi f\tau}d\tau.$$

Since $h(t; \tau)$ is assumed to be a complex Gaussian random variable, $H(f; t)$ is also a complex Gaussian random process. The correlation $\Phi(f_1, f_2; \Delta t)$ between the transfer function at two different frequencies and two different times as defined as

$$\begin{aligned}\Phi\left(f_1, f_2;\Delta t\right) &= E\left[H\left(f_1;t\right)H^*\left(f_2;t+\Delta t\right)\right]\\ &= \int_{-\infty}^{\infty} \phi\left(\tau;\Delta t\right)e^{-j2\pi\left(f_2-f_1\right)\tau}d\tau\end{aligned}$$

Thus the correlation between two frequencies for the WSSUS model (and at two times) depends only on the frequency difference. If we let $\Delta t = 0$ then we obtain

$$\Phi\left(\Delta f;0\right) = \int_{-\infty}^{\infty} \phi\left(\tau;0\right)e^{-j2\pi\left(\Delta f\right)\tau}d\tau$$

As the frequency separation becomes larger the correlation in the response between those two frequencies generally decreases. The smallest frequency separation, B_c, such that the correlation of the response at two frequencies separated by B_c is zero is called the coherence bandwidth of the channel. It is related to the delay spread by

$$B_c \approx \frac{1}{\tau_{\max}}$$

The rms delay spread and coherence bandwidth are important measures for narrowband channels. The performance of an equalizer for narrowband channels often does not depend on the exact delay power profile, but simply on the rms delay spread.

Now consider the time-varying nature of the channel. In particular, consider $\Phi(\Delta f; \Delta t)$, which is the correlation between the responses of the channel at two frequencies separated by Δf and at times separated by Δt. For $\Delta f = 0$ $\Phi(0; \Delta t)$ measures the correlation between two responses (at the same frequency) but separated in time by Δt. The Fourier transform gives the Doppler power spectral density

$$S(\lambda) = \int_{-\infty}^{\infty} \phi(0;\gamma) e^{-j2\pi\lambda\gamma} d\gamma.$$

The Doppler power spectral density gives the distribution of received power as a function of frequency shift. Since there are many paths coming from different directions and the receiver is moving, these paths will experience different frequency shifts. Consider a situation where a vehicle is moving toward a base station with velocity ν.

Example

If we assume that there are many multipath components that arrive with an angle uniformly distributed over $[0, 2\pi]$, then the Doppler spectral density is given by

$$S(\lambda) = \frac{1}{2\pi f_m}\left[1-\left(\lambda/f_m\right)^2\right]^{-1/2}, \quad 0 \le |\lambda| \le f_m$$

where $f_m = \nu f_c/c$, f_c is the center frequency and c is the speed of light (3×10^8 m/s). For example, a vehicle moving at 100 m/s with 1 GHz center frequency has maximum Doppler shift of 33.3 Hz. A vehicle moving at 30 m/s would have a maximum Doppler shift of 10 Hz. Thus most of the power is either at the carrier frequency plus 10 Hz or at the carrier frequency minus 10 Hz. The corresponding autocorrelation function is the inverse Fourier transform and is given by

$$\begin{aligned}\Phi(0,\gamma) &= \int_{-\infty}^{\infty} S(\lambda) e^{j2\pi\lambda\gamma} d\lambda \\ &= J_0\left(2\pi f_m \gamma\right)\end{aligned}$$

The channel correlation and Doppler spread are illustrated in Figs. 9.23 and 9.24 for vehicle velocities of 10 km/hour and 100 km/hour. From these figures it is clear that a lower vehicle velocity implies a small spread in the spectrum of the received signal and a larger correlation between the fading at different times. It is often useful for the receiver in a digital communication system to estimate the fading level. The faster the fading level changes the harder it is to estimate. The product of maximum Doppler spread f_m times the data symbol duration T is a useful tool for determining the difficulty in estimating the channel response. For $f_m T$ products much smaller than 1, the channel is easy to estimate while for $f_m T$ much larger than 1, the channel is hard to estimate. Channel estimation can improve the performance of coded systems as shown in the last section of this chapter. The availability of channel information is sometimes called "side information."

If the channel is not time varying (i.e., time invariant), then the responses at two different times are perfectly correlated so that $\Phi(0; \Delta t) = 1$. This implies that $S(\lambda) = \delta(f)$.

The largest value of λ for which $S(\lambda)$ is nonzero is called the Doppler spread of the channel. It is related to the coherence time T_c, the largest time difference for which the responses are correlated by

$$B_d = \frac{1}{T_c}$$

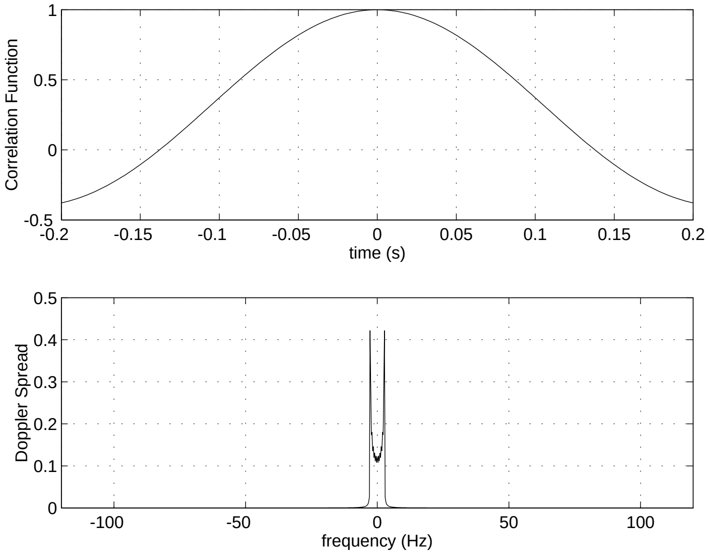

FIGURE 9.23 Channel correlation function and Doppler spread for f_c = 1 GHz, ν = 10 km/hour.

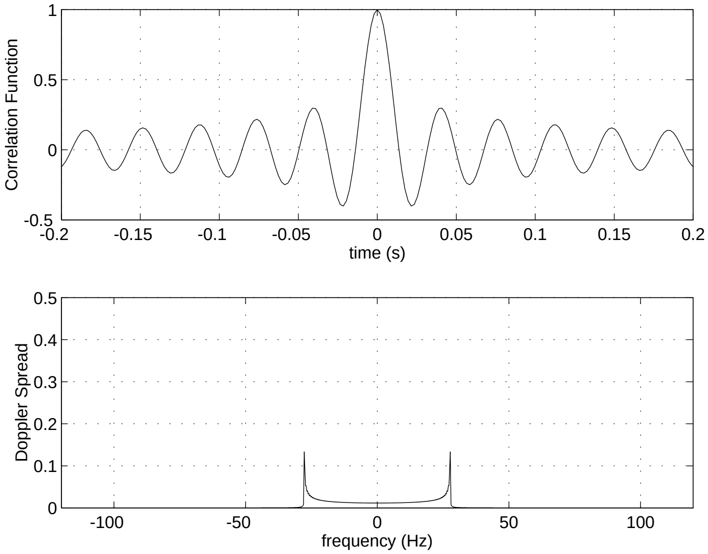

FIGURE 9.24 Channel correlation function and Doppler spread for f_c = 1 GHz, ν = 100 km/hour.

GSM Model

The GSM (Global System for Mobile Communications) model was developed in order to compare different coding and modulation techniques. The GSM model is a special case of the general WSSUS model described in the previous section. The model consists of N_p paths, each time varying with different power levels. In Fig. 9.25 one example of the delay power profile for a GSM model of an urban environment is shown. In the model each path's time variation is modeled according to a Doppler spread for a uniform angle of arrival spread for the multipath. Thus the vehicle velocity determines the time selectivity for each path. The power delay profile shown below determines the frequency selectivity of the channel.

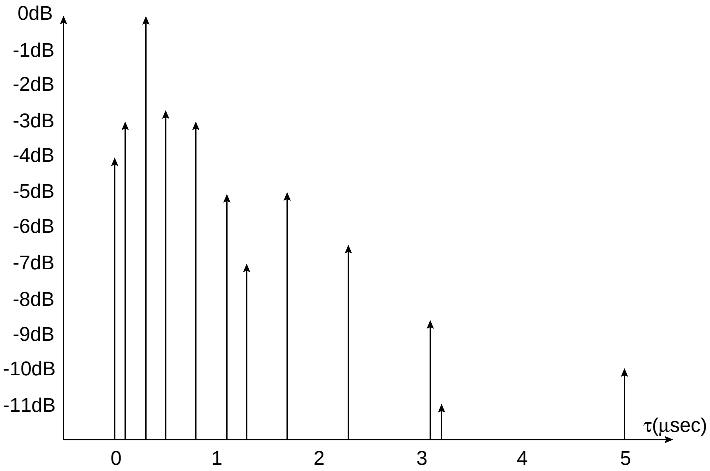

FIGURE 9.25 Power delay profile for the GSM model for typical urban channel.

TABLE 9.6 Parameters for Power Delay Profile GSM Model of Urban Area

Path	Delay (μ sec)	Average Power (dB)
1	0.0	–4.0
2	0.1	–3.0
3	0.3	0.0
4	0.5	–2.6
5	0.8	–3.0
6	1.1	–5.0
7	1.3	–7.0
8	1.7	–5.0
9	2.3	–6.5
10	3.1	–8.6
11	3.2	–11.0
12	5.0	–10.0

In Table 9.6 the parameters for the GSM model are given. The usefulness of this model is that it gives communication engineers a common channel to compare the performance of different designs.

Propagation Loss

The fading discussed above is referred to as short-term fading as opposed to long-term fading. Long-term fading refers to shadowing of the receiver from the transmitter due to terrain and buildings. The time scale for long-term fading is much longer (on the order of seconds or minutes) than the time scale for short-term fading. It is generally modeled as lognormal. That is the received power (in dB) has a normal (or Gaussian) distribution.

In this section we discuss the received power as a function of distance from the receiver. Suppose we have a transmitter and receiver separated by a distance d. The transmitter and receiver have antennas with gain G_t and G_r respectively. If the transmitted power is P_l the received power is

$$P_r = P_t G_r G_t \left(\frac{\lambda}{4\pi d} \right)^2$$

where $\lambda = c/f$ is the wavelength of the signal. The above equation holds in free space without any reflections or multipath of any sort.

Now consider the case where there is an additional path due to a single reflection from the ground. The multipath has a different phase from the direct path. If we assume the reflection from the ground causes a 180 degree phase change, then for large distances relative to the heights of the antennas the relation between the transmitted power and the received power changes to

$$P_r = P_t G_r G_t \frac{h_1^2 h_2^2}{d^4}$$

where h_1 and h_2 are the heights of the transmitting and receiving antenna. Thus the relation of received power to distance becomes an inverse fourth power law, or equivalently, the power decreases 40 dB per decade of distance. Experimental evidence for a wireless channel shows that the decrease in power with distance is 20 dB per decade near the base station, but as the receiver moves away, the rate of decrease increases. There are other models based on experimental measurements in different cities that give more complicated expressions for the path loss as a function of distance, antenna height, and carrier frequency. See [1] for further details.

Shadowing

In addition to the multipath effect on the channel and the propagation loss there is an effect due to shadowing. If a power measurement at a fixed distance from the transmitter was made there would be local variations due to constructive and destructive interference (discussed previously). At a fixed distance from the transmitter we would also have fluctuations in the received power because of the location of the receiver relative to various obstacles (e.g., buildings). If we measured the power over many locations separated by a distance of a wavelength or more from a given point we would see that this average would vary depending on the location of measurement. Measurements with an obstacle blocking the direct line-of-sight path would have much smaller averages than measurements without the obstacle. These fluctuations due to obstacles are called “shadowing.” The fluctuation in amplitude changes much slower than that due to multipath fading. Multipath fading changes as the receiver moves about a wavelength (30 cm for a carrier frequency of 1 GHz) in distance while shadowing causes fluctuations as the receiver moves about 10 m or more in distance.

The model for these fluctuations is typically that of a log-normal distributed random variable for the received power. Equivalently, the power received expressed in dB is a Gaussian distributed random variable with the mean being the value determined by the propagation loss. The variance is dependent on the type of structures where the vehicle is located and varies from about 3 to 6 dB. The fluctuations, however, are correlated. If $\nu(d)$ is a Gaussian random process modeling the shadowing process (in dB) at some location, then the model for the correlation between the shadowing at distance d_1 and the shadowing at distance d_2 is

$$E\left[\nu\left(d_1\right)\nu\left(d_2\right)\right] = \sigma^2 \exp\left\{-\left|d_1 - d_2\right| / d_0\right\}$$

where d_0 is a parameter that determines how fast the correlation decays with distance. If the velocity is known, then the correlation with time can be determined from the correlation in space. A typical value for d_0 is 10 m. Because shadowing is relatively slow, it can be compensated for by power control algorithms.

Performance with (Time and Frequency) Nonselective Fading

In this section we derive the performance of different modulation techniques with nonselective fading. We will ignore the propagation loss and shadowing effect and concentrate on the effects due only to multipath fading. First the error probability conditioned on a particular fading level is determined. Then the conditional error probability is averaged with respect to the distribution of the fading level.

Coherent Reception, Binary Phase Shift Keying (BPSK)

First consider a modulator transmitting a BPSK signal received with a faded amplitude. The transmitted signal is

$$s(t) = \sqrt{2P}b(t)\cos(2\pi f_c t)$$

where $b(t)$ is a data bit signal consisting of a sequence of rectangular pulses of amplitude +1 or –1. The received signal is

$$r(t) = R\sqrt{2P}b(t)\cos(2\pi f_c t + \phi) + n(t)$$

where $n(t)$ is additive white Gaussian noise with two-side power spectral density $N_0/2$. Assuming the receiver can accurately estimate the phase, the demodulator (matched filter) output at time kT is

$$z_k = R\sqrt{E}b_{k-1} + \eta_k$$

where $E = PT$ is the transmitted energy, b_{k-1} is the data bit transmitted during the time interval $[(k-1)T, kT]$, and η_k is a Gaussian random variable with mean 0 and variance $N_0/2$. The random variable R represents the attenuation due to fading ($R = |X|$) or fading level and has probability density

$$p_R(r) = \begin{cases} 0, & r < 0 \\ \dfrac{r}{\sigma^2} e^{-r^2/2\sigma^2} & r \geq 0 \end{cases}$$

The density function determines the probability that the fading is between any two levels as

$$P\{a < R \leq b\} = \int_a^b p_R(r)\,dr.$$

The error probability for a given fading level R is

$$P_e(R) = Q\left(\sqrt{\frac{2ER^2}{N_0}}\right).$$

The unconditional error probability is the average of the conditional error probability for a given fade level with respect to the density of the fading level.

$$P_e = \int_{r=0}^{\infty} p_R(r) Q\left(\sqrt{\frac{2Er^2}{N_0}}\right) dr$$

$$= \frac{1}{2} - \frac{1}{2}\sqrt{\frac{\bar{E}/N_0}{1+\bar{E}/N_0}}.$$

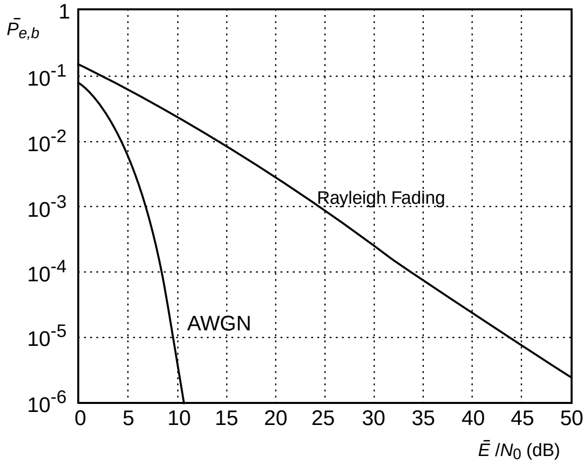

FIGURE 9.26 Bit error probability for BPSK with Rayleigh fading.

The error probability is shown in Fig. 9.26 for the case of no fading (additive white Gaussian noise) and Rayleigh fading. For the additive white Gaussian noise channel the error probability decreases exponentially with signal-to-noise ratio, E/N_0. However, with fading the decrease in error probability is much slower. In fact, for large E/N_0 the error probability is

$$P_e \simeq \frac{1}{4E/N_0}.$$

Thus for high E/N_0, the error probability decreases inverse linearly with signal-to-noise ratio.

To achieve an error probability of 10^{-5} requires a signal-to-noise ratio of 44.0 dB, whereas in additive white Gaussian noise the required signal-to-noise ratio for the same error probability is 9.6 dB. Thus fading causes a loss in signal-to-noise ratio of 34.4 dB. This loss in performance is at the same average received power. The cause of this loss is the fact that the signal amplitude sometimes is very small and causes the error probability to be close to 1/2. Of course, sometimes the signal amplitude is large and results in a very small error probability (say 0). However, when we average the error probability the result is going to be much larger than the error probability at the average signal-to-noise ratio because of the highly nonlinear nature of the error probability as a function of signal amplitude without fading.

While the specific error probabilities change when the modulation changes the general nature of the error probabilities remain the same. That is, without fading the error probability decreases exponentially with signal-to-noise ratio, while with fading the error probability decreases inverse linearly with signal-to-noise ratio. This typically causes a loss in performance of between 30 and 40 db and forces a designer to consider mitigation techniques as will be discussed subsequently.

BPSK with Diversity

To overcome this loss in performance (without just increasing power) a number of techniques are applied. Many of the techniques attempt to receive the same information with independent fading statistics. This is generally called diversity. The diversity could be the form of L different antennas suitably separated so that the fading on different paths from the transmitter are independent. The diversity could be in the form of transmitting the same data L times suitably separated in time so that the fading is independent.

In any case, consider a system with L independent paths. The receiver demodulates each path coherently. Assume that the receiver also knows exactly the faded amplitude on each path. The decision statistics are then given by

$$z_l = r_l \sqrt{E} b + \eta_l, \quad l = 1, 2, \ldots, L$$

where r_l are Rayleigh η_l is Gaussian, and b represents the data bit transmitted, which is either +1 or –1. The optimal method to combine the demodulator outputs can be derived as follows. Let $p_1(z_1 \ldots, z_L | r_1, \ldots, r_L)$ be the conditional density function of $z_1, \ldots, z_L$ given the transmitted bit is +1 and the fading amplitude is $r_1, \ldots, r_L$. The unconditional density is

$$p_1\left(z_1, \ldots, z_L, r_1, \ldots, r_L\right) = p_1\left(z_1, \ldots, z_L \middle| r_1, \ldots, r_L\right) p\left(r_1, \ldots, r_L\right)$$

The conditional density of z_1 given $b = 1$ and r_1, is Gaussian with mean $r_l\sqrt{E}$ and variance $N_0/2$. The joint distribution of $z_1, \ldots, z_L$ is the product of the marginal density functions. The optimal combining rule is derived from the ratio

$$\begin{aligned}\Lambda &= \frac{p_1\left(z_1, \ldots, z_L, r_1, \ldots, r_L\right)}{p_{-1}\left(z_1, \ldots, z_L, r_1, \ldots, r_L\right)} \\ &= \exp\left\{\frac{4}{N_0} \sum_{l=1}^{L} z_l r_l \sqrt{E}\right\}.\end{aligned}$$

The optimum decision rule is to compare Λ with 1 to make a decision. Thus the optimal rule is

$$\sum_{l=1}^{L} r_l z_l \underset{b=-1}{\overset{b=+1}{\gtrless}} 0$$

The error probability with diversity L can be determined using the same technique as used without diversity. The expression for error probability is

$$P_e(L) = P_e(1) - \frac{1}{2} \sum_{k=1}^{L-1} \frac{(2k)!}{k!k!} \left(1 - 2P_e(1)\right)\left(P_e(1)\right)^k \left(1 - P_e(1)\right)^k.$$

The error probability as a function of the signal-to-noise ratio is shown in Fig. 9.27. The signal-to-noise ratio in this case is defined as $E_b/N_0 = E * L/N_0$ where E is the energy transmitted per transmitting antenna or time diversity. Thus we assume that LE_b is the energy needed to have the signal received with L independent fading amplitudes. If we had L receiving antennas, then the performance as a function of the transmitting energy would be L times better. In any case, we plot the error probability as a function of the total received energy. In the case of diversity transmission, the energy transmitted per bit E_b is LE. For a fixed E_b, as L increases, each transmission contains less and less energy, but there are more transmissions over independent faded paths. In the limit, as L becomes large using the weak law of large numbers it can be shown that

$$\lim_{L \to \infty} P_e(L) = Q\left(\sqrt{\frac{2\bar{E}_b}{N_0}}\right)$$

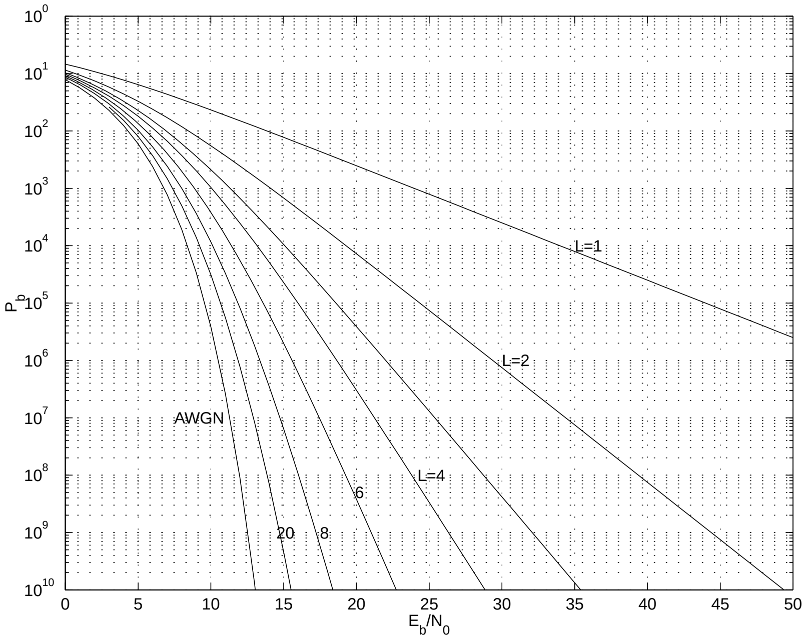

FIGURE 9.27 Error probability for BPSK (coherent demodulation) with and without Rayleigh fading.

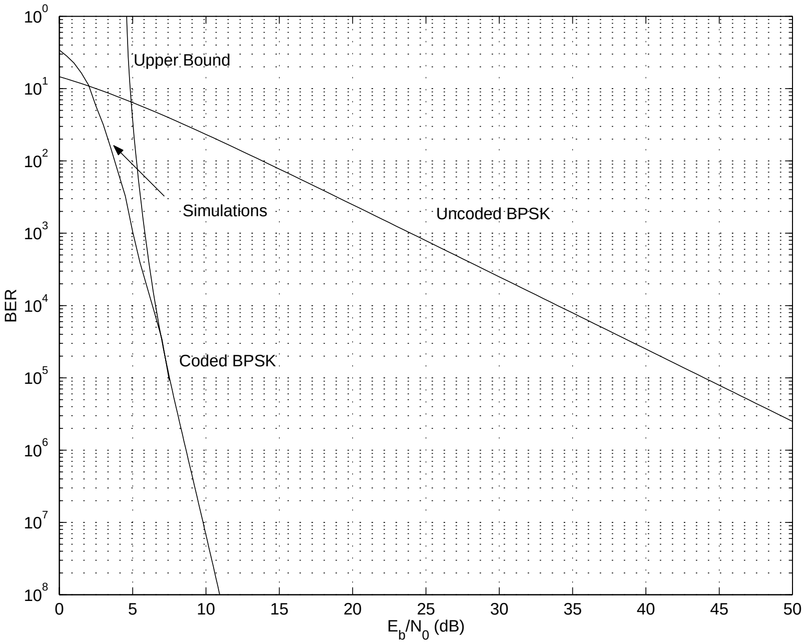

FIGURE 9.28 Error probability for BPSK (coherent demodulation) with Rayleigh fading and convolutional coding.

For large signal-to-noise ratio the error probability with diversity L is decreasing as $1/(E_b/N_0)^L$. While these curves show it is possible to get back to the performance with additive white Gaussian noise by using sufficient resources (diversity), it is possible to do even better with the right coding. In Fig. 9.28 we show the performance of a rate 1/2 constraint length 7 convolutional code on a Rayleigh faded channel (independent fading on each bit) where the receiver knows the fading level (side information) for each bit and can appropriately weight the metric in the decoder. Notice that the required E_b/N_0 for 10^{-5} bit error probability is about 7.5 dB, which is less than that required for uncoded BPSK without fading. The gain compared to uncoded performance is more than 36 dB.

Fundamental Limits

The fundamental limits on performance can be determined for a variety of circumstances. Here we assume that the transmitter has no knowledge of the fading amplitude and assume the modulation in binary phase shift keying. When the receiver knows exactly the amplitude (and phase) of the fading process we say that side information is available. The maximum rate of transmission (in bits/symbol) is called the capacity of the channel C. If an error control code of rate r information bits/channel use is used, then reliable (arbitrarily small error probability) is possible provided the rate is less than the capacity. For the case of side information available this condition is

$$r < C = 1 - \int_{r=0}^{\infty}\int_{y=-\infty}^{\infty} f(r)\, g(y) \log_2\left(1 + e^{-2y\beta}\right) dy\, dr$$

where $f(r) = 2r\exp\left\{-r^2\right\}$, $\beta = \sqrt{2\bar{E}/N_0}$ and

$$g(y) = \frac{1}{\sqrt{2\pi}} \exp\left\{-\left(y - \sqrt{2\bar{E}r^2/N_0}\right)^2 \Big/ 2\right\}.$$

If the receiver does not know the fading amplitude (but still does coherent demodulation) then we say no side information is available. The rate at which reliable communication is possible in this case satisfies

$$r < C = 1 - \int_{r=0}^{\infty}\int_{y=-\infty}^{\infty} p(y|1) \log_2\left(1 + \frac{p(y|0)}{p(y|1)}\right) dy$$

where

$$p(y|0) = \int_0^{\infty} f(r) \frac{1}{\sqrt{2\pi N_0}} e^{-\left(y - \sqrt{E}r\right)^2 / N_0} dr$$

and

$$p(y|1) = \int_0^{\infty} f(r) \frac{1}{\sqrt{2\pi N_0}} e^{-\left(y + \sqrt{E}r\right)^2 / N_0} dr$$

If the receiver makes a hard decision about each modulated symbol and the receiver knows the fading amplitude, then the capacity is

$$C = \int_0^{\infty} f(r)\left[1 + p(r)\log_2\left(p(r)\right) + \left(1 - p(r)\right)\log_2\left(1 - p(r)\right)\right] dr$$

where $p(r) = Q\left(\sqrt{\frac{2\bar{E}r^2}{N_0}}\right)$. For a receiver that does not know the fading amplitude and makes hard decisions on each coded bit, the capacity is given by

$$C = 1 + \bar{p}\log_2\left(\bar{p}\right) + \left(1-\bar{p}\right)\log_2\left(1-\bar{p}\right)$$

where

$$\bar{p} = \frac{1}{2} - \frac{1}{2}\sqrt{\frac{\bar{E}/N_0}{\bar{E}/N_0+1}}.$$

Finally if the transmitter is not restricted to binary phase shift keying but can use any type of modulation, then the capacity when the receiver knows the fading level is

$$C = \int_0^\infty f\left(r\right)\frac{1}{2}\log_2\left(1+2\bar{E}r^2/N_0\right)dr$$

In Fig. 9.29 we show the minimum signal-to-noise ratio $E_b/N_0 = E/N_0/C$ per information bit required for arbitrarily reliable communication as a function of the code rate ($r = C$) being used. In this figure the top curve (a) is the minimum signal-to-noise ratio necessary for reliable communication with hard decisions and no side information. The second curve (b) is the case of hard decisions with side information. The third curve (c) is the case of soft decisions with side information and binary modulation (BPSK). The bottom curve (d) is the case of unrestricted modulation and side information available at the receiver. There is about a 2 dB gap between hard decisions and soft decisions when side information is available. There is an extra one dB degradation in hard decisions if the receiver does not know the amplitude. A roughly similar degradation in performance is also true for soft decisions with and without side information. The model shown here assumes that the fading is constant over one symbol duration,

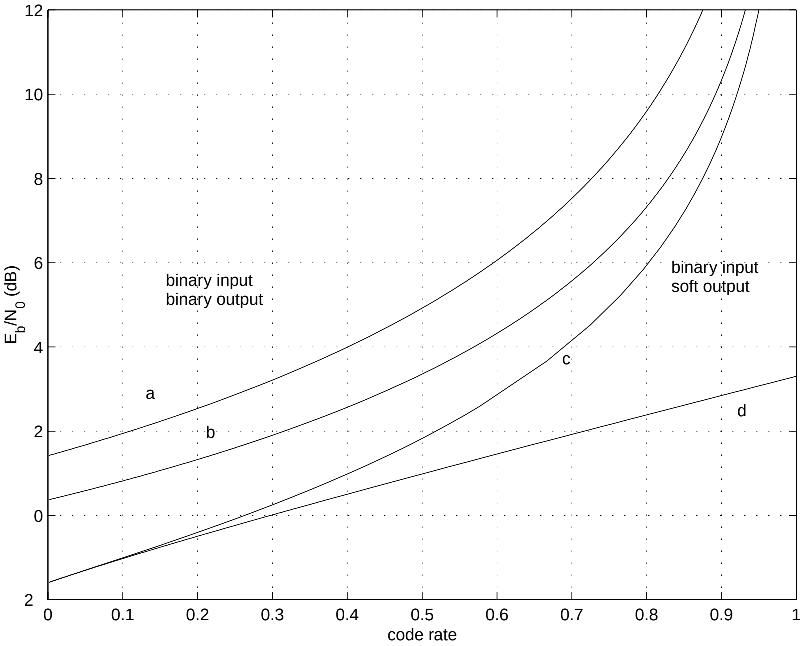

FIGURE 9.29 Capacity of Rayleigh faded channel with coherent detection.

but independent from one symbol to the next. However, for the case of the receiver knowing the fading level (side information) the capacity actually does not depend on the time selectivity as long as the fading is constant for at least one symbol duration. When there is no side information, the capacity gets larger when there is less selectivity. In this case the receiver can better estimate the channel. In fact, as the channel coherence time becomes large, the capacity without side information approaches the capacity with side information.

As can be seen in Fig. 9.29 it is extremely important that some form of encoding be used with fading. The required signal-to-noise ratio for small error probabilities has decreased from on the order of 45 dB for an uncoded system to a mere 2 dB for a coded system. When a repetition code is used, the error probability can be made to decrease exponentially with signal-to-noise ratio provided that we use a large number of antennas or repeat the same symbol a large number of times, which results in a small rate of transmission (information bits/modulated symbol). However, with error control coding such as a convolutional code and independent fading we can greatly improve the performance. The minimum required signal-to-noise ratio is no different than an unfaded channel when very low rate coding is used. For rate 1/2 coding, the loss in performance is less than 2 dB compared to an unfaded channel.

In conclusion, multipath fading causes the signal amplitude to vary and the performance of typical modulation techniques to degrade by tens of dB. However, with the right amount of error control coding, the required signal-to-noise ratio can be decreased to less than 2 dB of the required signal-to-noise ratio for a additive white Gaussian channel when the code rate is 0.5.

Reference

1. Pahlavan, K. and A. H. Levesque, *Wireless Information Networks,* John Wiley & Sons, New York, 1995.

9.5 Electromagnetic Interference (EMI)

Alfy Riddle

Fundamentals of EMI

Electromagnetic interference (EMI) is a potential hazard to all wireless and wired products. Most EMI concerns are due to one piece of equipment unintentionally affecting another piece of equipment, but EMI problems can arise within an instrument as well. Often the term electromagnetic compatibility (EMC) is used to denote the study of EMI effects. The following sections on generation of EMI, shielding of EMI, and probing for EMI will be helpful in both internal product EMI reduction and external product EMI compliance.

EMI compliance is regulated in the U.S. through the Federal Communications Commission (FCC). Specifically, Parts 15 and 18 of the Code of Federal Regulations (CFR) govern radiation standards and standards for industrial, scientific, and medical equipment. In Europe, Publication 22 from the Comite International Special des Perturbations Radioelectriques (CISPR) governs equipment radiation. Although the primary concern is compliance with radiation standards, conduction of unwanted signals onto power lines causes radiation from the long power lines, so conducted EMI specifications are also included in FCC Part 15 and CISPR 22 [1,2].

Figure 9.30 shows the allowed conducted EMI. FCC and CISPR specifications do not set any limits above 30 MHz. All of the conducted measurements are to be done with a line impedance stabilization network (LISN) connected in the line. The LISN converts current-based EMI to a measurable voltage. The LISN uses series inductors of 50 μH to build up a voltage from line current interference, and 0.1 μF capacitors couple the noise voltage to 50 ohm resistors for measurement [1]. Capacitors of 1 μF also bridge the output so the inductors see an AC short. The measurements in Fig. 9.30 are reported in dBμV, which is dB with respect to 1 μV. Both FCC and CISPR measurements specify an RF bandwidth of at least 100 kHz. The CISPR limitations given in Fig. 9.30 denote that a quasi-peak (QP) detector should

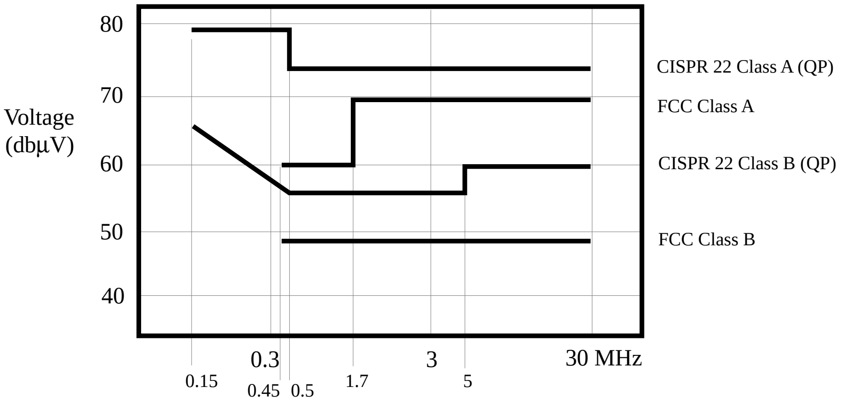

FIGURE 9.30 Conducted EMI specifications, measured with LISN.

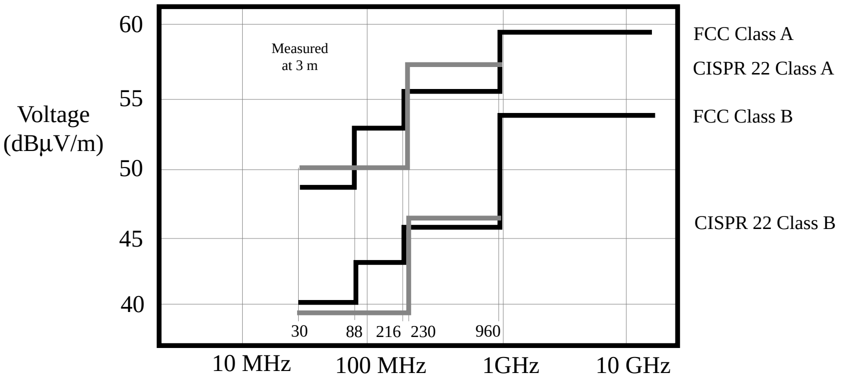

FIGURE 9.31 Radiated EMI specifications referred to 3 m.

be used. The QP detector is more indicative of human responses to interference. CISPR specifications for an averaging detector are 10 dB below that of the QP detector. FCC specifications require a QP detector. Both FCC and CISPR limitations have two classes. Class A is basically for industrial use, while Class B is for residential use.

Both CISPR and FCC radiated EMI specifications begin at 30 MHz. Fig. 9.31 shows the radiation limits for CISPR and FCC Classes A and B [1,2]. Because these measurements are made with an antenna, they are specified as a field strength in dB referenced to 1 μV/m. The measurement distances for radiation limits varies in the specifications, but all of the limits shown in Fig. 9.31 are referred to 3 m. Other distances can be derived by reducing the limits by 20 dB for every factor of ten increase in distance.

Generation of EMI

Almost any component can generate EMI. Oscillators, digital switching circuits, switching regulators, and fiber-optic transmitters can radiate through PCB traces, inductors, gaps in metal boxes, ground loops, and gaps in ground planes [1].

Switching Regulators

Because switching regulators have a fundamental frequency below 30 MHz and switch large currents at high speed, they can contribute to both conducted and radiated emissions. Very careful filtering is required so switching regulators do not contaminate ground planes with noise. The input filters on switching

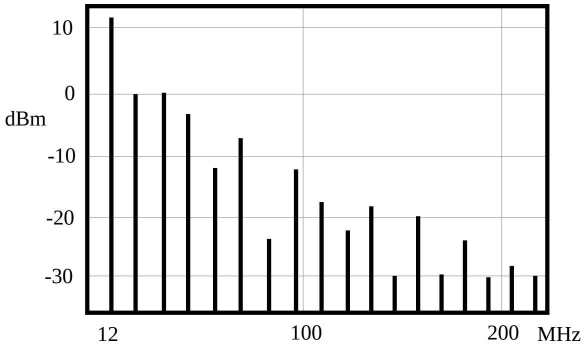

FIGURE 9.32 Harmonic clock spectra.

regulators are just as important as the output filters because the noise can travel to other power supplies and out to the line [3].

Digital Switching

Digital networks have several characteristics that increase EMI. Digital networks tend to have many lines switching simultaneously. The currents on the lines add in phase and increase radiation. Also, as CMOS digital circuits increase in clock frequency they require more current to drive their loads. Increasing both the current and the frequency creates more di/dt noise through the inductive connection from ICs to ground [4]. The fast switching of digital waveforms produces harmonics decades beyond the oscillator fundamental frequency. Fig. 9.32 shows the spectra from a typical 12 MHz crystal square-wave clock oscillator. Note that even though the output appears as a square wave, both even and odd harmonics are present. The harmonics of this oscillator fall off at roughly 20 dB/decade. As will be seen in the next section, most sources of coupling increase at about 20 dB/decade, which causes not only a relatively flat coupling spectrum, but significant EMI at ten or even 100 times the oscillator frequency. While this 12 MHz clock oscillator is at a very low frequency, similar phenomena happens with the laser drivers for high speed fiber-optic networks that operate with clocks of 2.5 GHz and higher.

Coupling

Any inductor is a potential source of coupling and radiation. Ribbon cables act like very long coupling loops and can spread signals or power supply noise all over an instrument and out to the outside world. Fundamentally, lengths of wire radiate an electric field and loops of wire radiate a magnetic field. The electric field, E_{Far}, far from a short radiator, is given by Eq. (9.138) [1]. Eq. (9.138) is in volts per meter where I is the element current, l is the element length, λ is the radiation wavelength, and r is the distance from the radiating element to the measured field. Because the field strength is inversely proportional to frequency, EMI coupling tends to increase with frequency. The far magnetic field, H_{Far}, due to a current loop is given in A/m by Eq. (9.139). In Eq. (9.139) a is the radius of the loop, c is the speed of light, I is the current in the loop, and r is the distance from the loop to the measured radiation.

$$E_{Far} = 377\, I\, l \Big/ \left(2 \lambda \mathrm{r}\right) \tag{9.138}$$

$$H_{Far} = \omega^2\, a^2\, \mu\, I \Big/ \left(1508\, c\, r\right) \tag{9.139}$$

Cabling

Cables form a source of radiation and susceptibility. In general it is the signal on the shield of a coaxial cable or the common-mode signal on twisted pairs that generates most of the radiation [1]. However, even high-quality coaxial cables will leak a finite amount of signal through their shields. Multiple braids, solid outer conductors, and even solder-filled braid coaxial cables are used to increase shielding. Twisted pair cables rely on twisting to cancel far field radiation from the differential mode. The effectiveness of the twisting reduces as frequency increases [1].

Shielding

Shielding is the basic tool for EMC work. Shielding keeps unwanted signals out and potential EMI sources contained. For the most part, a heavy metal box with no seams or apertures is the most effective shield. While thin aluminum enclosures with copper tape over the seams appear to enclose the RF currents, in fact they are a poor substitute for a heavy gauge cast box with an EMI gasket. It has been said that if spectrum analyzer manufacturers could make their instruments any lighter, primarily by leaving out some of the expensive casting, they would. The basic equation for shielding is given in Eq. (9.140) [5].

$$S = A + R + B \tag{9.140}$$

In Eq. (9.140), A is the shield absorption in dB, R is the shield reflection in dB, and B is a correction factor for multiple reflections within the shield [5]. Shield effectiveness depends on the nature of the field. Purely electric fields are well isolated by thin conductive layers while purely magnetic fields are barely attenuated by such layers. Magnetic fields require thick layers of high permeability material for effective shielding at low frequencies. Plane waves contain a fairly high impedance mix of electric and magnetic fields that are both reflected and absorbed by thin metal layers provided the frequency is high enough. One of the subtle points in EMI shielding is that any slot can destroy shielding effectiveness. It is the length of a slot in comparison to a wavelength that determines how easily a wave can pass through the slot [5].

Measurement of EMI

EMI compliance must be verified. Unfortunately, EMI measurements are time consuming, tedious, plagued by local interference sources, and often of frustrating variability. The FCC requires measurements to be verified at an Open Area Test Site (OATS) [2]. Many manufactures use a local site or a shielded TEM cell to estimate FCC compliance during product development. With care, OATS and TEM cell measurements can be correlated [6]. In any case, even careful EMI measurements can wander by several dB so most manufacturers design for a healthy margin in their products.

Open Area Test Site (OATS)

A sketch of an OATS site is given in Fig. 9.33a. OATS testing involves setting the antenna at specified distances from the device under test (DUT). FCC and CISPR regulations use distances of 3,10, and

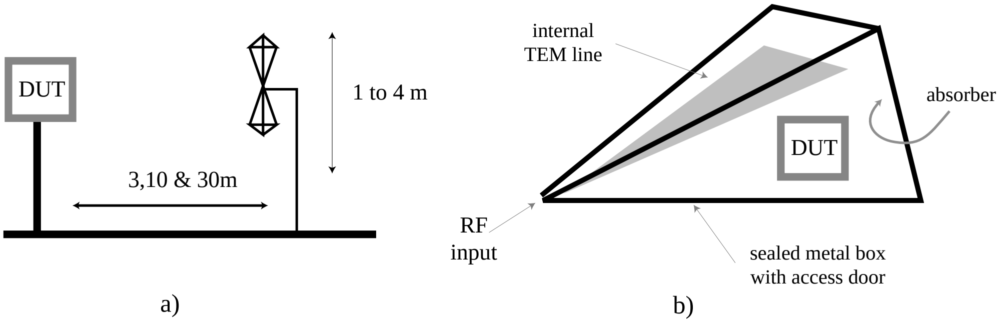

FIGURE 9.33 EMI measurements methods: a) OATS; and b) TEM cell.

30 meters depending on the verification class [1,2]. The antenna height must also be varied to account for ground reflections. Finally, the DUT must be rotated about all axes and the antenna must be utilized to test the DUT under radiation by both horizontally and vertically polarized fields.

TEM Cell

TEM cells are a convenient and relatively low cost method for making accurate and well-isolated EMI measurements [2,7]. A sketch of one configuration of TEM cell is shown in Fig. 9.33b [2]. The TEM cell uses a transmission line in a box to create a TEM field for testing devices. The box is driven from a narrow end and usually expands into an area where the DUT can be placed. The box terminates in a resistor surrounded by RF absorber. For EMI measurements the DUT must be placed away from the box walls and rotated about each axis so that all possible radiated waves can be measured.

Probes

EMI probes can be a very effective way of solving EMI problems. Articles have been written on building probes and commercial probes are available that provide a flat frequency response [8]. These probes can be used to "sniff" around a device until signals with the same spectral spacing as the EMI problem can be found. For clocks and switching power supplies, a close examination of the spectral spacing will indicate the fundamental frequency, which can be traced to a component on a schematic. In the time domain the suspected EMI source can be used to trigger an oscilloscope with the probed signal as the oscilloscope input. If the trace is stable, then the suspected EMI source has been found. Electric field probes are based on Eq. (9.138) and can be as simple as a wire extending from a connector. Magnetic field probes can be as simple as a loop of wire completing the path from a connector's center pin to its flange. A rectangular loop of length l with the near side a distance a from a current source I, and having the far side a distance b from the current source will yield the voltage given in Eq. (9.141). With all small probes it is useful to have at least a 6 dB pad after the probe to establish a load and minimize reflections.

$$V = j\,\omega\, l\, \mu\, I \ln\left(b/a\right)\Big/\left(2\,\pi\right) \tag{9.141}$$

Summary

EMI problems create an inexhaustible supply of work for those in the field. The EMC field has well documented requirements and a long history of measurement. Many excellent sources of information exist for those working in this area [1,2,5,9].

References

1. Paul, C.R., *Introduction to Electromagnetic Compatibility*, John Wiley & Sons, New York, 1992.
2. Morgan, D., *A Handbook for EMC Testing and Measurement*, Peter Peregrinus Ltd., London, 1994.
3. Lee, F.C. and Yu, Y., Input-Filter Design for Switching Regulators, *IEEE Trans. Aerosp. and Electron. Sys.*, 627–634, September 1979.
4. Dolle, M., Analysis of Simultaneous Switching Noise, *IEEE ISCAS*, 904–907, 1995.
5. Ott, H.W., *Noise Reduction Techniques in Electronic Systems*, John Wiley & Sons, New York, 1976.
6. Wilson, P., On Correlating TEM Cell and OATS Emission Measurements, *IEEE Trans. EMC*, 1–16, February 1995.
7. Konigstein, D., and Hansen, D., A New Family of TEM-Cells with Enlarged bandwidth and Optimized Working Volume, *Proc. 7th Int'l. Zurich Symp. on EMC*, 127–132, March 1987.
8. Johnson, F., Simple "Homemade" Sensors Solve Tough EMI Problems, *Electron. Design*, 109–114, November 8, 1999.
9. Kodali, V.P. and Kanda, M., *EMC/EMI Selected Readings*, IEEE Press, Piscataway, NJ, 1996.

9.6 Material Properties

9.6.1 Metals

Mike Golio

Metals serve several different functions in the realization of RF and microwave products. These functions include:

- The wire or guided wave boundary material for circuits and transmission media.
- The carrier or structural support for dielectric substrates or semiconductor chips.
- The heat sink for devices or circuits that exhibit high power density.
- The reflector element for antennas or screen room applications.

Each of these functions imposes different electrical, thermal, chemical, and mechanical requirements on the metal material selection. Thus the optimum metal for each application will vary. Consideration of a wide range of material properties for each metal is needed to choose an appropriate metal for most applications.

Resistance, Resistivity, and Conductivity

A first-order consideration in the choice of metals for many electrical applications is the electrical resistance of the metal conductor. DC resistance of a metal rod is given by

$$R = \frac{\rho L}{A} \tag{9.142}$$

where R is the resistance of the rod, ρ is the resistivity of the metal, L is the length of the rod, and A is the cross-sectional area of the rod. The DC electrical properties of metals are also sometimes discussed in terms of conductivity. Conductivity is the inverse of resistivity given by

$$\sigma = \frac{1}{\rho} \tag{9.143}$$

where σ is the conductivity of the material. For most applications, high concductivity, or conversely, low resistivity, is desirable. The resistivity of a number of metals is listed in Table 9.7.

TABLE 9.7 Electrical Resistivity at Room Temperature of Several Metals in $10^{-8}\ \Omega$ m

Metal	Electrical Resistivity
Aluminum	2.7
Beryllium	34.0
Chromium	12.6
Copper	1.7
Gold	2.3
Lead	21.1
Magnesium	4.5
Manganese	144
Molybdenum	5.5
Nickel	7.1
Palladium	10.7
Platinum	10.7
Silver	1.6

TABLE 9.8 Temperature Coefficient of Metal Resistivity at Room Temperature in (1/K)

Metal	Temp. Coefficient of Resistivity
Aluminum	4.38×10^{-3}
Copper	3.92×10^{-3}
Silver	3.71×10^{-3}
Gold	3.61×10^{-3}

The resistivity of metal is also a function of temperature. For small perturbations in temperature, this temperature dependence may be characterized by the equation

$$\alpha = \frac{1}{\rho}\frac{\partial \rho}{\partial T} \tag{9.144}$$

where α is the temperature coefficient of resistivity. The measured temperature dependence of resistivity changes as a function of the nominal temperature and can vary significantly at temperatures near 0 K, or well above room temperature. For most applications, a low value for the temperature coefficient of resistivity is desirable. Table 9.8 presents the temperature coefficient of resistivity at room temperature for several metals that might be chosen for their low resistivity values.

Skin Depth

An electromagnetic field can penetrate into a conductor only a minute distance at microwave frequencies. The field amplitude decays exponentially from its surface value according to

$$A = e^{-x/\delta_s} \tag{9.145}$$

where x is the normal distance into the conductor measured from the surface, and δ_s is the skin depth. The skin depth or depth of penetration into a metal is defined as the distance the wave must travel in order to decay by an amount equal to e^{-1} = 0.368 or 8.686 dB. The skin depth δ_s is given by

$$\delta_s = \frac{1}{\sqrt{\pi f \mu \sigma}} \tag{9.146}$$

where f is the frequency, σ is the metal conductivity, and μ is the permeability of the metal given as

$$\mu = \mu_o \mu_r \tag{9.147}$$

with μ_o equal to the permeability of free space and μ_r the relative permeability of the metal. For most metals used as conductors for microwave and RF applications, the relative permeability, μ_r = 1. The relative permeability of ferroelectric materials such as iron and steel are typically on the order of several hundred.

Skin depth is closely related to the shielding effectiveness of a metal since the attenuation of electric field strength into a metal can be expressed as in Eq. (9.145). For static or low frequency fields, the only method of shielding a space is by surrounding it with a high-permeability material. For RF and microwave frequencies, however, a thin sheet or screen of metal serves as an effective shield from electric fields.

Skin depth can be an important consideration in the development of guided wave and reflecting structures for high frequency work. For the best conductors, skin depth is on the order of microns for 1 GHz fields. Since electric fields cannot penetrate very deeply into a conductor, all current is concentrated

TABLE 9.9 Thermal Conductivities of Typical Metals (W/m K) at Room Temperature

Metal	Thermal Conductivity
Silver	419
Copper	395
Gold	298
Aluminum	156
Brass	101
Lead	32
Kovar	17

near the surface. As conductivity or frequency approach infinity, skin depth approaches zero and the current is contained in a narrower and narrower region. For this reason, only the properties of the surface metal affect RF or microwave resistance. A poor conductor with a thin layer of high conductivity metal will exhibit the same RF conduction properties as a solid, high conductivity structure.

Heat Conduction

One of the uses of metal in the development of RF and microwave parts and modules is as a heat spreader. For many applications that involve high power density electronic components, the efficient removal of heat is of great importance in order to preserve component reliability. Section 3.1 discusses heat transfer fundamentals and Section 3.8 discusses hardware reliability in greater detail.

The one-dimensional heat flow equation that applies to metals (as well as other media) is given as

$$q = kA\frac{\partial T}{\partial x} \tag{9.148}$$

where q is the heat flow, k is the thermal conductivity of the metal, A is the cross-sectional area for heat flow, and $\frac{\partial T}{\partial x}$ the temperature gradient across the metal. For applications where good heat sinking characteristics are desired, high thermal conductivity, k, is desirable. Table 9.9 lists thermal conductivity values for several metals.

Temperature Expansion

Because RF and microwave components often must operate over a wide range of temperatures, consideration of the coefficient of linear expansion of the metals must be included in making a metal selection for many applications. When temperature is increased, the average distance between atoms increases. This leads to an expansion of the whole solid body with increasing temperature. The changes to the linear dimension of the metal can be characterized by

$$\beta = \frac{1}{l}\frac{\Delta l}{\Delta T} \tag{9.149}$$

where β is called the coefficient of linear expansion, l is the linear dimension of the material, ΔT is the change in temperature, and Δl is the change in linear dimension arising from the change in temperature.

Linear expansion properties of metals are important whenever metallic structures are bonded to other materials in an electronic assembly. When two materials with dissimilar thermal expansion characteristics are bonded together, significant stress is experienced during temperature excursions. This stress can result in one or both of the materials breaking or cracking and this can result in degraded electrical performance or catastrophic failure. The best choice of metals to match thermal linear expansion properties is, therefore, determined by the thermal coefficient of linear expansion of the material that is used with the metal. Kovar, for example, is often chosen as the metal material of preference for use as a carrier when

TABLE 9.10 Thermal Coefficient of Linear Expansion of Some of the Materials Used in Microwave and RF Packaging Applications (at Room Temperature, in 10^{-6}/K)

Material	Thermal Coefficient of Expansion
Dielectrics	
Aluminum nitride	4
Alumina 96%	6
Beryllia	6.5
Diamond	1
Glass-ceramic	4–8
Quartz (fuzed)	0.54
Metals	
Aluminum	23
Beryllium	12
Copper	16.5
Gold	14.2
Kovar	5.2
Molybdenum	5.2
Nickel	13.3
Platinum	9
Silver	18.9
Semiconductors	
GaAs	5.9
Silicon	2.6
Silicon Carbide	2.2

alumina dielectric substrates are used to fabricate RF or microwave guided wave elements. Although Kovar is neither a superior electrical conductor nor a superior thermal conductor, its coefficient of linear expansion is a close match to that of the dielectric material, alumina. Table 9.10 presents the coefficients of linear expansion for several metals as well as other materials that are often used for RF and microwave circuits.

Chemical Properties

The chemical properties of metals can be especially important in the selection of metals to be used for semiconductor device contacts and in integrated circuits. Metal is used extensively in the development of transistors and ICs. Uses include:

- the contact material to establish ohmic and rectifying junctions,
- the interconnect layers, and
- the material used to fabricate passive components such as inductors and transmission line segments.

For these applications, the chemical properties of the metal when exposed to heat and in contact with the semiconductor material play a significant role in the metal selection criteria. The process of fabricating a semiconductor device often involves hundreds of individual process steps and exposure to significant thermal cycling. The temperature ranges associated with device fabrication will far exceed the environment the final device will be exposed to.

For silicon processes, for example, aluminum (or its alloys) is often the metal chosen for contacts and interconnects. Aluminum has high conductivity, but it is also chosen because it adheres well to silicon and silicon dioxide and because it does not interact significantly with silicon during the thermal cycling associated with processing. In contrast, gold also has high conductivity, but its use is typically avoided in silicon fabrication facilities because gold forms deep levels (traps) in silicon that dramatically degrade device performance. Other metals of specific interest in silicon processing include gallium and antiminide, which are often used in the formation of ohmic contacts.

Because interconnects continue to shrink in size as fabricated devices continue to be scaled down, interconnect resistance has begun to pose significant limitations on the levels of integration that can be achieved. One solution to extend these limits is to use copper rather than aluminum for interconnect metal. Copper's higher conductivity translates directly into improved interconnect performance. Rapid progress is being made in this area.

The formation of good ohmic contacts and Schottky barriers is critical to the fabrication of most GaAs devices. Different metals react chemically in distinct ways when exposed to a GaAs surface and high temperature. Metals such as gold, tin, and zinc tend to form ohmic contacts when placed in contact with a GaAs surface. In contrast, aluminum, titanium, and nickel normally form Schottky barriers on GaAs. In order to obtain optimum electrical conductivity and still produce good contacts, sandwiched layers of different metals are sometimes used. For example, a thick layer of gold is often utilized over layers of titanium and platinum to produce Schottky barrier contacts. When this technique is employed, the titanium resting on the surface of the GaAs forms the Schottky barrier, the platinum serves as a diffusion barrier to keep the gold and titanium from diffusing together, and the gold is used to produce a low resistance connection to the contact pads or remaining IC circuitry.

Certain metals can also react with GaAs to produce undesirable effects. Chromium, for example, produces undesirable deep levels in GaAs that can degrade device performance.

Weight

Over the past several decades a dominant trend in the development of electronic circuits has been the continued reduction of size and weight. Although much of this progress has been made possible by the continued scaling of semiconductor devices and ICs, metal portions of many electronic assemblies still dominate the weight of the system. Metal density can be an important factor in choosing metals for certain applications. Table 9.11 presents the density in g/cm^3 for several metals of interest.

TABLE 9.11 Density of Several Metals in g/cm^3

Metal	Density
Aluminum	2.7
Beryllium	1.85
Copper	8.93
Gold	19.4
Kovar	7.7
Molybdenum	10.2
Nickel	8.9
Platinum	21.45
Silver	10.5

References

Halliday, D. and Resnick, R., *Fundamentals of Physics*, John Wiley & Sons, New York, 1970.
Schroder, D. K., *Semiconductor Material and Device Characterization*, John Wiley & Sons, New York, 1990.
Plonus, M. A., *Applied Electromagnetics*, McGraw-Hill, New York, 1978.
Elliott, D. J., *Integrated Circuit Fabrication Technology*, McGraw-Hill, New York, 1982.
Collin, R. E., *Foundations for Microwave Engineering*, McGraw-Hill, New York, 1966.
Smith, A. A., *Radio Frequency Principles and Applications*, IEEE Press, New York, 1998.

9.6.2 Dielectrics

K.F. Etzold

Basic Properties

When electrical circuits are built, the physical environment consists of conductors separated from each other by insulating materials. Depending on the application, the properties of the insulating materials are chosen to satisfy requirements of low conductivity, a high or low dielectric permittivity, and desirable loss properties. In most cases the high field properties of the materials do not play a role (certainly not in the usual signal processing applications). This is also true with respect to electrical breakdown. However, there are exceptions. For instance, in transmitters the fields can be very large and the choice of insulators has to reflect those conditions. In semiconductor devices dielectric breakdown can be a problem that must be considered, but in many cases it is actually tunneling through the dielectric that is responsible for charge transport. In DRAM the leakage currents in the memory storage capacitor must be small enough to give a charge half-life of about one second over the full temperature range. In Flash memories the charge is transferred via tunneling to the controlling site in the FET where it must then remain resident for years. This requires a very good insulator. In most applications it is desirable that the material properties be independent of the strength of the applied field. This is not always true and there are now materials becoming available that can be used as transmission line phase shifters for steerable antennas, taking advantage of the field dependent dielectric permittivity.

Probably the most important property of dielectrics in circuit applications is the dielectric permittivity, often colloquially called the dielectric constant. This quantity relates the electric field in the material to the free charge on the surfaces. Superficially the connection between this property and the application of dielectrics in a circuit seems rather tenuous. Consider now, however, the capacity C of a device

$$C = \frac{q}{V} \tag{9.150}$$

where q is the charge on the plates and V the voltage across the device. Usually in a discrete capacitor (understood here as a circuit element), we would like store as much charge as possible in a given volume. Therefore, if we can somehow double the stored charge, the capacity C will double. What allows us to do this is the choice of the material that fills the device. Thus the material in this example has twice the charge storage capability or dielectric permittivity. This quantity is typically labeled by the Greek letter epsilon (ε).

Consider, as an example, a parallel plate capacitor. This simple geometry is easily analyzed, and in general we can calculate the capacity of a device exactly if it is possible to calculate the electric field. For the parallel plate device the capacity is

$$C = \varepsilon^{*} \frac{A}{d}, \tag{9.151}$$

where A is the area, and d the separation between the plates. If the material between the plates is vacuum, ε = 8.85*10^{-12} F/m, or in units that are a little easier to remember, 8.85 pF/m. The unit of capacity is the Farad. Using Eq. (9.151) a capacitor with 1m x 1m plates and with a separation of 1m has a capacity of 8.85 pF, neglecting edge effects, i.e., assuming parallel field lines between the plates, which clearly will not be the case here unless a special, guarded geometry is chosen (to guard a circuit, conductors at the same potential are placed nearby). There are no field lines between equipotentials and thus there are no contributions to the capacity. We can consider Eq. (9.151) for the capacity as a definition of dielectric permittivity. In general, the capacity is proportional to ε and the general expression for the capacity of a device is

$$C = \varepsilon^{*} \text{ geometry factor.} \tag{9.152}$$

Also, for practical applications the dielectric permittivity is usually specified relative to that of a vacuum. Thus,

$$\varepsilon = \varepsilon_0^{*} k. \tag{9.153}$$

Here ε_0 is redefined as the dielectric permittivity of vacuum (8.85 pF/m) and k is the relative dielectric permittivity, most often referred to as simply, but somewhat inaccurately, the dielectric permittivity or the dielectric constant; k of course is dimensionless. As an example, the dielectric permittivity of typical Glass-Epoxy circuit board is 4.5, where this is understood to be the relative dielectric permittivity. On physical grounds all materials have a dielectric permittivity greater than 1. Also, for the same reason, the dielectric permittivity of a vacuum has no frequency dependence. In Table 9.12 the important properties of some typical engineering insulating materials are given.

TABLE 9.12 Properties of Some Typical Engineering Insulating Materials

Material	k	Loss	Frequency	Resistivity
Vacuum	1.00	0	All	Zero
Air	1.0006	0		
Glass Vycor 7910	3.8	$9.1*10^{-4}$		
Glass Corning 0080	6.75	$5.8*10^{-2}$		
Al_2O_3	8.5	10^{-3}	1 MHz	
Teflon (PTFE)	2.0	$2*10^{-4}$	1 MHz	10^{17}
Arlon 25N circuit board	3.28	$2.5*10^{-3}$	1 MHz	
Epoxy-glass circuit board	4.5			
Beryllium oxide	7.35			
Diamond	5.58			10^{16}
PZT (lead zirconium oxide)	~1000			
Undoped silicon	11.8			
TaO_5	28			
Quartz (SiO_2)	3.75–4.1	$2*10^{-4}$		
Mica (Ruby)	6.5–8.7	$3.5*10^{-4}$		
Water	78.2	0.04	1 MHz	

Note that for crystalline materials the dielectric permittivity is not isotropic, i.e., the permittivity depends on the orientation of the crystal axes relative to the electric field direction. The angular variation is directly related to the spatial symmetry of the crystal.

So far, we have treated dielectrics as essentially perfect and lossless insulators that allow energy storage greater than that in a vacuum. However, as can be seen from the fact that the table has a loss factor column, frequency-dependent energy losses will occur in all materials (except, again, in a vacuum). As could be anticipated, there are a number of loss mechanisms. Perhaps the easiest loss mechanism to deal with conceptually is the low frequency conductivity of the material. If there is a current flow as a result of an applied field, energy will be dissipated. The DC conductivity can be due to the basic properties of the materials, such as the presence of impurities and their associated energy levels. It can also be due to crystalline defects, and conduction can take place along the surfaces of crystallites that constitute many materials (for example, ceramics). Most often, suitable materials can be selected based on desired properties. In Table 9.12 the conductivity for selected materials is presented. It is seen that some natural and man-made materials have an extremely low conductivity. Indeed the time constant for loss of charge for a free-floating (disconnected) device can be weeks. The time constant τ (in seconds) of a RC network is defined as

$$\tau = RC \tag{9.154}$$

where R is the resistance in parallel with the capacitor C (R is in Ohms and C in Farads). Consider Teflon (PTFE), for example. The DC resistivity at room temperature (25°C) is 10^{17} ohm cm.

Therefore, for this material, the time constant for the charge to decay to 1/e of its original value is 23 days using the dielectric permittivity of 2.0 from Table 9.12. This demonstrates that insulating materials exist for the cabling and supporting structures that are suitable for applications where only the smallest leakage can be tolerated. An example would be systems that measure very small charges, such as quartz-based force transducers and accelerometers.

Frequency Dependence of the Properties

We need now to consider the behavior at all user frequencies. These extend from DC into the microwave and optical range. In this range a number of different loss mechanisms have to be considered. But before this can be done, the definition of the dielectric permittivity needs to be extended so that AC effects can be properly considered. The losses are accounted for if an imaginary component is added to the definition of the dielectric permittivity. Thus

$$\varepsilon = \varepsilon' - j^{*}\varepsilon'' \qquad (9.155)$$

where ε′ is the real part of the dielectric permittivity and j is the square root of –1. The existence of losses is now explicitly included by the imaginary quantity ε″. It is also obvious that the term "permittivity" as a property of dielectrics is somewhat of a misnomer and is partly historical. In fact both the real and imaginary parts are functions of frequency. As is often the case in describing physical parameters that are complex (in the mathematical sense) the two quantities in Eq. (9.155) are actually related. This is a consequence of the fact that the electromagnetic behavior is governed by Maxwell's equations, the absence of discontinuities, and also that causality holds, a statement that relates to the time evolution of electric fields. Thus the so-called Kramers-Kronig equations relate the two quantities [1]

$$\begin{aligned}
&\varepsilon'(\omega) = \frac{1}{\pi^{*}}\int \frac{\varepsilon''}{x-\omega}\,dx;\\
&\varepsilon''(\omega) = \frac{1}{\pi^{*}}\int \frac{\varepsilon'}{x-\omega}\,dx;\\
&-\infty < \lim\text{its} < +\infty\\
&\omega = 2\pi \text{frequency}
\end{aligned} \qquad (9.156)$$

where the dependence of the real and imaginary parts of ε on frequency is now explicitly stated and where the integrals are the Cauchy principal values. Thus we only need to know the real or imaginary parts and the corresponding complimentary part can be calculated. For instance, if we know the real part of the dielectric response over the full frequency range we can calculate the losses by integration. Even if our knowledge of the real part (capacity) is only over a limited frequency range, the complementary part (loss) can often still be estimated, albeit with reduced accuracy.

Let us now discuss the behavior of dielectrics between the frequency extremes of DC and the optical range. At optical frequencies there is a relation from Maxwell's equations that relates the optical index of refraction to the dielectric and magnetic properties. Most dielectrics are nonmagnetic so the magnetic susceptibility is just that of free space, μ_0. The optical index of refraction n is given by

$$n = \sqrt{\frac{\varepsilon}{\mu_0}}. \qquad (9.157)$$

This is of interest because the optical index for all materials varies only over a fairly narrow range, which also relates to the dielectric properties at high (optical) frequencies. Vacuum has an index of one. Many insulators have an index near two, which means that the dielectric permittivity is around four. High optical indices are rare and one of the highest ones known is that of diamond, which has an index of 2.42 (hence the sparkle) and therefore a calculated dielectric permittivity of 5.81. The measured value is 5.58 at low frequencies. Thus there is a slight inconsistency between these values and one would expect a value equal to or slightly higher than 5.58.

Consider now the other end of the frequency range. At low frequencies (Fig. 9.34, up to about 1 GHz) the dielectric permittivity for different materials has a much wider range. Here a small diversion is necessary. We need to address the question of what gives rise to dielectric constants greater than one. The attribute that allows additional charge to be placed on the plates of a capacitor is the (bulk) polarizability of the material or the ability to deposit charge on interfaces associated with the contacts or grain boundaries. Note that except for amorphous ones, most materials are made up of aggregates of small crystallites. The solid then consists of adjacent crystallites separated by a "grain boundary." The properties of the grain boundary can be vastly different from the properties within a crystallite.

The polarizability can take various forms. It can be in the form of permanent dipoles that are observed, for example, in water or PZT. For many materials there is no permanent polarization but there is an

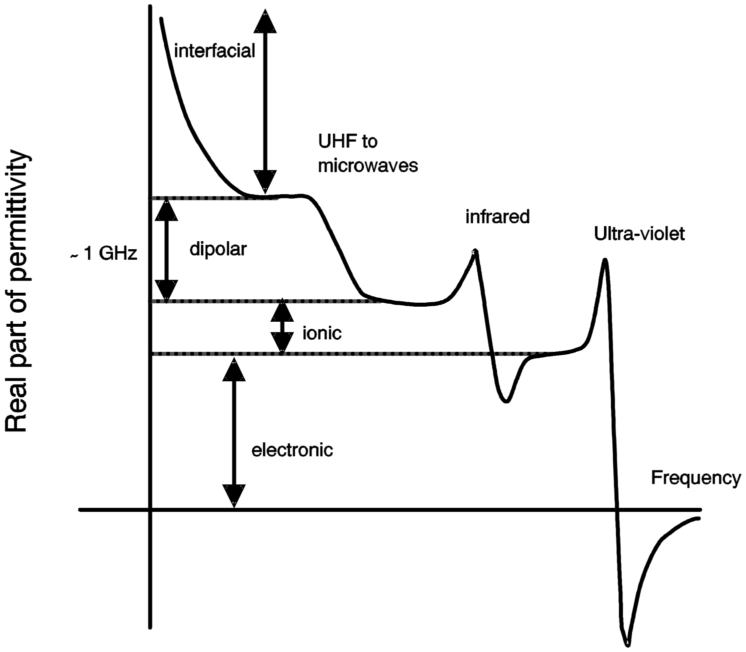

FIGURE 9.34 Adapted from Kittel, C., *Introduction to Solid State Physics,* 3rd ed., John Wiley & Sons, New York, 1967.

induced polarization caused by an externally applied field. The latter materials typically have relatively low dielectric constants, up to about 20. Materials that have permanent dipoles can have very high dielectric constants (up to about 20,000 and higher) especially in the presence of cooperative effects. These same cooperative effects imply the presence of a structural phase transition typically in a temperature range of somewhat below room temperature up to several hundred °C depending on the material. The inherent (molecular) polarization does not disappear above the phase transition where the materials change from ferroelectric to paraelectric, but the long-range order (domains) that prevails at temperatures below the phase transition temperature (the Curie temperature) disappears. This kind of behavior is typical of PZT and many other perovskites. (A perovskite is a crystal with a specific crystal geometry. Many of the materials with this kind of geometry have recently become technologically important; examples are PZT and $BaTiO_3$). Water is an example of a material whose molecules are polarized permanently but which does not have a ferroelectric phase, a phase in which the dipolar vector for a large number of molecules point in the same direction.

Let us now describe the trend of the dielectric permittivity over the entire frequency range. As discussed earlier, at very high (optical) frequencies the dielectric permittivity tends to have its lowest value (up to ~4) and increases as the frequency decreases toward DC. What connects these end points? Where do the changes take place and do they need to be considered in the RF and microwave regime? The general trend of the dielectric permittivity as a function of frequency is shown in Fig. 9.34. As can be seen, there are several regimes in which the dielectric permittivity is changing. At each transition the interaction mechanism between the field and the material is different.

Consider the low frequency extreme in Fig. 9.34. The low frequency rise in the permittivity is attributable to interface effects. These take place at the contacts or in the bulk of the material at the grain boundaries. Charge is able to accumulate at these interfaces and thereby able to contribute to the total capacity or dielectric permittivity. As the frequency is raised, eventually the system can no longer follow these time-dependent charge fluctuations and the dielectric permittivity settles to a value equal to the one without the interface charges. As a widely discussed phenomenon (papers on ferroelectrics or high permittivity thin films), surface and interface effects can take place in ferroelectric (for example PZT)

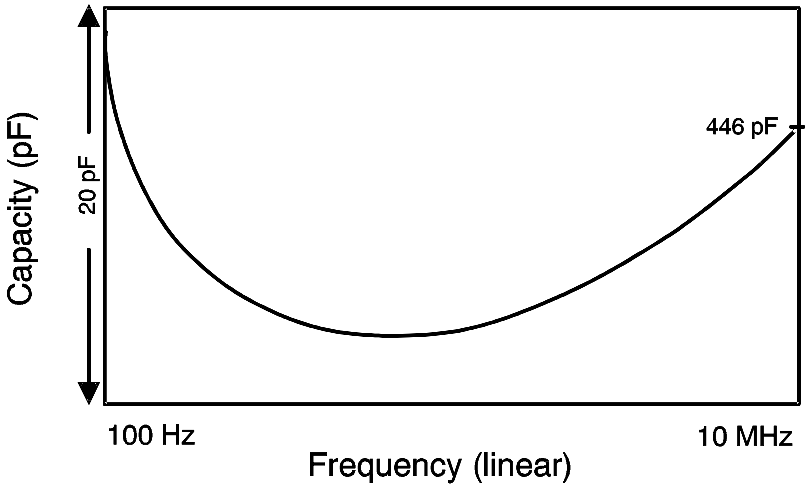

FIGURE 9.35

and non-ferroelectric materials such as $BaTiO_3$ or glassy amorphous materials. Barium titanates are the materials for chip capacitors.

A manifestation of this low frequency effect is memory or dielectric relaxation that is attributable to the same interface behavior. This relaxation can be readily observed if a capacitor is charged or discharged over long periods of time. Consider a discharged capacitor that is suddenly connected to a steady-state source such as a DC power supply or battery. If we measure the current in this circuit after a long time we will not find a zero current, as we would expect after the capacitor is fully charged. Rather, a slowly decreasing current is observed in the circuit. This current is not due to DC current leakage or a current variation associated with the RC time permittivity of the capacitor and the charging circuit. A leakage current would eventually become unvarying and the time constant of the charging RC circuit is much shorter than the observed decay. It is also observed that the capacitor returns some of this low charging current. If the power supply is suddenly removed and the leads of the capacitor are connected to the current meter we see the initial ordinary discharge from the capacitor. After this discharge is completed, a small, slowly decaying current in the opposite direction from the charging current is observed. It is also, of course, opposite to the residual charging current described above. These relaxation currents are due to charge that slowly accumulates on the various interior interfaces in the device. An example of areas where charge often becomes resident is the interface between the contacts and the dielectric. Of course the charge is returned when the capacitor is discharged. By way of contrast if there is leakage in a device there is no stored charge.

As a concrete example, consider the variation of the capacity of a commercial 470 pF chip capacitor as a function of frequency, shown in Fig. 9.35. We observe the increase of the capacity due to interface effects as the frequency decreases. However, somewhat unexpectedly, the response does not flatten or drop at high frequencies, as Fig. 9.34 implies. Instead the capacity goes through a minimum and then rises again. This rise is due to a parasitic effect, a resonance in the capacitor and the test jig. The unavoidable resonant elements are the lead inductance and the inherent capacity of the device. All capacitors exhibit this phenomenon. Indeed above the resonance the impedance can become positive and the device behaves like an inductor! In bypass applications (i.e., larger value capacitors) this usually requires paralleling capacitors of different values (and therefore different resonance frequencies) to obtain a composite capacitor that has a negative reactance over a wider frequency range. Manufacturers of chip capacitors have also developed devices with a particularly low inductance. In any case, the rise in the response toward high frequencies in Fig. 9.35 is not a material property, but rather is a consequence of the physical construction of the device. Therefore, the low frequency behavior of this chip capacitor is comparable to that shown in Fig. 9.34, modified for the resonance. As can be seen for the 470 pF capacitor, the interface effect can be neglected at frequencies above 2 to 3 MHz.

Returning now to the material dependent dielectric behavior as a function of frequency. As the frequency is increased, the next polarizability is associated with the material rather than interfaces. Perovskites have oxygen vacancies that will exhibit a dipolar polarization. This effect can have associated frequencies as low as 100 MHz. It can therefore play a role in chip capacitors, which are typically made from mixed or doped perovskites. Therefore, frequency-dependent effects can appear in these devices at relatively low frequencies. However, it is possible to control the number of vacancies in the manufacturing process so that in most cases this effect will be small.

As the frequency is increased again, into the range above 1 GHz, there will be contributions due to the ionic separation of the components of a material. For instance, in PZT the electronic charge cloud associated with a unit cell is slightly distorted. Therefore, the octahedron associated with the unit cell has a dipole moment, which will contribute to the polarization. Again, as the frequency of the applied field or voltage is raised, eventually these charges will no longer be able to follow the external field and the polarization, and therefore the dielectric permittivity will decrease to a new plateau.

The only polarization left at this point is the electronic contribution, i.e., the distortion induced in the electronic cloud of the material by the external field. Note that this is an induced polarization unlike the permanent polarization in water molecules or PZT. This happens at optical frequencies, hence the diamond example earlier in the section.

The above view of the dielectric behavior of many materials is somewhat idealized. In fact, the transition from one regime to another is usually not characterized by a single, well-located (in frequency) transition, but is presented to highlight the various mechanisms that enhance the dielectric permittivity. Most often there are multiple mechanisms resulting in a distribution of relaxation times. This in turn causes the transitions in Fig. 9.34 to be smeared out. In fact, the more typical behavior is that of the "Universal Law." Here the dielectric permittivity follows a power law typically with an exponent less than one. In many materials this behavior is observed over many decades of frequency. Thus the observed response follows

$$\varepsilon(\omega) - \varepsilon_\infty = \varepsilon_0 \omega^{(n-1)}, \tag{9.158}$$

with $0 < n < 1$. Interestingly this relation holds (at least for some perovskites) over as many as 12 orders of magnitude.

Measurements

The measurement of devices was initially done with a bridge circuit that is an AC modification of the Wheatstone bridge. The method essentially involves manually finding a pair of values representing the capacitance and dissipation factor. This is done by adjusting calibrated resistors to balance a bridge circuit and observing a minimum voltage across the diagonal terminals of the bridge. Because this is a manual method it is slow and tedious, particularly because the two values are interacting, necessitating an adjustment of the first value after the minimum was found for the second value. It is therefore a slowly converging cyclic adjustment. Classical AC bridges are also limited to low frequencies (below approximately 1 MHz).

In recent years the measurement of capacity and the loss of devices has become significantly easier with the development of fixed frequency or swept impedance meters by commercial vendors. At moderate frequencies, up to about 100 MHz, the measurement is typically done as a 4-terminal measurement. Two terminals deliver a known AC current (I). The complex voltage (V) with its corresponding phase angle relative to the phase of the exciting current across the device is measured with another pair of terminals. The complex impedance (Z) is then given by the AC equivalent of Ohm's law

$$Z = V/I. \tag{9.159}$$

TABLE 9.13

Measured Quantity	Series Equivalent	Parallel Equivalent
$\lvert Z\rvert$	$\sqrt{R^2 + X^2}$	
$\lvert Y\rvert$		$\sqrt{G^2 + B^2}$
Θ	$\mathrm{Tan}^{-1}(X/R)$	$\mathrm{Tan}^{-1}(B/G)$
C	$-1/(\omega X)$	B/ω
Q	$\lvert X\rvert/R$	$\lvert B\rvert/G$
D	$R/\lvert X\rvert$	$G/\lvert B\rvert$

The transformations between the measured quantity $\lvert Z\rvert$ and the associated phase angle Θ, and the engineering values of the capacity and loss for a series equivalent circuit and parallel equivalent are given in Table 9.13.

It should be remembered that a lossy two terminal capacitor necessarily has to be represented either as an ideal capacitor connected in series with its loss equivalent resistor or as the two equivalent elements connected in parallel. In the series column the resistance R and the capacity C are in series. In the parallel column the (equivalent) conductance G and inverse reactance B are connected in parallel. For the parallel connection the measured quantity is typically the admittance Y. The quality factor Q and the dissipation factor D are also included in the table. These transformations allow us to find any of the desired values.

It is possible to force an adjustable DC voltage across the current terminals. This allows a measurement of the capacity of the device as a function of an applied steady-state bias field. This application is particularly important in the analysis of semiconductor devices where the junction properties have strong field dependencies. An example is the acquisition of capacity vs. voltage or CV curves. Another example is the characterization of phase shifter materials for phased array antennas, mentioned at the beginning of this article.

At higher frequencies, i.e., above about 100 MHz, it not possible to accurately measure the current or voltage, primarily because of the aberrations introduced by the stray capacities and stray inductances in the connections. It is similarly difficult to measure the current and voltages without interactions between them. Because of this, the impedance measurement is instead made indirectly and is based on reflections in a transmission line using directional couplers that are capable of separating traveling waves going in the forward or reverse direction. Network analyzers exist that are designed to measure the transmission and reflection on a 50 ohm transmission line over a very wide range of frequencies. Thus if a complex impedance terminates such a line, the impedance of the terminating device can be determined from the reflected signals. In fact, the complex reflection coefficient Gamma (Γ) is given by

$$\Gamma = \frac{Z - Z_0}{Z + Z_0} \tag{9.160}$$

where Z is the reflecting impedance and Z_0 is the impedance of the instrument and transmission line (usually 50 ohms). This can be inverted to solve for the unknown impedance

$$Z = Z_0^* \frac{\Gamma + 1}{\Gamma - 1}. \tag{9.161}$$

Both the 4-terminal and the network analyzer impedance measurement methods place the sample at the terminals of the respective analyzer. In fact, it is often desirable to make an *in situ* measurement requiring cables. An example is the characterization of devices that are being probed on a silicon wafer. To accommodate this requirement many instruments have the capability to move the reference plane from the terminals to the measurement site. An accurate, purely resistive 50 ohm termination is placed at the actual test site. The resulting data is used to calibrate the analyzer. An internal algorithm does a little more than simply remeasure the calibration resistor. Two other measurements are also necessary to compensate for imperfections in the network analyzer and the cabling. The compensation is made for an imperfect directional coupler and direct reflection or imperfect impedance match at the sample site. This is accomplished with additional measurements with an open circuit and a short circuit in addition to the 50 ohm standard at the sample site. Using this data one can recalculate the value of the unknown at the end of the cable connections to remove the stray impedances. Similar compensations can be made for the four-terminal measurement at lower frequencies.

References

1. A. K. Jonscher, *Dielectric Relaxation in Solids*, Chelsea Dielectric Press, London, 1983.
2. C. Kittel, *Introduction to Solid State Physics*, 3rd Ed., John Wiley & Sons, New York, 1967.
3. J. D. Baniecki, *Dielectric Relaxation Of Barium Strontium Titanate and Application to Thin Films For DRAM Capacitors*, Ph.D. Dissertation, Columbia University, New York, 1999.
4. Hewlett Packard, Instruction Manuals for the HP4194A Impedance and Gain/Phase Analyzer and HP8753C Network Analyzer with the 85047A S-Parameter Test Set.

9.6.3 Ferroelectric and Piezoelectric Materials

K.F. Etzold

Piezoelectric materials have been used extensively in actuator and ultrasonic receiver applications, while **ferroelectric** materials (in thin film form) have recently received much attention for their potential use in nonvolatile (NV) memory applications. We will discuss the basic concepts in the use of these materials, highlight their applications, and describe the constraints limiting their uses. This section emphasizes properties that need to be understood for the effective use of these materials but are often very difficult to research. Among the properties discussed are **hysteresis** and **domains**.

Ferroelectric and piezoelectric materials derive their properties from a combination of structural and electrical properties. As the name implies, both types of materials have electric attributes. A large number of materials that are ferroelectric are also piezoelectric. However, the converse is not true. Pyroelectricity is closely related to ferroelectric and piezoelectric properties via the symmetry properties of the crystals.

Examples of the classes of materials that are technologically important are given in Table 9.14. It is apparent that many materials exhibit electric phenomena that can be attributed to ferroelectric, piezoelectric, and **electret** materials. It is also clear that vastly different materials (organic and inorganic) can exhibit ferroelectricity or piezoelectricity, and many have actually been commercially exploited for these properties.

As shown in Table 9.14, there are two dominant classes of ferroelectric materials, ceramics and organics. Both classes have important applications of their piezoelectric properties. To exploit the ferroelectric

TABLE 9.14 Ferroelectric, Piezoelectric, and Electrostrictive Materials

Type	Material Class	Example	Applications
Electret	Organic	Waxes	No recent
Electret	Organic	Fluorine based	Microphones
Ferroelectric	Organic	PVF2	No known
Ferroelectric	Organic	Liquid crystals	Displays
Ferroelectric	Ceramic	PZT thin film	NV-memory
Piezoelectric	Organic	PVF2	Transducer
Piezoelectric	Ceramic	PZT	Transducer
Piezoelectric	Ceramic	PLZT	Optical
Piezoelectric	Single crystal	Quartz	Freq. control
Piezoelectric	Single crystal	LiNbO3	SAW devices
Electrostrictive	Ceramic	PMN	Actuators

property, recently a large effort has been devoted to producing thin films of **PZT** (lead [Pb] Zirconate Titanate) on various substrates for silicon-based memory chips for nonvolatile storage. In these devices, data is retained in the absence of external power as positive and negative **polarization**. Organic materials have not been used for their ferroelectric properties but have seen extensive application as electrets (the ability to retain a permanent charge). Liquid crystals in display applications are used for their ability to rotate the plane of polarization of light but not their ferroelectric attribute.

It should be noted that the prefix *ferro* refers to the permanent nature of the electric polarization in analogy with the magnetization in the magnetic case. It does not imply the presence of iron, even though the root of the word means iron. The root of the word piezo means pressure; hence the original meaning of the word piezoelectric implied “pressure electricity” — the generation of electric field from applied pressure. This early definition ignores the fact that these materials are reversible, allowing the generation of mechanical motion by applying a field.

Mechanical Characteristics

Materials are acted on by forces (stresses) and the resulting deformations are called strains. An example of a strain due to a force to the material is the change of dimension parallel and perpendicular to the applied force. It is useful to introduce the coordinate system and the numbering conventions that are used when discussing these materials. Subscripts 1, 2, and 3 refer to the x, y, and z directions, respectively. Displacements have single indices associated with their directions. If the material has a preferred axis, such as the poling direction in PZT, the axis is designated the z or 3 axis. Stresses and strains require double indices such as xx or xy. To make the notation less cluttered and confusing, contracted notation has been defined. The following mnemonic rule is used to reduce the double index to a single index:

$$\begin{array}{ccc} 1 & 6 & 5 \\ xx & xy & xz \\ & 2 & 4 \\ & yy & yz \\ & & 3 \\ & & zz \end{array}$$

This rule can be thought of as a matrix with the diagonal elements having repeated indices in the expected order, then continuing the count in a counterclockwise direction. Note that $xy = yx$, etc. so that subscript 6 applies equally to xy and yx.

Any mechanical object is governed by the well-known relationship between stress and strain,

$$\mathbf{S} = \mathbf{sT} \tag{9.162}$$

where **S** is the strain (relative elongation), **T** is the stress (force per unit area), and **s** contains the coefficients connecting the two. All quantities are tensors; **S** and **T** are second rank, and **s** is fourth rank. Note, however, that usually contracted notation is used so that the full complement of subscripts is not visible. PZT converts electrical fields into mechanical displacements and vice versa. The connection between the two is via the d and g coefficients. The d coefficients give the displacement when a field is applied (motion transmitter), while the g coefficients give the field across the device when a stress is applied (motion receiver). The electrical effects are added to the basic Eq. (9.162) such that

$$\mathbf{S} = \mathbf{sT} + \mathbf{dE} \tag{9.163}$$

where **E** is the electric field and **d** is the tensor that contains the electromechanical coupling coefficients. The latter parameters are reported in Table 9.15 for representative materials. One can write the matrix equation [Eq. (9.163)],

TABLE 9.15 Properties of Well-Known PZT Formulations (Based on the Original Navy Designations)

	Units	PZT4	PZT5A	PZT5H	PZT8
ε_{33}	—	1300	1700	3400	1000
d_{33}	10^{-2} Å/V	289	374	593	225
d_{13}	10^{-2} Å/V	–123	–171	–274	–97
d_{15}	10^{-2} Å/V	496	584	741	330
g_{33}	10^{-3} Vm/N	26.1	24.8	19.7	25.4
k_{33}	—	70	0.705	0.752	0.64
T_{Θ}	°C	328	365	193	300
Q	—	500	75	65	1000
ρ	g/cm^3	7.5	7.75	7.5	7.6
Application	—	High signal	Medium signal	Receiver	Highest signal

$$\begin{bmatrix} S_1\\ S_2\\ S_3\\ S_4\\ S_5\\ S_6 \end{bmatrix} = \begin{bmatrix} s_{11} & s_{12} & s_{13} & & & \\ s_{12} & s_{11} & s_{13} & & 0 & \\ s_{13} & s_{13} & s_{33} & & & \\ & & & s_{44} & & \\ & 0 & & & s_{44} & \\ & & & & & 2\left(s_{11}-s_{12}\right) \end{bmatrix} \begin{bmatrix} T_1\\ T_2\\ T_3\\ T_4\\ T_5\\ T_6 \end{bmatrix} + \begin{bmatrix} 0 & 0 & d_{13}\\ 0 & 0 & d_{13}\\ 0 & 0 & d_{33}\\ 0 & d_{15} & 0\\ d_{15} & 0 & 0\\ 0 & 0 & 0 \end{bmatrix} \begin{bmatrix} E_1\\ E_2\\ E_3 \end{bmatrix} \tag{9.164}$$

Note that **T** and **E** are shown as column vectors for typographical reasons; they are in fact row vectors. This equation shows explicitly the stress-strain relation and the effect of the electromechanical conversion.

A similar equation applies when the material is used as a receiver:

$$\mathbf{E} = -\mathbf{gT} + \left(\varepsilon^{\mathrm{T}}\right)^{-1}\mathbf{D} \tag{9.165}$$

where **T** is the transpose and **D** the electric displacement. The matrices are not fully populated for all materials. Whether a coefficient is nonzero depends on the symmetry. For PZT, a ceramic given a preferred direction by the poling operation (the z-axis), only d_{33}, d_{13}, and d_{15} are nonzero. Also, again by symmetry, $d_{13} = d_{23}$ and $d_{15} = d_{25}$.

Applications

Historically the material that was used earliest for its piezoelectric properties was single-crystal quartz. Crude sonar devices were built by Langevin using quartz transducers, but the most important application was, and still is, frequency control. Crystal oscillators are today at the heart of every clock that does not derive its frequency reference from the AC power line. They are also used in every color television set and personal computer. In these applications at least one (or more) "quartz crystal" controls frequency or time. This explains the label "quartz," which appears on many clocks and watches. The use of quartz resonators for frequency control relies on another unique property. Not only is the material piezoelectric (which allows one to excite mechanical vibrations), but the material has also a very high mechanical "Q" or quality factor (Q > 100,000). The actual value depends on the mounting details, whether the crystal is in a vacuum, and other details. Compare this value to a Q for PZT between 75 and 1000. The Q factor is a measure of the rate of decay and thus the mechanical losses of an excitation with no external drive. A high Q leads to a very sharp resonance and thus tight frequency control. For frequency control it has been possible to find orientations of cuts of quartz that reduce the influence of temperature on the vibration frequency.

Ceramic materials of the PZT family have also found increasingly important applications. The piezoelectric but not the ferroelectric property of these materials is made use of in transducer applications. PZT has a very high efficiency (electric energy to mechanical energy coupling factor k) and can generate high-amplitude ultrasonic waves in water or solids. The coupling factor is defined by

$$k^2 = \frac{\text{energy stored mechanically}}{\text{total energy stored electrically}} \tag{9.166}$$

Typical values of k_{33} are 0.7 for PZT 4 and 0.09 for quartz, showing that PZT is a much more efficient transducer material than quartz. Note that the energy is a scalar; the subscripts are assigned by finding the energy conversion coefficient for a specific vibrational mode and field direction and selecting the subscripts accordingly. Thus k_{33} refers to the coupling factor for a longitudinal mode driven by a longitudinal field.

Probably the most important applications of PZT today are based on ultrasonic echo ranging. Sonar uses the conversion of electrical signals to mechanical displacement as well as the reverse transducer property, which is to generate electrical signals in response to a stress wave. Medical diagnostic ultrasound and nondestructive testing systems devices rely on the same properties. Actuators have also been built but a major obstacle is the small displacement which can conveniently be generated. Even then, the required drive voltages are typically hundreds of volts and the displacements are only a few hundred angstroms. For PZT the strain in the z-direction due to an applied field in the z-direction is (no stress, $\mathbf{T} = 0$)

$$s_3 = d_{33}E_3 \tag{9.167}$$

or

$$s_3 = \frac{\Delta d}{d} = d_{33}\frac{V}{d} \tag{9.168}$$

where s is the strain, E the electric field, and V the potential; d_{33} is the coupling coefficient which connects the two. Thus

$$\Delta d = d_{33}V \tag{9.169}$$

Note that this expression is independent of the thickness d of the material but this is true only when the applied field is parallel to the displacement. Let the applied voltage be 100 V and let us use PZT8 for which d_{33} is 225 (from Table 9.15). Hence Δd = 225 Å or 2.25 Å/V, a small displacement indeed. We also note that Eq. (9.167) is a special case of Eq. (9.163) with the stress equal to zero. This is the situation when an actuator is used in a force-free environment, for example, as a mirror driver. This arrangement results in the maximum displacement. Any forces that tend to oppose the free motion of the PZT will subtract from the available displacement with the reduction given by the normal stress-strain relation, Eq. (9.162).

It is possible to obtain larger displacements with mechanisms that exhibit mechanical gain, such as laminated strips (similar to bimetallic strips). The motion then is typically up to about 1 millimeter but at a cost of a reduced available force. An example of such an application is the video head translating device to provide tracking in VCRs.

There is another class of ceramic materials that recently has become important. **PMN** (lead [Pb], Magnesium Niobate), typically doped with ≈10% lead titanate) is an **electrostrictive** material that has seen applications where the absence of hysteresis is important. For example, deformable mirrors require

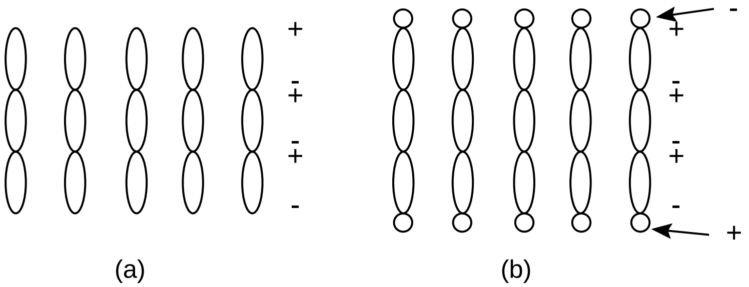

FIGURE 9.36 Charge configurations in ferroelectric model materials: (a) uncompensated and (b) compensated dipole arrays.

repositioning of the reflecting surface to a defined location regardless of whether the old position was above or below the original position.

Electrostrictive materials exhibit a strain that is quadratic as a function of the applied field. Producing a displacement requires an internal polarization. Because the latter polarization is induced by the applied field and is not permanent, as it is in the ferroelectric materials, electrostrictive materials have essentially no hysteresis. Unlike PZT, electrostrictive materials are not reversible; PZT will change shape on application of a field and generate a field when a strain is induced. Electrostrictive materials only change shape on application of a field and, therefore, cannot be used as receivers. PZT has inherently large hysteresis because of the domain nature of the polarization.

Organic electrets have important applications in self-polarized condenser (or capacitor) microphones where the required electric bias field in the gap is generated by the diaphragm material rather than by an external power supply.

Structure of Ferroelectric and Piezoelectric Materials

Ferroelectric materials have, as their basic building block, atomic groups that have an associated electric field, either as a result of their structure or as result of distortion of the charge clouds that make up the groups. In the first case, the field arises from an asymmetric placement of the individual ions in the group (these groupings are called unit cells). In the second case, the electronic cloud is moved with respect to the ionic core. If the group is distorted permanently, then a permanent electric field can be associated with each group. We can think of these distorted groups as represented by electric dipoles, defined as two equal but opposite charges separated by a small distance. Electric dipoles are similar to magnetic dipoles which have the familiar north and south poles. The external manifestation of a magnetic dipole is a magnetic field and that of an electric dipole an electric field.

Figure 9.36(a) represents a hypothetical slab of material in which the dipoles are perfectly arranged. In actual materials the atoms are not as uniformly arranged, but, nevertheless, from this model there would be a very strong field emanating from the surface of the crystal. The common observation, however, is that the fields are either absent or weak. This effective charge neutrality arises from the fact that there are free, mobile charges available that can be attracted to the surfaces. The polarity of the mobile charges is opposite to the charge of the free dipole end. The added charges on the two surfaces generate their own field, equal and opposite to the field due to the internal dipoles. Thus the effect of the internal field is canceled and the external field is zero, as if no charges were present at all [Fig. 9.36(b)].

In ferroelectric materials a crystalline asymmetry exists that allows electric dipoles to form. If the dipoles are absent the internal field disappears. Consider an imaginary horizontal line drawn through the middle of a dipole. We can see readily that the dipole is not symmetric about that line. The asymmetry thus requires that there be no center of inversion when a material is in the ferroelectric state.

All ferroelectric and piezoelectric materials have phase transitions at which the material changes crystalline symmetry. For example, in PZT there is a change from tetragonal or rhombohedral symmetry to cubic as the temperature is increased. The temperature at which the material changes **crystalline**

phases is called the **Curie temperature**, T_{Θ}. For typical PZT compositions the Curie temperature is between 250 and 450°C.

A consequence of a phase transition is that a rearrangement of the lattice takes place when the material is cooled through the transition. Intuitively we would expect that the entire crystal assumes the same orientation throughout as the temperature passes through the transition. By orientation we mean the direction of the preferred crystalline axis (say the tetragonal axis). Experimentally it is found, however, that the material breaks up into smaller regions in which the preferred direction and thus the polarization is uniform. Note that cubic materials have no preferred direction. In tetragonal crystals the polarization points along the c-axis (the longer axis) whereas in rhombohedral lattices the polarization is along the body diagonal. The volume in which the preferred axis is pointing in the same direction is called a domain and the border between the regions is called a domain wall. The energy of the multidomain state is slightly lower than the single-domain state and is thus the preferred configuration. The direction of the polarization changes by either 90° or 180° as we pass from one uniform region to another. Thus the domains are called 90° and 180° domains. Whether an individual crystallite or grain consists of a single domain depends on the size of the crystallite and external parameters such as strain gradients, impurities, etc. It is also possible that the domain extends beyond the grain boundary and encompasses two or more grains of the crystal.

Real materials consist of large numbers of unit cells, and the manifestation of the individual charged groups is an internal and an external electric field when the material is stressed. Internal and external refer to inside and outside of the material. The interaction of an external electric field with a charged group causes a displacement of certain atoms in the group. The macroscopic manifestation of this is a displacement of the surfaces of the material. This motion is called the piezoelectric effect, the conversion of an applied field into a corresponding displacement.

Ferroelectric Materials

PZT ($PbZr_xTi_{(1-x)}O_3$) is an example of a ceramic material that is ferroelectric. We will use PZT as a prototype system for many of the ferroelectric attributes to be discussed. The concepts, of course, have general validity. The structure of this material is ABO_3 where A is lead and B is one or the other atoms, Ti or Zr. This material consists of many randomly oriented crystallites that vary in size between approximately 10 nm and several microns depending on the preparation method. The crystalline symmetry of the material is determined by the magnitude of the parameter x. The material changes from rhombohedral to tetragonal symmetry when $x > 0.48$. This transition is almost independent of temperature. The line that divides the two phases is called a **morphotropic phase boundary** (change of symmetry as a function of composition only). Commercial materials are made with $x \approx 0.48$, where the d and g sensitivity of the material is maximum. It is clear from Table 9.15 that there are other parameters that can be influenced as well. Doping the material with donors or acceptors often changes the properties dramatically. Thus niobium is important to obtain higher sensitivity and resistivity and to lower the Curie temperature. PZT typically is a p-type conductor and niobium will significantly decrease the conductivity because of the electron Nb^{5+} contributes to the lattice. The Nb ion substitutes for the **B-site** ion Ti^{4+} or Zr^{4+}. The resistance to depolarization (the hardness of the material) is affected by iron doping. Hardness is a definition giving the relative resistance to depolarization. It should not be confused with mechanical hardness. Many other dopants and admixtures have been used, often in very exotic combinations to affect aging, sensitivity, etc.

The designations used in Table 9.15 reflect very few of the many combinations that have been developed. The PZT designation types were originated by the U.S. Navy to reflect certain property combinations. These can also be obtained with different combinations of compositions and dopants. The examples given in the table are representative of typical PZT materials, but today essentially all applications have their own custom formulation. The name PZT has become generic for the lead zirconate titanates and does not reflect Navy or proprietary designations.

When PZT ceramic material is prepared, the crystallites and domains are randomly oriented, and therefore the material does not exhibit any piezoelectric behavior [Fig. 9.37(a)]. The random nature of

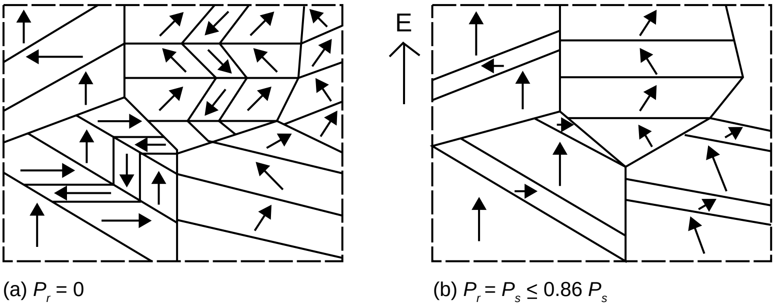

FIGURE 9.37 Domains in PZT, as prepared (a) and poled (b).

the displacements for the individual crystallites causes the net displacement to average to zero when an external field is applied. The tetragonal axis has three equivalent directions 90° apart and the material can be poled by reorienting the polarization of the domains into a direction nearest the applied field. When a sufficiently high field is applied, some but not all of the domains will be rotated toward the electric field through the allowed angle 90° or 180°. If the field is raised further, eventually all domains will be oriented as close as possible to the direction of the field. Note however, that the polarization will not point exactly in the direction of the field [Fig. 9.37(b)]. At this point, no further domain motion is possible and the material is saturated. As the field is reduced, the majority of domains retain the orientation they had with the field on leaving the material in an oriented state which now has a net polarization. This operation is called poling and is accomplished by raising the temperature to about 150°C, usually in oil to avoid breakdown. Raising the temperature lowers the **coercive field**, E_c and the poling field of about 30–60 kV/cm is applied for several minutes. The temperature is then lowered but it is not necessary to keep the applied field turned on during cooling because the domains will not spontaneously re-randomize.

Electrical Characteristics

Before considering the dielectric properties, consider the equivalent circuit for a slab of ferroelectric material. In Fig. 9.38 the circuit shows a mechanical (acoustic) component and the static or clamped capacity C_o (and the dielectric loss R_d) which are connected in parallel. The acoustic components are due to their motional or mechanical equivalents, the compliance (capacity, C) and the mass (inductance, L). There will be mechanical losses, which are indicated in the mechanical branch by R. The electrical branch has the clamped capacity C_o and a dielectric loss (R_d), distinct from the mechanical losses. This configuration will have a resonance that is usually assumed to correspond to the mechanical thickness mode but can represent other modes as well. This simple model does not show the many other modes a slab (or rod) of material will have. Thus transverse, plate, and flexural modes are present. Each can be represented by its own combination of L, C, and R. The presence of a large number of modes often causes difficulties in characterizing the material since some parameters must be measured either away from the

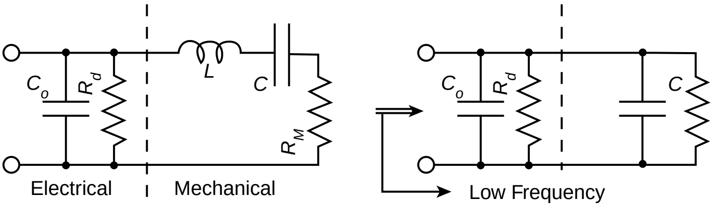

FIGURE 9.38 Equivalent circuit for a piezoelectric resonator. The reduction of the equivalent circuit at low frequencies is shown on the right.

resonances or from clean, non-overlapping resonances. For instance, the clamped capacity (or clamped dielectric constant) of a material is measured at high frequencies where there are usually a large number of modes present. For an accurate measurement these must be avoided and often a low-frequency measurement is made in which the material is physically clamped to prevent motion. This yields the static, non-mechanical capacity, C_o. The circuit can be approximated at low frequencies by ignoring the inductor and redefining R and C. Thus, the coupling constant can be extracted from the value of C and C_o. From the previous definition of k we find

$$k^2 = \frac{\text{energy stored mechanically}}{\text{total energy stored electrically}} = \frac{CV^2/2}{\left(C+C_o\right)V^2/2} = \frac{1}{\frac{C_o}{C}}+1 \qquad (9.170)$$

It requires charge to rotate or flip a domain. Thus, there is charge flow associated with the rearrangement of the polarization in the ferroelectric material. If a bipolar, repetitive signal is applied to a ferroelectric material, its hysteresis loop is traced out and the charge in the circuit can be measured using the Sawyer Tower circuit (Fig. 9.39). In some cases the drive signal to the material is not repetitive and only a single cycle is used. In that case the starting point and the end point do not have the same polarization value and the hysteresis curve will not close on itself.

The charge flow through the sample is due to the rearrangement of the polarization vectors in the domains (the polarization) and contributions from the static capacity and losses (C_o and R_d in Fig. 9.38). The charge is integrated by the measuring capacitor which is in series with the sample. The measuring capacitor is sufficiently large to avoid a significant voltage loss. The polarization is plotted on a X-Y oscilloscope or plotter against the applied voltage and therefore the applied field.

Ferroelectric and piezoelectric materials are lossy. This will distort the shape of the hysteresis loop and can even lead to incorrect identification of materials as ferroelectric when they merely have nonlinear conduction characteristics. A resistive component (from R_d in Fig. 9.38) will introduce a phase shift in the polarization signal. Thus the display has an elliptical component, which looks like the beginnings of the opening of a hysteresis loop. However, if the horizontal signal has the same phase shift, the influence of this lossy component is eliminated, because it is in effect subtracted. Obtaining the exact match is the function of the optional phase shifter, and in the original circuits a bridge was constructed with a second measuring capacitor in the comparison arm (identical to the one in series with the sample). The phase was then matched with adjustable high-voltage components that match C_o and R_d.

This design is inconvenient to implement and modern Sawyer Tower circuits have the capability to shift the reference phase either electronically or digitally to compensate for the loss and static components. A contemporary version, which has compensation and no voltage loss across the integrating capacitor,

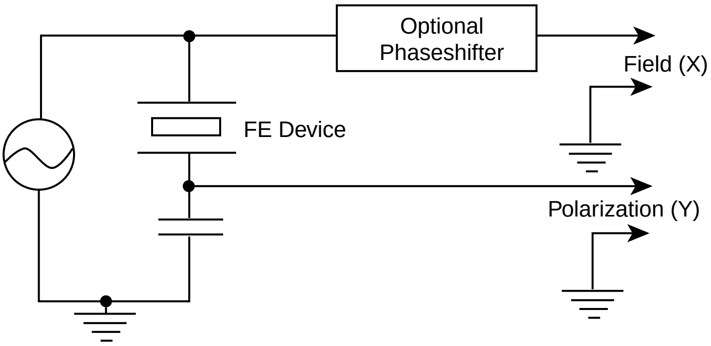

FIGURE 9.39 Sawyer Tower circuit.

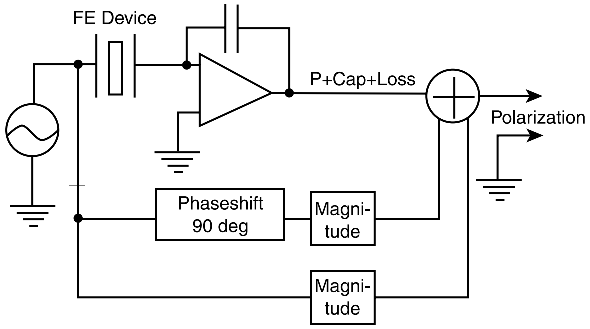

FIGURE 9.40 Modern hysteresis circuit. An op amp is used to integrate the charge; loss and static capacitance compensation are included.

is shown in Fig. 9.40. The op-amp integrator provides a virtual ground at the input, reducing the voltage loss to negligible values. The output from this circuit is the sum of the polarization and the capacitive and loss components. These contributions can be canceled using a purely real (resistive) and a purely imaginary (capacitive, 90° phase shift) compensation component proportional to the drive across the sample. Both need to be scaled (magnitude adjustments) to match them to the device being measured and then have to be subtracted (adding negatively) from the output of the op amp. The remainder is the polarization. The hysteresis response for typical ferroelectrics is frequency dependent and traditionally the reported values of the polarization are measured at 50 or 60 Hz.

The improved version of the Sawyer Tower (Fig. 9.41) circuit allows us to cancel C_o and R_d and the losses, thus determining the active component. This is important in the development of materials for ferroelectric memory applications. It is far easier to judge the squareness of the loop when the inactive components are canceled. Also, by calibrating the "magnitude controls" the values of the inactive components can be read off directly. In typical measurements the resonance is far above the frequencies used, so ignoring the inductance in the equivalent circuit is justified.

The measurement of the dielectric constant and the losses is usually very straightforward. A slab with a circular or other well-defined cross-section is prepared, electrodes are applied, and the capacity and loss are measured (usually as a function of frequency). The relative dielectric permittivity is found from

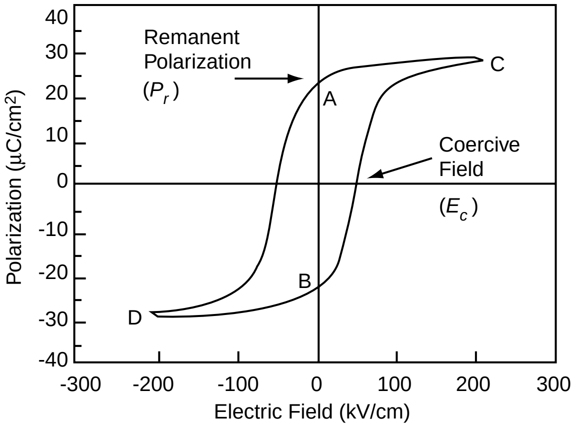

FIGURE 9.41 Idealized hysteresis curve for typical PZT materials. Many PZT materials display offsets from the origin and have asymmetries with respect to the origin. The curve shows how the remanent polarization $(\vec{P}_r)$ and the coercive field $(\vec{E}_c)$ are defined. While the loop is idealized, the values given for the polarization and field are realistic for typical PZT materials.

$$C = \varepsilon_o k \frac{A}{t} \tag{9.171}$$

where A is the area of the device and t the thickness. In this definition (also used in Table 9.15) k is the relative dielectric permittivity and ε_o is the permittivity of vacuum. Until recently, the relative dielectric permittivity, like the polarization, was measured at 50 or 60 Hz (typical powerline frequencies). Today the dielectric parameters are typically specified at 1 kHz or higher, which is possible because impedance analyzers with high-frequency capability are readily available. To avoid low-frequency anomalies, even higher frequencies such as 1 MHz are often selected. This is especially the case when evaluating PZT or non-ferroelectric high k thin films. Low frequency anomalies can be present but are not modeled in the equivalent circuit (Fig. 9.37). These are typically due to interface layers. These layers will cause both the resistive and reactive components to rise at low frequencies producing readings that are not representative of the dielectric material properties (see Section 9.6.2).

A piezoelectric component often has a very simple geometric shape, especially when it is prepared for measurement purposes. There will be mechanical resonances associated with the major dimensions of a sample piece. The resonance spectrum will be more or less complicated, depending on the shape of a sample piece. If the object has a simple shape, then some of the resonances will be well separated from each other and can be associated with specific vibrations and dimensions (modes). Each of these resonances has an electrical equivalent, and inspection of the equivalent circuit shows that there will be a resonance (minimum impedance) and an antiresonance (maximum impedance). Thus an impedance plot can be used to determine the frequencies and also the coupling constants and mechanical parameters for the various modes.

Ferroelectric and High Epsilon Thin Films

While PZT and other ferroelectric (FE) bulk materials have had major commercial importance, thin films prepared from these materials have only recently been the focus of significant research efforts. In this section the material properties and process issues will be discussed. Because of the potentially large payoff, major efforts have been directed at developing the technologies for depositing thin films of ferroelectric and non-ferroelectric but high epsilon (high dielectric permittivity) thin films.

A recent trend has been the ever increasing density of dynamic random access memory (DRAM). The data storage capacitor in these devices is becoming a major limiting factor because its dielectric has to be very thin in order to achieve the desired capacitance values to yield, in turn, a sufficient signal for the storage cell. It is often also desirable to have nonvolatile operation (no data loss on power loss). These two desires have, probably more than anything else, driven the development of high epsilon and FE thin films. Of course, these are not the only applications of FE films. Table 9.16 lists the applications of FE (nonvolatile, NV) and high epsilon films (volatile) and highlights which of the properties are important for their use. It is seen that NV memory application is very demanding. Satisfying all these requirements simultaneously has produced significant challenges in the manufacture of these films.

Perhaps the least understood and to some extent still unsolved problem is that of fatigue. In nonvolatile memory applications the polarization represents the memory state of the material (up ≡ bit 1; down ≡ bit 0). In use the device can be switched at the clock rate, say 100 MHz. Thus for a lifetime of 5 years

TABLE 9.16 Material Properties and Applications Areas

	Ferroelectric	Epsilon	Polarization	Coercive Field	Leakage	Aging	Electro-Optical	Electro-Mechanical
NV RAM	X		X	X	X	X		
DRAM		X			X	X		
Actuator				X				X
Display	X				X	X	X	
Optical Modulator	X				X	X	X	

the material must withstand $\simeq 10^{16}$ polarization reversals or large field reversals. Typical candidate materials for ferroelectric applications are PZTs with the ratio of zirconium to titanium adjusted to yield the maximum dielectric constant and polarization. This maximum will be near the morphotropic phase boundary for PZT. Small quantities of other materials can be added, such as lanthanum or niobium to modify optical or switching characteristics. The Sol-Gel method discussed below is particularly suitable for incorporating these additives. Devices made from materials at the current state of the art lose a significant portion of their polarization after 10^{10} to 10^{12} cycles, rendering them useless for their intended memory use because of the associated signal loss. This is a topic of intensive investigation and only one proprietary material has emerged that might be suitable for memory use (Symetric Corporation).

High epsilon non-ferroelectric materials are of great interest for DRAM applications. As an example, major efforts are extant to produce thin films of mixtures of barium and strontium titanate (BST). Dielectric constants of 600 and above have been achieved (compared to 4 to 6 for silicon oxides and nitrides).

In applications for FE films, significant opportunities also exist for electro-optical modulators for fiber-optic devices and light valves for displays. Another large scale application is actuators and sensors. For the latter the electromechanical conversion property is used and large values of d_{33} (the conversion coefficient) are desirable. However, economically the importance of all other applications are, and probably will be in the foreseeable future, less significant than that of memory devices.

Integration of ferroelectric or nonferroelectric materials with silicon devices and substrates has proved to be very challenging. Contacts and control of the crystallinity and crystal size and the stack structure of the capacitor device are the principal issues. In both volatile and nonvolatile memory cells the dielectric material interacts with the silicon substrate. Thus an appropriate barrier layer must be incorporated while which at the same time is a suitable substrate on which to grow the dielectric films. A typical device structure starts with an oxide layer (SiO_x) on the silicon substrate followed by a thin titanium layer which prevents diffusion of the final substrate layer, platinum (the actual growth substrate). If electrical contact to the silicon is desired, ruthenium based barrier layer materials can be used. These are structurally similar to the FE or high epsilon films.

While the major effort in developing thin films for data storage has been in the films described above, a significant effort has recently been made to produce low epsilon films. In contemporary logic chips the device speed is not only determined by the speed of the active devices but also by the propagation delay in the interconnect wiring. To reduce the delay the conductivity of the metal must be increased (hence the use of copper as conductors) and the dielectric separating the conductors must have as low as possible dielectric permittivity. Materials for this purpose are now also being developed in this film form.

Significant differences have been observed in the quality of the films depending on the nature of the substrate. The quality can be described by intrinsic parameters such as the crystallinity (i.e., the degree to which non-crystalline phases are present). The uniformity of the orientation of the crystallites also seems to play a role in determining the electrical properties of the films. In the extreme case of perfect alignment of the crystallites of the film with the single crystal substrate an epitaxial film is obtained. These films tend to have the best electrical properties. In addition to amorphous material, other crystalline but non-ferroelectric phases can be present. An example is the pyrochlore phase in PZT. These phases often form incidentally to the growth process of the desired film and usually degrade one or more of the desired properties of the film (for instance the dielectric constant). The pyrochlore and other oxide materials can accumulate between the Pt electrode and the desired PZT or BST layer. The interface layer is then electrically in series with the desired dielectric layer and degrades its properties. The apparent reduction of the dielectric constant which is often observed in these films as the thickness is reduced can be attributed to the presence of these low dielectric constant layers.

There are many growth methods for these films. Table 9.17 lists the most important techniques along with some of the critical parameters. Wet methods use metal organic compounds in liquid form. In the Sol-Gel process the liquid is spun onto the substrate. The wafer is then heated, typically to a lower, intermediate temperature (around 300°C). This spin-on and heat process is repeated until the desired thickness is reached. At this temperature only an amorphous film forms. The wafer is then heated to

TABLE 9.17 Deposition Methods for PZT and Perovskites

	Process Type	Rate nm/min	Substrate Temperature	Anneal Temperature	Target/Source
Wet	Sol-Gel	100 nm/coat	RT	450–750	Metal organic
Wet	MOD	300 nm/coat	RT	500–750	Metal organic
Dry	RF sputter	.5–5	RT–700	500–700	Metals and oxides
Dry	Magnetron sputter	5–30	RT–700	500–700	Metals and oxides
Dry	Ion beam sputter	2–10	RT–700	500–700	Metals and oxides
Dry	Laser sputter	5–100	RT–700	500–700	Oxide
Dry	MOCVD	5–100	400–800	500–700	MO vapor and carrier gas

between 500 and 700°C usually in oxygen and the actual crystal growth takes place. Instead of simple long-term heating (order of hours), rapid thermal annealing (RTA) is often used. In this process the sample is only briefly exposed to the elevated temperature, usually by a scanning infrared beam. It is in the transition between the low decomposition temperature and the firing temperature that the pyrochlore tends to form. At the higher temperatures the more volatile components have a tendency to evaporate, thus producing a chemically unbalanced compound that also has a great propensity to form one or more of the pyrochlore phases. In the case of PZT, 5 to 10% excess lead is usually incorporated which helps to form the desired perovskite material and compensates for the loss. In preparing Sol–Gel films it is generally easy to prepare the compatible liquid compounds of the major constituents and the dopants. The composition is then readily adjusted by appropriately changing the ratio of the constituents. Very fine quality films have been prepared by this method, including epitaxial films.

The current semiconductor technology is tending toward dry processing. Thus, in spite of the advantages of the Sol-Gel method, other methods using physical vapor deposition (PVD) are being investigated. These methods use energetic beams or plasma to move the constituent materials from the target to the heated substrate. The compound then forms *in situ* on the heated wafer (≃500°C). Even then, however, a subsequent anneal is often required. With PVD methods it is much more difficult to change the composition since now the oxide or metal ratios of the target have to be changed or dopants have to be added. This involves the fabrication of a new target for each composition ratio. MOCVD is an exception here; the ratio is adjusted by regulating the carrier gas flow. However, the equipment is very expensive and the substrate temperatures tend to be high (up to 800°, uncomfortably high for semiconductor device processing). The laser sputtering method is very attractive and it has produced very fine films. The disadvantage is that the films are defined by the plume that forms when the laser beam is directed at the source. This produces only small areas of good films and scanning methods need to be developed to cover full size silicon wafers. Debris is also a significant issue in laser deposition. However, it is a convenient method to produce films quickly and with a small investment. In the long run MOCVD or Sol-Gel will probably evolve as the method of choice for realistic DRAM devices with state of the art densities.

Defining Terms

A-site: Many ferroelectric materials are oxides with a chemical formula ABO_3. The A-site is the crystalline location of the A atom.

B-site: Analogous to the definition of the A-site.

Coercive field: When a ferroelectric material is cycled through the hysteresis loop the coercive field is the electric field value at which the polarization is zero. A material has a negative and a positive coercive field and these are usually, but not always, equal in magnitude to each other.

Crystalline phase: In crystalline materials the constituent atoms are arranged in regular geometric ways; for instance in the cubic phase the atoms occupy the corners of a cube (edge dimensions ≈2–15 Å for typical oxides).

Curie temperature: The temperature at which a material spontaneously changes its crystalline phase or symmetry. Ferroelectric materials are often cubic above the Curie temperature and tetragonal or rhombohedral below.

Domain: Domains are portions of a material in which the polarization is uniform in magnitude and direction. A domain can be smaller, larger, or equal in size to a crystalline grain.

Electret: A material that is similar to ferroelectrics but charges are macroscopically separated and thus are not structural. In some cases the net charge in the electrets is not zero, for instance when an implantation process was used to embed the charge.

Electrostriction: The change in size of a non-polarized, dielectric material when it is placed in an electric field.

Ferroelectric: A material with permanent charge dipoles which arise from asymmetries in the crystal structure. The electric field due to these dipoles can be observed external to the material when certain conditions are satisfied (ordered material and no charge on the surfaces).

Hysteresis: When the electric field is raised across a ferroelectric material the polarization lags behind. When the field is cycled across the material the hysteresis loop is traced out by the polarization.

Morphotropic phase boundary (MPB): Materials that have a MPB assume a different crystalline phase depending on the composition of the material. The MPB is sharp (a few percent in composition) and separates the phases of a material. It is approximately independent of temperature in PZT.

Piezoelectric: A material that exhibits an external electric field when a stress is applied to the material and a charge flow proportional to the strain is observed when a closed circuit is attached to electrodes on the surface of the material.

PLZT: A PZT material with a lanthanum doping or admixture (up to approximately 15% concentration). The lanthanum occupies the A-site.

PMN: Generic name for electrostrictive materials of the lead (Pb) magnesium niobate family.

Polarization: The polarization is the amount of charge associated with the dipolar or free charge in a ferroelectric or an electret, respectively. For dipoles the direction of the polarization is the direction of the dipole. The polarization is equal to the external charge that must be supplied to the material to produce a polarized state from a random state (twice that amount is necessary to reverse the polarization). The statement is rigorously true if all movable charges in the material are reoriented (i.e., saturation can be achieved).

PVF2: An organic polymer that can be ferroelectric. The name is an abbreviation for polyvinyledene difluoride.

PZT: Generic name for piezoelectric materials of the lead (Pb) zirconate titanate family.

Remanent polarization: The residual or remanent polarization of a material after an applied field is reduced to zero. If the material was saturated, the remanent value is usually referred to as the polarization, although even at smaller fields a (smaller) polarization remains.

References

J. C. Burfoot and G. W. Taylor, *Polar Dielectrics and Their Applications*, Berkeley: University of California Press, 1979.

H. Diamant, K. Drenck, and R. Pepinsky, *Rev. Sci. Instrum.,* 28, 30, 1957.

T. Hueter and R. Bolt, *Sonics,* New York: John Wiley and Sons, 1954.

B. Jaffe, W. Cook, and H. Jaffe, *Piezoelectric Ceramics,* London: Academic Press, 1971.

M. E. Lines and A. M. Glass, *Principles and Applications of Ferroelectric Materials,* Oxford: Clarendon Press, 1977.

R. A. Roy and K. F. Etzold, Ferroelectric film synthesis, past and present: a select review, *Mater. Res. Soc. Symp. Proc.,* 200, 141, 1990.

C. B. Sawyer and C. H. Tower, *Phys. Rev.,* 35, 269, 1930.

Z. Surowiak, J. Brodacki, and H. Zajosz, *Rev. Sci. Instrum.,* 49, 1351, 1978.

Further Information

IEEE Transactions on Ultrasonics, Ferroelectrics, and Frequency Control (UFFC).

IEEE Proceedings of International Symposium on the Application of Ferroelectrics (ISAF) (these symposia are held at irregular intervals).

Materials Research Society, Symposium Proceedings, vols. 191, 200, and 243 (this society holds symposia on ferroelectric materials at irregular intervals).

K.-H. Hellwege, Ed., *Landolt-Bornstein: Numerical Data and Functional Relationships in Science and Technology,* New Series, Gruppe III, vols. 11 and 18, Berlin: Springer-Verlag, 1979 and 1984 (these volumes have elastic and other data on piezoelectric materials).

American Institute of Physics Handbook, 3rd ed., New York: McGraw-Hill, 1972.

D. E. Kotecki et al., (BaSr)TiO_3 dielectrics for future stacked-capacitor DRAM, *IBM J. Res. Dev.,* 43, 367, 1999.

Grill, V. Patel, Novel low-k Dual Phase Materials Prepared by PECVD, *Mat. Res. Soc. Proc.,* Spring Meeting 2000 (San Francisco).

9.6.4 Semiconductors

Mike Harris

Semiconductor is a class of materials that can generally be defined as having an electrical resistivity in the range of 10^{-2} to 10^{9} ohm-cm.[1] Addition of a very small amount of impurity atoms can make a large change in the conductivity of the semiconductor material. This unique materials property makes all semiconductor devices and circuits possible. The amount of free charge in the semiconductor and the transport characteristics of the charge within the crystalline lattice determine the conductivity. Device operation is governed by the ability to generate, move, and remove free charge in a controlled manner. Material characteristics vary widely in semiconductors and only certain materials are suitable for use in the fabrication of microwave and RF devices.

Bulk semiconductors, for microwave and RF applications, include germanium (Ge), silicon (Si), silicon carbide (SiC), gallium arsenide (GaAs), and indium phosphide (InP). Electronic properties of these materials determine the appropriate frequency range for a particular material. Epitaxial layers of other important materials are grown on these host substrates to produce higher performance devices that overcome basic materials limitations of homogeneous semiconductors. These specialized semiconductors include silicon germanium, gallium nitride, aluminum gallium arsenide, and indium gallium arsenide among others. Many of the advanced devices described in Chapter 7 are made possible by the optimized properties of these materials. Through the use of "bandgap engineering," many of the material compromises that limit electronic performance can be overcome with these hetero-structures.

Electron transport properties determine, to a large extent, the frequency at which the various semiconductors are used. On the basis of maturity and cost, silicon will dominate all applications in which it can satisfy the performance requirements. Figure 9.42 is a plot showing the general range of frequencies over which semiconductor materials are being used for integrated circuit applications. It should be noted that the boundary tends to shift to the right with time as new device and fabrication technologies emerge. Discrete devices may be used outside these ranges for specific applications.

This section provides information on important materials properties of semiconductors used for microwave and RF applications. Basic information about each semiconductor is presented followed by tables of electronic properties, thermal properties, and mechanical properties. In order to use these materials in microwave and RF applications, devices and circuits must be fabricated. Device fabrication requires etching and deposition of metal contacts and this section provides a partial list of etchants for these semiconductors along with a list of metallization systems that have been used to successfully produce components.

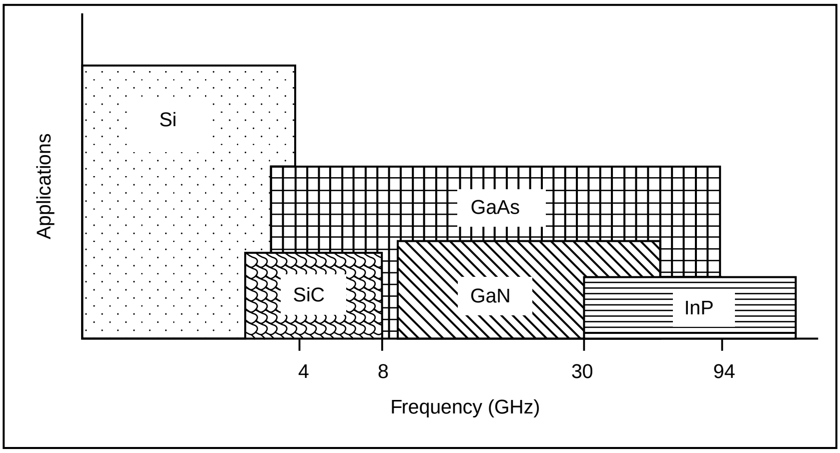

FIGURE 9.42 Frequency range for semiconductor materials.

Silicon

Silicon is an elemental semiconductor that is by far the best known and most mature. A measure of the maturity of silicon is the fact that it is available in 300-mm (12″) diameter wafers. Single crystal silicon wafers are made from electronic grade silicon, which is one of the most refined materials in the world, having an impurity level of no more than one part per billion. Silicon and germanium have the same crystal structure as diamond. In this structure, each atom is surrounded by four nearest neighbor atoms forming a tetrahedron as shown in Figure 9.43. All of the atoms in the diamond lattice are silicon. Silicon is a "workhorse" material at lower frequencies; however, its electron transport properties and low bulk resistivity limit its application in integrated circuit form to frequencies typically below 4 GHz. Silicon-based discrete devices such as PIN diodes find application at higher frequencies.

Si wafers are available with dopant atoms that make them conductive. Wafers having phosphorus impurities are n-type containing excess electrons. Boron-doped wafers are p type and have an excess of holes. Flats are cut on the wafers to distinguish between conductivity types and crystal orientation as shown in Fig. 9.44.[2]

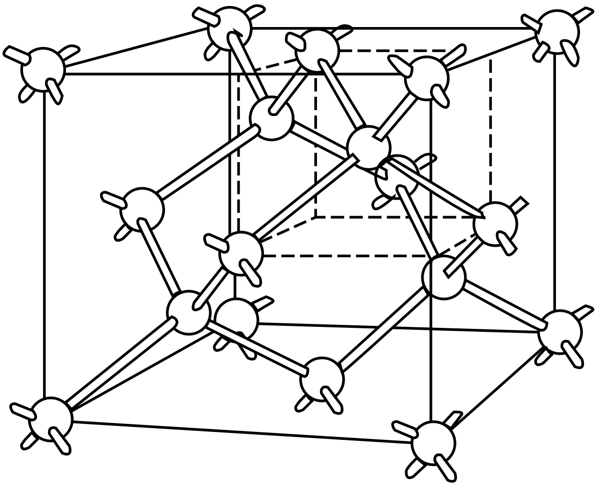

FIGURE 9.43 Cyrstalline structure of Si.

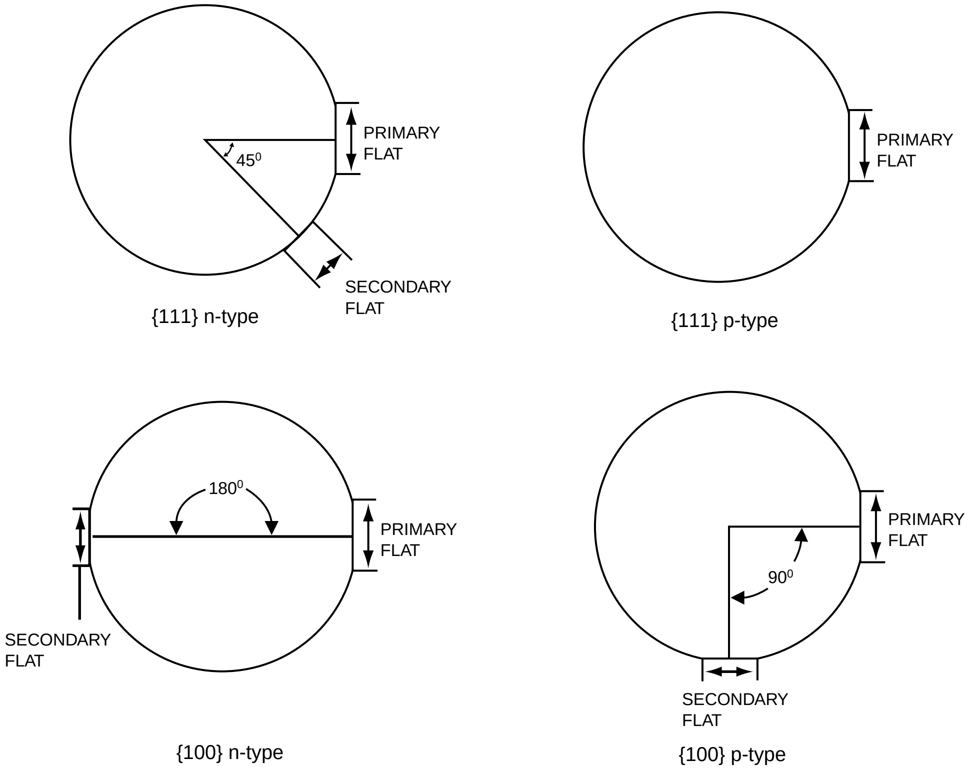

FIGURE 9.44 Silicon wafer type identification (Sze, VLSI Technology, Ref. 2).

Silicon is an indirect band gap material meaning that when an electron and hole recombine, the energy produced is dissipated as a lattice vibration. This should be compared to material like gallium arsenide that is direct gap. When an electron and hole recombine in GaAs, energy is released in the form of light.

Gallium Arsenide

Silicon is the most widely used semiconductor to make electronic devices, however, there are compounds that perform functions beyond the physical limits of the electronic properties of silicon. There are many different kinds of compound semiconductor materials, but the most common material combinations used in microwave and RF applications come from the group III and group V elements.

Gallium arsenide has a zincblende crystalline structure and is one of the most important compound semiconductors. Zincblende consists of two interpenetrating, face-centered cubic (fcc) sublattices as seen in Fig. 9.45. One sublattice is displaced by 1/4 of a lattice parameter in each direction from the other sublattice, so that each site of one sublattice is tetrahedrally coordinated with sites from the other sublattice. That is, each atom is at the center of a regular tetrahedron formed by four atoms of the opposite type. When the two sublattices have the same type of atom, the zincblende lattice becomes the diamond lattice as shown above for silicon. Other examples of compound semiconductors with the zincblende lattice include indium phosphide and silicon carbide.

GaAs wafers, for microwave and RF applications, are available in 4″ and 6″ diameters. Six-inch wafers are currently used for high speed digital and wireless applications and will be used for higher frequency applications as demand increases. Figure 9.46 shows the standard wafer orientation for semi-insulating GaAs. The front face is the (100) direction or 2 degrees off (100) toward the [110] direction. Figure 9.47 shows the different edge profiles that occur when etching GaAs. These profiles are a function of the crystal orientation as seen in the diagram.[3]

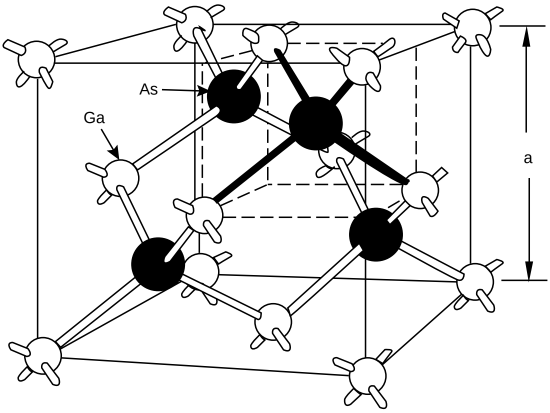

FIGURE 9.45 Zinc blende crystalline structure of gallium arsenide (GaAs).

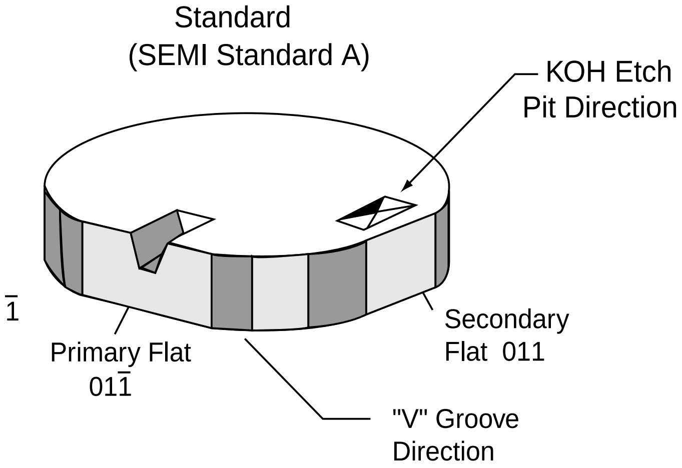

FIGURE 9.46 Standard wafer orientation for semi-insulating GaAs.

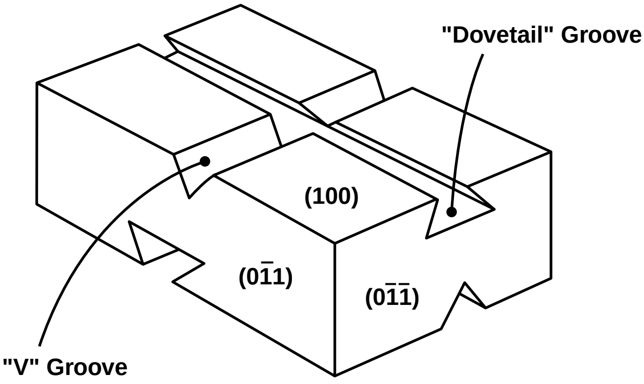

FIGURE 9.47 Orientation-dependent etching profiles of GaAs[3].

Figure 9.48 is a plot of the bandgap energy of various semiconductors as a function of temperature.[4] GaAs has a bandgap energy at room temperature of 1.43 eV compared to 1.12 eV for silicon. This means that the intrinsic carrier concentration of GaAs can be very low compared to silicon. Since the intrinsic

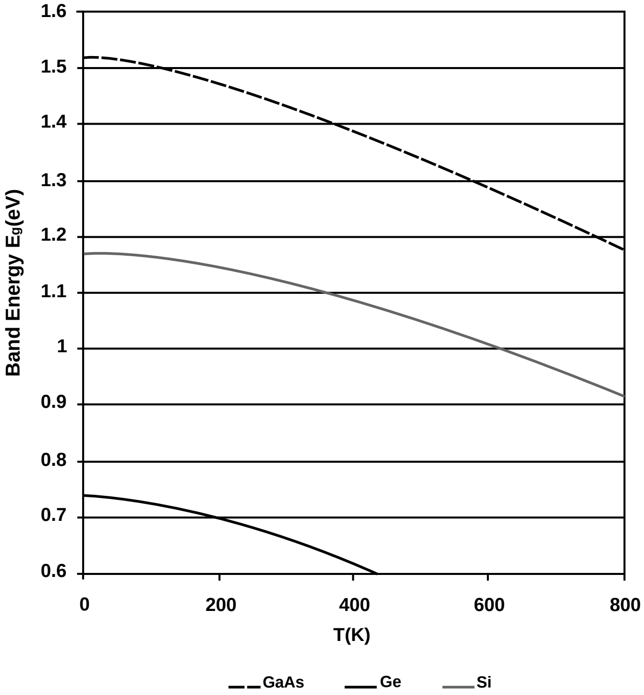

FIGURE 9.48 Energy bandgaps of GaAs, Si, and Ge as a function of temperature (after Sze, Ref. 3).

carrier concentration in gallium arsenide is less than that in silicon, higher resistivity substrates are available in gallium arsenide. High resistivity substrates are desirable since they allow the active region of a device to be isolated using a simple ion implantation or mesa etching. Availability of high resistivity gallium arsenide substrates is one reason that this material has found such widespread use for microwave and wireless applications.

The ability to move charge is determined by the transport characteristics of the material. This information is most often presented in the charge carrier velocity electric field characteristic as shown in Figure 9.49.[5] For low values of electric field, the carrier velocity is linearly related to the electric field

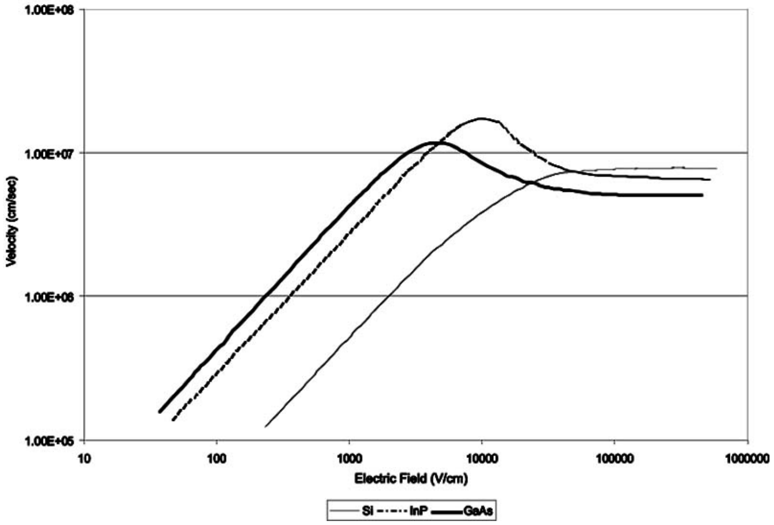

FIGURE 9.49 Electron velocity as a function of electric field for common semiconductors (after Bahl, Ref. 5).

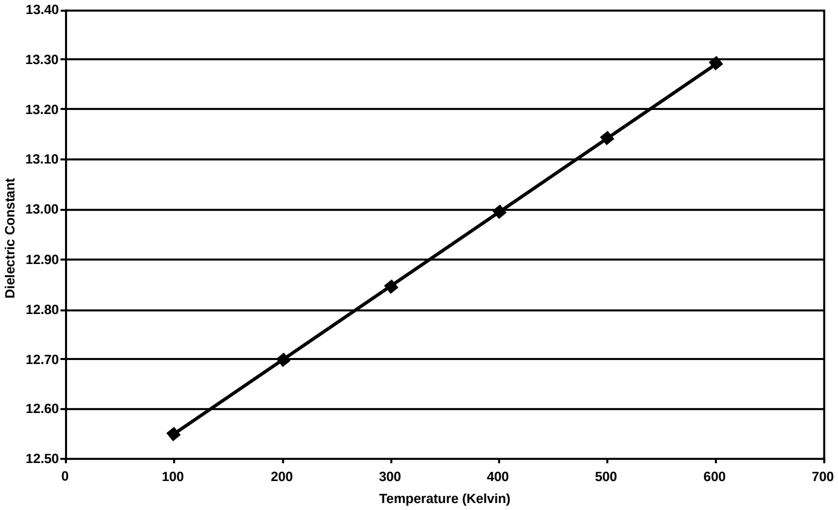

FIGURE 9.50 Relative dielectric constant of GaAs as a function of temperature.

strength. The proportionality constant is the mobility and this parameter is important in determining the low field operation of a device. Generally a high value of mobility is desired for optimum device performance. Since the mobility of electrons in gallium arsenide is about six times that of silicon, gallium arsenide is a more attractive material for high frequency RF and high-speed digital applications. This mobility advantage along with the availability of high resistivity substrates makes gallium arsenide the preferred and most widely used semiconductor material for these applications.[5]

The relative dielectric constant of GaAs is of critical importance in the design of monolithic microwave integrated circuits (MMICs). This parameter is used to determine the width of transmission lines used to interconnect transistors. The characteristic impedance of the transmission line is a function of the relative dielectric constant, the substrate thickness, and the width of the line. Figure 9.50 shows how the relative dielectric constant behaves with temperature. Microwave and RF designs must accommodate this variation over the expected temperature range of operation.

Reliable design and use of GaAs-based MMICs depends on keeping the device channel temperature below a certain absolute maximum level. Channel temperature is defined by the equation,

$$\mathbf{Tch} = \mathbf{Tsink} + \theta \times \mathbf{P}$$

where **Tch** is the channel temperature in (K), and **Tsink** is the heat sink temperature in (K). θ is the thermal resistance defined as L/kA, where L is the thickness of the GaAs substrate, k is the thermal conductivity of GaAs, and A is the area of the channel. **P** is the power dissipated (W). Thermal conductivity is a bulk material property that varies with temperature. Figure 9.51 shows the variation in thermal conductivity as a function of temperature for various semiconductors. At temperatures on the order of 100 K, the thermal conductivity of GaAs approaches that of copper.

III-V Heterostructures

A new class of high performance materials, based on GaAs and InP, has been developed using advanced epitaxial processes such as molecule beam epitaxy (MBE). These materials have heterojunctions that are formed between semiconductors having different compositions and bandgaps. The bandgap discontinuity can provide significant improvement in the transport properties of the material and allows optimization of device characteristics not possible with homojunctions. In FET devices, the current density can be high while retaining high electron mobility. This is possible because the free electrons are separated from their donor atoms and are confined to a region where the lattice scattering is minimal. Table 9.18 lists

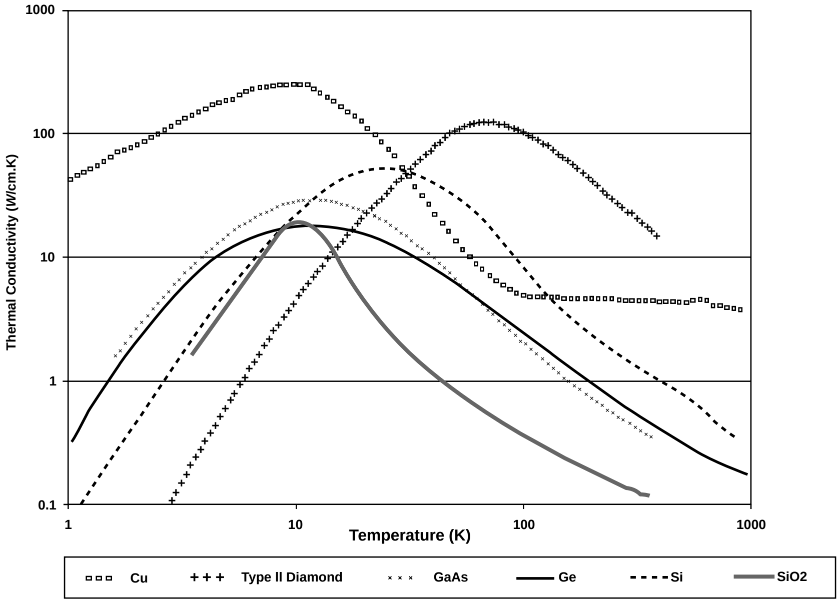

FIGURE 9.51 Thermal conductivity of various materials as a function of temperature (after Sze, Ref. 4).

TABLE 9.18 Common Heterostructures Used for Microwave and RF Applications

$Al_xGa_{1-x}As/GaAs$
$Al_xIn_{x-1}As/InGaAs$
$Al_xGa_{1-x}As/In_yGa_{1-y}As/GaAs$
InGaAs/InP
$Al_xIn_{x-1}As/InP$

the most common hetero-structures for microwave and RF applications. Material compositions vary and are designated by mole fraction using subscripts. In order to match the lattice spacing of GaAs, $Al_{0.25}Ga_{0.75}As$ is routinely used as shown in the diagram of Fig. 9.52. This diagram also shows the compounds that are lattice matched to InP. When a compound is formed with materials that have different lattice spacing, there is strain in the material and under certain conditions, improved performance is possible. This materials system is called pseudomorphic. Figure 9.53 is a cross-section diagram of a double pulsed doped pseudomorphic layer structure used for microwave power transistors.

Indium Phosphide

Indium phosphide (InP) is an important compound semiconductor for microwave and RF devices due to its physical and electronic properties. Some of the most important properties of InP are high peak electron velocity, high electric field breakdown, and relatively high thermal conductivity. Three-inch diameter bulk, semi-insulating InP wafers are available and four-inch diameter wafers are being validated. Indium phosphide has a zincblende crystalline structure like gallium arsenide and its lattice constant is 5.8687 angstroms compared to 5.6532 angstroms for GaAs. This materials property is important in the growth of hetero-structures as discussed below. Bulk InP is used in the fabrication of opto-electronic devices but is not used directly for microwave and RF applications. In microwave and RF devices, InP is used as a substrate for epitaxial growth to support GaInAs/AlInAs pseudomorphic high electron mobility transistors. This material system has proved to be a more desirable choice for microwave power amplifiers and millimeter-wave low noise amplifiers.

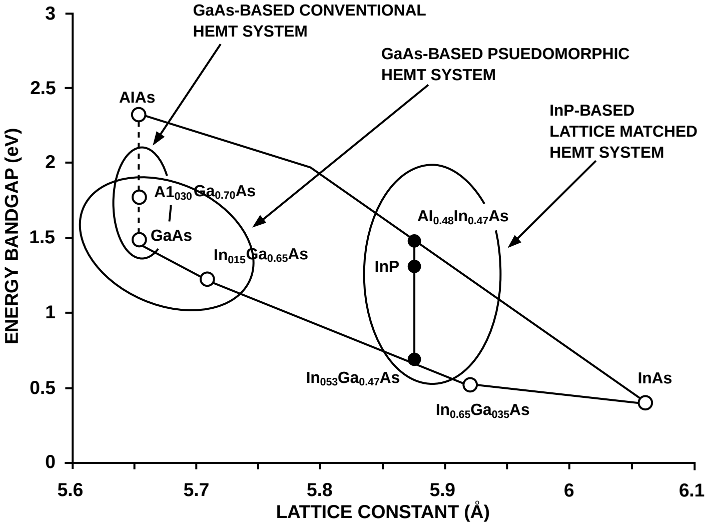

FIGURE 9.52 Energy bandgap and associated lattice constants for II-V hetero-structures.

	Thickness	Dopant	Doping
N^+ GaAs Cap	500 Å	Si	$5.0 \times 10^{18} cm^{-3}$
i AlGaAs Donor	300Å	None	-------
Si Planar Doping	-------	Si	$5.0 \times 10^{12} cm^{-2}$
i AlGaAs Spacer	20 Å	None	---------
i In GaAs Channel	120Å	None	---------
i GaAs Spacer			
Si Planar Doping	-------	Si	$1.2 \times 10^{12} cm^{-2}$
S/L Buffer	1000Å	None	---------
i GaAs Buffer	5000Å	None	---------
GaAs Substrate			

FIGURE 9.53 Double pulsed doped pseudomorphic HEMT layer structure. (From Quantum Epitaxial Designs. With permission.)

A fundamental design goal for microwave and RF device engineers, is to achieve the best electron transport properties possible within the reliability, breakdown, and leakage requirements of the application. Transition from GaAs/AlGaAs high electron mobility transistors to pseudomorphic GaAs/InGaAs/AlGaAs HEMTs resulted in significant improvements in device capability for both low noise and power applications.[6] This was due primarily to the increased electron velocity associated with the smaller electron effective mass in InGaAs compared to GaAs. However, the InAs lattice parameter of about 0.606 nm is considerably larger than the GaAs lattice constant of 0. 565 nm, and due to strain effects the compositional limit of psuedomorphic InGaAs on GaAs substrates is limited to about x = 0.30. One method to achieve higher InAs content in the InGaAs channel is to use an indium phosphide substrate with a lattice constant of 0.587 nm. This newer generation of HEMTs devices uses $In_{0.53}Ga_{0.47}As$ channel lattice matched to InP substrates. InP-based pseudomorphic HEMTs with $In_xGa_{1-x}As$ channel compositions of up to about x = 0.80 have achieved improvements in performance capability for both low noise and power amplifier applications compared to the best GaAs-based devices.

InP-based MMICs require semi-insulating substrates with resistivities from 10^{-6} to 10^{-8} ohm cm. To achieve such resistivities, in nominally undoped crystals would require the residual donor concentration to be reduced by a factor of at least 10^6 from current values. This is not practical and an alternate method is required that employs acceptor doping to compensate the residual donors. In principal, any acceptor can compensate the donors. However, because bulk indium phosphide crystals commonly have a short range variation of at least 5% in donor and acceptor concentration, the maximum resistivity that can be obtained by compensation with shallow acceptors in the absence of p-n junction formation, is only about 15 ohm cm. Resistivities in the semi-insulating range are usually obtained by doping with a deep acceptor such as iron (Fe). Fe is by far the most widely used deep acceptor to produce semi-insulating substrates. As a substitutional impurity, Fe is generally stable under normal device operating temperatures. At high temperatures there is concern of possible diffusion of Fe into the epitaxial layer leading to adverse effects on the devices. Diffusion studies of Fe in InP at temperature of 650°C for four hours indicated virtually no change from the control sample.[7]

Use of InP materials is sometimes restricted by its cost. InP substrates are significantly more costly than those made from GaAs, and even more so when compared to silicon. In addition, the technology of indium phosphide substrate manufacturing is much more difficult than for GaAs or silicon. This situation is not simply the result of lower market demand but is linked fundamentally to the high vapor pressure of phosphorus that creates an obstacle to the synthesis of single crystal boules of larger diameters. While 8-inch silicon substrates and 6-inch GaAs substrates are the rule in commercial fabrication, indium phosphide substrates are still primarily 2 inch. Three-inch diameter wafers are becoming available and 4-inch wafers are being validated. New concepts of single crystal growth may provide larger diameter wafers at low cost leading to wider acceptance of this compound semiconductor for microwave and RF applications.

Silicon Carbide

Silicon carbide possesses many intrinsic material properties that make it ideal for a wide variety of high power, high temperature, and high frequency electronic device applications. In comparison with silicon and gallium arsenide, SiC has greater than 2.5x larger bandgap, 3x greater thermal conductivity, and a factor of 10 larger breakdown electric field. These characteristics enable SiC devices to operate at higher temperatures and power levels, with lower on-resistances, and in harsh environments inaccessible to other semiconductors. However, electron transport properties may limit SiC applications to frequencies less than 10 GHz. While excellent prototype SiC devices have been demonstrated, SiC devices will not be widely available until material quality improves and material cost drops.[8]

SiC belongs to a class of semiconductors commonly known as "wide bandgap," which makes it, among other things, less sensitive to increased temperatures. Properly designed and fabricated SiC devices should operate at 500°C or higher, a realm that Si does not even approach. Furthermore, the thermal conductivity of SiC exceeds even that of copper; any heat produced by a device is therefore quickly dissipated. The inertness of SiC to chemical reaction implies that devices have the potential to operate even in the most caustic of environments. SiC is extremely hard and is best known as the grit coating on sandpaper. This hardness again implies that SiC devices can operate under conditions of extreme pressure. SiC is extremely radiation hard and can be used close to reactors or for electronic hardware in space. Properties of particular importance to the microwave and RF device design engineer are high electric field strength and relatively high saturation drift velocity.

SiC exists not as a single crystal type, but as a whole family of crystals known as polytypes. Each crystal structure has its own unique electrical and optical properties.[9,10] Polytypes differ not in the relative numbers of Si and C atoms, but in the arrangement of these atoms in layers as illustrated in Fig. 9.54. The polytypes are named according to the periodicity of these layers. For example, one of the most common polytypes is called 6H, which means a hexagonal type lattice with an arrangement of 6 different Si+C layers before the pattern repeats itself. In total, more than 200 different polytypes of SiC have been shown to exist, some with patterns that do not repeat for hundreds of layers. The exact physical properties of SiC depend on the crystal structure adopted. Some of the most common structures used are 6H, 4H, and 3C, the last being the one cubic form of SiC.

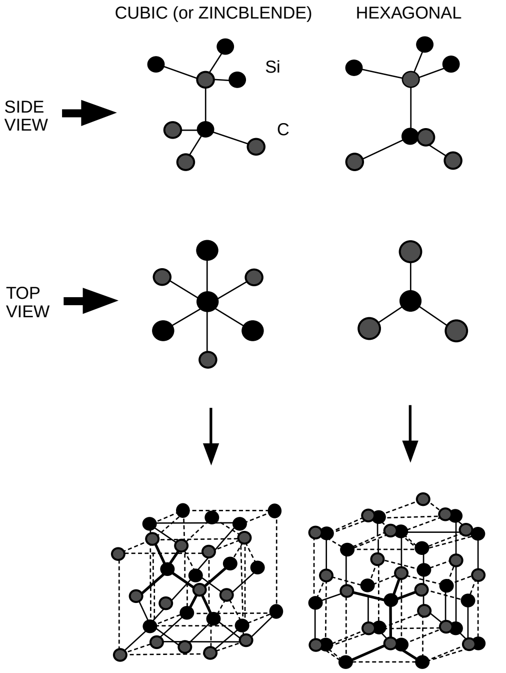

FIGURE 9.54 Difference between the cubic and hexagonal polytypes of SiC. (From Virgil B. Shields, 1994. With permission.)

Silicon carbide (SiC) is also emerging as a substrate material that may meet the challenging requirements for GaN growth.[11,12] Type 6H-SiC is lattice matched to within 3.5% of GaN compared to 16% for sapphire.[13] SiC has a thermal conductivity that is over 10 times higher than sapphire.

Figure 9.55 compares the energy band and lattice constants of the conventional III-V semiconductor material systems shown in the circle and the wide gap semiconductors. As shown in the figure, SiC is reasonably lattice matched to GaN and makes a good candidate for a substrate material.

Gallium Nitride

Gallium nitride in the wurtzite form (2H polytype) has a bandgap of 3.45 eV (near UV region) at room temperature. It also forms a continuous range of solid solutions with AlN (6.28 eV) and a discontinuous range of solid solutions with InN (1.95 eV). The wide bandgap, the heterojunction capability, and the strong atomic bonding of these materials make them good candidates for RF and microwave devices. Other pertinent device-related parameters include a good thermal conductivity of 1.5 W/cm-K, a type I heterojunction with AlN and AlGaN alloys, large band discontinuities with resultant large interface carrier concentrations, and a large breakdown voltage.

Intrinsic material properties of gallium nitride combined with hetero-structure designs are producing revolutionary improvement in output power for microwave devices. GaN-based FET devices have demonstrated power densities of near 10 W/mm of gate width compared to 1 W/mm for the best GaAs-based devices.[14] GaN has a bandgap of 3.45 eV compared to 1.43 eV for GaAs. This property leads to orders of magnitude lower thermal leakage. GaN has a thermal conductivity almost 3 times higher than GaAs, a parameter that is critically important for power amplifier applications. The dielectric breakdown strength of GaN is a factor of 2 greater than GaAs, further supporting the consideration of this material for microwave power amplifier applications. A key limitation in the development of GaN devices is the fact that there is no native GaN substrate. Currently, GaN must be deposited on host substrates such as sapphire or SiC.

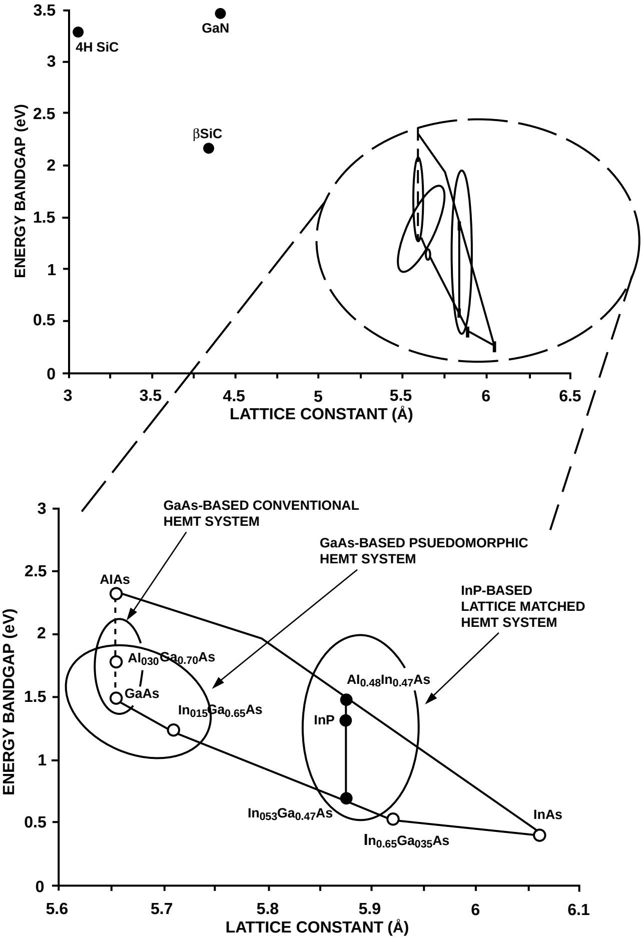

FIGURE 9.55 Comparison of conventional and wide bandgap materials.

GaN, AlN, and InGaN have a polar wurtzite structure as shown in Fig. 9.56 and epitaxial films of these materials typically grow along the polar axis. Although the polarity of these nitrides has been studied by a number of techniques, many results in the literature are in conflict.[15] The wurtzite lattice can be considered as two interpenetrating hexagonal close-packed lattices. The wurtzite structure has a tetrahedral arrangement of four equidistant nearest neighbors, similar to the GaAs zincblende structure.

Electron transport in GaN is governed by the electron mobility. Low field electron mobility, in bulk wurtzite GaN, is limited by charged states that are dislocation related, as well as by isolated donor ions and phonons. With no dislocations or donor ions, the 300°K phonon-limited mobility is near 2000 cm^2/V-s. Combined scattering effects reduce the mobility for both highly-doped and lightly-doped material, for a given dislocation density. Dislocation density depends on the nucleation methods used at growth initiation, usually ranging from $3 \times 10^9/cm^2$ to $3 \times 10^{10}/cm^2$.[16]

The average drift velocity at high fields in bulk GaN, or in GaN MODFETs, is expected to be above 2×10^7 cm/s. These high fields extend increasingly toward the drain with higher applied drain-source voltage. The average transit velocity is $>1.25 \times 10^7$ cm/s when only the effective gate length is considered, without the extended high-field region. This result is consistent with an average drift velocity of ~2×10^7 cm/s over an extended region.

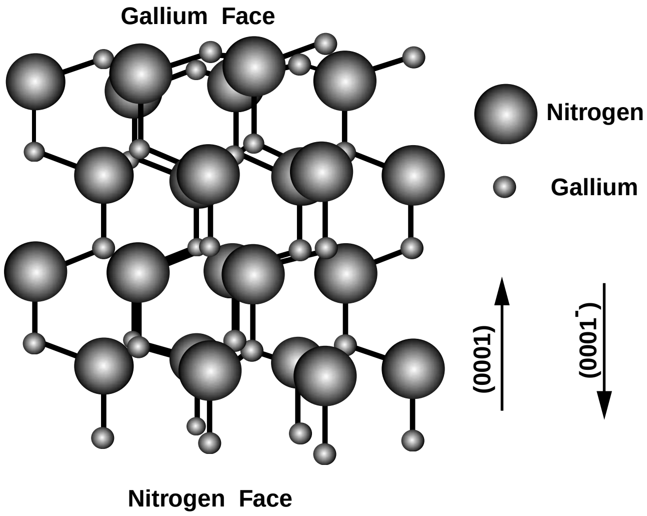

FIGURE 9.56 Wurtzite structure of GaN (Hellman[15] used with permission).

Growth of GaN and its related compounds is dominated by metal-organic vapor phase epitaxy (MOVPE) or MOCVD metal-organic chemical vapor deposition, techniques with obvious advantages in fields where high throughput is required. Molecular beam epitaxy (MBE) is also used to grow GaN films. The III-nitride community grows films of GaN and related nitride materials using hetero-epitaxial growth routes because of the lack of bulk substrates of these materials. This results in films containing dislocations because of the mismatches in the lattice parameters and the coefficients of thermal expansion between the buffer layer and the film and/or the buffer layer and the substrate. These high concentrations of dislocations may also limit the performance of devices.

Advanced growth procedures, including selective area growth (SAG) and lateral epitaxial overgrowth (LEO) techniques for GaN deposition, are being used specifically to significantly reduce the dislocation density. The latter technique involves the initial vertical growth of a configuration and material composition through windows etched in an SiO_2 or Si_3N_4 mask previously deposited on an underlying GaN seed layer and the subsequent lateral and vertical growth of a film over and adjacent to the mask. Reduction in the number of defects in the material and growth of GaN on larger diameter wafers will lead to the production of GaN-based devices and circuits for microwave and higher frequency applications.

Selected Material Properties

Table 9.19 contains the most common material properties on semiconductors used for microwave and RF applications. Sources of information in this table include textbooks, articles, and World Wide Web sites. Web sites are a convenient way to find materials data and several of the sites used to prepare Table 9.19 are listed in Table 9.20. Most of these sites include detailed references that will provide the user with more extensive information. When using these material properties in the design of components, it is recommended that the user examine the temperature and frequency behavior of the specific property before finalizing the design.

Etching Processes for Semiconductors

Table 9.21 lists typical etching processes for the various semiconductors described in this section.

Ohmic and Schottky Contacts

Table 9.22 is a list of metallizations that have been used to successfully fabricate low resistance ohmic contacts for drain and source contacts in FET devices and low leakage Schottky barrier contacts for metal semiconductor diode gates.

TABLE 9.19 Selected Material Properties of Semiconductors for Microwave and RF Applications

Property	Si	SiC	InP	GaAs	GaN
Atoms/cm^3	5.0×10^{22}	3.95×10^{22}	4.43×10^{22}	4.96×10^{22}	
Atomic weight	28.09	40.1	72.90	72.32	41.87
Breakdown Field (V/cm)	3×10^{5} [32]	20×10^{4} 3C-SiC[27] 30×10^{5} 4H-SiC[27]	5×10^{5} [32]	6×10^{5}	$>10 \times 10^{5}$
Crystal structure	Diamond	Zincblende	Zincblende	Zincblende	Wurtzite
Density (g/cm^3)	2.3283[23]	4.787[23]	5.316[33]	6.1[23]	
Dielectric constant	11.8[23]	9.75[17] 9.66[18]	12.4[23]	12.5[23]	9[35]
Effective mass m*/m$_0$ Electron	1.1	0.37 3C-SiC[19] 0.45 6H-SiC[20]	0.067[23]	0.068[23]	0.22[35,36]
Electron Affinity, eV	4.05[31]	—	4.38[31]	4.07[31]	3.4[34]
Energy Gap (eV) at 300 K	1.107[23]	2.403 3C-SiC[23] 3.101 6H-SiC[23]	1.29[31]	1.35[31]	3.34[37]
Intrinsic carrier concentration (cm^{-3})	1.45×10^{10} [23]	3×10^{6} 3C-SiC[21] 10^{15}–10^{16} 6H-SiC[22]	1.6×10^{7} [23]	1.8×10^{6} [23]	3-6 $\times 10^{9}$ [23]
Lattice constant (Angstroms)	5.431[31]	4.3596[27]	5.860[31]	5.651[31]	3.190[38]
Linear Coeff. of thermal expansion (10^{-6} K^{-1})	2.49[23]	5.48[22]	4.6[23]	5.4[23]	5.6[27]
Melting point (K)	1685[23]	3070[23]	1335[31]	1511[31]	—
Electron mobility (cm^2/V-S) μ_m	1900[23]	1000 3C-SiC[24] 600 6H-SiC[24]	4600[23]	8800[23]	1000[39]
Holes mobility μ_p (cm^2/V-S)	500[23]	40 3C-SiC[24] 40 6H-SiC[24]	150[23]	400[23]	30[39]
Optical phonon energy (eV)	.063 eV[31]	—	0.43[31]	0.35[31]	.912[40]
Refractive index	3.42[23]	2.65 3C-SiC[25] 2.72 6H-SiC[26]	3.1[31]	3.66[31]	2.7[41] (at band edge)
Resistivity, intrinsic (Ω-cm)	1000[31]	150 3C-SiC[27] $>10^{12}$ 4H-SiC[27]	8.2×10^{7} [31]	3.8×10^{8} [31]	$>10^{13}$ [27]
Specific heat (J/kg°K)	702[23]	640[28]	310[31]	325[32]	847.39[42]
Thermal conductivity at 300°K (Watt/cm°K)	1.24[23]	3.2 3C-SiC[29] 4.9 6H-SiC[30]	.77[32]	.56[31]	1.3[43]

TABLE 9.20 World Wide Web Sites for Semiconductor Material Properties

http://www.ioffe.rssi.ru/SVA/NSM/Nano/index.html
http://mems.isi.edu/mems/materials/
http://www.webelements.com/webelements/elements/
http://www.sensors-research.com/senres/materials.htm
http://nsr.mij.mrs.org/
http://nina.ecse.rpi.edu/shur/nitride.htm

TABLE 9.21 Etching Processes for Various Semiconductors

Etchant	Substrate and Conditions	Applications	Etch Rate	Ref.
15 HNO_3, 5 CH_3COOH, 2 HF (planar)	Si	For general etching	Variant	44
110 ml CH_3COOH, 100 ml HNO_3, 50 ml HF, 3 g I_2 (iodine etch)	Si	For general etching	Variant	45
KOH solutions; hydrazine (a) KOH (3–50%) (b) 60 hydrazine, 40 H_2O	(100) Si 70–90 C, SiO_2 unmasked 110 C, 10 min, unmasked	For texturing and V grooving solar etch (no texturizing) for diffuse-reflectivity texturizing	Variant	46
28% by weight KOH at 90–95°C	[100] Si, with oxide mask	V-shaped channel etching for optical waveguides	~2 microns/min	47
3CH3OH, 1H3PO4, 1H2O2	[110], [100], Ga [111]GaAs	Preferential structural etching	~2 microns/min, except Ga[111] reduced twofold	48
3 ml HPO_4, 1 ml H_2O_2, 50 ml H_2O	GaAs, 300 K with Shipley 1813 mask	Wet etch	~.1 microns/min	
BCL_3 Gas, reactive ion etch	GaN, BCL_3, 150 W, 10 mTorr	Slow etching, used to obtain a vertical profile for mesa isolation	~.02 microns/min	

TABLE 9.22 Metallization Systems for Ohmic and Schottky Barrier Contacts

Contact	SiC	GaAs	GaN	InP
Ohmic contact mettalization	Ta, Al/Ti, Ni, Ti, Mo, Ta[50]	Au/Ge/Ni, In, Sn, Ag and Ag alloys, Au, Ni[52]	Ti/Al/Ni/Aun-GaN Ni/Aup-GaN[53]	Au and Au alloys, near noble transition metals (Co, Ni, Ti, Pd, Pt)[49]
Schottky gate mettalization	Au and Au alloys[50]	Ti/Pt/Au multilayer structures, Au alloys[51]	Ni/Au/Ti n-GaN Aup-GaN[53]	For AlInP/InP 15% Al superlattice, 20% Al quantum well[52]

References

1. Yu, P.Y. and Cardona M., *Fundamentals of Semiconductors,* New York, Springer-Verlag, 1999, 1.
2. Sze, S.M., Ed., *VLSI Technology,* New York, McGraw-Hill, 1983, 35.
3. Sumitomo Electric III-V Semiconductors Specifications, 32.
4. Sze, S.M., Ed., *Physics of Semiconductors,* New York, John-Wiley & Sons, 1981, 15, 43.
5. Bahl, I. and Bhartia P., *Microwave Solid State Circuit Design*, New York, John Wiley & Sons, 1988, 307.
6. Pearsall, T.P., *Properties, Processing and Applications of Indium Phosphide,* Eisele, H. and Haddad, G.I., Eds., INSPEC, London, 2000, 40.
7. Katz, A., *Induim Phosphide and Related Materials: Processing, Technology and Devices,* Byrne, E.K. and Katz, A., Eds., Boston, Artech House, 1992, 169.
8. Brandes G.R., Growth of SiC Boules and Epitaxial Films for Next Generation Electronic Devices, American Physical Society Centennial Meeting, March 20–26, Atlanta, GA, 1999.
9. von-munch, W., Silicon Carbide, in *Physik der Elemete der* IV. Gruppe und der III-V Verbindungen, K.-H. Hellwege, Ed. Berlin, Heidelberg, Springer-Verlag, 1982, 132–142.
10. Powell, J. A., Pirouz, P., and Choyke, W.J., Growth and Characterization of Silicon Carbide Polytypes for Electronic Applications, in *Semiconductor Interfaces, Microstructures, and Devices: Properties and Applications,* Feng Z.C., Ed. Bristol, United Kingdom, Institute of Physics Publishing, 1993, 257–293.

11. Mohammad, S.N., Salvador A.A and Morkoc Hardel, Emerging Gallium Nitride Based Devices, *Proceedings of the IEEE*, 83, 10, 1306–1355, Oct. 1995.
12. Lin, M.E., Sverdlov, B., Zhou, G.L., and Morkoc, H., A Comparative Study of GaN Epilayers Grown on Sapphire and SiC Substrates by Plasma-assisted Molecular-beam Epitaxy, *Appl. Phys. Lett.*, 62, 26, 3479–3481, 1993.
13. Lin, M.E. et al. Low Resistance Ohmic Contacts on Wide Band-gap GaN, *Appl. Phys. Lett.*, 64, 1003–1005, 1994.
14. Sheppard, S., Doverspike, K., Leonard, M., Pribble, W., Allen, S., and Palmour, J., Improved Operation of GaN/AlGaN HEMTS on Silicon Carbide, International Conference on Silicon Carbide and Related Materials 1999, Paper 349.
15. Hellman, E.S., The Polarity of GaN: a Critical Review. *Materials Research Society Internet Journal*, Vol 3, Res 3, May 19, 1998.
16. Eastman, L., Chu, K., Schaff, W., Murphy, M.,Weimann, M., and Eustis, T., High Frequency AlGaN/GaN MODFET's, *Materials Research Society Internet Journal*, Vol. 2, Res 2, August 12, 1997.
17. Patrick, L., Choyke, W.J., *Physics Review Journal*, 2, 2255, 1977.
18. Choyke, W.J., *NATO ASI Ser. E, Applied Sciences*, 185, and references therin, 1990.
19. Suzuki, A., Ogura A., Furukawa, K., Fujii, Y., Shigeta, M., and Nakajima, S., *Journal of Applied Physics*, 64, 2818, 1988.
20. Wessels, B.W. and Gatos, J.C., *Journal of Physics Chemical Solids*, 15, 83, 1977.
21. Anikin, M.M., Zubrilov, A.S., Lebedev, A.A., Sterlchuck, A.M., and Cherenkov, A.E., *Fitz. Tekh. Polurpovdn.*, 24, 467, 1992.
22. Schackelford, J., Alexander, W., and Parker, J., Eds., *CRC Materials Science and Engineering Handbook*, 2nd ed., Boca Raton, FL, CRC Press, 1994, 304.
23. Lide, D.R., Properties of Semiconductors, *CRC Handbook of Chemistry and Physics*, 12–98, 1999–2000 ed. Boca Raton, FL, CRC Press, 2000.
24. http://vshields.jpl.nasa.gov/windchime.html.
25. Schaffer, P.T.B. and Naum, R.G., *Journal of Optical Society of America*, 59, 1498, 1969.
26. Scaffer, P.T.B., *Applied Optics*, 10, 1034, 1977.
27. Yoder, M.N.,*Wide Bandgap Semiconductor Materials and Devices* , 43, 10, 1634, 1966.
28. Kern, E.L., Hamill, H.W., Deem, H.W., and Sheets, H.D., *Mater Res. Bull.*, 4, 107, 1969.
29. Morelli, D., Hermans, J., Bettz, C., Woo, W.S., Harris, G.L., and Taylor, C., *Inst. Physics Conf. Ser.*, 137, 313–6, 1990.
30. Parafenova, I.I., Tairov, Y.M., and Tsvetkov, V.F., *Sov. Physics-Semiconductors*, 24, 2, 158–61, 1990.
31. http://www.ioffe.rssi.ru/SVA/NSM/Nano/index.html.
32. Garland, C.W. and Parks, K.C., *Journal Applied Physics*, 33, 759, 1962.
33. http://mems.isi.edu/mems/materials/measurements.cgi?MATTAG=galliumarsenidegaas-bulk&PAGE_SIZE=20.
34. Benjamin, M.C., Wang, C., Davis, R.F., and Nemanich, R.J., *Applied Phys. Letter*, 64, 3288, 1994.
35. Mohammad, S.N. and Morkoc, H., *Prog. Quant. Electron.*, 20, 361, 1996.
36. Barker, A.S. and Ilegems, M., *Phys. Rev. B*, 7, 743, 1973.
37. Maruska, H.P. and Tietjen, J.J., *Appl. Phys. Lett.*, 15, 327, 1969.
38. Shur, M.S. and Khan, A.M., *Mat. Res. Bull.*, 22, 2, 44, 1977.
39. Bhapkar, U.V. and Shur, M. S. , *Journal of Applied Physics*, 82, 4, 1649, 1997.
40. Chin, V. W. L., Tansley, T. L., andOsotchan, T., *Journal of Applied Physics*, 75, 7365, 1994.
41. Billeb, A., Grieshhaber, W., Stocker, D., Schubert, E.F., and Karlicek, R.F., *Applied. Physics. Letter*, 69, 2953, 1996.
42. Koshchenko, V.I., Grinberg, Ya, K.H., and Demidienko, A.F., *Inorganic Matter*, 11, 1550–3, 1984.
43. Sichel, E.K. and Pankove, J.I., *J. Phys. Chem. Solids*, 38, 330, 1977.
44. Ruynun, W.R., *Semiconductor Measurements and Instrumentation*, McGraw-Hill, New York, 1975, 129, Table 7.3, Chaps. 1, 2, 7, 9.

45. Integrated Circuit Silicon Device Technology; X-Chemical Metallurgical Properties of Silicon, ASD-TDR-63-316, Vol. X, AD 625, 985. Research Triangle Inst., Research Triangle Park, North Carolina.
46. Baroana, C.R. and Brandhorst, H.W., *IEEE Photovoltaic Spec. Conf. Proc.*, Scottsdale, AZ, 44–48, 1975.
47. http://peta.ee.cornell.edu/~jay/res/vgroove/
48. Merz, J.L. and Logan, R.A., *J. Appl. Physics*, 47, 3503, 1976.
49. Pearshall, T.P., Processing Technologies, in *Properties, Processing, and Applications of Induim Phosphide,* Katz A. and Pearshall, T.P., Eds., Inspec, London, 2000, 246.
50. Harris, G.L., SiC Devices and Ohmic Contacts, in *Properties of SiC,* Harris, G.L, Kelner, G., and Shur, M., Eds., Inspec, London, 1995, 233, 243.
51. Misssous, M., Interfaces and Contacts, in *Properties of Gallium Arsenide*, Morgan, D.V. and Wood, J., Eds., Inspec, London, 1990, 386–387.
52. Lammasniemi, J., Tappura K., and Smekalin K., *Applied Physics Letter*, 65, 20, 2574–5, 1998.
53. Edgar, J. H., Strite, S., Akasaki, I., Amano, H., and Wetzel, C., Specifications, characterisation and applications of GaN based devices, in *Properties, Processing and Applications of Gallium Nitride and Related Semiconductors,* Mohney, S.E., Ed., Inspec, London, 1999, 491–96.

Golio, Mike "Appendix A: Mathematics, Symbols and Physical Constants "
The RF and Microwave Handbook
Editor in Chief Mike Golio
Boca Raton: CRC Press LLC,2001

APPENDIX A

Mathematics, Symbols, and Physical Constants

Greek Alphabet

	Greek letter	Greek name	English equivalent		Greek letter	Greek name	English equivalent
Α	α	Alpha	a	Ν	ν	Nu	n
Β	β	Beta	b	Ξ	ξ	Xi	x
Γ	γ	Gamma	g	Ο	ο	Omicron	ŏ
Δ	δ	Delta	d	Π	π	Pi	p
Ε	ε	Epsilon	ĕ	Ρ	ρ	Rho	r
Ζ	ζ	Zeta	z	Σ	σ	Sigma	s
Η	η	Eta	ē	Τ	τ	Tau	t
Θ	θ ϑ	Theta	th	Υ	υ	Upsilon	u
Ι	ι	Iota	i	Φ	ϕ φ	Phi	ph
Κ	κ	Kappa	k	Χ	χ	Chi	ch
Λ	λ	Lambda	l	Ψ	ψ	Psi	ps
Μ	μ	Mu	m	Ω	ω	Omega	ō

International System of Units (SI)

The International System of units (SI) was adopted by the 11th General Conference on Weights and Measures (CGPM) in 1960. It is a coherent system of units built form seven *SI base units,* one for each of the seven dimensionally independent base quantities: they are the meter, kilogram, second, ampere, kelvin, mole, and candela, for the dimensions length, mass, time, electric current, thermodynamic temperature, amount of substance, and luminous intensity, respectively. The definitions of the SI base units are given below. The *SI derived units* are expressed as products of powers of the base units, analogous to the corresponding relations between physical quantities but with numerical factors equal to unity.

In the International System there is only one SI unit for each physical quantity. This is either the appropriate SI base unit itself or the appropriate SI derived unit. However, any of the approved decimal prefixes, called *SI prefixes,* may be used to construct decimal multiples or submultiples of SI units.

It is recommended that only SI units be used in science and technology (with SI prefixes where appropriate). Where there are special reasons for making an exception to this rule, it is recommended always to define the units used in terms of SI units. This section is based on information supplied by IUPAC.

Definitions of SI Base Units

Meter—The meter is the length of path traveled by light in vacuum during a time interval of 1/299 792 458 of a second (17th CGPM, 1983).

Kilogram—The kilogram is the unit of mass; it is equal to the mass of the international prototype of the kilogram (3rd CGPM, 1901).

Second—The second is the duration of 9 192 631 770 periods of the radiation corresponding to the transition between the two hyperfine levels of the ground state of the cesium-133 atom (13th CGPM, 1967).

Ampere—The ampere is that constant current which, if maintained in two straight parallel conductors of infinite length, of negligible circular cross-section, and placed 1 meter apart in vacuum, would produce between these conductors a force equal to 2×10^{-7} newton per meter of length (9th CGPM, 1948).

Kelvin—The kelvin, unit of thermodynamic temperature, is the fraction 1/273.16 of the thermodynamic temperature of the triple point of water (13th CGPM, 1967).

Mole—The mole is the amount of substance of a system which contains as many elementary entities as there are atoms in 0.012 kilogram of carbon-12. When the mole is used, the elementary entities must be specified and may be atoms, molecules, ions, electrons, or other particles, or specified groups of such particles (14th CGPM, 1971).

Examples of the use of the mole:

1 mol of H_2 contains about 6.022×10^{23} H_2 molecules, or 12.044×10^{23} H atoms
1 mol of HgCl has a mass of 236.04 g
1 mol of Hg_2Cl_2 has a mass of 472.08 g
1 mol of Hg_2^{2+} has a mass of 401.18 g and a charge of 192.97 kC
1 mol of $Fe_{0.91}S$ has a mass of 82.88 g
1 mol of e^- has a mass of 548.60 μg and a charge of –96.49 kC
1 mol of photons whose frequency is 10^{14} Hz has energy of about 39.90 kJ

Candela—The candela is the luminous intensity, in a given direction, of a source that emits monochromatic radiation of frequency 540×10^{12} hertz and that has a radiant intensity in that direction of (1/683) watt per steradian (16th CGPM, 1979).

Names and Symbols for the SI Base Units

Physical quantity	Name of SI unit	Symbol for SI unit
length	meter	m
mass	kilogram	kg
time	second	s
electric current	ampere	A
thermodynamic temperature	kelvin	K
amount of substance	mole	mol
luminous intensity	candela	cd

SI Derived Units with Special Names and Symbols

Physical quantity	Name of SI unit	Symbol for SI unit	Expression in terms of SI base units	
frequency[1]	hertz	Hz	s^{-1}	
force	newton	N	$m\ kg\ s^{-2}$	
pressure, stress	pascal	Pa	$N\ m^{-2}$	$=m^{-1}\ kg\ s^{-2}$
energy, work, heat	joule	J	N m	$= m^2\ kg\ s^{-2}$
power, radiant flux	watt	W	$J\ s^{-1}$	$= m^2\ kg\ s^{-3}$
electric charge	coulomb	C	A s	
electric potential, electromotive force	volt	V	$J\ C^{-1}$	$= m^2\ kg\ s^{-3}\ A^{-1}$

Physical quantity	Name of SI unit	Symbol for SI unit	Expression in terms of SI base units	
electric resistance	ohm	Ω	$\mathrm{V\ A^{-1}}$	$= \mathrm{m^2\ kg\ s^{-3}\ A^{-2}}$
electric conductance	siemens	S	Ω^{-1}	$= \mathrm{m^{-2}\ kg^{-1}\ s^3\ A^2}$
electric capacitance	farad	F	$\mathrm{C\ V^{-1}}$	$= \mathrm{m^{-2}\ kg^{-1}\ s^4\ A^2}$
magnetic flux density	tesla	T	$\mathrm{V\ s\ m^{-2}}$	$= \mathrm{kg\ s^{-2}\ A^{-1}}$
magnetic flux	weber	Wb	V s	$= \mathrm{m^2\ kg\ s^{-2}\ A^{-1}}$
inductance	henry	H	$\mathrm{V\ A^{-1}\ s}$	$= \mathrm{m^2\ kg\ s^{-2}\ A^{-2}}$
Celsius temperature[2]	degree Celsius	°C	K	
luminous flux	lumen	lm	cd sr	
illuminance	lux	lx	$\mathrm{cd\ sr\ m^{-2}}$	
activity (radioactive)	becquerel	Bq	$\mathrm{s^{-1}}$	
absorbed dose (of radiation)	gray	Gy	$\mathrm{J\ kg^{-1}}$	$= \mathrm{m^2\ s^{-2}}$
dose equivalent (dose equivalent index)	sievert	Sv	$\mathrm{J\ kg^{-1}}$	$= \mathrm{m^2\ s^{-2}}$
plane angle	radian	rad	1	$= \mathrm{m\ m^{-1}}$
solid angle	steradian	sr	1	$= \mathrm{m^2\ m^{-2}}$

[1] For radial (circular) frequency and for angular velocity the unit rad $\mathrm{s^{-1}}$, or simply $\mathrm{s^{-1}}$, should be used, and this may not be simplified to Hz. The unit Hz should be used only for frequency in the sense of cycles per second.

[2] The Celsius temperature θ is defined by the equation:

$$\theta/°\mathrm{C} = T/\mathrm{K} - 273.15$$

The SI unit of Celsius temperature interval is the degree Celsius, °C, which is equal to the kelvin, K. °C should be treated as a single symbol, with no space between the ° sign and the letter C. (The symbol °K, and the symbol °, should no longer be used.)

Units in Use Together with the SI

These units are not part of the SI, but it is recognized that they will continue to be used in appropriate contexts. SI prefixes may be attached to some of these units, such as milliliter, ml; millibar, mbar; megaelectronvolt, MeV; kilotonne, ktonne.

Physical quantity	Name of unit	Symbol for unit	Value in SI units	
time	minute	min	60 s	
time	hour	h	3600 s	
time	day	d	86 400 s	
plane angle	degree	°	(π/180) rad	
plane angle	minute	′	(π/10 800) rad	
plane angle	second	″	(π/648 000) rad	
length	ångstrom[1]	Å	10^{-10} m	
area	barn	b	$10^{-28}\ \mathrm{m^2}$	
volume	litre	l, L	$\mathrm{dm^3}$	$= 10^{-3}\ \mathrm{m^3}$
mass	tonne	t	Mg	$= 10^3$ kg
pressure	bar[1]	bar	10^5 Pa	$= 10^5\ \mathrm{N\ m^{-2}}$
energy	electronvolt[2]	eV (= $e \times$ V)	$\approx 1.60218 \times 10^{-19}$ J	
mass	unified atomic mass unit[2,3]	u (= $m_a(^{12}\mathrm{C})/12$)	$\approx 1.66054 \times 10^{-27}$ kg	

[1] The ångstrom and the bar are approved by CIPM for "temporary use with SI units," until CIPM makes a further recommendation. However, they should not be introduced where they are not used at present.

[2] The values of these units in terms of the corresponding SI units are not exact, since they depend on the values of the physical constants e (for the electronvolt) and N_a (for the unified atomic mass unit), which are determined by experiment.

[3] The unified atomic mass unit is also sometimes called the dalton, with symbol Da, although the name and symbol have not been approved by CGPM.

Physical Constants

General

Equatorial radius of the earth = 6378.388 km = 3963.34 miles (statute).

Polar radius of the earth, 6356.912 km = 3949.99 miles (statute).

1 degree of latitude at 40° = 69 miles.

1 international nautical mile = 1.15078 miles (statute) = 1852 m = 6076.115 ft.

Mean density of the earth = 5.522 g/cm^3 = 344.7 lb/ft^3

Constant of gravitation (6.673 ± 0.003) × 10^{-8} cm^3 gm^{-1} s^{-2}.

Acceleration due to gravity at sea level, latitude 45° = 980.6194 cm/s^2 = 32.1726 ft/s^2.

Length of seconds pendulum at sea level, latitude 45° = 99.3575 cm = 39.1171 in.

1 knot (international) = 101.269 ft/min = 1.6878 ft/s = 1.1508 miles (statute)/h.

1 micron = 10^{-4} cm.

1 ångstrom = 10^{-8} cm.

Mass of hydrogen atom = (1.67339 ± 0.0031) × 10^{-24} g.

Density of mercury at 0°C = 13.5955 g/ml.

Density of water at 3.98°C = 1.000000 g/ml.

Density, maximum, of water, at 3.98°C = 0.999973 g/cm^3.

Density of dry air at 0°C, 760 mm = 1.2929 g/l.

Velocity of sound in dry air at 0°C = 331.36 m/s – 1087.1 ft/s.

Velocity of light in vacuum = (2.997925 ± 0.000002) × 10^{10} cm/s.

Heat of fusion of water 0°C = 79.71 cal/g.

Heat of vaporization of water 100°C = 539.55 cal/g.

Electrochemical equivalent of silver 0.001118 g/s international amp.

Absolute wavelength of red cadmium light in air at 15°C, 760 mm pressure = 6438.4696 Å.

Wavelength of orange-red line of krypton 86 = 6057.802 Å.

π Constants

π = 3.14159 26535 89793 23846 26433 83279 50288 41971 69399 37511

$1/\pi$ = 0.31830 98861 83790 67153 77675 26745 02872 40689 19291 48091

π^2 = 9.8690 44010 89358 61883 44909 99876 15113 53136 99407 24079

$\log_e \pi$ = 1.14472 98858 49400 17414 34273 51353 05871 16472 94812 91531

$\log_{10} \pi$ = 0.49714 98726 94133 85435 12682 88290 89887 36516 78324 38044

$\log_{10} \sqrt{2\pi}$ = 0.39908 99341 79057 52478 25035 91507 69595 02099 34102 92128

Constants Involving e

e = 2.71828 18284 59045 23536 02874 71352 66249 77572 47093 69996

$1/e$ = 0.36787 94411 71442 32159 55237 70161 46086 74458 11131 03177

e^2 = 7.38905 60989 30650 22723 04274 60575 00781 31803 15570 55185

$M = \log_{10} e$ = 0.43429 44819 03251 82765 11289 18916 60508 22943 97005 80367

$1/M = \log_e 10$ = 2.30258 50929 94045 68401 79914 54684 36420 67011 01488 62877

$\log_{10} M$ = 9.63778 43113 00536 78912 29674 98645 –10

Numerical Constants

$\sqrt{2}$ = 1.41421 35623 73095 04880 16887 24209 69807 85696 71875 37695

$3\sqrt{2}$ = 1.25992 10498 94873 16476 72106 07278 22835 05702 51464 70151

$\log_e 2$ = 0.69314 71805 59945 30941 72321 21458 17656 80755 00134 36026

$\log_{10} 2$ = 0.30102 99956 63981 19521 37388 94724 49302 67881 89881 46211

$\sqrt{3}$ = 1.73205 08075 68877 29352 74463 41505 87236 69428 05253 81039

$\sqrt[3]{3}$ = 1.44224 95703 07408 38232 16383 10780 10958 83918 69253 49935

$\log_e 3$ = 1.09861 22886 68109 69139 52452 36922 52570 46474 90557 82275

$\log_{10} 3$ = 0.47712 12547 19662 43729 50279 03255 11530 92001 28864 19070

Symbols and Terminology for Physical and Chemical Quantities

Name	Symbol	Definition	SI unit
	Classical Mechanics		
mass	m		kg
reduced mass	μ	$\mu = m_1 m_2/(m_1 + m_2)$	kg
density, mass density	ρ	$\rho = M/V$	kg m^{-3}
relative density	d	$d = \rho/\rho^{\theta}$	1
surface density	ρ_A, ρ_S	$\rho_A = m/A$	kg m^{-2}
specific volume	ν	$\nu = V/m = 1/\rho$	m^3 kg^{-1}
momentum	p	$\boldsymbol{p} = mv$	kg m s^{-1}
angular momentum, action	L	$\mathrm{l = r \times p}$	J s
moment of inertia	I, J	$I = \Sigma m_i r_i^2$	kg m^2
force	F	$\boldsymbol{F} = \mathrm{d}\boldsymbol{p}/\mathrm{d}t = ma$	N
torque, moment of a force	$\boldsymbol{T}$, $(\boldsymbol{M})$	$\mathrm{T = r \times F}$	N m
energy	E		J
potential energy	E_p, V, Φ	$E_\mathrm{p} = -\int \boldsymbol{F} \cdot \mathrm{d}s$	J
kinetic energy	E_k, T, K	$e_\mathrm{k} = (1/2)mv^2$	J
work	W, w	$w = \int \boldsymbol{F} \cdot \mathrm{d}s$	J
Hamilton function	H	$H(q, p)$ $= T(q, p) + V(q)$	J
Lagrange function	L	$L(q, \dot{q})$ $\mathrm{T}(q, \dot{q}) - V(q)$	J
pressure	p, P	$p = F/A$	Pa, N m^{-2}
surface tension	γ, σ	$\gamma = \mathrm{d}W/\mathrm{d}A$	N m^{-1}, J m^{-2}
weight	G, (W, P)	$G = mg$	N
gravitational constant	G	$F = Gm_1 m_2/r^2$	N m^2 kg^{-2}
normal stress	σ	$\sigma = F/A$	Pa
shear stress	τ	$\tau = F/A$	Pa
linear strain, relative elongation	ε, e	$\varepsilon = \Delta l/l$	1
modulus of elasticity, Young's modulus	E	$E = \sigma/\varepsilon$	Pa
shear strain	γ	$\gamma = \Delta x/d$	1
shear modulus	G	$\mathrm{G} = \tau/\gamma$	Pa
volume strain, bulk strain	θ	$\theta = \Delta V/V_0$	1
bulk modulus,	K	$K = -V_0(\mathrm{d}p/\mathrm{d}V)$	Pa
compression modulus	η, μ	$\tau_{x,z} = \eta(\mathrm{d}v_x/\mathrm{d}z)$	Pa s
viscosity, dynamic viscosity			
fluidity	ϕ	$\phi = 1/\eta$	m kg^{-1} s
kinematic viscosity	ν	$\nu = \eta/\rho$	m^2 s^{-1}
friction coefficient	μ, (f)	$F_\mathrm{frict} = \mu F_\mathrm{norm}$	1
power	P	$P = \mathrm{d}W/\mathrm{d}t$	W
sound energy flux	P, P_a	$P = \mathrm{d}E/\mathrm{d}t$	W
acoustic factors			
reflection factor	ρ	$\rho = P_\mathrm{t}/P_0$	1
acoustic absorption factor	α_a, (α)	$\alpha_\mathrm{a} = 1 - \rho$	1
transmission factor	τ	$\tau = P_\mathrm{tr}/P_0$	1
dissipation factor	δ	$\delta = \alpha_\mathrm{a} - \tau$	1

Fundamental Physical Constants

Summary of the 1986 Recommended Values of the Fundamental Physical Constants

Quantity	Symbol	Value	Units	Relative Uncertainty (ppm)
Speed of light in vacuum	c	299 792 458	ms^{-1}	(exact)
Permeability of vacuum	μ_o	$4\pi \times 10^{-7}$	$\mathrm{N\ A}^{-2}$	
		= 12.566 370614 …	$10^{-7}\ \mathrm{N\ A}^{-2}$	(exact)
Permittivity of vacuum	ϵ_o	$1/\mu_o c^2$		
		= 8.854 187 817 …	$10^{-12}\ \mathrm{F\ m}^{-1}$	(exact)
Newtonian constant of gravitation	G	6.672 59(85)	$10^{-11}\ \mathrm{m}^3\ \mathrm{kg}^{-1}\ \mathrm{s}^{-2}$	128
Planck constant	h	6.626 0755(40)	10^{-34} J s	0.60
$h/2\pi$	$\hbar$	1.054 572 66(63)	10^{-34} J s	0.60
Elementary charge	e	1.602 177 33(49)	10^{-19} C	0.30
Magnetic flux quantum, $h/2e$	Φ_o	2.067 834 61(61)	10^{-15} Wb	0.30
Electron mass	m_e	9.109 3897(54)	10^{-31} kg	0.59
Proton mass	m_p	1.672 6231(10)	10^{-27} kg	0.59
Proton-electron mass ratio	$m_\mathrm{p} j m_e$	1836.152701(37)		0.020
Fine-structure constant, $\mu_o ce^2/2h$	α	7.297 353 08(33)	10^{-3}	0.045
Inverse fine-structure constant	α^{-1}	137 035 9895(61)		0.045
Rydberg constant, $m_e c\alpha^2/2h$	R_∞	10 973 731.534(13)	m^{-1}	0.0012
Avogadro constant	$N_{A'}L$	6.022 1367(36)	$10^{23}\ \mathrm{mol}^{-1}$	0.59
Faraday constant, $N_A e$	F	96 485.309(29)	$\mathrm{C\ mol}^{-1}$	0.30
Molar gas constant	R	8.314 510(70)	$\mathrm{J\ mol}^{-1}\ \mathrm{K}^{-1}$	8.4
Boltzmann constant, R/N_A	k	1.380 658(12)	$10^{-23}\ \mathrm{J\ K}^{-1}$	8.5
Stafan-Boltzmann constant, $(\pi^2/60)k^4/\hbar^3c^2$	σ	5.670 51(19)	$10^{-8}\ \mathrm{W\ m}^{-2}\ \mathrm{K}^{-4}$	34
Non-SI units used with SI				
Electronvolt, $(e/\mathrm{C})\mathrm{J} = \{e\}\mathrm{J}$	eV	1.602 17733(40)	10^{-19} J	0.30
(Unified) atomic mass unit, 1 u = $m_\mathrm{u} = 1/12m(^{12}\mathrm{C})$	u	1.660 5402(10)	10^{-27} kg	0.59

Note: An abbreviated list of the fundamental constants of physics and chemistry based on a least-squares adjustment with 17 degrees of freedom. The digits in parentheses are the one-standard-deviation uncertainty in the last digits of the given value. Since the uncertainties of many entries are correlated, the full covariance matrix must be used in evaluating the uncertainties of quantities computed from them.

PERIODIC TABLE OF THE ELEMENTS

Key to Chart

Atomic Number → 50
Symbol → Sn
1995 Atomic Weight → 118.710
Oxidation States → +2 +4
Electron Configuration → -18-18-4

	1	2	3	4	5	6	7	8	9	10	11	12	13	14	15	16	17	18	
New Notation	1	2	3	4	5	6	7	8	9	10	11	12	13	14	15	16	17	18	
Previous IUPAC Form	Group		IIIA	IVA	VA	VIA	VIIA		VIIIA		IB	IIB	IIIB	IVB	VB	VIB	VIIB		
CAS Version	IA	IIA	IIIB	IVB	VB	VIB	VIIB		VIII		IB	IIB	IIIA	IVA	VA	VIA	VIIA	VIIIA	Shell
	1 H +1 -1 1.00794 1																	2 He 0 4.002602 2	K
	3 Li +1 6.941 2-1	4 Be +2 9.012182 2-2											5 B +3 10.811 2-3	6 C +2 +4 -4 12.0107 2-4	7 N +1 +2 +3 +4 +5 -1 -2 -3 14.00674 2-5	8 O -2 15.9994 2-6	9 F -1 18.9984032 2-7	10 Ne 0 20.1797 2-8	K-L
	11 Na +1 22.989770 2-8-1	12 Mg +2 24.3050 2-8-2											13 Al +3 26.981538 2-8-3	14 Si +2 +4 -4 28.0855 2-8-4	15 P +3 +5 -3 30.973761 2-8-5	16 S +4 +6 -2 32.066 2-8-6	17 Cl +1 +5 +7 -1 35.4527 2-8-7	18 Ar 0 39.948 2-8-8	K-L-M
	19 K +1 39.0983 -8-8-1	20 Ca +2 40.078 -8-8-2	21 Sc +3 44.955910 -8-9-2	22 Ti +2 +3 +4 47.867 -8-10-2	23 V +2 +3 +4 +5 50.9415 -8-11-2	24 Cr +2 +3 +6 51.9961 -8-13-1	25 Mn +2 +3 +4 +7 54.938049 -8-13-2	26 Fe +2 +3 55.845 -8-13-2	27 Co +2 +3 58.933200 -8-15-2	28 Ni +2 +3 58.6934 -8-16-2	29 Cu +1 +2 63.546 -8-18-1	30 Zn +2 65.39 -8-18-2	31 Ga +3 69.723 -8-18-3	32 Ge +2 +4 72.61 -8-18-4	33 As +3 +5 -3 74.92160 -8-18-5	34 Se +4 +6 -2 78.96 -8-18-6	35 Br +1 +5 -1 79.904 -8-18-7	36 Kr 0 83.80 -8-18-8	-L-M-N
	37 Rb +1 85.4678 -18-8-1	38 Sr +2 87.62 -18-8-2	39 Y +3 88.90585 -18-9-2	40 Zr +4 91.224 -18-10-2	41 Nb +3 +5 92.90638 -18-12-1	42 Mo +6 95.94 -18-13-1	43 Tc +4 +6 +7 (98) -18-13-2	44 Ru +3 101.07 -18-15-1	45 Rh +3 102.90550 -18-16-1	46 Pd +2 +3 106.42 -18-18-0	47 Ag +1 107.8682 -18-18-1	48 Cd +2 112.411 -18-18-2	49 In +3 114.818 -18-18-3	50 Sn +2 +4 118.710 -18-18 -4	51 Sb +3 +5 -3 121.760 -18-18-5	52 Te +4 +6 -2 127.60 -18-18-6	53 I +1 +5 +7 -1 126.90447 -18-18-7	54 Xe 0 131.29 -18-18-8	-M-N-O
	55 Cs +1 132.90545 -18-8-1	56 Ba +2 137.327 -18-8-2	57* La +3 138.9055 -18-9-2	72 Hf +4 178.49 -32-10-2	73 Ta +5 180.9479 -32-11-2	74 W +6 183.84 -32-12-2	75 Re +4 +6 +7 186.207 -32-13-2	76 Os +3 +4 190.23 -32-14-2	77 Ir +3 +4 192.217 -32-15-2	78 Pt +2 +4 195.078 -32-17-1	79 Au +1 +3 196.96655 -32-18-1	80 Hg +1 +2 200.59 -32-18-2	81 Tl +1 +3 204.3833 -32-18-3	82 Pb +2 +4 207.2 -32-18-4	83 Bi +3 +5 208.98038 -32-18-5	84 Po +2 +4 (209) -32-18-6	85 At (210) -32-18-7	86 Rn 0 (222) -32-18-8	-N-O-P
	87 Fr +1 (223) -18-8-1	88 Ra +2 (226) -18-8-2	89** Ac +3 (227) -18-9-2	104 Rf +4 (261) -32-10-2	105 Db (262) -32-11-2	106 Sg (266) -32-12-2	107 Bh (264) -32-13-2	108 Hs (269) -32-14-2	109 Mt (268) -32-15-2	110 Uun (271) -32-16-2	111 Uuu (272)	112 Uub							-O-P-Q

* Lanthanides	58 Ce +3 +4 140.116 -19-9-2	59 Pr +3 140.90765 -21-8-2	60 Nd +3 144.24 -22-8-2	61 Pm +3 (145) -23-8-2	62 Sm +2 +3 150.36 -24-8-2	63 Eu +2 +3 151.964 -25-8-2	64 Gd +3 157 .25 -25-9-2	65 Tb +3 158.92534 -27-8-2	66 Dy +3 162.50 -28-8-2	67 Ho +3 164.93032 -29-8-2	68 Er +3 167.26 -30-8-2	69 Tm +3 168.93421 -31-8-2	70 Yb +2 +3 173.04 -32-8-2	71 Lu +3 174.967 -32-9-2	-N-O-P
** Actinides	90 Th +4 232.0381 -18-10-2	91 Pa +5 +4 231.03588 -20-9-2	92 U +3 +4 +5 +6 238.0289 -21-9-2	93 Np +3 +4 +5 +6 (237) -22-9-2	94 Pu +3 +4 +5 +6 (244) -24-8-2	95 Am +3 +4 +5 +6 (243) -25-8-2	96 Cm +3 (247) -25-9-2	97 Bk +3 +4 (247) -27-8-2	98 Cf +3 (251) -28-8-2	99 Es +3 (252) -29-8-2	100 Fm +3 (257) -30-8-2	101 Md +2 +3 (258) -31-8-2	102 No +2 +3 (259) -32-8-2	103 Lr +3 (262) -32-9-2	-O-P-Q

The new IUPAC format numbers the groups from 1 to 18. The previous IUPAC numbering system and the system used by Chemical Abstracts Service (CAS) are als o shown. For radioactive elements that do not occur in nature, the mass number of the most stable isotope is given in parentheses.

References

1. G. J. Leigh, Editor, *Nomenclature of Inorganic Chemistry*, Blackwell Scientific Publications, Oxford, 1990.
2. *Chemical and Engineering News*, 63(5), 27, 1985.
3. Atomic Weights of the Elements, 1995, *Pure & Appl. Chem.*, 68, 2339, 1996.

Electrical Resistivity

Electrical Resistivity of Pure Metals

The first part of this table gives the electrical resistivity, in units of 10^{-8} Ω m, for 28 common metallic elements as a function of temperature. The data refer to polycrystalline samples. The number of significant figures indicates the accuracy of the values. However, at low temperatures (especially below 50 K) the electrical resistivity is extremely sensitive to sample purity. Thus the low-temperature values refer to samples of specified purity and treatment.

The second part of the table gives resistivity values in the neighborhood of room temperature for other metallic elements that have not been studied over an extended temperature range.

Electrical Resistivity in 10^{-8} Ω m

T/K	Aluminum	Barium	Beryllium	Calcium	Cesium	Chromium	Copper
1	0.000100	0.081	0.0332	0.045	0.0026		0.00200
10	0.000193	0.189	0.0332	0.047	0.243		0.00202
20	0.000755	0.94	0.0336	0.060	0.86	0.00280	
40	0.0181	2.91	0.0367	0.175	1.99		0.0239
60	0.0959	4.86	0.067	0.40	3.07		0.0971
80	0.245	6.83	0.075	0.65	4.16		0.215
100	0.442	8.85	0.133	0.91	5.28	1.6	0.348
150	1.006	14.3	0.510	1.56	8.43	4.5	0.699
200	1.587	20.2	1.29	2.19	12.2	7.7	1.046
273	2.417	30.2	3.02	3.11	18.7	11.8	1.543
293	2.650	33.2	3.56	3.36	20.5	12.5	1.678
298	2.709	34.0	3.70	3.42	20.8	12.6	1.712
300	2.733	34.3	3.76	3.45	21.0	12.7	1.725
400	3.87	51.4	6.76	4.7		15.8	2.402
500	4.99	72.4	9.9	6.0		20.1	3.090
600	6.13	98.2	13.2	7.3		24.7	3.792
700	7.35	130	16.5	8.7		29.5	4.514
800	8.70	168	20.0	10.0	34.6	5.262	
900	10.18	216	23.7	11.4		39.9	6.041

T/K	Gold	Hafnium	Iron	Lead	Lithium	Magnesium	Manganese
1	0.0220	1.00	0.0225		0.007	0.0062	7.02
10	0.0226	1.00	0.0238		0.008	0.0069	18.9
20	0.035	1.11	0.0287		0.012	0.0123	54
40	0.141	2.52	0.0758		0.074	0.074	116
60	0.308	4.53	0.271		0.345	0.261	131
80	0.481	6.75	0.693	4.9	1.00	0.557	132
100	0.650	9.12	1.28	6.4	1.73	0.91	132
150	1.061	15.0	3.15	9.9	3.72	1.84	136
200	1.462	21.0	5.20	13.6	5.71	2.75	139
273	2.051	30.4	8.57	19.2	8.53	4.05	143
293	2.214	33.1	9.61	20.8	9.28	4.39	144
298	2.255	33.7	9.87	21.1	9.47	4.48	144
300	2.271	34.0	9.98	21.3	9.55	4.51	144
400	3.107	48.1	16.1	29.6	13.4	6.19	147
500	3.97	63.1	23.7	38.3		7.86	149
600	4.87	78.5	32.9			9.52	151
700	5.82		44.0			11.2	152
800	6.81		57.1			12.8	
900	7.86					14.4	

Electrical Resistivity in 10^{-8} Ω m (continued)

T/K	Molybdenum	Nickel	Palladium	Platinum	Potassium	Rubidium	Silver
1	0.00070	0.0032	0.0200	0.002	0.0008	0.0131	0.00100
10	0.00089	0.0057	0.0242	0.0154	0.0160	0.109	0.00115
20	0.00261	0.0140	0.0563	0.0484	0.117	0.444	0.0042
40	0.0457	0.068	0.334	0.409	0.480	1.21	0.0539
60	0.206	0.242	0.938	1.107	0.90	1.94	0.162
80	0.482	0.545	1.75	1.922	1.34	2.65	0.289
100	0.858	0.96	2.62	2.755	1.79	3.36	0.418
150	1.99	2.21	4.80	4.76	2.99	5.27	0.726
200	3.13	3.67	6.88	6.77	4.26	7.49	1.029
273	4.85	6.16	9.78	9.6	6.49	11.5	1.467
293	5.34	6.93	10.54	10.5	7.20	12.8	1.587
298	5.47	7.12	10.73	10.7	7.39	13.1	1.617
300	5.52	7.20	10.80	10.8	7.47	13.3	1.629
400	8.02	11.8	14.48	14.6			2.241
500	10.6	17.7	17.94	18.3			2.87
600	13.1	25.5	21.2	21.9			3.53
700	15.8	32.1	24.2	25.4			4.21
800	18.4	35.5	27.1	28.7			4.91
900	21.2	38.6	29.4	32.0			5.64

T/K	Sodium	Strontium	Tantalum	Tungsten	Vanadium	Zinc	Zirconium
1	0.0009	0.80	0.10	0.00016		0.0100	0.250
10	0.0015	0.80	0.102	0.000137	0.0145	0.0112	0.253
20	0.016	0.92	0.146	0.00196	0.039	0.0387	0.357
40	0.172	1.70	0.751	0.0544	0.304	0.306	1.44
60	0.447	2.68	1.65	0.266	1.11	0.715	3.75
80	0.80	3.64	2.62	0.606	2.41	1.15	6.64
100	1.16	4.58	3.64	1.02	4.01	1.60	9.79
150	2.03	6.84	6.19	2.09	8.2	2.71	17.8
200	2.89	9.04	8.66	3.18	12.4	3.83	26.3
273	4.33	12.3	12.2	4.82	18.1	5.46	38.8
293	4.77	13.2	13.1	5.28	19.7	5.90	42.1
298	4.88	13.4	13.4	5.39	20.1	6.01	42.9
300	4.93	13.5	13.5	5.44	20.2	6.06	43.3
400		17.8	18.2	7.83	28.0	8.37	60.3
500		22.2	22.9	10.3	34.8	10.82	76.5
600		26.7	27.4	13.0	41.1	13.49	91.5
700		31.2	31.8	15.7	47.2		104.2
800		35.6	35.9	18.6	53.1		114.9
900			40.1	21.5	58.7		123.1

Electrical Resistivity of Pure Metals (continued)

Element	*T*/K	Electrical Resistivity $10^{-8}\ \Omega$ m
Antimony	273	39
Bismuth	273	107
Cadmium	273	6.8
Cerium	290–300	82.8
Cobalt	273	5.6
Dysprosium	290–300	92.6
Erbium	290–300	86.0
Europium	290–300	90.0
Gadolinium	290–300	131
Gallium	273	13.6
Holmium	290–300	81.4
Indium	273	8.0
Iridium	273	4.7
Lanthanum	290–300	61.5
Lutetium	290–300	58.2
Mercury	273	94.1
Neodymium	290–300	64.3
Niobium	273	15.2
Osmium	273	8.1
Polonium	273	40
Praseodymium	290–300	70.0
Promethium	290–300	75
Protactinium	273	17.7
Rhenium	273	17.2
Rhodium	273	4.3
Ruthenium	273	7.1
Samrium	290–300	94.0
Scandium	290–300	56.2
Terbium	290–300	115
Thallium	273	15
Thorium	273	14.7
Thulium	290–300	67.6
Tin	273	11.5
Titanium	273	39
Uranium	273	28
Ytterbium	290–300	25.0
Yttrium	290–300	59.6

Electrical Resistivity of Selected Alloys

Values of the resistivity are given in units of 10^{-8} Ω m. General comments in the preceding table for pure metals also apply here.

Alloy Aluminum-Copper

Wt % Al	273 K	293 K	300 K	350 K	400 K
99[a]	2.51	2.74	2.82	3.38	3.95
95[a]	2.88	3.10	3.18	3.75	4.33
90[b]	3.36	3.59	3.67	4.25	4.86
85[b]	3.87	4.10	4.19	4.79	5.42
80[b]	4.33	4.58	4.67	5.31	5.99
70[b]	5.03	5.31	5.41	6.16	6.94
60[b]	5.56	5.88	5.99	6.77	7.63
50[b]	6.22	6.55	6.67	7.55	8.52
40[c]	7.57	7.96	8.10	9.12	10.2
30[c]	11.2	11.8	12.0	13.5	15.2
25[f]	16.3[aa]	17.2	17.6	19.8	22.2
15[h]	—	12.3	—	—	—
19[g]	10.8[aa]	11.0	11.1	11.7	12.3
5[e]	9.43	9.61	9.68	10.2	10.7
1[b]	4.46	4.60	4.65	5.00	5.37

Alloy—Copper-Nickel

Wt % Cu	273 K	293 K	300 K	350 K	400 K
99[c]	2.71	2.85	2.91	3.27	3.62
95[c]	7.60	7.71	7.82	8.22	8.62
90[c]	13.69	13.89	13.96	14.40	14.81
85[c]	19.63	19.83	19.90	2032	20.70
80[c]	25.46	25.66	25.72	26.12[aa]	26.44[aa]
70[i]	36.67	36.72	36.76	36.85	36.89
60[i]	45.43	45.38	45.35	45.20	45.01
50[i]	50.19	50.05	50.01	49.73	49.50
40[c]	47.42	47.73	47.82	48.28	48.49
30[i]	40.19	41.79	42.34	44.51	45.40
25[c]	33.46	35.11	35.69	39.67[aa]	42.81[aa]
15[c]	22.00	23.35	23.85	27.60	31.38
10[c]	16.65	17.82	18.26	21.51	25.19
5[c]	11.49	12.50	12.90	15.69	18.78
1[c]	7.23	8.08	8.37	10.63[aa]	13.18[aa]

Alloy—Aluminum-Magnesium

Wt % Al	273 K	293 K	300 K	350 K	400 K
99[c]	2.96	3.18	3.26	3.82	4.39
95[c]	5.05	5.28	5.36	5.93	6.51
90[c]	7.52	7.76	7.85	8.43	9.02
85	—	—	—	—	—
80	—	—	—	—	—
70	—	—	—	—	—
60	—	—	—	—	—
50	—	—	—	—	—
40	—	—	—	—	—
30	—	—	—	—	—
25	—	—	—	—	—
15	—	—	—	—	—
10[b]	17.1	17.4	17.6	18.4	19.2
5[b]	13.1	13.4	13.5	14.3	15.2
1[a]	5.92	6.25	6.37	7.20	8.03

Alloy—Copper-Palladium

Wt % Cu	273 K	293 K	300 K	350 K	400 K
99[c]	2.10	2.23	2.27	2.59	2.92
95[c]	4.21	4.35	4.40	4.74	5.08
90[c]	6.89	7.03	7.08	7.41	7.74
85[c]	9.48	9.61	9.66	10.01	10.36
80[c]	11.99	12.12	12.16	12.51[aa]	12.87
70[c]	16.87	17.01	17.06	17.41	17.78
60[c]	21.73	21.87	21.92	22.30	22.69
50[c]	27.62	27.79	27.86	28.25	28.64
40[c]	35.31	35.51	35.57	36.03	36.47
30[c]	46.50	46.66	46.71	47.11	47.47
25[c]	46.25	46.45	46.52	46.99[aa]	47.43[aa]
15[c]	36.52	36.99	37.16	38.28	39.35
10[c]	28.90	29.51	29.73	31.19[aa]	32.56[aa]
5[c]	20.00	20.75	21.02	22.84[aa]	24.54[aa]
1[c]	11.90	12.67	12.93[aa]	14.82[aa]	16.68[aa]

Alloy—Copper-Gold

Wt % Cu	273 K	293 K	300 K	350 K	400 K
99[c]	1.73	1.86[aa]	1.91[aa]	2.24[aa]	2.58[aa]
95[c]	2.41	2.54[aa]	2.59[aa]	2.92[aa]	3.26[aa]
90[c]	3.29	4.42[aa]	3.46[aa]	3.79[aa]	4.12[aa]
85[c]	4.20	4.33	4.38[aa]	4.71[aa]	5.05[aa]
80[c]	5.15	5.28	5.32	5.65	5.99
70[c]	7.12	7.25	7.30	7.64	7.99
60[c]	9.18	9.13	9.36	9.70	10.05
50[c]	11.07	11.20	11.25	11.60	11.94
40[c]	12.70	12.85	12.90[aa]	13.27[aa]	13.65[aa]
30[c]	13.77	13.93	13.99[aa]	14.38[aa]	14.78[aa]
25[c]	13.93	14.09	14.14	14.54	14.94
15[c]	12.75	12.91	12.96[aa]	13.36[aa]	13.77
10[c]	10.70	10.86	10.91	11.31	11.72
5[c]	7.25	7.41[aa]	7.46	7.87	8.28
1[c]	3.40	3.57	3.62	4.03	4.45

Alloy—Copper-Zinc

Wt % Cu	273 K	293 K	300 K	350 K	400 K
99[b]	1.84	1.97	2.02	2.36	2.71
95[b]	2.78	2.92	2.97	3.33	3.69
90[b]	3.66	3.81	3.86	4.25	4.63
85[b]	4.37	4.54	4.60	5.02	5.44
80[b]	5.01	5.19	5.26	5.71	6.17
70[b]	5.87	6.08	6.15	6.67	7.19
60	—	—	—	—	—
50	—	—	—	—	—
40	—	—	—	—	—
30	—	—	—	—	—
25	—	—	—	—	—
15	—	—	—	—	—
10	—	—	—	—	—
5	—	—	—	—	—
1	—	—	—	—	—

Alloy—Gold-Palladium

Wt % Au	273 K	293 K	300 K	350 K	400 K
99[c]	2.69	2.86	2.91	3.32	3.73
95[c]	5.21	5.35	5.41	5.79	6.17
90[i]	8.01	8.17	8.22	8.56	8.93
85[b]	10.50[aa]	10.66	10.72[aa]	11.100[aa]	11.48[aa]
80[b]	12.75	12.93	12.99	13.45	13.93
70[c]	18.23	18.46	18.54	19.10	19.67
60[b]	26.70	26.94	27.01	27.63[aa]	28.23[aa]
50[a]	27.23	27.63	27.76	28.64[aa]	29.42[aa]
40[a]	24.65	25.23	25.42	26.74	27.95
30[b]	20.82	21.49	21.72	23.35	24.92
25[b]	18.86	19.53	19.77	21.51	23.19
15[a]	15.08	15.77	16.01	17.80	19.61
10[a]	13.25	13.95	14.20[aa]	16.00[aa]	17.81[aa]
5[a]	11.49[aa]	12.21	12.46[aa]	14.26[aa]	16.07[aa]
1[a]	10.07	10.85[aa]	11.12[aa]	12.99[aa]	14.80[aa]

Alloy—Gold-Silver

Wt % Au	273 K	293 K	300 K	350 K	400 K
99[b]	2.58	2.75	2.80[aa]	3.22[aa]	3.63[aa]
95[a]	4.58	4.74	4.79	5.19	5.59
90[j]	6.57	6.73	6.78	7.19	7.58
85[j]	8.14	8.30	8.36[aa]	8.75	9.15
80[j]	9.34	9.50	9.55	9.94	10.33
70[j]	10.70	10.86	10.91	11.29	11.68[aa]
60[j]	10.92	11.07	11.12	11.50	11.87
50[j]	10.23	10.37	10.42	10.78	11.14
40[j]	8.92	9.06	9.11	9.46[aa]	9.81
30[a]	7.34	7.47	7.52	7.85	8.19
25[a]	6.46	6.59	6.63	6.96	7.30[aa]
15[a]	4.55	4.67	4.72	5.03	5.34
10[a]	3.54	3.66	3.71	4.00	4.31
5[i]	2.52	2.64[aa]	2.68[aa]	2.96[aa]	3.25[aa]
1[b]	1.69	1.80	1.84[aa]	2.12[aa]	2.42[aa]

Alloy—Iron-Nickel

Wt % Fe	273 K	293 K	300 K	350 K	400 K
99[a]	10.9	12.0	12.4	—	18.7
95[c]	18.7	19.9	20.2	—	26.8
90[c]	24.2	25.5	25.9	—	33.2
85[c]	27.8	29.2	29.7	—	37.3
80[c]	30.1	31.6	32.2	—	40.0
70[b]	32.3	33.9	34.4	—	42.4
60[c]	53.8	57.1	58.2	—	73.9
50[d]	28.4	30.6	31.4	—	43.7
40[d]	19.6	21.6	22.5	—	34.0
30[c]	15.3	17.1	17.7	—	27.4
25[b]	14.3	15.9	16.4	—	25.1
15[c]	12.6	13.8	14.2	—	21.1
10[c]	11.4	12.5	12.9	—	18.9
5[c]	9.66	10.6	10.9	—	16.1[aa]
1[b]	7.17	7.94	8.12	—	12.8

Alloy—Silver-Palladium

Wt % Ag	273 K	293 K	300 K	350 K	400 K
99[b]	1.891	2.007	2.049	2.35	2.66
95[b]	3.58	3.70	3.74	4.04	4.34
90[b]	5.82	5.94	5.98	6.28	6.59
85[k]	7.92[aa]	8.04[aa]	8.08	8.38[aa]	8.68[aa]
80[k]	10.01	10.13	10.17	10.47	10.78
70[k]	14.53	14.65	14.69	14.99	15.30
60[i]	20.9	21.1	21.2	21.6	22.0
50[k]	31.2	31.4	31.5	32.0	32.4
40[m]	42.2	42.2	42.2	42.3	42.3
30[b]	40.4	40.6	40.7	41.3	41.7
25[k]	36.67[aa]	37.06	37.19	38.1[aa]	38.8[aa]
15[i]	27.08[aa]	26.68[aa]	27.89[aa]	29.3[aa]	30.6[aa]
10[i]	21.69	22.39	22.63	24.3	25.9
5[b]	15.98	16.72	16.98	18.8[aa]	20.5[aa]
1[a]	11.06	11.82	12.08[aa]	13.92[aa]	15.70[aa]

[a] Uncertainty in resistivity is ± 2%.

[b] Uncertainty in resistivity is ± 3%.

[c] Uncertainty in resistivity is ± 5%.

[d] Uncertainty in resistivity is ± 7% below 300 K and ± 5% at 300 and 400 K.

[e] Uncertainty in resistivity is ± 7%.

[f] Uncertainty in resistivity is ± 8%.

[g] Uncertainty in resistivity is ± 10%.

[h] Uncertainty in resistivity is ± 12%.

[i] Uncertainty in resistivity is ± 4%.

[j] Uncertainty in resistivity is ± 1%.

[k] Uncertainty in resistivity is ± 3% up to 300 K and ± 4% above 300 K.

[m] Uncertainty in resistivity is ± 2% up to 300 K and ± 4% above 300 K.

[a] Crystal usually a mixture of α-hep and fcc lattice.

[aa] In temperature range where no experimental data are available.

Resistivity of Selected Ceramics (Listed by Ceramic)

Ceramic	Resistivity (Ω-cm)
Borides	
Chromium diboride (CrB_2)	21×10^{-6}
Hafnium diboride (HfB_2)	$10–12 \times 10^{-6}$ at room temp.
Tantalum diboride (TaB_2)	68×10^{-6}
Titanium diboride (TiB_2) (polycrystalline)	
85% dense	$26.5–28.4 \times 10^{-6}$ at room temp.
85% dense	9.0×10^{-6} at room temp.
100% dense, extrapolated values	$8.7–14.1 \times 10^{-6}$ at room temp.
	3.7×10^{-6} at liquid air temp.
Titanium diboride (TiB_2) (monocrystalline)	
Crystal length 5 cm, 39 deg. and 59 deg. orientation with respect to growth axis	$6.6 \pm 0.2 \times 10^{-6}$ at room temp.
Crystal length 1.5 cm, 16.5 deg. and 90 deg. orientation with respect to growth axis	$6.7 \pm 0.2 \times 10^{-6}$ at room temp.
Zirconium diboride (ZrB_2)	9.2×10^{-6} at 20°C
	1.8×10^{-6} at liquid air temp.
Carbides: boron carbide (B_4C)	0.3–0.8

Dielectric Constants

Dielectric Constants of Solids

These data refer to temperatures in the range 17–22°C.

Material	Freq. (Hz)	Dielectric constant	Material	Freq. (Hz)	Dielectric constant
Acetamide	4×10^8	4.0	Diphenylmethane	4×10^8	2.7
Acetanilide	—	2.9	Dolomite ⊥ optic axis	10^8	8.0
Acetic acid (2°C)	4×10^8	4.1	Dolomite ‖	10^8	6.8
Aluminum oleate	4×10^8	2.40	Ferrous oxide (15°C)	10^8	14.2
Ammonium bromide	10^8	7.1	Iodine	10^8	4
Ammonium chloride	10^8	7.0	Lead acetate	10^8	2.6
Antimony trichloride	10^8	5.34	Lead carbonate (15°C)	10^8	18.6
Apatite ⊥ optic axis	3×10^8	9.50	Lead chloride	10^8	4.2
Apatite ‖ optic axis	3×10^8	7.41	Lead monoxide (15°C)	10^8	25.9
Asphalt	$<3 \times 10^4$	2.68	Lead nitrate	6×10^7	37.7
Barium chloride (anhyd.)	6×10^7	11.4	Lead oleate	4×10^8	3.27
Barium chloride ($2H_3O$)	6×10^7	9.4	Lead sulfate	10^4	14.3
Barium nitrate	6×10^7	5.9	Lead sulfide (15°C)	16^8	17.9
Barium sulfate (15°C)	10^8	11.40	Malachite (mean)	10^{12}	7.2
Beryl ⊥ optic axis	10^4	7.02	Mercuric chloride	10^8	3.2
Beryl ‖ optic axis	10^4	6.08	Mercurous chloride	10^8	9.4
Calcite ⊥ optic axis	10^4	8.5	Naphthalene	4×10^8	2.52
Calcite ‖ optic axis	10^4	8.0	Phenanthrene	4×10^8	2.80
Calcium carbonate	10^4	6.14	Phenol (10°C)	4×10^8	4.3
Calcium fluoride	10^4	7.36	Phosphorus, red	10^8	4.1
Calcium sulfate ($2H_2O$)	10^4	5.66	Phosphorus, yellow	10^8	3.6
Cassiterite ⊥ optic axis	10^{12}	23.4	Potassium aluminum sulfate	10^8	3.8
Cassiterite ‖ optic axis	10^{12}	24	Potassium carbonate (15°C)	10^8	5.6
d-Cocaine	5×10^8	3.10	Potassium chlorate	6×10^7	5.1
Cupric oleate	4×10^8	2.80	Potassium chloride	10^4	5.03
Cupric oxide (15°C)	10^8	18.1	Potassium chromate	6×10^7	7.3
Cupric sulfate (anhyd.)	6×10^7	10.3	Potassium iodide	6×10^7	5.6
Cupric sulfate ($5H_2O$)	6×10^7	7.8	Potassium nitrate	6×10^7	5.0
Diamond	10^8	5.5	Potassium sulfate	6×10^7	5.9

Material	Freq. (Hz)	Dielectric constant	Material	Freq. (Hz)	Dielectric constant
Quartz ⊥ optic axis	3×10^7	4.34	Sodium carbonate ($10H_2O$)	6×10^7	5.3
Quartz ∥ optic axis	3×10^7	4.27	Sodium chloride	10^4	6.12
Resorcinol	4×10^8	3.2	Sodium nitrate	—	5.2
Ruby ⊥ optic axis	10^4	13.27	Sodium oleate	4×10^8	2.75
Ruby ∥ optic axis	10^4	11.28	Sodium perchlorate	6×10^7	5.4
Rutile ⊥ optic axis	10^8	86	Sucrose (mean)	3×10^8	3.32
Rutile ∥ optic axis	10^8	170	Sulfur (mean)	—	4.0
Selenium	10^8	6.6	Thallium chloride	10^4	46.9
Silver bromide	10^4	12.2	*p*-Toluidine	4×10^8	3.0
Silver chloride	10^4	11.2	Tourmaline ⊥ optic axis	10^4	7.10
Silver cyanide	10^4	5.6	Tourmaline ∥ optic axis	10^4	6.3
Smithsonite ⊥ optic axis	10^{12}	9.3	Urea	4×10^8	3.5
Smithsonite ∥ optic axis	10^{10}	9.4	Zircon ⊥, ∥	10^8	12
Sodium carbonate (anhyd.)	6×10^7	8.4			

Dielectric Constants of Ceramics

Material	Dielectric constant 10^4 Hz	Dielectric strength Volts/mil	Volume resistivity Ohm-cm (23°C)	Loss Factor[a]
Alumina	4.5–8.4	40–160	10^{11}–10^{14}	0.0002–0.01
Corderite	4.5–5.4	40–250	10^{12}–10^{14}	0.004–0.012
Forsterite	6.2	240	10^{14}	0.0004
Porcelain (dry process)	6.0–8.0	40–240	10^{12}–10^{14}	0.0003–0.02
Porcelain (wet process)	6.0–7.0	90–400	10^{12}–10^{14}	0.006–0.01
Porcelain, zircon	7.1–10.5	250–400	10^{13}–10^{15}	0.0002–0.008
Steatite	5.5–7.5	200–400	10^{13}–10^{15}	0.0002–0.004
Titanates (Ba, Sr, Ca, Mg, and Pb)	15–12.000	50–300	10^8–10^{13}	0.0001–0.02
Titanium dioxide	14–110	100–210	10^{13}–10^{18}	0.0002–0.005

Dielectric Constants of Glasses

Type	Dielectric constant At 100 MHz (20°C)	Volume resistivity (350°C megohm-cm)	Loss factor[a]
Corning 0010	6.32	10	0.015
Corning 0080	6.75	0.13	0.058
Corning 0120	6.65	100	0.012
Pyrex 1710	6.00	2,500	0.025
Pyrex 3320	4.71	—	0.019
Pyrex 7040	4.65	80	0.013
Pyrex 7050	4.77	16	0.017
Pyrex 7052	5.07	25	0.019
Pyrex 7060	4.70	13	0.018
Pyrex 7070	4.00	1,300	0.0048
Vycor 7230	3.83	—	0.0061
Pyrex 7720	4.50	16	0.014
Pyrex 7740	5.00	4	0.040
Pyrex 7750	4.28	50	0.011
Pyrex 7760	4.50	50	0.0081
Vycor 7900	3.9	130	0.0023
Vycor 7910	3.8	1,600	0.00091
Vycor 7911	3.8	4,000	0.00072
Corning 8870	9.5	5,000	0.0085
G. E. Clear (silica glass)	3.81	4,000–30,000	0.00038
Quartz (fused)	3.75 4.1 (1 MHz)	—	0.0002 (1 MHz)

[a] Power factor × dielectric constant equals loss factor.

Properties of Semiconductors

Semiconducting Properties of Selected Materials

	Minimum energy gap (eV)		$\frac{dE_g}{dT}$ × 10^4	$\frac{dE_g}{dP}$ × 10^6	Density of states electron effective mass m_{d_n}	Electron mobility and temperature dependence		Density of states hole effective mass	Hole mobility and temperature dependence	
Substance	R.T.	0 K	eV/°C	eV·cm²/kg	(m_o)	μ_n (cm²/V·s)	–x	m_{d_p} (m_o)	μ_p (cm²/V·s)	–x
Si	1.107	1.153	–2.3	–2.0	1.1	1,900	2.6	0.56	500	2.3
Ge	0.67	0.744	–3.7	±7.3	0.55	3,80	1.66	0.3	1,820	2.33
αSn	0.08	0.094	–0.5		0.02	2,500	1.65	0.3	2,400	2.0
Te	0.33				0.68	1,100		0.19	560	
III–V Compounds										
AlAs	2.2	2.3				1,200			420	
AlSb	1.6	1.7	–3.5	–1.6	0.09	2..	1.5	0.4	500	1.8
GaP	2.24	2.40	–5.4	–1.7	0.35	300	1.5	0.5	150	1.5
GaAs	1.35	1.53	–5.0	+9.4	0.068	9,000	1.0	0.5	500	2.1
GaSb	0.67	0.78	–3.5	+12	0.050	5,000	2.0	0.23	1,400	0.9
InP	1.27	1.41	–4.6	+4.6	0.067	5,000	2.0		200	2.4
InAs	0.36	0.43	–2.8	+8	0.022	33,000	1.2	0.41	460	2.3
InSb	0.165	0.23	–2.8	+15	0.014	78,000	1.6	0.4	750	2.1
II–VI Compounds										
ZnO	3.2		–9.5	+0.6	0.38	180	1.5			
ZnS	3.54		–5.3	+5.7		180			5 (400°C)	
ZnSe	2.58	2.80	–7.2	+6		540			28	
ZnTe	2.26			+6		340			100	
CdO	2.5 ± 0.1		–6		0.1	120				
CdS	2.42		–5	+3.3	0.165	400		0.8		
CdSe	1.74	1.85	–4.6		0.13	650	1.0	0.6		
CdTe	1.44	1.56	–4.1	+8	0.14	1,200		0.35	50	
HgSe	0.30				0.030	20,000	2.0			
HgTe	0.15		–1		0.017	25,000		0.5	350	
Halite Structure Compounds										
PbS	0.37	0.28	+4		0.16	800		0.1	1,000	2.2
PbSe	0.26	0.16	+4		0.3	1,500		0.34	1,500	2.2
PbTe	0.25	0.19	+4	–7	0.21	1,600		0.14	750	2.2
Others										
ZnSb	0.50	0.56			0.15	10				1.5
CdSb	0.45	0.57	–5.4		0.15	300			2,000	1.5
Bi_2S_3	1.3					200			1,100	
Bi_2Se_3	0.27					600			675	
Bi_2Te_3	0.13		–0.95		0.58	1,200	1.68	1.07	510	1.95
Mg_2Si		0.77	–6.4		0.46	400	2.5		70	
Mg_2Ge		0.74	–9			280	2		110	
Mg_2Sn	0.21	0.33	–3.5		0.37	320			260	
Mg_3Sb_2		0.32				20			82	
Zn_3As_2	0.93					10	1.1		10	
Cd_3As_2	0.55				0.046	100,000	0.88			
GaSe	2.05		3.8						20	
GaTe	1.66	1.80	–3.6			14	–5			
InSe	1.8					9000				
TlSe	0.57		–3.9		0.3	30		0.6	20	1.5
$CdSnAs_2$	0.23				0.05	25,000	1.7			
Ga_2Te_3	1.1	1.55	–4.8							
α-In_2Te_3	1.1	1.2			0.7				50	1.1
β-In_2Te_3	1.0								5	
$Hg_5In_2Te_8$	0.5								11,000	
SnO_2									78	

Band Properties of Semiconductors

Part A. Data on Valence Bands of Semiconductors (Room Temperature)

		Band curvature effective mass (expressed as fraction of free electron mass)			
Substance	Heavy holes	Light holes	"Split-off" band holes	Energy separation of "split-off" band (eV)	Measured light hole mobility (cm²/V·s)
Semiconductors with Valence Bands Maximum at the Center of the Brillouin Zone ("F")					
Si	0.52	0.16	0.25	0.044	500
Ge	0.34	0.043	0.08	0.3	1,820
Sn	0.3				2,400
AlAs					
AlSb	0.4			0.7	550
GaP				0.13	100
GaAs	0.8	0.12	0.20	0.34	400
GaSb	0.23	0.06		0.7	1,400
InP				0.21	150
InAs	0.41	0.025	0.083	0.43	460
InSb	0.4	0.015		0.85	750
CdTe	0.35				50
HgTe	0.5				350

Semiconductors with Multiple Valence Band Maxima

		Band curvature effective masses			
Substance	Number of equivalent valleys and directions	Longitudinal m_L	Transverse m_T	Anisotropy $K = m_L/m_T$	Measured (light) hole mobility cm²/V·s
PbSe	4 "L" [111]	0.095	0.047	2.0	1,500
PbTe	4 "L" [111]	0.27	0.02	10	750
Bi_2Te_3	6	0.207	~0.045	4.5	515

Part B. Data on Conduction Bands of Semiconductors (Room Temperature Data)

Single Valley Semiconductors

Substance	Energy gap (eV)	Effective mass (m_o)	Mobility (cm²/V·s)	Comments
GaAs	1.35	0.067	8,500	3 (or 6?) equivalent [100] valleys 0.36 eV above this maximum with a mobility of ~50
InP	1.27	0.067	5,000	3 (or 6?) equivalent [100] valleys 0.4 eV above this minimum
InAs	0.36	0.022	33,000	Equivalent valleys ~1.0 eV above this minimum
InSb	0.165	0.014	78,000	
CdTe	1.44	0.11	1,000	4 (or 8?) equivalent [111] valleys 0.51 eV above this minimum

Multivalley Semiconductors

			Band curvature effective mass			
Substance	Energy Gap	Number of equivalent valleys and direction	Longitudinal m_L	Transverse m_T	Anisotropy $K = m_L/m_T$	Comments
Si	1.107	6 in [100] "Δ"	0.90	0.192	4.7	
Ge	0.67	4 in [111] at "L"	1.588	~0.0815	19.5	
GaSb	0.67	as Ge (?)	~1.0	~0.2	~5	
PbSe	0.26	4 in [111] at "L"	0.085	0.05	1.7	
PbTe	0.25	4 in [111] at "L"	0.21	0.029	5.5	
Bi_2Te_3	0.13	6			~0.05	

Resistance of Wires

The following table gives the approximate resistance of various metallic conductors. The values have been computed from the resistivities at 20°C, except as otherwise stated, and for the dimensions of wire indicated. Owing to differences in purity in the case of elements and of composition in alloys, the values can be considered only as approximations.

	Diameter			Diameter	
B. & S. Gauge	mm	mills 1 mil = .001 in	B. & S. gauge	mm	mills 1 mil = .001 in
10	2.588	101.9	26	0.4049	15.94
12	2.053	80.81	27	0.3606	14.20
14	1.628	64.08	28	0.3211	12.64
16	1.291	50.82	30	0.2546	10.03
18	1.024	40.30	32	0.2019	7.950
20	0.8118	31.96	34	0.1601	6.305
22	0.6438	25.35	36	0.1270	5.000
24	0.5106	20.10	40	0.07987	3.145

B. & S. No.	Ohms per cm	Ohms per ft	B. & S. No.	Ohms per cm	Ohms per ft
Advance (0°C) $Q = 48. \times 10^{-6}$ ohm cm			Brass $Q = 7.00 \times 10^{-6}$ ohm cm		
10	.000912	.0278	10	.000133	.00406
12	.00145	.0442	12	.000212	.00645
14	.00231	.0703	14	.000336	.0103
16	.00367	.112	16	.000535	.0163
18	.00583	.178	18	.000850	.0259
20	.00927	.283	20	.00135	.0412
22	.0147	.449	22	.00215	.0655
24	.0234	.715	24	.00342	.104
26	.0373	1.14	26	.00543	.166
27	.0470	1.43	27	.00686	.209
28	.0593	1.81	28	.00864	.263
30	.0942	2.87	30	.0137	.419
32	.150	4.57	32	.0219	.666
34	.238	7.26	34	.0348	1.06
36	.379	11.5	36	.0552	1.68
40	.958	29.2	40	.140	4.26
Aluminum $Q = 2.828 \times 10^{-6}$ ohm cm			Climax $Q = 87. \times 10^{-6}$ ohm cm		
10	.0000538	.00164	10	.00165	.0504
12	.0000855	.00260	12	.00263	.0801
14	.000136	.00414	14	.00418	.127
16	.000216	.00658	16	.00665	.203
18	.000344	.0105	18	.0106	.322
20	.000546	.0167	20	.0168	.512
22	.000869	.0265	22	.0267	.815
24	.00138	.0421	24	.0425	1.30
26	.00220	.0669	26	.0675	2.06
27	.00277	.0844	27	.0852	2.60
28	.00349	.106	28	.107	3.27
30	.00555	.169	30	.171	5.21
32	.00883	.269	32	.272	8.28
34	.0140	.428	34	.432	13.2
36	.0223	.680	36	.687	20.9
40	.0564	1.72	40	1.74	52.9

B. & S. No.	Ohms per cm	Ohms per ft	B. & S. No.	Ohms per cm	Ohms per ft
Constantan (0°C) $Q = 44.1 \times 10^{-6}$ ohm cm			Excello $Q = 92. \times 10^{-6}$ ohm cm		
10	.000838	.0255	10	.00175	.0533
12	.00133	.0406	12	.00278	.0847
14	.00212	.0646	14	.00442	.135
16	.00337	.103	16	.00703	.214
18	.00536	.163	18	.0112	.341
20	.00852	.260	20	.0178	.542
22	.0135	.413	22	.0283	.861
24	.0215	.657	24	.0449	1.37
26	.0342	1.04	26	.0714	2.18
27	.0432	1.32	27	.0901	2.75
28	.0545	1.66	28	.114	3.46
30	.0866	2.64	30	.181	5.51
32	.138	4.20	32	.287	8.75
34	.219	6.67	34	.457	13.9
36	.348	10.6	36	.726	22.1
40	.880	26.8	40	1.84	56.0
Copper, annealed $Q = 1.724 \times 10^{-6}$ ohm cm			German silver $Q = 33. \times 10^{-6}$ ohm cm		
10	.0000328	.000999	10	.000627	.0191
12	.0000521	.00159	12	.000997	.0304
14	.0000828	.00253	14	.00159	.0483
16	.000132	.00401	16	.00252	.0768
18	.000209	.00638	18	.00401	.122
20	.000333	.0102	20	.00638	.194
22	.000530	.0161	22	.0101	.309
24	.000842	.0257	24	.0161	.491
26	.00134	.0408	26	.0256	.781
27	.00169	.0515	27	.0323	.985
28	.00213	.0649	28	.0408	1.24
30	.00339	.103	30	.0648	1.97
32	.00538	.164	32	.103	3.14
34	.00856	.261	34	.164	4.99
36	.0136	.415	36	.260	.794
40	.0344	1.05	40	.659	20.1
Eureka (0°C) $Q = 47. \times 10^{-6}$ ohm cm			Gold $Q = 2.44 \times 10^{-6}$ ohm cm		
10	.000893	.0272	10	.0000464	.00141
12	.00142	.0433	12	.0000737	.00225
14	.00226	0.688	14	.000117	.00357
16	.00359	.109	16	.000186	.00568
18	.00571	.174	18	.000296	.00904
20	.00908	.277	20	.000471	.0144
22	.0144	.440	22	.000750	.0228
24	.0230	.700	24	.00119	.0363
26	.0365	1.11	26	.00189	.0577
27	.0460	1.40	27	.00239	.0728
28	.0580	1.77	28	.00301	.0918
30	.0923	2.81	30	.00479	.146
32	.147	4.47	32	.00762	.232
34	.233	7.11	34	.0121	.369
36	.371	11.3	36	.0193	.587
40	.938	28.6	40	.0487	1.48

B. & S. No.	Ohms per cm	Ohms per ft	B. & S. No.	Ohms per cm	Ohms per ft
Iron $Q = 10. \times 10^{-6}$ ohm cm			Manganin $Q = 44. \times 10^{-6}$ ohm cm		
10	.000190	.00579	10	.000836	.0255
12	.000302	.00921	12	.00133	.0405
14	.000481	.0146	14	.00211	.0644
16	.000764	.0233	16	.00336	.102
18	.00121	.0370	18	.00535	.163
20	.00193	.0589	20	.00850	.259
22	.00307	.0936	22	.0135	.412
24	.00489	.149	24	.0215	.655
26	.00776	.237	26	.0342	1.04
27	.00979	.299	27	.0431	1.31
28	.0123	.376	28	.0543	1.66
30	.0196	.598	30	.0864	2.63
32	.0312	.952	32	.137	4.19
34	.0497	1.51	34	.218	6.66
36	0.789	2.41	36	.347	10.6
40	.200	6.08	40	.878	26.8
Lead $Q = 22. \times 10^{-6}$ ohm cm			Molybdenum $Q = 5.7 \times 10^{-6}$ ohm cm		
10	.000418	.0127	10	.000108	.00330
12	.000665	.0203	12	.000172	.00525
14	.00106	.0322	14	.000274	.00835
16	.00168	.0512	16	.000435	.0133
18	.00267	.0815	18	.000693	.0211
20	.00425	.130	20	.00110	.0336
22	.00676	.206	22	.00175	.0534
24	.0107	.328	24	.00278	.0849
26	.0171	.521	26	.00443	.135
27	.0215	.657	27	.00558	.170
28	.0272	.828	28	.00704	.215
30	.0432	1.32	30	.0112	.341
32	.0687	2.09	32	.0178	.542
34	.109	3.33	34	.0283	.863
36	.174	5.29	36	.0450	1.37
40	.439	13.4	40	.114	3.47
Magnesium $Q = 4.6 \times 10^{-6}$ ohm cm			Monel Metal $Q = 42. \times 10^{-6}$ ohm cm		
10	.0000874	.00267	10	.000798	.0243
12	.000139	.00424	12	.00127	.0387
14	.000221	.00674	14	.00202	.0615
16	.000351	.0107	16	.00321	.0978
18	.000559	.0170	18	.00510	.156
20	.000889	.0271	20	.00811	.247
22	.00141	.0431	22	.0129	.393
24	.00225	.0685	24	.0205	.625
26	.00357	.109	26	.0326	.994
27	.00451	.137	27	.0411	1.25
28	.00568	.173	28	.0519	1.58
30	.00903	.275	30	.0825	2.51
32	.0144	.438	32	.131	4.00
34	.0228	.696	34	.209	6.36
36	.0363	1.11	36	.331	10.1
40	.0918	2.80	40	.838	25.6

B. & S. No.	Ohms per cm	Ohms per ft	B. & S. No.	Ohms per cm	Ohms per ft
*Nichrome $Q = 150. \times 10^{-6}$ ohm cm			Silver (18°C) $Q = 1.629 \times 10^{-6}$ ohm cm		
10	.0021281	.06488	10	.0000310	.000944
12	.0033751	.1029	12	.0000492	.00150
14	.0054054	.1648	14	.0000783	.00239
16	.0085116	.2595	16	.000124	.00379
18	.0138383	.4219	18	.000198	.00603
20	.0216218	.6592	20	.000315	.00959
22	.0346040	1.055	22	.000500	.0153
24	.0548088	1.671	24	.000796	.0243
26	.0875760	2.670	26	.00126	.0386
28	.1394328	4.251	27	.00160	.0486
30	.2214000	6.750	28	.00201	.0613
32	.346040	10.55	30	.00320	.0975
34	.557600	17.00	32	.00509	.155
36	.885600	27.00	34	.00809	.247
38	1.383832	42.19	36	.0129	.392
40	2.303872	70.24	40	.0325	.991
Nickel $Q = 7.8 \times 10^{-6}$ ohm cm			Steel, piano wire (0°C) $Q = 11.8 \times 10^{-6}$ ohm cm		
10	.000148	.00452	10	.000224	.00684
12	.000236	.00718	12	.000357	.0109
14	.000375	.0114	14	.000567	.0173
16	.000596	.0182	16	.000901	.0275
18	.000948	.0289	18	.00143	.0437
20	.00151	.0459	20	.00228	.0695
22	.00240	.0730	22	.00363	.110
24	.00381	.116	24	.00576	.176
26	.00606	.185	26	.00916	.279
27	.00764	.233	27	.0116	.352
28	.00963	.294	28	.0146	.444
30	.0153	.467	30	.0232	.706
32	.0244	.742	32	.0368	1.12
34	.0387	1.18	34	.0586	1.79
36	.0616	1.88	36	.0931	2.84
40	.156	4.75	40	.236	7.18
Platinum $Q = 10. \times 10^{-6}$ ohm cm			Steel, invar (35% Ni) $Q = 81. \times 10^{-6}$ ohm cm		
10	.000190	.00579	10	.00154	.0469
12	.000302	.00921	12	.00245	.0746
14	.000481	.0146	14	.00389	.119
16	.000764	.0233	16	.00619	.189
18	.00121	.0370	18	.00984	.300
20	.00193	.0589	20	.0156	.477
22	.00307	.0936	22	.0249	.758
24	.00489	.149	24	.0396	1.21
26	.00776	.237	26	.0629	1.92
27	.00979	.299	27	.0793	2.42
28	.0123	.376	28	.100	3.05
30	.0196	.598	30	.159	4.85
32	.0312	.952	32	.253	7.71
34	.0497	1.51	34	.402	12.3
36	.0789	2.41	36	.639	19.5
40	.200	6.08	40	1.62	49.3

B. & S. No.	Ohms per cm	Ohms per ft	B. & S. No.	Ohms per cm	Ohms per ft
Tantalum $Q = 15.5 \times 10^{-6}$ ohm cm			Tungsten $Q = 5.51 \times 10^{-6}$ ohm cm		
10	.000295	.00898	10	.000105	.00319
12	.000468	.0143	12	.000167	.00508
14	.000745	.0227	14	.000265	.00807
16	.00118	.0361	16	.000421	.0128
18	.00188	.0574	18	.000669	.0204
20	.00299	.0913	20	.00106	.0324
22	.00476	.145	22	.00169	.0516
24	.00757	.231	24	.00269	.0820
26	.0120	.367	26	.00428	.130
27	.0152	.463	27	.00540	.164
28	.0191	.583	28	.00680	.207
30	.0304	.928	30	.0108	.330
32	.0484	1.47	32	.0172	.524
34	.0770	2.35	34	.0274	.834
36	.122	3.73	36	.0435	1.33
40	.309	9.43	40	.110	3.35
Tin $Q = 11.5 \times 10^{-6}$ ohm cm			Zinc (0°C) $Q = 5.75 \times 10^{-6}$ ohm cm		
10	.000219	.00666	10	.000109	.00333
12	.000348	.0106	12	.000174	.00530
14	.000553	.0168	14	.000276	.00842
16	.000879	.0268	16	.000439	.0134
18	.00140	.0426	18	.000699	.0213
20	.00222	.0677	20	.00111	.0339
22	.00353	.108	22	.00177	.0538
24	.00562	.171	24	.00281	.0856
26	.00893	.272	26	.00446	.136
27	.0113	.343	27	.00563	.172
28	.0142	.433	28	.00710	.216
30	.0226	.688	30	.0113	.344
32	.0359	1.09	32	.0180	.547
34	.0571	1.74	34	.0286	.870
36	.0908	2.77	36	.0454	1.38
40	.230	7.00	40	.115	3.50

Credits

Material in Section XII was reprinted from the following sources:

D. R. Lide, Ed., *CRC Handbook of Chemistry and Physics,* 76th ed., Boca Raton, Fla.: CRC Press, 1992: International System of Units (SI), conversion constants and multipliers (conversion of temperatures), symbols and terminology for physical and chemical quantities, fundamental physical constants, classification of electromagnetic radiation.

W. H. Beyer, Ed., *CRC Standard Mathematical Tables and Formulae,* 29th ed., Boca Raton, Fla.: CRC Press, 1991: Greek alphabet, conversion constants and multipliers (recommended decimal multiples and submultiples, metric to English, English to metric, general, temperature factors), physical constants, series expansion, integrals, the Fourier transforms, numerical methods, probability, positional notation.

R. J. Tallarida, *Pocket Book of Integrals and Mathematical Formulas,* 2nd ed., Boca Raotn, Fla.: CRC Press, 1991: Elementary algebra and geometry; determinants, matrices, and linear systems of equations; trigonometry; analytic geometry; series; differential calculus; integral calculus; vector analysis; special functions; statistics; tables of probability and statistics; table of derivatives.

J. F. Pankow, *Aquatic Chemistry Concepts,* Chelsea, Mich.: Lewis Publishers, 1991: Periodic table of the elements.

J. Shackelford and W. Alexander, Eds., *CRC Materials Science and Engineering Handbook,* Boca Raton, Fla.: CRC Press, 1992: Electrical resistivity of selected alloy cast irons, resistivity of selected ceramics.

APPENDIX B
Microwave Engineering Appendix

John P. Wendler
M/A — Com Components
Business Unit

Attenuator Design Values

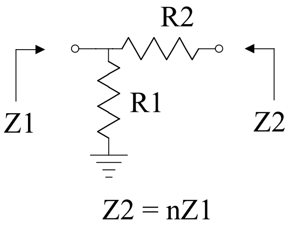

FIGURE 1 Equivalent circuit for a minimum loss pad.

TABLE 1 Minimum Loss Matching Pad Resistance Values as a Function of Transformation Ratio For Z1 = 1 Ohm, 50 Ohms, and 75 Ohms

n	r1	r2	R1	R2	R1	R2	
Z2/Z1	Z1 = 1	Z1 = 1	Z1 = 50	Z1 = 50	Z1 = 75	Z1 = 75	Loss [dB]
1.1	3.3166	0.3317	165.8	16.6	248.7	24.9	2.7
1.2	2.4495	0.4899	122.5	24.5	183.7	36.7	3.8
1.3	2.0817	0.6245	104.1	31.2	156.1	46.8	4.5
1.4	1.8708	0.7483	93.5	37.4	140.3	56.1	5.2
1.5	1.7321	0.8660	86.6	43.3	129.9	65.0	5.7
1.6	1.6330	0.9798	81.6	49.0	122.5	73.5	6.2
1.7	1.5584	1.0909	77.9	54.5	116.9	81.8	6.6
1.8	1.5000	1.2000	75.0	60.0	112.5	90.0	7.0
1.9	1.4530	1.3077	72.6	65.4	109.0	98.1	7.3
2.0	1.4142	1.4142	70.7	70.7	106.1	106.1	7.7
2.1	1.3817	1.5199	69.1	76.0	103.6	114.0	8.0
2.2	1.3540	1.6248	67.7	81.2	101.6	121.9	8.2
2.3	1.3301	1.7292	66.5	86.5	99.8	129.7	8.5
2.4	1.3093	1.8330	65.5	91.7	98.2	137.5	8.7
2.5	1.2910	1.9365	64.5	96.8	96.8	145.2	9.0
2.6	1.2748	2.0396	63.7	102.0	95.6	153.0	9.2
2.7	1.2603	2.1424	63.0	107.1	94.5	160.7	9.4
2.8	1.2472	2.2450	62.4	112.2	93.5	168.4	9.6
2.9	1.2354	2.3473	61.8	117.4	92.7	176.1	9.8
3.0	1.2247	2.4495	61.2	122.5	91.9	183.7	10.0
3.1	1.2150	2.5515	60.7	127.6	91.1	191.4	10.1

TABLE 1 (continued) Minimum Loss Matching Pad Resistance Values as a Function of Transformation Ratio For Z1 = 1 Ohm, 50 Ohms, and 75 Ohms

n	r1	r2	R1	R2	R1	R2	
Z2/Z1	Z1 = 1	Z1 = 1	Z1 = 50	Z1 = 50	Z1 = 75	Z1 = 75	Loss [dB]
3.2	1.2060	2.6533	60.3	132.7	90.5	199.0	10.3
3.3	1.1978	2.7550	59.9	137.7	89.8	206.6	10.5
3.4	1.1902	2.8566	59.5	142.8	89.3	214.2	10.6
3.5	1.1832	2.9580	59.2	147.9	88.7	221.9	10.8
3.6	1.1767	3.0594	58.8	153.0	88.3	229.5	10.9
3.7	1.1706	3.1607	58.5	158.0	87.8	237.1	11.0
3.8	1.1650	3.2619	58.2	163.1	87.4	244.6	11.2
3.9	1.1597	3.3630	58.0	168.2	87.0	252.2	11.3
4.0	1.1547	3.4641	57.7	173.2	86.6	259.8	11.4
4.1	1.1500	3.5651	57.5	178.3	86.3	267.4	11.6
4.2	1.1456	3.6661	57.3	183.3	85.9	275.0	11.7
4.3	1.1415	3.7670	57.1	188.3	85.6	282.5	11.8
4.4	1.1376	3.8678	56.9	193.4	85.3	290.1	11.9
4.5	1.1339	3.9686	56.7	198.4	85.0	297.6	12.0
4.6	1.1304	4.0694	56.5	203.5	84.8	305.2	12.1
4.7	1.1271	4.1701	56.4	208.5	84.5	312.8	12.2
4.8	1.1239	4.2708	56.2	213.5	84.3	320.3	12.3
4.9	1.1209	4.3715	56.0	218.6	84.1	327.9	12.4
5.0	1.1180	4.4721	55.9	223.6	83.9	335.4	12.5
5.1	1.1153	4.5727	55.8	228.6	83.6	343.0	12.6
5.2	1.1127	4.6733	55.6	233.7	83.5	350.5	12.7
5.3	1.1102	4.7739	55.5	238.7	83.3	358.0	12.8
5.4	1.1078	4.8744	55.4	243.7	83.1	365.6	12.9
5.5	1.1055	4.9749	55.3	248.7	82.9	373.1	13.0
5.6	1.1034	5.0754	55.2	253.8	82.8	380.7	13.1
5.7	1.1013	5.1759	55.1	258.8	82.6	388.2	13.2
5.8	1.0992	5.2764	55.0	263.8	82.4	395.7	13.3
5.9	1.0973	5.3768	54.9	268.8	82.3	403.3	13.3
6.0	1.0954	5.4772	54.8	273.9	82.2	410.8	13.4
6.1	1.0937	5.5776	54.7	278.9	82.0	418.3	13.5
6.2	1.0919	5.6780	54.6	283.9	81.9	425.9	13.6
6.3	1.0903	5.7784	54.5	288.9	81.8	433.4	13.6
6.4	1.0887	5.8788	54.4	293.9	81.6	440.9	13.7
6.5	1.0871	5.9791	54.4	299.0	81.5	448.4	13.8
6.6	1.0856	6.0795	54.3	304.0	81.4	456.0	13.9
6.7	1.0842	6.1798	54.2	309.0	81.3	463.5	13.9
6.8	1.0828	6.2801	54.1	314.0	81.2	471.0	14.0
6.9	1.0814	6.3804	54.1	319.0	81.1	478.5	14.1
7.0	1.0801	6.4807	54.0	324.0	81.0	486.1	14.1
7.1	1.0789	6.5810	53.9	329.1	80.9	493.6	14.2
7.2	1.0776	6.6813	53.9	334.1	80.8	501.1	14.3
7.3	1.0764	6.7816	53.8	339.1	80.7	508.6	14.3
7.4	1.0753	6.8819	53.8	344.1	80.6	516.1	14.4
7.5	1.0742	6.9821	53.7	349.1	80.6	523.7	14.5
7.6	1.0731	7.0824	53.7	354.1	80.5	531.2	14.5
7.7	1.0720	7.1826	53.6	359.1	80.4	538.7	14.6
7.8	1.0710	7.2829	53.6	364.1	80.3	546.2	14.6
7.9	1.0700	7.3831	53.5	369.2	80.3	553.7	14.7
8.0	1.0690	7.4833	53.5	374.2	80.2	561.2	14.8
8.1	1.0681	7.5835	53.4	379.2	80.1	568.8	14.8
8.2	1.0672	7.6837	53.4	384.2	80.0	576.3	14.9
8.3	1.0663	7.7840	53.3	389.2	80.0	583.8	14.9
8.4	1.0654	7.8842	53.3	394.2	79.9	591.3	15.0
8.5	1.0646	7.9844	53.2	399.2	79.8	598.8	15.0
8.6	1.0638	8.0846	53.2	404.2	79.8	606.3	15.1

TABLE 1 (continued) Minimum Loss Matching Pad Resistance Values as a Function of Transformation Ratio For Z1 = 1 Ohm, 50 Ohms, and 75 Ohms

n Z2/Z1	r1 Z1 = 1	r2 Z1 = 1	R1 Z1 = 50	R2 Z1 = 50	R1 Z1 = 75	R2 Z1 = 75	Loss [dB]
8.7	1.0630	8.1847	53.1	409.2	79.7	613.9	15.2
8.8	1.0622	8.2849	53.1	414.2	79.7	621.4	15.2
8.9	1.0614	8.3851	53.1	419.3	79.6	628.9	15.3
9.0	1.0607	8.4853	53.0	424.3	79.5	636.4	15.3
9.1	1.0599	8.5855	53.0	429.3	79.5	643.9	15.4
9.2	1.0592	8.6856	53.0	434.3	79.4	651.4	15.4
9.3	1.0585	8.7858	52.9	439.3	79.4	658.9	15.5
9.4	1.0579	8.8859	52.9	444.3	79.3	666.4	15.5
9.5	1.0572	8.9861	52.9	449.3	79.3	674.0	15.6
9.6	1.0565	9.0863	52.8	454.3	79.2	681.5	15.6
9.7	1.0559	9.1864	52.8	459.3	79.2	689.0	15.7
9.8	1.0553	9.2865	52.8	464.3	79.1	696.5	15.7
9.9	1.0547	9.3867	52.7	469.3	79.1	704.0	15.7
10.0	1.0541	9.4868	52.7	474.3	79.1	711.5	15.8

$$R_1 = \frac{Z_1\left(n+\sqrt{n^2-n}\right)}{n-1+\sqrt{n^2-n}} \qquad R_2 = Z_1\sqrt{n^2-n} \qquad \frac{P_O}{P_A} = \frac{1}{n}\left(\frac{1}{1+\sqrt{\frac{1}{n}}}\right)^2$$

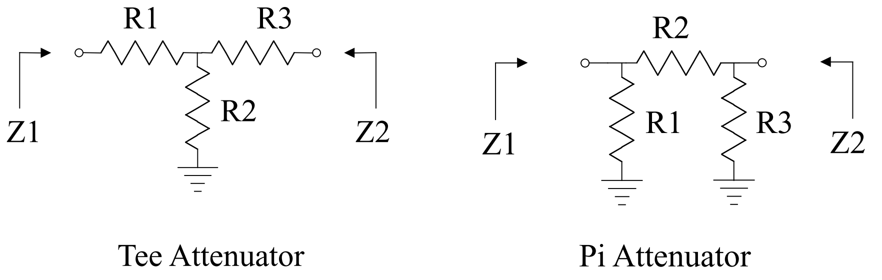

(a) (b)

FIGURE 2 (a) Equivalent circuit for a Tee attenuator; (b) Equivalent circuit for a Pi attenuator.

TABLE 2 Tee- and Pi-Pad Resistor Values for Zo = 1 Ohm and Zo = 50 Ohms

				Tee	Tee	Pi	Pi
Loss	Voltage	r1, r3, g1, g3	r2, g2	R1, R3	R2	R1, R3	R2
[dB]	Atten	Z1 = Z2 = 1	Z1 = Z2 = 1	Z1 = Z2 = 50	Z1 = Z2 = 50	Z1 = Z2 = 50	Z1 = Z2 = 50
0.1	0.98855	0.0058	86.8570	0.3	4342.8	8686.0	0.6
0.2	0.97724	0.0115	43.4256	0.6	2171.3	4343.1	1.2
0.3	0.96605	0.0173	28.9472	0.9	1447.4	2895.6	1.7
0.4	0.95499	0.0230	21.7071	1.2	1085.4	2171.9	2.3
0.5	0.94406	0.0288	17.3622	1.4	868.1	1737.7	2.9
0.6	0.93325	0.0345	14.4650	1.7	723.2	1448.2	3.5
0.7	0.92257	0.0403	12.3950	2.0	619.7	1241.5	4.0
0.8	0.91201	0.0460	10.8420	2.3	542.1	1086.5	4.6
0.9	0.90157	0.0518	9.6337	2.6	481.7	966.0	5.2
1.0	0.89125	0.0575	8.6667	2.9	433.3	869.5	5.8
1.2	0.87096	0.0690	7.2153	3.4	360.8	725.0	6.9
1.4	0.85114	0.0804	6.1774	4.0	308.9	621.8	8.1
1.6	0.83176	0.0918	5.3981	4.6	269.9	544.4	9.3
1.8	0.81283	0.1032	4.7911	5.2	239.6	484.3	10.4
2.0	0.79433	0.1146	4.3048	5.7	215.2	436.2	11.6

TABLE 2 (continued) Tee- and Pi-Pad Resistor Values for Zo = 1 Ohm and Zo = 50 Ohms

				Tee	Tee	Pi	Pi
Loss	Voltage	r1, r3, g1, g3	r2, g2	R1, R3	R2	R1, R3	R2
[dB]	Atten	Z1 = Z2 = 1	Z1 = Z2 = 1	Z1 = Z2 = 50	Z1 = Z2 = 50	Z1 = Z2 = 50	Z1 = Z2 = 50
2.2	0.77625	0.1260	3.9062	6.3	195.3	396.9	12.8
2.4	0.75858	0.1373	3.5735	6.9	178.7	364.2	14.0
2.6	0.74131	0.1486	3.2914	7.4	164.6	336.6	15.2
2.8	0.72444	0.1598	3.0490	8.0	152.5	312.9	16.4
3.0	0.70795	0.1710	2.8385	8.5	141.9	292.4	17.6
3.2	0.69183	0.1822	2.6539	9.1	132.7	274.5	18.8
3.4	0.67608	0.1933	2.4906	9.7	124.5	258.7	20.1
3.6	0.66069	0.2043	2.3450	10.2	117.3	244.7	21.3
3.8	0.64565	0.2153	2.2144	10.8	110.7	232.2	22.6
4.0	0.63096	0.2263	2.0966	11.3	104.8	221.0	23.8
4.2	0.61660	0.2372	1.9896	11.9	99.5	210.8	25.1
4.4	0.60256	0.2480	1.8921	12.4	94.6	201.6	26.4
4.6	0.58884	0.2588	1.8028	12.9	90.1	193.2	27.7
4.8	0.57544	0.2695	1.7206	13.5	86.0	185.5	29.1
5.0	0.56234	0.2801	1.6448	14.0	82.2	178.5	30.4
5.5	0.53088	0.3064	1.4785	15.3	73.9	163.2	33.8
6.0	0.50119	0.3323	1.3386	16.6	66.9	150.5	37.4
6.5	0.47315	0.3576	1.2193	17.9	61.0	139.8	41.0
7.0	0.44668	0.3825	1.1160	19.1	55.8	130.7	44.8
7.5	0.42170	0.4068	1.0258	20.3	51.3	122.9	48.7
8.0	0.39811	0.4305	0.9462	21.5	47.3	116.1	52.8
8.5	0.37584	0.4537	0.8753	22.7	43.8	110.2	57.1
9.0	0.35481	0.4762	0.8118	23.8	40.6	105.0	61.6
9.5	0.33497	0.4982	0.7546	24.9	37.7	100.4	66.3
10.0	0.31623	0.5195	0.7027	26.0	35.1	96.2	71.2
10.5	0.29854	0.5402	0.6555	27.0	32.8	92.6	76.3
11.0	0.28184	0.5603	0.6123	28.0	30.6	89.2	81.7
11.5	0.26607	0.5797	0.5727	29.0	28.6	86.3	87.3
12.0	0.25119	0.5985	0.5362	29.9	26.8	83.5	93.2
12.5	0.23714	0.6166	0.5025	30.8	25.1	81.1	99.5
13.0	0.22387	0.6342	0.4714	31.7	23.6	78.8	106.1
13.5	0.21135	0.6511	0.4425	32.6	22.1	76.8	113.0
14.0	0.19953	0.6673	0.4156	33.4	20.8	74.9	120.3
14.5	0.18836	0.6830	0.3906	34.1	19.5	73.2	128.0
15.0	0.17783	0.6980	0.3673	34.9	18.4	71.6	136.1
15.5	0.16788	0.7125	0.3455	35.6	17.3	70.2	144.7
16.0	0.15849	0.7264	0.3251	36.3	16.3	68.8	153.8
16.5	0.14962	0.7397	0.3061	37.0	15.3	67.6	163.3
17.0	0.14125	0.7525	0.2883	37.6	14.4	66.4	173.5
17.5	0.13335	0.7647	0.2715	38.2	13.6	65.4	184.1
18.0	0.12589	0.7764	0.2558	38.8	12.8	64.4	195.4
18.5	0.11885	0.7875	0.2411	39.4	12.1	63.5	207.4
19.0	0.11220	0.7982	0.2273	39.9	11.4	62.6	220.0
19.5	0.10593	0.8084	0.2143	40.4	10.7	61.8	233.4
20.0	0.10000	0.8182	0.2020	40.9	10.1	61.1	247.5
20.5	0.09441	0.8275	0.1905	41.4	9.5	60.4	262.5
21.0	0.08913	0.8363	0.1797	41.8	9.0	59.8	278.3
21.5	0.08414	0.8448	0.1695	42.2	8.5	59.2	295.0
22.0	0.07943	0.8528	0.1599	42.6	8.0	58.6	312.7
22.5	0.07499	0.8605	0.1508	43.0	7.5	58.1	331.5
23.0	0.07079	0.8678	0.1423	43.4	7.1	57.6	351.4
23.5	0.06683	0.8747	0.1343	43.7	6.7	57.2	372.4
24.0	0.06310	0.8813	0.1267	44.1	6.3	56.7	394.6
24.5	0.05957	0.8876	0.1196	44.4	6.0	56.3	418.2
25.0	0.05623	0.8935	0.1128	44.7	5.6	56.0	443.2

TABLE 2 (continued) Tee- and Pi-Pad Resistor Values for Zo = 1 Ohm and Zo = 50 Ohms

Loss [dB]	Voltage Atten	r1, r3, g1, g3 Z1 = Z2 = 1	r2, g2 Z1 = Z2 = 1	Tee R1, R3 Z1 = Z2 = 50	Tee R2 Z1 = Z2 = 50	Pi R1, R3 Z1 = Z2 = 50	Pi R2 Z1 = Z2 = 50
26.0	0.05012	0.9045	0.1005	45.2	5.0	55.3	497.6
27.0	0.04467	0.9145	0.0895	45.7	4.5	54.7	558.6
28.0	0.03981	0.9234	0.0797	46.2	4.0	54.1	627.0
29.0	0.03548	0.9315	0.0711	46.6	3.6	53.7	703.7
30.0	0.03162	0.9387	0.0633	46.9	3.2	53.3	789.8
31.0	0.02818	0.9452	0.0564	47.3	2.8	52.9	886.3
32.0	0.02512	0.9510	0.0503	47.5	2.5	52.6	994.6
33.0	0.02239	0.9562	0.0448	47.8	2.2	52.3	1116.1
34.0	0.01995	0.9609	0.0399	48.0	2.0	52.0	1252.5
35.0	0.01778	0.9651	0.0356	48.3	1.8	51.8	1405.4
36.0	0.01585	0.9688	0.0317	48.4	1.6	51.6	1577.0
37.0	0.01413	0.9721	0.0283	48.6	1.4	51.4	1769.5
38.0	0.01259	0.9751	0.0252	48.8	1.3	51.3	1985.5
39.0	0.01122	0.9778	0.0224	48.9	1.1	51.1	2227.8
40.0	0.01000	0.9802	0.0200	49.0	1.0	51.0	2499.8
41.0	0.00891	0.9823	0.0178	49.1	0.9	50.9	2804.8
42.0	0.00794	0.9842	0.0159	49.2	0.8	50.8	3147.1
43.0	0.00708	0.9859	0.0142	49.3	0.7	50.7	3531.2
44.0	0.00631	0.9875	0.0126	49.4	0.6	50.6	3962.1
45.0	0.00562	0.9888	0.0112	49.4	0.6	50.6	4445.6

Note: P_i values are duals of Tee values.

$$a = \sqrt{\frac{P_{Z_2}}{P_{Z_1}}} \qquad R_{1T} = \left(\frac{2}{(1-a^2)} - 1\right)Z_1 - \frac{2a}{(1-a^2)}\sqrt{Z_1 Z_2}$$

$$R_{2T} = 2\sqrt{Z_1 Z_2}\,\frac{a}{(1-a^2)}$$

$$R_{3T} = \left(\frac{2}{(1-a^2)} - 1\right)Z_2 - \frac{2a}{(1-a^2)}\sqrt{Z_1 Z_2}$$

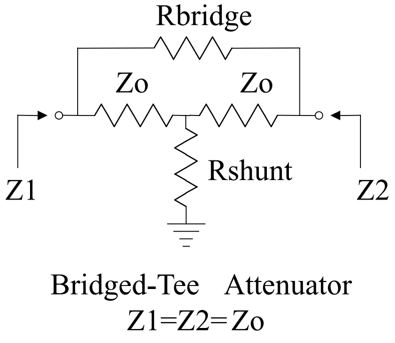

FIGURE 3 Equivalent circuit for a Bridged-T attenuator.

TABLE 3 Bridged-T Attenuator Resistance Values for Zo = 1 Ohm, 50 Ohms, 75 Ohms

Loss [dB]	Voltage Atten	Bridge Arm Z1 = Z2 = 1	Shunt Arm Z1 = Z2 = 1	Bridge Arm Z1 = Z2 = 50	Shunt Arm Z1 = Z2 = 50	Bridge Arm Z1 = Z2 = 75	Shunt Arm Z1 = Z2 = 75
0.1	0.98855	0.0116	86.3599	0.6	4318.0	6477.0	0.9
0.2	0.97724	0.0233	42.9314	1.2	2146.6	3219.9	1.7
0.3	0.96605	0.0351	28.4558	1.8	1422.8	2134.2	2.6
0.4	0.95499	0.0471	21.2186	2.4	1060.9	1591.4	3.5
0.5	0.94406	0.0593	16.8766	3.0	843.8	1265.7	4.4
0.6	0.93325	0.0715	13.9822	3.6	699.1	1048.7	5.4
0.7	0.92257	0.0839	11.9151	4.2	595.8	893.6	6.3

TABLE 3 (continued) Bridged-T Attenuator Resistance Values for Zo = 1 Ohm, 50 Ohms, 75 Ohms

Loss [dB]	Voltage Atten	Bridge Arm Z1 = Z2 = 1	Shunt Arm Z1 = Z2 = 1	Bridge Arm Z1 = Z2 = 50	Shunt Arm Z1 = Z2 = 50	Bridge Arm Z1 = Z2 = 75	Shunt Arm Z1 = Z2 = 75
0.8	0.91201	0.0965	10.3650	4.8	518.3	777.4	7.2
0.9	0.90157	0.1092	9.1596	5.5	458.0	687.0	8.2
1.0	0.89125	0.1220	8.1955	6.1	409.8	614.7	9.2
1.2	0.87096	0.1482	6.7498	7.4	337.5	506.2	11.1
1.4	0.85114	0.1749	5.7176	8.7	285.9	428.8	13.1
1.6	0.83176	0.2023	4.9440	10.1	247.2	370.8	15.2
1.8	0.81283	0.2303	4.3428	11.5	217.1	325.7	17.3
2.0	0.79433	0.2589	3.8621	12.9	193.1	289.7	19.4
2.2	0.77625	0.2882	3.4692	14.4	173.5	260.2	21.6
2.4	0.75858	0.3183	3.1421	15.9	157.1	235.7	23.9
2.6	0.74131	0.3490	2.8656	17.4	143.3	214.9	26.2
2.8	0.72444	0.3804	2.6289	19.0	131.4	197.2	28.5
3.0	0.70795	0.4125	2.4240	20.6	121.2	181.8	30.9
3.2	0.69183	0.4454	2.2450	22.3	112.2	168.4	33.4
3.4	0.67608	0.4791	2.0872	24.0	104.4	156.5	35.9
3.6	0.66069	0.5136	1.9472	25.7	97.4	146.0	38.5
3.8	0.64565	0.5488	1.8221	27.4	91.1	136.7	41.2
4.0	0.63096	0.5849	1.7097	29.2	85.5	128.2	43.9
4.2	0.61660	0.6218	1.6082	31.1	80.4	120.6	46.6
4.4	0.60256	0.6596	1.5161	33.0	75.8	113.7	49.5
4.6	0.58884	0.6982	1.4322	34.9	71.6	107.4	52.4
4.8	0.57544	0.7378	1.3554	36.9	67.8	101.7	55.3
5.0	0.56234	0.7783	1.2849	38.9	64.2	96.4	58.4
5.5	0.53088	0.8836	1.1317	44.2	56.6	84.9	66.3
6.0	0.50119	0.9953	1.0048	49.8	50.2	75.4	74.6
6.5	0.47315	1.1135	0.8981	55.7	44.9	67.4	83.5
7.0	0.44668	1.2387	0.8073	61.9	40.4	60.5	92.9
7.5	0.42170	1.3714	0.7292	68.6	36.5	54.7	102.9
8.0	0.39811	1.5119	0.6614	75.6	33.1	49.6	113.4
8.5	0.37584	1.6607	0.6021	83.0	30.1	45.2	124.6
9.0	0.35481	1.8184	0.5499	90.9	27.5	41.2	136.4
9.5	0.33497	1.9854	0.5037	99.3	25.2	37.8	148.9
10.0	0.31623	2.1623	0.4625	108.1	23.1	34.7	162.2
10.5	0.29854	2.3497	0.4256	117.5	21.3	31.9	176.2
11.0	0.28184	2.5481	0.3924	127.4	19.6	29.4	191.1
11.5	0.26607	2.7584	0.3625	137.9	18.1	27.2	206.9
12.0	0.25119	2.9811	0.3354	149.1	16.8	25.2	223.6
12.5	0.23714	3.2170	0.3109	160.8	15.5	23.3	241.3
13.0	0.22387	3.4668	0.2884	173.3	14.4	21.6	260.0
13.5	0.21135	3.7315	0.2680	186.6	13.4	20.1	279.9
14.0	0.19953	4.0119	0.2493	200.6	12.5	18.7	300.9
14.5	0.18836	4.3088	0.2321	215.4	11.6	17.4	323.2
15.0	0.17783	4.6234	0.2163	231.2	10.8	16.2	346.8
15.5	0.16788	4.9566	0.2018	247.8	10.1	15.1	371.7
16.0	0.15849	5.3096	0.1883	265.5	9.4	14.1	398.2
16.5	0.14962	5.6834	0.1759	284.2	8.8	13.2	426.3
17.0	0.14125	6.0795	0.1645	304.0	8.2	12.3	456.0
17.5	0.13335	6.4989	0.1539	324.9	7.7	11.5	487.4
18.0	0.12589	6.9433	0.1440	347.2	7.2	10.8	520.7
18.5	0.11885	7.4140	0.1349	370.7	6.7	10.1	556.0
19.0	0.11220	7.9125	0.1264	395.6	6.3	9.5	593.4
19.5	0.10593	8.4406	0.1185	422.0	5.9	8.9	633.0
20.0	0.10000	9.0000	0.1111	450.0	5.6	8.3	675.0
20.5	0.09441	9.5925	0.1042	479.6	5.2	7.8	719.4
21.0	0.08913	10.2202	0.0978	511.0	4.9	7.3	766.5
21.5	0.08414	10.8850	0.0919	544.3	4.6	6.9	816.4

TABLE 3 (continued) Bridged-T Attenuator Resistance Values for Zo = 1 Ohm, 50 Ohms, 75 Ohms

Loss [dB]	Voltage Atten	Bridge Arm Z1 = Z2 = 1	Shunt Arm Z1 = Z2 = 1	Bridge Arm Z1 = Z2 = 50	Shunt Arm Z1 = Z2 = 50	Bridge Arm Z1 = Z2 = 75	Shunt Arm Z1 = Z2 = 75
22.0	0.07943	11.5893	0.0863	579.5	4.3	6.5	869.2
22.5	0.07499	12.3352	0.0811	616.8	4.1	6.1	925.1
23.0	0.07079	13.1254	0.0762	656.3	3.8	5.7	984.4
23.5	0.06683	13.9624	0.0716	698.1	3.6	5.4	1047.2
24.0	0.06310	14.8489	0.0673	742.4	3.4	5.1	1113.7
24.5	0.05957	15.7880	0.0633	789.4	3.2	4.8	1184.1
25.0	0.05623	16.7828	0.0596	839.1	3.0	4.5	1258.7
26.0	0.05012	18.9526	0.0528	947.6	2.6	4.0	1421.4
27.0	0.04467	21.3872	0.0468	1069.4	2.3	3.5	1604.0
28.0	0.03981	24.1189	0.0415	1205.9	2.1	3.1	1808.9
29.0	0.03548	27.1838	0.0368	1359.2	1.8	2.8	2038.8
30.0	0.03162	30.6228	0.0327	1531.1	1.6	2.4	2296.7
31.0	0.02818	34.4813	0.0290	1724.1	1.5	2.2	2586.1
32.0	0.02512	38.8107	0.0258	1940.5	1.3	1.9	2910.8
33.0	0.02239	43.6684	0.0229	2183.4	1.1	1.7	3275.1
34.0	0.01995	49.1187	0.0204	2455.9	1.0	1.5	3683.9
35.0	0.01778	55.2341	0.0181	2761.7	0.9	1.4	4142.6
36.0	0.01585	62.0957	0.0161	3104.8	0.8	1.2	4657.2
37.0	0.01413	69.7946	0.0143	3489.7	0.7	1.1	5234.6
38.0	0.01259	78.4328	0.0127	3921.6	0.6	1.0	5882.5
39.0	0.01122	88.1251	0.0113	4406.3	0.6	0.9	6609.4
40.0	0.01000	99.0000	0.0101	4950.0	0.5	0.8	7425.0
41.0	0.00891	111.2018	0.0090	5560.1	0.4	0.7	8340.1
42.0	0.00794	124.8925	0.0080	6244.6	0.4	0.6	9366.9
43.0	0.00708	140.2538	0.0071	7012.7	0.4	0.5	10519.0
44.0	0.00631	157.4893	0.0063	7874.5	0.3	0.5	11811.7
45.0	0.00562	176.8279	0.0057	8841.4	0.3	0.4	13262.1

Return Loss, Reflection Coefficient, VSWR, and Mismatch Loss

TABLE 4 Conversion Between Return Loss, Reflection Coefficient, VSWR, and Mismatch Loss

Return Loss [dB]	Reflection Coefficient (Rho)	VSWR ( ):1	Mismatch Loss [dB]	Return Loss [dB]	Reflection Coefficient (Rho)	VSWR ( ):1	Mismatch Loss [dB]
Infinite	0.0000	1.00	0.00	33.00	0.0224	1.05	0.00
50.00	0.0032	1.01	0.00	32.00	0.0251	1.05	0.00
49.00	0.0035	1.01	0.00	31.00	0.0282	1.06	0.00
48.00	0.0040	1.01	0.00	30.00	0.0316	1.07	0.00
47.00	0.0045	1.01	0.00	29.00	0.0355	1.07	0.01
46.00	0.0050	1.01	0.00	28.00	0.0398	1.08	0.01
45.00	0.0056	1.01	0.00	27.00	0.0447	1.09	0.01
44.00	0.0063	1.01	0.00	26.00	0.0501	1.11	0.01
43.00	0.0071	1.01	0.00	25.00	0.0562	1.12	0.01
42.00	0.0079	1.02	0.00	24.00	0.0631	1.13	0.02
41.00	0.0089	1.02	0.00	23.00	0.0708	1.15	0.02
40.00	0.0100	1.02	0.00	22.00	0.0794	1.17	0.03
39.00	0.0112	1.02	0.00	21.00	0.0891	1.20	0.03
38.00	0.0126	1.03	0.00	20.00	0.1000	1.22	0.04
37.00	0.0141	1.03	0.00	19.50	0.1059	1.24	0.05
36.00	0.0158	1.03	0.00	19.00	0.1122	1.25	0.06
35.00	0.0178	1.04	0.00	18.50	0.1189	1.27	0.06
34.00	0.0200	1.04	0.00	18.00	0.1259	1.29	0.07

TABLE 4 (continued) Conversion Between Return Loss, Reflection Coefficient, VSWR, and Mismatch Loss

Return Loss [dB]	Reflection Coefficient (Rho)	VSWR ( ):1	Mismatch Loss [dB]	Return Loss [dB]	Reflection Coefficient (Rho)	VSWR ( ):1	Mismatch Loss [dB]
17.50	0.1334	1.31	0.08	6.02	0.5000	3.00	1.25
17.00	0.1413	1.33	0.09	6.00	0.5012	3.01	1.26
16.50	0.1496	1.35	0.10	5.80	0.5129	3.11	1.33
16.00	0.1585	1.38	0.11	5.60	0.5248	3.21	1.40
15.50	0.1679	1.40	0.12	5.40	0.5370	3.32	1.48
15.00	0.1778	1.43	0.14	5.20	0.5495	3.44	1.56
14.50	0.1884	1.46	0.16	5.11	0.5556	3.50	1.60
14.00	0.1995	1.50	0.18	5.00	0.5623	3.57	1.65
13.50	0.2113	1.54	0.20	4.80	0.5754	3.71	1.75
13.00	0.2239	1.58	0.22	4.60	0.5888	3.86	1.85
12.50	0.2371	1.62	0.25	4.44	0.6000	4.00	1.94
12.00	0.2512	1.67	0.28	4.40	0.6026	4.03	1.96
11.50	0.2661	1.73	0.32	4.20	0.6166	4.22	2.08
11.00	0.2818	1.78	0.36	4.00	0.6310	4.42	2.20
10.50	0.2985	1.85	0.41	3.93	0.6364	4.50	2.25
10.00	0.3162	1.92	0.46	3.80	0.6457	4.64	2.34
9.80	0.3236	1.96	0.48	3.60	0.6607	4.89	2.49
9.60	0.3311	1.99	0.50	3.52	0.6667	5.00	2.55
9.54	0.3333	2.00	0.51	3.40	0.6761	5.17	2.65
9.40	0.3388	2.03	0.53	3.20	0.6918	5.49	2.83
9.20	0.3467	2.06	0.56	3.00	0.7079	5.85	3.02
9.00	0.3548	2.10	0.58	2.80	0.7244	6.26	3.23
8.80	0.3631	2.14	0.61	2.60	0.7413	6.73	3.46
8.60	0.3715	2.18	0.65	2.40	0.7586	7.28	3.72
8.40	0.3802	2.23	0.68	2.20	0.7762	7.94	4.01
8.20	0.3890	2.27	0.71	2.00	0.7943	8.72	4.33
8.00	0.3981	2.32	0.75	1.80	0.8128	9.69	4.69
7.80	0.4074	2.37	0.79	1.74	0.8182	10.00	4.81
7.60	0.4169	2.43	0.83	1.60	0.8318	10.89	5.11
7.40	0.4266	2.49	0.87	1.40	0.8511	12.44	5.60
7.36	0.4286	2.50	0.88	1.20	0.8710	14.50	6.17
7.20	0.4365	2.55	0.92	1.00	0.8913	17.39	6.87
7.00	0.4467	2.61	0.97	0.80	0.9120	21.73	7.74
6.80	0.4571	2.68	1.02	0.60	0.9333	28.96	8.89
6.60	0.4677	2.76	1.07	0.40	0.9550	43.44	10.56
6.40	0.4786	2.84	1.13	0.20	0.9772	86.86	13.47
6.20	0.4898	2.92	1.19	0.00	1.0000	Infinite	Infinite

Notes:

1. Return Loss = -20*log(|Rho|)
2. Mismatch Loss = -10*log(1-|Rho|^2)
3. VSWR = (1+|Rho|)/(1-|Rho|)

Waveguide Components

TABLE 5 Waveguide Performance and Dimensions

		TE10 Cutoff	Recommended Frequency Range		Theoretical Attenuation		Inside Dimensions			Outside Dimensions			Wall					Hole
EIA WR-	Mil-W-85E RG( )/U	Frequency [GHz]	Min [GHz]	Max [GHz]	Fmin [dB/100']	Fmax [dB/100']	a [inches]	b [Inches]	Tolerance ± [Inches]	[Inches]	[Inches]	Tolerance ± [Inches]	Thickness [Inches]	Material	Contact Flange	Choke Flange	Cover Flange	Pattern Figure
3	139	173.5726	220.00	325.00	503.90	352.59	0.0340	0.0170	0.00020	4.156	(Diameter)	0.001		Silver				
4	137	137.2434	170.00	260.00	371.25	246.94	0.0430	0.0215	0.00020	3.156	(Diameter)	0.001		Silver				
5	135	115.7151	140.00	220.00	303.47	190.96	0.0510	0.0255	0.00025	2.156	(Diameter)	0.001		Silver				
7	136	90.7918	110.00	170.00	210.19	133.39	0.0650	0.0325	0.00025	1.156	(Diameter)	0.001		Silver				
8	138	73.7683	90.00	140.00	151.38	97.26	0.080	0.040	0.0003	0.156	(Diameter)	0.001		Silver				
10		59.0147	75.00	110.00			0.100	0.050	0.0005	0.180	0.130	0.002	0.040					1
12		48.3727	60.00	90.00	122.71	82.37	0.122	0.061	0.0005	0.202	0.141	0.002	0.040	Brass			387	1
12	99	48.3727	60.00	90.00	77.46	51.99	0.122	0.061	0.0005	0.202	0.141	0.002	0.040	Silver				1
15		39.8748	50.00	75.00	89.78	61.41	0.148	0.074	0.0010	0.228	0.154	0.002	0.040	Brass			385	1
15	98	39.8748	50.00	75.00	56.67	38.76	0.148	0.074	0.0010	0.228	0.154	0.002	0.040	Silver				1
19		31.3908	40.00	60.00			0.188	0.094	0.0010	0.268	0.174	0.002	0.040					1
22		26.3458	33.00	50.00	48.33	32.89	0.224	0.112	0.0010	0.304	0.192	0.002	0.040	Brass			383	1
22	97	26.3458	33.00	50.00	30.50	20.76	0.224	0.112	0.0010	0.304	0.192	0.002	0.040	Silver				1
28		21.0767	26.50	40.00	28.00	19.20	0.280	0.140	0.0015	0.360	0.220	0.002	0.040	Aluminum				1,2
28		21.0767	26.50	40.00	34.32	23.53	0.280	0.140	0.0015	0.360	0.220	0.002	0.040	Brass		600	599	1,2
28	96	21.0767	26.50	40.00	21.66	14.85	0.280	0.140	0.0015	0.360	0.220	0.002	0.040	Silver				1,2
34		17.3573	22.00	33.00			0.340	0.170	0.0020	0.420	0.250	0.003	0.040					
42	121	14.0511	18.00	26.50	16.86	12.40	0.420	0.170	0.0020	0.500	0.250	0.003	0.040	Aluminum	425	598	597	1,2
42	53	14.0511	18.00	26.50	20.66	15.19	0.420	0.170	0.0020	0.500	0.250	0.003	0.040	Brass	425	596	595	1,2
42	66	14.0511	18.00	26.50	13.04	9.59	0.420	0.170	0.0020	0.500	0.250	0.003	0.040	Silver	425	596A	595	1,2
51		11.5715	15.00	22.00			0.510	0.255	0.0025	0.590	0.335	0.003	0.040					2
62		9.4879	12.40	18.00	7.88	5.80	0.622	0.311	0.0025	0.702	0.391	0.003	0.040	Aluminum				2
62	91	9.4879	12.40	18.00	9.66	7.11	0.622	0.311	0.0025	0.702	0.391	0.003	0.040	Brass		541	419	2
62	107	9.4879	12.40	18.00	6.10	4.49	0.622	0.311	0.0025	0.702	0.391	0.003	0.040	Silver				2
75		7.8686	10.00	15.00			0.750	0.375	0.003	0.850	0.475	0.003	0.050					2
90	67	6.5572	8.20	12.40	5.29	3.66	0.900	0.400	0.003	1.000	0.500	0.003	0.050	Aluminum		136A	135	2
90	52	6.5572	8.20	12.40	6.48	4.49	0.900	0.400	0.003	1.000	0.500	0.003	0.050	Brass		40A	39	2
112	68	5.2598	7.05	10.00	3.39	2.63	1.122	0.497	0.004	1.250	0.625	0.004	0.064	Aluminum		137A	138	2
112	51	5.2598	7.05	10.00	4.15	3.23	1.122	0.497	0.004	1.250	0.625	0.004	0.064	Brass		52A	51	2
137	106	4.3014	5.85	8.20	2.42	1.91	1.372	0.622	0.004	1.500	0.750	0.004	0.064	Aluminum		440A	441	
137	50	4.3014	5.85	8.20	2.96	2.34	1.372	0.622	0.004	1.500	0.750	0.004	0.064	Brass		343A	344	
159		3.7116	4.90	7.05			1.590	0.795	0.004	1.718	0.923	0.004	0.064					

TABLE 5 (continued) Waveguide Performance and Dimensions

EIA WR-	Mil-W-85E RG( )/U	TE10 Cutoff Frequency [GHz]	Recommended Frequency Range		Theoretical Attenuation		Inside Dimensions		Tolerance ± [Inches]	Outside Dimensions		Tolerance ± [Inches]	Wall Thickness [Inches]	Material	Contact Flange	Choke Flange	Cover Flange	Hole Pattern Figure
			Min [GHz]	Max [GHz]	Fmin [dB/100']	Fmax [dB/100']	a [inches]	b [Inches]		[Inches]	[Inches]							
187	95	3.1525	3.95	5.85	1.70	1.18	1.872	0.872	0.005	2.000	1.000	0.005	0.064	Aluminum		406A	407	
187	49	3.1525	3.95	5.85	2.09	1.45	1.872	0.872	0.005	2.000	1.000	0.005	0.064	Brass		148B	149A	
229		2.5771	3.30	4.90			2.290	1.145	0.005	2.418	1.273	0.005	0.064					
284	75	2.0780	2.60	3.95	0.91	0.62	2.840	1.340	0.005	3.000	1.500	0.005	0.080	Aluminum		585	584	
284	48	2.0780	2.60	3.95	1.11	0.76	2.840	1.340	0.005	3.000	1.500	0.005	0.080	Brass		54B	53	
340	113	1.7357	2.20	3.30	0.65	0.45	3.400	1.700	0.005	3.560	1.860	0.005	0.080	Aluminum			554	
340	112	1.7357	2.20	3.30	0.80	0.56	3.400	1.700	0.005	3.560	1.860	0.005	0.080	Brass			553	
430	105	1.3724	1.70	2.60	0.48	0.32	4.300	2.150	0.005	4.460	2.310	0.005	0.080	Aluminum			437A	
430	104	1.3724	1.70	2.60	0.59	0.39	4.300	2.150	0.005	4.460	2.310	0.005	0.080	Brass			435A	
510		1.1572	1.45	2.20			5.100	2.550	0.005	5.260	2.710	0.005	0.080					
650	103	0.9079	1.12	1.70	0.26	0.17	6.500	3.250	0.005	6.660	3.410	0.005	0.080	Aluminum			418A	
650	69	0.9079	1.12	1.70	0.32	0.21	6.500	3.250	0.005	6.660	3.410	0.005	0.080	Brass			417A	
770	205	0.7664	0.96	1.45	0.20	0.13	7.700	3.850	0.005	7.950	4.100	0.005	0.125	Aluminum				
975	204	0.6053	0.75	1.12	0.14	0.09	9.750	4.875	0.010	10.000	5.125	0.010	0.125	Aluminum				
1150	203	0.5132	0.64	0.96	0.11	0.07	11.500	5.750	0.015	11.750	6.000	0.015	0.125	Aluminum				
1500	202	0.3934	0.49	0.75	0.07	0.05	15.000	7.500	0.015	15.250	7.750	0.015	0.125	Aluminum				
1800	201	0.3279	0.41	0.63	0.05	0.04	18.000	9.000	0.020	18.250	9.250	0.020	0.125	Aluminum				
2100		0.2810	0.35	0.53	0.04	0.03	21.000	10.500	0.020	21.250	10.750	0.020	0.125	Aluminum				
2300		0.2566	0.32	0.49	0.04	0.03	23.000	11.500	0.020	23.250	11.750	0.020	0.125	Aluminum				

Notes:

1. Conductivity of 63.0e6 Mhos/Meter used for Silver.
2. Conductivity of 37.7e6 Mhos/Meter used for Aluminum.
3. Conductivity of 25.1e6 Mhos/Meter used for Brass.
4. Loss is inversely proportional to the square root of conductivity.

Source:

1. Balanis, C.A., *Advanced Engineering Electromagnetics*, John Wiley & Sons, New York, 1990.
2. Catalog, Microwave Development Labs, Natick, MA.
3. Catalog, Aerowave Inc, Medford, MA.
4. Catalog, Formcraft Tool Co, Chicago, IL.
5. Catalog, Penn Engineering Components, No. Hollywood, CA.

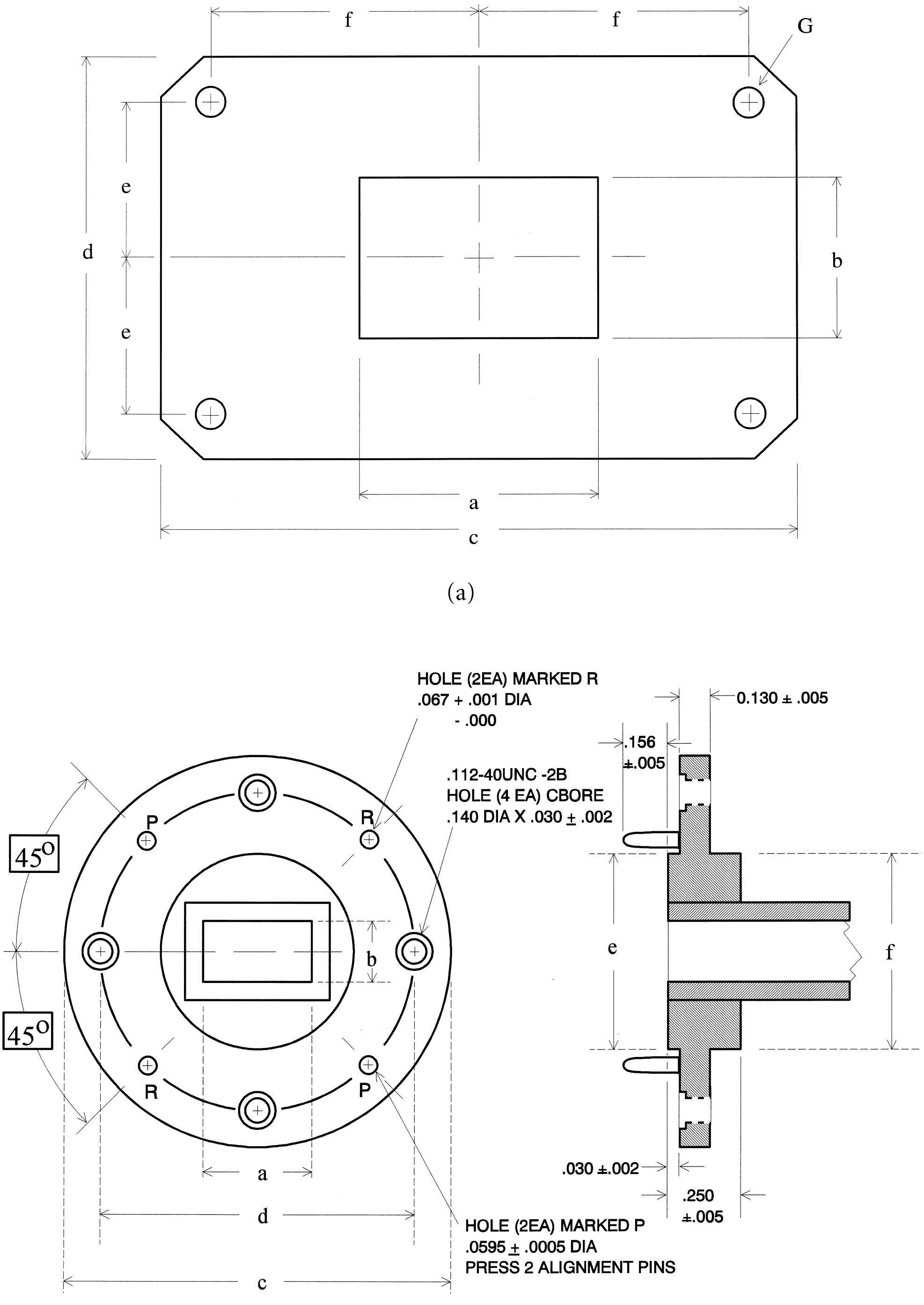

(a)

(b)

FIGURE 4 (a) Standard waveguide flange dimensions (rectangular flange); (b) Standard waveguide flange dimensions (circular flange).

TABLE 6 Waveguide Flange Dimensions

Rectangular Flange Dimensions

WR-()	a [inches] (Ref.)	b [inches] (Ref.)	c [inches] ±0.015	d [inches] ±0.015	e [inches] ±0.005	f [inches] ±0.005	G [inches-dia] ±0.0015
28	0.280	0.140	0.750	1.750	0.265	0.250	0.1175
42	0.420	0.170	0.875	0.875	0.335	0.320	0.1175
51	0.510	0.255	1.313	1.313	0.497	0.478	0.1445
62	0.620	0.311	1.313	1.313	0.478	0.497	0.1445
75	0.750	0.375	1.500	2.500	0.560	0.520	0.1445
90	0.900	0.400	1.625	1.625	0.610	0.640	0.1705
112	1.122	0.497	1.875	1.875	0.676	0.737	0.1705

Circular Flange Dimensions

WR-()	a [inches] (Ref.)	b [inches] (Ref.)	c [inches] +0.000 –0.002	d [inches] BSC.	e [inches] ±0.005	f [inches] ±0.005
10	0.1	0.05	0.75	0.5625	0.375	0.312
12	0.122	0.061	0.75	0.5625	0.375	0.312
15	0.148	0.074	0.75	0.5625	0.375	0.312
19	0.188	0.094	1.125	0.9375	0.5	0.468
22	0.224	0.112	1.125	0.9375	0.5	0.468
28	0.28	0.14	1.125	0.9375	0.5	0.468
42	0.42	0.17	1.125	0.9375	0.625	0.625

Coaxial Cables

TABLE 7 Flexible Coax Specifications

RG-()/U	Mil-C-17/()	Zo	Loss dB/100' @1 MHz	Loss dB/100' @10 MHz	Loss dB/100' @100 MHz	Loss dB/100' @1000 MHz	Center Conductor	Outer Conductor	Jacket	Outside Diameter [Inches]	Dielectric	Velocity Factor [%]	Capacitance pF/foot	Dielectric Core Diameter [inches]	Maximum Voltage [RMS]
8		52	0.16	0.56	1.9	7.4	#13 Stranded Bare Copper .058 Dia	Bare Copper Braid, 97%	Black PVC	0.405	Polyethylene	66	29.5	0.285	3700
8A	[3] 163	52	0.16	0.56	1.9	7.4	#13 Stranded Bare Copper .058 Dia	Bare Copper Braid, 97%	Black PVC, Noncontaminating	0.405	Polyethylene	66	29.5	0.285	3700
9		51	0.18	0.62	2.1	8.2	#13 Stranded Silver Coated Copper .086 Dia	Double Braid, Silver Coated Inner, Bare Copper Outer, 97%	Gray PVC, Noncontaminating	0.42	Polyethylene	66	30	0.28	3700
9B	[4] 164	50					#13 Stranded Silver Coated Copper .089 Dia	Double Braid, Silver Coated Inner, Bare Copper Outer, 97%	PVC	0.36	Polyethylene	66		0.285	3701
11	[6]	75	0.19	0.66	2	7.1	#18 Stranded Tinned Copper .048	Bare Copper Braid, 97%	Black PVC	0.405	Flame Retardant Semi-Foam Polyethylene	66	20.5	0.285	300
11A		75	0.19	0.66	2	8.5	#18 Stranded Tinned Copper .048	Bare Copper Braid, 97%	Black PVC, Noncontaminating	0.405	Polyethylene	66	20.5	0.285	3700
58	[28]	50	0.42	1.5	5.4	22.8	#20 Tinned Copper .035 Dia	Tinned Copper Braid, 95%	Black PVC, Noncontaminating	0.193	Polyethylene	66	30.8	0.116	1400
58A		50	0.42	1.5	5.4	22.8	#20 Solid Bare Copper .035 Dia	Tinned Copper Braid, 95%	Black PVC	0.193	Polyethylene	66	30.8	0.116	1400
58C	155	50	0.42	1.5	5.4	22.8	#20 Tinned Copper .035 Dia	Tinned Copper Braid, 95%	Black PVC, Noncontaminating	0.193	Polyethylene	66	30.8	0.116	1400
59	[29]	75	0.6	1.1	3.4	12	#23 Solid Bare Copper Covered Steel .023 Dia	Bare Copper Braid, 95%	Black PVC, Noncontaminating	0.241	Polyethylene	66	20.5	0.146	1700
59B		75	0.6	1.1	3.4	12	#23 Solid Bare Copper Covered Steel .023 Dia	Bare Copper Braid, 95%	Black PVC, Noncontaminating	0.241	Polyethylene	66	20.5	0.146	1700
62A	[30]	93	0.25	0.85	2.7	8.7	#22 Solid Bare Copper Covered Steel .023 Dia	Bare Copper Braid, 95%	Black PVC, Noncontaminating	0.242	Semi-solid Polyethylene	84	13.5	0.146	750

TABLE 7 (continued) Flexible Coax Specifications

RG-()/U	Mil-C-17/()	Zo	Loss dB/100' @1 MHz	Loss dB/100' @10 MHz	Loss dB/100' @100 MHz	Loss dB/100' @1000 MHz	Center Conductor	Outer Conductor	Jacket	Outside Diameter [Inches]	Dielectric	Velocity Factor [%]	Capacitance pF/foot	Dielectric Core Diameter [inches]	Maximum Voltage [RMS]
62B	[91] 97	93	0.31	0.9	2.9	11	#24 Solid Bare Copper Covered Steel .025 Dia	Bare Copper Braid, 95%	Black PVC, Noncontaminating	0.242	Semi-solid Polyethylene	84	13.5	0.146	750
63	[31]	125	0.19	0.52	1.5	5.8	#22 Solid Bare Copper Covered Steel .025 Dia	Bare Copper Braid, 97%	Black PVC, Noncontaminating	0.405	Semi-solid Polyethylene	84	9.7	0.285	750
71	[90]	93	0.25	0.85	2.7	8.7	#22 Solid Bare Copper Covered Steel .025 Dia	Double Braid, Tinned Copper Outer, Bare Copper Inner, 98%	Black Polyethylene	0.245	Semi-solid Polyethylene	84	13.5	0.146	750
122	[54] 157	50	0.4	1.7	7	29	#22 Stranded Tinned Copper .030 Dia	Tinned Copper Braid, 95%	Black PVC, Noncontaminating	0.16	Polyethylene	66	30.8	0.096	1400
141	[59] 170	50					#18 Solid Silver Coated Copper Covered Steel .037 Dia	Silver Coated Copper Braid, 94%	Fluorinated Ethylene-Propylene	0.17	TFE Teflon	69.5		0.116	1400
141A		50	0.34	1.1	3.9	13.5	#18 Solid Silver Coated Copper Covered Steel .037 Dia	Silver Coated Copper Braid, 94%	Tinted Brown Fiberglass	0.187	TFE Teflon	69.5	29.2	0.116	1400
142	[60] 158	50	0.34	1.1	3.9	13.5	#18 Solid Silver Coated Copper Covered Steel .037 Dia	Double Silver Coated Copper Braid, 94%	Tinted Brown Fluorinated Ethylene-Propylene	0.187	TFE Teflon	69.5	29.2	0.116	1400
174	[119] 173	50	1.9	3.3	8.4	34	#26 Stranded Bare Copper Covered Steel .019 Dia	Tinned Copper Braid, 90%	Black PVC Jacket	0.11	Polyethylene	66	30.8	0.059	1100
178	[93] 169	50					#30 Stranded Silver Coated Copper Covered Steel .012 Dia	Silver Coated Copper Braid, 96%	Fluorinated Ethylene-Propylene	0.071	TFE Teflon	69.5		0.033	750
178B		50	2.6	5.6	14	46	#30 Solid Silver Coated Copper Covered Steel .012 Dia	Silver Coated Copper Braid, 96%	White Fluorinated Ethylene-Propylene	0.071	TFE Teflon	69.5	29.2	0.033	750

179	[94]	75	3	5.3	10	24	#30 Solid Silver Coated Copper Covered Steel .012 Dia	Silver Coated Copper Braid, 95%	Tinted Brown Fluorinated Ethylene-Propylene	0.1	TFE Teflon	69.5	19.5	0.062	900
180	[95]	95	2.4	3.3	5.7	17	#30 Solid Silver Coated Copper Covered Steel .012 Dia	Silver Coated Copper Braid, 95%	Tinted Brown Fluorinated Ethylene-Propylene	0.141	TFE Teflon	69.5	15.4	0.102	1100
187	[68] 94	75					#30 Solid Silver Coated Copper Covered Steel .012 Dia	Silver Coated Copper Braid, 92.3%	Fluorinated Ethylene-Propylene	0.1	TFE Teflon	69.5		0.063	900
212	[73] 162	50	0.26	0.83	2.7	9.8	#15.5 Solid Silver Coated Copper .0556 Dia	Double Silver Coated Copper Braid, 95%	Black PVC Noncontaminating	0.332	Polyethylene	66	30.8	0.185	2200
213	[74] 163	50	0.18	0.62	2.1	8.2	#13 Stranded Bare Copper .089 Dia	Bare Copper Braid 97%	Black PVC Noncontaminating	0.405	Polyethylene	66	30.8	0.285	3700
214	[75] 164	50	0.17	0.55	1.9	8	#13 Stranded Silver Coated Copper .089 Dia	Double Silver Coated Copper Braid, 97%	Black PVC Noncontaminating	0.425	Polyethylene	66	30.8	0.285	3700
216	[77]	75	0.19	0.66	2	7.1	#18 Stranded Tinned Copper .048	Double Bare Copper Braid 95%	Black PVC Noncontaminating	0.425	Polyethylene	66	20.5	0.285	3700
223	[84]	50	0.35	1.2	4.1	14.5	#19 Solid Silver Coated Copper .034 Dia	Double Silver Coated Copper Braid, 95%	Black PVC Noncontaminating	0.212	Polyethylene	66	30.8	0.117	1700
303	[111] 170	50	0.34	1.1	3.9	13.5	#18 Solid Silver Coated Copper Covered Steel .037 Dia	Silver Coated Copper Braid, 95%	Tinted Brown Fluorinated Ethylene-Propylene	0.17	TFE Teflon	69.5	29.2	0.116	1400
316	[113] 172	50	1.2	2.7	8.3	29	#26 Stranded Silver Coated Copper Covered Steel .020 Dia	Silver Coated Copper Braid, 95%	White Fluorinated Ethylene-Propylene	0.098	TFE Teflon	69.5	29.2	0.06	900

Note: Mil-C-17/() part numbers were revised. Initial specification numbers are shown in brackets, current specification numbers are unbracketed.
Source:
Mil-C-17G
Mil-C-17G Supplement 1
Belden Master Catalog, Belden Wire & Cable Co, Richmond, IN.

TABLE 8 Semirigid Coax Specification

RG-()/U	Mil-C-17 Part Number M17/	Zo	Loss [dB/100 ft] Power [W] @500 MHz	Loss [dB/100 ft] Power [W] @1 GHz	Loss [dB/100 ft] Power [W] @3 GHz	Loss [dB/100 ft] Power [W] @5 GHz	Loss [dB/100 ft] Power [W] @10 GHz	Loss [dB/100 ft] Power [W] @18 GHz	Loss [dB/100 ft] Power [W] @20 GHz	Center Conductor Material	Center Conductor Diameter	Outer Conductor	Outside Diameter [Inches]	Dielectric	Dielectric Constant (1 GHz)	Max Capacitance pF/foot	Dielectric Diameter [inches]	Maximum Voltage (60Hz) [RMS]
	154-00001	50 ± 3.0	42 14	60 10	100 6	140 4.5	190 3.1		280 2	Silver Plated Copper Coated Steel	0.008 ±0.0005	Copper	0.034 ±0.001	Solid PTFE	2.03	29.9	0.026 ±0.001	750
	154-00002	50 ± 3.0	42 14	60 10	100 6	140 4.5	190 3.1		280 2	Silver Plated Copper Coated Steel	0.008 ±0.0005	Tin-Plated Copper	0.034 ±0.002	Solid PTFE	2.03	29.9	0.026 ±0.001	750
	151-00001	50 ± 2.5	28 45	40 32	70 18	90 13	130 9		190 65	Silver Plated Copper Coated Steel	0.0113 ±0.0005	Copper	0.047 ±0.001	Solid PTFE	2.03	29.9	0.037 ±0.001	1000
	151-00002	50 ± 2.5	28 45	40 32	70 18	90 13	130 9		190 6.5	Silver Plated Copper Coated Steel	0.0113 ±0.0005	Tin-Plated Copper	0.047 +0.002 –0.001	Solid PTFE	2.03	29.9	0.037 ±0.001	1000
405	133-RG-405	50 ± 1.5	15 180	22 130		50 54	80 35		130 20	Silver Plated Copper Coated Steel	0.0201 ±0.0005	Copper	0.0865 ±0.001	Solid PTFE	2.03	29.9	0.066 ±0.002	5000
	133-00001	50 ± 1.5	15 180	22 130		50 54	80 35		130 20	Silver Plated Copper Coated Steel	0.0201 ±0.0005	Tin-Plated Copper	0.0865 +0.002 –0.001	Solid PTFE	2.03	29.9	0.066 ±0.002	5000
	133-00002	50 ± 1.5	15 180	22 130		50 54	80 35		130 20	Silver Plated Copper	0.0201 ±0.0005	Copper	0.0865 ±0.001	Solid PTFE	2.03	29.9	0.066 ±0.002	5000
	133-00003	50 ± 1.5	15 180	22 130		50 54	80 35		130 20	Silver Plated Copper	0.0201 ±0.0005	Tin-Plated Copper	0.0865 +0.002 –0.001	Solid PTFE	2.03	29.9	0.066 ±0.002	5000
	133-00004	50 ± 1.5	15 180	22 130		50 54	80 35		130 20	Silver Plated Nickel Copper Coated Steel	0.0201 ±0.0005	Copper	0.0865 ±0.001	Solid PTFE	2.03	29.9	0.066 ±0.002	5000
	133-00005	50 ± 1.5	15 180	22 130		50 54	80 35		130 20	Silver Plated Nickel Copper Coated Steel	0.0201 ±0.0005	Tin-Plated Copper	0.0865 +0.002 –0.001	Solid PTFE	2.03	29.9	0.066 ±0.002	5000
	133-0006	50 ± 1.5	15 180	22 130		50 54	80 35		130 20	Silver Plated Copper Coated Steel	0.0201 ±0.0005	Copper	0.0865 ±0.001	Solid PTFE	2.03	29.9	0.066 ±0.002	5000

	133-00007	50 ± 1.5	15 180	22 130		50 54	80 35		130 20	Silver Plated Copper Coated Steel	0.0201 ±0.0005	Tin-Plated Copper	0.086 +0.0021 –0.001	Solid PTFE	2.03	29.9	0.066 ±0.002	5000
	133-00008	50 ± 1.5	15 180	22 130		50 54	80 35		130 20	Silver Plated Copper	0.0201 ±0.0005	Copper	0.0865 ±0.001	Solid PTFE	2.03	29.9	0.066 ±0.002	5000
	133-00009	50 ± 1.5	15 180	22 130		50 54	80 35		130 20	Silver Plated Copper	0.0201 ±0.0005	Tin-Plated Copper	0.0865 +0.002 –0.001	Solid PTFE	2.03	29.9	0.066 ±0.002	5000
	133-00010	50 ± 1.5	15 180	22 130		50 54	80 35		130 20	Silver Plated Nickel Copper Coated Steel	0.0201 ±0.0005	Copper	0.086 ±0.001	Solid PTFE	2.03	29.9	0.066 ±0.002	5000
	133-00011	50 ± 1.5	15 180	22 130		50 54	80 35		130 20	Silver Plated Nickel Copper Coated Steel	0.0201 ±0.0005	Tin-Plated Copper	0.086 +0.002 –0.001	Solid PTFE	2.03	29.9	0.066 ±0.002	5000
402	130-RG-402	50 ± 1.0	8 600	12 450	21 250	29 180	45 120		70 70	Silver Plated Copper Coated Steel	0.0362 ±0.0007	Copper	0.141 ±0.001	Solid PTFE	2.03	29.9	0.1175 ±0.001	5000
	130-00001	50 ± 1.0	8 600	12 450	21 250	29 180	45 120		70 70	Silver Plated Copper Coated Steel	0.0362 ±0.0007	Tin-Plated Copper	0.141 +0.002 –0.001	Solid PTFE	2.03	29.9	0.1175 ±0.001	5000
	130-00002	50 ± 1.0	8 601	12 451	21 251	29 181	45 121		70 71	Silver Plated Nickel Copper Coated Steel	0.0362 ±0.0007	Copper	0.141 ±0.001	Solid PTFE	2.03	29.9	0.1175 ±0.001	5000
	130-00003	50 ± 1.0	8 602	12 452	21 252	29 182	45 122		70 72	Silver Plated Nickel Copper Coated Steel	0.0362 ±0.0007	Tin-Plated Copper	0.141 +0.002 –0.001	Solid PTFE	2.03	29.9	0.1175 ±0.001	5000
	130-00004	50 ± 1.0	8 603	12 453	21 253	29 183	45 123		70 73	Silver Plated Copper Coated Steel	0.0362 ±0.0007	Copper	0.141 ±0.001	Solid PTFE	2.03	29.9	0.1175 ±0.001	5000
	130-00005	50 ± 1.0	8 604	12 454	21 254	29 184	45 124		70 74	Silver Plated Copper Coated Steel	0.0362 ±0.0007	Tin-Plated Copper	0.141 +0.002 –0.001	Solid PTFE	2.03	29.9	0.1175 ±0.001	5000
	130-00006	50 ± 1.0	8 605	12 455	21 255	29 185	45 125		70 75	Silver Plated Nickel Copper Coated Steel	0.0362 ±0.0007	Copper	0.141 ±0.001	Solid PTFE	2.03	29.9	0.1175 ±0.001	5000

TABLE 8 (continued) Semirigid Coax Specification

RG-()/U	Mil-C-17 Part Number M17/	Zo	Loss [dB/100 ft] Power [W] @500 MHz	Loss [dB/100 ft] Power [W] @1 GHz	Loss [dB/100 ft] Power [W] @3 GHz	Loss [dB/100 ft] Power [W] @5 GHz	Loss [dB/100 ft] Power [W] @10 GHz	Loss [dB/100 ft] Power [W] @18 GHz	Loss [dB/100 ft] Power [W] @20 GHz	Center Conductor Material	Center Conductor Diameter	Outer Conductor	Outside Diameter [Inches]	Dielectric	Dielectric Constant (1 GHz)	Max Capacitance pF/foot	Dielectric Diameter [inches]	Maximum Voltage (60Hz) [RMS]
	130-00007	50 ± 1.0	8 606	12 456	21 256	29 186	45 126		70 76	Silver Plated Nickel Copper Coated Steel	0.0362 ±0.0007	Tin-Plated Copper	0.141 +0.002 –0.001	Solid PTFE	2.03	29.9	0.1175 ±0.001	5000
	130-00008	50 ± 1.0	8 607	12 457	21 257	29 187	45 127		70 77	Silver Plated Copper Coated Steel	0.0362 ±0.0007	Aluminum	0.141 ±0.001	Solid PTFE	2.03	29.9	0.1175 ±0.001	5000
	130-00009	50 ± 1.0	8 608	12 458	21 258	29 188	45 128		70 78	Silver Plated Copper Coated Steel	0.0362 ±0.0007	Aluminum	0.141 ±0.001	Solid PTFE	2.03	29.9	0.1175 ±0.001	5000
	130-00010	50 ± 1.0	8 609	12 459	21 259	29 189	45 129		70 79	Silver Plated Nickel Copper Coated Steel	0.0362 ±0.0007	Aluminum	0.141 ±0.001	Solid PTFE	2.03	29.9	0.1175 ±0.001	5000
	130-00011	50 ± 1.0	8 610	12 460	21 260	29 190	45 130		70 80	Silver Plated Nickel Copper Coated Steel	0.0362 ±0.0007	Aluminum	0.141 ±0.001	Solid PTFE	2.03	29.9	0.1175 ±0.001	5000
	130-00012	50 ± 1.0	8 611	12 461	21 261	29 191	45 131		70 81	Silver Plated Copper Coated Steel	0.0362 ±0.0007	Silver Plated Copper	0.141 +0.002 –0.001	Solid PTFE	2.03	29.9	0.1175 ±0.001	5000
	130-00013	50 ± 1.0	8 612	12 462	21 262	29 192	45 132		70 82	Silver Plated Nickel Copper Coated Steel	0.0362 ±0.0007	Silver Plated Copper	0.141 +0.002 –0.001	Solid PTFE	2.03	29.9	0.1175 ±0.001	5000
401	129-RG-401	50 ± 0.5	4.5 1900	7.5 1400	11 750		33 350	48 200	— —	Silver Plated Copper	0.0641 ±0.001	Copper	0.250 ±0.001	Solid PTFE	2.03	29.9	0.209 ±0.002	7500
	129-00001	50 ± 0.5	4.5 1900	7.5 1400	11 750		33 350	48 200	— —	Silver Plated Copper	0.0641 ±0.001	Tin-Plated Copper	0.250 +0.002 –0.001	Solid PTFE	2.03	29.9	0.209 ±0.002	7500

Notes: Attenuation/Power Ratings are maximum values for families.
Sources: Mil-C-17/130E
Semi-Rigid Coaxial Cable Catalog, Micro-Coax Components, Inc, Collegeville, PA.

Metal Compatibility (See MIL-STD-889B)

Single Sideband and Image Reject Mixers

TABLE 10 Maximum Tolerable Phase Error (Degrees) for Single Sideband and Image Reject Mixers as a Function of Suppression and Amplitude Imbalance

Amplitude Imbalance [dB]	Suppression												
	–10 dBc	–13 dBc	–15 dBc	–17 dBc	–20 dBc	–23 dBc	–25 dBc	–27 dBc	–30 dBc	–33 dBc	–35 dBc	–37 dBc	–40 dBc
0.00	35.10	25.24	20.17	16.08	11.42	8.10	6.44	5.12	3.62	2.56	2.04	1.62	1.15
0.05	35.10	25.24	20.16	16.08	11.42	8.09	6.43	5.10	3.61	2.54	2.01	1.58	1.10
0.10	35.09	25.23	20.16	16.07	11.40	8.07	6.40	5.07	3.56	2.48	1.93	1.48	0.94
0.15	35.08	25.22	20.14	16.05	11.38	8.04	6.36	5.02	3.48	2.37	1.78	1.28	0.58
0.20	35.08	25.21	20.13	16.03	11.35	7.99	6.30	4.94	3.37	2.20	1.55	0.94	
0.25	35.06	25.19	20.10	16.00	11.30	7.93	6.22	4.84	3.23	1.97	1.20		
0.30	35.05	25.17	20.07	15.96	11.25	7.86	6.13	4.72	3.04	1.63	0.49		
0.35	35.03	25.14	20.04	15.92	11.19	7.77	6.01	4.57	2.79	1.12			
0.40	35.01	25.11	20.00	15.87	11.12	7.66	5.87	4.38	2.48				
0.45	34.99	25.07	19.96	15.81	11.03	7.54	5.72	4.17	2.08				
0.50	34.96	25.04	19.91	15.75	10.94	7.40	5.53	3.91	1.50				
0.55	34.93	24.99	19.85	15.68	10.84	7.25	5.32	3.61					
0.60	34.90	24.95	19.79	15.60	10.72	7.07	5.08	3.25					
0.65	34.87	24.90	19.73	15.51	10.60	6.88	4.81	2.80					
0.70	34.83	24.84	19.65	15.42	10.46	6.66	4.50	2.21					
0.75	34.79	24.78	19.58	15.32	10.31	6.42	4.13	1.32					
0.80	34.75	24.72	19.49	15.21	10.15	6.16	3.70						
0.85	34.70	24.65	19.41	15.10	9.97	5.86	3.18						
0.90	34.66	24.58	19.31	14.98	9.78	5.53	2.52						
0.95	34.61	24.50	19.21	14.84	9.58	5.16	1.53						
1.00	34.55	24.42	19.10	14.70	9.35	4.73							
1.10	34.44	24.24	18.87	14.40	8.86	3.65							
1.20	34.31	24.05	18.62	14.06	8.28	1.83							
1.30	34.17	23.84	18.34	13.67	7.61								
1.40	34.02	23.61	18.03	13.25	6.80								
1.50	33.86	23.35	17.69	12.78	5.82								
1.60	33.68	23.08	17.32	12.25	4.53								
1.70	33.50	22.79	16.92	11.67	2.52								
1.80	33.30	22.48	16.48	11.01									
1.90	33.09	22.14	16.00	10.28									
2.00	32.86	21.78	15.49	9.44									
2.10	32.63	21.39	14.93	8.47									
2.20	32.37	20.98	14.31	7.31									
2.30	32.11	20.54	13.64	5.87									
2.40	31.83	20.07	12.90	3.81									
2.50	31.54	19.56	12.08										
2.60	31.23	19.03	11.17										
2.70	30.90	18.45	10.13										
2.80	30.56	17.83	8.93										
2.90	30.21	17.17	7.48										
3.00	29.83	16.46	5.59										
3.10	29.44	15.68	2.41										
3.20	29.03	14.84											
3.30	28.60	13.92											
3.40	28.16	12.91											
3.50	27.69	11.77											
3.60	27.19	10.47											
3.70	26.68	8.94											
3.80	26.14	7.02											
3.90	25.57	4.24											
4.00	24.98												
4.10	24.35												
4.20	23.69												
4.30	23.00												
4.40	22.27												
4.50	21.49												
4.60	20.67												
4.70	19.79												
4.80	18.86												
4.90	17.85												
5.00	16.76												

Notes: Example: An image reject mixer requires 25 dB of unwanted image suppression, and a maximum amplitude imbalance of 1 dB is expected between the channels. Looking at the intersection of the 1 dB row and –25 dBc column shows that a maximum interchannel phase imbalance of 9.35 degrees is tolerable.
Suppression [dBc] = 10 log ((1 – 2 a cos(p) + a^2) / (1 + 2 a cos(p) + a^2)) where a is the voltage ratio amplitude imbalance and p is the phase imbalance.

Power, Voltage and Decibels

TABLE 11 Power, Voltage, dB Conversion Table

dB	Power Factor	Voltage Factor	dB	Power Factor	Voltage Factor	dB	Power Factor	Voltage Factor	dB	Power Factor	Voltage Factor
0	1	1	9	7.943282347	2.818382931	34	2511.886432	50.11872336	60	1000000	1000
0.1	1.023292992	1.011579454	9.5	8.912509381	2.985382619	35	3162.27766	56.23413252	61	1258925.412	1122.018454
0.2	1.047128548	1.023292992	10	10	3.16227766	36	3981.071706	63.09573445	62	1584893.192	1258.925412
0.3	1.071519305	1.035142167	11	12.58925412	3.548133892	37	5011.872336	70.79457844	63	1995262.315	1412.537545
0.4	1.096478196	1.047128548	12	15.84893192	3.981071706	38	6309.573445	79.43282347	64	2511886.432	1584.893192
0.5	1.122018454	1.059253725	13	19.95262315	4.466835922	39	7943.282347	89.12509381	65	3162277.66	1778.27941
0.6	1.148153621	1.071519305	14	25.11886432	5.011872336	40	10000	100	66	3981071.706	1995.262315
0.7	1.174897555	1.083926914	15	31.6227766	5.623413252	41	12589.25412	112.2018454	67	5011872.336	2238.721139
0.8	1.202264435	1.096478196	16	39.81071706	6.309573445	42	15848.93192	125.8925412	68	6309573.445	2511.886432
0.9	1.230268771	1.109174815	17	50.11872336	7.079457844	43	19952.62315	141.2537545	69	7943282.347	2818.382931
1	1.258925412	1.122018454	18	63.09573445	7.943282347	44	25118.86432	158.4893192	70	10000000	3162.27766
1.5	1.412537545	1.188502227	19	79.43282347	8.912509381	45	31622.7766	177.827941	71	12589254.12	3548.133892
2	1.584893192	1.258925412	20	100	10	46	39810.71706	199.5262315	72	15848931.92	3981.071706
2.5	1.77827941	1.333521432	21	125.8925412	11.22018454	47	50118.72336	223.8721139	73	19952623.15	4466.835922
3	1.995262315	1.412537545	22	158.4893192	12.58925412	48	63095.73445	251.1886432	74	25118864.32	5011.872336
3.5	2.238721139	1.496235656	23	199.5262315	14.12537545	49	79432.82347	281.8382931	75	31622776.6	5623.413252
4	2.511886432	1.584893192	24	251.1886432	15.84893192	50	100000	316.227766	76	39810717.06	6309.573445
4.5	2.818382931	1.678804018	25	316.227766	17.7827941	51	125892.5412	354.8133892	77	50118723.36	7079.457844
5	3.16227766	1.77827941	26	398.1071706	19.95262315	52	158489.3192	398.1071706	78	63095734.45	7943.282347
5.5	3.548133892	1.883649089	27	501.1872336	22.38721139	53	199526.2315	446.6835922	79	79432823.47	8912.509381
6	3.981071706	1.995262315	28	630.9573445	25.11886432	54	251188.6432	501.1872336	80	100000000	10000
6.5	4.466835922	2.11348904	29	794.3282347	28.18382931	55	316227.766	562.3413252	81	125892541.2	11220.18454
7	5.011872336	2.238721139	30	1000	31.6227766	56	398107.1706	630.9573445	82	158489319.2	12589.25412
7.5	5.623413252	2.371373706	31	1258.925412	35.48133892	57	501187.2336	707.9457844	83	199526231.5	14125.37545
8	6.309573445	2.511886432	32	1584.893192	39.81071706	58	630957.3445	794.3282347	84	251188643.2	15848.93192
8.5	7.079457844	2.66072506	33	1995.262315	44.66835922	59	794328.2347	891.2509381	85	316227766	17782.7941
86	398107170.6	19952.62315	–5.5	0.281838293	0.530884444	–35	0.000316228	0.017782794	–69	1.25893E-07	0.000354813
87	501187233.6	22387.21139	–6	0.251188643	0.501187234	–36	0.000251189	0.015848932	–70	0.0000001	0.000316228
88	630957344.5	25118.86432	–6.5	0.223872114	0.473151259	–37	0.000199526	0.014125375	–71	7.94328E-08	0.000281838
89	794328234.7	28183.82931	–7	0.199526231	0.446683592	–38	0.000158489	0.012589254	–72	6.30957E-08	0.000251189
90	1000000000	31622.7766	–7.5	0.177827941	0.421696503	–39	0.000125893	0.011220185	–73	5.01187E-08	0.000223872
91	1258925412	35481.33892	–8	0.158489319	0.398107171	–40	0.0001	0.01	–74	3.98107E-08	0.000199526
92	1584893192	39810.71706	–8.5	0.141253754	0.375837404	–41	7.94328E-05	0.008912509	–75	3.16228E-08	0.000177828
93	1995262315	44668.35922	–9	0.125892541	0.354813389	–42	6.30957E-05	0.007943282	–76	2.51189E-08	0.000158489
94	2511886432	50118.72336	–9.5	0.112201845	0.334965439	–43	5.01187E-05	0.007079458	–77	1.99526E-08	0.000141254
95	3162277660	56234.13252	–10	0.1	0.316227766	–44	3.98107E-05	0.006309573	–78	1.58489E-08	0.000125893
96	3981071706	63095.73445	–11	0.079432823	0.281838293	–45	3.16228E-05	0.005623413	–79	1.25893E-08	0.000112202
97	5011872336	70794.57844	–12	0.063095734	0.251188643	–46	2.51189E-05	0.005011872	–80	0.00000001	0.0001
98	6309573445	79432.82347	–13	0.050118723	0.223872114	–47	1.99526E-05	0.004466836	–81	7.94328E-09	8.91251E-05
99	7943282347	89125.09381	–14	0.039810717	0.199526231	–48	1.58489E-05	0.003981072	–82	6.30957E-09	7.94328E-05
100	10000000000	100000	–15	0.031622777	0.177827941	–49	1.25893E-05	0.003548134	–83	5.01187E-09	7.07946E-05
0	1	1	–16	0.025118864	0.158489319	–50	0.00001	0.003162278	–84	3.98107E-09	6.30957E-05
–0.1	0.977237221	0.988553095	–17	0.019952623	0.141253754	–51	7.94328E-06	0.002818383	–85	3.16228E-09	5.62341E-05
–0.2	0.954992586	0.977237221	–18	0.015848932	0.125892541	–52	6.30957E-06	0.002511886	–86	2.51189E-09	5.01187E-05
–0.3	0.933254301	0.966050879	–19	0.012589254	0.112201845	–53	5.01187E-06	0.002238721	–87	1.99526E-09	4.46684E-05
–0.4	0.912010839	0.954992586	–20	0.01	0.1	–54	3.98107E-06	0.001995262	–88	1.58489E-09	3.98107E-05
–0.5	0.891250938	0.944060876	–21	0.007943282	0.089125094	–55	3.16228E-06	0.001778279	–89	1.25893E-09	3.54813E-05
–0.6	0.87096359	0.933254301	–22	0.006309573	0.079432823	–56	2.51189E-06	0.001584893	–90	0.000000001	3.16228E-05
–0.7	0.851138038	0.922571427	–23	0.005011872	0.070794578	–57	1.99526E-06	0.001412538	–91	7.94328E-10	2.81838E-05
–0.8	0.831763771	0.912010839	–24	0.003981072	0.063095734	–58	1.58489E-06	0.001258925	–92	6.30957E-10	2.51189E-05
–0.9	0.812830516	0.901571138	–25	0.003162278	0.056234133	–59	1.25893E-06	0.001122018	–93	5.01187E-10	2.23872E-05
–1	0.794328235	0.891250938	–26	0.002511886	0.050118723	–60	0.000001	0.001	–94	3.98107E-10	1.99526E-05
–1.5	0.707945784	0.841395142	–27	0.001995262	0.044668359	–61	7.94328E-07	0.000891251	–95	3.16228E-10	1.77828E-05
–2	0.630957344	0.794328235	–28	0.001584893	0.039810717	–62	6.30957E-07	0.000794328	–96	2.51189E-10	1.58489E-05
–2.5	0.562341325	0.749894209	–29	0.001258925	0.035481339	–63	5.01187E-07	0.000707946	–97	1.99526E-10	1.41254E-05
–3	0.501187234	0.707945784	–30	0.001	0.031622777	–64	3.98107E-07	0.000630957	–98	1.58489E-10	1.25893E-05
–3.5	0.446683592	0.668343918	–31	0.000794328	0.028183829	–65	3.16228E-07	0.000562341	–99	1.25893E-10	1.12202E-05
–4	0.398107171	0.630957344	–32	0.000630957	0.025118864	–66	2.51189E-07	0.000501187	–100	1E-10	0.00001
–4.5	0.354813389	0.595662144	–33	0.000501187	0.022387211	–67	1.99526E-07	0.000446684			
–5	0.316227766	0.562341325	–34	0.000398107	0.019952623	–68	1.58489E-07	0.000398107			

Notes:

1. Multiply by appropriate factor.
2. Use voltage factor to convert S-parameters.

Microstrip Impedances

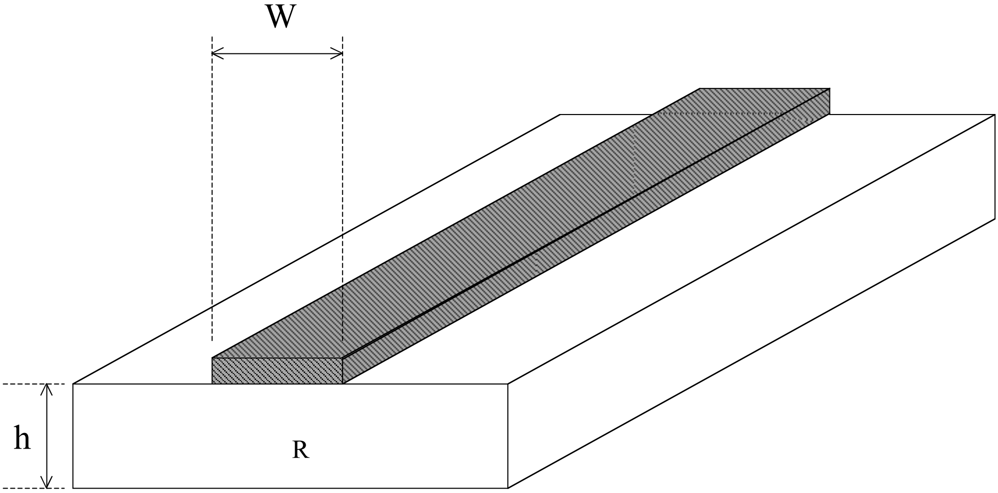

FIGURE 12

TABLE 12a Zero Thickness Microstrip Dimensions, Effective Dielectric Constant, and PUL Capacitance and Inductance for Er = 2.2

Zo [Ohms]	W/h	Keff	pF/cm	nH/mm	Zo [Ohms]	W/h	Keff	pF/cm	nH/mm
1	250.3363	2.1861	49.3192	0.0493	57	2.5199	1.8500	0.7959	2.5860
2	123.5739	2.1728	24.5846	0.0983	58	2.4514	1.8471	0.7816	2.6294
3	81.4007	2.1601	16.3417	0.1471	59	2.3854	1.8443	0.7678	2.6727
4	60.3537	2.1480	12.2218	0.1955	60	2.3218	1.8416	0.7544	2.7160
5	47.7490	2.1364	9.7510	0.2438	61	2.2603	1.8389	0.7415	2.7592
6	39.3615	2.1253	8.1046	0.2918	62	2.2010	1.8362	0.7290	2.8024
7	33.3816	2.1146	6.9294	0.3395	63	2.1437	1.8336	0.7170	2.8456
8	28.9051	2.1044	6.0485	0.3871	64	2.0883	1.8310	0.7053	2.8887
9	25.4299	2.0946	5.3639	0.4345	65	2.0347	1.8285	0.6939	2.9318
10	22.6550	2.0851	4.8166	0.4817	66	1.9829	1.8259	0.6829	2.9749
11	20.3889	2.0760	4.3692	0.5287	67	1.9327	1.8235	0.6723	3.0179
12	18.5040	2.0673	3.9967	0.5755	68	1.8919	1.8214	0.6620	3.0612
13	16.9121	2.0589	3.6817	0.6222	69	1.8447	1.8190	0.6520	3.1042
14	15.5503	2.0508	3.4120	0.6688	70	1.7990	1.8166	0.6423	3.1471
15	14.3723	2.0429	3.1784	0.7152	71	1.7548	1.8143	0.6328	3.1900
16	13.3435	2.0354	2.9743	0.7614	72	1.7119	1.8120	0.6236	3.2329
17	12.4375	2.0280	2.7943	0.8075	73	1.6704	1.8097	0.6147	3.2757
18	11.6337	2.0210	2.6344	0.8536	74	1.6301	1.8075	0.6060	3.3186
19	10.9159	2.0141	2.4915	0.8994	75	1.5910	1.8053	0.5976	3.3614
20	10.2711	2.0075	2.3631	0.9452	76	1.5531	1.8031	0.5894	3.4041
21	9.6889	2.0010	2.2469	0.9909	77	1.5163	1.8010	0.5814	3.4469
22	9.1607	1.9948	2.1414	1.0365	78	1.4806	1.7988	0.5736	3.4896
23	8.6793	1.9887	2.0452	1.0819	79	1.4458	1.7968	0.5660	3.5322
24	8.2389	1.9828	1.9571	1.1273	80	1.4121	1.7947	0.5586	3.5749
25	7.8346	1.9771	1.8761	1.1726	81	1.3793	1.7926	0.5514	3.6175
26	7.4621	1.9715	1.8014	1.2177	82	1.3474	1.7906	0.5443	3.6601
27	7.1178	1.9661	1.7323	1.2628	83	1.3164	1.7886	0.5375	3.7027
28	6.7988	1.9608	1.6682	1.3078	84	1.2862	1.7867	0.5308	3.7453
29	6.5024	1.9557	1.6085	1.3528	85	1.2568	1.7847	0.5243	3.7878

TABLE 12a (continued) Zero Thickness Microstrip Dimensions, Effective Dielectric Constant, and PUL Capacitance and Inductance for Er = 2.2

Zo [Ohms]	W/h	Keff	pF/cm	nH/mm	Zo [Ohms]	W/h	Keff	pF/cm	nH/mm
30	6.2263	1.9507	1.5529	1.3976	86	1.2282	1.7828	0.5179	3.8303
31	5.9686	1.9458	1.5010	1.4424	87	1.2003	1.7809	0.5117	3.8728
32	5.7274	1.9410	1.4523	1.4871	88	1.1732	1.7791	0.5056	3.9152
33	5.5013	1.9364	1.4066	1.5318	89	1.1467	1.7772	0.4996	3.9577
34	5.2890	1.9319	1.3636	1.5763	90	1.1210	1.7754	0.4938	4.0001
35	5.0892	1.9274	1.3231	1.6208	91	1.0959	1.7736	0.4882	4.0424
36	4.9009	1.9231	1.2849	1.6653	92	1.0714	1.7718	0.4826	4.0848
37	4.7231	1.9189	1.2488	1.7096	93	1.0476	1.7700	0.4772	4.1272
38	4.5550	1.9147	1.2146	1.7539	94	1.0243	1.7683	0.4719	4.1695
39	4.3959	1.9107	1.1822	1.7982	95	1.0016	1.7665	0.4667	4.2118
40	4.2450	1.9067	1.1515	1.8424	96	0.9795	1.7658	0.4617	4.2552
41	4.1018	1.9028	1.1223	1.8865	97	0.9579	1.7651	0.4569	4.2987
42	3.9658	1.8990	1.0945	1.9306	98	0.9369	1.7644	0.4521	4.3421
43	3.8363	1.8953	1.0680	1.9746	99	0.9163	1.7637	0.4475	4.3855
44	3.7129	1.8917	1.0427	2.0186	100	0.8962	1.7629	0.4429	4.4289
45	3.5953	1.8881	1.0185	2.0625	101	0.8767	1.7621	0.4384	4.4722
46	3.4831	1.8846	0.9955	2.1064	102	0.8575	1.7613	0.4340	4.5154
47	3.3758	1.8811	0.9734	2.1502	103	0.8389	1.7605	0.4297	4.5586
48	3.2733	1.8778	0.9523	2.1940	104	0.8206	1.7596	0.4255	4.6018
49	3.1751	1.8745	0.9320	2.2378	105	0.8028	1.7588	0.4213	4.6449
50	3.0811	1.8712	0.9126	2.2814	106	0.7855	1.7579	0.4172	4.6880
51	2.9909	1.8680	0.8939	2.3251	107	0.7685	1.7570	0.4132	4.7310
52	2.9044	1.8649	0.8760	2.3687	108	0.7519	1.7561	0.4093	4.7740
53	2.8214	1.8618	0.8588	2.4122	109	0.7357	1.7552	0.4054	4.8169
54	2.7416	1.8587	0.8422	2.4557	110	0.7198	1.7543	0.4016	4.8599
55	2.6648	1.8558	0.8262	2.4992	111	0.7043	1.7534	0.3979	4.9027
56	2.5910	1.8528	0.8108	2.5426	112	0.6892	1.7524	0.3943	4.9456
113	0.6744	1.7515	0.3907	4.9884	132	0.4484	1.7330	0.3327	5.7964
114	0.6600	1.7505	0.3871	5.0312	133	0.4389	1.7321	0.3301	5.8387
115	0.6459	1.7496	0.3837	5.0739	134	0.4296	1.7311	0.3275	5.8810
116	0.6320	1.7486	0.3803	5.1166	135	0.4206	1.7302	0.3250	5.9232
117	0.6185	1.7477	0.3769	5.1593	136	0.4117	1.7292	0.3225	5.9654
118	0.6053	1.7467	0.3736	5.2020	137	0.4030	1.7283	0.3201	6.0076
119	0.5924	1.7457	0.3704	5.2446	138	0.3945	1.7273	0.3177	6.0498
120	0.5798	1.7447	0.3672	5.2872	139	0.3862	1.7264	0.3153	6.0920
121	0.5675	1.7438	0.3640	5.3298	140	0.3781	1.7254	0.3130	6.1342
122	0.5554	1.7428	0.3609	5.3723	141	0.3702	1.7245	0.3107	6.1763
123	0.5436	1.7418	0.3579	5.4148	142	0.3624	1.7236	0.3084	6.2185
124	0.5321	1.7408	0.3549	5.4573	143	0.3547	1.7226	0.3062	6.2606
125	0.5208	1.7399	0.3520	5.4998	144	0.3473	1.7217	0.3039	6.3027
126	0.5097	1.7389	0.3491	5.5422	145	0.3400	1.7208	0.3018	6.3448
127	0.4989	1.7379	0.3462	5.5846	146	0.3328	1.7199	0.2996	6.3868
128	0.4884	1.7369	0.3434	5.6270	147	0.3259	1.7190	0.2975	6.4289
129	0.4780	1.7360	0.3407	5.6694	148	0.3190	1.7181	0.2954	6.4709
130	0.4679	1.7350	0.3380	5.7118	149	0.3123	1.7172	0.2934	6.5130
131	0.4580	1.7340	0.3353	5.7541	150	0.3058	1.7163	0.2913	6.5550

Notes: Calculation of W/H has an error of less than 1%.

Source: Gupta, K.C., Garg, R., Bahl, I., Bhartia, P., *Microstrip Lines and Slotlines,* 2nd Ed., Artech House, Norwood, MA, 1996, 103.

TABLE 12b Zero Thickness Microstrip Dimensions, Effective Dielectric Constant, and PUL Capacitance and Inductance for Er =3.78

Zo [Ohms]	W/h	Keff	pF/cm	nH/mm	Zo [Ohms]	W/h	Keff	pF/cm	nH/mm
1	190.5772	3.7382	64.4927	0.0645	26	5.4498	3.1668	2.2831	1.5433
2	93.9049	3.6989	32.0763	0.1283	27	5.1890	3.1537	2.1940	1.5994
3	61.7511	3.6619	21.2770	0.1915	28	4.9474	3.1410	2.1113	1.6553
4	45.7086	3.6271	15.8817	0.2541	29	4.7230	3.1287	2.0345	1.7110
5	36.1035	3.5942	12.6477	0.3162	30	4.5140	3.1167	1.9629	1.7666
6	29.7137	3.5632	10.4941	0.3778	31	4.3190	3.1051	1.8961	1.8221
7	25.1593	3.5337	8.9578	0.4389	32	4.1365	3.0938	1.8335	1.8775
8	21.7508	3.5059	7.8070	0.4997	33	3.9655	3.0827	1.7747	1.9327
9	19.1053	3.4794	6.9133	0.5600	34	3.8050	3.0720	1.7195	1.9878
10	16.9935	3.4542	6.1994	0.6199	35	3.6539	3.0616	1.6676	2.0428
11	15.2694	3.4301	5.6162	0.6796	36	3.5116	3.0514	1.6185	2.0976
12	13.8357	3.4072	5.1309	0.7389	37	3.3773	3.0414	1.5722	2.1524
13	12.6252	3.3853	4.7210	0.7978	38	3.2504	3.0317	1.5284	2.2070
14	11.5899	3.3643	4.3702	0.8566	39	3.1302	3.0222	1.4869	2.2616
15	10.6946	3.3442	4.0666	0.9150	40	3.0164	3.0130	1.4475	2.3160
16	9.9129	3.3249	3.8014	0.9732	41	2.9083	3.0039	1.4101	2.3703
17	9.2247	3.3064	3.5678	1.0311	42	2.8056	2.9951	1.3745	2.4246
18	8.6143	3.2885	3.3605	1.0888	43	2.7080	2.9864	1.3406	2.4787
19	8.0694	3.2714	3.1754	1.1463	44	2.6150	2.9780	1.3082	2.5327
20	7.5800	3.2549	3.0090	1.2036	45	2.5263	2.9697	1.2774	2.5867
21	7.1382	3.2389	2.8586	1.2607	46	2.4417	2.9615	1.2479	2.6406
22	6.7375	3.2235	2.7222	1.3175	47	2.3609	2.9536	1.2197	2.6943
23	6.3724	3.2086	2.5978	1.3743	48	2.2836	2.9458	1.1927	2.7480
24	6.0386	3.1942	2.4840	1.4308	49	2.2097	2.9381	1.1669	2.8016
25	5.7321	3.1803	2.3794	1.4871	50	2.1389	2.9306	1.1421	2.8552
51	2.0711	2.9233	1.1183	2.9086	101	0.5140	2.7126	0.5439	5.5488
52	2.0060	2.9160	1.0954	2.9620	102	0.5008	2.7099	0.5383	5.6008
53	1.9435	2.9089	1.0734	3.0152	103	0.4878	2.7071	0.5328	5.6529
54	1.8840	2.9020	1.0523	3.0685	104	0.4752	2.7043	0.5274	5.7048
55	1.8268	2.8952	1.0320	3.1217	105	0.4630	2.7016	0.5222	5.7568
56	1.7719	2.8886	1.0124	3.1748	106	0.4511	2.6989	0.5170	5.8086
57	1.7190	2.8820	0.9935	3.2278	107	0.4394	2.6961	0.5119	5.8605
58	1.6682	2.8756	0.9752	3.2807	108	0.4281	2.6934	0.5069	5.9123
59	1.6192	2.8693	0.9577	3.3336	109	0.4171	2.6907	0.5020	5.9640
60	1.5720	2.8631	0.9407	3.3865	110	0.4064	2.6880	0.4972	6.0157
61	1.5265	2.8569	0.9243	3.4392	111	0.3960	2.6853	0.4924	6.0674
62	1.4826	2.8509	0.9084	3.4919	112	0.3858	2.6826	0.4878	6.1190
63	1.4402	2.8450	0.8931	3.5446	113	0.3759	2.6800	0.4832	6.1706
64	1.3993	2.8392	0.8782	3.5971	114	0.3663	2.6774	0.4788	6.2221
65	1.3597	2.8334	0.8638	3.6496	115	0.3569	2.6747	0.4744	6.2736
66	1.3215	2.8278	0.8499	3.7021	116	0.3477	2.6721	0.4701	6.3251
67	1.2845	2.8222	0.8364	3.7545	117	0.3388	2.6696	0.4658	6.3765
68	1.2488	2.8167	0.8233	3.8068	118	0.3301	2.6670	0.4616	6.4279
69	1.2142	2.8113	0.8106	3.8591	119	0.3217	2.6644	0.4575	6.4793
70	1.1807	2.8060	0.7982	3.9113	120	0.3134	2.6619	0.4535	6.5307
71	1.1482	2.8008	0.7862	3.9635	121	0.3054	2.6594	0.4496	6.5820
72	1.1168	2.7956	0.7746	4.0156	122	0.2976	2.6569	0.4457	6.6333
73	1.0863	2.7905	0.7633	4.0676	123	0.2900	2.6544	0.4418	6.6845
74	1.0568	2.7855	0.7523	4.1196	124	0.2826	2.6520	0.4381	6.7358
75	1.0282	2.7805	0.7416	4.1716	125	0.2754	2.6496	0.4344	6.7870
76	1.0004	2.7756	0.7312	4.2235	126	0.2683	2.6472	0.4307	6.8382
77	0.9735	2.7737	0.7215	4.2776	127	0.2615	2.6448	0.4271	6.8893
78	0.9474	2.7717	0.7120	4.3316	128	0.2548	2.6424	0.4236	6.9405
79	0.9220	2.7696	0.7027	4.3855	129	0.2483	2.6401	0.4201	6.9916

TABLE 12b (continued) Zero Thickness Microstrip Dimensions, Effective Dielectric Constant, and PUL Capacitance and Inductance for Er =3.78

Zo [Ohms]	W/h	Keff	pF/cm	nH/mm	Zo [Ohms]	W/h	Keff	pF/cm	nH/mm
80	0.8974	2.7675	0.6936	4.4393	130	0.2420	2.6378	0.4167	7.0427
81	0.8735	2.7653	0.6848	4.4929	131	0.2358	2.6355	0.4134	7.0938
82	0.8503	2.7630	0.6762	4.5465	132	0.2298	2.6332	0.4101	7.1449
83	0.8277	2.7606	0.6677	4.6000	133	0.2239	2.6309	0.4068	7.1959
84	0.8058	2.7582	0.6595	4.6534	134	0.2182	2.6287	0.4036	7.2469
85	0.7845	2.7557	0.6514	4.7067	135	0.2126	2.6265	0.4004	7.2980
86	0.7639	2.7532	0.6436	4.7599	136	0.2072	2.6243	0.3973	7.3490
87	0.7438	2.7506	0.6359	4.8130	137	0.2019	2.6221	0.3943	7.3999
88	0.7242	2.7481	0.6284	4.8660	138	0.1968	2.6200	0.3912	7.4509
89	0.7052	2.7454	0.6210	4.9190	139	0.1917	2.6179	0.3883	7.5019
90	0.6868	2.7428	0.6138	4.9718	140	0.1869	2.6158	0.3853	7.5528
91	0.6688	2.7401	0.6068	5.0246	141	0.1821	2.6137	0.3825	7.6037
92	0.6513	2.7374	0.5999	5.0773	142	0.1775	2.6116	0.3796	7.6546
93	0.6344	2.7347	0.5931	5.1300	143	0.1729	2.6096	0.3768	7.7055
94	0.6178	2.7320	0.5865	5.1826	144	0.1685	2.6076	0.3741	7.7564
95	0.6018	2.7292	0.5801	5.2351	145	0.1642	2.6056	0.3713	7.8073
96	0.5861	2.7265	0.5737	5.2875	146	0.1600	2.6036	0.3687	7.8582
97	0.5709	2.7237	0.5675	5.3399	147	0.1560	2.6017	0.3660	7.9091
98	0.5561	2.7209	0.5615	5.3922	148	0.1520	2.5998	0.3634	7.9599
99	0.5417	2.7182	0.5555	5.4444	149	0.1481	2.5979	0.3608	8.0108
100	0.5277	2.7154	0.5497	5.4966	150	0.1444	2.5960	0.3583	8.0616

Notes: Calculation of W/H has an error of less than 1%.

Source: Gupta, K.C., Garg, R., Bahl, I., Bhartia, P., *Microstrip Lines and Slotlines,* 2nd Ed., Artech House, Norwood, MA, 1996, 103.

TABLE 12c Zero Thickness Microstrip Dimensions, Effective Dielectric Constant, and PUL Capacitance and Inductance for Er =5.75

Zo [Ohms]	W/h	Keff	pF/cm	nH/mm	Zo [Ohms]	W/h	Keff	pF/cm	nH/mm
1	154.1545	5.6626	79.3758	0.0794	55	1.3098	4.1200	1.2310	3.7239
2	75.8057	5.5818	39.4035	0.1576	56	1.2664	4.1088	1.2074	3.7864
3	49.7547	5.5068	26.0920	0.2348	57	1.2248	4.0978	1.1846	3.8488
4	36.7611	5.4372	19.4449	0.3111	58	1.1847	4.0869	1.1627	3.9112
5	28.9839	5.3723	15.4628	0.3866	59	1.1461	4.0763	1.1415	3.9734
6	23.8117	5.3116	12.8127	0.4613	60	1.1089	4.0658	1.1210	4.0355
7	20.1263	5.2548	10.9235	0.5352	61	1.0731	4.0555	1.1012	4.0976
8	17.3689	5.2014	9.5094	0.6086	62	1.0386	4.0453	1.0821	4.1596
9	15.2296	5.1512	8.4118	0.6814	63	1.0054	4.0353	1.0636	4.2214
10	13.5223	5.1037	7.5357	0.7536	64	0.9733	4.0305	1.0464	4.2859
11	12.1289	5.0589	6.8204	0.8253	65	0.9423	4.0265	1.0297	4.3507
12	10.9706	5.0163	6.2257	0.8965	66	0.9124	4.0222	1.0136	4.4153
13	9.9929	4.9759	5.7236	0.9673	67	0.8836	4.0178	0.9979	4.4797
14	9.1570	4.9375	5.2942	1.0377	68	0.8557	4.0132	0.9827	4.5439
15	8.4343	4.9008	4.9229	1.1077	69	0.8288	4.0084	0.9679	4.6080
16	7.8035	4.8659	4.5987	1.1773	70	0.8028	4.0035	0.9535	4.6719
17	7.2484	4.8324	4.3133	1.2466	71	0.7777	3.9985	0.9394	4.7357
18	6.7562	4.8004	4.0602	1.3155	72	0.7534	3.9933	0.9258	4.7993
19	6.3169	4.7697	3.8342	1.3841	73	0.7299	3.9881	0.9125	4.8628
20	5.9225	4.7403	3.6312	1.4525	74	0.7072	3.9828	0.8996	4.9261
21	5.5666	4.7119	3.4479	1.5205	75	0.6853	3.9774	0.8870	4.9893
22	5.2438	4.6847	3.2817	1.5883	76	0.6641	3.9720	0.8747	5.0524
23	4.9499	4.6584	3.1302	1.6559	77	0.6435	3.9665	0.8628	5.1153
24	4.6812	4.6331	2.9916	1.7232	78	0.6236	3.9609	0.8511	5.1781
25	4.4346	4.6087	2.8644	1.7902	79	0.6044	3.9554	0.8397	5.2408

TABLE 12c (continued) Zero Thickness Microstrip Dimensions, Effective Dielectric Constant, and PUL Capacitance and Inductance for Er =5.75

Zo [Ohms]	W/h	Keff	pF/cm	nH/mm	Zo [Ohms]	W/h	Keff	pF/cm	nH/mm
26	4.2075	4.5851	2.7471	1.8571	80	0.5858	3.9498	0.8287	5.3034
27	3.9979	4.5623	2.6388	1.9237	81	0.5678	3.9442	0.8178	5.3659
28	3.8037	4.5402	2.5384	1.9901	82	0.5503	3.9386	0.8073	5.4283
29	3.6233	4.5187	2.4451	2.0563	83	0.5334	3.9329	0.7970	5.4905
30	3.4554	4.4980	2.3581	2.1223	84	0.5171	3.9273	0.7870	5.5527
31	3.2988	4.4778	2.2769	2.1881	85	0.5012	3.9217	0.7771	5.6148
32	3.1523	4.4583	2.2010	2.2538	86	0.4859	3.9161	0.7676	5.6768
33	3.0151	4.4393	2.1297	2.3193	87	0.4710	3.9105	0.7582	5.7387
34	2.8863	4.4208	2.0628	2.3846	88	0.4566	3.9049	0.7490	5.8005
35	2.7652	4.4028	1.9997	2.4497	89	0.4427	3.8994	0.7401	5.8623
36	2.6511	4.3853	1.9403	2.5147	90	0.4292	3.8938	0.7314	5.9239
37	2.5434	4.3682	1.8842	2.5795	91	0.4161	3.8883	0.7228	5.9855
38	2.4417	4.3516	1.8311	2.6441	92	0.4034	3.8829	0.7144	6.0470
39	2.3455	4.3353	1.7808	2.7087	93	0.3912	3.8774	0.7063	6.1085
40	2.2543	4.3195	1.7331	2.7730	94	0.3793	3.8720	0.6983	6.1699
41	2.1678	4.3040	1.6878	2.8373	95	0.3677	3.8667	0.6904	6.2312
42	2.0856	4.2889	1.6448	2.9014	96	0.3565	3.8614	0.6828	6.2925
43	2.0075	4.2741	1.6037	2.9653	97	0.3457	3.8561	0.6753	6.3537
44	1.9289	4.2588	1.5645	3.0288	98	0.3352	3.8508	0.6679	6.4148
45	1.8591	4.2449	1.5272	3.0926	99	0.3250	3.8456	0.6607	6.4759
46	1.7926	4.2312	1.4916	3.1562	100	0.3152	3.8405	0.6537	6.5369
47	1.7291	4.2178	1.4576	3.2198	101	0.3056	3.8354	0.6468	6.5979
48	1.6684	4.2048	1.4250	3.2832	102	0.2963	3.8304	0.6400	6.6588
49	1.6104	4.1919	1.3938	3.3464	103	0.2874	3.8254	0.6334	6.7197
50	1.5549	4.1794	1.3638	3.4096	104	0.2787	3.8204	0.6269	6.7806
51	1.5017	4.1671	1.3351	3.4727	105	0.2702	3.8155	0.6205	6.8414
52	1.4507	4.1550	1.3076	3.5356	106	0.2620	3.8107	0.6143	6.9022
53	1.4018	4.1431	1.2811	3.5985	107	0.2541	3.8059	0.6082	6.9629
54	1.3549	4.1315	1.2556	3.6612	108	0.2464	3.8011	0.6022	7.0236
109	0.2389	3.7964	0.5963	7.0842	130	0.1255	3.7101	0.4942	8.3525
110	0.2317	3.7918	0.5905	7.1449	131	0.1217	3.7065	0.4902	8.4127
111	0.2247	3.7872	0.5848	7.2055	132	0.1180	3.7030	0.4863	8.4729
112	0.2179	3.7827	0.5792	7.2660	133	0.1144	3.6996	0.4824	8.5331
113	0.2113	3.7782	0.5738	7.3265	134	0.1110	3.6962	0.4786	8.5933
114	0.2049	3.7738	0.5684	7.3871	135	0.1076	3.6928	0.4748	8.6535
115	0.1987	3.7694	0.5631	7.4475	136	0.1044	3.6895	0.4711	8.7137
116	0.1927	3.7651	0.5580	7.5080	137	0.1012	3.6863	0.4675	8.7739
117	0.1869	3.7608	0.5529	7.5684	138	0.0982	3.6830	0.4639	8.8341
118	0.1813	3.7566	0.5479	7.6288	139	0.0952	3.6799	0.4603	8.8943
119	0.1758	3.7524	0.5430	7.6892	140	0.0923	3.6767	0.4569	8.9544
120	0.1705	3.7483	0.5382	7.7496	141	0.0896	3.6737	0.4534	9.0146
121	0.1653	3.7443	0.5334	7.8099	142	0.0869	3.6706	0.4500	9.0748
122	0.1603	3.7403	0.5288	7.8703	143	0.0842	3.6676	0.4467	9.1350
123	0.1555	3.7363	0.5242	7.9306	144	0.0817	3.6647	0.4434	9.1952
124	0.1508	3.7324	0.5197	7.9909	145	0.0792	3.6618	0.4402	9.2553
125	0.1462	3.7286	0.5153	8.0512	146	0.0768	3.6589	0.4370	9.3155
126	0.1418	3.7248	0.5109	8.1115	147	0.0745	3.6561	0.4339	9.3757
127	0.1375	3.7210	0.5066	8.1717	148	0.0723	3.6533	0.4308	9.4359
128	0.1334	3.7173	0.5024	8.2320	149	0.0701	3.6505	0.4277	9.4961
129	0.1294	3.7137	0.4983	8.2922	150	0.0680	3.6478	0.4247	9.5562

Notes: Calculation of W/H has an error of less than 1%.

Source: Gupta, K.C., Garg, R., Bahl, I., Bhartia, P., *Microstrip Lines and Slotlines,* 2nd Ed., Artech House, Norwood, MA, 1996, 103.

TABLE 12d Zero Thickness Microstrip Dimensions, Effective Dielectric Constant, and PUL Capacitance and Inductance for Er = 9.4

Zo [Ohms]	W/h	Keff	pF/cm	nH/mm	Zo [Ohms]	W/h	Keff	pF/cm	nH/mm
1	120.1221	9.2047	101.2010	0.1012	24	3.4066	7.1750	3.7229	2.1444
2	58.8859	9.0280	50.1125	0.2004	25	3.2161	7.1309	3.5630	2.2269
3	38.5353	8.8676	33.1101	0.2980	26	3.0409	7.0885	3.4157	2.3090
4	28.3901	8.7212	24.6268	0.3940	27	2.8791	7.0475	3.2797	2.3909
5	22.3208	8.5871	19.5493	0.4887	28	2.7293	7.0079	3.1537	2.4725
6	18.2864	8.4635	16.1735	0.5822	29	2.5902	6.9697	3.0366	2.5538
7	15.4132	8.3493	13.7691	0.6747	30	2.4609	6.9326	2.9276	2.6348
8	13.2647	8.2433	11.9712	0.7662	31	2.3403	6.8967	2.8258	2.7156
9	11.5985	8.1445	10.5771	0.8567	32	2.2275	6.8619	2.7306	2.7961
10	10.2695	8.0521	9.4653	0.9465	33	2.1220	6.8281	2.6413	2.8764
11	9.1854	7.9655	8.5584	1.0356	34	2.0229	6.7952	2.5574	2.9564
12	8.2846	7.8841	7.8050	1.1239	35	1.9221	6.7606	2.4780	3.0356
13	7.5248	7.8074	7.1695	1.2116	36	1.8364	6.7301	2.4037	3.1152
14	6.8754	7.7348	6.6264	1.2988	37	1.7556	6.7004	2.3336	3.1947
15	6.3143	7.6661	6.1571	1.3853	38	1.6792	6.6715	2.2673	3.2740
16	5.8248	7.6009	5.7477	1.4714	39	1.6070	6.6434	2.2045	3.3530
17	5.3942	7.5389	5.3875	1.5570	40	1.5386	6.6159	2.1449	3.4319
18	5.0126	7.4798	5.0682	1.6421	41	1.4738	6.5891	2.0884	3.5105
19	4.6722	7.4234	4.7833	1.7268	42	1.4122	6.5629	2.0346	3.5890
20	4.3668	7.3694	4.5276	1.8110	43	1.3537	6.5373	1.9834	3.6673
21	4.0913	7.3178	4.2968	1.8949	44	1.2981	6.5122	1.9346	3.7454
22	3.8416	7.2683	4.0876	1.9784	45	1.2451	6.4877	1.8880	3.8233
23	3.6143	7.2207	3.8971	2.0616	46	1.1946	6.4638	1.8436	3.9010
47	1.1465	6.4403	1.8011	3.9786	99	0.1530	5.8352	0.8139	7.9771
48	1.1005	6.4173	1.7604	4.0560	100	0.1472	5.8268	0.8052	8.0518
49	1.0567	6.3948	1.7215	4.1332	101	0.1417	5.8184	0.7966	8.1265
50	1.0148	6.3728	1.6841	4.2103	102	0.1365	5.8102	0.7883	8.2012
51	0.9747	6.3596	1.6494	4.2901	103	0.1314	5.8021	0.7801	8.2758
52	0.9364	6.3507	1.6165	4.3711	104	0.1265	5.7942	0.7720	8.3504
53	0.8997	6.3412	1.5849	4.4519	105	0.1217	5.7864	0.7642	8.4251
54	0.8646	6.3312	1.5543	4.5323	106	0.1172	5.7787	0.7565	8.4997
55	0.8309	6.3208	1.5248	4.6124	107	0.1128	5.7712	0.7489	8.5742
56	0.7987	6.3100	1.4963	4.6923	108	0.1086	5.7638	0.7415	8.6488
57	0.7678	6.2989	1.4687	4.7719	109	0.1046	5.7565	0.7342	8.7234
58	0.7382	6.2875	1.4421	4.8512	110	0.1006	5.7493	0.7271	8.7979
59	0.7098	6.2759	1.4163	4.9303	111	0.0969	5.7423	0.7201	8.8725
60	0.6826	6.2641	1.3914	5.0091	112	0.0933	5.7354	0.7133	8.9470
61	0.6564	6.2521	1.3673	5.0877	113	0.0898	5.7286	0.7065	9.0216
62	0.6313	6.2400	1.3439	5.1661	114	0.0864	5.7219	0.6999	9.0961
63	0.6072	6.2278	1.3213	5.2443	115	0.0832	5.7154	0.6934	9.1707
64	0.5841	6.2156	1.2994	5.3223	116	0.0801	5.7090	0.6871	9.2452
65	0.5619	6.2032	1.2781	5.4001	117	0.0771	5.7026	0.6808	9.3197
66	0.5406	6.1909	1.2575	5.4777	118	0.0743	5.6964	0.6747	9.3943
67	0.5201	6.1786	1.2375	5.5552	119	0.0715	5.6903	0.6687	9.4688
68	0.5004	6.1662	1.2181	5.6325	120	0.0688	5.6843	0.6627	9.5434
69	0.4814	6.1539	1.1992	5.7096	121	0.0662	5.6785	0.6569	9.6179
70	0.4632	6.1417	1.1809	5.7866	122	0.0638	5.6727	0.6512	9.6925
71	0.4457	6.1295	1.1631	5.8634	123	0.0614	5.6670	0.6456	9.7670
72	0.4289	6.1173	1.1458	5.9401	124	0.0591	5.6615	0.6401	9.8416
73	0.4127	6.1053	1.1290	6.0166	125	0.0569	5.6560	0.6346	9.9162
74	0.3972	6.0933	1.1127	6.0931	126	0.0548	5.6506	0.6293	9.9907
75	0.3822	6.0814	1.0968	6.1694	127	0.0527	5.6454	0.6241	10.0653
76	0.3679	6.0696	1.0813	6.2456	128	0.0508	5.6402	0.6189	10.1399
77	0.3540	6.0579	1.0662	6.3217	129	0.0489	5.6351	0.6138	10.2146
78	0.3407	6.0464	1.0516	6.3977	130	0.0471	5.6301	0.6088	10.2892
79	0.3279	6.0350	1.0373	6.4736	131	0.0453	5.6252	0.6039	10.3638

TABLE 12d (continued) Zero Thickness Microstrip Dimensions, Effective Dielectric Constant, and PUL Capacitance and Inductance for Er = 9.4

Zo [Ohms]	W/h	Keff	pF/cm	nH/mm	Zo [Ohms]	W/h	Keff	pF/cm	nH/mm
80	0.3156	6.0236	1.0233	6.5494	132	0.0436	5.6204	0.5991	10.4385
81	0.3038	6.0125	1.0098	6.6251	133	0.0420	5.6157	0.5943	10.5131
82	0.2924	6.0014	0.9965	6.7007	134	0.0404	5.6111	0.5897	10.5878
83	0.2815	5.9905	0.9836	6.7762	135	0.0389	5.6065	0.5850	10.6625
84	0.2709	5.9797	0.9710	6.8517	136	0.0375	5.6021	0.5805	10.7372
85	0.2608	5.9691	0.9588	6.9271	137	0.0361	5.5977	0.5761	10.8119
86	0.2510	5.9586	0.9468	7.0024	138	0.0347	5.5934	0.5717	10.8867
87	0.2416	5.9482	0.9351	7.0777	139	0.0334	5.5892	0.5673	10.9614
88	0.2326	5.9380	0.9237	7.1529	140	0.0322	5.5850	0.5631	11.0362
89	0.2239	5.9280	0.9125	7.2281	141	0.0310	5.5809	0.5589	11.1110
90	0.2155	5.9180	0.9016	7.3032	142	0.0298	5.5770	0.5547	11.1858
91	0.2074	5.9083	0.8910	7.3782	143	0.0287	5.5730	0.5507	11.2606
92	0.1997	5.8986	0.8806	7.4532	144	0.0276	5.5692	0.5467	11.3354
93	0.1922	5.8891	0.8704	7.5281	145	0.0266	5.5654	0.5427	11.4103
94	0.1850	5.8798	0.8605	7.6031	146	0.0256	5.5617	0.5388	11.4852
95	0.1781	5.8706	0.8507	7.6779	147	0.0247	5.5581	0.5350	11.5600
96	0.1715	5.8616	0.8412	7.7528	148	0.0237	5.5545	0.5312	11.6350
97	0.1651	5.8526	0.8319	7.8276	149	0.0229	5.5510	0.5274	11.7099
98	0.1589	5.8439	0.8228	7.9023	150	0.0220	5.5476	0.5238	11.7848

Notes: Calculation of W/H has an error of less than 1%.

Source: Gupta, K.C., Garg, R., Bahl, I., Bhartia, P., *Microstrip Lines and Slotlines,* 2nd Ed., Artech House, Norwood, MA, 1996, 103.

TABLE 12e Zero Thickness Microstrip Dimensions, Effective Dielectric Constant, and PUL Capacitance and Inductance for Er = 9.8

Zo [Ohms]	W/h	Keff	pF/cm	nH/mm	Zo [Ohms]	W/h	Keff	pF/cm	nH/mm
1	117.6023	9.5914	103.3045	0.1033	57	0.7347	6.5379	1.4963	4.8615
2	57.6329	9.4030	51.1424	0.2046	58	0.7059	6.5254	1.4691	4.9421
3	37.7044	9.2322	33.7840	0.3041	59	0.6783	6.5128	1.4428	5.0224
4	27.7700	9.0767	25.1237	0.4020	60	0.6519	6.5000	1.4174	5.1025
5	21.8272	8.9344	19.9408	0.4985	61	0.6265	6.4870	1.3927	5.1824
6	17.8771	8.8035	16.4952	0.5938	62	0.6022	6.4740	1.3689	5.2621
7	15.0641	8.6827	14.0413	0.6880	63	0.5788	6.4609	1.3458	5.3415
8	12.9606	8.5706	12.2066	0.7812	64	0.5564	6.4477	1.3234	5.4208
9	11.3295	8.4662	10.7841	0.8735	65	0.5349	6.4346	1.3017	5.4999
10	10.0285	8.3688	9.6496	0.9650	66	0.5142	6.4214	1.2807	5.5788
11	8.9673	8.2775	8.7244	1.0557	67	0.4944	6.4082	1.2603	5.6575
12	8.0857	8.1917	7.9558	1.1456	68	0.4753	6.3951	1.2405	5.7360
13	7.3419	8.1109	7.3075	1.2350	69	0.4570	6.3820	1.2213	5.8144
14	6.7063	8.0345	6.7535	1.3237	70	0.4395	6.3690	1.2026	5.8927
15	6.1572	7.9622	6.2749	1.4118	71	0.4226	6.3561	1.1844	5.9708
16	5.6782	7.8937	5.8573	1.4995	72	0.4064	6.3432	1.1668	6.0488
17	5.2568	7.8285	5.4900	1.5866	73	0.3908	6.3305	1.1497	6.1266
18	4.8834	7.7664	5.1644	1.6733	74	0.3758	6.3179	1.1330	6.2043
19	4.5503	7.7071	4.8738	1.7595	75	0.3614	6.3053	1.1168	6.2820
20	4.2515	7.6505	4.6131	1.8452	76	0.3476	6.2929	1.1010	6.3595
21	3.9820	7.5963	4.3778	1.9306	77	0.3343	6.2807	1.0857	6.4368
22	3.7377	7.5443	4.1645	2.0156	78	0.3215	6.2685	1.0707	6.5141
23	3.5154	7.4944	3.9703	2.1003	79	0.3092	6.2565	1.0561	6.5913
24	3.3122	7.4464	3.7926	2.1846	80	0.2974	6.2447	1.0419	6.6684
25	3.1259	7.4002	3.6296	2.2685	81	0.2860	6.2329	1.0281	6.7455

TABLE 12e (continued) Zero Thickness Microstrip Dimensions, Effective Dielectric Constant, and PUL Capacitance and Inductance for Er = 9.8

Zo [Ohms]	W/h	Keff	pF/cm	nH/mm	Zo [Ohms]	W/h	Keff	pF/cm	nH/mm
26	2.9545	7.3557	3.4795	2.3522	82	0.2751	6.2214	1.0146	6.8224
27	2.7962	7.3128	3.3408	2.4355	83	0.2646	6.2100	1.0015	6.8993
28	2.6497	7.2713	3.2124	2.5185	84	0.2545	6.1987	0.9887	6.9760
29	2.5138	7.2312	3.0930	2.6012	85	0.2448	6.1876	0.9762	7.0528
30	2.3873	7.1923	2.9819	2.6837	86	0.2355	6.1766	0.9640	7.1294
31	2.2693	7.1547	2.8781	2.7659	87	0.2265	6.1658	0.9520	7.2060
32	2.1591	7.1182	2.7811	2.8478	88	0.2179	6.1552	0.9404	7.2825
33	2.0558	7.0827	2.6901	2.9295	89	0.2096	6.1447	0.9291	7.3590
34	1.9590	7.0483	2.6046	3.0109	90	0.2016	6.1344	0.9180	7.4355
35	1.8614	7.0124	2.5237	3.0916	91	0.1939	6.1242	0.9071	7.5118
36	1.7777	6.9805	2.4480	3.1727	92	0.1865	6.1142	0.8965	7.5882
37	1.6987	6.9494	2.3766	3.2535	93	0.1794	6.1044	0.8862	7.6645
38	1.6241	6.9191	2.3090	3.3342	94	0.1726	6.0947	0.8760	7.7408
39	1.5535	6.8896	2.2450	3.4146	95	0.1660	6.0852	0.8661	7.8170
40	1.4867	6.8609	2.1843	3.4948	96	0.1597	6.0758	0.8565	7.8932
41	1.4233	6.8328	2.1266	3.5749	97	0.1536	6.0666	0.8470	7.9693
42	1.3632	6.8053	2.0718	3.6547	98	0.1478	6.0575	0.8377	8.0455
43	1.3060	6.7785	2.0197	3.7343	99	0.1422	6.0486	0.8286	8.1216
44	1.2517	6.7523	1.9699	3.8138	100	0.1368	6.0398	0.8198	8.1977
45	1.1999	6.7266	1.9225	3.8931	101	0.1316	6.0312	0.8111	8.2737
46	1.1507	6.7015	1.8772	3.9721	102	0.1266	6.0227	0.8026	8.3498
47	1.1037	6.6770	1.8339	4.0510	103	0.1217	6.0143	0.7942	8.4258
48	1.0588	6.6529	1.7924	4.1298	104	0.1171	6.0062	0.7860	8.5018
49	1.0161	6.6293	1.7527	4.2083	105	0.1127	5.9981	0.7780	8.5778
50	0.9752	6.6149	1.7158	4.2895	106	0.1084	5.9902	0.7702	8.6538
51	0.9361	6.6054	1.6810	4.3722	107	0.1043	5.9824	0.7625	8.7298
52	0.8988	6.5953	1.6474	4.4545	108	0.1003	5.9748	0.7549	8.8057
53	0.8630	6.5846	1.6150	4.5365	109	0.0965	5.9673	0.7476	8.8817
54	0.8289	6.5735	1.5837	4.6182	110	0.0928	5.9600	0.7403	8.9576
55	0.7961	6.5619	1.5536	4.6996	111	0.0893	5.9527	0.7332	9.0336
56	0.7648	6.5501	1.5245	4.7807	112	0.0859	5.9456	0.7262	9.1095
113	0.0826	5.9387	0.7194	9.1855	132	0.0396	5.8280	0.6101	10.6295
114	0.0795	5.9318	0.7126	9.2614	133	0.0381	5.8232	0.6052	10.7056
115	0.0765	5.9251	0.7060	9.3374	134	0.0366	5.8185	0.6005	10.7818
116	0.0736	5.9185	0.6996	9.4133	135	0.0352	5.8139	0.5958	10.8579
117	0.0708	5.9120	0.6932	9.4893	136	0.0339	5.8093	0.5912	10.9341
118	0.0681	5.9057	0.6870	9.5652	137	0.0326	5.8049	0.5866	11.0102
119	0.0655	5.8994	0.6808	9.6412	138	0.0314	5.8005	0.5821	11.0864
120	0.0630	5.8933	0.6748	9.7172	139	0.0302	5.7962	0.5777	11.1626
121	0.0606	5.8873	0.6689	9.7931	140	0.0290	5.7920	0.5734	11.2389
122	0.0583	5.8814	0.6631	9.8691	141	0.0279	5.7879	0.5691	11.3151
123	0.0561	5.8756	0.6574	9.9451	142	0.0269	5.7838	0.5649	11.3914
124	0.0540	5.8699	0.6517	10.0211	143	0.0258	5.7799	0.5608	11.4677
125	0.0519	5.8643	0.6462	10.0971	144	0.0249	5.7760	0.5567	11.5440
126	0.0499	5.8588	0.6408	10.1731	145	0.0239	5.7722	0.5527	11.6203
127	0.0480	5.8534	0.6354	10.2492	146	0.0230	5.7684	0.5487	11.6966
128	0.0462	5.8482	0.6302	10.3252	147	0.0221	5.7647	0.5448	11.7730
129	0.0445	5.8430	0.6250	10.4013	148	0.0213	5.7611	0.5410	11.8494
130	0.0428	5.8379	0.6200	10.4773	149	0.0205	5.7576	0.5372	11.9258
131	0.0411	5.8329	0.6150	10.5534	150	0.0197	5.7541	0.5334	12.0022

Notes: Calculation of W/H has an error of less than 1%.

Source: Gupta, K.C., Garg, R., Bahl, I., Bhartia, P., *Microstrip Lines and Slotlines,* 2nd Ed., Artech House, Norwood, MA, 1996, 103.

TABLE 12f Zero Thickness Microstrip Dimensions, Effective Dielectric Constant, and PUL Capacitance and Inductance for Er = 11.6

Zo [Ohms]	W/h	Keff	pF/cm	nH/mm	Zo [Ohms]	W/h	Keff	pF/cm	nH/mm
1	107.9253	11.3278	112.2672	0.1123	26	2.6229	8.5446	3.7502	2.5351
2	52.8209	11.0843	55.5270	0.2221	27	2.4782	8.4928	3.6003	2.6246
3	34.5132	10.8654	36.6506	0.3299	28	2.3444	8.4426	3.4615	2.7138
4	25.3888	10.6674	27.2364	0.4358	29	2.2202	8.3942	3.3325	2.8026
5	19.9316	10.4873	21.6044	0.5401	30	2.1047	8.3473	3.2124	2.8912
6	16.3052	10.3226	17.8617	0.6430	31	1.9970	8.3019	3.1003	2.9794
7	13.7232	10.1712	15.1973	0.7447	32	1.8884	8.2543	2.9948	3.0667
8	11.7929	10.0313	13.2059	0.8452	33	1.7964	8.2125	2.8967	3.1545
9	10.2964	9.9016	11.6625	0.9447	34	1.7101	8.1718	2.8045	3.2420
10	9.1031	9.7809	10.4321	1.0432	35	1.6291	8.1324	2.7178	3.3293
11	8.1299	9.6682	9.4289	1.1409	36	1.5527	8.0939	2.6361	3.4163
12	7.3215	9.5625	8.5958	1.2378	37	1.4807	8.0565	2.5589	3.5031
13	6.6397	9.4632	7.8932	1.3340	38	1.4128	8.0201	2.4859	3.5897
14	6.0573	9.3696	7.2931	1.4294	39	1.3485	7.9846	2.4168	3.6759
15	5.5541	9.2812	6.7747	1.5243	40	1.2877	7.9499	2.3513	3.7620
16	5.1153	9.1975	6.3226	1.6186	41	1.2301	7.9161	2.2890	3.8478
17	4.7294	9.1180	5.9249	1.7123	42	1.1754	7.8830	2.2299	3.9335
18	4.3875	9.0424	5.5725	1.8055	43	1.1235	7.8507	2.1735	4.0189
19	4.0826	8.9703	5.2581	1.8982	44	1.0742	7.8192	2.1199	4.1041
20	3.8091	8.9016	4.9760	1.9904	45	1.0273	7.7883	2.0687	4.1890
21	3.5625	8.8358	4.7215	2.0822	46	0.9827	7.7654	2.0207	4.2758
22	3.3390	8.7728	4.4908	2.1736	47	0.9402	7.7532	1.9762	4.3653
23	3.1357	8.7124	4.2807	2.2645	48	0.8998	7.7401	1.9334	4.4545
24	2.9499	8.6543	4.0887	2.3551	49	0.8612	7.7262	1.8922	4.5432
25	2.7796	8.5984	3.9125	2.4453	50	0.8244	7.7117	1.8526	4.6315
51	0.7893	7.6966	1.8145	4.7195	101	0.0957	6.9814	0.8726	8.9017
52	0.7558	7.6810	1.7778	4.8072	102	0.0917	6.9719	0.8635	8.9837
53	0.7238	7.6650	1.7425	4.8945	103	0.0880	6.9625	0.8545	9.0657
54	0.6933	7.6487	1.7084	4.9816	104	0.0844	6.9534	0.8458	9.1477
55	0.6641	7.6322	1.6755	5.0683	105	0.0809	6.9444	0.8372	9.2297
56	0.6362	7.6154	1.6438	5.1548	106	0.0776	6.9356	0.8287	9.3116
57	0.6095	7.5985	1.6131	5.2410	107	0.0744	6.9269	0.8205	9.3936
58	0.5840	7.5815	1.5835	5.3270	108	0.0714	6.9185	0.8124	9.4756
59	0.5596	7.5643	1.5549	5.4127	109	0.0684	6.9102	0.8044	9.5576
60	0.5363	7.5472	1.5273	5.4982	110	0.0656	6.9020	0.7967	9.6396
61	0.5139	7.5301	1.5005	5.5835	111	0.0630	6.8940	0.7890	9.7216
62	0.4925	7.5129	1.4747	5.6686	112	0.0604	6.8862	0.7815	9.8036
63	0.4721	7.4959	1.4496	5.7535	113	0.0579	6.8786	0.7742	9.8857
64	0.4525	7.4789	1.4253	5.8382	114	0.0555	6.8710	0.7670	9.9677
65	0.4337	7.4620	1.4018	5.9227	115	0.0533	6.8637	0.7599	10.0498
66	0.4158	7.4452	1.3790	6.0071	116	0.0511	6.8565	0.7530	10.1318
67	0.3986	7.4286	1.3569	6.0913	117	0.0490	6.8494	0.7461	10.2139
68	0.3821	7.4121	1.3355	6.1753	118	0.0470	6.8425	0.7394	10.2960
69	0.3663	7.3957	1.3147	6.2592	119	0.0450	6.8357	0.7329	10.3781
70	0.3512	7.3795	1.2945	6.3430	120	0.0432	6.8290	0.7264	10.4602
71	0.3367	7.3635	1.2749	6.4266	121	0.0414	6.8225	0.7201	10.5423
72	0.3228	7.3477	1.2558	6.5101	122	0.0397	6.8161	0.7138	10.6245
73	0.3095	7.3321	1.2373	6.5935	123	0.0381	6.8099	0.7077	10.7067
74	0.2967	7.3166	1.2193	6.6768	124	0.0365	6.8037	0.7017	10.7888
75	0.2845	7.3014	1.2018	6.7600	125	0.0350	6.7977	0.6957	10.8711
76	0.2728	7.2864	1.1847	6.8430	126	0.0336	6.7919	0.6899	10.9533
77	0.2616	7.2716	1.1682	6.9260	127	0.0322	6.7861	0.6842	11.0355
78	0.2508	7.2570	1.1520	7.0089	128	0.0309	6.7804	0.6786	11.1178
79	0.2405	7.2426	1.1363	7.0918	129	0.0296	6.7749	0.6730	11.2001
80	0.2306	7.2285	1.1210	7.1745	130	0.0284	6.7695	0.6676	11.2824

TABLE 12f Zero Thickness Microstrip Dimensions, Effective Dielectric Constant, and PUL Capacitance and Inductance for Er = 11.6

Zo [Ohms]	W/h	Keff	pF/cm	nH/mm	Zo [Ohms]	W/h	Keff	pF/cm	nH/mm
81	0.2211	7.2146	1.1061	7.2572	131	0.0273	6.7642	0.6622	11.3647
82	0.2121	7.2009	1.0916	7.3398	132	0.0261	6.7590	0.6570	11.4471
83	0.2033	7.1874	1.0774	7.4224	133	0.0251	6.7539	0.6518	11.5294
84	0.1950	7.1741	1.0636	7.5049	134	0.0240	6.7489	0.6467	11.6118
85	0.1870	7.1611	1.0501	7.5873	135	0.0231	6.7440	0.6417	11.6943
86	0.1793	7.1483	1.0370	7.6697	136	0.0221	6.7392	0.6367	11.7767
87	0.1719	7.1357	1.0242	7.7520	137	0.0212	6.7345	0.6318	11.8592
88	0.1649	7.1233	1.0117	7.8343	138	0.0203	6.7300	0.6271	11.9417
89	0.1581	7.1111	0.9994	7.9166	139	0.0195	6.7255	0.6223	12.0242
90	0.1516	7.0992	0.9875	7.9988	140	0.0187	6.7210	0.6177	12.1067
91	0.1454	7.0874	0.9758	8.0810	141	0.0179	6.7167	0.6131	12.1893
92	0.1394	7.0759	0.9645	8.1632	142	0.0172	6.7125	0.6086	12.2718
93	0.1337	7.0646	0.9533	8.2453	143	0.0165	6.7084	0.6042	12.3545
94	0.1282	7.0535	0.9424	8.3274	144	0.0158	6.7043	0.5998	12.4371
95	0.1230	7.0426	0.9318	8.4095	145	0.0152	6.7003	0.5955	12.5197
96	0.1179	7.0319	0.9214	8.4916	146	0.0146	6.6964	0.5912	12.6024
97	0.1131	7.0214	0.9112	8.5736	147	0.0140	6.6926	0.5870	12.6851
98	0.1085	7.0111	0.9013	8.6556	148	0.0134	6.6889	0.5829	12.7679
99	0.1040	7.0010	0.8915	8.7377	149	0.0128	6.6852	0.5788	12.8506
100	0.0998	6.9911	0.8820	8.8197	150	0.0123	6.6817	0.5748	12.9334

Notes: Calculation of W/H has an error of less than 1%.

Source: Gupta, K.C., Garg, R., Bahl, I., Bhartia, P., *Microstrip Lines and Slotlines,* 2nd Ed., Artech House, Norwood, MA, 1996, 103.

TABLE 12g Zero Thickness Microstrip Dimensions, Effective Dielectric Constant, and PUL Capacitance and Inductance for Er =11.9

Zo [Ohms]	W/h	Keff	pF/cm	nH/mm	Zo [Ohms]	W/h	Keff	pF/cm	nH/mm
1	106.5298	11.6168	113.6899	0.1137	55	0.6453	7.8084	1.6947	5.1265
2	52.1270	11.3637	56.2223	0.2249	56	0.6179	7.7908	1.6626	5.2139
3	34.0530	11.1365	37.1049	0.3339	57	0.5918	7.7731	1.6316	5.3009
4	25.0454	10.9312	27.5710	0.4411	58	0.5667	7.7554	1.6016	5.3878
5	19.6583	10.7446	21.8678	0.5467	59	0.5428	7.7375	1.5726	5.4744
6	16.0785	10.5741	18.0780	0.6508	60	0.5199	7.7197	1.5446	5.5607
7	13.5298	10.4175	15.3802	0.7536	61	0.4980	7.7019	1.5176	5.6469
8	11.6245	10.2730	13.3640	0.8553	62	0.4771	7.6841	1.4914	5.7328
9	10.1474	10.1390	11.8014	0.9559	63	0.4571	7.6664	1.4660	5.8186
10	8.9696	10.0144	10.5558	1.0556	64	0.4379	7.6488	1.4414	5.9041
11	8.0091	9.8981	9.5403	1.1544	65	0.4195	7.6313	1.4176	5.9895
12	7.2113	9.7891	8.6970	1.2524	66	0.4020	7.6140	1.3946	6.0748
13	6.5385	9.6867	7.9859	1.3496	67	0.3852	7.5968	1.3722	6.1598
14	5.9637	9.5902	7.3784	1.4462	68	0.3691	7.5797	1.3505	6.2447
15	5.4672	9.4991	6.8538	1.5421	69	0.3536	7.5628	1.3295	6.3295
16	5.0342	9.4128	6.3961	1.6374	70	0.3389	7.5462	1.3090	6.4142
17	4.6534	9.3309	5.9937	1.7322	71	0.3247	7.5297	1.2892	6.4987
18	4.3160	9.2531	5.6370	1.8264	72	0.3112	7.5134	1.2699	6.5831
19	4.0152	9.1789	5.3189	1.9201	73	0.2982	7.4973	1.2511	6.6674
20	3.7454	9.1081	5.0334	2.0134	74	0.2858	7.4814	1.2329	6.7516
21	3.5020	9.0404	4.7759	2.1062	75	0.2739	7.4658	1.2152	6.8356
22	3.2816	8.9755	4.5424	2.1985	76	0.2625	7.4504	1.1980	6.9196
23	3.0810	8.9134	4.3298	2.2905	77	0.2516	7.4352	1.1812	7.0035
24	2.8977	8.8536	4.1355	2.3820	78	0.2411	7.4202	1.1649	7.0873
25	2.7297	8.7961	3.9572	2.4732	79	0.2311	7.4055	1.1490	7.1711

TABLE 12g (continued) Zero Thickness Microstrip Dimensions, Effective Dielectric Constant, and PUL Capacitance and Inductance for Er =11.9

Zo [Ohms]	W/h	Keff	pF/cm	nH/mm	Zo [Ohms]	W/h	Keff	pF/cm	nH/mm
26	2.5751	8.7408	3.7930	2.5641	80	0.2215	7.3910	1.1335	7.2547
27	2.4324	8.6874	3.6413	2.6545	81	0.2123	7.3767	1.1185	7.3383
28	2.3004	8.6359	3.5009	2.7447	82	0.2035	7.3627	1.1038	7.4218
29	2.1779	8.5861	3.3704	2.8345	83	0.1950	7.3489	1.0895	7.5053
30	2.0640	8.5378	3.2489	2.9240	84	0.1869	7.3353	1.0755	7.5887
31	1.9578	8.4911	3.1355	3.0132	85	0.1791	7.3220	1.0619	7.6721
32	1.8513	8.4425	3.0288	3.1014	86	0.1717	7.3089	1.0486	7.7554
33	1.7607	8.3995	2.9295	3.1902	87	0.1646	7.2960	1.0356	7.8386
34	1.6756	8.3577	2.8362	3.2787	88	0.1577	7.2834	1.0230	7.9219
35	1.5956	8.3171	2.7485	3.3669	89	0.1512	7.2709	1.0106	8.0051
36	1.5204	8.2776	2.6658	3.4549	90	0.1449	7.2588	0.9985	8.0882
37	1.4494	8.2391	2.5877	3.5426	91	0.1389	7.2468	0.9868	8.1713
38	1.3824	8.2016	2.5139	3.6301	92	0.1331	7.2350	0.9752	8.2544
39	1.3190	8.1651	2.4440	3.7173	93	0.1276	7.2235	0.9640	8.3375
40	1.2591	8.1295	2.3777	3.8043	94	0.1223	7.2122	0.9530	8.4206
41	1.2023	8.0947	2.3147	3.8910	95	0.1172	7.2011	0.9422	8.5036
42	1.1484	8.0607	2.2548	3.9775	96	0.1124	7.1902	0.9317	8.5866
43	1.0973	8.0275	2.1979	4.0639	97	0.1077	7.1795	0.9214	8.6696
44	1.0487	7.9951	2.1436	4.1499	98	0.1033	7.1691	0.9113	8.7526
45	1.0026	7.9633	2.0918	4.2358	99	0.0990	7.1588	0.9015	8.8356
46	0.9586	7.9500	2.0446	4.3263	100	0.0949	7.1487	0.8919	8.9185
47	0.9168	7.9367	1.9994	4.4167	101	0.0909	7.1388	0.8824	9.0015
48	0.8770	7.9226	1.9560	4.5067	102	0.0872	7.1292	0.8732	9.0845
49	0.8391	7.9078	1.9143	4.5962	103	0.0836	7.1197	0.8641	9.1674
50	0.8029	7.8923	1.8742	4.6854	104	0.0801	7.1104	0.8552	9.2504
51	0.7684	7.8762	1.8356	4.7743	105	0.0768	7.1012	0.8466	9.3333
52	0.7354	7.8598	1.7984	4.8628	106	0.0736	7.0923	0.8380	9.4163
53	0.7040	7.8429	1.7626	4.9510	107	0.0705	7.0835	0.8297	9.4992
54	0.6740	7.8258	1.7280	5.0389	108	0.0676	7.0749	0.8215	9.5822
109	0.0648	7.0665	0.8135	9.6652	130	0.0266	6.9243	0.6752	11.4107
110	0.0621	7.0583	0.8056	9.7481	131	0.0255	6.9190	0.6698	11.4940
111	0.0595	7.0502	0.7979	9.8311	132	0.0245	6.9138	0.6645	11.5774
112	0.0571	7.0423	0.7903	9.9141	133	0.0235	6.9086	0.6592	11.6608
113	0.0547	7.0345	0.7829	9.9971	134	0.0225	6.9036	0.6541	11.7442
114	0.0524	7.0269	0.7756	10.0801	135	0.0216	6.8987	0.6490	11.8276
115	0.0503	7.0195	0.7685	10.1632	136	0.0207	6.8939	0.6440	11.9110
116	0.0482	7.0122	0.7615	10.2462	137	0.0198	6.8892	0.6391	11.9945
117	0.0462	7.0050	0.7546	10.3293	138	0.0190	6.8845	0.6342	12.0780
118	0.0443	6.9980	0.7478	10.4123	139	0.0182	6.8800	0.6294	12.1615
119	0.0424	6.9911	0.7412	10.4954	140	0.0174	6.8756	0.6247	12.2451
120	0.0407	6.9844	0.7346	10.5785	141	0.0167	6.8713	0.6201	12.3287
121	0.0390	6.9778	0.7282	10.6617	142	0.0160	6.8670	0.6156	12.4123
122	0.0374	6.9714	0.7219	10.7448	143	0.0154	6.8628	0.6111	12.4959
123	0.0358	6.9651	0.7157	10.8280	144	0.0147	6.8588	0.6067	12.5795
124	0.0343	6.9589	0.7096	10.9112	145	0.0141	6.8548	0.6023	12.6632
125	0.0329	6.9528	0.7036	10.9944	146	0.0135	6.8509	0.5980	12.7469
126	0.0316	6.9469	0.6978	11.0776	147	0.0130	6.8471	0.5938	12.8306
127	0.0302	6.9411	0.6920	11.1608	148	0.0124	6.8433	0.5896	12.9144
128	0.0290	6.9354	0.6863	11.2441	149	0.0119	6.8396	0.5855	12.9982
129	0.0278	6.9298	0.6807	11.3274	150	0.0114	6.8361	0.5814	13.0820

Notes: Calculation of W/H has an error of less than 1%.

Source: Gupta, K.C., Garg, R., Bahl, I., Bhartia, P., *Microstrip Lines and Slotlines,* 2nd Ed., Artech House, Norwood, MA, 1996, 103.

TABLE 12h Zero Thickness Microstrip Dimensions, Effective Dielectric Constant, and PUL Capacitance and Inductance for Er =12.88

Zo [Ohms]	W/h	Keff	pF/cm	nH/mm	Zo [Ohms]	W/h	Keff	pF/cm	nH/mm
1	102.3159	12.5596	118.2135	0.1182	24	2.7402	9.5011	4.2841	2.4676
2	50.0315	12.2746	58.4323	0.2337	25	2.5791	9.4384	4.0991	2.5619
3	32.6633	12.0197	38.5483	0.3469	26	2.4309	9.3779	3.9288	2.6559
4	24.0084	11.7903	28.6339	0.4581	27	2.2942	9.3197	3.7715	2.7494
5	18.8329	11.5823	22.7043	0.5676	28	2.1677	9.2635	3.6258	2.8427
6	15.3941	11.3928	18.7648	0.6755	29	2.0503	9.2091	3.4905	2.9355
7	12.9460	11.2191	15.9610	0.7821	30	1.9316	9.1518	3.3637	3.0273
8	11.1161	11.0591	13.8660	0.8874	31	1.8324	9.1020	3.2463	3.1197
9	9.6977	10.9111	12.2425	0.9916	32	1.7397	9.0536	3.1365	3.2117
10	8.5668	10.7736	10.9487	1.0949	33	1.6528	9.0068	3.0335	3.3035
11	7.6446	10.6455	9.8939	1.1972	34	1.5714	8.9612	2.9369	3.3950
12	6.8787	10.5255	9.0182	1.2986	35	1.4948	8.9170	2.8459	3.4862
13	6.2329	10.4130	8.2799	1.3993	36	1.4228	8.8739	2.7602	3.5772
14	5.6812	10.3071	7.6492	1.4993	37	1.3549	8.8320	2.6792	3.6678
15	5.2048	10.2071	7.1046	1.5985	38	1.2908	8.7911	2.6027	3.7582
16	4.7893	10.1125	6.6296	1.6972	39	1.2302	8.7513	2.5302	3.8484
17	4.4239	10.0228	6.2119	1.7952	40	1.1729	8.7125	2.4614	3.9383
18	4.1003	9.9376	5.8418	1.8927	41	1.1186	8.6745	2.3962	4.0280
19	3.8117	9.8565	5.5117	1.9897	42	1.0672	8.6375	2.3341	4.1174
20	3.5529	9.7791	5.2155	2.0862	43	1.0184	8.6014	2.2751	4.2066
21	3.3196	9.7051	4.9483	2.1822	44	0.9721	8.5791	2.2205	4.2989
22	3.1082	9.6342	4.7061	2.2778	45	0.9281	8.5645	2.1693	4.3928
23	2.9159	9.5663	4.4856	2.3729	46	0.8863	8.5487	2.1202	4.4863
47	0.8465	8.5321	2.0731	4.5794	99	0.0845	7.6726	0.9333	9.1471
48	0.8086	8.5147	2.0278	4.6720	100	0.0808	7.6620	0.9233	9.2331
49	0.7726	8.4967	1.9843	4.7643	101	0.0774	7.6516	0.9136	9.3192
50	0.7383	8.4781	1.9425	4.8562	102	0.0740	7.6415	0.9040	9.4052
51	0.7056	8.4591	1.9023	4.9478	103	0.0709	7.6315	0.8946	9.4912
52	0.6744	8.4397	1.8635	5.0390	104	0.0678	7.6218	0.8855	9.5773
53	0.6447	8.4201	1.8263	5.1299	105	0.0649	7.6123	0.8765	9.6633
54	0.6163	8.4002	1.7903	5.2206	106	0.0621	7.6030	0.8677	9.7494
55	0.5893	8.3802	1.7557	5.3109	107	0.0595	7.5938	0.8591	9.8354
56	0.5634	8.3601	1.7223	5.4010	108	0.0569	7.5849	0.8506	9.9215
57	0.5388	8.3399	1.6900	5.4908	109	0.0545	7.5761	0.8423	10.0076
58	0.5152	8.3198	1.6588	5.5804	110	0.0521	7.5675	0.8342	10.0937
59	0.4928	8.2996	1.6288	5.6697	111	0.0499	7.5592	0.8262	10.1798
60	0.4713	8.2796	1.5997	5.7588	112	0.0477	7.5509	0.8184	10.2659
61	0.4508	8.2596	1.5716	5.8477	113	0.0457	7.5429	0.8107	10.3521
62	0.4312	8.2397	1.5443	5.9365	114	0.0437	7.5350	0.8032	10.4382
63	0.4125	8.2200	1.5180	6.0250	115	0.0418	7.5273	0.7958	10.5244
64	0.3946	8.2005	1.4925	6.1133	116	0.0400	7.5198	0.7885	10.6106
65	0.3775	8.1811	1.4678	6.2015	117	0.0383	7.5124	0.7814	10.6968
66	0.3611	8.1619	1.4439	6.2895	118	0.0367	7.5052	0.7744	10.7830
67	0.3455	8.1429	1.4207	6.3774	119	0.0351	7.4981	0.7676	10.8693
68	0.3306	8.1242	1.3982	6.4652	120	0.0336	7.4912	0.7608	10.9556
69	0.3163	8.1057	1.3763	6.5528	121	0.0321	7.4844	0.7542	11.0419
70	0.3026	8.0874	1.3551	6.6402	122	0.0308	7.4778	0.7477	11.1282
71	0.2895	8.0694	1.3346	6.7276	123	0.0294	7.4713	0.7413	11.2146
72	0.2770	8.0517	1.3146	6.8148	124	0.0282	7.4649	0.7350	11.3009
73	0.2651	8.0342	1.2952	6.9020	125	0.0270	7.4587	0.7288	11.3873
74	0.2536	8.0169	1.2763	6.9890	126	0.0258	7.4526	0.7227	11.4737
75	0.2427	8.0000	1.2579	7.0759	127	0.0247	7.4467	0.7167	11.5602
76	0.2323	7.9833	1.2401	7.1628	128	0.0236	7.4409	0.7109	11.6466
77	0.2222	7.9669	1.2227	7.2496	129	0.0226	7.4352	0.7051	11.7331
78	0.2127	7.9507	1.2058	7.3363	130	0.0217	7.4296	0.6994	11.8197
79	0.2035	7.9348	1.1894	7.4229	131	0.0207	7.4241	0.6938	11.9062

TABLE 12h (continued) Zero Thickness Microstrip Dimensions, Effective Dielectric Constant, and PUL Capacitance and Inductance for Er =12.88

Zo [Ohms]	W/h	Keff	pF/cm	nH/mm	Zo [Ohms]	W/h	Keff	pF/cm	nH/mm
80	0.1947	7.9192	1.1734	7.5095	132	0.0198	7.4188	0.6883	11.9928
81	0.1864	7.9039	1.1578	7.5960	133	0.0190	7.4136	0.6829	12.0794
82	0.1783	7.8889	1.1425	7.6825	134	0.0182	7.4085	0.6775	12.1660
83	0.1707	7.8741	1.1277	7.7689	135	0.0174	7.4035	0.6723	12.2527
84	0.1633	7.8596	1.1133	7.8552	136	0.0166	7.3986	0.6671	12.3393
85	0.1563	7.8453	1.0992	7.9415	137	0.0159	7.3938	0.6621	12.4261
86	0.1496	7.8314	1.0854	8.0278	138	0.0152	7.3891	0.6570	12.5128
87	0.1431	7.8176	1.0720	8.1140	139	0.0146	7.3845	0.6521	12.5996
88	0.1370	7.8042	1.0589	8.2002	140	0.0140	7.3800	0.6473	12.6863
89	0.1311	7.7910	1.0461	8.2864	141	0.0134	7.3756	0.6425	12.7732
90	0.1255	7.7781	1.0336	8.3725	142	0.0128	7.3713	0.6378	12.8600
91	0.1201	7.7654	1.0215	8.4587	143	0.0122	7.3671	0.6331	12.9469
92	0.1149	7.7529	1.0095	8.5448	144	0.0117	7.3630	0.6286	13.0338
93	0.1100	7.7407	0.9979	8.6309	145	0.0112	7.3590	0.6241	13.1207
94	0.1052	7.7288	0.9865	8.7169	146	0.0107	7.3551	0.6196	13.2077
95	0.1007	7.7171	0.9754	8.8030	147	0.0103	7.3512	0.6152	13.2946
96	0.0964	7.7056	0.9645	8.8890	148	0.0098	7.3475	0.6109	13.3817
97	0.0922	7.6944	0.9539	8.9751	149	0.0094	7.3438	0.6067	13.4687
98	0.0883	7.6833	0.9435	9.0611	150	0.0090	7.3402	0.6025	13.5558

Notes: Calculation of W/H has an error of less than 1%.

Source: Gupta, K.C., Garg, R., Bahl, I., Bhartia, P., *Microstrip Lines and Slotlines,* 2nd Ed., Artech House, Norwood, MA, 1996, 103.

TABLE 12i Zero Thickness Microstrip Dimensions, Effective Dielectric Constant, and PUL Capacitance and Inductance for Er =35

Zo [Ohms]	W/h	Keff	pF/cm	nH/mm	Zo [Ohms]	W/h	Keff	pF/cm	nH/mm
1	61.2525	33.5453	193.1947	0.1932	57	0.1141	20.3209	2.6380	8.5709
2	29.6179	32.3412	94.8478	0.3794	58	0.1063	20.2652	2.5890	8.7093
3	19.1302	31.3265	62.2321	0.5601	59	0.0990	20.2113	2.5417	8.8477
4	13.9141	30.4569	46.0216	0.7363	60	0.0923	20.1591	2.4961	8.9860
5	10.8011	29.7005	36.3573	0.9089	61	0.0860	20.1087	2.4521	9.1243
6	8.7367	29.0345	29.9561	1.0784	62	0.0801	20.0598	2.4096	9.2626
7	7.2699	28.4417	25.4132	1.2452	63	0.0746	20.0126	2.3686	9.4010
8	6.1757	27.9094	22.0275	1.4098	64	0.0695	19.9670	2.3289	9.5393
9	5.3291	27.4273	19.4101	1.5722	65	0.0648	19.9228	2.2906	9.6776
10	4.6555	26.9878	17.3286	1.7329	66	0.0604	19.8801	2.2534	9.8160
11	4.1073	26.5845	15.6351	1.8918	67	0.0562	19.8389	2.2175	9.9543
12	3.6529	26.2124	14.2315	2.0493	68	0.0524	19.7990	2.1827	10.0928
13	3.2705	25.8674	13.0501	2.2055	69	0.0488	19.7604	2.1490	10.2312
14	2.9445	25.5460	12.0424	2.3603	70	0.0455	19.7232	2.1163	10.3697
15	2.6635	25.2453	11.1732	2.5140	71	0.0424	19.6872	2.0846	10.5082
16	2.4189	24.9629	10.4161	2.6665	72	0.0395	19.6525	2.0538	10.6468
17	2.2042	24.6968	9.7510	2.8180	73	0.0368	19.6189	2.0239	10.7855
18	2.0144	24.4452	9.1623	2.9686	74	0.0343	19.5865	1.9949	10.9242
19	1.8358	24.1924	8.6351	3.1173	75	0.0319	19.5551	1.9667	11.0630
20	1.6891	23.9716	8.1658	3.2663	76	0.0298	19.5249	1.9394	11.2018
21	1.5569	23.7610	7.7427	3.4145	77	0.0277	19.4957	1.9127	11.3407
22	1.4372	23.5597	7.3594	3.5619	78	0.0258	19.4674	1.8869	11.4796
23	1.3284	23.3669	7.0106	3.7086	79	0.0241	19.4402	1.8617	11.6187
24	1.2292	23.1820	6.6918	3.8545	80	0.0224	19.4139	1.8372	11.7578
25	1.1385	23.0043	6.3995	3.9997	81	0.0209	19.3884	1.8133	11.8970

TABLE 12i (continued) Zero Thickness Microstrip Dimensions, Effective Dielectric Constant, and PUL Capacitance and Inductance for Er =35

Zo [Ohms]	W/h	Keff	pF/cm	nH/mm	Zo [Ohms]	W/h	Keff	pF/cm	nH/mm
26	1.0554	22.8334	6.1304	4.1442	82	0.0195	19.3639	1.7900	12.0362
27	0.9790	22.6972	5.8857	4.2907	83	0.0181	19.3402	1.7674	12.1755
28	0.9087	22.6289	5.6670	4.4429	84	0.0169	19.3173	1.7453	12.3149
29	0.8438	22.5532	5.4624	4.5939	85	0.0157	19.2952	1.7238	12.4544
30	0.7840	22.4719	5.2708	4.7437	86	0.0147	19.2739	1.7028	12.5940
31	0.7286	22.3863	5.0911	4.8925	87	0.0137	19.2533	1.6823	12.7336
32	0.6774	22.2977	4.9222	5.0403	88	0.0127	19.2334	1.6624	12.8733
33	0.6300	22.2069	4.7633	5.1873	89	0.0119	19.2142	1.6429	13.0131
34	0.5861	22.1148	4.6136	5.3333	90	0.0111	19.1957	1.6238	13.1530
35	0.5453	22.0220	4.4724	5.4787	91	0.0103	19.1778	1.6052	13.2929
36	0.5074	21.9291	4.3390	5.6233	92	0.0096	19.1605	1.5871	13.4329
37	0.4723	21.8365	4.2128	5.7673	93	0.0089	19.1439	1.5693	13.5730
38	0.4397	21.7445	4.0933	5.9107	94	0.0083	19.1278	1.5520	13.7132
39	0.4093	21.6536	3.9800	6.0535	95	0.0078	19.1122	1.5350	13.8535
40	0.3811	21.5638	3.8724	6.1959	96	0.0072	19.0972	1.5184	13.9938
41	0.3549	21.4755	3.7702	6.3378	97	0.0067	19.0828	1.5022	14.1342
42	0.3305	21.3889	3.6730	6.4792	98	0.0063	19.0688	1.4863	14.2747
43	0.3078	21.3039	3.5805	6.6203	99	0.0059	19.0553	1.4708	14.4152
44	0.2867	21.2208	3.4923	6.7610	100	0.0055	19.0422	1.4556	14.5559
45	0.2670	21.1396	3.4081	6.9014	101	0.0051	19.0297	1.4407	14.6966
46	0.2487	21.0603	3.3278	7.0416	102	0.0047	19.0175	1.4261	14.8374
47	0.2317	20.9831	3.2510	7.1814	103	0.0044	19.0058	1.4118	14.9782
48	0.2158	20.9078	3.1776	7.3211	104	0.0041	18.9945	1.3978	15.1191
49	0.2010	20.8346	3.1073	7.4605	105	0.0038	18.9836	1.3841	15.2601
50	0.1873	20.7635	3.0399	7.5998	106	0.0036	18.9730	1.3707	15.4012
51	0.1745	20.6944	2.9753	7.7388	107	0.0033	18.9629	1.3575	15.5423
52	0.1625	20.6272	2.9134	7.8778	108	0.0031	18.9530	1.3446	15.6835
53	0.1514	20.5621	2.8539	8.0166	109	0.0029	18.9436	1.3319	15.8247
54	0.1411	20.4989	2.7967	8.1553	110	0.0027	18.9344	1.3195	15.9661
55	0.1314	20.4377	2.7418	8.2939	111	0.0025	18.9256	1.3073	16.1074
56	0.1224	20.3784	2.6889	8.4324	112	0.0023	18.9170	1.2954	16.2489
113	0.0022	18.9088	1.2836	16.3904	132	0.0006	18.7969	1.0956	19.0896
114	0.0020	18.9009	1.2721	16.5320	133	0.0005	18.7928	1.0872	19.2321
115	0.0019	18.8932	1.2608	16.6736	134	0.0005	18.7889	1.0790	19.3747
116	0.0018	18.8858	1.2497	16.8153	135	0.0005	18.7851	1.0709	19.5173
117	0.0016	18.8786	1.2387	16.9571	136	0.0004	18.7815	1.0629	19.6600
118	0.0015	18.8717	1.2280	17.0989	137	0.0004	18.7779	1.0551	19.8027
119	0.0014	18.8651	1.2175	17.2407	138	0.0004	18.7745	1.0473	19.9454
120	0.0013	18.8587	1.2071	17.3826	139	0.0003	18.7713	1.0397	20.0882
121	0.0012	18.8524	1.1970	17.5246	140	0.0003	18.7681	1.0322	20.2310
122	0.0012	18.8465	1.1870	17.6666	141	0.0003	18.7650	1.0248	20.3738
123	0.0011	18.8407	1.1771	17.8087	142	0.0003	18.7621	1.0175	20.5167
124	0.0010	18.8351	1.1675	17.9508	143	0.0003	18.7592	1.0103	20.6596
125	0.0009	18.8297	1.1580	18.0930	144	0.0002	18.7565	1.0032	20.8026
126	0.0009	18.8245	1.1486	18.2352	145	0.0002	18.7538	0.9962	20.9456
127	0.0008	18.8195	1.1394	18.3775	146	0.0002	18.7513	0.9893	21.0886
128	0.0008	18.8146	1.1304	18.5198	147	0.0002	18.7488	0.9825	21.2316
129	0.0007	18.8100	1.1215	18.6622	148	0.0002	18.7464	0.9758	21.3747
130	0.0007	18.8055	1.1127	18.8046	149	0.0002	18.7441	0.9692	21.5178
131	0.0006	18.8011	1.1041	18.9471	150	0.0002	18.7419	0.9627	21.6609

Notes: Calculation of W/H has an error of less than 1%.

Source: Gupta, K.C., Garg, R., Bahl, I., Bhartia, P., *Microstrip Lines and Slotlines,* 2nd Ed., Artech House, Norwood, MA, 1996, 103.

TABLE 12j Zero Thickness Microstrip Dimensions, Effective Dielectric Constant, and PUL Capacitance and Inductance for Er =85

Zo [Ohms]	W/h	Keff	pF/cm	nH/mm	Zo [Ohms]	W/h	Keff	pF/cm	nH/mm
1	38.5925	79.6824	297.7560	0.2978	26	0.3739	51.7462	9.2288	6.2387
2	18.3705	75.6651	145.0765	0.5803	27	0.3349	51.4124	8.8583	6.4577
3	11.6859	72.5009	94.6738	0.8521	28	0.3000	51.0886	8.5150	6.6757
4	8.3710	69.9235	69.7318	1.1157	29	0.2688	50.7757	8.1961	6.8930
5	6.3982	67.7680	54.9189	1.3730	30	0.2409	50.4745	7.8994	7.1095
6	5.0937	65.9270	45.1398	1.6250	31	0.2159	50.1850	7.6226	7.3253
7	4.1695	64.3277	38.2191	1.8727	32	0.1935	49.9076	7.3640	7.5407
8	3.4821	62.9184	33.0733	2.1167	33	0.1734	49.6422	7.1218	7.7557
9	2.9517	61.6613	29.1034	2.3574	34	0.1554	49.3886	6.8947	7.9702
10	2.5309	60.5285	25.9513	2.5951	35	0.1393	49.1467	6.6813	8.1845
11	2.1895	59.4981	23.3904	2.8302	36	0.1249	48.9161	6.4804	8.3986
12	1.8946	58.5089	21.2622	3.0618	37	0.1119	48.6966	6.2911	8.6125
13	1.6651	57.6611	19.4840	3.2928	38	0.1003	48.4877	6.1124	8.8263
14	1.4696	56.8730	17.9682	3.5218	39	0.0899	48.2891	5.9435	9.0400
15	1.3012	56.1365	16.6614	3.7488	40	0.0806	48.1003	5.7835	9.2537
16	1.1551	55.4455	15.5236	3.9740	41	0.0723	47.9210	5.6319	9.4673
17	1.0274	54.7949	14.5245	4.1976	42	0.0648	47.7509	5.4881	9.6810
18	0.9153	54.4535	13.6748	4.4306	43	0.0581	47.5893	5.3514	9.8947
19	0.8165	54.1607	12.9202	4.6642	44	0.0521	47.4361	5.2213	10.1085
20	0.7290	53.8383	12.2376	4.8950	45	0.0467	47.2907	5.0975	10.3224
21	0.6514	53.4976	11.6179	5.1235	46	0.0418	47.1529	4.9794	10.5364
22	0.5825	53.1467	11.0534	5.3498	47	0.0375	47.0222	4.8667	10.7505
23	0.5211	52.7921	10.5375	5.5743	48	0.0336	46.8984	4.7590	10.9648
24	0.4664	52.4383	10.0645	5.7972	49	0.0301	46.7810	4.6561	11.1792
25	0.4176	52.0888	9.6297	6.0185	50	0.0270	46.6697	4.5575	11.3938
51	0.0242	46.5643	4.4631	11.6085	101	0.0001	44.8028	2.2106	22.5503
52	0.0217	46.4644	4.3726	11.8234	102	0.0001	44.7963	2.1888	22.7720
53	0.0195	46.3698	4.2857	12.0385	103	0.0001	44.7901	2.1674	22.9936
54	0.0175	46.2801	4.2023	12.2538	104	0.0001	44.7842	2.1464	23.2153
55	0.0156	46.1952	4.1221	12.4693	105	0.0001	44.7787	2.1258	23.4371
56	0.0140	46.1148	4.0449	12.6849	106	0.0001	44.7734	2.1056	23.6589
57	0.0126	46.0386	3.9707	12.9008	107	0.0001	44.7685	2.0858	23.8808
58	0.0113	45.9665	3.8992	13.1168	108	0.0000	44.7638	2.0664	24.1027
59	0.0101	45.8982	3.8302	13.3330	109	0.0000	44.7593	2.0474	24.3247
60	0.0091	45.8335	3.7637	13.5495	110	0.0000	44.7551	2.0287	24.5467
61	0.0081	45.7722	3.6996	13.7661	111	0.0000	44.7511	2.0103	24.7688
62	0.0073	45.7142	3.6376	13.9829	112	0.0000	44.7473	1.9923	24.9908
63	0.0065	45.6592	3.5777	14.1999	113	0.0000	44.7437	1.9745	25.2130
64	0.0059	45.6072	3.5198	14.4170	114	0.0000	44.7404	1.9572	25.4351
65	0.0052	45.5579	3.4638	14.6344	115	0.0000	44.7371	1.9401	25.6573
66	0.0047	45.5112	3.4095	14.8519	116	0.0000	44.7341	1.9233	25.8795
67	0.0042	45.4670	3.3570	15.0696	117	0.0000	44.7312	1.9068	26.1018
68	0.0038	45.4252	3.3061	15.2875	118	0.0000	44.7285	1.8906	26.3241
69	0.0034	45.3856	3.2568	15.5056	119	0.0000	44.7259	1.8746	26.5464
70	0.0030	45.3481	3.2089	15.7238	120	0.0000	44.7235	1.8589	26.7688
71	0.0027	45.3126	3.1625	15.9422	121	0.0000	44.7212	1.8435	26.9911
72	0.0024	45.2789	3.1174	16.1607	122	0.0000	44.7190	1.8284	27.2135
73	0.0022	45.2471	3.0736	16.3794	123	0.0000	44.7169	1.8135	27.4360
74	0.0020	45.2169	3.0311	16.5982	124	0.0000	44.7149	1.7988	27.6584
75	0.0018	45.1884	2.9897	16.8172	125	0.0000	44.7131	1.7844	27.8809
76	0.0016	45.1614	2.9495	17.0363	126	0.0000	44.7113	1.7702	28.1034
77	0.0014	45.1358	2.9104	17.2556	127	0.0000	44.7097	1.7562	28.3259
78	0.0013	45.1115	2.8723	17.4750	128	0.0000	44.7081	1.7425	28.5484
79	0.0011	45.0886	2.8352	17.6946	129	0.0000	44.7066	1.7289	28.7710
80	0.0010	45.0669	2.7991	17.9142	130	0.0000	44.7052	1.7156	28.9936

TABLE 12j (continued) Zero Thickness Microstrip Dimensions, Effective Dielectric Constant, and PUL Capacitance and Inductance for Er =85

Zo [Ohms]	W/h	Keff	pF/cm	nH/mm	Zo [Ohms]	W/h	Keff	pF/cm	nH/mm
81	0.0009	45.0463	2.7639	18.1340	131	0.0000	44.7038	1.7025	29.2162
82	0.0008	45.0268	2.7296	18.3539	132	0.0000	44.7026	1.6896	29.4388
83	0.0007	45.0084	2.6962	18.5739	133	0.0000	44.7014	1.6768	29.6614
84	0.0007	44.9909	2.6636	18.7941	134	0.0000	44.7002	1.6643	29.8840
85	0.0006	44.9744	2.6317	19.0143	135	0.0000	44.6992	1.6519	30.1067
86	0.0005	44.9587	2.6007	19.2347	136	0.0000	44.6981	1.6398	30.3293
87	0.0005	44.9439	2.5704	19.4551	137	0.0000	44.6972	1.6278	30.5520
88	0.0004	44.9299	2.5408	19.6757	138	0.0000	44.6963	1.6160	30.7747
89	0.0004	44.9166	2.5118	19.8963	139	0.0000	44.6954	1.6043	30.9974
90	0.0003	44.9040	2.4836	20.1171	140	0.0000	44.6946	1.5929	31.2201
91	0.0003	44.8921	2.4560	20.3379	141	0.0000	44.6938	1.5816	31.4429
92	0.0003	44.8808	2.4290	20.5588	142	0.0000	44.6931	1.5704	31.6656
93	0.0002	44.8701	2.4026	20.7798	143	0.0000	44.6924	1.5594	31.8883
94	0.0002	44.8600	2.3767	21.0009	144	0.0000	44.6917	1.5486	32.1111
95	0.0002	44.8504	2.3515	21.2220	145	0.0000	44.6911	1.5379	32.3339
96	0.0002	44.8414	2.3267	21.4432	146	0.0000	44.6905	1.5273	32.5567
97	0.0002	44.8328	2.3025	21.6645	147	0.0000	44.6899	1.5169	32.7794
98	0.0001	44.8247	2.2788	21.8859	148	0.0000	44.6894	1.5067	33.0022
99	0.0001	44.8170	2.2556	22.1073	149	0.0000	44.6889	1.4966	33.2250
100	0.0001	44.8097	2.2329	22.3288	150	0.0000	44.6884	1.4866	33.4478

Notes: Calculation of W/H has an error of less than 1%.

Source: Gupta, K.C., Garg, R., Bahl, I., Bhartia, P., *Microstrip Lines and Slotlines,* 2nd Ed., Artech House, Norwood, MA, 1996, 103.

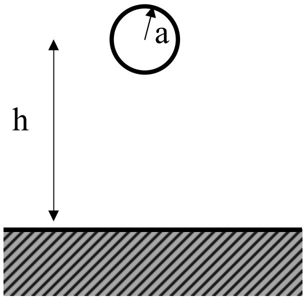

$$L_{WIREoverGND} = \frac{\mu_0 \mu_r}{2\pi} \cosh^{-1} \frac{h}{a} \quad \text{(nH/m)} \qquad \text{for } h >> a$$

FIGURE 5 Inductance of a wire over a ground plane. When consistent units are used for the wire radius, a, and the height over the ground plane, h, the formula provides an estimate of the inductance per unit length in (nH/m).

Bondwires, Ribbons, Mesh

The assembly of semiconductor and hybrid integrated circuits for microwave and millimeter-wave frequencies generally requires the use of gold bondwires, ribbons, or mesh. The impedance of the interconnection must be accounted for in a good design. Unfortunately, there is no single accepted electrical model. The complexity required of the model will depend on the frequency of operation and the general impedance levels of the circuits being connected. At low frequencies and moderate to high impedances, the connection is frequently modeled as an inductor (sometimes in series with a resistor); at high frequencies, a full 3-D electromagnetic simulation may be required for accurate results. At intermediate points it may be modeled as a high impedance transmission line or as a lumped LC circuit. Note that the resistances of the RF interconnects should be included in the design of extremely low-noise circuits as they will affect the noise figure. In connecting a semiconductor die to package leads, it may also be necessary to model the mutual inductances and interlead capacitances in addition to the usual self-inductances and shunt capacitance. Figure 5 illustrates one method of modeling bond wire inductance that has been shown adequate for many microwave applications. More sophisticated methods of modeling bond wires, ribbon or mesh are described in the references.

References

1. Grover, F.W., *Inductance Calculations*, Dover Publications, New York, Available through Instrument Society of America, Research Triangle Park, NC.
2. Caulton, M., Lumped Elements in Microwave Circuits, in *Advances in Microwaves 1974,* Academic Press, New York, 1974, 143–202.
3. Wadell, B. C., *Transmission Line Design Handbook,* Artech House, Boston, MA, 1991, 151–155.
4. Terman, F.E., *Radio Engineer's Handbook,* McGraw-Hill, New York, 1943, 48–51.
5. Caverly, R. H., Characteristic impedance of integrated circuit bond wires, *IEEE Transactions on Microwave Theory and Techniques,* MTT-34, 9, September 1986, 982–984.
6. Kuester, E. F., Chang, D. C., Propagating modes along a thin wire located above a grounded dielectric slab, *IEEE Transactions on Microwave Theory and Techniques,* MTT-25, 12, December 1977, 1065–1069.
7. Mondal, J. P., Octagonal spiral inductor measurement and modelling for MMIC applications, *Int. J. Electronics,* 1990, 68, 1, 113–125.
8. MIL-STD-883E, Test Method Standard, Microcircuits U.S. Department of Defense, Washington, D.C.